Proceedings of:

The Fifteenth Annual Meeting

The American Society for Precision Engineering

October 22-27, 2000
DoubleTree Paradise Valley Resort
Scottsdale, Arizona

The American Society for Precision Engineering (ASPE) is a multidisciplinary professional and technical society concerned with research and development, design, manufacture and measurement of high accuracy components and systems. ASPE activities encompass relevant aspects of mechanical, electronic, optical and production engineering, physics, chemistry, and computer and materials science. Membership is open to anyone interested in any aspect of precision engineering.

Founded in 1986, ASPE provides a new focus for a diverse but important community. Other professional organizations have covered aspects of precision engineering, always as a sideline to their principal goals. ASPE is based on the core of generic concepts necessary to achieve precision in any application; independent of discipline, ASPE intends to be the focus for precision technology — and to represent all facets from research to application.

ASPE — The American Society for Precision Engineering
301 Glenwood Avenue, Suite 205, Raleigh, NC 27603
P.O. Box 10826, Raleigh, NC 27605-0826
Phone (919) 839-8444 Fax (919) 839-8039

Preface

This book comprises the proceedings of the 2000 Annual Meeting. The contributions reflect the authors' opinions and are published as presented to ASPE, without change. Their inclusion in this publication does not necessarily constitute endorsement by the ASPE, or its editorial staff.

Individual readers of this book and nonprofit libraries acting for them are permitted to make fair use of the material contained in this book to be used in teaching or research; provided they copy said paper in total, as written by the author. Permission is granted to quote excerpts from the scientific or technical works in this book with proper acknowledgment of the source to include: The author's name, the book name, and the ASPE tag line. Reproduction of figures and tables is likewise permitted from the contents of this book, provided that the same acknowledgment of the same source and content is printed.

Any other type reproduction, systematic copying or multiple reproduction of any material in this book is expressly prohibited except with the written permission of the ASPE editorial staff, addressed to the Society's headquarters.

ISBN 1-887706-24-0

2000

American Society for Precision Engineering
301 Glenwood Avenue, Suite 205
Raleigh, NC 27603

Printed in the United States of America

Welcome Note

The American Society for Precision Engineering celebrates its Fifteenth Annual Meeting this year in Scottsdale, Arizona. The remarkable growth and success of the Society is reflective of the increasing importance of precision engineering in a wide variety of fields of endeavor, from manufacturing to microelectronics to basic science. The Society serves as a focus for precision engineers across all of these fields. The Annual Meeting has evolved into a premier international forum for the exchange of ideas and presentation of research results relating to precision engineering, metrology, controls, and system integration. Precision engineers and scientists from private industry, government laboratories, and universities meet to learn about the latest developments and to exchange ideas about the future directions of these technologies.

This year's meeting continues the tradition of offering two full days of tutorials presented by some of the foremost precision engineers and scientists in the world. Many participants cite the tutorial program as one of the most valuable features of the meeting. The technical sessions and poster presentations offer the latest research results in the areas of ultraprecision machining, metrology, controls, precision grinding, micro-positioning, material processing, design, precision transducers, surface profilometry, machine tool metrology, and error compensation. The commercial exhibit will provide attendees with the opportunity to view and discuss the latest precision engineering equipment, products, and services that are commercially available. The open forum will give attendees the opportunity to express their opinions and pose questions for discussion by the group, enhancing the exchange of information.

The conference organizing committee is proud to present the program for the Fifteenth Annual Meeting of the ASPE. We welcome your participation.

Welcome to Scottsdale.

2000 ASPE Meeting Organizing Committee

Steven C. Fawcett – Chairman – Axsun Technologies, Inc.

Chris Arcona, Norton Company, Saint-Gobain Abrasives
Vivek G. Badami, Tropel Corporation
Debra Krulewich Born, Lawrence Livermore National Laboratory
John H. Bruning, Tropel Corporation
Jeffrey W. Carr, Lawrence Livermore National Laboratory
James F. Cuttino, University of North Carolina at Charlotte
Bradley N. Damazo, National Institute of Standards and Technology
David W. Davis, Precitech, Inc.
Thomas A. Dow, North Carolina State University
Helen E. Fawcett, Axsun Technologies, Inc.
Kenneth P. Garrard, North Carolina State University
Anthony E. Gee, Cranfield University
Andrew J. Hazelton, Nikon Research Corporation of America
Bradley H. Jared, Corning Inc.
Thomas R. Kurfess, Georgia Institute of Technology
Don A. Lucca, Oklahoma State University
Steven J. Ludwick, Aerotech, Inc.
Don L. Martin, Lion Precision
Michele H. Miller, Michigan Technological University
Yoshiharu Namba, Chubu University
Steven M. Scott, Reflexite Precision Technology Centre
Alexander H. Slocum, Massachusetts Institute of Technology
Marianna Slocum, Department of Defense
Alex Sohn, North Carolina State University
Irving F. Stowers, Lawrence Livermore National Laboratory
Hooman Tajbakhsh, ETEC Systems, Inc.
E. Clayton Teague, National Institute for Standards and Technology
Daniel C. Thompson, Production Technology, Inc.
David L. Trumper, Massachusetts Institute of Technology
R. Ryan Vallance, University of Kentucky
Andrew D. Woodfin, University of North Carolina at Charlotte
David H. Youden, Eastman Kodak Company

2000 Scholarship Recipients

Andrew D. Woodfin, University of North Carolina at Charlotte
R.V. Jones Memorial Scholarship

Nagasubramaniyan Chandrasekaran, Oklahoma State University
David W. Hamby, Oklahoma State University
Vincent C. Vigliano, The Pennsylvania State University

2000 Annual Meeting

Contents

Preface . . . . . *ii*

Welcome Note . . . . . *iii*

Organizing Committee — 2000 Scholarship Recipients . . . . . *iv*

Sponsor Members . . . . . *vi*

Cooperating Sponsors—Technical Exhibitors . . . . . *vii*

Program . . . . . *viii*

Keynote Speaker . . . . . *ix*

2000 Lifetime Achievement Award . . . . . *x*

Executive Forum/Commercial Session/Open Forum *1*

Technical Paper Index *2-12*

Technical Papers *15-607*

Authors Index *609-612*

Sponsor Members of the ASPE

3M Company
St. Paul, MN 55144-1000
Contact: William J. Bryan
(651) 575-1465

ADCOLE Corporation
Marlborough, MA 01752
Contact: Addison D. Cole
(508) 485-9100

ADE Technologies, Inc.
Auburndale, MA 02466
Contact: Jon Allen
(617) 831-8012

Agilent Technologies
Santa Rosa, CA 95403
Contact: Paul Lomeli
(707) 577-5514

Brown & Sharpe
North Kingstown, RI 02852
Contact: David H. Genest
(401) 886-2358

Chardon Tool & Supply Company, Inc.
Chardon, OH 44024
Contact: Weldon Bennett
(440) 286-6440

Contour Fine Tooling, Inc.
Marlborough, NH 03455
Contact: Jeffrey Tomlin
(603) 876-4908

Corning Inc.
Science & Technology Division
Corning, NY 14831
Contact: Dan E. Luttrell
(607) 974-3393

Cranfield Precision, Div. of Landis Lund
A Western Atlas Corporation
Cranfield, Bedford MK43 OAL, England
Contact: Edric M. E. Brown
011-44-1234-754222

DAC International, Inc.
Carpinteria, CA 93013
(805) 684-8307
Contact: James W. Drain

Dover Instrument Corporation
Westboro, MA 01581
Contact: Philip M. Greene
(508) 366-1456

Fabreeka International, Inc.
Stoughton, MA 02072
Contact: Robert P. Haley
(781) 341-3655

Fisba Optik, LLC
Rochester, NY 14620
Contact: John J. Nemechek
(716) 473-3990

Lawrence Livermore National Laboratory
Livermore, CA 94550
Contact: Robert Burleson
(925) 423-1967

Lion Precision
St. Paul, MN 55126
Contact: Don L. Martin
(651) 484-6544

Mahr Federal, Inc.
Providence, RI 02940
Contact: Robert A. Frick
(401) 784-3313

MicroE Systems, Inc.
Natick, MA 01760
Contact: Donald K. Mitchell
(508) 903-5000

Moore Tool Company, Inc.
Bridgeport, CT 06607
Contact: Thomas L. Hannon
(203) 366-3224

Nano Corporation
Tokyo 146-0085, Japan
011-81-3-3751-3311
Contact: Akira Hayashi

New Way Machine Components
Aston, PA 19014
Contact: Andrew J. Devitt
(610) 494-6700

Precitech, Inc.
Keene, NH 03431
Contact: David W. Davis
(603) 357-2511

Professional Instruments Company
Hopkins, MN 55343
Contact: James Arneson
(952) 933-1222

Reflexite-Precision Technology Center
West Henrietta, NY 14586
Contact: Steven M. Scott
(716) 272-0309

Seagate Technology
Scotts Valley, CA 95067
Contact: Bernd M. Seeger
(831) 439-3781

Tropel Corporation
60 O'Connor Road
Fairport, NY 14450
Contact: John H. Bruning
(716) 388-3400

Zygo Corporation
Middlefield, CT 06455
Contact: Robert A. Smythe
(860) 347-5101

Cooperating Sponsors

Elsevier Science, Inc.
euspen – European Society for Precision Engineering and Nanotechnology
Japan Society for Precision Engineering

Technical Exhibitors

ADE Phase Shift
ADE Technologies
A. G. Davis / AA Gage
Bal-tec
Center for Precision Metrology—University of North Carolina at Charlotte
Chardon Tool
Contour Fine Tooling, Inc.
CoorsTek
Digital Instruments, Veeco Metrology Group
Dover Instrument Corporation
Fabreeka International, Inc.
Heidenhain Corporation
Herzan Industries
K & Y Diamond, Ltd.
Lion Precision
Machine Dynamics Research Lab.—Penn State University
Mahr Federal
Metrology Perspectives Group, LLC
Minus K Technology, Inc.
Moore Nanotechnology Systems LLC
New Way Machine Components, Inc.
Precision Engineering Center—North Carolina State University
Precitech, Inc.
Professional Instruments Company, Inc.
SDL Queensgate, Ltd.
SNU Precision Company, Ltd.
Techmetals, Inc.
Tropel Corporation
Veeco Metrology Group
Zygo Corporation

Program

2000 ASPE Annual Meeting

Time	Sun., Oct. 22	Mon., Oct. 23	Tues., Oct. 24	Wed., Oct. 25	Thurs., Oct. 26	Fri., Oct. 27
8:00	Registration		Registration and Continental Breakfast			
9:00	Tutorials	Tutorials + Executive Forum	Session I Novel Systems	Session III Lithography	Session VI Micro/Mezo	Technical Tours
10:00	Break	Break				
11:00	Tutorials	Tutorials + Executive Forum	Break			
12:00			Session II Surface Metrol.- Forms	Session IV CMM Metrology	Session VII Precision Fab. II - Fluidics	
1:00			Lunch and Committee Meetings	Awards Lunch and Business Meeting	Lunch and Roundtable Discussions	
2:00	Tutorials	Tutorials + Executive Forum	Commercial Session	Poster Paper Session	Session VIII Precision Fab III - Cutting	
3:00	Break	Break				
4:00	Tutorials	Tutorials + Executive Forum	Break			
5:00			Poster Paper Session	Session V Precision Fab. I - Manufacturing	Open Forum	
6:00			Hospitality Hour	Hospitality Hour		
7:00	Student Reception	Keynote Address				
8:00		Welcome Reception	Open Evening	Dinner		
9:00						

Keynote Speaker

William L. Warren

Monday, October 23, 6:30 p.m.

Session Chair: Steven C. Fawcett, Axsun Technologies, Inc.

William L. Warren: Dr. Warren received his B.S. and Ph.D. degrees in Engineering Science from The Pennsylvania State University in 1986 and 1990, respectively. He is currently at the Defense Advanced Research Projects Agency as a program manager on Mesoscopic Machines, Mesoscale Integrated Conformal Electronics, Water and Air Purification, and Molecular Electronics programs. He has been a principal senior member of the technical staff in the electronic ceramics division at Sandia National Laboratories since 1990. He specializes in electronic component manufacturing, molecular electronics, water purification and desalination, and electronic characteristics and defect properties in electronic ceramics such as silicon dioxide, silicon nitride, buried oxides, phosphors, and ferroelectrics. Research projects involve the basic understanding of the operation and degradation of semiconductor and ferroelectric memories. He is the author of over 180 publications, the editor of three conference proceedings, has over 150 scientific presentations and has four patents issued on semiconductor memories and infra-red detectors. He is a recipient of the 1997 R&D 100 award for protonic memory devices, of the Industry Week 1997 Innovation and Technology Award, of the 1998 Discover Magazine Award, American Ceramic Society's Henry Award (1995), the Frank Fenlon Award at the Pennsylvania State University, the Xerox Materials Research Award (1986 & 1991), and the 1995 IEEE NSREC and HEART outstanding paper awards. He is a member of the Materials Research Society, American Ceramic Society, Electron Spin Resonance Society, Golden Key National Honor Society, and Sigma Xi. He has organized or co-organized five international conferences (MRS, EMRS, SSDM and IEEE SISC).

"Precision Manufacturing: Come On, Cut Me a 'Fine' Break"

The talk will be on precision manufacturing of mesoscale machines, precision manufacturing of tomorrow's electronics and precision manufacturing of "forgotten" electronics. We will provide numerous examples of how precision manufacturing is not only nice to have, but was absolutely necessary for energy-efficient and reliable machines. Such machines include vacuum pumps, blowers, micro-climate control devices and gyroscopes to name a few.

Next, we will march towards self-assembly and how this enables a new-era of cost-effective manufacturing for not only for next generation "Lilliputian" electronics, but also for manufacturing in the most general case. It is anticipated that hierarchical self-assembly processes may be the only way to bridge the chasm between the nano-world and the macro-world.

The last part of the talk will be on a new way to manufacture electronic components (resistors, capacitors, inductors, batteries, antennae) in a conformal way. The goal of this program is to direct-write functional materials on low-temperature substrates. This ability will open up a new opportunity to build electronics on the physical structure. Further out, we envisage this as an ability to fabricate living, or morphing machines.

2000 Lifetime Achievement Award

Robert J. Hocken

The 2000 ASPE Lifetime Achievement Award is presented to Professor Robert J. Hocken in recognition of his contributions to the art and science of precision engineering, and to the education and training of a new generation of precision engineers and metrologists.

Bob Hocken earned B. A. degrees in both physics and mathematics from Oregon State University and M. A. and Ph. D. degrees in physics from the State University of New York at Stony Brook. His doctoral work, completed in 1973, included an early application of heterodyne laser interferometry in precision metrology – in particular to the measurement of the refractive index of xenon near its liquid-gas phase transition. During 1974-75, Bob continued his work in experimental critical point thermodynamics as an NBS-NRC Postdoctoral Fellow in the Heat Division of the National Bureau of Standards (since 1988, the National Institute of Standards and Technology – NIST). In 1975 he joined the permanent staff of NBS as a physicist in the Dimensional Technology Section. Over the next dozen years or so, Bob assumed positions of increasing technical leadership and responsibility, becoming a Group Leader in Dimensional Metrology, Chief of the Automated Production Technology Division, and finally Chief of the Precision Engineering Division.

During his years at NIST, Bob earned an international reputation for technical excellence through his pioneering work in error modeling, error mapping, and software correction of coordinate measuring machines (CMMs) and machine tools, the large-scale metrology of liquid natural gas container ships, and the applications of stabilized lasers to problems of high-accuracy metrology. In the latter area, Bob lead the design and construction of a precise polarimeter for measurements of sugar concentration, an interferometer for measuring long-term dimensional stability of beryllium, and the original tracking interferometer system (now commercially available as the laser tracker). In addition to his technical work and administrative duties at NIST, Bob played a leadership role in the development of the widely used ASME/ANSI B89.4 performance evaluation standard for CMMs. He later made significant contributions towards writing the ASME/ANSI B5.54 and B5.57M standards for the performance evaluation of CNC machining centers, turning centers, and lathes.

In 1989 Bob left NIST and assumed the Norvin Kennedy Dickerson, Jr., Distinguished Professorship of Precision Engineering in the Department of Mechanical Engineering and Engineering Science at the University of North Carolina at Charlotte. He catalyzed the creation, and serves as Director, of the UNCC Center for Precision Metrology which is a widely recognized center of excellence for state-of-the-art graduate studies and research in areas of design, manufacturing, processes, and controls relating to precision metrology. Bob recruited an excellent faculty of recognized experts in their respective areas of precision engineering. He also created an Industrial Affiliates Program whose members fund student research on generic core problems in manufacturing metrology. In 1998 the Center was funded by the National Science Foundation and designated as an Industry/University Cooperative Research Center, charged with advancing precision metrology in areas of significant industrial relevance. Graduates of the Center for Precision Metrology are currently applying their skills at many of the country's leading companies in precision manufacturing and metrology.

Bob Hocken is a Charter Member of ASPE, has served on numerous ASPE committees and has been twice elected to the Board of Directors. In addition, he has served the Society for many years by teaching a very successful series of popular tutorials at our Annual Meetings. Bob is an Active Member of the International Institution for Production Engineering Research (CIRP), a member of the American Physical Society, a Senior Member and Fellow of the Society for Manufacturing Engineers, and a member of the American Society for Mechanical Engineers. Among his many honors and awards are Gold and Silver Medals from the U. S. Department of Commerce, the F. W. Taylor International Research Award from SME, and the F. W. Taylor Medal from CIRP. Most recently, Bob was awarded the First Citizens Bank Scholars Medal from UNCC, the University's highest honor for scholarship and intellectual inquiry.

Executive Forum

Monday, October 23, 8:00 a.m. – 5:00 p.m.

Session Chair: John H. Bruning, Tropel Corporation

The ASPE Executive Forum will be conducted again this year on Monday, October 23, 2000, just prior to the start of the formal ASPE meeting and overlapping one day with the Tutorial Program. The session will be organized and chaired by John H. Bruning of Tropel Corporation. As in previous years, the program combines business and technology issues of contemporary interest to leaders and executives in the precision engineering community. The program will consist of a continental breakfast, morning and afternoon talks, a lunch break and ample time to network with speakers and peers. The morning will be an interactive session devoted primarily to business issues. The first of the morning speakers will discuss what characterizes an excellent company – from an investor's perspective. We are in the negotiation phase for a speaker to cover "the essentials of B2B (e-business) for small companies". Dr. Chris Evans of NIST will conclude the morning session with a discussion of the Department of Commerce's Advanced Technology Program including a number of interesting case studies.

Dr. Robert Hocken will lead off the more technical aspect of the session with a discussion of trends in micro and meso-scale manufacturing. Dr. Tallis Chang of the Jet Propulsion Laboratory will review NASA's future stellar interferometry mission designed to locate planetary systems outside of our solar system. Dr. S. V. Sreenivasan will describe new results and applications for "step-and-flash" lithography – a low cost lithography approach with ultrahigh resolution.

Corporate Sponsors of the ASPE are welcome to send one attendee to the Executive Forum free of charge. Additional participants from the same Corporate Sponsor or from other organizations will be charged a fee of $125.

Commercial Session

Tuesday, October 24, 2:00 – 3:30 p.m.

Session Chair: James F. Cuttino, University of North Carolina at Charlotte

The Commercial Session will take place early in the week on Tuesday afternoon. This is a special session where company representatives are invited to make brief presentations on new products associated with precision engineering. In this session, conference participants will have the opportunity to receive timely information on new technologies that have been commercialized into products and services. The presentations will contain details and technical specifications of current product offerings, as well as information on advances that can be expected in the near future.

Open Forum

Thursday, October 26, 4:00 – 5:30 p.m.

Session Co-Chairs: Keith Carlisle, Lawrence Livermore National Laboratory, and Thomas A. Dow, North Carolina State University

The Open Forum was created to encourage dissemination of new and significant results, as well as observations on precision engineering subjects. All interested conference participants can sign up at the Conference Registration Table for short, informal presentations.

Technical and Poster Paper Index

The technical program for the 2000 ASPE Annual Meeting contains 155 papers on precision engineering advances. Papers that lent themselves to significant verbal interaction, concise but important discoveries, or strongly visual or tactile subjects have been selected for the poster session. Authors will be present to discuss their work on Tuesday, October 24, from 4:00 to 5:30 p.m., and again on Wednesday, October 25, from 2:00 to 3:30 p.m.

Session I
Novel Systems

Tuesday, October 24, 2000, 8:30 a.m. - 10:15 a.m.

Session Co-Chairs: Steven C. Fawcett (Axsun Technologies, Inc.) and David H. Youden (Eastman Kodak Co.)

Welcome Remarks
S. C. Fawcett, Annual Meeting Chairman

1. **A Telecommunications Overview for Precision Engineers (Invited Paper)***
   D. E. Luttrell (Corning Incorporated) . . . . . page 15
2. **A Tactile Micro Gripper with Piezoelectric Actuator Based on Microsystem Technology**
   F. Qiao, H. Wurmus (Ilmenau Technical University) . . . . . page 16
3. **Wafer-Level Assembly of Hybrid Microsystems***
   B. J. Nelson, B. Vikramaditya, G. Yang, J. Gaines (University of Minnesota), and E. Enikov (University of Arizona) . . . . . page 20
4. **Instrument for Setting Radio Telescope Surfaces**
   D. H. Parker, J. M. Payne, J. W. Shelton, T. L. Weadon (The National Radio Astronomy Observatory) . . . . . page 21

Session II
Surface Metrology — Forms

Tuesday, October 24, 2000, 10:45 a.m. - 12:30 p.m.

Session Co-Chairs: Debra Krulewich Born (Lawrence Livermore National Laboratory), and Don L. Martin (Lion Precision)

1. **Recent Advances in Separation of Roughness, Waviness and Form (Invited Paper)**
   J. Raja, B. Muralikrishnan, S. Fu, X. Liu (University of North Carolina at Charlotte) . . . . . page 25
2. **Measurement of the Absolute Diameter of Cylindrical Gages by Grazing Incidence Interferometry**
   V. G. Badami, P. Venkataraman, A. W. Kulawiec, J. H. Bruning (Tropel Corporation) . . . . . page 31
3. **Development of 2D Angle Probe for Flatness Metrology of Large Silicon Wafer**
   W. Gao, S. Kiyono (Tohoku University), E. T. Kanai (University of Washington), and P. S. Huang (SUNY at Stony Brook) . . . . . page 35
4. **Optical Reference Profilometer with Improved Thermal Stability**
   S. R. Clark, J. E. Greivenkamp, R. M. Richard, J. M. Sasián (University of Arizona) . . . . . page 39

* *Extended abstract not available at press time*

Poster Session

Tuesday, October 24, 2000, 4:00 p.m. – 5:30 p.m. and Wednesday, October 25, 2000, 2:00 p.m. – 3:30 p.m.

Session Chair: Andrew D. Woodfin (University of North Carolina at Charlotte)

PROCESSES

Machining

1. ***The Micro Diamond Cutting of Steel Using Electrolysis****
   J.-H. Ahn, H.-S. Lim, S.-M. Son (Pusan National University) . . . . . page 41
2. ***Three-dimensional Machining of Optical Quality Surfaces***
   M. A. Cerniway, T. A. Dow (North Carolina State University) . . . . . page 42
3. ***Which of the Material Properties Dominates Surface Roughness of Diamond Turned Plastics***
   K. Horio, M. Nabeshima (Saitama University) . . . . . page 46
4. ***An Optimization of Geometries of Ball-end Mill for High Speed Machining***
   N.-K. Kim, S.-C. Chung (Hanyang University) . . . . . page 50
5. ***Proposal of Magnetic-field Assisted Cutting for Improvement of Machinability***
   F. Nakano (Olympus Co. Ltd.), K. Yanagihara, Y. Tani (The University of Tokyo),
   H. Yamaguchi (Utsunomiya University), and Y. Kanda (Toyo University) . . . . . page 54
6. ***Ductile-regime Turning of Brittle Materials by Single Point Diamond***
   I. Ogura, Y. Okazaki (Mechanical Engineering Laboratory, AIST/MITI) . . . . . page 58
7. ***High Speed Machining of Deep Groove by Using Slender End Mills***
   H. Onozuka, Y. Asakawa, M. Sawa, Y. Maeda, M. Kikuchi, Y. Koguchi (Hitachi, Ltd.) . . . . . page 62
8. ***Diamond Turning of CaF_2 for Nanometric Surface***
   J. Yan, K. Syoji, T. Kuriyagawa, K. Tanaka (Tohoku University), and
   H. Suzuki (Toyohashi University of Technology) . . . . . page 66
9. ***Ultraprecision Cutting of α-ß Titanium Alloy***
   H. Yasui, S. Sakamoto, M. Kawada, S. Kondo (Kumamoto University), and
   A. Hosokawa (Kanazawa University) . . . . . page 70

Grinding

1. ***Investigation of a Novel Tool Concept for Ductile Grinding of Optical Glass***
   E. Brinksmeier, R. Malz, W. Preuß (University of Bremen) . . . . . page 74
2. ***Micro Crack-free Scratching of Silicon Under External Hydrostatic Pressure***
   N. Chandrasekaran, R. Komanduri (Oklahoma State University), and M. Yoshino, T. Aoki
   (Tokyo Institute of Technology) . . . . . page 78
3. ***Investigation of the Surface Integrity of Precision Machined Single Crystal Silicon***
   C. L. Chao (Tam-Kang University), K. J. Ma, S. C. Sheu (Chung-Cheng Institute of Technology),
   and H. Y. Lin, F. Y. Chang (MIRL, Industrial Technology Research Institute) . . . . . page 82
4. ***Thermal Effects in Vibration Assisted Grinding***
   P. Chen, M. H. Miller (Michigan Technological University), W. Qu (Dana Corporation), and
   A. Chandra (Iowa State University) . . . . . page 86
5. ***Investigations on the Coolant Supply in Precision Dicing***
   H. H. Gatzen, J. Zeadan (Hanover University) . . . . . page 90
6. ***Effects of Crystallographic Orientation on Tool Wear and Machining Forces in Silicon***
   R. D. Grejda, E. R. Marsh (The Pennsylvania State University) . . . . . page 94

* *Extended abstract not available at press time*

7. ***Static Modeling of Grinding Wheel***
H.-S. Lee, K. Sadasue, Y. Ito, T. Wakabayashi (Nihon University) . . . . . *page 98*

8. ***The Grindability of Stainless Steel Using ULID (Ultrasonic In-process Dressing) Method***
S.-W. Lee, H.-D. Jeong (Pusan National University), and H.-Z. Choi (Korea Institute of Industrial Technology) . . . . . *page 102*

9. ***Ductile Regime Nanocutting of Silicon Nitride***
J. A. Patten, R. Fesperman (University of North Carolina-Charlotte), and W. Gao (Tohoku University) . . . . *page 106*

Polishing, Lapping and ECM

1. ***Lapping of Ceramics Using Metallic-abrasive Lapping Tools***
A. Barylski (Technical University of Gdánsk) . . . . . *page 110*

2. ***Fine Grinding and Mechano-chemical Polishing for Brittle Hard-disk Substrate Manufacturing****
F.-Y. Chang, H.-Y. Lin, T.-C. Wu (MIRL, Industrial Technology Research Institute) . . . . . *page 114*

3. ***Particulate Dynamic Action of a Polishing Lap***
A. E. Gee, D. F. Williams (Cranfield University) . . . . . *page 115*

4. ***Fracture Strength Evaluation of Semiconductor Silicon Wafering Process Induced Damage***
S.-M. Jeong, S.-E. Park, H.-L. Lee (Yonsei University), and H.-S. Oh (Posco-Huls Co., Ltd.) . . . . . *page 119*

5. ***Study of Dimensional Limitations of Electro-chemical Micro-machining***
J. Kozak, K. P. Rajurkar (University of Nebraska-Lincoln) . . . . . *page 124*

6 ***Electrochemical Polishing of Indium Tin Oxide Film***
C.-C. Tsai, J. C. Lin (National Central University), and F.-Y. Chang, H.-Y. Lin, T.-C. Wu (MIRL/ITRI) . . . . . *page 128*

7. ***Optical Fabrication in the Optics Research Group***
H. van Brug, S. M. Booij (Delft University of Technology), R.-J. M. van der Bijl (DeCOS, TNO/TPD), and O. W. Fähnle (FISBA-Optik AG) . . . . . *page 132*

Manufacturing (Precision Mass Production)

1. ***Precision Replication of Optics***
D. D. Gill, T. A. Dow, A. Sohn (North Carolina State University) . . . . . *page 136*

2. ***Development of One-stop Machining System for ϕ300mm Silicon Wafer***
L. Zhou, H. Eda, H. Nakano, R. Kondo, J. Shimizu (Ibaraki University), and K. Watanabe (Hitachi Via-Mechanics Pte., Ltd.) . . . . . *page 140*

Non-Conventional Processes

1. ***Knowledge Management for Process Diagnostics and Improvement***
S. H. Bui, J. Raja (University of North Carolina at Charlotte) . . . . . *page 144*

2. ***Maskless Laser Patterning of Metal Lines from Metal Powders***
H. Hidai, H. Tokura (Tokyo Institute of Technology) . . . . . *page 148*

3. ***Novel Grinding Tools for Machining Precision Micro Parts of Hard and Brittle Materials***
H.-W. Hoffmeister, A. Wenda (Technical University of Braunschweig) . . . . . *page 152*

4. ***A Novel Polymer Processing Assisted by Infrared Radiation to Attain a High Precision Transcription***
Y. Kurosaki, K. Sato (University of Electro-Communications) . . . . . *page 156*

5. ***A Study on Fabrication and Application of Micro Tool by Using High Speed Chemical Etching***
J.-M. Park, S.-H. Kim, S.-C. Jeong, H.-D. Jeong, J. W. Park, Y.-H. Moon (Pusan National University) . . . . . *page 160*

* *Extended abstract not available at press time*

6. ***Non-straight Profile Cutting on Glass Using Hot Air Jet***
E. S. Prakash, K. Sadashivappa (Bapuji Institute of Engineering and Technology), V. Joseph (University BDT College of Engineering), and M. Singaperumal (Indian Institute of Technology) . . . . . page 164

7. ***Development of Surface Texture Creation Device for Microscopic Areas Using AFM Stylus***
K. Shirai, Y. Kobayashi (Nihon University). . . . . page 168

8. ***Wire EDM Slicing of Monocrystalline Silicon Ingot***
Y. Uno, A. Okada, Y. Okamoto (Okayama University), and T. Hirano (Tokyo Advanced Technologies Co., Ltd.). . . . . page 172

EQUIPMENT, MACHINES & INSTRUMENTS

Design and Testing

1. ***Focused Ion Beam Shaped Micro-cutting Tools for Fabricating Curvilinear Features***
D. P. Adams (Sandia National Laboratories), and M. J. Vasile, Y. N. Picard (Louisiana Tech University) . . . page 176

2. ***Design of a Linear High Precision Ultrasonic Piezoelectric Motor***
M. G. Bauer, T. A. Dow (North Carolina State University). . . . . page 180

3. ***Affordable, Compact, Research Single Point Diamond Turning Machine***
A. D. Bohart, P. Collins, S. Faulk, C. Halvorson, M. McClellan, K. Shillito (Schafer Corporation) . . . . . page 184

4. ***New Technology and Novel Design Make Sub-micron Production Practical***
M. Clarke, M. G. Pierse, M. M. W. Knuefermann, R. R. F. Read (Cranfield Precision) . . . . . page 187

5. ***A Non-contact Linear Motion System and Its Application***
R. S. Cortesi, A. H. Slocum (Massachusetts Institute of Technology) . . . . . page 191

6. ***High Stiffness Air Bearing Design and Experiments for CMP Machines***
P. Greene, Z. Shang, D. Bittner (Dover Instrument Corporation) . . . . . page 195

7. ***Development of a Linear Motor Drive Testbed and Initial Thermal Behavior Results***
K. Harper, B. N. Damazo, A. Donmez (National Institute of Standards and Technology). . . . . page 199

8. ***Design of a Piezo Actuator for Cryogenic Environments***
M. D. Heinrich, T. A. Dow (North Carolina State University) . . . . . page 203

9. ***Incident Angle Auto-alignment of Ellipsometer Using Precision 3-Axis Stage with Kinematic Coupling***
J.-H. Jeong, S.-L. Park, D.-G. Gweon (Korea Advanced Institute of Science and Technology) . . . . . page 207

10. ***Characterization of Porous Graphite Air Bearings***
B. R. Knapp, B. P. O'Connor, E. R. Marsh (The Pennsylvania State University). . . . . page 211

11. ***Cast Monolithic Hydrostatic Journal Bearings***
M. S. Kotilainen, A. H. Slocum (Massachusetts Institute of Technology) . . . . . page 215

12. ***Development of a Spherical Motor Manipulated by Four Wires***
H. Nagasawa, S. Honda (Tokyo Metropolitan Institute of Technology). . . . . page 219

13. ***Fabrication of an In-pipe Mobile Microrobot with the 3D Steering Mechanism***
M. Ono, S. Kato, M. Shirakawa, T. Hamano (Nippon Institute of Technology) . . . . . page 223

14. ***Application of Design of Experiment Techniques to Estimate CMM Measurement Uncertainty***
A. Piratelli-Filho (University of Brasilia), and B. Di Giacomo (University of São Paulo) . . . . . page 227

15. ***System Modeling and Identification of a Precision Fast Tool Servo System***
S. Rakuff, J. Cuttino (University of North Carolina at Charlotte), and D. Schinstock (Tulsa University) . . . . page 231

16. ***Investigations Into Spindle Error Motions Using a Modified Loading Device***
A. K. Sharma (The Boeing Company), and S. R. Patterson (University of North Carolina at Charlotte) . . . page 236

17. ***Precision Radial Magnetic Bearing***
T. Shinshi, C. Iijima, X. Zhang, K.-B. Choi, K. Sato, A. Shimokohbe (Tokyo Institute of Technology) . . . . . page 240

18. ***High-Speed Metal Bellows Earthworm-type In-pipe Microrobot***
M. Shirakawa, M. Ono, S. Kato (Nippon Institute of Technology) . . . . . page 244

19. ***Kinematic Couplings for Pallets in Flexible Assembly Systems***
R. R. Vallance (University of Kentucky), and A. H. Slocum (Massachusetts Institute of Technology) . . . . . page 248

20. ***Evaluation of Machine Tool Contouring Accuracy at High Feed Rates***
C. P. Wang, R. Griffin (Optodyne, Inc.), and M. Omari, D. Ajao (General Motors Corporation) . . . . . page 252

21. ***A Lathe Tool Translator for Form Error Reduction in Diamond Turning***
S. C. Woody, S. T. Smith (University of North Carolina at Charlotte) . . . . . page 256

22. ***Experimental Study on Motion Accuracy of CNC Machine Tool with Ball Screw Drive System***
K. Yamazaki, Y. Kawahara, Y. Kagawa, J. Liu (University of California, Davis), J. Braasch (Johannes Heidenhain GmbH), and M. Fujishima, M. Mori (Mori Seiki Co., Ltd.) . . . . . page 260

23. ***Air Bearing Design Optimization***
F. Zhao, C. A. Andersson, J. R. Singh, C. Emmons (M Cubed Technologies, Inc.) . . . . . page 264

Controls

1. ***Intelligent Controller for Magnetostrictive Micropositioning Device for Ultra-Precision***
J. C. Campos Rubio (Federal University of Minas Gerais), J. G. Duduch, A. V. Porto (University of São Paulo), F. G. Santoro (A.U.R.A., Inc. – Cerro Tololo Inter-American Observatory), and A. E. Gee (Cranfield University) . . . . . page 268

2. ***Optimal Parameter Turning of Feed Drive Systems to Minimize Quadrant Protrusion Errors***
M.-S. Kim, S.-C. Kim, S.-C. Chung (Hanyang University) . . . . . page 272

3. ***Rapid Calibration of Cutting Force Control System Using Motor Currents in End Milling Processes***
S.-C. Kim, S.-C. Chung (Hanyang University) . . . . . page 276

4. ***Sub-milliKelvin On-off Temperature Controller***
K. M. Lawton, S. R. Patterson (University of North Carolina at Charlotte), and V. G. Badami (Tropel Corporation) . . . . . page 280

5. ***Multipoint Temperature Control Using Thermoelectric Modules***
J. Ouyang, H. D. Tran (University of New Mexico), and P.-T. Ton-Nu (Intel Corporation) . . . . . page 284

6. ***Error Calibration and Real Time Compensation System for the Chip Mounting Machine Using the Kinematic Ball Bar***
H. J. Pahk, J. H. Kim, C. H. Lee, J. H. Moon (Seoul National University) . . . . . page 288

7. ***Integrated Real Time Compensation System for Thermally Induced Volumetric Errors in Commercial CNC Machine Tools***
H. J. Pahk, S. W. Lee, S. Kim, S. W. Yoon (Seoul National University) . . . . . page 292

8. ***Development of the Standard Application Program Interface (API) for Open FA Controller in Japan***
S. Ueno (Technical Research Institute of JSPMI), H. Inoue (FANUC Ltd.), S. Chino (Mitsubishi Electric Corp.), Y. Hoshino (MAKINO Milling Machine Co., Ltd.), and M. Uneme (MORI SEIKI Co. Ltd.) . . . . . page 296

9. ***The Control of Six Degree-of-Freedom Magnetically Suspended Stage***
C. Wang (University of North Carolina at Charlotte) . . . . . page 300

Analysis and Modeling

1. ***Real Time Estimation of Temperature Distribution in a Ball Screw System Using Observer and Adaptive Algorithm***
J.-Y. Ahn, T.-H. Kim, S.-C. Chung (Hanyang University) . . . . . page 304

2. ***Rapid Machine Design***
E. Bamberg, A. H. Slocum (Massachusetts Institute of Technology) . . . . . page 308

3. ***A Correlation Analysis Between Micro-waviness of Magnetic Disk Surface and Electromagnetic Conversion Characteristics at the Head/Disk Interface***
S. Hara, T. Oosone (Nagaoka University of Technology) . . . . . page 312

4. ***Development of an Independent Real-time Position Feedback Device for CNC Machining Operations***
B. Jokiel, Jr., L. F. X. Bieg, M. Ensz (Sandia National Laboratories). . . . . page 316

5. ***Hybrid Simulation and Experimental Method of Uncertainty Analysis***
J. G. Salsbury (Mitutoyo America Corporation) . . . . . page 320

6. ***Effect of Laminating Period of Ceramics Superlattice Coating Film on its Mechanical Properties***
S. Shimada, H. Takai (Osaka University), and H. Tanaka, N. Ikawa (Osaka Electro-Communication University) . . . . . page 324

7. ***Wear Behavior of Different Mating Parts***
J. Shivakumar, K. Sadashivappa, Y. Vrushabhendrappa, K. V. Jayadevappa (Bapuji Institute of Engineering and Technology). . . . . page 328

Micro-Electro-Mechanical Systems and Nanotechnology

1. ***Automatic Surface Damage Exploring and Repairing System by Precise Micro Robots***
H. Aoyama, S. Miyamoto (University of Electro-Communications). . . . . page 332

2. ***Simulation for Laser Trapping on Arbitrary Shaped Particles***
J. Bai, Y. Takaya, T. Miyoshi, S. Takahashi (Osaka University) . . . . . page 336

3. ***Development of a Miniature Posture Device Carved into a Parallel Linkage****
Y. Funaki, S. Honda (Tokyo Metropolitan Institute of Technology) . . . . . page 340

4. ***Fabrication of an In-pipe Microrobot Movable in Sheep's Small Intestine***
S. Kato, H. Akita, K. Miyajima, T. Sugaya, Y. Kasai, N. Kato (Nippon Institute of Technology) . . . . . page 341

5. ***Self-alignment of Microparts Using Liquid Surface Tension – Examination of the Alignment Characteristics***
K. Sato, K. Ito, S. Hata, A. Shimokohbe (Tokyo Institute of Technology) . . . . . page 345

6. ***Micro Multi-point Sheet Electrode for Auditory Brainstem Implant***
H. Takahashi, T. Ejiri, M. Nakao, K. Matsumoto, Y. Hatamura, N. Nakamura, K. Kaga (The University of Tokyo), and T. Herve (Grenoble University) . . . . . page 349

Novel Systems

1. ***Design of a Precision Electro Discharge Micro Milling Machine***
K.-F. Hii, X. Zhao, R. R. Vallance (University of Kentucky) . . . . . page 353

2. ***The New Long Range Multi-axis Nanopositioner Using Inertial Slider/Walking Method***
J. Y. Shim, H. Chung, D.-G. Gweon (Korea Advanced Institute of Science and Technology). . . . . page 357

METROLOGY

Instrumentation, Design and Testing

1. ***New Artifacts for Calibration of Large CMMs***
M. Bartscher, K. Busch, M. Franke, H. Schwenke, F. Wäldele (Physikalisch-Technische Bundesanstalt) . . page 361

2. ***A Method of Optimal Design for Minimization of Force Ripple in Long Stroke Precision Linear Actuator with BLPMM***
M. J. Chung, M. G. Lee, D.-G. Gweon (Korea Advanced Institute of Science and Technology). . . . . page 365

* *Extended abstract not available at press time*

3. **A High Precision Linear Measuring System**
T. B. Eom, J. W. Han (Korea Research Institute of Standards and Science) . . . . . page 369

4. **Development of an Ultraprecise Positioning Stage Travelling on a Grating**
S. Honda (Tokyo Metropolitan Institute of Technology) . . . . . page 373

5. **Development of a Measuring Instrument for Grinding Wheel Peripheral Shapes**
M. Izumi, H.-S. Lee, T. Wakabayashi (Nihon University), and S. Inoue (Makino Seiki Co., Ltd.) . . . . . page 377

6. **Analysis of PZT Tube Scanner Motion Using Newly Designed Sensing Mechanism**
H. Jung, J. Y. Shim, D.-G. Gweon (Korea Advanced Institute of Science and Technology) . . . . . page 381

7. **Comparative Analysis of Halbach and Conventional Linear Motors for Precision Positioning and High Speed Control**
M. G. Lee, M. J. Chung, S. Q. Lee, D.-G. Gweon (Korea Advanced Institute of Science and Technology) . page 385

8. **Form and Length Measurements Using a Modified Commercial Form Measuring Instrument**
F. Lüdicke, O. Jusko, H. Reimann (Physikalish-Technische Bundesanstalt). . . . . page 389

9. **Development of Long Depth of Focus Optical Microscopy Using Software-confocal Method and its Application to 3-D Profile Measurement**
K. Mitsui, T. Uno (Keio University). . . . . page 393

10. **A Micro Coordinate Measurement System with Virtual Contact Probe**
K. W. Ng, K. S. Moon, C. R. Friedrich (Michigan Technological University), and Z. K. Ling (Ford Motor Co.). . . . . page 397

11. **Enhancements to the Pellissier H5 Hydrostatic Level**
D. H. Parker, J. W. Shelton, B. Radcliff (The National Radio Astronomy Observatory) . . . . . page 401

12. **A Detachable Step Gage for the Calibration of Vertical Machining Centers and Bridge Type Coordinate Measuring Machines**
A. R. Sousa, C. A. Schneider (Federal University of Santa Catarina) . . . . . page 405

13. **Design and Use of a Precision Bearing Analyzer**
V. C. Vigliano, E. R. Marsh (The Pennsylvania State University) . . . . . page 409

Surface and Subsurface

1. **A Convolved Multi-Gaussian Probability Distribution for Surface Topography Applications**
J. D. Cogdell (The Timken Company). . . . . page 413

2. **Subsurface Microstructure Effects on Frequency Characteristics of Polished Quartz Oscillator Discs**
T. Kaneeda, Y. Yokota, D. Nishiyama, (Okayama University of Science), T. Miyawaki (Wakou Kikou Co., Ltd.), and S. Yokomizo (Okayama Prefecture Office, Industry Development Division) . page 417

3. **Surface Topography Analysis of Silicon Wafers by a Chromameter**
G. Udupa, B. K. A. Ngoi (Nanyang Technological University). . . . . page 421

Form and Geometry

1. **Error Budget by Constraints**
S. K. Eisenbies, R. J. Hocken (University of North Carolina at Charlotte) . . . . . page 425

2. **A Study on Model Building of Free-form Curves**
Feng G., Zhang G., Xie Z., Wang C. (Tianjin University) . . . . . page 429

3. **On-Machine Profile and Straightness Measurement of a Linear Slide***
E. H. K. Fung, S. M. Yang (The Hong Kong Polytechnic University). . . . . page 433

4. **Self-calibration for 2-Dimensional Precision Stages Based on Circle Closure Principle**
X. Lu, H. D. Tran (University of New Mexico) . . . . . page 434

* *Extended abstract not available at press time*

5. ***Shape Error Measurement of a Parabolic Mirror Using the Ray Tracing and the Fringe Scanning Method***
T. Nomura, K. Kamiya, S. Okuda, K. Yamazaki (Toyama Prefectural University), and H. Tashiro, K. Yoshikawa (Toyama University) . . . . . page 438

6. ***Profile Tolerance Zones with Control Points***
T. M. Ketahara Pasupathy, R. G. Wilhelm (University of North Carolina at Charlotte), and G. A. Hetland (Hutchinson Technologies Ltd.) . . . . . page 442

7. ***Precision Interferometer Measurement of Ultrahigh Precision Grate Base****
S. Peng (Chinese Academy of Science). . . . . page 446

8. ***Accurate Profile Measurement by an Interferometer***
X-F. Qiang, W. Gao, S. Kiyono (Tohoku University) . . . . . page 447

9. ***A Method for Non-contact Measurement of Free-form Surfaces Based on CMM***
Xu Y., Zhang G., Xie Z., Feng G., Wang C. (Tianjin University) . . . . . page 451

10. ***In-process Roundness Measurement System for Cylindrical Machine Parts of Small Diameter with Run-out Error Compensation***
R. Yamada (Nagaoka National College of Technology), and T. Takei, K. Yanagi (Nagaoka University of Technology). . . . . page 454

11. ***Automatic Measurement of Large Surface Planeness***
Zhang J., Lei T., Chen Y. (Academy of Machinery Science & Technology) . . . . . page 458

Analysis and Modeling

1. ***A Proposed Method for the Dimensional Metrology of Non-rigid Objects***
K. L. Blaedel, D. W. Swift (Lawrence Livermore National Laboratory), H. Tajbakhsh (ETEC Systems, Inc.), S. R. Patterson (University of North Carolina at Charlotte), and D. C. Thompson (Production Technology Inc.) . . . . . page 462

2. ***Data Filtering Using Measured Surface Normals***
R. Edgeworth (Intel Corporation), and R. G. Wilhelm (University of North Carolina at Charlotte) . . . . . page 465

3. ***Plate Calibration Methods for Two-dimensional Stages***
J. Fu, R. J. Hocken (University of North Carolina-Charlotte), G. X. Zhang (Tianjin University) . . . . . page 469

4. ***Comparison Study of Areal Functional Parameters for Rough Surfaces***
X. Q. Jiang, L. Blunt, K. J. Stout (The University of Huddersfield) . . . . . page 473

5. ***An Accurate and Robust Stereo Algorithm with a Variable Window for Measurement of 3D Shapes***
G.-B. Kim, S.-C. Chung (Hanyang University) . . . . . page 477

6. ***Volumetric Error Identification and Measured Data Correction for On-machine Measurement and Inspection Systems***
K.-D. Kim, S.-C. Chung (Hanyang University) . . . . . page 481

7. ***The Interaction of Measuring Errors and Workpiece Errors in Feature Evaluation Algorithms***
E. P. Morse (University of North Carolina at Charlotte), and J. G. Salsbury (Mitutoyo America Corporation) . . . . . page 485

8. ***A Novel Practical Approach to Cylindricity Evaluation: An Experimental Report***
G. Singh (Mahr Federal), O. Devillers (INRIA), and F. P. Preparata (Brown University) . . . . . page 489

9. ***An Artificial Intelligent Measuring Sequence Path Planning for CMM***
Wu Y., Liu S., Zhang G. (Tianjin University) . . . . . page 493

* *Extended abstract not available at press time*

Optics and Interferometry

1. **Investigation of Subsurface Damage of II-VI Semiconductors Using Photoluminescence**
   D. W. Hamby, D. A. Lucca (Oklahoma State University) . . . . . page 497
2. **Second Order Distortion of Grazing Incidence Interferometric Measurements**
   P. D. Knight, Jr., S. R. Patterson (University of North Carolina at Charlotte) . . . . . page 501
3. **Compensation of Phase Change Upon Reflection in White Light Interferometry**
   M.-C. Park, S.-W. Kim (Korea Advanced Institute of Science and Technology) . . . . . page 505
4. **A Compact Interferometric Surface Characterization Device**
   A. D. Woodfin, F. Farahi, R. J. Hocken (University of North Carolina at Charlotte) . . . . . page 509
5. **Dual Mode Phase Measurement of Heterodyne Optical Interferometry**
   N.-B. Yim, M.-S. Kim, S.-W. Kim (Korea Advanced Institute of Science and Technology) . . . . . page 513

Session III
Lithography

Wednesday, October 25, 2000, 8:30 a.m. – 10:15 a.m.

Session Co-Chairs: Andrew J. Hazelton (Nikon Research Corporation of America) and Hooman Tajbakhsh (ETEC Systems, Inc.)

1. **Nikon Electron Projection Lithography System: Mechanical and Metrology Issues (Invited Paper)**
   W. T. Novak, D. Watson (Nikon Research Corporation of America), and Y. Yoda (Nikon Corporation). . . . . page 517
2. **High-NA Camera for an EUVL Microstepper**
   L. C. Hale, R. M. Hudyma, J. S. Taylor, R. L. Thigpen, C. A. Chung (Lawrence Livermore National Laboratory). . . . . page 521
3. **Nullifying Acceleration Forces in Nano-positioning Stages for Sub-0.1μm Lithography Tool for 300mm Wafers**
   Y. B. P. Kwan, E. L. Loopstra (ASM Lithography B.V.). . . . . page 525
4. **Development of a Vertical Wafer Stage for High-vacuum Applications**
   E. Beckert, A. Hoffmann, C. Schäffel (IMMS GmbH), E. Saffert (Technical University of Ilmenau), and U.-C. Kirschstein (Leica Lithography Systems GmbH) . . . . . page 529

Session IV
CMM Metrology

Wednesday, October 25, 2000, 10:45 a.m.- 12:30 p.m.

Session Co-Chairs: Vivek G. Badami (Tropel Corporation) and Andrew D. Woodfin (University of North Carolina at Charlotte)

1. **A Giant Magneto Resistive (GMR) Eddy Current Sensor for Use as a Zero Width Coordinate Measuring Machine Probe (Invited Paper)**
   S. T. Smith, T. Dogaru (University of North Carolina at Charlotte) . . . . . page 533
2. **A New Design for a Three-dimensional Measurement Probe**
   A. Sohn, T. A. Dow, E. A. Marino (North Carolina State University) . . . . . page 537
3. **Development of a Special CMM for Dimensional Metrology on Microsystem Components**
   U. Brand, T. Kleine-Besten, H. Schwenke (Physikalish-Technische Bundesanstalt) . . . . . page 542
4. **Design and Testing of a High Speed, 5-DOF, Coordinate Measuring Machine with Parallel Kinematic Structure**
   J. C. Ziegert (University of Florida). . . . . page 547

Session V

Precision Fabrication I — Manufacturing

Wednesday, October 25, 2000, 4:00 p.m. – 5:30 p.m.

Session Co-Chairs: A. E. Gee (Cranfield University) and Alex Sohn (North Carolina State University)

1. **Multi-layered Circuit Board Precisely Pressed/Damascened on Glass Plates**
   M. Nakao, J. Kumaki, K. Matsumoto, Y. Hatamura (The University of Tokyo) . . . . . page 551
2. **Production of a Rayleigh-Taylor Instability Target**
   R. D. Day, N. Elliott, J. Elliott, V. Gomez, T. Pierce, D. Hatch, G. Rivera, E. Armijo, P. Gobby, M. Brooks, B. Hennike, L. Rodriguez, J. Bartos (Los Alamos National Laboratory). . . . . page 555
3. **Bending Deflections Due to Scribe-induced Residual Stresses**
   B. Austin, B. Love, T. A. Dow, J. Eischen, R. O. Scattergood (North Carolina State University) . . . . . page 559
4. **Investigations on the Tool Plate Preparation for Nanogrinding**
   H. H. Gatzen, H. Siekmann (Hanover University). . . . . page 563

Session VI

Micro/Mezo

Thursday, October 26, 2000, 8:30 a.m. – 10:15 a.m.

Session Co-Chairs: Jeffrey W. Carr (Lawrence Livermore National Laboratory) and Bradley H. Jared (Corning Incorporated)

1. **Micro Mechanical Manufacturing Processes – Capabilities and Barriers****
   J. Hillesheim, R. Heitkamp (Remmele Engineering)
2. **Microfactory and a Design Evaluation Method for Miniature Machine Tools**
   N. Mishima, K. Ashida, T. Tanikawa, H. Maekawa, K. Kaneko, M. Tanaka (Mechanical Engineering Laboratory, AIST, MITI) . . . . . page 567
3. **Performance Evaluation of a Parallel Cantilever Biaxial Micropositioning Stage**
   E. G. Amatucci, N. G. Dagalakis, J. A. Kramar, F. E. Scire (National Institute of Standards and Technology) . . . . . page 571
4. **Micro-lathe to Machine Micro-parts**
   Y. Okazaki, (Mechanical Engineering Laboratory, AIST/MITI), and T. Kitahara (Shonan Institute of Technology) . . . . . page 575

Session VII

Precision Fabrication II – Fluidics

Thursday, October 26, 2000, 10:45 a.m. – 12:30 p.m.

Session Co-Chairs: Thomas A. Dow and Kenneth P. Garrard (North Carolina State University)

1. **Microfluidic Control Using MEMS (Invited Paper)***
   J. Collier, D. Wroblewski, T. G. Bifano (Boston University) . . . . . page 579
2. **Precision Generation of Optical Elements Using Drop-on-demand Technology**
   H.-J. Trost, W. R. Cox, C. Guan, D. J. Hayes, R. Hoenigman, D. B. Wallace (MicroFab Technologies, Inc.). . . . . page 580

* *Extended abstract not available at press time*
** *Abstract not available at press time*

3. **Nano-positional Detection Using Laser Trapping Probe for Microparts**
Y. Takaya, S. Takahashi, T. Miyoshi (Osaka University) . . . . . *page 584*

4. **Rapid Prototyping of Microfluidic Components**
W. C. Jackson, W. Leger, G. P. Lopez, H. D. Tran (University of New Mexico) . . . . . *page 588*

Session VIII
Precision Fabrication III — Cutting

Thursday, October 26, 2000, 2:00 p.m. – 3:30 p.m.

Session Co-Chairs: James F. Cuttino (University of North Carolina at Charlotte) and Don A. Lucca (Oklahoma State University)

1. **Dynamic Forces and Energy Dissipation in Vibration Diamond Cutting of Copper**
E. Brinksmeier, J. Schmütz (University of Bremen) . . . . . *page 592*

2. **Characteristics of Micro Groove Machining for the Mold of PDP Barrier Ribs**
H.-D. Jeong, I.-H. Cho, S.-C. Jeong, J.-M. Park (Pusan National University) . . . . . *page 596*

3. **Chipping of Sintered Cutting Tools – Mechanism and its Prediction**
K. Uehara (Toyo University), J. Herai (Kiriu Machine Mfg. Co. Ltd.), and T. Ishikawa (Mikasa Sangyo Co. Ltd.) . . . . . *page 600*

4. **The Effects of Fluids on the Deformation and Ductile-to-Brittle Transition of Silicon**
J. A. Patten, S. V. Mumford (University of North Carolina at Charlotte) . . . . . *page 604*

Technical Papers

A S P E

Wafer-Level Assembly of Hybrid Microsystems

B. J. Nelson, B. Vikramaditya, G. Yang, J. Gaines, E. Enikov*

University of Minnesota
Minneapolis, MN 55455, E-mail: nelson@me.umn.edu
*Currently with the University of Arizona

The assembly of microparts directly onto micromachined silicon wafers allows one to design MEMS devices using incompatible microfabrication processes and to develop truly 3D microsystems. The drawback, however, is the microassembly step. Microassembly tasks differ from their macro counterparts primarily due to two reasons: very high precision requirements and the vastly different physics that dominate in the micro domain. These two differences indicate that sensor based manipulation strategies are required. For example, the current state-of-the art in the manufacture of microdevices requiring complex manipulation entails hand assembly using an optical microscope and probes or small tweezers, a very costly manufacturing step. In this talk two different types of wafer-level microassembly tasks will be presented. In the first, electroplated parts are assembled onto micromachined silicon wafers using visual servoing strategies. In the second task, self-assembly strategies are exploited to develop electromagnetic microactuators for dual-stage disk drives.

Instrument for Setting Radio Telescope Surfaces

David H. Parker,* John M. Payne,† John W. Shelton,‡ Timothy Lee Weadon§
The National Radio Astronomy Observatory¶
Key Words: radio telescope, panel setting, inclinometer calibration, coordinate measurement machine, laser ranging

1 Introduction

The Green Bank Telescope (GBT) [1] is a 100-meter radio telescope under construction by The National Radio Astronomy Observatory in Green Bank, WV. The GBT incorporates a first-of-its-kind active surface that will be adjusted under a closed-loop laser metrology system [2] to correct surface deflections. The goal is to maintain a reflector surface accuracy of 0.220-mm rms in order to operate down to 3-mm wavelengths (100 GHz). The reflector is made up of 2004 individual panels, each of which is manufactured to a section of a 60-meter focal length paraboloid surface to an accuracy of 0.075-mm rms. The panels rest on 2209 motor-driven actuators that adjust the surface to correct for deflections in the telescope backup structure. A bracket on each actuator joins the corners of four panels, so each actuator moves the four adjacent panel corners as a single unit and thus the relative location of the four corners remains fixed.

Each panel is measured in a 4" X 6" grid on a coordinate measurement machine (CMM) before painting. A cardinal point, near each corner of the panel, is masked before painting in order to retain a reference to the CMM measurements. The CMM data is best-fit to the design surface, and the relative height of the "as built" cardinal points are calculated.

Radio telescope panels are traditionally adjusted to the fixed paraboloid shape, using conventional surveying techniques or photogrammetry. Fine adjustments are later made using a microwave holography technique. For the GBT holography, the goal is an accuracy of 0.100 mm on a 0.5 X 0.4 meter pixel spacing, i.e., holography can not resolve the step discontinuity between panels. Due to the unique architecture of the GBT, the panels do not have to be adjusted to the design paraboloid as accurately (since the final adjustments can be made by the actuators) as a fixed-surface telescope. However, the relative heights of the four panels is of greater concern. Laser rangers are used to measure retroreflectors, which are calibrated with respect to the cardinal points, located in the corner of a panel at each actuator--thus completing the final link in the chain between the CMM measurements and the telescope reflector paraboloid.

2 The Panel Setting Tool

A new instrument had to be designed for this application in order to set the relative heights of four panel corners to an accuracy of 0.050 mm, *in situ*. The accuracy of the instrument is around 0.015 mm, or 3 times better than the required mechanical adjustment precision. The instrument incorporates a dual-axis inclinometer, a sighting telescope, four digital indicators, a barcode reader, and a handheld computer. See Figure 1. The dual-axis inclinometer is used to reference the instrument with respect to the gravity vector. The sighting telescope is used to orient the instrument along a radial line to the vertex. This combination orients the instrument platform direction vectors. The four digital indicators measure the distance to each cardinal point with respect to the instrument platform. The barcode reader scans an identification number for each panel corner, which is used as the pointer to the offset calculated from the CMM data and the location to calculate the surface normal vector at that point for a given elevation angle of the reflector. The handheld computer is used to correct actual digital indicator measurements at the actual instrument orientation to distances that would be measured by an ideal instrument tangent to the surface.

* Green Bank, WV, dparker@nrao.edu, (304)456-2121
† Tucson, AZ, jpayne@nrao.edu, (520)882-8250 X118
‡ Green Bank, WV, jshelton@nrao.edu, (304)456-2117
§ Green Bank, WV, tweadon@nrao.edu, (304)456-2120
¶ The National Radio Astronomy Observatory is operated by Associated Universities, Inc. under cooperative agreement with the National Science Foundation.

The instrument is attached to the center of the actuator bracket via a temporary stud extension screwed to a stud in the center of the bracket. This is simply to hold the instrument in place for the measurement, i.e., the orientation of the instrument is not important--except that it is oriented about its z-axis to point to the vertex. The instrument case and computer is operated from an adjacent panel in order to avoid distortions by standing on the panel under measurement. See Figure 2. The difference between the ideal and desired offsets is displayed for the technician to make mechanical adjustments, and thus bring the four corners into the desired relative positions. An adjustment tool was designed with a dial and pointer, calibrated in thousandths of an inch in order to facilitate making a precise adjustment and minimize iterations. See Figure 3.

3 Calibrations

The dual-axis inclinometers must be calibrated to an accuracy of about 15 arcseconds over the entire +/- 25 degree range. The inclinometer is mounted on a square lock and calibrated in the lab with respect to the block, before being mounted on the platform. This calibration is performed in a basement lab on an 8-foot surface plate leveled to about 2 seconds. Calibration of the dual axes is achieved by generating compound angles, measuring the inclinometer outputs, and doing a best-fit of the sine of the generated angles to a function with 10 terms--including cross terms. The compound angles are generated by a combination of a 21-inch sine bar and angle blocks used to rotate the inclinometers about the axis normal to the sine bar. The sine bar is set at 0, 15, and 25 degrees. Angle blocks are used to rotate the mounting block at 15-degree increments through a full 360 degrees, for each sine bar angle, for a total of 72 data points.

The instrument platform accurately locates the geometry of the four digital indicators and a mechanical reference for the inclinometer base block in order to orient the inclinometer with respect to the indicators. The instrument platform also has a mechanical reference to orient the platform and align the telescope to a reference target in the lab. The combination instrument platform and digital indicators are calibrated with only a level surface plate, and can thus be checked in the field. The hardware/software integration was tested using a 12"x12" granite sine plate and angle blocks to rotate the instrument about the axis normal to the sine plate.

4 Results

Since this was not in the original scope of work for the contractor (COMSAT Inc.), negotiations were required to implement the plan. NRAO developed and built three instruments and the work was performed by a joint team of NRAO technicians and COMSAT ironworkers. The specification was set at +/- 0.050 mm, which was limited by the precision of the mechanical adjustment. The corners were actually set to 0.030-mm rms, and the average time required to adjust a set of corners was 12 minutes.

5 Conclusions

By maintaining dimensional traceability of the GBT panels from the manufacturing floor to the telescope reflector, providing a cardinal point on the panels to facilitate matching the panels at the corners, and use of the panel setting tool and the laser metrology system, the GBT will be the first radio telescope surface to be set to high accuracy by dimensional metrology and at an unprecedented spatial resolution.

6 References

[1] http://info.gb.nrao.edu
[2] David H. Parker and John M. Payne, "Metrology System for the Green Bank Telescope", Proc. ASPE 1999 Annual Meeting, Vol. 20, p.21-24.

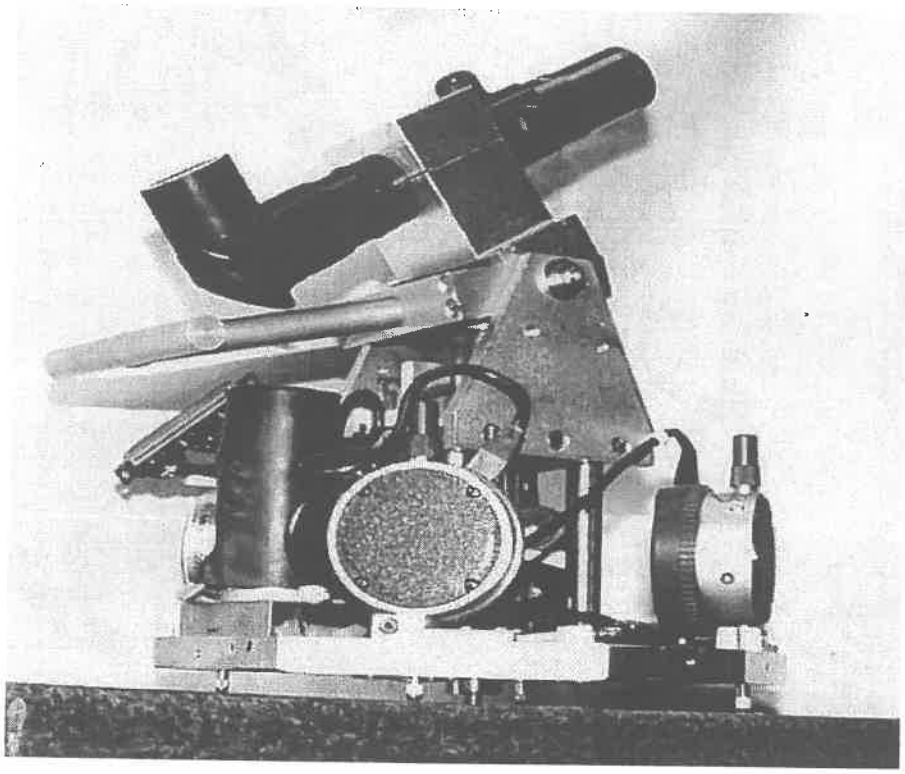

Figure 1

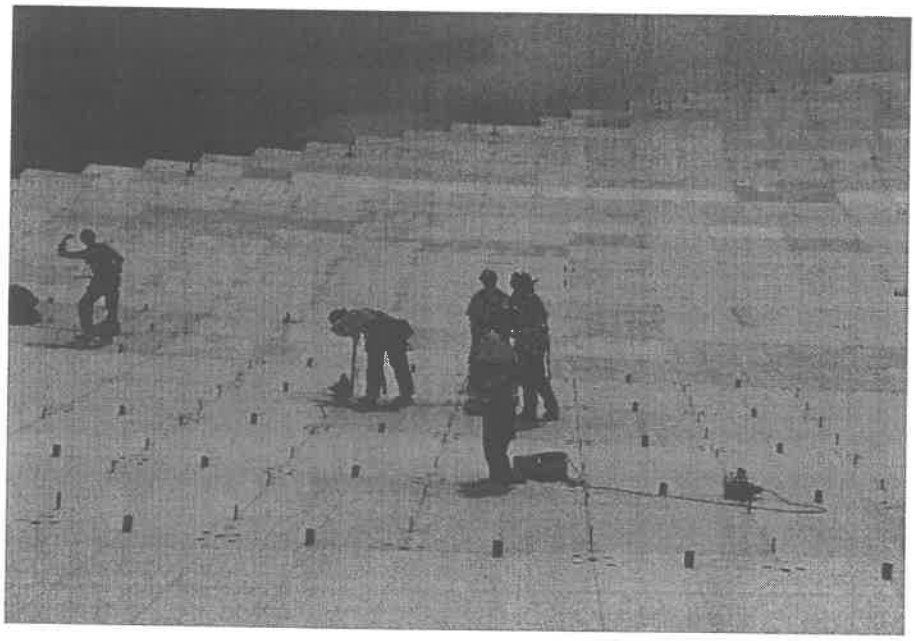

Figure 2

Figure 3

Recent Advances in Separation of Roughness, Waviness and Form

Raja J, Muralikrishnan B, Fu S, Liu X
Center for Precision Metrology
The University of North Carolina at Charlotte
Charlotte, NC 28223

1 Introduction

A typical engineering surface consists of a range of spatial frequencies. The high frequency or short wavelength components are referred to as roughness, the medium frequencies as waviness and low frequency components as form. Figure 1 illustrates this.

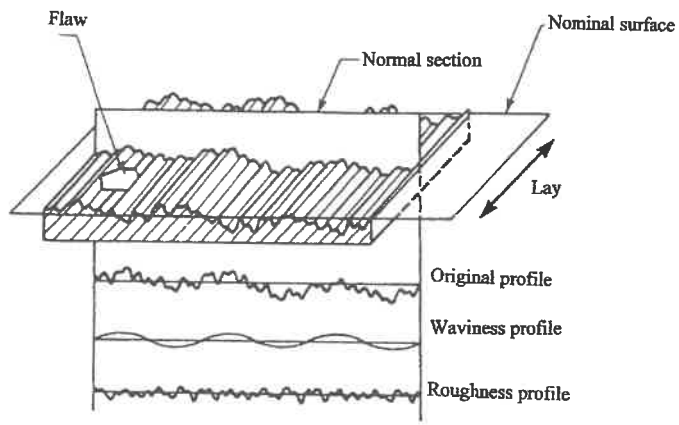

Figure 1 Roughness and waviness in a surface [1]

In the early days, different instruments and measurement techniques were adopted to capture the different wavelength regimes. Visual assessment using microscopy was used to identify any torn material or micro burr, stylus based instruments to obtain roughness and other special instruments to get form information. Today, with the availability of increasingly sophisticated gages and sensors, we have an overlap of measuring capability.

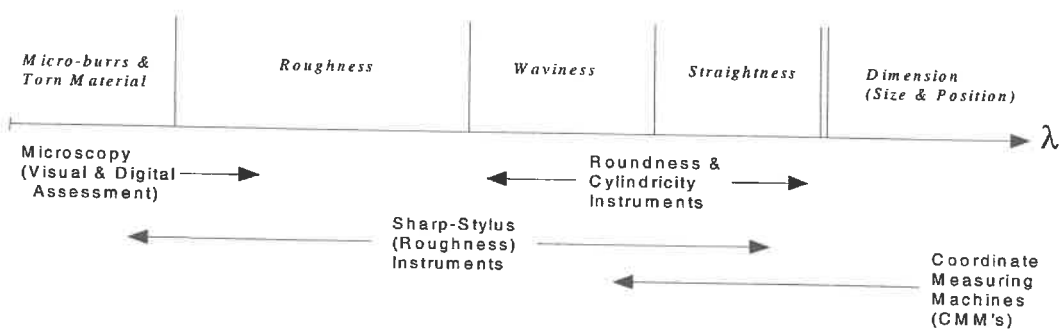

Figure 2 Metrology measurement spectrum [2]

A typical stylus based instrument can capture roughness, waviness and form. A roundness measuring instrument can also gather straightness data and a CMM can get both dimensional information and form. Figure 2 shows the current metrology

measurement spectrum. As the bandwidth of measurement instruments increase, it has become essential to separate surface profile data into meaningful wavelength regimes before numerical characterization.

Historically, it has been accepted that different aspects of the manufacturing process generate the different wavelength regimes and these affect the function of the part differently [3]. By separating surface profile into various bands, we can map the frequency spectrum of each band to the manufacturing process that generated it. Thus, filtering of surface profiles serves as a useful tool for process control and diagnostics.

While engineers commonly trace manufacturing process variations based on surface profile data, mapping functional performance of a component based on surface profile information has been a challenge. The different wavelength regimes play a key role in critical parts like crankshafts and bearings. Thus, separation of signal into various bandwidths has to be viewed from a functional standpoint as well.

Digital filtering is a common practice to separate a signal into various regimes [4]. Analog RC filters have been replaced by the now common Gaussian filters. This paper reviews recent advances in filtering surface data including bandpass filters for process specific analysis and functional correlation, multiresolution analysis using wavelets, robust filters and morphological filters.

2 Current filtering practice

The earliest filter used in surface metrology is the analog RC filter. The 2RC digital filter [1] simulates the characteristics of the analog 2RC network. The transfer functions of the 2RC lowpass filter and highpass filter are

$$\frac{Output}{Input} = \left(1 - ik\,\lambda/\lambda_c\right)^{-2}, \quad \frac{Output}{Input} = \left(1 - ik\,\lambda_c/\lambda\right)^{-2}$$

respectively, where $i = \sqrt{-1}$ and $k = 1/\sqrt{3} = 0.577$. The 2RC filter does not have linear phase characteristics. The digital 2RC filter overcomes many of the shortcomings of the analog RC filter [4]. Whitehouse proposed a new RC filter with linear phase [5]. The most widely used filter today is the Gaussian filter [1]. The weighting function and transmission characteristic of a Gaussain lowpass filter are

$$S(x) = \frac{1}{\alpha\lambda_c}\exp\left[-\pi\left(\frac{x}{\alpha\lambda_c}\right)^2\right]$$

$$\frac{A_{output}}{A_{input}} = \exp\left(\pi\left(\alpha\frac{\lambda_c}{\lambda}\right)^2\right)$$

respectively. Where $\alpha = \sqrt{\ln 2/\pi} = 0.4697$. The important property of Gaussian filter is linear phase characteristics and 50% transmission at the cutoff to simplify analysis of waviness.

3 Recent Developments

The advances in the field of digital signal processing and increasing computational capability have led to new developments in surface filtering.

3.1 Mapping process conditions

To analyze surface texture appropriately, the different wavelength components should be separated reasonably by applying filters with different cutoff, i.e., in figure 3 $\lambda_f, \lambda_c, \lambda_s$ are cutoffs for form, waviness and roughness. Figure 4 is a piston pin bore profile and its power spectral density(PSD). The PSD shows the different wavelengths and their sources. The short wavelengths are generated by tool radius and long wavelengths by guideway error. Chatter is clearly visible in the medium wavelength band.

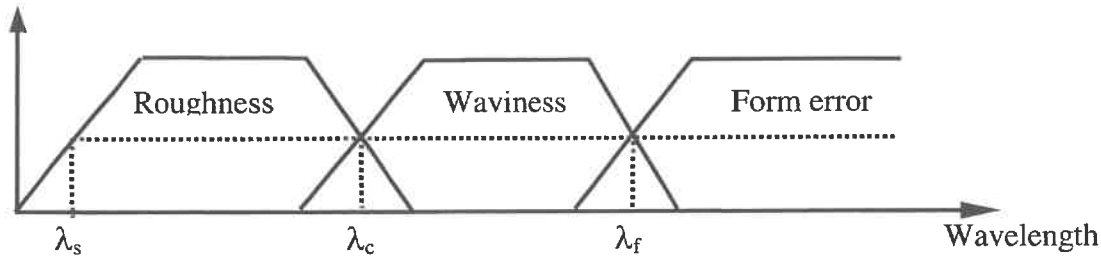

Figure 3 Separation of surface into frequency bands

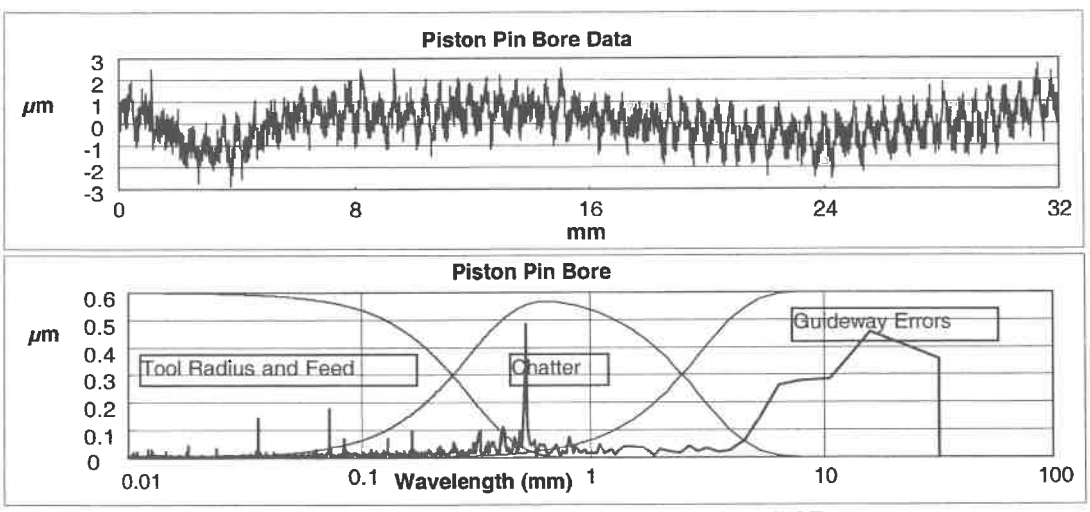

Figure 4 Piston pin bore profile and its PSD

3.2 Function critical components

Functional performance of a part is usually determined by different wavelengths on a surface. From a study by Marlburg [2], the middle wavelength components are critical to a diesel engine crankshaft pin's performance because they are relative to localized loading and ultimate failure of the bearing. It is necessary to control long wavelength aspects in a reasonable level for proper fit and short wavelength components for tribological requirements. Bandpass filtering is needed to separate those function

critical wavelength components. Figure 5 shows the result from bandpass filtering of a crankshaft pin profile.

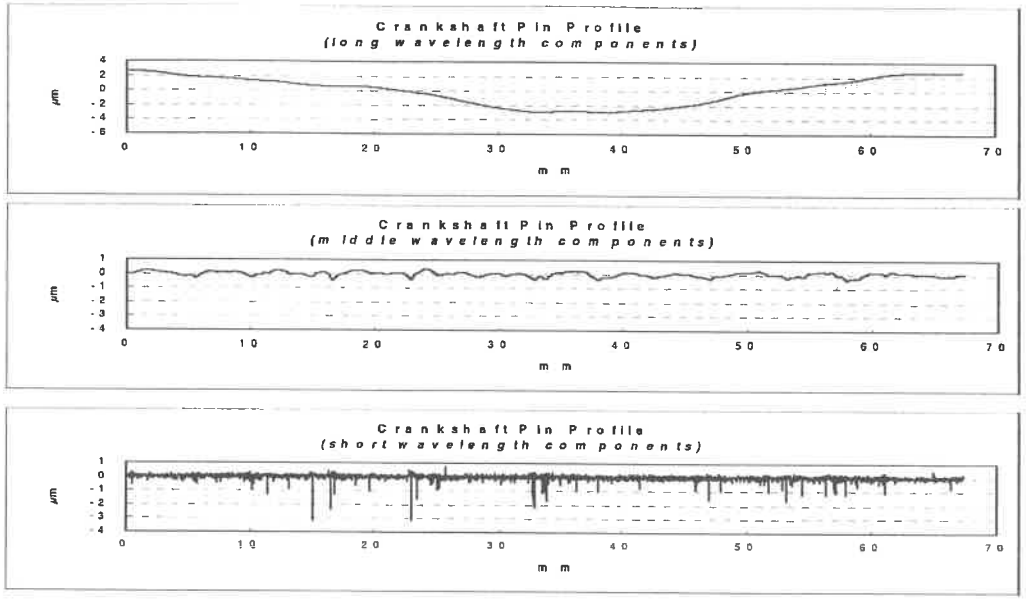

Figure 5 Bandpass filtering of a crankshaft pin profile

3.3 Filtering with wavelet transform

The fundamental idea behind wavelet analysis is to analyze signal according to scale. Wavelet analysis provides a flexible time-scale window localized on time-scale plane. If we look at a signal with a large window, we would notice gross features. Similarly, if we look at a signal with a small window, we would notice fine features. The result in wavelet analysis is to see both the fine and the gross features. This makes wavelets interesting and useful.

The primary study on the application of multiresolution analysis (MRA) for analyzing multi-scale engineering surfaces are presented by Chen, Liu and Raja [6][7]. As octave filter banks, wavelets can be used to decompose signal into different bands with different scales, which is also called multiresolution analysis of signal [8]. In MRA, the dyadically dilated wavelets constitute a bank of octave band pass filters and the dilated scaling functions form a low pass filter bank. The efficient implementation of discrete wavelet transform (DWT) is to get successive approximations of signal by applying the low pass filter bank and successive details of signal by applying the band pass filter bank. DWT appears to have great potential for analyzing multi-scale features in engineering surfaces due to its properties of good time-scale localization and flexible time-scale resolution. In order to analyze engineering surface texture, multi-scale approximations of original texture at different resolution levels will be extracted by DWT. This will give us a clear overview of the multi-scale features of surface texture. Then the separation of multi-scale features based on wavelength can be made according to the information provide by the multi-scale approximations. A polished surface profile is considered for wavelet filtering. In the multi-resolution approximation shown in figure

6, only long wavelengths in the profile are seen below level 5. The rougher structure appears from level 5 to 9. In approximations over level 9, more and more fine structures are added. We can reconstruct the profiles by combining the levels 1~5, levels 5~9 and levels 9~13. Various families of wavelets can be used for MRA. Each one has its own advantages and limits. Spline wavelets are recommended to be used in ISO/TS 16610-4 [9].

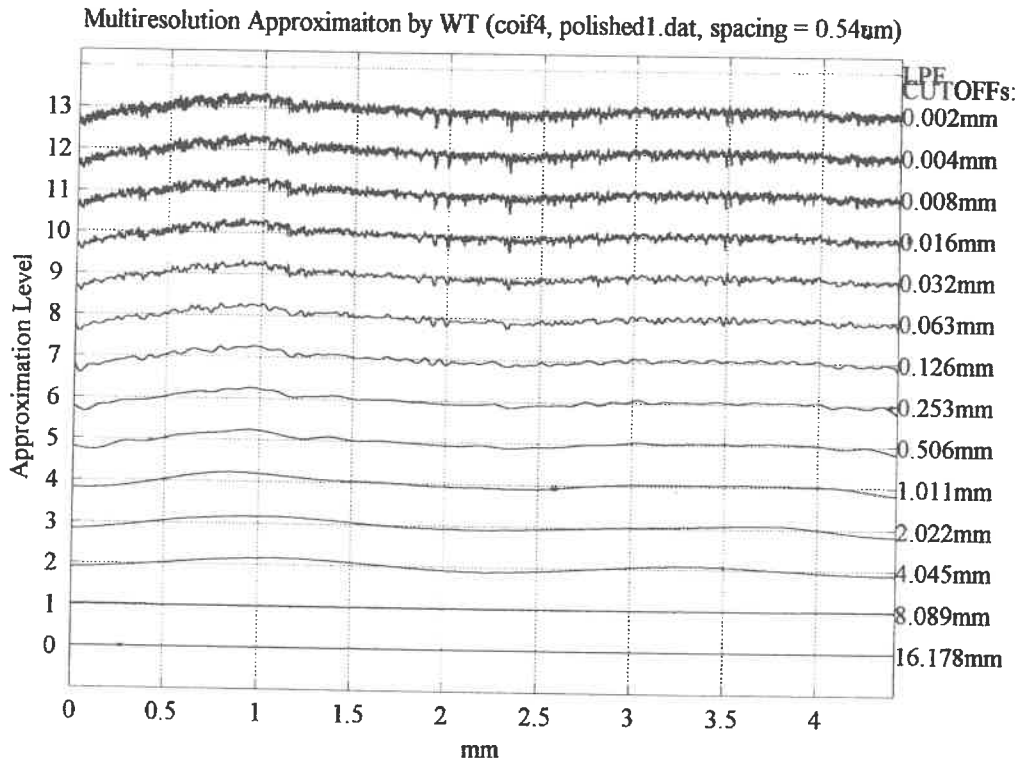

Figure 6 Wavelet decomposition of polished surface profile

3.4 Robust filters

Robust filters are filters that are tolerant against outliers. There are two types of robust spline filters : non-periodic robust filters for filtering open profiles and periodic robust filters for closed profiles. Since robust spline filters are non-linear, the weighting function can not be given. The filter equation for both kinds of robust spline filters are specified in ISO/TS 16610-8 [10]. Another robust filter that has been proposed is the robust Gaussian regression filter, the definition for which can be found in ISO/TR 16610-10[11]. With its regression approach and robust algorithm this filter evaluates measured surface profiles without loss of data in the marginal sections.

3.5 Morphological filters

Mathematically, morphological filters are defined using Minkowski sums. There are two major morphological operations (dilation and erosion) and two secondary morphological operations (opening and closing). The basic concepts of morphological operations and filters are addressed in ISO/TS 16610-5[12]. The computation part is

defined in ISO/TS 16610-6[13] and the scale space techniques is described in ISO/TS16610-7[14].

4 Conclusions

Advances in filtering techniques enable us today to separate the different wavelength regimes without any distortions. It is easy to specify and implement well defined bandwidths using digital filters. Current research emphasis is in the area of multiresolution analysis and more robust filters. The need to establish stable manufacturing process and provide functional correlation for components will require finer bandwidth analysis in the future. Case studies to demonstrate process control and functional analysis with these new and powerful tools will be a task for the future.

5 References

1 ASME B46.1, Surface Texture (Surface Roughness, Waviness, and Lay), 1995.

2 Marlburg, M. C., "A Unified Methodology for the Application of Surface Metrology", Ph.D. dissertation, University of Warwick, UK, and University of North Carolina at Charlotte, USA.

3 Whitehouse, D. J., "Surfaces – a Link between Manufacture and Function", Proc. Instn. Mech. Engrs, Vol. 192, 179-188, 1978.

4 J. Raja and V. Radhakrishnan, "Digital filtering of surface profiles",Wear, Vol 57, 1979, 147-155

5 Whitehouse, D. J., "Improved Type of Wavefilter for Use in Surface-finish Measurement", Proc Instn Mech Engrs, 306-318, 1967-68, 3K.

6 Chen X., Raja J., Simanapalli S., "Multi-scale of engineering surface', Int. J. Mach. Tools Manufacts. Vol. 35, No.2.

7 Liu X., and Raja J., "Analyzing engineering surface texture using wavelet filter", SPIE Vol. 2825.

8 S. Mallat, "A theory for multiresolution signal decomposition: the wavelet representation", IEEE Trans. On Pattern Analysis and Machine Intell., Vol. 11, pp. 674-693, July 1989.

9 ISO/TS 16610-4, Geometrical Product Specification (GPS) – Data extraction techniques by sampling – Part 8: Spline Wavelets.

10 ISO/TS 16610-8, Geometrical Product Specification (GPS) – Data extraction techniques by sampling and filtration – Part 8: Robust spline filters.

11 ISO/TS 16610-10, Geometrical Product Specification (GPS) – Data extraction techniques by sampling and filtration – Part 10: Robust Gaussian Regression filter.

12 ISO/TS 16610-5, Geometrical Product Specification (GPS) – Data extraction techniques by sampling and filtration – Part 5: Basic concepts of morphological operations and filters.

13 ISO/TS 16610-6, Geometrical Product Specification (GPS) – Data extraction techniques by sampling and filtration – Part 6: Morphological operations and filters.

14 ISO/TS 16610-7, Geometrical Product Specification (GPS) – Data extraction techniques by sampling and filtration – Part 7: Morphological scale space techniques.

MEASUREMENT OF THE ABSOLUTE DIAMETER OF CYLINDRICAL GAGES BY GRAZING INCIDENCE INTERFEROMETRY

V.G. Badami, P. Venkataraman, A. W. Kulawiec and J. H. Bruning
Tropel Corporation, Fairport, NY 14450, USA

1.0 Introduction

Grazing incidence interferometry has been applied successfully to the measurement of the form of cylindrical parts [1]. An extension of this technique for the measurement of absolute diameter by comparison with a calibrated artifact of similar diameter (typically within 4-10 μm) has been described previously [2]. This limitation is directly attributable to the 2π phase ambiguity inherent in this kind of measurement, and necessitates the use of a series of calibrated artifacts to cover a range of diameters. This paper describes a further extension that permits absolute diameter measurements over an extended dynamic range (over 25 mm with sub-micron resolution) using only one calibration master. Sources of measurement uncertainty are identified and discussed briefly. Results of absolute diameter measurement are compared with traditional two-point contact measurements and are observed to agree to better than ±0.1μm.

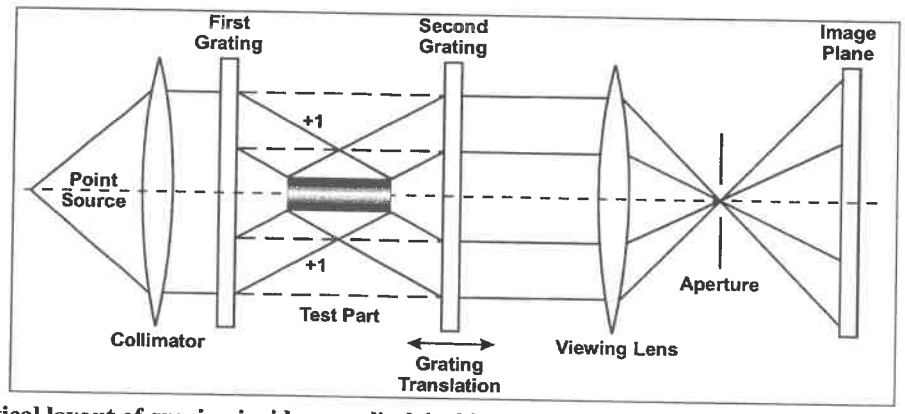

Figure 1: Optical layout of grazing incidence cylindrical interferometer

2.0 Principle of operation

Interferometric inspection of cylinders uses high precision diffractive optical elements to produce wavefronts which precisely match the surface of a perfect cylinder (see Figure 1). The first diffracted orders (+1 for OD parts and –1 for ID parts) from these circular diffractive elements produce a converging cone (diverging for ID parts) of light which strikes the part at grazing incidence. The zero order beam remains undeviated and provides the reference wavefront. The beam reflected from the part provides the test wavefront and interferes with the zero order diffracted beam at the second grating. The annular fringe pattern is imaged by a lens onto a CCD camera. An aperture located between the lens and the image plane is used to block unwanted diffracted orders. Deviations of the test cylinder from a perfect cylinder show up as phase differences in the interference pattern. Conventional phase measuring interferometry (PMI) is used to obtain accurate surface height data over the entire surface of the cylinder. The second grating is moved to modulate the fringes for PMI.

The deviations from a perfect cylinder are analyzed by fitting a series of orthogonal polynomials (Legendre-Fourier polynomials [3]) to the raw data. The constant term of this fit is referred to as the constant phase term or the 'piston' term, and is typically discarded. The higher order polynomial coefficients are representative of the magnitudes of the common form errors encountered in typical industrial parts. In contrast to traditional contact roundness gages, the non-contact/interferometric nature of this technique enables rapid measurement (less than 1 minute) of the entire surface of the cylinder.

3.0 Theory of absolute diameter measurement

Measurement of the absolute diameter of a cylinder is based on the observation that the constant or average phase ('piston') term is proportional to the diameter of the part. This term is typically discarded during a form

measurement as it contains no form information and is similar to radius suppression in traditional roundness measurement. The piston term is similar to the radius of a best fit cylinder fit to a cylindrical form data set. Figure 2 shows the dependence of the output of the interferometer on the diameter of the part. A change in the average diameter of the part results in a proportional change in the piston term. The constant of proportionality is known as the fringe sensitivity S and is the change in diameter corresponding to 2π radians (one fringe) of phase change. However, this variation is cyclical due to the fact that the interferometer ultimately measures the phase difference which is a periodic quantity with a period of 2π radians. This implies that two parts with diameters differing by a dimension corresponding to 2π radians of phase change, or one fringe, are indistinguishable. In other words, unless some method is available to determine the number of integral fringes between the two diameters, the diameter is known only to within the unambiguous range of one fringe. This phenomenon is referred to as phase ambiguity and is a drawback common to many forms of interferometry.

Differences in diameter may be tracked without ambiguity within 2π radians of phase change. This property may be exploited [2] to measure the diameter of a part by comparison to a calibrated master with the *a priori* restriction that the parts do not differ in diameter by more than one fringe (typically 4-10 μm).

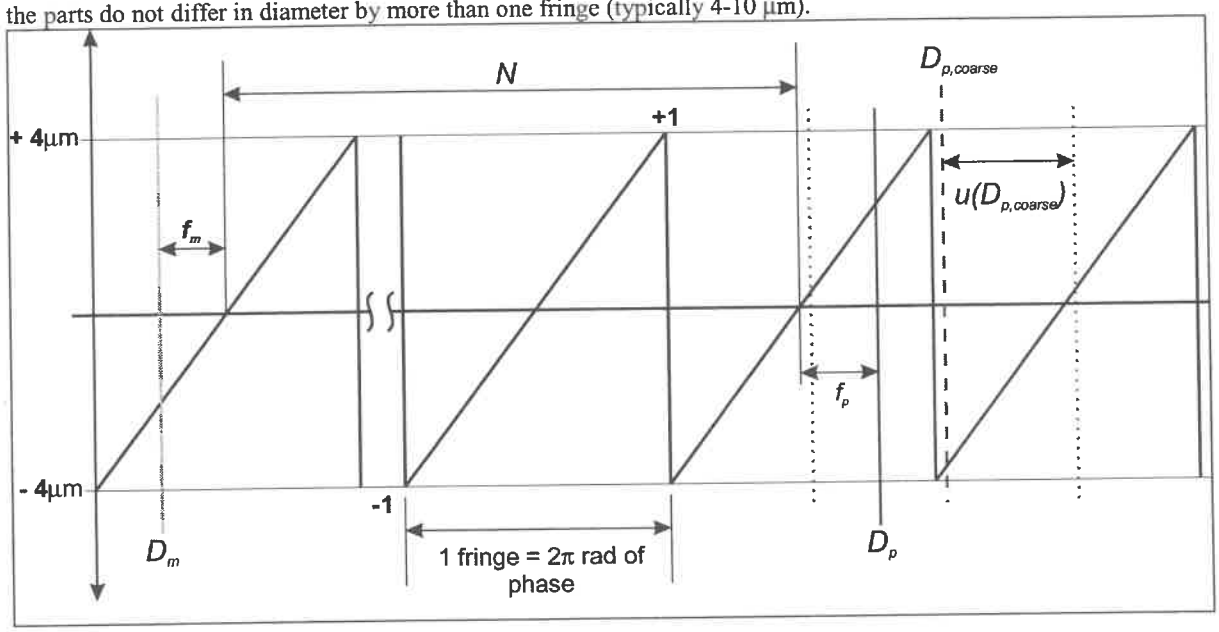

Figure 2: Principle of absolute diameter measurement

The measurement of parts that exhibit large differences in diameter (greater than one fringe) relative to the master requires resolution of the phase ambiguity. The principle of this measurement is illustrated in Figure 2. The measurement is a comparison measurement with the instrument zero being determined by the diameter of a calibrated master D_m. The number of integral fringes N, between the diameter of the master and test part may be determined from a relatively inaccurate estimate (hereafter referred to as the coarse measurement) $D_{p,coarse}$, of the diameter of the part under test, the sensitivity S, and the measured piston term for the master f_m. A refined estimate of the diameter of the test part may be obtained from

$$D_p = D_m + S(N + f_m + f_p) \tag{1}$$

where f_p is the measured piston term for the test part. In order to determine N without ambiguity, the uncertainty $u(D_{p,coarse})$ associated with the coarse measurement cannot exceed one half fringe. This is represented graphically in Figure 2 by the two dotted lines disposed in a symmetric fashion about the coarse estimate $D_{p,coarse}$. It can be shown that the sensitivity S is equal in magnitude to the pitch of the gratings or alternately, one fringe is equivalent to the grating pitch. It is significant to note that the sensitivity is independent of the wavelength of the source used to illuminate the part. The unambiguous range is then equal to the grating pitch and the maximum uncertainty of the coarse measurement is half the grating pitch. For a typical grating pitch of 8 μm, this imposes an accuracy requirement of ± 4 μm on the coarse measurement. For a typical part diameter of 25 mm, this represents a relatively trivial measurement with an instrument such as a micrometer. This requirement may be further relaxed by increasing

the grating pitch at the expense of the achievable resolution. This technique is essentially similar to the Method of Excess Fractions [4].

4.0 Measurement procedure

This technique is tested by measuring five XXX Grade steel gage pins ranging in size from 5 to 25 mm in diameter. All pins are approximately 50 mm long. The separation of the gratings remains unchanged during the measurement, except for the motion required to modulate the fringes for PMI. The measurement was made at a nominal air temperature of 20°C with the temperature of the air in the vicinity of the pin being measured and recorded as each pin was measured. A maximum change in temperature of approximately 0.2°C was recorded over the entire measurement period of approximately four hours.

The average diameter of each of the pins was determined by comparison to steel gage blocks. The measurement was made on a LVDT based comparator between a flat anvil and a spherical diamond stylus. The diameter of the pin was measured along two mutually orthogonal diameters at five equispaced sections along the pin. The measured values are corrected for the effects of temperature and Hertzian deformation. The average of these corrected measurements is considered to be the average diameter of the pin.

The zero reference is set by measuring the calibrated master and recording the piston term. The master is then replaced with the test part and a measurement is performed to obtain a piston term for the test part. The pins are aligned with the optical axis of the interferometer before each measurement. The piston term reported by the machine is used in the computation of the average diameter. In this particular case, the nominal size of the gage pins is used as the coarse estimate of the diameter as the tolerance requirements on the XXX pin ensure that the accuracy requirement on the coarse measurement is met. This estimate is used to determine the integral number of fringes between the master and the test part. This information is then combined according to Equation 1 with the piston terms obtained for the master and test to provide a refined measure of the average diameter of the part.

Table 1: Sources of uncertainty in absolute diameter measurement

S. No	Source of uncertainty	S. No	Source of uncertainty
1	Value of grating pitch	7	Error due to support plate
2	Size of master	8	Phase change upon reflection
3	Thermal effects on part size	9	Computation of constant phase term
4	Frequency stability of laser source	10	Evaluation of phase
5	Change in refractive index due to environmental factors	11	Tilt and decenter of the part
6	Change in grating separation	12	Wavefront aberrations

There are a number of sources of uncertainty in the measurement which are summarized in Table 1. The sources of uncertainty impact various aspects of the measurement. The uncertainty associated with the value of the grating pitch directly affects the gain of the measurement. The uncertainty in the size of the master is an uncertainty in the zero setting or offset of the instrument. Further, differences in temperature from 20°C result in uncertainties in the diameter of the part and master. The remaining terms are uncertainties in the measured piston term. They constitute sources of uncertainty which contribute a change in the measured phase not directly attributable to the average diameter of the part. Sources 3-4 contribute to the change in measured phase by virtue of the fact that the path lengths of the test and measurement beams are slightly different and are analogous to a unbalanced displacement measuring interferometer in this regard. The frequency stability of the source only affects the measured phase by virtue of this imbalance, but does not affect the sensitivity (unlike a displacement measuring interferometer). Changes in grating separation between successive measurements either due to thermal expansion or non-repeatability of the initial position of the moving grating during PMI affect the result through the path imbalance. The uncertainty due to phase change upon reflection is a subtle effect that stems from the fact that this phase change is variable and depends of the material and surface finish of the part. This results in a contribution to the measured piston term that is not related to the average diameter. This can be significant particularly when the master and test exhibit significantly different material and surface properties. There is also an uncertainty associated with the evaluation of the measured phase by PMI. Tilt and decenter of the part relative to the optical axis of the machine also have the potential to affect the average diameter value. Further, the system utilizes a high quality collimator to collimate the beam incident upon the grating. Any aberrations in the wavefront can also cause changes in the average phase as different portions of the grating/wavefront are utilized for measuring parts of different sizes.

5.0 Results of measurement and future work

The results of measurement are shown in Figure 3. Nine experimental runs are shown. The 5 mm pin has been chosen as the calibration master. In each run, the pins are measured in sequence from the smallest to the largest. A least squares line is fit to the diameters of the pins as measured by two-point contact measurement and as reported by the grazing incidence interferometer with a nominal grating pitch value of 8μm. The slope of this line is seen to deviate from unity by approximately 40 ppm. This suggests an uncertainty in the value of the grating pitch at the sub-nanometer level which is well within the uncertainty for this quantity. The grating pitch is adjusted by this amount to achieve unit slope. Figure 3 shows deviations from this line with unit slope. The maximum residual is observed to be approximately 0.12 μm. The maximum spread of the measurement is approximately 0.04 μm which is considerably lesser than the maximum deviation. These results should be viewed in the context of the uncertainty associated with the two-point contact measurement of the pins, which is represented by the error bars in the figure. The current best estimate of this uncertainty is 0.15 μm (k=2). This suggests that the uncertainty of the measurement is dominated by the uncertainty in the average diameter of the pins. No significant drift is seen in the measurement.

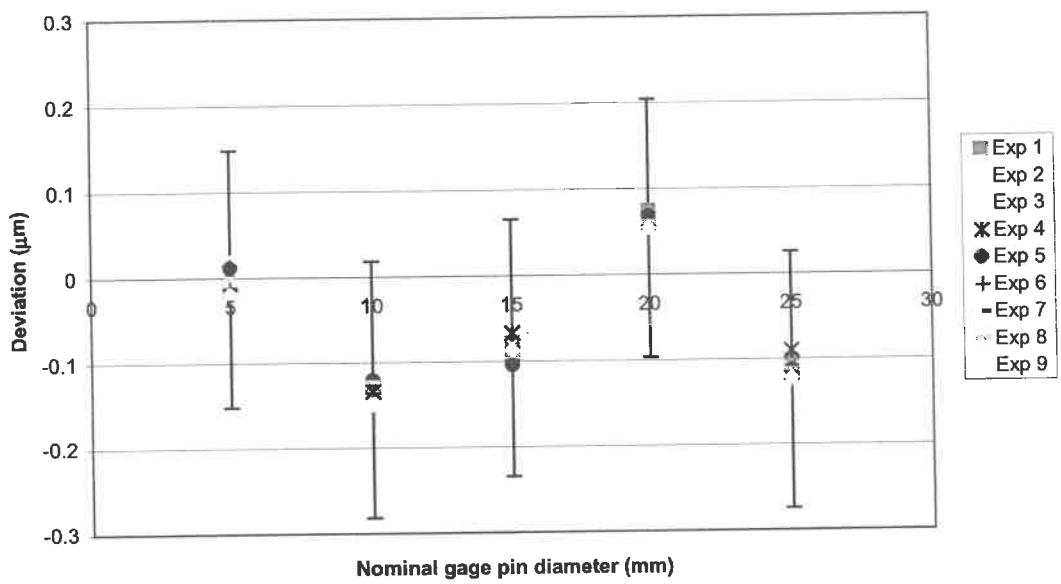

Figure 3: Results of absolute diameter measurement with 5mm pin as the calibrated master

Several additional investigations are currently underway. In order to further characterize the accuracy of this technique, better estimates of the pin diameters are required. An uncertainty statement for the measurement is currently under development. Possible systematic errors which provide opportunities for mapping are being investigated.

The measurement of absolute average diameter using a grazing incidence interferometer over large dynamic ranges has been demonstrated. The maximum observed error relative to the current best estimates of the average diameter from two-point contact measurement is 0.12 μm. Currently, the largest source of uncertainty is the size of the pins. This technique demonstrates the potential for the measurement of absolute diameter with sub-micron accuracies in conjunction with a form measurement over the entire surface of the cylinder under test.

References

1. Dresel, T., Schwider, J., Wehrhahn, A., and Babin, S., "Grazing incidence interferometry applied to the measurement of cylindrical surfaces," *Opt. Eng.* **34**, 3531-3535 (1995).
2. Kulawiec, A. W., Fleig, J. F., and Bruning, J. H., "Interferometric Measurement of Absolute Dimensions of Cylindrical Surfaces," *Proc. of the 12th ASPE Annual Meeting, Norfolk, VA,* 25-28 (1997).
3. Glenn, P., "Set of orthonormal surface error descriptors for near-cylindrical optics," *Opt. Eng.*, Vol. 23 No. 4, 384-390 (1984).
4. Born, M. and Wolf, E., *Principles of Optics*, Pergammon Press, 291(1964).

Development of 2D Angle Probe for Flatness Metrology of Large Silicon Wafer

Wei Gao [1], Edward T. Kanai [2], Peisen S. Huang [3], and Satoshi Kiyono [1]

[1] Department of Mechatronics and Precision Engineering, Tohoku University, Sendai, 980-8579 JAPAN
[2] Department of Mechanical Engineering, University of Washington, Seattle, WA 98195-2600, USA
[3] Department of Mechanical Engineering, SUNY at Stony Brook, Stony Brook, NY 11794-2300, USA

1. INTRODUCTION

Flatness is a critical parameter of silicon wafers for making integrated circuits, and measurement of wafer flatness is an essential process for both wafer manufactures and device manufacturers. Meanwhile, to make devices with improved functionality at a reduced cost, the design rule (width of the device pattern) has been becoming smaller and the silicon wafer size has been becoming larger. It is predicted that the design rule and wafer size will be 130nm, 300mm in 2002, and 35nm, 450mm in 2014, respectively [1]. This brings a big challenge to the metrology of wafer flatness. The site flatness of a wafer is required to be at the same level as the design rule, and the tolerance for the global flatness over the whole wafer is also very tight. To properly evaluate the flatness of such large wafers, improved metrology techniques with nanometric accuracy and high measurement speed must be developed.

In this project, we aim to develop a new scanning multi-probe system based on the concept of error separation [2], which can measure the flatness of 300mm and/or 400mm silicon wafers with high accuracy and high measurement speed. Two two-dimensional angle probes are used for error separation [3][4]. The probes detect the two-dimensional local surface slopes at two points on the wafer surface. The profile (flatness) of the wafer can be separated from the motion errors of the scanning stage (Z-directional error, pitching and rolling) by using the probe outputs. To realize nano-metrology of wafer flatness, two-dimensional angle probes with high resolution and high accuracy must be used. Since there are no commercially available angle probes that can detect the two-dimensional local slope of a surface, development of such probes is of high priority in this project.

In this paper, a prototype angle probe was designed and built. The probe utilizes the principle of autocollimation [5]. Different optical detection devices (photo-detectors) were used in the probe for the purpose of comparison. Principle and calibration results of the probe are reported.

2. PRINCIPLE OF 2D ANGLE PROBE

A two-dimensional (2D) angle probe is basically used for detecting the two-dimensional tilt of a surface as shown in Figure 1. Two-dimensional local slopes of the surface can also be detected by such a probe. The simplest way to construct a 2D angle probe is to utilize the method of optical lever. As can be seen in Figure 1, a laser beam is projected onto the sample surface. The optical spot of the reflected beam on a photo-detector with a distance L from the sample surface will move in the X and Y directions if the sample tilts around the X and Y axes. The two-dimensional components of the tilt $\Delta\alpha$ and $\Delta\beta$ can be calculated from the moving distances Δx and Δy of the spot on the photo-detector as follows:

$$\Delta\alpha = \Delta y / L \tag{1}$$

$$\Delta\beta = \Delta x / L \tag{2}$$

This method is simple but errors arise when distance L changes. In this study, we employ the technique of autocollimation to solve this problem. As shown in Figure 2, an objective lens is placed between the sample and the photo-detector. If the photo-detector is placed at the focal position of the lens, the relationship between the tilt and the readout of the photo-detector becomes:

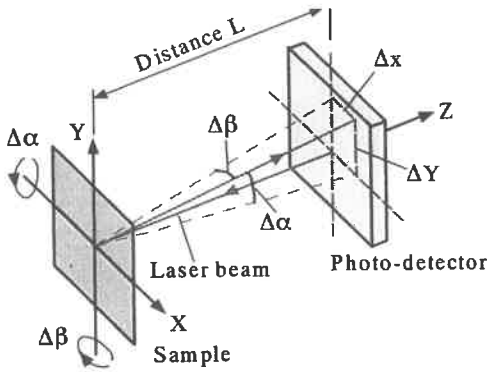

Figure 1 Two-dimensional tilt of a surface

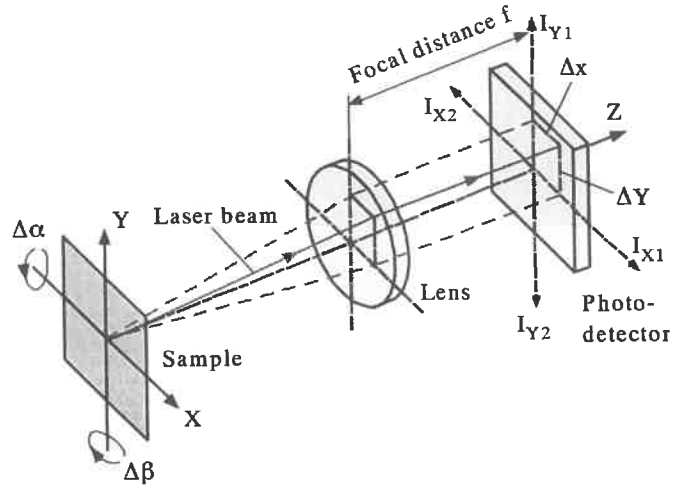

Figure 2 Detection of 2D tilt by autocollimation

$$\Delta\alpha = \Delta y / f \tag{3}$$

$$\Delta\beta = \Delta x / f \tag{4}$$

where f is the focal distance of the lens. As can be seen in Equations (3) and (4), the distance between the sample surface and the autocollimation unit consisting of the lens and the photo-detector does not affect the angle detection.

In the case of flatness metrology of silicon wafer, local slopes of the wafer surface are very small and the sensitivity of the angle probe is required to be very high. The sensitivity of the angle probe based on autocollimation can be improved by choosing a lens with a long focal distance. However, this will influence the compactness of the angle probe. In this paper, we discuss how to improve the sensitivity of the angle probe without increasing the focal distance of the lens by choosing proper photo-detectors.

The two-dimensional position sensing device (PSD) is widely used to detect the position of a light spot in two dimensions. PSDs have the advantage of good linearity. Position detection is also not affected by the intensity distribution of the light spot. Let the sensitive length of the PSD be L_P in both X and Y directions, the two-dimensional position can be calculated from the optical-electric currents I_{X1}, I_{X2}, I_{Y1}, and I_{Y2} through the following equations:

$$\Delta x = \frac{L_P}{2}\frac{(I_{X1} - I_{X2})}{(I_{X1} + I_{X2})} \tag{5}$$

$$\Delta y = \frac{L_P}{2}\frac{(I_{Y1} - I_{Y2})}{(I_{Y1} + I_{Y2})} \tag{6}$$

It can be seen that the sensitivity of a 2D PSD is mainly determined by the sensitive length. A PSD with short sensitive length is preferred for getting high sensitivity. A sensitive length of 0.1mm is proper for our purpose but commercially available PSDs typically have sensitive length of several millimeters. That means the required sensitivity of angle detection is difficult to achieve by choosing a PSD as the photo-detector. Another parameter to determine the sensitivity of a PSD is the noise current. The noise current level of a 2D PSD is several times larger than that of a one-dimensional (1D) PSD. From this point of view, it is easier to achieve higher sensitivity by using 1D PSDs. Figure 3 shows a 2D angle probe using two 1D PSDs. The sensitive directions of the PSDs are set along the X-axis and Y-axis, respectively.

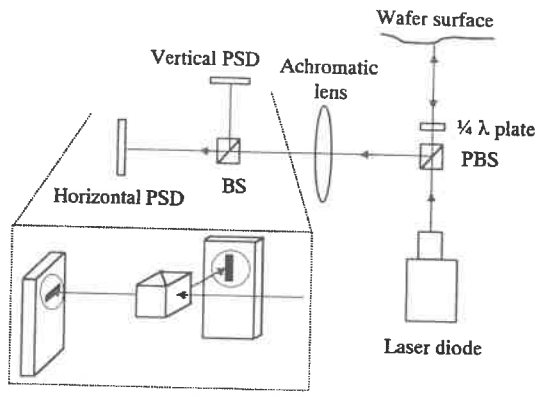

Figure 3 Two-dimensional angle probe using two one-dimensional PSDs

Another possible photo-detector is the quadrant photodiode (PD). As shown in Figure 4, a quadrant PD is placed at a position that is slightly apart from the focal point of the lens so that a light spot with a width of D_P is generated on the PD. For simplicity, the light spot is assumed to be rectangular. The two dimensional position of the light spot can be calculated by:

$$\Delta x = \frac{D_P}{2}\frac{(I_1 + I_4) - (I_2 + I_3)}{(I_1 + I_2 + I_3 + I_4)} \tag{7}$$

$$\Delta y = \frac{D_P}{2}\frac{(I_1 + I_2) - (I_3 + I_4)}{(I_1 + I_2 + I_3 + I_4)} \tag{8}$$

It can be seen that the sensitivity of the quadrant PD for position detection is mainly determined by the width of the light spot on the sensitive window of the PD. The width of the light spot can be changed to get a proper sensitivity of position detection by adjusting the position of the PD relative to the focal position of the lens along the optical axis of the autocollimation unit. Extremely high sensitivity can be achieved by using this technique.

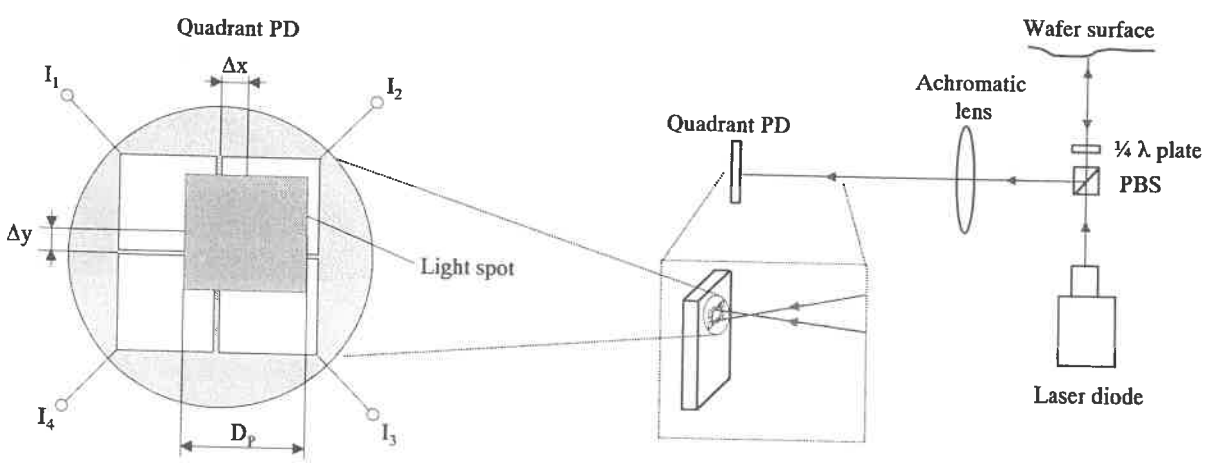

Figure 4 Two-dimensional angle probe using a quadrant PD

It should be pointed out that if the shape of the light spot is not rectangular but round, the relationships shown in Equations (7) and (8) will be nonlinear.

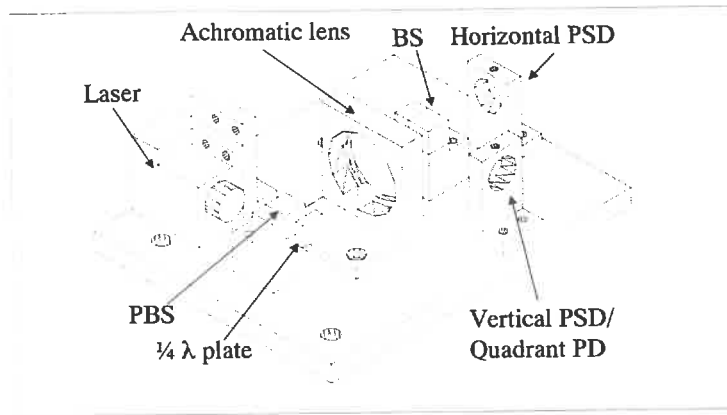

Figure 5 A prototype 2D angle probe

3. EXPERIMENTS

A prototype 2D angel probe was designed and built to investigate the basic characteristics of using different photo-detectors. Figure 5 shows a schematic view of the probe. Two one dimensional PSDs and a quadrant PD were used as the photo-detectors in the same probe for comparison. A laser diode was used as the optical source for compactness. The probe was designed to be within 90mm x 60mm x 20mm in size. An achromatic lens with a focal distance of 40mm was employed as the objective lens.

Figure 6 shows the result of calibration. The position of the PD was carefully adjusted to get high sensitivity of angle detection. It can be seen that the sensitivity of using quadrant PD is much higher than that of using PSD. The non-linearity of the PD output was caused by the round shape of the light spot.

4. CONCLUSIONS

A two-dimensional angle probe has been designed for measuring the flatness of large wafers. To improve the sensitivity of angle detection, the method of using two one-dimensional PSDs, and that of using a single quadrant PD as the photo-detectors have been theoretically discussed and experimentally investigated. It has been confirmed that the method of using a quadrant PD could reach higher sensitivity.

ACKNOWLEDGMENTS

This project is conducted under a JSPS Grant-in-Aid for Scientific Research (No.12555032). It is also supported by a NSF/JSPS Joint Research Grant.

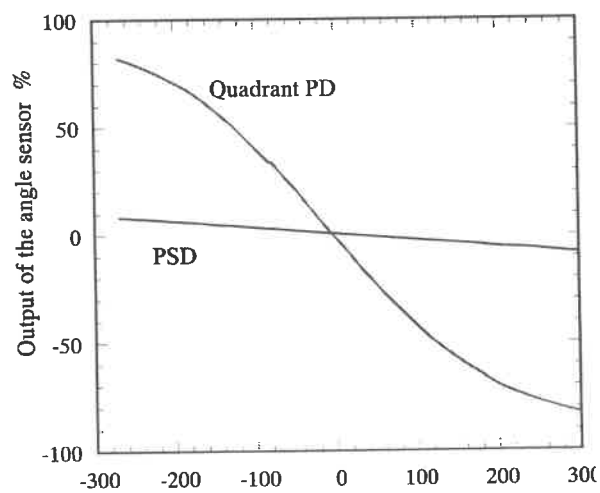

Figure 6 Calibration result

REFERENCES:

[1] International SEMATECH: International Technique Roadmap for Semiconductors: 1999 edition.

[2] D. J. Whitehouse: Some theoretical aspects of error separation techniques in surface metrology, J Phys E: Sci Instrum, 9, (1976), 531-536,

[3] W.Gao, et al.: Measurement and control of rolling of precision stage, Prof. of 1997 IEEE Int. Conf. on Intelligent Processing Systems, Beijing, (1997), 70-74.

[4] S. Kiyono, et al: A differential laser autocollimation probe for on-machine measurement, Precision Engineering, 15-2, (1993), 68-76.

[5] A.E.Ennos and M.S.Virdee: High accuracy profile measurement of quasi-conical mirror surfaces by laser autocollimation, Precision Engineering, 4-1, (1982), 5-8.

Optical Reference Profilometer with Improved Thermal Stability

Stephan R. Clark, John E. Greivenkamp, Ralph M. Richard, José M. Sasián
Optical Sciences Center, University of Arizona, Tucson, AZ 85721
Voice: (520)-626-5410, Fax: (520)-621-9691
Src@u.arizona.edu

The optical reference profilometer (1) utilizes a $\lambda/20$ reference mirror and a metrology frame to create, what is essentially a contact Fizeau interferometer. A Fizeau interferometer measures height deviations of the part under test from a reference surface. In interferometry, this deviation is measured in fringes. Instead of using fringes, the optical reference profilometer uses a laser distance measuring interferometer coupled with an air-bearing stylus to provide the deviation measurement from the reference flat. The separation between the part under test and the reference must be constant during the measurement. In order to maintain a constant separation, a metrology/metering frame is used. The basic metrology frame connects the part and the reference flat, and it consists of three super-invar rods, a super-invar base plate. The optical reference is mounted on top of the three rods with the optical surface facing down toward the test part. This frame is placed kinematically on top of an x-y roller-bearing translation stage, which moves the frame and test part under the air-bearing stylus assembly.

The benefits of this system are discussed in more detail in a previous paper (1), so only a short summary of these benefits will be given here. The main benefit of this design is the de-coupling of the z-axis motion of the stage from the part-reference separation. The measurement of any point on the test piece is the relative distance between the part and the optical reference. This distance is held constant by the three metering rods. Any z-axis motion errors of the stage cannot change this distance; therefore the measurement is insensitive to this error. This feature enables the use of a roller-bearing stage instead of a more expensive air-bearing stage.

The second benefit of this design comes from the mechanical separation of the stylus assembly from the metrology frame. Because the stylus rests (approx. weight 0.1g) on top of the part being measured, only the relative distance from the part to the reference flat is measured. This makes it possible to use an aluminum bridge to hold the stylus assembly instead of an athermalized support structure.

In an attempt to increase the long-term stability of the previously described system (1), a series of mechanical upgrades have been implemented. The data measurements taken by the first generation system were over a short time period and on low slope parts, so thermal expansion errors in the x and y positions were not significant. However, for longer runs (3-5 hours for example) this expansion can have a very large effect. The second-generation machine reduces these effects by adding a special metering rod network to couple the lateral positioning interferometers, used to monitor the x and y positions of the test part, to a defined test part center. This network also helps reduce deadpath errors and overall air path lengths because the cube interferometers for the DMI can now be placed closer to their respective stage mirrors. The metering rod network references the x and y positions on the part relative to the system center reducing the thermal sensitivity of the part position. Because the stylus assembly is mechanically

independent from the frame-stage combination, it is possible for the location of the center of the stylus to shift in x or y from the system center during a measurement cycle. Therefore, it is necessary to monitor the x and y position of the stylus assembly relative to the system center. The stylus position is also referenced via this metering rod network. This makes it possible to correct for any lateral position shifts the stylus may experience.

The addition of the stylus position monitoring system is still in the development stages; therefore the results presented will be made with the x-y lateral positioning reference structure only. The stylus position monitoring system presented will contain theoretical effects on the measurement accuracy of the system.

References

[1] S. Clark, M. North-Morris, J. Greivenkamp, " Stylus Profilometer with an Optical Reference", in *Optical Fabrication and Testing Technical Digest*,OSA, 1998, vol. 12, p 155-156.

Keywords: Metrology Instrumentation, Surface Figure Measurements

The Micro diamond cutting of steel using Electrolysis

Jung Hwan Ahn, Pusan National University, School of Mech. Engineering
Han Seok Lim, Pusan National University, RIMT
Seong Min Son, Pusan National University, Dept. of Mechanical and Intelligent Systems Eng.
Mount. 30, ChangJeon-Dong, KeumJeong-Ku
Pusan 609-735, KOREA
Business Phone: 82-51-510-2333, Fax: 82-51-514-0685, email: semson@hyowon.pusan.ac.kr

This paper presents a new method that cut steel with diamond tool using electrolysis. The cutting with diamond tool is one of the most important technologies to manufacture precision parts. There are many various applications in the fields of product of optical, electric, and electronic parts such as magnetic disk, polygon mirror, spherical non-spherical mirror and copier drum, etc.

It is merit to cut a high sharp and precision shape with diamond tool, because it is possible to make edge radius of tool very sharpness. However, conventional diamond cutting method cannot be applied to steel cutting, because there is a excessive wear of the diamond tool due to high chemical activity with iron in high temperature.

So, we intend to apply electrolysis to micro diamond cutting. The basic principle of the cutting method is as follows. The steel workpiece is oxidized continuously by electrolysis in cutting process and the diamond tool cut the layer. The oxidized layer grows along the previous formed shape. We can get the desired shape by the repeats of this work. It is possible to expect the reduction of cutting force, because the diamond tool removes only the weak area by electrolysis. And the reduction of cutting force suppresses excessive wear of diamond tool due to chemical activity with steel. In a simple preparation experiment, the diamond tool maintained the sharpness of tool edge after cut ten 0.3/0.5mm groove on steel(20mm in diameter) with 3 /5micron depth of cut, 1000 rpm of cutting speed.

Key Words: Diamond Tool, Electrolysis

3-DIMENSIONAL MACHINING OF OPTICAL QUALITY SURFACES

Matthew A. Cerniway, Thomas A. Dow
North Carolina State University, Raleigh, NC

INTRODUCTION

Primary techniques for the production of optical quality surface finishes are turning and ruling. A third technique, milling, has been excluded from mass production due to the complexity of the machinery required to produce 3-dimensional (3-D) shapes and the increased machining time required to achieve finishes equivalent to other techniques. The research reported here focuses on the feasibility of a production technique utilizing stacked piezoelectric actuators to move the tool relative to the workpiece. The stiffness of the actuators and the ability to control their position at high speed and high resolution provide the capability to produce optical finishes and reduce the manufacturing time necessary to create complex amorphous contours.

Mounted on a Nanoform 600, a piezoelectrically actuated linear mill, called the UltraMill (UM), becomes capable of true 3-axis machining. Conventional milling encounters problems with varying angular cutting speeds during the machining of spherical contours, while the UM has the ability to uncouple the relative speed of the work piece and the tool. In addition, the UM has the potential to operate at speeds that are an order of magnitude higher than present day spindles. Equating the cutting frequency of the UM to its rotary counter part, an operating frequency of 17 kHz is equivalent to 1 million rpm.

The current effort involves a study of the unique cutting dynamics of the piezoelectrically actuated linkage system, evaluating the operational envelope of its 3-dimensional cutting ability and the UM's use in diamond milling of traditionally non-diamond tool capable materials, i.e. ferrous metals or ceramics.

DESIGN

Theory of Motion

The elliptical tool path produced by the geometry in Figure 1 is the result of two principles: first, the summation of two orthogonal sine waves will produce a circular path; and two, the strain of piezoelectric ceramics is a linear function of the voltage supplied. Two actuators support the tool and their motion makes it rotate and translate in the plane of the paper to produce the path shown. By changing the length of a, b and c, the shape of the path can be changed from circular to elliptical as shown on the left hand side of Figure 1.

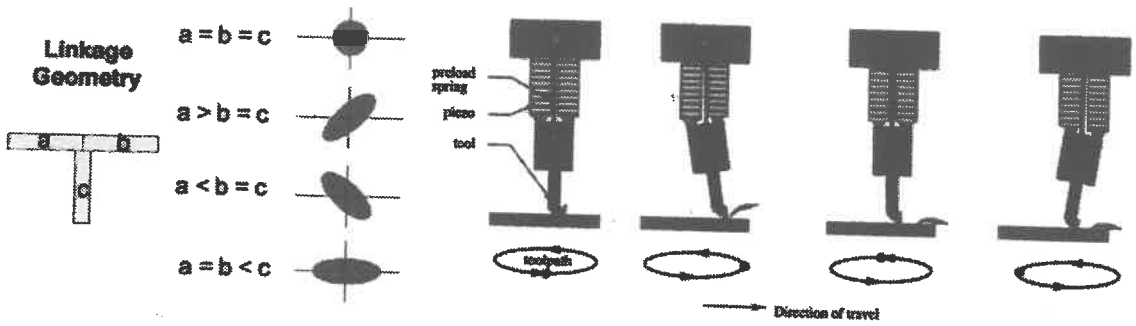

Figure 1. UltraMill Cutting Motion via Linkage Geometry

Advantages of Motion

The peak-to-valley (P-V) surface finish of an elliptically driven tool is:

$$\text{UM Elliptical: } P-V = \frac{bf^2}{8a^2} \qquad \text{Circular: } P-V = \frac{f^2}{8R}$$

where f is the distance indexed per cycle and a and b are the respective major and minor axes of the ellipse. If a and b are equal, the path becomes circular and the equation reduces to the "circular" P-V expression (note: R is the radius of the circular motion). A large major to minor axis ratio would result in reduced P-V surface roughness. The surface finish can also be improved by increasing the apparent tool rotation (operating frequency), increasing the radius of motion or reducing forward speed of the tool.

Another advantage of the UM is the ability to uncouple the relative speed of the work piece and tool. For a turning operation, the surface speed of the tool decreases as it approaches the center of the part. For a rotating tool, the surface speed changes with the contact point on the flute of the tool. Varying cutting speeds over the surface of the part produces less than optimal results. With the constant cutting velocity of the UM, 3-D optical quality surfaces are now possible.

Recent findings also show an elliptical tool path reduces the cutting forces from a third to a half and nearly eliminates thrust forces [1]. In addition, surface roughness is reduced by up to 3.5 times over standard milling. Finally, a strong correlation exists between the diamond tool wear and the effective contact time of the tool and part associated with the elliptical cutting motion [2]. This reduced wear suggests that diamond machining of ferrous metals may be possible since chemical wear of the diamond tool is reduced.

EXPERIMENTAL APPARATUS

Design of Prototype

A prototype constructed at the PEC produces an elliptical tool path with a major to minor axis ratio of 9.4:1. This device, illustrated in Figure 2, consists of two 25 mm, high-voltage piezoelectric stacks each having a longitudinal displacement of 20 µm. Path motion was verified using a dual-channel fiber-optic displacement-measuring gauge (Opto-Acoustics® Angstrom

Resolver®) capable of sub-µm detection and evaluations of cutting trial specimens using a white light interferometer (Zygo® New View®). Figure 2 shows a sketch of the structure on the right along with details of the operating features on the left. The components include a cutter head that holds the diamond tool, the two piezoelectric stacks and the cam-loaded wire for preloading the actuators to prevent tensile loading.

Bandwidth: DC – 400 Hz (0 – 18000 rpm equivalent)
1st Natural Frequency: ~500 Hz
Piezo Material: PZWT100 (Kinetic Ceramics, Inc.)
- Modulus of Elasticity: ~3000 ksi
- Elongation: ~ 0.1% of Overall Stack Length
- Density: 7.75 gm/cm^3
- Active System Mass: 17.854 gm

Elliptical Tool Path:
- Major Axis: 89.8917 µm
- Minor Axis: 9.6154 µm

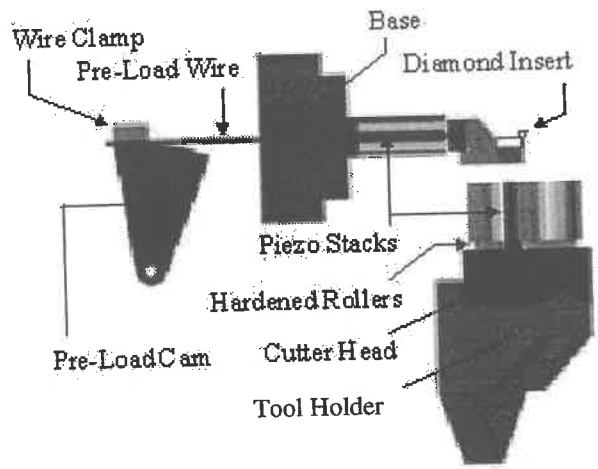

Figure 2. Main Components of UltraMill

Cutting Experiments

Initial cutting experiments have been directed towards understanding the cutting dynamics. Mounting a series 1100 aluminum blank on an ASG-2500 Diamond Turning Machine, three types of test have been conducted. The first was to measure the tool path and any resulting inlet and/or outlet effects with a series of plunge cuts. The second type of test consisted of machining flat optical surfaces. The third test involved surface texturing and surface pattern creation on the µm to nm level was investigated; that is, creating constant depth and spaced surface features on mold masters as might be used for injection molding of anti-glare plastic surfaces.

RESULTS

UM Frequency	= 300 Hz
Cross Feed Rate	= 0.1 mm/min
Spindle Speed	= 1 rpm
Surface Rough (rms)	= 20 nm
Diamond Radius	= 1.02 mm
Part Radius	= 22.58 mm

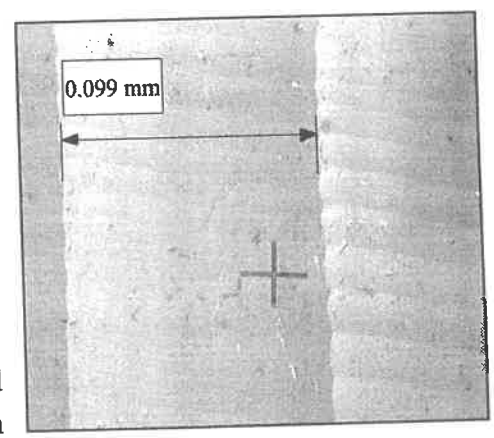

Figure 3. Turning with UltraMill

Figure 3 shows a micrograph of a flat surface machined with the UM. The cross feed rate and spindle speed shown should produce cusps with the 0.1 mm spacing shown. The features in the vertical direction are a result of the motion of the UM. Note that these features are not exactly aligned with the tool

motion meaning that the tool face is not exactly perpendicular in the cutting direction. However, the surface finish is excellent and indicates optical quality surfaces are possible.

CONCLUSIONS AND FUTURE WORK

Analysis of the cutting dynamics through both simulated and actual cutting experiments has established control parameters for the precise control of the UM. The UM has been used to machine flat and textured surfaces with RMS surface finishes ranging from 6 to 25 nm. The knowledge obtained in these initial tests also forms the foundation from which to expand the systems capabilities to the ultimate goal of radically contoured surface production.

A compact, high-speed (> 8 kHz) version of the UltraMill is under development. Once completed it will replace the low-speed version for use in the 3-D cutting trials. These experiments will also examine the feasibility of milling different materials such as plastics, infrared optical materials and ferrous metals.

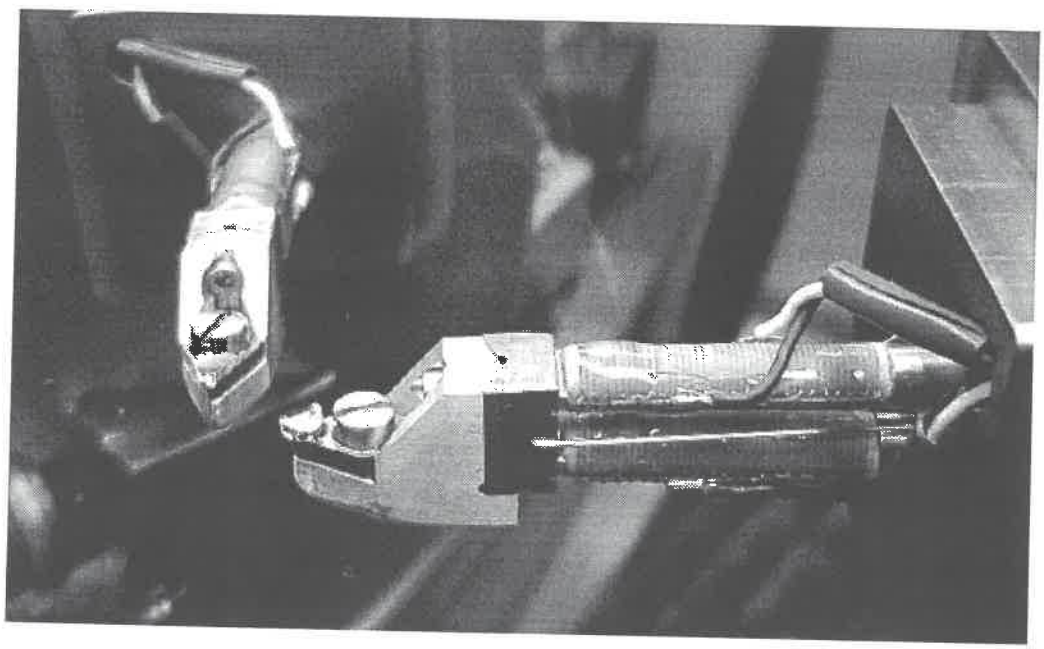

Figure 4. Photograph of UM (cover removed) reflected in machined aluminum sphere.

REFERENCES

1. Ahn, Jung-Hwan, et.al., "Improvement of Micro-machining Accuracy by 2-Dimensional Vibration Cutting," ASPE 1999 Annual Meeting, Vol. 20, pp 150-153, 1999.
2. Brinksmeier, E. and Glabe, R., "Elliptical Vibration Cutting of Steel with Diamond Tools," ASPE 1999 Annual Meeting, Vol. 20, pp 163-166, 1999.

Which of the material properties dominates surface roughness of diamond turned plastics

Ken'ichiro Horio, Masaru Nabeshima
Mechanical Engineering Department, Saitama University
255 Shimo-okubo, Urawa, Saitama 3388570, JAPAN

1. Introduction

Plastics are very useful materials as their specific gravity is small and as we can design and adjust desirable property of the material to some extent. If you intend to use the plastics to micro parts or fine parts, high accuracy or small surface roughness is needed. To attain these, diamond turning is a possible candidate by economical or engineering point of view. But there are a lot of kinds of plastics and it is thought that attainable surface roughness depends on the kind of plastics. That sort of application has already been popular in optical fields. For example, material of eyeglasses has changed from glass to plastics. Contact lenses are plastics machined with diamond turning. Much more applications of changing from metal or other to plastics are expected. However machinability, especially micro-machinability of the plastics has not been revealed yet, though most plastics are so softer than metals or ceramics

This study is concerned with the question that which of the material property of plastics have effect to the attainable surface roughness.

2. Experiments

This study was performed experimentally. Table 1 shows experimental conditions. Cutting tests with round nose diamond tool were conducted. We used the apparatus of fly cutting method. Five kinds of plastics were evaluated. Those were, polycarbonates (PC), polystyrene (PS), polymethylmethacrylate (PMMA), polyamide 6 (PA) and high-density polyethylene (HDPE). In the cutting tests both a new (sharp) tool and an old (dull) tool were used, and both feed rate and depth of cut were altered. ZYGO New View 100, an optical surface profiler, evaluated the surface

Table 1 Experimental condition

Material	Polycarbonates, PC Polystyrene, PS Polymethylmethacrylate, PMMA Polyamide6, PA High density polyethylene, HDPE
Tool	Single crystalline diamond (Nose radius=5mm) Sharp tool / Worn tool
Depth of cut	2--40 μm
Feed rate	2--80 μm/rev
Cutting speed	600m/min
Cutting method	Fly cutting
Coolant	Nothing / Dry air

roughness and an optical microscope observed the surface.

From the experimental result for diamond turned plastics, the depth of cut did not affect their surface roughness. On the contrary, it was proven that the feed rate influenced for the surface roughness, especially in PS as shown in Fig.1. It is clear, because the theoretical roughness is defined by nose radius of tool and the feed rate.

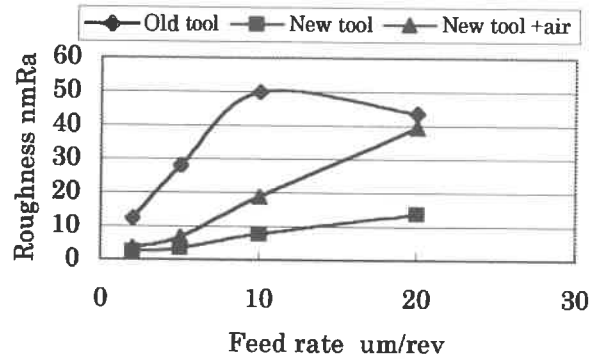

Fig.1 Influence of feed rate to surface roughness in diamond turning of PS

3. The factor that seems to affect the surface roughness.

Next four is mentioned as the factor, which seems to affect the surface roughness in ultra-precision cutting of the plastics.

(a) Condition of tool edge

It is good the result which there are no chipping and abrasion at the edge of the tool in order to prove from the experimental result. As the plastic is fundamentally a soft material, and it can be easily influenced by condition of the tool edge, it seems to obtain the good surface roughness by carrying out the cutting by choosing thing of which the condition of the edge is good as much as possible.

(b) Feed rate

As mentioned above, small feed rate tends to get good surface. Though actual roughness values are more than that of theoretical ones, it happened that smaller the feed rate is more smooth the surface becomes. However once it becomes too small as 2 μm/rev, the surface cannot improve at all.

(c) Tensile strength

Generally speaking tensile strength of a material is a primary factor of the surface roughness at metal cutting, because the yield shearing stress is correlated to the tensile strength. When the tensile strength is high, it is thought that the surface roughness on a machined surface is bad because large shear stress is needed to remove the material.

Fig.2 shows the relation between the tensile strength of each material and the surface roughness on same experimental conditions. Since it becomes the right riser almost, it is proven that there is to some extent correlation between the tensile strength and the surface roughness on the graph, if HDPE is removed in this figure. Though HDPE was cut from the reason that tensile strength was small in this study, experimental result is different from expected one.

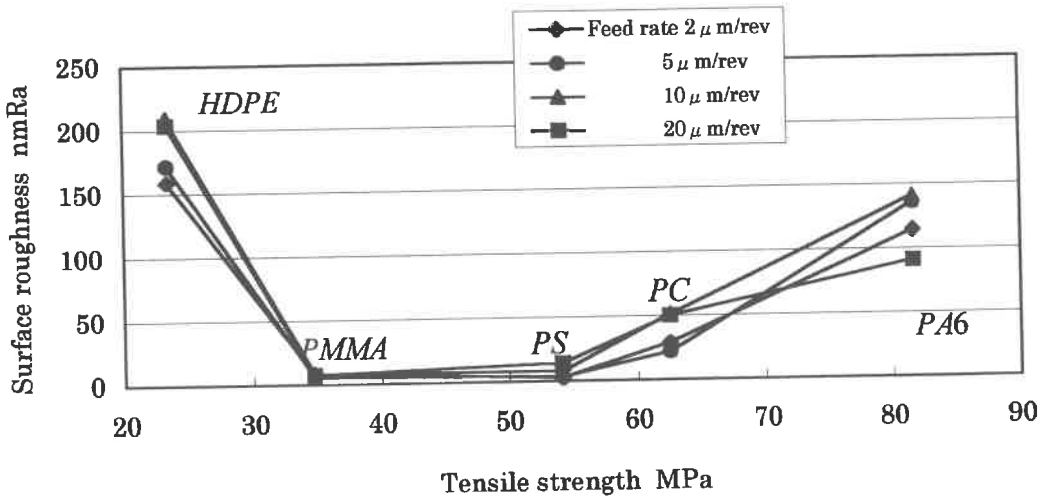

Fig.2 Relation between tensile strength and surface roughness of plastics

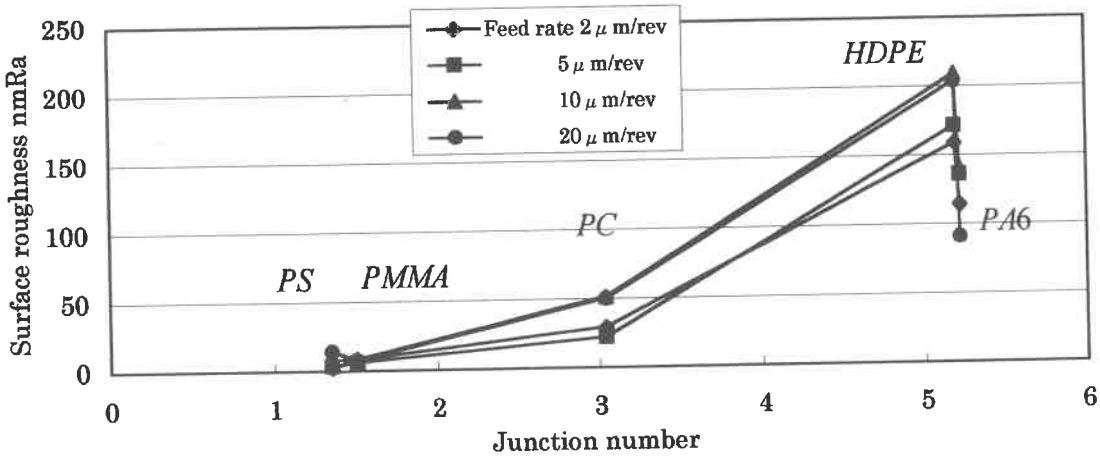

Fig.3 Relation between junction number and surface roughness of plastics

(d) Degree of crystallization (Junction number)

Fig.3 shows the relation between junction number of the materials and the surface roughness. The graph shows the tendency that is almost fixed with the right riser, and the relationship between the junction numbers seems to influence it than the relationship between tensile strength and surface roughness of machined surface.

The junction number is defined to a number of molecular chain per unit cross section in a material. The number is related to degree of crystallization, which is a proportion of crystallized parts in the material. Actually at PS, PMMA or PVC (polyvinyl chloride) it all consists of the amorphous region and PC slightly has the crystal region, and PA, PP (polypropylene), PE and so on

have much more regions. It is considered that this fact agrees with the experimental result and that the degree of crystallization affects the surface roughness.

4. Discussion

The plastic is the giant molecule structurally cohering in secondary coupling force based on van der Waals force among molecular chains as an essential point unlike the metal. The microscopic mechanism of the plastic destruction was considered as follows.

(1) It becomes an unequal distribution from the viewpoint of the molecular level, when it applied even in on the macroscopically uniform external force. The force works to not only interatomic coupling in molecular chain but also the secondary coupling.

(2) Extended coupling is cut off, when the external force is increased. Though the coupling of the circumference shoulders the loss to some extent, the cutting similarly continues.

(3) A micro crack is generated after the cutting of the coupling is accumulated. Such micro cracks arise in here and there on the workpiece. The micro crack becomes macroscopic crack by accumulating or combining.

(4) With cutting the secondary coupling where the resistance is less than the first coupling, the macroscopic crack grows and brings about the last destruction.

On this sequence, the destruction of plastic is mainly upon the secondary coupling part, and a part of destruction of the primary coupling seems to contribute less.

5. Conclusion

The derived conclusions from this study are as follows.

(1) Degree of crystallization of the material shows a good correlation to the generated surface roughness. As the junction number is a scale of the degree of crystallization, if the junction number is low, the surface roughness of the diamond turned one is expected to good surface.

(2) In four materials except HDPE good correlation between the tensile strength and the surface roughness is shown. HDPE's surface roughness is the worst during five kinds of plastics though the tensile strength of that is the lowest.

(3) Good surface roughness is obtained by using a good conditioned, that is new and sharp tool.

(4) Lower the feed rate is, better the surface roughness is. The feed rate is more effective to the surface roughness than the depth of cut.

(5) Polystyrene is the most sensitive to effect of the factors to the surface roughness. The best result within our experiments of 2.3nmRa (average roughness) was obtained using new tool, 5μm feed rate and 2μm depth of cut.

(6) The experimental factors are not susceptive when PMMA is machined. The surface roughness is roughly good. You can get a good surface steadily when using PMMA.

An Optimization of Geometries of Ball-End Mill for High Speed Machining

Nam-Kyu Kim and Sung-Chong Chung

MAnufacturing Systems & Control LABoratory
School of Mechanical Engineering
Hanyang University, Haengdang Dong 17, Sungdong Gu, Seoul 133-791, KOREA

Abstract : In this paper, the geometries of ball-end mill are developed mathematically and simulated. The cutting coefficients for the prediction of the cutting forces are acquired by two-dimensional orthogonal cutting experiments of SKD11. Through the geometric and cutting force model, geometric optimal solutions of ball-end mill that can minimize the stress of the tip at the cutting edge and the total cutting force in the tool, are searched by the genetic algorithm. A stress analysis at cutting edge is the basis of designing cutting edge geometry and the results play an important role over the tool life and the cutting forces of ball-end milling. After optimizing ball-end mill geometries, the cutting forces are compared with a conventional un-optimized ball-end mill.

Keywords : High Speed Machining, Ball-End Mill, Optimization, Genetic Algorithm, Helix Angle, Rake Angle, Relief Angle, Cutting Forces

1. Introduction

The high speed machining(HSM) is one of the most effective way to improve the machining accuracy and productivity of fabricating dies and moulds. Previous cutting methods are based on deep cutting and low speed feeding condition. The HSM, however, is based on shallow cutting and high speed feeding conditions. This reduces the burden on the cutting edge of the tool, which prolongs the tool life and realizes the high quality surface finishes. The essential conditions for realizing the HSM are the use of high speed spindle, a cutting tool for high cutting speed and dynamically well balanced tool attachment system. Cutting tools for the HSM require high rigidity during high speed rotating, good dynamical balance and good wear characteristics.

As a tool for the HSM of sculptured surfaces of difficult-to-cut workpiece, the ball-end mill is extensively used. There have been significant researches reported in modeling mechanics of helical flat-end milling, but little work has been done on the mechanics of ball-end milling. Since the geometries of ball-end mill are so complicated, many researchers have studied geometries and cutting mechanics. The geometric parameters of ball-end mill, i.e., relief angle, helix angle, rake angle and cutting speeds vary along helical flutes. Also, for the different geometric parameters, the cutting coefficients, i.e., shear, friction angle, etc., vary along helical flutes. Because cutting forces during ball-end milling influence the deflection the tool and surface finishes of products, its prediction is important. Over different geometries and material of ball-end mill, the cutting forces show different values. Consequently, the mechanistic model requires large amount of cutting tests and acute mathematical models, and can be applicable to just a particular workpiece material-cutter only. If the cutting force can be predicted accurately and reduced by the optimized ball-end mill, the productivity of fabricating dies and moulds will be increased.

In this paper, the geometries of ball-end mill are representated mathematically and simulated. The cutting force coefficients are acquired by two-dimensional orthogonal turning experiments with SKD11 that is the material for the pipe form and heat-treated to HRC40. Then the results are used for the prediction of cutting forces of ball-end mill. Through the geometric and the cutting force models, geometric optimal parameters of ball-end mill that can minimize the stress of cutting edge and the total cutting force in the tool, are searched by the genetic algorithm. A stress analysis of the tool tip at the cutting edge is the basis of designing cutting edge geometry and the results affect tool wear and cutting forces of ball-end milling. After optimizing ball-end mill geometries, the cutting forces compared with a conventional un-optimized ball-end mill.

2. Orthogonal cutting force coefficients

In this section, in order to predict cutting forces of ball-end milling, the cutting force coefficients are

acquired by two-dimensional orthogonal turning experiments with SKD11.

In general, an elemental cutting edge of ball-end mill can assume an oblique cutting edge. And the oblique cutting process can be analyzed as an orthogonal cutting process in the plane containing the cutting velocity vector and the chip flow direction vector. Fig. 1 is a graphical representation of chip geometry and a relationship of cutting forces for orthogonal cutting. In Fig. 1, the cutting force F_p and thrust force F_q are defined in equation (1).

$$F_p = \frac{\cos(\beta-\gamma_o)}{\cos(\phi_o+\beta-\gamma_o)}\frac{\tau_s bh}{\sin(\phi_o)}$$
$$F_q = \frac{\sin(\beta-\gamma_o)}{\cos(\phi_o+\beta-\gamma_o)}\frac{\tau_s bh}{\sin(\phi_o)} \quad (1)$$

Where ϕ_o : orthogonal shear plane angle
τ_s : shear stress, β : friction angle, γ_o : rake angle
b : width of cut, h : uncut chip thickness

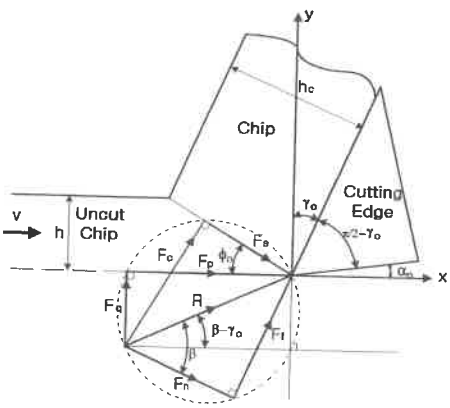

Fig. 1 Chip Geometry and relationship of cutting forces for orthogonal cutting

Tungsten carbide(WC) cutting tools with four kinds of rake angles for orthogonal cutting experiments are coated TiAlN. The depth of cut is from 0.06 to 0.15 (mm) and spindle rotational speed is from 85 to 440 (rpm). Fig. 2 is an aspect of orthogonal cutting experiment.

The cutting ratio r, which is used to determine orthogonal shear angle ϕ_o, can be calculated by measuring a cut chip thickness with micrometer. The orthogonal shear angle ϕ_o and the cutting ratio r are expressed in equation (2) and (3).

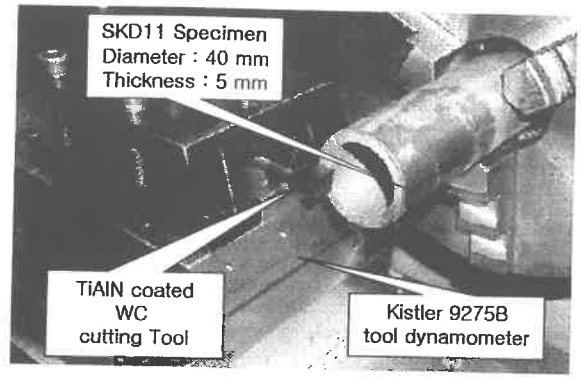

Fig. 2 Orthogonal cutting experiment

$$\phi_o = \tan^{-1}\left(\frac{r\cos(\gamma_o)}{1-r\sin(\gamma_o)}\right) \quad (2)$$

$$r = c_1 t^{c_2}$$
$$c_1 = 49.826\, V^{-0.76} f_r^{0.36} + 4.66\gamma_o + 10.0 \quad (3)$$
$$c_2 = 19.12\, V^{-0.33} f_r^{1.33} + 0.16\gamma_o + 1.12$$

Where, t : uncut chip thickness
V : cutting velocity (m/min)
f_r : feedrate (mm/min)

Equation(4) expresses the friction angle β and average shear stress τ_s is equation(5).

$$\beta = 47.60\, V^{-3.33} f_r^{-0.66} + 1.28\gamma_o + 0.6381 \quad (4)$$
$$\tau_s = 1144.20\ MPa \quad (5)$$

3. Ball-end mill geometries and cutting force model

In order to analyze cutting forces of ball-end mill, the geometric definition and the calculation of uncut chip thickness are required. Fig. 3 depicts the radial uncut chip thickness of ball-end mill on the z_j location in the axial direction from the tip of the ball. The point O_1 is the present center of rotating end mill and O_2 is previous one. Therefore, the uncut chip thickness $t(\theta_{ij})$ is the value which subtracts $D(\theta_{ij})$, the length of $\overline{O_1P_1}$, from the local radius $R(z_j)$.

$$t(\theta_{ij}) = R(z_j) - D(\theta_{ij}) \quad (6)$$

$$R(z_j) = \sqrt{R^2 - z_j^2} \quad (7)$$

$$D(\theta_{ij}) = -f_r \sin\theta_{ij} + \sqrt{R(z_j)^2 - (1-\sin^2\theta_{ij}) f_r^2} \quad (8)$$

Where, i : index number of cutting edge
j : location in the axial direction, R : ball radius

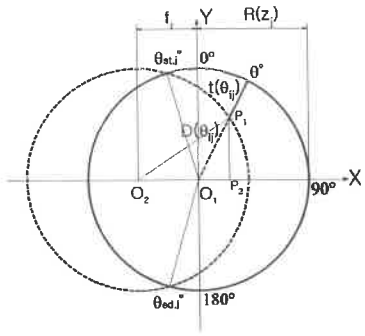

Fig. 3 Radial uncut chip thickness

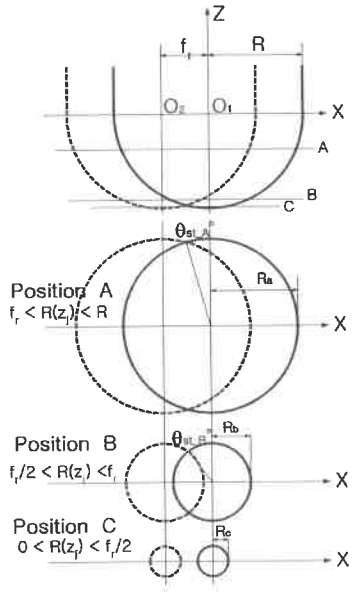

Fig. 4 The start and end cutting point along axial location

The start and end cutting point is expressed by

$$\theta_{st,j} = -\sin^{-1}\left(-\frac{f_r}{2R(z_j)}\right) \quad , \quad \theta_{ed,j} = \sin^{-1}\left(-\frac{f_r}{2R(z_j)}\right) + \pi \qquad (9)$$

The local helix angle $\lambda_{sj}(z_j)$ varies along the location of elemental cutting edge.

$$\lambda_{sj}(z_j) = \tan^{-1}\left(\frac{R(z_j)}{R}\tan\lambda\right) \qquad (10)$$

The angular position of elemental cutting edge can be calculated from Fig. 4 and equation (9).

$$\theta_{ij}(\Theta, z_j) = \Theta - \frac{z_j}{R}\tan\lambda_{sj} - (i-1)\frac{2\pi}{n} \qquad (11)$$

Where, Θ : tool rotation angle, n : number of tooth

The total cutting forces are expressed as the function of tool rotation angle Θ from y-axis and the tip.

$$F_x(\Theta) = \sum_{i=1}^{n}\sum_{j=1}^{k}\Big[-dF_{Rij}\sin\kappa_j\sin\theta_{ij} - dF_{Tij}\cos\theta_{ij} - dF_{Aij}\cos\kappa_j\sin\theta_{ij}\Big]dz \qquad (12)$$

$$F_y(\Theta) = \sum_{i=1}^{n}\sum_{j=1}^{k}\Big[-dF_{Rij}\sin\kappa_j\cos\theta_{ij} + dF_{Tij}\cos\theta_{ij} - dF_{Aij}\cos\kappa_j\cos\theta_{ij}\Big]dz \qquad (13)$$

$$F_z(\Theta) = \sum_{i=1}^{n}\sum_{j=1}^{k}\Big[-dF_{Rij}\cos\kappa_j - dF_{Aij}\sin\kappa_j\Big]dz \qquad (14)$$

Where, $\kappa_j = \cos^{-1}\left(\frac{R-z_j}{R}\right)$

The tangential, radial and axial elemental cutting force is the function of edge cutting coefficients and cutting force coefficients.

$$dF_t = K_{te}dS + K_{tc}t(\theta_{ij})db \qquad (15)$$

$$dF_r = K_{re}dS + K_{rc}t(\theta_{ij})db \qquad (16)$$

$$dF_a = K_{ae}dS + K_{ac}t(\theta_{ij})db \qquad (17)$$

The cutting force coefficients are evaluated by equation (18), (19) and (20), and edge cutting coefficients are evaluated by orthogonal cutting test.

$$K_{tc} = \frac{\tau_s}{\sin\phi_n}\frac{\cos(\beta-\gamma_n) + \tan\eta_c\sin\beta\tan\lambda_s}{c} \qquad (18)$$

$$K_{rc} = \frac{\tau_s}{\sin\phi_n\cos\lambda_s}\frac{\sin(\beta-\gamma_n)}{c} \qquad (19)$$

$$K_{ac} = \frac{\tau_s}{\sin\phi_n}\frac{\cos(\beta-\gamma_n)\tan\lambda_s - \tan\eta_c\sin\beta}{c} \qquad (20)$$

$$K_{te} = 14.99(N/mm)$$
$$K_{re} = 60.56(N/mm) \qquad (21)$$
$$K_{ae} = 0(N/mm)$$

Where, η_c : chip flow angle

$$c = \sqrt{\cos^2(\phi_n + \beta - \gamma_n) + \tan^2\eta_c\sin^2\beta}$$

4. Tool tip stress analysis

The stress at the tip of cutting edge is considered as a common denominator which can account for the particular optimal geometries of ball-end mill. Therefore, the normalized stress can be expressed

equation (22) and a purely geometrical relationship, which depends only on the clearance angle α, the rake angle γ_n and the inclination angle λ_s.

$$\bar{\sigma}_r = \cos^2\lambda_s \frac{\sin\left(\alpha+\frac{\delta}{2}\right)\sin\frac{\delta}{2}\left(\frac{\delta}{2}+\frac{\sin\delta}{2}\right)-\cos\left(\alpha+\frac{\delta}{2}\right)\cos\frac{\delta}{2}\left(\frac{\delta}{2}-\frac{\sin\delta}{2}\right)}{\left(\frac{\delta}{2}\right)^2-\left(\frac{\sin\delta}{2}\right)^2} \tag{22}$$

Where, $\delta = 90^\circ - \gamma_n - \alpha$: wedge angle

5. Optimization of ball-end mill geometry

In this section, through the geometric, cutting force model and the normalized stress model, geometrical optimal parameters, i.e., the helix angle, the rake angle and the relief angle of ball-end mill that can minimize the value of object function consisting of the stress at the tip of cutting edge and cutting forces during the cutting operation, are searched by the genetic algorithm. When design variables exist out of the feasible region, the value of penalty function of tool deflection constraint increases, and then the value of fitness function which is composed of the original object function and the penalty function becomes much bigger.

$$\min\ F(x,\rho_k) = f(x) + P(x,\rho_k) \tag{23}$$

$$\lim_{k\to\infty}\rho_k = \infty,\ \lim_{x\to feasible} P(x,\rho_k) = 0 \tag{24}$$

Where, k : generation number, $F(x,\rho_k)$: fitness function

$f(x)$: object function, $P(x,\rho_k)$: penalty function

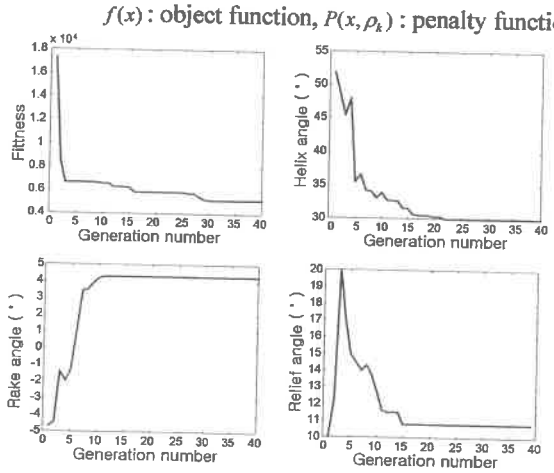

Fig. 5 Optimization results

Fig. 5 depicts optimization results of geometric parameters of two flutes, 10mm diameter ball-end mill. Fitness value converges to about 5000 after 40 generation.

In Fig. 6, the absolute value of cutting forces with optimized ball-end mill is small for the conventional one in Fig. 7. The depth cut is 3mm axially and slot cutting, and the feed per tooth is 0.01mm/tooth.

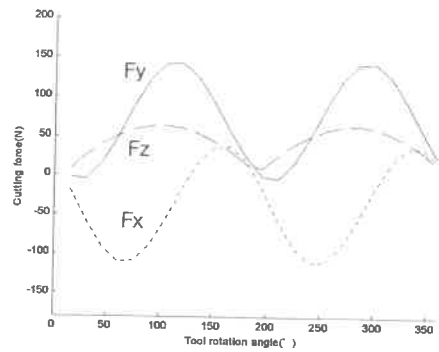

Fig. 6 Cutting forces with optimized ball-end milling

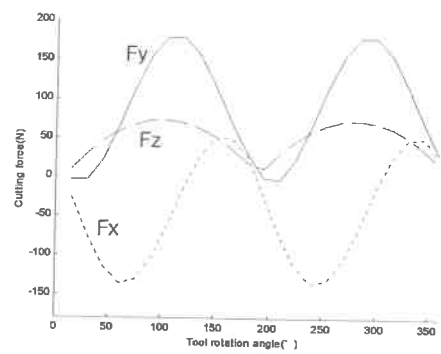

Fig. 7 Cutting forces with conventional ball-end milling

6. Conclusion

In this paper, the geometries of ball-end mill are developed mathematically and simulated. Through the geometric and the cutting force model, geometrical optimal solutions of ball-end mill that can minimize the stress at the cutting edge and the total cutting force in the tool, are searched by the genetic algorithm.

References

1. Warren R. Devries, 1991, Analysis of material removal processes, Springer-Verlag
2. David E. Goldberg, 1989, Genetic algorithm in search, optimization, and machine learning, Addison Wesley Longman, Inc.
3. S. Kaldor, 1986, "A Common Denominator for Optimal Cutting Tool Geometry", Annals of the CIRP, Vol.35, No.1, pp.41-44
4. G. Yucesan, Y. Altintas, 1996, "Prediction of Ball End Milling Forces", Journal of Engineering for Industry, Vol.118, February, pp.95-103

Proposal of Magnetic-Field Assisted Cutting for Improvement of Machinability

F. Nakano[1], K. Yanagihara[2], H. Yamaguchi[3], Y. Tani(2)[2], and Y. Kanda[4]

[1]Olympus Co. Ltd., Ishikawa 2951, Hachiouji-Shi, Tokyo, Japan

[2]Institute of Industrial Science, The University of Tokyo, Roppongi 7-22-1, Minato-Ku, Tokyo, Japan

Tel: +81-3-3402-6231 ext. 2226, Fax: +81-3-5411-3908, e-mail: kiyoshi@martini.iis.u-tokyo.ac.jp

[3]Utsunomiya University, Youtou 7-1-2, Utsunomiya-Shi, Tochigi, Japan

[4]Toyo University, Kujirai Nakanodai 2900, Kawagoe-Shi, Saitama, Japan

1 INTRODUCTION

Recently, considerable attention has been drawn to the decreasing of cutting fluid with respect to environmental issues [1]. However, a reduction of cutting fluid will cause problems such as shortening of the tool life. Therefore the total comprehension of cutting phenomena, for example, clarification of the cutting mechanism, the development of new coating technology and new cutting tool to improve tool life, and the establishment of a method for prediction of tool wear was intended to be a significant advance towards solutions for the above problems [2][3][4].

On the other hand, there are some interesting reports that discuss the decrease of tool wear and changes in the machinability of work material by magnetic effects, in the field of tribology. The purpose of this study is to apply this tribological knowledge and the unique properties of work material by using magnetic effects to strategically improve hard-to-cut materials. In particular, it focuses on development and establishment of Magnetic-Field Assisted Cutting (MFAC). As a result of experimental study of MFAC, the improvement of tool life was achieved, and the suppression of chatter vibration and improvement of surface roughness were accomplished in the cutting of austenitic stainless steel.

2 EXPERIMENTAL ENVIRONMENT

Some papers in tribology reported that there is a possibility that a magnetic field may change the friction among material contacts and the mechanical properties of materials [5][6]. It may also improve the machinability.

Table 1: Cutting conditions.

Experiment No.	(1)	(2)
Cutting speed m/min	120	80
Feed mm/rev	0.5	0.2
Depth of cut mm	2	1
Work material	ISO 683-13 11 type Austenitic Stainless Steel	
Tool material	P30	
Insert	SNGA120408	
Holder	ESBNR2020	
Coolant	None	

Thus continuous turning tests were carried out using an OKUMA LS-450 lathe. The cutting conditions used are listed in Table 1. Turning tests were carried out using a 50mm diameter, 400mm long bar. ISO standard P30 SNGA120408 inserts were clamped to a ESBNR2020 tool holder. In order to inspect influence in different cutting temperature, the cutting speed of 120m/min with a comparatively heavy load condition and the cutting speed of 80m/min with a comparatively light load condition were selected, as listed in Table 1.

Figure 1 shows the tool holder and the insert with Nd-Fe-B magnets (Sumitomo Special Metal Co., NEOMAX, 5.0 × 2.3 × 1.0, 10 pieces). The number of magnets was considered to apply sufficient magnetic power on the tool to cause some magnetic effects, and the position of the magnets on the tool holder was determined to be the point nearest the tool edge providing the swarf did not make contact with the magnets.

Figure 2 shows the FEM analysis result with the magnetic field as reference. The strength of the magnetic field was 5-7mT near the cutting edge, according to the measurement.

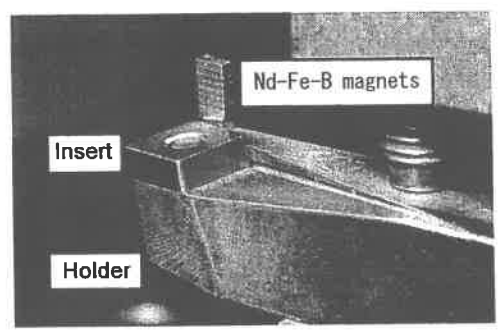

Figure 1: Tool holder and insert with Nd-Fe-B magnets.

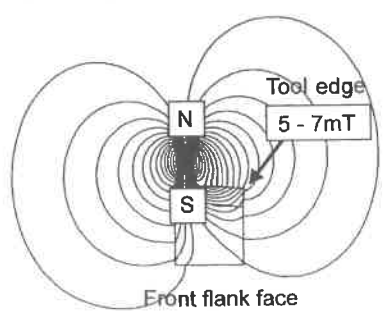

Figure 2: FEM analysis of magnetic field.

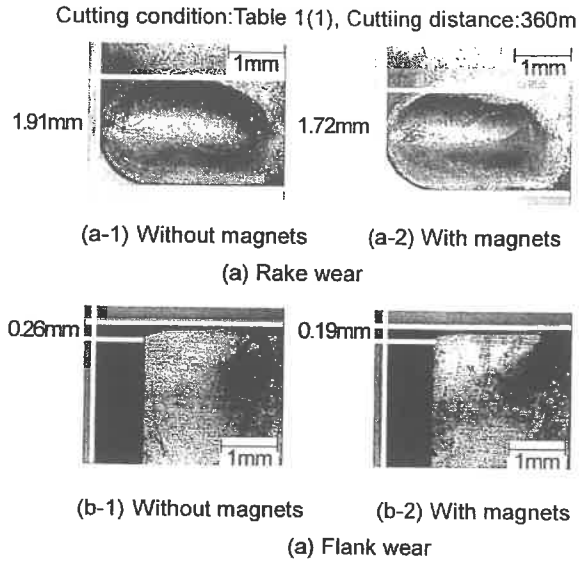

Figure 3: Difference of tool wear by the presence of magnetic field.

3 EFFECTS OF MFAC

3.1 Improvement of wear of a cemented carbide tool

Figure 3 shows the difference in tool wear effected by the presence of the magnetic field. Figures (a-1) and (a-2) show the rake faces, and figures (b-1) and (b-2) show the flank faces. After cutting, it was noted that tool wear in MFAC was less than that in normal dry cutting.

The difference in flank wear effected by the presence of the magnetic field is shown in Figure 4. The tool life of MFAC is 1.2-1.5 times longer than that of normal cutting.

Common cemented carbide tools are sintered with tungsten carbide (WC) as the main ingredient and 3-20% cobalt (Co) as cement. One of the factors in tool wear is considered that the cobalt cement comes out of the subsurface of the tool and is washed away because high temperature and high pressure are generated around the cutting area by the high cutting energy, as shown figure 5 [7]. The binding force among WC particles is weakened by losing Co binder. Finally that makes tool wear.

In order to confirm the Co density, SEM-EDX analyses at each tool flank face were held. Co concentration after normal cutting was 7.8wt% which is an increase of 2.6wt% since 5.2wt% as the value before the test. Though its concentration after MFAC was the same. Therefore applying magnetic power near the cutting area prevented tool wear .

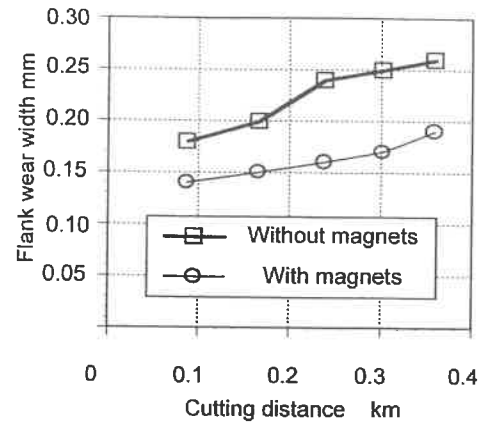

Figure 4: Difference of flank wear with or without magnets under the condition of Table 1(1).

Under light load cutting condition of Table 1 (2), the difference in tool wear was hardly apparent because cutting condition was too light to generate the Co movement. However, the surface roughness in MFAC was found to be 10-40% better than that in normal cutting, as shown in Figure 6.

Surface roughness is often concern with the adhesion of work material. The difference in the adhesion of the work material to the flank face of the tool effected by the presence of the magnetic filed is shown in Figure 7. The adhesion in MFAC was less than that in normal cutting. Therefore magnetic field has the effect to reduce the adhesion of work material and produce better surface roughness.

3.2 Influence on cutting forces in MFAC

In order to ascertain the change of machinability, as mentioned above, FFT analysis of the cutting forces in normal cutting and MFAC was performed. The cutting experiment involved increasing the overhang of the tool from 20mm, the normal position, to 37mm from the edge of the tool post. The change of machinability effected by the presence of the magnetic field to be distinguished easily as chatter vibration.

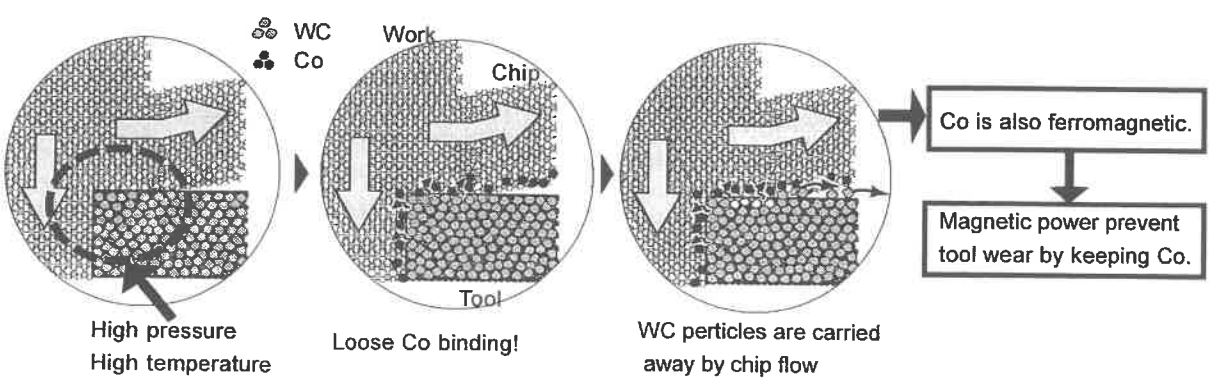

Figure 5: Mechanism of cemented carbide tool wear improvement.

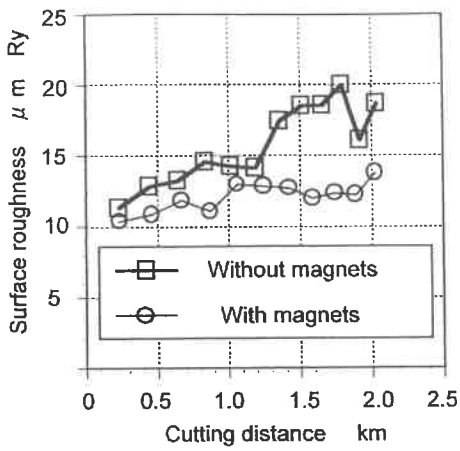

Figure 6: Difference of surface roughness with or without magnets under the condition of Table 1(2).

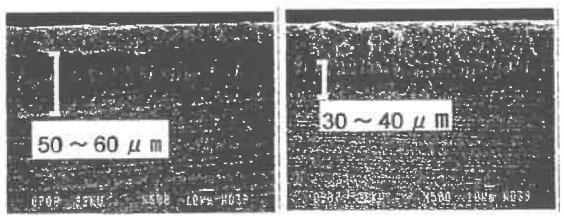

(a)Without magnetic-field (b)With magnetic-field

Figure 7: Difference of adhesion of work material to flank face of tool by the presence of magnetic field.

Figures 8 (a) and (b) show the spectrum of thrust cutting force in normal cutting and in MFAC, respectively, with a 5mT magnetic field. The main spectrum peak of the chatter vibration at around 6 kHz is clearly observed in Figure 8 (a), but was absolutely suppressed by the application of the 5mT magnetic field, as seen in Figure 8(b). The cause of this suppression may not be the magnetic field, but may be dynamic properties such as the change in tool weight caused by attaching the magnets on the tool.

Therefore it was investigated whether the weight increase affects the dynamic behavior by attaching dummy weights that weighed as much as the magnets. Consequently the suppression of chatter vibration did not occur under this condition. Thus it was concluded that the chatter vibration was suppressed by the magnetic field.

Figure 9 shows the relationship between magnetic flux density and amplitude of chatter vibration. The amplitude of chatter vibration clearly depended upon the magnetic flux density on the tool edge.

3.3 Mechanism of improving machinability

The improvement of surface roughness and the suppression of chatter vibration were found as mentioned above. In this paragraph, the possible causes of these effects is stated. The investigations focused on next three magnetic influences upon tool material, contact environment between tool and work, work material, were considered.

At first, TiN coated tools and Al_2O_3 ceramic tools were tested in MFAC to confirm the relationship between the phenomena and the magnetism of tool material. Then the chatter vibration was suppressed while

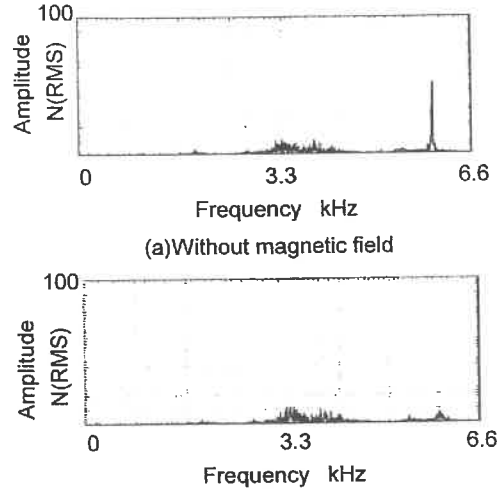

(a)Without magnetic field

(b)With magnetic field(5mT)

Figure 8: FFT analyses of thrust cutting forces.

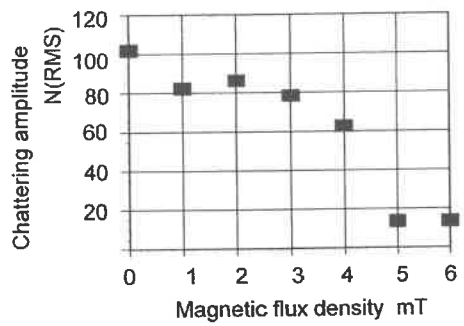

Figure 9: Relationship between magnetic flux density and chattering amplitude of thrust cutting forces.

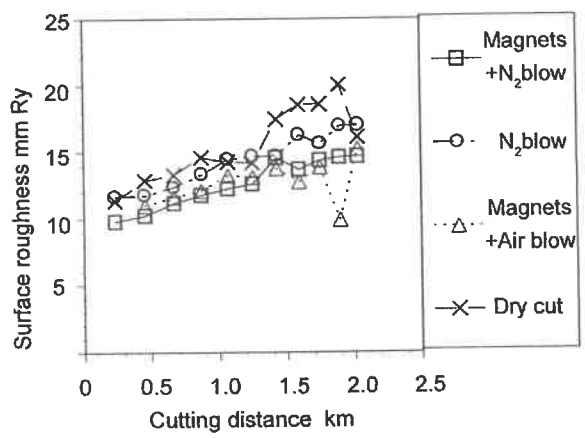

Figure 10: Difference of magnetic effect on machined surface by the presence of oxygen.

using tools of both materials. In short, the phenomena have no relation to magnetism of tool material.

Second, it was investigated whether the magnetic field affects the environment of the contacts. Some reports stated that the magnetic field could change the wear pattern from severe to mild, by promoting the oxidation of the material surface. Then four different cutting patterns were chosen to confirm the relationship between magnetic field and environment. Two of them were normal dry cutting and nitrogen gas blow cutting, to investigate the difference in surface roughness caused by

Table 2: Cutting conditions of invar alloy.

Cutting speed m/min	80
Feed mm/rev	0.2
Depth of cut mm	0.25
Work	Invar alloy
Tool material	P30
Insert	SNGA120408
Holder	ESBNR2020
Coolant	Dry (no use)

Table 3: Difference of surface roughness in machining of invar alloy .

Theoretical	6.25 μ m Ry
Without magnets	11.3 μ m Ry
With magnets	8.4 μ m Ry

the presence of oxygen. The other two were air blow cutting with a magnetic field and nitrogen blow cutting with a magnetic field, to investigate the effect of the presence of the magnetic field. Figure 10 shows the change in surface roughness under each blow condition. It shows that the N_2 blow cutting was superior to normal dry cutting. However, the MFAC data obtained under both the air and N_2 blow conditions were much better than both normal and N_2 blow cutting without the magnetic field. The improvement of surface roughness may have some relationships to the presence of oxygen. However, the magnetic field around the cutting area had a stronger effect on the surface roughness. Accordingly the above phenomena had negligible concern with the presence of oxygen.

Lastly, martensitic stainless steel (ISO type No.683-13 4), copper, brass, and aluminum alloy (ISO AlMg 2.5 type) were used as the work material in MFAC, and it was confirmed whether the effects depend on work materials. Consequently the phenomena were observed only for austenitic stainless steel.

Therefore the magnetic field may relate to a special property of only austenitic stainless steel. Because it was reported that a magnetic field can cause a magnetic-field-induced martensitic transformation of work material to austenitic stainless steel [8]. Thus, its possibility was experimented another work material which can make itseif magnetic-field-induced martensitic transformation.

4 APPLICATION OF MFAC TO CUTTING OF INVAR ALLOY

Invar alloy is a hard-to-cut material which can undergo a magnetic-field-induced martensitic transformation. If the suppression of chatter vibration and surface roughness in cutting austenitic stainless steel is related to the magnetic-field-induced martensitic transformation, the machinability of invar alloy may be improved by MFAC as well.

Using the cutting conditions listed in Table 2, an MFAC test on invar alloy was carried out. Subsequently, all components of cutting forces during MFAC of invar alloy were smoother than those during normal cutting. The surface roughness in MFAC was better than that in normal cutting, as shown in Table 3.

Considering the consequences mentioned above, it was proven that the magnetic-field-induced martensitic transformation improved the machinability of work material, and prevented the fluctuation of cutting forces. It also suppressed the chatter vibration, and improved the surface roughness.

5 CONCLUSIONS

The influences of a magnetic field on the cutting of materials have been analyzed in various cutting experiments. Conclusions based on these experiments are as follows.

(1)The tool life of a cemented carbide tool was improved 1.2-1.5 times that under normal cutting conditions by applying a magnetic field near the cutting area.

(2)The reason for the above result is that the magnetic field prevented Co as the tool cement from coming out of the tool subsurface .

The following result was obtained only in cutting austenitic alloy.

(3)When MFAC was applied in cutting austenitic stainless steel, the improvement of surface roughness and the suppression of chatter vibration were accomplished due to a magnetic-field-induced martensitic transformation; this was also the case in cutting invar alloy.

6 ACKNOWLEDGMENTS

Substantial support and cooperation have been offered by Mitsubishi Material Co. Ltd. and Sumitomo Special Metal Co. Ltd.. Fruitful suggestions were given by Mr. K. Karino of Mitsubishi Material Co. Ltd., and experimental support was provided by Mr. K. Yasui of Toyo Univ.. The authors express their appreciation to them.

8 REFERENCES

[1]F. Klocke, G.Eisenblatter, 1997, Dry Cutting, Annals of the CIRP, 42/2:519-526.

[2]J. C. Hanmann, F. Le Maltre, D. Guillot, 1994, Selective Transfer Built-up Layer Displacement in High-Speed Machining -Consequences on Tool Wear and Cutting Forces, Annals of the CIRP, 43/1:69-72.

[3]P. Chen, 1992, High-Performance Machining of SiC Whisker-Reinforced Aluminum Composite by Self-Propelled Rotary Tools, Annals of the CIRP, 41/1:59-62.

[4]K. Uehara, M. Sakurai, T. Ikeda, 1992, On the Problem of Thermoelectric Current in Metal Cutting, Annals of the CIRP, 41/1:75-78.

[5]M. K. Muju, A. Gosh, 1977, A MODEL OF ADHESIVE WEAR IN PRESENCE OF A MAGNETIC FIELD, Wear, 41:103-116.

[6]M. K. Muju, A. Gosh, 1980, EFFECT OF A MAGNETIC FIELD ON THE DIFFUSIVE WEAR OF CUTTING TOOLS, Wear, 58:137-145.

[7]E. M. Trent, M. Met, 1952, Some Factors Affecting Wear on Cemented Carbide Tools, Proc. I. MEC. E, 166:64-74.

[8]Z. Nishiyama, 1994, MARTENSITIC TRANSFORMATION, ACADEMIC PRESS INC., London, p.299.

Ductile-Regime Turning of Brittle Materials by Single Point Diamond

Ichiro Ogura, Yuichi Okazaki
Manufacturing Machinery Division
Mechanical Engineering Laboratory, AIST, Tsukuba 305-8564, Japan

1. Introduction

To realize new types of optical devices having minute patterns above aspheric profiles, a new precision cutting technique for optical glass is required. It is well known that brittle materials, such as glass or silicon, can be machined crack free when the depth of cut is fixed at less than a certain critical amount[1]. This is called ductile mode cutting. There have been many studies on the brittle-ductile transition process to clarify the mechanism of brittle material machining or develop manufacturing techniques for ductile mode cutting. Blake and Scattergood investigated the critical depth of cut for single crystals of germanium and silicon using a diamond-turning lathe[2]. Brinksmeier et al. experimentally tested a plunge-cut technique for silicon and germanium[3]. Schinker cut several types of glasses using high-speed radial cutting with single diamond tools[4].

This report presents our experimental results on the machining of brittle materials using a practical ultra-precision lathe. Four machining types comprising subdivisions of ductile and brittle modes were defined to provide detailed descriptions of the experimental results. Machining experiments on BK7 and SiC were conducted in several different atmospheres. The maximum depth of groove in the ductile mode and the critical depth of tool indentation calculated from previous theoretical analysis were compared.

2. Outline of Experiment

2.1 Experimental procedure

Fig. 1 shows the experimental setup in this study. This system is an ultra-precision lathe with a fast tool servo (FTS) for single point diamond turning. Using a piezoelectric actuator, the FTS can control depth of cut at a 2 nm resolution, and its frequency response is 2 kHz. A diamond cutting tool is set on the FTS. The radius of the cutting tool is 0.2 mm, and the rake angle is 0 degree. The rotation speed of the spindle axis is 90 rpm.

The work is attached to the spindle axis by a vacuum chuck. In this study, BK7, SiC, and vitreous silica were used for cutting work. The diameter of these works was 30 mm, and the hickness was 5 mm.

The computer input a command signal with a profile like the teeth of a saw, as shown in Fig. 1, to the servo system, and an inclined plunge cut was applied to the work material three times per rotation. The cutting depth was 4 microns.

Before cutting, several types of reagents were applied to the surface of the work, and the machining atmosphere was changed. In this stury, eight machining atmospheres were selected: dry, water, heptane, octane, methanol, ethanol, and propanol for the BK-7 and SiC cutting experiments, and triethylamine for BK-7 only. Changing the cutting radius, we conducted three cutting experiments with each atmosphere. In this manner we obtained nine grooves of inclined plunge cut for each atmosphere.

After the cutting experiments, the surfaces of the works were observed by Nomarski differential interference microscope, and the machining types, as described in the next section, were distinguished. The amount of tool infeed was calculated from the starting point of the cutting mark, and depth of groove

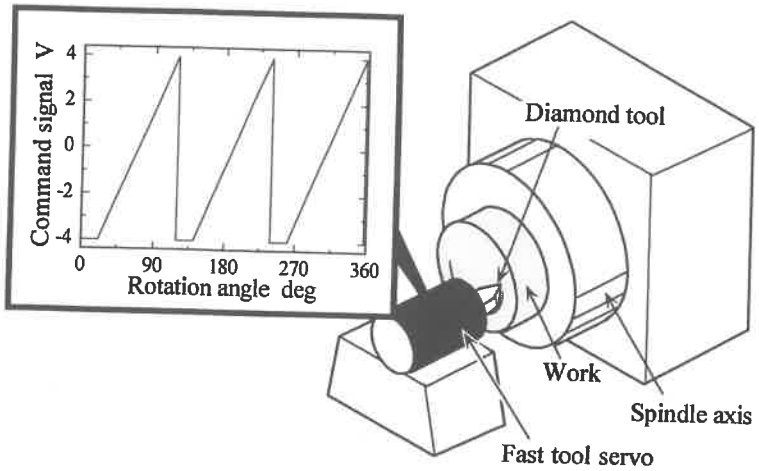

Fig. 1 Ultra-precision lathe with fast tool servo

was measured by a surface topographic measurement apparatus (Talyscan, Rank Taylor Hobson). The resolution of this apparatus is 3 nm. Finally, we obtained the relationships under several types of atmospheres between tool infeed, depth of groove, and groove state.

2.2 Definition of machining types

The brittle mode or ductile mode is confirmed when a brittle material is machined. These two modes are distinguished according to whether cracks or damage occur in the machined surface. In this study, four machining types comprising subdivisions of ductile and brittle modes were defined to provide detailed descriptions of the experimental results.

Figs. 2(a) to (d) show typical machining types. These results were obtained by Nomarski microscope observation. Type 1 has narrow grooves with no cracks. This type occurs by plastic deformation of the surface material. Almost all cases of this type have a depth of less than 100 nm. Type 2 has wider and deeper grooves than type 1, but also it has no damage. This type is realized in ductile mode, and is the most suitable machining type for damage-free machining of brittle materials. Type 3 has damaged grooves with lateral cracks. There are some cracks around the grooves, but no major destruction in the grooves. Type 4 is overall brittle mode machining. Many cracks and factures are confirmed around the grooves.

3. Results

3.1 BK7 cutting experiments

Fig. 3 shows the results of the BK7 cutting experiments in a water atmosphere. The tool infeed is plotted on the x axis, and the depth of the cut measured by Talyscan on the y axis. Both of the axes are denoted in logarithmic values. The line in this graph is y = x, indicating the same value for depth of groove and tool infeed.

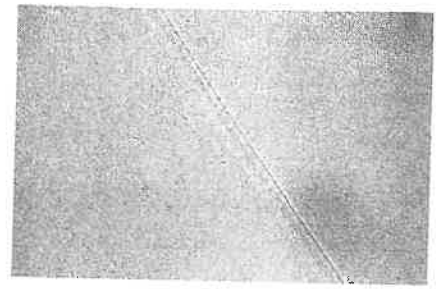

(a) Type 1

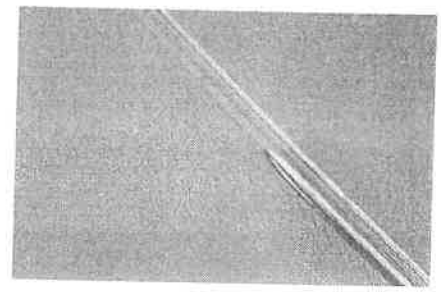

(b) Type 2

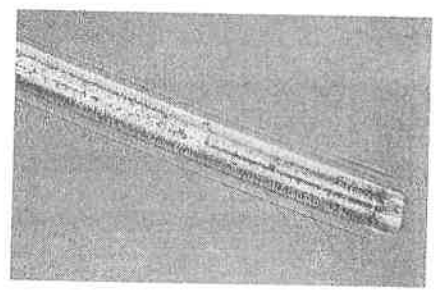

(c) Type 3

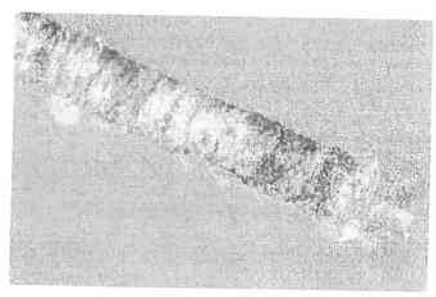

(d) Type 4

Fig. 2 Machining types in brittle material cutting

From this figure, it is clear that except for type 4, the depth of groove is less than the tool infeed, because of the compliance of the lathe. In the case of type 4, there is a large fracture in the groove, so the depth of groove is larger than the tool infeed. The depths of grooves for type 1 and type 2 differ by about 0.5 to 0.7 micron at the same tool infeed. This results from the spring back of the material in type 1, and the fact that the tip of the cut material in type 2 flows on the rake plane of the cutting tool. In the case of type 2, although a part of this area overlaps with type 3, an almost linear relationship is obtained between the tool infeed and depth of groove. If individual type 2 can be obtained, ductile mode cutting will be realized.

Fig. 4 shows the results under several types of atmospheres. This figure shows how the four machining types are obtained in each atmosphere. Under dry condition, no individual machining type is obtained at 0.2 micron. Stable cutting therefore cannot be expected in this atmosphere. In the heptane, octane, methanol, and ethanol atmospheres, however, there are areas in which individual type 2 can be obtained. Especially in the methanol and ethanol atmospheres, such areas exist from 0.2 to 1.2 microns, indicating good atmospheres for practical machining. Using propanol, however, type 2 is covered by type 3 from 0.25 micron, so that it is not suitable for stable machining. Under a triethylamine atmosphere, type 3 exists from 0.2 micron cutting. It therefore appears that this condition is not good for ductile machining. In microscopic observations, no cracks were found around the groove although many cracks could be observed inside the groove. Hence, it is considered that crack propagation is the main machining mechanism of this atmosphere.

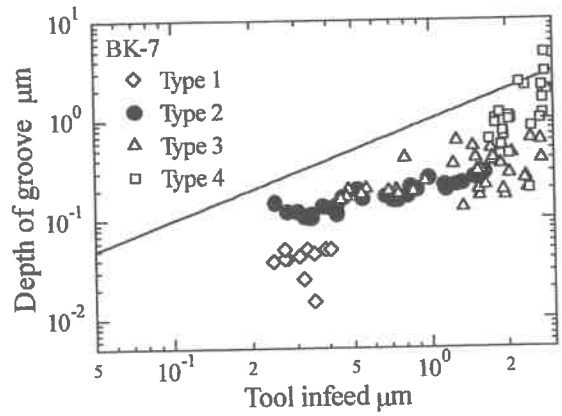

Fig. 3 Results of cutting experiments (BK7)

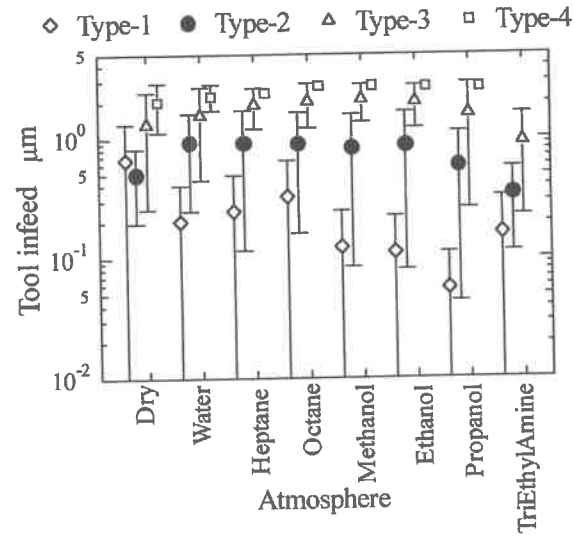

Fig. 4 Machining types under various atmospheres

3.2 SiC cutting experiments

We conducted the same experiments on SiC as for BK7. No significant difference was observed except under dry condition, indicating that SiC is a material that is less affected by the atmosphere compared with BK7.

Figs. 5(a) and (b) show two sets of machining results under a dry atmosphere. Fig. 5(a) shows normal cutting, and Fig. 5(b) shows vibration cutting, which was realized by the addition of FTS minute vibrations to the plunge cut. The amplitude of vibration was 0.1 micron in the cutting direction. From (b), it can be seen that the type 2 cutting groove can be obtained at 0.1 to 0.5 micron tool infeed. The reason for this result is that minute cutting reduces the friction between the cutting tool and the material.

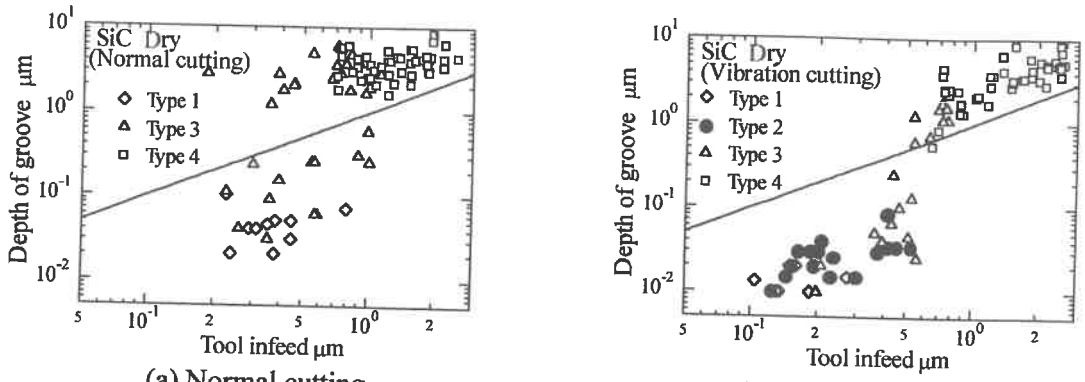

(a) Normal cutting (b) Vibration cutting

Fig. 5 Results of cutting experiments (SiC)

3.3 Relationship between experimental results and theoretical values

Under a water atmosphere, BK7, SiC, and vitreous silica were cut and each maximum depth of groove in type 2 was observed. Table 1 shows the results.

This table also shows the critical depth of indentation calculated from Griffith's theory. This value is calculated as follows.

$$d_c \approx \frac{E}{H_V}\left(\frac{K_{IC}}{H_V}\right)^2$$

Table 1 Calculated d_c and observed results

Materials			BK7	SiC	Vitreous silica
Fracture toughness	K_{IC}	MPa m$^{1/2}$	0.2	4	0.75
Young's modulus	E	GPa	81.5	420	70
Hardness	H_V	GPa	5.1	24	6
Critical depth of indentation	d_c	μ m	0.025	0.49	0.18
Observed maximum depth of groove in type 2		μ m	0.2	0.5	0.1

From this table, it is seen that nearly the same values of depth are confirmed for SiC and vitreous silica. On the other hand, the observed value for BK7 significantly differs from the theoretical value. However, there is a report that the maximum depth of cut in BK7 ductile mode was 0.25 micron at a rake angle of 45 degrees and a cutting speed of 20 m/s[3]. The result of our experiment is close to this result. It is therefore considered that the critical depth of cut in BK7 becomes much larger than the indentation.

4. Summary

This study report describes our experimental results on the machining of optical glasses and brittle materials for the realization of brittle material machining. BK7 and SiC were cut in several different atmospheres by an ultra-precision lathe. For BK7, methanol and ethanol provided the best conditions for ductile cutting. Vibration cutting was effective for SiC dry cutting. The relationship between the observed maximum depth of groove in type 2 and the calculated critical depth of indentation was investigated. In the case of SiC and vitreous silica, nearly the same values for depth were confirmed, whereas the values for BK7 were significantly different.

References

1) T. Bifano, T. Dow, and R. Scattergood: Ductile Regime Grinding: A New Technology for Machining Brittle Materials. ASME, J. Eng. Ind., **113**, 5 (1991), 184.
2) P. N. Blake and R. O. Scattergood: Ductile-Regime Machining of Germanium and Silicon. J.Am.Ceram.Soc., **73**, 4 (1990), 949.
3) E. Brinksmeier, W. Preuβ, and O. Riemer: From Friction to Chip Removal. An Experimental Investigation of the Microcutting Process. Proc. 8th Intern. Prec. Eng. Seminar (1995), 335.
4) M. G. Schinker: Subsurface Damage Mechanisms at High-Speed Ductile Machining of Optical Glasses. Prec. Eng., **13**, 3 (1991), 208.

HIGH SPEED MACHINING OF DEEP GROOVE BY USING SLENDER END MILLS

Hideaki Onozuka* , Yohei Asakawa* , Masashi Sawa* , Yukio Maeda*
Motohiro Kikuchi** , Yoshio Koguchi**
*Production Engineering Research Laboratory , Hitachi , Ltd.
292 Yoshida-cho , Totsuka-ku , Yokohama 244-0817 , Japan
**Kokubu Works , Hitachi , Ltd.
1-1-1 Kokubu-cho , Hitachi 316-8501 , Japan

1. Introduction

By the improvement of machine tools and cutting tool material , cutting efficiency has been increased in late years. End mills are commonly used for machining of grooves for some mechanical parts. But during the machining of narrow and deep grooves , slender end mills are broken so often that cutting efficiency is hard to be increased. This paper describes high efficient and precision machining of oxygen free copper to produce deep groove which is 2.2mm in width and 16mm in depth.

2. Experimental Procedure and Conditions

A vertical machining center (YASDA YBM-640V) was used for the cutting experiments. Maximum spindle revolution is 20000rpm , and HSK shank which has high repetition accuracy in tool exchanging was adopted. And maximum feed rate is 10000mm/min for each x , y , z axis. Objective work shape is shown in Fig.1 and shape of end mill used for experiments is shown in Fig.2. The run out of end mill was managed to be within 5μm.

Experimental setup and cutting method are shown in Fig.3 and Fig.4. Piezo-electric dynamometer (Kistler 9257B) was used for measuring cutting forces , and specimen was fixed on the dynamo meter. Round trip cutting was adopted for roughing of the grooves , and sholder cutting was adopted for finishing of inside of the grooves. In order to evaluate the stability against the chatter vibration, end mill was fed in slant direction that radial depth of cut could be increased according to the cutting position , and stability limit of radial depth of cut was determined by the wave shape of cutting forces and observation of the machined surface. Cutting conditions are shown in Table 1.

3. Experimental Results and Discussion

3.1 Tool Life of Slender End Mills at Roughing Process

Effects of cutting conditions on the tool life of end mills were evaluated. Axial depth of cut (*Ad*) and feed rate (*Sz*) were taken up for the experiment. Those parameters are changed at a constant cutting efficiency , and it is equivalent to changing the aspect ratio of the chip shape. Fig.5 shows the correlation between the aspect ratio of the chip and tool life. It is found that end mills are easy to be broken at conditions of small *Ad*/*Sz* , in other words at conditions of small *Ad* and large *Sz*. Fig.6 shows the measured cutting forces during the machinig of groove. It is found that cutting force becomes very large at the position of dead end of the groove. On the other hand , breakage of the end mills occurred at this position necessarily. The cause of the breakage was thought to be the large force at the position of dead end of the groove , and forces at the dead end tend to become large at conditions of small *Ad*/*Sz*. The reason is thought as follows ; generated chips are usualy removed from the machined groove by cutting

fluid , but they become hard to be removed at a condition of high feed speed because of the viscosity of cutting fluid , and chips are sandwitched between the end mill and inside face of the dead end.

Thus it is found that large Ad/Sz condition is suitable for the cutting condition at roughing , and then Ad=0.5mm , Sz=0.02mm/tooth are selected.

3.2 Finishing Method of Groove

3.2.1 Prevention of residues

Unevenness which has an equivalent pitch to depth of cut was found inside of the groove by round trip cutting , and it came almost 40μm. Those unevenness were thought to be caused by the bending of end mill. In order to remove it , finishing end mills are applied. Fig.7 shows the finished surface of the groove. Large amount of residues are found on the finished surface , and they exist only on the area of 5mm from the bottom. It is equivalent to the pitch of cutting edges of end mill which has 2mm diameter and 30° helix angle. Pitch of cutting edges (p) is expressed as follows , by using cutter radius (r) , number of teeth (n) , and helix angle (β) ;

$$p = \frac{r \cdot 2\pi}{n \cdot \tan\beta}$$

In the case of applied finishing end mill , pitch of cutting edges is 5.4mm according to above equation.

The cause of residue generation was thought to be the bending of the end mill. Number of simultaneously acting cutting edges changes while tool rotating[2) , so bending of the end mill varies. Then chip generation was interrupted , and chips remained on machined surface as residues as shown in Fig.8. Thus in order to avoid residue generation , maximum number of simultaneously acting cutting edge is required to be 1. Fig.9 shows the correlation between helix angle and the number of simultaneously acting cutting edges in the case of cutter diameter is 2mm , number of theeth is 2 , axial depth of cut is 16mm. According to this figure , the following can be described ;

(1)In the case of applied finishing end mill , maximum number of simultaneously acting cutting edges is 3.

(2)In order to obtain single simultaneously acting cutting edge , helix angle is required to be less than 11° .

However , small helix angle sometimes cause the decrease of stability against chatter vibration , then stability limit was evaluated for each helix angle.

3.2.2 Correlation between helix angle and stability limit

End mill was fed in slant direction that radial depth of cut could be increased according to the cutting position. Radial depth of cut was changed by the range of 0～0.5mm under the condition of fixed feed rate and spindle revolution. Both down milling and up milling were applied for the experiments. Fig.10 shows the correlation between helix angle and stability limit. According to this figure , the following can be described ;

(1)Stability limit becomes small at small helix angle.

(2)Stability limits of down milling is larger than those of up milling.

(3)Residues are not generated at the condition of helixangle 11° unless chatter vibration occurs.

4. Conclusions

As the results , within the range of these experimental conditions , it was clarified that :

(1)In order to avoid the end mill breakage in high efficiency , large axial depth of cut and small feed rate

are suitable for roughing condition.

(2)Helix angle of finishing end mills must be at the condition of which simultaneously acting cutting edges is single in order to avoid the residue generation.

(3)Helix angle of finishing end mills must be as large as possible in order to avoid chatter vibration.

5. References

1) Y.Fujii , H.Iwabe , M.Suzki : Effect of Dynamic Behaviour of End Mill in Machining on Work Accuracy , JSPE , (1977) 807 (in Japanese).

2) Tlusty , J. and MacNeil : Dynamics of cutting forces in end milling , P. , Annals of the CIRP , 24-1(1975) 21

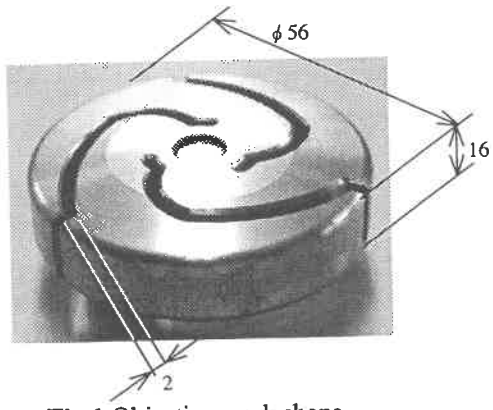

Fig.1 Objective work shape

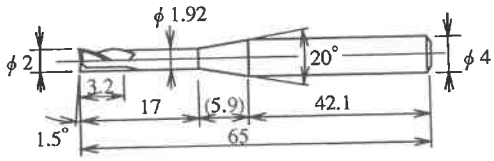

Fig.2 Geometry of applied end mill

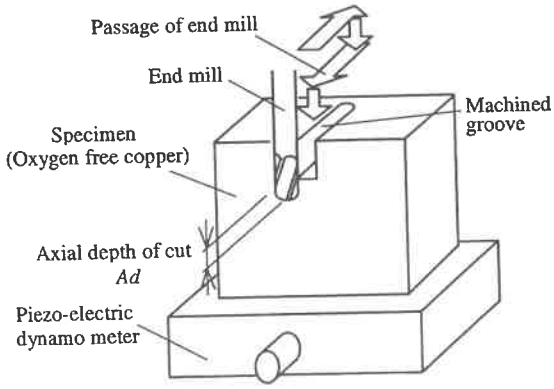

Fig.3 Experimental set up for roughing of the grooves

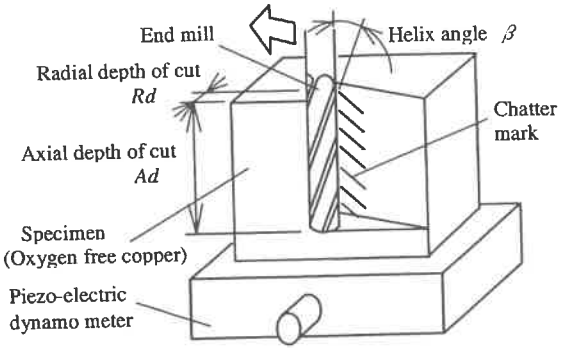

Fig.4 Experimental set up and cutting method for finishing of groove and evaluation of stability limit against chatter

Table 1 Cutting conditions

Tool	End Mill ϕ 2 , L=17mm WC (TiAlN coated)	
Work	Oxygen Free Copper	
Cutting Conditions	Roughing	Spindle revolution 10000min^{-1} Axial depth of cut (*Ad*) 0.1～0.5mm Feed rate (*Sz*) 0.02～0.1mm/tooth
	Finishing	Spindle revolution 10000min^{-1} Axial depth of cut (*Ad*) 16mm Radial depth of cut (*Rd*) 0～0.5mm Feed rate (*Sz*) 0.01mm/tooth
Cutting Fluid	Oil	

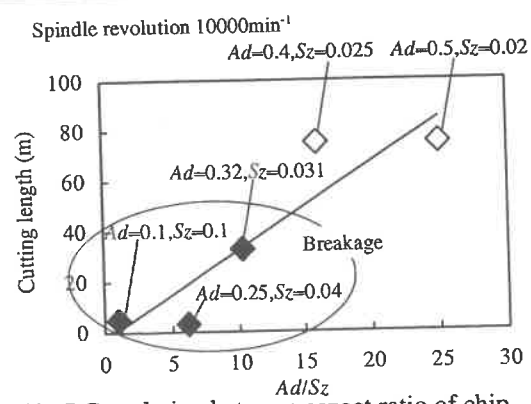

Fig.5 Correlation between aspect ratio of chip shape and tool life

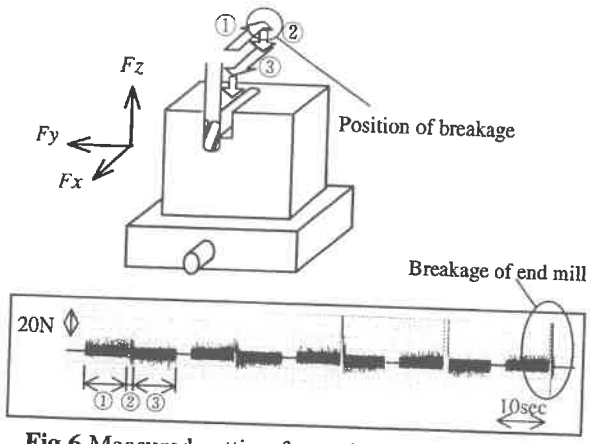

Fig.6 Measured cutting force during the round trip cutting (Fx)

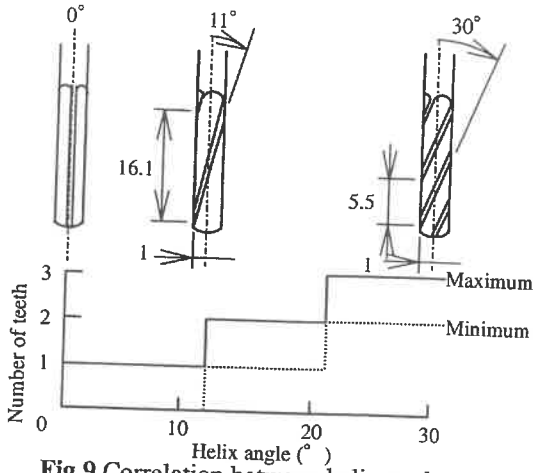

Fig.9 Correlation between helix angle and number of simultaneously acting edges

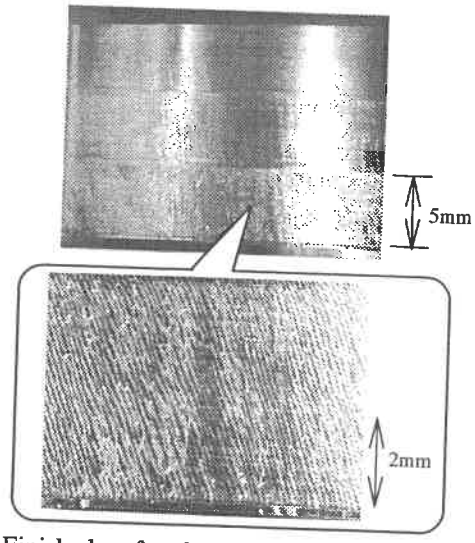

Fig.7 Finished surface by using end mill with helix angle 30°

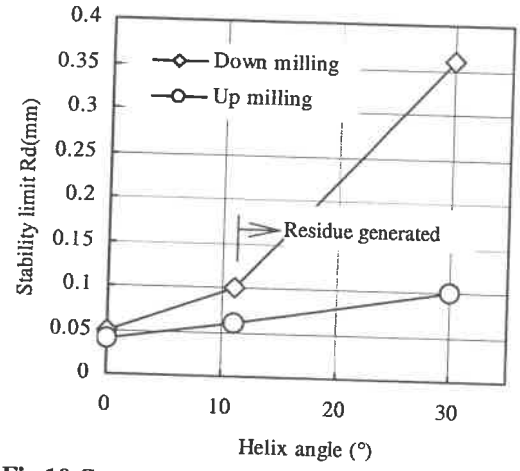

Fig.10 Correlation between helix angle and stability limit

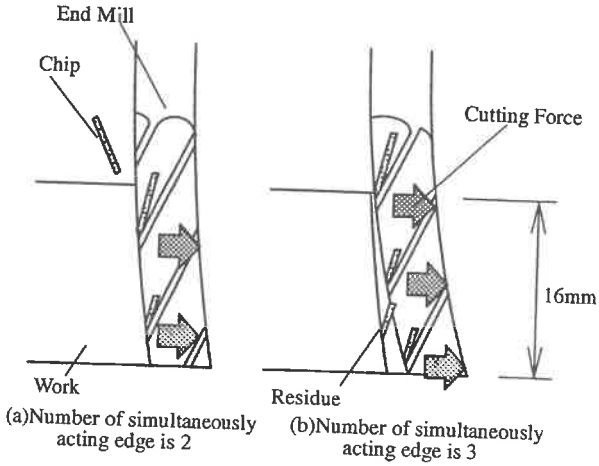

Fig.8 Mechanism of residue generation in finishing

Diamond Turning of CaF_2 for Nanometric Surface

Jiwang Yan [a*], Katsuo Syoji [a], Tsunemoto Kuriyagawa [a]
Kenji Tanaka [a] and Hirofumi Suzuki [b]

[a] *Department of Mechatronics and Precision Engineering, Tohoku University*
Aramaki-Aoba-01, Auba-ku, Sendai, 980-8579, Japan
[*] *E-mail: yanjw@pm.mech.tohoku.ac.jp*
[b] *Department of Production Systems Engineering, Toyohashi University of Technology*
Tempaku-cho, Toyohashi, 441-8580, Japan

Abstract

Single crystal calcium fluoride is an excellent optical material for both ultraviolet and infrared wavelength ranges with important applications. Currently, calcium fluoride optical component is produced by polishing subsequent to grinding and/or lapping. In this paper, the authors investigated the possibility of machining calcium fluoride by single point diamond turning for fabricating high quality optical surface directly. It is found that due to the unique thermal property of calcium fluoride, a special type of crack occurs when the tool feed is smaller than a critical value during wet cutting. To solve this problem, two approaches are carried out: dry cutting and large feed wet cutting. Nanometric ductile surface is obtained with forming continuous chip.
Key words: calcium fluoride, fluorite, diamond turning, ductile regime machining, optical surface

1. Introduction

Single crystal calcium fluoride (CaF_2), usually known as fluorite, is a transparent colorless crystal having the fluorite crystal structure. The cleavage plane is (111) plane. Some of the main properties (optical, mechanical, thermal) of CaF_2 are listed in table 1. For comparison, the corresponding items of single crystal silicon are also listed in the same table. CaF_2 is an excellent optical material having extremely good permeability and refractive index from 0.125μm wavelength ultraviolet range to 12μm wavelength infrared range. It also has good water-resistance, thermal-resistance and chemical stability. Therefore, it has been widely used as lenses, prisms and windows for various advanced optical instrument. Moreover, CaF_2 is considered to be the most prospective lens substrate material for the lithography equipment (stepper) of the future semiconductor manufacturing industry. On the other hand, CaF_2 is a typical brittle material, having very low fracture toughness and low hardness. The thermal conductivity index of CaF_2 is also extremely low, approximately 1/17 of that of silicon. On the contrary, the thermal expansion coefficient of CaF_2 is very large, 5.8 times of that of silicon. Conventionally, CaF_2 is finished by polishing subsequent to grinding and lapping. However, it is difficult or even impossible for polishing to attain high form accuracy when fabricating complex components such as aspheric surface, free-form surface and diffractive optics. Therefore in this paper, the authors carried out the single point diamond turning experiments in order to examine the possibility of the direct fabrication of CaF_2 optical surface without polishing.

Table 1 Optical, mechanical and thermal property of CaF_2 and a comparison with silicon

Property	CaF_2	Silicon
Permeable wavelength (μm)	0.125~12	1.2~15
Reflection loss (%)	5.6 (4 μm)	46.1 (10 μm)
Crystal structure / Cleavage plane	Fluorite / (111)	Diamond / (111)
Knoop hardness (kg/mm^2)	158.3	1150
Young's modulus (GPa)	75 (25°C)	170
Thermal conductivity index (cal/cmSec°C)	0.0232 (36°C)	0.39 (40°C)
Coefficient of thermal expansion (10^{-6}/°C)	24 (20~60°C)	4.15 (10~50°C)
Melting point (°C)	1360	1420
Specific heat (cal/g°C)	0.204 (0°C)	0.168 (25°C)

2. Experimental Procedure

In a previous report[1], the authors put forward a new method for ductile regime turning, where the straight-nosed diamond tool is used instead of the round-nosed tool[2) 3)]. This method enables the thinning of undeformed chip thickness in the nanometric range over the entire cutting region, and at the same time provides significant cutting width ensuring the plain strain conditions. Compared to the traditional method, it has the consistency in chip thickness hence provides an effective means for studying brittle-ductile transition behavior[4]. This method is also proved to be capable of large feed ductile regime turning which improves both machining efficiency and tool life. Accordingly, the experiments in this paper are carried out using straight-nosed diamond tools.

The experiments are carried out on a commercially available ultra-precision lathe having a hydrostatic bearing spindle. The machine enables the cutting tool to move along X and Z-axis, and to rotate along the B-axis which is necessary for the adjustment of the cutting edge angle. Single crystal CaF_2 wafers with (111) orientation, 50mm in diameter, 5mm in thickness are machined. The tool rake angle is varied from 0 to -60°. The cutting edge radius is estimated to be ~40 nm before cutting. Undeformed chip thickness is varied from 0 to 1 micrometers by adjusting the cutting edge angle and the tool feed rate in the ranges of 0.1~1°, 0~60μm/rev respectively. Face turning is performed and cutting speed is varied in the range of 47~235 m/min. For wet cutting, kerosene, kerosene mist, water, dehydrated methanol and acetone are used as coolant respectively.

3. Results and Discussion

3.1 Thermal crack generation in wet cutting

In the cutting of single crystal silicon using the straight nosed diamond tool, as the tool feed rate is decreased at a constant cutting edge angle, the cutting mode transits from brittle to ductile[1]. This

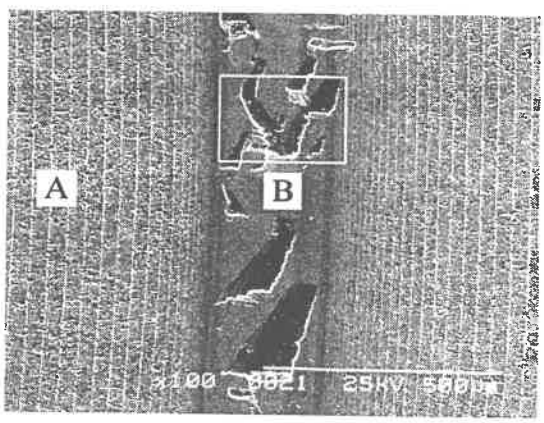

Fig.1 SEM photograph of CaF_2 surface machined under varied feed rate when using kerosene as the coolant, showing different micro-fractures occurred in large feed region (A) and small feed region (B) respectively.

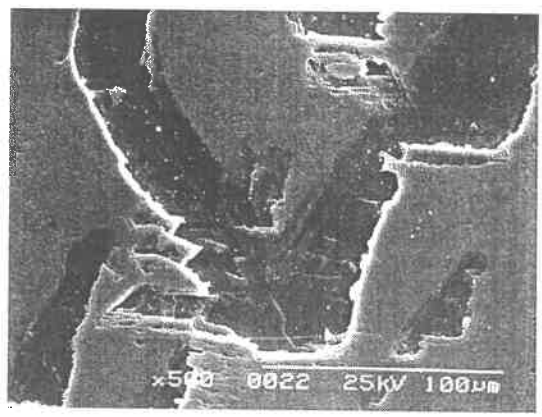

Fig.2 Detailed SEM photograph of the micro-fracture in the small feed region (B) of Fig.1, showing the flat crack surfaces and cleavage structure.

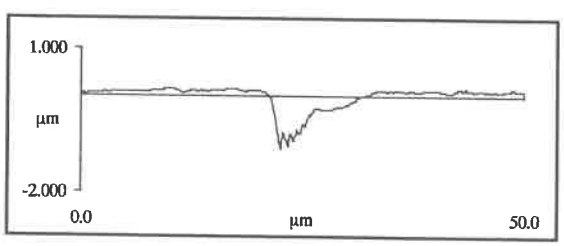

Fig.3 Sectional profile of a crack occurred in large feed region (A), cutting direction from right to left.

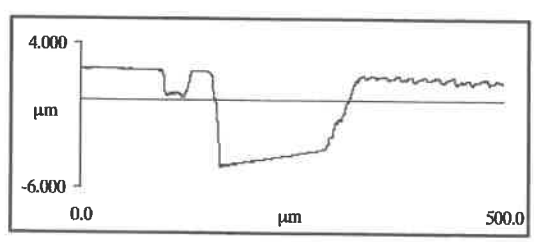

Fig.4 Sectional profile of a crack occurred in small feed region (B), cutting direction from left to right.

phenomenon is commonly observed for other hard brittle materials such as germanium and glass. However, in the cutting of CaF_2, when either kind of coolant is applied, extraordinarily large cracks occurred after the tool feed rate is decreased below a critical value. As an example, a scanning electron microscope (SEM) photograph of the CaF_2 surface machined under varied feed rate when kerosene is used as coolant is shown in Fig.1 (tool rake angle -30°, cutting edge angle 1.53°). In the large feed region (A), micro-fractures of size in the order of 10μm occurred densely, whereas in the small feed region (B), fractures as large as a few hundreds of micrometers occurred. Fig.2 shows the detailed SEM photograph of such a large crack in B region. The crack surfaces are generally smooth and the cleavage structure can be observed at the crack corner. Fig.3 shows the sectional profile of a micro crack in A region, measured by Form Talysurf along the cutting direction. The profile is curved as the V-shape, consisting of waviness on the bottom. This kind of crack is generated in front of the cutting edge during cutting, as discussed in cutting single crystal silicon[5]. Fig.4 shows the sectional profile of a crack in B region. The profile takes on the U-shape, consists flat bottom surface and steep wall surfaces. The depth of the crack reaches 6 μm, more than 3 time of that of Fig.3. Moreover, it is also found that the occurrence of the cracks in A region shows a strong crystallographic effect whereas those in B region do not.

Similar phenomenon is observed when either of the other types of coolant is used. Consequently, the crack generation of B region is considered to be due to the thermal aspects and resulted from the unique thermal property of CaF_2. As known from the cutting principles, the cutting heat generated from material deformation causes the temperature of the cutting point to rise significantly. Then after the tool pass, due to the rapid cooling effect of the coolant, the surface temperature drops suddenly. The above heating-cooling process yields tensile stress in the surface layer. As a result, cleavage fracture occurs. Here we term this kind of crack the "thermal crack". Unlike the cracks in region A, which are formed by the cutting force, the thermal crack is initiated due to the thermal stress. The thermal crack generation is especially significant for single crystal CaF_2 due to its extremely low thermal conductivity index and high thermal expansion coefficient. This kind of thermal property leads to great difference in both the temperature and the stress state between the outer surface layer and the internal region. Moreover, the thermal crack generation is particularly apt to occur when cutting at very low tool feed. Because the temperature rise in the cutting region depends on the heat quantity of per tool pass and the tool pass number on the constant area of machined surface, at an extremely low tool feed rate large quantity of cutting heat accumulates in the surface layer and the cutting temperature rises very high before being cooled.

3.2 Dry cutting

To avoid the thermal crack generation in wet cutting, one possible approach would be dry cutting. In dry cutting, there is no sudden cooling so the cutting heat in the surface layer can transmit to the internal region.

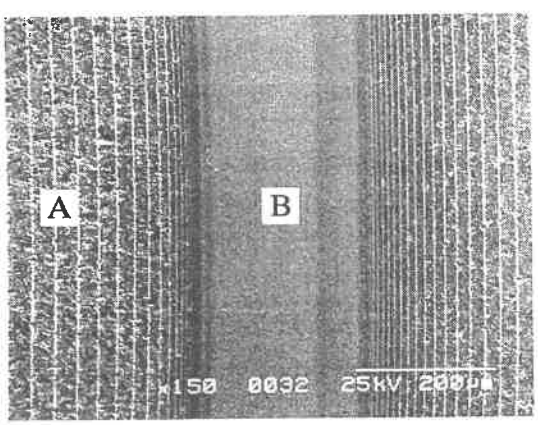

Fig.5 SEM photograph of CaF_2 surface machined under varied feed rate in dry cutting, showing micro-fractures occurred in large feed region (A) and no crack in small feed region (B).

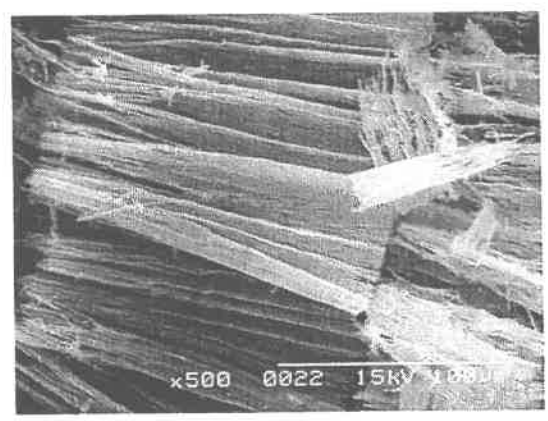

Fig.6 SEM photograph of CaF_2 ductile chips in dry cutting, indicating the material removal via plastic deformation.

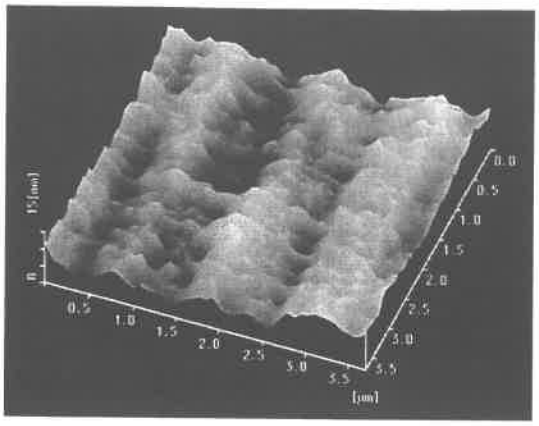

Fig.7 AFM image of CaF_2 surface machined under the feed rate of 1μm/rev in dry cutting, having the roughness of approximately 15nm Rmax.

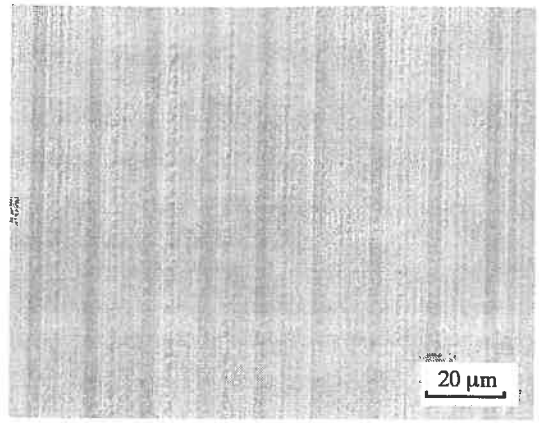

Fig.8 Nomarski photograph of CaF_2 surface machined under the feed rate of 15μm/rev in wet cutting, showing no thermal crack generation.

Thus the temperature difference and tensile stress decrease. Fig.5 shows the SEM photograph of the machined surface under varied feed rate of dry cutting. In region A, the same as Fig.1, micro-fractures occurred. However, in region B, good ductile surface is obtained without any visible crack. Fig.6 shows the SEM photograph of the CaF_2 ductile chips. The chips are continuous and similar to those of metal cutting, indicating the material is removed through plastic deformation. Fig.7 shows the AFM image of the CaF_2 surface, dry cut under the tool feed rate of 1μm/rev and the cutting edge angle of 0.57°. The surface is very smooth and has the surface roughness of approximately 15nm Rmax.

3.3. Large feed wet cutting

Another attempt for avoiding the thermal crack is large feed wet cutting. At large feed rate, the tool pass number and then the cutting heat on a constant surface area is decreased hence the surface temperature does not rise significantly. In this case, crack does not occur though the coolant is applied. In cutting with the straight-nosed diamond tool, by controlling the cutting edge angle to be small enough, undeformed chip thickness can be decreased to nanometer range even at a large tool feed up to a few tens of micrometers per revolution, thus ductile regime turning at large feed becomes possible.

Fig.8 shows the Nomarski photograph of the CaF_2 surface machined under the feed rate of 15μm/rev and the cutting edge angle of 0.12°, using kerosene as coolant. Although the coolant is applied during cutting, no thermal crack is generated. The surface is in good ductile mode with a surface roughness of 36nm Rmax.

4. Summary

Single crystal calcium fluoride is machined using single point diamond turning. It is found that coolant has significant effect on the machined surface quality. Due to the low thermal conductivity index and high thermal expansion coefficient of calcium fluoride, a special kind of crack, termed as thermal crack occurs when tool feed rate is smaller than a critical value during wet cutting. It is proved that dry cutting and wet cutting at large tool feed by using straight nosed tool are effective methods to solve this problem. Nanometric ductile surface is obtained with forming continuous chip on calcium fluoride.

References

1) J. Yan, K. Syoji, H. Suzuki and T. Kuriyagawa: *J. JSPE*, **64**, 9, (1998) 1345.
2) W. S. Blackly and R. O. Scattergood: *Prec. Eng.*, **13**, 2 (1991) 95.
3) T. Nakasuji, S. Kodera, S. Hara, H. Matsunaga, N. Ikawa and S. Shimada: *Ann. CIRP*, **39**, 1 (1990) 89.
4) J. Yan, K. Syoji, T. Kuriyagawa and H. Suzuki: *Proc. ASPE 13th Annual Meeting*, **18** (1998) 128.
5) J. Yan, K. Syoji and T. Kuriyagawa: *J. JSPE*, **65**, 7 (1999) 1008.

Ultra-Precision Cutting of α–β Titanium Alloy

Heiji YASUI*, Shigehiko SAKAMOTO*, Masaki KAWADA*, Sumihisa KONDO* and Akira HOSOKAWA**

* Dept. of Mechanical Engineering & Materials Science, Kumamoto University, Kumamoto 860-8555, JAPAN
** Dept. of Mechanical System Engineering, Kanazawa University, Kanazawa 920-8667, JAPAN

1. Introduction

The titanium alloys are expected to be increasingly used as the high quality components in a wide field of industries because of their excellent mechanical and chemical properties. In order to produce the value-added high quality components of titanium alloys, the productive machining technic of high dimension accuracy with high smoothness surface for titanium alloys is required. The request, however, has not been still filled sufficiently in high precision cutting, especially in ultra-precision cutting because of few researches in addition to the difficult-to-cut materials.

From the point of view, the research aims to establish high quality machining method of titanium alloys. In this research, first of all, the ultra-precision cutting of α–β titanium alloy with a single crystal diamond bite which is generally used in ultra-precision cutting of various kinds of materials such as aluminum alloys, copper alloys and so on is examined. From the results, it is found that the diamond bite is not available for ultra-precision cutting of α–β titanium alloy because of extremely high bite wear rate. Then a coated cemented carbide bite is applied to a series of experiments for the investigation of the surface roughness and tool life in ultra-precision cutting of α–β titanium alloy.

2. Experimental procedure

The experiments are carried out by face-turning the workpiece with the ultra-precision lathe. The overview of experimental setup is shown in **Fig. 1**. The experimental conditions are summarized in Table 1 . Workpiece materials used are pure titanium, β titanium alloy (Ti-22Al-4V) and α-β titanium alloy (Ti-6Al-4V). The shape of workpiece used is ϕ50mm in diameter and 20mm in thickness. Two kinds of cutting tools which are a single crystal diamond bite and a coated cemented carbide bite are used in this experiment. Cutting fluids used are two kinds of oil types. The difference between those is due to the different extreme additives included in cutting fluid. The observation and roughness measurement of the turned workpiece surfaces are done with Nomarski type of differential interference microscope, SEM and surface interferometer (WYKO TOPO-3D).

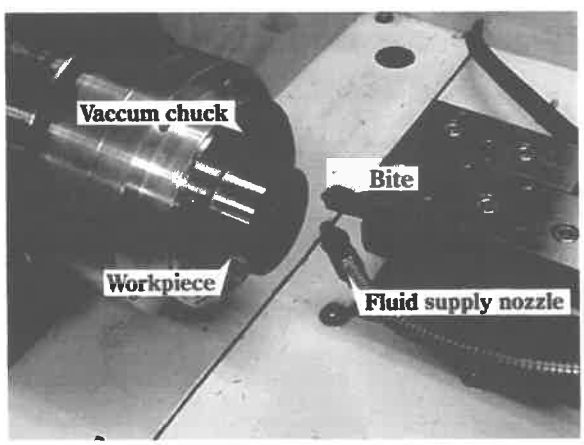

Fig. 1 Overview of experimental setup

Table 1 Experimental conditions

Machine tool:	Ultra-precision Lathe ULC-100A, Toshiba Machine CO.,LTD.
Cutting tool:	Single crystal diamond bite Nose radius: 0.5 mm Coated cemented carbide bite Nose radius: 0.2 mm Rake angle: 0 deg, Relief angle: 7 deg
Workpiece material:	Pure titanium (JIS class 2) Ti-22V-4Al (β titanium alloy) Ti-6Al-4V (α–β titanium alloy)
Cutting fluid:	Oil type cutting fluid (Type A, Type B)
Cutting conditions	Cutting speed: V = 45 m/min Depth of cut: d = 5 μm/rev Feed rate: f = 2 μm/rev

3. Results and Discussions

3.1 Ultra-precision cutting with diamond bite

Figure 2 shows the rake face of single crystal diamond bite after face-turning of β titanium alloy and α-β

titanium alloy at cutting length L=80m. In spite of short cutting length, the enormous wear together with cutting traces is found out on the cutting point of the diamond bite. **Figure 3** shows the microscopic photograph and WYKO image of α-β titanium surface face-turned. The face-turned surface consists of the fine cutting grooves and its 3D surface roughness is about 140nm (P-V). **Figure 4** shows the EPMA images of rake face of the single crystal diamond bite after face-turning of α-β titanium. It is obvious that elements of titanium, aluminum and vanadium included in the α-β titanium in addition to carbon being the element of diamond are detected from the turned bite face. From the results, it is inferred that the adhesion of α-β titanium to the cutting bite edge face is related to the enormous bite wear and the largely surface roughness in short cutting length. Consequently, it is considered that the diamond bite is unsuited for ultra-precision cutting of titanium alloys.

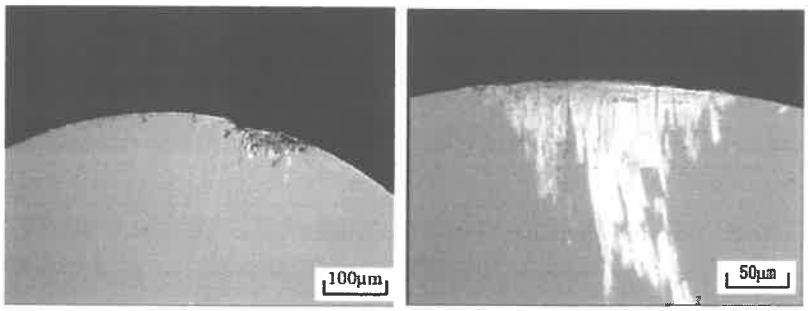

(a) β titanium alloy (L=80m) (b) α–β titanium alloy (L=80m)

Fig. 2 Microscopic photographs of single crystal diamond bite face after face-turning of β titanium alloy and α–β titanium alloy (N=500rpm, V=60m/min, d=5μm, f=2μm/rev, cutting fluid: Type A)

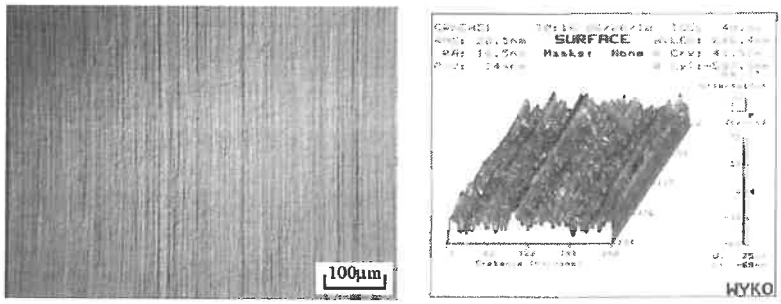

Fig. 3 Microscopic photograph and WYKO image of face-turned α–β titanium alloy surface (N=500rpm, V=60m/min, d=5μm, f=2μm/rev, cutting fluid: Type A)

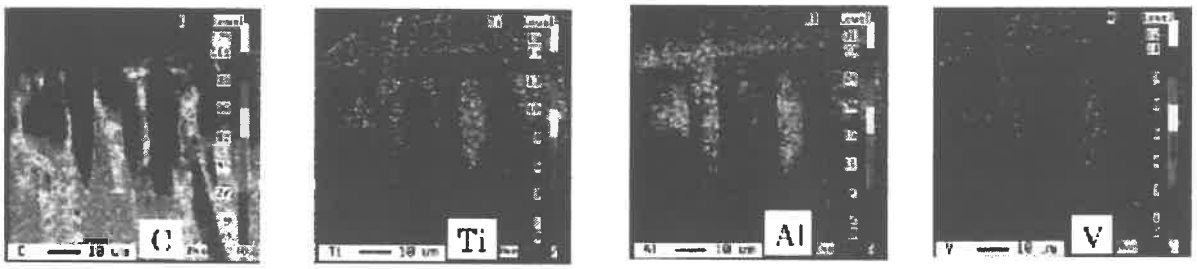

Fig.4 EPMA images of single crystal diamond bite face after face-turning of α–β titanium alloy (N=500rpm, V=60m/min, d=5μm, f=2μm/rev, cutting fluid: Type A)

3.2 Ultra-precision cutting with coated cemented carbide bite

Figure 5 shows the microscopic photographs and WYKO images of face-turned titanium and titanium alloy surfaces with coated cemented carbide bite under using oil type cutting fluid (Type A). For comparison, in the figure, the corroded surfaces are also shown. **Figure 5(a), 5(b) and 5(c)**, however, are for pure titanium, β titanium alloy and α–β titanium alloy, respectively. From the microscopic photographs for pure titanium and β titanium alloy, crystal grains are clear to be observed on the face-turned surface. From the microscopic photograph for face-turned α–β titanium alloy, on the other hand, crystal grains are difficult to be observed. The crystal grains cannot be found as well on the corroded surface of face-turned α–β titanium alloy. The reason is considered that α–β titanium alloy is composed of much finer crystals than pure titanium and β titanium alloy. According to the 2D measurement of the surface roughness with WYKO, it is found that the crystal grain boundary step is about 100nm in pure titanium and about 70nm in β titanium alloy, respectively. As shown in **Fig. 5(a) and 5(b)**, the 3D surface roughness in face-turned pure titanium and β titanium is about 220nm(P-V) and about 140nm(P-V), respectively. Accordingly the surface roughness of pure titanium and β titanium alloy are considerably influenced by

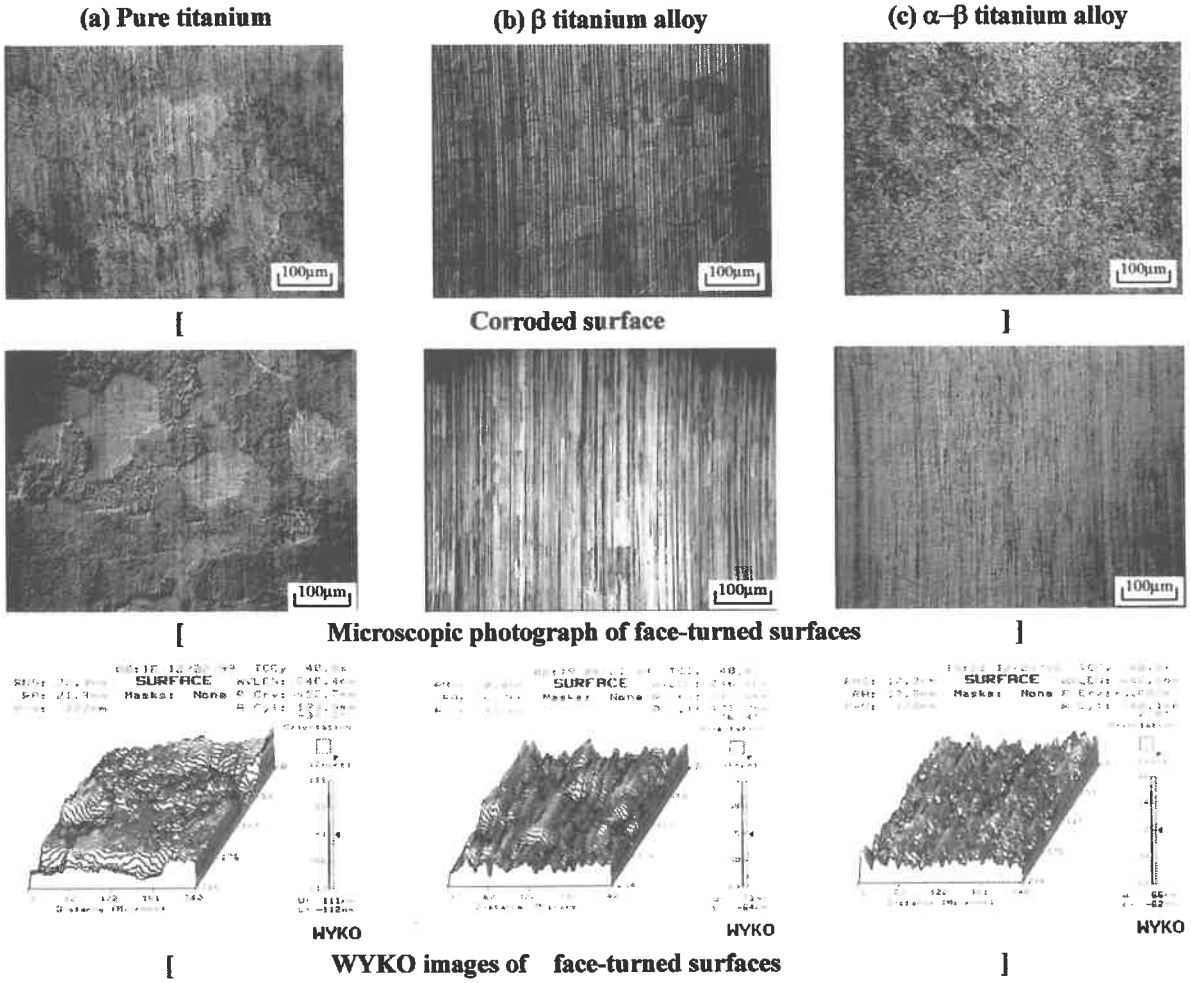

Fig. 5 Microscopic photographs and WYKO images of face-turned titanium and titanium alloy surfaces and their corroded surfaces
(N=500rpm, V=60m/min, d=5μm, f=2μm/rev, cutting fluid: Type A)

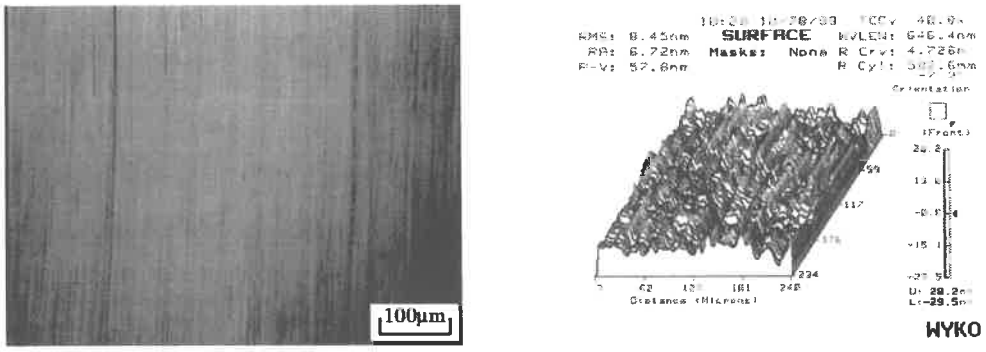

Fig. 6 Microscopic photograph and WYKO 3D image of α–β titanium alloy face-turned with coated cemented carbide bite under using oil type cutting fluid (Type B)
(N=500rpm, V=60m/min, d=5μm, f=2μm/rev)

crystal grain boundary step. The crystal grain boundary step in α–β titanium alloy, on the other hand, has little influence on the surface roughness.

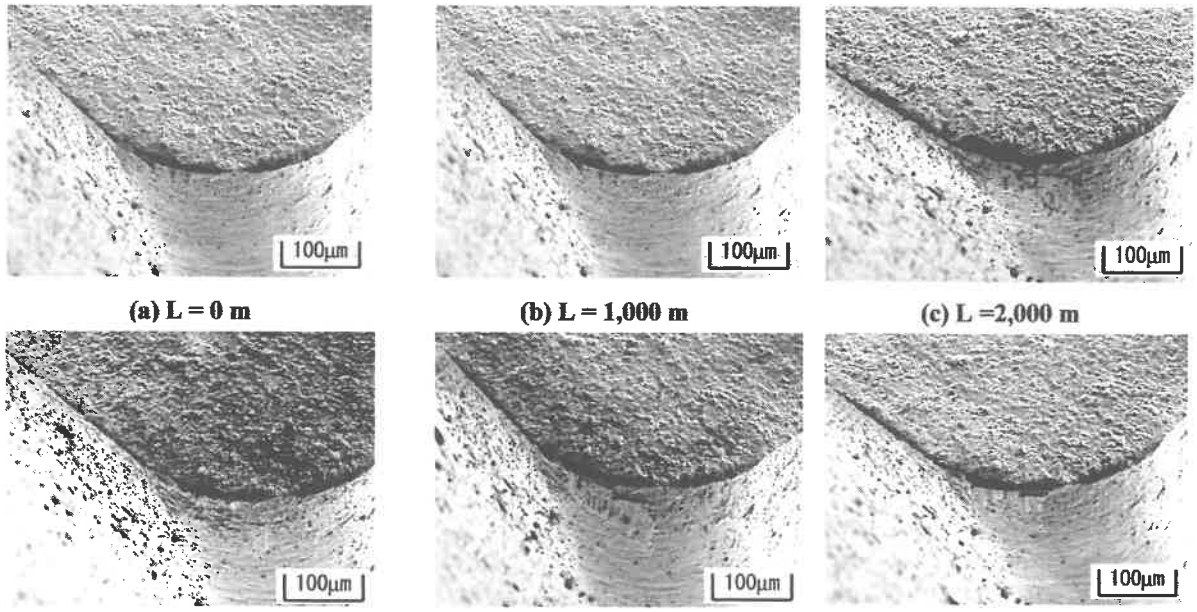

(a) L = 0 m (b) L = 1,000 m (c) L =2,000 m

(d) L = 3,000 m (e) L = 4,000 m (f) L = 5,000 m

Fig.7 Change of coated cemented carbide bite face with cutting length (N=500rpm, V=60m/min, d=5μm, f=2μm/rev, cutting fluid: Type B)

Figure 6 shows the microscopic photograph and WYKO image of face-turned α–β titanium alloy surface with coated cemented carbide bite under using oil type cutting fluid (Type B). Comparing with face-turned α–β titanium alloy surface under using cutting fluid (Type A), which is shown in **Fig.5 (c)**, from the photograph, it is found that the face-turned surface is smooth though the cutting grooves are observed as well. The 3D finished surface roughness is also improved up to 60nm (P-V). The improvement in surface roughness is considered to be caused by the difference between the additives containing in cutting fluid of type A and type B. From the results, it is referred that the type of cutting fluid effects the ultra-precision turning characteristics of titanium and titanium alloys. It is important that the most suitable cutting fluid for ultra-precision cutting of α–β titanium alloy is selected.

Figure7 shows the change of coated carbide bite face with face-turning process of α–β titanium alloy under using oil type cutting fluid (Type B). It is obvious from the figure that the rake and relief faces of coated cemented bite have little wear until cutting length of about 5km which is much longer than 80m at which the enormous wear of diamond bite is shown in **Fig.2**. In the case of kerosene used generally as cutting fluid in ultra-precision cutting, however, it was found that both wears of rake and relief faces of coated cemented bite became considerably large in cutting length of about 200m[1].

4. Summary

The coated cemented carbide bite used in the research is available for ultra-precision cutting of α–β titanium alloy because the bite wear is so small in the cutting length of about 5km and the finished surface roughness is smoother than 60nm (P-V). The surface roughness of ultra-precision face-turned α–β titanium alloys depends considerably on the kind of cutting fluid. By using the special oil type cutting fluid including the extreme pressure additives, the surface roughness is attainable smoother than 60nm (P-V) though it is rougher than 500nm (P-V) for kerosene used generally as the cutting fluid in ultra-precision cutting.

Acknowledgement

The authors would like to thank Toshiba Machine Co., Ltd., Osaka Diamond Industrial Co., Ltd., Yushiro Chemical Industry Co., Ltd., UEX Co., Ltd. and Daido Steel Co., Ltd for providing cutting fluids and titanium workpiece materials. A part of this research is supported by Grant-In-Aid for Scientific Research, 1998, in Japan.

References

[1] H.Yasui, S.Sakamoto, M.Kawata, A.Fujimori: "Effect of Cutting Fluid on Surface Roughness in Ultra-Precision Cutting of Titanium Alloys", Proceedings of Spring Annual Meeting of JSPE, (2000), pp.231.

Investigation of a novel tool concept for ductile grinding of optical glass

Ekkard Brinksmeier; Rüdiger Malz; Werner Preuß

Laboratory for Precision Machining, University of Bremen

Introduction

In this work a novel tool concept for ductile grinding of optical glass is presented. In contrast to coventional precision grinding technologies, electroplated coarse grained diamond wheels with grain sizes of approx. 100 µm are used in order to obtain longer tool life and thus achieving ductile grinding of large aspheric shapes. The essential requirement for a successful application of coarse grained diamond wheels in ductile grinding of optical glass is the generation of a special grinding wheel topography consisting of flattened grains with a very constant peripheral envelope, resulting in a minimized radial runout of the grinding wheel (cf. fig. 1) [Kan95].

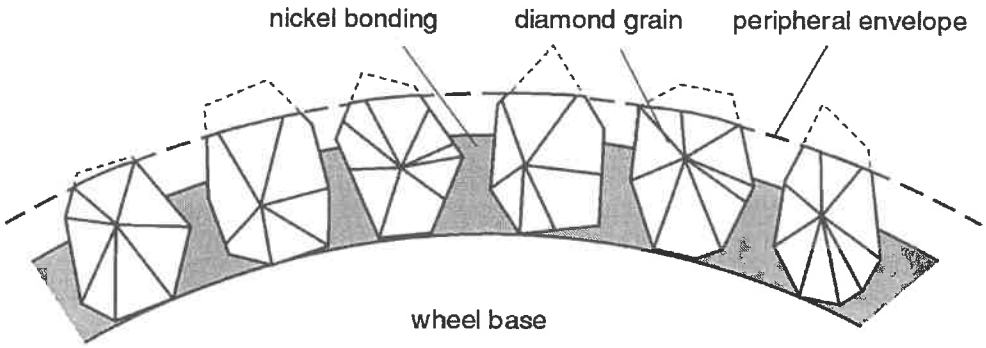

Fig. 1: Intended grinding wheel topography after dressing.

In a first step, a special dressing technology for coarse grained diamond wheels was developed. The dressing time was found to be strongly dependent on the dressing wheel speed. The suitability of the novel tool concept for ductile grinding was tested in surface grinding of SF6 glass. Ductile mode was achieved with similar cutting parameters as known from precision grinding with fine grained wheels [Bif88].

Experimental

The experimental setup for the dressing and grinding experiments is shown in fig. 2. In dressing configuration the grinding wheel performs the infeed motion in x-direction, while the dressing wheel oscillates in z-direction. For the surface grinding experiments x is the feed direction, while the infeed motion is carried out by the workpiece in y-direction. The glass workpiece is mounted on a vacuum chuck below the grinding wheel. The radial error motions of the air bearing dressing and grinding spindles are less than 25 nm. Precision stages with a resolution of 0.1 µm were used for motion in x-, y-, z-directions. The resolution in y-direction is improved to 10 nm due to a 5° tilt of the stage. Grinding forces are recorded with a Kistler 9256 piezo electric transducer with a threshold < 0,002 N. Both dressing and grinding operations are performed by supplying a coolant emulsion.

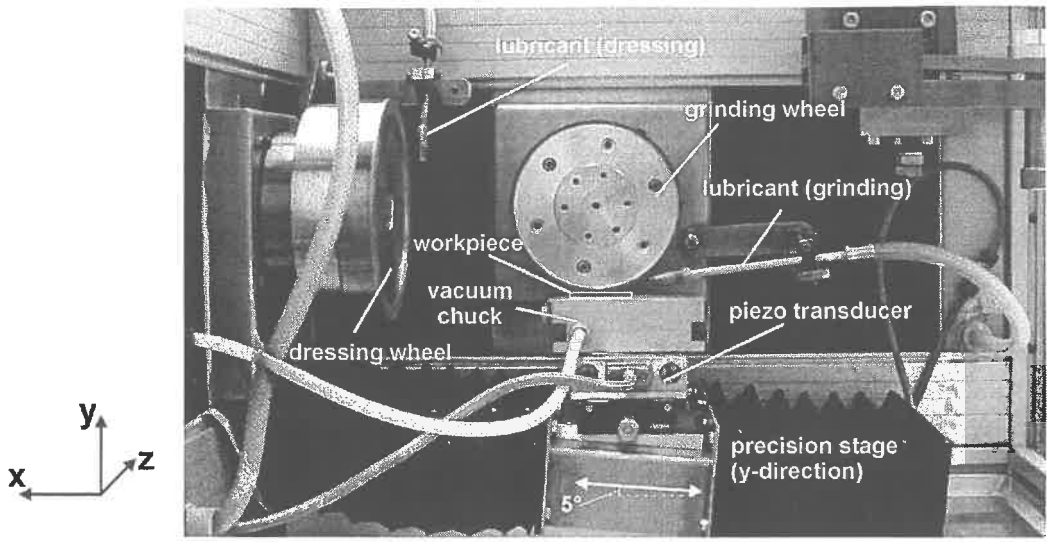

Fig. 2: Experimental setup for dressing and surface grinding with coarse grained diamond wheels.

Dressing of coarse grained diamond wheels

For dressing the diamond grinding wheels only the diamond tops were machined, since the electroplated wheels exhibit a single abrasive layer. Cutting the grain tops results in flattened diamonds on a constant peripheral envelope, so that the number of diamond grains active in the grinding process is increased significantly. Moreover, the hard bonding material leads to a reduced probability of grain tear-out, compared to resin or metal bonded grinding wheels.

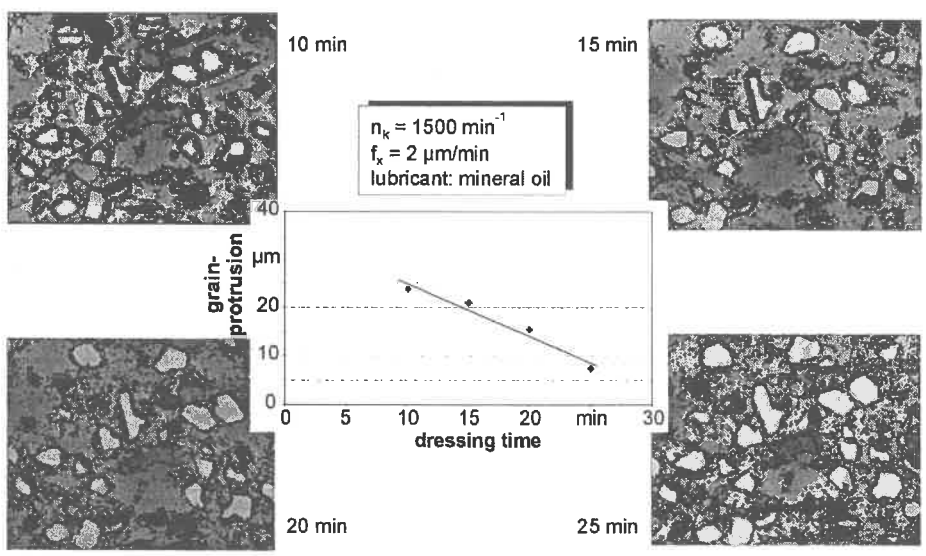

Fig. 3: Grain protrusion vs. dressing time.

For studying the material removal mechanisms and -rates, experiments were performed for different dressing wheel speeds (600 rpm - 1500 rpm). Feed rate was $f_x = 2$ µm/min. The dressing wheel was a D15 metal bonded diamond cup wheel. The removal rate was characterized by investigating the grain protrusion on replicas of the wheel topography with a white-light interferometer. The change of wheel topography with increasing dressing time is shown in fig. 3. The slope of the measured average grain protrusion plotted vs. dressing time

reflects the material removal rate. The maximum material removal rate was obtained for the lowest dressing wheel speed of $n_k = 600$ rpm.

Dressing of the diamond wheels was performed with a grinding wheel speed $v_c = 30$ m/s which is also the cutting speed in the subsequent grinding experiments. With a feed rate $f_x = 2$ µm/min and a dressing wheel speed $n_k = 600$ rpm radial grinding wheel runout of less than 2 µm was obtained. The radial runout was investigated using a Mahr inductive dial comparator with a resolution of 0.2 µm.

Grinding experiments

The material removal mechanism for precision grinding of SF6 glass with electroplated coarse grained diamond wheels was studied in several grinding experiments. In fig. 4 roughness R_a is shown for different feed rates and depths of cut. The roughness R_a is strongly influenced by the feed rate v_f, while the depth of cut has a considerably lower effect on surface topography. For $v_f = 1$ mm/min ductile material removal is obtained for all investigated depths of cut. Increasing the feed rate from 1 mm/min to 5 mm/min leads to semi-ductile material response. Further increase of the feed rate from 5 mm/min to 10 mm/min results in brittle material removal. Only for a depth of cut $a_e = 1$ µm semi-ductile surface topography was reached even with $v_f = 10$ mm/min.

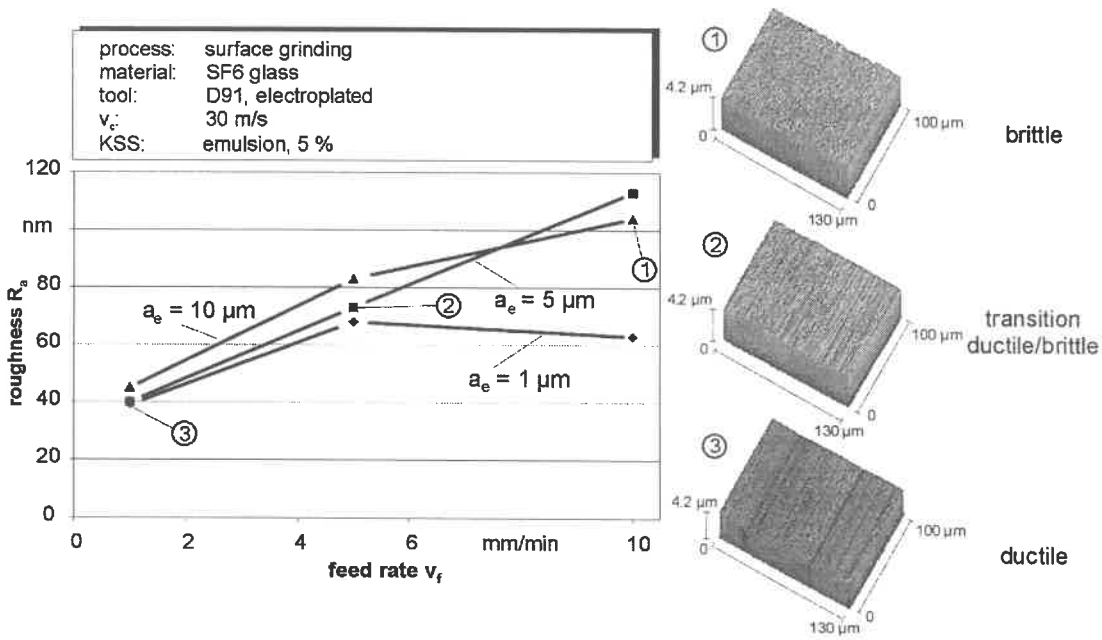

Fig. 4: Roughness R_a and material removal mechanisms vs. feed rate v_f for SF6 glass.

In a number of publications (cf. [Kom97]) the existence of a critical undeformed chip thickness for ductile machining of glass is postulated. The undeformed chip thickness h_{cu} for surface grinding is given by

$$h_{cu} = \frac{a_e \cdot v_f}{v_c} \qquad (1)$$

with depth of cut a_e, feed rate v_f and cutting speed v_c. In our experiments we found different material removal mechanisms even for constant undeformed chip thickness h_{cu} depending on feed rate v_f. This hints at the existence of a critical feed rate as described by Blackley and

Scattergood for diamond turning of brittle materials [Bla91]. Below this feed rate, microfracture induced in the uncut shoulder will not replicate below the cut surface plane (cf. fig. 5). Consequently, constant undeformed chip thickness can result in both, ductile or brittle material removal, depending on the ratio of feed rate to depth of cut.

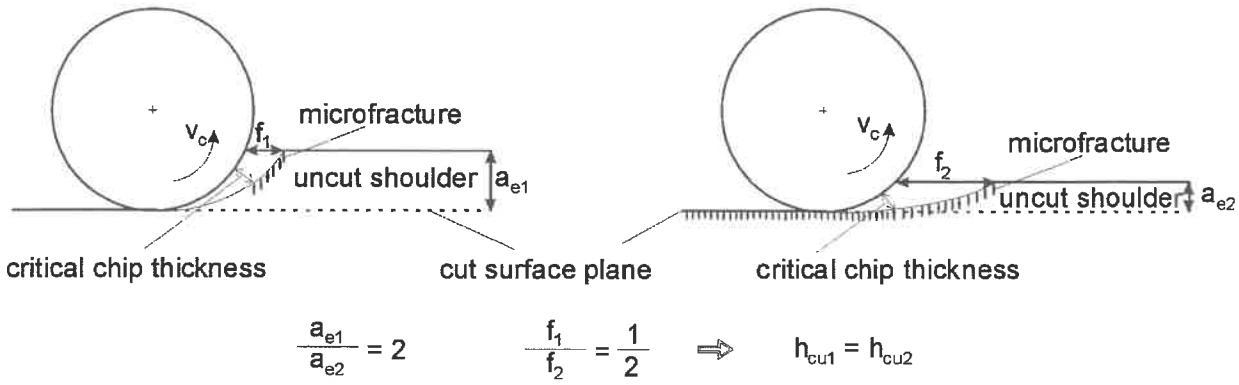

Fig. 5: Effect of feed rate and depth of cut on surface topography.

Conclusion

We have shown that coarse grained diamond wheels with grain sizes of appr. 100 µm can be successfully applied for ductile grinding of glass. The essential requirement for ductile material removal is a very constant peripheral envelope of the diamond tops which has to be in the range of the depth of cut of a few micron. Dressing of the electroplated grinding wheels was performed by grinding the diamond tops with a diamond cup wheel. A radial runout of less than 2 µm was achieved.

Grinding experiments were performed with different feed rates and depths of cut. The achieved roughness R_a was found to be strongly influenced by the feed rate v_f. For v_f = 1 mm/min ductile material removal was achieved even with a depth cut a_e = 10 µm.

Further investigations will focus on the application of our surface grinding process to contour grinding of aspherical shapes. We expect, that the surface quality achieved in surface grinding will improve by a contour grinding process due to the superimposing tracks of the grains.

Acknowlegement

The authors thank the Deutsche Forschungsgemeinschaft DFG for funding this research project.

References

[Bif88] Bifano, T.G.: Ductile-regime grinding of brittle materials. Diss. North Carolina State University, 1988.

[Bla91] Blackley, W. S.; Scattergood, R. O.: Ductile-regime machining model for diamond turning of brittle materials. Precision Engineering, Vol. 13 No. 2, 1991. pp. 95-103.

[Kan95] Kanai, A.; Miyashita, M.; Sato, M.; Daito, M.: Proposal of High Productivity in Ductile Mode Grinding of Brittle Materials. Proc. ASPE 10th Annual Meeting, Austin, Texas, Oct.1995. pp. 167-170.

[Kom97] Komanduri, R.; Lucca, D. A.; Tani, Y.: Technological advances in fine abrasive processes. Keynote Paper, Annals of the CIRP, 46/2/1997. pp. 545-596.

MICRO CRACK-FREE SCRATCHING OF SILICON UNDER EXTERNAL HYDROSTATIC PRESSURE

Naga Chandrasekaran, Masahiko Yoshino[1], Takayuki Aoki[1], Ranga Komanduri
Mechanical and Aerospace Engineering, Oklahoma State University, Stillwater, OK 74078
[1] Tokyo Institute of Technology, Tokyo, Japan

1. INTRODUCTION

Silicon is widely used in the semiconductor electronic industries for integrated circuits and for optical components in high resolution thermal imaging systems. These precision components require a high degree of surface finish and form accuracy with minimal surface and subsurface damage. It has been observed that the tendency for subsurface defects, such as micro cracks to develop in the case of brittle materials decreases with decrease in the undeformed chip thickness and almost disappear below a critical value of depth of cut, < 1 μm [1-5]. This is because at low depths of cut, the stresses generated by the high negative rake angle tools may not reach the values required to generate median vents in brittle materials. It has also been suggested that at very shallow depths of cut, the energy required to propagate cracks may be larger than the energy required for plastic yielding resulting in material removal by plastic deformation [2].

Alternately, it is possible that such large negative rake angle tools can induce significant hydrostatic pressure to plastically deform the material around the tool [5]. Nakasuji et al. [6] reported that negative rake angle tools enabled higher cut depths before the occurrence of brittle fracture. From Bridgman's work [5] it is well known that the hydrostatic pressure can increase the strain at fracture even in a nominally brittle material, such as chalk, marble, cast iron etc. In the current study, the possibility of generating micro crack-free silicon surfaces under a range of external hydrostatic pressure (0 to 400 MPa) and scratch depths (0 to 1.5 μm) and consequently, increasing the brittle-to-ductile transition (BDT) depth is investigated (both experimental and numerical) in detail. More details are given elsewhere [8].

2. EXPERIMENTAL AND NUMERICAL APPROACH

Pin-on-disc type scratch tests were conducted on (111) silicon surface under various external hydrostatic pressures (0 to 400 MPa) and scratch depths (0.1 to 1.5 μm) using a specially designed high external hydrostatic pressure machining apparatus [4]. The scratch speed was maintained constant at 5 mm/s. A single crystal diamond pin with an edge radius of 17 μm was used in the experiments. The resulting scratches were examined in an SEM and an optical interference microscope (MicroXam) to evaluate the influence of scratch depth and hydrostatic pressure on the nature of the scratches produced (smooth versus fractured surfaces). To simulate dislocation generation and propagation during indentation and retraction of silicon, mesoplasticity FEM technique under plane strain conditions was used [9]. Indentation simulations were performed on the (111) silicon surface for a depth of 2.5 μm. Friction at the interface of indenter and workmaterial was not considered for simplicity.

3. RESULTS AND DISCUSSION

3.1. Scratch Experiments Under External Hydrostatic Pressure (EHP)

Figures 1 (a) and (b) are SEM micrographs of the scratch tracks on silicon at 0 and 400 MPa external hydrostatic pressure (EHP), respectively, at a scratch depth of ~ 0.6 μm. It can be seen that at 0 MPa

EHP condition [Figure 1 (a)], the material removal is accompanied by brittle fracture due to the generation of lateral cracks and their growth outside the scratch track. Figure 1 (b), on the other hand, shows a smooth surface on the application of 400 MPa EHP. The SEM images indicate that for a given scratch depth, the external hydrostatic pressure (EHP) plays an important role in minimizing machining defects, such as microcracks, and producing smooth surfaces.

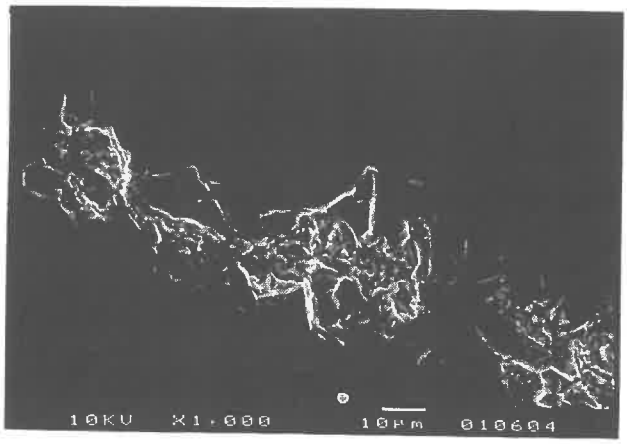

(a)

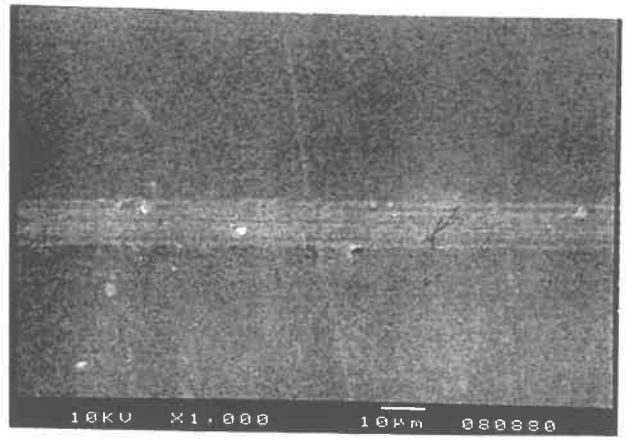

(b)

Figure 1 SEM micrographs of scratch tracks on silicon at (a) 0 MPa and (b) 400 MPa EHP

Figure 2 shows the variation of the crack-ratio (ρ) with scratch depth (d) for different hydrostatic pressure conditions where ρ is the total length of the cracks along unit groove length. It can be seen from Figure 2 that the critical scratch depth (d_c) for zero crack-ratio (ρ=0, no defects) increases with increase in the external hydrostatic pressure. For example, the critical scratch depth (d_c) for zero crack-ratio is ~0.11 μm at 0 MPa EHP. With increasing scratch depth (d), ρ increases and reaches a value of unity (100% fracture) at a scratch depth, d ~ 0.55 μm. When EHP is increased to 400 MPa, ρ remains at zero as the scratch depth increases up to ~0.4 μm. Beyond this point, ρ increases with increasing groove depth and approaches 100% at d ~ 2 μm. It can, therefore, be seen that the critical depth of cut can be increased with increase in EHP. The EHP tends to compensate the tensile stresses generated during the scratching process which in effect suppresses the crack generation and growth.

3.2. Mesoplasticity FEM Simulation - Indentation-Retraction on (111) Silicon Surface

The principal and hydrostatic stress distributions showed the generation of compressive stresses just beneath the indenter during indentation and tensile stresses outside the perimeter of the indenter during retraction [8]. Figure 3 shows the variation of the maximum tensile principal stress and compressive hydrostatic stress (hydrostatic pressure) with depth of indentation and after retraction, respectively. The retracted depth corresponds to the depth at which the force curve during retraction reaches zero force. Figure 3 shows that the maximum hydrostatic pressure increases at a higher rate than the tensile principal stress during indentation and at maximum indentation depth the hydrostatic pressure is ~ 4 times higher than the tensile principal stress. After retraction, the tensile principal stress increases further. However, the hydrostatic pressure decreases significantly as observed from the stress distribution plots [8]. This combination of stress variation can result in an increase in the defect density in the workmaterial after retraction as will be shown below. To investigate the effect of

external hydrostatic pressure (EHP) on the deformation and fracture in the indentation-retraction process, the stress distribution and the defect density distribution (η) were calculated under EHP from 0 to 400 MPa from the FEM simulation. With increasing EHP, the stress distribution in the workmaterial was observed to transform from a tensile to a compressive resulting in a decrease in the magnitude of defect generation [8].

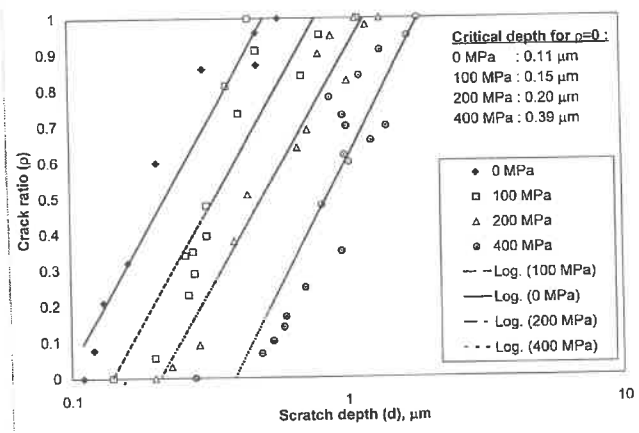

Figure 2 Variation of the crack-ratio with the scratch depth under various EHP

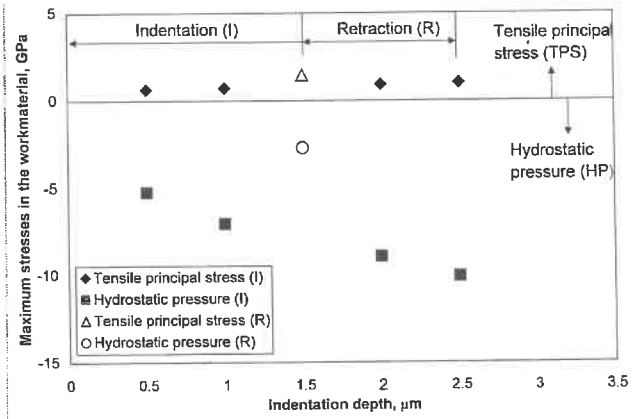

Figure 3 Stress variation in the workmaterial using mesoplasticity FEM results

Figures 4 (a) and (b) show the variation of the maximum value of the defect density (η) in the workmaterial at various depths of indentation and after retraction, respectively, for different EHP conditions. The defect density for a particular indentation depth and hydrostatic pressure condition is higher after retraction than at maximum indentation depth due to the combination of stress variation [Figure 3]. Figure 4 also shows an increase in the magnitude of η with increasing indentation depth and decreasing EHP (both during indentation and after retraction). This can be attributed to the increasing compressive hydrostatic stress and decreasing tensile principal stress in the workmaterial. Thus, at a critical defect density of ~0.3 GPa for example, the critical indentation depth after retraction increases from ~0.3 μm at 0 MPa EHP to ~1 μm at 400 MPa EHP. The increase in the critical depth is ~3 times with the application of 400 MPa external hydrostatic pressure. Earlier, the experimental results also showed a similar increase in the critical depth by ~3 times on the application of 400 MPa external hydrostatic pressure [Figure 2]. Based on the experimental and simulation results, it appears feasible to increase the brittle-to-ductile transition (BDT) depth in finishing of brittle materials under EHP.

4. CONCLUSIONS

The feasibility of generating micro crack-free silicon surfaces under external hydrostatic pressure was investigated in detail. Scratch experiments were performed on the (111) silicon surface at external hydrostatic pressures (EHP) varying from zero to 400 MPa. On the numerical side, plane strain indentation-retraction simulations were conducted using the mesoplasticity FEM technique. Both, the experimental and the simulation results show that the hydrostatic pressure plays an important role in minimizing fracture and producing smoother surfaces. The results also indicate an increase in the brittle-to-ductile transition (BDT) depth with increasing hydrostatic pressure. The change in the behavior from brittle to ductile of hard and brittle materials with decreasing depth is attributed to

the high effective negative rake angle presented by the tool. Such high negative rake angles generate significant hydrostatic pressure around the tool which in effect reduces the tensile stresses resulting in the generation of smooth surfaces on brittle materials.

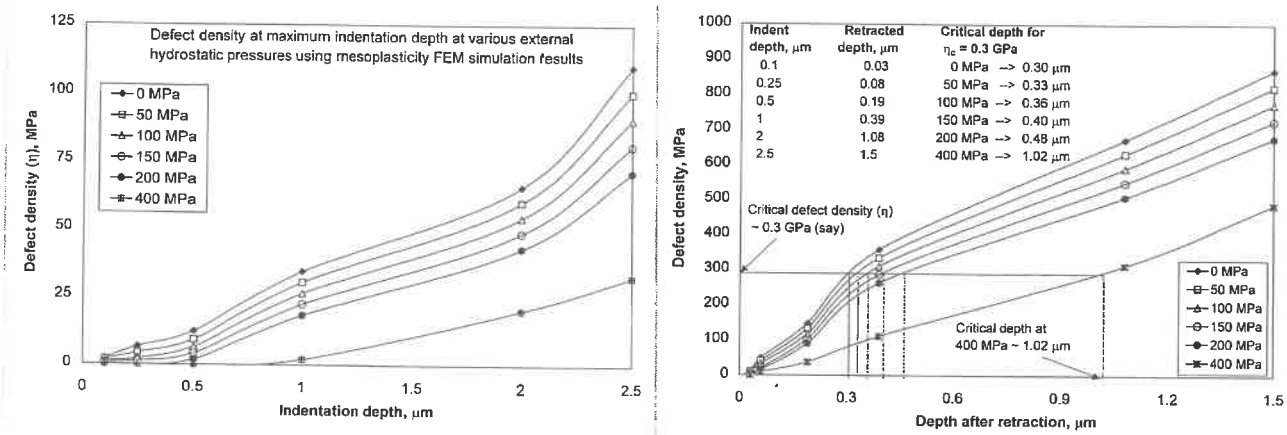

(a) (b)

Figures 4 Variation of defect density (a) with indentation depth and (b) after retraction under EHP

ACKNOWLEDGEMENTS

This work was supported by a grant from the US-Japan co-operative program on High Efficiency, Damage-free Finishing of Advanced Ceramics and Glasses (INT-9603002). The authors thank the U.S. National Science Foundation and the Ministry of Education of Japan for support of this work. One of the authors (R.K.) also acknowledges the support from the DOD EPSCoR program on the Finishing of Advanced Ceramics and the MOST Chair for Intelligent Manufacturing.

REFERENCES

[1] K. E. Puttick, M. R. Rudman, K. J. Smith, A. Franks, and K. Lindsey, "Single Point Diamond Machining of Glasses," Proc. R. Soc. Lond. A, 426, (1989), pp. 19-30

[2] P. N. Blake and R. O. Scattergood, "Ductile-Regime Machining of Germanium and Silicon," J. Am. Cer. Soc., 73/4, (1990), pp. 949-957

[3] T. Shibata, S. Fujii, E. Makino, and M. Ideda, "Ductile-Regime Turning Mechanism of Single Crystal Silicon," Precision Engineering, 18, (1996), pp. 129-137

[4] M. Yoshino, T. Aoki, T. Shirakashi, and R. Komanduri, "Some Experiments On the Scratching of Silicon," Int. J. Mech. Sci., (in print, 2000)

[5] R. Komanduri, D. A. Lucca, Y. Tani, "Technological Advances in Fine Abrasive Processes," Annals of CIRP, 46/2, (1997), pp. 545-596

[6] T. Nakasuji, S. Kodera, S. Hara, H. Matsunaga, N. Ikawa, and S. Shimada, "Diamond Turning of Brittle Materials for Optical Components," Annals of CIRP, 39/1, (1990), pp. 89-92

[7] P. W. Bridgman, "The Effect of Hydrostatic Pressure On the Fracture of Brittle Substances," J. Appl. Phys., 18, (1947), pp. 246-259

[8] N. Chandrasekaran, M. Yoshino, T. Aoki, and R. Komanduri, "On the Micro Crack-Free Scratching of Silicon Under External Hydrostatic Pressure," submitted for publication

[9] M. Yoshino, T. Shiina, and T. Shirakashi, "FEM Simulation of Dislocation Behavior in an FCC Metal," Computer Modeling and Simulation in Engineering, 2, (1997), pp. 218-226

INVESTIGATION OF THE SURFACE INTEGRITY OF PRECISION MACHINED SINGLE CRYSTAL SILICON

~~C. L. Chao~~[1], K. J. Ma[2], S.C. Sheu[2], H. Y. Lin[3] and F. Y. Chang[3]

[1] Department of Mechanical Engineering, E790, Tam-Kang University, No.151 Ying-Chuan Road, Tamsui, Taipei Hsien-251, Taiwan, R.O.C (Email: clchao@mail.taipeilink.net)

[2] Department of Mechanical Engineering, Chung-Cheng Institute of Technology, Ta-Hsi, Taoyuan, Taiwan-335, R.O.C.

[3] MEMS Division, MIRL, Industrial Technology Research Institute, Chu-Tung, Hsin-Chu, Taiwan-310, R.O.C.

EXTENDED ABSTRACT

Single crystal silicon, having many advanced physical and mechanical properties, is now widely used in the semiconductor industry (account for more than 90% of the semiconductor devices) and infrared optics. In order to machine the 300mm~400mm silicon wafer to the specified surface roughness and flatness, precision ELID (electrolytic in-process dressing) diamond grinding and CMP (chemical-mechanical polishing) were employed in this study to replace the conventional grinding, etching and polishing routine. Various machining conditions such as wheel grain size, spindle speed, feedrate, ELID conditions and CMP parameters were studied in the present research. The ELID-ground and CMPed specimens were subsequently examined using OM, SEM and AFM to ensure the quality of surface. Sub-surface damage layer of the machined surface was also investigated using high resolution transmission electron microscope (HRTEM) and chemical etching techniques. It was found that sub-surface cracks generated by diamond grinding process could in some cases penetrate up to 20μm deep into the surface. Although the subsequent CMP process could improve the surface roughness to a Ra of 1nm, sub-surface cracks could be revealed by chemical etching if it were not fully removed. From the viewpoint of material removal rate and uniformity among the CMP parameters tested in this study, condition with down force of 10psi, pad speed of 20rpm, carrier speed of 40rpm and oscillation speed of 2mm/sec could obtain the best result. However, down force of 5psi, pad speed of 10rpm, carrier speed of 30rpm and oscillation speed of 2mm/sec gave the best surface roughness. The results of XTEM showed that for specimens ELID-ground by #1200 and #2000 wheels the micro-cracks could sometimes penetrate 20μm into the surface. Although the CMP process can improve the surface to a Ra ~ 1nm and no apparent flaws observed under the x400 OM, this did not guarantee the sub-surface was free from defects. This means that grinding-induced cracks are sometimes just too deep to be removed by the subsequent CMP process if the form accuracy is to be maintained. The results showed that #4000, #6000 ELID grinding process followed by CMP process proved to be a feasible combination to obtain a crack-free surface with sub-nanometer surface roughness.

Keywords: ELID grinding, CMP, Silicon wafer, sub-surface damage

Experiment Setup

ELID Grinding: A Nachi RGS20N ELID grinding machine was used in this study for carrying out grinding experiments. The power supply and metal bond diamond wheels were made by Fuji (ELIDer 630) and Noritake respectively. Shown schematically in Figure 2 is the lay-out of the grinding experiments. The (100) silicon wafer was placed on the work spindle which was set to rotate at a relatively low speed (100~400rpm). The grinding head was set to operate at the speed of 1000 to 3000rpm. The feed rates, peak voltages and peak currents ranged respectively from 2μm/min to 8μm/min, from 30V to 60V and from 2A to 10A. A pulse duration (Ton/off) of 2μSec and gap of 0.4mm were used in the study.

Chemical Mechanical Polishing: The CMP experiments were carried out on a Westech (model 372M) CMP machine (Fig. 3) and the machining conditions were as following: pad speed up to 20rpm, carrier speed up to 42rpm, down force ranged from 3 to 12psi, backpressure 2psi, oscillation velocity up to 8mm/sec and slurry flow rate was 200ml/min. SC-1 (diluted with D.I. water SC–1 : H_2O = 1 : 2) and ZrO_2 (diluted with D.I. water ZrO_2 : H_2O = 1 : 3) were the slurry tested in this study. A special pattern was photo-etched (1.5μm deep) onto wafer at nine different positions so that the MRR and non-uniformity (n.u.% = $[\delta h_{max}-\delta h_{min}]/[2*\delta h_{ave}]$) could be measured.

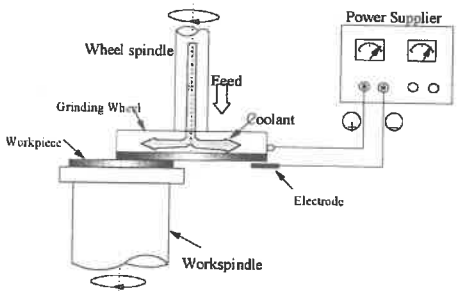

Fig. 2 Schematic representation of the setup of grinding experiments

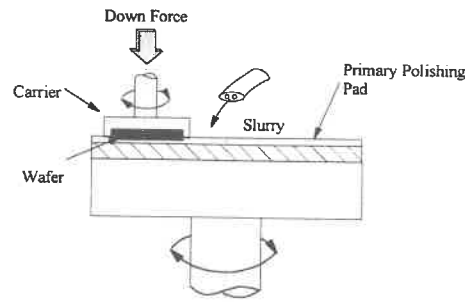

Fig. 3 Schematic of the CMP machine

Results and Discussions

MRR and surface obtained: Shown in Fig. 4 is the MRR of different points on the wafer under various down pressure and it is clear that a good balance between MRR and uniformity can be reached by applying down pressure of 10psi. The surface roughness, non-uniformity and MRR achieved by applying different down force and pad speed were shown in Fig. 5, Fig. 6 and Fig. 7 respectively.

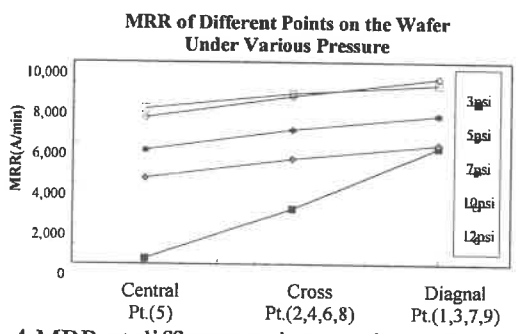

Fig. 4 MRR at different points on the wafer

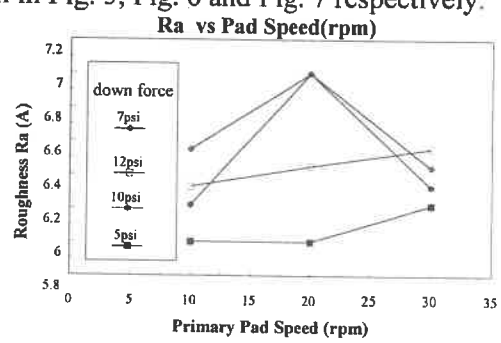

Fig. 5 Surface roughness obtained under various down forces and pad speeds

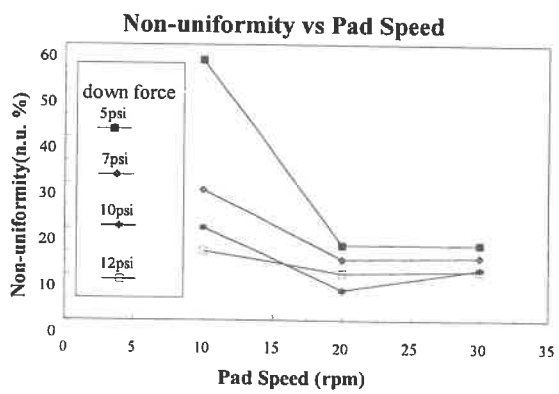

Fig. 6 Non-uniformity under different down force and pad speed

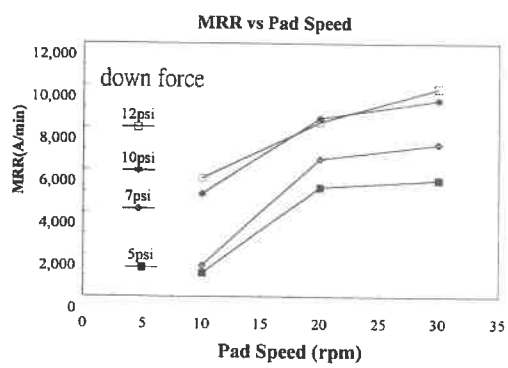

Fig. 7 MRR achieved under different down force and pad speed

Sub-surface damaged layer: The ground/polished specimens were subsequently examined with cross-section transmission electron microscopy (XTEM) and etching technique to reveal the defect structure of sub-surface damage layer. The results of XTEM showed that for specimens ground by #1200 wheels the micro-cracks could sometime penetrate 20μm into the surface. Shown in Figure 8 are the AFM and HRTEM micrographs of the ELID ground silicon surfaces using #6000 diamond wheel 60V, 10A, 3000/100rpm and feedrates of 8μm/min. Single crystal substrate covered by an amorphous layer of 10~30nm in thickness when thick oxide layer and high feedrate was used. While grinding with thick oxide layer and low feedrate excess attritious wear might occurs and the generated friction heat/force introduced a thicker amorphous layer(up to 80nm) and the dislocation distributed layer (up to 200nm) underneath it.

Shown in Fig. 9(a) and (b) are the optical microscopy of #1200P(#1200 ground +CMP) sample before and after etched by HF acid(50wt% HF 10ml, $K_2Cr_2O_7$ 5g, H_2O 5ml). The apparently defect-free CMPed surface(Ra<1nm) was actually full of hidden cracks (Fig. 9). This means that a superb surface does not guarantee the sub-surface is free of defects and the 20μm cracks are just too deep to be removed by the subsequent CMP process if the form accuracy is to be maintained. The possible reason for the grinding-induced cracks to be "hidden" is that they are refilled by neighboring materials during the CMP process via plastic flow.

No hidden cracks were observed when the #4000P, #6000P (#4000, #6000 ground+CMPed for 5min.) samples were etched. This demonstrates that as long as the grinding-induced cracks are within working depth of CMP process it is possible to remove them completely.

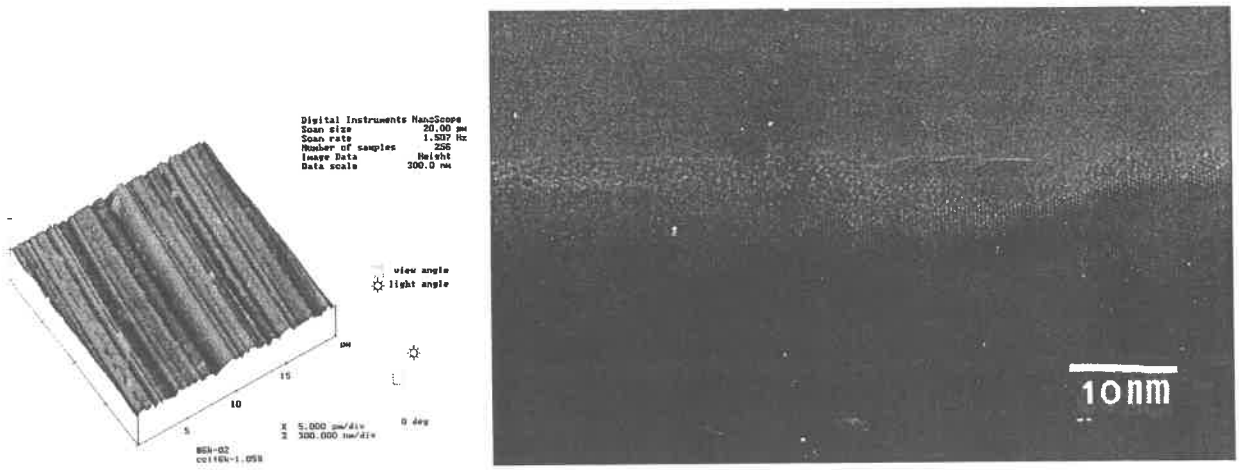

Fig. 8 AFM and HRTEM micrographs of the ELID ground silicon surfaces using #6000 diamond wheel (60V, 10A, 3000/100rpm, 8μm/min), zone axis : [110]

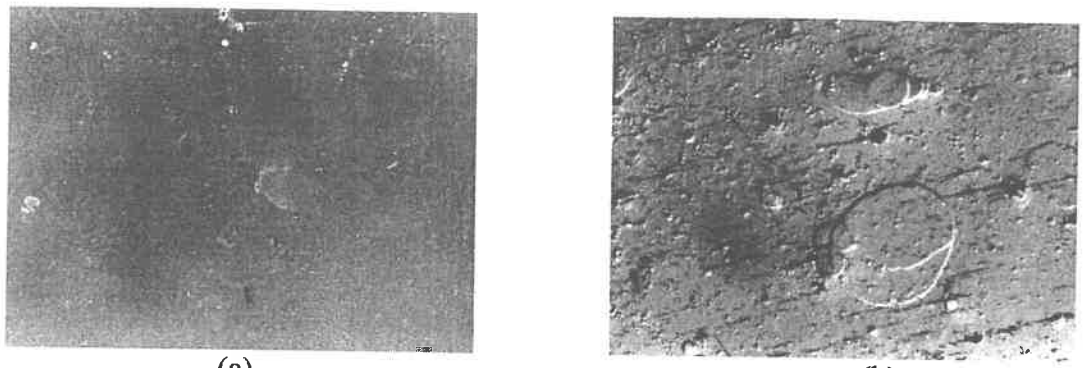

(a) (b)

Fig. 9 Optical microscopy of #1200P(#1200 ground +CMP) sample (a) before and (b) after etched by HF acid for 6 minutes

Conclusions

1. Generally, the finer the diamond grit used in ELID grinding wheel, the better surface quality (Ra, Rq values) could be obtained
2. From the viewpoint of material removal rate and uniformity among the CMP parameters tested in this study, condition with down force of 10psi, pad speed of 20rpm, carrier speed of 40rpm and oscillation speed of 2mm/sec could obtain the best result. However, down force of 5psi, pad speed of 10rpm, carrier speed of 30rpm and oscillation speed of 2mm/sec gave the best surface roughness.
3. A superb surface does not guarantee the sub-surface is free of defects and the grinding-induced cracks are sometime just too deep to be removed by the subsequent CMP process if the form accuracy is to be maintained.
4. The #4000, #6000 ELID grinding process followed by CMP process proved to be a feasible combination to obtain a crack-free surface with sub-nanometer surface roughness.

References

Abe, T. (1991) "A Future Technology for Silicon Wafer Processing for ULSI", Precision Engineering, p.251

Bifano, T.G. , Dow , T.G. and Scattergood , R.O. (1991) "Ductile-Regime Grinding : A New Technology for Machining Brittle Materials , Trans, " ~~ASME.J.Engg. for industry~~ , 113, p.184.

Blake, P.N. and Scattergood, R.O. (1990) "Ductile-Regime Machining of Germanium and Silicon," J. Am. Ceram. Soc., Vol.73, No.4, p.949

Chao, C.L. (1991) Cranfield Institute of Technology, PhD Thesis, U.K.

Chao, .L.; Chen, G.L., Sheu, C.C. and Lin, H.Y. 1999 "Investigations of Properties of the Oxide Layer in ELID Grinding", Proc. of the 3rd Conf. On Nanotechnology and Micro-systems, May 4-5, ITRI, Hsin-Chu, Taiwan, pp2-43 ~ 2-50

Itoh, N.; Ohmori, H.; Kasai, T.; Karaki-Doy, T. and Horio, K. 1998 "Characteristics of ELID Surface Grinding by Fine Abrasive Metal-Resin Bonded Wheel", Int. J. Japan Soc. Pre. Eng., Vol.32, No.4, p.273

Tonshoff , H.K. , Schmieden , W. , Inasaki. , V. , Konig , W. and Spur , G. (1990) "Abrasive Machining of Silicon, " ~~Annals of the CIRP~~ ,39 ,2 , p.621.

Ohmori, H.; Takahashi, I. And Nakagawa, T. 1990 "Mirror Surface Grinding of Silicon Wafers with Electrolytic In-Processing Dressing", Ann. CIRP, Vol.39, No.1, p.329

Ohmori, H. and Nakagawa, T. (1995) "Analysis of Mirror Surface Generation of Hard and Brittle Materials by ELID Grinding with Superfine Grain Metakkic Bond Wheels", Annals of the CIRP, Vol.44/1, p.287

Puttick, K.E.; Whitmore, L.C.; Chao, C.L. and Gee, A.E; (1994) Phil. Mag. A., 69(1), p.91

Shibata, T.; Fujii, S.; Makino, E. and Ikeda, M. (1996) Precision Eng. Vol.18, No2/3, p.129

Shimada, S.; Ikawa, N.; Inamura, T.; Takazawa, N.; Ohmori, H. and Sata, T. (1995) "Brittle-Ductile Transition Phenomena in Micro-indentation and Micro-machining," Annals of the CIRP Vol.44, No.1, p.523

Thermal Effects in Vibration Assisted Grinding

P. Chen, W. Qu[1], M. H. Miller, A. Chandra[2]
Michigan Technological University, Houghton, MI

Introduction

Compared to other machining processes, grinding is a high energy process that generates significant heat. A number of researchers have investigated thermal aspects of grinding and other machining processes. Of particular interest are the total heat generated and its partitioning between the workpiece and elsewhere (chips, coolant, wheel) [1-5].

The amount of heat that enters the workpiece is important because it impacts the quality of the finished part. Excessive temperature can lead to workpiece burn, thermal softening, and dimensional distortion. In addition to workpiece effects, heat generation in the grinding process accelerates wheel wear and necessitates coolant usage. Temperature also influences the mechanism of material removal: temporary softening of the workpiece, due to high temperatures, promotes ductile flow in the grinding of brittle materials. (In one of our tests the temperature rose to more than 400 °C at a point 40 μm below the surface.)

Colwell showed that the introduction of high frequency vibrations to the grinding process reduces the incidence of thermal cracking [6]. Markov [7] and Ishikawa et al. [8] observed that high frequency vibrations permit better coolant penetration. Moreover, several researchers have observed that high frequency vibration reduces machining force and thus machining energy [9,10]. Chandra et al. observed that high frequency modulation can reduce the depth of penetration of median cracks in Pyrex glass [11]. This paper further investigates the effect of high frequency vibrations on grinding temperatures. It describes tests at moderate vibration frequencies (up to 3 kHz) and ultrasonic frequencies. Based on measurements of grinding energy and workpiece temperature, estimates of the portion of heat energy that enters the workpiece (the energy partition) are made.

Grinding Tests at Moderate Vibration Frequencies (0 to 3 kHz)

Force and temperature measurements were made during surface up-grinding experiments in which the workpiece could be vibrated (or "modulated") vertically at frequencies up to 3 kHz. Figure 1 shows the experimental setup. A 10.2 x 25.4 mm steel workpiece is glued onto a workpiece holder that is in turn clamped to a magnetostrictive actuator. The actuator vibrates sinusoidally in the Z direction. An E type thermocouple threads into the workpiece parallel to the work surface in the Y direction. Its tip touches the workpiece at its centerline 3 to 4 mm below the surface. The grinding wheel is aluminum oxide. The actuator assembly attaches to a three-axis force dynamometer. A data acquisition system simultaneously records the dynamometer and thermocouple signals.

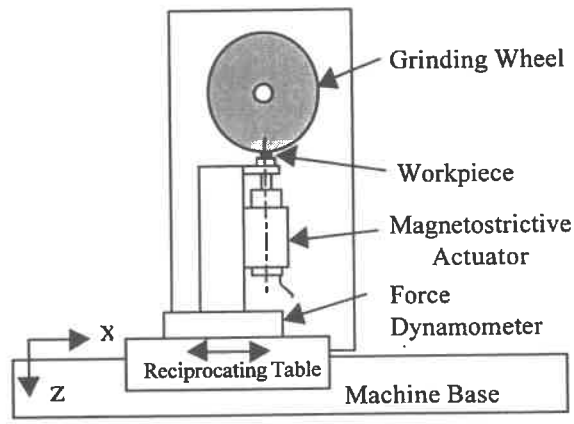

Figure 1: Setup for vibration assisted surface grinding experiments

Table 1: Grinding conditions

Workpiece mat'l	4140 mild steel Hardness : RC31 25.4 x 10.2 x 10 mm
Grinding wheel	Carborundum 32AR46-JV40 178 mm dia. x 12.7 mm
Wheel speed	26.6 m/s
Table speed	0.038 m/s
Wheel depth of cut	10 μm (dry tests) 25 μm (wet tests)
P-V vibration ampl.	7.5 μm
Vibration frequency	0, 1, 2, and 3 kHz (dry tests) 0 and 3 kHz (wet tests)

[1] Currently at Dana Corporation
[2] Currently at Iowa State University

Table 1 outlines the conditions for the experimental trials. Force and temperature measurements were made during a single traverse of the grinding wheel across the work surface. Before each measurement pass we made a preparatory pass under the same conditions. This preparatory pass was necessary to properly set the depth of cut for the measurement pass. Without it, a vibration assisted pass would remove more material than a no-vibration pass. A set of tests was performed dry (without coolant) at vibration frequencies ranging from 0 to 3 kHz. We also performed a set of tests with coolant both without vibration and with 3 kHz vibration.

Figure 2 shows the workpiece temperature during dry grinding with and without 3 kHz vibration. The temperature starts at an ambient of 22.5°C, climbs to a peak temperature after the grinding wheel passes by, and then gradually decreases (eventually returning to ambient). The high frequency component of these signals is electrical noise. For the case without modulation, the peak temperature is 49.2 °C. With 3 kHz modulation, the peak temperature is 40.5 °C.

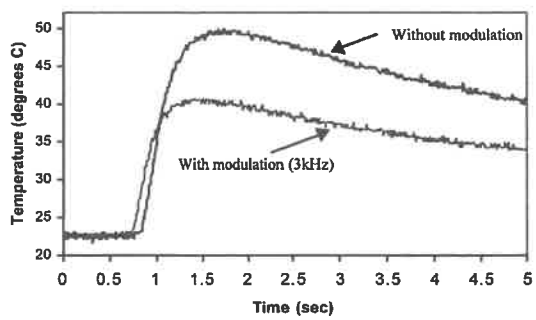

Figure 2: Temperature under dry condition as measured by thermocouple 3.8 mm below work surface

Table 2: Summary of force and temperature measurements for dry grinding tests at 10 μm depth of cut

Modulation Freq. (kHz)	Avg. Force (N)	Avg. Peak Temp. Rise (°C)
0	14.5	26.5
1	13.1	21.1
2	12.5	19.0
3	12.3	17.6

Table 2 presents the average results of the grinding tests performed under dry conditions. Four tests were performed at each condition and averaged. From 0 kHz to 3 kHz, the average force decreases by 15% and the average peak temperature rise decreases by 34%.

Experiments were also performed with coolant. To increase overall temperatures and improve the signal-to-noise ratio, we increased the depth of cut to 25 μm for the tests with coolant. With 3 kHz modulation the average measured force decreased from 23.3 to 21.3 N (8.6% reduction), and the average peak temperature rise decreased from 18.0 to 14.3 °C (21% reduction).

Estimate of Energy Partition

The results from the previous section show that modulation has a greater influence on temperature than on force. The temperature drop is a result of both a reduction in total energy (proportional to force) and a reduction in the energy partition (or the portion of the total energy that flows into the workpiece). Based on the experimental results we determined how modulation influences the energy partition.

The total power can be estimated as:

$$P_{total} = F_c V \tag{1}$$

where F_c is the cutting force and V is the cutting speed. For the unmodulated dry case, the total cutting power is (14.5 N)(26.6 m/s) = 386 W.

The workpiece heating power is:

$$P_{work} = q'w \tag{2}$$

where q' is the heat power per unit length of the heat source and w is the width of the workpiece. To estimate q', we adopted the moving line source model of Carslaw and Jaeger [12]. It calculates the temperature rise in a semi-infinite body at any (x,z) position due to a line source parallel to the y direction that moves in the x direction. The temperature rise in the workpiece is:

$$T(x,z) - T_o = \frac{2q'}{\pi k} e^{\frac{vx}{2\alpha}} K_o \left[\frac{v\left(x^2 + z^2\right)^{1/2}}{2\alpha} \right] \tag{3}$$

where T_o is the ambient temperature; k and α are the work material's conductivity and diffusivity, respectively; v is the table feed rate; K_o is the modified Bessel function of the second kind; and q' is the heat power per unit length of the line source. For our experiments, z was approximately 3.8 mm and x changes with time according to $x = vt$. To estimate q', we guessed a q' and attempted to match the maximum temperature from Equation (3) with the maximum temperature from the experiments at the location of the thermocouple. We also estimated q' based on a moving strip source model [12] and found that the results were nearly the same; we concluded that the small depth of cut in our experiments makes

the width of the strip source small enough that the line source is a reasonable representation.

Figure 3 shows a plot of the experimentally measured temperature for a dry unmodulated case as well as a plot of temperature as calculated from Equation (3). To generate the modeled plot, a q' value of 29,610 W/m was assumed. With a workpiece width (or line source length) of 10.2 mm, the estimated heat power into the workpiece is then (29610)(0.0102)=302 W.

The energy partition, R_w, is defined as the portion of the total energy that flows into the workpiece. In the unmodulated case, R_w is 302/386 = 78%. Table 3 summarizes the effect of modulation on the energy partition for the dry and wet cases. The energy partition decreases as frequency increases.

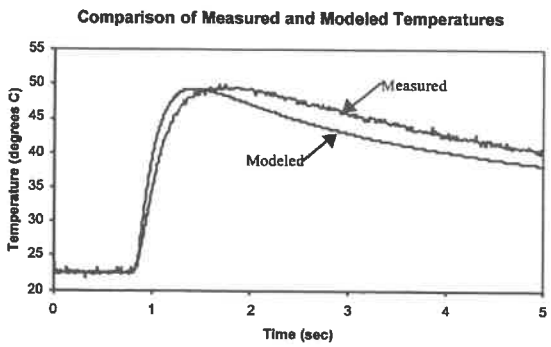

Figure 3: Comparison of measured temperature for the no modulation case alongside temperature as calculated from Equation (3)

Table 3: Summary of effect of modulation on energy partition

Coolant Use	Modulation Freq. (kHz)	Energy Partition Percentage
dry	0	78
	1	68
	2	65
	3	60
wet	0	33
	3	28

Temperature Near Work Surface

In all the experiments described above, the temperature rise in the workpiece is modest because it is measured 3.8 mm below the surface. We performed additional temperature measurements with the thermocouple positioned closer to the work surface. Figure 4 shows the temperature for z values (distance from thermocouple tip to work surface) ranging from 0.04 mm to 3.8 mm. The absolute temperature reduction near the surface is several hundred degrees.

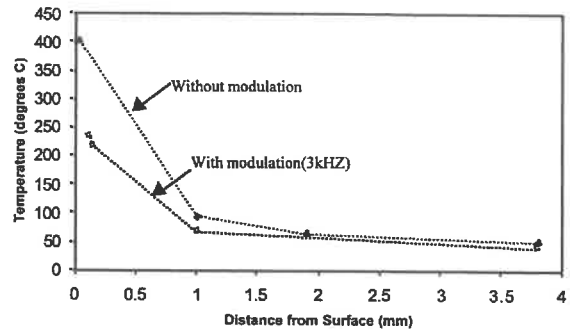

Figure 4: Temperature at varying depths below the grinding surface

Grinding Tests at Ultrasonic Frequency

To further explore the influence of modulation frequency and amplitude on the grinding process , we performed additional tests at a modulation frequency of 40 kHz. Table 4 summarizes the conditions for these experiments. The wheel was dressed once with a diamond nib before beginning the experiments but not before every test.

Table 4: Grinding conditions

Workpiece mat'l	Steel, Hardness: RC19 12.34 x 6.24 x 3.0 mm
Grinding wheel	Carborundum 32AR46-JV40 178 mm dia. x 12.7 mm
Truing Speed	0.353mm/s
Wheel speed	26.6 m/s
Table speed	0.025 m/s
Wheel depth of cut	10 μm
P-V vibration ampl.	0, 0.9, 1.8, 2.8 μm
Vibration frequency	40 kHz

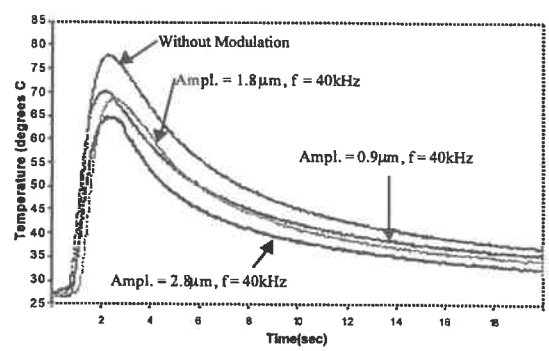

Figure 5: Temperature under dry grinding as measured by thermocouple 1.99 mm below work surface

Figure 5 shows the effect of vibration amplitude on grinding temperatures. For the case without modulation, the peak temperature is 78.1 °C. With

40 kHz modulation and peak-to-valley amplitude of 2.8 μm, the peak temperature is 64.9 °C.

Table 5: Summary of force and temperature measurements for dry grinding tests with 40 kHz modulation

P-V Modulation Ampl. (μm)	Avg. Force (N)	Avg. Peak Temperature Rise (°C)
0	28.50	52.60
0.9	22.19	50.20
1.8	21.06	41.51
2.8	19.34	37.85

Table 5 presents the average results of the grinding tests performed under dry conditions at 40 kHz. Three tests were performed at each condition and averaged. Increasing the modulation amplitude from 0 to 2.79 μm reduces the average force by 31% and the average peak temperature rise by 28%. The energy partition factors for these tests were all approximately 30% and did not change significantly with amplitude. However, the small workpiece used in this test invalidates the semi-infinite assumption used in calculating partition factors. Note that the measured forces in these tests are higher than those in the 0–3 kHz set. This is due to a harder workpiece material.

Conclusions

Vibration assisted grinding experiments at relatively modest frequencies as well as ultrasonic frequency indicate that modulation reduces cutting force and temperature. Modulation at 3 kHz and 7.5 μm amplitude reduced the force by 15% and peak temperature rise by 34% over the unmodulated case. Modulation at 40 kHz and 2.8 μm amplitude reduces the cutting force by 31% and the peak temperature rise by 28% over the unmodulated case. The reduction in temperature is on the order of several hundred degrees near the work surface. Somewhat surprisingly, moderate modulation frequencies appear to produce as much benefit as ultrasonic frequencies (with reduced amplitudes). The effect of frequency and amplitude on energy partition requires further study. The mechanisms for the force and temperature reduction are currently under investigation.

Acknowledgments

This work was supported in part by NSF grant numbers DMI9610454 and DMI9875251. The authors thank Hiroshi Hashimoto for use of the ultrasonic actuator.

References

[1] Snoeys, R., M. Maris and J. Peters, "Thermally Induced Damage in Grinding," *Annals of the CIRP*, Vol. 27, No. 2, 1978, pp. 571-581.

[2] Shaw, M. C., "A Simplified Approach to Workpiece Temperatures in Fine Grinding," *Annals of the CIRP*, Vol. 39, 1990, pp. 345-347.

[3] Kohli, S., C. Guo and S. Malkin, "Energy Partition to the Workpiece for Grinding with Aluminum Oxide and CBN Abrasive Wheels," *J. Eng. Ind.*, Vol. 117, 1995, pp. 160-168.

[4] Chang, C.C. and A.Z. Szeri, "A Thermal Analysis of Grinding," *Wear*, Vol. 216, 1998, pp. 77-86.

[5] Kato, T. and H. Fujii, "Energy Partition in Conventional Surface Grinding," *J. of Mfg Sci. and Eng.*, Vol. 121, No. 3, 1999, pp. 393-398.

[6] Colwell, L.V., "The Effects of High-Frequency Vibrations in Grinding," *Trans. ASME*, 1956, pp. 837-846.

[7] Markov, A. I., *Ultrasonic Machining of Intractable Materials*, Illife Books, London, 1966.

[8] Ishikawa, K., H. Suwabe, T. Nishide and M. Uneda, "A Study on Combined Vibration Drilling by Ultrasonic and Low-Frequency Vibrations for Hard and Brittle Materials," *Precision Engineering*, Vol. 22, No. 4, 1998, pp. 196-205.

[9] Moriwaki, T. and E. Shamoto, "Ultrasonic Elliptical Vibration Cutting," *Annals of the CIRP*, Vol. 44, No. 1, 1995, pp. 31-34.

[10] Astashev, V. K., "Effect of Ultrasonic Vibration of a Single-Point Tool on the Process of Cutting," *Journal of Machinery Manufacture and Reliability*, No. 3, pp. 65-70, 1992.

[11] W. Qu, M. H. Miller , A. Chandra, "Effect of Modulation on Single Grit Scratch Tests," *Proc. of ASPE Annual Meeting*, 1998, pp. 618 – 621.

[12] Carslaw, H. S. and J. C. Jaeger, *Conduction of Heat in Solids*, 2nd Edition, Oxford University Press, 1959.

Investigations On the Coolant Supply in Precision Dicing

Hans H. Gatzen, Jeihad Zeadan
Institute for Microtechnology, Hanover University, Germany

Key words: Outside diameter grinding, dicing, coolant supply.

Abstract---Outside diameter grinding is used extensively to machine semiconductor materials and advanced ceramics. The cutting grit typically is diamond. If exposed to a temperature exceeding 900°C, it will react with the oxygen in the air and will loose its structural integrity. Therefore, an appropriate cooling is of utmost importance. To analyze the coolant flow, a computational approach to determine the channel available to the cutting zone was compared to actual coolant flow measurements. A relationship between coolant flow and cutting force was established.

I. Introduction

Outside diameter grinding is used extensively to machine semiconductor materials and advanced ceramics [1]. Due to their high Vickers hardness, the cutting grit typically is diamond. During cutting, a substantial amount of heat is created in the contact zone between tool and workpiece. These diamond grains react with oxygen in the air when exposed to a temperature exceeding 900°C [2,3]. Therefore, dicing requires the use of coolant and applying an appropriate amount is therefore essential for achieving optimal grinding results. An investigation was conducted to determine the parameters effecting the otimal coolant flow to the active cutting area.

II. Volume Flow in the Cutting zone

A. Volume Calculation by Geometry Analysis

During dicing, the chip space (V_{cs}) between the grinding wheel and the workpiece, provides space to absorb volume removed (M). It also serves as a coolant delivery path into the cutting zone. A mathematical description of the coolant flow rate Q may be found by describing the chip space available per unit time and subtracting the actual volume of the chips removed. The remaining volume per time interval is available for the coolant flow, establishing the actual flow rate (Q) in the cutting zone. By dividing Q by the cross sectional area A between the dicing wheel, the parameter Q'_A may be derived which describes the amount of cooling supplied to the cutting area in the active gap.

$\dot{M}$ is the volume rate of material removed, it depends on the feed rate (v_f), the wheel depth of cut (t), and the width of the dicing wheel (b) [2]. $\dot{M}$ can be calculated according to equation 1.1 as:

$$\dot{M} = v_f \cdot t \cdot b \tag{1.1}$$

To determine the actual volume of the chip space, the following method was applied. First, the actual three dimensional work piece surface profile at the bottom of a kerf was determined by white light interferometry. Next the three dimensional wheel profile was measured, also using white light interferometry. As depicted in Figure 1, the chip space volume may be now determined, as long as we make proper assumptions for the diamonds of the wheel profile to be in contact with the ground workpiece profile. Also, since we wanted to calculate a flow rate, the volume was divided by unit time, with the actual volume per time dependent on the dicing wheel's rotational velocity. The chip space per time $\dot{V}_{cs}$ thus equals the volume rate $\dot{V}_{B+D}$ below the wheel section (binder plus embedded diamonds), minus the volume rate above the workpiece surface. The latter one was established by taking the volume rate of the complete measurement area $\dot{V}_{co}$ and substracting the volume rate of the work piece surface profile $\dot{V}_{wp}$.

LIST OF SYMBOLS

A	Cross section	$\dot{V}_{cs}$	Time dependent chip space
M	Volume removed	$\dot{V}_{wp}$	Time dependent volume below the workpiece surface
$\dot{M}$	Volume removal rate	b	With of the dicing wheel
Q	Flow Rate	t	Depth of cut
Q'_A	Flow rate divided by the cross sectional area	n_c	Rotational speed
$\dot{V}_{B+D}$	Volume rate below the wheel section	v_c	Cut speed
$\dot{V}_{co}$	Time dependent complete measuring range	v_{nj}	Nozzle jet velocity
V_{cs}	Chip space	v_f	Feed rate

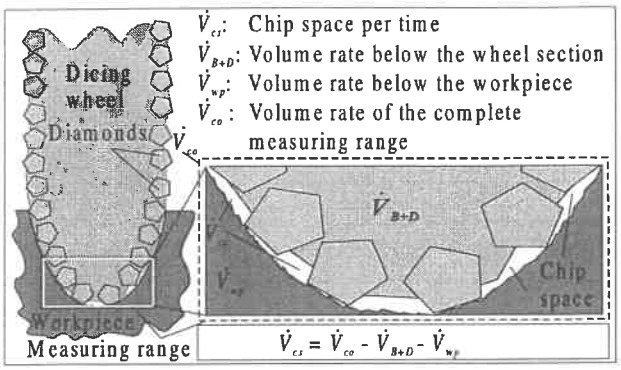

Fig. 1: Cross section of a dicing wheel cutting a workpiece

To allow a statistical evaluation the measurements were repeated on 20 different dicing wheel locations. The data compounded were saved in ASCII format for the numerical volume calculation. These data represent the individual measurement series which were recorded during the white light interferometry measurements. A program developed specifically for this application allowed a separation of the data stored. The volume defined by the topography measurements was then determined using two alternative methods.

The first method analyzed the respective measurement series individually and independently from each other. To do so, a polynomial, which approximates each one of the series, was calculated by applying the Gaussian interpolation method (Fig. 2). The resulting data allowed to determine the volume integral of the space below the surface described by the polynomials. Consecutively, the total result was computed by summing up the individual calculation results.

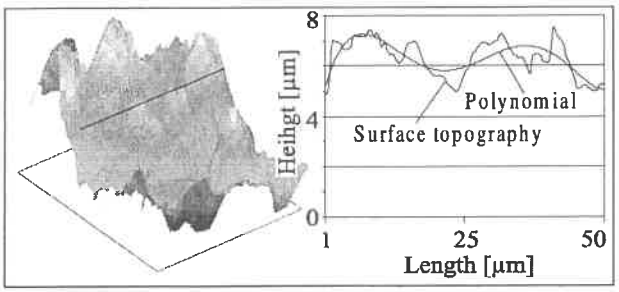

Fig. 2: Cross sectional approximation during dicing wheel volume commutation

The second method made use of the FEM program Advanced Visual Systems (AVS) to do the calculations required. The program allowed to calculate the volume enclosed below a surface topography. A comparison of both results showed a good agreement between both calculation methods.

Once $\dot{V}_{cs}$ was calculated and, assuming that the entire chip space is available for the coolant as well as the chipping products, Q'_A was determined according to equation 1.2. A represents the contact area between the dicing wheel and the work piece.

$$Q'_A = (\dot{V}_{cs} - \dot{M}) / A \tag{1.2}$$

B. Volume Measurement by Experimentally Determining the Coolant Flow

The conventional approach to determine the volume flow is to use a guide blade immediately behind the wheel to collect the coolant. The guide blade diverts the used coolant directly into an external container for volume measurement. However, for small dicing wheels with a wheel width below 300 µm, this method proved to be unsuitable. A puddle of coolant is forming around the gap during the dicing process as the coolant is diverted sideways, thus falsifying the test results. Furthermore, the flanges holding the dicing wheel tend to cause coolant to swirl greatly, allowing coolant following the wheel outside the gap to reach the guide blade. To achieve more accurate results, a method was devised which collects the coolant directly at the cutting zone. Figure 3 shows the schematics of the approach taken: a workpiece holder was equipped with a groove with a progressive depth. A bore in the groove serving as an exit orifice was connected to an external duct. The duct consisted of a transparent plastic tube allowing to observe the presence of air bubbles. A groove was ground into the workpiece, then it was glued to the workpiece holder with boths channels formed by the respective grooves lining up. During a consecutive test cut, the groove was cut open which then allowed to collect the coolant flowing through the cutting zone.

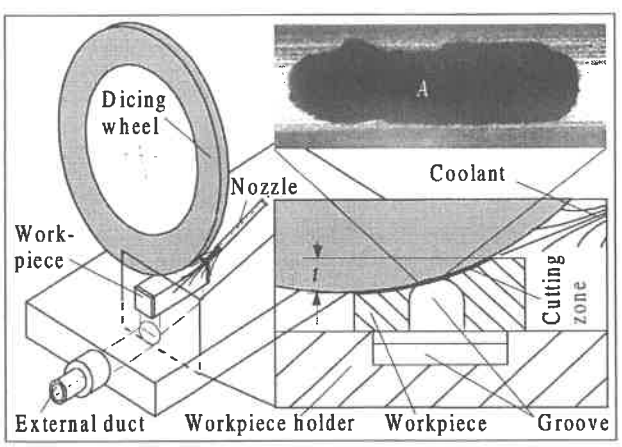

Fig. 3: Schematic representation of the devise set up to measure the coolant flow in the cutting zone

Previously to executing the test cut, the position was calculated at which a kerf would intersect with the groove and would form a predetermined cross section. During a test, the rotating dicing wheel was fed to the calculated position and, by doing so, the upper cut in the workpiece was executed. Due to the continuous coolant flow, the coolant passing through the cutting zone was redirected into the lower groove and collected through the exiting tube while measuring the coolant flow per time. The coolant flow in the cutting zone was smaller than 0.01 ml per cutting pass. For that reason, the measurement was better suited for static tests and therefore was executed at zero feed rate ($v_f = 0$). To avoid errors due to workpiece motion, the calculated workpiece position was maintained throughout the tests.

C. Comparison of the Theoretical and Experimental Results

Figure 4 depicts a comparison of Q'_A determined by numerical calculation and through coolant flow experiments in the cutting zone for two different dicing wheels in a worn state. The chosen cut speed applied for the experimental investigations was matching the time base chosen during the numerical calculation.

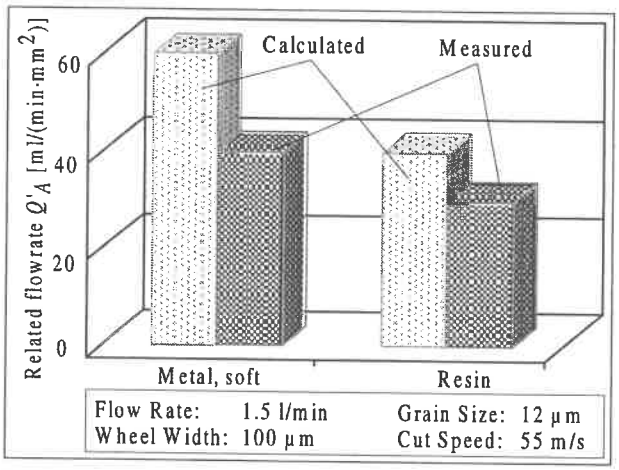

Fig. 4: A comparison between the calculated and the measured related flow rate in the cutting zone

For a soft metal bonded wheel a Q'_A of 60 ml/(min.mm^2) was calculated while a resin bonded wheel resulted in a Q'_A of 38 ml/(min.mm^2). The reason may be found in diamond grains with a higher protrusion breaking off the relative porous resin binder which leads to a smaller chip space.

Experimental data for the actual fluid flow were appr. 37 ml/(min.mm^2) for a metal bonded wheel and 24 ml/(min.mm^2) for a resin bonded one. For these tests, the coolant supply rate was 1.5 l/min. This correlates to appr. 60% of the calculated amount. The difference between the numerically and the experimentally determined Q'_A values may be attributed to the flow characteristics of the coolant jet (laminar, which is desirable, or turbulent), the adhesion of the coolant at the interface between wheel and workpiece fringe areas, as well as to the coolant backflow. An increase of the volume flow rate into the cutting zone, and therefore an approximation towards the theoretical value, may be accomplished by modifying the coolant nozzles' jets. Areas of improvement for coolant nozzles are a reduction of the pressure drop and avoiding turbulence in the coolant jet.

In operation ($v_f > 0$mm/s) $\dot{V}_{co}$ not only contains coolant but also chips. As a for instance the volume flow for a feed rate of 1 mm/s and a cut depth of 1 mm relates to a material volume rate of $1.0*10^8$ µm^3/s. This amount roughly represents only 2% of the calculated time related volume of the available chip space.

III. Relative Velocity between Dicing Wheel and Nozzle Jet

During cutting, the rotating dicing wheel transports the coolant into the cutting area. Therefore, the magnitude of Q'_A depends among other on the cutting speed [2]. Figure 5 depicts the relative velocity between the dicing wheel and the nozzle jet (v_c/v_{nj}) as a function of the rotational velocity (n_c) and the relative volume flow Q'_A. The figure shows clearly an increase of Q'_A with decreasing v_c/v_{Nj}. Due to the fact that the nozzle jet velocity (v_{nj}) is limited, the pressure drop at the nozzles, v_c/v_{nj} decreases when v_c increases. Therefore, the actual coolant flow decreases with increasing rotational velocity. This issue may be addressed by modifying the jet nozzles in a controlled fashion. Also, it was observed that the exit tube showed air bubbles indicating the presence of air in the cutting zone.

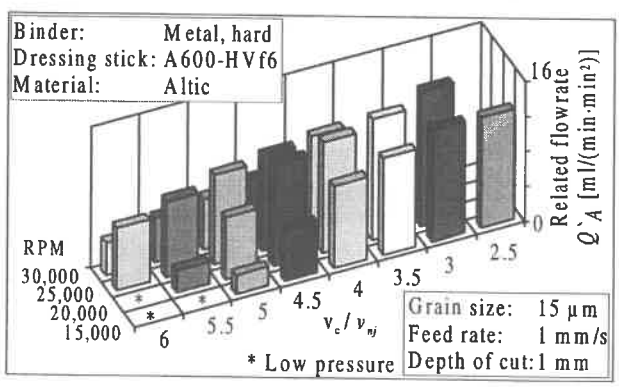

Fig. 5: Q'_A as a function of the velocity between the dicing wheel and the nozzle jet

In case of too low a coolant velocity, a negative pressure is forming in the cutting zone, preventing coolant from reaching the cutting zone. This phenomenon is caused by the rotating wheel being surrounded by an air cushion due to frictional effects, which mainly depend on the wheel's surface roughness [4]. This air cushion is forming a barrier in front of the dicing wheel, preventing the coolant to enter the cutting zone.

IV. Cutting Performance under Improved Coolant Supply Conditions

By appropriately modifying the nozzle design, a compact coolant jet showing laminar flow over a long distance could be achieved. The effect of such an optimized coolant jet on the cutting results was verified by measuring the cutting forces. Figure 6 depicts the tangential forces for resin bonded wheels as a function of the nozzle jet velocity. Using the modified nozzle resulted in a reduction of the cutting forces. Such an optimal coolant flow may be expected to positively influence the cutting process in multiple ways. The two most important effects were expected to be an optimal heat transfer [5] which kept the diamonds sharp and a reduction of friction due to the fluid film. Both are reducing wheel wear and workpiece subsurface damage due to thermal load. Furthermore, an optimal coolant supply also results in the cleaning of cutting chips from the dicing wheel, further reducing the pressure between dicing wheel and workpiece in the cutting area. While a breakdown of the influence of the various effects was not attempted during this work, the relationship between coolant supply and cutting force clearly emphasizes the importance of an appropriate coolant supply.

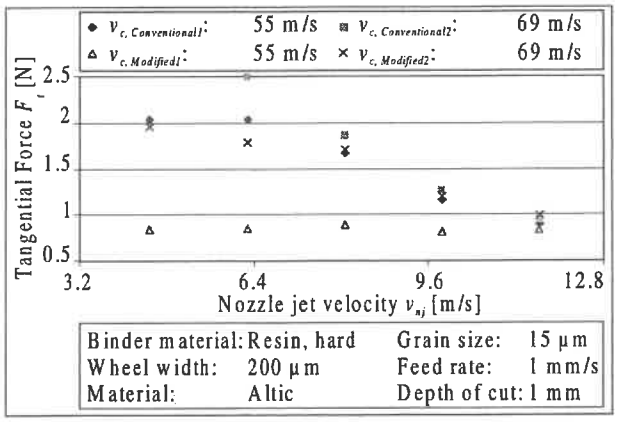

Fig. 6: Tangential cutting force as a function of the nozzle jet velocity

V. Conclusion

By comparing a computational approach of determining the cutting zone with coolant flow measurements, the effectiveness of a coolant supply could be judged. The computational approach was based on numerical surface analyses data based on white light interferometry measurements. For the experimental approach, a measurement system was devised allowing to pick up the coolant flow directly at the cutting zone, thus avoiding errors in measuring the actual coolant flow rate typical for conventional systems.

It could be proven that a compact coolant jet with laminar flow substantially contributes to achieving an optimal cutting process. Most desirable is a nozzle creating a compact jet maintaining a laminar flow over a distance as great as possible. It further coud be proven that such a coolant system substantially reduces the cutting forces and wheel wear. The reduction was attributed to better heat transfer, lower friction at the effective cutting area, and better cleaning off the chips from the dicing wheel.

References

[1] Gatzen, H.H.: Dicing challenges in microelectronics and micro electro-mechanical systems, Proceedings, MicroMat 2000, Berlin 2000

[2] Spur, G.: Keramikbearbeitung (Ceramics machining) Carl Hanser Verlag, München, Wien 1989

[3] Brinksmeier, E., Heinzel, C.: Aufgaben und Auswahl von Kühlschmierstoffen (Purpose and selection of coolants), Proceedings, DIF Conference, Bremen 1995, pp. 1-32

[4] Trmal, G.; Kaliszer, H.: Delivery of cutting fluids in grinding, Chartered Mechanical Engineer 238, 1976, pp. 35-39

[5] Wobker, H. G.: Schleifen keramischer Schneidstoffe (Grinding of ceramics cutting tools), Dissertation, IFW, Hanover University, Hanover 1992

EFFECTS OF CRYSTALLOGRAPHIC ORIENTATION ON TOOL WEAR AND MACHINING FORCES IN SILICON

Robert D. Grejda, Eric R. Marsh
Machine Dynamics Research Laboratory
The Pennsylvania State University
University Park, PA 16802

Introduction

As the electronics industry pushes to meet tight geometric form and surface finish tolerances on larger silicon wafers, rapid and cost effective advancements of the silicon machining processes are needed. Recent progress by researchers such as Tricard have shown promise in reducing the finishing time for a silicon wafer using fixed abrasives on high throughput grinding machines [1]. Grinding silicon is an excellent alternative to the slow material removal of the conventional lapping process; however, silicon has the advantage of being a diamond turnable material based upon its chemical composition [2]. Tool wear is not negligible resulting in an increase in machining forces, loss of control over part geometry, and an increase in sub-surface damage. Previous work on the crystallographically similar diamond suggests that machining silicon along preferred crystallographic orientations may lower machining forces and mitigate tool wear [3]. This study focuses on the effect, if any, of crystallographic orientation on extending the track length (tool life) for diamond machining of silicon.

Experimental Setup

The flycutting machine tool is shown in Figure 1. The machine base is a Moore plain way No. 3 with DC gearmotors providing XZ travel. The air bearing spindle is a Professional Instruments 4R with integral AC motor. A HP 35670A dynamic signal analyzer is used to capture the cutting forces measured by the Kistler MiniDyn 3-Component Dynamometer - Type 9256. A sampling rate of 800 Hz was typically used to take full advantage of the high bandwidth capabilities of the Kistler while allowing sufficient sample time to capture the entire pass of the diamond tool over the entire workpiece (many minutes long for most feed rates). Some tests were sampled at higher rates and then digitally filtered afterwards to match the bandwidth of the dynamometer. In both cases, proper use of analog anti-alias filtering was observed.

Five tools with different geometries were tested until the surface finishes were of visibly poor quality (as characterized by a significant diffraction grating appearance in the surface). The test parameters are outlined in Table 1.

Table 1: Silicon cutting test parameters.

Test	DOC	Rad	Feed	Spindle	Speed	Rake	Sample	Chip thick	Track/pass
	µm	*mm*	*µm*	*RPM*	*m/min*	*degrees*	*#*	*µm*	*km*
0	5	4.88	25	240	115	-30	2/3	1.15	0.03
1	5	4.88	3	477	228	-30	2/4	0.13	0.27
2	5	5.08	25	477	228	0	1/4	1.13	0.03
3	5	1.52	6	477	228	0	1/3	0.50	0.13
5	5	1.60	6	477	228	-30	1/3	0.50	0.13

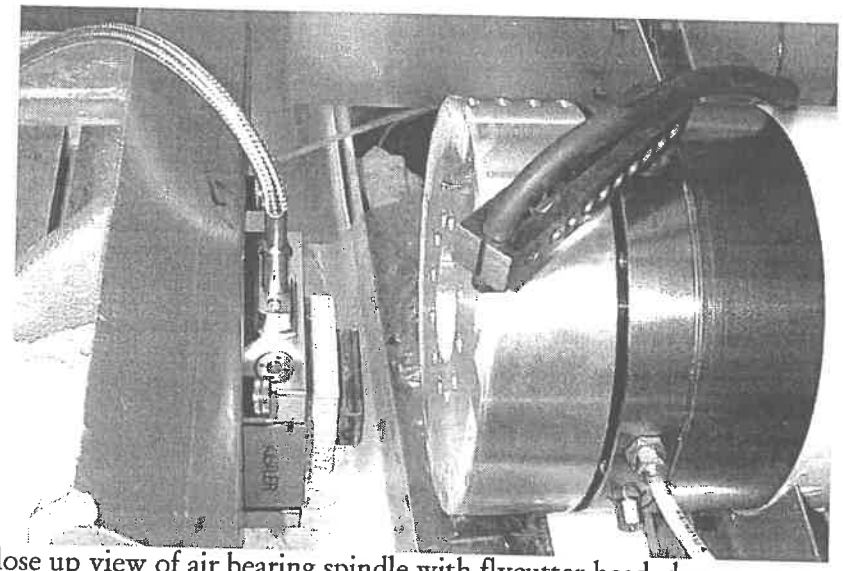

Figure 1: Close up view of air bearing spindle with flycutter head, dynamometer, and silicon workpiece. A hose for coolant is shown above the workpiece/tool contact point.

Results

Each tool was tested until the forces became high and the surface finish was visibly poor. Additional pre-tests were performed to verify that good surfaces could be made with fresh diamond tools. Figure 2 shows a typical good surface made with a new (0.4 kilometer track length) tool.

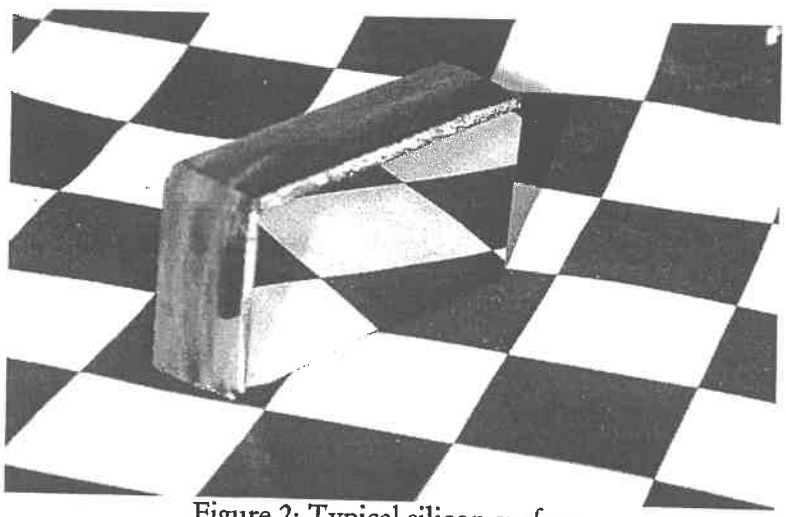

Figure 2: Typical silicon surface.

The intermittent contact of flycutting provides a convenient reference for removing any low frequency artifacts that may occur because of thermal gradients from changing coolant flow (the location at which the coolant impinges upon the dynamometer changes during the test). A typical force trace with many revolutions of cutting is shown in Figure 3.

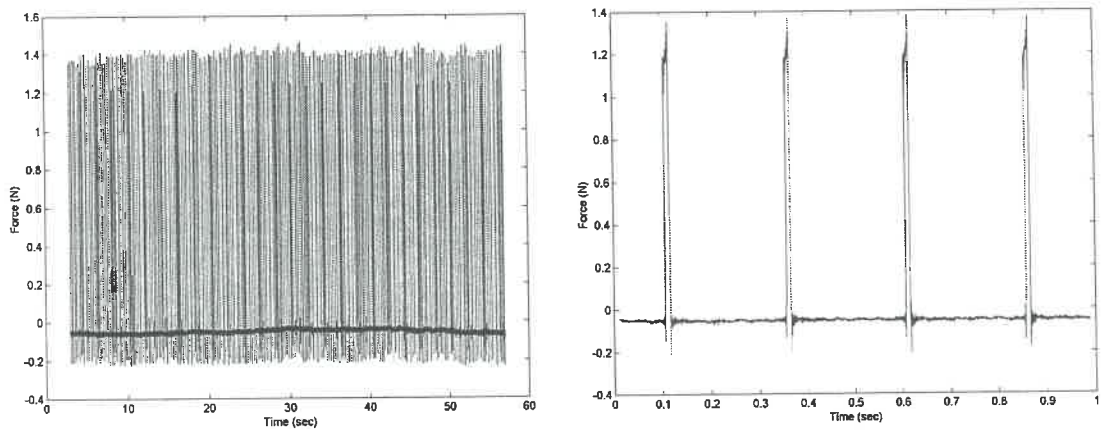

(a) (b)

Figure 3: (a) Long cutting force time capture with several hundred passes over the workpiece and (b) Four consecutive flycutting passes over the silicon workpiece.

Close up inspection of a typical cutting force trace reveals the fine detail as the tool cuts the 19 mm length workpiece, as shown in Figure 4.

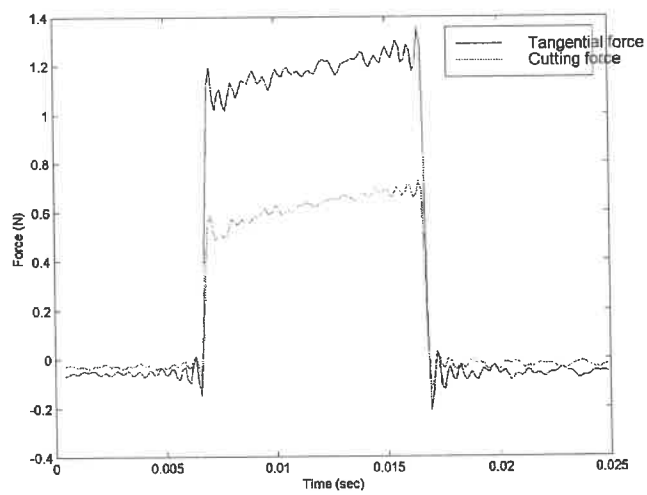

Figure 4: Close up of cutting and tangential forces from one cut over the workpiece.

Data from pre-tests performed at varying depths of cut show that the specific cutting energy does not remain constant, as shown in Figures 5 and 6. However, the cutting forces do remain constant when normalized by the effective chip thickness given by Equation 1.

$$t_c = f\sqrt{\frac{2h}{R}} \tag{1}$$

where t_c is the effective chip thickness, f is the feed per revolution of the cutting tool, h is the depth of cut, and R is the tool nose radius.

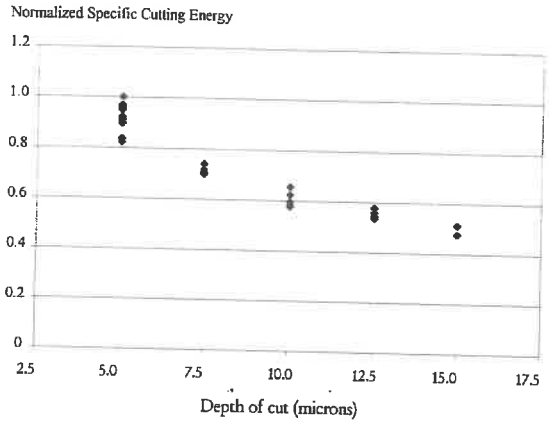

Figure 5: Normalized specific cutting energy.

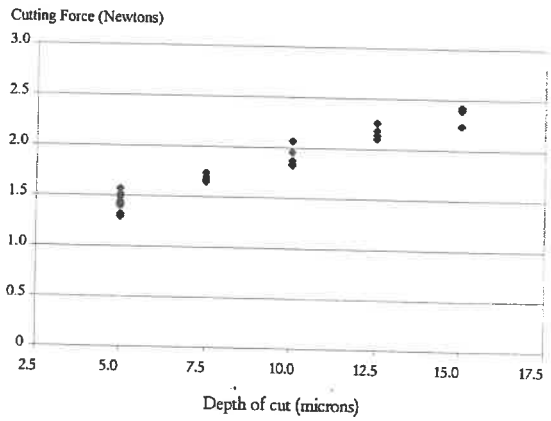

Figure 6: Cutting force vs. depth of cut.

Conclusions

A series of tests were undertaken to explore diamond tool wear in the intermittent cutting of brittle materials, specifically silicon. The test results show that workpieces requiring on the order of three kilometers of track length can be made with low tool wear and excellent surface finish. With longer track lengths, the tool forces (and presumably tool wear) begin a roughly linear increase as surface finish steadily worsens. No catastrophic tool failures were observed, only slow changes as the track length increases. Interestingly, the specific cutting energy did not remain constant with depth of cut, suggesting that there are significant friction forces in the cutting of silicon. These findings support published results emphasizing the importance of a large clearance angle on the tool and hints that aggressive cuts may be the most efficient way to remove material. That is, tool life may turn out to scale with track length, not volume indicating that machining parameters for silicon should be chosen to minimize track length by taking heavier cuts.

Acknowledgements

The authors would like to thank Mark Piscotty of Lawrence Livermore National Laboratory and David Arneson of Professional Instruments Company.

References

[1] Tricard, Marc. "Fixed Abrasive Vertical Spindle™ ." Conference Presentation. 1999.
[2] Paul, E., Evans, C., et al. "Chemical aspects of tool wear in single point diamond turning." *Precision Engineering*, 1996.
[3] Kim, George. "Technical details of silicon machining behavior from a diamond toolmaker's perspective." *Proceedings of ASPE Spring Topical Meeting on Silicon Machining*, 1998.

Keywords:
silicon, crystallographic orientation, diamond turning

Static modeling of grinding wheel

Hwa-Soo LEE, Kojiro SADASUE, Yujiro ITO and Tadashi WAKABAYASHI

Department of Mechanical Engineering, College of Science & Technology,
Nihon University.
1-8-14 Kanda-Surugadai, Chiyoda-ku, Tokyo, 101-8308, Japan

Abstract

In this study, in order to clarify dynamic phenomena of grains in the contact area with workpiece, a dynamic model of wheel is proposed and an experimental evaluation of this model for applications to dynamic analysis is carried out. As the first step of this study, a static wheel model is proposed in which rigid spherical grain particles are suspended by simple bonds having static stiffness k. In this study, elastic deformation of wheel is evaluated by FEM and by three points bending test. As the results of these considerations, it is confirmed that the wheel model proposed in this study can be used to the static analysis on elastic deformations in contact area with workpiece.

Key words : Grinding wheel, Contact stiffness, Static Stiffness, Static analysis.

1. Introduction

Static and dynamic phenomena in grinding operations are affected by dynamics between grinding wheel and workpiece consisting of workpiece, grinding wheel and contact stiffnesses. In these parameters, contact stiffness between wheel and workpiece has been analyzed by applying the theory of Hertzian contact so far/1, 2, 3/. In these analysis, elastic deformations in contact area are discussed by using elastic modulus and Poisson' ratio of grinding wheel under the assumption that wheel is uniform continuous body. As well known, however, wheel consisting of abrasive grain, bond and void is not actually uniform continuous body. Furthermore, the number of abrasive grains in small contact area in grinding operation is finite. Consequently, it may be some problems that wheel is assumed to be a uniform continuous body in order to analyze the dynamic phenomena in contact area.

This study aims to propose a kinetic model of wheel used to analyze the phenomena in contact area between wheel and workpiece and to prove the propriety of the proposed model analytically and experimentally. As the first step of this study, a static model consisting of rigid spherical abrasive grains and bonds connecting successive two grains which has static stiffness k is proposed. In this study, in order to clarify the propriety of the proposed kinetic model, theoretical analysis by finite element method and experimental analysis by three point bending tests are carried out.

2. Analytical approach

2.1 Kinetic model of wheel

Figure 1 shows an image of three-dimensional uniform arrangement of idealized sphere grain in a grinding wheel and/or abrasive stick. A kinetic model in which bond is connecting successive two bonds as shown in Figure 2 is proposed. Assuming that these sphere grains are arranged uniformly in grinding wheel and/or abrasive stick, amount of static stiffness k connecting two grains can be calculated by the following a method.

Assuming that the model shown in Figure 2 is a unit of grain arrangement, volume percentage of grain in wheel Vg can be shown as the function of total number of grains N as:

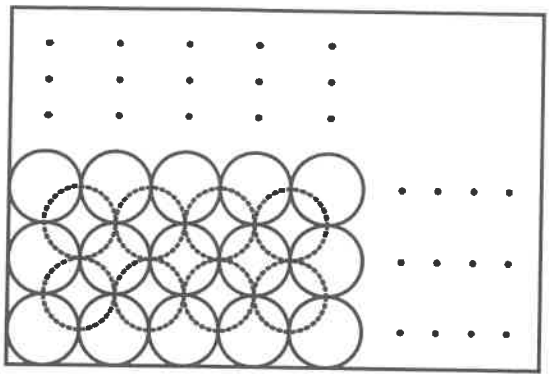

Figure 1 Ideal arrangement of sphere abrasive grains

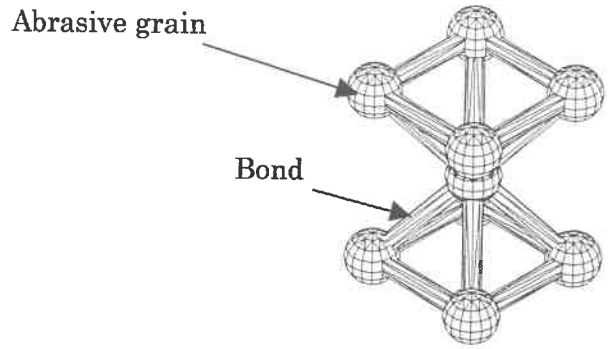

Figure 2 Unit of kinetic model of grain arrangement

$$V_g = \frac{\left(4/3\right)\pi r^3 \times N}{V} \quad (1)$$

Where V is a volume of whole wheel. Distance between successive two grains can also be calculated geometrically as a function of volume percentage of grain in wheel.

2.2 Calculation of static stiffness k

Supporting an abrasive stick shown in Figure 3 in two points, displacement of the center where load P is applying is shown as follows.

$$\delta = \frac{PL^3}{48E'I'} \quad (2)$$

Where L is the length of stick, E' and I' are equivalent elastic modulus and moment of inertia of area respectively. On the other hand, analyzing the relation between load P and the displacement at loading point δ in three points bending test by finite element method, these relation can be shown as a function of P and k.

Grinding stick	WA60 J V	WA120 J V
Grain size	#60 (=0.25[mm])	#120 (=0.105[mm])
Grain volume percentage	50 [%]	50 [%]

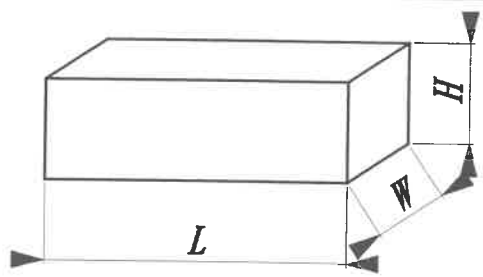

Stick	Width [mm]	Height [mm]	Length [mm]
1	8.0	5.7	40
2	4.0	5.7	40
3	5.0	7.1	40
4	7.5	6.9	40
5	5.7	8.0	40
6	5.7	4.0	40

Figure 3 Abrasive sticks used in experiment

$$\delta = \alpha \frac{P}{k} \quad (3)$$

Where, α is a coefficient obtained in FEM, which is determined by the number of springs and the arrangement of abrasive grains. From the relation shown in Equations (2) and (3), static stiffness of each bond k can be obtained as a function of E' and I'.

$$k = \frac{48E'I'}{L^3} \cdot \alpha \quad (4)$$

2.3 Analytical results

In the method shown above, the coefficients α are calculated and shown in Figure 4. According to the calculated results, it is known that α has a tendency to decrease with the increase of volume percentage of grains in wheel.

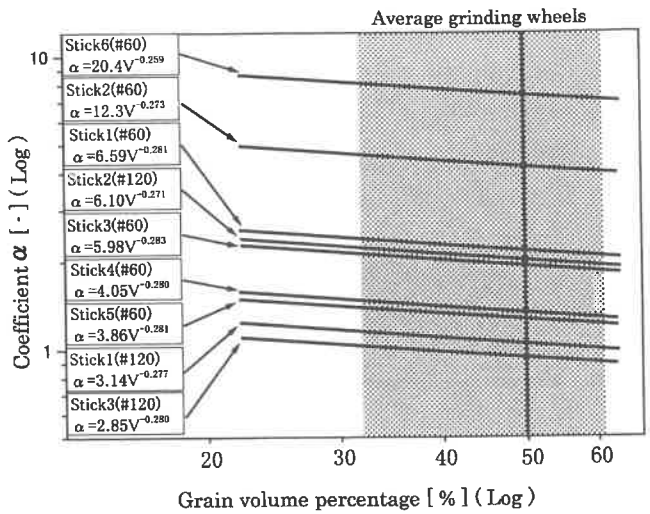

Figure 4 Analyzed results

3. Experiments and results

Experimental results of three points bending test for WA60JV and WA120JV are shown in Figure 5 and 6 respectively. From these figures showing the relations between relative load and relative displacement, it can be known that their relations depend on the geometrical shapes and sizes of abrasive stick. Equivalent elastic modulus E' obtained from the inclinations of the test results shown in Figure 5 and 6 are shown in Table 1. In this table, static stiffness k and equivalent moment of inertia of area I' obtained form the theoretical analysis described above are also shown. These analytical results show that equivalent elastic modulus E' and equivalent moment of inertia I' vary depending on the geometrical shape of tested abrasive stick. On the other hand, the static stiffness k are constant independently from the geometrical shape and are almost 8.00[N/μm] for #60 stick and 4.00[N/μm] for #120 stick respectively. This tendency means that the equivalent elastic modulus of the whole abrasive stick, which has been assumed to be constant, changes depending on the geometrical shape, but the static stiffness k of the basic unit of abrasive stick is independent from the shape. Consequently, using the kinetic model proposed in this study, elastic phenomena of grinding wheel may be analyzed independently from geometrical shape of wheel and/or stick.

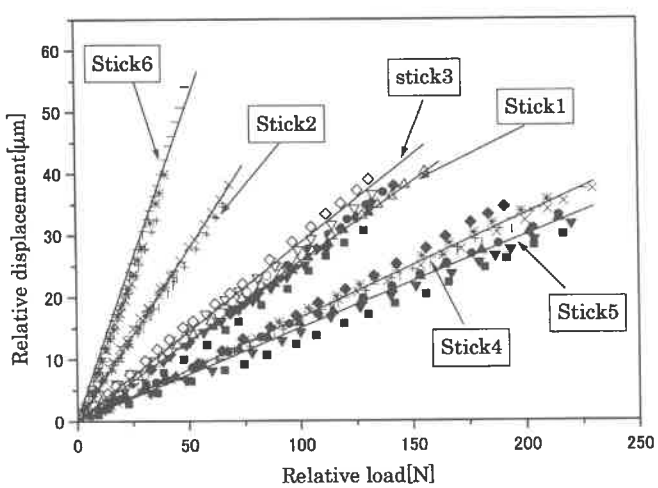

Figure 5 Results of three points bending tests (#60)

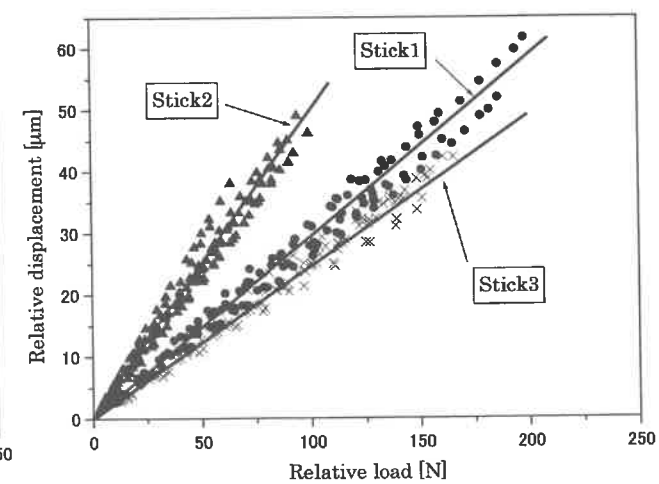

Figure 6 Results of three points bending tests (#120)

Table 1 Analyzed results

	Stick	Equivalent elastic modulus E[kN/ mm²]	Static stiffness k[N/μm]	Equivalent moment of inertia of area I [mm⁴]
#60	1	41.5	8.42	123
	2	40.7	7.97	61.7
	3	32.5	7.24	149
	4	39.9	8.29	205
	5	36.9	8.61	243
	6	43.3	7.32	30.4
#120	1	37.3	3.67	123
	2	44.3	4.33	61.7
	3	35.7	3.80	149

According to the test results, it is known that static stiffness in #60 stick is two times larger than the stiffness in #120 stick. From such tests results, it may be considered that the amount of static stiffness changes by the size effect of bond connecting successive two abrasive grains as follows. That is, since the size of bond may be considered to be changed with the grain size, the length of bond in #60 stick is two times longer than the length of bond in #120 stick and the sectional area of bond in #60 stick is four times larger than one in #120 stick as shown in Figure 7. It means that the amount of static stiffness k shown in Figure 2 is affected by the bond size and then the amount of k in #60 stick may be two times larger that one in #120 stick. From such a consideration, the test results shown above may be understood easily.

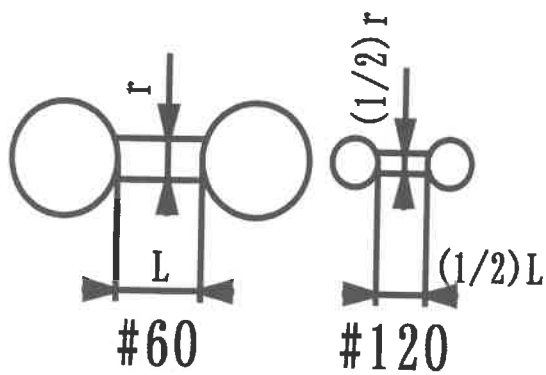

Figure 7 Bond sizes

4. Conclusions

(1) A static model for analyzing the elastic phenomena of wheel is proposed.

(2) As the results of theoretical and experimental analysis, it is clarified that the model proposed in this study can be used to analyze the elastic phenomena of wheel.

Acknowledgement

The authors would like to appreciate to the Science and Research Foundation of the Japanese Ministry of Education for financial supporting of this research (C 12650125).

References

1) Riichi Fukuda, Tooru Tokiwa, "A Study on the Contact Stiffness between Grinding Wheel and Workpiece", Journal of JSPE, Vol.40, No.10(1974), P.809.

2) R. H. Brown, K. Saito and M. C. Shaw, "Local Elastic Deflections in Grinding", Annals of the CIRP Vol. XVIV (1971), P.105.

3) K. Nakayama, J. Brecker and M. C. Shaw, "Grinding Wheel elasticity", Trans. ASME, Journal of Engineering for Industry, May (1971), P. 609.

THE GRINDABILITY OF STAINLESS STEEL USING ULID (ULTRASONIC IN-PROCESS DRESSING) METHOD

S. W. Lee[a], H. D. Jeong[a] and H. Z. Choi[b]
[a] *School of Mechanical Engineering, Pusan National Univ.*
Changjun-dong San 30, Pusan 609-735, Korea
[b] *Korea Institute of Industrial Technology*
35-3, HongChonRi, IbJangMyun, ChonAnSi 330-825, Korea

Abstract

Because of the high toughness and low thermal conductivity, stainless steel is very difficult material to machine. It is also reported that the chemical interaction between stainless steel workpiece and alumina wheel causes the poor grindability. From these reasons, grinding time is larger and form accuracy is worse when the material ground with alumina wheel.

By applying CBN or diamond wheel, the cutting depth can be increased and the dressing interval can be expanded. However, the impurities at grinding can easily get attached to the wheel surface and caused clogging phenomena.

In this study, the Ultrasonic In-Process Dressing (ULID) method was suggested to prevent the clogging phenomena of the wheel surface and decrease the wheel wear. Finally, it can be found that the surface roughness with the ULID method is better than that without it. When stainless steel was ground with the CBN wheel, the wheel wear with ULID was about 36% less than that without it. The change of surface roughness and wheel wear is small with the use of ULID. The ULID is also effective to prevent clogging of wheel by removing the impurities among the grains.

Key words : Ultrasonic In-Process Dressing (ULID), Ultrasonic vibration, Clogging, Wheel wear, Surface roughness

1. Introduction

Improvements in surface integrity and productivity can be achieved by using appropriate grinding wheels and grinding conditions. For the precise grinding, the grinding characteristics of the wheel should always be kept consistent[1]. Many studies have been done in the field of grinding with the CBN and diamond wheels[2]. These wheels are good for keeping the shape as it has little wear. Because of the clogging phenomena, however, it is difficult to keep the fresh surface of the wheel. Finally, burning is caused on the surface of ground workpiece. To prevent all of these, a suitable dressing method should be used for the wheels. The ultrasonic vibration is used as one of the methods to get the high surface integrity. A lot of researches on the ultrasonic vibration are carried out to promote the grinding characteristics and surface integrity[3],[4],[5].

The Ultrasonic In-Process Dressing (ULID) is suggested to prevent the clogging phenomena and decrease wheel wear in the grinding process with the CBN & diamond wheels. It intends to decrease the wheel wear and get the high surface integrity. The surface integrity of ground workpiece and wheel wear in grinding with ULID is compared with that without it.

2. Principle of Ultrasonic Dressing

The ULID is a dressing method to prevent the clogging of the wheel by removing the impurities among the grains with the ultrasonic vibration.

Fig. 1 shows the ultrasonic unit and vibration mode. If high voltage by the ultrasonic generator is provided to the ultrasonic transducer, it changes to the vibration with the amplitude of about 2～3 ㎛. It will be amplified by a corn and horn. The desired amplitude in the tip of the horn can be obtained by optimal designing of the corn and horn. The ultrasonic unit using this experiment has the resonance frequency of 20 ㎑. The amplitude of the horn tip was 30 ㎛.

Fig. 2 shows the principle of the ultrasonic dressing. The vibration force by the up-and-down motion of the horn and the explosion force of the cavitation in the coolant are transmitted to the wheel surface and then the impurities are removed. These forces are extremely small but they are enough to eliminate the impurities among the wheel grains owing to the resonance frequency of the horn. In this way, the ULID method keeps the fresh wheel surface by preventing the clogging phenomena.

3. Experimentation

In this experiment, the resin bond diamond wheel and vitrified bond CBN one were used. For the workpiece, stainless steel (SUS420J2) and mold material (STD11) were used. The value of hardness after heat treatment were about H_{RC} 44～46 and H_{RC} 56～58, respectively.

Table 1
Experimental conditions

Machine	Surface grinder	
Wheel	Vitrified bond CBN wheel (B120H150V3, ϕ300×11×127)	
	Resin bond diamond wheel (TC400R125BG5, ϕ300×11×127)	
Dresser	Rotary diamond dresser (ϕ100, 2,500 rpm	
Workpiece	SUS420J2	After heat treatment, H_{RC} 44 ~ 46
	STD 11	After heat treatment, H_{RC} 56 ~ 58
Depth of cut	10, 20, 40 μm	
Gap(l)	0.05, 0.1, 0.15mm	
Coolant	Emulsion 4%	
Ultrasonic Unit	Power	1,500 W
	Frequency	20 kHz
	Amplitude	30 μm
	Coolin	Air cooling
	Horn Material	Al 7075

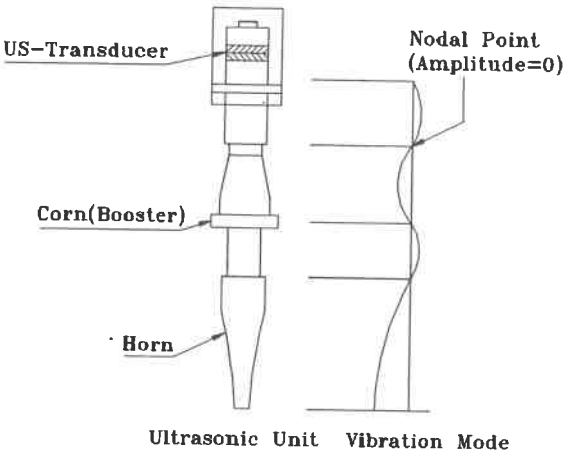

Fig. 1 Schematic of ultrasonic unit and vibration mode

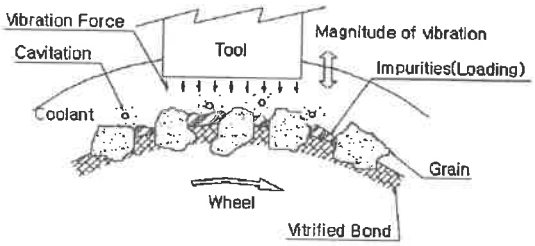

Fig. 2 Principle of Ultrasonic In-Process Dressing (ULID)

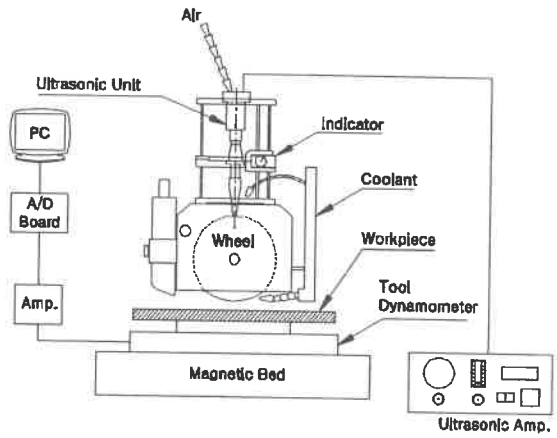

Fig. 3 Schematic of experimental equipment

The ultrasonic dressing unit was attached to the upper part of the spindle housing of the surface grinder (Fig. 3). To control the gap between the horn and wheel, a height gauge was used. The tip of the horn was shaped similar to the profile of the wheel. The compressed air was used to cool down the ultrasonic transducer and the coolant was provided into the tip of the horn.

The wheel wear and the surface integrity of ground workpiece were compared in the case with and without ULID. It was also observed that the ultrasonic dressing removed the impurities, which took place on the wheel surface. The experimental conditions are shown in Table 1.

4. Experimental results

4.1 Photograph of wheel surface

The wheel surface was observed to find the clogging phenomena. Fig. 4(a) is the photograph of the wheel surface ground up to V_w'= 20,000mm^3/mm without ULID. It shows that the clogging phenomena were generated by the impurities of the workpiece. The white part in the photograph indicates that the clogging was generated.

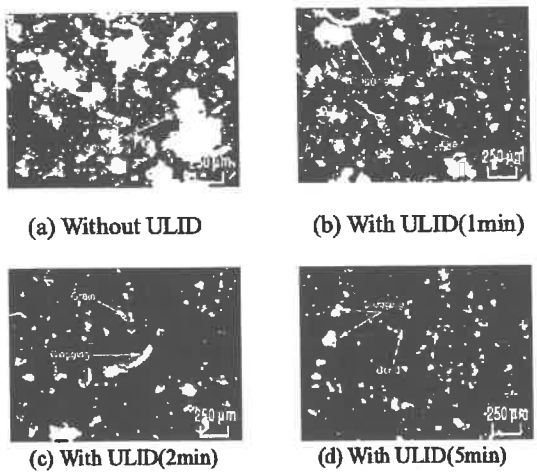

(a) Without ULID (b) With ULID(1min)

(c) With ULID(2min) (d) With ULID(5min)

Fig. 4 Photograph of CBN wheel surface

The photograph of the wheel in cases of ultrasonic dressing time of 1, 2, and 5 minutes, respectively, are shown in Fig. 4(b), (c), and (d). The impurities are not removed completely though the ultrasonic dressing time increases. The reason is that the ultrasonic dressing is an indirect dressing method without contact between horn and wheel.

Fig. 5 shows the surface of the ground workpiece, in the cases with and without ULID. The stainless steel was ground with the diamond wheel when V_w'= 100mm^3/mm. The cutting depth was between 10 μm and 40 μm. Because of the toughness of stainless steel, the surface of ground workpiece with ULID was better than that without it.

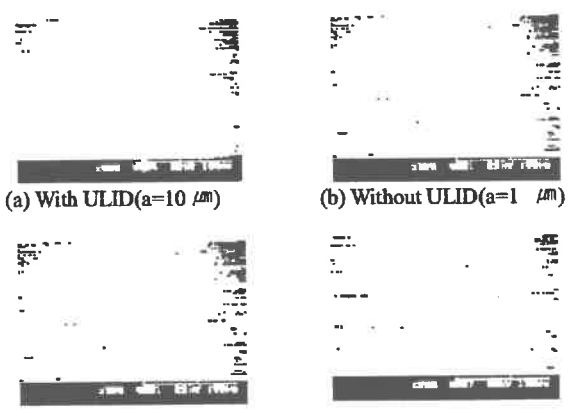

(a) With ULID(a=10 μm) (b) Without ULID(a=1 μm)

(c) With ULID(a=40 μm) (d) Without ULID(a=4 μm)

Fig. 5 SEM of ground workpiece surface

4.2 Photograph of ground workpiece

Fig. 6 shows the wheel wear, in the case with and without ULID when stainless steel was ground with the CBN and diamond wheels.

Fig. 6(a) shows the wear of CBN wheel until the material removal per unit active wheel width reached 20,000mm3/mm. The wheel wear with ULID was about 0.171mm and 0.269mm without it. Fig. 6(b) shows the results for the diamond wheel. The wheel wear was about 0.05mm without ULID and 0.044mm with it. The material removal was 1,200mm^3/mm. The wheel wear in grinding with ULID was less than that without it. The ULID method should be effective to prevent clogging of wheel.

4.3 Surface Roughness

Fig. 7 shows a graph of the surface roughness, depending on whether there is the ULID when the stainless steel was groundb the CBN wheel in the depth of cut of 2 μm. It is found that the surface roughness was deteriorated as V_w' increased. As found in this graph, the Rz value of the conventional grinding without the ULID was greater than that with the ULID by approximately 0.3 ~0.8 μm. The change of the surface roughness value without the ULID was about 1. μm while that with the ULID only was about 0.7 μm in the grinding of stainless steel with the V_w' ranging to 2,500mm^3/mm. Therefore, if the ULID is used, a fine grinding surface can be obtained.

As shown in Fig. 8, the depth of cut was set as 1 μm and the gap between the horn and wheel surface was changing from 0.05 through 0.1 to 0.15mm to investigate the effect of the ULID according to the gap.

The most optimal surface roughness was came out when the gap was 0.05mm. The ULID is an indirect dressing method, removing the impurities among the grains by the vibration force of the horn and cavitation explosion force generated in the coolant. Therefore, in case the gap between the wheel surface and horn was great, their forces were so little that the effect of the ultrasonic dressing disappeared.

The surface roughness with the gap of 0.15mm between the horn and wheel surface was better than that of 0.1mm. This is the reason that the vibration force is transmitted through the wheel to the ground surface, but that the removal force of the impurities among the grains is small in case of 0.1mm. In case of 0.15mm, however, the better surface roughness was came out, as the vibration force became so small.

5. Conclusion

The conclusions are as follows

1. The ULID is effective to prevent clogging of grinding wheel b removing the impurities among the grains.
2. The surface roughness of ground workpiece with ULID was better than that without it.
3. When stainless steel was ground with the CBN wheel, the wheel wear with ULID was about 36% less than that without it.
4. The ULID had the best effect when the gap between ultrasonic horn and wheel surface was 0.05mm.
5. If the ULID is used, a fine surface can be obtained.

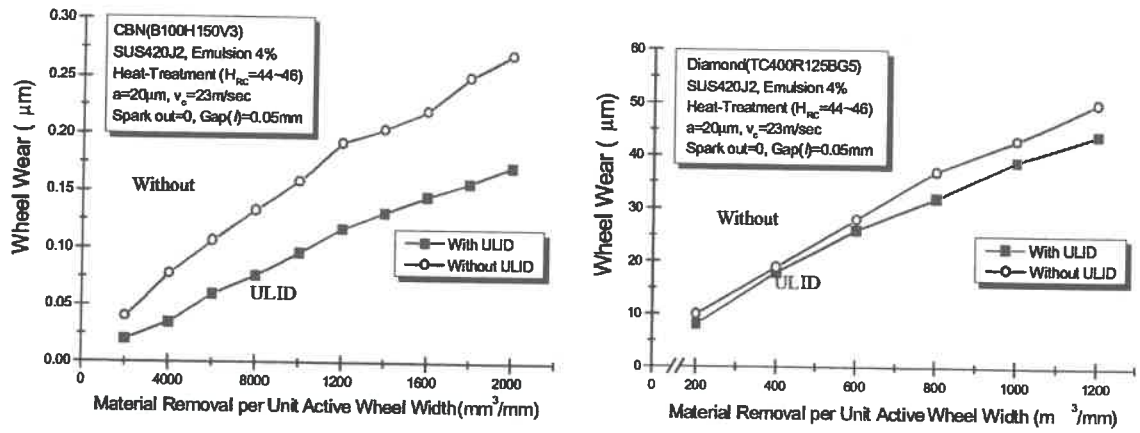

(a) The CBN wheel wear

(b) The diamond wheel wear

Fig. 6 Wheel wear according to material removal per unit active wheel width

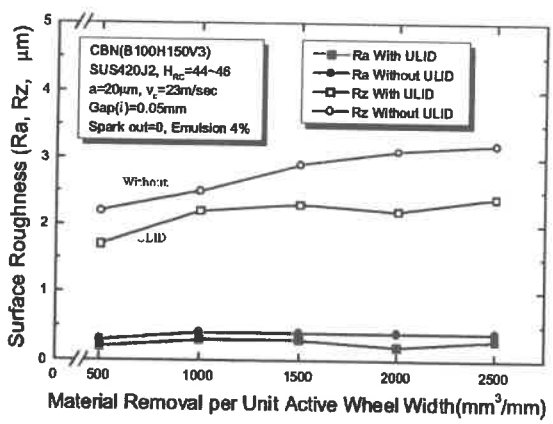

Fig. 7 Influence of Ultrasonic In-Process Dressing on surface roughness

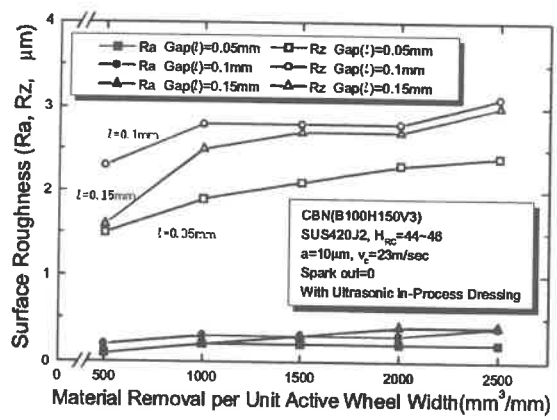

Fig. 8 Surface roughness for different gap(l)

6. Reference

[1] Komanduri, R.," A New Technique of Dressing and Conditioning Resin Bonded Superabrasive Grinding Wheel" , Annal of CIRP, Vol.29, pp. 239～243, 1980.

[2] Choi, H. Z., Lee, S. W, and Park, S. I., " A Study the Grinding Technologies for Manufacturing Ball Screws" , CIRP International Seminar on Improving Machine-Tool Performance, pp. 475～486, 1998.

[3] Yasushi Ikuse, Takeshi Nonokawa, Noritugu Kawabata, Takehiko Kamo, Yoshihiko Yuzawa and Kuniaki Unno, " Development of New Ultrasonic Dressing Equipment " , J. of JSPE,Vol. 61, No. 7, pp. 986 ～990, 1995.

[4] Yeiji Iasui, Hiroshi Nakazono, Hideo Tsuwa," Improvement of Grinding Performance by Ultrasonic Dressing " , J. of JSME, Vol. 39, No. 10, pp. 54 ～59, 1973

[5] Berlyaev et al, B. V., " The Effect of Ultrasonic Wheel Dressing on the Grinding Process " , Machines & Tooling, Vol. 49, No. 11, pp. 53～54, 1978.

Ductile regime Nanocutting of Silicon Nitride

John A. Patten, Wei Gao, Ronnie Fesperman, University of North Carolina at Charlotte

Research has been carried out to evaluate the ductile regime machining of silicon nitride. The Nanocut II device, an experimental cutting instrument, was used to produce cuts in silicon nitride with single point diamond tools (-45 degree rake angle). This device controls the depth of cut to within a nanometer, and measures the cutting and thrust forces (in mN) with sub-mN resolution. Actual depths of cut ranged from 250 to 600 nanometers, and the corresponding forces were less than .2 N. From this data the force ratios (Fc/Ft, the apparent coefficient of friction) were calculated. These values ranged from 1.7 to 4.

Keywords: silicon nitride, ductile machining, ductile-brittle transition, CMP, vibration assisted machining.

Introduction

Ductile cutting of ceramics in general, and silicon nitride in particular, is possible by either controlling the depth of cut (below the critical ductile to brittle transition) or by thermally heating the material to soften and possibly toughen its response to deformation (Shin, 2000). The goal of this present research is to perform controlled depth of cut experiments while simultaneously monitoring the cutting and thrust forces. This data, depth of cut and forces, together with tool geometry, cutting conditions (speed, feed) and material property data are being used in a collaborative research project to model and simulate the machining of ceramics (Hocken, 1999).

Results

All cuts in this range, actual depths of cut as measured on an AFM of 250 to 600 nm, resulted in purely ductile material removal with no evidence of brittle fracture. Subsequent cutting test on a commercial diamond turning machine (DTM) indicated that the ductile to brittle transition threshold for this material was approximately 10 micrometers (Patten, 2000b). The resulting surface finish of the cuts was comparable to the as received polished conditions of 25 to 100 nm Ra.

Discussion

Three different types of cuts were performed: Cuts were made in room air (Figures 1 & 2), vibration assisted cuts, and cutting with chemical-mechanical-polishing (CMP) slurries (Figures 3 & 4). The cuts made in air resulted in the highest cutting forces compared to vibration and slurry assisted machining (Figures 1 & 3). Vibration assisted machining involved vibrating the sample, normal to the tool, with a PZT stack, at 200 Hz with an amplitude of 1 to 2 nm. The vibration assisted machining resulted in reduced cutting and thrust forces compared to non-vibrating cuts made in room air (Figures 3 & 4). Cuts made

with CMP slurries showed a reduced cutting force and increased thrust force (Figures 3 & 4). Cutting tests with combined vibration and slurry assisted cutting resulted in forces in-between those of just vibration or fluid alone (Figures 3 & 4).

The (as received) silicon nitride samples were polished to a surface roughness of 25 to 100 nm Ra. This relatively rough surface, and the corresponding porous polycrystalline structure of the material, made it difficult to obtain accurate depth of cut comparisons between the various cutting processes. Therefore the origins of the reduced forces associated with vibration or slurry assisted machining, compared to cutting in air, can not at this time be positively determined. The reduced forces could be due to a material or process condition changes. The material's behavior, such as yield strength, or the chip formation process, including shear and friction processes, could have changed as a result of the vibration or CMP slurry. Alternately, the depth of cut may be different, even though the programmed depth of cuts were the same (the results are indicated for programmed depth of cut of 1000 nm and 1500 nm, but the actual depth of cut, as measured on an AFM were between 250 nm and 600 nm). The latter could arise if the material's response to the vibration or slurry resulted in a change in surface characteristics, such as hardness. Future tests on a nanoindenter and DTM will shed some additional insight into the observed phenomena.

Conclusions

Ductile regime cutting of silicon nitride is possible in the nanometric range. Cutting forces can be significantly reduced by employing vibration and/or fluid assisted cutting action. Vibration assisted cutting also lowers the thrust force, while fluid assisted cutting raised the thrust force compared to dry cutting in air. This latter phenomenon is similar to that experienced with deforming silicon (Patten, 2000a). The combination of vibration and fluid assisted machining resulted in intermediate effects for the thrust force, i.e. the thrust forces for combined vibration and fluid assisted machining fell in-between those cuts using just vibration or fluid alone. The force ratio Fc/Ft, the apparent coefficient of friction (Figure 5), was greatest for the vibration assisted machining and least for the fluid assisted machining. This former result is influenced most by the significant decrease in thrust force during vibration assisted machining. It is possible, that the vibration acted to "break-up" the surface and thus reduce the thrust force. (the vibration is in the thrust direction and not the cutting direction). The lower force ratios obtained with the fluid may be due to lubricity associated with the slurry provided at the contact surfaces. The combination of vibration and fluid assisted machining, by reducing the cutting force, should result in reduced tool wear. The one unanswered question is why the fluid alone caused a decrease in the cutting force but an increase in the thrust force. One possible explanation, is that the fluid increased the apparent hardness of the material, resulting in less penetration and a corresponding smaller depth of cut which would subsequently reduce the cutting force.

Acknowledgements

This work was partially supported by a National Science Foundation REU grant. J. Patten also wishes to thank Caterpillar Inc. for providing the silicon nitride sample material.

References

Hocken, R.J., Patten, J.A., Cherukuri, H. , Machining of Ceramics, NSF research project, # EEC-9903838,(Win Aung Program Manager)

Patten, John A., Mumford, Sherman, V., The Effects of Fluids on the Deformation and Ductile-Brittle Transition for Silicon, ASPE 15 th Annual Conf., Oct. 2000 (these same proceedings)

Patten, John, A., Ductile regime machining of silicon nitride, The Third International Symposium on Advances in Abrasive Technology (ISAAT2000), October 30-November 2, 2000 Tokai Univ., Pacific Center, Hawaii

Shin, Y.C., et al., Laser Assisted Machining, Machining Technology Vol. 11, No. 3, Third Quarter 2000, Machining Technology Association of the Society of Manufacturing Engineers (SME)

Figure 1 Cutting Forces vs Depth of Cut

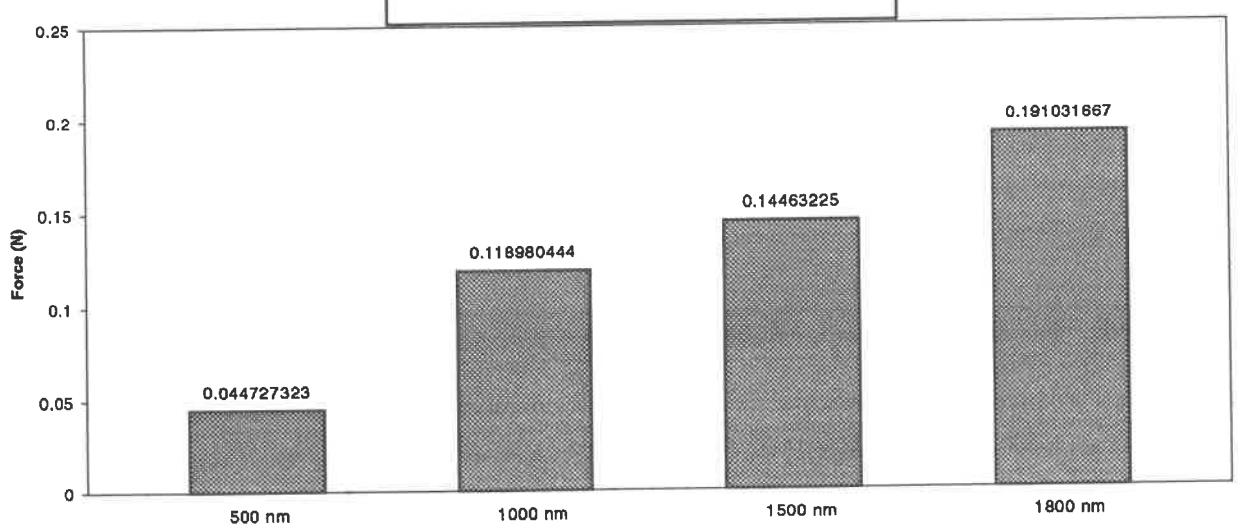

Figure 2 Thrust Force vs Depth of Cut

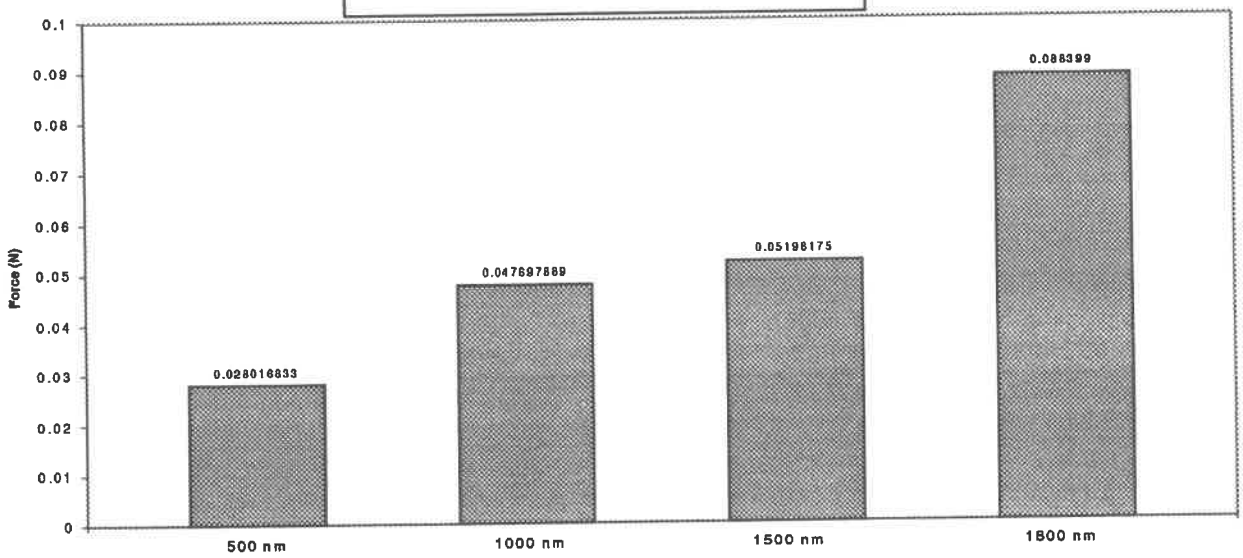

Figure 3 Cutting Force, Depth, Vibration and Fluid

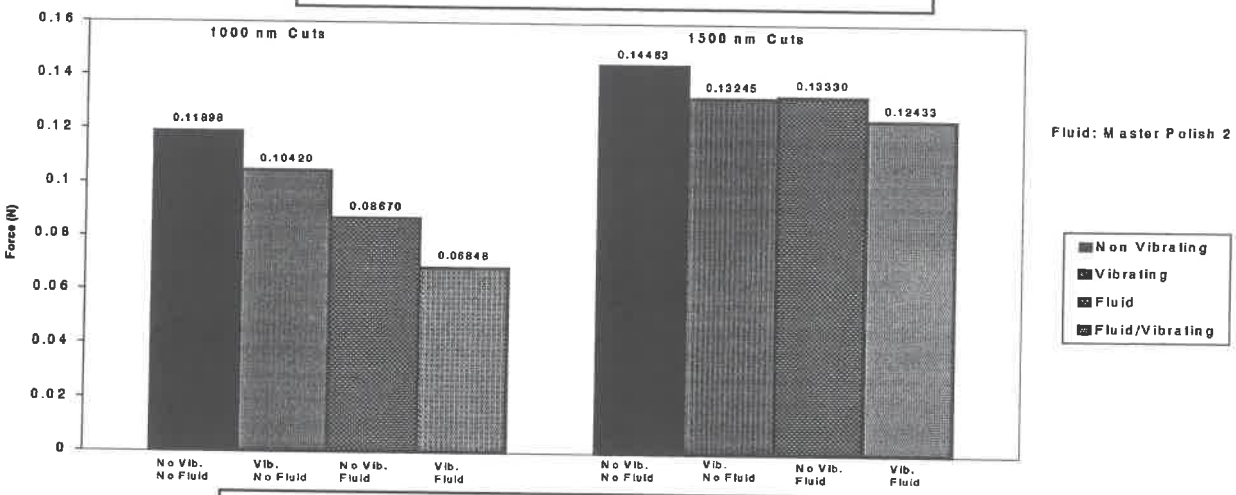

Figure 4 Thrust Force, Depth, Vibration and Fluid

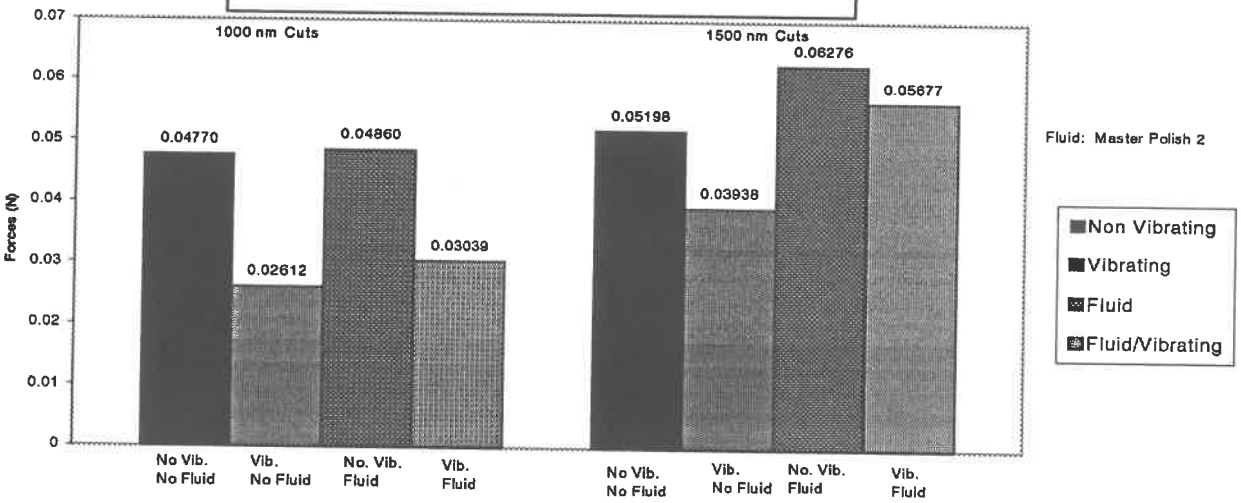

Figure 5 Apparent Cofficient of Friction, Depth, Vibration and Fluid

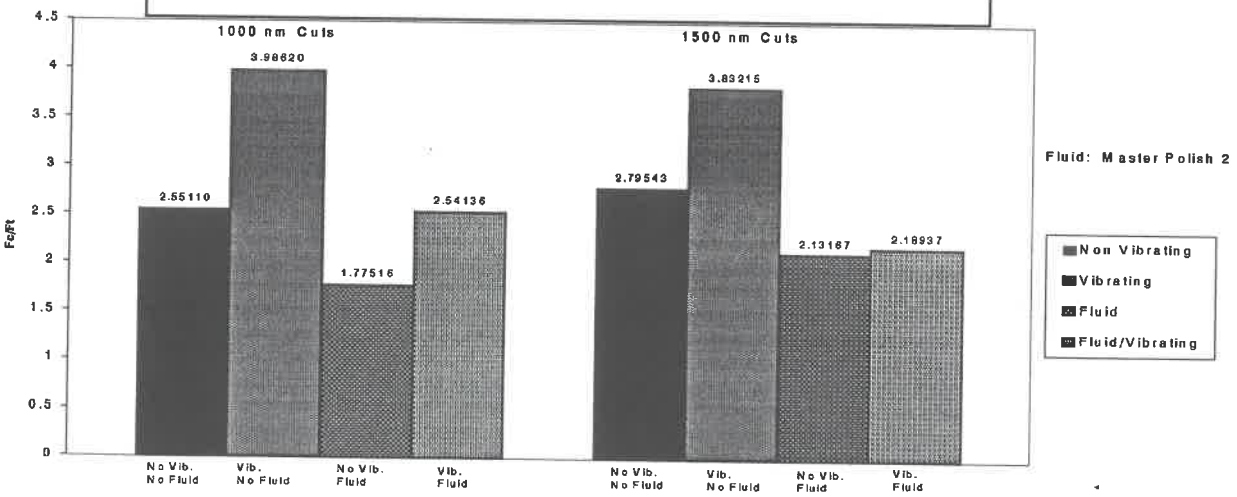

LAPPING OF CERAMICS USING METALLIC-ABRASIVE LAPPING TOOLS

Adam BARYLSKI
Technical University of Gdansk, Faculty of Mechanical Engineering
G. Narutowicza 11/12, 80-952 Gdansk, Poland

1. Introduction

Lapping is one of the most common finishing operations used on flat or cylindrical surfaces. A good surface finish has an important effect on the live and friction of the components. Geometrical structure of the lapped surface has good properties in sliding joints - the valleys in the surface roughness of the contacting bodies can serve as local reservoirs for lubricants, as well as in stationary joints because of the high bearing ratio. Lapping systems is characterised by the set of many structural, material and surface properties connected with the workpiece, lap, abrasive particles and the lapping machine. The lap - a tool used in lapping - has an essential influence on the dimensional and shape accuracy.

In mechanical lapping of flat surfaces, commonly used are metallic discs; frequently of cast iron, steel or copper [7-9]. The components of such a machining systems are characterised by many properties, above all are mechanical, material and surface [4,5]. These are all related to the workpiece, the lapping disk and abrasion suspensions. Necessary for realising the process is the continuous drop dosage of abrasion suspensions or periodical drop dosage of abrasion paste. This is done for the lapping medium.

Besides single-metal based abrasive discs, possible also are bimetal constructions e.g. cast iron-copper or cast iron-steel discs [1]. The working surface of bimetal discs contains elements from hard and soft materials the effect of which the composite versions are more resistant to wear than their counterparts. Further, the composite designs are better carriers of abrasive micrograins, and there appears in them dosage of lapping medium thus facilitating smooth lapping process. This comes about particularly because of single-layer distribution of abrasive micrograins in the machining zone. The micrograins that fall off the disc are quickly removed by the moving workpiece or by separators and do not take part at all in lapping. Such dosages of abradants often appear in excess in workshop practice. Having known the conditions for conventional discs, it is purposeful to seek unconventional tool constructions. Below is presented one of such solutions: glued metal discs [6].

2. Construction of tools

The constructional principle of abrasion metal discs is that abrasive insertions are spread uniformly on the working surface of a metal base [2,3]. During lapping by means of such tools only the machining of fluid is dosed, and that by drop. The tool body is of cast-iron Z1250 (184-194 HB) and of ferrite-perlite matrix. For cast iron Zl250 the tool is cast such as to keep phosphorus sulphur contents minimum, and also controlled to keep manganese within low content range.

In the first constructional version abrasive insertions on silicon carbide base (or electrocorundum, alumina base) are distributed symmetrically on the tool surface, such that both perpendicular and circular profiles appear (Fig.1a). Other solutions are possible. These insertions are of ceramic binding and are produced chiefly for files for heads in polishing

technology. In the second tool version, abrasive elements of circular shape pellets are produced by mixing boron carbide BC4000 micrograins with electrographite micrograins and epoxide resins (Fig.1b).

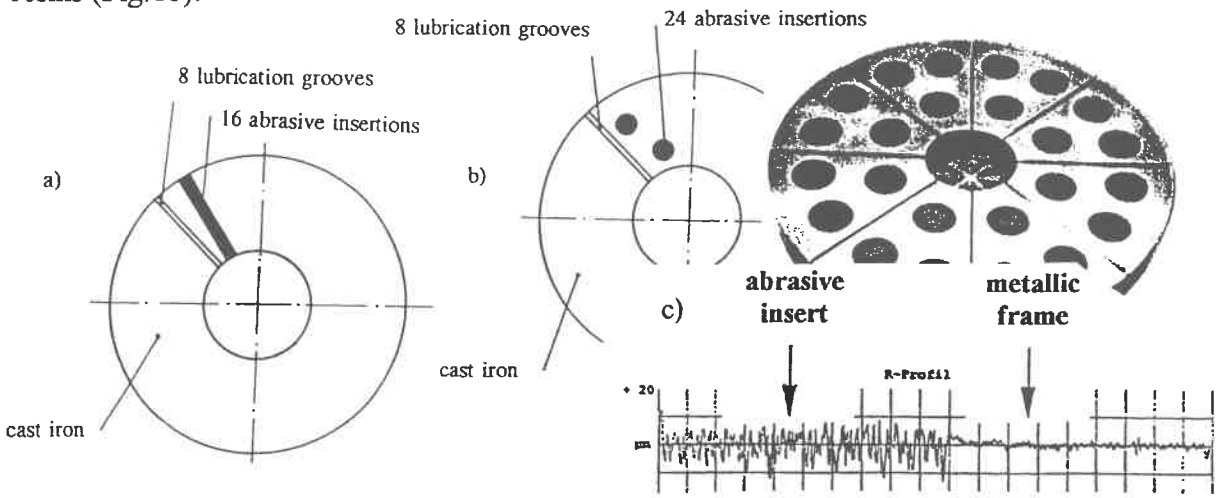

Fig.1. Lapping tools with abrasive elements: a) version I, b) version II, c) profilogram of an active surface of the lap (1-cast iron, 2-abrasive insertions)

.3. Some results of investigations on lapping

Analyses were made concerning yield of machining using abrasive-metallic discs; surface roughness and tool wear. The results show roughly double increase in lapping yield and almost double fall in quality by reason of worsened surface roughness. The wear of single-metal based tools (cast iron material) is about the same as obtained for insertions built on the following bases: abrasion-electrographite, abrasion-copper. Only in cases of insertions of ceramic binding is there obtained significant increase in tool wear intensity. The figure 2-4 present an investigation on the use of one-sided lapping discs in lapping flat surfaces of ceramic parts.

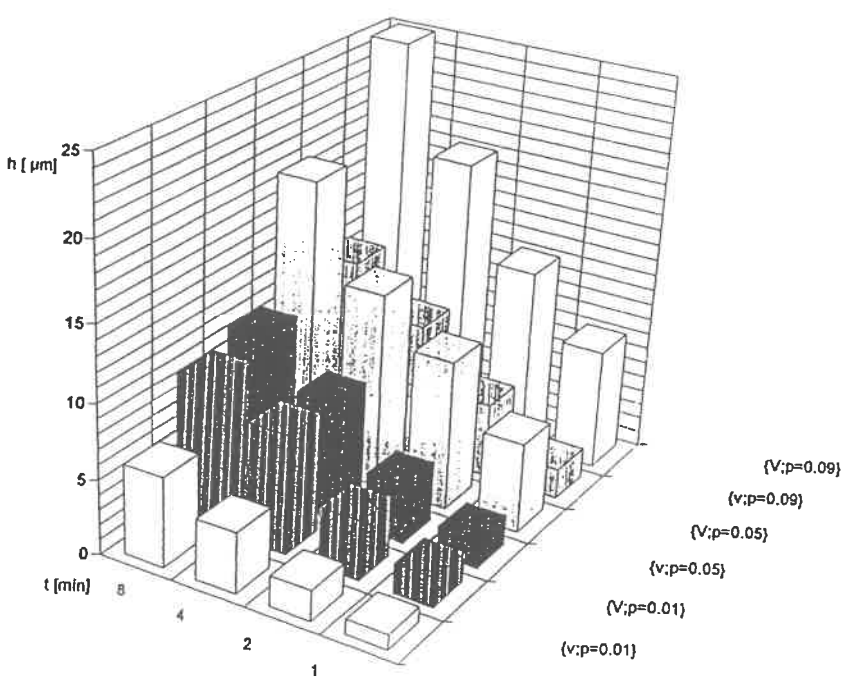

Fig.2. Attrition of Al_2O_3-ZrO_2 ceramic parts in lapping of abrasive-metallic tools (v=18.2 m/min, V=40.7 m/min)

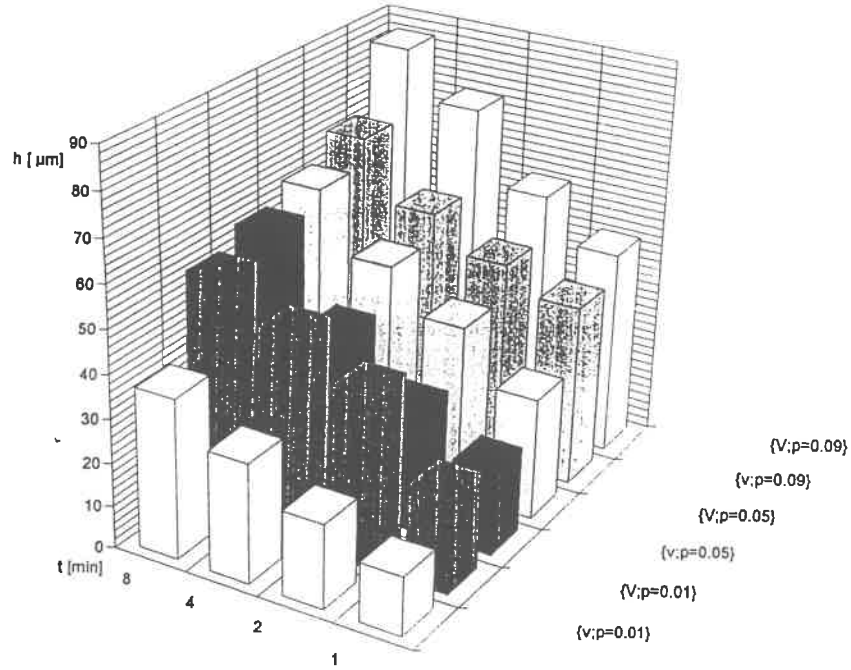

Fig.3. Attrition of Al_2O_3 (95%) ceramic parts in lapping of abrasive-metallic tools (v=18.2 m/min, V=40.7 m/min)

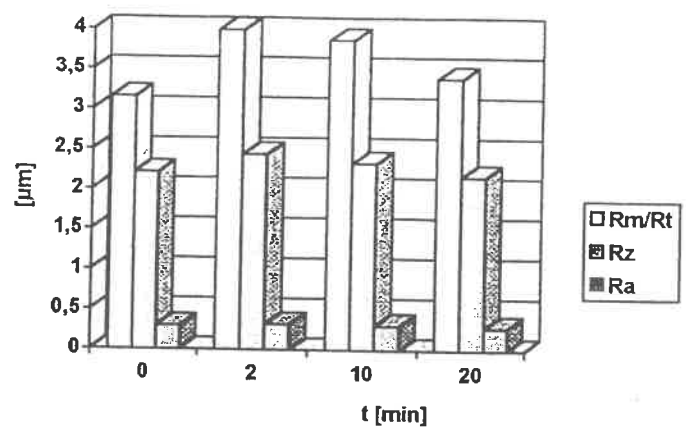

Fig.4. Surface roughness of Al_2O_3 (97%) ceramic parts after lapping (v=40.7 m/min, p=0.06 MPa)

4. Conclusion

The abrasive-metallic tools treated here are characterised by the fact that it is possible to make use of scrapped off micrograins in activating the surface of tool cast iron body. Choice of characteristic of insertions can simplify optimisation of preliminary treatment micrograins. This is significant in cases of superhard abradants, which are expensive. Glue joining of abrasive insertions with metal bases seems here to be the correct technology. In the case of abrasive-metallic there appears intensified surface lapping with little fall in workmanship quality. Linear wear of metallic part of the tool is comparable with that for single-metal based cast iron disc, especially when electrographite and copper concentration of insertions as well as the kind of grooving, the working surface of the disc; plus conditions of tool generation. The constructions given here can be extended to cover tools for lapping holes and shape surfaces.

References

[1] Barylski A.: Fundamentals of flat surface lapping with single-disk. Zesz. Nauk. P. Gdan. 491, Mechanika 67, 1992, 3-196 (in Polish)

[2] Barylski A.: Flat lapping tool, especially for preliminary lapping. Patent, PL, 172327, 1997.

[3] Barylski A.: Flat lapping tool, especially for final lapping. Patent, PL, 172330, 1997.

[4] Barylski A.: Influence of lapping conditions and parameters of the surface contamination. X National Conference on Industrial Tribology, 1993, Dehra Dun, India, 280-289.

[5] Barylski A.: Theoretical and experimental fundamentals of flat surface lapping on disk lapping machine. International Progress in Precision Engineering. Proc. of VII International Precision Engineering Seminar, 1993, Kobe, Japan, suppl., 1-15.

[6] Higiuda Y., Karikomi K., Nakagawa T., Sata T.: Manufacturing of a sintered cast iron plate with fixed abrasives and its lapping abilities. Ann. CIRP, 1981, No 1, 227-231.

[7] Ishikawa K., Ichikawa K., Suwabe H.: A basic study on corrective techniques to recovering accuracy of deteriorated lapping plate. Bull. Japan Soc. of Prec. Eng., 1988, No 3, 234-236.

[8] Ishikawa K., Ichikawa K., Suwabe H., Takagi H.: Nippon Kikai Gakai Ronbunshu c. Hen., 1989, No 515, 1759-1764.

[9] Kling J., Matthias E.: Workpiece material removal and lapping wheel wear in plate and planeparallel lapping. Ann. CIRP, 1986, No 1, 219-222.

Fine Grinding and Mechano-Chemical Polishing for Brittle Hard-Disk Substrate Manufacturing

Fuh-Yu Chang, Hung-Yi Lin, Tung-Chuan Wu

Micro-Electro-Mechanical Systems Research Div., Mechanical Industry Research Laboratories, Industrial Technology Research Institute

M200, MIRL/ITRI, Bldg. 22, 195-3 Chung Hsing Rd., Section 4, Chutung, Hsinchu, Taiwan 310, ROC

Phone: 886(Taiwan)-3-5917775 Fax: 886(Taiwan)-3-5826104

E-mail: 870656@itri.org.tw

The substrate material chosen for new hard-disk product development in today's industry is frequently glass-ceramic or glass instead of the traditional nickel–phosphorous-coated aluminum (Al/NiP). The reasons for this change are principally for increasing hard-disk data storage density and decreasing weight. This industry shift from aluminum-based hard-disk substrate to brittle material substrates presents new challenges in high-precision machining. Today's fabrication techniques for the brittle hard-disk substrates generally rely on double-side lapping and polishing. Such fabrication processes are slow, usually requiring hours for processing a single batch of disk substrates, to achieve the surface finish and flatness required of disk substrates, and therefore make the cost of brittle material hard-disk substrates is still much higher than the conventional aluminum-based hard-disk substrates. In this paper a study to apply ultraprecision double–side grinding and mechano-chemical polishing for developing a more efficient fabrication method with higher finished disk quality for glass-ceramic hard-disk substrate manufacturing is reported.

In order to obtain better surface roughness and flatness before polishing, a double-side fixed-abrasives surface grinding process, normally known fine grinding process, was used. The kinematics of fine grinding are equivalent to lapping but the use of small size bonded superabrasives leads to very fine ground disk surface (roughness Ra <30 nm) with high removal rates. In the grinding process the temperature distribution of the top and bottom grinding wheels used were controlled by the circulation cooling system inside the wheels to prevent thermal distortion to get high dimension and shape accuracy of ground disks. As to the polished surface property, the polishing recipes were investigated by different commercial slurries and by different abrasives such as ZrO_2, Al_2O_3, SiO_2 and CeO_2 used in the homemade slurries. In addition, some chemicals were added into the slurries to obtain cleaner surface and to reduce possible scratches during polishing. The removal rate, the surface roughness, the surface topography and the depth of damage layer were considered as the indices of choosing the right polishing slurry combinations. The experimental results show that for the glass-ceramic hard disk substrates used CeO_2 slurry is a better choice for the first step polishing. For the second step polishing both SiO_2 and ZrO_2 slurries are suitable. The finished surface roughness and flatness of the second polished disk substrates are less than 5 Å and 2 μm.

Keywords: hard disk substrate, glass-ceramic, fine grinding, polishing

Particulate Dynamic Action of a Polishing Lap

A. E. Gee* & D. F. Williams
School of Industrial & Manufacturing Science, Cranfield University,
Cranfield, Bedford, MK43 0AL, UK

1. Lap Action: Micro and Macro Particulate Mechanics

Earlier studies (Gee 1996, Gee & Williams 1999) considered mechanical ablative actions of abrasive grains , modelled as kinematic micromechanical processes both at the particulate level and as macroscopic areal averaging processes. The latter were subdivided according to whether the lap was resilient ('hard') or yielding ('soft') and then either elastic (as used for semiconductor wafers) or viscous (as in pitch used in the optics industry).

Single-point indenter and ruling studies for machining investigations showed sharp scale transition at a depth of about 1μm between brittle chipping at the 10μm scale and plastic deformation permitting spatial fidelity at the nanometric level and lower (Gee et al 1992). These collated very much with hard and soft lap-actions which have distinct modes in working brittle materials.

Hard lap 'hogging' involves the disordered generation of brittle-chips whose geometry is determined by brittle-fracture. The action is dominated by chip size, which, together with surface damage and roughness were all of the order of 10μm. Grains dig in and roll or slide to ablate material at high rates so that the workpiece form converges towards that of the lap.

Changing to a soft yielding lap (elastic polymer material or viscous pitch), a major action is to permit abrasive particles to autonomously self-align whilst sheared *en-masse* over certain geometrical forms (planar, spherical and cylindrical). By this action, they microscopically ablate the surface to improve finish readily to the order of 1nm R_a, as much as four orders below the rough-hogging level. Such action is compatible with observations made relating to single point machining and in turn to the grinding of brittle materials. A plastic regime, existing at scales below some critical depth for fracture, would permit material removal without the divergent unstable crack growth downward into the material which leads to classical conchoidal fracture observed in glassy materials. Shearing action observed in single point experiments using tools with high negative rake-angles would model closely the actions of a sliding grit particle made up of facets embracing large included angles (Gee 1996, Puttick et al 1989).

2. Likelihood of Abrasive Grain Rolling During Polishing

It has been observed that abrasive grains of mean diameter well in excess of 1μm can generate surfaces whose finishes have roughness R_a~1nm (Gee and Williams 1999). Such fine finish is achieved in the plastic ablative mode as brittle chips are orders larger (Gee et al 1992). This being so, were rolling of any particle a putative action, it would be expected to emboss spatial features plastically into the surface; these are likely to be of a scale to ~0.3x the mean particle diameter i.e. >300nm, more than two orders greater than the 1nm finish typically measured. Rolling action is therefore extremely unlikely to contribute to such finish.

Having eliminated rolling, the ablative action is constrained to fixed grain orientation in roll and (by symmetry) angular pitch but with lateral freedom in yaw plus in-plane sliding. It may therefore be envisaged that fine surface finish is achieved by grain facets aligned with the surface acting to ablate asperities by 'scrape-planing' action, as suggested by Strong (1938).

3. Response of Elastic Lap

The action of an abrasive particle carried by elastic lap material is related to force applied and thence to the amplitude of height variations imposed as the particle passes over asperities. Linear elastic lap forcing action on the rising side of asperities may therefore be expected to be independent of frequency and solely a function of roughness amplitude. On the 'falling' side, depending on the relaxation characteristics and response time, the grain may or may not follow the slope depending on its steepness with respect to the response of the particle/lap material. Since the input shearing action is essentially random and omni-directional the rising effect may be expected to dominate.

4. Response of Viscous Lap

In the case of abrasive action using a pitch-lap, the force on a grain moving near-normally into the lap is a linear function of its velocity through the viscous pitch medium, i.e. to the grain sink-velocity normal to the surface, deriving from its endeavours to follow surface deviations. Assuming the input forcing function (surface roughness) to be spatially/temporally sinusoidal, (for the purposes of illustration) the sink-rate is a linear function of frequency and amplitude. In-going the depth of a grain in the pitch H is given by:

$$H = A\sin \omega t \qquad \text{(eq.1)}$$

where A is the zero-peak amplitude and ω is the temporal radial frequency. A lap/surface shearing velocity S m/s will 'scan' the roughness spatial frequency of f cycles/m to yield $\omega = 2\pi fS$ rad/s.

From SPM scans of a pitch-lap we obtained the size and distribution of particles. Typically four particles of 10μm are found in a square of side 40μm leading to an estimate of the sustained force on each particle of 60μg (Gee & Williams 1999).

If we approximate the grain to a sphere of radius r moving at sink-rate v m/s in a medium of viscosity η, Stokes' Law applies in respect of the sustaining/reacting force F:

$$F = 6\pi\eta rv$$

If, as a start-point, we consider a sphere of radius 0.5μm travelling with velocity 1μm/s in the medium of viscosity 10^8 Pas (Ns/m^2) or 10^9 Poise, (see section 6), the force on it will be:

$$F = 6\pi\ 10^8\ (0.5\ 10^{-6})10^{-6} \sim 1\text{mN} \sim 100\text{mg}. \qquad \text{(eq.2)}$$

Consider now the sink-rate pertaining from endeavouring to follow, at lap-shear velocity S m/s, a surface of spatial frequency f cycles/m and amplitude A m. From eq.1 above, the sink motion is given by:

$$H = A\sin \omega t = A\sin 2\pi fSt \ \text{(in m)} \ \text{ where } \omega = 2\pi fS \text{ rad/s.}$$

The instantaneous sink-rate of the grain into the pitch is $v = \omega A\cos \omega t$ (in m/s) $= 2\pi fSA\cos 2\pi\ fSt$ whose maximum (sink-rate) value is: $v_{max} = 2\pi fSA$ m/s.

SPM scans of hard-lapped surfaces generated using grits progressing down to 1200 (Fig.1) show a typical spatial period of 15μm (f ~7.5×10^4 cycles/m) and semi-pk-pk amplitude (A) of 1μm. If the lap is shearing over the work-piece at S = 0.2m/s, and the typical deviating 'input' to any one grit particle is perhaps 1/10 of the roughness amplitude (0.1μm), we have:

$$v_{max} = 2\pi\ fSA = 2\pi\ 7.5 \times 10^4 \times 0.2 \times 0.1\mu\text{m/s} = \sim 10\text{mm/s}.$$

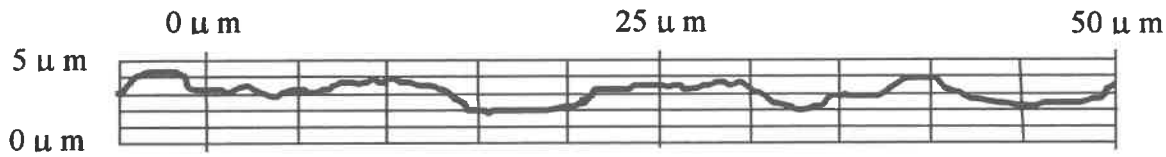

4 depressions are seen at about 15μm wavelength;
each is about 2 μ m deep x about 10 μ m long; they are generally convex depressions having steeper sides near the highest areas between the depressions.

Fig. 1 SPM scan of typical roughed glass

We can now scale the above starting point equation (eq.2) to measurement-derived scales of velocity, from 1μm/s to 10mm/s (i.e by 10^4), and grain diameter, from 1 to 10μm (i.e. by 10). The force applying to each particle scales from 100mg by a factor of 10^5 to 10kg. This remarkably high value is close to the typical loading on a lap.

In the plastic regime where single-point loads of the order of grams cause ductile deformation (Gee et al 1992), plainly, at much lower forces before such hypothetical kg order forces are invoked, the asperity or roughness peak capable of generating such a velocity component will have yielded and been plastically deformed by the highly raked typical grit facet presenting as discussed previously (Gee 1996).

It is likely that material will be plastically deformed into the corresponding 'valley' component of the surface roughness and that the total lap system will autonomously settle on a net level corresponding to some material loss in the form of chips washed/swept away. Such action appears to allow for volumetric redistribution with a proportion of the material regressed into the surface in the form of a 'worked' layer as discussed by Twyman (1952 p56).

5. Amplitude/Frequency Variation

The dynamic force applying to a polishing grain in a pitch-lap is a linear function of the forced sink-rate i.e. to both amplitude and frequency of any cyclic forcing function (the surface roughness). Progressive reduction of amplitude during polishing by selective peak 'flattening' will generate two cross-sectional inflections where there was one before. This will be accompanied by a corresponding increase in frequency as the spatial components get smaller. To a first approximation it might be expected that the correspondence is linear and that the forced sink-rate remains approximately constant as frequency increases and amplitude reduces. In turn, this would be expected to cause little variation in the lap drive force/frictional characteristics as polishing progresses.

6. The Issue of Pitch Viscosity

Although pitch in its various forms remains a highly viscous fluid, it approaches an apparently solid state at low temperatures. Its softening point temperature is used to indicate the relative 'hardness' of the pitch and for glass polishing purposes this is usually between about 40 and 90 C. The softening temperature is

defined by a standard test (ring and ball) to termine the temperature at which the pitch viscosity falls to a standard value of 800 Ns/m^2 (8,000 Poise). The actual viscosity-temperature function is highly non-linear but appears of similar form for most pitches (Kirk-Othmer 1997). The viscosity rises very rapidly below the softening point temperature (Fig 2) but it appears that the material remains essentially viscous.

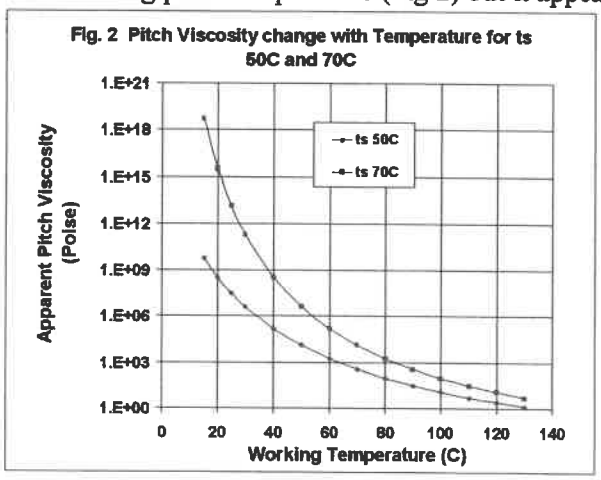

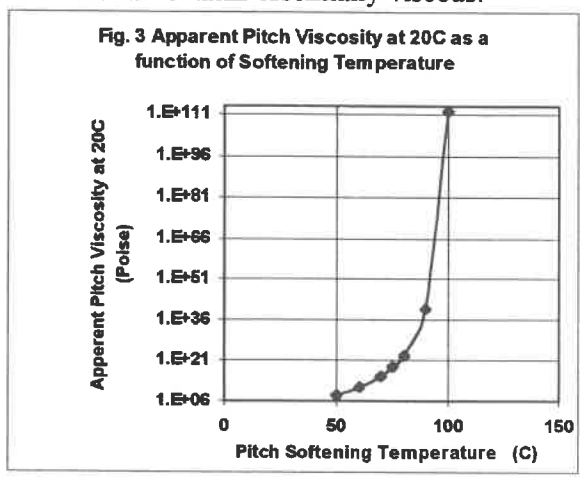

Fig 3. shows apparent viscosity at a working temperature of 20C for a range of softening temperatures. values of 10^9 to 10^{11} Poise being typical. For the 'soft' pitch grades used in polishing (softening temperature about 50C) the working temperature viscosity would be about 10^9 to 10^{10} Poise, yielding to long impress. Pitch also has a very low coefficient of thermal conductivity so that any heat generated locally due to frictional effects is likely to remain local for appreciable time thus causing potentially large local reductions of viscosity compared with the surrounding material (Briggs and Popper 1954). It has been suggested (Gee 1996) that this autonomously compensates for inconsistency in pitch mixtures.

7. REFERENCES

D.K.H. Briggs and F. Popper 1954 "Thermal Conductivity of Coal Tar Pitch" Fuel vol 33 p222

A.E.Gee 1996 "Modelling the mechanics of free particulate abrasive polishing from the viewpoint of single-point processes" Proc SPIE vol 2775, pp611-618

A E Gee, R C Spragg, K E Puttick & M R Rudman 1992 "Single-point Diamond Form-finishing of Glasses and other Macroscopically Brittle Materials" Proc SPIE vol 1573 pp 39-48

A E Gee & D F Williams 1999 "Single Point Contributions to Free Abrasive Polishing" ASPE Conference, Monterey CA, Proc ASPE vol 20 pp501-503

R.E. Kirk et al, eds., 1997 *Kirk-Othmer Encyclopedia of Chemical Technology* (4th edn.) vol 23 p696

K. E. Puttick, M. R. Rudman, K. J. Smith, A. Franks and K. Lindsey 1989, "Single-point diamond machining of Glasses" Proc Roy Soc Lond A vol. 426 pp19-30

F.Twyman, 1952 *Prism and Lens Making,* (2nd edn.) Hilger & Watts, London (republished Adam Hilger/IoP Publishing, Bristol 1988)

8. ACKNOWLEDGEMENTS

Commencement of this work resulted from discussion of ruling experiments on glass between AEG and Prof J. Strong, U.Massachusetts, Amherst, MA and further discussions are acknowledged with Mr E. Palmer of Hampton, Middx. SPM measurements were undertaken by Dr S. Dunn of Cranfield University.

FRACTURE STRENGTH EVALUATION OF SEMICONDUCTOR SILICON WAFERING PROCESS INDUCED DAMAGE

Seong-Min Jeong[1)], Sung-Eun Park[1)], Han-Seog Oh[1)2)], Hong-Lim Lee[1)]
1) Department of Ceramic Engineering, Yonsei University, Seoul, Korea
2) R&D Center, Posco-Huls Co.Ltd., Chonan, Choongchungnam-Do, Korea

Introduction

Recently, fracture strength test has been introduced to evaluate the damage of silicon wafer. There have been several works to observe and analyze mechanical damage in silicon wafers and to demonstrate optimum process condition. So far, 3 point bending strength was measured after cutting wafers into the rectangular type specimens and also the biaxial strength was measured by piston-on-3-ball test for 4in wafers[1-2]. In case of strength measurement after cutting wafers into small parts, the maximum load is concentrated on the cut edge, so that it is very difficult to represent the strength of the overall wafer surface owing to the edge effect. In case of measurement by piston-on-3-ball test, the maximum load is concentrated on the face area of the piston(diameter=5mm), therefore, it is unable to detect the damage which is only slightly deviated from the center of the wafer.

Therefore, in this study, a new testing method, "ring-on-ring biaxial strength test", was adapted to get the more reliable data for 8in wafers. Therefore, in this study, a new testing method, "ring-on-ring biaxial strength test", was adapted to get the more reliable data for 8in wafers. To analyze stress and displacement distribution of wafer under ring-on-ring test, stress analysis was performed using finite element method. Angle lapping method was also used to measure the damage of Sawn, Lapped, Etched and Polished wafers, respectively. The fracture strength test was used to evaluate the damage of Sawn, Lapped, Etched and Polished wafers. The results of angle lapping method were compared with those of fracture strength test.

Experiment

1 Equipments and finite element analysis

UTM(Universal Test Machine, H10K-C, Hounsfield Test Equipment, U.K.) was used in this study together with the ring-on-ring fixture. In the ring-on-ring fixture, the diameter of the upper ring was designed as 140mm and that of the lower ring was designed as 170mm, to fit the diameter(200mm) of the wafer [3]. Since the upper ring and lower ring must be put into a coaxial circle, 3 fixing pins were set to fix the wafer into its center. The load cell(maximum load:10000N) of UTM was set together with the ring-on-ring fixture.

The biaxial strength of the wafers measured by the ring-on-ring test can be determined by the expression (1) [4].

$$\sigma = \frac{3P}{4\pi t^2}[2(1+\nu)\ln\frac{a}{b} + \frac{(1-\nu)(a^2-b^2)}{R^2}] \qquad (1)$$

where P is the load, t is the thickness of wafer, ν is the Poisson's ratio, a is the radius of the supporting ring, b is the radius of the ring and R is the radius of the wafer.

In the real system, the load cell is set on the ring-on-ring fixture, however, the load distribution is not known on the wafer. Therefore, the load stress on the wafer was calculated by Finite Elemente Analysis. ANSYS package was used for finite element analysis [5].

2. Depth of damage evaluation by angle lapping method

The angle lapping, so called section polishing, is a technique to observe the defects of the wafers. By this method, the section surface is observed after lapping the tilted surface. To observe the damage better, dry oxidation at 800 ℃ for 4 hours and wet oxidation at 1100 ℃ for 80 minutes are performed before the selective etching and observation. [6]. Nomarski microscope(Nikon, Japan) was used for observation. Fig. 1 shows the locations of the four samples taken from the wafer; one sample was taken from the center and other three were taken from three edges of the wafer as shown in Fig. 1. After cutting a wafer into 2 pieces, one was applied to the dry oxidation process and the other was applied to the wet oxidation process. One sample at center and 3 samples at edges were to be observed.

3. Fracture strength evaluation of wafer using ring-on-ring test

The fracture strength evaluation was performed by the ring-on-ring test. The wafering process is commonly

composed of sawing, lapping, etching and polishing processes, so that the sawn, lapped, etched and polished wafers,

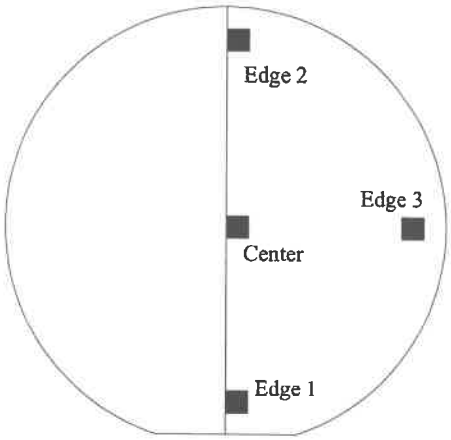

Fig. 1. Schematic diagram showing the locations of the samples (Center, Edge 1, Edge 2 and Edge 3) to measure DOD.

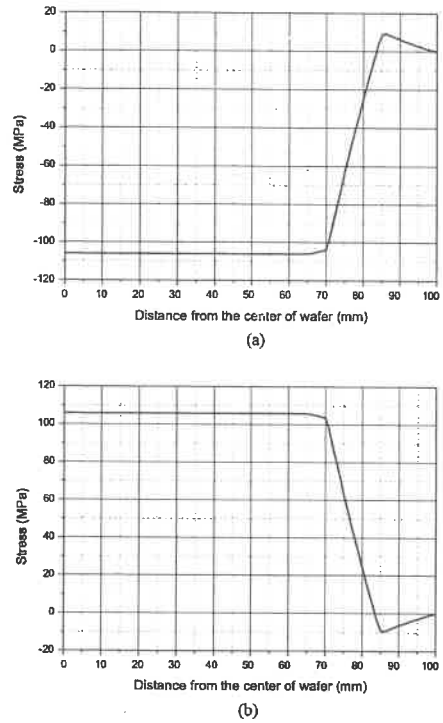

Fig. 2. Surface stress distribution of the wafer in the ring-on-ring test, calculated for a 725mm thick 8 inch wafer loaded under 5000N. (a) upper face (b) lower face

respectively, were analyzed to observe the residual damage produced in each wafering processes. Especially, when polishing1 was compared with polishing2, polishing2 process was better than polishing1 process.

Results and discussion

1. Stress distribution in ring-on-ring test

Fig. 2 shows the stress distribution on the upper and the lower faces of the wafer as a function of the distance from the center of the wafer when 5000N was loaded on the wafer of 725 ㎛ thickness and 8in diameter. As can be seen in Fig. 2, the compressive stress of 106MPa is uniformly loaded on the upper face of the wafer and the tensile stress of 106MPa is loaded on the lower face of the wafer. The stress is rapidly decreased from the supporting ring to the loading ring so that the stress is nearly 0 at the edge of the wafer. Therefore, the damage located in the central area inside loading ring of the wafer can be precisely calculated without reflecting the edge effect on strength because of the uniform load in the central area of 70mm radius. This area corresponds to 49% of the entire wafer surface area, which means that this ring-on-ring method can detect the surface damage on wafer better than any other existing damage evaluating method.

2. Depth of damage measurement by angle lapping method

For comparison with fracture strength evaluation method, the depth of damage was measure by angle lapping method. The damage length was multiplied by the value of sine(grinding angle) to obtain DOD(depth of damage). The obtained DOD values are represented in Fig. 3. The values of DOD decrease according to the order of the processes, sawing->lapping->etching->polishing, which is generally adapted wafering process as shown in Fig. 3. This means that the damage of Sawn wafer is highest and the damage of wafer is removed by progress of lapping, etching, polishing processes. The damage was more remarkably observed for the samples processed through dry

oxidation rather than those processed through wet oxidation. This means that damage can be observed more clearly by dry oxidation process than by wet oxidation process. It was observed that the damage at the edge was more severe than that at the center of the wafer. This means that the edge is more heavily damaged compared with the center of the wafer. Because the sample quantity selected from edge site is more than that from center site, the probability of finding severe damage in edge is assumed to be higher. It is also probable that the larger damages cannot be found in the selected parts rather than can be found at some other places because DOD was measured for the ultimately small part of the wafer. Therefore, it is reasonable to compare the maximum values of DOD for all processes regardless of the positions(center or edge).

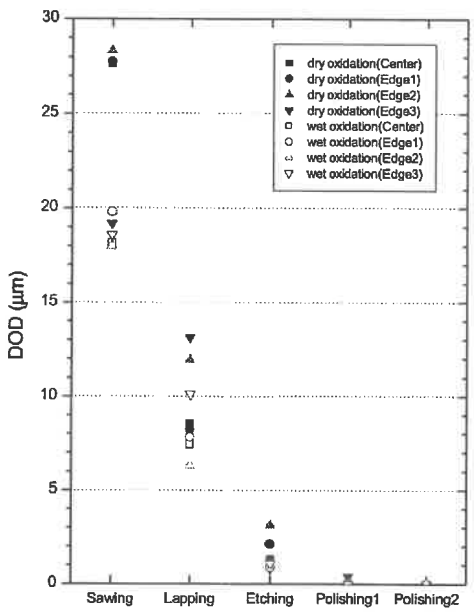

Fig. 3. DOD measured by angle lapping after heat treating wafer for various processes.

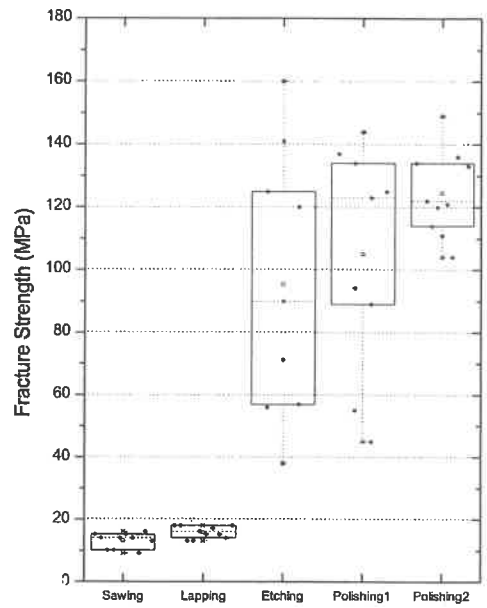

Fig. 4. Fracture strength of wafers for various processes in ring-on-ring test.

3. Fracture strength analysis for wafer with ring-on-ring test

The fracture strength analysis for sawn, lapped, etched and polished wafers, respectively, was performed by ring-on-ring test. Fig. 4 shows the fracture strength by ring-on-ring test. The maximum damage existing inside the circle with radius of 70mm is considered to determine the strength of the wafer. The wafer of the lower strength showed the smaller variation of strength and the wafer of the higher strength showed the larger variation of the strength as shown in Fig. 4. This is because the strength is inversely proportional to depth of damage. The strength increases gradually to the order of sawing->lapping->etching->polishing process because the damage decreases gradually in this order. Therefore, it could be confirmed that the damage of Sawn wafer was highest and the damage of wafer was gradually removed according to the progress of lapping, up to etching and up to polishing processes.

4. Comparison with fracture strength and depth of damage

The fracture strength value obtained by ring-on-ring test was compared with the depth of damage obtained by angle lapping method. Generally, the strength is inversely proportional to the root of the depth of damage. In other words, the larger the damage of wafer is, the lower the strength value is. In fracture mechanics, strength and damage have the relation as the following expression (2).

$$K_{IC} = \sigma_f Y \sqrt{a_f} \qquad (2)$$

where K_{IC} is the fracture toughness, σ_f the fracture strength, Y the geometric factor and a_f the damage. Since K_{IC} is the material constant and Y is the constant value related to the loading system, the size and shape of the specimen and the damage, it can be understood that the damage is inversely proportional to the square of the strength of the specimen.

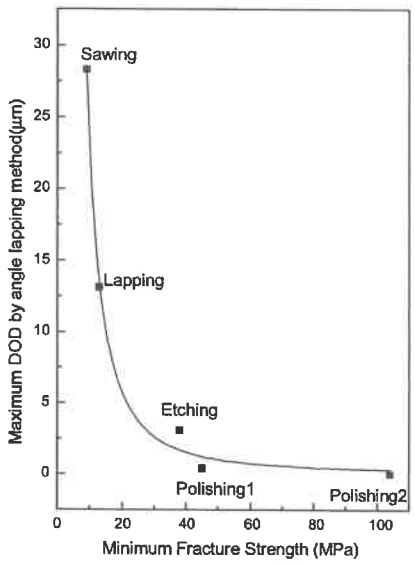

Fig. 5. Curve fitting of maximum depth of damage measured by angle lapping method as a function of the measured maximum fracture strength.

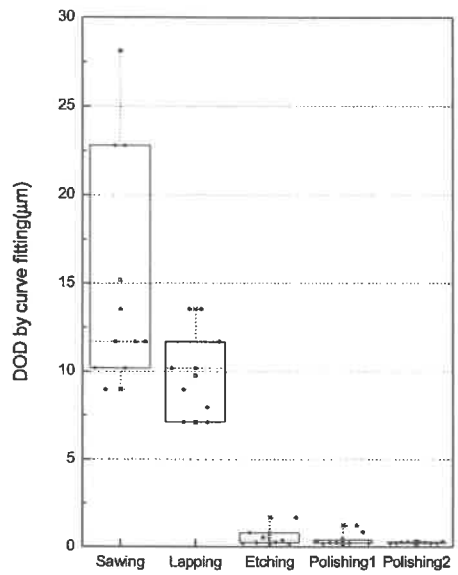

Fig. 6. Depth of damage obtained from the fitting of fracture strength of wafers for various processes in ring-on-ring test.

The values of the maximum depth of damage for various processes measured by angle lapping method are plotted in Fig. 5 together with the minimum fracture strength measured by ring-on-ring test for curve fitting. In real system, the maximum value of damage is more meaningful to control the condition of wafering processes and the fracture strength will have smallest value for the largest damage. Therefore Fig. 5 shows the plots of maximum value of damage obtained by the angle lapping method against the minimum value of fracture strength of the sawn, lapped, etched and polished samples to fit the two parameter power fitting function which is expressed as Equation (3) [7].

$$y = y_0 + \frac{A_1}{x^2} \tag{3}$$

where y_0 is Y offset, A_1 the amplitude, y DOD calculated by the angle lapping method, and x the strength measured by the ring-on-ring test. y_0 and A_1 are the constants 0.108 and 2270.0, respectively, obtained by the curve fitting from Fig. 5.

Fig. 6 shows depth of damage values obtained by curve fitting from the ring-on-ring strength data shown in Fig. 5 using the two parameter power fitting function. In general, the samples with the smaller damage(polishing, etching) showed smaller variation, on the other hand, the samples with the larger damage(sawing, lapping) showed larger variation, which is considered to be related to the variation in strength data. Though the variation of DOD was smaller when DOD was larger, the variation of strength becomes larger, due to the inverse proportion of the strength to DOD value. Although the variation of damage was larger when damage was smaller, the variation of the strength was not so large as can be seen in Fig. 5.

In contrast to the strength data given in Fig. 4, depth of damage value becomes smaller in the order of sawing->lapping->etching->polishing processes as shown in Fig. 6. Comparing depth of damage values in the processes

etching and polishing, about half of the wafers passed through etching process had zero depth of damage value, however, more than half of the wafers passed through polishing process had zero DOD, that is, the damage decreased gradually to zero as the wafering proceeds.

Conclusions

A new damage analyzing technique, ring-on-ring test, was suggested to the wafering process of 200mm Si wafer and analyzed the damage of Sawn, Lapped, Etched and Polished wafers, respectively. The depth of damage obtained by angle lapping method, the existing damage measuring technique, decreased in the order of sawing->lapping->etching->polishing process. The values of fracture strength obtained by ring-on-ring test increased according to the order of sawing->lapping->etching->polishing process.

Acknowledgment

The authors wish to thank Mz. J.S.Choi in PHC for helpful gathering samples and Dr. Shaker Sadasivam, Mr. B.S.Kang in PHC R&D Center for their contribution.

Reference

[1] Seong-Min Lee, Sung-Min Sim, Yong-Wuk Chung, Young-Kwan Jang and Hee-Kang Cho, "Fracture Strength Measurement of Silicon Chips", *Jpn. J. Appl. Phys.*, **36** 3374-3380 (1997).

[2] K. McGuire, S. Danyluk, T. L. Baker, J. W. Rupnow and D. McLaughlin, "The Influence of Backgrinding on the Fracture Strength of 100mm Diameter (111) p-type Silicon Wafers", *J. Mater. Sci.*, **32** 1017-1024 (1997).

[3] Hong-Lim Lee, Sung-Eun Park, Seong-Min Jeong and Han-Seog Oh, "Ring-on-ring strength test for 200mm Si wafer to analyze depth of damage", to be published.

[4] Dinesh K. Shetty, Alan R. Rosenfield, Paula McGuire, Giraaj K. Bansal, and Winston H. Duckworth, "Biaxial Flexure Tests for Ceramics", *Ceramic Bulletin*, **59**[12] 1193-7 (1980)

[5] Swanson, J. A. ANSYS-Engineering Analysis System User's Manual, Swanson Analysis System, Inc., Houston, PA.

[6] Han-Seog Oh, Jong-Rok Kim, Tae-Hyeong Kim, Jae-Jun Yu, Hong-Lim Lee, Ju-Hyeon Lee, Douglas Rice, "The Characterization of Process Induced Damage of Silicon Wafering Process – Mechanical Damage", Electrochemical Society Proceeding Volume 99-1, 100-108 (1999)

[7] F. Shimura, "Crystal Characterization", pp215-278 in Chapter Semiconductor Silicon Crystal, Ed by F. Shimura, Academic Press, Inc., London (1989)

STUDY OF DIMENSIONAL LIMITATIONS OF ELECTRO-CHEMICAL MICRO-MACHINING

Jerzy Kozak, Kamlakar P. Rajurkar
Center for Nontraditional Manufacturing Research
University of Nebraska-Lincoln, Lincoln, NE

Introduction. Electrochemical Machining (ECM) has established itself as one of the major alternatives to conventional methods of machining difficult - to - cut materials of and/or generating complex contours, without inducing residual stress and tool wear. It has been applied in diverse industries such as aerospace, automotive and electronics, to manufacture airfoils and turbine blades, die and mold, artillery projectiles, surgical implants and prostheses, etc. [1]. Moreover with recent advances in machining accuracy and precision, based on the development of advanced electrochemical metal-removal processes, demonstrate that the ECM can be effectively used for micro-machining components in the electronics and precision industries [2].

This paper presents a study of detail-transfer by ECM as applicable to micro-machining capabilities. The application of integrating laser with ECM process to improve micro-ECM operations is also presented.

Experimental Results and Analysis of Detail-Transfer in ECM. Electrochemical Machining is employed in micro machining for the copying of mini-features of the cathodic tool electrode onto the anodic surface of the workpiece, i.e. "detail transfer" by ECM (Figure 1a), and for manufacturing mini-shapes, slots, groves and micro-holes without the use of a profile electrode (Figure 1b).

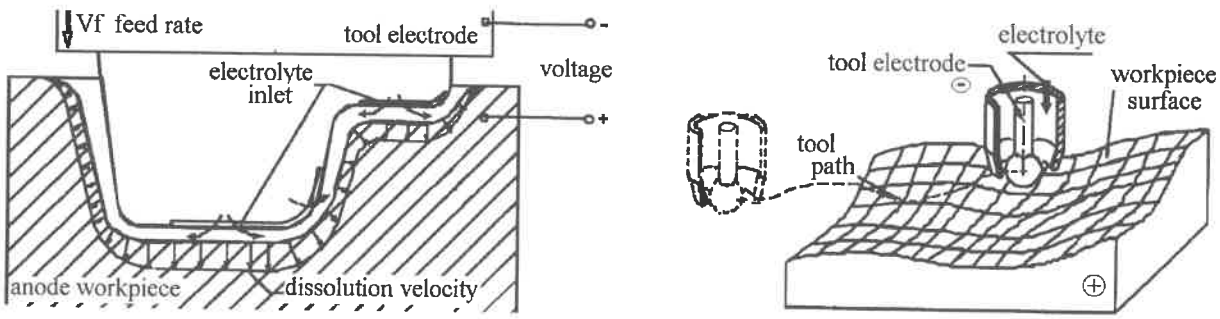

a) b)

Fig.1. Electrochemical machining (ECM) using: a) contoured tool electrode, b) numerically controlled non-profiling tool electrode

In most applications, a high rate of machining is maintained by feeding the tool electrode towards the workpiece with a constant feed rate. A steady state is reached in which the machining surface maintains a fixed shape as it recedes in the direction of the tool feed. The equilibrium surface of the anode resembles the tool shape, but is not congruent with it. The difference in shape is particularly significant for the copying of mini-features.

The results of theoretical and experimental investigations of the relationship between the characteristic shape dimensions, imported upon the anode-workpiece surface by the micro-features of the cathode-tool electrode under given machining conditions are presented. This research included the study of electrochemical copying of slots, mini-holes, and grooves and insulating groove features, which are shown in Figures 2, 3, 4 and 5 [4]. Mini-features are defined as those whose dimensions are below 5 S_f (for example, b, h, d < 5 S_f), where S_f is equilibrium gap size in a steady-state ECM process:

$$S_f = \kappa \cdot K_V \frac{U - E}{V_f}$$

where κ is electrical conductivity of electrolyte, K_V is the electrochemical machinability coefficient, which is defined as the volume of material dissolved per unit electrical charge, U is working voltage, E is total overpotential of electrode processes, and V_f is the feed rate of tool electrode.

The experimental investigations were performed on a sinking electrochemical machine tool with a 10% $NaNO_3$ water solution. Workpieces were made of die steel (0.7% Cr, 1.6% Ni, 0.25% Mo, 0.7% Mn, 0.55% C) treated to 55 HRC hardness. The tests were carried out with special electrodes having different mini-features. The

tool electrode was fitted with lateral walls ensuring one-dimensional flow of electrolyte. Design of experiments is used to determine the effects of four significant parameters namely the equilibrium gap size, the characteristic feature dimensions (h, b, or d), inlet pressure p(in) and feature position on the tool electrode. Graphs illustrating the most interesting relationships for the chosen ECM parameters are shown below.

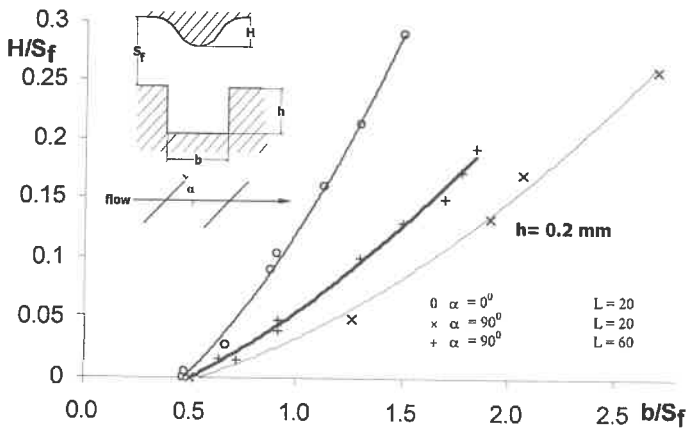

Fig. 3. Detail transfer height vs. relative groove width b/S_f

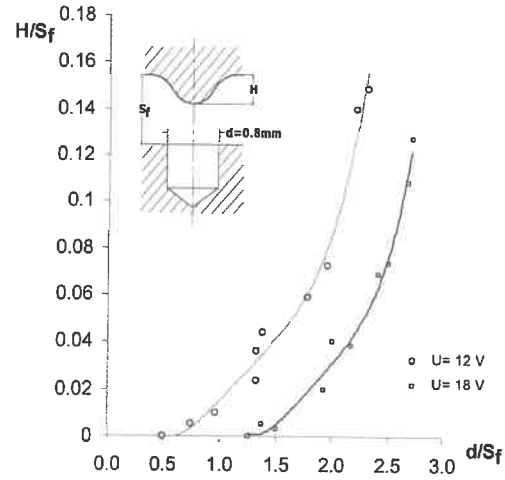

Fig.4. Detail transfer height vs. diameter hole d/S_f

The shape details transfer and its dimensions depend not only on the dimensional features of the tool electrode and equilibrium gap size but also on position details in the gap (distance to inlet of electrolyte L and slope of features to flow direction α), working voltage, and hydrodynamic conditions.

The influence of position details on the gap is shown in Figures 3. Two limiting orientation of the grooves with respect to the flow are investigated: flow transverse to the grooves $\alpha = 0°$ and flow parallel to the grooves $\alpha = 90°$. Results are shown in Figure 3. The difference in results for various α is related to the distribution of diffusion layer thickness on the anode surface.

The effect of voltage on copying of mini-holes on the tool electrode is shown in Figure 4. Under the same conditions, in particular at S_f = constant, intensity of heating increases occur as a result of increased voltage. This factor causes a limiting effect on the accuracy of copying of smaller features on the tool electrode.

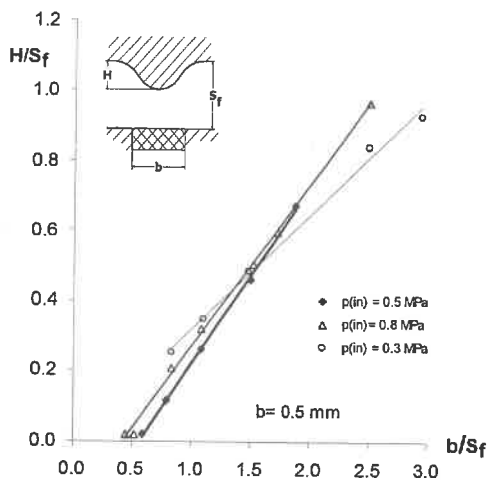

Fig. 5. Detail transfer height vs. insulating relative groove width b/S_f

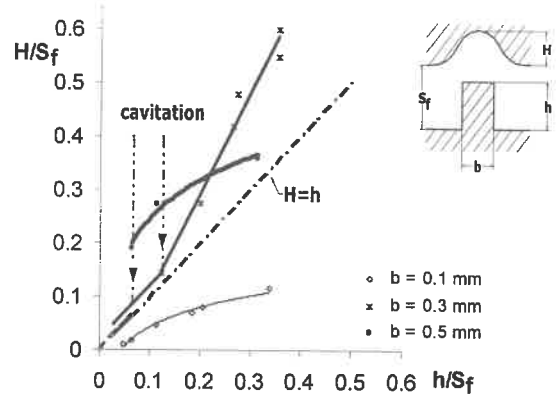

Fig.6. Detail transfer height vs. feature relative height h/S_f

The Figures 5 and 6 illustrates the influence of hydrodynamics on copying process. The effect of inlet pressure of the electrolyte is shown in Figure 5 for copying insulating grooves. Disturbances of copying of rectangular projections by cavitation phenomena can be seen in Figure 6.

The transfer of mini-features of the tool electrode on the anode workpiece are connected with problem of limiting conditions of ECM from the point of view of copying. Of particular importance is geometric limitation in

copying, i.e. the limiting dimension below which the transfer of details from tool does not occur. The limiting dimension of the features depends mainly on its shape, the equilibrium gap size and working voltage. In an example for copying holes, on the tool electrode and insulating grooves, the limiting dimensions were following: d_L = (0.7-1.4) S_f in Figure 4 and b_L = (0.4-0.6) S_f in Figure 5.

On the basis of these investigations it can be concluded that ECM process includes "damping" of small disturbances of primary electric fields between the electrodes. If details on the tool electrode produce a change of intensity of the primary electric field at the anode below (0.07- 0.14) U/S_f, the detail transfer will not take place.

Therefore, for improveming shape accuracy and simplification of tool design, the gap size during ECM should be as small as possible. Additionally, reducing non-uniformity in the electrical conductivity and other physical conditions, which are significant for dissolution process, needs more stable gap state. All these requirements for ECM performance at continuous working voltage are very limited. The minimum practical tool gap size, which may be employed, is however constrained by the onset of unwanted electrical discharges. This short circuit reduce the surface quality of the workpiece, and lead to electro-erosive wear of the tool-electrode, and usually hinders machining progress. Intense heating, hydrogen generation and sometimes choking phenomena, and cavitation within the gap can lead to evaporation and subsequent gas evolution. This gas is believed to cause the onset of electrical discharge. All these constraints in continuous ECM can be eliminated, also the requirements with the point of view of machining accuracy can be achieved, by application of pulse voltage in the electrochemical microshaping and smoothing [5]. Additional positive effects can be achieved by introducing special complex controlling movement of the tool electrode. Thus, the continuous ECM can be replaced with a discrete process, resulting in the reduction of gap size below 0.1 [mm] and improving micro-shaping accuracy.

Micro-ECM with Laser. The laser activation of the electrode processes during electrochemical dissolution (ECM) and/or deposition (electroforming) is required for localised enhanced dissolution/deposition of material for improvement accuracy and productivity of micro-areas being machined (deposited). The laser beam in provides an acceleration of electrochemical reactions during non-destructive illumination of metal-workpieces. The results of experimental investigations of laser electrochemical micro machining (LECMM) are described below. The experiments carried out using the experimental set up, which consists of electrochemical shaping and laser assistance systems. CO_2 laser with 20W power and power supply 20V and 50A for ECM is used for LECMM. The workpiece *W* is mounted on a sample holder, which is attached to a controlled table capable of micron precision movement in the X-Y directions. The scheme of experimental set up is shown in Figure 7

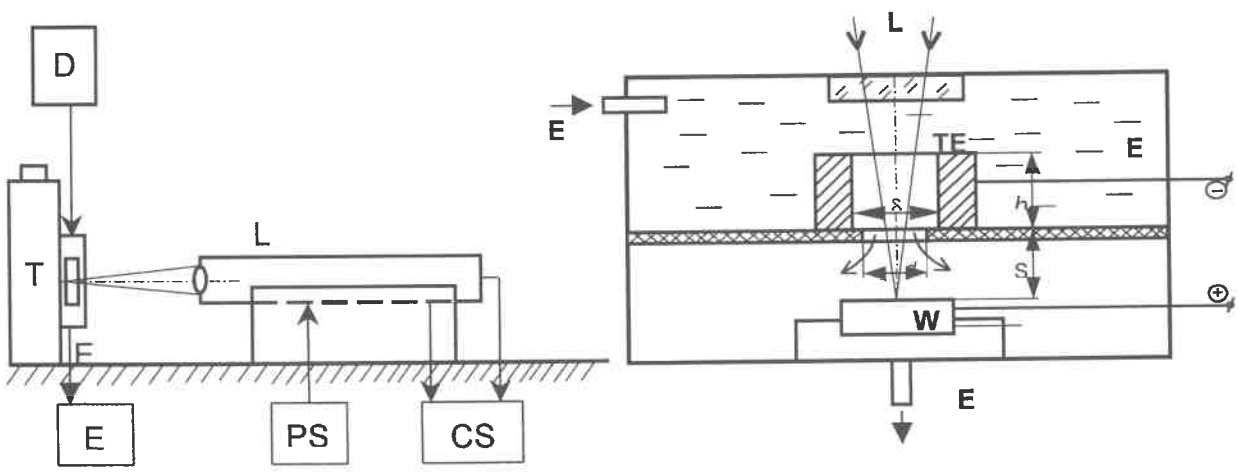

Fig 7. Experimental system for Laser Electrochemical Micro-Machining (LECMM): D-drive, T-workpiece table, E-electrolyte supply, L-laser, PL-power supply, CS-cooling system, W-workpiece, TE-electrode, E-electrolyte

The following settings were used during experiments: distance between cathode and anode – S = 5 mm; interelectrode voltage U = 0 – 30 V; current density i = from 4 A/cm^2 to 40 A/cm^2, flow rate Q = 1.14 l/min and machining time t = 60 -180 s. Experiments were performed on chromium steel using 15 % NH_4NO_3 electrolyte.

Figure 8 shows the results of experiments carried out at i = 19 - 20 A/cm^2 In this case it is observed that there is not significant difference between the metal removal rates in ECM and LECMM. However, the profile shapes are different. In LECMM the profile shape has more sharp edges and is more uniform and smoother profile than in ECM.

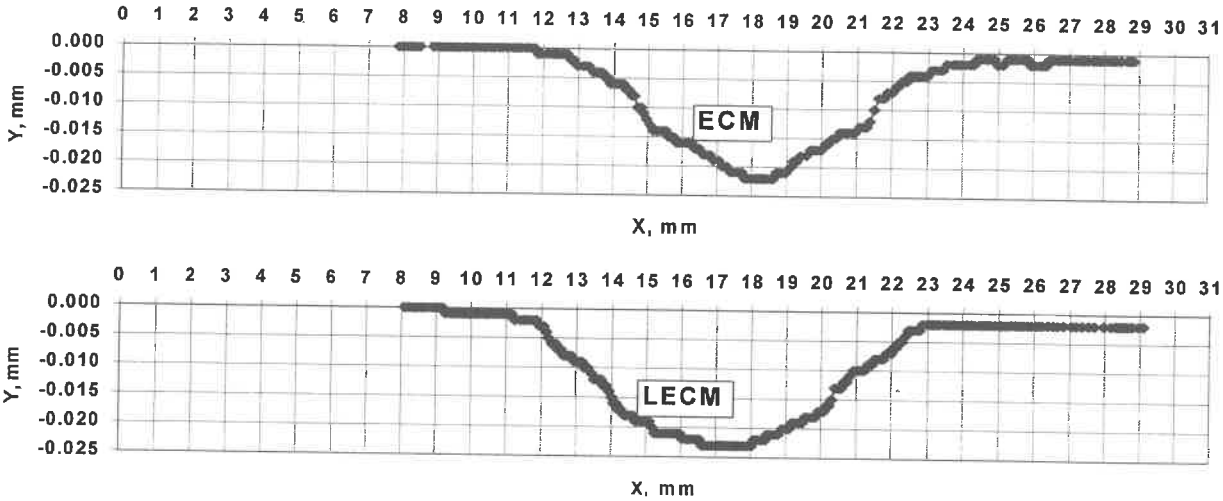

Fig. 8. Profile of machined surfaces after ECM and LECM
Parameters: material: LH15, electrolyte: 15% NH4NO3, i = 19 A/cm^2,
U = 24 V, S = 5 mm, t_m = 120 s, Q_v = 1.14 l/min

Results were significantly different, when electrochemical dissolution is performed at low current density with passivation phenomena occurring in the process. For example, at: i = 4.4 A/cm^2, U = 12 V, L = 2.7 mm, Q_v = 1.14 l/min, t = 90 s. The difference in the profile shapes for ECM and LECMM and increases in process localization are shown in Figure 9.

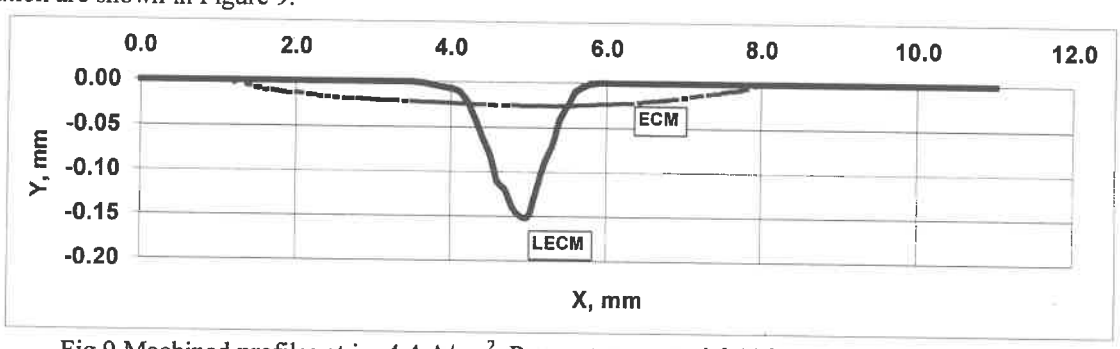

Fig.9.Machined profiles at i = 4.4 A/cm^2. Parameters: material: NC6, electrolyte: 15% NH_4NO_3,
U = 12 V, L = 2.7 mm, t_m = 90 s, Q_V = 1.14 l/min

Conclusions. Study of micro-ECM process demonstrate that an ECM using small gap and pulse current, and a laser assistance of ECM can be effectively used for improving of micro-machining processes by increasing localization of anodic dissolution and increase of metal removal rate.

References

1. Rajurkar K., P., McGeough J., A., Kozak J., De Silva A., Annals of the CIRP Vol.48/2, pp. 569-579,1999
2. Datta M., IBM Journal of Research and Development Vol. 42, No. 5, pp. 655-669, 1998
3. Datta M., et all., J. Electrochemical Soc., Vol. 136, No.8, pp. 2251-2256, 1989
4. Kozak J., Rajurkar K. P., Sarwade R. N., Proceed. Symposium on Electrochemical Microfabrication, Phoenix, 180 th Meeting of Electrochemical Society, Inc., Phoenix, 1991
5. Kozak J., Rajurkar K., P., Wei B., Transaction of the ASME, J. of Engineering for Industry Vol.116, 3, pp. 316-323, 1994

Key words: electrochemical micro-machining, accuracy, dimensional limitation, pulse current, laser activation

Electrochemical Polishing of Indium Tin Oxide Film

'Chih-Chang Tsai, *Fuh-Yu Chang, *Hung-Yi Lin, Jing-Chie-lin, *Tung-Chuan Wu,
Department of Mechanical Engineering, National Central University
Chungli, Tao-yuan, Taiwan 320, R.O.C.
Phone: 886(Taiwan)-3-4267395 Fax: 886(Taiwan)-3-5826104
E-mail: s8323041@cc.ncu.edu.tw
*Micro-Electro-Mechanical Systems Research Div., Mechanical Industry Research Laboratories, Industrial Technology Research Institute
M200, MIRL/ITRI, Bldg.22, 195-3 Chung Hsing Rd., Section 4, Chutung, Hsinchu, Taiwan 310, ROC
Phone: 886(Taiwan)-3-5917775 Fax: 886(Taiwan)-3-5826104

Abstract

Electrochemical polishing has been used in this study to improve the surface conformation of Indium tin oxide film (ITO). After sputtering deposition, the surface roughness of the ITO film is not good enough in the application of future Organic Light-Emitting Diodes (OLED). The OLED displays should further be improved for their performance, especially long-life with stable yield quality. Chemical Mechanical Planarization (CMP) process is currently a practice method for obtaining flat surface. However, a substitute method with lower cost is more competitive. In this work, electrochemical polishing was found as to improve the surface conformation of the ITO film.

I. Introduction

Since Indium tin oxide film has high transparency and good conductivity, so it is broadly applied to displayer system such as Liquid Crystal Displayer (LCD) and Plasma Displayer, etc. as electrode. When it is applied to photo displayer system, such as LCD and Plasma Displayer, etc., its conductivity request is also especially **high, and its surface resistance has to < 10Ω-cm²**. Except for the request of low resistance, there are also other requests such as surface roughness, defect size, workability, chemical stability, film formation temperature, sample size and production cost, etc. Generally, the conductivity of the ITO film will increase according to the temperature of film formation. Mainly, the temperature increment will contribute the forming of crystal formation with high conductivity. There are many kinds of process technology of Indium tin oxide film, such as electron gun deposition, spray, direct current electroplating or high frequency spattering, etc. Reactive direct-current sputtering process has the uniformity of the largest area and the process of bulk production, and therefor it is widely applied to the bulk production of the LCD. Relatively, to produce the indium tin oxide film substrate with large uniformity area and the quality of bulk production, the target with high density (99%) and high concentration (99.99%) has to be used. Increasing the mechanical intensity and the heat conductivity of target is a must to gain higher

sedimentation rate of the ITO film, smoother surface and lower resistance. In traditional surface flatting process, CMP method is mainly used to produce the ITO film with high flatness. Since its cost is too expensive, we use a low cost process technology-Electropolishing (EP) method to improve its surface condition instead. From the experiment, we can notedly discover its surface average roughness has decrease from primary 4 nm to 1.2 nm. And thou the result is incomparable with CMP (Ra<0.5nm), but relatively, we flat the surface of the ITO films with the simplest method.

II. Experimental details

(a) Sample preparation

The sample used in the experiment is prepared with DC sputtering deposited method, its target is the composite oxide of indium and tin (90wt% In_2O_3 + 10wt% SnO_2, 99.99% purity); substrate is 10cm x 10cm corning 7059 glass substrate, then the substrate is cut into 2cm x 2cm for further testing after the sedimentation of indium tin oxide film. After the substrate is cut into certain size, the sample is cleaned with normal cleaning and then is blown to dry with nitrogen. Mostly, the purpose of this cleaning is to prevent dust and oil sticking on the sample surface because it will influence the experiment result.

(b) Electrochemical testing

Place 2cm x 2cm Indium tin oxide film substrate in Teflon work electrolytic cell (such as shown in figure 1). We use constant potential instrument measuring system to do dynamic potential scanning, constant potential, constant voltage test with platinum (Pt) as auxiliary electrode, standard calomel electrode (SCE) as reference electrode. And the electrobath is the solution of HCl, HNO_3, H_2O.

(c) Sample observation and resistance measurement

Sample observing is mainly done to observe surface condition, we use atomic force microscope (AFM) to measure the surface condition changes of the ITO film before and after, to differ surface changes condition of the film; using four points probe to measure surface resistance. Finally, we use SEM to observe the film surface condition of large area after polishing.

III. Large area electrochemical polishing construction

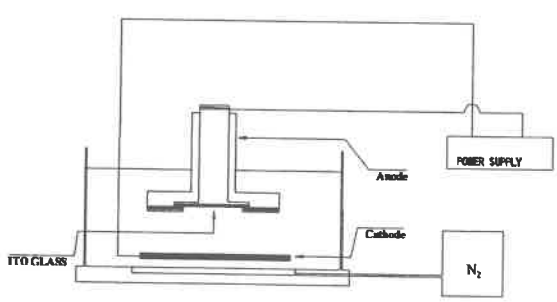

Figure 1 Large area electrochemical polishing construction.

IV. Results

Figure 2 shows the comparison between EP and CMP, and show significant difference. EP method still cannot reach the same level of CMP, but we discover a kind of low cost method to produce the ITO film with high flatness. In the past reference of EP, we learn that the important parameter are current density and the concentration, the temperature of etching solution, sample and the distance between electrode. In the experiment, we search EP area of the ITO film with constant potentiometer. Figure 3 is the result of dynamic polarization test of the ITO film in the mixture of diluted HCl, HNO_3, H_2O. In figure 3, we can know the current and voltage property of the ITO in this solution.

In this figure, we can discover when voltage is increasing, its current changes will not vary; it also represents that the ITO film surface is always protected by the forming of a layer of inert film. According to the theory of EP, we can know that the result we get can be used to be EP within this area. Figure 4 shows the relationship between voltage and time when EP. Through figure 3, we choose the voltage range between 0.5 ~ 3V, time as 1000 seconds, etching solution is the mixture of HCl, HNO_3, H_2O, sample and electrode distance as variable. In the experiment result we find sample and electrode distance will influence the polished surface roughness such as shown in figure 5. In the relationship between different etching solution concentration and surface roughness, we discover the higher the concentration of etching solution, the smoother its etched surface will be.

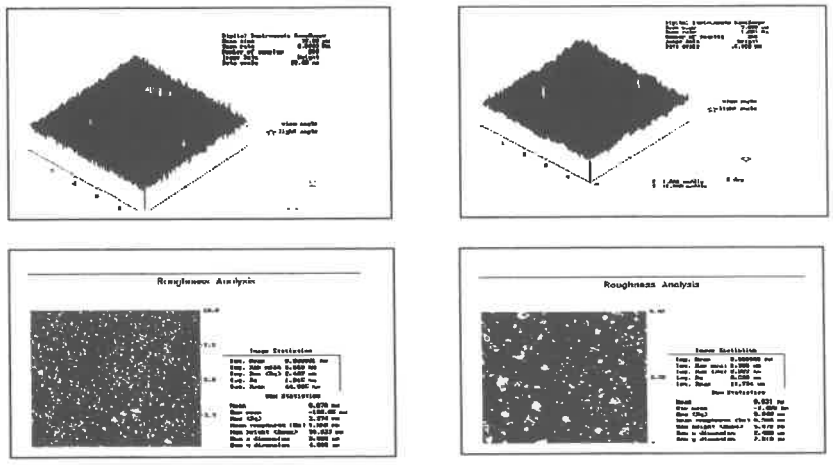

(a) (b)

Figure 2 (a) The ITO film, which is polished with EP (b) The ITO film, which is polished with CMP

V. Conclusions

This research confirms that ITO film can be electro-polished with cathode bias resistance in HCl and HNO_3 solutions, it also proves that electro-polishing method can significantly reduce the average surface roughness. This result displays that ITO film can have good market competitive potential in electrochemical etching of HCl and HNO_3 solutions. The continuing research of this project will put stress in improving the electric current and voltage distribution during electro-polishing.

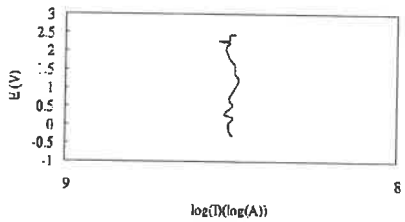

Figure 3 The dynamic polarization test of film in solution.

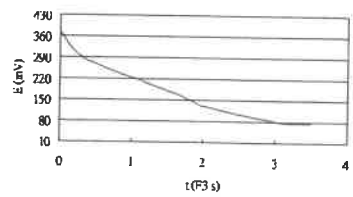

Figure 4 The measured E-t figure of film in solution.

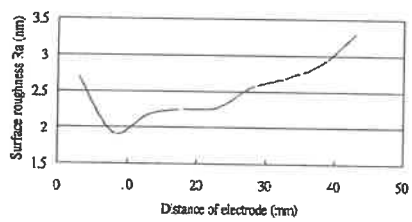

Figure 5 The influence of electrode distance towards surface average roughness.

VI. References

1. K. B. SUNDARAM, V. H. DESAI "Electropolishing of silicon using hydrazine", Journal of Material Science: Materials in Electronics, 1997, pp. 99
2. Wang, J. J.; Lambers, E. S.; Pearton, S. J.; Ostling, M.; Zetterling, C.-M.; Grow, J. M.; Ren "ICP etching of SiC", Solid-State Electronics, Volume: 42, Issue: 12, December, 1998, pp. 2283-2288
3. Kuo, Yue, "Reactive ion etching of indium tin oxide by SiCl4-based plasmas-substrate temperature effect", Vacuum, Volume: 51, Issue: 4, December 1, 1998, pp. 777-779
4. Van Den Meerakker, J. E. A. M.; Baarslag, P. C.; Walrave, W.; Vink, T.; Daams, J. L. C., "On the homogeneity of sputter-deposited ITO films Part II. Etching behaviour", Thin Solid Films, Volume: 266, Issue: 2, October 1, 1995, pp. 152-156

Optical Fabrication in the Optics Research Group

Hedser van Brug, Silvia M. Booij
Optics Research Group, Delft University of Technology, Lorentzweg 1, NL-2628 CJ Delft
The Netherlands (e-mail: brug@optica.tn.tudelft.nl)
Robert-Jaap M. van der Bijl
DeCOS, TNO/TPD, Delft, The Netherlands
Oliver W. Fähnle
FISBA-OPTIK AG, St. Gallen, Switzerland

Introduction

Within the Optics Research Group there has been, and still is an interest in optical fabrication. The group had its own optical workshop in which the experimental work could be carried out. Recently, the optical workshop has been taken over by TNO/TPD and is now operated under the name Delft Center of Optical Surfaces (DeCOS), both for production and research. The research in the field of optical fabrication is carried out within DeCOS, with coaching by staff members of the Optics Research Group. The work reported here is the result of about ten years of research. The reported research ranges from process optimization and control to the design of new types of production machines and production methods.

Bowl-feed polishing

The first research to be elaborated upon is bowl-feed polishing [1]. Bowl-feed polishing is also referred to as super-polishing. During bowl-feed polishing, the sample oscillates horizontally (28 strokes/min) over the rotating pitch lap, similar to conventional polishing. The basic difference with traditional (fresh-feed) polishing is the use of a bowl with a suspension of polishing compound in water, rotating with the same speed as the pitch lap. Because of the centrifugal and gravitational forces, the particles of the polishing compound in the suspension move to the perimeter and to the bottom of the bowl. This is confirmed by the fact that the polishing compound sinks visibly to the bottom within one hour if no obstacles are placed in the rotating bowl. For an impression of the bowl-feed configuration, see Fig.1. The super-polishing starts with a stirrer in the bowl, which provides a fairly homogeneous distribution of the polishing compound in the bowl. Then, a continuous deposition of new polishing compound occurs on the pitch lap, because the suspension flows over its edges. If a good contact between the rotating pitch lap and the sample surface is obtained, the stirrer is removed. Now the particles in the suspension start sinking and the amount of polishing compound arriving on the pitch lap decreases gradually until finally only pure water flows over the lap. Since the compound particles are broken and pushed into the pitch during polishing, the surface of the pitch lap becomes increasingly smoother. In its turn, this smooth lap surface extremely reduces the sample surface roughness. The setup used to characterize the sample roughness was a modified Linnik interference microscope. Using this setup we arrived at an accuracy of 0.02 nm. The starting surface roughness was about 0.5 nm (RMS) and this roughness was reduced to 0.15 nm (RMS) by bowl-feed polishing.

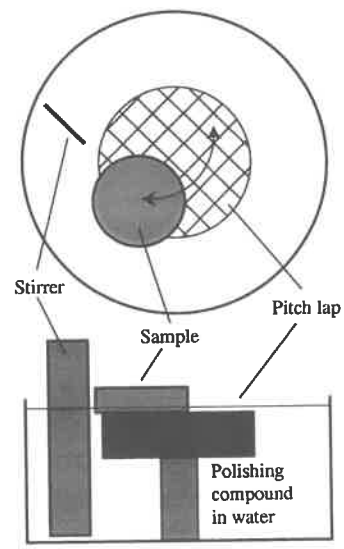

Fig.1: Top and side views of the bowl-feed polishing instrument.

FAUST and WAGNER

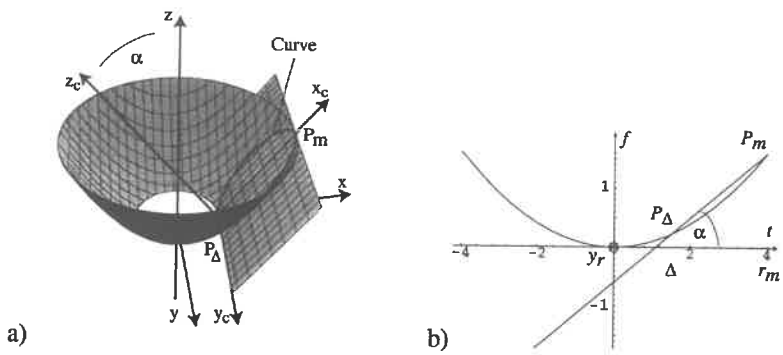

Fig.2: A schematic representation of the FAUST and WAGNER methods. In a) the surface and the intersecting plane are indicated in 3D view where in b) a cross section is shown. The smallest and largest radial positions are given.

In this section two new asphere production methods will be discussed. Starting with the description of a rotationally symmetric surface shape to be generated, it is possible to calculate the intersection curve of that shape with a plane, see Fig.2. This plane has to pass through the minimum and maximum radial position to be present in the surface. The idea is now to create a tool that machines an optical surface along this intersection curve. At the end of the machining the shape of the optical surface will then be the desired one. If the machining is carried out with a line-contact (a machining band), the method is called FAUST [2,3]: Fabrication of Aspheric Ultra-precise Surfaces using a Tube. If on the other hand point contact machining is employed, the method is called WAGNER [4,5]: Wear-based Aspherics Generator based on a Novel Elliptical Rotator. Since within the FAUST method the machining is carried out along a line contact, the orientation of the contact line between the machining band and the surface determines the shape of the surface being generated. Within WAGNER a stop has to be included in the machine to stop the machining as soon as the desired removal has been obtained. Owing to this stop, the differences in removal rate for different radial positions on the surface will not be a problem. By using FAUST of WAGNER the problem of producing high accuracy aspherical surfaces is shifted to the problem to produce an accurate path along which the machining takes place. The required accuracy of the machining path is less stringent than that of the optical surface owing to the advantageous error propagation factor between machining path errors and surface shape errors.
The same tool, shaped in the form of the intersection curve, can be used to produce differently shaped surfaces by changing the angle under which it is positioned above the surface. Within the WAGNER setup we use only elliptical tool paths. It has been shown that by using an elliptical tool-path, all types of conical surfaces can be produced. Both FAUST and WAGNER can be used to produce on-axis as well as off-axis surfaces and they use loose abrasive load controlled machining. Within WAGNER the point contact consists of a small cup wheel placed under an angle such that effectively the wheel makes a small area contact with the workpiece. First results with WAGNER showed an rms roughness values of below 5 nm. The FAUST setup is presently under construction and the first results are expected by the end of the year 2000.

Fluid Jet Polishing

Recently, a new shaping and finishing technique has been introduced. This technique is referred to as Fluid Jet Polishing (FJP) [6,7]. On one hand we knew the principle behind bowl-feed polishing and on the other hand we knew that it is possible to cut glass and metal with high-pressure abrasive slurry jets. This gave us the idea to investigate the use of a low-pressure abrasive slurry jet to shape and finish optical

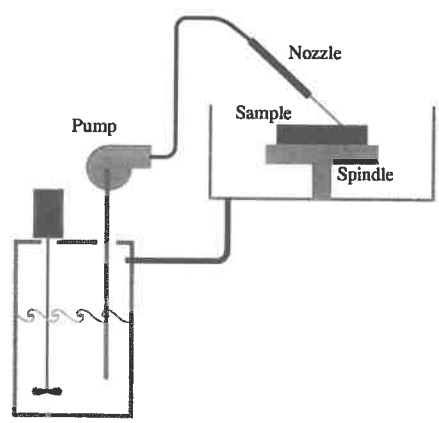

Fig. 3: The FJP setup, comprising of a tank (containing the slurry), a stirrer, a pump, a nozzle and a glass sample on a spindle.

surfaces. Using a simple membrane pump (0 – 10 bar) we pump the slurry of water and abrasive particles from a tank and guide it through a nozzle to the surface, see Fig.3. There the fluid jet is, after hitting the surface, forced to flow laterally to the surface such that the particles apply a shear force to the surface. This results in a ductile removal of material. A 1 mm diameter nozzle results in a 3 mm spot size where material is being removed. Starting with a rough surface (rms roughness of 300 nm) it was found that the surface gets smoother by the FJP process (typical end roughness of 5 – 15 nm rms) and that the removal rate is about 3μm/min. If a smooth surface is processed, it was found that the surface finish was maintained (no degradation), and that the removal rate is lower by about a factor of ten as compared to a rough starting surface. The main features of FJP are its in process cooling and debris removal, the re-use of slurry and thereby low environmental pollution and low production cost (low consumables consumption), and its simple setup. It can be used to process all types of materials (plastics, ceramics, metals, and crystals) and with a proper computer control it can be used to shape all kinds of surfaces.

iTIRM

The acronym iTIRM stands for intensity-detecting total internal reflection microscopy [8]. The idea behind iTIRM originates from total internal reflection microscopy (TIRM), where light illuminates the surface from within under an angle exceeding the angle of total reflection, and a microscope is used to inspect the surface, from above. There where defects are present, light will be scattered and will show up in the microscope image. All defects free areas will remain dark since the light will be totally reflected. We have extended this method such that it can be used for in-process monitoring. During processing the microscope can not be positioned above the surface. Therefore we decided to use the reflected light intensity as an indicator of defects and/or state of roughness on the surface. It has recently been shown that iTIRM can be used for process investigation (optimization purposes) and for in-process monitoring as watch-dog for process errors and as indicator for the end of process. Figure 4 shows the iTIRM setup (as used for in-process measurements) together with some results from a polishing experiment. It can clearly be seen that the iTIRM signal increases with time, indicating a decreasing roughness. With time the increase gets less until it finally levels out, indicating that the end result of this polishing step has been reached. The sudden drop in intensity in the left-hand-side result is caused by insufficient lubrication which shows that iTIRM is well suited as process monitor.

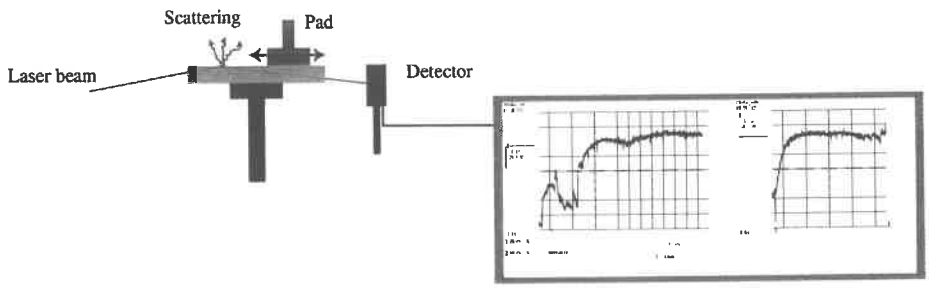

Fig. 4: iTIRM setup and measurement result (see text).

Nomarski

In many optical workshops a Nomarski microscope is used as a quick tool to qualitatively investigate the status of a surface. Our idea was to take the histogram of the Nomarski images to get more quantitative information on the surface quality [9]. A histogram gives information on how often a given gray value is present in an image. For a perfectly smooth surface the Nomarski image should contain only one single gray value. For surfaces that contain some roughness, the histograms of the Nomarski images show a peak with a certain width. It is expected for the peak width to be linked to the rms surface roughness. Since a Nomarski microscope compares two adjacent points on the surface (shearing interferometry), the gray value in the image is linked to the slope in the surface. In Fig.5 an example is given of a Nomarski image taken from a sample that contains tool marks. From this Nomarski image the histogram was taken and converted from gray values to corresponding slope values. A broad structure can be seen

with two clear sub-peaks. These peaks indicate the presence of tool-marks. Tool-marks will in general be present as lines or steps in the surface. This leads to the presence in the Nomarski images of many points having one of two gray values, one gray value for the up-going slope, and one for the down-going slope.

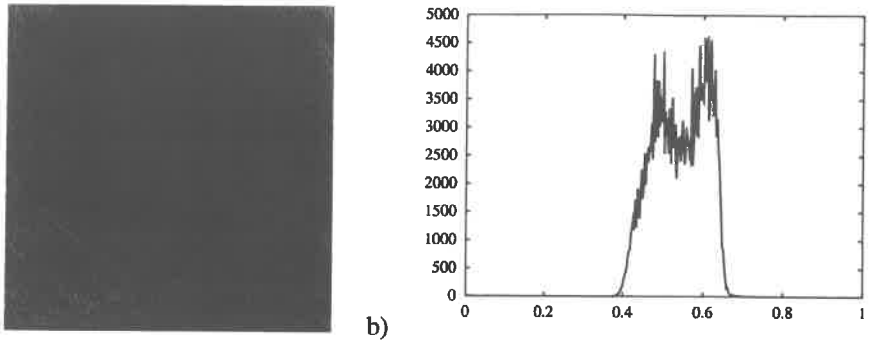

Fig. 5: Nomarski image of a surface showing tool marks and its histogram. The double peaked structure in b) indicates the tool marks.

Conclusions

The investigations within the Optics Research Group, in the field of optical fabrication, have been shown to be very divers. It consists work in the field of shaping (FAUST, WAGNER, and FJP), finishing (Bowl-feed polishing and FJP), and characterization (iTIRM, Nomarski microscopy, and Linnik microscopy).

The authors like to thank the co-workers in the Optical Workshop: Rosindro Partosoebroto, Rob Kuiper and Bob den Dulk.

References

[1] Johannes van Wingerden, Hans J. Frankena, and Bertram A. van der Zwam, "Production and measurement of superpolished surfaces," *Optical Engineering* **31**(5), pp. 1086 – 1092

[2] O. W. Fähnle, H. van Brug, C. J. van der Laan, and H. J. Frankena, "Loose abrasive line-contact machining of aspherical optical surfaces of revolution," *Applied Optics* **36**(19), pp. 4483 – 4489

[3] O. W. Fähnle, H. van Brug, C. J. van der Laan, and H. J. Frankena, "Generation of on-axis and off-axis conic surfaces of revolution by applying a tubular tool," *Applied Optics* **36**(19), pp. 4490 – 4496

[4] Oliver W. Fähnle, Hedser van Brug, and Hans J. Frankena, "Wear-based aspherics generator based on a novel elliptical rotator," *Optical Engineering* **37**(8), pp. 2343 – 2350

[5] Hedser van Brug and Oliver W. Fähnle, "WAGNER: machine construction and operation considerations," in *Optical Fabrication and Testing*, OSA Technical Digest (Optical Society of America, Washington DC, 2000), pp. 122 – 124

[6] Oliver W. Fähnle, Hedser van Brug, and Hans J. Frankena, "Fluid Jet Polishing of Optical Surfaces," *Applied Optics* **37**(28), pp. 6771 – 6773

[7] Silvia M. Booij, Hedser van Brug, and Oliver W. Fähnle, "A mathematical model for machining spot in Fluid Jet Polishing," in *Optical Fabrication and Testing*, OSA Technical Digest (Optical Society of America, Washington DC, 2000), pp. 70 – 72

[8] Robert-Jaap M. van der Bijl, Oliver W. Fähnle, and Hedser van Brug, "Subsurface damage measurements as a tool for process monitoring," in *Proceedings of the ASPE 1999 Annual Meeting* (American Society for Precision Engineering, Raleigh, NC 1999), pp. 606 – 609

[9] Hedser van Brug, Silvia M. Booij, Oliver W. Fähnle, and Robert-Jaap M. van der Bijl, "Quantitative surface characterization using a Nomarski microscope," in *Optical Fabrication and Testing*, OSA Technical Digest (Optical Society of America, Washington DC, 2000), pp. 91 – 93

PRECISION REPLICATION OF OPTICS

David D. Gill, Thomas A. Dow, Alex Sohn
North Carolina State University, Raleigh, NC

INTRODUCTION

Advancements in the fields of optical communication, photonics and display technologies require the development of high volume, high precision production methods. As signal traffic continues to increase on fiber optic networks, there is a need to perform switching without converting the optical signal to an electric signal. These switches, often called Micro Optical Electro-Mechanical Systems (MOEMS), must be fast, durable, highly transmissive, and thermally stable. Video displays on laptop computers and personal organizers are increasing in quality and there is a constant demand for wider viewing angle and screens with increased brightness and clarity. Display applications also require components that are thin, precisely located over a large area, and highly transmissive. Both fields require high-volume, low-cost fabrication and assembly techniques.

Molded polymers fulfill many of the requirements for these parts, but still present challenges. For example current production methods for MOEMS rely on integrated circuit technologies such as lithography and flip-chip construction. These methods require many steps with precision alignments of successive masks to produce the desired features. The components are built up from silicon in the z dimension and then separated from the substrate and rotated to produce in-plane optical networks on the substrate [1]. Replicated polymer optics would serve well in this application if they could be thermally stable throughout the wide temperature operating range and provide long service life. One potential solution is to mold the polymer optics in a thin layer on a thermally stable substrate [2]. Such optics could be cast in a UV curable polymer [3] (low volume production, low capital investment) or injection molded (high volume production, high capital investment). The application of thin polymer optics on a thermally stable substrate would also benefit the field of display technology where laptop and personal organizer screens require microlenses and optical waveguides on the glass screen substrate to broaden the viewing angle or to sense the touch-input device.

The goal of this research involves the development of processes capable of accurately reproducing sub-micron optical features over small and large areas as well as rapidly co-molded these features on thermally stable substrates.

REPLICATION TECHNIQUES

UV Cure Molding

UV cured polymers have been extensively used for creating soft contact lenses and also for replicating thin optical surfaces on top of glass and plastic substrates [7, 8]. This process was studied to evaluate the capability to reproduce nanometer sized features on the mold and also the speed and repeatability of the process.

An aluminum mold was diamond turned with the mold cavity 350 μm deep. The monomer was cast into the aluminum mold and the mold placed in a vacuum chamber to remove entrained air

bubbles. Upon removal from the vacuum chamber, a glass plate was placed over the cavity. UV illumination cross-linked the monomer and it adhered to the glass plate. While features were accurately replicated within a few nanometers, this process is quite slow. To reduce the cycle time of this operation, investigation into injection molding was initiated.

Injection Molding

To achieve the goal of precision replication of sub-micron features in thin moldings over a large substrate in injection molding, the research has been divided into four stages :

The first stage investigated the transfer of feature and form from the mold to the molded part. Previous research [4, 5, 6] reported the molding variables that affect feature transfer, but further study is warranted for optical components. Tests were conducted using a diamond-turned mold producing a 25 mm diameter plano-convex lens with center thickness of 3.5 mm. The plano mold half had features ranging between 0.5 and 16 μm width with depths less than 21 nm.

The second stage will investigate the injection molding of part geometries onto thermally stable substrates such as glass, and quartz using the convex half of the mold in conjunction with a plano substrate located in the fixed side of the mold base.

The third stage of the project will combine the molding of very thin parts onto thermally stable substrates.

The fourth stage will investigate the transfer of micron and sub-micron features within the very thin parts on thermally stable substrates, possibly incorporating precision slides to produce in-plane optics.

Concave-Plano Lens A Van Dorn, 75 ton hydraulic injection molding machine was used to fabricate test lenses. Two mold halves, one plano (fixed half) and the other concave (to make a convex lens) were diamond turned from aluminum and installed in the mold bases on the machine. VEREX 1301 polystyrene (Nova Chemicals) was injection molded with varying hold times, cooling times, and barrel temperature profiles to determine the optimum parameters for form and feature transmission. An injection pressure of 11.4 MPa was held constant for all trials. The hold time was varied between 2 and 20 seconds while maintaining a constant injection pressure, barrel temperature profile, and cooling time. Subsequently, the in-mold cooling time was varied between 4 and 20 seconds while maintaining a constant barrel temperature profile, holding time, and injection pressure.

The barrel temperature test varied the temperatures at the three control locations along the injection barrel. The machine controls the temperature using a PID controller that monitors the temperature at the front and rear of the barrel and at the injection nozzle. Electric heater bands at each location maintains the desired temperature. The temperatures were varied between 215°C and 265°C. The process temperature range published for the polystyrene is between 190°C and 274°C, but the entire range was not available using the other molding parameters as set due to the melt and flow characteristics of the polymer.

RESULTS AND DISCUSSION

UV Cure Molding Figure 1 illustrates the quality of the UV polymer replication. Figure 1(a) is a white-light interferometer trace of a diamond turned mold and Figure 1(b) is an inverted trace of the plastic replica. The surface has the characteristic features of diamond turning with a slightly-damaged tool resulting in a rms roughness of 20 nm. The feed rate for this surface is

about 20 μm per revolution. The replicated surface is inverted to make it easy to compare the mold and replica. The small features of the tool (some less than 10 nm) are copied with impressive fidelity using UV cure polymers.

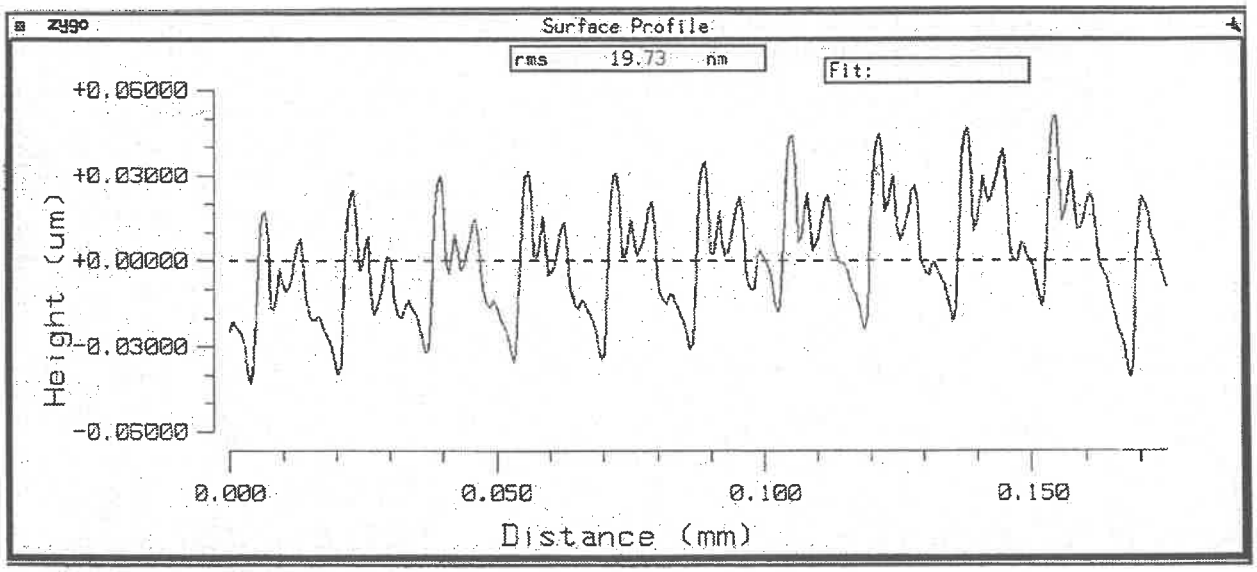

Figure 1 (a). White Light interferometer trace of diamond turned aluminum mold surface

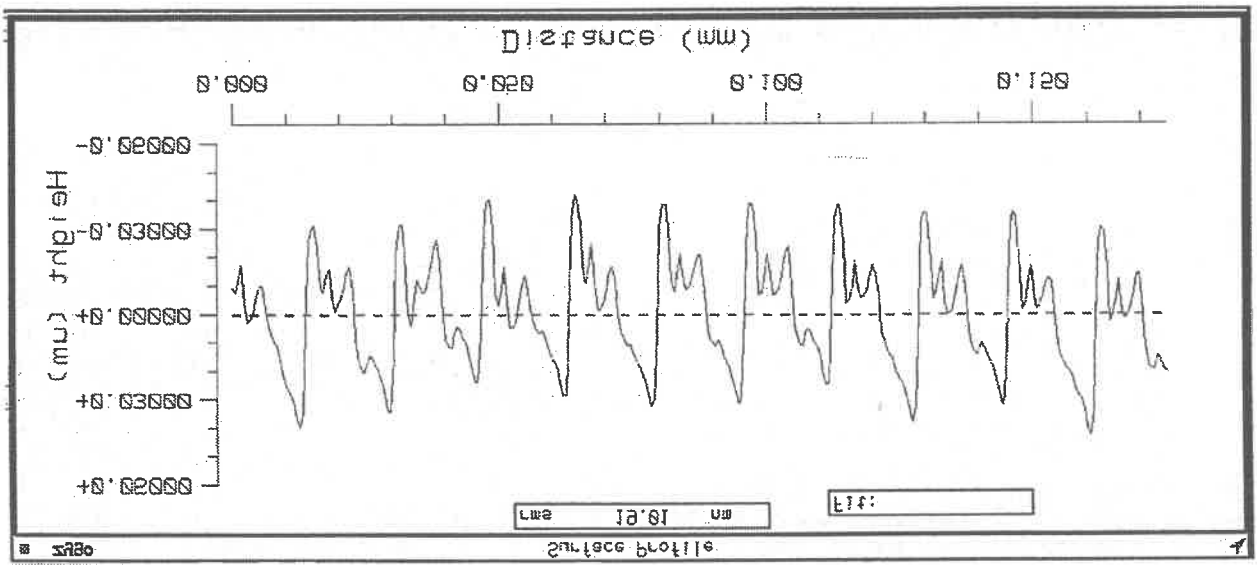

Figure 1(b). Inverted white-light interferometer trace of UV cured polymer replica

Figure 2 shows a top-down view of the center of a second diamond turned mold. In this case the feed rate 20 μm using a 3 mm tool radius. The theoretical height of the features is 15 nm.

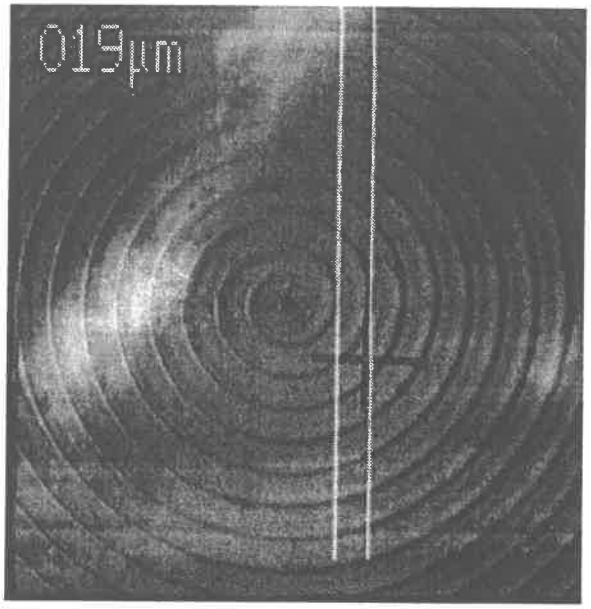

Figure 2. Micrograph of center of UV Replicated sphere

Injection Molding A large number of test parts were fabricated with varying packing time, barrel temperature and barrel temperature. The figure of merit selected was the peak-to-valley error on the flat side of the molded lens. Flat features are the most difficult to mold so this measurement was deemed a useful comparison. A significant reduction in form error (on the order of 75%) was observed as the time was increased from 1 to 10 seconds. The influence of cooling time was less apparent. While a slight downward trend was observed (increased cooling time reduced form error), more scatter in the data also existed for these tests. The results of the barrel temperature profile tests showed similar scatter. Additional tests are in progress to better define the trends.

REFERENCES

1. G. Zhou et al., "New Approach for Nonsilicon Micromachined Three-Dimensional Multilevel Diffractive Optical Elements," *SPIE proc.*, 1999, vol. 3879, pp. 88-95.
2. L. Baraldi and R.E. Kunz, "High Precision Molding of Integrated Optical Structures," *SPIE Proc.*, 1993, vol.1992, pp.21-29
3. M. Tanagami et al., "Low-Wavefront Aberration and High-Temperature Stability Molded Micro Fresnel Lens," *IEEE Photonics Tech. Letters*, Nov. 1989, vol. 1, pp.384-385
4. S.Y. Chou, P.R. Krauss, P.J. Renstrom, "Imprint of Sub-25nm Vias and Trenches in Polymers,", *Applied Physics Letters*, 1995, vol. 67, n.21, pp.3114-3116
5. O. Kemmann, C. Schaumburg, L. Weber, "Micro Moulding Behaviour of Engineering Plastics," *SPIE Proc.*, 1999, vol. 3680-1, pp464-471
6. M. Yoshii, H. Kuramoto, Y. Ochai, "Experimental Study of the Transcription of Minute Grooves by Injection Molding (II)", *Polym. Eng. Sci.*, V38, n.9, Sept. 1998, pp.1587
7. Blough, G., et. al., "Single-point diamond turning and replication of visible and near-infrared diffractive optical elements", Applied Optics, Vol 36, No 20, 1997, p 4648.
8. Anagnostis, J, et.al., "Replication of high fidelity surface relief structures", ASPE Spring Topical Meeting, Vol 19, 1999, pg 29.

DEVELOPMENT OF ONE-STOP MACHINING SYSTEM FOR ϕ300MM SILICON WAFER

Libo ZHOU*, Hiroshi EDA*, Kazushi WATANABE**,
Hirotami NAKANO*, Ryo KONDO* and Jun SHIMIZU*

* Ibaraki University, Nakanarusawa 4-12-1, Hitachi-shi, JAPAN 316-8511
** Hitachi Via-Mechanics Pte. Ltd, 2100 Kami-Imaizumi, Ebina-shi, JAPAN 243-0488

1. Introduction

According to the roadmap of the semiconductor industry, the silicon wafer will be shifted from ϕ200mm (8") to ϕ300mm (12") by the year 2003. Presently the manufacturing of silicon wafer is mainly done by lapping, etching and polishing. These free slurry methods achieve better surface roughness only when smaller abrasives are applied, therefore, require multi-stage equipments and multi-stage processes. The current pressure-controlled process is also unable to fulfill the requirement of global flatness as the wafer size is increased. To combat the problems of throughput rate, post-process cleaning, environmental impact as well as to achieve the total surface integrity of ϕ300 silicon wafer, the semiconductor industry is looking for a fixed abrasive solution as the alternative.

This research project has successfully developed an advanced manufacturing system, using fixed abrasive grinding wheel instead of free sully, to provide a totally integrated environment to achieve one-stop machining. The key component developed for this system is the giant magnetostrictive actuator, which is used to precisely position the grinding head against the workpiece for non-defect grinding, and to control the posture of the silicon wafer as well to achieve the flatness over ϕ300mm global area.

2. One-stop grinding machine

Fig.1 is the external view of the newly developed one-stop grinding machine, which has two aerostatic spindles configured level facing each other to eliminate the gravity effect. Both spindles come with built-in AC servomotors and rotate at 1.8~18000 rpm with the maximum run-out of 0.02μm. The left spindle, to hold the workpiece, is equipped with a vacuum chuck made of porous ceramics to attain high rigidity, while mounted on the right spindle is the diamond grinding wheel.

As the details shown in Fig.2, the grinding machine has two degrees of freedom. The linear motion along X direction is given to the work spindle, while the Z directional motion to the wheel spindle. The guide way used is aerostatic box type with six-plane constraint. The tables are designed as 5 times long as the maximum linear stroke of 200mm, and driven by a

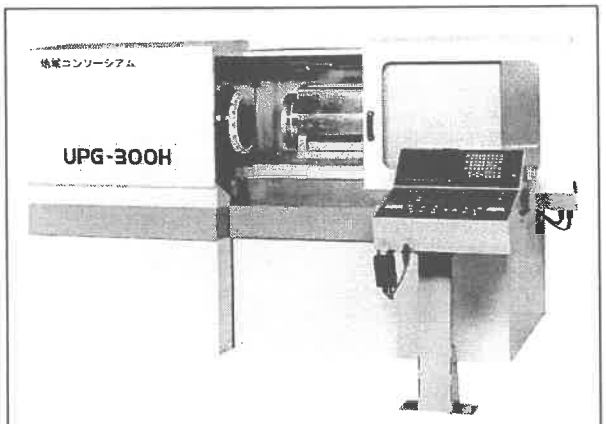

Fig.1 Newly developed one-stop grinding machine

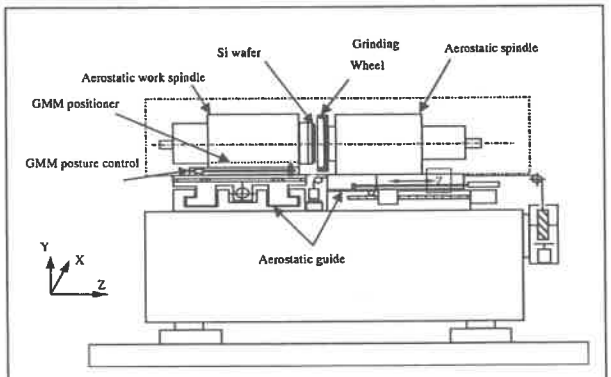

Fig.2 Machine structure and key components

Table 1 specifications and conditions

Specification	Property	Movement
Wheel spindle	Aerostatic bearing, built-in motor	1.8~1800rpm
Work spindle	Aerostatic bearing, built-in motor	1.8~18000rpm
X, Z linear guide	Aerostatic bearing, AC servo motor	10nm/200mm
Position	GMM actuator	1nm/2μm
Posture	GMM actuator	10nm/5μm
Conditions	**Property**	**Dimension**
Wheel	SD3000N150DK200B	300D-3W-3X-40T
Coolant	Pure water	20°C
Workpiece	Silicon wafer	300D-0.8t
Operational parameters	Wheel speed V	40~1500rpm
	Work speed v	20~500rpm
	Infeed rate F	0.5~20μm/min
	Infeed Z	2~20μm

set of precisely lapped lead screw together with a servomotor. All motion errors in pitching, rolling and yawing are less than 0.15μm over 200mm length, and the positioning resolution is as good as 10nm.

It is placed as shown in Fig.9 so that the grinding wheel and silicon wafer are half overlapped. The loop stiffness is about 100N/μm. The plunge grinding is adapted for the current research to avoid the variation in the contact area and thereby the grinding pressure, which normally leads to lower the quality of flatness. By disengaging the screw nut, the table of the Z-axis also moves by a low friction pneumatic cylinder which creates a constant the grinding force/pressure. This function is used for the final finishing, instead of the spark-out. The specifications and experimental conditions are summarized in Table 1.

3. Precision positioner

One of the core technologies of this grinding machine is its precision positioner, which is used to give the fine depth of cut and to control the posture of the silicon wafer against the grinding wheel. Fig.3 is the conceptual design of the positioner. The table consists of two pieces of parallel plate (600×600mm). They are wire cut into such shapes that the top plate linearly gives elastic deformation in Z direction while the bottom plate gives elastic deformation in yawing, rolling and pitching directions.

The actuator newly developed to drive this positioner is made of GMM (giant magnetostrictive material). Comparing to the piezo material, the GMM offers much better performance in displacement range, resolution, response speed and output power. Fig.4 shows the GMM actuator and the table actually developed. Four GMM actuators are employed; Actuator 1 and 2 for rotational motion around X, Z axes, Actuator 3 for rotational motion around Y axis and Actuator 4 for linear motion along Z axis. Each actuator comes with a capacitive sensor to form a closed feedback loop. Fig.5 is the control diagram for the positioner, which is comprised of a position controller, a current controller and a power amplifier. The symbols used in Fig.5 are the position reference value x^*, the actual position x, and the current reference value i^* and the actual current i. The detailed diagrams of the position controller and the current controller are respectively shown in Fig.6 and Fig. 7.

The position controller is built on a single PC board, which is equipped with a PowerPC 604e processor for fast floating-point calculation at 333MHz, a 16-bit ADC with of 4μs sampling time, 14-bit DAC with 5μs setting time. The position controller firstly compares the position reference value x^*, which is generated by a signal generator, with the ADC output x from the capacitive sensor. The error signal then regulates the current reference value i^* by means of the proportional

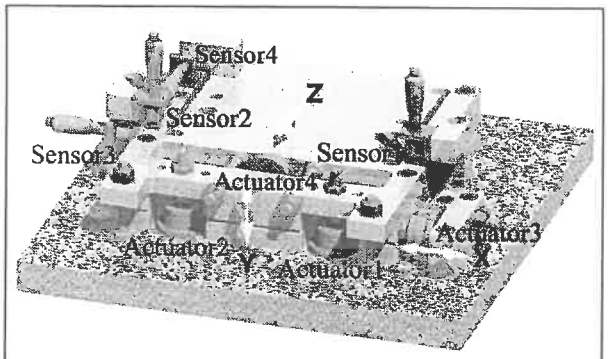

Fig.3 Position and posture control table

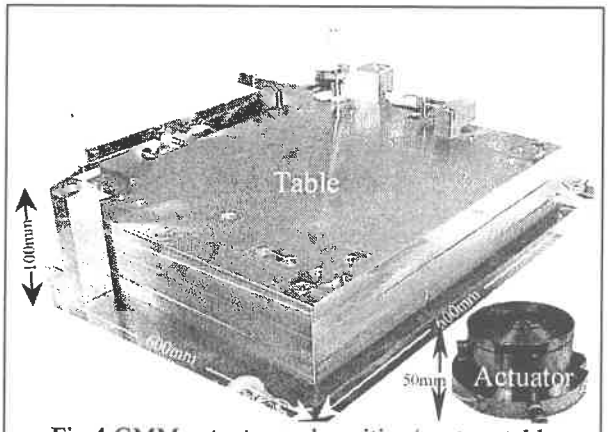

Fig.4 GMM actuator and position/posture table

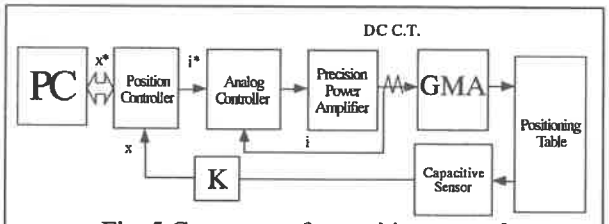

Fig. 5 Component for position control

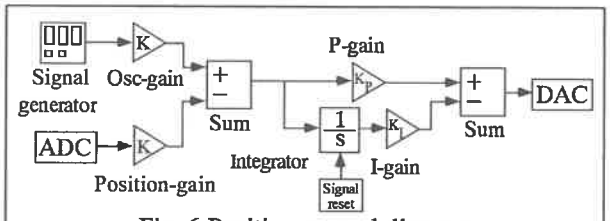

Fig. 6 Position control diagram

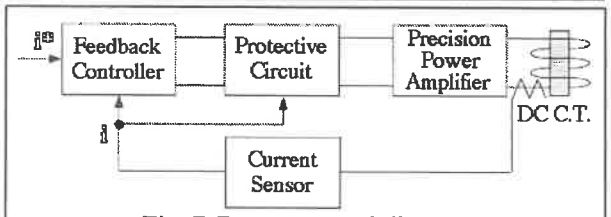

Fig. 7 Current control diagram

control gain or P-gain, and the integral gain or I-gain.

The actual current i flowing into the GMM actuator is detected by the DC current transducer and amplified by the current sensor. A feedback control is done in the current controller so that the actual current matches the current reference value.

The performance of the positioner has been evaluated with 500kgf payload. It is found that the positioner has about 2μm actuating range as it is designed. Fig.8 shows step responses of the table at the 10nm and 6.25Å. At such large payload, the motion error is less than 1Å. Being mounted on the positioner, the workpiece spindle is able to offer very fine depth of cut to achieve the ductile mode material removal and to align the posture to achieve high global flatness.

4. Grinding test

Infeed grinding is applied at the position shown in Fig.9, where the wheel is aligned half overlapping with the silicon wafer. The operational conditions are co-listed in Table 1. The cutting path formed on the wafer by each abrasive is dependent only upon the rotational speed ratio v/V of the wafer against the wheel. Examples given in Fig.9 are $v/V = 0.02$ and $v/V = 0.46$. For each case, the cutting path is denser in the center than that in the fringe. The wafer after grinding therefore tends to be concave (Fig.10a). On the other hand, tilting the wafer around X-axis makes its ground profile convex (Fig.10b). The flatness can be significantly achieved if the appropriate condition is chosen to offset these two factors. A typical result attained is shown in Fig.11 that has the global flatness of 0.2μm over ϕ300mm diameter.

The result in Fig.9 also shows that each cutting edge forms 50 passes for both $v/V = 0.02$ (or 1/50) and $v/V = 0.46$ (or 23/50), but with different locus. It is meant that the denominator m of irreducible fraction v/V of Eq (1) determines the number of the cutting path as grinding reaches the steady state.

$$\frac{v}{V} = \frac{n}{m} \qquad (1)$$

where n, m are integers, n/m is irreducible. Once the grinding reaches the steady state, the cutting edge goes over the same path. In order to achieve a better surface roughness, the cutting path density, namely, the denominator should not be too low. Fig.12 compares the surface roughness resulted from different rotation speed combination. The cutting path at $v/V = 495/1500$ (or 33/100) is three times denser than that at $v/V = 50/1500$ (or 1/30). It is clearly proven that the density of cutting path contributes in the surface roughness improvement. In the meantime, an

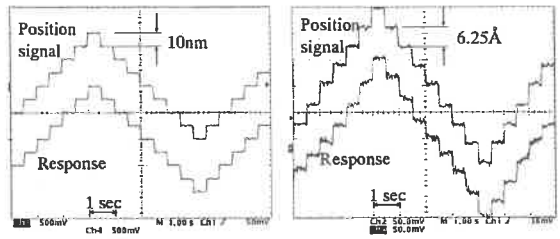

Fig. 8 Positioning resolution at 500kgf payload

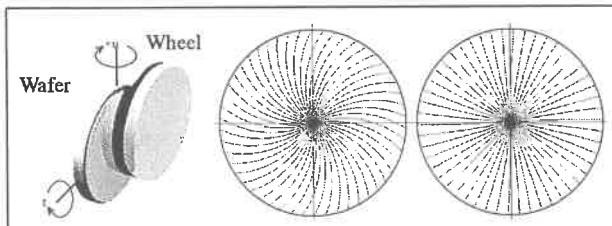

Infeed grinding method v/V=0.02, v/V=0.46

Fig.9 Grinding method and cutting path formed

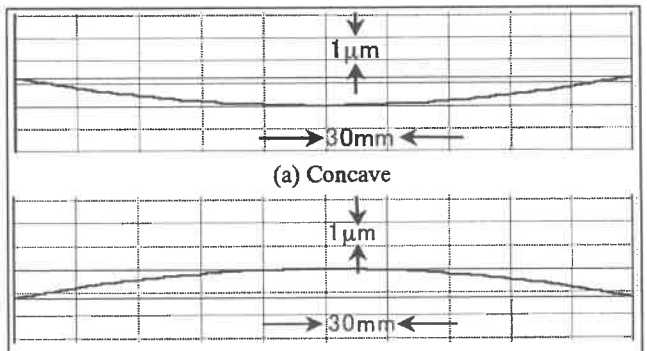

Fig.10 Alignment and profile control

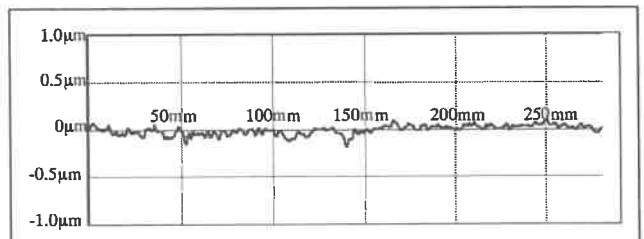

Fig. 11 Global flatness achieved

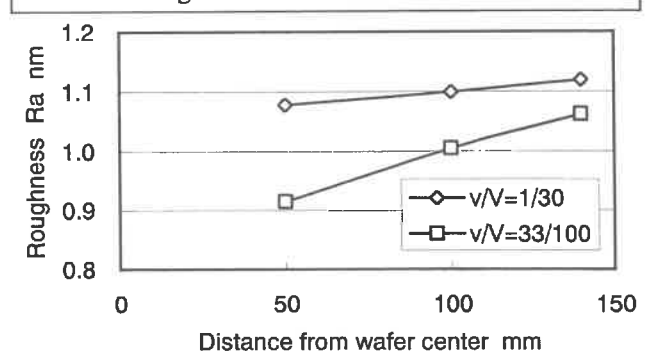

Fig.12 Cutting path density and roughness

excessive m takes a long time to reach the steady state, which often leads to the burn marks on the wafer surface. Fig.13 is the critical condition of burn mark, which is discovered by a series of experiment. The results spell out as long as the operational parameters meet the Eq.(2) that the burn mark is avoidable.

$$Z\left(\frac{V}{F}\right)^2 \le a \qquad (2)$$

where a is a constant dependent on the properties of the wheel and workpiece. In the current condition, a is about $4 \sim 5\times10^4$. In Eq.(2), F/V stands for the depth of cut per wheel revolution. A finer depth of cut normally leads to a better surface roughness, but risks more in burn mark.

In order to make a homogenous ground surface, the operational parameters need further to fulfill the condition in Eq.(3).

$$V\frac{Z}{F} = k\cdot m \quad (k: \text{a natural number}) \qquad (3)$$

Shown in Fig.14 are three typical patterns with $m = 300$ that the cutting path forms. When $0 \le k < 1$, grinding has yet reached to its steady state and there are some places where the cutting path is lacking. When $k = 1$, the wafer is most uniformly ground. When $k > 1$, there are some places having the cutting path multiplied. When k takes other natural number than 1, the cutting paths are homogenously distributed, but multiply cut by the same abrasives. This fact deepens the cutting marks and results in a rough surface. Fig. 15 shows the experimental results corresponding to the parameter settings in Fig.14, in which the best the roughness is achieved at $k = 1$.

The final finishing is done under a constant force controlled between 0.15~1.5kgf. The ground 3D profile is given in Fig.16 which show that roughness is below 1nm.

5. Conclusion

In this research, an advanced grinding machine with the capability of one-stop finishing for ϕ300mm Si wafer has been developed. The core technology is the GMM actuated positioner which is able to move half a ton of payload at the resolution of 5 Å. By optimizing the operational parameters, the first trail test has achieved the result of surface roughness Ra<1nm and global flatness less than 0.2μm over ϕ300mm.

Acknowledgement

This research was partially sponsored by the Regional Consortium from New Energy and Industrial Technology Development Organization, the Grand-in-Aid for Exploratory Research (No.10875029) and the Regional Joint Research (No. 11792007) from the Ministry of Education, Science and Culture of Japan.

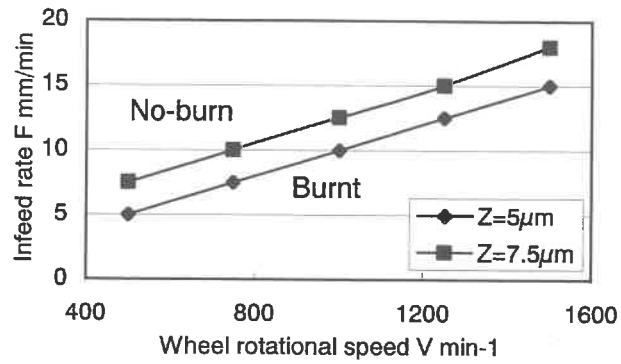

Fig.13 Critical condition of burn mark

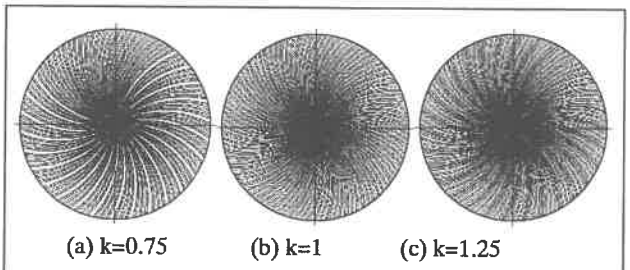

(a) k=0.75 (b) k=1 (c) k=1.25

Fig.14 Pattern formed by cutting path

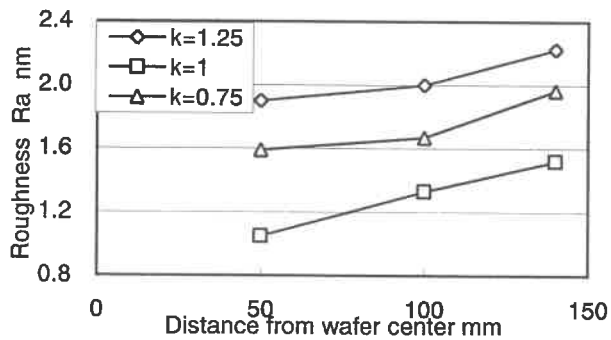

Fig.15 Effect of the cutting path distribution

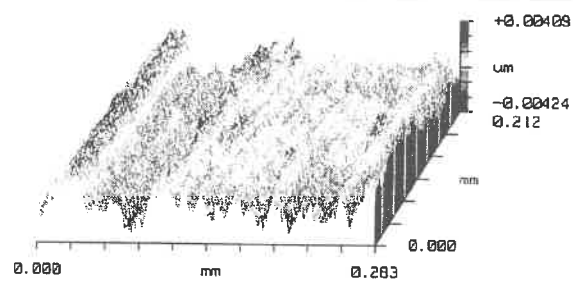

3D Ra=0.922nm 2D Ra=0.808nm

Fig. 16 Surface roughness achieved

Knowledge Management for Process Diagnostics and Improvement

Son H. Bui and Jay Raja
Center for Precision Metrology
University of North Carolina at Charlotte
Charlotte, NC 28223

1.0 Introduction

This paper describes the benefits and features of knowledge management for process diagnostics and improvement. Large corporations are in search of better ways to diagnose and improve manufacturing processes. They are examining techniques to manage their knowledge and share it with others in the organization in order to make better decision in process diagnostics. Currently, they create and maintain knowledge in isolated systems targeted at specific workgroups. Therefore, for users outside of the workgroup, that knowledge is virtually invisible and unreachable. They often spend time looking for it, recreate it, or do their job without it. In a global environment with significant outsourcing of parts manufacturing this leads to inefficiencies. The use of computers, coupled with the connectivity of computer systems makes computer based knowledge management a feasible solution to organize information. This addresses the broad process of locating, organizing, transferring, and more efficiently using the information and expertise within a company. With the help of Internet, knowledge management has the potential to provide engineers a tool for process diagnosis and improvement. This paper describes a prototype system for managing surface texture information for process and function related diagnostics.

2.0 Features

Definition of knowledge Management is the conceptualizing of an organization as an integrated knowledge system, and the management of the organization for effective use of that knowledge [1]. The knowledge management system offers a unique way to manage information and share it with everyone in an organization. This provides people better ways to diagnose and improve manufacturing process. This system is accessible through a web browser with an Internet connection.

The knowledge management system is designed using Microsoft Site Server and Microsoft SQL Server. These tools work in conjunction with existing Microsoft Internet Information Server and NT technologies, such as Active Server Page. Microsoft Site Server is a powerful intranet server, optimized for Microsoft Windows NT Server with Internet Information Server, for publishing and finding information easier and faster [2]. It can help organizations streamline the information-sharing process by providing content authors with a structured submission, posting, and approval process. Users can easily find and use information for process diagnostics and improvement.

2.1 Content Management

The system provides the user better ways to management content and deploy it to others. It allows a content provider to submit, tag, and edit content using Web Interface. Site editor can then approve, edit, and enforce uniform guideline for content [2]. After a site editor approves a submitted content, this content is deployed to destination Web servers securely and is grouped and indexed into catalog used for searching.

Figure 1 shows how the content provider submits a roughness parameter paper. The user drags a file in a folder and then attaches attributes related to surface parameter, such as parameter type, title and abstract. This content is then transferred to a content editor for approving before adding to catalog used in the search engine or published as shown in figure 2.

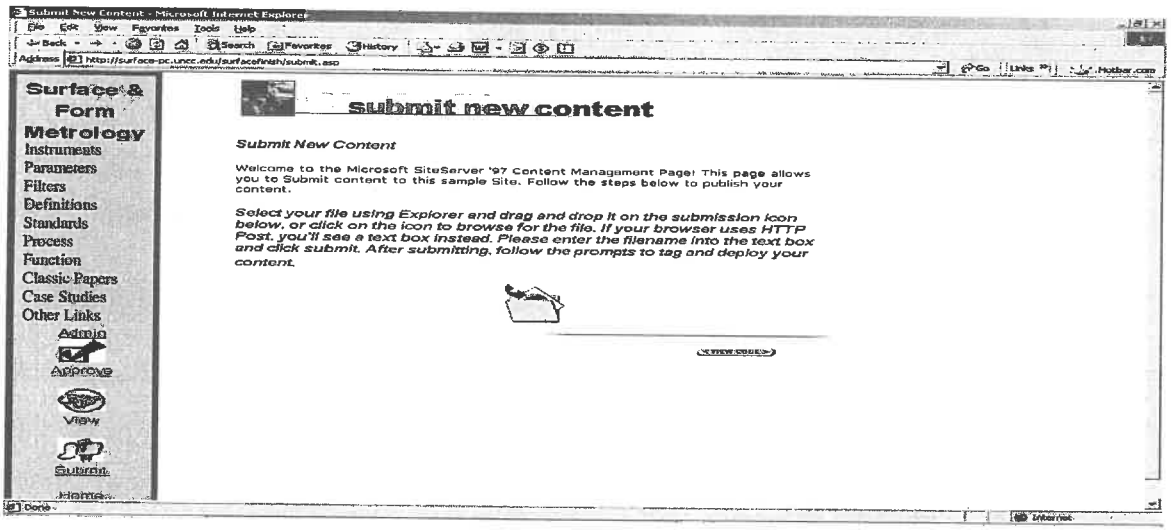

Figure 1. Roughness parameter is submitted to a content editor

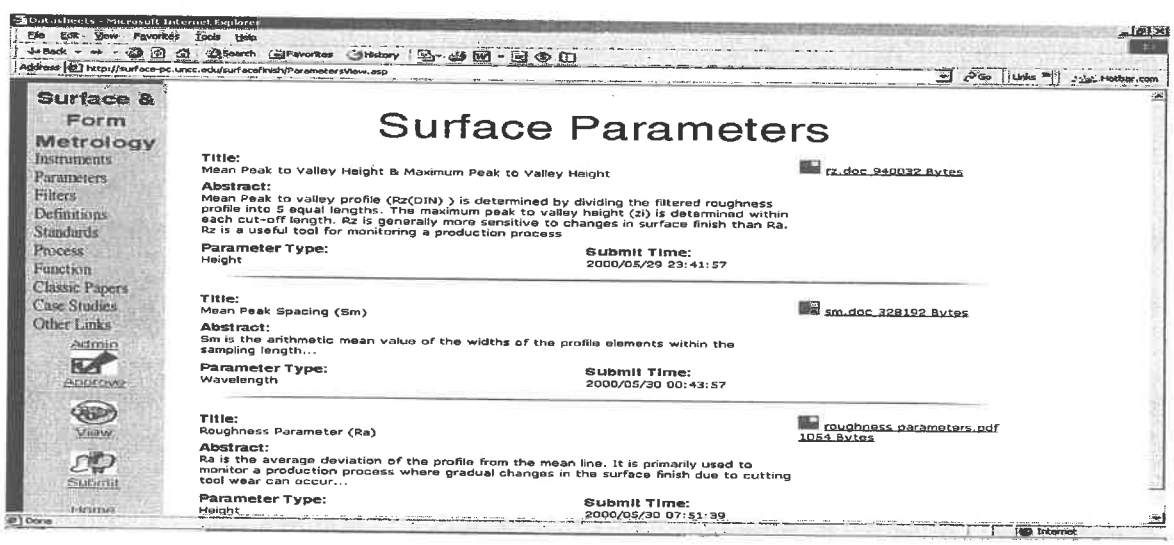

Figure 2. Information of surface parameter after it is approved

2.2 Knowledge Manager

Knowledge Manager provided in the system uses the rich information created by content management or the existing service making it useful to other. Users can easily browse, search, share, and subscribe to relevant information with a centralized Web-based application. Knowledge Manager is considered as information portals, which are shown in figure 3 [2]. Instead of looking for information based on a general search, the user can move toward categorized and personalized information. People in an organization can decide what information is available through the portal and can obtain information passively or actively. With tagged content, the user can quickly search information based on specific category, such as parameters, case studies, and instruments. The information can be periodically scanned and sent to the user based on their interests. The user can have information emailed or pushed to them instead of going to the portal.

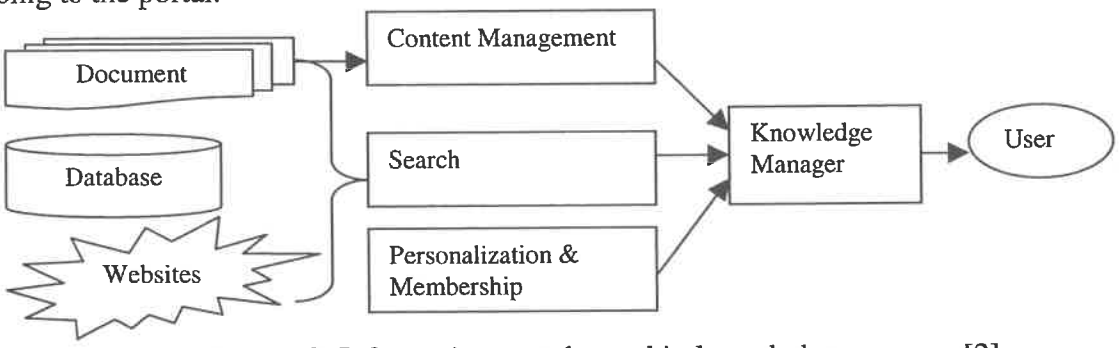

Figure 3. Information portals used in knowledge manager [2]

Figure 4 shows a search center provided in the Knowledge Manager. The keyword "roughness" is searched in Parameters category; the result gives the user Mean Peak to Valley height including its abstract, and URL that links to the paper of this parameter.

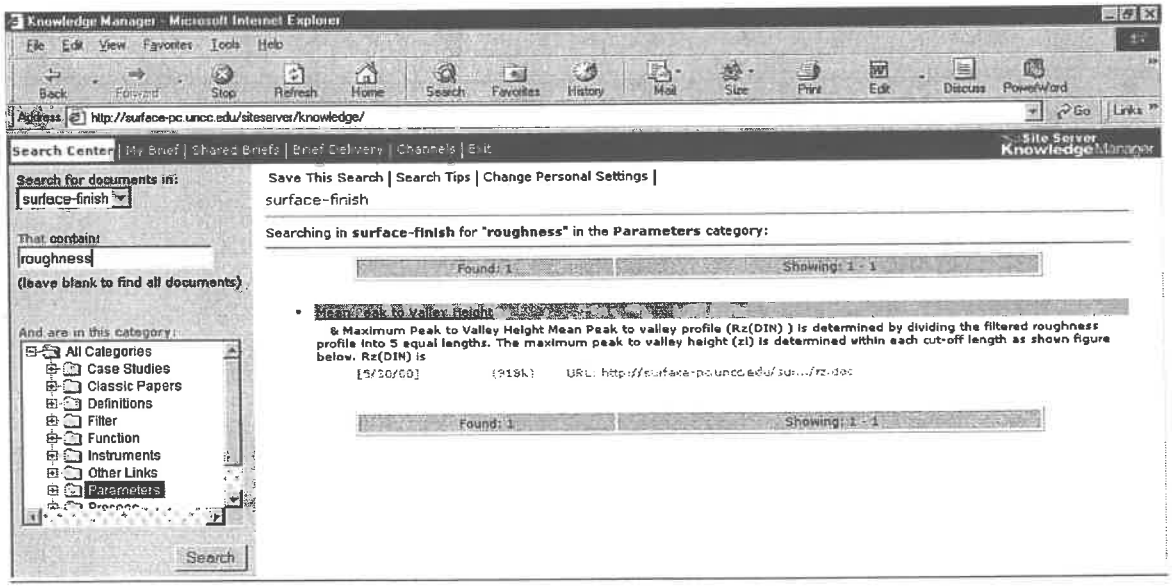

Figure 4. Search center in knowledge manager

2.3 Personalization

Personalization provided in the system makes a complex site easy to use by providing solutions that use strategies to address individual needs and promote individual success [3]. Engineers can customize for example a "My Metrology" page by retrieving information based on their interests from information portal, such as standards, filters, or some information related to surface and form metrology. This gives engineers more knowledge on specific manufacturing process that they want to learn. This helps them to diagnose problems in a process quickly.

3. Conclusion

The current prototype system covers surface metrology and it will be expanded to include form, process, and function related information. Knowledge management tools offer a more efficient way to manage information and deploy it to others in an organization. It is very helpful in process diagnostics and improvement. The benefits of this system are:

- Awareness: everyone in a company knows where to look for knowledge to diagnose and improve a manufacturing process. This saves engineers time and effort.
- Accessibility: all individuals can use the combined knowledge and experience in the context of their own roles
- Availability: with the help of Internet, knowledge can be used wherever it is need and whether from a plant, office, home, on the road, or at the vendor's site.

4. Preferences

1. Nick Apostolopoulos, Joey Bernal, Steve Edens, Robert Howard, Stephen Howard, Mike Kendzierski, Steven Livingstone, Craig McQueen, Marco Tabini, Alex Toussaint, Peter Watt, " Professional Siteserver 3.0", Wrox Press Ltd., Birmingham, United Kingdom.
2. Southon, Gray. "Introduction to Knowledge Management." 11 May 2000. < http://www.uts.edu.au/fac/hss/Departments/DIS/km/introduct.htm> (July 11 2000).
3. Martinez,Margaret . "Personalizing E-Learning." < http://www.trainingplace.com/source/research/masspersonalization.htm >(June 2000).

MASKLESS LASER PATTERNING OF METAL LINES FROM METAL POWDERS

Hirofumi Hidai, Hitoshi Tokura

Department of Mechanical Sciences and Engineering, Tokyo Institute of Technology, 2-12-1 O-okayama, Meguro, Tokyo, 152-8552 JAPAN, hidai@ctrl.titech.ac.jp, htokura@ctrl.titech.ac.jp

ABSTRACT

In this paper, a new, simple, high-speed method of selective metal deposition on glass substrates is proposed. The method is as follows: metal powder is placed on a glass substrate, then an argon ion laser is irradiated through the glass from the other side. Soda glass, Pyrex glass and silica glass were used as substrates, aluminum and copper powders, with grain sizes of 7.0μm and 4.6μm, respectively, were chosen. The beam of an argon ion laser (Coherent, DBW20) was used at 488nm wavelength, because the glasses have high transparency of visible light. Both aluminum and copper can be deposited on all the glasses. Aluminum deposited on the soda glass were 80μm - 800μm in width and 10μm - 120μm in height. The deposited aluminum and copper had high conductivity and resistances of 0.017Ω/mm - 0.64Ω/mm and 0.0014Ω/mm - 0.2Ω/mm, respectively.

INTRODUCTION

There is a growing need for the deposition of metal films on insulators that are used in devices such as SOIs (silicon on insulators), and TFT-LCDs (thin film transistor liquid crystal displays). These applications have three important requirements: high speed, fine quality and low cost.

In particular, the use of focused lasers for direct writing or maskless patterned depositions have been extensively described in the literatures, for instance: LCVD (laser-induced chemical vapor deposition) [1], LIFT (laser-assisted forward transfer)[2], laser-assisted deposition from organo-metallic solutions[3], laser enhanced electro- [4] or electroless [5] plating, and photothermal decomposition of metal-doped polymer films[6].

In this paper, a new, simple, high-speed method of selective metal deposition on glass substrates is proposed, in which metal powders placed on a glass substrate are irradiated by a laser through the glass from the other side.

The thickness and width of the deposited metal were observed as functions of scanning speed and laser power. The conductivity of deposited metal was estimated.

EXPERIMENTAL

Soda glass, Pyrex glass and silica glass were used as substrates, because they are popular materials and their thermal properties were varied as shown in Table 1. Aluminum and copper powders, with grain sizes of 7.0μm and 4.6μm, respectively, were chosen.

In the experiments, the beam of an argon ion laser (Coherent, DBW20) was used at 488nm wavelength, because the glasses have high transparency of visible light. The laser beam was focused by a convex lens, with a focal length of 170mm, down to a spot size of about 120μm. Glass substrates

Table 1 Properties of glass substrates

	Softening point ℃	Thermal expansion coefficient* $\times 10^{-7}K^{-1}$	Transmission rate %
Soda glass	735	99	Approximately 90
Pyrex glass	820	32	90-95
Silica glass	1600	5.5	90-95

* at 5 – 300 ℃

and metal powder were placed on an electronically controlled X-Y-Z stage, as shown in fig. 1.

Table 2 shows experimental conditions. The thickness of the metal powder layer was approximately 2mm and the power was compressed with a roller.

After irradiation, excessive or loosely adhered powder was brushed off, then the substrate was cleaned by ultrasonication.

RESULTS AND DISCUSSION

Laser irradiation of the glasses

The laser beam was focused on glass substrates, hence the glass substrates could be damaged, even when metal powder was not placed on the glass substrates. The laser beam (laser power: 7W maximum, exposure time: 60s, no scanning) was irradiated on each glass without metal powder. As a result, we found that there were no changes, except for the soda glass which became slightly warmer. Therefore, absorption of the glasses is considered to be negligible in this paper.

Irradiation of the metal powder on the glass

Glass substrates, metal powders, laser power and scanning speed were varied in deposition experiments. Both aluminum and copper were deposited on all the glasses under certain irradiation conditions. Fig. 2 shows scanning electron micrographs of the deposited metal lines at a laser power of 7W and scanning speed of 1mm/s.

These micrographs show that metal powders are deposited well. Fig.2 (a) shows aluminum deposited on soda glass. Each individual powder grain remains and cracks are observed on the glass due to rapid heating by laser irradiation and cooling. Aluminum deposited on Pyrex glass did not differ from that on soda glass. On the other hand, aluminum powder on silica glass was different from the others. In some parts of the deposited aluminum, grain shape could not be recognized. There were no cracks on the glass because silica glass has good

Table 2 Experimental conditions

Laser	Ar ion laser
Wavelength	488nm
Power	0 - 7.0 W
Beam mode	TEM_{00}
Scanning speed of moving stage	0.1 - 5.0mm/s
Substrate	Soda, Pyrex, silica glass
Thickness of substrate	2mm
Metal Powder (grain size)	Al (7μm), Cu (4.6μm)
Powder layer thickness	2mm

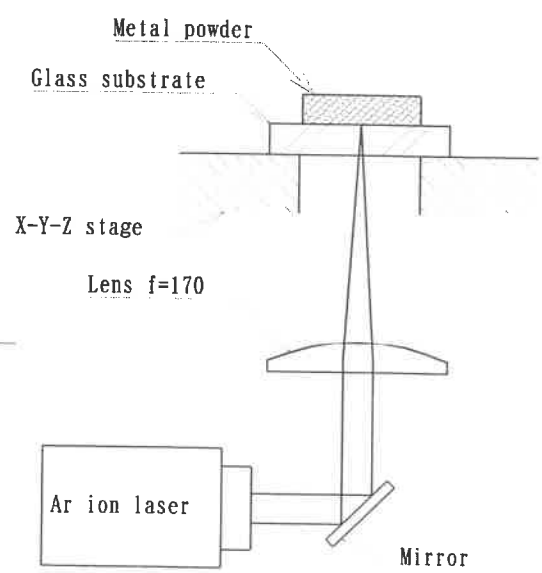

Fig.1. Illustration of the experimental setup

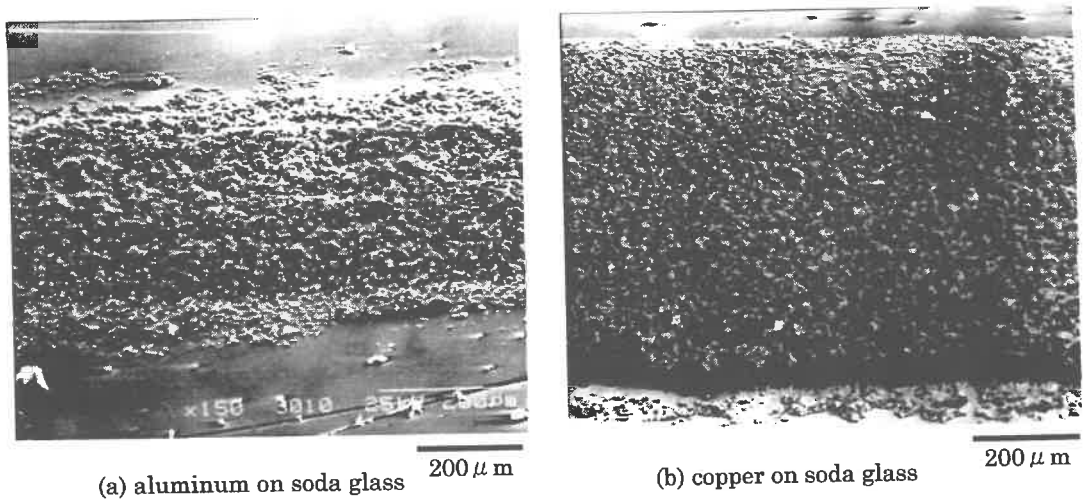

(a) aluminum on soda glass (b) copper on soda glass

Fig. 2. SEM micrographs of the deposited metals on glasses: laser power 7W,scanning speed 1.0mm/s.

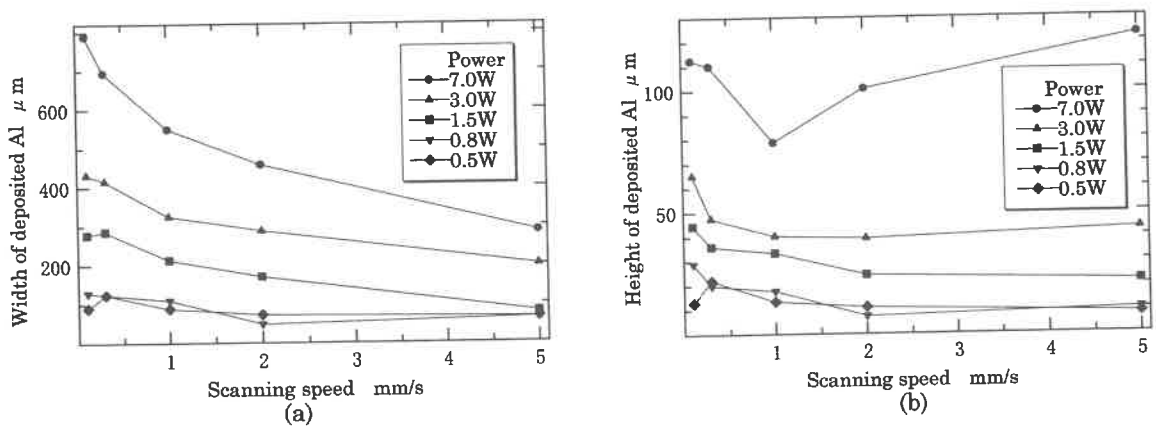

Fig. 3. Scanning speed dependence of the thickness and width of the deposited line

thermal protection. Copper deposited on soda glass is shown in fig.2 (b). Detachment is recognized at the interface of the glass substrate and the deposited copper.

Influence of the laser power and scanning speed was investigated in each glass and powder. Metal powder deposited on glasses better with increasing laser power and decreasing scanning speed. Aluminum was conductive on any glass. Copper was also deposited on all three types of glass, but adhesion strength on silica glass was poor, so the deposited copper was easily detached during brushing or washing in an ultrasonic bath. Copper deposited on soda glass and Pyrex glass was conductive, but on silica glass it was not conductive under any condition. Both metals adhered strongest to the soda glass and poorest to the silica glass. This result was due to a difference in the softening point.

Width and height of the deposited aluminum on the soda glass were measured using an optical microscope, and results are shown in fig.3. As scanning speed became slower and laser power became larger, both width and height became larger. However, width was not smaller than 80μm because the diameter of the laser spot was approximately 120μm.

Resistance values of the deposited metal were measured by the double bridge method. They

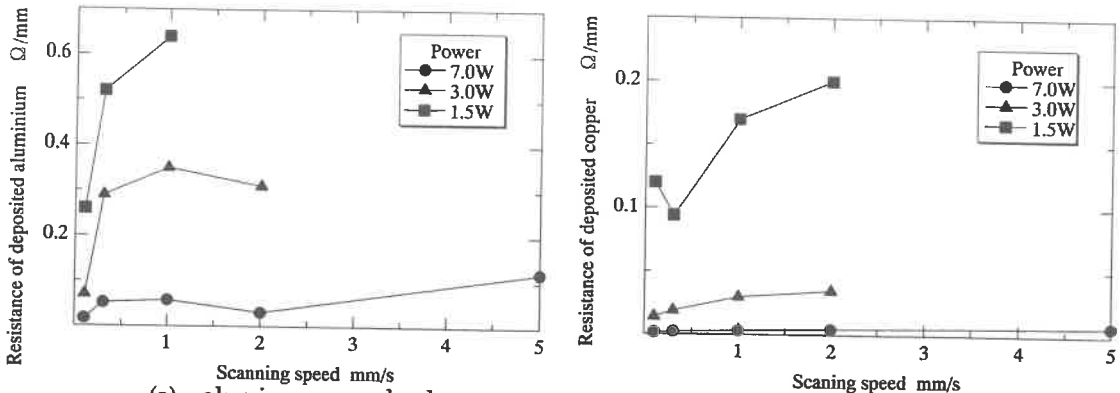

(a) aluminum on soda glass (b) copper on soda glass

Fig. 4. Resistance of metal lines as a function of scanning speed and laser power

could be divided into good conductor (<1 Ω/mm) and poor conductor(>1M Ω/mm). When the deposited metals were poor conductors, there were gaps in the deposited metals. For the deposited aluminum and copper having good conductivity, resistance values are shown in fig. 4. That of aluminum was 0.017Ω/mm - 0.64Ω/mm, and that of copper was 0.0014Ω/mm - 0.2Ω/mm. In both cases, resistance values decreased with increasing laser power and decreasing scanning speed.

CONCLUSIONS

A novel method of metal deposition on glass substrates is proposed. The method is as follows: metal powder is placed on a glass substrate, then an argon ion laser is irradiated through the glass from the other side. Aluminum and copper can be deposited on soda, Pyrex and silica glass. The deposited aluminum and copper had high conductivity and resistances of 0.017Ω/mm - 0.64Ω/mm and 0.0014Ω/mm - 0.2Ω/mm, respectively.

REFERENCE

1. G. E. Blonder, G. S. Higashi and C. G. Fleming: Laser Projection Patterned Aluminum Metallization for Integrated Circuit Applications, Appl. Phys. Lett., 50, 12 (1987) 766.
2. E. Pogarassy, C. Fuchs, F. Kerherve, G. Hauchecorne and J. Perriere: Laser-induced forward transfer: A new approach for the deposition of high T_c superconducting thin film, J Mater. Res., 4, 5 (1989) 1082.
3. Gupta and R. Jagannathan: Laser writing of copper lines from metalorganic films, Appl. Phys. Lett., 51, 26 (1987) 2254.
4. R. J. von Gutfeld, E. E. Tynan, R. L. Melcher and S. E. Blum: Laser enhanced electroplating and maskless pattern generarion, Appl. Phys. Lett., 35, 9 (1079) 651.
5. K. G. Mishra and r. K. Paramguru: Kinetics and mechanism of electroless deposition of copper, J. Electrochem. Soc., 143, 2 (1996) 510.
6. M. E. Gross, G. J. Fisanik, P. K. Gallagher, K. J. Schnoes and M. D. Fennell: Laser-initiated deposition reactions: Microchemistry in organogold polymer films, Appl. Phys. Lett. 47, 9 (1985) 923.

Novel Grinding Tools for Machining Precision Micro Parts of Hard and Brittle Materials.

Hans-Werner Hoffmeister, Andreas Wenda
Institute of Machine Tools and Production Technology
Technical University of Braunschweig, Germany

Summary

The production of miniaturized diamond grinding tools like abrasive pencils, profiled grinding blades and core drills, as well as, their optimal application is a field of research at the Institute of Machine Tools and Production Technology at the University of Braunschweig, Germany [1, 2].
Conventional micro grinding tools have limits in diameter, shape or diamond grit size. Our challenge was to exceed these limits.

State of the art in micro grinding

Micro grinding allows the production of microstructures or micro components in hard and brittle materials. Normally the products have demands on accuracy of 1-5 µm, and on the surfaces a roughness of 0.2 µm for $R_{z,DIN}$ or better. Conventional miniaturized tools for micro grinding are as follows: dicing blades with a minimum thickness of 15 µm and a standard diameter of 56 mm, abrasive pencils with a minimum diameter of approx. 200 µm, and core drills with a minimum diameter of approx. 900 µm (figure 1). In order to grind ceramics, glass or sintered carbide, diamond grains in different bonding systems (galvanic or sintered bonds), and different sizes are used. Further on, novel grinding tools with a CVD-Diamond coating as abrasive layer with a "diamond grain size" of approx. 1 to 12 µm were investigated (figure 1).

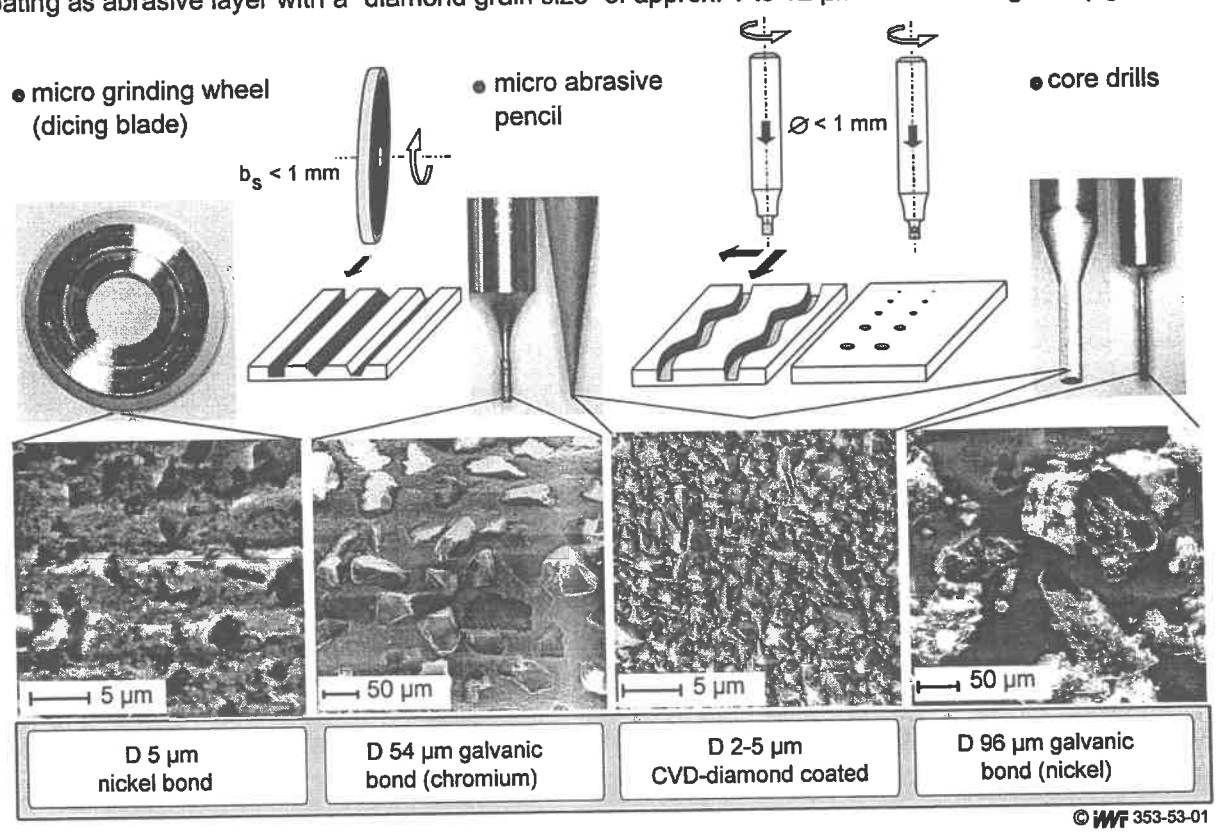

figure 1: Conventional and novel miniature grinding tools

While there are no limits in the choice of the diamond grain size for dicing blades, the minimum grain size for conventional miniaturized abrasive pencils and core drills is approx. 30 µm. The typical problems of the machined components are chipping at the edges and insufficient surface roughness caused by the large diamond grains.
In experiments, we tested the commercially available micro grinding tools to investigate their scope. The materials ground were silicon, glass, ceramic and sintered carbide. Varying the machining parameters (cutting speed, infeed, depth of cut), we measured the process forces, and the surface quality of the ground surface. We found that the available grinding blades met the requirements for micro grinding hard and brittle materials. However, grinding a specific profiled groove was still impossible. For the improvement of grinding blades with a thickness smaller than 150 µm, an ultra precision experimental set-up was built for profiling these grinding wheels. With the experimental set-up for profiling, we could manufacture a V-profile for a wheel thickness of 75 µm. The set-up allows us to define the angle between 0° and 180°.

Comparison of commercially available and novel CVD-Diamond micro abrasive pencils

We manufactured and used CVD diamond coated sintered carbide bodies as abrasive pencils and core drills. The advantages of these micro-grinding tools are the free shape of the sintered carbide bodies, and the small grain size of the diamonds in the CVD-Diamond layer. The CVD-Diamond coating was manufactured by the Fraunhofer-Institut für Schicht- und Oberflächentechnik in Braunschweig, Germany. Conventional miniature abrasive pencils broke easily grinding ceramic, sintered carbide or glass due to their insufficient stiffness, even for a minimal depth of cut and a rotational speed of 175,000 revs/min. For these materials CVD-Diamond coated abrasive pencils had a much better performance. However, for the machining of silicon, conventional micro abrasive pencils showed long tool-paths. With CVD-Diamond coated tools, however, we achieved the better surface roughness (figure 2) and smaller edge chipping.

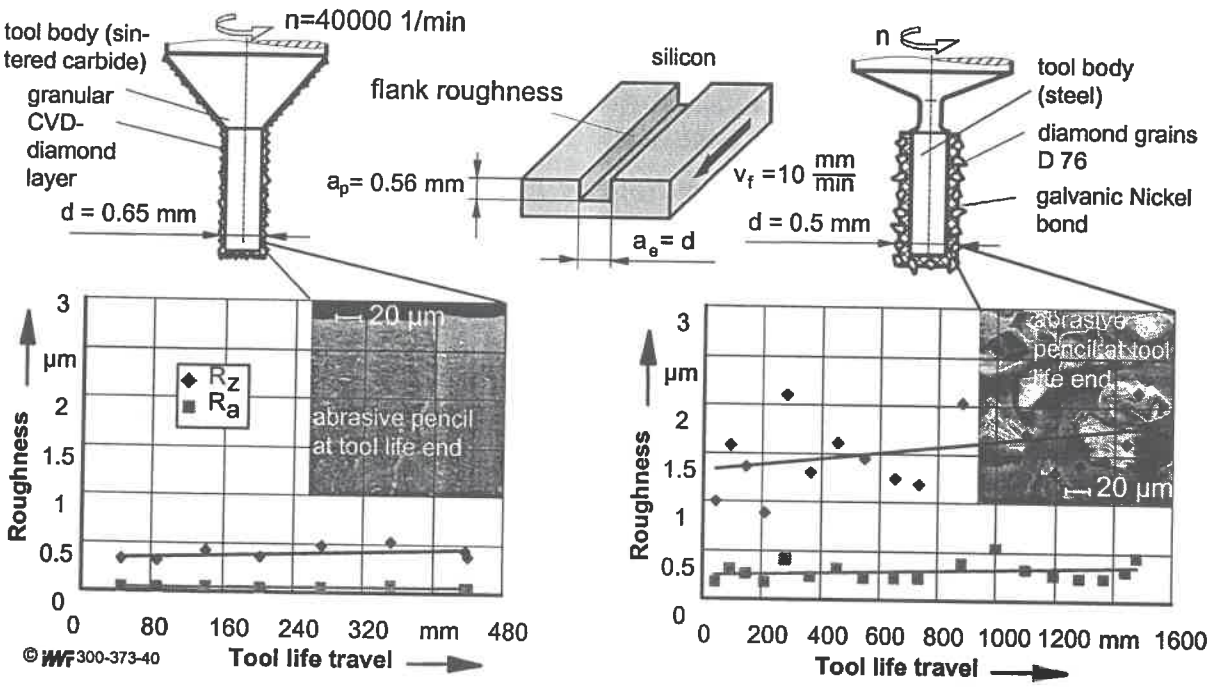

figure 2: Comparison of conventional and CVD-Diamond coated micro abrasive pencils

Several abrasive pencils like cylindrical or cone shaped (also stepped or shouldered) with a diameter of 40 µm to 1 mm were manufactured and tested to determine the required process conditions for their application.
Some general assertions can be made concerning the established variation in parameter size in grinding with CVD- Diamond coated micro abrasive pencils. The cutting speed must be set as high as possible based upon the limits of the spindle system used. A cutting speed above 2.5 meters per second, for example using a work tool with a diameter of 0.35 mm and a spindle rotation speed of 130,000 rotations

per minute, allows the grinding of silicon, glass, and sintered carbide to be relatively problem free. Furthermore, the run out of the work tool should be smaller than 10 µm; however, the permissible tolerance of the commercial work tool manufacturer is still in the higher range of this tolerance. In addition, the forward feed is dependent upon the characteristics of the work piece, the grinding requirements and the feed motion, and thereby, it should orientated by a process force measurement. Due to this, one must take into account the mechanical stability of the sintered carbide main bodies, as well as, the radial stiffness of the air-bearing spindle used. Furthermore, through the stress a flexible deformation occurs on the work piece. The typical process force was in the range of a few Newton. In addition, in order to achieve a functioning grinding process, one must guarantee the removal of the micro chips produced by the grinding process out of the working zone, and the removal of the small chips clinging to the diamond coating, through an intensive flushing for example with a cooling lubricant.
We established that work tool fracture was the most frequent cause of failure for micro shaft cutting tools. To get an idea of the permissible threshold for the process force for the micro abrasive pencils we performed many analytic calculations with the purpose of geometrical optimization. The theoretical values were compared with experimental results. The calculations were run through using the Hänchen-Decker method, and a sintered carbide work piece of K15. The permissible stress was calculated for the most various geometries. The result of this calculation was the curve pictured "theoretical threshold of force" in the graph in figure 3. Under this analytically calculated curve, cylindrical micro shaft work tools are theoretically continuously stabile. The labeled points in the diagram were experimentally determined fracture forces and process forces for non-destroyed work tools, which occurred through the cutting experiments with the varying work tool diameters. Work tool fractures, which occurred after a determined tool life (a minimum time of five minutes), were classified as fatigue fractures. All work tools which lie below the theoretical curve did not fracture. This means that the theoretical curve reproduces very well in reality.

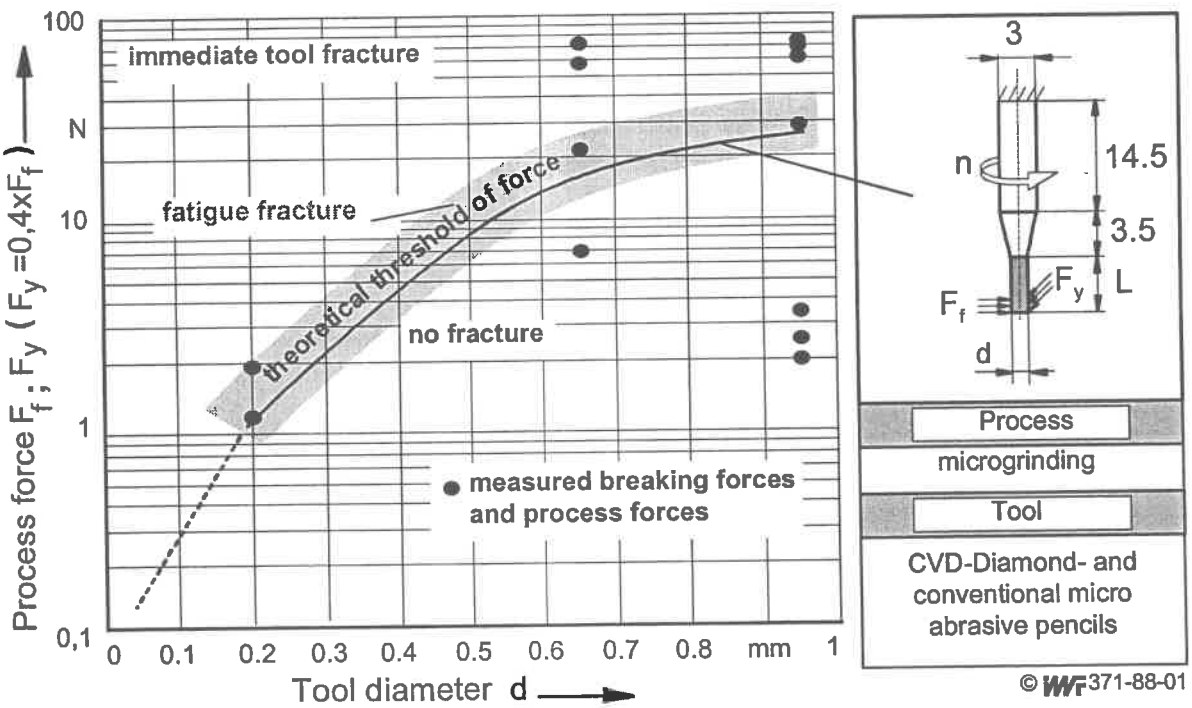

figure 3: Threshold for the process forces for micro abrasive pencils

In preparation of a grinding process, the parameter infeed and cutting depth, as well as, the cutting width must adapt to the permissible threshold for the process force. For example, the radial process forces during micro grinding with an abrasive pencil of 0.2 mm diameter are not to exceed the value of approximately 1 N. The results of this are very high requirements for the run out accuracy and dynamic stiffness of the machining systems. Finally, the tool shaft geometry was optimized by these analytic calculations to reduce stress fractures.

Application examples

Application fields of miniature grinding tools are production of moulding or extrusion tools, precision components like nozzles, microstructured surfaces and special products of precision engineering (MEMS). Figure 4 shows some possible microstructures ground in different materials.

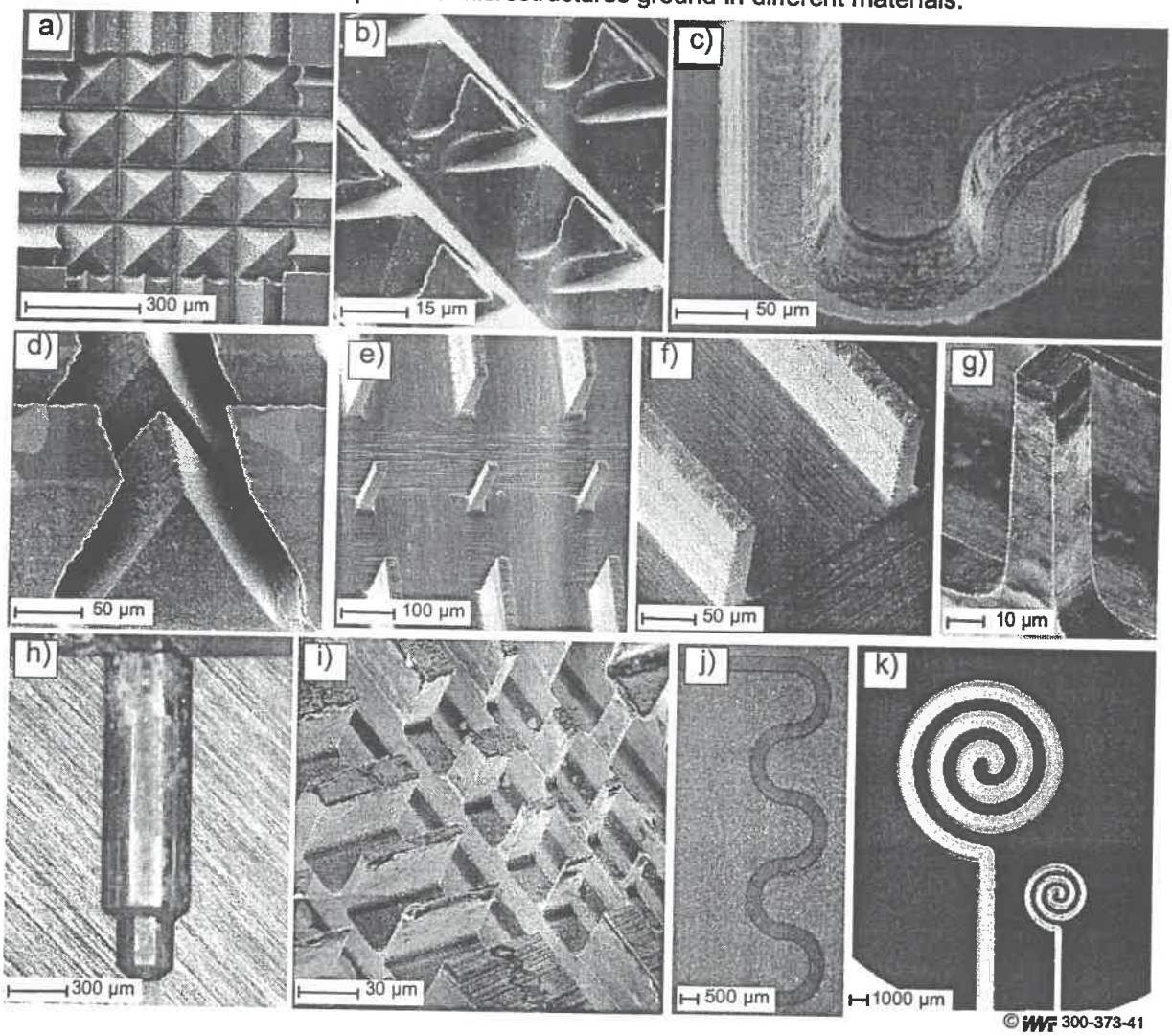

figure 4: Ground microstructures in silicon (a, b, c, k), glass (d), zirconium oxide (e, f), aluminium oxide (j), sintered carbide (g, h, i)

Outlook

Further miniaturization and optimization of the grinding process is planned. The automatisation of the machine tool for the tool shaping operations and the optimization of micro machining technology is the research for the future.

References

1 HOFFMEISTER, H.-W. ; WENDA, A.: *3D micromachining of single crystal silicon*. In: EUSPEN (proceedings of the 1st international conference and general meeting of the European society for precision engineering and nanotechnology), Bremen, Mai 31. - June 4. 1999, pp. 396-400

2 GÄBLER, J. ; SCHÄFER, L. , WENDA, A. ; HOFFMEISTER, H.-W.: *Developement and application of CVD diamond micro tools for milling and grinding*. In: EUSPEN (proceedings of the 1st international conference and general meeting of the European society for precision engineering and nanotechnology), Bremen, Mai 31. - June 4. 1999, pp. 434-438

A Novel Polymer Processing Assisted by Infrared Radiation to Attain a High Precision Transcription

Yasuo Kurosaki and Kimitoshi Sato
Department of Mechanical Engineering and Intelligent Systems
University of Electro-Commnications
Chofu, Tokyo 182-8585, Japan

1. Introduction

Some unfavorable phenomena often appear in plastics processed by polymer injection molding : shape deformation, residual stress, birefringence, and ill transcription. The ill transcription is one of the most fatal defects for precision components such as memory disks, camera lenses, electronic devices and parts of MEMS. It is therefore very important for polymer mold fabrication to obtain the high quality transcription of surface in plastics[1,2].

An innovative injection molding process was developed to improve transcription from a heat transfer point of view[3,4]. The process is able to improve both the optical quality and the transcribability of plastic components by applying infrared radiation through the window provided on the mold wall on the moving polymer melt injected in the mold cavity. In this paper, another novel processing having two stages such as a molding and a transcribing process is proposed to improve transcribability. The concept of this method is shown in Fig.1. In the first stage of the process, blank workpieces are processed by a conventional injection molding process. Then, in the second stage a blank workpiece is inserted into another precise mold with the wall transparent to infrared radiation having the primary surface to be transcribed, and is radiated by an external infrared radiation source. One of advantages is that the pressure in the second stage is quite low to compare with the first one. The window for infrared radiation is therefore enough to bear the pressure in the process. Further, the mold is quite simple, and the cost of this molding process is lower than the case of the moving polymer irradiated. Besides, the process cycle time is quite short.

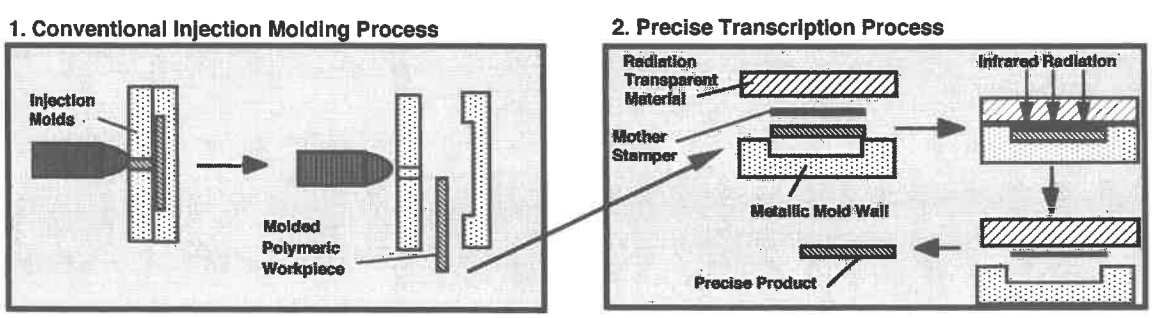

Fig.1 Schematic of the two-stage transcription process assited by infrared radiation

2. Experimental Setup

A two-stage transcription process system proposed here has two independent facilities. In the first stage, an injection molding system is used to process blank workpieces by conventional procedure; the workpieces in this stage not always require a high degree of accuracy. In the second stage, a special mold having a cavity with a window transparent to infrared radiation is prepared as shown in Fig.2. A workpiece molded in the first stage is inserted into the cavity, and is covered with an infrared-transparent glass plate (ZnSe); then, an infrared radiation of CO_2 laser is applied to the inserted one for certain duration about a few tens seconds. Since the temperature of the thin layer of resin near surface rises due to absorption of radiation, the fluidity of polymer in the thin layer consequently increases, and also the pressure in the cavity increases due to a volume expansion. The information "roughness" on the surface of the infrared-transparent glass contacted with the resin is able to be efficiently transcribed to the surface of workpiece.

In our experiment, a polystyrene disk, 25 mm in a diameter and 2 mm in thickness, was conventionally processed in the first stage. In the second stage, two kinds of precise mold were adopted; the details of those molds were shown in Fig.3. The first one shown in Fig.3 (a) has a ZnSe mold wall on the surface of which a few precise fine grooves were formed to evaluate the tanscribability. The details of the grooves are shown in Fig. 4. When this mold is used, the infrared radiation through the window directly radiates the surface of an inserted disk, and heats up the thin layer of resin. The second one shown in Fig.3 (b) has a thin metallic stamper plate pasted on the surface of ZnSe; in this experiment, a part of a mother stamper of CD disk, 0.3 mm in thickness, was used as a mother surface for transcription. The surface of the stamper faced

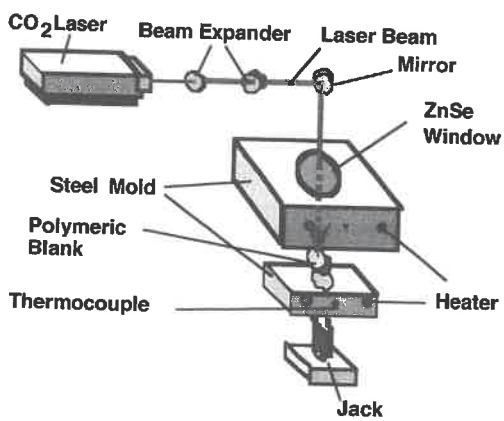

Fig.2 Experimental setup for the precise transcription process

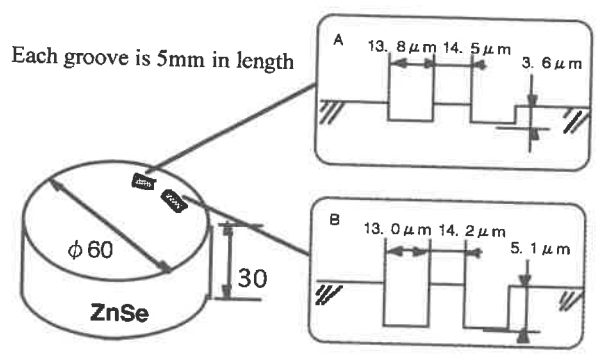

Fig.4 Geometry of grooves engraved on a ZnSe mold wall surface

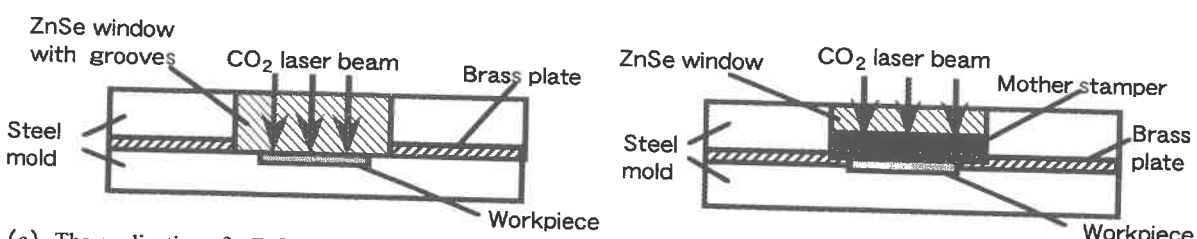

(a) The application of a ZnSe window having the grooves

(b) The application of a mother stamper

Fig.3 Details of precise mold system used in the secound-stage

to a radiation source was pained black to improve absorption of radiation. When the second mold is employed, the metallic stamper is heated by radiation, and then, the resin of polystyrene is heated by heat conduction from the heated stamper. A little longer time is, therefore, necessary for the latter to achieve a sufficient transcription.

3. Improvement of Transcribability in a Two-Stage Molding Process

First, experiment was conducted with the mold with no metallic stamper shown in fig.3 (a) to examine the feasibility of the proposed transcription molding process assisted by infrared irradiation. The effectiveness of replication of the grooves on the surface of ZnSe mold wall was defined as the ratio of height of protrusion on the workpiece to the depth of groove. Figure 5 shows the effect of the duration of irradiation on replication. It is seen that preferable transcription was achieved by direct irradiation for an appropriate duration despite of the depth of grooves.

Second, in the case using a mother metallic stamper, the depth of a sub-micron pit on the surface is measured by an atomic force microscope (AFM). The AFM photographs for both the surfaces of a mother stamper and a transcribed polymer processed with irradiation are shown in Figs. 6(a) and 6(b), respectively. Further, the influence of mold wall temperature measured by thermocouples mounted on the surface of a

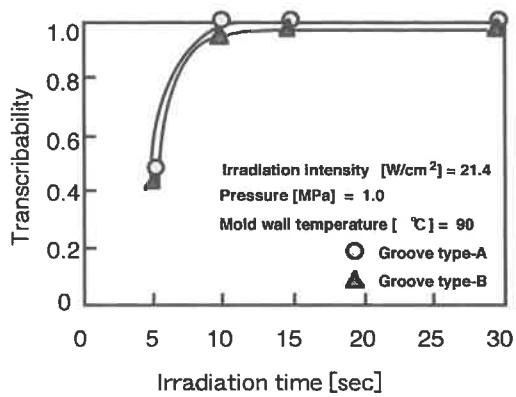

Fig.5 Influence of radiation on transcribability for the grooves on ZnSe mold surface

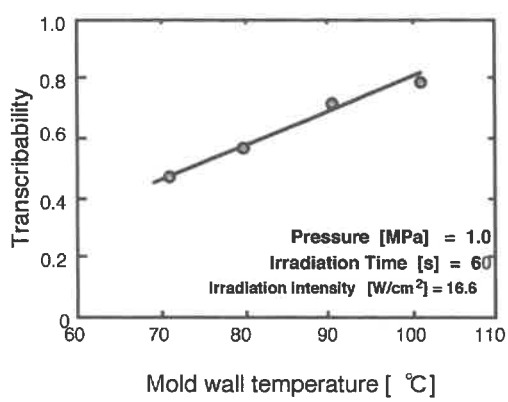

Fig.7 Influence of mold wall temperature on transcribability using the mother stamper

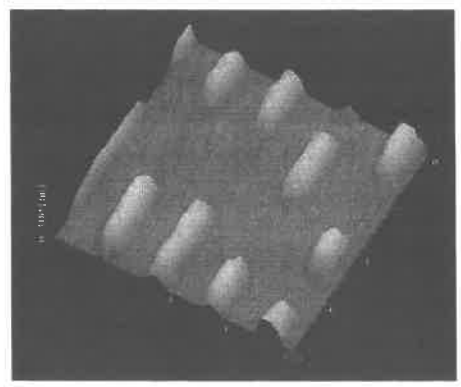

(a) Surface of a mother stamper

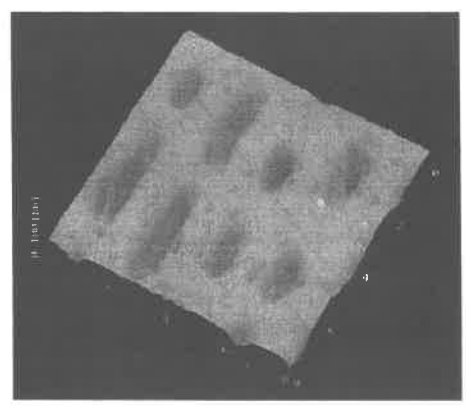

(b) Surface of a replicated workpiece

Fig.6 AFM imagesof stamper and workpiece

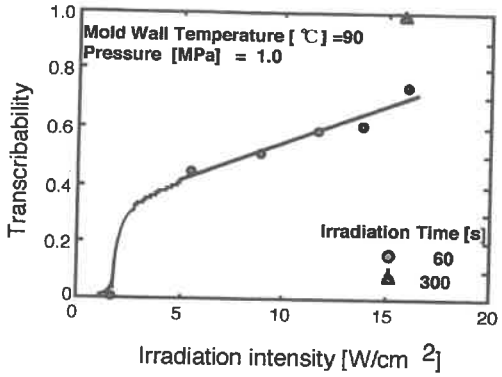

Fig.8 Influence of irradiation intensity on transcribability in the secondary transcription process

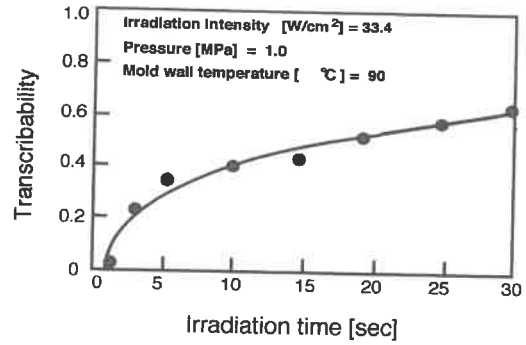

Fig.9 Influence of irradiation time on transcribability in the secondary transcription process

stamper on the transcription is shown in Fig. 7. From this figure, satisfactory feasibility is not obtained without irradiation in case of the mold wall temperature lower than a glass transition one of polymer. Figure 8 shows the influence of irradiation intensity on the transcription. Application of high radiation intensity results in favorable transcription in this process. The effect of time duration of irradiation on transcription in case of a CD stamper adopted is shown in Fig. 9. The temperature of resin surface contacted with a metallic stamper is raised promptly after radiation is supplied on the other surface of stamper; therefore, the sub-micron transcription is able to be completed in a few tens second processing.

4. Conclusion

The feasibility of this proposed procedure was experimentally examined using the system with a CO_2 laser beam as a radiation source and the ZnSe window transparent the beam. The transcription of a micro-scale information on the mold surface to the one of molded plastics was greatly improved by direct irradiation onto the polymer. Further, the sub-micron scale transcription such as pits of compact disks was experimentally confirmed by the two-stage transcription process. The proposed system has a feature: a conventional injection molding process is able to be employed in the first stage, and a molding system in the second stage is not necessary to bear high pressure and to be sophisticated. This system is feasible for processing high quality components such as optical or electrical devices, micro-scale devices and MEMS components.

References

1. M. J. Liou, N. P. Suh, "Reducing Residual Stresses in Molded Parts" Polymer Engineering and Science, Vol. 29, No. 7, (1989).
2. E. Brinksmeier, W. Preuss, "Basics of Precision Replication Techniques" Proceeding of the ASPE Spring Topical Meeting on Precision fabrication and Replication, Vol.19, pp.23-28 (1999).
3. Y. Kurosaki, I. Satoh, "A Precision Polymer Injection Molding Process Assisted by Infrared Radiation to Upgrade both Optical Quality and Transcribability" Proceeding of the ASPE Spring Topical Meeting on Precision fabrication and Replication, Vol.19, pp.46-49 (1999).
4. Y. Kurosaki, I. Satoh, T. Saito, "Heat Transfer Aspect to Upgrade the Quality of Plastics" Proceeding of the Symposium of Energy Engineering in the 21 Century, pp.84-95. (2000).

A Study on Fabrication and Application of Micro Tool by using High Speed Chemical Etching

Jun-min Park*, Sung-heon Kim*, S.C. Jeong*, Hae-do Jeong**, J.W. Park*, Y.H. Moon**
* School of Mechanical Engineering, Pusan National University, Pusan, Korea
**Graduate School of Precision Mechanical Engineering, Pusan National University, Pusan, Korea
Tel : +82-51-510-3210 Fax : +82-51-518-8442
E-mail : park918@hotmail.com , hdjeong@hyowon.pusan.ac.kr

1. Introduction

The method of micro tool fabrication has been studied in the fields of micro-machining, electronics, optics and medical instruments. Y. Yamagata[1], T. Waida[2], and T. Masuzawa[3] fabricated micro shaft using turning, grinding and WEDG (Wire Electro-Discharge Grinding) method, respectively. But grinding and turning method leaves mechanical damage layer to the tool and WEDM method requires complicated system.

In this study, the tool was fabricated by fluid-energy-enhanced chemical etching method to prevent the material from mechanical damage and shape accuracy degradation. The experimental setup was composed of high speed motor, chemical solution and several mm rod. A part of the rod was dipped in chemical solution and the rod rotated with high speed (1000-10000rpm). The main factors of diameter control are chemical concentration, reaction time, rpm and temperature. The surface of chemical solution around the rotating rod is pulled up by balance of surface tension and centrifugal force. This phenomenon makes a difficulty in getting clear shape of micro shaft. As a result, the lower part of the material to be the micro tool was fabricated in diameter of tens of μm with high speed rotation. And then, the micro shaft was finished by electropolishing method. The electrolyte was mixed by H_3PO_4(phosphoric acid), H_2SO_4(sulfuric acid), H_2O(water) 50%, 20%, 30%, respectively[4].

This type of micro shaft can be used in manufacturing one dimensional structures such as hole and lines in size of tens of μm. Thus the fabricated micro tool was applied to make a line with 30μm width. In this research, this process has the advantages of low cost and superior machine-ability for micro tools. The fluid-energy-enhanced etching method was successfully applied to make micro tool and the integration of the kinetic energy of circumference and the effect of etching, takes less time to fabricate the micro shaft than any other conventional methods.

2. Mechanism of corrosion erosion

Erosion corrosion phenomenon is corrosive property by the velocity difference between caustic liquid and interface of the metallic material. The shear force is increasing in surface of material by increasing of the caustic fluid velocity. When the shear force approaches the breakaway velocity, the chemical reacted layer of the material is removed the leakage part by cavitation phenomenon. The cavitation phenomenon is caused by metamorphosis of pressure difference between chemical fluid and surface of the metallic material. The burst pores break the immovable oxidation layer of the metallic material. The pressure difference is ruled by Bernoulli's law. And then, the lower part of the removed layer is appeared in the chemical solution. This phenomenon is continuously occurred interface of the material and chemical solution as shown Fig.1. The material to be micro tool was rotated with high speed (1,000~10,000rpm) to add the surface active energy. The experimental set-up is shown Fig.2. The micro shaft was fabricated several micrometers in the diameter by the high speed rotation, the cavitation and chemical attack.

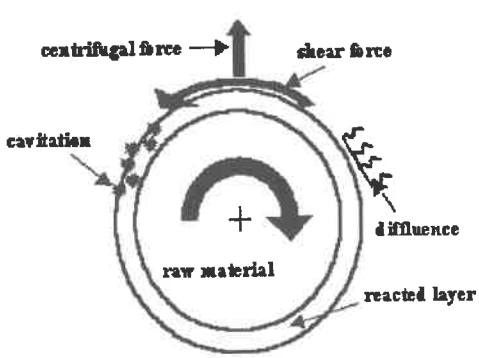

Fig. 1 mechanism of corrosion erosion

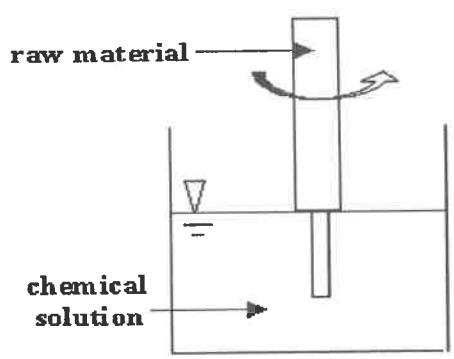

Fig. 2 schematic of micro tool fabrication

3. Fabrication of micro shaft

The micro shaft can be fabricated several micrometer in the diameter only using machining the chemical reactions of atoms level, and the shape of micro shaft is cleared as well. The process is removed not anisotropic machining but isotropic machining. Most of all, the system is not only simplified but also very low cost.

In this study, the chemical solution is mixed water(90wt%) with $FeCl_3$ (10wt%) to make the micro shaft. The material to be micro shaft is steel, and stainless steel. Discharging on the anode and the cathode, the anode(steel) is dissolved in the state of ionization, and the cathode generates the hydrogen gas. The ionized steel generates a ferrous hydroxide as a bonding state of hydroxyl ions. The ferric hydroxide is also resulted from reacting the ferrous hydroxide, water, and oxygen gas. The reaction between steel and the chemical solution is representatively shown (1) ~ (3). The SEM(Scanning Electron Microscope) of shafts is respectively shown as Fig. 3,4, and the experimental conditions are shown as table 1.

$$2Fe(s) + O_2(g) + 2H_2O(l) \rightarrow 2Fe(OH)_2(s) \quad (1)$$
$$6Fe(OH)_2(s) + O_2(g) \rightarrow 2Fe_3O_4 \square H_2O(s) + 4H_2O(l) \quad (2)$$
$$Fe_3O_4 \square H_2O(s) \rightarrow H_2O(l) + Fe_3O_4(s) \quad (3)$$

Table 1 experimental conditions of fabrication of micro shaft

Raw material	Steel, stainless steel
Rpm	1,000 ~ 10,000
Chemical solution	Water(90wt%) + $FeCl_3$ (10wt%)
Temperature	Room temperature
Machining time	10 min

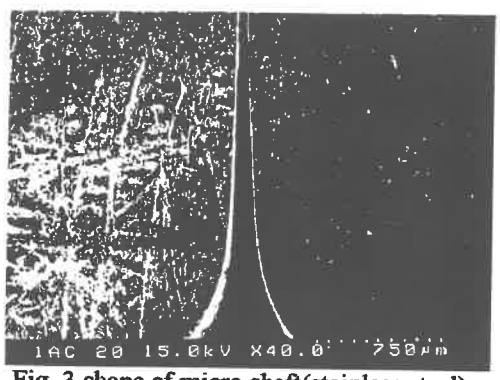

Fig. 3 shape of micro shaft(stainless steel)

Fig. 4 shape of micro shaft(steel)

4. Electropolishing

Electropolishing is decided by electrochemical dissolution between the anode and the cathode of atomic weight of materials, current, and machining time. The cathode is not change the shape but only expose the hydrogen gas. In the electropolishing process, the removal volume of the material is defined by Faraday's law.

$$m = \frac{AIt}{zF}.$$

where A : atomic weight, I : current, t : machining time, z : valence, F : Faraday's constant(96500C)

Thus, the removal rate per machining time is defined below equation.

$$m' = \frac{AIt}{zF}.$$

Especially, A/z(electrochemical equivalent) is a important factor in electropolishing process. The current efficiency is defined ;

$$\text{Current efficiency} = \frac{m'}{(A/zF)I}.$$

The current efficiency is affected by passivation, gas generation, etching, electrode gap distance, and electrolyte. The electropolishing is a super passivation process. Thus, the oxidation chromium layer appears on the material,

and the current efficiency is resulting in decreasing, and the surface roughness is not made progress any more. The relation of electrolyte and stainless steel is shown chemical reaction equation (4) ~ (6).

$$Cr(s) + O_2(g) + 2H_2O(l) \rightarrow Cr(OH)^-(aq) + 2H_2(g) \quad (4)$$
$$Cr(s) + H_3PO_4(aq) \rightarrow Cr(PO_4) + H_2(g) + H^+(aq) \quad (5)$$
$$Cr(s) + 3H_2SO_4(aq) \rightarrow Cr_2(SO_4)_3 + 3H_2(g) \rightarrow Cr_2O_3(s) \quad (6)$$

The electropolishing mechanism and the experimental set-up are shown as Fig. 5,6, respectively. The electrolyte used is mixed H_3PO_4(phosphoric acid), H_2SO_4(sulfuric acid), H_2O(water) 50%, 20%, 30%, respectively. The anode is the micro shaft, and the copper plate is used as the cathode. The condition of electropolishing is followed as table 2. According to the table 3, the electrochemical equivalent is calculated as the value of 27.52 (table 4). In the electropolishing process of the stainless steel, the experimental and theoretical removal rate values are compared in the table 5. As the results, the removal rate is to be estimated. From the results of relation the electrode gap and the surface roughness the electropolishing, the gap is related to the current efficiency. The surface roughness of the stainless steel is fine neither low current density(≥0.5 A/ $cm^{2)}$, nor high current density(≤1.5 A/ cm^2). The good electrode gap is 1mm as shown Fig. 7. From these results, the micro shaft was made a good shape and corrosion resistance (Fig.8).

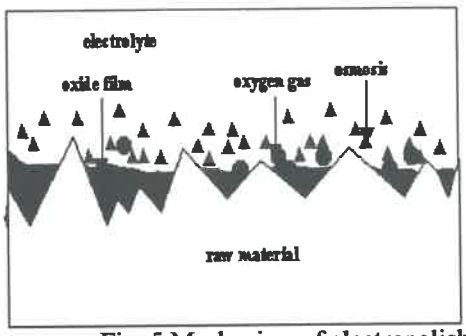

Fig. 5 Mechanism of electropolishing

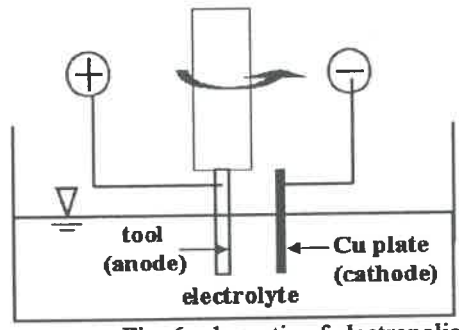

Fig. 6 schematic of electropolishing

Table 2 conditions of electropolishing (steel, stainless steel)

Power output	DC
Current	200 mA
Voltage	30 V
Pulse time (τ on, off)	5 μs
Polishing time	2 minute
Electrolyte	H_3PO_4 : 50wt%+ H_2SO_4 : 20wt%+ H_2O : 30wt%
Electrode gap	1 mm
Tool material	SUS 316L, steel (SKD 11)

Table 3 chemical properties and composition of stainless steel

Metal	Atomic weight	Valence	Weight %
Chromium	51.99	2	17.80
Iron	55.85	2	66.24
Manganese	54.94	2	0.80
Molybdenum	95.94	3	2.28
Nickel	58.71	2	12.19
Silicon	28.09	4	0.62

Table 4 A value of electrochemical equivalent for stainless steel

Element	Fe	Si	Mn	Ni	Cr	Mo
Chemical equivalent(A/z)	27.93	7.02	27.47	29.36	26.0	31.98
Quotient X/(A/z)	2.37	0.09	0.03	0.42	0.68	0.07
$(A/z)_{stainless\ steel}$	27.24					

Table 5 Experimental, theoretical removal rates and current efficiencies for stainless steel

Current density (A/ cm^2)	Machining rate (g min^{-1} cm^{-2})		
	Theoretical	Observed	Current efficiency(%)
0.5	0.00847	0.00831	98.1
0.7	0.01186	0.01161	97.9
1	0.01694	0.01649	97.3

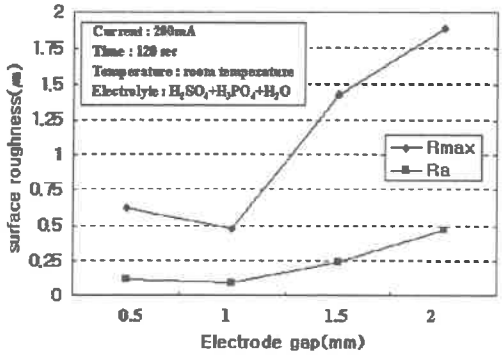

Fig. 7 relation electrode gap and surface roughness(electropolishing)

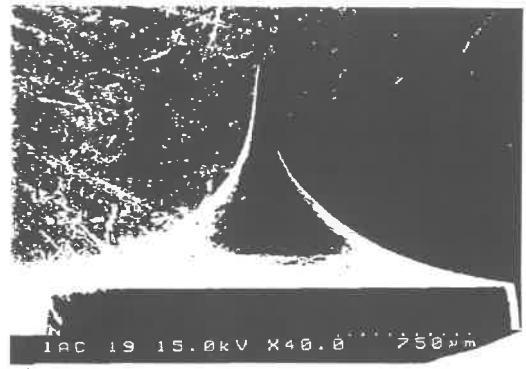

Fig. 8 SEM of micro shaft(after electropolishing)

6. Conclusions

In this study, A new method of micro shaft fabrication was introduced as high speed chemical etching and electropolishing. This method is dependent on the chemical solution, material, and machining time. The electropolishing made the micro shaft that has a very clear shape, and corrosion resistance. Thus, the micro shaft is to be a good micro tool. The micro shaft of the Fig. 9 has the radius of 2.5μm. The line in the Fig. 10 is applied by the machining of the stainless steel micro tool.

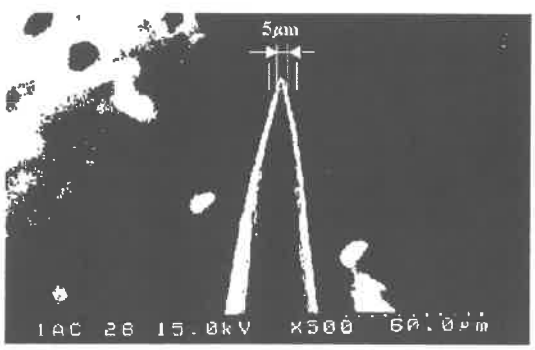

Fig. 9 SEM of micro shaft (radius = 5 μm)

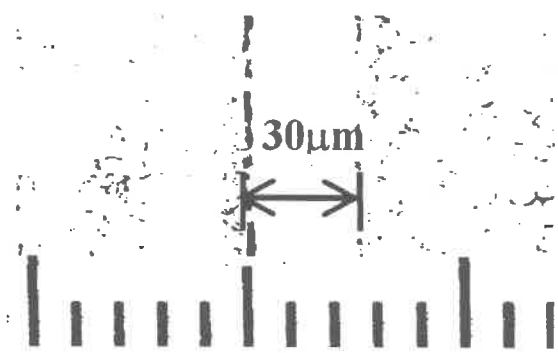

Fig. 10 optic microscope photograph of line machining(x500)

Reference

[1] Y. Yamagata, T. Higuchi, "Three-Dimensional Micro Fabrication by Precision Cutting Technique", JSPE, Vol.61, No.10, pp.1361-1364, 1995.

[2] T. Waida, K.Okano, "Micro-grinding of Micro-machine Component", JSPE, Vol. 61, No. 10, pp. 1365-1368, 1995.

[3] T. Masuzawa, M. Fujino, K. Kobayashi, "Wire Electro-Discharge Grinding For Micro Machining", Annals of the CIRP, Vol. 34, pp 431-424, 1985.

[4] J.B. Song, E.S. Lee, J.W. Park, " A Study on the Machining Characteristics of Electropolishing for Stainless Steel ", Vol.23, No.2, pp.279-286, 1999.

NON-STRAIGHT PROFILE CUTTING ON GLASS USING HOT AIR JET

E.S. Prakash[1] K. Sadashivappa[1] Vince Joseph[2] M. Singaperumal[3]
[1]Bapuji Institute of Engineering and Technology, Davangere – 577 004.
[2]University BDT College of Engineering, Davangere – 577 004.
[3]Indian Institute of Technology, Madras, Chennai – 600 036, India.
[1]Fax: (08192) 23261, E-mail: es_prakash@usa.net

Key words: *Thermal cutting, glass fabrication, lens cutting, non conventional cutting, profile cutting*

1.0 Introduction

Glass has failed in its use as a structural member, in spite of several good qualities, because of its high brittleness. However, glass has become an important non-replaceable material in some key areas because of its unique qualities such as transparent nature and excellent optical characteristics. Glass is inevitably an important component in any opto-instrument. The worthiness of any opto-instrument lies in the quality of lens and its fabrication method. Glass is also very useful as automobile and locomotive passenger car window shields. Glass finds as the only material suitable in case of microwave oven window because of its ability to tolerate higher temperatures without deformation. Cutting glass to very close tolerances without any irregularities at the edge for window glass is very important to prevent crossing of liquid and gaseous medium.

A novel glass cutting method by the above authors has been reported [1,2]. In this method, hot air jet issuing from a nozzle is impinged on the plate glass to be cut. The X-Y table, on which plate glass is kept, can be moved at required speed. Any complex profile could be easily and economically generated by the above method. This method avoids development of internal flaws and microcracks on the surface during cutting. Profiles generated by the new method are smoother as compared to that by diamond cutting. It is possible to maintain very close tolerances with the new glass cutting method. Experimental studies on temperature distribution and thermal strains in plate glass during thermal cutting were made and the results were reported earlier. Experiments were also conducted to determine the cutting speed and dwell time [3-5]. The principle of thermal cutting is explained elsewhere [6].

2.0 Experimental details

Experimental set up was arranged for cutting glass using hot air jet. It consists of a CNC X-Y table and hot air blower with an arrangement to vary stand off distance. Glass was placed on the X-Y table and moved under the stationary hot air jet issuing from the nozzle. Fig. 1 shows the crack propagation in glass using the hot air jet.

Experimental studies on thermal cutting of glass have shown that the thermal cutting time increases with the plate thickness. Glass of thickness varying from 2 to 20 mm were used for the experiments. Also dwell period is higher for larger thickness plate glass[6].

Fig. 1. Crack propagation

3.0 Non-straight profile cutting

It is difficult to cut non-straight profiles using conventional cutting using a diamond point tool in a single step. These disadvantages are very much inherent in the cutting method itself. The size and shapes obtained are always unpredictable.

The novel method of glass cutting using the hot air jet can be used to cut non-straight profiles such as sinusoidal, square, triangular, circle etc. Fig. 2 shows the sinusoidal profile cutting on plate glass of 3 mm thickness using the CNC X-Y table. Fig. 3 shows a circle cutting on ophthalmic lens of 3 mm thickness. Fig. 4 shows sinusoidal profile cutting on mirror glass of 2 mm thickness using the CNC table. Fig. 5 shows the V-thread cutting on art glass of 4 mm thick using the manual X-Y table. It is observed that the cutting speed for non-straight profiles is lower as compared to straight profiles. This requires further investigations. Profile cutting of non-straight shapes is more accurate with a CNC table.

Photographs of a few non-straight profiles cut using the new method are presented below.

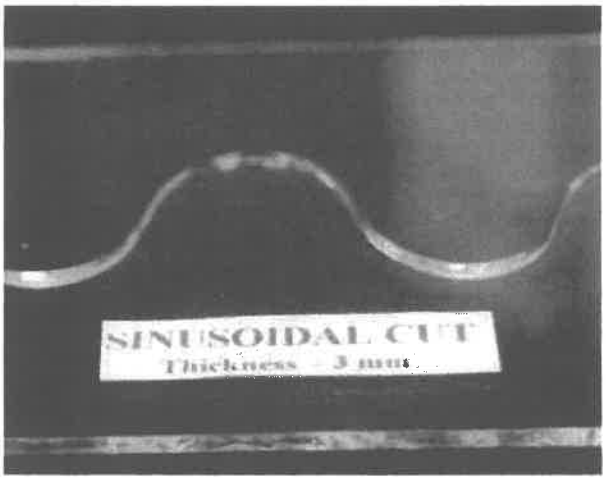

Fig. 2. Sinusoidal profile on plate glass

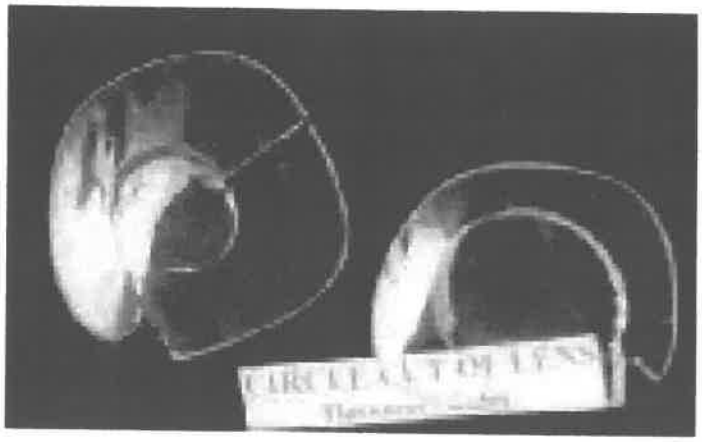

Fig. 3. Circle cutting on ophthalmic lens

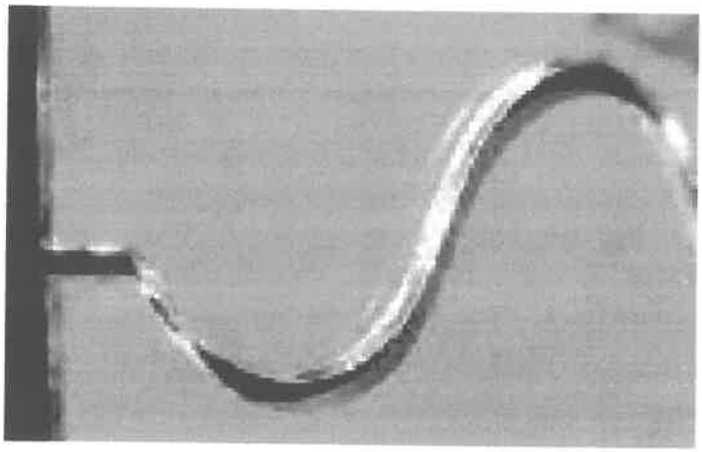

Fig. 4. Sinusoidal profile cutting on mirror glass

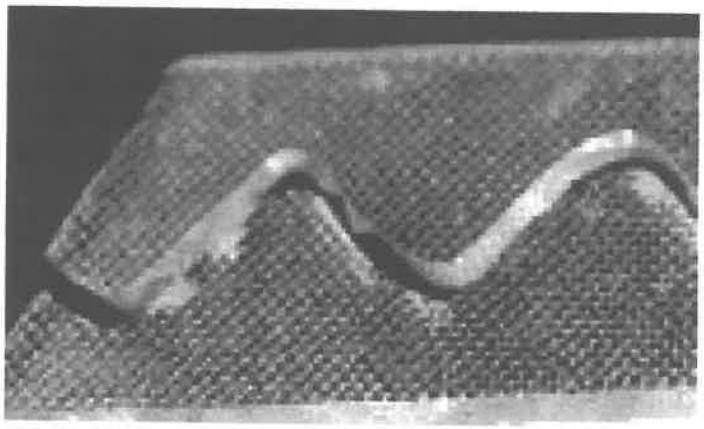

Fig. 5. V-thread cutting on art glass

The following part programs are used for cutting circle and sinusoidal shapes using Siemens 'Sinumerik 802S' [8].

```
N5 G90 G94 Z10 X4 F30
N10 G2 K20 I-7 AR=359.9
N20 M30
```

```
G5 G90 G94 Z30 X40 F100
N10 G2 K10 I-7 AR=180
N20 G3 K10 I-7 AR=180
N30 G2 K10 I-7 AR=180
N40 M30
```

4.0 Conclusions

It is not possible to cut non-straight profiles conventionally using a diamond point tool in a single step. Also glass wastage is more during cutting of non-straight profiles by conventional method. The new method of glass cutting using hot air jet can be applied successfully for cutting any non-straight profile to required size and shape in a single step. Non-straight profiles are used for decorative purposes, automotive car windows etc.

Acknowledgement

The authors wish to thank the AICTE New Delhi for sponsoring this research work.

References

1. K. Sadashivappa, C.S. Bhaskar Dixit, M. Singaperumal, Thermal cutting of plate glass, Proc. 11th Annual Meeting, ASPE, Vol 14, Monterey, USA, 551-556, 1996.
2. K. Sadashivappa, E.S. Prakash, M. Singaperumal, Compact portable air jet gun for thermal cutting of plate glass, Proc. 13th Annual Meeting, ASPE, St. Louis, Missouri, USA, 1998.
3. E.S. Prakash, K. Sadashivappa, Vince Joseph, M. Singaperumal, A study on thermal strains in plate glass during thermal cutting using hot air jet, Proc. 14th Annual Meeting, ASPE, Monterey, California, USA, 1999.
4. E.S. Prakash, K. Sadashivappa, Vince Joseph, M. Singaperumal, Strain measurement in plate glass during thermal cutting, Prof. of The First National Conf. on Precision Engineering, COPEN 2000, Indian Institute of Technology, Madras, Chennai, India, 117-122, Jan. 12-13, 2000.
5. E.S. Prakash, K. Sadashivappa, Vince Joseph, M. Singaperumal, Experimental study on glass cutting speed using hot air jet, Paper accepted for the 4th Intn. Conf. OPTO 2000 (Special session on innovative products, Lecture S10), Erfurt, Germany, May 11-12, 2000.
6. E.S. Prakash, K. Sadashivappa, Vince Joseph, M. Singaperumal, Nonconventional cutting of plate glass using hot airjet:Experimental studies, accepted for publication Ref. No. MECH 445, Int. J of Mechatronics, UK, June 2000.
7. E.S. Prakash, K. Sadashivappa, Vince Joseph, M. Singaperumal, Temperature distribution prediction in plate glass during thermal cutting and surface finish of cut surface, abstract accepted for the 19th AIMTDR Conf., Indian Institute of Technology, Madras, Chennai, India, Dec. 2000.
8. SIEMENS Sinumerik 802S Operation and Programming Software Version 2 Turning, User Manual, Edition 9.97, Sept 1997, pp8.25.
9. J.P. Holman, Heat Transfer, McGraw-Hill Book Co., Seventh Edn., Printed in Singapore, 1992.
10. Ernest O Doebelin, Measurement systems application and design, McGraw Hill Int. Edn., Fourth Edn., Singapore, 1990.

***

Development of Surface Texture Creation Device for Microscopic Areas using AFM Stylus

Kenji SHIRAI and Yoshikazu KOBAYASHI
Department of Computer Science, College of Engineering, Nihon University
Nakagawara, Tokusada, Tamura-machi, Koriyama, 963-8642, Japan

1. Introduction

Recent improvements in cutting and grinding technology have made very smooth, mirror finishing possible for machine processed surfaces. Although ever smoother surfaces have conventionally been sought where two parts meet, such as in moving sections, various adverse mechanical effects have arisen. These effects include increased friction between extremely smooth surfaces with roughness on the nanometer order. The stiction problem between a magnetic disk, used as a magnetic storage medium, and a head slider and increased separation resistance in plastic injection molds are some concrete examples. One method for dealing with the adverse effects arising from extreme surface smoothness, and thereby improving product functionality, is to create a fine roughness pattern, called a texture, on the surface. However, conventional texture creation equipment is large scale and the materials on which textures can be created are limited. There has been no compact, simple texture creation equipment. In this research a surface texture creation device for microscopic areas was developed using the AFM stylus from a commercial AFM device.

2. Outline of the system

In order to examine the tribological behavior of small surface areas, other researchers have developed several useful instruments[1)~4)]. Based on these instruments, we created a new apparatus. A schematic illustration of the apparatus, along with a photograph, are shown in Figs. 1(a) and (b) respectively. The apparatus consists primarily of four units :

(1) The moving stage units

(1-1) The XY-axes pulse-motor stage moves the specimen in the X and Y directions

(1-2) The Z-axis PZT stage moves the specimen in the Z direction

(2) The cantilever folder

(3)The laser displacement meter

(4) The controller and computer

The flow of data between each unit during operation is shown in Fig. 2. First, the specimen is pressed against the diamond stylus at the tip of the AFM cantilever by raising a Z axis PZT stage. Next, the contact load between the specimen and the stylus is estimated by measuring the deflection

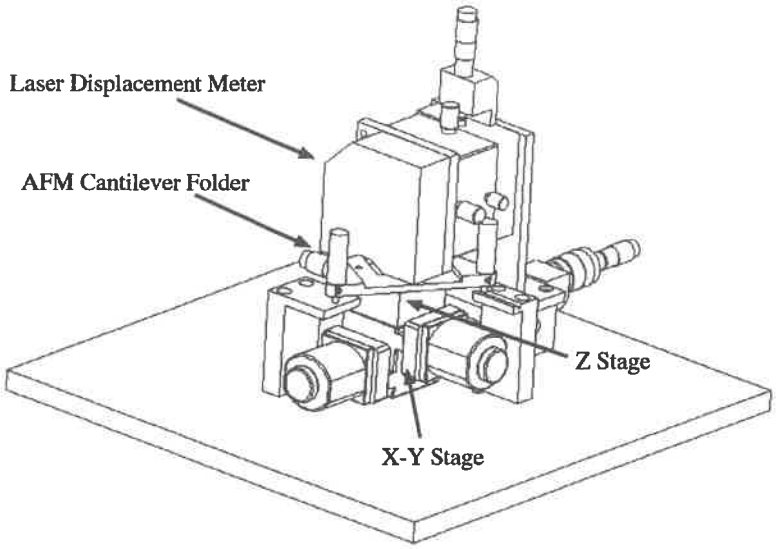

(a) Schematic illustration of developed apparatus

(b) Photograph of developed apparatus

Fig.1 Developed apparatus

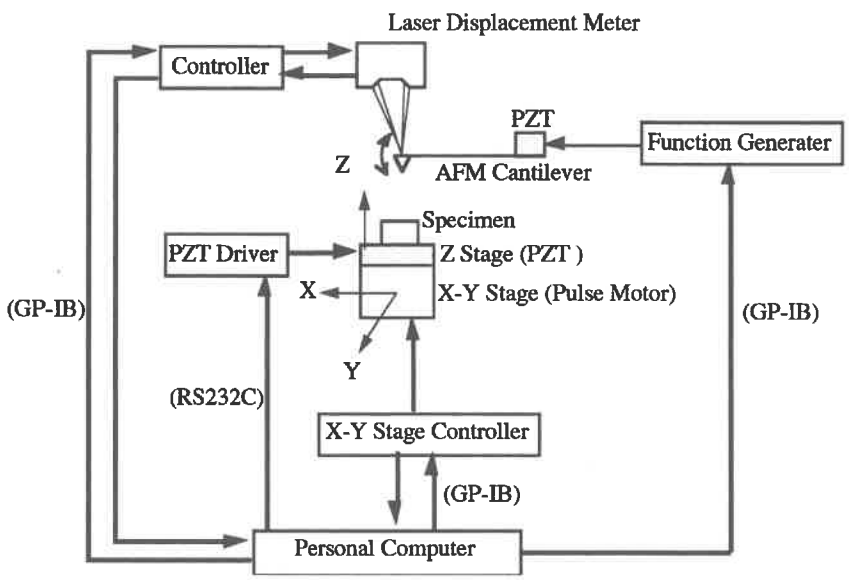

Fig.2 Diagram of data flow

of the cantilever with the laser displacement meter. To maintain the appropriate contact load, the computer monitors this deflection data and sends a feedback signal to the Z-axis PZT stage. By attaching the PZT to the end of the cantilever, the inertial force of oscillation is used for creating pressure marks or the influence of minute oscillation on the resultant scratching also can be studied. A photograph of the cantilever holder is shown in the Fig. 3. To create the intended texture, marking and scratching are achieved by movements along the X- and Y- axes, with height along Z-axis controlled. The interfaces between the units use GP-IB and RS232C. The specification for the

Fig.3 AFM Cantilever Folder

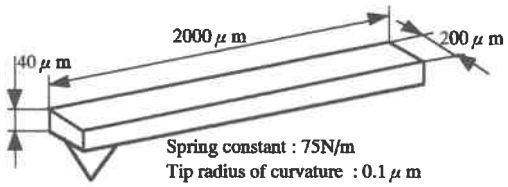

Fig.4 Dimensions of AFM Cantilever and mechanical condition

Table 1 Specification of the develped apparatus

(1) Makable area of texture	Min. 1μm*1μm Max. 10μm*10mm
(2) Resolution of cantilever deflection	Min. 10nm Max. 100μm

Table 2 Creating condition of texture

	(a) Line pattern	(b) Dot pattern
(1) Material	S50C[5]	S50C[5]
(2) Applied load	2.3mN	1.5mN

cantilever and other units of the apparatus are shown in Fig.4 and Table 1, respectively.

3. Experimental results

Two different types of texture were created using the apparatus described above: a line pattern, shown in Fig.5(a), and a dot pattern, shown in Fig.5(b). The conditions under which these patterns were achieved are shown in Table 2. As can be seen in Fig.5(a), the scratch process using this apparatus can be precisely controlled using an interface to CAD software. As noted in Table 2, the width of each scratch is approximately 3μm, while the depth is 1.5μm. A slight ridge is visible on both side of each scratch. Fig.5(b) shows the corresponding precision with which a dot pattern can be created. It is also possible to observe slight scratches cased by the sliding of the stylus on the specimen surface. These small scratches appear to be the result of deflection of the cantilever caused by vibration in the surrounding environment. The dimensions of each dot are approximately 2μm*2μm, while the depth is 1 μm.

4. Conclusion

The apparatus for surface-texture creation developed in this study used the AFM stylus from a commercial AFM device. It should prove helpful in the study of the tribological behavior of textured surfaces and in the creation of micro-texture on small surfaces. Such texture can be useful when dealing with the adverse effects arising from extreme surface smoothness, thereby improving product functionality. The described device can fit in an area of approximately 100 mm2, is easily transportable, reasonably precise, and relatively inexpensive. Since plastic deformation is used to create texture, there should be few material limitations.

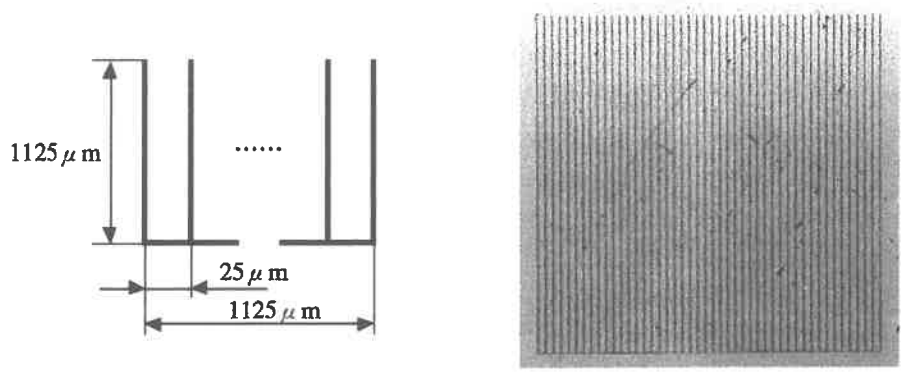

(a) Line pattern texture

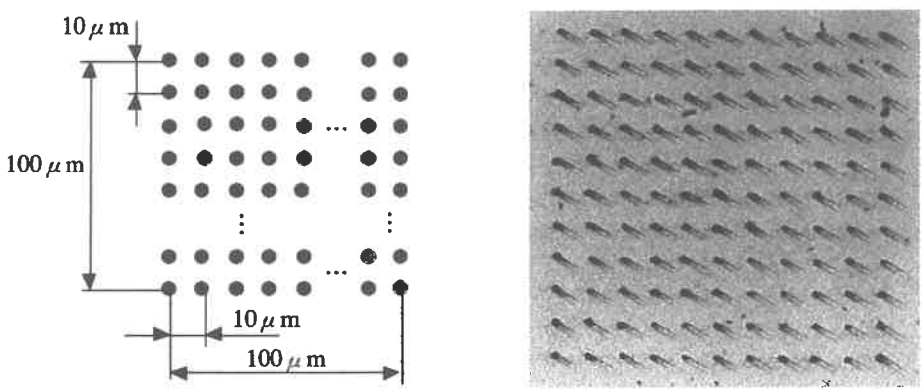

(b) Dot pattern texture

Fig.5 Experimental results

References

1) V.Jardret et al : Understanding and quantification of elastic and plastic deformation during a scratch test, Wear 218 (1998) .

2) Louis G. Hector and Steven R. Schmid : Simulation of asperity plowing in an atomic force microscope Part I : Experimental and theoretical methods, Wear 215 (1998).

3) Xiaodong Li and Bharat Bhushan : Micromechanical and tribological characterization of hard amorphous carbon coating as thin as 5nm for magnetic recording heads, Wear 220 (1998).

4)E.J.van Loenen at al : Direct writing in Si with a scanning tunneling microscope, Appl. Phys. Lett. Vol.55 No.13 (1989).

5) JIS G 4051-1979.

Wire EDM Slicing of Monocrystalline Silicon Ingot

Yoshiyuki UNO*, Akira OKADA*, Yasuhiro OKAMOTO*, Tameyoshi HIRANO**

* Okayama University, 3-1-1, Tsushimanaka, Okayama 700-8530, JAPAN
** Toyo Advanced Technologies Co.,Ltd., 5-3-38, Ujinahigashi, Minami-ku, Hiroshima 734-8501, JAPAN

1. Introduction

Monocrystalline silicon is one of the most important materials in the semiconductor industry because of its many excellent properties as a semiconductor. The manufacturing process of IC chip consists of various fine precision machining techniques, including monocrystallizing of silicon, slicing of ingot, lapping and polishing of wafer, photolithography and etching for integrated circuits, dicing and so on. In the slicing process, further improvements of efficiency and accuracy are strongly required, since the final flatness of wafer is significantly determined by this process.

Conventionally, inner diameter(ID) blade has been used for slicing silicon ingot[1]. However, some problems in efficiency are existed, that is, kerf loss is relatively large and the maximum crack of about 30 μm in depth is generated on the sliced surface resulted from mechanical machining. Moreover, this method is difficult to apply for larger-scale wafers of 12 or 16 inches diameter expected to be used in the near future. Then, multi wire saw has been gradually applied[2]. This method is performed by feeding thin piano wire to workpiece with slurry consisting of abrasives and cutting oil. In the method, many wafers can be sliced at the same time, kerf loss is relatively small, and it is applicable to large-scale wafer. However, there still remain the problems of slurry treatment and contamination of sliced surface.

From the above mentioned viewpoints, a new slicing method of monocrystalline silicon ingot by wire electrical discharge machining (WEDM) is proposed in this study. A silicon wafer used as substrate for epitaxial film growth has low resistivity in the order of 0.01 Ω•cm, which makes it possible to cut silicon ingot by WEDM[3)-5)]. And it is expected that the crack on the machined surface might be reduced, since the material removal is performed by repetition of micro crater due to a single discharge and the machining force acting on the workpiece in WEDM process is extremely small compared with that in conventional slicing methods. In this study, the possibility of slicing of silicon ingot by WEDM was discussed, and the machining properties such as cutting speed and surface roughness were experimentally investigated. Furthermore, the accuracy of wafer and the contamination on the machined surface was evaluated.

2. Experimental Procedures

Fig.1 shows the schematic diagram of experimental apparatus. In this machine, the discharge current pulse made by transistor switching circuit has relatively long duration and low intensity, different from conventional one made by condenser circuit. Therefore, it is expected that the electrode wear becomes very small. Then, the wire electrode used once is rewound around the drum and reused repeatedly, as shown in the figure. P-type monocrystalline silicon ingot of 40mm in thickness whose resistivity is 10^{-2} Ω•cm is used as a workpiece. Main machining conditions are shown in **Table 1**. The experiment using conventional WEDM with condenser circuit is also done for comparison. In this case, large discharge current for 1st cut and small one for 2nd cut are applied.

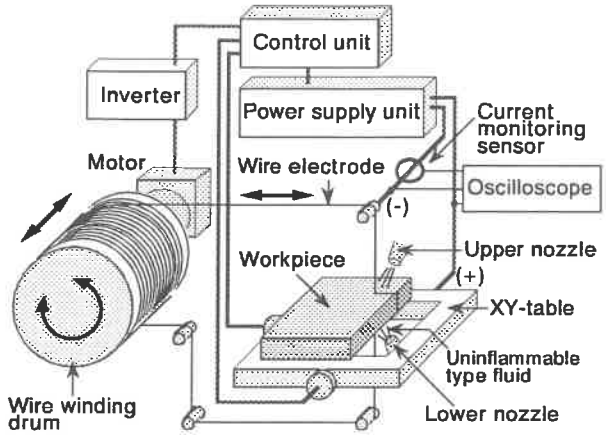

Fig.1 Schematic diagram of experimental apparatus

Table1 Machining conditions

Electrode	Molybdenum (ϕ180 μm)
Polarity	Electrode : (-)
Dielectric	Deionized water ($\rho > 10^6$ Ω·cm)
Gap voltage	u_i=100 [V]
Discharge current	i_e= 3, 12, 22 [A]
Discharge duration	t_e= 5, 10, 20, 40, 75 [μs]
Duty factor	τ = 15 [%]
Wire feed rate	F_w= 10.0 [m/s]
Wire tension	F= 0.6 [kgf]

3. Machining Properties

Fig.2 shows the variations of removal rate with discharge duration for various discharge currents. As can be seen in the figure, the removal rate increases with an increase of discharge current. And the removal rate takes maximum at about 20 μs in pulse duration, just like die-sinking EDM process. On the other hand, in case of conventional WEDM, they were 104mm^2/min and 10mm^2/min under 1st cut condition and 2nd cut one respectively. It was made clear that the removal rate of monocrystalline silicon by relatively long duration and low intensity current with transistor switching circuit was as large as that in conventional WEDM with condenser circuit. It was reported[6] that the Joule's heat generation played an important role in material removal in EDM for high resistance material. Also in this case, it is considered that the Joule's heat generation in addition to the heat conduction from arc column made a great contribution to material removal.

Fig.3 shows the variations of surface roughness. The surface roughness increases with the increases of discharge current and discharge duration. On the other hand, it was 21.5 μm for 1st cut and 7.6 μm for 2nd cut in conventional WEDM. It is reported that the surface roughness is about 20 μm in multi wire saw slicing applied so far. Furthermore, the removal of crack layer is actually performed after slicing process, and the thickness is more than 30 μm. Considering these results with the removal rate shown above, large discharge current and short pulse duration are suitable conditions, which leads to large removal rate and small surface roughness.

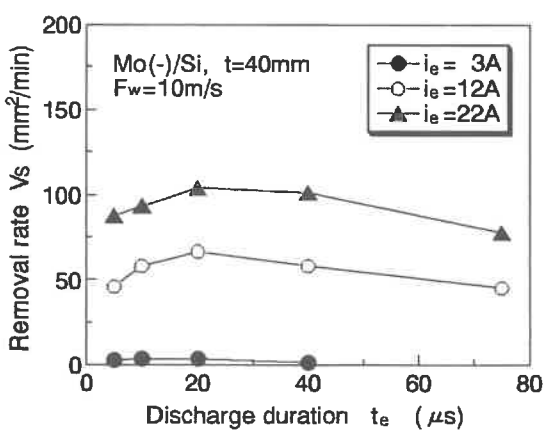

Fig.2 Variations of removal rate

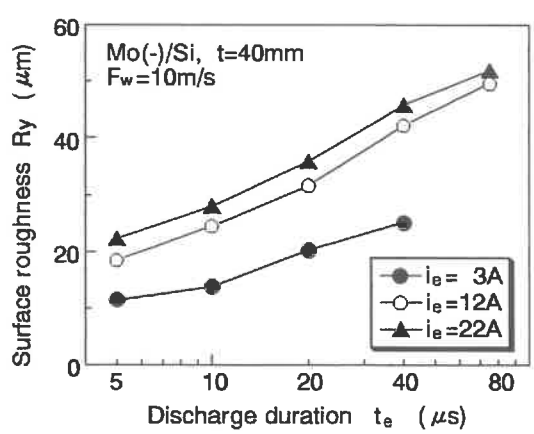

Fig.3 Variations of surface roughness

4. Surface Integrity

Fig.4 shows one of the longest cracks generated in sliced surface by WEDM. The crack length is about 20 μm as shown in the micrograph. On the other hand, they are about 20-30 μm in cases of ID blade and multi wire saw slicing. Therefore, this method is effective for high efficiency manufacturing of IC, since thinner crack layer leads to the shortening of time to remove the layer.

In order to investigate the contamination of machined surface, XPS(X-ray Photoelectron Spectro-scopy) analysis was carried out. **Fig.5** shows the results of analysis. The contamination layers such as oxidized layer and carbonized layer which had been generated by atmosphere after machining were removed by argon ion etching in the measurement chamber before analysis.As shown in the figure, oxygen exists on the machined surface in both cases. It is considered that the machined surface is oxidized by electrical discharge in deionized water or in air. Of course, contamination by oxygen is not desirable in semiconductor manufacturing process. However, it is allowable to some extent, since a few process for removing oxygen are actually performed after slicing process. In case of conventional WEDM, copper and zinc from wire material exist.

Copper is one of the most undesirable materials in semiconductor manufacturing process, since it tends to diffuse into the inside of silicon. Therefore, conventional WEDM is never applicable. On the other hand, molybdenum of wire material hardly adhere to the machined surface in case of this WEDM. It is considered that adhesion or diffusion of wire material can be reduced because of discharge current waveform made by transistor switching circuit.

Fig.4 Cross section of sliced surface

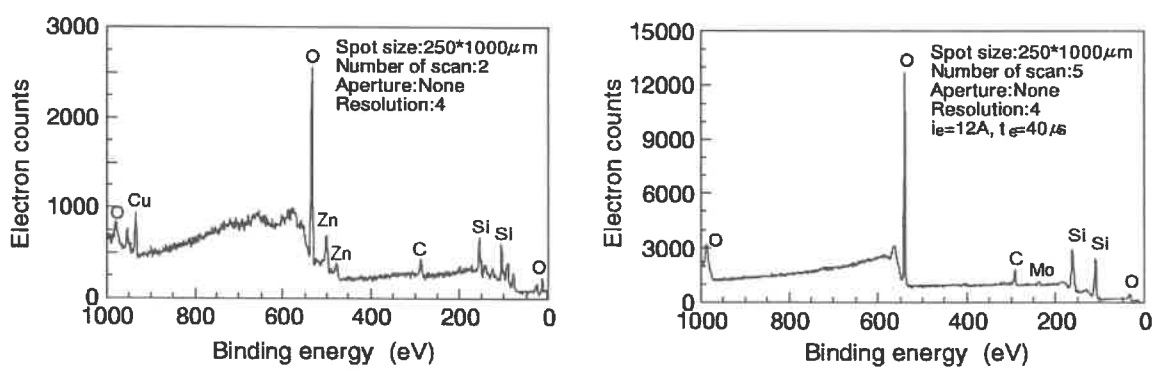

(a)Conventional WEDM with condenser circuit (b)WEDM with transistor switching circuit

Fig.5 Results of XPS analysis of sliced surface

5. Slicing of 6 inches Ingot

Next, slicing of 6 inches silicon ingot was carried out. **Fig.6** shows the relationship between displacement of wire and machining time. As shown in this figure, slicing speed decreases with an increase of workpiece width, and it takes about 140 min to slice 6 inches silicon ingot. That is, the average slicing speed is about 1.1mm/min. In the case of multi wire saw, it is 0.2-0.3mm/min . If multi slicing, in which many wafers are sliced at once can be realized like wire saw slicing, this WEDM slicing method is applicable as a high efficiency slicing method of silicon ingot.

Fig.7 shows TTV(Total Thickness Variation) and Warp of 6 inches wafer sliced by WEDM. Both values are the important dimensional parameters of wafer, that is, TTV is the difference between the maximum and minimum thickness, and Warp is defined as the difference between the maximum and minimum distances from a reference plane, as shown in the figure. Both values in the case of WEDM are almost the same as those in the case of wire saw. In addition, the kerf loss was about 250 μm, which is almost the same value as wire saw,too.

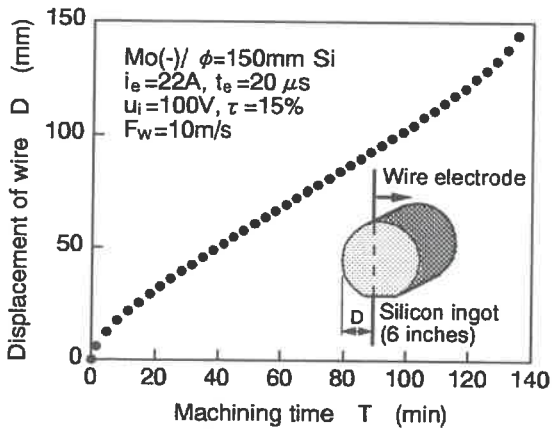

Fig.6 Displacement of wire in slicing of 6" ingot

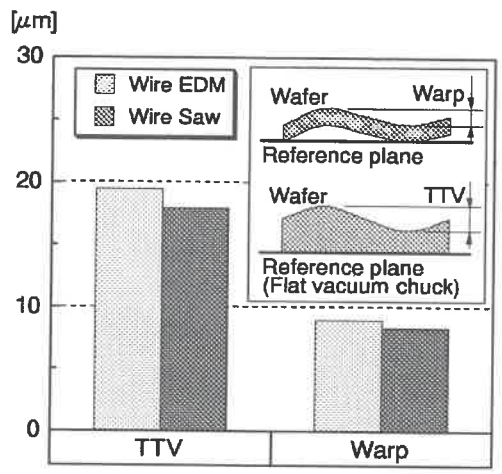

Fig.7 TTV and Warp of sliced 6" wafer

6. Conclusions

Main conclusions obtained in this study are as follows:

(1)Wire EDM has a possibility as a new slicing method of monocrystalline silicon ingot.

(2)The surface roughness by WEDM is as small as that by multi wire saw method used conventionally.

(3)Contamination due to adhesion and diffusion of wire electrode material to machined surface can be reduced by WEDM under the condition of low current and long discharge duration.

(4)The accuracy of wafer by this slicing method is almost the same as that by multi wire saw method. And, higher speed slicing is possible if a multi type WEDM slicing can be realized.

Acknowledgements

This work was partly supported by Electric Technology Research Foundation of Chugoku. The authors also would like to express their thanks to Sin-Etsu Handotai Co.,Ltd. and Sodick Co., Ltd. for their help through this research.

References

1) F.Shimura : Semiconductor Silicon Crystal Technology, Academic Press Inc. (1988) 186.

2) K.Makino et al. : Slicing by Multi Wire Saw, J.of the Society of Grinding Engineers, 41, 1(1997) 16-19.

3) D.Reynaerts et al.:Microstructuring of silicon by EDM, Sensors and Actuators, 60, 1-3 (1997) 212.

4) Y.Uno et al.:Fundamental Study on EDM of Single Crystalline Silicon, J.of JSPE, 63, 10(1997) 1459.

5) Y.Uno et al.:High Efficiency Fine Boring of Single Crystalline Silicon Ingot by Electrical Discharge Machining, Proc. of the 12th ASPE Annual Meeting (1997) 525-528.

6)T.Saeki et al.: Transient Workpiece Temperature Analysis in the EDM Processes of High Electric Resistance Materials Considering Joule Heating, J.of JSPE, 62, 3 (1996) 443.

FOCUSED ION BEAM SHAPED MICRO-CUTTING TOOLS FOR FABRICATING CURVILINEAR FEATURES

David P. Adams*, Michael J. Vasile, Yoosuf N. Picard
*Sandia National Laboratories, P.O. Box 5800, Albuquerque, NM, 87185
Institute for Micromanufacturing, Louisiana Tech University, Ruston, LA, 71272, USA

This work combines focused ion beam (FIB) sputtering and ultraprecision machining as a first step in fabricating polymer, ceramic and metal alloy microcomponents. Focused ion sputtering is used to shape a variety of miniature cutting tools including microgrooving / threading tools. Tools are made of cobalt M42 high speed steel or C2 grade tungsten carbide, and have cutting widths between 10 and 30 μm. FIB sputtering is useful for shaping tools, because this numerically controlled technique reproducibly affords sub-micron dimensional resolution, different tool geometries and sharp tool cutting edges. Micro-grooving /threading tools consist of nonplanar facets with well-defined lengths and relative angles. Facets provide back rake, side rake and clearance taper behind cutting edges. Selected results from ultraprecision machining are also presented. This includes lathe machining of helical grooves in PMMA and Macor™ cylindrical workpieces.
Keywords: *microtools; micromachining; ultraprecision*

INTRODUCTION

Alternative fabrication techniques are currently being explored to meet the manufacturing requirements of microsystems.[1] While a large variety of microcomponents and microelectromechanical devices have been demonstrated in recent years, most fabrication has involved inherently planar techniques, such as optical or x-ray lithography. Features are defined in polished substrates or thin film layers by exposure of a resist (using a mask) and etching. However, there is a desire to fabricate more complex shaped features in a variety of ceramics, metals and polymers. For example, nonprismatic features and nonplanar workpieces are needed for a variety of devices. These include micro-fluidic sensors, microinductors, and microactuators.

In present work focused ion beam sputtering is combined with ultra-precision machining. Focused ion beam (FIB) sputtering is used to shape micro-cutting tools intended for mechanical machining of various workpieces. FIB sputtering is attractive for fabricating micron-size tools or instruments, because this technique can precisely remove or add material. Most importantly, focused ion beam sputtering can be used to create and align a number of nonplanar features[2,3], such as facets required on cutting tools. Previous studies demonstrate FIB-sputtered microwrenches, microscalpels, and nanoindenters. Ultra-precision machining is beneficial for microfabrication, because of its accuracy and speed. The intent of current work is to fabricate micron size features over centimeter length scales in reasonable time. This is potentially achievable, since commercial ultra-precision machines have 5-nm resolution. Further, it is expected that tools having ~25 μm-diameters are robust and reproducibly define microscopic features. Initial work demonstrates that ~25 μm-diameter, FIB-fabricated micro-end mills machine trenches in polymethyl methacrylate (PMMA) and metal workpieces [4,5].

In this report, we present a number of cutting tools shaped by focused ion beam sputtering. This includes precision grooving/threading tools having well-defined cross-sections. Tools have sharp cutting edges with radii of curvature estimated to be 0.1 μm or less. Focused ion beam fabricated microtools are tested by machining helices into different workpiece materials.

PROCEDURE FOR SHAPING MICROTOOLS

Microtools are shaped by focused ion beam sputtering using a custom-made vacuum apparatus described previously [6]. A liquid metal ion gun produces a 20keV beam of gallium ions that is directed towards tool blanks. The ion beam has a Gaussian intensity distribution with a full-width at half-maximum diameter of 0.4 μm. In practice an operator outlines a desired shape for removal on a secondary electron image of the target, and an octapole deflection system steers the ion beam to designated areas with sub-micron resolution. Between sputter removal steps, a stage positions tools with 1 μm accuracy. This stage also provides for sample rotation with a minimum step size of 0.37°. Individual facets are sputtered with the tool blank fixed.

Tool blanks are purchased from National Jet, Inc. and are made of cobalt M42 high-speed steel or C2 micrograin tungsten carbide. The tool shank has a diameter of 1.02 mm and is brazed into a centerless ground mandrel. Tool mandrels are either 2.3 mm or 3.175 mm in diameter. One end of each tool is tapered by diamond grinding and polished; this end has a diameter of approximately 25 μm and is cylindrical over a length of 25 μm. The average rate of sputtering C2 tungsten carbide has been measured to be 0.76 μm^3/sec at near-normal incidence when using a beam current of 2.8nA.

FABRICATED MICROTOOLS

A number of different microtools have been shaped by focused ion beam sputtering and tested. This includes microgrooving/threading tools and micromilling tools. An example microgrooving tool is shown in Figure 1. This tool is made of tungsten carbide and contains facets intended for cutting and raking chips. The tool has a cutting edge width of 18 μm and a rectangular cutting cross-section. Tools are made with well-defined back rake and side rake angles as well as clearance taper angles behind cutting edges. Clearance for minimizing frictional drag of a tool results from the sputter yield dependence on ion beam/target incidence angle. This particular tool has 7° back rake and side rake angles. In general the time required to shape a tool in the FIB system depends on the amount of material sputtered and the composition of the tool. The microcutting tool shown in Figure 1 was fabricated in 4-5 hours using an ion current of 2.8 nAmps (measured in a Faraday cup). Energy-dispersive x-ray spectroscopy reveals that the low electron yield features in Figure 1 (dark regions on facets) are Co-rich and C-rich regions.

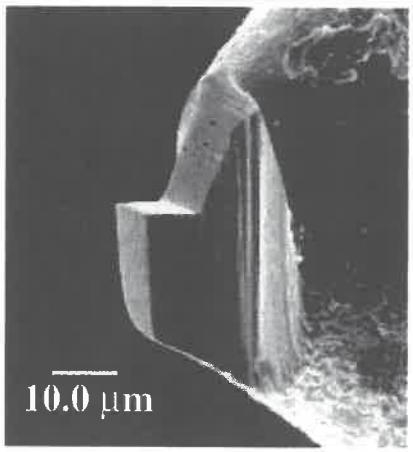

Figure 1. Tungsten carbide lathe microtool having a rectangular cross-section.

Microgrooving/threading tools are fabricated by ion beam sputtering to have a variety of shapes. This includes tools intended for cutting rectangular, trapezoidal and triangular cross-section grooves. A microtool having a triangular cross section is shown in Figure 2. This tungsten carbide tool has a 5° back rake angle. A particular ion beam/ target geometry is used to create extremely sharp cutting edges for this and all other microtools. In general, an edge created on the side of facets furthest from the ion source has the smallest radius of curvature. This effect is due to the Gaussian nature of the beam and is described in detail elsewhere[4]. A clear demonstration of a sub-micron radius of curvature along a cutting edge is shown in Figure 3.

This image is taken from a symmetrical 4-facet micromilling tool having a tool width of 12 μm. The projection shown in Figure 3 is parallel to the tool axis and the micrograph displays the intersection of two ion beam sputtered facets. It is estimated that FIB sputtered facet edges have radii of curvature of 0.1 μm or less.

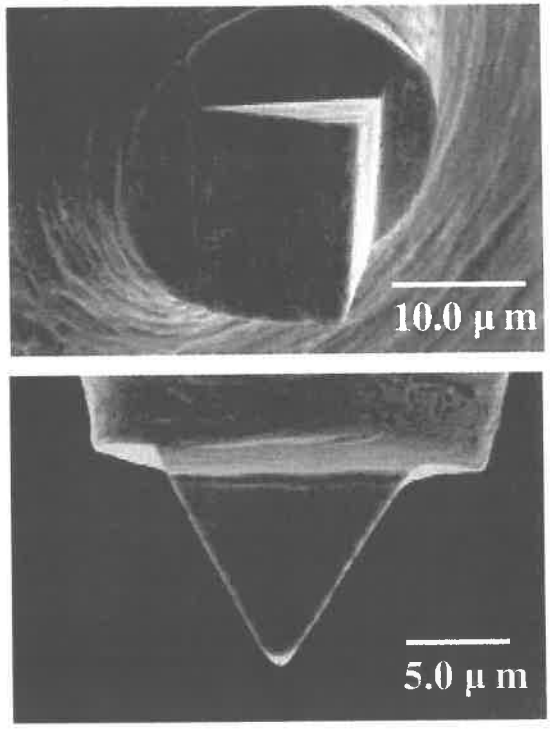

Figure 2. Tungsten carbide microtool having a triangular cross-section.

ULTRAPRECISION MACHINING

Focused ion beam fabricated microtools have been tested by machining a number of different materials including Al 6061-T6, PMMA and Macor™. For this we employ a Precitech Optimum 2000 lathe. According to manufacturer's specifications this instrument has linear laser holographic scales and read-head assemblies that provide stable positional feedback for both axes with 8.6 nm-resolution. Machining of different materials has consisted of cutting helices such as those shown in Figure 4. For these experiments water continuously flushes workpieces during ultra-precision machining. After machining, workpieces are rinsed with isopropyl alcohol. The scanning electron micrograph in Figure 4.a. shows portions of a groove cut in 1.38 mm diameter PMMA. The pitch is 50 μm and the total groove length is 420 mm. The total time to cut PMMA is approximately 30 seconds using a feed rate of 10 mm/min (single pass). Measurements with a calibrated scanning electron microscope show that the micromachined groove is consistently 13.1 μm wide over the entire cylinder length, and nearly the same as the tool width, 13.0 μm. Figure 4.b. shows a Macor cylinder machined with a focused ion beam fabricated microtool. A series of helices are machined along the length of this workpiece bounded by several bands also cut with the same microtool. The grooves machined into this Macor sample are 20 μm deep and involved 10 passes. No offset error from multiple passes is detected using high resolution SEM. Using a microscope focused on the microcutting tool we observe chip formation during ultraprecision machining.

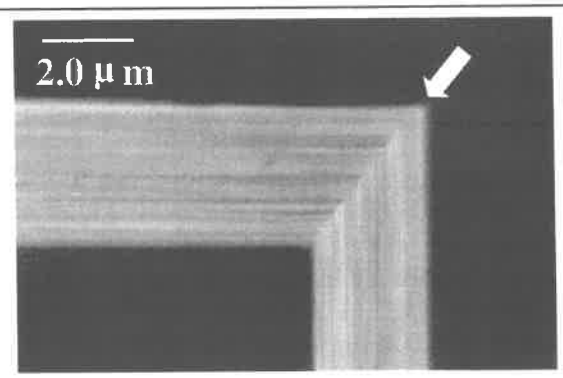

Figure 3. Sharp cutting edge of a four-side, tungsten carbide micro-end mill tool.

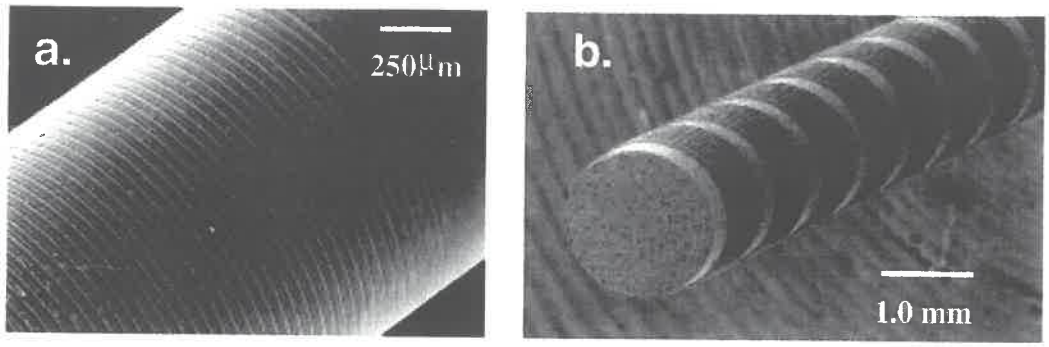

Figure 4. Cylindrical workpieces machined with FIB-fabricated microtools. Helical grooves are machined into (a.) PMMA, (b.) Macor ™

SUMMARY

This work successfully extends conventional machining techniques to the microscale in order to fabricate curvilinear features. Focused ion beam sputtering is used to shape micro-grooving / threading tools that have well defined back and side rake angles, cutting edge widths and cross-sectional shapes. A clear demonstration of cutting edges having sub-micron radius of curvature is presented. Focused ion beam tool fabrication has the advantage that almost any conceivable tool geometry can be fabricated on a scale that is well below those reached by grinding methods. This study demonstrates examples of micromachined curved features, including helices on cylindrical substrates.

ACKNOWLEDGEMENTS

The authors value the efforts of M.B. Ritchey (SNL) for SEM and S. Moncrief (LTU) for ultraprecision machining. MJV acknowledges support from the Louisiana Board of Regents. Part of this work was performed at Sandia National Laboratories and is supported by the United States Department of Energy under Contract No. DE-AC04-94AL85000. Sandia is a multiprogram laboratory operated by Sandia Corporation, a Lockheed Martin Company, for the United States Department of Energy.

REFERENCES

1. Thornell G and Johansson S, "Microprocessing at the Fingertips," *J. Micromech. Microeng.*, 1998, **8**, 251-262.
2. Ishitani T, Ohnishi T and Kawanami Y, "Micromachining and Device Transplantation Using Focused Ion Beam," *Jap. J. Appl. Phys.*, 1990, **29**, 2283-2287.
3. Vasile MJ, Biddick CJ and Schwalm SA, "Microfabrication by ion milling: The lathe technique," *J. Vac. Sci. Technol. B*, 1994, **12**, 2388.
4. Vasile MJ, Friedrich CR, Kikkeri B, and McElhannon R, "Micrometer-scale machining: tool fabrication and initial results," *J. Prec. Eng.*, 1996; **19 (2/3)**, 180-186.
5. Adams DP, Benavides GL, Vasile MJ, "Micrometer-scale machining of metals and polymers enabled by focused ion beam sputtering," *Mat. Res. Soc. Proc.*, 1999; **546**, 201-206.
6. Harriott LR, "A second generation focused ion beam micromachining system," *Proc. SPIE*, 1987; **773**, 190,

DESIGN OF A LINEAR HIGH PRECISION ULTRASONIC PIEZOELECTRIC MOTOR

Markus G.Bauer, Thomas A. Dow
North Carolina State University, Raleigh, NC 27695

INTRODUCTION

Ultrasonic piezoelectric motors can be designed to use either traveling waves or standing waves to generate motion. Piezoelectric standing wave motors, the emphasis of this work, use a combination of flexural, torsional or longitudinal vibrations of a piezoelectric actuator. One vibration produces a normal force, while the other vibration generates motion that is perpendicular to the normal force. This combination creates a friction based driving force between one stationary component, the motor, and the object to be moved. The amplitudes of the vibrations and the phase between them are the most important parameters that influence the performance of the motor. Variation of the phase alone can be used to control the motor. A phase of 0° between force and motion will not generate slideway motion, 90° results in maximum slidway velocity in one direction and 180° changes the direction of slideway motion.

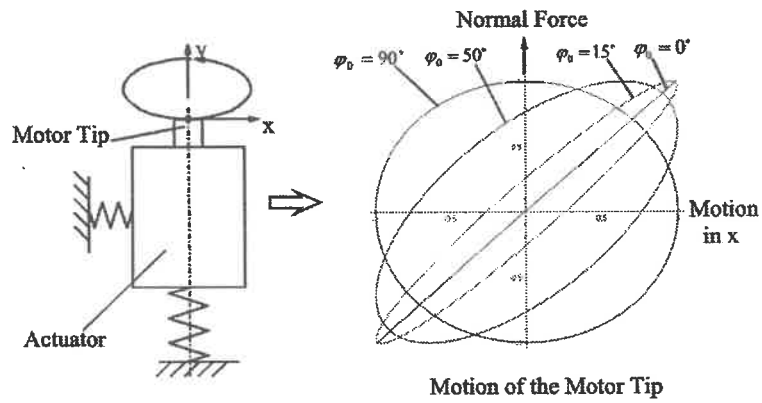

Figure 1: Influence of the phase between normal force and motion

Generally speaking, any structure that can be made to vibrate in orthogonal directions with sufficient magnitude can be used as a motor. A standing-wave motor produced by Nanomotion Ltd. is illustrated in Figure 2. This motor uses the first longitudinal resonance of the piezoelectric material to generate a sinusoidal normal force and the third bending resonance to generate a force in the direction of motion. It is made from a single block of piezoelectric material divided into 4 sections. Applying the voltage to different sections changes the direction of motion of the slideway. However, because both vibrations are excited using a single voltage, the phase between force and motion cannot be changed.

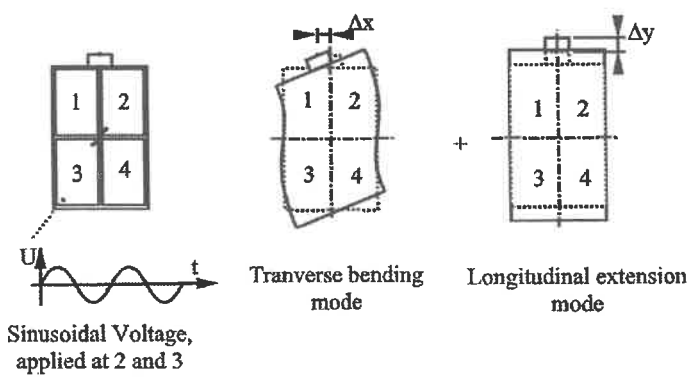

Figure 2: Nanomotion Motor, Mode Shapes

DESIGN OF NEW ACTUATOR

The objective of this project is to design an actuator that allows normal force and sliding motion to be controlled independently. The normal force can then be kept at an optimal level while the amplitude of the sliding motion and the phase angle between sliding motion and normal force can be used to control slideway direction and speed.

Methods of analysis

To implement the design objective, the motor must have one mode shape that will generate a normal force and one mode shape that generates only sliding motion (and no component of normal force). The resonant frequencies of these two modes must be close enough to each other (~500 Hz) so that a single excitation frequency will amplify the stroke in each direction by the resonance effect.

Analytical models of the actuators were used to approximate the system response. It is necessary to model the motor as a continuous dynamic system to include all natural frequencies. To allow an exact prediction of both natural frequencies and mode shapes, it is necessary to include all details of the design such as any glue joints that exist. As the motors grew in complexity, finite element analysis (FEA) was used to numerically determine all natural frequencies and mode shapes. The results were then analyzed and the dimensions of the system are optimized. This process was repeated until a system was obtained for which the two desired modes are at similar frequencies and have coincident nodes that can be used to attach a support.

Prototype designs

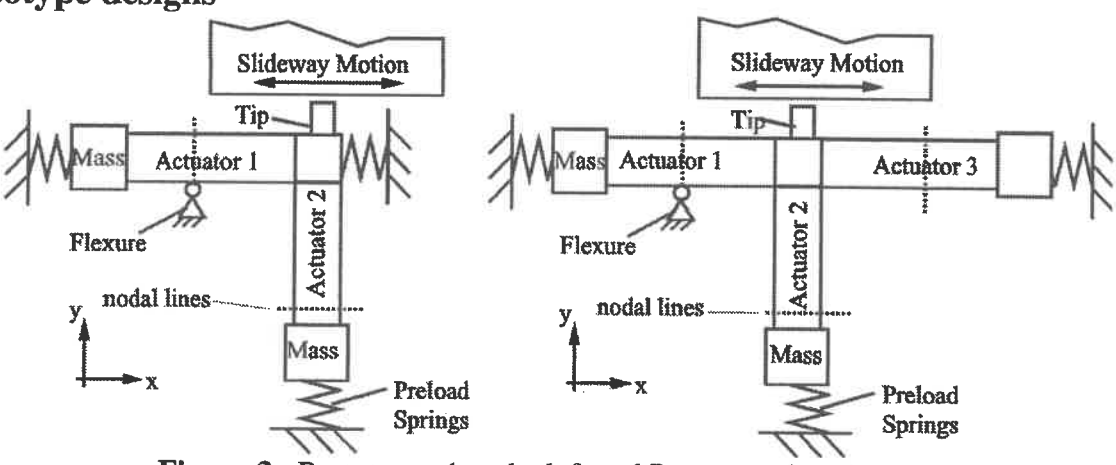

Figure 3. Prototypes 1 at the left and Prototype 2 at the right.

Prototype 1

The principle for the first two prototypes of the standing wave motor was to use two orthogonal actuators, as shown in Figure 3, and to excite each at one longitudinal resonance. Prototype 1, shown on the left, used two orthogonal piezoelectric actuators glued at right angles to a metal block to which the tip was attached. The two masses at the ends were added to adjust the position of the vibration nodes or points of zero amplitude. The location of these nodes is an important aspect of the design because this is where the motor is attached to the frame to support the drive loads.

Actuator 1 provides excitation in the direction of slideway motion, and Actuator 2 changes the normal load at the contact point between the ceramic tip on the motor and the slideway drive surface. Motion of the slideway to the right or the left depends on the phase angle between the motion of the drive piezoelectric actuator (Actuator 1) and the loading actuator (Actuator 2). The springs are used to preload the two actuators to keep them in compression and avoid damage to the brittle ceramic.

Experiments showed that, when Actuator 2 was excited with +/- 100V at 44.8kHz, the motor produced considerable slideway motion (in only one direction) and a pushing force of 5N. The excitation of actuator 1 does not influence the motor's performance significantly. A change in phase between both excitations changes the magnitude of the pushing force and slideway velocity to some extent, but does not allow a reversal of the direction of motion.

Prototype 2

The T-shaped geometry in Prototype 2 was introduced to create symmetry with respect to the bending motion of Actuator 1 when Actuator 2 is excited. In this design, the tip does not bend and no sliding motion is caused by excitation of Actuator 2. It is not possible to improve the behavior of the other actuator in the same way, because the tip has to be pressed against the slideway. When Actuators 1 and 3 are excited to generate sliding motion, bending motion occurs in Actuator 2. The dimensions of the motor can be chosen such that rotation of the tip is small, but it cannot be eliminated entirely by symmetry (as done for the other direction). Consequently, longitudinal excitation of Actuators 1 and 3 results in bending motion of Actuator 2, which in turn leads to bending in Actuators 1 and 3. Since bending of these is part of the mode that generates the normal force at the tip, the longitudinal excitation of Actuators 1 and 3 also results in a dynamic normal force at the tip. Thus, both modes are still coupled, although the advantage of this prototype is that the effect of one mode on the other is much smaller than in Prototype 1.

Experiments showed that a dynamic normal force of +/- 30N can be generated with a voltage of +/-100V applied at Actuator 2. Unlike Prototype 1, the excitation of Actuator 2 in Prototype 2 generates predominantly a dynamic normal force at the tip (the thrust force is very small). A maximum slideway velocity was measured at about 0.5m/s, when both actuators were simultaneously excited. The slideway velocity is about 15 to 20% higher in one direction than in the other, due to the coupling of both modes.

The major disadvantage of this motor is that the natural frequency of the mode that generates the thrust force is about 1.5kHz above the natural frequency that generates the normal force. This difference has to be minimized to at most 500 Hz for the motor to function. No matter how well the analysis is done to develop the motor it is virtually impossible to build it such that both resonances are at exactly the same frequency. It must be possible to modify the length or width of one actuator or the attached mass to fine-tune the motor. A way to do this has not been found, because all alterations of Prototype 1 and 2 influenced both mode shapes and resonant frequencies to about the same extent. If, for example, the length of one actuator is reduced, each individual resonance increases, but the difference between both resonances does not change significantly.

Prototype 3

The goal for Prototype 3, illustrated in Figure 4, is to eliminate the problem of the coupling between different mode shapes. The shape is basically the T-shaped Prototype 2 without the lower half of the T. This design also eliminates the glue joints found in the first two prototypes. It consists of two piezoelectric plates with a thin brass electrode between them. The electric field is applied between one of the electrodes on the outer surface (1) or (2) and the brass electrode in the center. Applying a sinusoidal voltage at the outer electrodes (1) extends and contracts the upper half of the actuator and thus excites the bending mode. An electric field that extends across the actuator will excite the longitudinal mode of vibration. This is done by applying voltage to the inner electrodes (2). Prototype 3 uses the fifth bending mode to generate a dynamic normal force and the 2nd longitudinal mode to generate sliding motion in a very similar manner to Prototype 2. Because these two modes are orthogonal, it is virtually impossible to have any interaction between them.

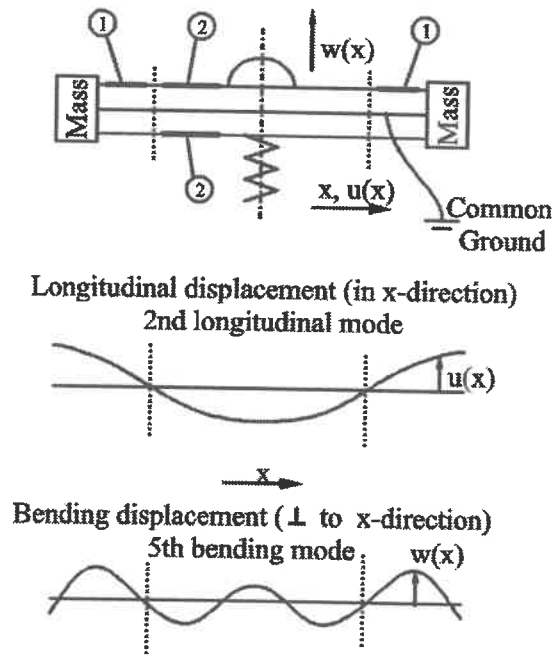

Figure 4: Prototype 3

Initial measurements of the frequency spectrum for the forces at the tip indicate that the resonances for the normal force and for the thrust force differ by about 2 kHz. This difference can be reduced by carefully adjusting the mass at the ends of the motor. Once the motor has been modified so that the normal force is large enough, and so that the difference between the resonance for the normal force and the resonance for the thrust force is less than 500 Hz, its performance can truly be assessed.

CONCLUSION

Prototype 1 and Prototype 2 are capable of producing a very large dynamic normal force, which exceeds the strength of the motor when the maximum electrical field is applied. Symmetry is used to reduce coupling between modes in Prototype 2. However, for these prototypes the extent of coupling between both modes of interest depends on specific dimensions of actuators and masses.

Coupling is no longer an issue for Prototype 3, because the bending mode and the longitudinal mode are naturally orthogonal and thus independent of one another.

Further experiments are underway to adjust both resonances to the same frequency and to evaluate the ability of Prototype 3 to generate the desired slideway motion.

REFERENCES

1) US Patent #5616980, April 1, 1997

Affordable, Compact, Research Single Point Diamond Turning Machine

Allen Bohart, Pat Collins, Scott Faulk, Dr. Craig Halvorson,
Dr. Michael McClellan, Dr. Keith Shillito
Schafer Corporation, Livermore, CA 94550

1. INTRODUCTION

Schafer Corporation's Energy and Environment Division has developed an affordable, compact single point diamond turning machine for production of experimental micro-machined parts. The system has been dubbed "SPRL", an acronym for Schafer Precision Research Lathe. Materials that have been machined with this system include copper, aluminum, polymer foams, aerogel and silicon.

The system was assembled and made operational in about 3 months from readily available commercial off-the-shelf parts, including two Aerotech ABL-2000 air-bearing stages with linear motors, an Aerotech DR-500 amplifier module, and an Aerotech Unidex 600 controller. The controller receives input from a standard Pentium-class PC running Windows NT 4.0 and Aerotech's U600 MMI software. The stages are directly mounted to an isolation table comprised of a 60" x 36" x 10" granite slab, and 4 Newport air isolation mounts. The spindle is an off the shelf 4-inch Blockhead spindle acquired from Professional Instruments, Inc, powered by a Hewlett-Packard 6228B DC power supply. A Cohu video camera with a 10x microscope objective is used for fine placement of the tool with respect to the part. The system is operated in a 12' by 24' clean room environment (Level 1000) to maximize temperature stability (to within ± ½ °F) and control airflow. Total expenditures for purchased components (excluding the existent granite slab and Newport isolation mounts) was less than $70K. The compact design of SPRL, shown in Figure 1, with direct mounting of the slides to the granite slab offers reduced vibration and minimized moment arms for the X and Y axis couplings.

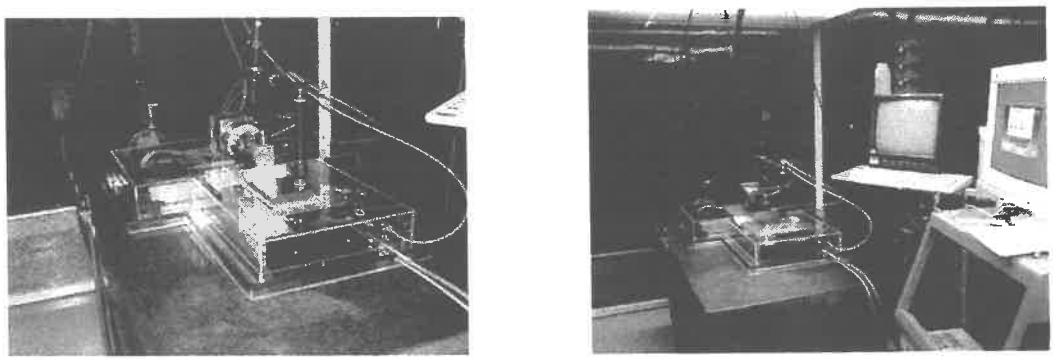

Figure 1. Views of the SPRL Machine

2. MACHINE CAPABILITIES

The Schafer SPRL is a single point diamond turning lathe that has exceptional capabilities, considering it's affordability and compactness. The machine is capable of 4 nm resolution on both axes, with the ability to produce sub-micron surface finishes. The stages consume only 0.3 cfm of compressed air, allowing the machine to be run with bottled nitrogen, instead of using an air compressor. The machine is programmable in RS-247, 447 CNC programming language and uses standard C libraries. Initial machining results are promising, with no discernible noise or vibration problems.

Typical parts produced on SPRL are copper and aluminum casting molds, foam spheres, and small-scale silicon optics. The casting molds are flats with various surface figures machined into them. Typical surface figures are sine waves and multi-modal sine waves with sub-micron amplitudes, and varying wavelengths. Spheres are machined using approximately 50 mg/cc polystyrene foam. The silicon optics are of varying surface figure, with 40-100 Å rms surface finishes. Samples of the various parts and materials that we have machined are shown in the figures below.

3. PERFORMANCE/EXAMPLES

As a custom designed machine SPRL has been built to produce parts that are required by the Department of Energy for the Inertial Confinement Program. It is capable of producing surfaces with roughness less that 100 Å rms and very detailed surface morphologies.

SPRL is used to produce generally small parts that are approximately 1000μm x 1000μm in area with the following types of features on the surfaces:

Ramps : These ramps range from 10μm to 400μm thickness.
Step: Step size of approximately 100μm.
Sine Waves : We have made a wide range from 1μm peak-to-valley, 20μm wavelength, and 20μm thickness to 40μm peak-to-valley, 200μm wavelength, and 20μm thickness.
Ramp/Sine Wave: 2μm peak-to-valley and 20μm wavelength on 10μm thick to 20μm thick ramp.

Several examples of the types of products we have machined are shown below.

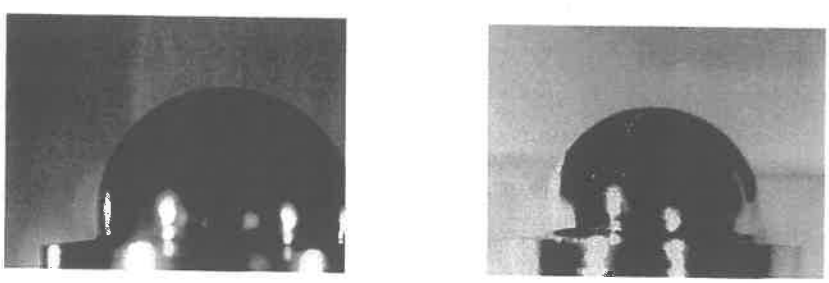

Figure 2. Copper Sphere Process Development for Polymer Foam Spheres

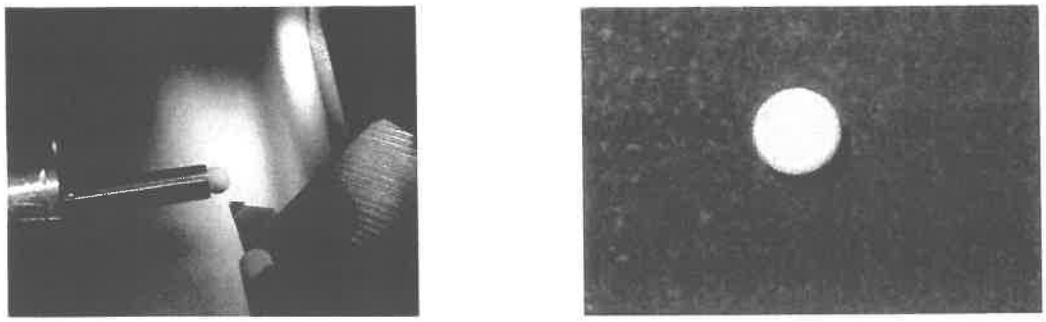

Foam machining in-process on SPRL

Completed sphere (4.5mm diam.,40mg/cc)

Figure 3. Polystyrene Foam Sphere

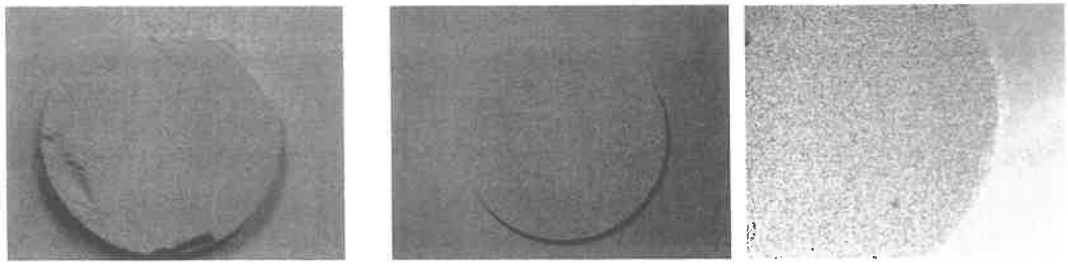

Original cast surface.

SPDT facing cut.

Fine pore structure.

Figure 4. Face cut of SiO_2 Aerogel (< 5 mg/cc density)

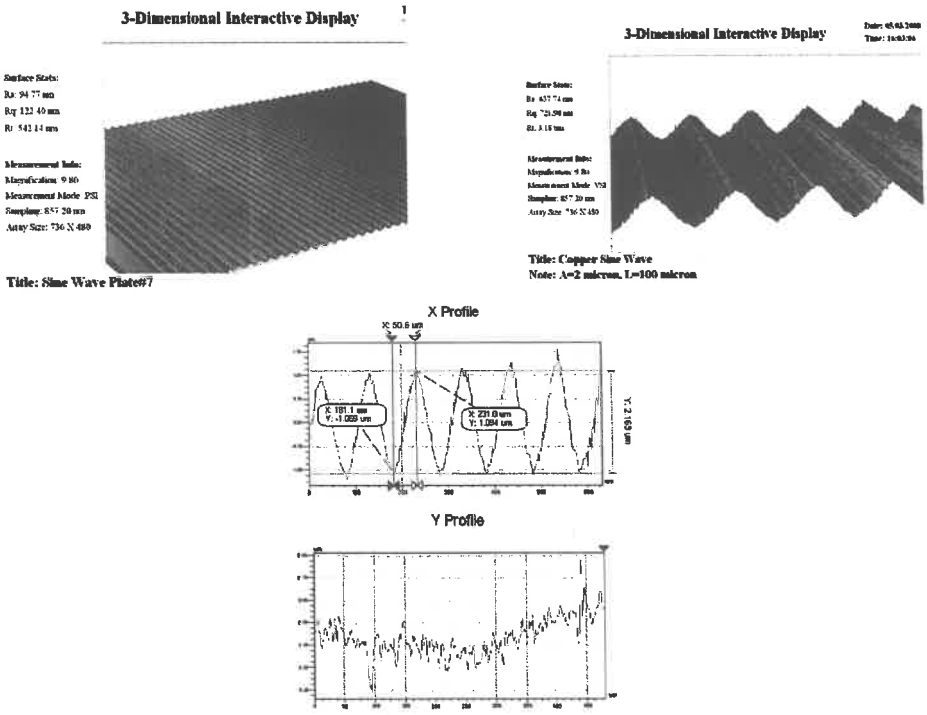

Figure 5. Copper Sine Wave Plate, Amplitude: 2μm , Wavelength: 100μm. Characterizations using VEECO White Light Interferometer.

New Technology and Novel Design make Sub-Micron Production Practical

Michael Clarke, Michael G. Pierse, Markus M.W. Knuefermann, Roger R.F. Read
Cranfield Precision, Cranfield, Bedfordshire, England

Introduction

This paper is based on the design and testing of the Cranfield Precision DeltaTurn40 lathe (Figure 1). This machine has been designed as a small chucking lathe for sub-micron production turning of complex parts in conventional materials and also hardened tool and bearing steels.

Initially, we will describe in detail how several new novel technologies have been brought together to challenge the way current machines are designed. We will then show how, in production, the machine is capable of producing parts with sub-micron size control at capabilities greater than *1.67* C_{pk}. The paper also presents results from on-going hard turning tool trials showing how the machine can obtain excellent surface finishes and hence challenge conventional grinding processes, even when bearing ratios are required that conventionally could not be achieved with turning.

Technical Developments

Figure 1: The DeltaTurn40

Due to the small size of the machine several novel technical developments were brought together making a unique machine tool that overcomes most of the errors normally found in precision machine tools.

The key elements brought to the machines design are:

- Voice coil motors
- Two axis encoder
- Hydrostatic bearings
- Space frame construction

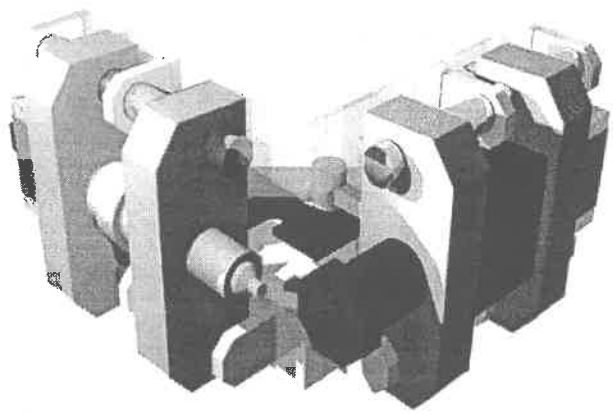

Figure 2: Construction

Voice Coil Motors - Based on the moving coil actuators used in loudspeakers, voice coil actuators apply linear force to both the X and Z axes on the machine. Linked with high-speed digital signal processing (DSP) they provide high dynamic performance, coupled with zero wear parts. Benefits include precise, frictionless positioning, high acceleration and stiffness, and also freedom from backlash and lateral disturbance - unlike conventional ballscrew drive systems. The motors are positioned to apply motive force directly onto the centre-line (and centre of gravity) of each axis to drive the workpiece and turret axes. The intersection of the force vectors also falls within the working volume of the machine.

Two Axis Encoder - The axis positioning system comprises a Heidenhain [1] grating plate with orthogonal graduations and reference marks (sometimes referred to as a tartan scale) and a non-contacting scanning head that detects reference and motions in both X and Z directions. On this machine the scale is mounted on spindle centre-line, off to the side of the Workslide Z axis, with the scanning head mounted off the side of the Toolslide X axis. With the system measurement point placed in this configuration, as close as possible to the cutting point and at precisely workpiece centreheight we are able to eliminate virtually all Abbé errors [2]. Several advantages quickly come to mind when utilising this system: -

- Axes positions measured directly and with reference to each other – not looped through base structure.
- Each axis motion is measured not only in the critical direction but also orthogonally, therefore any lateral or yaw error motion on either axis is sensed and is automatically corrected by the other axis.
- Orthogonality of machine axes is permanently determined by the precise grid pattern alignment on the encoder plate and can, if required, be further error corrected in software. Precise physical axis alignments are not required.
- No forces in the machine measuring loop.

Hydrostatic Bearings - The machine utilises round bar temperature controlled hydrostatic bearings on both linear axes, with a kinematically constrained (but not over constrained) configuration of pads, equispaced above and below the axis centreline to provide precision with ease of manufacture and assembly. The Workspindle can be specified with either air or hydrostatic bearings depending on the application. Hydrostatic bearings are utilised for smoothness of motion, high damping, high static and dynamic stiffness and enduring precision.

Space Frame Construction - Both axes on the machine are of lightweight construction to permit maximum acceleration. The axes are attached through the hydrostatic bearings to a triangulated space-frame 'Delta' base construction as shown above in Figure 2. This structure is supported on a system of isolation feet to the machine's enclosure. This base has been designed utilising FEA techniques to optimise placement and type of structural materials used to give a stiff, damped structure with a minimum of mass – the first measured natural frequency (highly damped) was 350Hz. This configuration allows for a compact machine design that can accommodate all the services for air and hydrostatics within its own enclosure without affecting the performance of the machine.

Tool Turret with Error Correction - To provide the capability of multiple operations on a part, the machine is fitted with an 8 position tool turret. To eliminate any machining errors due to non-repeatability of index, variation in the indexing positions are logged in both the X and Z planes and correction factors applied.

Production Manufacturing

Process Control - To maintain the consistency of size despite process related effects, (particularly tool wear) the automated part handling places each completed part in an integrated, dedicated air gauge measurement device with 0.1μm resolution of size for 100% inspection. Data for each of up to 5 critical features (OD, ID or length) is analysed for trend and correction factors are fed to the CNC controller for analysis and consequent change to tool position offsets. Detrimental middle-to-long-term thermal drifts are thus prevented from causing size fluctuation. Statistical Process Control techniques are applied to the finished part measurement data to monitor performance.

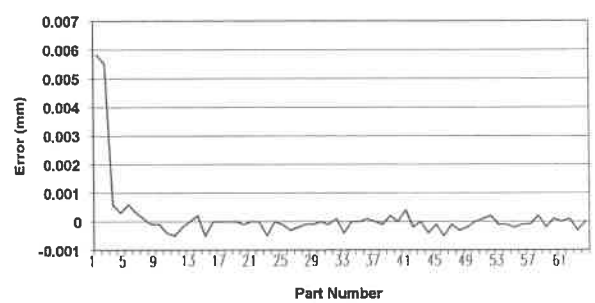

Figure 3: Diameter error log

Additionally, cutting force monitoring (X and Z) can be used to identify tool failure and to monitor the onset of tools reaching the end of their useful life. This all helps to make highly accurate extended production runs straightforward: Any error from the first part is applied 100% to the tool offset data to approach a correctly sized third part (part 2 is being machined whilst part 1 is being measured). From this point onwards an 8 part moving algorithm is used to control size variation due to tool wear and environment changes.

The chart in Figure 3 shows the measured size error, for the finish boring of 430F Stainless Steel to $\varnothing\ 5mm$. The processing was at $70\ ^{m}/_{min}$ surface speed (V_c) with a feedrate (f) of $0.03\ ^{mm}/_{rev}$ and $50\ \mu m$ depth of cut (doc).

It also shows the part size being established, and subsequently maintained for the production run.

The example below shows the ability of the machine to perform hard turning operations (replacing costly and time consuming grinding operations). CBN tool technology is used for the hard turning of steels, generally above *58 HRc*: both conventional and stainless steels have been processed on DeltaTurn. These processes are 'dry cutting', requiring no coolant or cutting lubricant, thus eliminating the environmental hazards of the removal and disposal of these fluids and compounds.

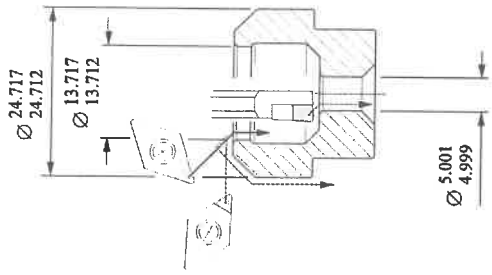

Material: 535A99 BS970: Part 1: 1983 (EN31), through hardened to *58-62 HRc*

- V_c = 225 $^m/_{min}$ (170 $^m/_{min}$ for 5 mm bore)
- f = 0.03 $^{mm}/_{rev}$
- *doc* = *0.05 mm* (2 passes)
- Standard Sumitomo CBN tools: -
- Inserts: DCMW070204BNX10NU
- Brazed tip bar: BNBB04BNX20

Figure 4: Component and data

Post-process analysis of the completed components displayed roundness errors of < *0.2 µm*, and concentricity errors between features of < *1 µm*. Surface Roughness values were achieved (in the hard turning of steel) to better than *100 nm* R_a. Such high quality roundness errors improve the part (∅) accuracy capability. To achieve the accuracies quoted within this paper it is important that sufficient stock is left on the component critical features prior to finishing to allow 2 cuts. The first cut is to clean up the part (to < *1 µm* run-out) which then allows the second cut (at consistent pressure) to achieve the excellent (< *0.2 µm*) roundness levels.

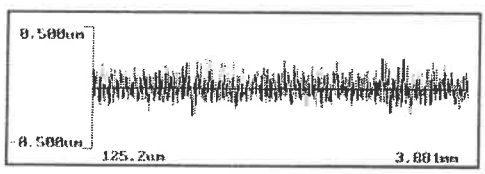

Figure 5: Bore surface roughness

The roughness trace shown in Figure 5 is from the *5 mm* bore of the part shown in Figure 4. The finish obtained was *75 nm* R_a. The machine has also been used with both PCD and natural diamond tools (on non-ferrous materials) to achieve roughness values of *~30 nm* R_a

Surface Finish - Recent work carried out on the DeltaTurn40 in co-operation with several industrial partners has proven the capability of the DeltaTurn40 not only to manufacture components with nanometric surface roughness, but it is also possible to maintain low surface finishes throughout the tool life. Typical surface finish requirements for precision components are between *100-200 nm* R_a, sometimes with a combination of different finish parameters being requested (e.g. R_a and bearing ratio).

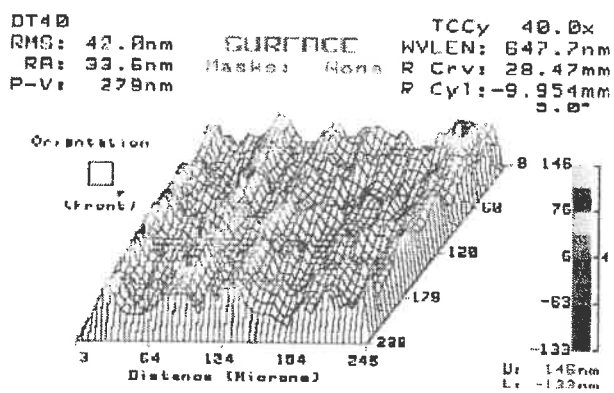

Figure 6: Surface plot of a turned component
R_a = 33 nm

A statistically designed set of experiments has been carried out on DeltaTurn40 in co-operation with De Beers Industrial Diamonds UK to prove the machine's capability to achieve low surface finish values [3].Figure 6 shows a 3D-plot of a component machined during these experiments recorded with a 3D optical surface profiler. At low feed rates it was possible to achieve surface finishes down to *31 nm* R_a. Statistical evaluation of the data gathered so far reveals an average surface roughness of *42 nm* R_a (Figure 7), at suitable cutting conditions.

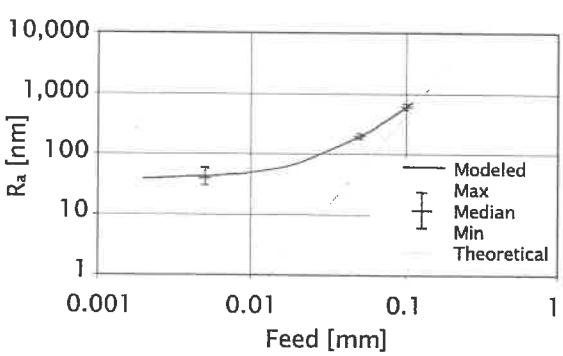

Figure 7: Finish vs. Feed (0.4 mm rad tool)

The disadvantage encountered when manufacturing these very good surfaces is the requirement for a low feed rate. The low feed rate not only increases cycle times, but also increases the contact time between tool and workpiece. Since tool wear in CBN cutting tools is roughly proportional to the contact time only a small number of components can be machined with any one tool. Combinations of higher feed rates and larger tool radii allow the manufacture of surface finishes in the order of *100 nm* R_a while reducing machining time by a factor of 20. This in turn increases the number of workpieces, which can be machined per cutting tool.

Tool life tests carried out on DeltaTurn40 show that under typical machining conditions CBN tools have a life in excess of *40-60 min* in contact with the workpiece. This exceeds tool manufacturers' tool life data (typically *30-45 min*) by a significant margin. During the tool lifetime surface finish drifts as the tool wears, but can be maintained within acceptable limits. Only when excessive tool wear occurs can a rapid drop off in surface finish be observed.

Modified surface finishes - The degree of process control achieved on DeltaTurn40 not only allows for very precise size and finish control, but also allows the designer to tailor the surface of the part in the sub-micron level as shown below.

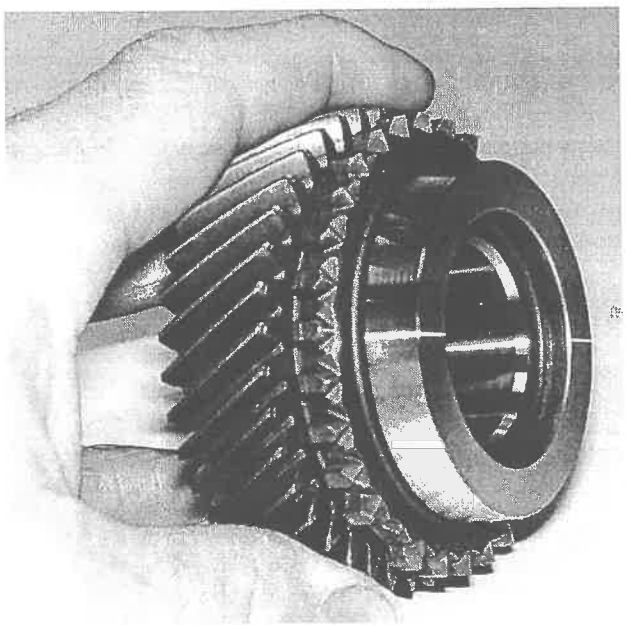

Figure 8: Synchro Cone

The taper of a Synchro cone normally has a specification for surface finish (R_a) and bearing ratio (*tp*). Bearing ratio is the length of bearing surface (expressed as a % of the measured length) at a specified depth below the highest peak of the surface and can be difficult to achieve with a turning process. On analysing the requirements it was found that by modifying the tool path in the sub-micron level the required finish could be achieved. The image below (Figure 9) shows a typical pattern used for Synchro cones, the surface has > *1 μm* deep grooves equispaced along the surface. The depth, length and spacing of these grooves is critical to bearing ratio, where as tool rad and feedrate determine the overall surface finish of the feature.

Figure 9: Surface image

Process trials – the next stage - Further work will focus on achieving the best level of surface finish while maintaining economic production rates, tool life and bearing ratios and will also look at interrupted cuts and better exploitation of the wiper tool geometry in achieving best possible surface finishes.

Conclusions

The above results have shown that by taking a global approach to machine design and applying optimised process parameters, sub-micron manufacturing tolerances at better than 1.66 capability ratios, with part roundness of *0.1 μm* and surfaces finishes below *75 nm* R_a are readily achievable in an automated production environment. The materials can be ferrous and non-ferrous, and can include hardened bearing and tool steels. Further work is now underway to use the DeltaTurn40 as a diamond turning machine including adding a vacuum chuck and optical toolset station.

---

1 Heidenhain, "Turning on a Micron", Drives & Controls, page56, Sept. 1998
2 Bryan,J.B. "The Abbe Principle Revisited: An Updated interpretation",
Precision Engineering, Vol 1, pages 129-132, 1979
3 M. Knuefermann, R. Read, R. Nunn, I. Clark, M. Fleming
"Ultra-precision turning of hardened steel with AMBORITE DBN45 on the DeltaTurn40 lathe"
Industrial Diamond Review, Vol. 60, No. 585, 2/2000

A Non-Contact Linear Motion System and Its Application

Roger S. Cortesi[1], Alexander H. Slocum[2]
Massachusetts Institute of Technology, Cambridge MA

The *Axtrusion* is a new linear motion concept developed by Professor Alexander Slocum and Roger Cortesi of the Massachusetts Institute of Technology's Mechanical Engineering Department. The name *Axtrusion* comes from the shape of the axis' cross section, which in principle is simple enough to be extruded. The Axtrusion is intended for use in applications where the emphasis is on high speed, no wear, and low error motions, such as in high-speed motion of workpieces in semiconductor manufacturing equipment. It is designed to enable air bearing systems to be competitive in price with high performance ball bearings systems while providing all the advantages of a non-contact motion system.

The functional requirements of the Axtrusion concept, shown in Figure 1, are:

- No contact between the way and the carriage, allowing for very high-speed operation and zero wear. The elimination of lubrication reduces maintenance requirement and machine downtime. Non-contact is also the primary means of reducing error motion.
- Moderate stiffness by using magnetically preloaded air bearings.
- The system should be insensitive to temperature changes, thereby reducing thermal growth.
- The geometry should remain simple, and minimal precision parts and features should be used to keep manufacturing inexpensive and easy.

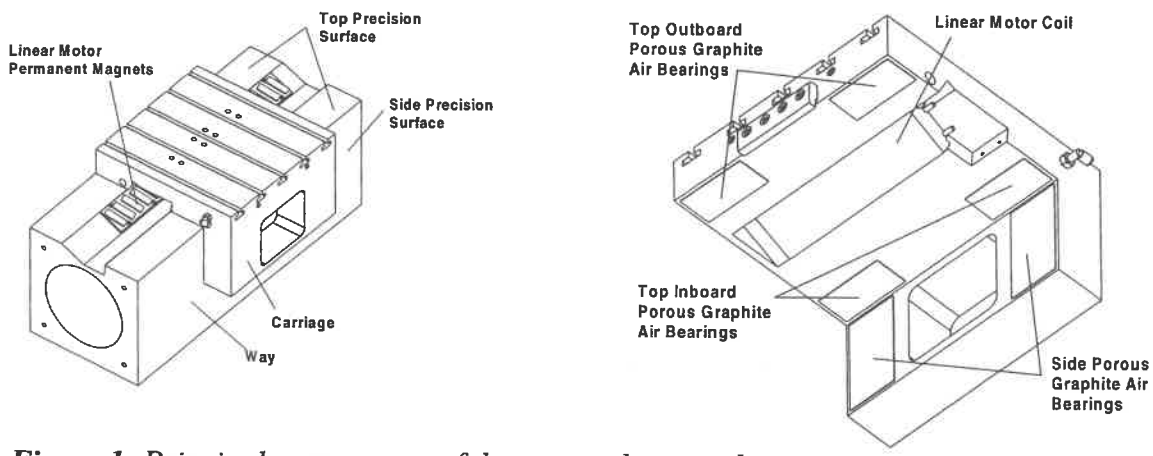

***Figure 1**: Principal components of the system that uses linear motor magnet attractive force at an inclined angle to preload all the bearing pads*

---

[1] Graduate student, Department of Mechanical Engineering, Massachusetts Institute of Technology
[2] Prof. of Mechanical Engineering, MIT Room 3-445, 77 Mass. Ave, Cambridge, MA 02139 USA
slocum@mit.edu

The attractive force between the motor coil and the magnet track preloads the bearings, which support the vertical and horizontal loads. By carefully choosing the groove angle and motor location, the designer can specify the amount of preload on each bearing pair. The pairs are the top outboard pair, the top inboard pair and the side pair. There have been many designs in the past that have used magnets to preload air bearings, but the Axtrusion appears to be the only design where a single magnet track can be placed to evenly preload all the carriage's bearings.

Porous graphite air bearings are quite easy to work with and can easily be replicated in place, which greatly simplifies the manufacturing process. The bearings and motor coil of the prototype were potted in-place in to the carriage, allowing the axis to be assembled in just under 2 hours. Granite was used for the ways because of a special characteristic: if cracked or chipped, the granite will fracture completely downward without creating the slightest crater rim. This allows the air bearings to continue to slide over the fracture unimpeded.

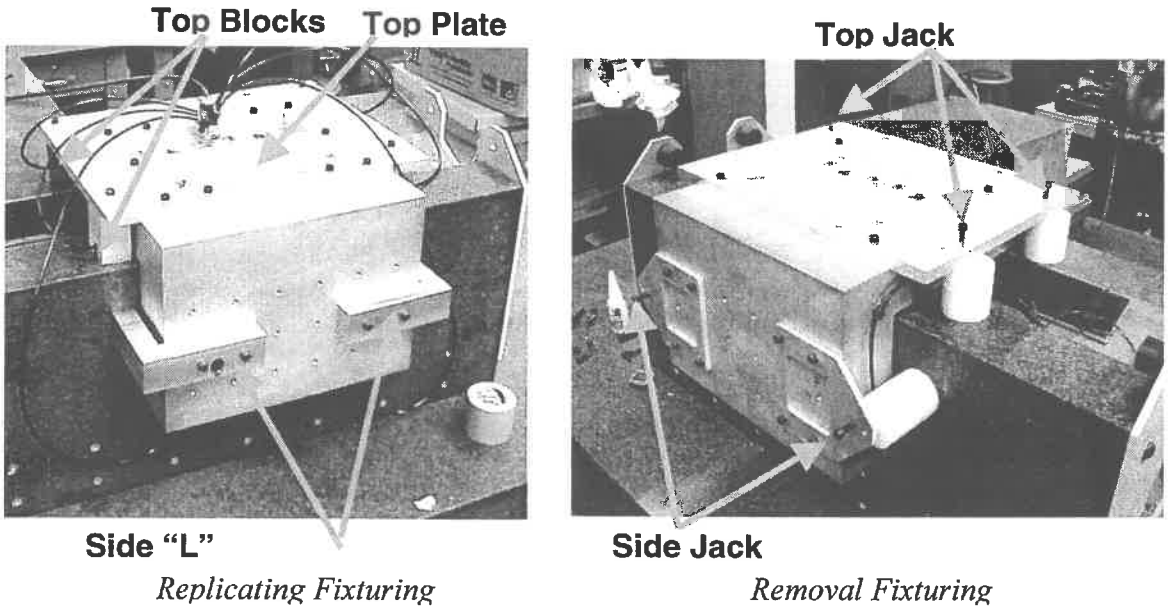

Replicating Fixturing *Removal Fixturing*

Figure 2: The replicating fixturing (left) allowed the assembly of the Axtrusion prototype in 2 hours. The jacks on the removal fixturing (right) are used to draw the motor coil away from the magnets enough to be able to remove the carriage from the way.

The static stiffness was measured by adding weights and recording the deflection with an interferometer. The vertical stiffness was found to be 422 N/micron with 100 psi air supply. The dynamic performance was determined by modal analysis. The animated modes are shown at http://pergatory.mit.edu/research/Cortesi/modal/modal.htm. The results are summarized in Table 1.

Freq [Hz]	Damping [%]	Magnitude [Output/Input]	Comments
362	3.8	48.11	Left front top air bearings moving the most.
487	1.9	5.5	Deformation of carriage spreading "hinge"
491	0.1	0.007	Carriage rocks back and forth, pure air bearings.
607	3.3	32.8	Main carriage mode with center oscillating in z.

***Table 1**: Modal analysis summary for the Axtrusion with 100 psi air supply to the bearings*

The accuracy of the Axtrusion is affected by the change of the magnetic attraction force as the open faced motor carriage passes over the permanent magnets. This primarily causes sinusoidal pitch errors. The maximum measured pitch error is 2.44 arc seconds; the maximum yaw error is 1.59 arc seconds. For a high-speed material handling system or a modest accuracy machine tool, this is insignificant. For higher precision systems, the magnets would need to be attached to the carriage and they would be attracted to a uniform steel plate rather than utilizing the linear motor.

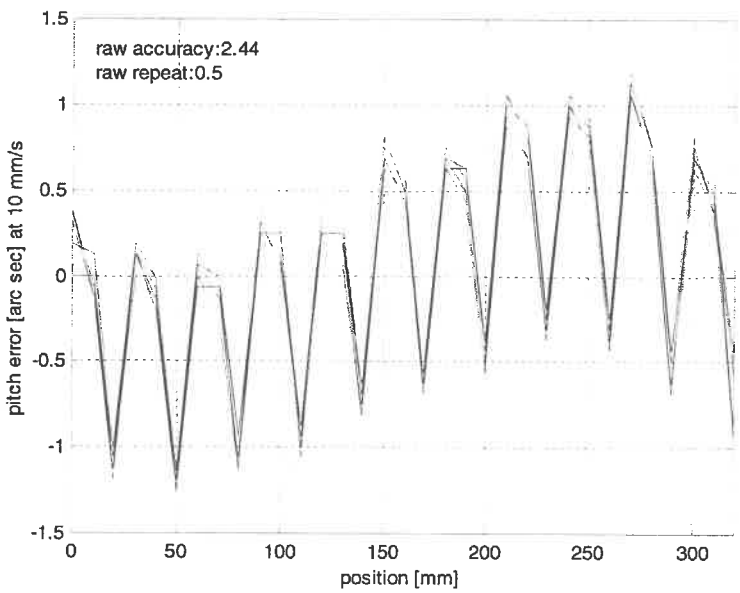

***Figure 3**: The pitch data for the Axtrusion prototype over 320 mm of travel.*

The Axtrusion is the basic building block for the *Minimill*, a desktop 3-axis milling machine. It uses two identical L's to make the machine structure for the X and Y axis.

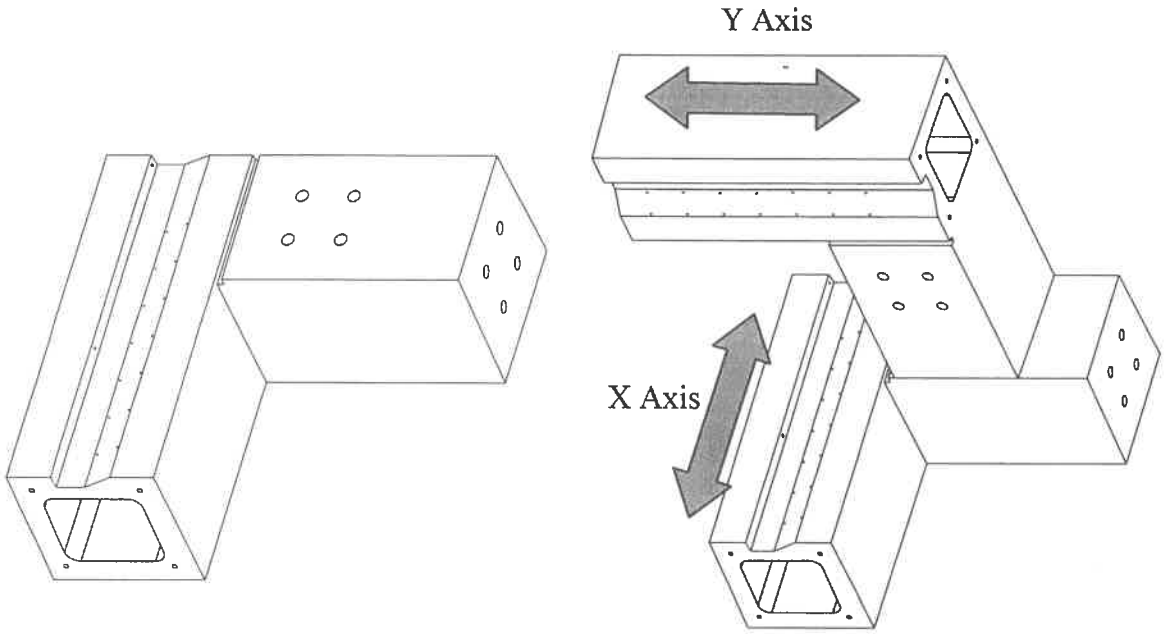

***Figure 4**: The two "L" structural concept for building the X and Y axis of the Minimill.*

Acknowledgements

The authors wish to thank the following people and companies for their generous help with this project:

- Andrew Devitt of New Way Bearings (http://www.newwaybearings.com/) for providing the porous graphite bearings, and his generous help and skill in aligning the system and then potting the bearings in place with DWH epoxy.
- Phil Greene of Dover Instrument Corp. (http://www.doverinstr.com/) for integrating the motor, scale, and control electronics, and assisting with the initial metrology measurements.
- Eli Razon of Anorad Corp. (http://www.anorad.com/) for providing the linear motor.
- Jerry Parrot and Mike Caputo of Rock of Ages Corp. (http://www.rockofages.com/) for providing the granite for the structure.

High Stiffness Air Bearing Design and Experiments for CMP Machines

Philip Greene, Zongren Shang, Douglas Bittner
Dover Instrument Corporation
Flanders Road, Westboro, MA 01581, USA

INTRODUCTION

The Chemical Mechanical Polishing (CMP) process has been developed for planarizing the dielectric layers that insulate the levels of metal interconnect in integrated circuit (IC) chips. Most CMP machines are currently using ball bearings in the main spindles and table spindles. However, along with the enhancement of the required surface performances and the prediction of increased levels of interconnect [1], the stiffness, speed, and error motion of spindles have become the key properties for achieving advanced CMP process requirements. Air bearing spindles are ideal alternative products for CMP machines. Air bearing spindles possess much lower error motion than ball bearings. In applying air bearing spindles into CMP machines, one of the most important properties of air bearing spindles is stiffness. This paper will present the results of the studies.

Because the critical performance parameters of CMP spindles are the most important factors for satisfying advanced CMP requirements for speed, error motion, and stiffness, the bearing selection and design should be carefully considered. Air bearings possess many advantages over ball bearings and oil-lubricated bearings. For instance, oil bearings produce friction heat at higher speeds and the oil degrades at higher temperatures. These are fatal problems of oil-lubricated bearings in the CMP process. Although ball bearings have some advantages over air-lubricated bearings, the error motion of ball bearings is much larger than that of air bearings. In addition, the PV value of ball bearings limits their application at high speeds, such as in the CMP process. Air bearings possess low error motion and high-speed characteristics. The major existing problem of air bearings is lower stiffness relative to oil bearings.

In order to achieve high stiffness of air bearing spindles for CMP applications, studies have been conducted on air bearing spindles. The pressure distribution of the air film became the target to reduce the side-flow effect for increasing the stiffness when using orifice-type restriction. In addition to the theoretical studies, experimental studies have also been conducted on the air bearing spindle. In the tests, the stiffness of the air bearing reached 8.7×10^8 N/m (4.97 lbs./μin) in the axial direction, and 1.9×10^9 N/m (11 lbs./μin) in the radial direction. All of the testing data of stiffnesses reached the target values from theoretical simulation within 10%. The spindle was also velocity tested to 6,500 rpm (390 meter/sec surface speed at the rotor periphery).

CONSIDERATIONS OF AIR BEARING DESIGN

Because of the high stiffness requirements, the bearing design should be carefully considered. In order to satisfy the specifications, the following issues need to be addressed:

1. Pressure ratio
2. Line feed coefficient
3. Pneumatic hammer
4. Airflow rate

In an air bearing design, the pressure ratio (outlet pressure of orifice/inlet pressure) is an important parameter because of its effect on loading capacity and stiffness. Due to the machining error, the pressure ratio was given between 0.55 to 0.75. This variation will give ~20% change in stiffness, which satisfies the specification requirements. However, once the pressure ratio was determined, the side flow of air caused a decrease in stiffness when using orifices as the restrictors. According to *Precision Machine Design* [2], a difference in the line feed correction coefficient ($1/\lambda$), which is a measure of side flow, may result in a significant change in stiffness. In order to increase the line feed coefficient, narrow and shallow grooves were used on the thrust bearings, while long and shallow pockets were used on the journal. (Fig.1).

The most common issue, which remains a serious concern, is pneumatic hammer. In order to reduce the restriction of airflow through the grooves (which increase the line feed coefficient), the depth and width of the grooves was relatively large. Consequently, these large grooves may cause pneumatic hammer. In an effort to counteract this occurrence, the grooves were reduced to the minimum size. This resulted in a reduction in the line feed coefficient, which in turn reduced the risk of pneumatic hammer. The width and depth of the grooves was 0.0125mm (0.0005").

The final concern was the airflow rate. There is no doubt that the air gap is the key parameter involved in the airflow rate. To satisfy the specification, the air gap could not be larger than 0.0127mm (0.0005"). In order to satisfy the stiffness requirements, the air gap had to be smaller than 0.0125mm, which also satisfied the air flow requirements.

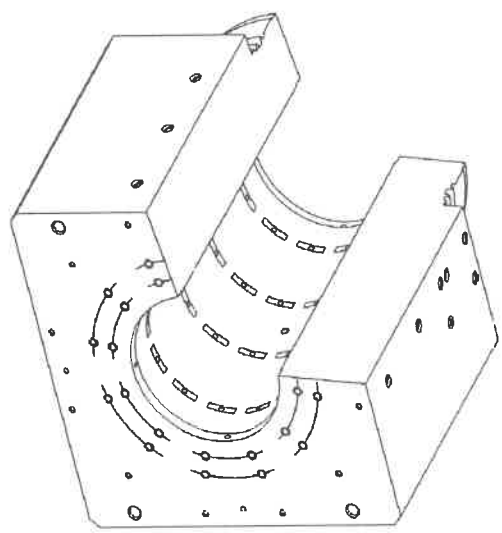

Fig. 1 Air Bearing Structure

EXPERIMENTAL RESULTS

The load versus displacement curves in both the radial and axial directions are illustrated in Figures 2 and 3. The displacements shown are of the bearing film only. The data was obtained by first measuring the combined displacements of the bearing film and the deformations of the bearing structure. The deformations of the structure alone were then measured. The differences between the two are the resultant displacements of the bearing film only.

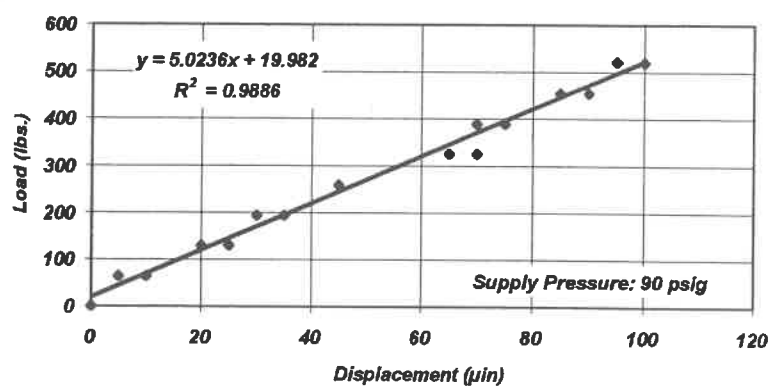

Fig. 2 Radial Load vs. Displacement

Capacitance probes measured the displacements and deformations, while an air cylinder applied the loads. The bearing supply pressure was operated at 90 psi.

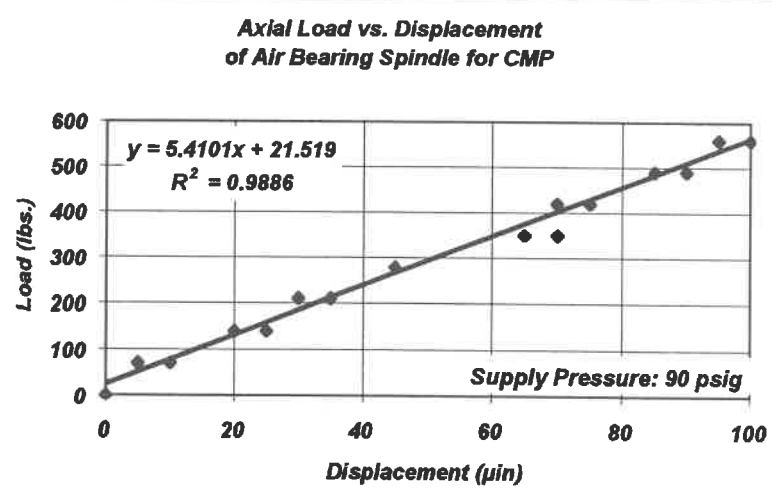

Fig. 3 Axial Load vs. Displacement

Below is a comparison of the theoretical and actual bearing stiffness and capacities:

	Calculated Stiffness	Calculated Load Capacity	Tested Stiffness	Tested Load Capacity
	Newton/meter	*Newton*	*Newton/meter*	*Newton*
Axial	8.89×10^8	2558	8.84×10^8	> 2180
Radial	1.03×10^9	2891	8.89×10^8	> 2180

CONCLUSIONS

1. The application of air bearings into the CMP process is feasible.
2. The stiffness requirements of most CMP machines (radial direction: 2.8×10^8 Newton/meter and axial direction: 6.13×10^8 Newton/meter) can be met by this design.
3. Both the pressure ratio and the line feed coefficient were reasonably designed. The pressure ratio was 0.57 and the line feed coefficient was 0.65.
4. The balance of the line feed coefficient and the pneumatic hammer should be considered when determining the depth and width of the grooves.
5. The error between theoretical calculation and experimental data is within 10%.

REFERENCES:

[1] *National Technology Roadmap for Semiconductors: Semiconductor Industry Association Report*, SEMATEC, Inc., Austin, TX, 1997.

[2] Slocum, Alexander.H., *Precision Machine Design*, Massachusetts Institute of Technology, Society of Manufacturing Engineers, Dearborn, MI, 1992.

Development of a Linear Motor Drive Testbed and Initial Thermal Behavior Results

Kari Harper, Brad Damazo, Alkan Donmez
Automated Production Technology Division
Manufacturing Engineering Laboratory
National Institute of Standards and Technology, Gaithersburg, MD

Introduction

The machine tool industry is moving toward using linear motors for both conventional and high speed machine tools due to many advantages: low maintenance, faster assembly times (compared with the more conventional ball screw drives), and improvements in both dynamics and accuracy. Linear motors are also used in ultra precise machine tools and coordinate measuring machines. On the other hand, lack of adequate information about the performance characteristics of such systems limits their widespread use. Therefore, as linear motors become more widely accepted, there is a need to develop methods to characterize their performance. A linear motor testbed has been established within the Manufacturing Engineering Laboratory of the National Institute of Standards and Technology (NIST) in support of this need. The testbed is used to investigate both measurement methods and key performance characteristics. For example, while the thermal characteristics of a linear motor are investigated, the influences of those thermal characteristics on the drive structure itself and thermal contributions to failure modes are also explored. Attention is given to determination of the most effective measurement methodologies for the overall performance of the drive.

Background

Over the last three decades, linear motors have been developed for a variety of different applications, most notably in transportation [1,2, for example] and for semiconductor fabrication [3,4, for example]. Applications in the entertainment [5,6], health [7] and nuclear industries [8] have also been documented.

Within the machine tool industry, acceptance of linear motors for machine drives has been gradually increasing. Widest acceptance has been seen in high speed, lower thrust applications such as the machining of large, monolithic aluminum aerospace parts [9]. This is, in fact, the type of application that Pritschow [10] concludes was most appropriate for linear drives in his comparison of linear and conventional (ballscrew) drives. Several recent areas of research strive to support the introduction of linear motor drives into machine tools by addressing particular aspects of these devices. Van Brussel and Van den Braembussche [11] and McNab and Tsao [12] each investigate the control of linear motion drives in light of the direct coupling of changes in load to the motor. Abdou and Tereshkovich [13] use finite element modeling of linear motor geometry and electric and magnetic field distribution to perform a static analysis of a linear motor drive, concluding that the cutting force affects factors such as flux and current densities and dissipated power more than the electric and magnetic field characteristics. Liebman and Trumper [14] address the issue of heat removal from the linear motor coil with an oil-cooled end-turn coil design.

Testbed Development

The linear motor drive testbed was developed to study the characteristics of such systems on machine tools that influence the machine tool accuracy as well as operational/maintenance requirements. It is

therefore important to create realistic structural, loading and other functional features that simulate the actual machining conditions. Since the metrology and condition monitoring are important aspects of the study, one of the design criteria was to accommodate various sensors and measurement instruments without obstructing the motion. The detailed description of the testbed design is given below.

The testbed is comprised of a synchronous (permanent magnet) type linear motor, ball bearing linear motion guides, a precision scale for position feedback and a precision motion axis controller, all selected to be typical of an industrial machine tool application. The components are assembled in a standard slideway configuration, mounted to a precision ground surface plate. While the testbed utilizes components typical of small-scale machine tools, the lessons learned can be scaled up to match the very high speed and high force applications found within, for example, the aerospace industry.

The linear motor is, of course, the heart of the testbed. A synchronous, ironcore motor was selected over the asynchronous type due to the higher force per unit area available in synchronous motors and the resulting broader applicability of this type of motor. The testbed motor has a peak force rating of 500 N, a coil mass of just 3 kg, a magnetic attractive force of about 2.5 kN, and a magnet track length of 1 m. Under the testbed design, velocity of up to 3 m/s is allowable with acceleration of up to 2 g.

In designing the testbed, several factors were kept in mind. Symmetry about the axis of motion was maintained whenever possible, to minimize the effect of thermal growth on the system and to ease wear on the linear motion guides through even loading. The scale used for position feedback was placed as close to the axis of motion as was practical in order to minimize Abbe error. Height of the drive above the linear motion guides was minimized for better dynamic stability. To achieve the current compact height, the scale was mounted flat along the baseplate, rather than vertically against a mounting block. While this necessitated that the scanning head be shimmed down from the underside of the carriage, it resulted in a lowered center of mass of the moving mass. These features can be seen in the end view schematic given in Figure 1.

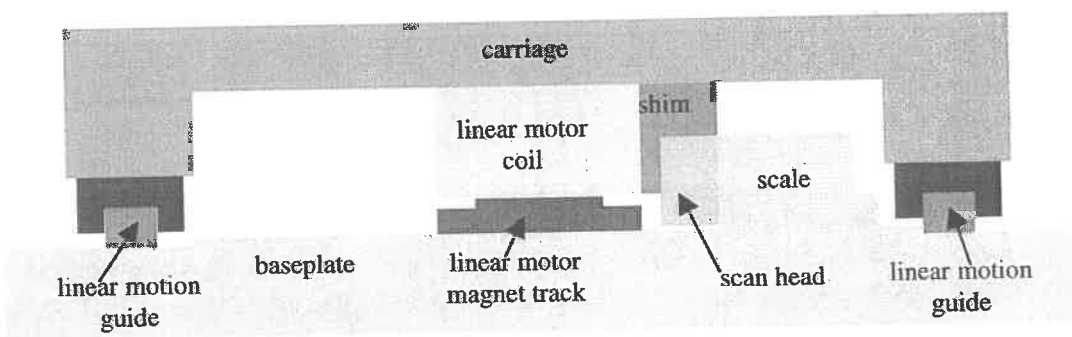

Figure 1: End view of linear motor drive testbed.

A solid model of the system was developed after component selection. A view of this model is shown in Figure 2. The solid model was used in the design finalization process to optimize testbed features. An example of such optimization is minimization of the moving mass. This is done through selection of an appropriate platen thickness and fillet radii combination to minimize the volume of the carriage while maintaining an acceptably low level of deflection under the magnetic attraction forces from the motor and

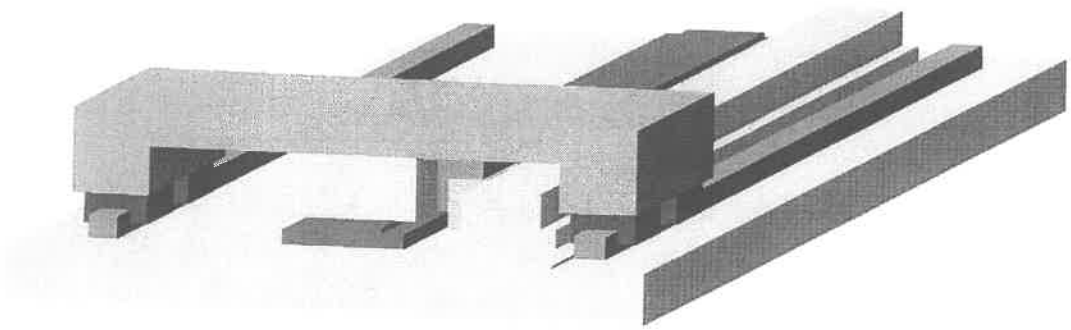

Figure 2: Solid model of the linear motor drive testbed design.

gravity. Figure 3 shows a mapping onto the carriage solid model of the finite element analysis-generated deflections. Maximum deflection was predicted by the model to be less than 4 μm with this carriage geometry. Planned future use of this model includes use for running "what if" scenarios for further study of thermal effects and use in the development of an accelerated life testing plan.

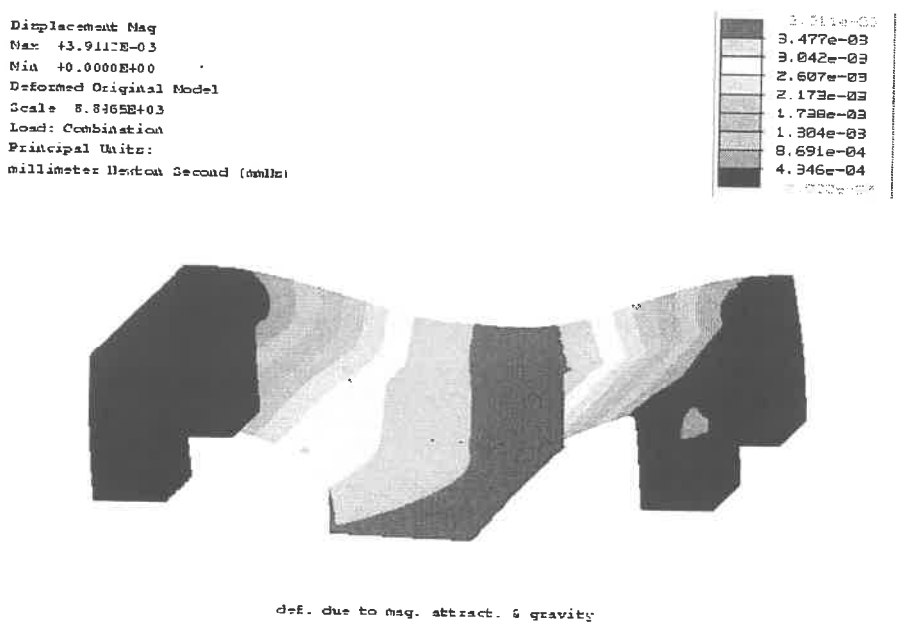

Figure 3: Exaggerated view of carriage deflection due to both the magnetic attraction forces of the motor and the effect of gravity.

The testbed has been instrumented with thermocouples, accelerometers and capacitance probes. An infrared imaging system has also been used to monitor, more qualitatively but on a more system-wide scope, the thermal behavior of the linear motor drive. Details of the metrology system, the experimental methodology, and initial thermal study results are given in the poster presentation.

Future Studies

In addition to more detailed thermal studies in those areas indicated by the initial work, the testbed will be used to investigate other performance issues related to the use of linear motors in machine tools and coordinate measuring machines. Dynamic stiffness and thrust ripple have been identified for early investigation.

References

[1] Kaga, Shigeo; Murai, Toshiaki, et al., "Characteristics of LSM Drive at the Yamanashi Maglev Test Line," *Quarterly Report of Railway Technical Research Institute,* v. 39, n. 2, p. 68-73, 1998.

[2] Byers, Donald C., "The Linear-Induction Motor in Transit: A Systems View," *Elevator World*, v. 46, n. 6, p. 90-94, 1998.

[3] Widdowson, G.P., Kuah, et al., "Design, Analysis and Testing of a Linear/Theta Motor for Semiconductor Applications," *Proceedings, IEEE International Conference on Power Electronics and Drive Systems*, v. 1, p. 357 –364, 1997.

[4] Kim, Won-Jong and Trumper, David L., "Linear Motor-Levitated Stage for Photolithography," *Annals of the CIRP*, v. 46, n. 1, p. 447-450, 1997.

[5] Bartel, Charles F. Jr., "Complex Motion Systems Spur Entertainment Industry." *Power Transmission Design*, v. 39, n. 8, p. 29-31, 1997.

[6] Elliott, N.J., "Novel Application of a Linear Synchronous Motor Drive", *Proceedings of the 1997 IEE Colloquium on Update on New Power Electronic Techniques*, n. 091, p. 8/1-8/5, 1997.

[7] Yamaguchi, Masaki and Kano, Yoshio, "Design Investigation of a Linear Motor for Artificial Heart Driving," *electrical Engineering in Japan,* v. 123, n.1, p.43-50, 1998.

[8] Khan, S. H., "Methods of Calculation of Magnetic Fields and Static characteristics of Linear Step Motors for Control Rod Drives of Nuclear Reactors," *IEEE Transactions on Magnetics,* v. 28, n. 5, p. 2227-2279, 1992.

[9] Smith, Patricia, L., "Leaning Toward Linear," *American Machinist*, v. 142, p. 88-98, March, 1999.

[10] Pritschow, Gunter, "A Comparison of Linear and Conventional Electromechanical Drives," *Annals of the CIRP*, Keynote Paper, v. 47, n. 2, p. 541-548, 1998.

[11] Van Brussel, H.; Van den Braembussche, P., "Robust Control of Feed Drives with Linear Motors," *Annals of the CIRP*, v. 47, n. 1, p. 325-328.

[12] McNab, Robert J.; Tsao, Tsu-Chin; "Stability and Control of Lienar Motor Feed Drives for the End Milling Process," *Proceedings of the ASME*, DSC-v. 64, p. 471-478, 1998.

[13] Abdou, George; Tereshkovich, William, "Finite Element Static Analysis of a Linear Motor Drive," *6th Industrial Engineering Research Conference Proceedings*, p. 592-597, 1997.

[14] Liebman, Michael K.; Trumper, David L., "Pushing the Thermal Limit in Linear Motors", *Proceedings of the 1998 ASPE Annual Meeting*, v. 18, p. 380-383, 1998.

DESIGN OF A PIEZO ACTUATOR FOR CRYOGENIC ENVIRONMENTS

Matias D. Heinrich, Thomas A. Dow
Precision Engineering Center, North Carolina State University

INTRODUCTION

The Next Generation Space Telescope (NGST) planned to launch in 2008 will utilize a large mirror with a diameter of approximately eight meters. The Hubble Space Telescope (HST) will be taken out of commission in 2010 and NGST will be a replacement that will also look at the infrared spectrum of light [1]. Because the transportation vehicle (Space Shuttle Orbiter) has a capacity for an object only 4.57 m in width, the new mirror must be able to fold for transportation. When the mirror is unfolded, the focal point will be adjusted by an array of actuators pushing along the non-reflective side of the mirror. These actuators must have high-resolution static position capability to adjust the optical surface and power off set-and-hold to conserve the onboard power supply. Some of the key requirements include 10 to 20 nm resolution, 6 mm of stroke and a mass less then 40 grams.

Linear motors utilizing piezoelectric actuators seem obvious solutions with products such as Burleigh's Inchworm or the New Focus Picomotor. However, piezo ceramics show extremely diminished strain in cryogenic temperatures (approximately one-sixth of that at room temperature). Recently, TRS Ceramics from State College, Pennsylvania, has developed a single crystal piezoelectric material. This material is capable of producing strains in cryogenic environments similar to those of conventional piezo ceramics at room temperature. This new technology brings the Inchworm and Picomotor back into contention.

Other challenges still remain to be addressed on these designs including size, weight and power off set-and-hold. One way to address the power off set-and-hold is to build the device such that a fine pitch screw is rotated inside a fixed nut to produce axial displacement. Because of the small pitch angle of the threads, axial load is not enough to overcome rotational friction thereby producing no motion.

DESIGN FOR PIEZOELECTRIC MOTORS

Traditionally, there are two types of precision motors: The first is an Inertia Clamp design that relies on the mass, acceleration and applied forces (including variations between static and dynamic friction) of the system. The second is an Active Clamp design that relies more heavily on static friction and clearance between actuators and displacing components.

INERTIA CLAMP DESIGN

Conventional piezoelectric ceramics are often used for precision motion control such as in the New Focus Picomotor [3] seen in Figure 1. This device depends on the difference between the static and dynamic coefficient of friction at the screw/nut interface to convert the small displacement of the piezoelectric crystal to a useful rotation of the screw. A slightly elongated nut can be distorted with a piezoelectric actuator (PZT). The rapid expansion coupled with the

inertia of the screw will force the threads on each side of the nut to slide in opposite directions. When the piezo is slowly retracted, the friction in the threads provides the torque to turn the screw in a stationary nut (not shown) and thus extend the end of the screw.

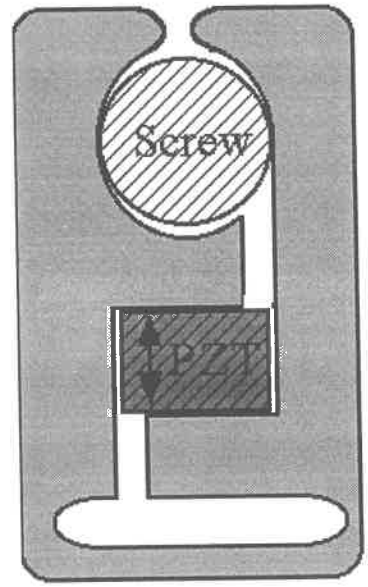

This is a relatively inexpensive device (~$400) but the current design is not acceptable for the cryogenic environment. First, the difference between the static and dynamic friction coefficients needed for the operation of the Picomotor may not be the same in space environment as at room temperature. Second, the strain available from the standard polycrystalline materials is severely reduced at low temperatures.

Another inertia clamping system was developed by Steward Observatory at the University of Arizona (see Figure 2). The design also utilizes a fine pitch screw but instead of piezoelectric actuation, it uses electromagnets to produce an impulse force. The impulse force accelerates the nut suspended by three flexures. The friction force between the nut and screw accelerates the screw but at the same time the nut is slowing down as it winds up the flexures. When the nut and screw reach the same velocity, the friction between the two is maximum and the flexures slow down and stop the nut and screw. The energy stored in the flexures then unwinds the nut and returns it to the nominal position returning

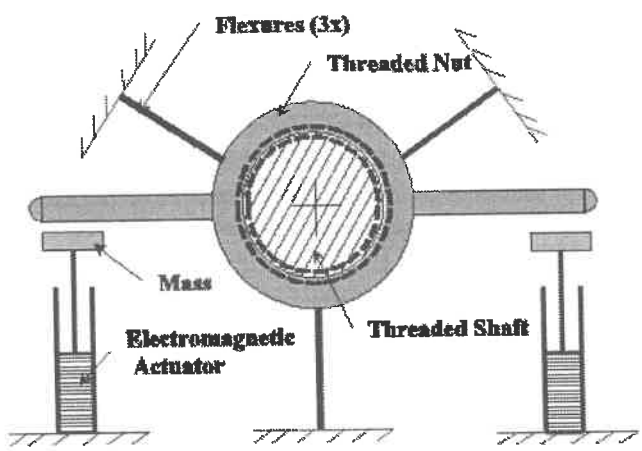

the screw with it. Since the screw slipped relative to the nut in the first part of the stroke, but not during the return part, the screw undergoes net rotational displacement and thus an axial displacement as well.

To model this system, a finite difference program was created that estimated the forces, displacements and directions of each component during one cycle. Variables such as the geometry of the screw and nut (diameter, mass), velocity of the mass when it hits the nut and properties of the flexures (thickness, length and width) were varied and the final displacement of

the screw was calculated. This model was used to study the sensitivity of the system to operating conditions (such as friction) and the dimensions of each component.

A major concern is magnitude and velocity dependence of the friction in a space environment and how much that will affect resolution and displacement. Smooth surfaces in a vacuum, such as space, tend to stick together and create very large friction coefficients. The friction will also produce a hysteresis effect when these motors switch directions. This hysteresis is due to the deforming nut (Picomotor) and flexures (Steward Observatory) not returning to the nominal position after every cycle.

Active Clamp Design

An active clamp design differs from an inertia clamp in that it relies on static friction to cause motion and clearance (or very little contact) for retraction. Burleigh's Inchworm [2] is a commercial example of such a design. These types of actuators rely on a clamping-displacing-unclamping-retracting cycle on a slideway or bar. The Precision Engineering Center has created an active clamping design based around a fine pitch screw similar to those mentioned above. The actuator, designated the "Cryoworm", uses one piezoelectric actuator for clamping a screw and a second actuator to cause rotation. The design of the clamping nut is shown in Figure 3. It was built around a slightly modified #8-80 screw where the threads were machined off on a portion. This portion allows the nut to clamp the screw on a smooth surface eliminating damage to threads and reducing wear of the alumina tip. Another threaded nut, which is attached to ground, converts the rotational motion into axial motion.

Two square waves, 90° out of phase, are used to drive the clamp and rotation actuators. Figure 4 shows 3 cycles of the clamp/rotation process. The process starts with the rotational actuator, which is energized at about 8 seconds in Figure 4. A large step in the displacement of the end of the screw accompanies this actuation step because the screw is pushed radially in the stationary nut and the screw tends to move axially due to the shape of the threads. The clamp actuator is then actuated (at 10 sec) to attach the screw to the clamping nut. This action also moves the screw in the nut and produces a step. The next step is to de-energize the rotational actuator (at 14 sec) which results in a drop in the displacement by removing the side load on the screw. Finally, the clamp force is removed from the screw at 16 sec and the new position of the end of the screw is reached. For the three cycles shown in Figure 4, the average motion for each step is 3.6 nm.

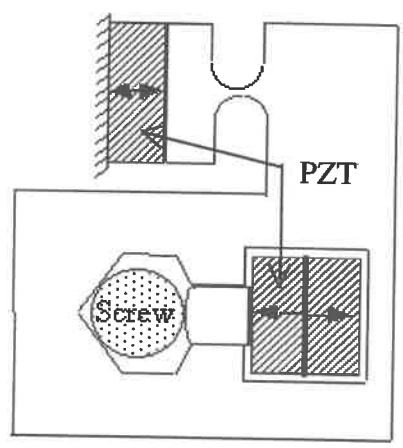

Figure 3: Clamping Nut of Cryoworm

There are a number of design issues that need to be addressed. A large preload on the end of the screw will reduce the step deflection discussed above by keeping the screw centered in the nut. The stiffness of the flexure both axially and rotationally plays an important role on the operation of the motor. If it is too stiff in bending, it will induce a lateral load on the screw but no rotation. If the axial stiffness is too low, it will waste the small stroke of the piezoelectric stack without

causing rotation. A possible solution is to redesign the clamping nut with two symmetrical rotational PZT's on either side of the screw. With this configuration, the forces created by the two bending flexures are cancelled out thereby transferring only a moment.

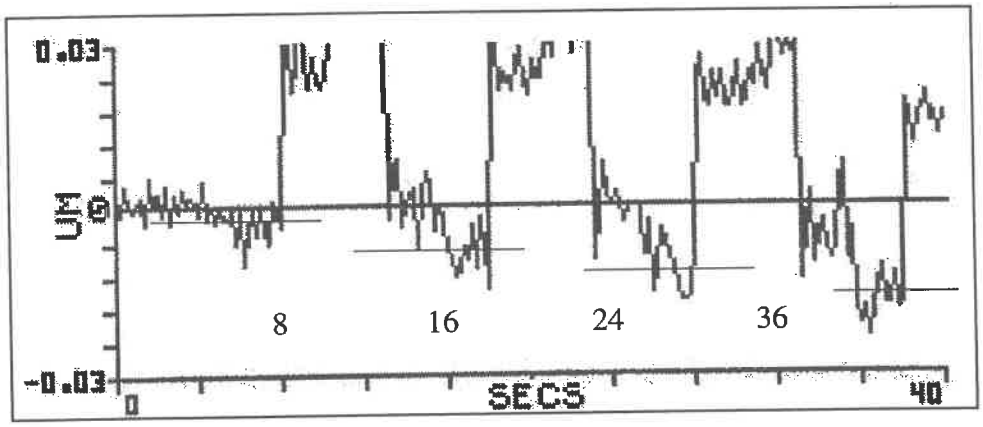

CONCLUSION

Two types of actuators have been discussed, inertia and active clamping. There are advantages and disadvantages to both types of actuators.

- The computer model indicated that the inertia clamping design is very sensitive to the magnitude of the friction between the nut and the screw as well as the variation in that friction with relative velocity. The initial energy from the actuator is coupled to the nut by friction and it is possible to make the screw end up clockwise or counterclockwise from the initial position by changing the input energy or the initial speed of the nut. Consequently, changing the friction coefficient can have a similar effect. Thus uncertainty in the frictional properties is the biggest unknown in this type of design.
- The active clamping design depends upon coupling the nut and the screw through a change in normal force rather than friction coefficient. Since the piezoelectric material has a very small stroke, this implies careful control of the shape and dimensions of the components. For an active clamping motor to be assembled and tested at room temperature and transported to space for operation, appropriate materials and designs must be used to accommodate the thermal expansion coefficients.

REFERENCES

1. Brown, R.A. Hubble Space Telescope Web Site. "HST Second Decade," http://sso.stsci.edu/second_decade/
2. Fasick, J.C., "Development of a Nanometer Resolution Constant Velocity Piezotranslator", MS These, N.C. State University, 1998.
3. New Focus.com web site. "MRA and Rotating Shafts". http://www.newfocus.com/Online_Catalog/6/145/1106/body.html

Incident Angle Auto-Alignment of Ellipsometer using Precision 3-Axis Stage with Kinematic Coupling

Jae-Hwa Jeong , Sung-Lim Park and Dae-Gab Gweon
Department of Mechanical Engineering, Korea Advanced Institute of Science and Technology,
373-1, Kusong-Dong, Yusong-gu, Tae-jon, 305-701, Korea

Introduction

The demand for high precision stage is increasing to obtain more accurate and precise results in many areas especially in the optical measurement systems and thin-film measurement systems. Ellipsometer is an optical measuring instrument for the characterization of, and observation of evens at, an interface or film between two media and is based on exploiting the polarization transformation that occurs as a beam of polarized light is reflected from or transmitted through the interface or film. It is known as a useful one for determining optical indices and thickness of thin films.

In ellipsometer the resulting polarization state of the reflected light is measured and the changes in amplitude and phase occurring upon reflection are determined. It is notable that the ellipsometry parameters ψ and Δ, not the physical quantity, are measured by an ellipsometer. Ellipsometry parameters are functions of the incidence angle and depend strongly on the incidence angle factor. So precise incident angle alignment is an important process and has influence on the accuracy of ellipsometry measurement.

In this paper, we propose a novel design of 3-axis (z-axis, pitch, roll) motion stage [1] and it is utilized for incident angle auto-alignment of ellipsometer. To develop several properties of stage, the kinematic coupling [2] is applied. The kinematic coupling has many advantages, such as closed form motion solution, high repeatability, low construction cost, and no play between mating parts. This novel device could have much influence on not only ellipsometer but also other precision and automation systems, such as, optical microscopes, scanning prove microscopes, reflection measurement systems and etc, where the device tilts and translates specimen or component. The incident angle auto-alignment of ellipsometer[3] consists of two steps, searching the spot and aligning to the center of detector. It is possible to align the incident angle automatically without additional apparatus by this algorithm.

Stage Design

Figure 1 shows the designed overall structure of the stage. Figure 2 presents the bottom of upper plate.

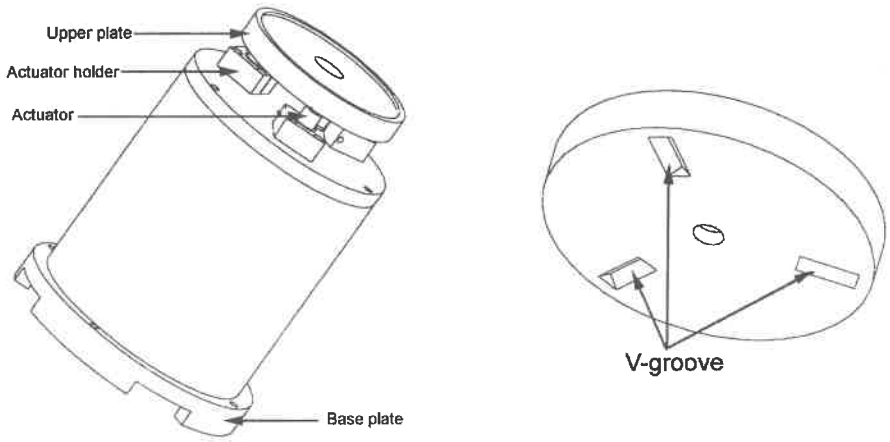

Fig. 1 Structure of 3-axis stage

This stage is composed of an upper plate, three actuators, and a base plate. There are three V-grooves symmetrically in the bottom of the upper plate. The specimen is fixed on the top of the upper plate. The end of each actuator is a ball that contacts with each V-groove. This configuration makes 6 points contact and gives us 6 independent constraints between upper plate and actuators. Generally speaking an object that is rigid requires 6 independent constraints to exactly constrain 6 degrees of freedom. So we can say that the degree of freedom of the upper plate relative to the actuators is zero. This kinematic coupling provides closed form motion solution, high repeatability, no play between mating parts, and several properties of kinematic design. We use ultrahigh resolution linear DC Motors made by PI instrument. These motors travel 25mm range with 0.06μm resolutions and have ball tips. Three actuators are controlled independently. The position and tilting angles of the upper plate are determined by the positions of actuators. So we can get 3-axis motions (z-axis, pitch, roll) of upper plate by controlling the positions of actuators. If we make actuators move with 0.06 μm resolutions, the stage provides 0.18 arcsec resolution over total range of 19.84 degrees in pitch and roll motion.

Auto-alignment algorithm

The incident angle alignment of ellipsometer is a process of centering the spot on the detector. If the alignment is carried out, we can have exact information about incident angle and have maximum intensity, in other words, we can get a large SNR. Incident angle and noise signals are sensitive factors to ellipsometric parameters, ψ and Δ. Most existing approaches have additional apparatus for alignment. But we would like to do this work automatically by using specimen stage only.

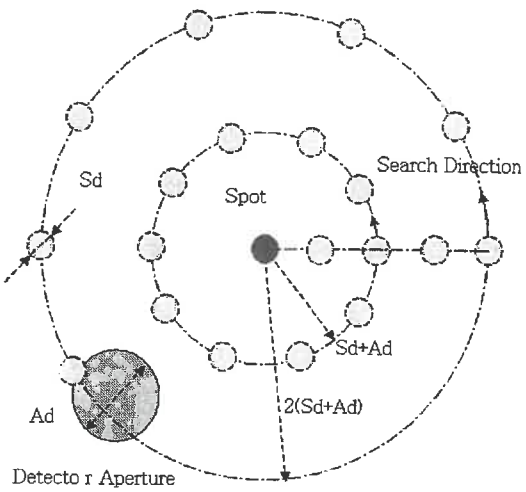

Fig. 3 Step 1 (Accessing)

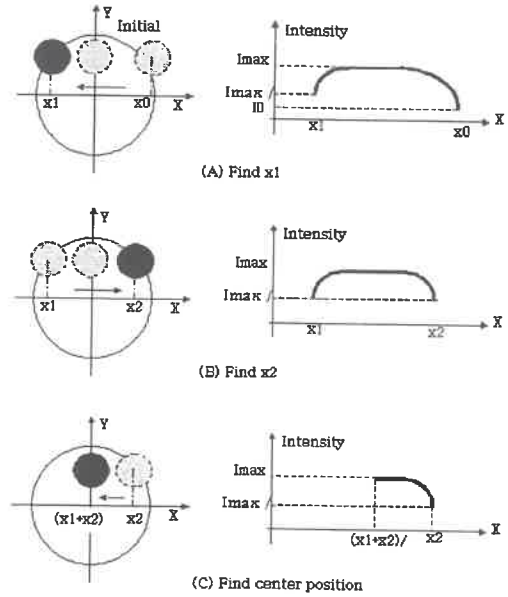

Fig. 4 Step 2 (Centering)

Incident auto-alignment algorithm consists of two steps. Figure 3 shows the schematic figure of the first step that is positioning the spot to detector aperture. The spot and detector aperture (photo diode) are on the detector plane in figure 3. Let's assume that initial position of the spot is the center of plane and the detector aperture is in the bottom of the plane. There isn't any overlapped area between spot and detector aperture, so there is no output intensity. And then we make the spot circle round through actuating the stage properly. If we don't detect any intensity, we increase the radius of circular motion. The incremental amount of radius is the sum of Sd and Ad, where Sd is a diameter of the spot and Ad is a diameter of the detector aperture. The circular motion of spot stops when there is some output signals and the first step is finished

Figure 4 presents the second step that is centering process. The intensity will be proportional to overlapped area. If we make the spot move along X-axis, the intensity varies just like figure 4-(A). We can know the maximum intensity value and stop the stage when the intensity is the half of maximum value. Then the position of the stage will be x1, we remember this. Next, we make the spot move along reverse X-axis, and find x2 position. Finally if we move the stage to middle position of x1 and x2, (x1+x2)/2, the alignment along X-axis is end. The aligning process along Y-axis is the same.

General incident angle alignment includes Z-axis alignment. However, this algorithm is related to 2-axis alignment only, pitch and roll.

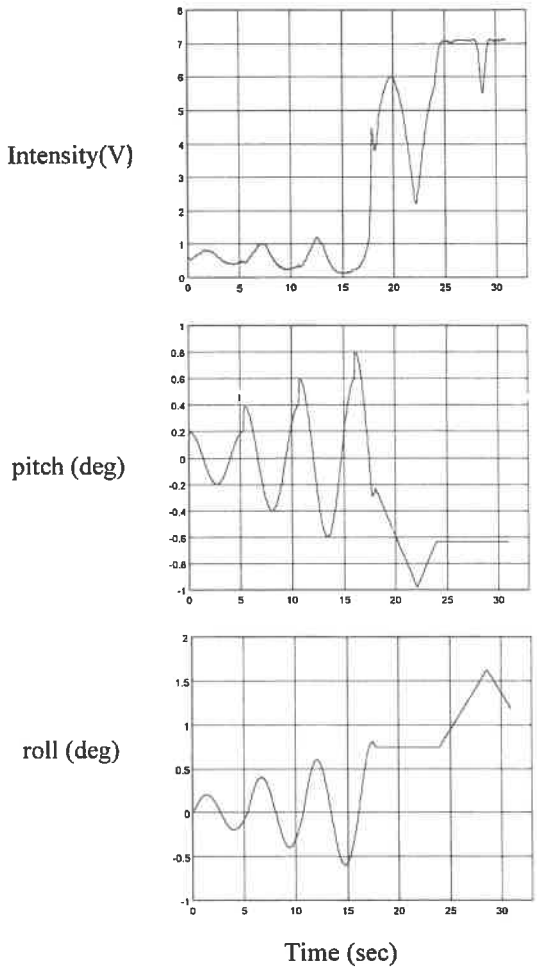

Fig. 5 Experimental result

Result and discussion

Figure 5 shows the experimental result. The configuration of experiment was very simple. The light of laser diode was reflected by mirror on the stage and reflected light was detected by photo diode. The top figure of result is the intensity variation during incident angle auto-alignment process. The second and third figures are the angle variations of stage, pitch and roll. The incremental angle of stage is 0.01 degree. The intensity is vibrating until 17 seconds because of the circular motion of spot, step 1. Next only pitch angle is varied to find center position along X-axis. Finally only roll angle is varied and the spot is aligned along Y-axis. The total elapsed time is 31 seconds.

In this paper we propose a novel 3-axis precision stage and incident angle auto-alignment algorithm without using additional apparatus. We expect that this work can have much influence on the precision and automation of system.

Acknowledgement

This work was supported by Korea Science and Engineering Foundation (KOSEF). The authors thank KOSEF for their financial support.

References

1. J.H. Jeong et al, "A new design and kinematic analysis of 3-axis motion stage for ellipsometer", *Proceedings of the ICMT'99*, Oct 1999, pp. 327-329.
2. A.H. Slocum, "Kinematic Couplings for precision fixturing – Part 1:Formulation of design parameters", *Precision Engineering*, Vol. 10, 1988, pp. 85-91.
3. Yasuaki Hayashi, "Automatic alignment correction system for an ellipsomteric monitor", *Rev. Sci. Instrum.* Vol. 60, No. 8, 1989, pp. 2800-2802.

CHARACTERIZATION OF POROUS GRAPHITE AIR BEARINGS

Byron R. Knapp, Brian P. O'Connor, Eric R. Marsh
Machine Dynamics Research Lab
The Pennsylvania State University, University Park, PA

Introduction

As the demand for higher precision machine tools and inspection equipment grows, there is a need for more precise bearing systems. The error motions of bearings with mechanical contact are dominated by the geometric and surface finish errors of their components [1]. Air bearings, however, do not have mechanical contact between elements and benefit from an air-film averaging effect. Furthermore, due to an absence of mechanical contact, the air bearing has virtually no friction to generate heat and cause wear.

An ideal air bearing would distribute the pressure equally across the entire bearing face to increase load capacity and stiffness. By using bearings with porous media compensation, the pressure distribution is nearly constant across the entire face of the air bearing. In addition to their inherent high stiffness and load carrying capacity, porous media air bearings offer better damping and stability characteristics compared to orifice compensated designs [2, 3].

A substantial amount of work has been done to improve the quality of porous graphite air bearings since the work published by Rasnick et al. [2]. The objective of this research is to develop an empirical stiffness model for porous graphite air bearings and verify this model using experimental modal and finite element analyses. The importance of establishing a model for structural performance is evident with respect to deterministic design.

Experimental Approach

Static load tests are performed on New Way Machine Components porous graphite air bearing pads. A 3-axis Kistler load cell is used to measure the applied force to the air pad. Lion Precision capacitance probes are mounted directly to the back of the air pad to measure the air-film thickness. The bearing pads are tested at supply pressures ranging from 350 kPa (50 psi) to 690 kPa (100 psi) in order to investigate the effect of supply pressure and air-film thickness on pad stiffness. An example of the load versus air-film displacement data is shown in Figure 1.

Load versus air-film displacement data from each static load test is curve fit to a polynomial. The experimental stiffness (K_{Static}) values are obtained by evaluating the derivative of the curve at specific air-film thicknesses. By normalizing the static stiffness by the supply pressure (P), air-film thickness (G), and effective bearing area (A), a constant stiffness factor (C_k) is found using Equation 1.

$$C_k \approx \frac{K_{Static}}{\left(\frac{A \cdot P}{G}\right)} \qquad (1)$$

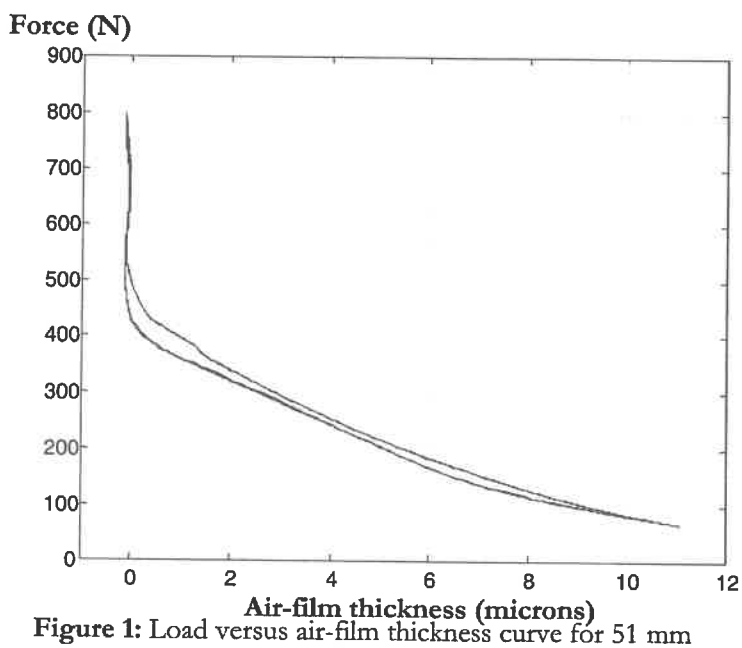

Figure 1: Load versus air-film thickness curve for 51 mm pad at 380 kPa supply.

The stiffness factor, C_k, shown graphically in Figure 2, is found by curve fitting a line to the normalized data. The slope of the line, C_k, is 0.26. The R^2 value for the regression is 0.95, meaning that the linear model is a very good approximation of the data.

It is interesting to note that Rasnick of Oak Ridge Y-12 used a similar method for approximating the stiffness [4]. He quotes a stiffness factor of 0.35 for a captured thrust porous graphite air bearing.

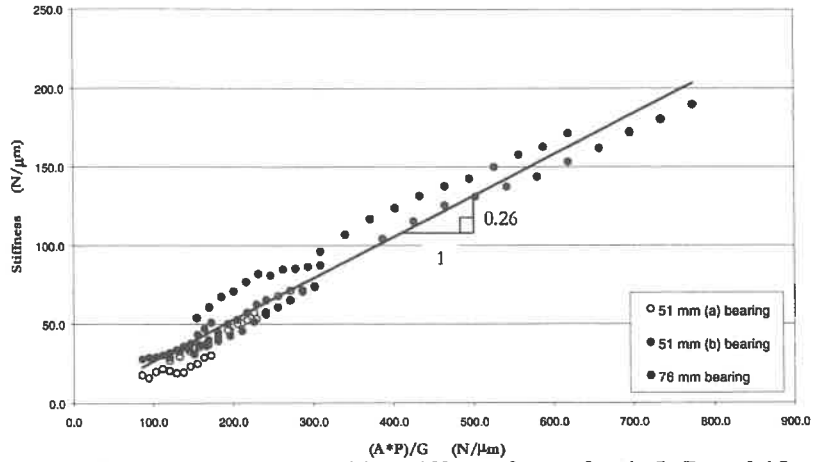

Figure 2: Porous graphite stiffness factor for 4, 5, 7, and 10 micron air-film thicknesses.

The static stiffness (K_{Static}) of the porous graphite air pad is calculated for air-film thicknesses greater than 3 microns as

$$K_{Static} = 0.26\left(\frac{A \cdot P}{G}\right) \tag{2}$$

For air-film thicknesses less than 3 microns, the stiffness does not change proportionally with A, P, and G. Therefore, Equation 2 cannot be applied for air-film thicknesses less than 3 microns.

Using static load tests to find the stiffness of a simple porous graphite air bearing pad has been shown a straightforward process. This same technique can be used to determine the stiffness characteristics of more complicated bearing systems as well. However, a more elegant approach is to determine the static stiffness using Experimental Modal Analysis (EMA). To determine the stiffness of the bearing using EMA, the modal mass and resonance must be determined. For a simple spring-mass oscillator, the stiffness is determined given the mass and natural frequency. Unfortunately, most bearing systems do not follow this simple model since the dynamics of the structure and the air layer become coupled.

To find the static stiffness of a New Way air bearing stage (box slide with four air pads and solid aluminum ram, shown in Figure 3), a modal analysis is conducted. The results of the experimental analysis are summarized in Table 1. The first six natural modes are below 2500 Hz; the first three modes reflect air layer dynamics, while the second three are predominately structural. Since the pitch, roll, and bounce modes involve compression of the air layer, they are the most influential in determining the air layer stiffness.

Table 1: Experimental modal results.

MODE	Frequency (Hz)	Damping (%)	DESCRIPTION OF MODE
1	870	5.0 %	Pitch
2	1020	5.9 %	Roll
3	1250	1.4 %	Bounce
4	1610	1.6 %	Box slide shear
5	1880	0.8 %	Box slide torsion
6	2230	1.5 %	Ram and slide bending

A finite element model of the linear air stage is developed using FEA software. The air stage, shown in Figure 3, is modeled in three parts: 1) ram and box slide – modeled as solid aluminum components; 2) porous graphite –modeled as aluminum with an 80% lower modulus of elasticity; 3) air layer – modeled as a 5x5 grid of discrete springs at each porous graphite-ram interface. J.M. Pitarresi uses a similar air layer finite element modeling technique (discrete springs) for the calculation of the dynamic stiffness of an air bearing pad [5]. In order to determine the variation of the stiffness of the air layer due to internal air pressure, a static analysis of a $^1/_8$ model of the box slide is conducted. The deflection of the box ranges from 6 to 12 microns under normal operating conditions, which results in a significant variation in the air layer stiffness. Therefore, the stiffness along the Y face is varied from k_y at the corner to $k_y/2$ at the center (based on the static stiffness model of Equation 2). The stiffness along the Z face is kept constant at $k_z = 0.6\ k_y$ because while the gap remains constant in that direction, the area is 60% of the area along the Y face.

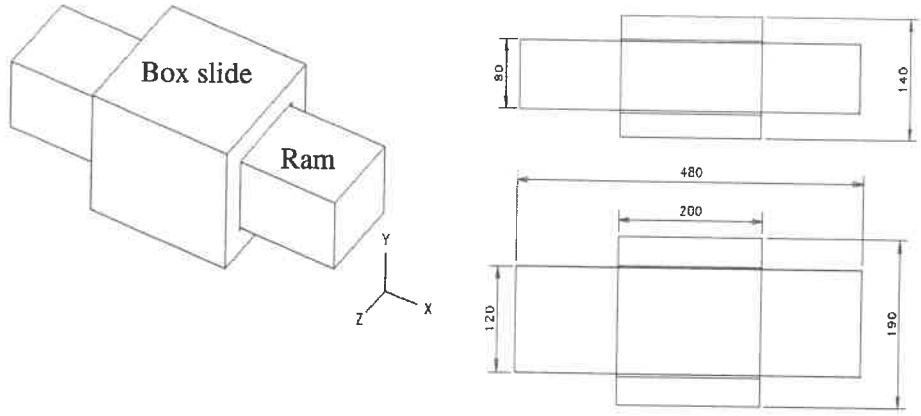

Figure 3: Finite element model of the air stage (dimensions in mm).

The air gap stiffness is determined by matching the experimental and finite element results. The stiffness of the discrete springs is varied until the first six frequencies of vibration match the experimental results. The stiffness in the Y direction is obtained by summing the discrete springs used to represent the air-layer. Unfortunately, due to inaccurate modeling (such as modeling the box slide as one solid piece, unmodeled damping, etc.), each individual mode converges to the experimental data at a slightly different air-layer stiffness. The air-layer stiffness which corresponds to the least amount of error, K_y = 560 N/micron, can be found in Table 2.

Table 2: Percent error in model updating.

Stiffness (N/µm)		% Error Between Experimental and Finite Element Analyses						RMS
Ky	Kz	Pitch	Roll	Bounce	Shear	Torsion	Bending	Error
385	482	-6	-13	-30	14	1	-14	6.5
403	503	-4	-12	-29	14	1	-13	6.2
420	525	-2	-10	-28	15	1	-13	6.0
438	547	-1	-9	-28	15	1	-12	5.8
455	569	1	-7	-27	15	2	-12	5.7
490	613	4	-5	-26	16	2	-11	5.4
525	657	6	-2	-25	16	2	-9	5.3
560	700	9	0	-23	17	3	-8	5.2
595	744	11	2	-23	17	3	-7	5.3
630	788	13	4	-22	18	3	-6	5.4
700	876	17	8	-20	19	4	-4	5.7

Using the results obtained from the FEA and the EMA, the static stiffness model of Equation 2 is verified. The air stage was tested at a supply pressure of 410 kPa. Since the static FEA of the box slide shows that the air-film thickness varies from 6 to 12 microns over the top face of the air stage, an average air-film gap of 9 microns is used. The air stage has two opposing pads; consequently the stiffness is doubled.

$$K_{Static} = C_k \frac{PA}{G} = 0.26 \frac{(410\,\text{kPa})(2)(120\,\text{mm})(200\,\text{mm})}{9\,\mu\text{m}} = 570\ \text{N/micron}$$

Conclusion

The calculated stiffness of 570 N/micron agrees within 5% of the stiffness predicted from the FEA analysis (560 N/micron). Thus, the static stiffness model developed proves to be very accurate in estimating the stiffness of the more complex linear air stage.

The results of this study advance the state of the art in precision machining and inspection through the development of design and measurement techniques for porous graphite air bearings. In addition, a method for finite element modeling of the stiffness of air-films in porous graphite air bearings is proposed.

Acknowledgements

This research was made possible through funding provided by Tropel Corporation, New Way Machine Components, the National Science Foundation, Kistler Instrument Corporation, and Lion Precision. In addition, the authors are grateful for the many hours of discussion, consulting, and testing contributed by David A. Arneson and Melvin J. Liebers from Professional Instruments Company and fellow MDRL graduate student Robert D. Grejda.

References

[1] Slocum, A.H. *Precision Machine Design.* Dearborn, Michigan: Society of Manufacturing Engineers, 1992.

[2] Sheinberg, S. A., and Shuster, V.G., *Machine and Tooling*, v 31, 1960, p 24-29.

[3] Sneck, H.J., "A Survey of Gas-Lubricated Porous Bearings." *Journal of Lubrication Technology*, October 1968, pp.804-809.

[4] Rasnick, W.H., Steger, P.J., Arehart, T.A., and Littleton, D.E. "Porous Graphite Air Bearing Components as Applied to Machine Tools," *SME Technical Report MRR74-02*, 1974.

[5] Pitarresi, J.M., and Haller, K.A. "An Air Layer Modeling Approach for Air and Air/Vacuum Bearings." *Journal of Manufacturing Science and Engineering*, v 119, August 1997, pp. 388-392.

Keywords

Porous Graphite Air Bearings, Modal Analysis, Finite Element Analysis

Cast Monolithic Hydrostatic Journal Bearings

Markku S. Kotilainen, Alexander H. Slocum
Massachusetts Institute of Technology, Cambridge, MA

Abstract

In this work a self-compensating hydrostatic journal bearing design, which eliminates all but one precision-manufacturing step, was manufactured and tested. Novel manufacturing methods for different sizes are introduced. The bearing sensitivity to manufacturing errors was analyzed computationally using statistical methods. These results were used to show that the introduced manufacturing methods are more cost effective than the traditional precision manufacturing methods for hydrostatic bearings, even when the performance variation is taken into account. Manufactured bearings were tested and the experimental results were compared with theoretical results and satisfactory agreement was achieved.

The bearing geometry is shown in Figure 1. The surface geometry on the internal surface achieves compensation and the bearing is able to carry load without any external restrictor devices, hence the name surface self-compensating hydrostatic bearing. This type of bearing generally achieves similar or slightly better performance as a bearing with fixed compensating devices (for example orifices or capillary tubes). Also, the bearing system is simplified since only single hydraulic line is needed and the number of parts is reduced. The only problematic question has been, how to manufacture the surface geometry, shown in Figure 1, on the internal surface of the bushing and how accurately they should be manufactured.

In order to manufacture the internal surface geometry, different casting and molding methods were explored. The most convenient and economically viable methods, especially for small quantities, are processes were the mold is broken after the part material has cooled. Such methods are, for example, sand casting and investment casting. Sand casting, in this case, requires a special core box to make the sand core with the desired geometry. Investment casting requires patterns for each produced part and due to the part geometry traditional pattern making methods were not applicable. Rapid prototyping methods offered the required versatility to produce the investment

casting patterns. These methods were selected for producing two different size prototype bearings..

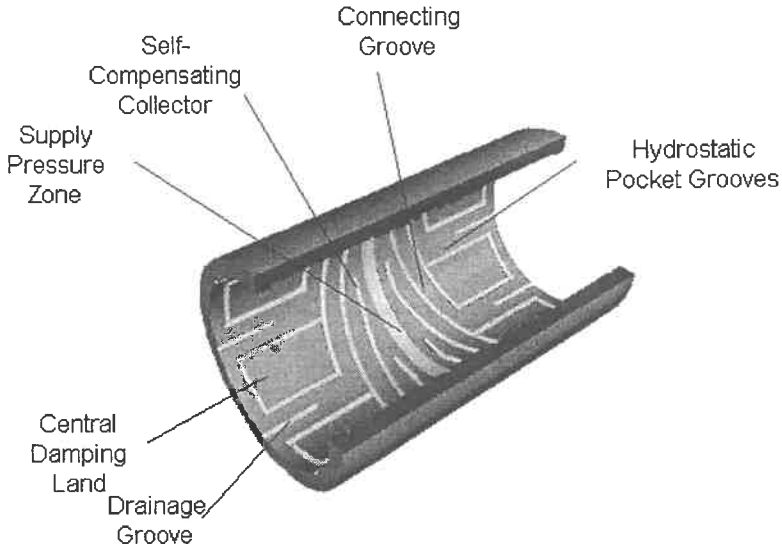

Figure 1 Cut open view of the bearing

The actual dimensional variation was measured from the manufactured parts. This information is used to determine the effect of manufacturing errors to the bearing performance. This was done by statistical methods (Monte-Carlo method). The distribution of the manufacturing variation was determined to follow Gaussian distribution by Chi-square test. Trends were searched with run test, but none were found. The static bearing performance is modeled with a hydraulic resistance network, where the bearing geometry is lumped into equivalent hydraulic resistances. The hydraulic resistance is calculated with the assumption of one dimensional, fully developed, highly viscous flow between two flat plates. If the area which is lumped into a single hydraulic resistance is small enough, the assumptions are very accurate.

The dimensional variation introduced by the manufacturing method is modeled by assigning each of the land widths a probability density function (pdf). This is obtained from measuring the bearings or estimated if the variation is not known. After pdf's are defined, Monte-Carlo method is used to compute the bearing force histogram. From this data it is possible to define the bearing

output (usually force) pdf. In the case of the 6" bearing the measured data will be used to perform the analysis. The standard deviation and the mean offset are $\sigma = 3\%$, $\Delta\mu = 4\%$ respectively. These correspond to approximately 0.2mm errors, which is a reasonable number for this size casting. Figure 2 shows the distribution at ecc=0.1 together with the overlaid normal distribution with the computed mean and standard deviation. Table 1 summarizes the results at different eccentricities.

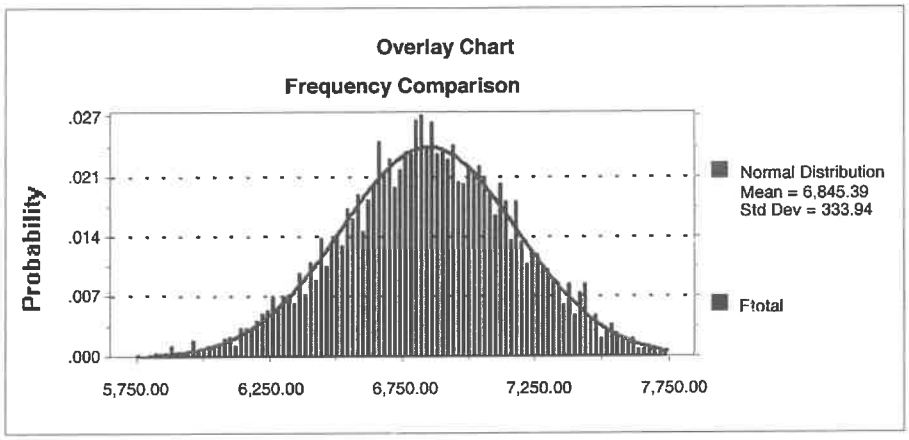

Figure 2 Bearing force distribution with ecc=0.1, $\Delta\mu = -4, \sigma = 3\%$ of groove width

TABLE 1 Summary of the results for $\Delta\mu = 4, \sigma = 3\%$ of the land widths case

Eccentricity	$F_{nominal}$	μ_F	σ_F	$\phi_{nominal}$	μ_ϕ	σ_ϕ
0.1	6832	6843	328	-28.1	-28.1	2.9
0.2	13139	13146	314	-28.2	-28.3	1.4
0.3	18563	18567	288	-28.5	-28.5	1.0
0.4	22966	22974	266	-28.8	-28.8	0.7
0.5	26387	26398	251	-29.1	-29.1	0.6

It was attempted to derive a variable that would combine the effects of manufacturing quality with the cost of the particular manufacturing method. This was done by integrating the computed pdf together with a quadratic cost function to calculate the mathematical expectation for the cost. This single number can then easily be compared between different manufacturing methods to determine the most cost effective. The power of this method is that it automatically takes the cost and

the accuracy of the manufacturing methods into account. The values of this number for the two methods introduced here varied between 1.3-2 times the manufacturing cost, depending on the calibration of the cost function.

Bearings were also tested and good agreement between predicted and measured results was achieved. As an example the initial stiffness (taken as a linear fit at 500N) results for the 6" bearing are presented in Table 3.

TABLE 2 Initial Stiffness at 250 psi

Measure	Value	Unit
Predicted Initial Stiffness	1770	N/μm
Measured Initial Stiffness	1915	N/μm
Difference	7.6	%

The combined radial and tilting error motion trace for multiple revolutions is shown in Figure 3. The maximum deviation from LSC is 0.20 μm and the mean deviation 0.05 μm. This test was run at 6 rpm and there are 10 revolutions in the error motion trace.

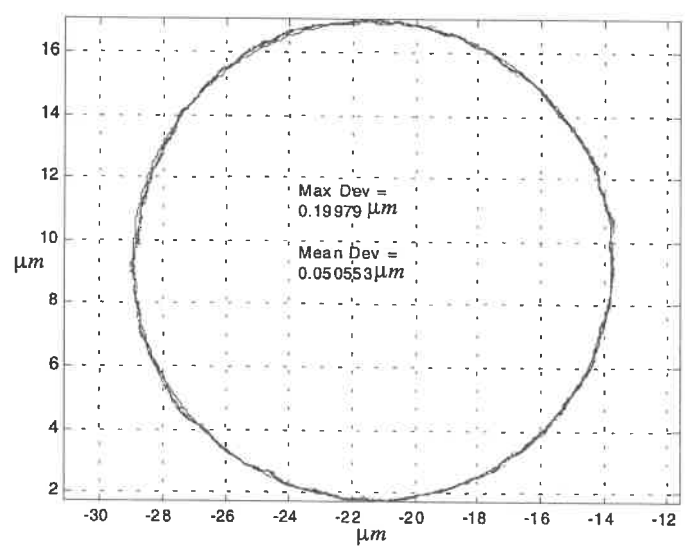

Figure 3 Error motion for multiple revolutions

DEVELOPMENT OF A SPHERICAL MOTOR MANIPULATED BY FOUR WIRES

Hirokazu Nagasawa and Satoshi Honda
Tokyo Metropolitan Institute of Technology, Tokyo, Japan

1. Introduction

Recently, redundant manipulators are highly regarded for having a lot of inherent advantage.[1)2)] However, the redundant manipulators mostly constitute a linkage mechanism installed redundant actuators at redundant joints for driving the redundant linkages, so, redundant manipulators become more bulky and projections for the actuators impede the motion of the manipulators. Moreover, as the driven axes for the actuators are intersect at the centre of the joint, structure of the redundant joint is more intricate. For the solution of these inconvenient, some spherical motors have been developed.[3)4)] One spherical motor is consist of a spherical cell made of steel and four ultrasonic motors. Other spherical motor composes a special planet gear mechanism. These spherical motors are still intricate and control algorithms are complicated.

In this paper, we present a novel spherical motor manipulated by four wires. The spherical motor can drive into three directions in rotation (i.e., pitch, roll and yaw). Structure of the spherical motor is compact and its mechanism is not intricate. Posture of the spherical motor is controlled by a simple algorithm in which lengths of four wires are regulated to reference lengths. The reference is calculated by a simple formula. The structure of the spherical motor manipulated by four wires and the principles of drive algorithm are described in this paper. Relationship between posture of the spherical motor and length of the wires are analyzed in theoretically. Optimal points to fix the tips of wires on the spherical cell and optimal points to pull the wires into the spherical concave shell are investigated in numerical calculations.

2. Structure and drive algorithm of the spherical motor

The spherical motor is consisted of a spherical cell, a spherical concave shell and four wires as shown in figure 1. The spherical cell is fitted on the spherical concave shell and slides on the spherical concave

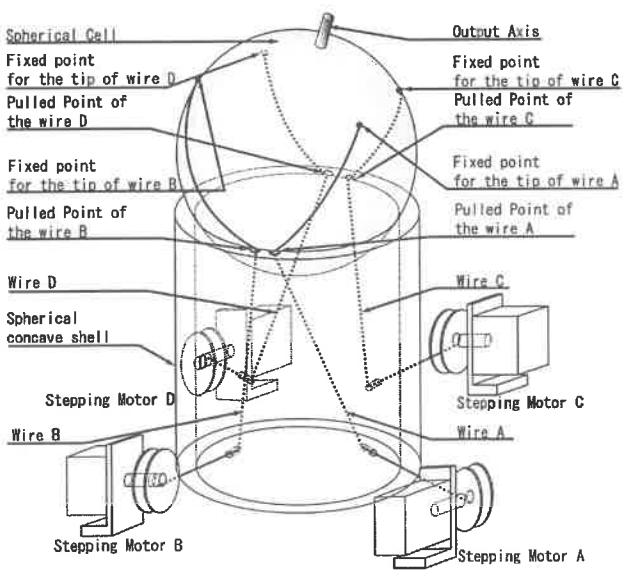

Figure 1. Structure of the spherical motor manipulated by four wires

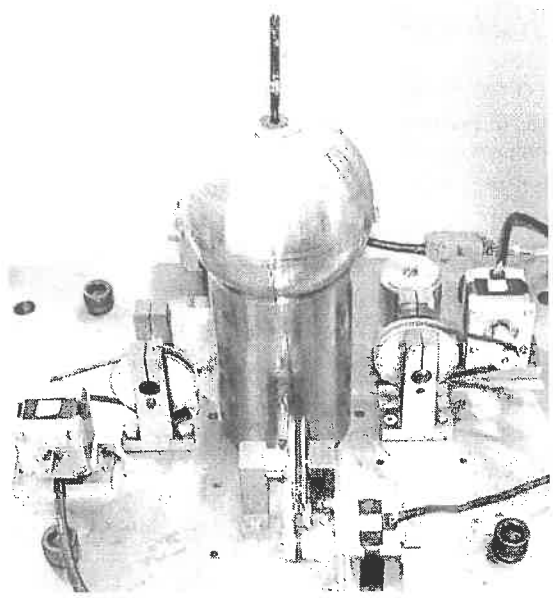

Figure 2. Spherical motor manipulated by four wires

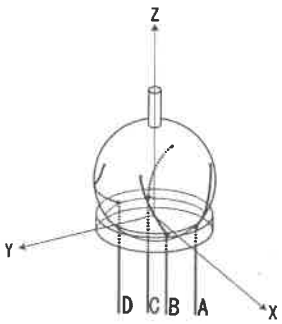

Figure 3-1 Standard posture

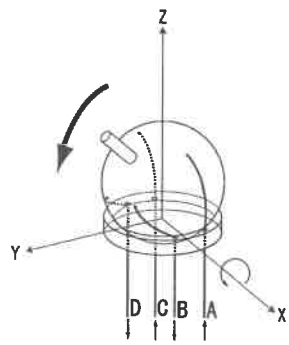

Figure 3-2 Rotation against Y-axis

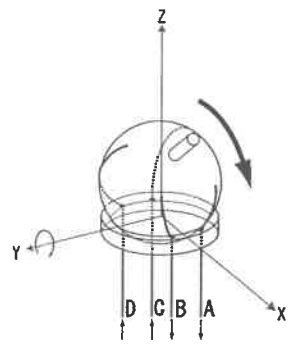

Figure 3-3 Rotation against X-axis

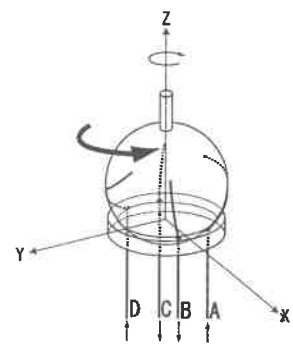

Figure 3-4 Rotation against Z-axis

shell like a spherical slide bearing. The tips of the wires are fixed on the spherical cell symmetrically and the wires are respectively guided into small holes around a rim of the spherical concave shell. Each wire is stretched between the fixed point on the spherical cell and the hole of the spherical concave shell. The wires lie on the spherical cell with the shortest wire in length without slacking the wires. Four wires are pulled or loosened by stepping motors respectively. The spherical cell rotates in the direction of the resultant tensions for four wires. Length of the wires decides the posture of the spherical motor.

The spherical motor is driven as shown figure 3. Coordinates frame and standard posture of the spherical motor are defined as shown in figure 3-1. If the wires of B and D are pulled/loosened and the wires of A and C are loosened/pulled simultaneously, the spherical cell rotates against the X-axis as shown in figure 3-2. If the wires of A and B are pulled/loosened and the wires of C and D are loosened/pulled simultaneously, the spherical cell rotates against the Y-axis as shown figure 3-3. If the wires of B and C are pulled/loosened and the wires of A and D are loosened/pulled simultaneously, the spherical cell rotates against the Z-axis as shown in figure 3-3.

3. Posture of the spherical motor and length of the wires

A certain posture of the spherical motor is represented by three angles as shown in figure 4. θv represents tilted angle between Z-axis of the coordinates frame and the output axis of the spherical cell. θh represents rotated angle against Z-axis of the coordinates frame after the tilt of θv is accomplished. θr represents spun angle against the output axis of the spherical cell after the tilt of θv and rotation of θh are accomplished.

In the standard posture, if the tip of the wire is fixed at a point of (P) which coordinates components against the coordinates frame are (Px, Py, Pz) and if the wires are pulled into a point of (Q) which components against the coordinates frame are (Qx, Qy, Qz), the wire length Lo becomes as follows;

$$Lo = R \times \cos^{-1}((Px \times Qx + Py \times Qy + Pz \times Qz)/R^2),$$

where R is radius of the spherical cell.

When the spherical cell is driven from the standard posture to the posture I which posture is represented by (θv, θh and θr), the fixed point of the wire moves to the point which coordinates components are (Pxa, Pya, Pza). The wire length La becomes as follows;

$$La = R \times \cos^{-1}((Pxa \times Qx + Pya \times Qy + Pza \times Qz)/R^2),$$

where Pxa, Pya and Pza are calculated by a following translate equation;

$$\begin{pmatrix} Pxa \\ Pya \\ Pza \end{pmatrix} = \begin{pmatrix} ACos\,\theta\,hCos\,\theta\,v - B\sin\theta\,h & -BCos\,\theta\,hCos\,\theta\,v - ASin\,\theta\,h & Cos\,\theta\,hSin\,\theta\,v \\ ASin\,\theta\,hCos\,\theta\,v + BCos\,\theta\,h & -BSin\,\theta\,hCos\,\theta\,v + ACos\,\theta\,h & Sin\,\theta\,hSin\,\theta\,v \\ -ASin\,\theta\,v & BSin\,\theta\,v & Cos\,\theta\,v \end{pmatrix} \begin{pmatrix} Px \\ Py \\ Pz \end{pmatrix},$$

where $A = Cos\,\theta\,rCos\,\theta\,h + Sin\,\theta\,rSin\,\theta\,h$, $B = Sin\,\theta\,rCos\,\theta\,h - Cos\,\theta\,rSin\,\theta\,h$.

Therefore, if the wire is pulled subtracted distance between Lo and La, the spherical cell is moved from the standard posture to the posture I . Additionally, if the spherical cell moves from the posture I to a

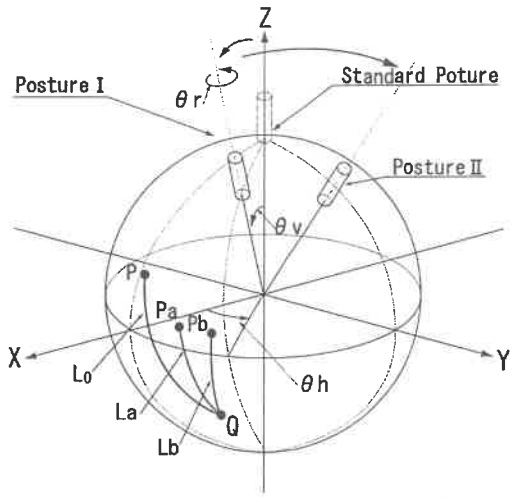

Figure 4. Coordinates fram and length of the wire

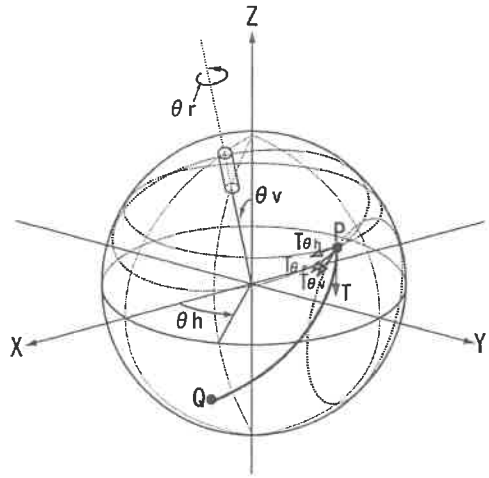

Figure 5. Distributed wire's tention at the fixed point on the spherical cell

posture Ⅱ, wire length (Lb) is calculated and the wire is pulled subtracted different between La and Lb in the same way.

4 Manipulated range of the spherical motor

The spherical motor can move in restricted range. The restricted range is defined by some geometrical necessities and some kinematical requirements. They are as follows; 1)the wires can not stretch over the half length of the outer circumference of the spherical cell because the wires are stretched along the shortest track of the spherical cell by its tension, 2)the wires are not tangled, 3)the tip on the wires are not moved under the guided holes around the rim of the spherical concave shell, 4)all of three components of the wire's tension distributed to the direction of θv, θh and θr at the tip of wire must exist because the spherical cell can not drive to all directions of θv, θh and θr if one of these components does not exit. Distributed wire's tensions at the fixed point on the spherical cell are shown in figure 5.

The manipulated range in which the spherical motor can move to all directions of θv, θh and θr and other geometrical necessities are obtained satisfactory is numerically analyzed. If the tip of wires fixed at the point which setting angles are ϕv and ϕh as shown figure 6, the manipulated range are shown in figure 7, figure 8 and figure 9. In these figures, the manipulated range depends on the setting angles of ϕv and ϕh. The manipulated range about θv and θh is estimated in figure 10. Total spaces on each θv-θh plane, which mean that the spherical motor can move to the three directions, are plotted in figure 10. When ϕv is 5 degree and ϕh is 5 degree about the setting angles, manipulated range about θv and θh becomes biggest. The manipulated range about range θr is estimated in figure 11. Total volumes, which mean that the spherical motor can move to the three directions, are plotted in figure 11. When ϕv is 5 degree and ϕh is 5 degree about the setting angles, manipulated range about θr becomes biggest.

5. Conclusions

The novel spherical motor manipulated by four wires is developed. The structure of the spherical motor is compact and its drive algorithm is simple. The spherical motor is manipulated into the goal posture by controlling length of the wires. The manipulated range become largest when θv is 5 degree and ϕh is 5 degree about the setting angles.

References

[1] Koichi Koganezawa: A fast and Singularity-free Solution of Inverse Kinematics for Redundant Manipulators, JRSJ, 16, 5, pp721-727 (1998).

[2] Kazuhito Hyodo, et al.: On Stiffness Control of Tendon-Driven Robotic Mechanism with Redundant

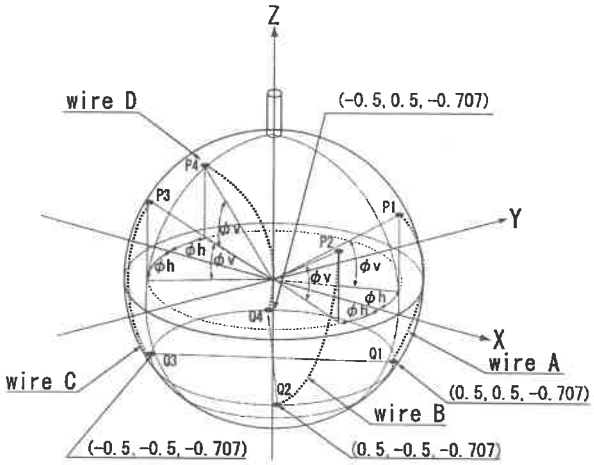

Figure 6. Setting angles (ϕv, ϕh) for the wires

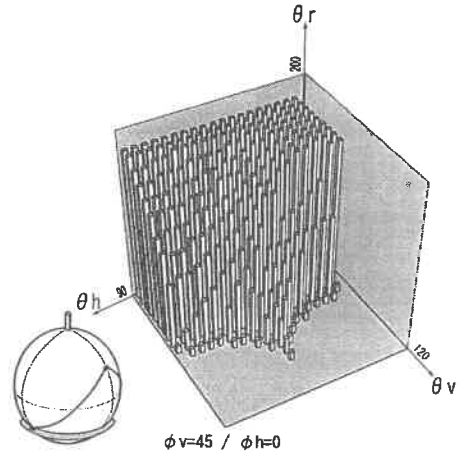

Figure 7. Manipulated range (ϕ v=45^0 , ϕ h=0^0)

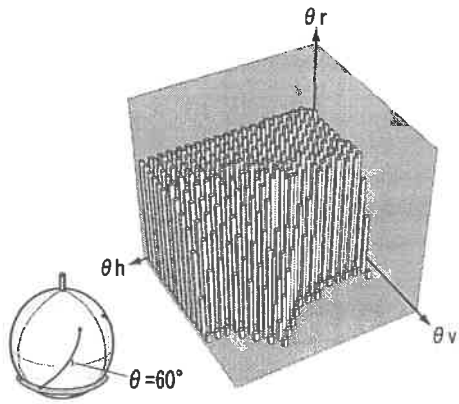

Figure 8. Manipulated range (ϕ v=45^0, ϕ h=0^0)

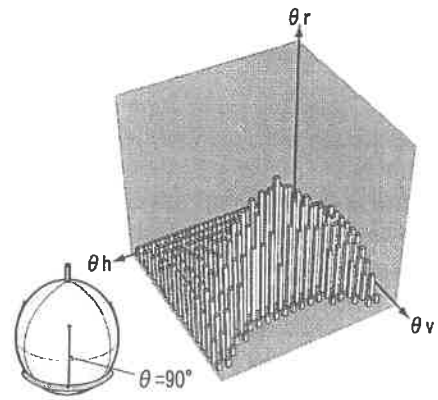

Figure 9..Manipulated range(ϕ v=45^0, ϕ h=0^0)

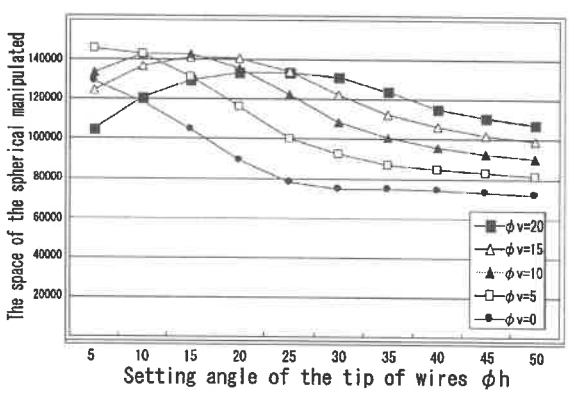

Figure 10. Estimation of the manipulated range for θv and θh

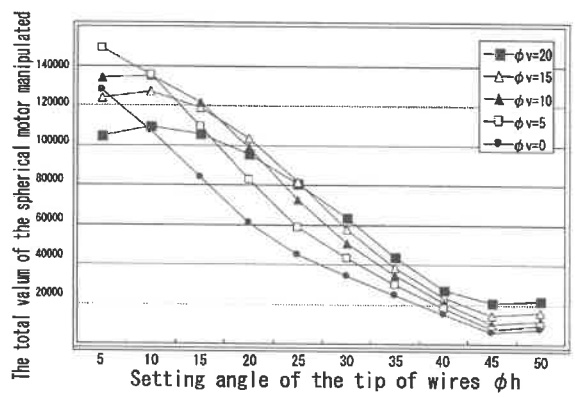

Figure 11. Estimation of the manipulated range for θr

Tendons", JRSJ, 17, 4, pp493-502 (1999).

[3]K. Kaneko, et al.: A Spherical DC Motor with Three Degree of Freedom, Dynamic Systems Measurement and Control of ASME, 111, p398 (1989).

[4]Shigeki Toyama, et al.: Development of a spherical ultrasonic motor, Proceedings of 9th annual meeting of Robotic Society of Japan, p39(1991).

FABRICATION OF AN IN-PIPE MOBILE MICROROBOT WITH THE 3D STEERING MECHANISM

Manabu ONO, Shigeo KATO,
Mizuyuki SHIRAKAWA and Toshiaki HAMANO

Nippon Institute of Technology
Miyashiro, Saitama 345-8501, JAPAN
Phone: +81-480-337725
FAX: +81-480-337745
E-mail: s984143@sstu.nit.ac.jp

Keywords: 3D, Steering-mechanism, In-pipe, Mobile, Microrobot

1. Introduction

In-pipe mobile microrobots which inspect thin pipes in the human body or pipelines have been researched. Takahashi has presented a inching microrobot which is 20 mm in diameter and driven by pneumatic pressure. It speed was 2.2 mm/s [1]. Kubota also has presented a inching microrobot which is 20 mm in diameter and driven by pneumatic pressure. Its speed was 13 mm/s with no load [2]. Miyagawa has presented a microrobot which is 23 mm in diameter and driven by electric motor. Its speed was 6 mm/s [3]. Kato has presented a in-pipe mobile microrobot which is 6.8 mm in diameter and driven by gas-liquid phases-change actuator. Its speed was 0.56 mm/s [4].

However, these mobile microrobots are able to move in the straight or the moderate curvature pipes, but are not able to pass the pipes with the junction. Pipes in pipelines or the human body have many Y Junctions. We fabricated a new in-pipe mobile microrobot with the 3D steering mechanism. The steering mechanism control is done by the combination of stretching or shrinking of four small bellows which are arranged in matrix. The front point of fixed four rubber bellows is able to displace about 8 mm for the arbitrary eight directions of each 45 degree in the 2D plane, if two or three bellows of fixed four rubber bellows are vacuumed.

2. Structure of the fabricated microrobot

The cross section of the fabricated microrobot is shown in Fig. 1. The microrobot is structured by a driving mechanism to move in the pipe and a steering mechanism to pass the Y junction of the pipe.

2.1 Steering Mechanism

The steering mechanism is structured by four rubber bellows arranged in the matrix. The rubber bellows are 5 mm in outer diameter, 2 mm in inner diameter and 20 mm long. The rubber bellows made of nitrile butyl rubber. Each rubber bellows is connected a thin tube which is 0.5 mm in inner diameter, 1000 mm long and feeds pneumatic and vacuum pressure to the bellows. The front, rear part of four rubber bellows are fixed by nylon strings.

2.2 Driving Mechanism

The driving mechanism is structured by three plastic bellows arranged in series. The

plastic bellows are 18 mm in outer diameter, 14 mm in inner diameter and 22 mm long. The plastic bellows are connected a thin tube which is 2 mm in inner diameter, 1000 mm long and feeds pneumatic and vacuum pressure to the bellows.

3. The control system of the microrobot

The control system of the microrobot is shown in Fig. 2. A computer controls seven electromagnetic valves through a valve controller. Three electromagnetic valves are used to drive the microrobot and another four electromagnetic valves are used to steer the microrobot. All feeding air-tubes are connected from the electromagnetic valves to all the bellows actuator. A air-compressor is connected to the entrance ports of the electromagnetic valves and a vacuum pump is connected to the exit ports of the electromagnetic valves.

3.1 Steering Principle of the Microrobot

The pneumatic pressure of 0.1 MPa and the vacuum pressure of -0.08 MPa are used for all the bellows. These two pressures are switched by four electromagnetic valves. First, the four bellows are given the pneumatic pressure before steering motion. If the vacuum pressure is given to two or three bellows and the pneumatic pressure is still given to another bellows, the four bellows bend their head to the vacuumed bellows. The steering mechanism is able to displace its head about 8 mm for the arbitrary eight directions of each 45 degrees in the two dimensional plane.

For example, if the bellows-1 and the bellows-2 are pressurized and

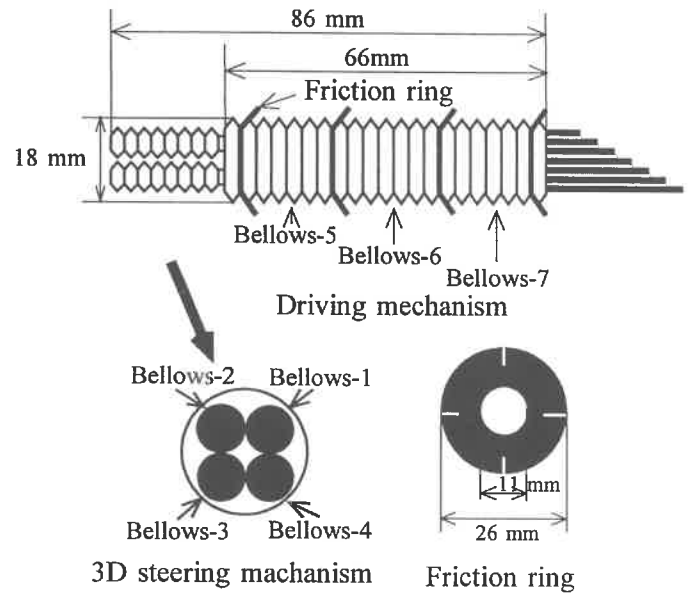

Fig. 1 Structure of microrobot

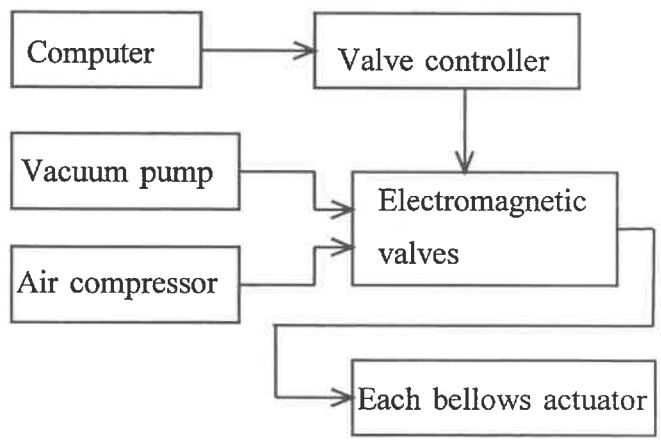

Fig. 2 The control system of the microrobot

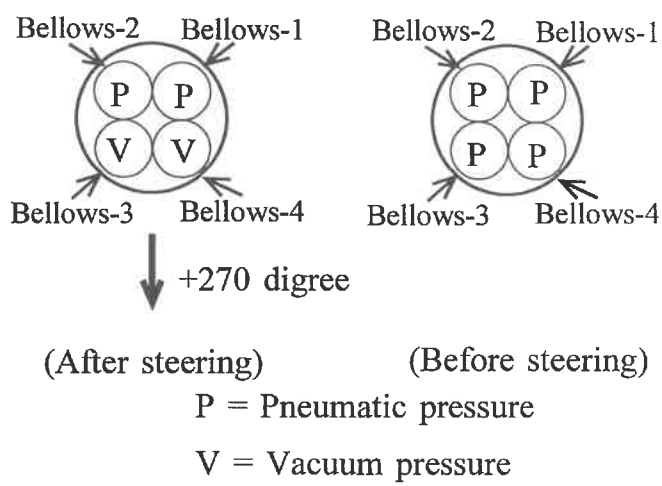

Fig. 3 Steering motion of the rubber bellows at the junction (Downward direction)

the bellows-3 and the bellows-4 are vacuumed, the four bellows bend their heads to the side of the bellows-3 and the bellows-4 . The displacement of their heads is 8 mm. Bending motion of the four rubber bellows at Y junction is shown in Fig. 3. In this case, the microrobot is steered to the downward direction.

When three bellows within the four bellows are vacuumed and one bellows is pressurized shown as Fig. 4, the microrobot is steered to the direction of 45 degree from horizontal and vertical direction.

3.2 Driving Principle of the Microrobot

The time-chart of the pneumatic pressure for the driving mechanism is shown in Fig. 5. The pneumatic pressure of 0.02 MPa and the vacuum pressure of -0.08 MPa are used for all the plastic bellows. First, all the plastic bellows shrunk by the vacuum pressure. Then the pneumatic pressure pulses are sequentially supplied to the front bellows, to the second bellows, and to the third bellows. A tractile wave generated by the stretching and shrinking motion of the three bellows goes to the backward direction in the flexible bellows. Consequently, the in-pipe mobile microrobot is able to move to the forward direction.

4. Moving characteristics of in the pipe

4.1 Moving speed of the Microrobot

The microrobot can move in the pipe, when pneumatic pressure and vacuum pressure are supplied to the bellows of the driving mechanism of the microrobot. The straight moving speed was measured. The supplied pneumatic

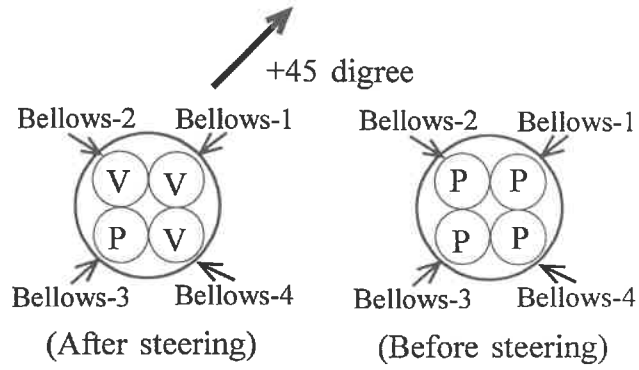

P = Pneumatic pressure

V = Vacuum pressure

Fig. 4 Steering motion of the rubber bellows at the junction (Direction of +45 degree)

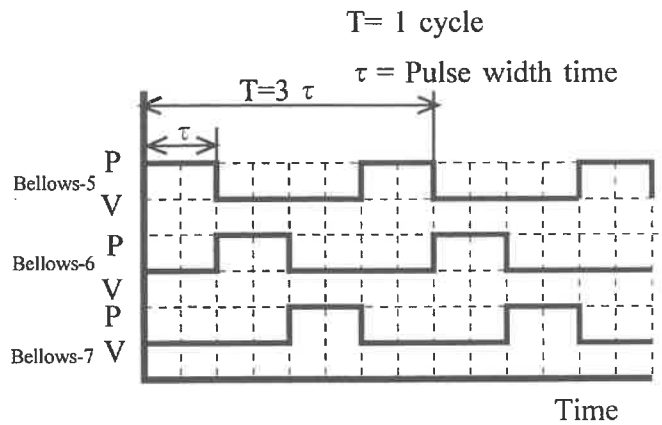

P = Pneumatic pressure

V = Vacuum pressure

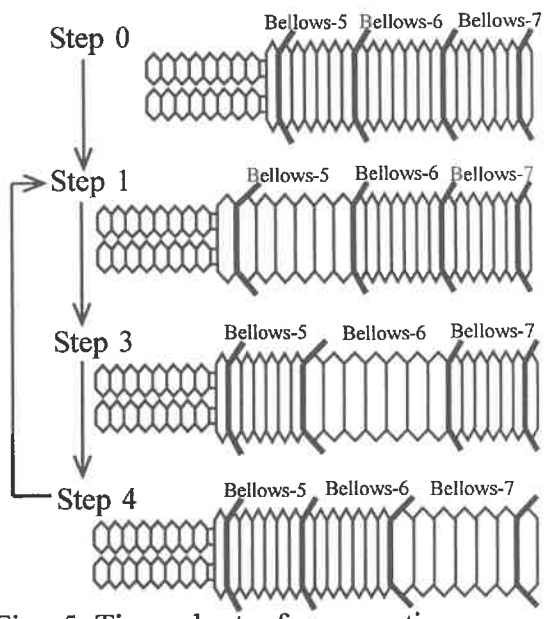

Fig. 5 Time chart of pneumatic pressure for the driving mechanism

pressure was 0.01 MPa and the vacuum pressure was -0.1 MPa. The measured straight moving speed is shown in fig. 6. The maximum speed of 33 mm/s was obtained at the cycle time of 0.3 seconds.

4.2 Steering characteristics

The Steering mechanism is steered to any direction of 45, 135, 225 and 315 degree. If the angle of 20 degree is desired, the angle of 0 degree is used to steer the microrobot. The photograph of the bending four bellows to +45 degree direction is shown in Fig. 6.

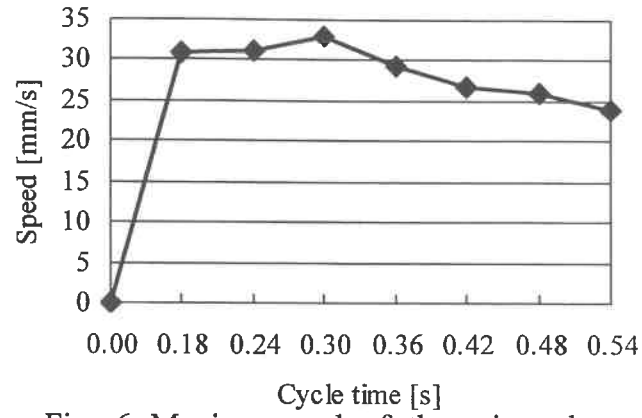

Fig. 6 Moving speed of the microrobot

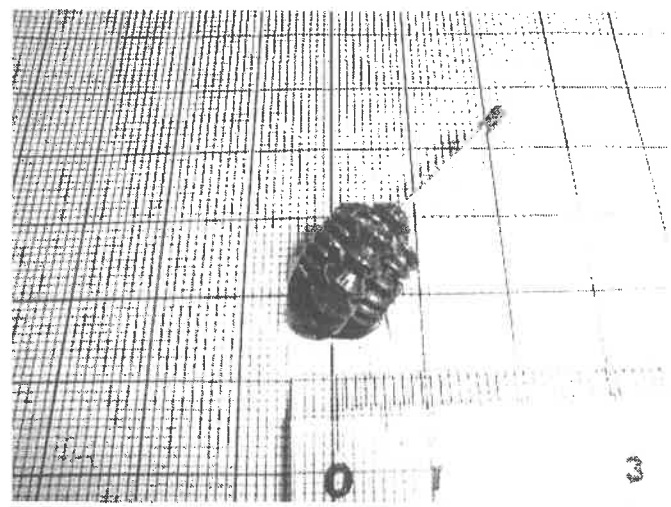
Fig. 7 The photograph of the bending steering mechanism (+45 degree direction)

5. Conclusions

(1) We fabricated of prototype of new in-pipe mobile microrobot with the very simple 3D steering mechanism.

(2) The vacuum pressure is given to one or two bellows. Then, four bellows bend their head to the vacuum bellows as the bimetal and the microrobot is steered to any way of the 3D junction.

(3) The microrobot was confirmed to move at the maximum speed of 33 mm/s at the Y junction.

REFERENCES:

[1] M. Takahashi, I. Hayashi, N. Iwatsuki, K. Suzumori, and N. Ohki: The Development of an In-pipe Microrobot Applying the Motion of an Earthworm, Journal of the Japan Society for Precision Engineering, Vol. 61, No. 1 (1995) pp. 90-94.

[2] M. Kubota, and T. Noritsugu: Development of In-pipe Mobile Robot using Pneumatic Soft-actuator, Proceedings of the 16th Annual Conference of the Robotics Society of Japan, Vol. 3, (1998) pp. 1085-1086.

[3] T. Miyagawa, K. Suzumori, M. Kimura, and Y. Hasegawa: Development of Micro-Inspection Robot for Small Piping, Proceedings of Tenth World Congress on the Theory of Machines and Mechanisms, Vol. 2, (1999) pp. 856-861.

[4] S. Kato and T. Noguchi: Fabrication of an In-pipe Mobile Micromachine Driven by a Gas-liquid Phase-change Actuator, Proceedings of Tenth World Congress on the Theory of Machines and Mechanisms, Vol. 2, (1999) pp. 862-867.

Application of design of experiment techniques to estimate CMM measurement uncertainty

ANTONIO PIRATELLI-FILHO[1], BENEDITO DI GIACOMO[2]
[1]University of Brasilia, Faculty of Technology, Dept. Mechanical Engineering, Brasilia, DF, Brazil
[2]University of São Paulo, Dept. Mechanical Engineering, São Carlos, SP, Brazil

1 - Introduction

Coordinate Measuring Machines (CMM) calibration has been widely investigated by researchers and the methods of mathematical modeling, comparison and performance tests are applied to determination of measurement uncertainty. Mathematical modeling is the method most suitable to determine the uncertainty of CMM measurements and its application involves the calibration of the CMM geometric errors. Its use request high price equipment such as laser interferometer and it is time consuming. The comparison method request a standard artifact identical to measuring part, but it is not suitable when there are different characteristics to be measured in a given piece [1]. The performance tests are not time consuming and request different artifacts to be carried out [2]. There are some international standards concerning application of performance tests and they are largely accepted among CMM users. The utilization of statistical methods may complement the analysis of the results and it may provide sufficient estimates of measurement uncertainty [3].

This work proposes a method to estimate Coordinate Measuring Machines (CMM) measurement uncertainty. The method proposed was carried out using a one-dimensional calibrated gauge and the statistical method of design of experiments. A performance test experiment was planned using this statistical technique to investigate the CMM error sources or CMM variables. An experimental design was selected among several designs of experiments with the purpose of reducing the amount of experimental runs. The experimentation was accomplished modifying the levels or values of the selected CMM variables to intentionally stimulate the variability of the results. The use of analysis of variance (ANOVA) allowed the determination of the most significant variables affecting the CMM errors and the measurement uncertainty associated to each experimental variable was determined.

2 - Experimental design

Design of experiments may be summarized as a group of techniques applied to investigate interrelation among several variables involved in a given phenomenon. Its application involves the planning of an experiment, the data acquisition and a statistical analysis. The first stage is carried out by selection of an experimental plan, as a function of the number of experimental variables investigated and the total number of trials or runs desired. After data acquisition, analysis of variance (ANOVA) technique is applied to identify the most significant variables influencing the result [4].

An engineering problem may be characterized as a system where external input variables are influencing the output variables and any experimental investigation must begin by its identification. In general, we can represent a function relating these variables as the equation 1, where y is the output variable and $x_1, x_2, \ldots, x_n$ are the input variables. This representation is in agreement with ISO Guide recommendation to assess measurement uncertainty [5].

$$y = (x_1, x_2, \ldots, x_n) \qquad (1)$$

The experimental plan establishes a given number of combinations of the experimental variables in its levels or values adopted. Many specific plans or designs have been used mainly at process and engineering design experimentation. The factorial design is largely used and an example is the 3^2 factorial design. The 3^2 design allows the investigation of two input variables in three levels or values

each by realizing nine experimental trials or runs. All combinations of these two variables in three levels are represented by an experimental array [4]. Equation 2 shows a function relating these two variables in a 3^2 factorial design.

$$y_{ijl} = \mu + \tau_i + \beta_j + (\tau\beta)_{ij} + \varepsilon_{ijl} \qquad (2)$$

In this equation, the Greek letter μ represents the arithmetic mean of all determined values of response variable. The letters τ and β represent the effects or change in response variable caused by changing the levels of input variables A and B, respectively. The effect τ_i is determined computing the difference between the mean of response variable (when variable A is at level i) minus μ. The effect β_j is determined in the same way. The response variable y can be estimated by the summation of the mean μ plus the effects τ_i and β_j, plus the effect of interaction between the variables A and B $(\tau\beta)_{ij}$. There would be a deviation caused by uncontrolled variables and it is the residual error represented by ε. When measuring the response variable y, the combined standard uncertainty may be determined by experimental variance V_{ijl} that is related to the uncertainties associated to the effects of variables A (σ_τ) and B (σ_β), interaction AB ($\sigma_{\tau\beta}$) and residual error (σ) and showed by equation 3 [3, 5].

$$V_{ijl} = \sigma_\tau^2 + \sigma_\beta^2 + \sigma_{\tau\beta}^2 + \sigma^2 \qquad (3)$$

These uncertainties at the right side of equation 3 are the components of variance and may be determined using the values of mean squares obtained when performing ANOVA [4]. The approach of determining uncertainty by using design of experiments and ANOVA was mentioned at ISO Guide to the expression of uncertainty in measurement (1993) and was used in recent publications [3, 6].

3 - CMM Application - results and discussion

The determination of measurement uncertainty using performance tests has some degrees of complexity due to the great number of variables influencing the measurement errors. The input variables are those that affect measurement uncertainty, like probe, machine structure and measurement strategy. The output variable y may be considered the measurement error. The relation imposed by equation 1 means that any change in $x_1, x_2, \ldots, x_n$ values become change in y value.

The input variables to be investigated must be those who promote high change in response variable. But, it is imposed by statistical theory that the effects observed when changing the levels of each variable must be independent and normally distributed with mean zero and standard deviation σ, or N.I.D.(0, σ). Thus, it is preferred continuous input variables instead of discrete input variables. After carefully study, it was considered as input variables the length course, the length measurement orientation in work volume and the position in work volume in wich length will be measured. These variables are influenced by other CMM error sources, such as geometric errors, and they are called operational variables in this work.

The traceability of measurements was performed by using ball bar gauges with combined standard uncertainty equal to 1 µm. The proposed method was carried out using a Moving Bridge CMM, work volume 350x400x300 mm, located at Metrology Laboratory, University of São Paulo, Brazil. The experimental device used to support ball bar over CMM is showed by figure 1. One touch trigger probe was used, with a stylus in vertical direction. The ball bar length was measured with CMM touching seven points each ball of the gauge. The own CMM software was used to determine the balls center-to-center length. The measurement error was determined by length measured minus calibrated and each value was determined three times.

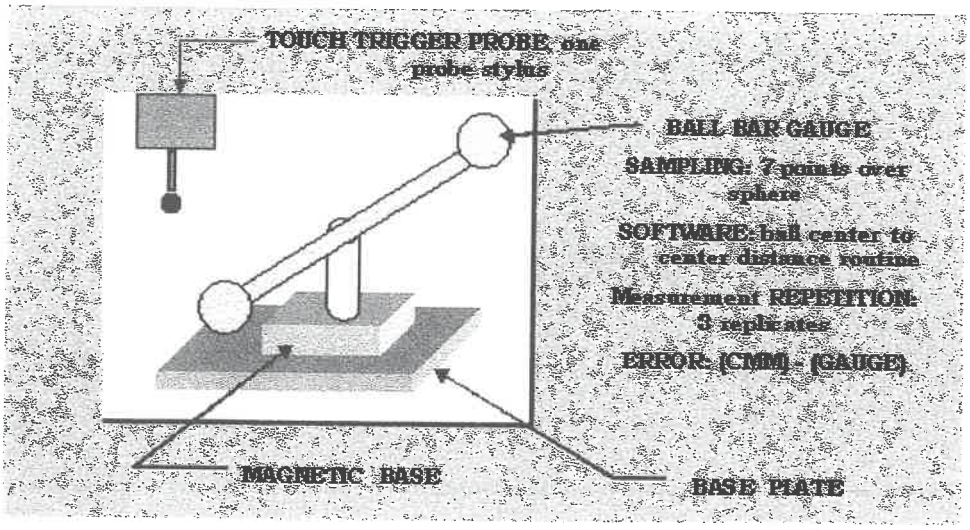

Figure 1 - Experimental construction

Instead of use factorial design, it was used a Taguchi L9 modified experimental plan to reduce the number of runs required to investigate five variables. This array is showed by table 1, where the letters A, B, C, D and E represents the variables (A) position along X-axis, (B) position along Y-axis, (C) position along Z-axis, (D) length measured, (E) orientation in work volume. The numbers 1 to 3 in A to D represent the levels of each variable, and E1 to E6 represent the levels of variable E. In this array, each line correspond to one run that is carried out combining the levels of the five variables.

Table 1 - L9 modified Taguchi array

RUN	A	B	C	D	E					
					E1	E2	E3	E4	E5	E6
1	1	1	1	1						
2	1	2	2	2						
3	1	3	3	3			RESULTS			
4	2	1	2	3						
5	2	2	3	1			(MEASUREMENT ERRORS)			
6	2	3	1	2						
7	3	1	3	2						
8	3	2	1	3						
9	3	3	2	1						

The mathematical model is showed in equation 4. The effects of input variables A, B, C, D and E are the Greek letters τ, β, γ, δ and η, respectively. The expression to determine measurement uncertainty was obtained applying error propagation and the result is showed in equation 5. In this equation, the components of variance σ_τ, σ_β, σ_γ, σ_δ and σ_η are estimates of standard uncertainty associated to variables A, B, C, D and E.

$$y_{ijloqw} = \mu + \tau_i + \beta_j + \gamma_l + \delta_o + \eta_q + \varepsilon_{ijloqw} \qquad (4)$$

$$\sigma_y^2 = \sigma_\tau^2 + \sigma_\beta^2 + \sigma_\gamma^2 + \sigma_\delta^2 + \sigma_\eta^2 + \sigma^2 \qquad (5)$$

These components of variance may be determined according to equations 6 to 10, where the values MSA, MSB, MSC, MSD and MSE are the mean squares deviation of variables A, B, C, D and E, obtained with ANOVA analysis. MSR is the residual mean squares deviation, associated to variables not considered in experimentation. The letters a, b, c, d and e are the level of variables and r is the replication number.

$$\hat{\sigma}_A^2 = \frac{MSA - MSR}{a \cdot e \cdot r} \quad (6)$$

$$\hat{\sigma}_B^2 = \frac{MSB - MSR}{b \cdot e \cdot r} \quad (7)$$

$$\hat{\sigma}_C^2 = \frac{MSC - MSR}{c \cdot e \cdot r} \quad (8)$$

$$\hat{\sigma}_D^2 = \frac{MSD - MSR}{d \cdot e \cdot r} \quad (9)$$

$$\hat{\sigma}_E^2 = \frac{MSE - MSR}{a \cdot a \cdot r} \quad (10)$$

The ANOVA results showed that the different orientations and ball bar lengths change the measurement errors in a statistically significant way (99%). The standard uncertainties were 1 μm (A), 1 μm (B), 2 μm (C), 4 μm (D) and 17 μm (E). The results were compared to performance test proposed by ANSI/ASME B89 standard and some complementary tests were performed to verify the uncertainty statements and the results were in agreement.

4 - Conclusion

The design of experiment techniques is a helpful tool to investigate the measurement uncertainty and its use is suitable when type A uncertainty sources are predominant. In the CMM application performed, it was found that the object orientation in CMM work volume answers for the main portion of measurement uncertainty. Besides, these techniques can be used to estimate uncertainty sources in industrial processes.

References

[1] B. Van Dorp et. al., *Traceability of CMM measurements*. Proceedings of American Society for Precision Engineering - ASPE Annual Meeting, Monterey, CA, USA, 1999.
[2] J.A. Bosch, *Coordinate Measuring Machines and Systems*. Marcel Dekker, New York, 1995. 444 p.
[3] A. Piratelli-Filho, *A method for Coordinate Measuring Machine performance evaluation using design of experiments*. São Carlos, University of São Paulo, Brazil, PhD Thesis, 1997.
[4] D.C. Montgomery, *Design and analysis of experiments*, John Wiley & Sons, New York, 1991. 649 p.
[5] International Organization for Standardization, ISO, GUM - Guide to the expression of uncertainty in measurement, 1993.
[6] M. Koike and H. Ishida, *Estimation of measurement uncertainty of Rockwell Hardness test using orthogonal array*. Proceedings of XV International Measurement Confederation - IMEKO World Conference, Osaka, Japan, 1999.

Acknowledgements

This work was supported by Conselho Nacional de Desenvolvimento Científico e Tecnológico - CNPq, Coordenação para Aperfeiçoamento de Pessoal – Capes and Fundação de Empreendimentos Científicos e Tecnológicos - FINATEC, Brazilian financing agencies.

SYSTEM MODELING AND IDENTIFICATION OF A PRECISION FAST TOOL SERVO SYSTEM

S. Rakuff[1](student), J. Cuttino[1], D. Schinstock[2]
[1]Mechanical Engr. and Engr. Science, The University of North Carolina at Charlotte, Charlotte, NC 28223
[2]Dept. of Mechanical Engineering, Tulsa University, Tulsa, OK 74104

Introduction

The Laser industry and the contact lens industry are among many industries to accentuate the need for Fast Tool Servo systems (FTS). FTS's enable diamond turning machines to produce non-axisymmetric components by moving the cutting tool in and out of the workpiece while the spindle rotates. The capability of producing non-axisymmetric parts makes it possible to produce products such as contact lenses for patients with astigmatisms, laser diode corrective lenses, and non-axisymmetric metrology artifacts. Reference [1] for example, utilizes a sinusoidal wave pattern cut along the z-axis of a cylinder to obtain optical instrument transfer functions. With FTS's, the artifact geometry can be expanded to generate periodic, non-axisymmetric waveforms about the rotary axis, thereby enhancing metrology capabilities. The FTS described in this paper is referred to as the *FTSii*. It has an operating frequency of up to 50Hz and a design range of motion of 2mm. The target accuracy is 25nm.

System configuration

The diamond tool is mounted on a monolithic flexure system that is driven by a voice coil actuator. The flexure consists of the tool shuttle, four leaf springs, and two stationary supports. It was machined using a wire EDM to avoid internal stresses. A C-code PID control program runs directly on an Analog Devices Sharc microprocessor mounted on a Precision Micro Dynamics signal processing card. The control loop runs at an interrupt frequency of 40kHz. The voltage signal from the controller is converted into a current by a high bandwidth, high power amplifier. The system is interfaced to the DTM by reading the encoders of the spindle and the x-axis with the DSP-card. An Excel Precision laser interferometer is used to feed back the actual position of the tool shuttle and has 10 nm resolution at a maximum slew rate of 0.7 m/s. Figure 1 illustrates the hardware interaction.

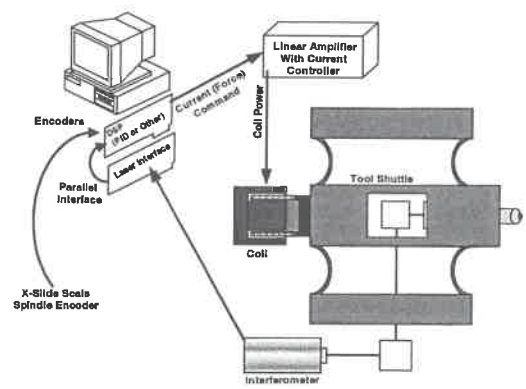

Fig. 1: System configuration

Controller considerations

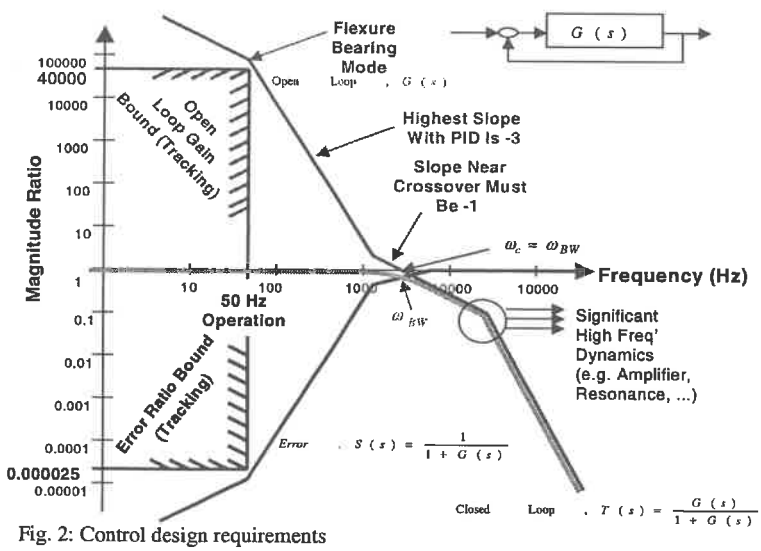

Fig. 2: Control design requirements

Figure 2 shows many of the important aspects of the position control design. Analysis indicates that in order to obtain an error to displacement ratio of 25nm to 1mm at 50 Hz operation of the *FTSii*, a small signal bandwidth of approximately 3 kHz is required for the position control system. This is a design requirement, and has several implications in terms of the mechanical, electrical, and control system designs. The current amplifier/controller for the coil must have a small signal bandwidth of approximately 30 kHz or greater. The mechanical system must not have any resonant modes below 3 kHz other than the main flexure mode that are excited by the actuation force. Finally, the digital position control implementation must have a servo update rate of 30 kHz or greater.

System identification

The system was modeled with the block diagram shown in Figure 3. The model is a time invariant single input single output system. Since the bandwidth of the mechanical system is small compared to the sampling frequency of 40kHz, effects from digital sampling have been assumed to be negligible. The permeability of the coil is assumed to be constant. Under this assumption, the relationship between the current flowing through the coil and the delivered force is linear. The force constant, K_f, is 29.2N/A, and the back-emf constant, K_b, is 21.4Ns/m.

Two possible sources of saturation have significant influence on the performance of the *FTSii*, the DSP card and the amplifier. It is relatively easy to keep the DSP card from saturating by carefully distributing proportional gain among the system components. The amplifier saturates at 8A due to the power supplies and has a maximum slew rate of 8V/μs.

The amplifier utilizes a current loop to improve system performance. To decouple the amplifier dynamics and the dynamics of the voice coil from the rest of the system, the bandwidth of the amplifier was designed to be at least one decade higher than the bandwidth of the system. A number of tests were conducted to bring the current loop up to 30kHz, ten times greater than the system's closed loop bandwidth of 3kHz. Therefore, the current loop could be modeled as a constant gain. The quantization effect of the digital laser interferometer and hysteresis of the flexure were also assumed to be negligible. The flexure system was specifically designed to behave as a second order spring mass damper system to optimize the control.

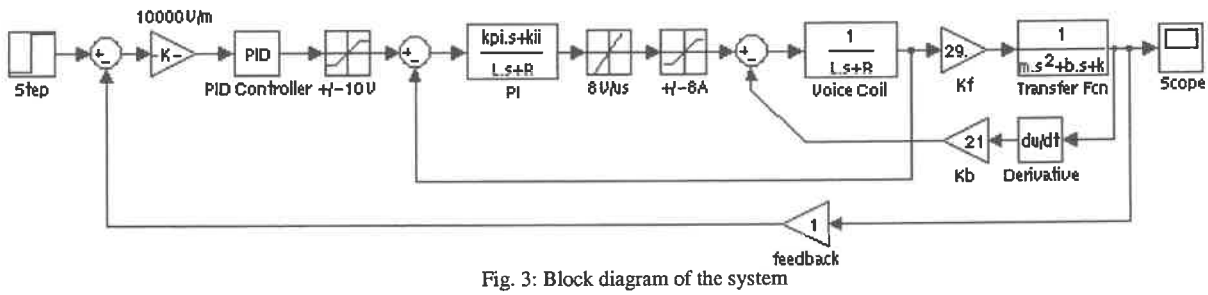

Fig. 3: Block diagram of the system

Determining plant parameters

The moving mass was verified by weighting all moving parts on electronic scales or computed by using dimensional data from the CAD files. In addition, the effective mass was estimated by adding one third of the mass of each leaf spring to the moving mass. The mass was calculated as 1.22 kg (without tool and clamp/bolts). In order to find the damping ratio ξ, the damping b, and the spring constant k, impact testing was performed. Figure 4 shows one set of test data for the first mode. The voice coil was attached to the flexure during testing, since it contributes additional mass and damping caused by Lorenz currents.

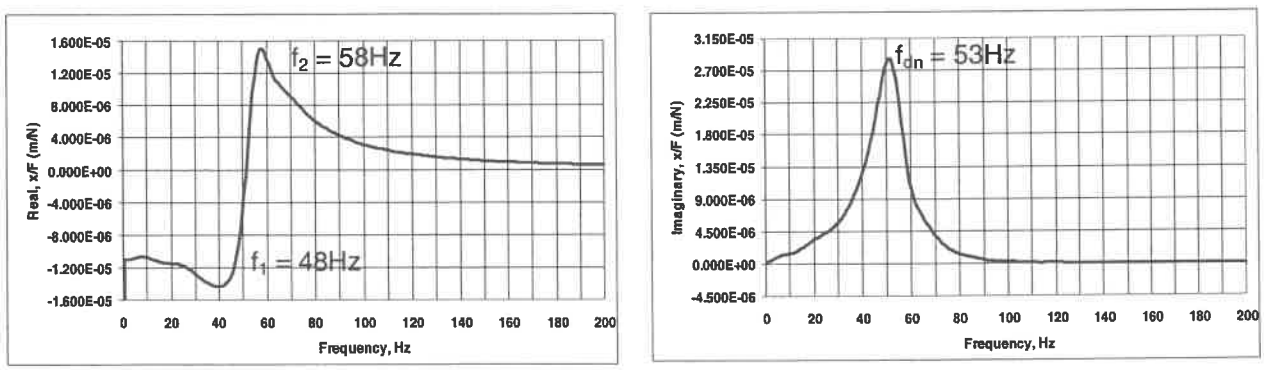

Fig. 4: Fundamental mode frequency response

The two graphs show a damped natural frequency of 53Hz. The damping ratio ξ can be determined by using [3]:

$$\xi_7 = \frac{\omega_2^{\,2} - \omega_1^{\,2}}{4\omega_{dn}^{\,2}} \tag{1}$$

The testing for the fundamental mode was repeated several times, resulting in a calculated damping ratio of

$$\xi = 0.165 \pm 0.002 \tag{2}$$

To calculate the undamped natural frequency, the following equations can be used.

$$\omega_n = \frac{\omega_{dn}}{\sqrt{1-\xi}} = \frac{328}{\sqrt{1-0.165}} rad/s = 359 rad/s \tag{3}$$

The damping, b, of this second order system is equal to

$$b = 2\xi m\omega_n = 144.8 \frac{Ns}{m} \tag{4}$$

For a second order spring mass damper system with no damping, the spring constant k is given as:

$$k = m\omega_n^{\ 2} = 1.222kg \cdot (359 rad/s)^2 = 157492 \frac{N}{m} \tag{5}$$

Tuning the controller

The PID controller for the FTSii was initially designed using the Ziegler-Nichols technique. In this method a unit step is applied to the closed loop system with the controller already installed. Initially, the controller gains, k_p, k_i, and k_d are set to zero. k_p is then increased until the system becomes oscillatory. For the ultimate-cycle method, k_p is then multiplied by 0.6. There are formulas to calculate the other gains with the period of the oscillations [3]. Unfortunately, the limited slew rate of the interferometer (0.7m/s) made it difficult to monitor these oscillations. Since the target applications for the FTSii are sinusoidal, the controller was tuned using a sinusoidal input only. This method is a very general approach and resulted in non-optimal controller gains.

A second approach was applied using Matlab and Simulink simulation packages. The Matlab/Control System toolbox was first used to model the linear system neglecting saturation effects [4]. A PID controller was then designed for this model using the root locus design GUI. The gains were then transferred to an equivalent model created in Simulink and verified. Saturation blocks were then added for DSP card and amplifier.

The transfer function for the PID controller can be written as:

$$TF(s) = k_d s + k_p + \frac{k_i}{s} = \frac{k_d s^2 + k_p s + k_i}{s} = \frac{k_d (s^2 + \frac{k_p}{k_d} s + \frac{k_i}{k_d})}{s} \tag{6}$$

The transfer function introduces two zeroes and one pole at the origin. By selecting a gain and the position of the zeros, the controller gains were determined. In a first design (Figure 4), the two zeros and the gain k_d were chosen in such a way that the Bode plot resembled the plot in Figure 2 and Reference [2], with an amplitude ratio of 90dB at 50Hz and crossover at 15000rad/s (2400 Hz). The results are shown in Figure 6.

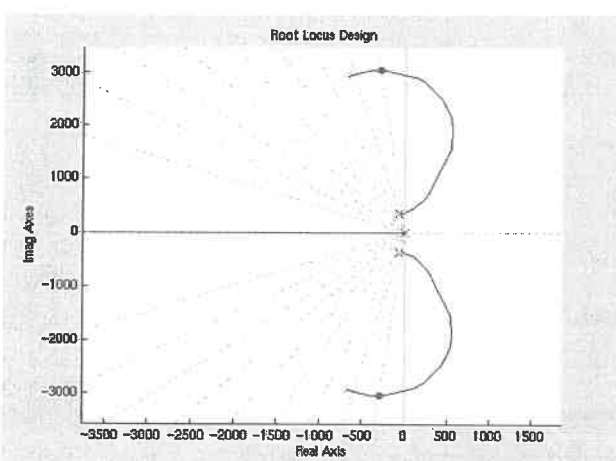

Fig. 5: Root locus of first controller design

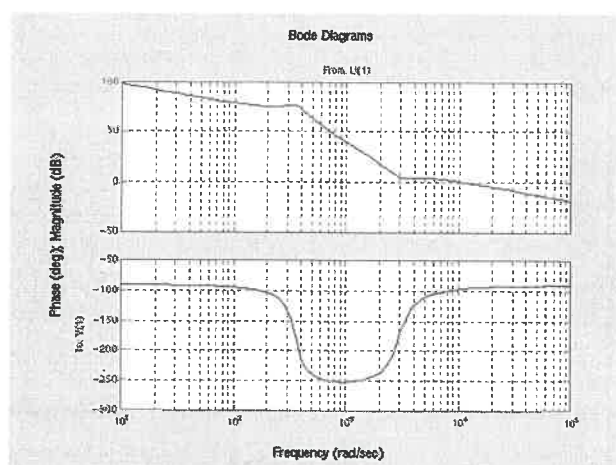

Fig. 6: Bode plot of first controller design

For stability, the phase margin should be greater than 70 degrees. Figure 6 shows that this criterion is met. The transfer function for the controller designed was therefore

$$TF_{PID} = \frac{k_d(s+669\pm 2925i)}{s} = \frac{0.05s^2+67.51s+454200}{s},\ k_d = 0.05\,\text{sec} \tag{7}$$

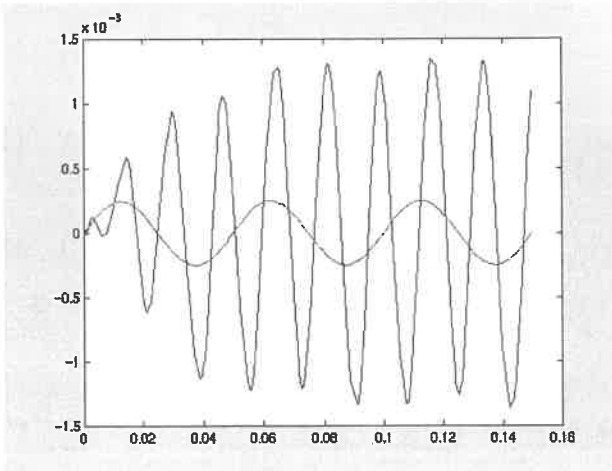

Fig. 7: Unstable system response

The root locus indicates that the derivative gain, k_d, should be greater than 0.02secs or less than 7μs for stability. Calculating the controller gains yielded:

$$k_d = 0.05\text{sec}\quad k_p = 26513\quad k_i = 178361240\text{sec}^{-1} \tag{8}$$

The gains were then exported to the Simulink model (Figure 3) to investigate how the non-linearities affected the system. Figure 7 shows the response of the non-linear system to a 20Hz, 250μm sinusoidal wave. It is obvious that the non-linear system is unstable. The equivalent linear system has minimal error and is stable if the non-linearities are removed.

A possible solution to the problem of saturation is to move the zeros in such a way that the system remains stable even with saturation effects. Figure 8 shows the zeros in different locations, which led to a new controller design. The Bode plots for this system are shown in Figure 9. The disadvantage of this design is that the crossover frequency is about one order of magnitude higher than in the previous design, thereby requiring a much larger bandwidth of the mechanical system.

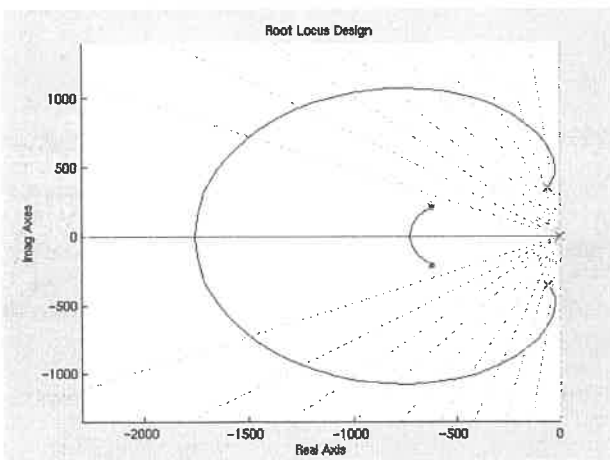

Fig. 8: Loci completely in left hand plane

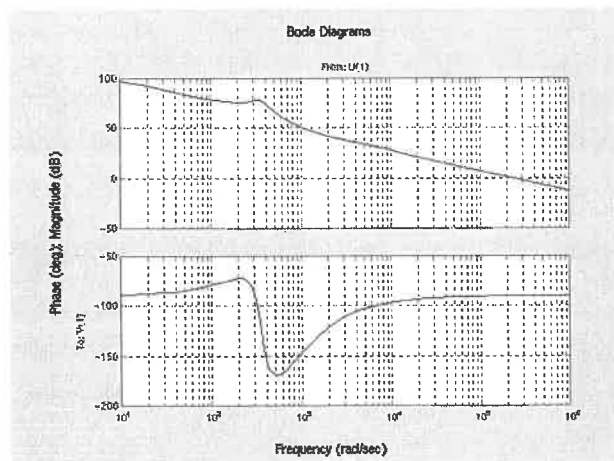

Fig. 9: Bode plot of stable system

The transfer function for this controller was

$$TF_{PID} = \frac{k_d(s+619\pm 215i)}{s} = \frac{s^2+1238s+429400}{s} \qquad k_d = 1 \tag{9}$$

Calculating the controller gains yielded

$$k_d=1\text{s}\quad k_p=1238\quad k_i=429400/\text{s} \tag{10}$$

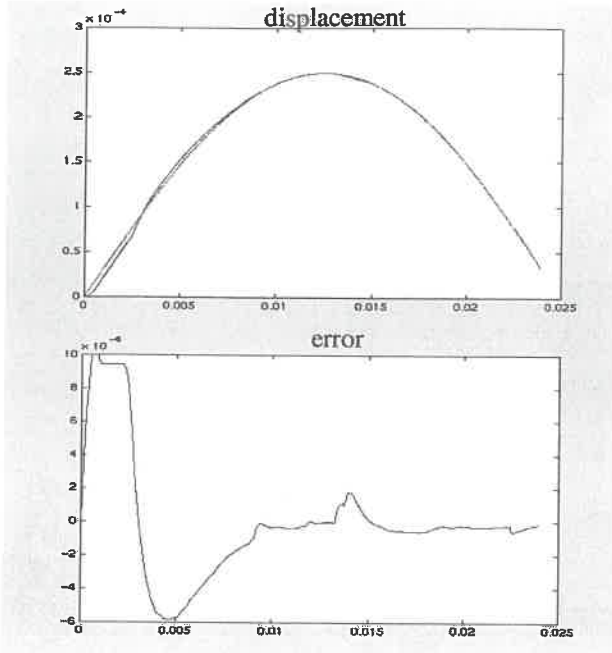

Fig. 10: System response of stable system

These gains were exported into the Simulink model again. From observation it can be seen, that the system has a stable response, even with the presence of saturation (Figure 10). However, the combination of saturation effects and non-optimized gains causes following errors as high as 10 µm. To minimize those errors and to improve the system's performance, the saturation limits need to be raised. At this time, the amplifier is limited to a maximum output of 2A. Once sufficient cooling for the heat sink of the amplifier is achieved, the amplifier should be able to deliver up to 8A.

Conclusion

Once the saturation limits of the amplifier are risen, the following error is expected to drop significantly. Currently, work is being done to interface FTSii with a diamond turning machine. A new housing has been designed that will contain the interferometer, the flexure, and a counterweight to reduce the moment exerted on the slide.

References

1. P. D. Knight, Jr. "Measurement of cylindrical parts by grazing incidence interferometry", Dissertation, University of North Carolina at Charlotte, expected publication September 2000.
2. Guang Lu, "System Identification and Modeling of a Precision Fast Tool Servo", Thesis, University of Alabama, 1999
3. William T. Thomson, Marie Dillon Dahleh, "Theory of Vibration with applications", 5th edition, Prentice Hall, 1998
4. William J. Palm III, "Modeling, Analysis, and Control of Dynamic Systems", 2nd edition, John Wiley and sons, inc.
5. Matlab/Control System Toolbox user's guide, Version 4.2, the Mathworks Inc.

Keywords: Fast Tool Servo, Diamond Turning, PID, Laser Interferometer

Investigations into Spindle Error Motions using a Modified Loading Device

Aditya K. Sharma
Manufacturing Research and Development
The Boeing Company, Seattle, WA 98124
and
Steven R. Patterson
Center for Precision Metrology
University of North Carolina at Charlotte, Charlotte, NC 28223

Keywords: CNC vertical machining center, Loading device, Spindle error analyzer, Axial and Asynchronous error motions

Introduction

Current measurement methods specified by ANSI/ASME B5.54-1993 and B89.3.4-1985 Standards[1, 2] for spindle error motions establish error motion characteristics of the spindle with no load applied to the spindle bearings. It is possible that the application of load to spindle bearings will result in either different error motions or a different response to the error motions, or both.

The objective of this study is to extend the application of a loading device designed and built in a previous study to investigate error motions of a Computer Numerically Controlled (CNC) machine tool spindle with tapered roller bearings and a constant preload mechanism.

Experimental Setup

The loading device is an external fixture that applies various axial loads to lower and upper bearings of a spindle. It combines traditional spindle testing with an artifact to study both spindle drift and error motions with the ability to conduct these tests under load while at speed. The details of loading device can be found in Reference [3].

In this study, design of the loading device has been modified for testing on a Monarch vertical machining center (VMC-75). A separate fixture was designed to mount the pair of magnets. To apply thrust load to the spindle bearing system, magnets are mounted to a collar that fits around the quill of the machine. The collar is made of Aluminum and has small clearance to fit onto the quill with various holes for mounting magnets that can be placed equal distance from the centerline of the spindle. Additionally, a new tool holder was modified by heat-shrinking a steel sleeve onto the straight dimension of the collet chuck. The sleeve allowed target plate to be mounted onto the tool holder. The spindle of this machine tool has tapered roller bearing and a constant preload throughout the range of speeds from 35 to 10,000 rpm.

Spindle error motion tests were conducted at various rpms using the modified loading device with an application of 140 lbs. of thrust load and under no load. The test set up for spindle error motions under load is shown in Figure 1. For tests under unloaded conditions, magnets are removed from the collar.

A commercially available, capacitance gauge based system is utilized to monitor spindle error motions under load and no load conditions. A calibrated load cell was used to monitor loads applied

to the spindle at a given air gap. The range of axial loads that can be achieved using the modified loading device is from 0-140lbs (623N) at an air gap of 0.125 inch (3mm).

To establish a relationship between unloaded and loaded spindle error motions, results of axial and radial error motions along with polar plots have been analyzed and reported.

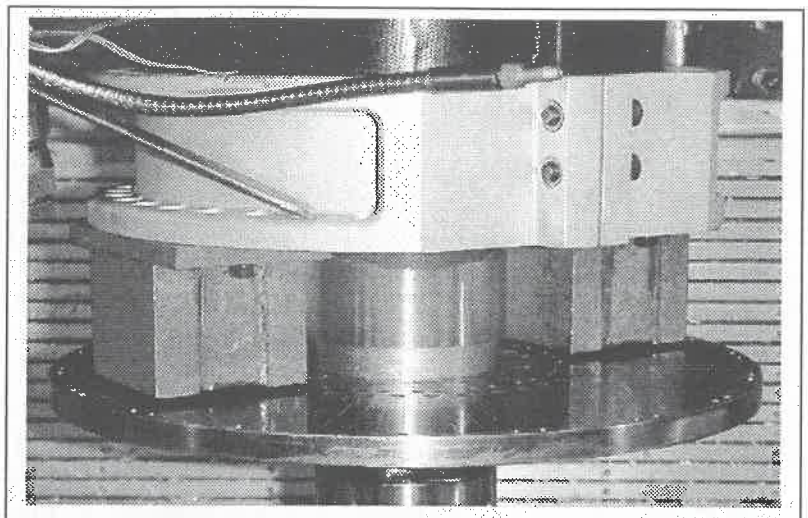

Figure 1 Setup for spindle error motions under load

Results of Spindle Error Motions under Loaded and Unloaded Conditions

Spindle error motions have been analyzed for Axial error motions and Asynchronous error motions. Tests at various loads and rpms were conducted according to the ANSI/ASME B5.54 standard specifically related to the axial and radial error motions for rotating sensitive direction.

In this study, tests conducted under the application of 140 lbs of axial load are reported. For radial error motion tests, only asynchronous error data have been analyzed and reported.

Axial Error Motions, Rotating Sensitive Direction

The axial error motion is defined as in and out motion of the spindle while it rotates. The data has been taken for 16 revolutions of spindle with 128 data points per revolutions. For axial error motion tests capacitance gage target eccentricity was minimized to avoid measurement errors. Figure 2 shows results of the axial error motion magnitudes under loaded and unloaded conditions and at various rpms.

Axial error motion was found to be higher at unloaded conditions of the spindle bearing system. The

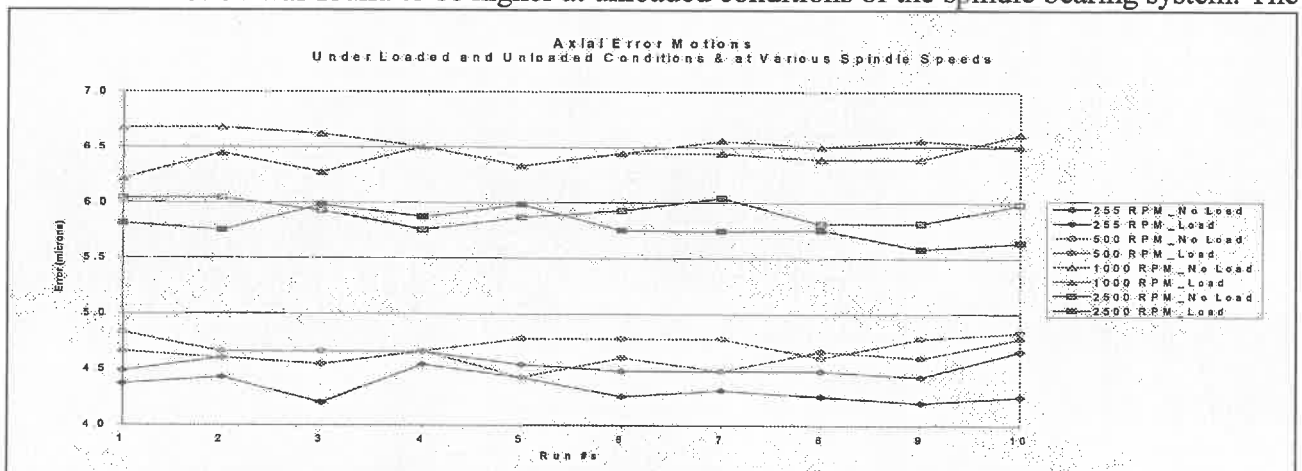

Figure 2 Axial error motions under loaded and unloaded conditions and at various spindle speeds

application of 140 lbs. of axial load reduced both the amounts of axial error and variations within

the measurements by approximately 0.25 and 0.15 micron respectively. It is possible that by increasing the amount of axial load may reduce either the magnitude of the axial error or the amount of variations within measurements or both.
At 500 rpm, the application of external load in this study did not affect spindle axial error motion. Similar results were obtained at spindle operating speeds of 1000 and 2500 rpm. However, the amount of axial error obtained was higher by approximately 0.60 micron at 1000 rpm than at 2500 rpm.

Radial Error Motion, Rotating Sensitive Direction
In capacitance gage measurement system data is acquired from the X and Y probes positioned 90 degrees to each other. The probes measure X and Y changes in position of the axis line of rotation and generates sine and cosine signals to produce a polar plot using Tlusty method [4,5]. For radial error measurements target eccentricity was maintained constant.

Figure 3 shows results of the asynchronous error motions recorded at various rpms, and under the applications of 140 lbs of axial load on spindle bearings and under unloaded conditions of the spindle.

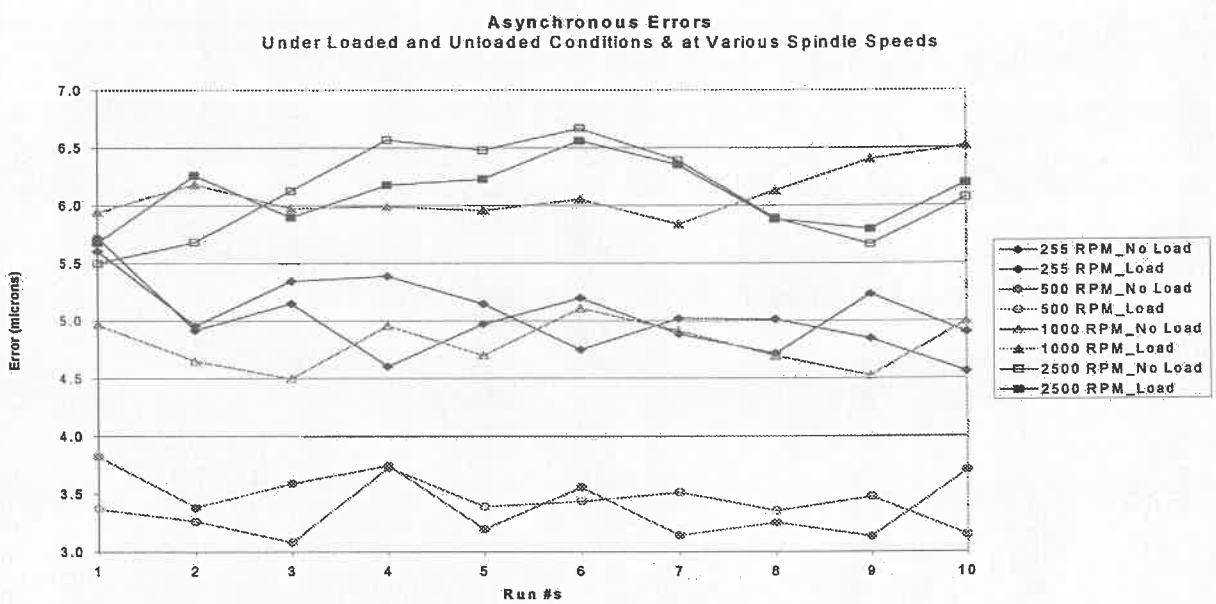

Figure 3 Asynchronous error motions under loaded and unloaded conditions and at various spindle speeds

For radial error motions at 255 rpm and 500 rpm, application of 140 lbs. of thrust load did not influence asynchronous error motions. However, variations in measurements obtained were approximately one and one-half times larger at 255 rpm than at 500 rpm.
At 1000 rpm, average asynchronous error motion increased by approximately 3 microns when axial load was applied to spindle bearing system. Further data analysis and measurements will be required to establish key factors that could cause spindle error motion to remain unchanged both under

loaded and unloaded conditions at 1000 rpm. Asynchronous error magnitude remained unchanged at 2500 rpm.

Conclusions and Future Work

A loading device previously designed and built to study spindle thermal drift was modified and utilized to investigate error motions under loaded and unloaded conditions. The maximum load and spindle operating speed were limited to 140 lbs. and 2500 rpm.

The magnitude of axial error motions under the application of 140 lbs. of external load did not change significantly when compared with the axial error motion without the application of load. However, variations within the measurements were found to be larger than the difference in the magnitudes of axial errors obtained under loaded and unloaded conditions.

Similar characteristics were obtained for asynchronous errors accept for measurements at 1000 rpm. At this rpm, asynchronous error increased under the application of 140 lbs. of axial load. However, more measurements and data analyses are necessary to establish spindle behavior at this rpm.

Future work will include comprehensive analysis of the data obtained with the modified loading device, and study of spindle thermal stability under loaded and unloaded conditions.

References

1. ANSI/ASME B5.54-1993, " Methods for Performance Evaluation of Computer Numerically Controlled Machining Centers," American Society of Mechanical Engineers, NY, 1992.
2. ANSI/ASME B89.3.4, "Axes of Rotation, Methods for Specifying and Testing" American Society of Mechanical Engineers, NY, 1985.
3. Sharma, A.K., "An Experimental Investigation into Thermal Spindle Growth Under Load", Masters Thesis, The University of North Carolina at Charlotte, 1997.
4. "Spindle Error Analyzer, Instructions Manual," Lion Precision, Inc., St. Paul, MN., 1996.
5. Tlusty, J. "System and methods of testing machine tools," Microtechnic, 13, 162-178, 1959.

PRECISION RADIAL MAGNETIC BEARING

Tadahiko Shinshi, Chihiro Iijima, Xiaoyou Zhang ,
Kee-Bong Choi , Kaiji Sato and Akira Shimokohbe

Precision and Intelligence Laboratory, Tokyo Institute of Technology, Yokohama, Japan

Introduction

Conventional air bearings of a high rotational accuracy have been widely used in precision machines. However the rotational accuracy of the air bearings decreases due to the unbalance force at a high speed and the disturbance force because of their low stiffness and damping. On the contrary, magnetic bearings can compensate motion errors caused by the unbalance and disturbance forces because of their active motion control capability. Moreover magnetic bearings are free from friction so that they are candidates for high accurate and high-speed bearings in the future. A precision magnetic stage and linear guides having positioning resolutions of several ten nanometers have been presented [1-2]. However there have been no magnetic bearings of nanometer rotational accuracy.

The goal of this research is to realize a magnetic bearing which has rotational accuracy of several nanometers at 10,000 rpm. As the first step, this paper discusses a precision radial magnetic bearing (PRMB) in which radial two-degree-of-freedom motions of the spindle are precisely controlled.

Precision Radial Magnetic Bearing

An experimental radial magnetic bearing is designed and constructed, as shown in Figures 1 and 2. The spindle motions in the X and Y directions are controlled by eight electromagnets. To support the other degrees of freedom of the spindle motion, thrust air bearings are used. The electromagnets are comprised of E-core laminations of Ni-Fe alloy and coils of 25 turns. The nominal air gap between the spindle and the electromagnets is 0.2 mm. The saturation current to the coil with which the flux density of the core as well as the electromagnetic force saturates is 10 A. The possible moving range of the spindle is between -100 and 100 μm which is restricted by touch-down bearings and measurement range of capacitance displacement sensors.

The spindle consists of one steel shaft with a flange as a sensor target, two Ni-Fe lamination rings facing electromagnets and one rotor of an induction motor. The mechanical surfaces of the spindle and electromagnets are finished precisely to prevent the magnetic disturbance force which is caused by variation of the magnetic reluctance due to gap errors between the electromagnets and the spindle. The maximum diameter of the spindle is 80 mm and its mass is 3.29 kg. The roundness of the sensor target is 30 nm. The spindle can be alternatively driven by the induction motor or compressed air. The displacements of the spindle in the X and Y directions are measured by two capacitance displacement sensors

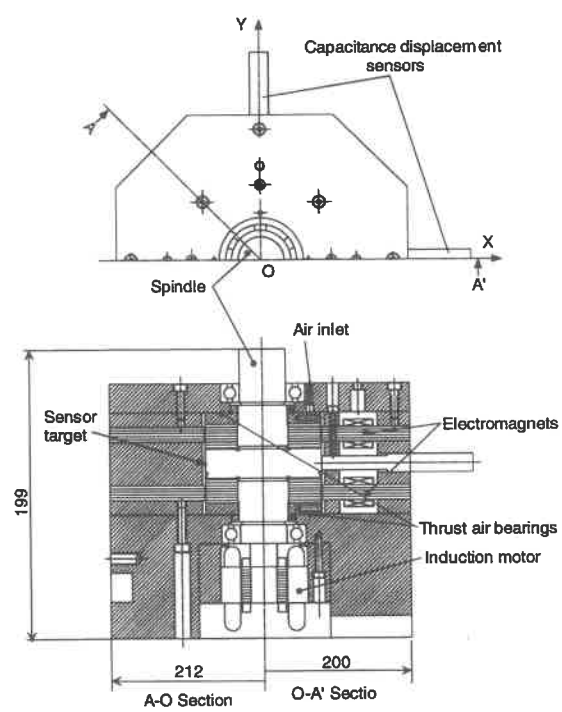

Figure 1: PRMB configuration

(ADE, Microsense 5130, 0.2 mm measuring range). The resolutions of the sensors are about 15 nm including signal acquisition and processing systems.

Control Scheme

A pair of electromagnets is necessary to generate a bidirectional force. In Figure 3, the electromagnetic force F to an object is predominantly controlled by two currents i_a and i_b. Because there is a infinite number of combination of i_a and i_b to generate a certain force, how to determine the currents must be discussed.

One of simple solutions is to work only one actuator of the two shown in Figure 4 (zero bias control). The primary advantage of this control is that the heat generation of the actuators can be minimized. On the contrary, the drawbacks are zero-force slew rate at zero coil current [3], and nonlinear relationship between the current and the force. Although the latter can be overcome by feedback linearization [4], the zero-force slew rate can not be compensated. The zero-force slew rate is undesirable for precise motion control because the electromagnets do not produce control forces when the currents are around zero.

The other solution is to work both coils simultaneously such that $i_a = i_0 + i$ and $i_b = i_0 - i$, where i_o is a fixed bias current and i is a command current (bias current control). This control scheme is widely used in the conventional magnetic bearings because they have linearity to the command current i without additional linearization and the force slew rate does not become to zero unless i_0 is zero. To generate the maximum force within the linear range of the command current and force with the push-pull scheme, i_0 should be the half of the saturation current. Such a large bias current generates a large amount of heat.

To overcome the zero-force slew rate and the heat generation, this paper proposes the partial bias control as shown in Figure 5. While the command current is within +/- i_0, the drive currents such that $i_a = i_0 + i$ and $i_b = i_0 - i$ are applied to the coils. On the contrary, the command current exceeds +/- i_0, one of the drive currents is made to zero.

Figure 6 shows the block diagram of the control system. The positioning controller consists of a states feed-

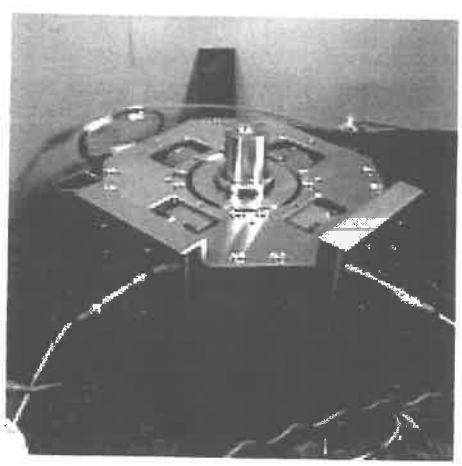

Figure 2: The prototype PRMB without upper thrust air bearings

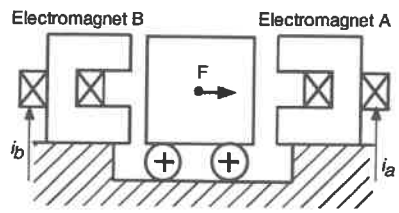

Figure 3: 1- DOF motion control using a pair of electromagnets

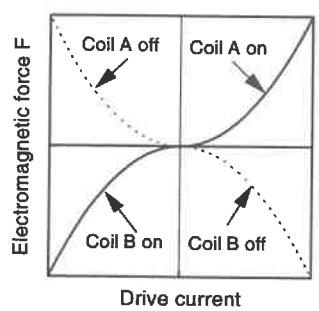

Figure 4: Zero bias control

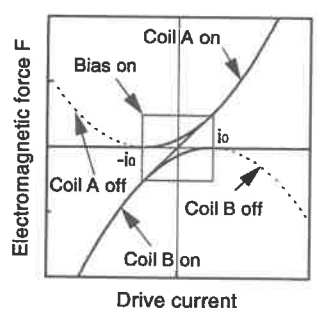

Figure 5: Partial bias control

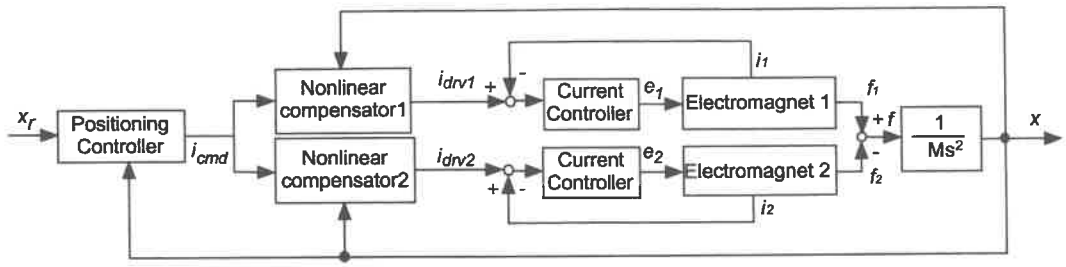

Figure 6 : Block diagram of the PRMB system

back controller and an observer. To decrease a time constant of the electromagnets, current feedback loops are used. Nonlinear compensators using the gap information linearize the relationship between the command current and the control force. Thus the zero-force slew rate and the nonlinearity of the actuators can be overcome by the partial bias control and the nonlinear compensator. Furthermore, the heat generation of the partial bias control can be made much smaller than that of the bias control when a smaller i_0 is used..

The PRMB is controlled by a DSP, 16 bit A/D and 14 bit D/A converters at 10 KHz sampling. The gain of the capacitance displacement sensor is 10 nm/mV. The positioning controller works so as to keep the gap constant. Strictly speaking, the measured gap does not indicate an real rotational accuracy because the profile errors of the sensor target is included in the displacement sensor outputs.

Experimental Results

Positioning and rotational accuracies of the spindle using the zero bias and the partial bias control (i_{max}=10A, i_0=1A)are compared with the same positioning and current feedback controllers. Figure 7 shows positioning resolutions using the zero bias and the partial bias control. In the X and Y directions, the positioning resolutions of the zero bias control are 40 nm. By the partial bias control, 20 nm positioning resolutions approximately as same as noise levels of the displacement sensors are achieved.

Figure 8 shows runouts of the rotational spindle using the zero bias and the partial bias control. A standard deviation σ is calculated using runout e during one turn of the spindle. The runout e is calculated by a following equation,

$$e = \sqrt{x^2 + y^2} \tag{1}$$

where x and y are displacement sensor outputs. The 3σ of the partial bias control at 500 rpm is under 10 nm. The repeatable runouts are shown at 1500 rpm. The runouts of the spindle gradually increase by the unbalance force as the spindle speed increases shown in Figure 9. The rotational accuracies of the partial bias control are better than those of the zero bias control.

Conclusions

As the first step to realize a precision magnetic bearing, a radial magnetic bearing was designed and constructed. The higher positioning resolutions and rotational accuracies than those of conventional magnetic bearings [5] were attained. The spindle using the partial bias control had 20 nm positioning resolutions in the X and Y directions at 0 rpm and 8.97 nm (3σ) rotational accuracy at 500 rpm. It is proved that the partial bias

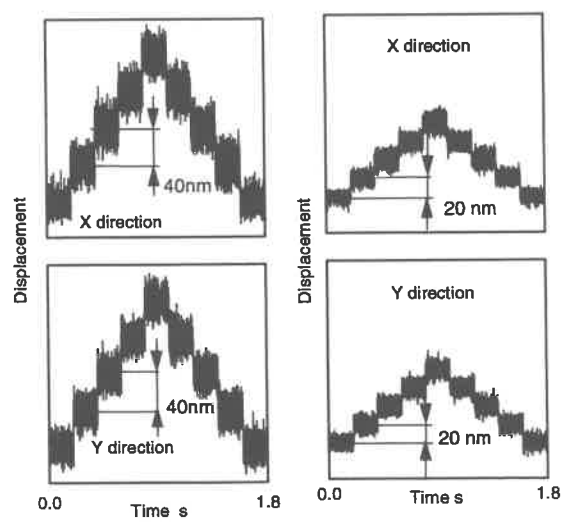

(1) Zero bias (2) Partial bias (i_0=1A)

Figure 7 : Positioning resolutions at 0 rpm

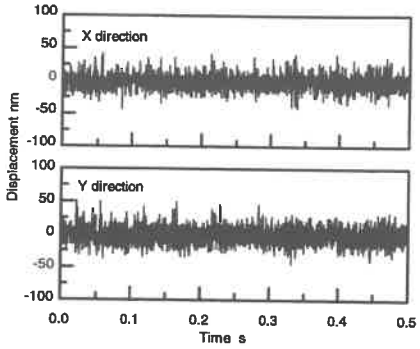

(1-1) Zero bias (500 rpm, 3σ=24.7 nm)

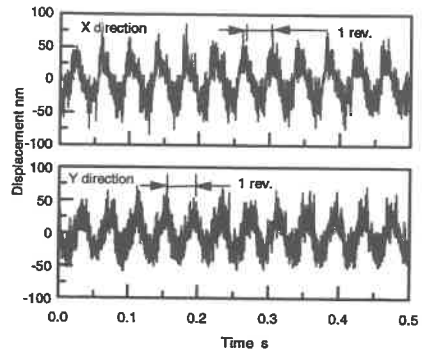

(1-2) Zero bias (1500 rpm, 3σ=35.7 nm)

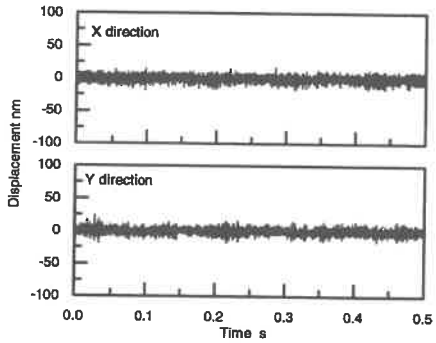

(2-1) Partial bias (i_0=1A, 500 rpm, 3σ=8.97 nm)

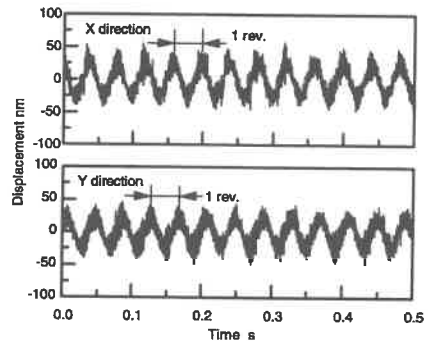

(2-2) Partial bias (i_0=1 A, 1500 rpm, 3σ=23.4 nm)

Figure 8 : Runouts at 500 and 1500 rpm

control is more suitable for improving positioning resolutions and rotational accuracies than the zero bias control.

The future works are evaluation of rotational accuracy in consideration of the roundness of the sensor target, measurement of the heat generation under the control and improvement of the rotational accuracies at a speed of over 1,000 rpm using the repetitive controller.

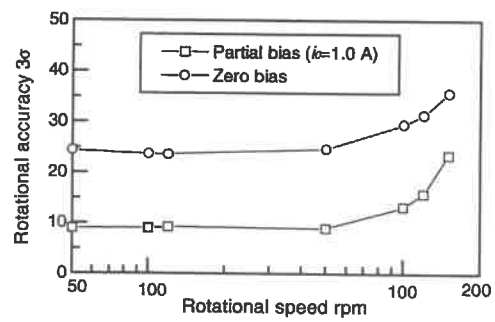

Figure 9 : Rotational accuracies

Acknowledgments

This research is supported in part by Grant-in-Aid for Scientific Research No. 11555049 from JSPS.

References

[1] M. E. Williams, D. L. Trumper and R. Hocken: Magnetic Bearing Stage for Photolithography, Annals of the CIRP, 42,1 (1993) 307-610.

[2] Won-Jong Kim and D. L. Trumper: Linear Motor-Levitated Stage for Photolithograph, Annals of CIRP, 46, 1(1997)447-450.

[3] E. H. Maslen, P. E. Allaire, M. D. Noh and C. K. Sortore: Magnetic Bearing Design for Reduced Power Consumption, Journal of Tribology, 118, October (1996) 839-846.

[4] A. Charara, J. D. Miras and B. Caron: Nonlinear Control of a Magnetic Levitation System Without Premagnetization, IEEE Transactions on Control Systems Technology, 4, 5 (1996) 513-523.

[5] Alexander H. Slocum, Precision Machine Design, Society of Manufacturing Engineers (1992) 629.

HIGH-SPEED METAL-BELLOWS EARTHWORM TYPE IN-PIPE MICROROBOT

Mizuyuki SHIRAKAWA, Manabu ONO and Shigeo KATO

Nippon Institute of Technology
Miyashiro, Saitama 345-8501, JAPAN
E-mail: s954258@stu.nit.ac.jp

Abstract

We fabricated a prototype of a new earthworm type microrobot which is able to move in the thin pipe with very high-speed. The microrobot is made by three flexible metal-bellows which is 6.8 mm in diameter and 20 mm long. The material for the bellows is nickel. The microrobot is driven by the pneumatic pressure and vacuum pressure. The maximum speed of 21 mm/s was obtained in the acrylic pipe of 9 mm in inner diameter. The maximum speed of 18 mm/s was obtained in the small intestine of a sheep held in an acrylic pipe.

***Keywords*:** High-speed, Metal-bellows, Earthworm, In-pipe, Microrobot

1. Introduction

In-pipe mobile microrobots which inspect or repair thin pipes in the atomic plants, pipelines, intestines or blood vessels have been developed. Kato et al. have presented an inchworm type and an earthworm type microrobot [1], [2]. Pneumatic pressure and vacuum pressure were used to drive these microrobots.

We fabricated a prototype of a new earthworm type microrobot which is able to move in the thin pipe with very high-speed. The microrobot is made by three flexible metal-bellows which is 6.8 mm in diameter and 20 mm long. The material for the bellows is nickel. The microrobot is connected with three thin tubes which are 1 mm in inner diameter, 1000 mm long and feed pneumatic and vacuum pressure to the microrobot. The air-feeding tubes are 2 times larger than the microrobot which we fabricated last years in their length and inner diameters. The pneumatic pressure of +0.035 MPa and the vacuum pressure of –0.085 MPa are used to drive the microrobot. These two pressures are switched by three electromagnetic valves. First, the vacuum pressures are supplied to the three metal-bellows. The microrobot is shrunk at that time. Then, the pneumatic pressure pulses are sequentially supplied to the top, the second and the third bellows. A tractile wave generated by the stretching and shrinking motion goes to the backward direction in the metal-bellows. The microrobot repeats such stretching and shrinking motion which leads to go forward direction. If we want to reverse the microrobot, the pneumatic pressure must be supplied from the third to the top bellows.

The microrobot is equipped with four friction-rings which are located at the joint of the metal-bellows. The rings are 9 mm in outer diameter and 0.3 mm thin made of vinyl chloride. These rings make friction force between the pipe and the microrobot. A ring makes the force of 0.08 N for the forward direction and 0.13 N for the backward direction in acrylic pipe of 9 mm in inner diameter. A ring also makes the force of 1.02 N for the forward direction and 1.21 N for the backward direction in the small intestine of sheep held in acrylic pipe of 9 mm in inner diameter.

The maximum speed of 21 mm/s was obtained in the acrylic pipe of 9 mm in inner diameter. The cycle time was 0.09 s. This speed is 1.2 times of former fastest speed of 18.2 mm/s The maximum speed of 18 mm/s was obtained in the small intestine of a sheep held in an acrylic pipe. The cycle time was 0.09 s. The intestine of a sheep is almost same as the large intestine of human child. This robot is also effective for inspect in the intestine of human child.

2. Structure of the fabricated microrobot

We fabricated a prototype of a new earthworm type microrobot which is able to move in the thin pipe with very high-speed. The microrobot is structured by a flexible metal-bellows. The cross section of the microrobot is shown in Fig. 1. The material for the bellows is nickel. The microrobot is 6.8 mm in inner diameter and 60 mm long. Three silicon air-tubes which feed pneumatic and vacuum pressure to the microrobot. The air-tubes are 0.5 mm in inner diameter, 1 mm in outer diameter which is put within inside of the metal-bellows. The air-tubes are put within outside of the metal-bellows which are 1 mm in inner diameter and 2 mm in outer diameter and 1000 mm long, because these thick tubes are easy to supply the air. Four friction-rings which are 9 mm in outer diameter, 4 mm in inner diameter and 0.3 mm thin are fixed at all ends of the bellows. The friction-rings are made of vinyl chloride These rings make friction force between the pipe and the microrobot.

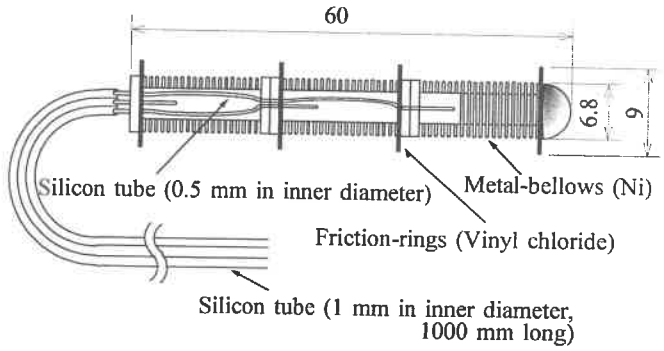

FIg. 1 Structure of the earthworm type microrobot

The moving principle of microrobot shown in Fig. 2.

① The vacuum pressures are supplied to the three metal-bellows. The microrobot shrinks at that time.
② The pneumatic pressure is supplied to the top bellows, the top bellows stretches.
③ The pneumatic pressure is supplied to the second bellows, and vacuum pressure in supplied to the top bellows, the second bellows stretches and the top bellows shrinks.
④ The pneumatic pressure is supplied to the third bellows, and vacuum pressure is supplied to the second bellows, the third bellows stretches and the second bellows shrinks.

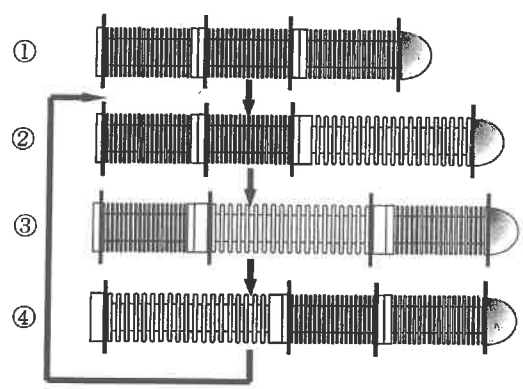

Fig. 2 Movement of tne earthworm type microrobot

A tractile wave generated by the stretching and shrinking motion goes to the backward direction in the metal-bellows. The microrobot repeats such stretching and shrinking motion which leads to go forward direction. If we want to reverse the microrobot, the pneumatic pressure must be supplied from the third to the top bellows.

3. Frictional force

Four friction-rings which fixed at ends of the bellows. The friction-rings made of vinyl chloride. These rings make friction force between the pipe and the microrobot. The friction forces made by the friction-rings are shown in Table. 1. A ring makes the force of 0.08 N for the forward direction and 0.13 N for the backward direction in acrylic pipe of 9 mm in inner diameter. A ring also makes the force of 1.02 N for the forward direction and 1.21 N for the backward direction in the small intestine of sheep held in acrylic pipe of 9 mm in inner diameter. The friction force is backward direction larger than forward direction. Consequently, the microrobot is able to go forward by these differences.

Table. 1 Frictional force

	Forward direction (N)	Backward direction (N)	Difference of both forces (N)
Acrylic pipe	0.08	0.14	0.06
Sheep's small intestine	1.03	1.21	0.18

4. Moving speed

An experimental apparatus for measuring the speed of the microrobot is shown in Fig. 3. A computer controls three electromagnetic valves through a valve controller. Three feeding air-tubes are connected from the electromagnetic valves to three metal-bellows and independently feed the pneumatic and the vacuum pressure to each metal-bellows. The vacuum pressure is –0.085 MPa and the pneumatic pressure is +0.03 MPa. The pulse width time is changed from 0.03 seconds to 0.3 second. The displacement of the metal-bellows is measured by the laser displacement indicator to calculate the virtual speed.

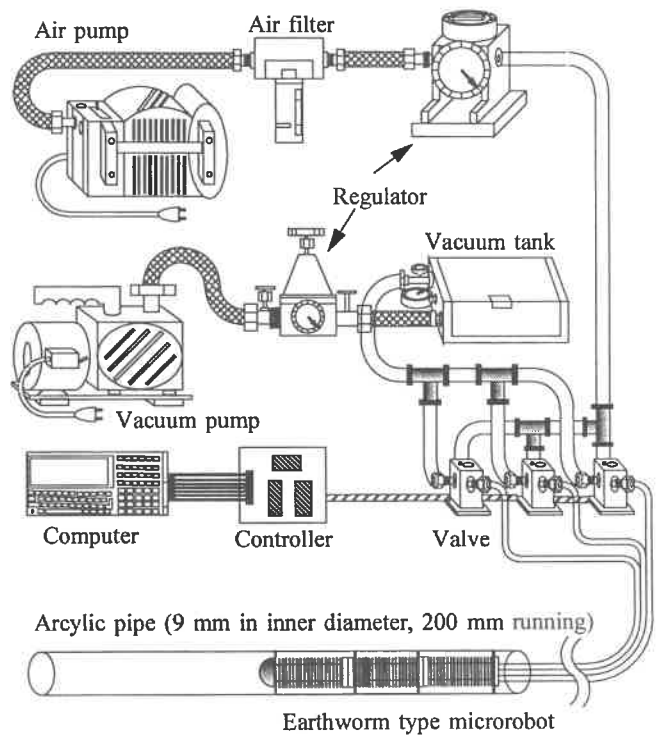

Fig. 3 Exprermental apparatus

The speed of the microrobot is shown in Fig. 4. The maximum speed of 21 mm/s was obtained in the acrylic pipe of 9 mm in inner diameter. The cycle time was 0.09 s. The maximum speed of 18 mm/s was obtained in the small intestine of a sheep held in an acrylic pipe. The cycle time was 0.09 s. The virtual speed of 25 mm/s was obtained in this cycle time was 0.06 s. The vertical traction force of 15 N was obtained in acrylic pipe.

5. Speed coefficient

The speed coefficient is shown in Fig. 5. The speed coefficient is a ratio of the real speed and the virtual speed. The speed coefficient of 0.8 was obtained in the acrylic pipe. The speed coefficient of 0.6 was obtained in the small intestine of a sheep held in an acrylic pipe. The speed coefficient of 0.8 in the acrylic pipe was higher than the small intestine of a sheep of 0.6, because the small intestine of a sheep are more flexible than metal-bellows. As a result, the real speed can be predicted by the virtual speed.

6. Conclusions

Fabrication of a prototype of a new earthworm type microrobot to inspect or to repair thin pipes in the human body or pipelines was performed. The followings are the conclusions of the fabrication.

(1) We fabricated a new earthworm type microrobot which is constructed by a metal-bellows which is 6.8 mm in outer diameter and 60 mm long. A plastic air feeding tubes which feeds pneumatic and vacuum pressure to the microrobot is 1 mm in inner diameter and vacuum pressure to the microrobot is 2 mm in inner diameter and 1000 mm long.

(2) Four friction-rings of vinyl chloride 9 mm in outer diameter are fixed at the metal-bellows. These friction-rings make friction force between the pipe and the microrobot. A ring makes the force of 0.08 N for the forward direction and 0.13 N for the backward direction in acrylic pipe of 9 mm in inner diameter. The ring makes the force of 1.02 N for the forward direction and 1.21 N for the backward direction in the small intestine of sheep held in acrylic pipe of 9 mm in inner diameter.

(3) The microrobot is able to move in an acrylic pipe of 9 mm in diameter. The maximum speed of 21 mm/s was obtained in the acrylic pipe of 9 mm in inner diameter. The cycle time was 0.09 s. The maximum speed of 18 mm/s was obtained in the small intestine of a sheep held in an acrylic pipe. The cycle time was 0.09 s. The virtual speed of 25 mm/s was obtained in the cycle time was 0.06 s. The vacuum pressure of –0.085 MPa and the pneumatic pressure of +0.03 MPa were used.

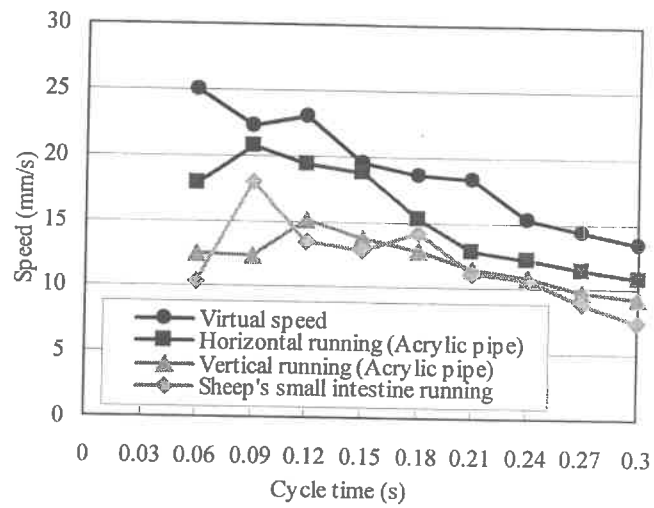

Fig. 4 Speed of the microrobot

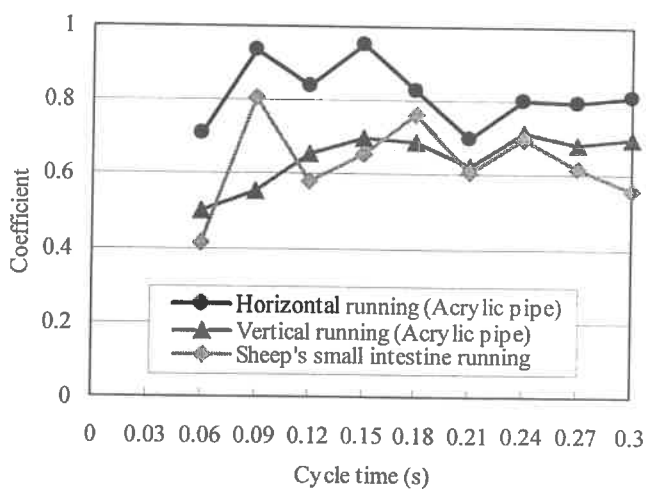

Fig. 5 Speed coefficient

(4) The speed coefficient of 0.8 and 0.6 were obtained in the acrylic pipe and in the small intestine of a sheep held in an acrylic pipe respectively. The acrylic pipe's speed coefficient was higher than the small intestine of a sheep's speed coefficient.

References:

[1] S. Kato, M. Shirakawa, M. Ohno and S. Fukumoto, *Proceedings from ASPE 1999 Annual Meeting* (1999), 37-40.

[2] S. Kato, M. Shirakawa, M. Ohno and M. Tabata, *Proceedings from ASPE 1999 Annual Meeting* (1999), 204-208.

Kinematic Couplings for Pallets in Flexible Assembly Systems

R. Ryan Vallance* and Alexander H. Slocum†

***Precision Systems Laboratory, University of Kentucky, Lexington, KY** [1]
†Precision Engineering Research Group, Massachusetts Institute of Technology, Cambridge, MA [2]

Abstract

Flexible assembly systems use conveyors to transfer products through a series of workstations. The product being assembled is typically held in a fixture mounted on top of a pallet. Conventional approaches for locating the pallets often use precision ground pins and bushings for location. This technique requires clearance between the pin and bushings to accommodate manufacturing variation and prevent binding. For one system, this clearance limits the repeatability of the pallet to 100 microns. For high-precision assembly operations, the non-repeatability of the pallet can be one of the largest sources of variation and lead to low quality or poor yields. This paper presents kinematic couplings as an exact constraint approach for locating pallets in flexible assembly systems. The paper describes a split-groove kinematic pallet used in a flexible assembly system for electrical connectors. The repeatability of the kinematic pallet was measured in factory-like conditions. The repeatability was within 10 microns, which is about an order of magnitude improvement over a leading industrial pallet.

***Keywords*:** kinematic couplings, pallets, flexible assembly systems, and assembly automation

Introduction

During the 1970s and 1980s, flexible assembly systems were developed as an alternative to hard automation that used fixed tooling and machinery. Flexible assembly systems offer the ability to produce a variety of products within the same production system, achieving small batch sizes (sometimes as low as one unit per batch). Flexible assembly systems collect independent workstations into an integrated system connected by a material handling system that transported pallets between workstations. Each pallet carries a fixture capable of holding one or more product assemblies. Powered conveyors with sensors and logical controls are frequently used as the material handling system. In the 1980s, several suppliers of assembly automation released product lines for constructing conveyor systems from modular components [1], and systems using these components are now standard practice within industry.

While designing a flexible assembly system for electrical connectors [2], the variation in pallet location was the largest source of error in the error budget [3]. This amount of variation prevented the connector from being reliably assembled at reasonable quality levels. Therefore, a new approach was developed that used kinematic couplings between the pallets and workstations. Kinematic couplings (and Kelvin clamps) are well-known deterministic mechanical solutions for precisely locating one object with respect to another [4],[5].

This paper presents kinematic couplings as a new alternative for precisely locating palletized fixtures on workstations in flexible assembly systems. The paper begins with a description of an industrial pallet system and the pallet's locating method. Then, the design of a split-groove kinematic pallet is presented. Repeatability measurements of the split-groove kinematic pallet are presented, and the kinematic pallet is shown to be repeatable within ± 0.005 mm (±0.0002 in), an order of magnitude improvement over the conventional pallet.

Conventional Pallet Designs

In one style of modular conveyor systems [6], the pallet is constructed from a molded polyimide frame, a steel or aluminum plate, and four hardened steel bushings. The plastic frame encloses the perimeter of the plate, and the entire assembly is joined by pressing the bushings into the frame and plate. These same bushings are used with ground

[1] *210-A CRMS Building, Lexington, KY 40506. http://www.engr.uky.edu/psl.*
[2] *Rm 3-455, 77 Massachusetts Institute of Technology, Cambridge, MA 02139, USA. http://pergatory.mit.edu.*

pins to locate the pallet at workstations. The precision ground pins, mounted on the workstation, slide into the bushings within the pallet. The precision ground pins are available in two varieties, one variety with a round profile and one with a diamond profile.

The locating method for this style of pallet is illustrated in Fig 1. The method usually uses one of the round pins and one of the pins with flats. The round pin constrains the translational degrees of freedom (in the plane), and the pin with flats constrains the rotational degree of freedom. With this approach to locating the pallet at the workstation, the clearance between the bushings and pins limits the repeatability. The clearance is necessary to accommodate manufacturing variation in the location of the bushings and the distance between the holes. The clearances limit the pallet repeatability to about ±0.05 mm (± 0.002 inches) in the plane [6].

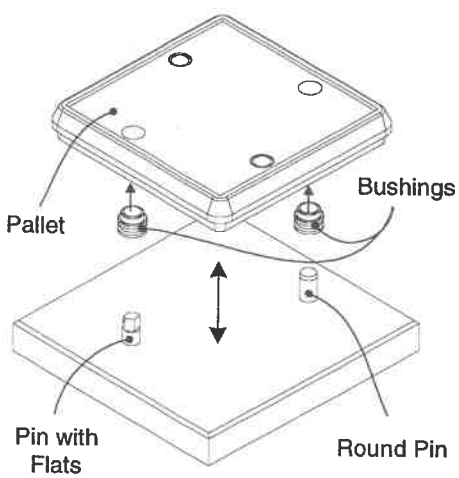

Fig 1: Position method for conventional pallets

Split-Groove Kinematic Pallet Design

Kinematic couplings are exact constraint [7] devices for positioning one body with respect to another body. Kinematic couplings come in many forms, but the two most common configurations are the Kelvin coupling and the three-groove coupling [8]. Kinematic couplings connect two bodies through six contact points, exactly enough for static equilibrium. This ensures that the coupled body is statically determinant.

Kinematic couplings derive three advantages by ensuring that the body is statically determinant. First, no strain is induced in the coupled body due to forced congruence between the coupled bodies. The second advantage is that a single preferred relative position between the two bodies exists (due to minimizing potential energy). The third advantage is that the coupling is deterministic, which means that its performance is predictable. Unfortunately, kinematic couplings also have some limitations. Since the contact between the bodies is limited to six points, the reactions at the contact points are distributed over very small areas. This Hertzian contact produces large stresses at the contact points. The deformation at the contact points that arises from the contact stress also limits the static stiffness between the coupled bodies.

For the kinematic pallets, an adaptable variant of the three-groove kinematic coupling was used. This variant, called a split-groove kinematic coupling, splits one of the grooves to provide a wide baseline to enhance packaging in space-limited systems. A split-groove kinematic coupling is illustrated in Fig 2. The six contact points exist between the flats of the vee-grooves and the balls. Vallance provides a technique for designing split-groove couplings and considering their stability to disturbance forces [2].

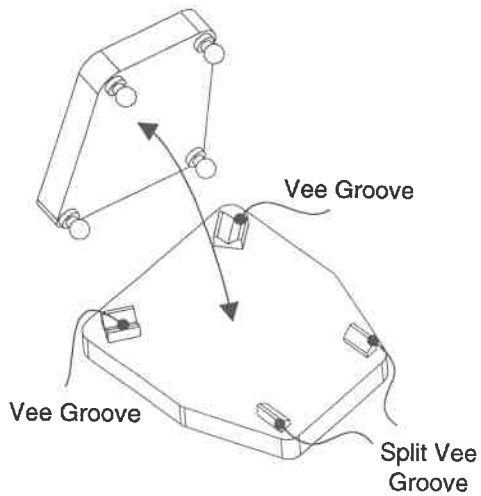

Fig 2: Split-groove kinematic coupling

The split-groove kinematic coupling was designed into a conventional assembly pallet by incorporating the balls into the fixture plate, which fastens onto the top of the conventional pallet. The vee-grooves were designed into the assembly workstation. The split-groove allowed the vee-grooves to straddle the width of the conveyor system and prevented the necessity for locating a vee-groove in the center of the conveyor system. The pallet was preloaded into the vee grooves using a set of permanent magnets. The magnetic preload was sized so that adequate stability existed for a range of

disturbance forces, but the preload was not excessive for manually lifting the pallet off of the workstation.

Fig 3 shows photographs of the split-groove kinematic pallet system designed for the connector flexible assembly system [2]. The vee-grooves and the permanent magnets in the assembly workstation can be seen in Fig 3 (a), and Fig 3 (b) shows the pallet coupled to the assembly workstation.

(a)

(b)

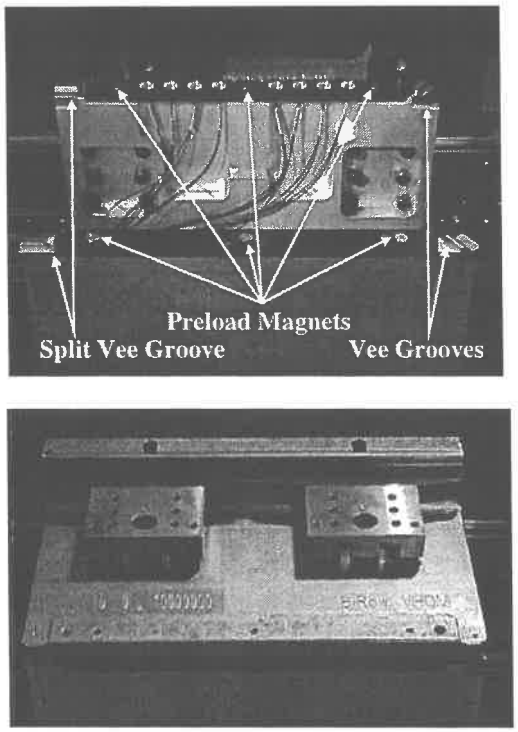

Fig 3: Split-groove kinematic coupling in assembly workstation

Pallet Repeatability Measurements

The repeatability of the split-groove kinematic pallet was assessed experimentally. The experiments were conducted on an instrumentation fixture, shown in Fig 4, which duplicated the geometry of the assembly workstation, including the split vee-groove, the conventional vee-grooves, and the preload magnets. The pallet was lifted and dropped onto the grooves by a pneumatically actuated plate. The lift plate was guided by die set bushings, and it separated from the pallet at the bottom of travel to prevent over constraining the pallet. Capacitive distance sensors were mounted around the pallet to measure the variation in the location of the pallet. Each sensor provided an analog signal (±10 V) proportional to the change in the distance between the face of the sensor and a steel target attached to the pallet (±50 μm). A 16-bit data acquisition system was configured to measure signals between ±5 V, providing a resolution around 0.76 nm/bit.

In factory-like conditions, the pallet was lifted and dropped thousands of times over two days, and the gap distance was measured each time. Fig 5 shows a plot of the four sensors' measurements in microns. The expansion and contraction of the pallet and fixture due to ambient temperature cycles produced a cyclic error with a period of 24 hours and maximum amplitude of 10 μm in Sensor 1. Additional variation due to the air compressor and pneumatic system produced a periodic trend with a period of approximately 2 hours. Even with the errors produced by the thermal and pneumatic cycles, the pallet was repeatable to within 10 μm. This represents a 10X improvement over conventional pallet location methods, which are only repeatable to about ±50 μm.

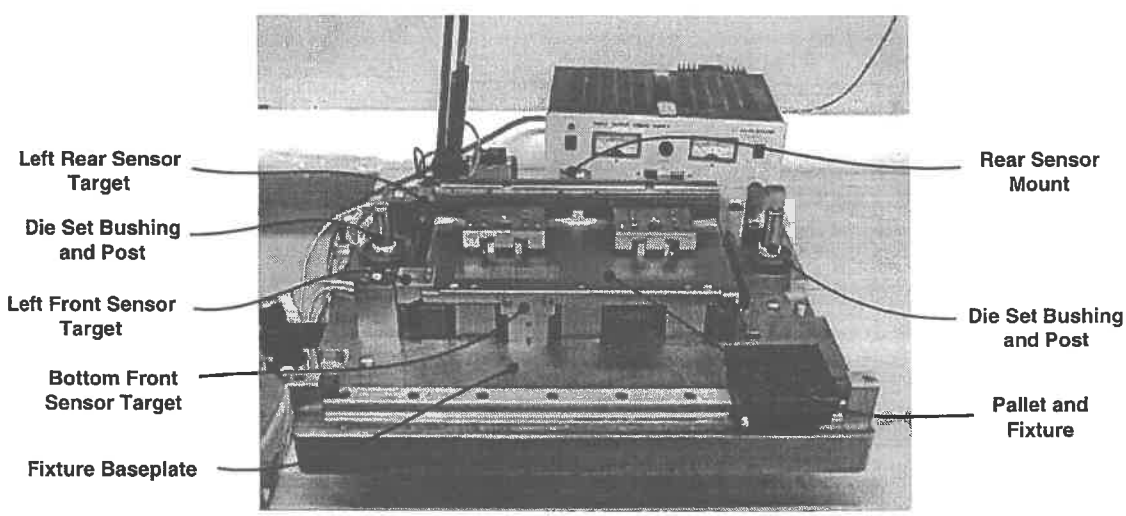

Fig 4: Experimental fixture for measuring pallet repeatability

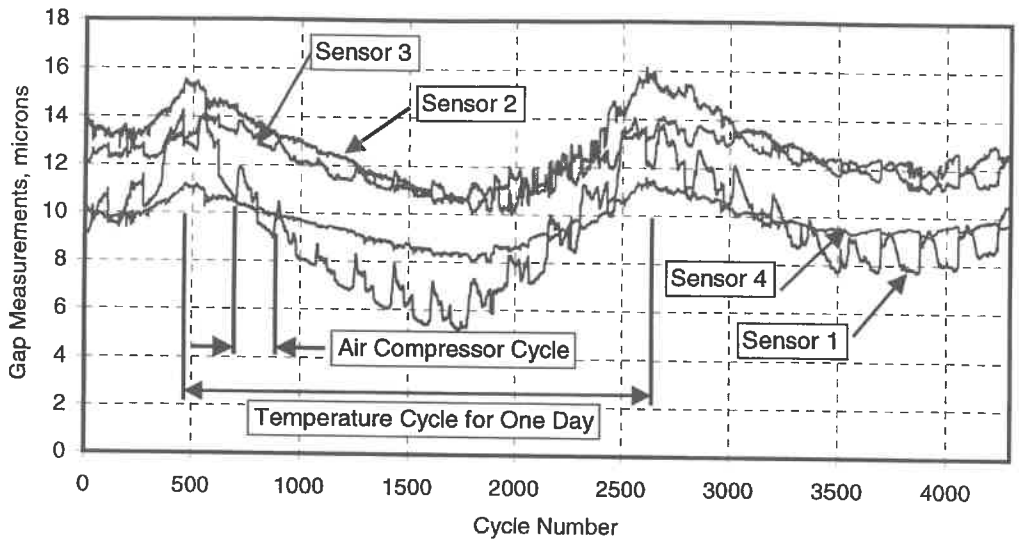

Fig 5: Repeatability measurements for split-groove kinematic pallet

Conclusions and Future Work

Kinematic couplings are an effective approach for improving the repeatability of pallets in flexible assembly systems. At least an order-of-magnitude improvement can be obtained by using a kinematic coupling rather than the standard approach of pins and bushings. A particular embodiment was described that used a split-groove kinematic coupling incorporated into the fixture that mounts on a conventional industry pallet. The repeatability of the kinematic pallet was about ±5 μm, including variation resulting from thermal expansion and pneumatic cycles. This improvement enables flexible assembly systems to be used for products with stringent precision requirements.

Although the benefits of kinematic pallets were demonstrated in this work, future work is needed to incorporate kinematic features into industry standard pallets. This would prevent having to incorporate the kinematic features into the fixture rather than in the conventional pallet. This will require collaboration with an industry partner that designs and manufactures modular conveyor systems.

Acknowledgements

This research was conducted at MIT with funding from Teradyne Connection Systems (Nashua, NH). The authors are grateful to Prof. David Trumper (MIT) for loaning us his capacitance sensors and instrument amplifiers for measuring pallet repeatability.

References

[1] Drexel, P. et al. "Modular Flexible Assembly System 'FMS' from Bosch". *Proceedings of the 3rd International Conference on Assembly Automation.* Stuttgart, Germany. 1982. p. 129-153.

[2] Vallance, R. R. *Precision Connector Assembly Automation.* Ph.D. Dissertation. Massachusetts Institute of Technology. Cambridge, MA. June, 1999.

[3] Donaldson, R. R. "Error Budgets". *Technology of Machine Tools, Vol. 5.* Machine Tool Task Force. Robert J. Hocken, Chairman. 1980.

[4] Slocum, A. "Design of Three-Groove Kinematic Couplings". *Precision Engineering.* Vol. 14, No. 2. April, 1992. p. 67-76.

[5] Schouten, C.H., P.C.J.N. Rosielle, and P.H.J. Schellekens. "Design of a Kinematic Coupling for Precision Applications". *Precision Engineering.* Vol. 20, No. 1. Jan. 1997. p. 46-52.

[6] Bosch Automation's catalog for TS-2 conveyor system. Bosch Automation Products. 816 E. Third St., Buchanan, MI. 49107. Publication No. 8981500127.

[7] Blanding, D.L. *Exact Constraint: Machine Design Using Kinematic Principles.* ASME Press. New York. 1999.

[8] Evans, C. *Precision Engineering: an Evolutionary View.* Cranfield Press. Bedford, UK. 1989.

Evaluation of Machine Tool Contouring Accuracy at High Feed Rates

Dr. Charles Wang and Bob Griffin
Optodyne, Inc. Compton, CA

Dr. Mohammed Omari and Dotun Ajao
General Motors Corporation
Metal Fabricating Division, Troy, MI

Recently, 5-axis high-precision high-speed milling machines have been developed specifically for die mold applications. To achieve the high precision and super-finishes, static positioning accuracy or repeatability is not enough. The acceptable contour will depend on several factors including cutter path complexity, machine static and dynamic accuracy, the machine acceleration and deceleration rate, the machine control system and compensation, data processing rate, etc.

The circular test provides a rapid and efficient way of measuring a machine tool's contouring accuracy. The circular tests show how the two axes work together to move the machine in a circular path. As the machine is traversing with multiple axes along a circular trajectory, each axis goes through sinusoidal acceleration, velocity and position changes. The measured circular path data will show any deviation the machine makes from a perfect circle. The shapes are diagnosed and correlated to servo mismatch, backlash, reversal spikes, squareness error, cyclic error, stick slip, machine vibrations, etc.

For high speed machining operations or die and mold manufacturing, machine tool contouring accuracy is very important. To achieve high quality and productivity, it is important to know what is the maximum feed rate while meeting the required accuracy. The standard verification of machine contouring accuracy is the use of circular tests. However, traditional test equipment is rather limited in its capability to measure small radius contours at high speed. For example, for most dies and molds the radius of curvatures are less than 50 mm and the feed rates are a few meters per minute, and it is more desirable to perform the contour tests at smaller radius and at high feed rate.

For the study here, a Laser/Ballbar developed by Optodyne is used. The Laser/Ballbar is based on a single-aperture Laser Doppler Displacement Meter (LDDM) and a flat mirror target. The major features are: the measurement is non-contact; the circular path radius can be varied continuously from less than 1 mm to 150 mm; all linear accuracy are traceable to NIST; the feed rate is up to 4 m/sec; the data rate is up to 1000 Hz; and the actual feed rate, velocity, and acceleration profiles can all be determined.

As compared to conventional telescoping ball bars, the Laser/Ballbar makes a 2-dimensional measurement. Both the x-coordinate and y-coordinate are measured to generate the circular path. The telescoping ball bar is a 1-dimensional measurement, only the radius changes along angular positions are measured. The angular positions are not measured but calculated by assuming the machine feed rate is a constant. Of course, the 2-dimensional Laser/Ballbar measurement will provide more information, such as feed rate or tangential velocity and acceleration.

1. Velocity control and acceleration/deceleration limitations:

Moving along a contour, the axis velocity and axis acceleration is continuously changing. For a circular path, the axis motion is a simple harmonic or sinusoidal motion. That is:

$$X(t) = R \sin \omega t$$

$$V(t) = dX/dt = \omega * R \cos \omega t = F \cos \omega t \qquad (1)$$

$$A(t) = dV/dt = -\omega * \omega * R \sin \omega t = -F*F/R \sin \omega t$$

Where X is the position, V is the velocity, A is the acceleration, R is the radius, ω is the angular velocity, F is the feed rate and t is the time.

For a constant feed rate F, the required acceleration is proportional to the square of the feed rate and inversely proportional to the radius of the circular contour. Hence, for a small radius or at high feed rate, the required acceleration/deceleration becomes very large. With a fixed maximum driving force, it is important to reduce the moving mass of the machine to achieve the required high acceleration.

2. Decrease in radius caused by response lags and acceleration/deceleration time:

For a circular contour of radius R and at a constant feed rate F, the decrease in radius dR caused by the response lags can be expressed as

$$dR = -(Tp*Tp/2 + Ts*Ts/2 + Ta*Ta/24) * F*F/R \qquad (2)$$

where Tp is the time constant for the position loop in sec, Ts is the time constant for the controller filtering circuit in sec, Ta is the time constant for acceleration/deceleration in sec, F is the feed rate in mm/sec, and R is the radius in mm.

To reduce the decrease in radius, it is important to keep the response time as short as possible. However, sometimes the smaller servo loop response time or larger servo loop gain may cause oscillations or vibrations. There are many methods, such as path error compensation, feed forward control, look ahead, etc that may be used to minimize the decrease in radius.

3. Decrease in radius caused by block processing delay or programming methods:
Two methods are available to program a machine to follow a circle. One is using the NC command G02/G03 or circular interpolation. The advantage of using circular interpolation is that the CNC does not process a large amount of NC blocks and rather dedicates its resources to moving the axes and tracking their positions.

The other method is the use of the command G01 or linear interpolation. Here many linear segments define the circular path. If the accuracy requirement of the circle is high, a large number of points will be needed. The CNC must continuously process this data while the machine is attempting to follow the path. Very often highly dense data is necessary to define a curve; hence the machine control system must manage this high data flow. In many cases, this high data rate may cause data starvation or the reduction in feed rate. Hence, the positioning accuracy of motion-control systems depends on how well controllers can execute linear and non-linear interpolation programs at high rates. The key is how to verify the effect.

Described here are tests performed at one of GM Metal Fabrication Division plants. Most of the tests were performed on a vertical spindle bridge design machining center with a work volume of 6.250 X 3.700 X 1.200 cubic meter. The maximum travel speed is 333 mm/sec. The controller is a Fanuc 15MB. Circular contours at various radii from 6.25 mm to 150 mm and at 20 mm/sec to 80 mm/sec have been performed.

1. Velocity and acceleration profiles:
For a circular contour, the axis motion is a sinusoidal function. Similarly, the velocity and acceleration are also sinusoidal. The shapes of these curves are very close to sinusoidal. This indicates good velocity and acceleration control. The peak displacements correspond to the radius of the circular path, the peak velocities correspond to the tangential velocity or feed rate, and the peak accelerations correspond to the centrifugal acceleration.

For circular path without velocity feedback or control, data was collected on a different machine. The displacement, velocity, and acceleration were measured. Although the displacement is close to sinusoidal, the velocity profile is close to a triangular shape and the acceleration profile is similar to a 2-level acceleration.

2. Various radii at a constant feed rate:
We have performed circular tests at radii of 6.25, 12.5, 25, 50, 75, 100, and 150 mm at a constant feed rate of 80 mm/sec. As shown in Table 1, the variations in circularity or non-roundness are relatively small, they vary from 28μm to 35μm. However, the decrease in radius is rather large, up to 403μm at 6.25 mm radius. Note that the measured radius error is inversely proportional to the nominal radius as expressed in Eq. 2. Also, the feed rates varied from +0.5 to –1.42 mm/sec.

3. Various feed rate with a constant radius:
We have performed circular tests of radius 100 mm at three different feed rates, 16.7, 50 and 133 mm/sec. The results are shown in Table 2. The differences in circularity are relatively

small from 58 μm at 50 mm/sec to 84 μm at 133 mm/sec, while the decreases in radius are relatively large from 75 μm at 50 mm/sec to 276 μm at 133 mm/sec. These results agree with the Eq. 2 very well.

In summary, using Optodyne's Laser/ballbar system, we have performed the circular contour tests at various radii down to 6.25 mm at high feed rates up to 80 mm/sec. The results agree with the theory very well. Because the measurement is non-contact, the circular contour radius can be varied continuously down to a few mm at a high feed rate up to a few m/sec. The setup time is short and the data rate is high. Because of these capabilities, the Laser/ballbar should be an essential tool for servo system, machine tool, and NC manufacture, for optimizing the motion control parameters and verifying the contouring accuracy.

Table 1. Changes in radius, circularity and feed rate versus various radii of the circular contour at a constant feed rate of 80 mm/sec.

Test #	Nominal radius mm	Changes in radius μm	Circularity μm	Changes in feed rate mm/sec
1	6.25	-403	32	-1.37
2	12.5	-216	31	+0.22
3	25	-109	28	+0.53
4	50	-52	29	+0.53
5	75	-32	35	+0.48
6	100	-21	32	+0.05
7	150	-8	35	+0.12
8	150 linear	+10	499	-4.6

Table 2. Changes in radius and circularity versus various feed rates of the circular contour at a constant radius of 100 mm.

Test #	Feed Rate mm/sec	Changes in radius μm	Circularity μm
1	16.7	+3	71
2	50	-35	58
3	133.3	-276	84

Key words: Dynamic testing, contouring accuracy, circular tests, small radius, and high feed rate.

A lathe tool translator for form error reduction in diamond turning

Shane C. Woody & Stuart T. Smith
Center for Precision Metrology, UNC Charlotte, Charlotte, NC 28223

Summary

This paper presents the design of a fine motion controller for nanometer level control of a lathe tool during diamond turning. Fine motion of the tool in the direction of cutting is achieved by a piezoelectric stack actuator with relative motion between the tool and base being monitored using a capacitance gage. Motion constraint is provided by a leaf type flexure providing a relatively high stiffness in off-axis directions. Mounting the translation stage on a wedge facilitates tool height adjustment. A squeeze clamp is incorporated in the wedge to hold the tool at the correct height and increase the stiffness of the complete system. The current design provides a fine motion control with a maximum range of 3 μm, a step response settling time of 12 ms and tool height adjustment of ± 2.5 mm with repeatable positioning, with suitable feedback, to within a few micrometers.

1.0 Introduction

This abstract presents the design and manufacture of a fine tool controller for the machining of profiled mandrels using a diamond turning machine. Particular emphasis is the fabrication of surfaces for applications such as replicated mirror optics for x-ray reflectometry where nanometer geometrical tolerances are necessary. The motivation for this project is the precise manufacture using replication of single or nested grazing incidence x-ray optical elements.

This development is part of a larger program to increase the accuracy of replicated x-ray optics by adjusting the profile of diamond turned mandrels to compensate systematic errors introduced throughout the manufacturing process. Replication involves the manufacture of a shaped mandrel that is subsequently used as the master form for electro-deposition of a relatively thick metallic film. It is this deposited film that is used as the finished optic. Each manufacturing stage introduces errors. In this study, it is speculated that these errors may be removed by adjusting the profile of the replication mandrel. For this to be possible, it is necessary that these errors are repeatable and the profiles of mandrel and finished optic can be measured. Profile measurement, both in-situ in the diamond turning machine and of finished products, will form a future component of this study.

2.0 Instrumentation Design

In general, the servo tool provides a translation range of 3 μm with a resolution of 1 nm. Additionally, a contact based, long trace profiling system with sub nanometer resolution is envisioned for development[i]. Adapting a high precision servo tool and profilometer system into a diamond turning center is a challenging design task. Thermal instability in working environments is inherently a dominant factor effecting repeatability of machining and subsequent profiling. This key issue is currently being investigated at UNCC for high precision diamond turning. One key point is to maintain a thermal equilibrium between the tool and spindle post. To retain the same working zone, the

spindle post should not expand at a faster rate than the tool post. For matching, the servo components are fabricated with stainless steel 303.

To position the cutting edge of the tool at the correct height (often coincident with the spindle axis), the tool stage incorporates a vertical adjustment in the base, figure 2.0.1. As shown, the vertical adjustment is achieved using a wedge guided by dovetail slides on each side. In general, the vertical stage consists of a base, wedge and platform. The base and platform are constrained in the *Z*-axis with respect to each other by two 'wishbone' flexure designs on the upper and lower sides. Side flexure systems generate high stiffness along the *Z*-axis and relatively low stiffness in the *Y*-axis direction. Thus, the base and wedge displace in the *Y*-axis as the wedge is displaced along the *Z*-axis using the micrometer. The wedge has a 5° taper on each side (a 10° wedge) and is separated in the middle of the *X* plane by a leaf type flexure. A bolt is then used to clamp the wedge to the dovetail slides once the tool height has been set. When the wedge is locked the three components of the tool carriage support are effectively a rigid body. The vertical stage assembly translates a total range of 5 mm and, with practice, a vertical resolution of 0.2 μm can be achieved.

A monolithic, tool translation flexure, figure 2.2, rigidly mounts to the top of the carriage platform, figure 2.1. Four leaf flexures are designed on each side of the tool mount to provide high axial stiffness and moderately high resonant frequency. Additionally, there are two further flexures underneath the carriage that are squeeze clamped to the platform. Consequently, the base flexures restrict the carriage from tilting about the *X* axis. A combination of conventional milling and wire EDM were used to produce the monolith. The tool carriage is designed with approximately 4 MN m^{-1} stiffness and a 400 Hz natural frequency.

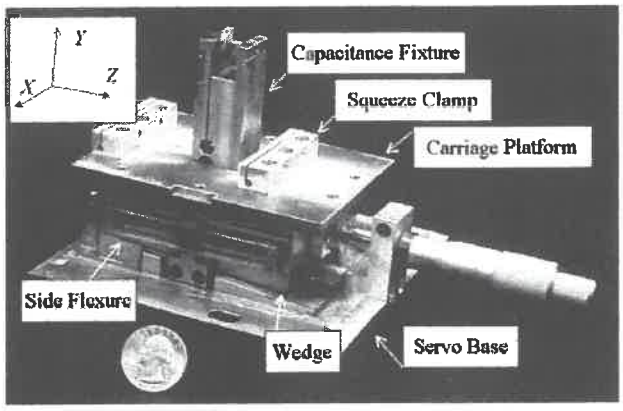

Figure 2.1: Servo tool capacitor fixture and vertical stage

A piezoelectric (PZT) stack actuator provides a single linear motion and uses capacitance gauging for closed loop control, figure 2.2. The PZT stack has a maximum range of 17 micrometers with an applied potential of 150 V. The use of capacitance sensor for closed loop control significantly reduces the hysteretic effects. In this design, the capacitance gage directly measures the local tool motion due to PZT expansion or contraction. The capacitive sensor consists of two aluminum coated glass slides. The base glass slide is approximately 1 mm in thickness and the central region is etched with a 20 μm step prior to coating of aluminum electrodes. A second slide bridges across the base plate and epoxy is applied to each corner. Glass slides of 0.2 mm

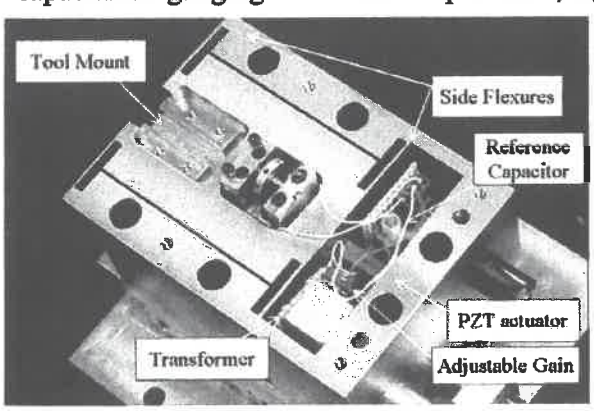

Figure 2.2: Tool translation flexure and capacitor electronics

thickness and aluminized on one face are chosen as the top slide to provide low stiffness. A ruby sphere is bonded with epoxy to the top slide to provide a contact point for transferring motion of the carriage to displacement of the thin glass slide electrode. The capacitance assembly mounts into a flexure tilt stage, figure 2.1. Maintaining low thermal drifts is mandatory for a 1 nm resolution metrology loop. Therefore, invar is chosen due to low thermal expansion properties for the fixture's components. A differential screw accommodates a fine adjustment mechanism and, with feedback, this can be controlled to better than 2 μm. The complete capacitor assembly and fixture is placed through a clearance hole in the tool carriage and bolts to the carriage platform. Fine differential adjustment is then utilized to bring the ruby sphere of the capacitance sensor into contact with the tool carriage. The contact is aligned with the diamond tool axis in order to minimize Abbe offset.

Servo electronics consist of a Thorlabs™ PZT amplifier, capacitance lock-in electronics and a PID controller. A separate circuit board is built to contain a variable gain preamplifier, adjustable reference capacitor and transformer. The reference capacitor and transformer circuit are used to null the measurement capacitor between a 1-10 μm contact range. Ideally, the reference and measurement capacitor should be mounted as close as possible to minimize added capacitance in the cabling. Thus, the electronic circuit board is designed to fit compactly in a pocket behind the tool carriage, figure 2.2. The gain potentiometer effectively changes the range of the servo while inversely affecting the resolution (i.e a higher resolution servo may be achieved by shortening the range). A commanded voltage is generated from LabView™ through a data acquisition board and transferred to the PID. The PID compares between the measurement capacitor signal and the command voltage to produce a corrective signal to the PZT controller.

Considering that the workpiece and servo tool may be doused with an oil or air bath, a thin walled environmental shell is utilized to prevent any oil from entering the carriage chamber and disrupting the electronics, figure 2.3. The shell is designed with a 1 mm wall thickness and made from aluminum 6061. Aluminum is chosen for the stress free properties and favorable high speed machining properties. Also, the shell is bolted directly to the tool carriage frame and moves with the platform when it is being adjusted for tool height. Lastly, the tool mounts in the carriage as shown and is rigidly clamped using an aluminum plate.

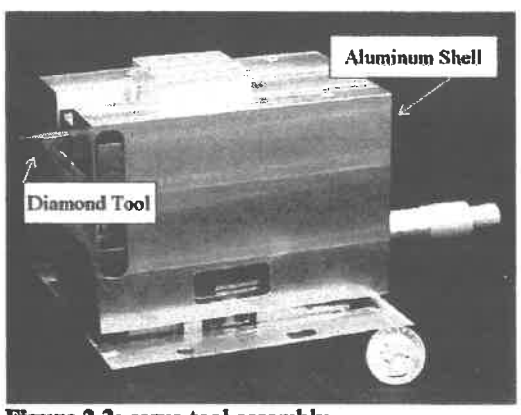

Figure 2.3: servo tool assembly

3.0 Performance Testing

Affectively, the servo tool is calibrated using a Hewlett Packard laser interferometer. During calibration, the demodulated capacitance voltage is compared to the laser displacement reading and a second order polynomial is used to fit the measured data. Next, the tool is tested to determine the fastest response time or limiting bandwidth. The response time is determined from the output from the capacitance gage when a step demand is fed into the PID controller. The servo's settling time is optimized by adjusting the three terms of the PID controller while monitoring the response in real time. Currently, the servo's optimal settling time is determined to be 12 ms.

Currently, research is underway to assess the servo tool's overall performance. Recent investigations include cutting step and sinusoidal profiles across the face of 4" diameter aluminum blanks. First, the tool servo is mounted into a Precitech diamond turning center with the PID controller and Capacitor lock-in located to the side of the Z-axis slide. These tests involve first facing the sample piece in several cutting passes until a P-V surface finish of between 50-100 Å is achieved. In the final pass, the *Z*-axis slide is translated towards the blank for a nominal depth of 0.5 μm and *X*-axis is slowed to 2 mm per minute. A sample is cut with a specified profile indenting every 0.3 cycles mm^{-1} and an increased 20 nm depth each cycle, figure 3.1. A Nanostep 2 is utilized to measure the subsequent surface profile. As shown, the steps increase approximately 20-25 nm each time. The surface roughness is determined to be 100-150 Å and, therefore, it is difficult to assess the servo's actual resolution from this early data. Typically, an approximate 50 Å surface finish is generated by a DTM. Initial performance testing revealed excessive tool tip wear. Future investigations aim to reduce tool tip wear for optimal servo performance. Additionally, current measurements indicate a rather large overshoot. This may be minimized by changing the settings in the PID controller. Initial results represent the first cutting tests generated by the servo. Thus, results shown are far from optimized and it is envisaged that more definitive performance measures will be presented in the near future.

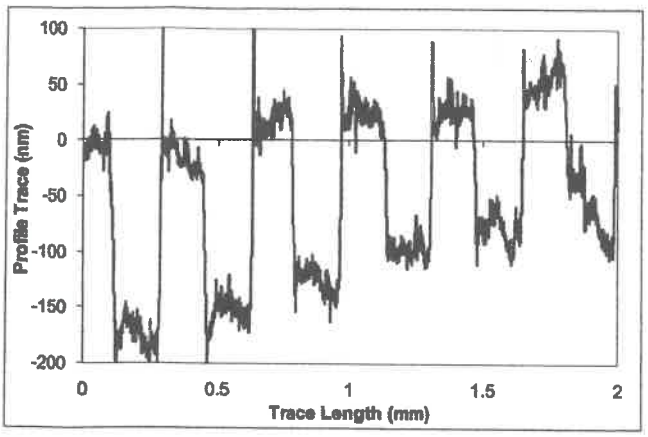

Figure 3.1: Steps machined into the face of an aluminum specimen

References

[i] Lindsey K., Smith S.T. and Robbie C.J., 1988, Sub-nanometer surface texture and profile measurement with 'Nanosurf 2', *Annals of the CIRP*, 37, 519-522

- Lindsey K. and Smith S.T., U. S. A. Patent No. 4 944 606 Precision Motion Slideways (1990)

Experimental Study on Motion Accuracy of CNC Machine Tool with Ball Screw Drive System

Kazuo Yamazaki[(1)], Yasuhiro Kawahara[(1)], Yoshihito Kagawa[(1)], Jiancheng Liu[(1)], Jan Braasch [(2)], Makoto Fujishima[(3)] , Masahiro Mori[(3)]

[(1)]: IMS-Mechatronics Laboratory, University of California, Davis, California

[(2)]: Johannes Heidenhain GmbH, Traunreut, Germany

[(3)]: Mori Seiki Co. Ltd., Nara, Japan

1. INTRODUCTION

Among many error sources that affect the machining accuracy, thermal induced error is most critical and difficult to deal with especially for high-speed machining which generate the heat in motion mechanism due to the repetition of high acceleration and deceleration. Because the error usually behaves in a random and non-repeatable manner and the accuracy of the feed drive system with a ball screw is greatly influenced by the thermal distortion of the ball screw generated in such high-speed motion.

The combination of a rotary encoder, ball screw and nut is a common configuration for the motion control system in most of the CNC machine tool systems available today. Under the high-speed and high-acceleration feed motion, the heat generation between the nut and a ball screw is extreme and above mentioned error will become unpredictable. This means that the axis position can not precisely determined from the reading of the rotational angle of the ball screw using a rotary encoder system. Therefore, the high-speed machine tools equipped with the rotary encoder feedback system should have some countermeasures to overcome the control inaccuracy caused by the thermal effects. For this purpose, some machine tools are equipped with the water based cooling system, which circulate the coolant in the harrow ball screws to maintain the temperature of the ball screw system as constant. But, this method is difficult to achieve the reliable operation and more expensive than the conventional system. In resent years, some of high-speed machine

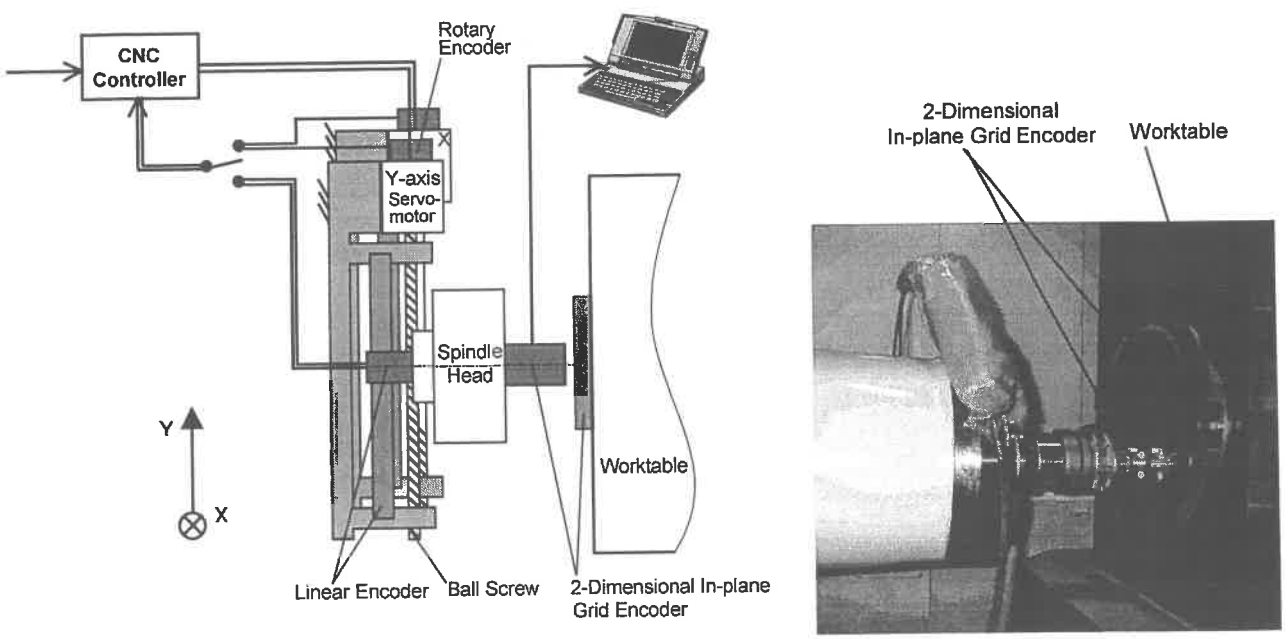

(a) Configuration of experimental setup (b) Setup view

Figure 1. Experimental setup

tools, especially linear motor machine tools, are equipped with linear encoder system. However, the real effectiveness is not clear in terms of suppression of the motion control error induced by thermal growth in the ball screw feed drive system.

therefore, an experimental study on the positioning error behavior of the high-speed horizontal axis machining center with ball screw (no ball screw cooling) and rotary encoder feedback system has been conducted(1). The study was to understand how the high-speed repetitive traverse motion by a ball screw influences the positioning error of the spindle head in time domain. The typical behavior of positioning accuracy deterioration was studied and the results have clearly shown that time history of a positioning error behavior has remarkable correlation with the speed of the traverse motion. In this paper, circular motion and triangle motion test, have been performed to clarify the two-dimensional motion control error behavior in the high-speed horizontal axis machining center equipped with ball screw.(no ball cooling) and rotary encoder feedback system. The obtained results were compared with the obtained results sing the linear encoder feedback, which is also equipped on the machining center as another positioning sensor.

2. VERIFICATION OF MOTION ACCURACY BASED REPETITIVE MOTION CONTROL

2.1 EXPERIMENTAL SETUP

Figure 1 shows the experimental setup. The two-dimensional in-plane grid encoder with a measurement range of 520mm was used for measuring the accurate spindle head position on the worktable. The machine tool is equipped with the rotary encoder and linear encoder, which

Table 1. Experimental apparatus

Machine Tool	High Speed CNC Horizontal Axis Machining Center
Rotary Encoder	FANAC
Linear Encoder	HEIDENHAIN
2-Dimensional Grid Encoder	HEIDENHAIN
Computer	Compaq PROLINEA 5100 Software:HEIDENHAIN ACCOM Ver.2.01

Table 2. Experimental condition

Initial spindle center position	X=420 mm Y=140, 380, 530
Traverse rate	1000, 5000, 10000
Motion trajectory	Circle(Dia.100mm Triangle(Hight 100mm)
Interbal time	2h

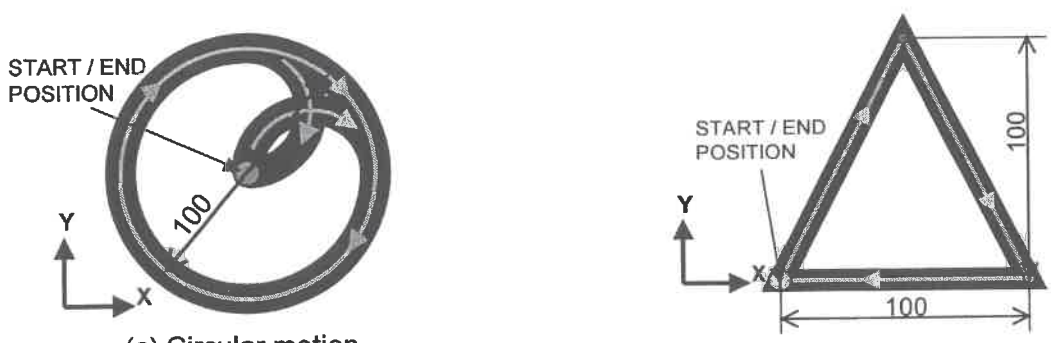

(a) Circular motion

(b) Triangle motion

Figure 2. Motion trajectory

measure the spindle head position along the ball screw and used for position feedback. These sensors are able to switch in the control system. Table 1 shows the experimental apparatus.

2.2 EXPERIMENTAL RESULTS AND DISCUSSION

Figure 2(a) shows the circular motion with 100 mm diameter obtained as a typical two-dimensional motion to the spindle head and figure 2(b) shows the isosceles triangle motion with 100mm base line and 100mm height obtained as a sharp corner motion. These tests are performed at the different position in height on the worktable and the different traverse rate. The test conditions are shown in Table2.

2.2.1 CIRCULAR MOTION TEST

Figure 3 shows an example of experimental results of the circular motion with rotary encoder feedback system in the condition of initial spindle position 140 mm and traverse rate 1000 mm/min, 5000 mm/min. From figure 3(a), it is found that in case of traverse rate 1000 mm/min, the trajectory profile error becomes larger with the running time is increased. As shown figure 3(b), however, in case of traverse rate is 5000 mm/min, the trajectory profile error becomes extremely larger with the increase of running time. The maximum positioning error is 36 μm in the case of traverse rate 10000 mm/min. It can be drawn that from figure 3 that the heat generation between the nut and the ball screw will result in motion error in the case of high traverse rate and this error

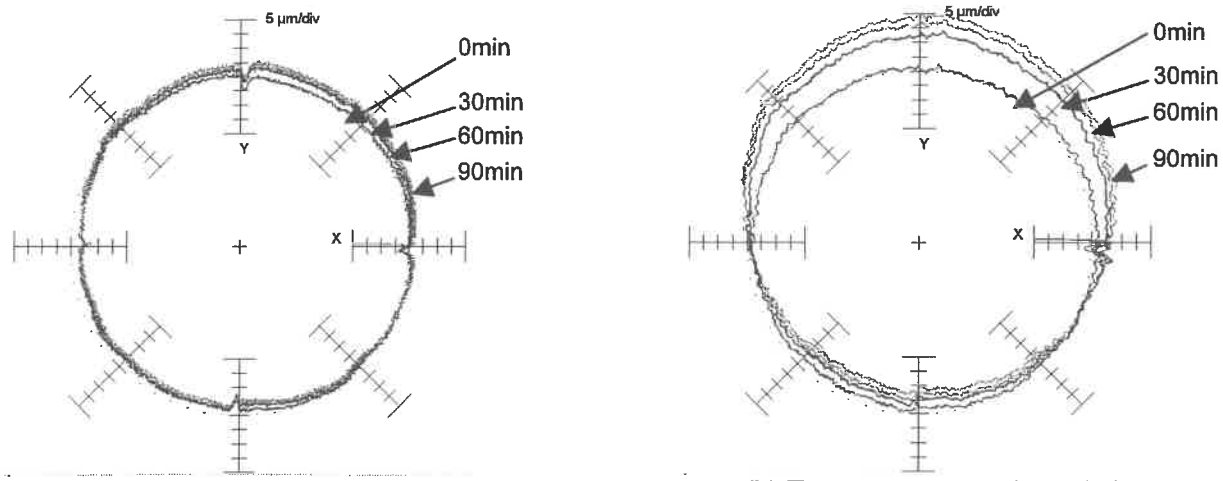

(a) Traverse rate 1000 mm/min (b) Traverse rate 5000 mm/min

Figure 3. Example of the circular motion test with rotary encoder (Initial spindle position y=140mm)

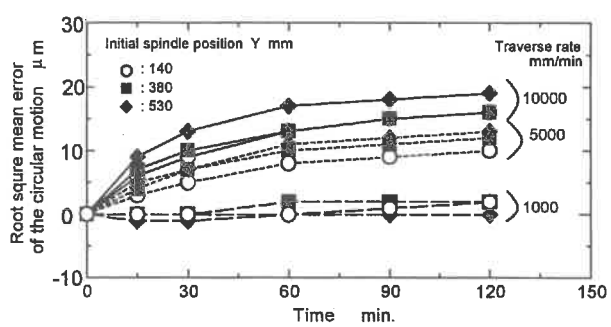

Figure 4. The time history of the circular motion error with rotary encoder feedback

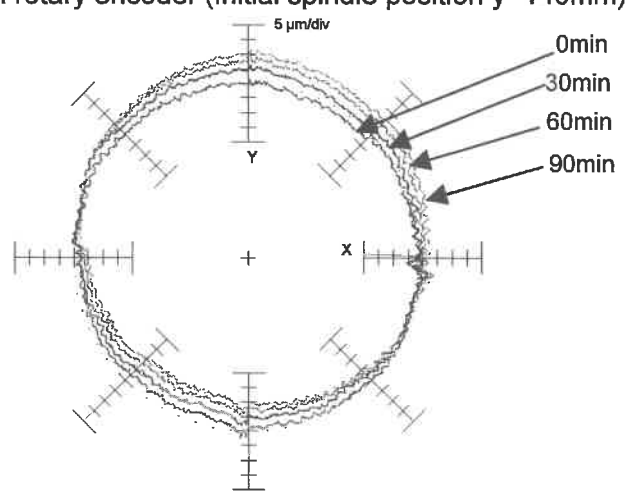

Traverse rate 5000 mm/min

Figure 5. The circular motion test with linear encoder (Initial spindle position y=140mm)

cannot be compensate with the rotary encoder feedback system. Figure 4 shows the time history of the root square mean error of the circular motion in various motion conditions. From this figure, it is found that with increase of the running time and traverse rate, the root square mean error becomes large. From this result, it can be deduced that the ball screw has a big thermal growth in both X and Y-axis with increase of the running time and traverse rate. In the first one-hour running, the thermal expansion increases rapidly. In worst case, the error caused by the thermal growth reaches 20 μm. After that, the ball screw gradually expands. Figure 5 shows an example of measured results with the linear encoder feedback in the same condition with figure 3. It is found that the linear encoder feedback has the small motion error in comparison with the error with the rotary encoder feedback. The maximum positioning error is 17 μm in the case of traverse rate 10000 mm/min. The root square mean error of the motion is reduced more than 50 % with the linear encoder feedback. It was found that from these measurement results the thermal growth is remarkable and there is a big difference between the position information reflected by the rotary encoder and the actual position measured directly by the linear encoder.

2.2.2 TRIANGLE MOTION TEST

Figure 6(a)(b) shows an example of experimental results of the triangle motion with rotary encoder feedback system and with linear encoder feedback system in the condition of initial spindle position 530 mm and traverse rate 10000 mm/min, respectively. The results show that the in the case of the rotary encoder feedback control, the motion error increases with running time. In the worst case of all test (shown in figure 6), the maximum error of corner position is 18 μm. However, the error is almost compensated with the linear encoder feedback control. The error is 2 μm.

3. SUMMARY

The positioning performance with the rotary encoder and linear scale feedback system for the ball screw drive systems was investigated. When the rotary encoder feedback is used for relatively high speed repetitive circular motion of the worktable, thermal expansion of the ball screw resulted in a maximum motion error of 36 μm and root square mean value 20 μm in the worst case. (a running time of 1 to 2 hours with a traverse rate 10,000mm/min) And in case of triangle motion, a maximum motion error was 18 μm in the worst case. . However, In the case of linear encoder feedback system, the thermal error can be dynamically monitored, so the motion error of the worktable was greatly reduced.

4. REFERENCES

1. K.Yamazaki, etc. "Experimental Study on Dynamic Accuracy Behavior of a High-speed CNC Machine Tool with Semi-closed and Fully-closed Feedback Control", proc. Of ASPE, annual meeting 462-466 (1997).

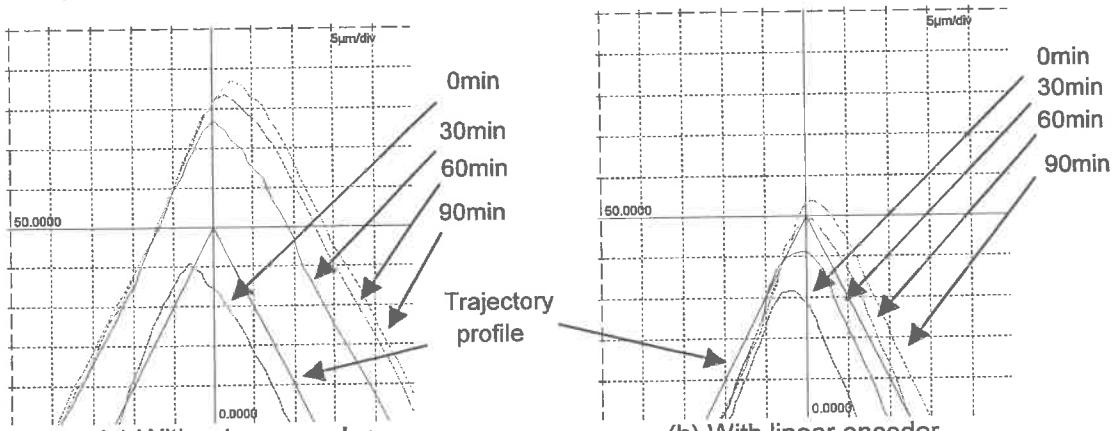

(a) With rotary encoder (b) With linear encoder

Figure 6. Example of the triangle motion test
(Traverse rate 10000mm/min, Initial spindle position y=530mm)

Air Bearing Design Optimization

Fuzhang Zhao and Clarence A. Andersson
Advanced Materials Division, M Cubed Technologies, Inc., Newark, DE 19711

Jai R. Singh and Craig Emmons
M Cubed Technologies, Inc., Monroe, CT 06468

1. Introduction

Air bearings widely used in precision engineering can be classified into two types: orifice and porous media. The air bearings discussed here refer to a porous graphite type. Many parameters influence the performance of air bearings. A model is needed which provides a design tool for motion system designers to correctly predict the performance of porous bearings. The modeling of fluid flow through porous material is well established. For the low permeability porous materials of greater thickness, Darcy equation was used [1]. For high permeability porous materials of smaller thickness, a modified Reynolds equation was used to study the viscous shear and stress jump at the interface between the porous material and the gas film [2]. The modeling of fluid flow through the atmosphere is mainly based on the classical Reynolds equation [3-5]. The key physical quantity to choose or control in an air bearing design is the permeability of a porous material. Although increasing the permeability of a porous media increases the efficiency of load capacity, it will decrease the stability of levitation. An optimum bearing should possess high efficiency of load capacity, high stiffness and good stability during levitation. In order to optimize the air bearing design, a novel simplified one-dimensional steady-state model was developed based on flow equilibrium. The model was divided into two parts: porous material pad and thin air layer. The Darcy equation was used to describe the air diffusing through a porous material pad. Film coefficient was successfully used to model the air releasing to the environment.

2. Modeling of Porous Air Bearings

When an air bearing is put in service, a supply air pressure p_0 is applied through a porous material pad with cross sectional area A, circumference c, and height H; and forms a gap layer with gap height h and gap pressure p_H. Air is released to the environment with film coefficient f, and ambient pressure p_∞. The model and the corresponding coordinate systems are shown in Figure 1.

To balance the flow in both the porous material pad (using Darcy equation) and in the air gap (using film coefficient), one may use the governing equations (Eqs. (1) & (3)) and boundary conditions (Eqs. (2), (4) and (5)),

$$\frac{d}{dx_1}\left(k_1 \frac{dp}{dx_1}\right) = 0 \quad where \;\; k_1 = \frac{\kappa}{\mu} \tag{1}$$

$$p\big|_{x_1=0} = p_0 \quad and \quad -\frac{\kappa}{\mu}\frac{dp}{dx_1}\Big|_{x_1=H} = q_H \tag{2}$$

$$\frac{d^2 p}{dx_2^2} - \alpha^2 p = 0 \;\; where \;\; \alpha = \sqrt{\frac{fc}{Ak_2}}, \;\; f = \frac{h^{\frac{3}{2}}}{12\mu\sqrt{L}} \quad and \quad k_2 = \frac{h^2}{12\mu} \tag{3}$$

$$-k_2 \frac{dp}{dx_2}\Big|_{x_2=0} = q_H \quad and \quad -k_2 \frac{dp}{dx_2}\Big|_{x_2=h} = 0 \tag{4}$$

$$p\Big|_{x_1=H} = p\Big|_{x_2=0} = p_H \tag{5}$$

where q is the fluid flow flux, κ is the permeability of porous material, μ is the viscosity of air and L is an effective length that makes the pressure drop to ambient pressure.

Solving equations assuming that k_1 is not a function of pressure, applying boundary conditions and eliminating q_H, one may derive the efficiency of load capacity as follows,

$$\eta = \frac{p_H A}{p_0 A} = \frac{p_H}{p_0} = \frac{1}{1+\theta} \quad where\ \theta = \frac{\alpha H k_2}{k_1} \frac{e^{2\alpha h} - 1}{e^{2\alpha h} + 1} \tag{6}$$

We define the θ as the dimensionless stability for an air bearing. In order to optimize both the efficiency of load capacity and the dimensionless stability, they have to be equalized. With $\theta = \eta$, Eq. (6) becomes,

$$\eta^2 + \eta - 1 = 0 \tag{7}$$

thus the maximum efficiency of load capacity, one of the roots, is 0.618.

Taking the derivative of η with respect to h and using the definition of stiffness, which is the slope of load-gap height curve, we define the dimensionless stiffness $\bar{S}$ as,

$$\bar{S} = -\frac{d\eta}{dh} h = 1.75(\eta - \eta^2) = \frac{S h}{p_0 A} \tag{8}$$

where S is stiffness.

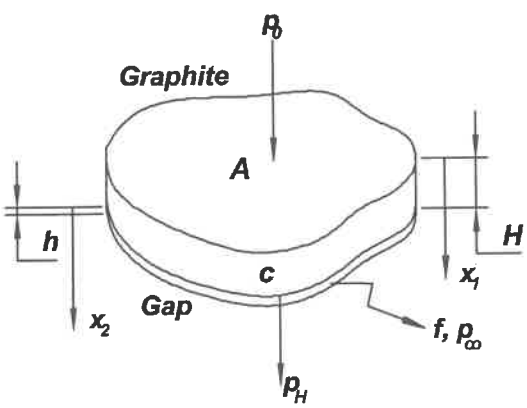

Fig. 1 Fluid flow model for air bearing.

Fig. 2 M Cubed Technologies' porous graphite air bearings.

In practice, k_1 is a linear function of pressure,

$$k_1 = a + b\,p \tag{9}$$

where a and b are constants determined by experiment. Considering that k_1 is a linear function of pressure, the dimensionless stiffness turns out to be,

$$\bar{S} = \frac{S h}{p_0 A} = \frac{7}{4} \frac{\left[1 + \frac{1}{2}\left(\frac{b}{a}\right) p_0\right]\eta - \left[1 + \frac{1}{2}\left(\frac{b}{a}\right) p_0 \eta\right]\eta^2}{1 + \frac{1}{2}\left(\frac{b}{a}\right) p_0 (1 + \eta^2)} \tag{10}$$

3. Applications of the Model

Theoretically, the maximum efficiency of load capacity is 61.8%. Experimentally, a 51-mm diameter circular bearing was used to test its maximum efficiency. When the bearing was loaded up to about 63% efficient at a gap height of 6.35 μm, it started to buzz audibly. As the efficiency was further increased, the bearing became vibrationally unstable. Therefore, a maximum efficiency of 60% of the load capacity is recommended in air bearing design.

In order to validate the model, stiffness comparisons between theory and experiment have been made. Both circular and rectangular graphite air bearings (Fig. 2) were tested.

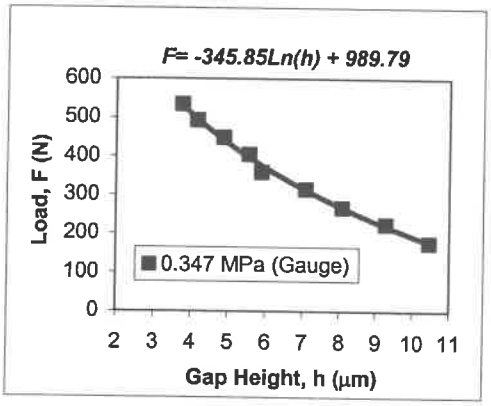

Fig. 3 Load as a function of lift for 51-mm diameter circular graphite bearing.

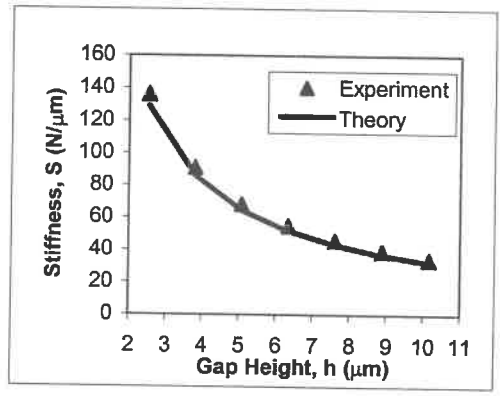

Fig. 4 Stiffness comparison between the model and experiment for 51- mm diameter circular bearing.

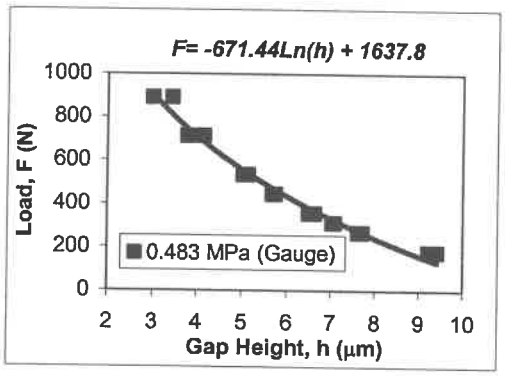

Fig. 5 Load as a function of lift for 76-mm by 51-mm rectangular bearing.

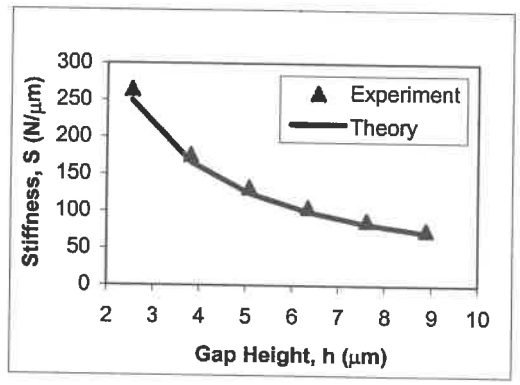

Fig. 6 Stiffness comparison between the model and experiment for 76-mm by 51-mm rectangular bearing.

The experimentally determined load-gap height curve for the 51-mm diameter circular bearing is shown in Figure 3. The experimentally derived stiffness versus gap height curve was determined based on the equation obtained from curve fitting given in Fig. 3. Using Eq. (10), the corresponding theoretical stiffness as a function of gap height was also calculated. As the circular bearing is 50.16% efficient at h=6.35 μm, the following parameters p_0=0.347 MPa, η=0.5016, A=2.027×10^{-3} m^2 and b/a=2.175×10^{-6} Pa^{-1} were used to evaluate the theoretical stiffness shown in Figure 4.

The model is equally applicable to air bearings with rectangular shape. The load was also measured with respect to the gap height for the 76-mm by 51-mm rectangular bearing shown in Figure 5. A stiffness-gap height curve with solid triangular legend was, similarly, derived from

the experimentally obtained load-gap height curve. Again, using Eq. (10), the corresponding theoretical stiffness as a function of gap height was calculated. As the rectangular bearing is 23.95% efficient at gap height of 6.35 μm, the following parameters p_0=0.483 MPa, η=0.2395, A=3.871×10^{-3} m^2 and b/a=2.175×10^{-6} Pa^{-1} were used to evaluate the theoretical stiffness shown in Figure 6.

The comparisons between experiment and theory show that the stiffness calculated from the current model is accurate. Therefore, it is feasible to use this model in air bearing design.

4. Concluding Remarks

A model that describes the functioning of porous air bearings has been derived. The model agrees well with the experiments. It is applicable to air bearings with a variety of shapes. The dimensionless stiffness and dimensionless stability were defined. In practice, the commonly used supply air pressures for porous air bearings are in the range of 0.345 to 0.552 MPa in gauge (50 to 80 psig). Air bearings with levitation heights of about 5.1 to 7.6 μm (200 to 300 μin) perform well since the bearing will tend to be pinned if it levitates too low above the working surface. On the other hand, it will tend to be vibrationally unstable if it flies too high. Although many parameters influence a bearing's function and behavior, the most important parameters are the efficiency of load capacity (or inversely the dimensionless stability) and bearing area. In making a porous air bearing the key physical property to choose or control is the efficiency of air diffusion through the porous media—permeability. As a general design rule, we propose the following guidelines:

1) In general, the efficiency of load capacity chosen in air bearing design must be less than or equal to 0.60. In other words, the dimensionless stability must be larger than or equal to 0.60.
2) If the bearing area is limited, stiffness can be improved by increasing the efficiency of load capacity close to 0.60.
3) If both a high stability and a high stiffness are required, a larger area with lower permeability material will be needed.

In fact, the first rule must be satisfied in making any porous air bearing before either the second rule or the third rule is applied.

5. References

[1] Park, J.E., Giles, Jr. G.E., Rasnick, W.H., and Steger, P.J., 1978, "Computation and Measurement of Flow Rate and Load Capacities for Graphite-Fed Externally Pressurized Gas Bearings", *Interim Report of Oak Ridge National Laboratory*.

[2] Li, W.-L., 1999, " Derivation of Modified Reynolds Equation—A Porous Media Model", ASME *Journal of Tribology*, Vol. 121, pp. 823-829.

[3] Faria, M.T.C., and Andres, L.S., 2000, "On the Numerical Modeling of High-Speed Hydrodynamic Gas Bearings", ASME *Journal of Tribology*, Vol. 122, pp. 124-130.

[4] Hu, Y., Jones, P.M., Chang, P.T., and Bogy, D.B., 1998, "Partial Contact Air Bearing Characteristics of Tripad Sliders for Proximity Recording", ASME *Journal of Tribology*, Vol. 120, pp. 272-280.

[5] Peng, J.-P., and Hardie, C.E., 1995, "A Finite Element Scheme for Determining the Shaped Rail Slider Flying Characteristics with Experimental Confirmation", ASME *Journal of Tribology*, Vol. 117, pp. 136-142.

INTELLIGENT CONTROLLER FOR MAGNETOSTRICTIVE MICROPOSITIONING DEVICE FOR ULTRA-PRECISION

J. C. Campos Rubio[1], J. G. Duduch[2], F. G. Santoro[3], A. V. Porto[2], A.E. Gee[4]

[1] Federal University of Minas Gerais, Mechanical Engineering Department
Av. Antonio Carlos 6627, Pampulha, 31270-901 Belo Horizonte, MG. Brazil.

[2] University of São Paulo, Escola de Engenharia de São Carlos
Caixa Postal 356, 13560-970 São Carlos, SP. Brazil.

[3] A.U.R.A., Inc. – Cerro Tololo Inter-American Observatory
Colina El Pino, s/n, Casilla 603, La Serena – Chile

[4] Cranfield University, School of Industrial and Manufacturing Science
Cranfield, Bedford, MK43 0AL - England

ABSTRACT

Generally, requirements such as high performance and small sizes for mechatronic systems, have led modern industry to design positioning systems with better characteristics of acceleration and positioning accuracy. The increasing demand for components with better metrological and finishing characteristics such as x-ray and infra-red lenses, has prompted the development of a number of types of micropositioning systems that are able to move machine elements in very small displacements with high levels of accuracy. In this work, it is proposed the use of a new type of actuator, which employs the properties of electromagnetic strain of certain metallic alloys (magnetostrictive actuators). Digital control systems that use control algorithms based on fuzzy logic (FL) and artificial neural networks (ANN) for micropositioning control are considered and their application proposed.

Key words: Micropositioning Devices, Magnetostrictive Actuators, Intelligent Control

INTRODUCTION

The fabrication of components with high form accuracy (1μm), low surface roughness (nm) and low subsurface damage such as for complex optical systems, demands the use of high precision positioning machines capable of following complex movements. Presently, this kind of components can be obtained by ultraprecision diamond turning and grinding machines.

The machine tool plays an important role in this kind of fabrication. In broad terms, to achieve adequate characteristics of positioning resolution and dynamic performance, ultraprecision machine tools must present extremely high overall structural stiffness and high dynamic performance servo mechanisms and control systems.

Ultraprecision displacement systems are not only required in machine tools but also in metrology systems and optical assembly systems. Examples of such systems are stylus and optical profilometers, optical and V.L.S.I. manufacturing systems.

This work presents the development of a type of modular architecture micropositioning system. The dynamic performance of the micropositioner, using digital control strategies based on Neural Network and Fuzzy Logic is presented and compared with results obtained by different authors. It is shown that the commissioning of the appropriate control technique permits the attenuation of instabilities and non-linearities of the

servosystem, permitting resolutions of the order of nanometres.

MICROPOSITIONING SYSTEM

Most commercial precision machine tools do not possess the required characteristics of accuracy and repeatability to machine brittle materials, correct systematic errors and possibly random errors for the fabrication of non-axysymmetric components. An additional system for the positioning and/or correction of errors is, therefore, desirable to attain the required characteristics of form, surface roughness and subsurface integrity.

Several types of device have been developed to accomplish the above. Figure 1 shows a schematic of a modular toolpost, which uses a leafspring guide system. [CAMPOS RUBIO et al, 1998].

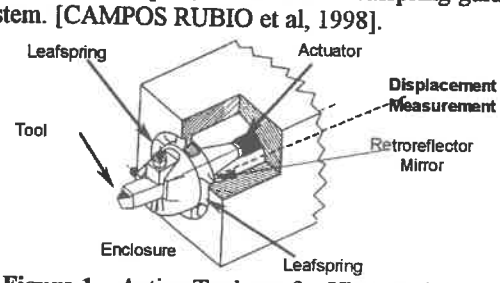

Figure 1 – Active Toolpost for Ultraprecision Machining [CAMPOS RUBIO et al, 1998]

The use of an appropriate drive system for positioning of precision elements is crucial. Several types of linear actuators could be mentioned here as a potential solution (e.g. hydraulic, pneumatic, fine screws, levers etc) but, in ultra-precision design, it is likely that there will be few design options for selection. In the case of ultra-fine tool displacement described in this work, solid state magnetostrictive actuators were chosen.

Magnetostrictive materials are able to transform an electric signal into linear movement within the range of a few micrometres [CAMPOS RUBIO et al, 1996]. The load carrying capacity of a magnetostrictive actuator can easily reach 1 kN and the bandwidth can be as high as several kHz. Magnetostrictive actuators are particularly suitable for fine positioning as they provide high positioning accuracy, fast time response, high stiffness and high bandwidth.

MICROPOSITIONER MODEL

The elements that make part of the dynamic system is described below using the appropriate mathematical formulation (mathematical model). Figure 2 shows the block diagram of the dynamic system.

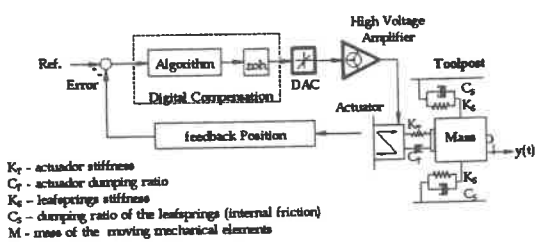

Figure 2 - Dynamic System Structure.

This system can basically be divided into two parts: The digital controller and the plant, which is composed by the remaining elements of the system (electro-mechanical system). The plant can be further divided into two distinct parts. One corresponds to the magnetostrictive actuator (MST) and the other to the moving mechanical elements.

Moving Mechanical Elements (Toolpost)

The toolpost moving mechanical elements mathematical model is shown in Equation 1 [MIRON, 1989], where ζ is the structural dumping ratio (0.08) and ϖ corresponds to the resonant frequency of the system (200 Hz) for a 650 g mass.

$$\frac{Y(s)}{X(s)} = \frac{2\cdot\xi\cdot\varpi_c\cdot\left(s+\frac{\varpi_c}{2\cdot\xi}\right)}{s^2+2\cdot\xi\cdot s+\varpi_c^{\,2}} \qquad (1)$$

Magnetostrictive Actuator

This component converts an electrical current into a proportional displacement. The mathematical model for this type of element, according to the literature [KANIZAR et al., 1995], is described as a second order system, where ζ is the dumping ratio and ω_n is the resonant frequency ($\omega_n = 2\pi f_r$).

An MP 50/6 Etrema Terfenol-D^R magnetoestrictive actuator was used, which has an expansion range of ±25 μm for the input signal of ±1.5 A.

$$\frac{X(s)}{I(s)} = \frac{K_{MST}\cdot\varpi_n^{\,2}}{s^2+2\cdot\xi\cdot s+\varpi_n^{\,2}} \qquad (2)$$

Table 1 – System Parameters

	Mechanical Elements	MST
Freq Response. (f_r)	450 Hz	5 kHz
Stiffness (k)	5.25 10^6 N/m	7 10^6 N/m
Dumping Ratio (ζ)	0.080	0.097
Gain (K_{iii})	452.39	1.66 10^{-5} m/A

There are two regimes of operation, one for several micrometre range where the effect is strictly amplitude proportional and that below this level where the effect diminishes with reducing amplitude. The former can be readily modeled as a (fixed) attenuation and phase lag; the latter indicates that, for ultraprecision control system settling, the effect is negligible [DUDUCH, 1993].

HYBRID CONTROLLER "PI *FUZZY* + D"

Due to inertia of the moving elements, there may be a motion after the driving signal is ceased. This characteristic makes the plant control extremely difficult.

Since traditional PID controllers are not adequate when the plant parameters vary [TAO & TAUR, 1995], the inclusion of Fuzzy Logic in a traditional PID controller has the objective of reducing the overshoot and diminishing the time response. Earlier observations (e.g., CAMPOS RUBIO et al., 1996) show that:

- Conventional PID controllers are easy to implement and are versatile. They have fast time response but are subject to overshoot.
- Being a fixed gain algorithm, for fast response and low steady state errors they may become unstable.
- Fuzzy controllers are less susceptible to variations in the plant, external noise, and instability, permitting lower steady-state errors and faster response. They are also adaptative and rugged .

Hybrid Controller

As a means of simplifying the implementation of the algorithm, a sequential arrangement of the two types of controllers was chosen.

Each **PID** element has a specific function and acts either on its own or together for one or more response characteristics [MIRON, 1989], as follows:

- ***Proportional*** (K_p) – decrease time response and error
- ***Integral*** (K_i) – reduces the steady state error
- ***Derivative*** (K_d) - increases stability.

Similarly to conventional **PID** gain, hybrid controller parameters can be adjusted, e.g., using Ziegler Nichols method. After adjusting the **PID** filter, the **PI** component is replaced by the ***Fuzzy*** system, resulting in a hybrid controller.

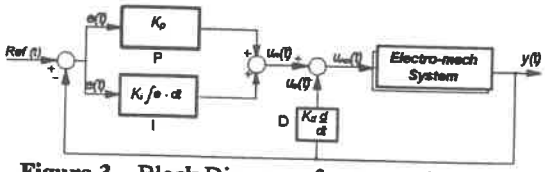

Figure 3 – Block Diagram of a conventional PID Controller.

Equations for the Hybrid Controller

Figure 3 shows the block diagram of a dynamic system controlled by a PID filter.

T – sampling time;
e(k) – input to the controller: e(k) = Ref(k) – y(k);
u(k) – output of the controller (kT).

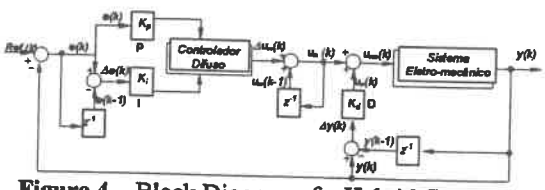

Figure 4 – Block Diagram of a Hybrid Controller "PI *difuso* + D".

In this work, the use of a hybrid "PI *fuzzy* + D" is proposed, where the integral and proportional parameters are generated by a fuzzy controller. Figure 4 shows the architecture of the system where the control signal ($u_{PID}(k)$) can be expressed as:

$$u_{pid}(k) = u_{pi}(k) - u_d(k) \tag{3}$$

generalizing,

$$u_{pid}(k) = K_{pi} \cdot \Delta u_{pi}(k) + u_{pi}(k-1) - K_d \cdot \left[\frac{\Delta y(k)}{T}\right] \tag{4}$$

$$u_{pid}(k-1) = K_{pi} \cdot \Delta u_{pi}(k-1) + u_{pi}(k-2) - K_d \cdot \left[\frac{\Delta y(k-1)}{T}\right] \tag{5}$$

which can be written in the incremental form as:

$$\Delta u_{pid}(k) = u_{pid}(k) - u_{pid}(k-1) \tag{6}$$

$$\Delta u_{pid}(k) = K_{pi} \cdot \left[\Delta u_{pi}(k) - \Delta u_{pi}(k-1)\right] + \left[u_{pi}(k-1) - u_{pi}(k-2)\right] - K_d \cdot \left[\frac{\Delta y(k) - \Delta y(k-1)}{T}\right] \tag{7}$$

In this manner, the mathematical principle, which defines the control law can be obtained as a function of the output of a PI system of the incremental type. This output can be expressed in the frequency domain as:

$$U_{pi}(s) = K_p^c \cdot E(s) + K_i^c \cdot \frac{E(s)}{s} \tag{8}$$

Where, K_p^c e K_i^c correspond to the proportional and integral gain of the controller PI and E(s), the following error signal. In the discrete form, Equation 8 becomes:

$$u_{pi}(k) = K_p \cdot e(k) + K_i \cdot T \cdot \sum_{n=0}^{k} e(n) \tag{9}$$

or,

$$\Delta u_{pi}(k) = K_p \cdot [e(k) - e(k-1)] + K_i \cdot T \cdot e(k) \tag{10}$$

$$\Delta u_{pid}(k) = \frac{u_{pi}(k) - u_{pi}(k-1)}{T} \tag{11}$$

or:

$$u_{pi}(k) = u_{pi}(k-1) + T \cdot \Delta u_{pi}(k) \tag{12}$$

As shown by MALKI et al. (1994), The term $T\Delta u_{pi}(k)$ can be replaced by a term which represents a fuzzy action of the incremental type $K_{PI}\ \Delta u_{PI\ fuzzy}(k)$, where K_{PI} is the gain of the fuzzy controller, so that:

$$u_{PI}(k) = u_{PI}(k-1) + K_{PI} \cdot \Delta u_{PIfuzzy}(k) \tag{13}$$

for $K_{PI}=1$:

$$\Delta u_{PIfuzzy}(k) = u_{PI}(k) + u_{PI}(k-1) \tag{14}$$

Using rules of the IF-THEN type, the fuzzy logic controller describes the relationship between the control action increment $\Delta u_{PI\ fuzzy}(k)$, the deviation of the desired value or The error e(k) at the same time and its variation "Δe(k) = e(k) - e(k-1)", thus:

$$\Delta u_{PIfuzzy}(k) = f\{e(k), \Delta e(k)\} \tag{15}$$

As can be seen, equations 10 and 15 are similar, showing that a fuzzy PI controller can replace a conventional PI. Equation 9 can be re-written as:

$$u_{PID}(k) = K_p \cdot e(k) + K_i \cdot \Delta e(k) - K_d \cdot \Delta y(k) \tag{16}$$

thus

$$\Delta u_{PIfuzzy}(k) \propto K_p \cdot e(k) + K_i \Delta e(k) \tag{17}$$

where K_p and K_i are the conventional PI controller gains. The difference is that, in the case of conventional PI the relationship is linear (constant gain) whereas in the fuzzy PI the relationship can be non-linear (variable parameters).

A Neural Network similar to the one shown in CAMPOS RUBIO et al, (1998) was used, with 5 neurons. Figure 5 shows the mapping of the fuzzy element of the hybrid controller using a neural network of two layers and 5 neurons on the intermediate layer.

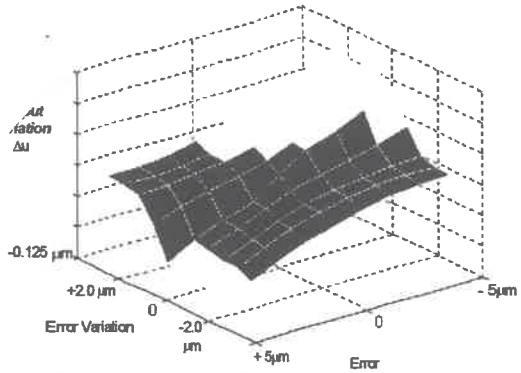

Figure 5 – Mapping of the Fuzzy Logic Controller

NUMERICAL SIMULATION AND EXPERIMENTAL TESTS

The servocontrollers were assessed in terms of time response and ability to reduce/eliminate perturbations.

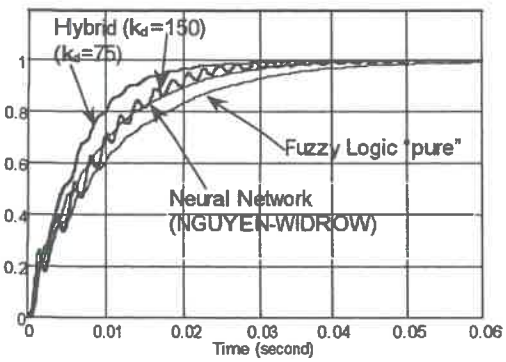

Figure 6. – Step Response.

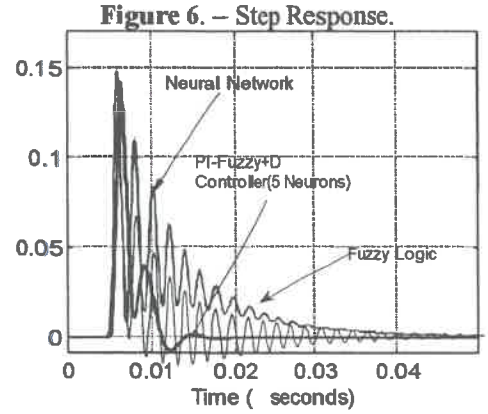

Figure 7. – Removal of Perturbation.

Figures 6 and 7 show the closed loop step and perturbation response using MATLAB® software.

The displacement amplitude using "PI *fuzzy*+D" is shown in Figure 8.

RESULTS AND DISCUSSIONS

The time response of the fuzzy neural-based controller was superior to the "pure" fuzzy. This is because of the need to interpolate values within the look-up table (linear interpolation in the case of "pure" fuzzy). PI *fuzzy* + D is an interesting option which aggregates the simplicity of the PID controller and greater control capabilities (variable gain) of PI *fuzzy* + D. It also proves adequate even

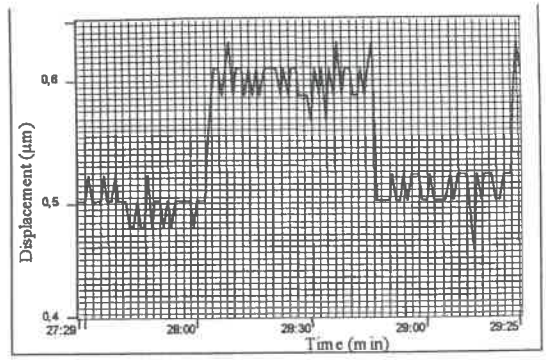

Figure 8 - PI fuzzy+D Displacement Test

in the presence of high level noise (Figure 8).

REFERENCES

CAMPOS RUBIO, J. C.; DUDUCH, J.; GEE, A. E.; PORTO, A. & LÊDO, H. (1996); *Comparison of control strategies for piezoelectric and magnetostrictive micropositioning devices for...* Proc. ASPE, Monterey. Vol. 14, pp 294-299

CAMPOS RUBIO, J. C.; SANTORO, F.; DUDUCH, J. & PORTO, A. (1996); *Algoritmo neural-fuzzy para controle de atuadores magnetoestrictivos.* VIII Congreso Chileno de Ing. Mec., Universidad de Concepcion, Concepcion, Chile. pp. 475-480.

CAMPOS RUBIO, J C; SANTORO, F; DUDUCH, J, PORTO, A & AE Gee (1998); *Neural Network controllers for magnetostrictive actuators.* Proc ASPE,,Vol 18, pp 264-269 (ann Meeting, St Louis, MO)

DUDUCH, J. G (1993); *Some Critical Aspects of Machine Design and Performance for the Machining of Brittle Materials*. Ph.D. Thesis, Cranfield Institute of Technology. England.

EDGE TECHNOLOGIES (1995): *Etrema Terfenol-D magnetoestrictive actuators* (catalog), Ames, Iowa.

KANIZAR, W.; LIU, D.; MOON, K. & SUTHERLAD, S. (1996); Magnetostrictive actuator-based micropositioner and its applications in turning. Proc. of SPIE, Vol. 2721, pp. 385-393.

MALKI, H., LI, H. & CHEN, G. (1994); New Design and Stability Analysis of Fuzzy Proportional-Derivative Control Systems. IEEE Transactions on Fuzzy Systems, Vol. 2, Nº 4, November. pp. 245 – 254.

MIRON, D. (1989); *Design of Feedback Control Systems*, HBS Publishers. New York, NY.

THE MATHWORKS, Inc. (1995); Neural Network Toolbox - For use with MATLAB®.

TZAFESTAS, S. & PAPANIKOLOPOULOS, N. (1990); Incremental Fuzzy Expert PID Control. IEEE Transactions on Industrial Electronics, Vol. 37, Nº 5, pp. 365 – 371.

YOJO, L. & MORAES, R. (1999); Avaliação de Controladores PID com Lógica Fuzzy. In Tech Brasil. Vol. 2, No 15 (May).pp.53-58.

MULTIPOINT TEMPERATURE CONTROL USING THERMOELECTRIC MODULES

Jian Ouyang*, Phuong-Thao Ton-Nu+, and Hy. D. Tran* §

* Dept. of Mechanical Engineering
University of New Mexico
Albuquerque, NM 87131

+ Intel Corporation
Rio Rancho, NM 87124

Abstract

Temperature control is a critical issue in precision engineering, especially for metrology structures and metrology frames. While oil shower and air showers have been shown to achieve millikelvin temperature stability, some applications do not permit oil shower or air shower systems (e.g. clean room environments). We demonstrate that by adding active temperature control to a structure, using thermoelectric devices for cooling or heating, we can maintain a structure at a more uniform temperature despite environmental temperature fluctuations. While it is not possible to maintain completely uniform temperature, it is possible to maintain temperature at selected points in the structure, where the sensors and actuators are located. Our objective is to demonstrate millikelvin temperature stability despite non-uniform external thermal disturbances. Some of the control issues that arise are cross coupling between different sensors and actuators, and effect of bias and drift of sensors (especially at millikelvin resolution). The analysis is based on a state variable finite difference thermal model. While state-space based control design may better handle cross coupling in the dynamics of the thermal system, simpler PID type controllers are easier to implement and test. The major advantages with active temperature control are that by separating the functions of temperature control from structural stability, one can choose materials for metrology structures based on structural criteria, independent of thermal properties. We will show initial experiments using a 4×4 array of thermoelectric coolers to control the temperature of an aluminum plate despite environmental disturbances. The results and control methods can be extended to large structures, such as metrology frames in lithography steppers. The advantages of this approach are not only better temperature control, but also superior dimensional control using inexpensive materials, and also more rapid thermal equilibration during equipment startup and shutdown.

Introduction

Thermally induced errors in precision mechanical structures are a major part of the error budget in precision mechanical systems, especially with lithography applications. With the increasing demand for improved minimum critical dimension (CD) in semi-conductor fabrication, the desire to maintain a dimensional stability of 10% of the CD (currently 0.18 μm) becomes increasingly challenging. In spite of the manufacturers' effort, there are always some residual thermal displacements that are related to coefficient of thermal expansion (CTE) of the materials of the structure, which is subject to the

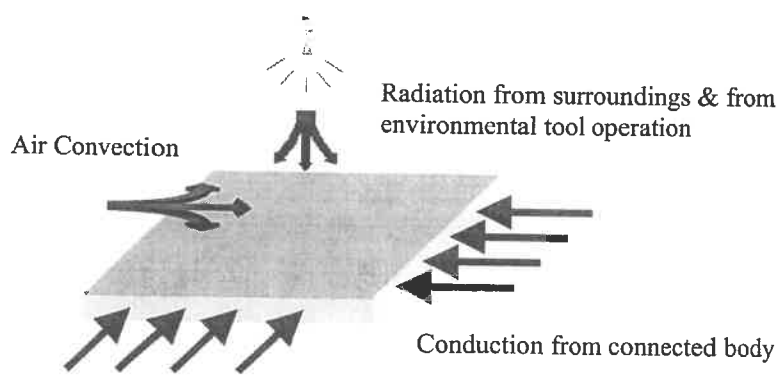

Fig. 1 Environmental Thermal Disturbances

§ Ouyang: ouyanj@unm.edu Tran: tran@me.unm.edu
This work is supported by DOD/ARO DAAD-19-99-1-0196

fluctuations of the surroundings. Therefore, it is desirable to maintain structures at a uniform temperature, regardless of environment. As an example, consider a 100mm square structure with a maximum 10nm of dimensional strain allowable to thermal effects. If the structure is made of super-invar (with a CTE of 0.63×10^{-6}/K), it is necessary to maintain its temperature at 160mK; however if the structure is made of aluminum (CTE of 22.5×10^{-6}/K), it is necessary to maintain the temperature should be kept within 5mK. However, aluminum has better specific stiffness, and is therefore more desirable mechanically. Active thermal control using a feedback control system emerges as a logical and practical solution.

Current techniques in the large equipment is to use air or oil shower to maintain the temperature; oil showers are not desirable in a clean room environment. Commercially available thermoelectric coolers (TEC) exploiting the Peltier effect and acting like solid-state heat pump with no moving parts are a very nearly ideal solution for small temperature ranges. With TECs, we can control structure temperature slightly above and below ambient temperature just by controlling current to the TEC; this allows isolation of a structure from possibly turbulent heat exchangers. We will describe the modeling of the system (4×4 TECs), and a proof-of-concept experiment and simulations for multipoint temperature control.

Heat transfer calculation

Consider the calculation shown in Figure 2.

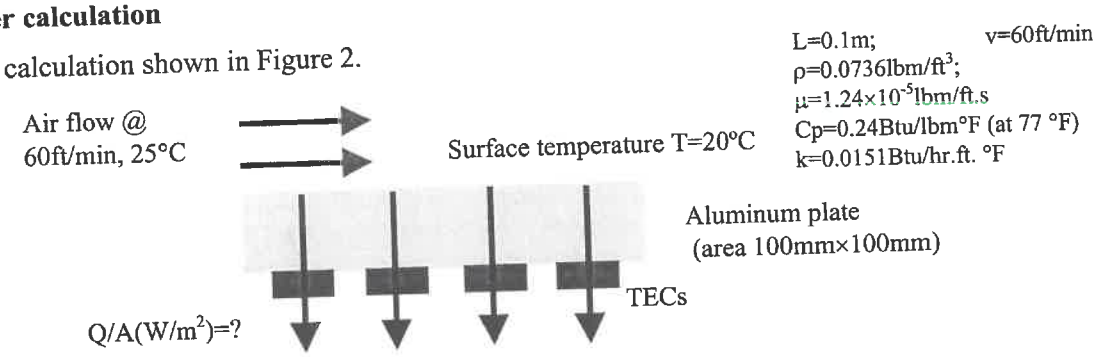

Fig. 2 Heat Transfer Calculation Setup

The heat convection coefficient of the surrounding air $h = \frac{N_u \times k}{L}$ (1)

For the design purpose, take average value for Nusselt number $N_{uL} = 0.664 \times \mathrm{Re}^{1/2} \times \mathrm{Pr}^{1/3}$ (2)

Equation (2) is applied when Reynolds number $\mathrm{Re} < 2\times10^5$, where $\mathrm{Re} = Lv\rho/\mu = 1947$ (3)

We can also calculate Prandtl number Pr as $\mathrm{Pr} = \mu C_p / k = 0.70951$ (4)

From (2), (3) and (4), we can obtain $N_{uL} = 26.132$ and $h = 1.203\,\mathrm{Btu/hr.°F.ft^2} = 7.22\,\mathrm{W/m^2K}$. With a total area of $0.01\mathrm{m}^2$, we have $Q = h \times A \times \Delta T = 0.361\,\mathrm{W}$. The air velocity of 60 ft/min is typical in laminar flow clean rooms (between 60 and 100 ft/min at the face of the HEPA filters). The average cooling power of a Ferrotec-USA module TE6302/065/018A is 5W, so an array of these modules provides more than sufficient cooling or heating power.

Experimental setup

Figure 3 shows a schematic concept for a temperature control experiment.

The temperature range we need to control is not large (±5 K), however the requirement for temperature precision is at millikelvin

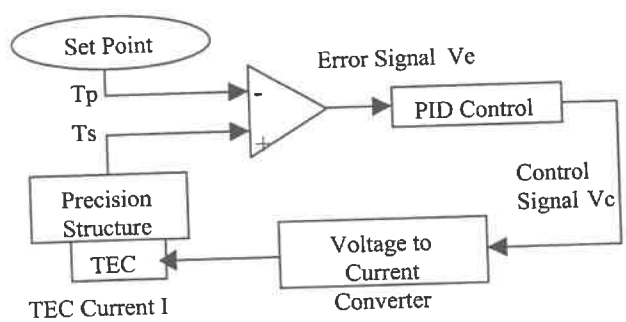

Fig. 3 Block Diagram

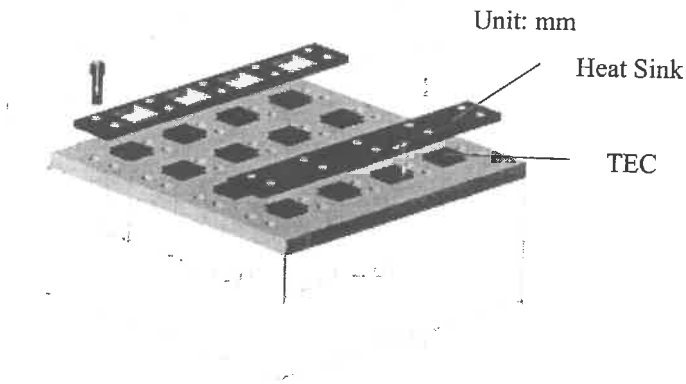

Fig. 4 Test Structure Assembly View

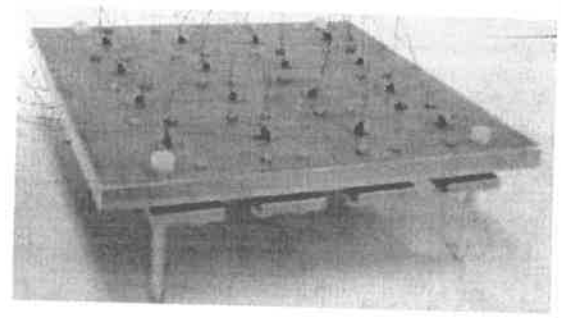

Fig. 5 Photograph of Test Structure

level. We choose thermistors for their high sensitivity and long term stability.

The test structure is an aluminum plate, shown in Figure 4 and Figure 5.

Finite Difference Model

The test structure is virtually cut into 4×4 parts as figure 6 shows and the sixteen elements are controlled by individual TECs and the temperature is measured individually by thermistors. However there exists thermal coupling between these elements. Coupling between diagonal elements (e.g. [1,1] and [2,2]) is smaller than between adjacent elements, and is omitted in the model. The effects of bolting holes are also omitted in the model. Since the system involves both conduction and surface convection effects, it is necessary to determine the Biot number that provides a measure of the temperature drop in the solid relative to the temperature difference between the surface and the fluid.

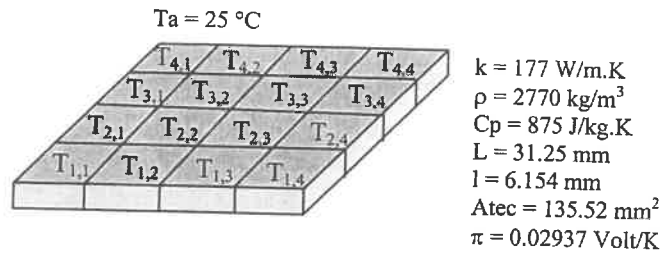

Fig. 6 Finite Difference Model

$$Bi = hL/k = 0.00334 < 0.1 \tag{5}$$

Hence the assumption of a uniform temperature distribution for each element is reasonable.
There are three types of elements for this model: inner ([2,2], [2,3], [3,2], [3,3]); corner ([1,1], [1,4], [4,1], [4,4]); side ([1,2], [1,3], [2,1], [3,1], [4,2], [4,3], [2,4], [3,4]).

- **Inner Nodes**

Take [2,2] as an example. By conservation of energy, we can obtain the following equation

$$\dot{T}_{2,2} = \frac{k}{\rho L^2 C_p}(T_{1,2} + T_{2,1} + T_{2,3} + T_{3,2} - 4T_{2,2}) - \frac{h}{\rho L^2 l C_p}(2L^2 - A_{tec})(T_{2,2} - T_a) - \frac{\pi}{\rho L^2 l C_p} I_{2,2} \tag{6}$$

- **Corner Nodes**

Take [2,2] as an example. By conservation of energy, we can obtain the following equation

$$\dot{T}_{1,1} = \frac{k}{\rho L^2 C_p}(T_{2,1} + T_{1,2} - 2T_{1,1}) - \frac{h}{\rho L^2 l C_p}(2L^2 - A_{tec} + 2Ll)(T_{1,1} - T_a) - \frac{\pi}{\rho L^2 l C_p} I_{1,1} \tag{7}$$

- **Side Nodes**

Take [1,2] as an example. By conservation of energy, we can obtain the following equation

$$\dot{T}_{1,2} = \frac{k}{\rho L^2 C_p}(T_{1,1} + T_{1,3} + T_{2,2} - 3T_{1,2}) - \frac{h}{\rho L^2 l C_p}(2L^2 - A_{tec} + Ll)(T_{1,2} - T_a) - \frac{\pi}{\rho L^2 l C_p} I_{1,2} \tag{8}$$

In equation (6), (7) and (8), the k-term is related with the heat conduction between different elements, h-term heat convection from the surroundings, π-term heat drawn by TEC. Here we omit the resistance and conductance effects of TEC to simplify the problem and assume that heat sinks attached to TECs work perfectly. It is also assumed that the temperature-related coefficients k, h, Cp and π are constant since the temperature range is within ±5 K.

Plugging in the value of parameters, we obtain the state-space equations of the system as follows.

$$\dot{\mathrm{T}} = \mathrm{AT} + \mathrm{BI} + \mathrm{D}T_a \tag{9}$$

$$\dot{\mathrm{T}} = (\dot{T}_{1,1} \;\; \dot{T}_{1,2} \;\; \dot{T}_{1,3} \;\; \dot{T}_{1,4} \;\; \dot{T}_{2,1} \;\; \dot{T}_{2,2} \;\; \dot{T}_{2,3} \;\; \dot{T}_{2,4} \;\; \dot{T}_{3,1} \;\; \dot{T}_{3,2} \;\; \dot{T}_{3,3} \;\; \dot{T}_{3,4} \;\; \dot{T}_{4,1} \;\; \dot{T}_{4,2} \;\; \dot{T}_{4,3} \;\; \dot{T}_{4,4})^T$$

$$\mathrm{T} = (T_{1,1} \;\; T_{1,2} \;\; T_{1,3} \;\; T_{1,4} \;\; T_{2,1} \;\; T_{2,2} \;\; T_{2,3} \;\; T_{2,4} \;\; T_{3,1} \;\; T_{3,2} \;\; T_{3,3} \;\; T_{3,4} \;\; T_{4,1} \;\; T_{4,2} \;\; T_{4,3} \;\; T_{4,4})^T$$

$$\mathrm{I} = (I_{1,1} \;\; I_{1,2} \;\; I_{1,3} \;\; I_{1,4} \;\; I_{2,1} \;\; I_{2,2} \;\; I_{2,3} \;\; I_{2,4} \;\; I_{3,1} \;\; I_{3,2} \;\; I_{3,3} \;\; I_{3,4} \;\; I_{4,1} \;\; I_{4,2} \;\; I_{4,3} \;\; I_{4,4})^T$$

$$A = \begin{pmatrix} \Phi & 0.0748E_4 & 0 & 0 \\ 0.0748E_4 & \Gamma & 0.0748E_4 & 0 \\ 0 & 0.0748E_4 & \Gamma & 0.0748E_4 \\ 0 & 0 & 0.0748E_4 & \Phi \end{pmatrix} \qquad \mathrm{B} = -0.00202\mathrm{E}_{16}\mathrm{I}$$

$$\mathrm{D} = (\mathrm{D}_1 \;\; \mathrm{D}_2 \;\; \mathrm{D}_2 \;\; \mathrm{D}_1)^T$$

$$\Phi = \begin{pmatrix} -0.1506914 & 0.0748 & 0 & 0 \\ 0.0748 & -0.2253961 & 0.0748 & 0 \\ 0 & 0.0748 & -0.2253961 & 0.0748 \\ 0 & 0 & 0.0748 & -0.1506914 \end{pmatrix} \qquad \mathrm{D}_1 = \begin{pmatrix} 0.0010914 \\ 0.0009961 \\ 0.0009961 \\ 0.0010914 \end{pmatrix}$$

$$\Gamma = \begin{pmatrix} -0.2253961 & 0.0748 & 0 & 0 \\ 0.0748 & -0.3001008 & 0.0748 & 0 \\ 0 & 0.0748 & -0.3001008 & 0.0748 \\ 0 & 0 & 0.0748 & -0.2253961 \end{pmatrix} \qquad \mathrm{D}_2 = \begin{pmatrix} 0.0009961 \\ 0.0009008 \\ 0.0009008 \\ 0.0009961 \end{pmatrix}$$

Where E_4 is a 4×4 identity matrix, O is a 4×4 zero matrix, E_{16} is a 16×16 identity matrix, T_a is the emperature of the surrounding air. This system is linear and controllable.

Summary

The results of the simulations and experiments will be presented at the conference.

References

. DeBra, D. B., Victor, R. A., and Bryan, J., "Shower and high pressure oil temperature control," *CIRP Annals* vol 35(1), p. 359-364, 1986.

'. *Technical Reference For Ferrotec Thermoelectric Cooling Modules*, Ferrotec America, Nashua, NH

. Huang, J. J., and DeBra, D. B., "Liquid Temperature Control for a Hydraulic Turning Machine," *IEEE Control Systems Magazine*, vol 17(4), p. 55-63, 1997.

. *Internaional Technology Roadmap for Semiconductors*, http://www.itrs.net/ntrs/publntrs.nsf

Error Calibration and Real Time Compensation System for the Chip Mounting Machine using the Kinematic Ball Bar

Heui Jae Pahk, Jung Hwan Kim, Chang Ha Lee, Jun Hee Moon
School of Mechanical Eng, Seoul National University, Seoul, Korea

1. Introduction

The chip mounting machines or the PCB chip mounters are widely used in variety of semiconductor manufacturing processes, where those chip mounters are for picking up electronic parts(called chips) from magazines loaded, then for inserting those chips into the PCB(Printed Circuit Board). The static/dynamic accuracy in the positioning/inserting processes plays great role in the performance of the chip mounters, and thus the accuracy enhauncement of the chip mounters has been desired for the manufacturers and users of the chip mounting machines. The laser interferometer or manufacturers' jig have been used for just simple checking of the machine positioning, although more comprehensive error calibration and compensation system is desired. The ball bar system has been used for quick check of accuracy of machine tools, and the comprehensive volumetric error calibration is possible with the enhaunced version of ball bar such as AVEC-100[1]. In this paper, a comprehensive error calibration method is proposed for the chip mounter, where positional errors, squareness error, straightness errors, angular errors, and the back lash error terms are assessed. The chip mounter is modeled with the kinematic configuration, and the volumetric error equations are derived from the kinematic chain of axis configuration. As the backlash error is observed as varying with the axis positioning, a new concept of two dimensional back lash error terms are considered and modeled accordingly. The modeled error terms are effectively added to the volumetric error equations of ball bar analysis algorithm developed, and thus efficient error calibrations are performed. Once the error calibration is performed, the real time error compensation procedures are followed and implemented in the chip mounter controller. The accuracy of chip mounting capability is enhaunced as much as three times in average, and thus the machine performnace is upgraded in terms of accuracy specification. As the on line measurement/compensation features are fully implemented, the developed techniques are readily applied to the manufacturing processes of chip mounters in SAMSUNG, and the acuracy enhauncement is performed.

2. Error Calibration and Modeling

2.1 Error modeling with kinematic ball bar system

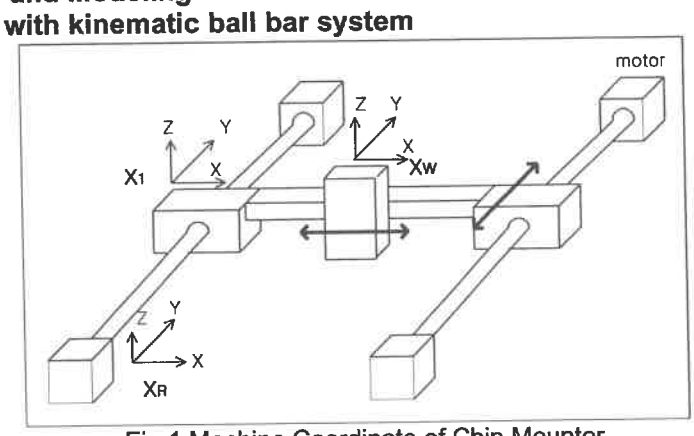

Fig 1.Machine Coordinate of Chip Mounter

Fig 1 shows the configuration of the chip mounter considered, where it has two guides along the Y axis, and the X axis guide on the gantry structure locating on the Y axis guides. Therefore two dimensional kinematic error models are possible, and the translational/rotational error terms are modeled as follows,

$$L(x) = \begin{bmatrix} x + \delta_{xx} \\ \delta x \end{bmatrix} \quad (2\text{-}1) \qquad L(y) = \begin{bmatrix} \delta \ \ -\alpha y \\ y + \delta_{yy} \end{bmatrix} \quad (2\text{-}2)$$

$$R(x)=\begin{bmatrix}1 & -\varepsilon_{zx}\\ \varepsilon_{zx} & 1\end{bmatrix} \quad (2\text{-}3) \qquad R(y)=\begin{bmatrix}1 & -\varepsilon_{zy}\\ \varepsilon_{zy} & 1\end{bmatrix} \quad (2\text{-}4)$$

The following formula are induced from the structure of chip mounter..

$$X_R = R(y)X_1 + L(y) \quad (2\text{-}5)$$

$$X_1 = R(x)X_W + L(x) \quad (2\text{-}6)$$

From (2-5), (2-6) X_W is like

$$X_W = R(x)^{-1}\left[R(y)^{-1}\left[X_R - L(y)\right] - L(x)\right] \quad (2\text{-}7)$$

Using translation & rotation matrix(2-1~4) errors can be derived.

$$\Delta X = \begin{bmatrix}\Delta x\\ \Delta y\end{bmatrix} = \begin{bmatrix}-\delta_{xx} - \delta_{xy} - \alpha y - \varepsilon_{zy} y - \varepsilon_{zx} y\\ -\delta_{yy} - \delta_{yx} - \varepsilon_{zx} x\end{bmatrix} \quad (2\text{-}8)$$

The relation ship between the radial error and the volumetric error is then as follows,

$$(R+\Delta R)^2 = (x+\Delta x)^2 + (y+\Delta y)^2 \quad (2\text{-}9)$$

thus the radial error is formed as following.

$$\begin{aligned}\Delta R &= \frac{1}{R}(x\Delta x + y\Delta y)\\ &= \frac{x}{R}(-\delta_{xx} - \delta_{xy} - \alpha y - \varepsilon_{zy} y - \varepsilon_{zx} y) + \frac{y}{R}(-\delta_{yy} - \delta_{yx} - \varepsilon_{zx} x)\end{aligned} \quad (2\text{-}10)$$

Eq(2-10) completes the error calibration of the chip mounter using the kinematic ball bar, and it can be used for the consequent error calibration/compensation procedures.

2.2 Compensation algorithm

The compensation algorithm calculates the compensation values from present and target coordinates and make the chip mounter move to the accurate position. The compensation value is determined by a machine controller using the following compensation formula, which is derived from the modeling information of X-Position Error, Y-Position Error , Y-Yaw Error, Y Straightness Error along X axis, X straightness Error along Y axis, X-Backlash, Y-Backlash.

The compensation formula defined by the structure of chip mounter are

$$\Delta X = \delta\,\mathrm{x(X)} - \delta\,\mathrm{x(Y)} + \mathrm{Backlash_X(X,Y)} \quad (2\text{-}11)$$

$$\Delta \mathrm{Y} = -\delta \mathrm{y(X)} + \delta \mathrm{y(Y)} + \alpha \mathrm{X} + \varepsilon_{zy}\mathrm{Xp} + \mathrm{Backlash_Y(X,Y)} \quad (2\text{-}12)$$

where the backlash terms are explained in the next sections.

3. Practical application

3.1 Configuration and Method of Experiment

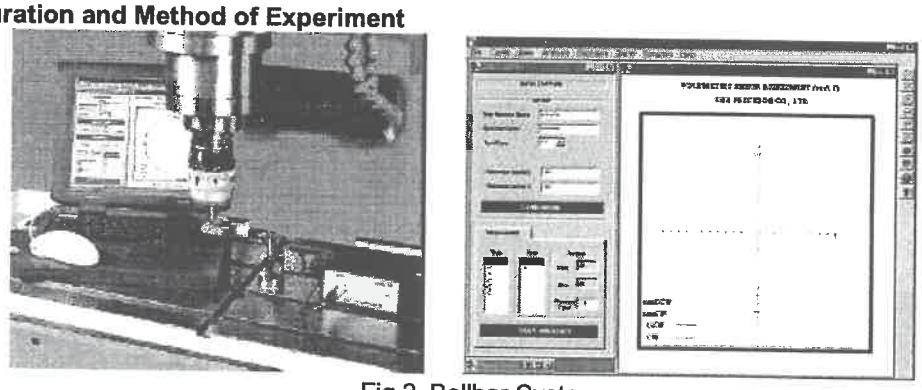

Fig 2. Ballbar System

The developed AVEC-100 ball bar system has been applied to the Samsung chip mounter(Model name :

CP-40), where the ball bar setup and configurations are shown in fig2.
In this experiment, the kinematic ball bar of 300mm radius(nominal length) and Invar calibrator is used to guarantee the length accuracy. A PC is connected to kinematic ball bar via sensor interface part and the controller of chip mounter by RS232C interface module to receive the signal that chip mounter moves to the measuring position and takes the data from kinematic ball bar at that time. The measurement procedures are performed along the contour path based on the point to point to movement of the chip mounter.
The backlash error is varying at the every point of X-Y plane because the yaw error along Y axis is great by the effect of the gantry type structure of chip mounter, where a drive motor is attached to only one ball screw. The kinematic ball bar (AVEC-100) software makes two dimensional backlash error from the measurements as follows.

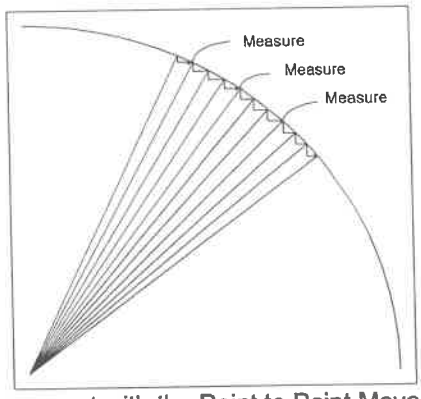

Fig 3 . Ball Bar Measurement with the Point to Point Movement of Machine

3.2 The Measurement and Modelling of Backlash

As is seen in Fig 4, backlash can be obtained by movement to the X+, X-, Y+, Y- direction at each measuring point around the circle. The formula (3-1) and (3-2) show the backlash modeling function out of measured backlash values with variables X, Y.

$$Backlash_X(X,Y) = AX + BY + CXY + D \qquad (3\text{-}1)$$

$$Backlash_Y(X,Y) = A'X + B'Y + C'XY + D' \qquad (3\text{-}2)$$

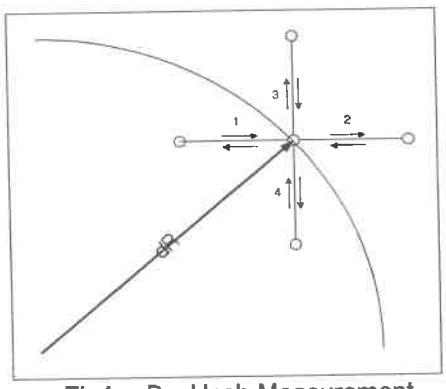

Fig4. Backlash Measurement

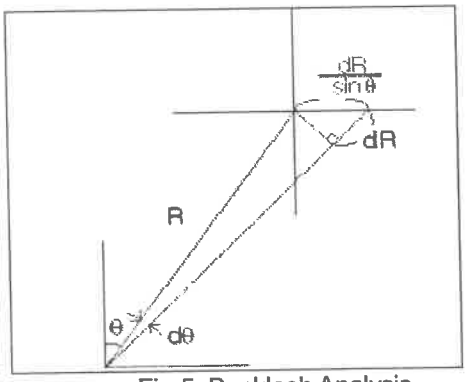

Fig 5. Backlash Analysis

3.3 Results

Using the kinematic ball bar, the errors of chip mounter are measured, calibrated, and compensated. To certify this effort, the errors are measured again after calibration. Also the pitch error along X, Y axis of the chip mounter are measured by the laser interferometer before and after compensation. As a result, we can see that accuracy of chip mounter is improved about 3 times. Fig 6, 7 show the measurement result of kinematic ball bar and Fig 8, 9 is the result of laser interferometer measurement before and after

compensation. Table 1 shows the comparison of accuracy with and without compensation.

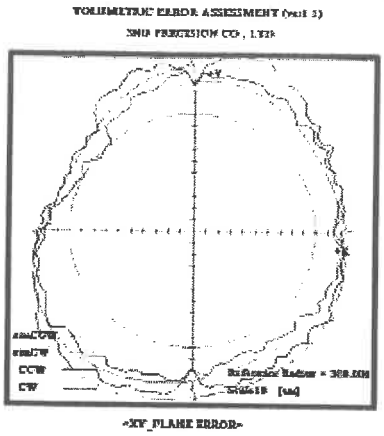

Fig 6. Before compensation

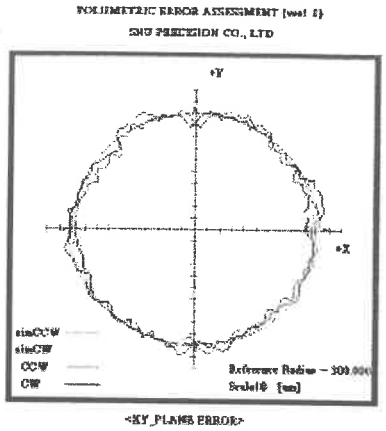

Fig 7. After compensation

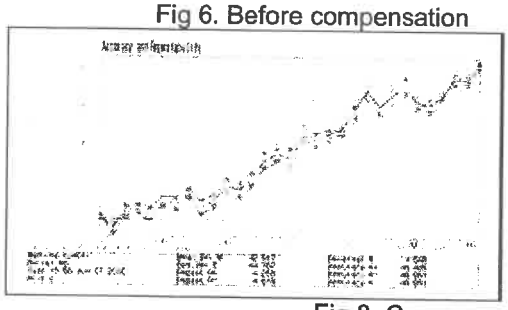

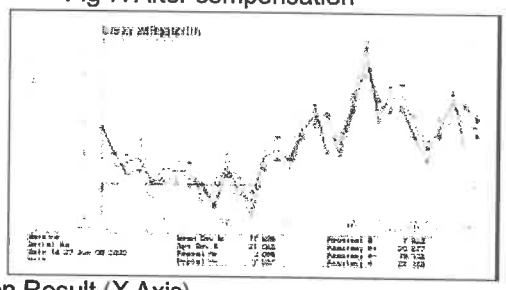

Fig 8. Compensation Result (X Axis)

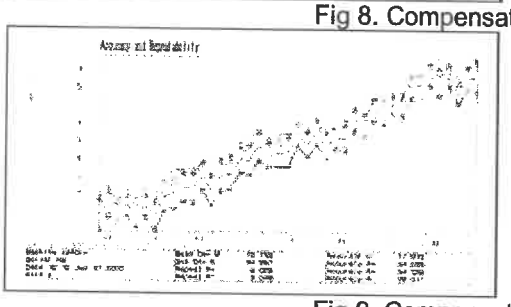

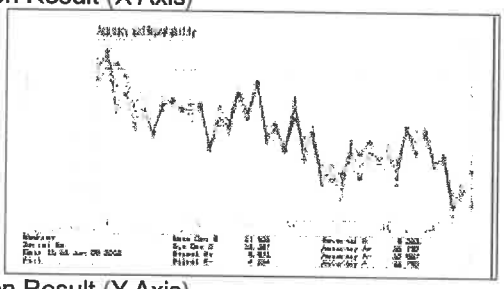

Fig 9. Compensation Result (Y Axis)

	X axis		Y axis	
	Accuracy	Backlash	Accuracy	Backlash
Before Compensation	46.931	4.548	99.017	17.913
After Compensation	22.183	1.530	36.792	9.263

Table 1. Compensation Result

4. Conclusion

A kinematic ball bar system is applied to semiconductor equipments such as chip mounter, where the PC controls the kinematic ball bar and controller of chip mounter using RS232C interface. Thus the on-line features of measurement/compensation is implemented. The accuracy has been enhaunced as much as about three times, and the machine accuracy specification has been uograded.

References

[1] AVEC-100 User Manual for Ball Bar System, SNU Precision, 1999

[2] A new technique for volumetric error assessment of CNC machine tools incorporating the ball bar measurement and the 3D volumetric error model, Heui Jae Pahk, Y.S.Kim, J.H.Moon, acceptef for publication to the Int.J.machine tools and manufacture, 1996

Integrated Real Time Compensation System for Thermally Induced Volumetric Errors in Commercial CNC machine tools

Heui Jae Pahk, Suk Won Lee, Suck Kim, Sung Won Yoon
School of Mechanical Engineering, Seoul National University, Seoul, Korea

1.Introduction

Thermally induced errors have been significant factors affecting the machine tool accuracy. The thermal errors generally come from the thermal deformations of the machine elements caused by heat sources that exist within the structure, ball screws, bearings, nuts, axis drive motors, friction on the way surfaces, cutting processes, the flow of coolant/lubricating oil, and the ambient temperature. Those thermal errors have been reported as much as about 70% of the total positioning error in the machine tool, and among them, the spindle thermal errors or spindle drifts have been considered as the dominant error components (e.g.[1]) In this paper, a measurement system for spindle thermal error and feed axis thermal error is developed and three methods of thermal error modeling are implemented for the spindle thermal error: multiple linear regression, neural network, and system identification; and the error modeling for feed axis thermal error is composed of geometric error and thermal error. In order to obtain the compensation values, the algorithm of the volumetric error map is programmed using the models. The coordinates of the machine tool controller are modified to compensate in real time in PC interfaced environment program. After the real tome compensation, the machine tool accuracy has been improved about 4-5 times.

2. Spindle thermal error measurement/modeling

2.1 Measurement system for the 5 DOF spindle thermal errors

There are 6 degree of freedom(6 DOF) components in the spindle error motion in machine tools[6]: two radial error motions, one axial motion, two tilting motions, and one indexing error motion. In view of the machine tool accuracy, the indexing error motion of spindle can be ignored and thus 5 DOF spindle thermal errors are considered in this paper.
Fig.1 shows the measurement setup of the 5 DOF spindle errors, where the jig of two master balls and 5 gap sensors are arranged around the PC interfaced environment. Temperature variations are also measured with the thermocouples around the machine tool structure.

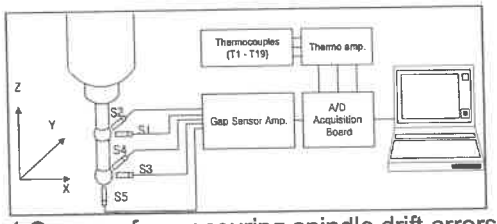

Fig.1 Sensors for measuring spindle drift errors.

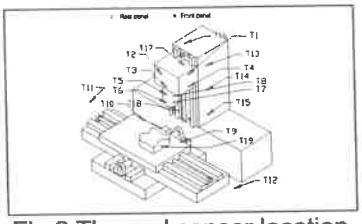

Fig.2 Thermal sensor location

Fig.2 shows the thermocouples located around the machine tool structure, where 8 sensors are located around the spindle and spindle housing, 8 sensors around the frame, 2 sensors for the ambient air temperature, and 1 sensor around the gap sensor jig. The on line measurement feature has been implemented, in order to measure the spindle thermal error with efficiency. When the total measurement time and the measurement interval are input, the PC controls the CNC machine to operate according to the programmed speed via the RS232C serial interface connection. At the time of measurement, the PC sends the command "M19"(typically for the FANUC controller) to the machine tool such that the machine spindle stops at the angle of reference pulse signal(zero degree) of the spindle encoder. Then the machine spindle stops, and the spindle error measurements as well as the temperature measurements are performed. After the measurement operation, the PC sends the command of spindle rotation to the machine tool, then the machine spindle rotates until the next command of measurement is given.

2.2 Spindle thermal error measurement and modeling

The developed thermal error measurement system has been applied to the three operation conditions of the CNC machine tool: (1) constant running condition (running at constant 3000 rpm) (2) progressive

running condition (progressively increasing/decreasing rpm at 10 min interval) (3) random running condition (running at random rpm). The machine tool is running at 3000rpm constantly during 4 hours, then machine stops during another 4 hours in constant running condition. In progressive running condition, the spindle rotation is progressively increasing from such as 0 rpm, 1000 rpm, 2000 rpm, and 3000 rpm, then the spindle rotation is progressively decreasing from such as 3000rpm, 2000rpm, 1000rpm, and 0 rpm. In random running condition, the machine tool is running at random. In fig.3, temperature variations around machine tool and thermal spindle errors are shown over time in each spindle running condition. From the above three spindle thermal error measurement cases at the three typical running condition of machine tool, a strong relationship can thus be suggested between the temperature data and the spindle thermal error data. Therefore the relationship can be obtained by the thermal error modeling procedures which will be explained in the next section.

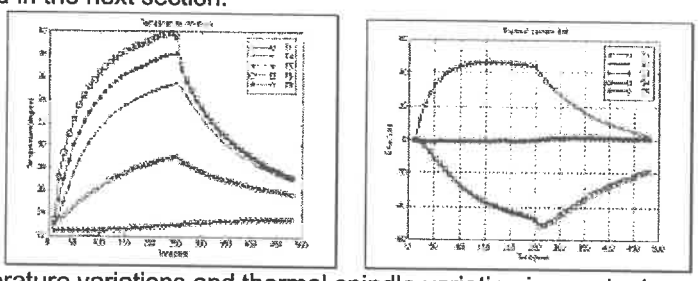

Fig.3a Temperature variations and thermal spindle variation in constant running condition

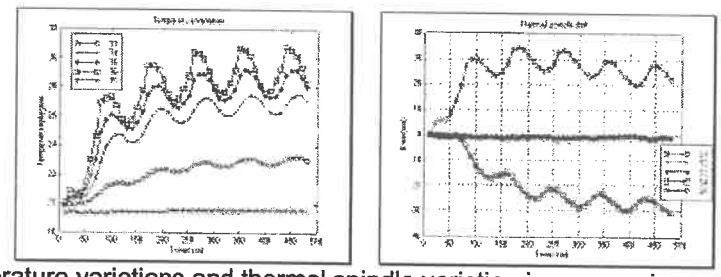

Fig.3b Temperature variations and thermal spindle variation in progressive running condition

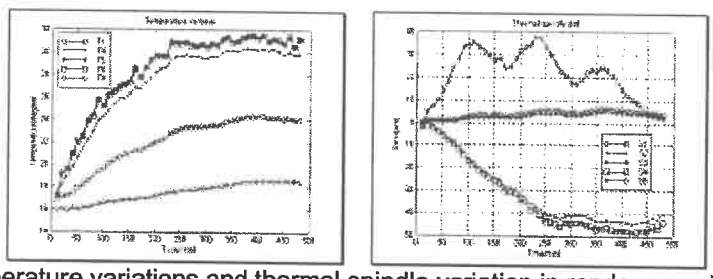

Fig.3c Temperature variations and thermal spindle variation in random running condition

2.3. Spindle thermal error modeling

There have been several methods of the thermal error modeling for the machine tool, and three different methods of thermal error modeling are implemented and tested in this paper: multiple linear regression model, neural network model, and the system identification model.

- Multiple linear regression model

The relationship between the temperature data and the spindle error can be modeled as the multiple linear regression model. Let t_l(l=1,2,....N) be the temperature data at several locations around the machine tool, then the thermal error component, y_1 can be modeled as linear relationship as follows.

$$y_1 = a_{11}t_1 + a_{12}t_2 + a_{13}t_3 + a_{14}t_4 + ... + a_{1n}t_n + b_1 \qquad (1)$$

where $a_{11}, a_{12}, a_{13}, a_{14}....a_{1n}$ are coefficient for temperature, b_1 is the constant for the thermal error model. Eq(1) can be extended to the 5 DOF spindle thermal errors, and thus can be represented in matrix form as follows

$$Y = AT \qquad (2)$$

Therefore the relationship between the thermal error and the temperature data can be found from equation(2), and the multiple linear regression model is completed.

- Neural network

The neural network is a kind of multiple nonlinear model in which the coefficients are called weights; and the coefficients are evaluated by training with an iterative technique called back propagation. Thus the neural network is appropriate to a system having the nonlinear relationship between the multiple inputs and the multiple outputs. There are three types of layers for the neural network: input layer, hidden layer, and output layer. For the thermal error application, the input layer is designed to consist of temperature data, output layer of the 5 DOF spindle thermal errors.

- System identification

In the system indentification model, the present thermal errors(at time t) are influenced by the present temperature data, the past temperature data, and the past thermal errors.

Let $X_t, X_{t-1}, X_{t-2}, \cdots X_{t-n}$ be the thermal errors at time t, t-1, t-2, ... t-n, respectively, and let $a_t, a_{t-1}, \cdots a_{t-n+1}$ be the temperature data at time t, t-1, ... t-n+1, respectively. Then the thermal errors $X_t, X_{t-1}, X_{t-2}, \cdots X_{t-n}$ can be related with the temperature data $a_t, a_{t-1}, \cdots a_{t-n+1}$. That is,

$$X_t - \phi_1 X_{t-1} - \phi_2 X_{t-2} - \cdots - \phi_n X_{t-n} = \theta_1 a_t - \theta_2 a_{t-1} - \theta_3 a_{t-2} - \cdots - \theta_m a_{t-m+1} \quad (3)$$

where, ϕ_n and θ_m are the model coefficients, and the integers n, m are heuristically chosen as 3, 2 repectively.

3. Feed axis thermal error measurement/modeling

3.1 Feed axis thermal error measurement

There are 3 translation errors(including 1 postional error and 2 straight errors) and 3 rotational errors(pitch, yaw, roll) along feed axis. The thermally induced translational errors, pitch, yaw errors are measured using the laser interferometer over time; and temperatures around machine tool are simultaneously measured with thermocouples. The measurement system for feed axis thermal error is shown in fig.5. The system is composed of PC interfaced devices such as program interfacing machine tool using RS232C and laser interferometer; and having acqusition system for temperature around machine tool. Temperature locations are selected, considering principal heat sources and associated thermal distortion; ball screw bearings, linear scale, environmental air, slide face in each axis.

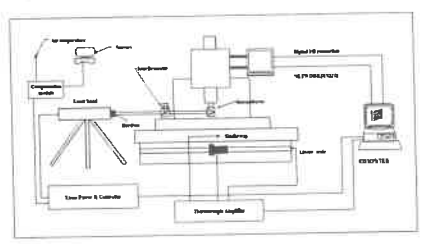

Fig.5 Setup for thermal feed axis error

3.1 Feed Axis Thermal Error Modeling

Feed axis error model is composed of geometric term and thermal term.Geometric term has factor of nominal coordinates in each axis and the thermal term has factors of temperatures around machine tool, that is,

$$Error(P,T) = Error_g(P) + Error_t(T) \quad (4)$$

Where each term is defined as following:

$$Error_g(P) = a_0 + a_1 P + a_2 P^2 + \ldots \quad (5)$$

$$Error_t(T) = m_1(T) * P + m_2(T) \quad (6)$$

Temperature variation and positional error including thermal/geometric error in X axis is shown in fig.6. It has been found that the longer feed axis, the more thermal error machine tool has. The first term in equation(6) has physical meaning that thermal error is related to the length and temperature. The rest of thermally induced feed axis errors such as straightness and angular errors are also modeled similarly, however, angular error and straightness error have less variation than positional error over time, while the

angular errors are usually amplified by the Abbe's offset principle.

3.2 Volumetric error map and real time compensation

The volumetric errors are calculated using the homogeneous transformation matrix(HTM) including spindle thermal error and the feed axis thermal error. The HTM is defined as follows,

$$T_r^n = \begin{bmatrix} O_{11} & O_{12} & O_{13} & P_x \\ O_{21} & O_{22} & O_{23} & P_y \\ O_{31} & O_{32} & O_{33} & P_z \\ 0 & 0 & 0 & 1 \end{bmatrix} \qquad (7)$$

where **O** is related to angular terms and **P** is related translational terms. The actual errors at every nominal position are calculated in each axis as follows:

$$S_{AP_t} = T_A^D T_D^E P_t(p) \qquad S_{AP_w} = T_A^C T_C^B P_w(p) \qquad Error = S_{AP_w} - S_{AP_t} \qquad (8)$$

Real time compensation system is developed using the modified PLC program in CNC controller. The compensation data in each axis calculated using the HTM, and are sent to the controller. The developed system has been applied to a practical CNC machine tool, and the diagonal error is measured with laser interferometer for verification. The result is shown in fig.7 where the error was greatly reduced typically about 4-5 times.

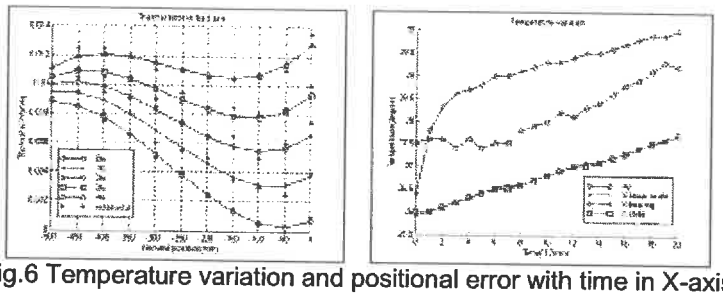

Fig.6 Temperature variation and positional error with time in X-axis

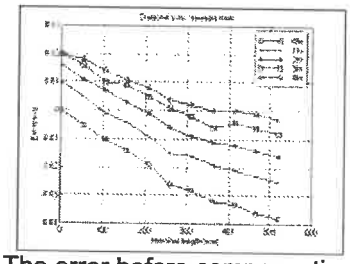

Fig.7a The error before compensation

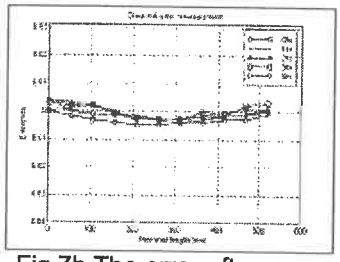

Fig.7b The error after compensation

4. Conclusion

Thermal error measurement and real tome compensation system has been successfully developed. The spindle thermal error and feed axis error including thermal and geometric error are modeled respectively. The real time compensation system is developed modifying the PLC program in CNC controller interfacing the PC which has algorithm calculating the volumetric error. After compensation, about 85% of error is removed. This result shows that the error modelings suggested have good performance.

REFERENCE

[1] Suk Won Lee, Development of thermal error measurement and compensation system for spindle and feed axis in CNC machine tool, Seoul National University, Korea, 2000

[2] J.B.Bryan, International status of thermal error research, Annals of the CIRP, Vol.16, pp.203-215, 1968

[3] E.R.McClure, Significance of thermal effect in manufacturing and metrology, Annals of CIRP, Vol.15, pp.61-66, 1967

[4] G.P.Sutton, Economy of accuracy, technology of machine tools, Vol.5: Machine tool accuracy, Lawrence Livermore National Laboratories, University of California, Livermore, CA., 1980

[5] R.Donaldson, D.C.Thompson, Design and performance of a small precision CNC turning machine, Annals of the CIRP, Vol.35, No. 1, pp. 373-376, 1986

Development of the Standard Application Program Interface (API) for Open FA controller in Japan

Shigeru UENO *,Hideaki.INOUE**,Shinichiro.CHINO***,Yoshihiro.HOSHINO****
and Masayoshi UNEME*****
*Technical Research Institute of JSPMI Higashikurume city, Tokyo,Japan
**FANUC Ltd, Yamanashi, Japan
***Mitsubishi Electric Corp., Itami, Japan
****, MAKINO Milling Machine Co.ltd, Atsugi, Japan
*****, MORI SEIKI Co.ltd, Nara, Japan

Introduction: Although an open architecture controller system has been told that it would becomes next generation controller system in FA area 1)2), there still are few manufacturers who introduce it in precision machining system. The reason is fully depending upon the lack of its standard systems and standard API. JOP (Japan Open System Promotion Group) has been conducted the CNC API standardization for three years. The specification of the API set PAPI (Principal Application Program Interface) has defined and becomes new Japanese standard. This paper describes its development concept and its test results. PAPI is consisted from two group API sets such as Basic API and Extended API. Also it is classified into three categories such as API for CNC, for servo systems, and for applications. It has about 90 functions of C languages, and supports standard services for Human-Machine-Interface (HMI) of NC, such as system control / manual operation / program management. The developed API has implemented into two existing different manufacturer's CNC system, and operated simultaneously by the single server PC that installed third vender's HMI.

Basic concept: It is a critical points to specify the meaning of an open architecture NC system. So that before starting its detail developments, the development group has discussed its classifications. Finally they agreed upon its basic points as follows. That is; this API should be developed for three types of open controllers such as 1) PC +proprietary NC type, 2) PC + NC card type and 3) Software NC on PC+I/O card type, as proprietary NC system still keep its strong position in the machine tool manufactures field. Figure 1 explains the configuration of these three types CNC systems. In the type 1), The controller is the existing CNC, which consists of the motion controller, and PLC. Setting from the API includes those processed directly by the motion controller and those passed to the PLC. Commands passed to the PLC are mediated with input information from the panel, etc. Type 2) consists of specially designed NC board, which includes PLC functions. API processing methods are similar to the type 1). Type 3) is so called software PC based controller. The controller is made according to an open agreement. In general, almost all basic processing is realized in the software on the PC.

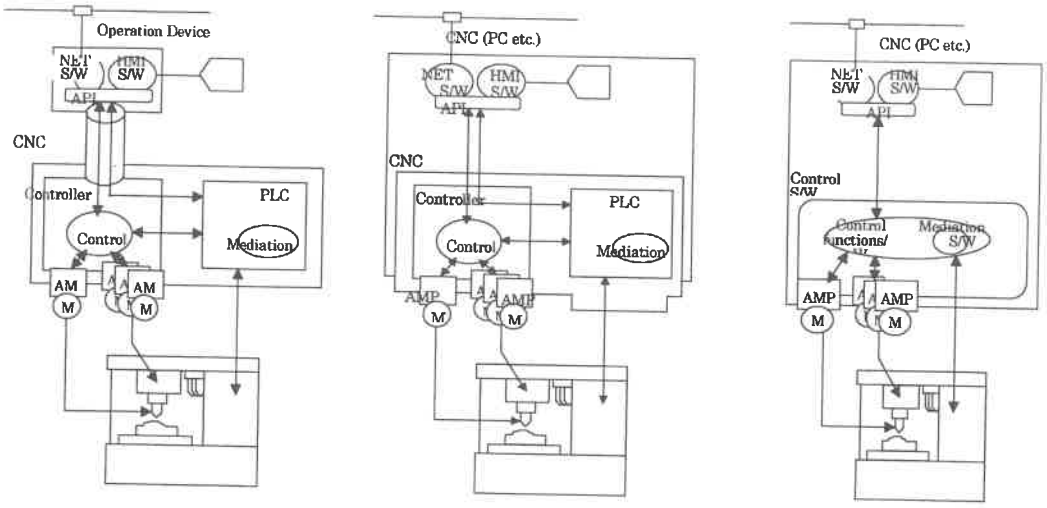

Type 1.

PC + Proprietary CNC

Type 2.

PC + NC Board

Type 3.

Software NC on PC + I/O

Figure 1. Existing CNC Configuration Type

CNC Model (CNC Function Block): PAPI offers the functions, which construct the HMI for the CNC model as shown in the Figure 2. This figure explains the function model of existing CNC system. Basically, Open architecture APIs should cover all kinds of information connections between the indicated functions. However, it may rather complicate and some of them has a difficulty to standardize at this moment. The major requirements are to monitor and control the total CNC systems, and not to modify its own servo conditions at the real time mode. So, the development target has concentrated into HMI functions.

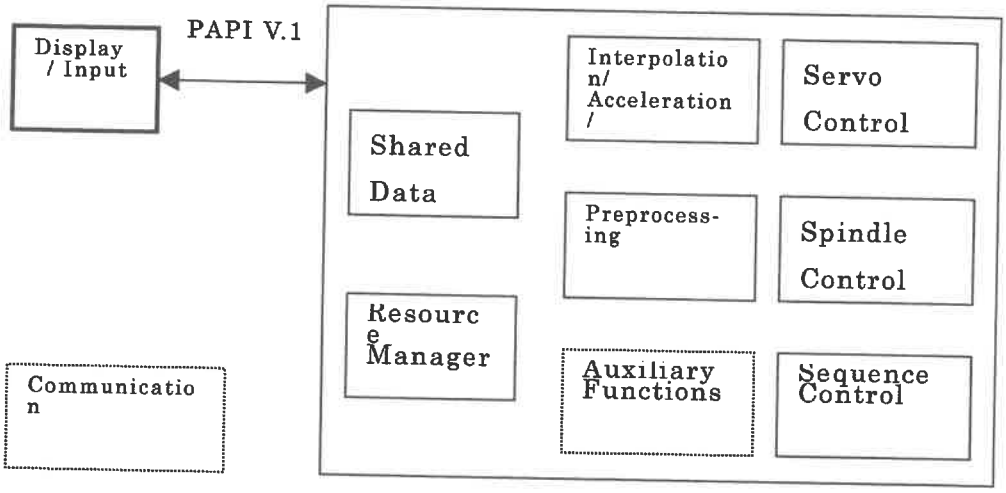

Figure 2. CNC System Function Block Diagram

According to the function blocks, it was classified into three categories with their functional characteristics. Category one is called as CNC system APIs that include Display, Input, Resource manager and Communication. Category two is called CNC Devices APIs that is consisted from Interpolation, Acceleration, Deceleration, Servo control, Spindle control and Sequence control. The final one, category three is called CNC Application APIs that include Shared data and Preprocessing (NC programming).

Figure 3 explains the relations between the category and target CNC systems. The horizontal axis indicates three possible types of CNC systems. Also it indicate the processing speed that required in PC system. In case of PC +proprietary NC type, processing speed in the PC does not required so much. On the contrary, fully software based CNC may be requested high data processing rate. The vertical column explains classified API category that will apply to the all kind of CNC systems. PAPI ver.1 covers major CNC system APIs, and some of CNC application and CNC device control APIs are also supported . Remained area are provided for the future extension.

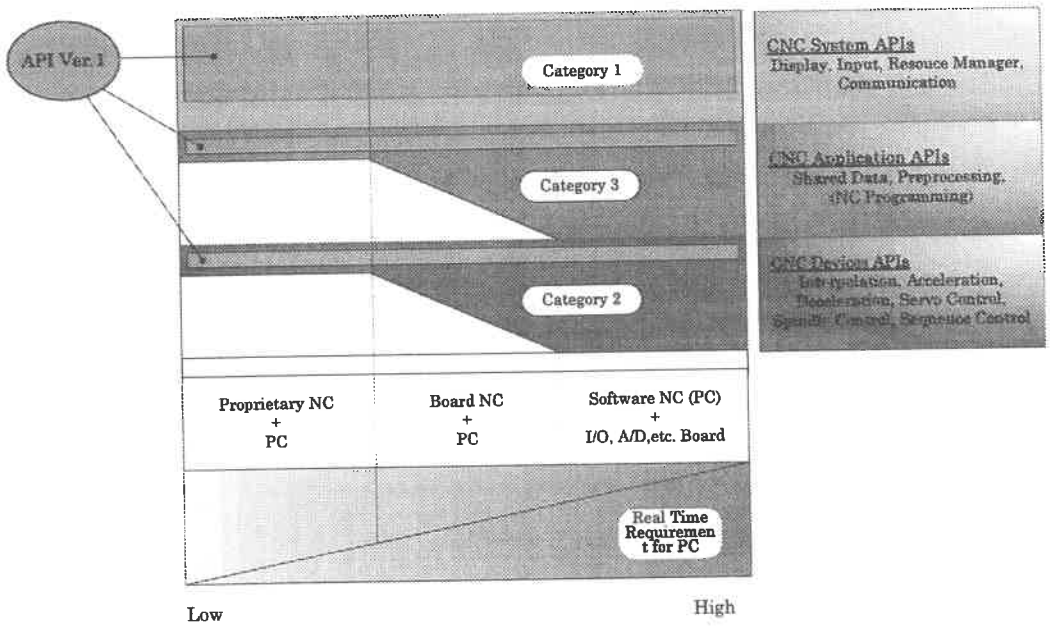

Figure 3. Category of CNC system and APIs

PAPI is consisted from two types APIs. The first is called "Basic API" and second is calle "Extended API". The "basic API" is defined to be mainly the set of functions that provid functions for monitoring the state of what is to be controlled and for managing the prograı parameters. .And "extended API" is defined to be mainly the set of functions that provid functions for operating what is to be controlled such as "start", "stop" and "operation mod change". Numbers of provided functions are 95, for the Basic; 49, and for the Extended;46.

Demonstration of developed API: To check its performance, the developed API has implemented into two existing different kind of CNC systems that are manufactured by MITSUBISHI Electronic Corp., and FANUC LTD., Basic control HMI has developed by Tokyo University Mitsuishi Lab. students. All system has installed in Windows NT system. Figure 4 shows the total configurations demonstrated at Mechatro-tech Japan in Nagoya, Oct.13-16, 1999. The aims of demonstration were to show that PAPI is actually implementable in commercial NCs, to show how PAPI is effective to realize a custom HMI, and to show that PAPI is also useful for the communication with upper level controllers. The demonstration results were quite successful, that connected two NC system could operate by the same HMI, and also could communicate with higher level controller that provides production-scheduling software. This result indicate that developed PAPI has a good ability and affinities with existing CNCs.

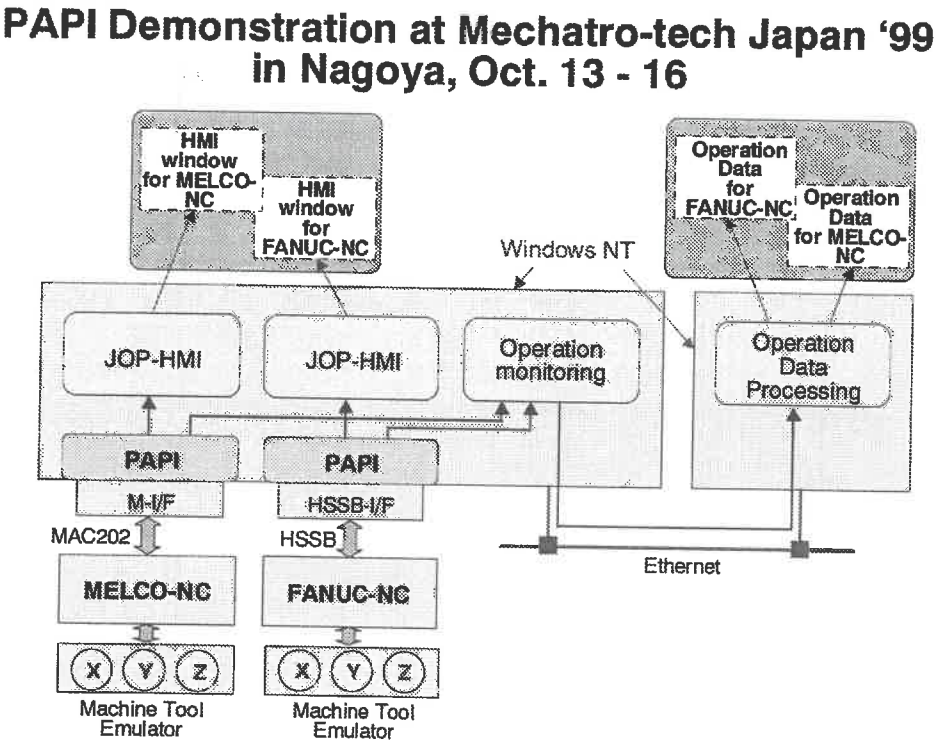

Figure 4. Demonstration Configuration in Mechatro-tech Japan 99

Reference

1)Requirements of Open, Modular Architecture Controllers for Applications in the Automotive Industry, Version 1.1,(1994),Chrysler, Ford, GM

2) Open Architecture Controls for Precision Machine Tools, Bradley N. Damazo et al, Proceedings of ASPE Spring Topical Meeting on Mechanisms and Controls for Ultra precision Motion, April 6-8, 1994, Tucson, AZ, pp.26-31.

The Control of Six Degree-of-Freedom Magnetically Suspended Stage

Chunhai Wang
Center for Precision Metrology, University of North Carolina at Charlotte

Abstract: This paper describes the controller design for a magnetically suspended stage with six degrees-of-freedom. The stage employs a single platen as the moving part with a large travel volume of 25mm × 25mm × 0.1mm. We will present the modeling of the platen taking into account motion couplings between the different movements, and a controller design that decouples the six-input six-output control into six separate single-input single-output controls. Results showing 0.3nm stepping performance are given.

1. Introduction

Fine motion stages are widely used in scanning probe microscopes. Magnetically suspended stages used for this purpose are a development of recent years[1-4]. They can possess the advantage of both long travel and high resolution. M. Holmes has developed a prototype of such a stage [5,6]. This paper addresses control related problems on the stage. It begins with an introduction of the stage, then the modeling and controller design for the stage. Finally a 0.3 nm step is shown.

2. The magnetically suspended stage

Figure 1 shows the magnetically suspended stage with some parts moved aside and some eliminated to show the key inside structure. The stage is composed of four linear motors, a floating platen and a metrology target and sensors etc. Dow Corning 200 fluid with viscosity of 10,000 cs is filled between the platen and the frame. The platen is designed to neutrally float in the fluid. Four linear motors provide the necessary force to suspend and servo the platen, which has a travel volume of 25mm×25mm×0.1mm. The metrology target is attached on the top of the platen and extends out of the fluid. Its positions are monitored by the three interferometers and three capacitive gauges. The stage is mounted on an air isolated optical table. The whole system is placed in a temperature controlled metrology lab.

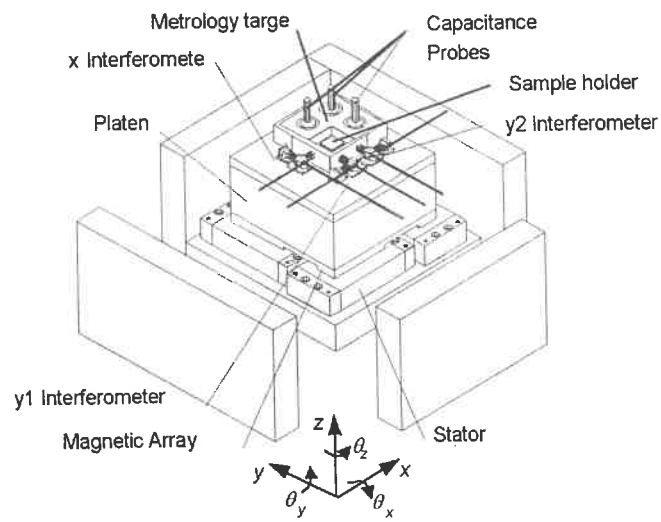

Figure 1 Magnetically suspended stage with the front frames moved aside, sensor mounts eliminated

3. Modeling

Fine motion control depends on accurate modeling. The stage has only one moving part – the platen as shown in figure 1. All movements in x, y, z, θ_x, θ_y and θ_z are realized by servoing the platen. The platen can be modeled as

$$\begin{bmatrix} x(s) \\ y(s) \\ z(s) \\ \theta_x(s) \\ \theta_y(s) \\ \theta_z(s) \end{bmatrix} = \begin{bmatrix} H_x(s) & 0 & 0 & 0 & H_{\theta_y x} & H_{\theta_z x} \\ 0 & H_y(s) & 0 & H_{\theta_x y} & 0 & H_{\theta_z y} \\ 0 & 0 & H_z(s) & H_{\theta_x z} & H_{\theta_y z} & 0 \\ 0 & 0 & 0 & H_{\theta_x}(s) & 0 & 0 \\ 0 & 0 & 0 & 0 & H_{\theta_y}(s) & 0 \\ 0 & 0 & 0 & 0 & 0 & H_{\theta_z}(s) \end{bmatrix} \begin{bmatrix} F_x(s) \\ F_y(s) \\ F_z(s) \\ T_{\theta_x}(s) \\ T_{\theta_y}(s) \\ T_{\theta_z}(s) \end{bmatrix} \quad (1$$

where s is Laplace transformation factor, $x(s)$, $y(s)$, $z(s)$, $\theta_x(s)$, $\theta_y(s)$ and $\theta_z(s)$ are the positions of the platen in x, y, z θ_x, θ_y and θ_z axes respectively, $F_x(s)$, $F_y(s)$, $F_z(s)$, $T_{\theta x}(s)$, $T_{\theta y}(s)$ and $T_{\theta z}(s)$ are the forces or torques applied to the platen in x, y, z, θ_x, θ_y and θ_z axes respectively, $H_i(s)$ (i= x, y, z, θ_x, θ_y and θ_z) are the transfer functions of the platen in each separate degree-of-freedom respectively, and $H_{ij}(s)$ (i= θ_x, θ_y, θ_z and j=x, y, z) are the coupling transfer

functions from the torques that are applied for angular movements to linear motions. Motion couplings occur when the rotary axes do not pass the point where the test sample is located. In this stage, the linear motors are placed at the bottom of the platen while the test sample is located at one corner of the metrology target (see figure 1). None of the rotary axes passes the sample. Whenever there is an torque applied to the platen, there will be an accompanied motion in x, y or z, as well as the desired angular motion.

4. Digital controller design

The stage is a typical multi-input multi-output system. However, to avoid making the controller very complex, it is preferable to decouple the six-input six-output stage to six single-input single-output controls. Please note that the coupling motions occur only from angular to linear ones, but not visa versa. Therefore angular controllers can be designed independently. Once they are determined their coupling motions to linear ones are also definite or predictable. Then the linear motion controller can be designed to take into account the couplings from the angular controls. Digital controllers employing state design are used here[7]. For the convenience of mathematic calculation, it is assumed that angular controllers use angular position and velocity as their describing states while linear controllers use linear position and velocity as their states.

(1) θ_z controller

The model of the platen in θ_z can be described in state space as

$$\boldsymbol{\theta}_z(k+1) = \boldsymbol{\Phi}_{\theta_z}\boldsymbol{\theta}_z(k) + \boldsymbol{\Gamma}_{\theta_z}T_{\theta_z}(k) \tag{2}$$

$$\theta_z(k) = \mathbf{H}\boldsymbol{\theta}_z(k) \tag{3}$$

where $\boldsymbol{\theta}_z = \begin{bmatrix}\theta_z & \dot{\theta}_z\end{bmatrix}^T$, $\mathbf{H} = [1 \;\; 0]$, $\boldsymbol{\Phi}_{\theta_z}$ and $\boldsymbol{\Gamma}_{\theta_z}$ are the matrices representing the platen transfer function in the discrete domain, and they are equivalent to the transfer function $H_{\theta_z}(s)$, k is the sequence number of control cycles, T_{θ_z} is the servoing torque applied for θ_z motion. The control diagram for θ_z is shown in figure 2. To eliminate the residual error between the input and output, an integrator $\theta_{zI}(k)$ is necessary, which is

$$\theta_{zI}(k+1) = \theta_{zI}(k) + \theta_z(k) - \theta_{zd}(k) = \theta_{zI}(k) + \mathbf{H}\boldsymbol{\theta}_z(k) - \theta_{zd}(k) \tag{4}$$

where θ_{zd} is the desired position and θ_z is the actual position. Augmenting the integrator, model (2) becomes

$$\begin{bmatrix}\theta_{zI}(k+1)\\ \boldsymbol{\theta}_z(k+1)\end{bmatrix} = \begin{bmatrix}1 & \mathbf{H}\\ 0 & \boldsymbol{\Phi}_{\theta_z}\end{bmatrix}\begin{bmatrix}\theta_{zI}(k)\\ \boldsymbol{\theta}_z(k)\end{bmatrix} + \begin{bmatrix}0\\ \boldsymbol{\Gamma}_{\theta_z}\end{bmatrix}T_{\theta_z}(k) - \begin{bmatrix}1\\ 0\end{bmatrix}\theta_{zd}(k) \tag{5}$$

The control law, following equation (5), is

$$T_{\theta_z}(k) = -\begin{bmatrix}K_{\theta_z I} & \mathbf{K}_{\theta_z}\end{bmatrix}\begin{bmatrix}\theta_{zI}(k)\\ \boldsymbol{\theta}_z(k)\end{bmatrix} + \mathbf{K}_{\theta_z}\mathbf{N}\theta_{zd}(k) \tag{6}$$

where $[K_{\theta_z I} \;\; \mathbf{K}_{\theta_z}]$ is the gain matrix, which can be determined using the *Matlab* function *acker* based on the coefficient matrix in equation (5), $\mathbf{N}$ is a matrix to convert the input θ_{zd} to a reference state, $\mathbf{N}=[1,0]^T$. The estimator is to give angular velocity information that is not measured directly by the interferometers and capacitive gauges.

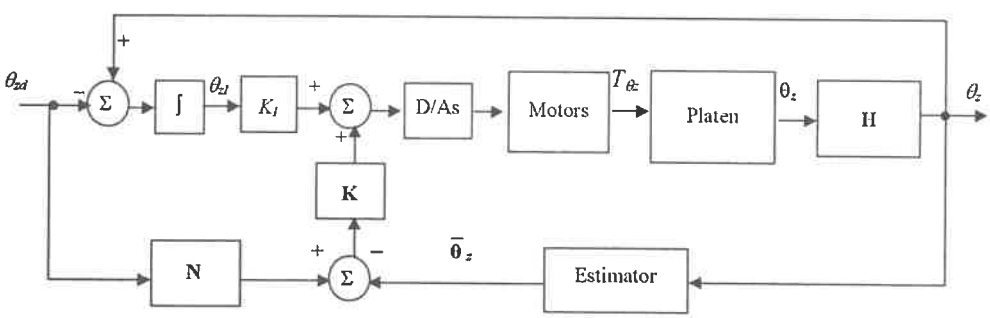

Figure 2 Control diagram for θ_z

(2) θ_y controller

Similar to that of θ_z, the model of θ_y can be described as

$$\boldsymbol{\theta}_y(k+1) = \boldsymbol{\Phi}_{\theta_y}\boldsymbol{\theta}_y(k) + \boldsymbol{\Gamma}_{\theta_y}T_{\theta_y}(k) \tag{7}$$

$$\theta_y(k) = \mathbf{H}\boldsymbol{\theta}_y(k) \tag{8}$$

where $\mathbf{\Phi}_{\theta_y}$ and $\mathbf{\Gamma}_{\theta_y}$ are the matrix coefficients equavalent to the transfer function $H_{\theta_y}(s)$, T_{θ_y} is the torque applied for θ_y motion. Augmenting a similar integrator θ_{yI} to model (7) results

$$\begin{bmatrix} \theta_{yI}(k+1) \\ \boldsymbol{\theta}_y(k+1) \end{bmatrix} = \begin{bmatrix} 1 & \mathbf{H} \\ 0 & \mathbf{\Phi}_{\theta_y} \end{bmatrix} \begin{bmatrix} \theta_{yI}(k) \\ \boldsymbol{\theta}_y(k) \end{bmatrix} + \begin{bmatrix} 0 \\ \mathbf{\Gamma}_{\theta_y} \end{bmatrix} T_{\theta_y}(k) - \begin{bmatrix} 1 \\ \mathbf{0} \end{bmatrix} \theta_{yd}(k) \tag{9}$$

where θ_{yd} is the desired angular position. The control law, following equation (9), is

$$T_{\theta_y}(k) = -\begin{bmatrix} K_{\theta_y I} & \mathbf{K}_{\theta_y} \end{bmatrix} \begin{bmatrix} \theta_{yI}(k) \\ \boldsymbol{\theta}_y(k) \end{bmatrix} + \mathbf{K}_{\theta_y} \mathbf{N} \theta_{yd}(k) \tag{10}$$

where $[K_{\theta_y I} \quad \mathbf{K}_{\theta_y}]$ is the gain matrix, which can also be determined using the *Matlab* function *acker* based on the coefficient matrix in equation (9), **N** is the matrix to convert input θ_{yd} to a reference state, $\mathbf{N}=[1,0]^T$.

(3) x controller

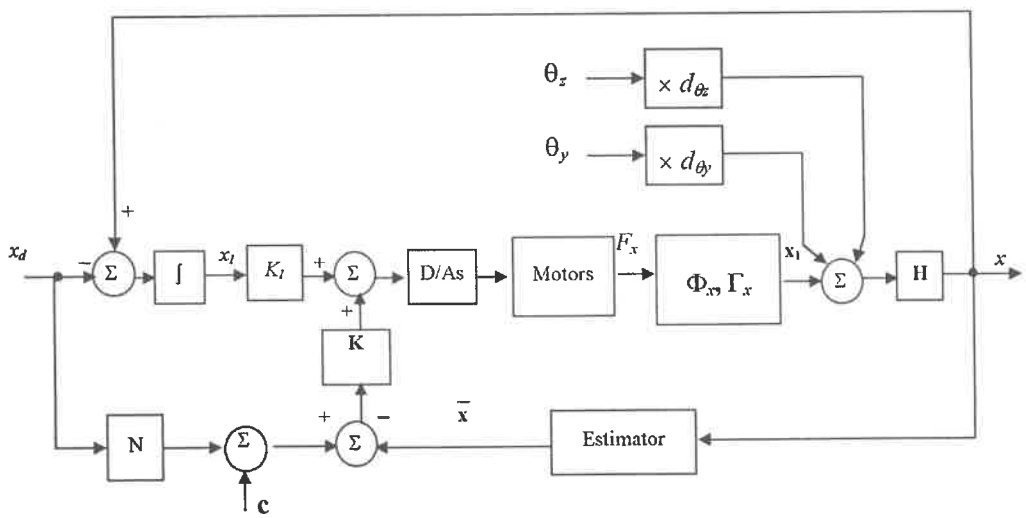

Figure 3 the x control

As far as the pure linear motion in x is considered, it has a similar model to that of angular motion, as

$$\mathbf{x}_1(k+1) = \mathbf{\Phi}_x \mathbf{x}_1(k) + \mathbf{\Gamma}_x F_x(k) \tag{11}$$

where $\mathbf{\Phi}_x$ and Γ_x are the matrix representing transfer function $H_x(s)$ in state space. However the motion coupling from θ_y and θ_z to x must be considered for fine control. In this case the x controller can be modified as shown in figure 3. The new x motion model becomes

$$\mathbf{x}(k+1) = \mathbf{x}_1(k+1) + \boldsymbol{\theta}_y(k+1) d_{\theta_y} + \boldsymbol{\theta}_z(k+1) d_{\theta_z} \tag{12}$$

$$x(k) = \mathbf{H}\mathbf{x}(k) \tag{13}$$

where d_{θ_y} and d_{θ_z} are respective distances that couple angular motions in θ_y and θ_z into linear motion in x.

Combining equations (2), (7), (11) and (12) results in

$$\mathbf{x}(k+1) = \mathbf{\Phi}_x \mathbf{x}_1(k) + \mathbf{\Gamma}_x F_x(k) + \mathbf{\Phi}_{\theta_y} \boldsymbol{\theta}_y(k) d_{\theta_y} + \mathbf{\Gamma}_{\theta_y} T_{\theta_y}(k) d_{\theta_y} + \mathbf{\Phi}_{\theta_z} \boldsymbol{\theta}_z(k) d_{\theta_y} + \mathbf{\Gamma}_{\theta_z} T_{\theta_z}(k) d_{\theta_z} \tag{14}$$

Since $\mathbf{x}_1(k) = \mathbf{x}(k) - \boldsymbol{\theta}_y(k) d_{\theta_y} - \boldsymbol{\theta}_z(k) d_{\theta_z}$, equation (14) can be rewriten as

$$\mathbf{x}(k+1) = \mathbf{\Phi}_x \mathbf{x}(k) + \mathbf{\Gamma}_x F_x(k) + \mathbf{c}_x(k) \tag{15}$$

where $\mathbf{c}_x(k) = (\mathbf{\Phi}_{\theta_y} - \mathbf{\Phi}_x)\boldsymbol{\theta}_y(k) d_{\theta_y} + \mathbf{\Gamma}_{\theta_y} T_{\theta_y}(k) d_{\theta_y} + (\mathbf{\Phi}_{\theta_z} - \mathbf{\Phi}_x)\boldsymbol{\theta}_z(k) d_{\theta_z} + \mathbf{\Gamma}_{\theta_z} T_{\theta_z}(k) d_{\theta_z}$. $\mathbf{c}(k)$ is the motion coupling from $\theta_y(k)$ and $\theta_z(k)$ to $\mathbf{x}(k+1)$. To eliminate the residual error between the actual position x and desired position x_d, an integrator is also included

$$x_I(k+1) = x_I(k) + x(k) - x_d(k) = x_I(k) + \mathbf{H}\mathbf{x}(k) - x_d(k) \tag{16}$$

and arriving at the augmented model

$$\begin{bmatrix} x_I(k+1) \\ \mathbf{x}(k+1) \end{bmatrix} = \begin{bmatrix} 1 & \mathbf{H} \\ 0 & \mathbf{\Phi}_x \end{bmatrix} \begin{bmatrix} x_I(k) \\ \mathbf{x}(k) \end{bmatrix} + \begin{bmatrix} 0 \\ \mathbf{\Gamma}_x \end{bmatrix} F_x(k) + \begin{bmatrix} -x_d(k) \\ \mathbf{c} \end{bmatrix} \tag{17}$$

from which the corresponding control law is obtained

$$F_x(k) = K_I x_I - \mathbf{K}\mathbf{x}(k) + \mathbf{K}(\mathbf{N}x_d - \mathbf{c}) \tag{18}$$

(4) θ_x, y and z control

θ_x controller has a similar mathematical form as the θ_y and θ_z controllers except some variables are replaced with their θ_x counterparts. The y and z controllers have similar forms as x except the corresponding variables are replaced with their counterparts.

5. Step response

With the new model and controller, stable motions and positioning are observed. Figure 4 shows the 0.3nm step response of the stage.

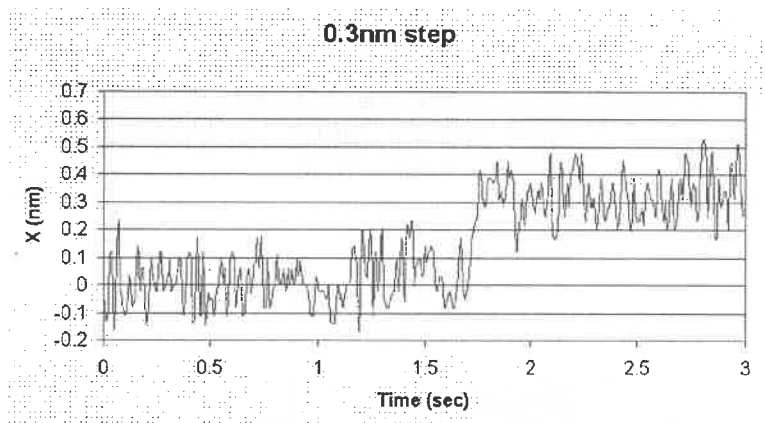

Figure 4 0.3 nm step

6. Conclusion

The modeling and control of the platen is investigated with consideration of the motion couplings. The couplings occur from angular motions to linear motions, but not in reverse direction. This phenomenon forms the basis for decoupling the six-input six-output platen control system into six separate single-input single-output controls. The angular controllers are designed independently, and the linear controllers are designed taking into account the couplings from angular motions.

Acknowledgments

The research is funded by the National Science Foundation under the grant No. 2975990126, and carried out in the Center for Precision Metrology (an NSF I/UCRC), University of North Carolina at Charlotte.

References

[1] Holmes M., "Analysis and Design of Magnetically-Suspended Precision Motion Control Stage", Master's Thesis, Department of Electrical Engineering, UNCC Charlotte, NC, 1994

[2] Holmes M., Trumper D., Hocken R., "Atomic-scale precision motion stage (the angstrom stage)", *Annals of The CIRP*, Vol. 44, pp. 455-460, 1995

[3] Ludwick S., Trumper D. and Holmes M., "Modeling and Control of a Six Degree-of-Freedom Magnetic/Fluidic Motion Control Stage", *IEEE Transactions on Control System Technology*, Vol. 4, No. 5, 1996.

[4] W. Kim, D. Trumper and J. Bryan, "linear motor-levitated stage for photolithography", *Annals of the CIRP*, vol. 46, pp. 447-450, 1997

[5] M.L. Holmes, "Analysis and Design of a Long Range Scanning Stage", PhD's Thesis, Department of Electrical Engineering, UNCC Charlotte, NC, 1998

[6] Holmes M., Hocken R., Trumper D., "The long-range scanning stages- a novel platform for scanned-probe microscopy" *Precision Engineering*, Vol. 24 , No. 3, 2000

[7]G.F. Franklin, J.D. Powell, M. Workman, "Digital Control of Dynamic Systems", third edition, Addison-Wesley, 1998

Real Time Estimation of Temperature Distribution in a Ball Screw System Using Observer and Adaptive Algorithm

Joong-Yong Ahn, Tae-Hoon Kim and Sung-Chong Chung

MAnufacturing Systems & Control LABoratory
Department of Mechanical Design & Production Engineering
Hanyang University, SungdongGu, Seoul 133-791, KOREA

Abstract : So far empirical models have been mainly studied for real-time application of thermal error compensation scheme in machine tools. However, the empirical models are somewhat unreliable because they cannot estimate correctly for the untested conditions. This paper describes a new approach to estimate the unknown heat inputs and temperature distribution in real time based on an analytical model. A 1-dimensional heat transfer problem is modeled with state space equations. And then observer is designed to estimate the intensity of heat source and the whole temperature field in real time using frequency domain approach and low pass filter. Thermal process is time-variant because parameters in thermal process are the function of temperature. So, a recursive parameter identification of adaptive algorithm is used to enhance the estimation accuracy of temperature distribution as well as heat inputs. To verify the reliability of the proposed real-time estimator, heat inputs and temperatures are estimated by observer and with measurements from two points of a ball screw system in case of the presence of measurement noise.

Keywords : Adaptive Algorithm, Ball Screw System, Inverse Heat Conduction Problem(IHCP), Mode Reduction, Observer, Recursive Parameter Estimation, State Space Equation

1. Introduction

Thermal error is the most important factor that affects the accuracy of precision machine tools since thermal error comprises 40-70% of the workpiece error in precision machining[1]. Attention is paid to software error compensation with the increase of computer capability[2]. The accuracy is determined by the estimation accuracy of thermal error model. Some empirical models are used to relate temperature measurements to thermal deformation[3]. But it is a tedious task to obtain empirical error models and these models are not accurate enough, and are unreliable for untested inputs. As for numerical solutions, FEM and FDM methods are not appropriate to the real time compensation since they consume much computation time[4]. The previous research using IHCP is studied under assumption that confined to case that the reference model is known precisely[5].

In this paper, the temperature distribution of ball screw system is estimated with a few number of temperature measurements. First, thermal process is modeled as state space equations using modal analysis and mode reduction for a 1-dimensional heat transfer problem. For a real time estimation of heat inputs and temperatures, observer is designed using the concept of low pass filter. A recursive parameter identification is used to enhance the estimation accuracy for various thermal conditions. The application results to a ball screw show that the proposed method gives the solution to the real-time estimation of temperature distribution.

2. Modeling of heat transfer

2.1 Modal analysis

The governing equation and boundary conditions of 1-dimensional unsteady state heat conduction problem are given in general form by

$$L_{cond}[T(x,t)] + M\frac{\partial T(x,t)}{\partial t} = Q(x,t) \qquad \text{(1-a)}$$

$$B_L[T(x,t)]_{x=0} = l(t), \quad B_R[T(x,t)]_{x=L} = r(t) \qquad \text{(1-b)}$$

To change Eq. (1-b) into a homogeneous boundary condition, the solution of Eq. (1-a) is assumed as

$$T(x,t) = \Theta(x,t) + g(x)l(t) + h(x)r(t) \qquad (2)$$

where, $g(x)$ and $h(x)$ are polynomials which make homogeneous boundary condition about $\Theta(x,t)$.

From Eq. (1) and (2), a nonhomogeneous differential equation is given by Eq. (3). If the solution of Eq. (3) is assumed as $\Theta(x,t) = \theta(x)\eta(t)$, an eigenvalue problem is acquired as Eq. (4)

$$\begin{aligned} L_{cond}[\Theta(x,t)] + M\frac{\partial \Theta(x,t)}{\partial t} \\ = Q(x,t) - \{l(t)L[g(x)] + \dot{l}(t)Mg(x)\} \\ - \{r(t)L[h(x)] + \dot{r}(t)Mh(x)\} \end{aligned} \qquad (3)$$

$$L_{cond}[\theta(x)] - \Lambda M\theta(x) = 0 \qquad \text{(4-a)}$$

$$B_L[\theta(x)]_{x=0}=0,\quad B_R[\theta(x)]_{x=L}=0 \tag{4-b}$$

The solution of Eq. (4) yields an infinite set of eigenvalues λ_n and corresponding eigenfunctions $\theta_n(x)$. When it is assumed that the solution of Eq. (3) is given by Eq. (5) based on expansion theorem, uncoupled ordinary differential equation set is acquired as Eq. (6).

$$\Theta(x,t)=\sum_{n=1}^{\infty}\theta_n(x)\eta_n(t) \tag{5}$$

$$\dot{\eta}_n(t)+\Lambda_n\eta_n(t)=N_n(t),\quad n=1,2,\cdots \tag{6}$$

where, $N_n(t)$ is generalized heat input.

For the heat convection problems, the same procedure is applied to eigenvalues, eigenfunctions and uncoupled ordinary differential equation set.

2.2 State space equation by mode reduction

In Eq. (6), the mode reduction is required because it is inefficient and impossible to formulate the state space equation with infinite modes. A criterion is established to aid in the elimination of modes to be used in the solution. Firstly, s_N can be defined in the following way

$$s_N^2=\sum_{i=1}^{N}\left(\frac{\theta_i(a_H)}{\Lambda_i}\right)^2 \tag{7}$$

where N is the number of modes used in the approximation. N increases until Eq. (8) becomes violated.

$$\frac{s_N}{s_{N+1}}\geq\beta,\quad 0<\beta<1 \tag{8}$$

where, β is the proportion of s_N and s_{N+1}, which define relative accuracy of results. After N is determined, the state space equation [Eq. (9)] is composed with a finite number of selected modes. If the sensor location is $b_T(0\leq b_T\leq L)$, output $y(t)$ is given by Eq. (10)

$$\dot{\mathbf{x}}(t)=\mathbf{A}\mathbf{x}(t)+\mathbf{B}u(t)-\mathbf{D}\mathbf{z}(t) \tag{9}$$

$$y(t)=T(b_T,t)=\mathbf{C}\mathbf{x}(t)+\mathbf{E}\mathbf{z}(t) \tag{10}$$

where,

$$\mathbf{A}=\begin{bmatrix}\nwarrow & & \\ & -\Lambda & \\ & & \searrow\end{bmatrix}=\begin{bmatrix}-\Lambda_1 & & & \\ & -\Lambda_2 & & \\ & & \ddots & \\ & & & -\Lambda_N\end{bmatrix}$$

$$\mathbf{B}=[\theta_1(a_H)\ \theta_2(a_H)\ \cdots\ \theta_N(a_H)]^T$$

$$\mathbf{C}=[\theta_1(b_T)\ \theta_2(b_T)\ \cdots\ \theta_N(b_T)]$$

$$\mathbf{D}=\begin{bmatrix}\leftarrow\mathbf{D}_1\rightarrow\\ \leftarrow\mathbf{D}_2\rightarrow\\ \vdots\\ \leftarrow\mathbf{D}_N\rightarrow\end{bmatrix}=\begin{bmatrix}G_1^* & G_1 & H_1^* & H_1\\ G_2^* & G_2 & H_2^* & H_2\\ \vdots & \vdots & \vdots & \vdots\\ G_N^* & G_N & H_N^* & H_N\end{bmatrix}$$

$$\mathbf{E}=[g(b_T)\ 0\ h(b_T)\ 0]$$

$$\mathbf{x}(t)=\{\eta_1(t)\ \eta_2(t)\ \cdots\ \eta_N(t)\}^T,\quad u(t)=q(t)/k$$

$$\mathbf{z}(t)=[l(t)\ \dot{l}(t)\ r(t)\ \dot{r}(t)]^T$$

3. Observer design

In general, estimation of heat input is a focus in IHCP. The objective of this paper is to estimate the thermal deformation with the temperature field in real-time. The estimation of temperature distribution is important as well as the one of heat input.

The IHCP can be interpreted as a frequency-domain transfer system relating the estimated heat flux $\hat{U}$ to the true heat flux U and the measurement noise N,

$$\hat{U}(s)=G_U(s)U(s)+G_N(s)N(s) \tag{11}$$

To derive the relationship between G_U and G_N, consider the structure of the IHCP as depicted in the block diagram of Fig. 1. Measurement signal Y^* is given as

$$Y^*=Y+N=G_HY+N \tag{12}$$

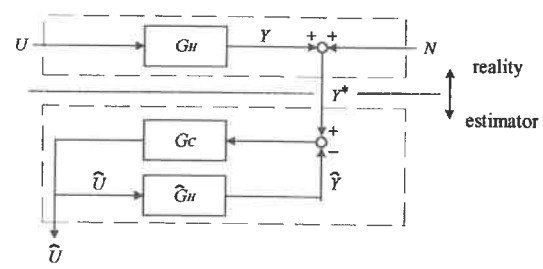

Fig. 1 Block diagram of IHCP solution

A reference model $\hat{G}_H$ was assumed to be time-invariant and known precisely in the previous research[5]. However, Thermal process is time-variant in reality because parameters in thermal process ,e.g., heat convection coefficient, thermal diffusivity coefficient, are the function of temperature. So, $\hat{G}_H$ is estimated recursively and G_C is updated by adaptive algorithm in this paper. The closed-loop transfer function of the feedback loop implemented in the estimator,

$$\hat{U} = \frac{G_C}{1+G_C\hat{G}_H} Y^* \tag{13}$$

characterizes the behavior of the solution algorithm. G_U and G_N are found by combining Eqs. (14) and (15). Finally, $\hat{U}$ is given as Eq. (16)

$$G_U = \frac{G_C\hat{G}_H}{1+G_C\hat{G}_H} \qquad G_N = \frac{G_C}{1+G_C\hat{G}_H} \tag{14}$$

$$G_N = G_U\hat{G}_H^{-1} \tag{15}$$

$$\hat{U} = G_N(s)Y^*(s) \tag{16}$$

The amplification of measurement noise $|G_N|$ for a given passband of the signal transfer function G_U can be minimized by maximizing the roll-off of $|G_U|$[5]. Therefore, we formulate a transfer function G_U satisfying the desired filtering properties by Butterworth analog filter design. The adaptive algorithm is applied to the observer to estimate the time-variant thermal parameter as shown in Fig. 2. It is based on the error reduction of the estimated temperature at another point.

4. Application to ball screw

Using the proposed method, the temperature distribution of a ball screw system is estimated. The schematic diagram of an actual ball screw system is shown in Fig. 3. Table 1 shows the specification of the ball screw.

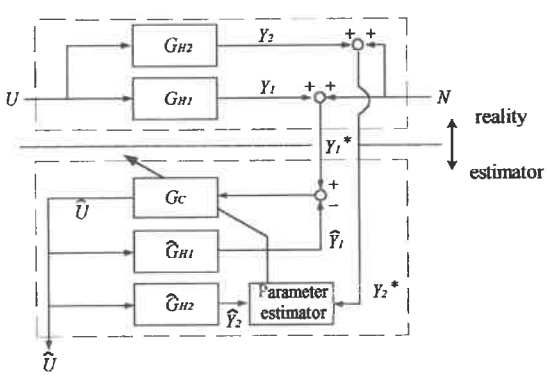

Fig. 2 Block diagram of proposed IHCP solution

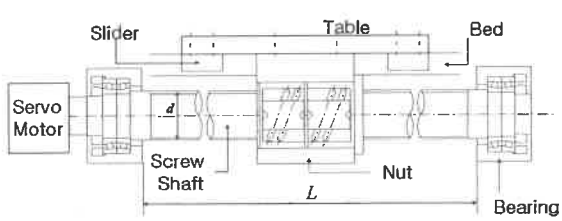

Fig. 3 Schematic diagram of a ball screw [6]

Table 1 Specification of ball screw [6]

Material	SCM415H
Diameter (d)	40×10^{-3} m
Screw length (L)	0.5 m
Heat capacity (C)	5700 J/℃
Thermal diffusivity (α)	1.67×10^{-5} m^2/s
Heat conductivity (k)	60.5 W/m℃

The nut traverses a specific zone and the shaft rotates at a constant speed. In this case, boundary conditions and heat inputs can be assumed as Fig. 4. It is assumed that the boundary condition at motor side is an insulation condition, and that the boundary condition at the opposite side of motor is a convection condition. The heat input generated by the nut is assumed as a distributed heat input at the specific zone and the heat inputs at the bearings are assumed as concentrated heat inputs. When the nut traverses between a_1 and a_2, the distributed heat input is given by Eq. (17) which is the modified equation of Otsuka's [6]. From the experiments by Kakino [7], it is shown that the heat inputs generated by friction at the bearings are proportional to the heat input intensity generated at the nut. Consequently, it can be assumed that the thermal behavior of the ball screw system is SISO system.

$$q_{nut}(t) = \frac{n\cdot\pi}{30}\cdot T_f(t)\cdot z\cdot\frac{a_2-a_1}{L} \tag{17}$$

where, n = rotation speed (rpm)
$T_f(t)$ = friction torque (Nm)
z = motion ratio

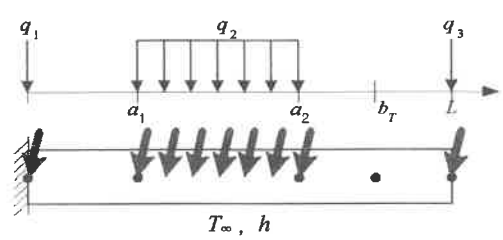

Fig. 4 Simulation model of ball screw

The operation conditions and parameters for simulation are acquired with reference to experiments by Otsuka et. al [6]. In this paper, convection coefficient is varying in time. For state space equation, 5 modes are selected when β is 0.999. Fig. 5 and Fig. 6 show the estimated heat input q_{nut} and temperatures without adaptive algorithm. Heat input is well estimated when convective coefficient is equal to the initial coefficient but not estimated well when thermal parameter of real plant is different from the one of the reference plant. Nonetheless, temperatures

are fairly estimated without adaptation algorithm except that the estimated temperature at $x = 0.25$ is not matched to the measurement when convective coefficient of real plant is different from the one of the reference plant.

Fig. 7 and Fig. 8 show the estimated heat input and temperatures by adaptive algorithm. Heat input is well estimated though convective coefficient is different from the one of reference plant. Tmperatures are well estimated by adaptation algorithm at $x = 0.25$ and $x = 0.43$ even when convective coefficient of real plant is not equal to the one of the reference plant.

5. Conclusion

In this paper, 1-dimensional heat transfer problems were modeled with the continuous state space equation through mode reduction technique. After deriving IHCP solution in a frequency-domain, the observer was designed with the Butterworth low pass filter. And then, adaptation algorithm was applied so as to estimate the time-variant parameter in actual thermal process. The temperature distribution of a ball screw was estimated with temperature measurements in case of the presence of noise. Although the heat input was not estimated well, the temperatures are estimated fairly with only fixed observer. When adaptation algorithm is applied to the observer, the heat input and the temperatures are estimated precisely regardless of time-variant thermal parameters.

References

1. J. Bryan, 1990, "International Status of Thermal Error Research", *Annals of the CIRP*, Vol.39, No.2, pp.645-656.
2. J. S. Chen and C. C. Ling, 1996, " Improving the Machine Accurary Through Machine Tool Metrology and Error Correction", *The Int. Jr. of Adavanced Manufacturing Technology*, Vol.11, pp.198-205.
3. T. Moriwaki and C. Zhao, 1992, "Prediction of Thermal Deformation of Machining Center by Applying Neural Network", *JSME(C)*, Vol.58, No.550, pp.1932-1937.
4. S. C. Chung and J. K. Park, 1992, "Thermal Expansion Analysis of the Ball Screw System by Finite Difference Methods", *KSPE*, Vol.9, No.4, pp.44-57.
5. J. Blum and W. Marquardt, 1997, "An Optimal Solution to Inverse Heat Conduction Problems Based on Frequency-Domain Interpretation and Observers", *Numerical Heat Transfer*, Vol.32, pp.453-478.
6. J. Otsuka, S. Fukada and N. Obuchi, 1984, "A Study of Thermal Expansion of Ball Screw -In case of Constant Preload-", *Precision Machine*, Vol.50, No.4, pp.646-651.
7. Y. Kakino, K. Mori, 1988, "A Study of Compensation of Thermal Displacement of the Ball Screw in NC Machine Tools", JSPE, Vol.54, No.9, pp.1753-1758.

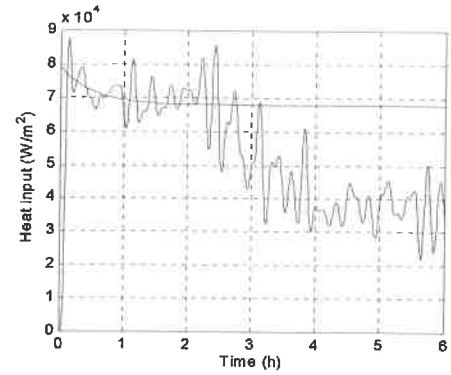

Fig. 5 Estimation of heat input by fixed observer

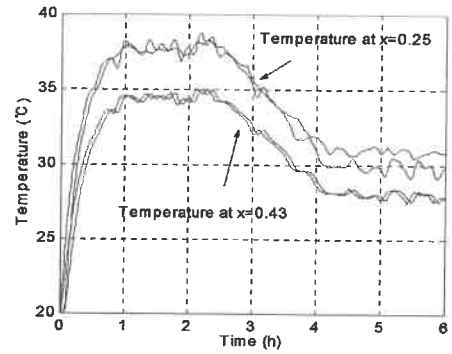

Fig. 6 Estimation of temperature by fixed observer

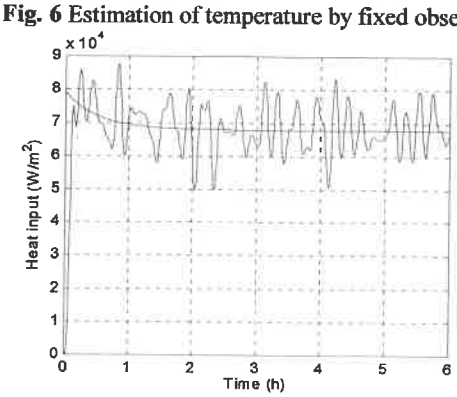

Fig. 7 Estimation of heat input with adaptation algorithm

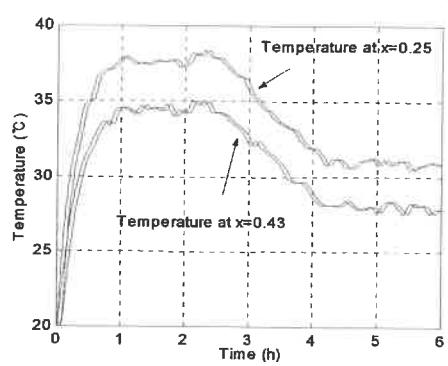

Fig. 8 Estimation of temperature with adaptation algorithm

Rapid Machine Design

Eberhard Bamberg[1], Alexander H. Slocum[2]
Massachusetts Institute of Technology, Cambridge MA

The methodology of rapid machine design attempts to shorten design-to-manufacture time of production equipment by using advanced engineering tools such as Computer Aided Design systems (CAD) and Finite Element Analysis (FEA) during the conceptual design phase. It is hypothesized that by identifying the best of all available design concepts, overall development time can be shortened. Further time savings result from building machine components out of fabricated structures instead of casts. This eliminates the need for making molds and other specialized tooling systems, and provides a high degree of flexibility in terms of changing the design and/or making modifications to design specifications.

Fabricated Structures

Traditionally, the base and other major components of a machine tool have been made of gray or nodular cast iron, which has the advantages of low cost and good damping, but the disadvantage of heavy weight. Casting is a net-shaping process whereby molten metal is poured into a mold, thereby assuming its shape upon solidification. In modern equipment design, lightweight structures are desirable because of ease of transportation, higher natural frequencies, and lower inertial forces of moving members [Kalpakjian]. Lightweight designs are a basic goal in rapid machine design and require fabrication processes such as mechanical fastening (bolts and nuts) of individual components and welding. A fabricated design consists of pre-cut stock materials such as plates, tubes, channels, and angles which are joined together to form the structure. Such stock items are available in a wide range of sizes and shapes and have some highly desirable mechanical properties such as formability, machinability and weldability. Of special interest are round and rectangular tubes whose closed cross sections have a very high stiffness-to-weight ratio.

In rapid machine design, fabrication is the preferred technique because of the following key advantages:

- Low fixed costs make it highly suitable for low to medium production volume.
- Fabrication can easily be done in-house, making the need for outsourcing obsolete.
- Use of highly standardized materials ensures high availability and competitive prices.
- Fabrication equipment is rather inexpenssive.
- Minimum tooling costs. Fabricated structures only need some form of fixturing which is universally applicable. No expensive molds are required.

1. Research Engineer, Department of Mechanical Engineering, MIT Room 3-470, Cambridge, MA 02139
2. Professor of Mechanical Engineering, MIT Room 4-445, 77 Mass Ave., Cambridge, MA 02139

- Minimum lead time. No proprietary tooling such as molds are required, shortening design-to-manufacture time.
- Great scalability. No re-tooling required when scaling the design to change available workvolume.
- High flexibility. Design changes are not impaired by existing tooling, making alterations inexpensive and easy to implement.
- Modular components can initially be fabricated separately and then joined whenever it is convenient.

However, fabricated structures have also a few disadvantages associated. These include:

- Comparably high variable costs prohibit large production volumes.
- Structures generally need stress-relief either through thermal or vibrational relaxation.
- All welds should be reasonably accessible, imposing sometimes hard to meet design constraints.
- Fabricated structures have much less damping compared to cast-iron based designs, requiring other forms of damping such as constrained layer damping.

Despite the shortcomings listed above, designing and building a machine as a fabricated structure has the big advantage of a much lighter design with a substantially shorter lead-time compared to a cast design. This is especially true for the case where the base is built from round tubes as opposed to flat plates, because round structures offer better strength-to-weight ratios and are more readily available.

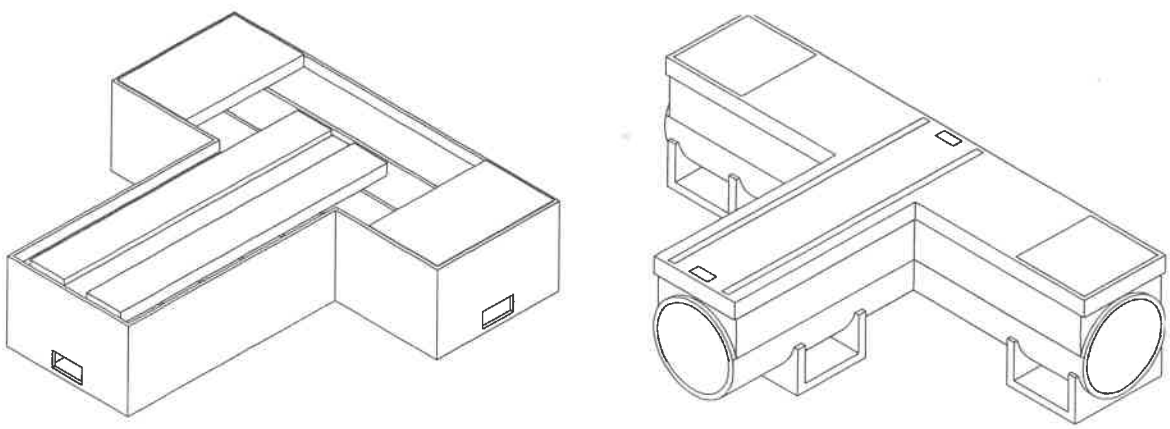

FIGURE 1. Conventional base built from plates vs. base built from round tubes

Constrained Layer Damping

Welded machine tool structures provide easy scalability in terms of size and outstanding flexibility in terms of fast design and fabrication; however, damping of the structure is a very critical issue. Unlike cast iron or polymer concrete-based components, welded steel plates have virtually no internal damping and are therefore prone to unwanted vibrations. Filling the structure with concrete or sand adds damping but also a great deal of unwanted weight. A better

approach is the use of constrained layer damping where a viscoelastic layer is squeezed between the structure and one or more constraining layers. Kinetic energy from relative motion between the structure and the constraining layer as it occurs during bending or twisting gets dissipated into heat by the viscoelastic layer. This mechanism introduces damping into the system, thereby limiting the structure's response to excitation frequencies near its modes. Unfortunately, existing shear layer damping designs tend to be costly to implement.

For machine structures, internal damping designs are most appropriate because they allow to maximize the structural cross sections, resulting in excellent strength-to-weight ratios. For tubular structures, constrained layer damping can be reasonably easy achieved with the ShearDamper™[1] design (Figure 2). Here, the constraining layers are created by cutting 8 slots starting from both ends of the tube until the cuts almost meet in the center of the tube. Next, a sheet of damping material (ISODAMP™ C-1002[2]) with adhesive on one side is wrapped around the split tube and the entire assembly inserted into the tubular machine structure. As the next step, the ends are sealed off with silicon and the gap between the damping layer and the outer structure is being filled with either epoxy or VibraDamp™[3], a lower-cost alternative to epoxy which is essentially epoxy resin heavily filled with inert material.

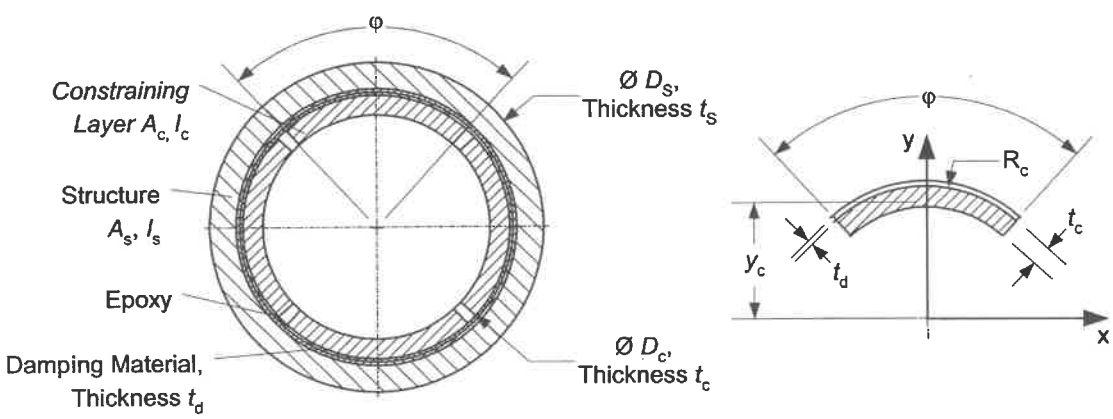

FIGURE 2. ShearDamper™ design parameters

While the ShearDamper design offers good performance, due to its complex design it also adds significantly to the cost of the structure. Next, alternative designs are presented with the following idea: replace the split tube with less expensive structural materials and possibly increase the damping performance even further. Concrete, for instance, is very inexpensive and has a respectable amount of damping built-in. This new design would make use of "sausage-like" damping sheet enclosures which are inserted into the structural tube. The bottom ends are closed off and the center of this assembly is supported by a thin-walled tube. Finally, the four sausages are evenly filled with concrete with an expanding agent added. The added grout agent, which contains aluminum powder, oxidizes during the curing of the concrete,

1. ShearDamper™ is registered trademark of AESOP Inc.
2. ISODAMP is a trademark licensed to AERO company
3. VibraDamp is a registered trademark of Philadelphia Resins

thereby producing little hydrogen bubbles. The gas causes the concrete to expand and counteracts its tendency to shrink during the curing. In fact, when dosed properly, the volume actually increases a bit, causing the damping material to be pressed against the inner diameter of the structural tube as well as against the outer diameter of the central supporting tube. The pressure exerted will be large enough to create enough friction to keep the damping sheet from sliding along those two surfaces. If this wasn't the case, damping performance would not be as good as anticipated. The inner support tube can either be a round or a square tube and, provided that its stiffness is properly tuned to that of the concrete constraining layer, can add a significant amount of extra damping. Once the concrete is cured, the ends are cut off and the concrete is sealed with a layer of coating that prevents moisture from entering the system.

The new constrained layer damping design offers significantly improved damping performance at only a fraction of the cost of a conventional system. The improvement can be seen in Figure 3. The sand- and concrete filled designs as well as the ShearDamper design exhibit vibration in excess of 8 ms, while the novel concrete designs have no measurable vibration after 3 and 2 ms, respectively.

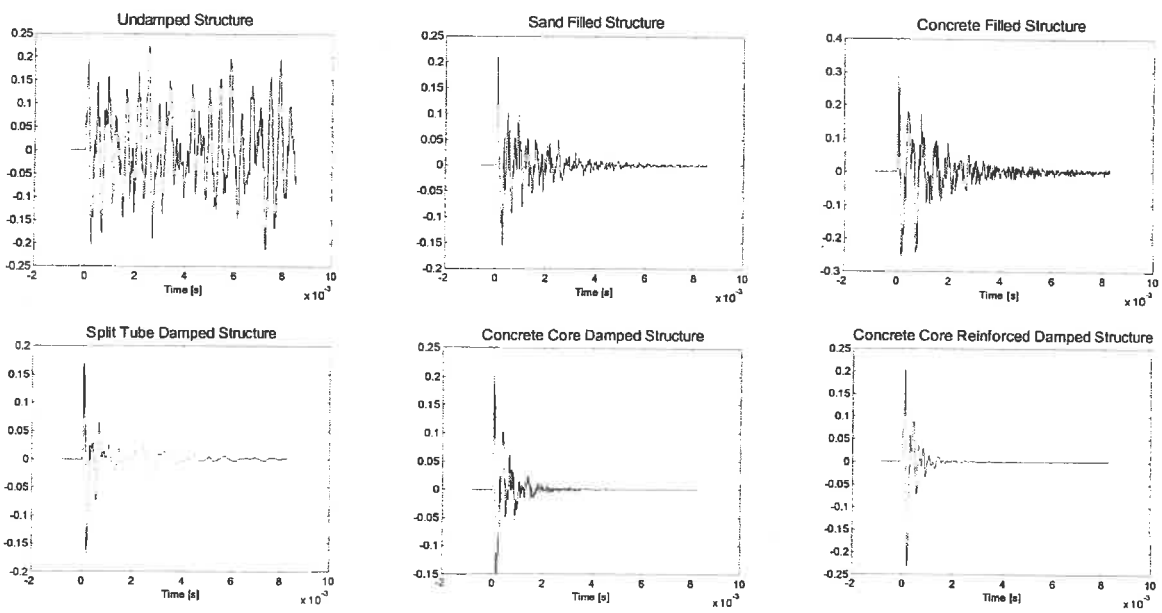

FIGURE 3. Time response for various damping designs

References

Kalpakjian, S., *Manufacturing Engineering and Technology*, Addison Wesley, p. 611, 1995.

Slocum, A.H., Marsh, E.R., Smith, D.H., New Daper Design for Machine Tool Structures: the Replicated Internal Viscous Damper, Precision Engineering Journal of the American Society for Precision Engineering, Vol. 16, July, pp. 174-183, 1994.

Marsh, E.R., Slocum, A.H., *Integrated Approach to Structural Damping*, Precision Engineering Journal of the American Society for Precision Engineering, Vol. 18, Apr-May, pp. 103-109, 1996.

A Correlation Analysis between Micro-Waviness of Magnetic Disk Surface and Electromagnetic Conversion Characteristics at the Head/Disk Interface

S. Hara, and T. Oosone
Nagaoka University of Technology
Nagaoka, Niigata, 940-2188 Japan

Introduction

In order to increase the information storage density of HDD, it is strongly required to reduce the flying height of the magnetic head. For its realization, the head slider has been advanced to smaller size, i.e. nano-slider or pico-slider. And then, magnetic disks are needed to be as flat as possible even in the short wavelength band. The head slider cannot fly over the disk following the irregularity of the surface if the wavelength of the irregularity is too short [1,2]. Such surface irregularity whose wavelength is shorter or comparable to the head slider length is called "Micro-Waviness".

Interferometry can be a useful tool to assess such surface waviness of magnetic disks and many optical interferometers are put on the market. "OptiFLAT"® by Phase Shift Technology Inc. is a representative white light interferometer, with which macroscopic surface profiles over the whole area of the disk may be measured and evaluated. Authors build an instrument to measure the circumferential surface profile of the disk and proved the measurement accuracy and suitability of obtained results of the white light interferometer. In addition authors investigated the correlation between the surface geometry (roughness, waviness and form) and fluctuation of the head/medium spacing

Circumferential profile measuring instrument

First of all in this study, a stylus instrument with extremely light load was developed to measure envelope curves along the circumferential tracks of disk surface (see Figure1 and Table 1). The instrument employs diamond stylus and high accuracy static air bearing rotated in very row revolution speed. It was estimated that the repeatability of the instrument is less than 0.5nm.

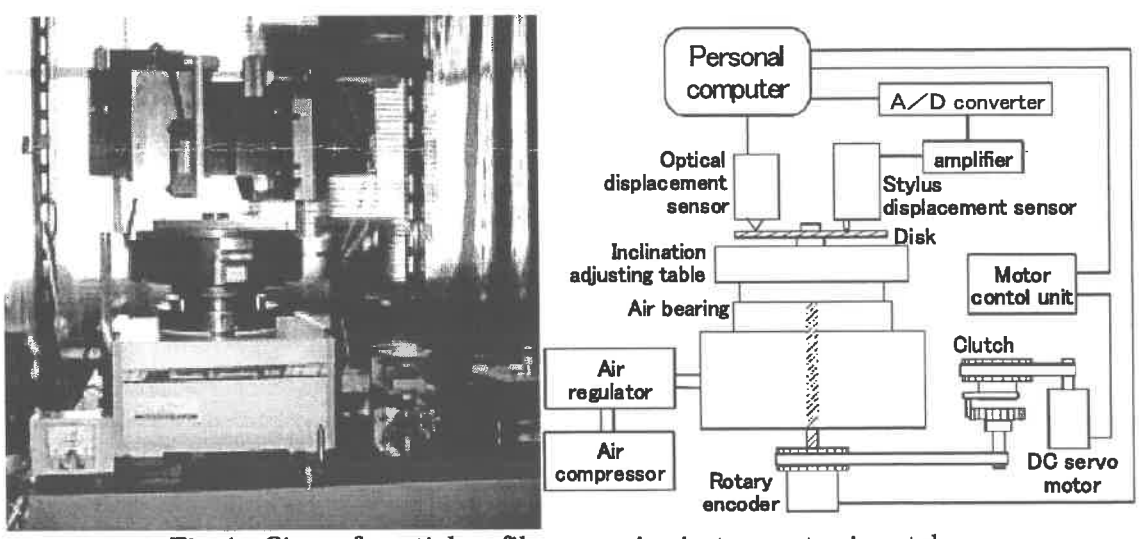

Fig. 1 Circumferential profile measuring instrument using stylus

Table 2 shows the prepared aluminum and glass sample disks. Considering the head slider size and its follow-up motion to disk surface, measuring length of 15mm was selected. Applying a 500μm low pass filter, a quite good agreement of the waviness parameter was obtained between the processed profiles with the developed instrument and the OptiFlat as shown on figure 2 and 3. One advantage of the developed instrument is that it has wider surface wavelength band than another because of shorter sampling spacing.

Table 1 Measuring conditions of the stylus instrument

Stylus tip radius	10 μm
Stylus load	0.2 mN
Vertical resolution	0.1 nm
Measuring speed	100 μm/s
Measuring length	15 mm
Sampling interval	2 μm

Table 2 Sample disks

	3.5 inch Aluminum disk	2.5 inch Glass disk
Surface finish	Mechanical texture	Polished
Ra (λc= 80 mm)	≈ 1 nm	≈ 0.2 nm
Wa (λc= 80 mm, λw= 5 mm)	0.4 ...1.5 nm	0.4 ...1.0 nm
Track for measurement	r= 30 mm	r= 20 mm
Number of samples	14	8

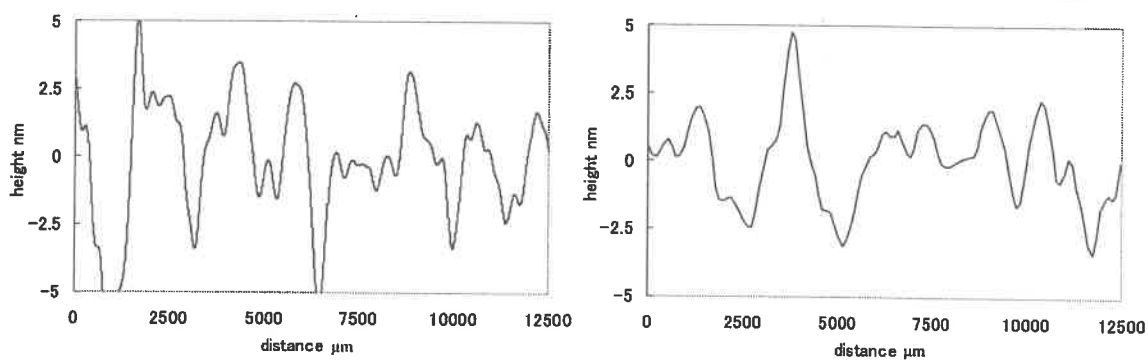

(a) Stylus (b) OptiFLAT

Fig. 2 Circumferential profiles obtained using stylus instrument and OptiFLAT

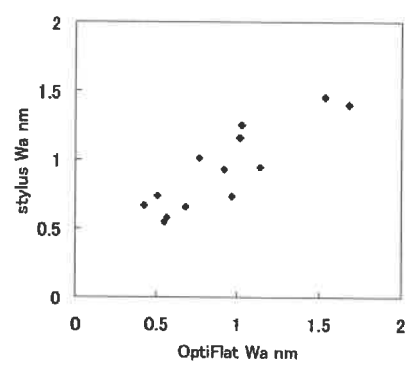

Fig. 3 Correlation between OptiFLAT *Wa* and Stylus *Wa*

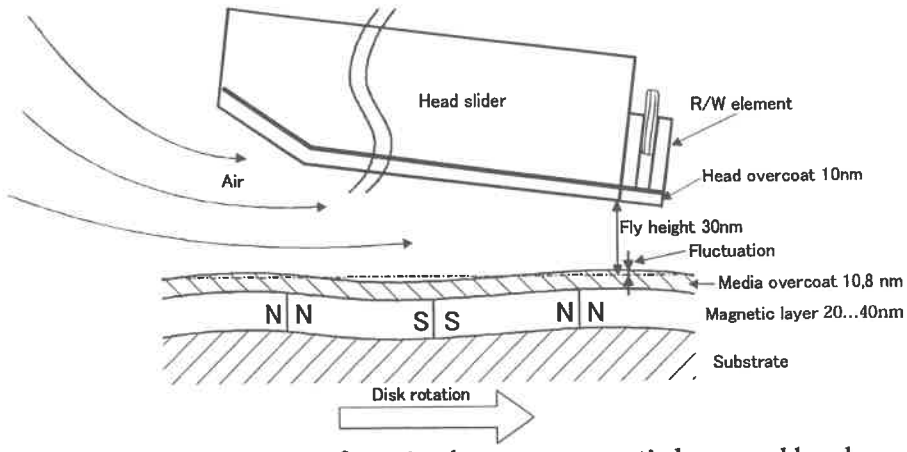

Fig. 4 Fluctuation of spacing between magnetic layer and head

Correlation of the Readout Signal to the surface micro-waviness

The amplitude modulation of the head readout signal is affected by the spacing between the head and the magnetic layer. The schematic of the head slider flotation is shown in figure 4. The relationship between the readout signal V and the spacing d is described as follows [3].

$$V = \frac{9\Delta\rho J W M_r \delta(g+t)}{8\sqrt{2}\, t\, g\, M_{mr}} \tan^{-1} \frac{g}{2(d+a)} \tag{1}$$

Where, g denotes shield gap spacing of the magnetic head, a denotes transition parameter of the magnetic layer, d denotes the head/medium spacing. Other parameters can be regarded to be constant when considering the fluctuation of the spacing. Putting actual values of the g and a, the relation ship can be rewritten as follows

$$\Delta d / d_0 \approx -2(\Delta v / v_0) \tag{2}$$

Where, Δd denotes fluctuation of the spacing, d_0: the mean spacing (50 nm), Δv: fluctuation of the readout signal, v_0: the mean readout signal (1.6 ... 2 V). Then, the fluctuation of the readout signal can be converted into the fluctuation of the spacing.

The readout signals of all the sample disks were measured using a disk tester. Conditions of the test were shown in table 3. Example of the result is shown in figure 5. Two curves, (a) and (b), have similar amplitude and waveform, even though the two curves were obtained in completely different principle.

The relationship between the amplitude of the profile and fluctuation of the spacing was investigated using the parameter *Wa*. Figure 6 shows the *Wa* values of 14 aluminum disks

Table 3 Conditions for measuring Read-Out-signal

	Al disk	Glass disk
Write freq.	10 MHz	
Speed	5400 rpm	
Head-slider	MR, Nano-slider	
Radius	30 mm	20 mm
Sampling	5 MHz (3.4 mm)	5 MHz (2.3 mm)

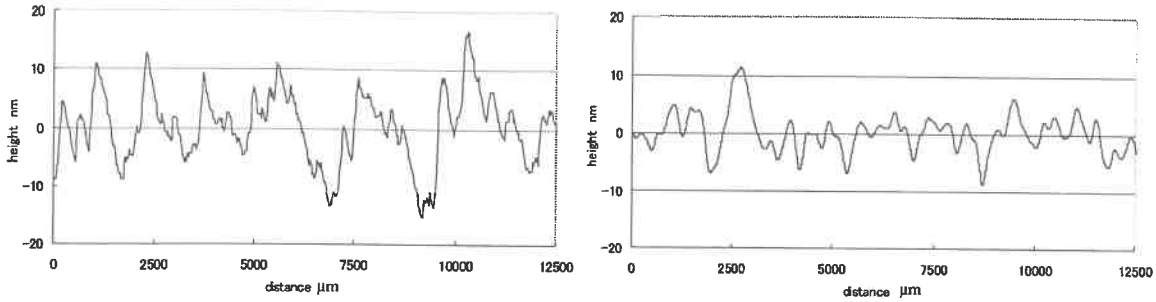

(a) Head readout signal (b) Stylus

Fig. 5 Circumferential profiles calculated from the head readout signal and obtained using stylus

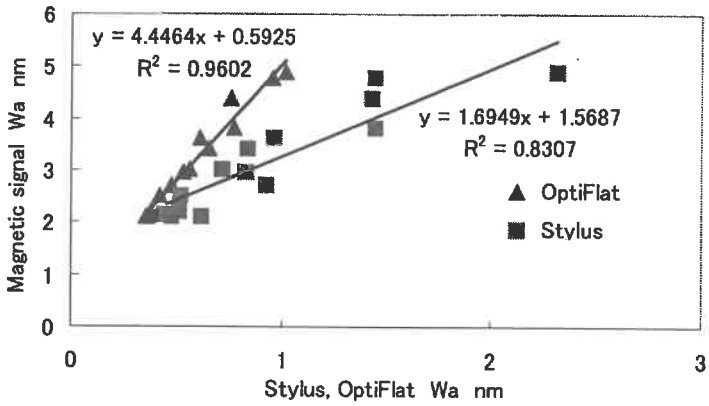

Fig. 6 Correlation between magnetic Wa and Magnetic-Waviness and Aluminum 3mm HPF

when applying the 3mm high pass filter. The correlation was best when the cutoff of the high pass filter was 3mm, which is about the same as the length of the head slider. It can be concluded that the disk micro-waviness has a great influence on the physical head-disk separation or the information storage density of HDD.

Conclusions

1) A quite good agreement of the waviness parameter was obtained between the processed profiles with the developed instrument and the OptiFlat.
2) The correlation between the amplitude modulation of the readout signal and the amplitude of the micro waviness was best when applying the 3mm high pass filter. It is about the same as the length of the employed head slider.

References

[1] Wei Yao, David Kuoa and Jing Gui : Effects of disc Micro-Waviness in an ultra-high density magnetic recording system, Proc. of Interface Tribology Towards 100 Gbit/in², (1999)31
[2] P. Yim, P. Wang, Z. Li, T. Dansen, S. Choa & H. J. Lee : The Role of Disk Surface Waviness on Baseline Instability of MR Head, IEEE Transactions on Magnetics, 35, 2(1999)758.
[3] H. Neal Betram : Theory of Magnetic Recording, Cambridge Univ. Pr, (1994).

Development of an Independent Real-time Position Feedback Device for CNC Machining Operations

Bernhard Jokiel, Jr., Lothar F.X. Bieg, Mark Ensz
Sandia National Laboratories[1], Albuquerque, New Mexico

Keywords: real-time, feedback, spatial, coordinate, metrology

1. Introduction

Sandia National Laboratories'(SNL) low volume manufacturing of a highly diversified product line has created new manufacturing and inspection challenges. Statistical process control (SPC) has been utilized in the past at SNL by influencing the manufacturing process based on trends. However, SPC techniques are most useful when applied to high volume manufacturing. With lot sizes decreasing, and product diversity increasing, the desire to eliminate or minimize independent product inspection has grown.

In order to effectively get the product right every time total process control (TPC) methods are being investigated and implemented. Under TPC quality is built into the process, where all attributes influencing the production process are detected, analyzed, and controlled, preferably in real-time. To date, feedback on machine tools and other manufacturing hardware has been limited to sensing motion at often large distances away from the actual point of operation (i.e. – encoders on ball screw or scales adjacent to guideways), sometimes including a volumetric error correction algorithm. Industry and University publications attribute up to 80% of the part errors to thermal and geometric effects and inaccuracies.

In response to the need within SNL for TPC, a novel device for real-time, in-situ measurement of the position of a milling spindle relative to the worktable is currently being developed at SNL under a three-year lab-directed research & development (LDRD) project. This new measuring device is capable of tracking and providing real-time feedback of the position of a milling head relative to the worktable during machining operations, independent from the machine tool's controller and axis feedback systems.

2. Measurement Device Overview

The main design objectives were (1) to build a relatively inexpensive device that was thermally stable, (2) easy to transport, (3) easily adaptable to different machine architectures and (4) yields very precise measurements suitable for feedback for error correction (3μm).

2.1. Design and Construction

The device proposed and constructed is a three revolute joint serial linkage arm (Figure 1). Joints one and two are constructed of Invar for thermal stability and utilize ABEC grade 7 ball bearings for smooth, accurate motion. The joint axes of joints one and two are constructed to be mutually perpendicular and intersecting. Alumina rods 305mm long, selected for their thermal stability and high stiffness to weight ratio, connect joint three to joint two and from joint three to the probe ball. ABEC grade 7 bearings are also used in joint three. The workvolume of the device is approximately a 1.2m diameter sphere.

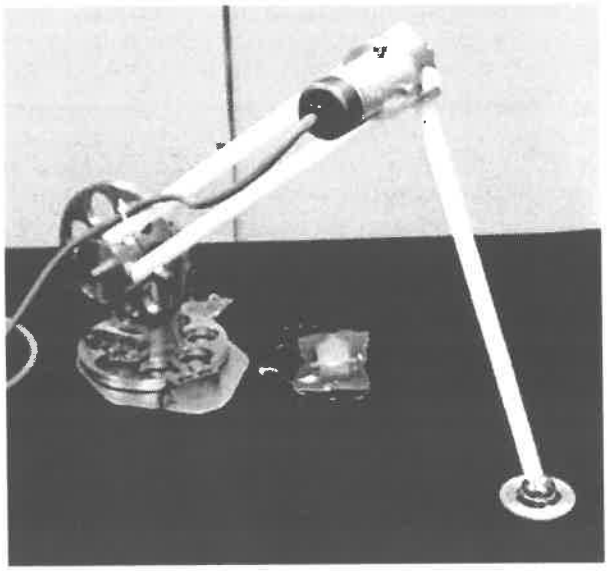

Figure 1 – 3-DOF serial linkage measurement device.

[1] Sandia is a multiprogram laboratory operated by Sandia Corporation, a Lockheed Martin Company, for the United States Department of Energy under Contract DE-AC04-94AL85000.

2.2. Position Feedback System

Two types of encoders were considered for feedback. The first was a SNL built disk encoder made of a Renishaw 0.1μm flexible scale wound around a precision-ground Invar disk, yielding a resolution of 3counts/arcsec. The second was a Canon K-1 with 81,000counts/revolution K-1 using an 80x interpolator yields a resolution of 5counts/arcsec. Extensive testing of repeatability and accuracy of these two encoders referenced to a Zeiss RT05 rotary table (certified 1arcsec accuracy) showed that the SNL encoders were significantly more repeatable than the K-1 (Figure 2). With proper calibration the SNL encoders are expected to exhibit better than 5arcsec accuracy, which is very comparable to the K-1.

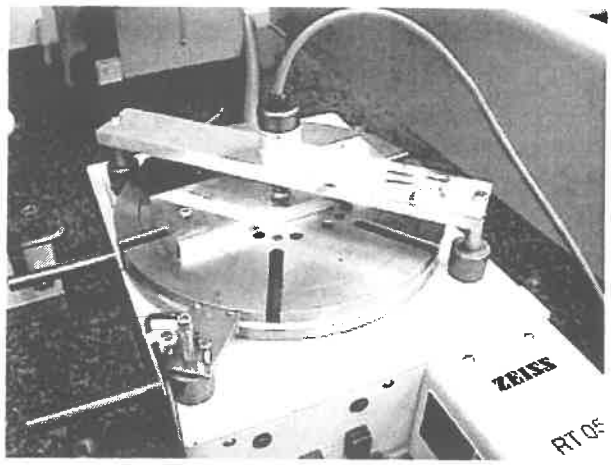

Figure 2 – Experimental test setup of SNL and K-1 encoders versus Zeiss RT05.

In light of the experimental results, the SNL Renishaw scale encoders were chosen for joints one and two. The final grind on the disk periphery and the joint shaft bore for each joint were completed in the same setup and on the machine to minimize form error and radial error motion of the disk relative to the joint axis centerline. The Canon K-1 encoder was chosen to be used on joint three for its compact size and low mass (80g).

3. Proposed Device Implementation

3.1. Machine Tool Metrology Frame

The primary use of the device is as a metrology frame to measure in real-time motion occurring between a point near the tool tip of a milling machine and the coordinate system of the workpiece being manufactured. In this mode the base of the device is connected to the machine tool's table near the workpiece with the probe tip attached to a point on the milling head near spindle nose by a magnetic kinematic coupling (Figure 3). The device is then aligned electronically to the axes of the machine tool. The probe tip then may be disconnected and used to probe the tool and the workpiece blank to establish the geometry of the part and tool setup relative to the metrology frame.

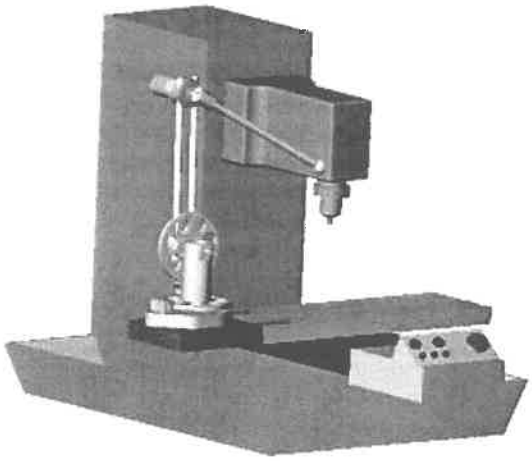

Figure 3 – Conceptual picture of measuring device installed on small milling machine.

During the execution of a part program, the relative motion of the worktable and milling head are sensed by the device. Positional errors that occur are sensed in-situ, and fed into the control loop of the machine tool for compensation. In this manner, positional errors in the machine tool from thermal or geometric effects may be compensated during motion. It is important to note here that this is a three-DOF measurement device, while there are 21 errors in a three-axis machine tool that combine into six errors between the tool tip and the part frame. Therefore it takes three of these devices to capture all of the errors or at least a second three-axis attachment to capture the rotational errors. Due to budgetary constraints, only one device is currently being built and tested at this time.

3.2. Manual Probing

In addition to part and tool setup and checking on the machine tool (section 3.1), geometric features of a part may be directly measured at particular intervals during pauses in the machining cycle. The probe

ball may be detached from the kinematic mount on the machine and used as a manual coordinate measuring machine (CMM). The entire device also may be removed from the machine tool and taken to a surface plate (or other measurement location), where it may be used as a portable CMM.

4. Uncertainty Analysis

4.1. Governing Equation for Position

The equation for the position of the probe center point relative to the base reference frame via a serial linkage is easily determined by Equation 1 from the Devanvit-Hartenburg parameters (DHP) appearing in Table 1. Figure 4 shows the geometrical significance of the DHP on a single link.

$$ {}^{G}P_{Tool} = {}^{G}T_1\,{}^{1}T_2\,{}^{2}T_3\,{}^{3}P_{Tool} \qquad where: $$

$$ {}^{i}T_j = \begin{bmatrix} \cos(\theta_j) & -\sin(\theta_j) & 0 & a_{i,j} \\ \sin(\theta_j)\cos(\alpha_{i,j}) & \cos(\theta_j)\cos(\alpha_{i,j}) & -\sin(\alpha_{i,j}) & -\sin(\alpha_{i,j})S_j \\ \sin(\theta_j)\sin(\alpha_{i,j}) & \cos(\theta_j)\sin(\alpha_{i,j}) & \cos(\alpha_{i,j}) & \cos(\alpha_{i,j})S_j \\ 0 & 0 & 0 & 1 \end{bmatrix} \tag{1} $$

Table 1 – Nominal DHP for measurement device.

Link Length (mm)	Twist Angle (deg)	Offset Distance (mm)	Joint Angle (deg)
a_{G1}=0	α_{G1}=0	S_1=123	θ_1=variable
a_{12}=0	α_{12}=90	S_2=0	θ_2=variable
a_{23}=305	α_{23}=0	S_3=0	θ_3=variable

	${}^{3}x_{tool}$ (mm)	${}^{3}y_{tool}$ (mm)	${}^{3}z_{tool}$ (mm)
${}^{3}P_{tool}$	305	0	0

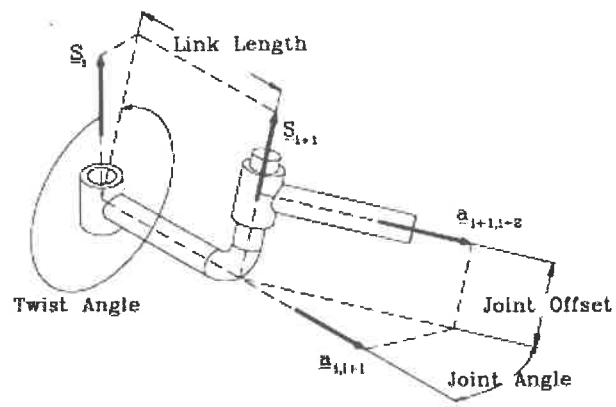

Figure 4 – The DHP are the physical dimensions of a link in a serial chain.

4.2. Error Budget

Uncertainty in the DHP stems from a variety of factors including thermal effects, encoder accuracy and repeatability, imparted mechanical loads, imparted gravitational loads, bearing error motions (radial, face, tilt and motions) and device calibration. A total of 40 factors were considered to contribute to the uncertainty in the 13 DHP for the device. For brevity, only the combined uncertainties in the DHP are shown (Table 2). Interested readers are encouraged to contact the authors for a complete listing of all of the uncertainty contributors.

Table 2 – DHP estimated uncertainties.

Model Parameter	Combined Uncertainty	Units
θ_1	0.000021	rad
S_1	0.003	mm
a_{12}	0.003	mm
α_{12}	0.000022	rad
θ_2	0.000010	rad
S_2	0.003	mm
a_{23}	0.005	mm
α_{23}	0.000022	rad
θ_3	0.000010	rad
S_3	0.003	mm
Ptool3 - X	0.005	mm
Ptool3 - Y	0.002	mm
Ptool3 - Z	0.006	mm

4.3. Uncertainty Calculation and Workspace Mapping

Since the DHP are the basic kinematic parameters of a serial device, they are not inherently cross-coupled. Since the calibration process relies on direct inspection the measured DHP will not become cross-coupled during calibration. Under these circumstances the combined uncertainty at the probe point may be calculated assuming that the effects of the DHP uncertainties act independently from each other and are therefore uncorrelated. In compliance with the ANSI/NCSL *U.S. Guide to the Expression*

of Uncertainty in Measurement, a type "A" analysis was conducted using the combined uncertainty rule in Equation 2. Where x consists of the DHP.

Using Maple to symbolically derive the 13 partial derivatives of Equation 1 and MATLAB to evaluate them with their respective individual uncertainties, the combined uncertainty occurring at the probe point was evaluated and mapped over device's workspace. From this analysis the maximum combined uncertainty in the reported position of the tool tip is 18 μm (Figure 5).

$$u_p = \sqrt{\sum_{i=1}^{13}\left(\frac{\partial P}{\partial x_i}u_{x_i}\right)^2} \tag{2}$$

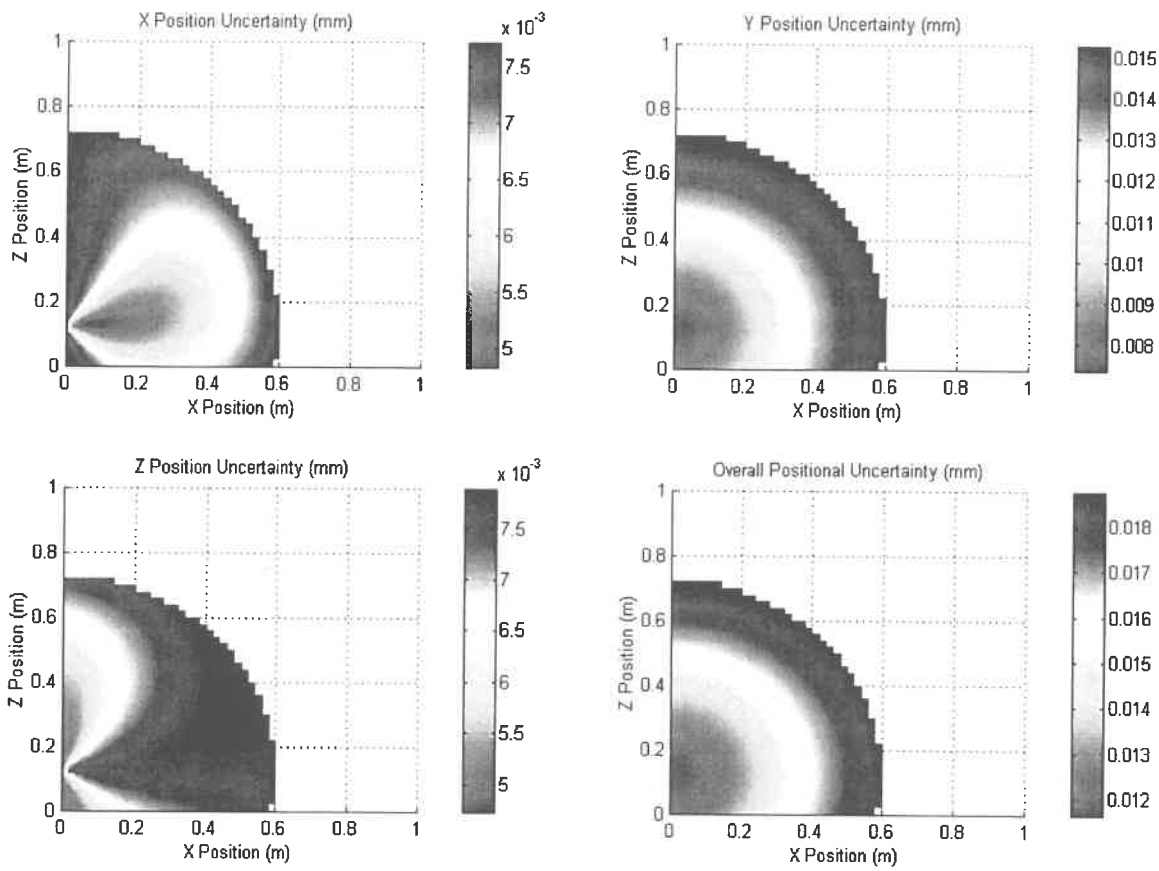

Figure 5 – Combined uncertainty map at probe point.

5. Conclusions and Future Work

A prototype portable and multi-use metrology frame and CMM has been designed and analyzed, and is currently in its final phase of assembly and interfacing. The prototype system will be able to independently measure, feedback, and compensate relative motion measurements occurring between a milling head and part being produced with an uncertainty between 12-18 μm. Recent improvements in Rensiahw's flexible scale product line to 50nm resolution may also be implemented in which case the uncertainty in the reported position of the probe tip will drop to 10 μm. Calibration and testing of the prototype and implementation on a small CNC milling machine is expected to be completed in December.

6. Acknowledgements

The authors would like to thank the following people for their hard work and support: Paul Cunningham, Clinton J. Atwood, Doug Abrams, John Cressup, Henry Apodaca and Tyler Donnell.

Hybrid Simulation and Experimental Method of Uncertainty Analysis

James G. Salsbury
Mitutoyo America Corporation, Aurora, Illinois, USA

1. Introduction

According to the scope of the *Guide to the Expression of Uncertainty in Measurement* (GUM) [1], the general rules for evaluating and expressing uncertainty that are established in the GUM are for various fields and levels of accuracy. The GUM specifically states that its principles are designed to cover a broad range of measurements including shop floor and production measurements, laboratory calibrations, and applied research and development measurements. The measurement uncertainty examples found in the GUM and in the published literature, however, are generally applicable only to calibrations and advanced measurement techniques. Little practical guidance is available for the various common industrial dimensional measurements that are found in places such as on production shop floors and in quality assurance laboratories.

In this paper, a general methodology for uncertainty analysis is presented that combines simulation and experimental techniques and is in accordance to the principles of the GUM. The hybrid technique brings together the concepts of measurement uncertainty simulation [2,3,4] with industrial developed practices in experimentally testing the repeatability of production measurement processes [5]. The developed approach is particularly applicable to situations where individual gages or measuring instruments are used for a variety of measurement tasks, such as is common in production measurements. The hybrid technique is applicable from simple measurement tasks, such as measuring diameter with a micrometer, to complex tasks, such as measurements made with coordinate measuring machines (CMMs).

2. General Uncertainty Model for Independent Contributors

Following the philosophy of the GUM, a measurement is an attempt to estimate the value of a specific measurand. The lack of knowledge in the value of the measurand from a particular measurement process is expressed by an estimation of the uncertainty of the measurement. In accordance to the GUM, the uncertainty is represented by the combined standard uncertainty, $u_C(y)$, for a measurement result y. If all contributors to the uncertainty can be treated as independent, then the combined standard uncertainty can be determined by the positive square root of

$$u_c^2(y) = \sum_{i=1}^{N} \left(\frac{\partial f}{\partial x_i} \right)^2 u^2(x_i) \qquad (1)$$

where $u(x_i)$ represents the standard uncertainty of any one of the N independent quantities that contribute to the uncertainty of the measurement, and partial derivatives $\partial f / \partial x_i$ are the sensitivity coefficients that relate the change of the output estimate, the measurement result y, to the input estimates x_i. The governing equation for the measurement process is defined by

$$y = f(x_i) \qquad \text{for } i = 1 \text{ to } N \qquad (2)$$

To estimate the combined standard uncertainty, it is necessary to best determine the quantities influencing the measurement result, estimate the standard uncertainties associated with the contributors, and calculate the appropriate sensitivity coefficients. In estimating the standard uncertainties, the GUM recognizes two

separate types, those evaluated by statistical methods (Type A), and those evaluated by other means, such as the application of sound scientific or engineering judgment (Type B). In practice, many uncertainty analyses use a combination of Type A and B techniques [1,6]. In the hybrid approach introduced in this paper, Type A and B estimates are not formally used, but rather the combined standard uncertainty of a measurement is determined directly through a combination of simulation and experimental techniques.

3. Description of the Hybrid Approach

In the hybrid approach, a Type A statistical experiment is specially developed such that particular input estimates, x_j, are allowed to influence the measurement result while the other independent input estimates have negligible effect. These other input estimates are then estimated using a Monte Carlo simulation technique and are labeled, $\hat{x}_i$, to distinguish them from x_j. The equation of the measurement process can therefore be written in the form

$$y = f(\hat{x}_i, x_j) \quad \text{for } i, j = 1 \text{ to } N \text{ and } i \neq j \tag{3}$$

where y is again the output estimate and $\hat{x}_i$ and x_j represent estimates of all the influence quantities determined to be significant to the measurement process. Using the governing equation for the measurement process in the form of Eq. (3), the simulated input estimates $\hat{x}_i$ are then numerically inserted into the independent statistical experiment that is dependent only on x_j. In this manner the uncertainty due to the $\hat{x}_i$ are propagated into the Type A experiment that was originally only sensitive to the x_j. A statistical analysis of this hybrid experiment is then used to directly estimate the combined standard uncertainty of the measurement result y. This process is shown graphically in Fig. 1. The hybrid approach is motivated by situations where it is more economical and practical to develop Type A experiments that are sensitive to specific independent contributors instead of using Type B knowledge or where it is difficult to directly determine the appropriate sensitivity coefficients of Type B estimates of standard uncertainties.

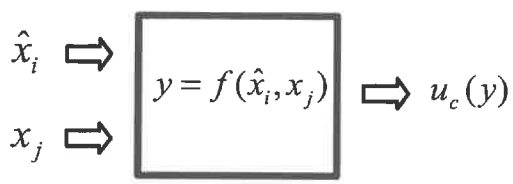

Fig. 1. Using the hybrid simulation and experimental method to estimate the combined standard uncertainty of a measurement process.

4. Hybrid Uncertainty Method Applied to a CMM

To demonstrate the usefulness of the hybrid method for estimating the uncertainty of complex measuring systems, the method is applied to a CMM process. Though there is no well-accepted method for estimating the uncertainty of CMM results, there is literature available that discusses the errors in measurements made with CMMs [7,8], and standards are available for testing their performance [9,10]. The difficulty lies in transposing the general knowledge of CMM capabilities into uncertainty estimates for particular measurement tasks. This problem is compounded by the fact that CMMs are used for a wide variety of measurements and that these measurements can be made in many different manners. While information regarding single point measuring uncertainty may be available, how that uncertainty propagates into the myriad of potential coordinate measurement processes is quite challenging.

The hybrid approach is implemented by developing a measurement experiment that is sensitive to particular x_j. Monte Carlo simulation techniques are then used to propagate additional input estimates,

$\hat{x}_i$, into the experiment assuming that the experiment was previously not sensitive to the $\hat{x}_i$. For CMMs, the hybrid approach is particularly useful if the simulation inputs can be generated within the CMM software and propagated into actual measurement data in-situ. This is the approach that was developed and is discussed here.

4.1 Generating and Propagating Simulation Values In-situ

The majority of commercially available CMM software is quite powerful and resides on advanced computing platforms. Using the features within the CMM software it is often possible to develop the necessary code to generate the Monte Carlo simulation values in real time during CMM operation. In addition, it is also necessary to be able to propagate the simulation values into the actual measurement results. The approach taken here is to simulate coordinate point measuring errors and then propagate them into the actual measured points. This is done on a point-by-point basis for each coordinate prior to the calculation and evaluation of the measured geometry. In this manner, the measurement uncertainty represented in the simulation process is propagated through the measurement algorithms of the CMM software.

The process of generating and propagating the simulation values in-situ is shown in Fig. 2. For each actual measured coordinate point, (X_i, Y_i, Z_i), the associated errors, $(\delta X_i, \delta Y_i, \delta Z_i)$, are generated by sampling from the appropriate estimated distribution. This process creates a set of new measurement points, (X_i', Y_i', Z_i'), which are then evaluated by the CMM software according to the feature being measured. Fig. 2 shows an example of a circle diameter being measured; D' is the final calculated diameter of the circle, and the function f represents the algorithm used to calculate the circle diameter from the set of n data points. This process would be repeated a number of times according to how the experiment was designed, and the statistics for D' would be used to estimate the combined standard uncertainty for the measurement of the diameter.

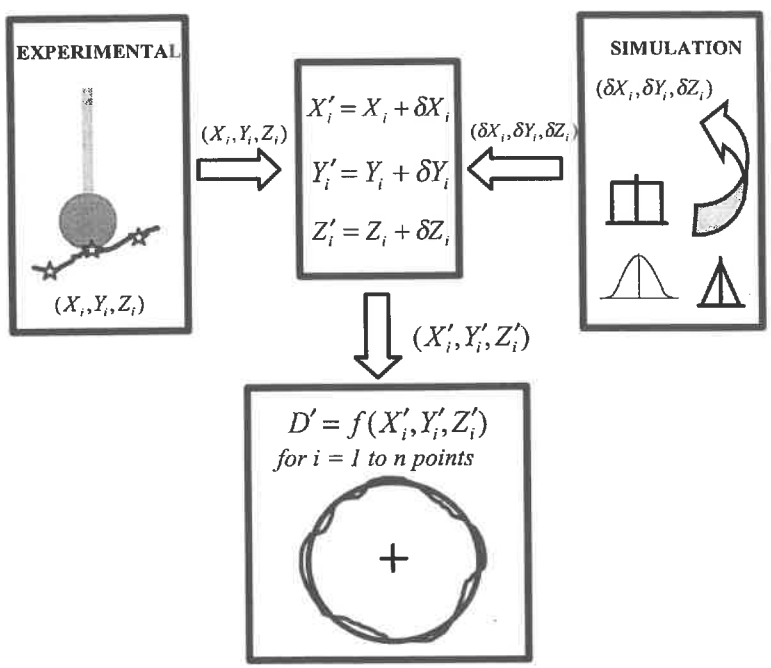

Fig. 2. In-situ generation and propagation of simulated values into the experimental results.

4.2 Hybrid Uncertainty Implementation on a CMM

The hybrid uncertainty technique is implemented on a CMM for the measurement of the diameter of a small bore. Based on performance test results, and for example purposes here, the standard uncertainty of the point measuring capability of the CMM is estimated to be 2 μm in each of the three axes directions. A Monte Carlo simulation is created within the measurement software so that each actual point is modified as discussed earlier and as shown in Fig. 2. For example purposes, a circle diameter is measured using three equally spaced points.

The bore on the actual workpiece is measured using three points and the least-squares circle fitting algorithm resident in the CMM software. A single part is measured 30 times. Between trials, the probe stylus is recalibrated using normal operating procedures. The program is also created to randomly change the exact locations of the measured points. The points are rotated around the bore and shifted slightly along the axis of the bore. The points are, however, always measured using an equally spaced sampling strategy. The standard deviation of the 30 measured diameters, which represents the combined standard uncertainty of the measurement process, is calculated.

Using the hybrid approach, the combined standard uncertainty is estimated to be 5.13 μm. For comparison, the results of the experiment are also processed without the use of the hybrid module enabled in the CMM software. These results, which are now simply a Type A study, are combined with the Type B estimate of the point measuring uncertainty and the sensitivity coefficient for circle measurements using three points [11]. Using this approach, the combined standard uncertainty is estimated at 4.87 μm. This value differs by about 5% from the result of the hybrid method; this difference is within expected statistical variation indicating the proper functionality of the hybrid approach. The hybrid approach has the advantage, however, of being able to be used for any type of CMM measurement.

5. Acknowledgments

This work was made possible by the research facilities available within the Center for Precision Metrology at the University of North Carolina at Charlotte. The author would like to thank Dr. Robert Hocken, the National Science Foundation, and all the industrial affiliate members who support the Center.

6. References

[1] *Guide to the Expression of Uncertainty in Measurement*, ISO, Geneva, Switzerland, 1995.
[2] Phillips, S. D., Borchardt, B., Sawyer, D., Estler, W. T., Ward, D., Eberhardt, K., Levenson, M. S., McClain, M., Melvin, B., Hopp, T., and Shen Y., "The Calculation of CMM Measurement Uncertainty via The Method of Simulation by Constraints," *Proc ASPE*, 1997, 16, 443-446.
[3] Balsamo, A., Di Ciommo, M., Mugno, R., Rebaglia, B. I., Ricci, E., and Grella, R., "Evaluation of CMM Uncertainty Through Monte Carlo Simulations," *Annals of CIRP*, 1999, 48, 425-428.
[4] Kunzmann, H., Trapet, E., and Waldele, F., "Concept for the Traceability of Measurements with Coordinate Measuring Machines," *Proc 7th IPES*, 1993, 41-52.
[5] *Measurement Systems Analysis Reference Manual*, AIAG, Troy, MI, 1995.
[6] ISO/TS 14253-2:1999, *Estimation of uncertainty in GPS measurement.*
[7] Phillips, S. D., Borchardt, B., and Caskey, G., "Measurement Uncertainty Considerations for Coordinate Measuring Machines," NISTIR 5170, NIST, Gaithersburg, MD, April 1993.
[8] Phillips, S. D., "Performance Evaluations," in *Coordinate Measuring Machines and Systems*, Bosch, J. A. (ed.), Marcel Dekker, New York, NY, 1995.
[9] ASME B89.4.1-1997, *Methods for Performance Evaluation of Coordinate Measuring Machines.*
[10] ISO 10360-2:1994, Performance assessment of coordinate measuring machines.
[11] Hopp, T. H., "The Sensitivity of Three-Point Circle Fitting," NISTIR 5501, NIST, 1994.

Effect of Laminating Period of Ceramics Superlattice Coating Film on Its Mechanical Properties

Shoichi Shimada, Hideyoshi Takai
Department of Precision Science and Technology, Osaka University,
2-1 Yamada-oka, Suita, Osaka 565-0871 Japan

Hiroaki Tanaka, Naoya Ikawa
Osaka Electro-Communication University,
18-8 Hatsu-cho, Neyagawa, Osaka 572-8530 Japan

Background

Ceramics superlattice, which has a laminated structure of heterogeneous ceramics combination in nanometric scale, is one of the most promising approaches as a highly functional coating film. As the ceramics superlattice shows high indentation hardness and thermal stability, it is expected to use as a wear-resistant coating films on the surfaces subjected to severe frictional contact such as cutting tools and slide ways. For example, it is reported that TiN/VN epitaxial monocrystalline superlattice film shows remarkable hardness enhancement [1]. The indentation hardness of the superlattice film depends on its laminating period and reaches the maximum value of H_V = 55 GPa at the period of 5.2 nm. This value corresponds to the hardness of more than twice as high as that of TiN or VN homogeneous films. Polycrystalline TiN/AlN superlattice film also shows the maximum hardness of 40 GPa at the period of 2.5 nm [2][3]. This value is approximately 1.6 times as high as that of TiN homogeneous film. However, the mechanism of hardness enhancement has not been understood well due to the difficulties in highly reliable measurement of mechanical properties and observation of microstructure of the superlattice film.

In this paper, to clarify the correlation between laminating period and mechanical properties of ceramics superlattice and to establish the guidelines for design of highly functional superlattice coating films, molecular dynamics (MD) computer simulations of uniaxial compression testing are carried out on TiN/ZrN superlattice films with various laminating periods.

MD modeling of ceramics superlattice

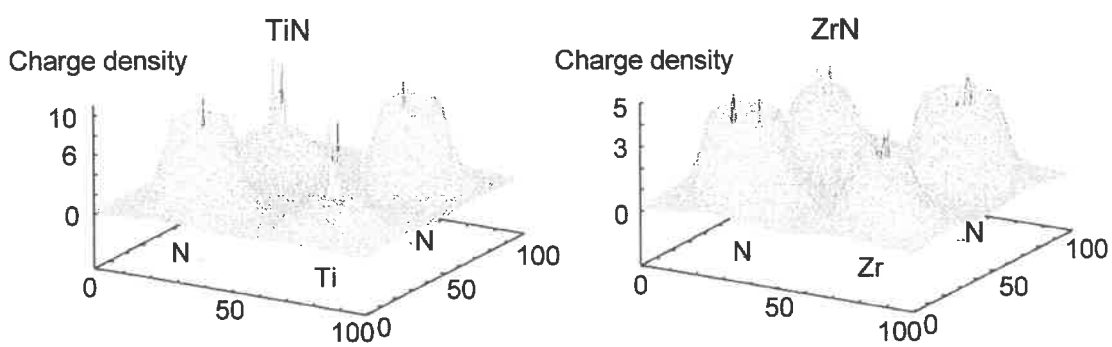

	Atomic charge	Charge Shift[%]
Ti	19.5543312	0.888833236
N	7.2590904	1.037012914

	Atomic charge	Charge Shift[%]
Zr	36.3990352	0.90997588
N	7.2060296	1.0294328

Fig.1 First-principle calculation of electronic charge density distribution in TiN and ZrN

MD simulation is an useful method to analyze accurately the atomistic behavior of the deformation or fracture process of an atomic solid model. For the analysis, three-demensional (3-D) TiN/ZrN superlattice model with various laminating periods are used assuming the interatomic potential functions based on the modified embedded atom method (MEAM) [4]. Figure 1 shows electric charge density distribution of TiN and ZrN calculated by the use of a full potential linearized augmented plane wave package for calculating crystal properties (WIEN97) [5]. The MEAM potential parameters regarding electric charge density distribution are determined by fitting the density distribution between N and Ti and Zr with that of the calculated distribution of valence electrons. The other parameters are determined by fitting the cohesive energy, elastic modulus, atomic volume and interatomic distance with those of measured values.

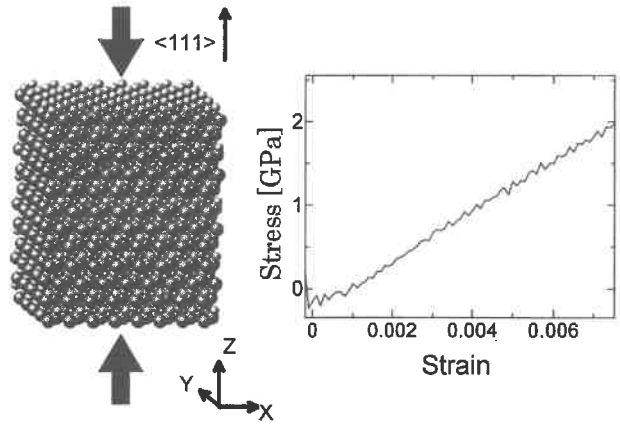

Fig.2 Uniaxial compression testing for TiN and ZrN

To analyze the deformation behavior of monocrystalline TiN and ZrN, MD simulation of uniaxial compression testing are carried out using 3-D model as shown in Fig. 2. Both of TiN and ZrN models have (111) top plane in z-direction and periodic boundaries are applied in x, y and z-directions. Young's modulus is calculated from the stress-strain curve when the model is compressed in z-direction. The Young's modulus of TiN and ZrN obtained from the simulations are 340 GPa and 390 GPa, respectively, which are 10-15 % smaller than those of measured values.

Figure 3(a) shows the MD model of TiN/ZrN superlattice for uniaxial compression testing. The thin layers of TiN and ZrN with same thickness are alternately laminated in <111> direction. The laminating periods of the models used in the simulation are 1.5, 3.0 and 6.1 nm. In addition, the monolayer-laminating model (Ti/N/Zr/N/Ti/N/Zr/N----) is also used as the model of an extremely

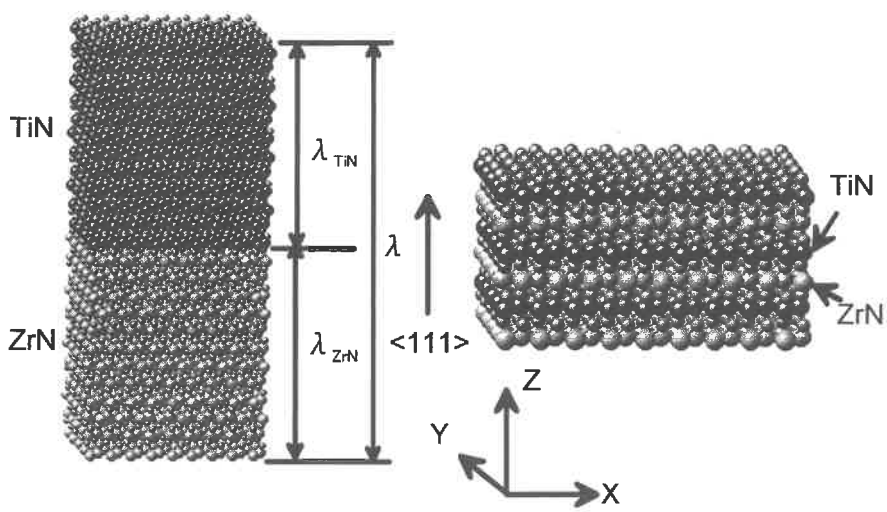

(a)Laminating period
λ =1.5 , 3.0 , 6.1nm
(λ TiN : λ ZrN = 1:1)

(b)Monolayer laminating

Fig.3 Uniaxial compression testing for TiN/ZrN supperlattice

WEAR BEHAVIOR OF DIFFERENT MATING PARTS

J. Shivakumar K. Sadashivappa Y. Vrushabhendrappa K.V. Jayadevappa

Bapuji Institute of Engineering and Technology,Davanagere-577 004

Fax: (08192)23261, E-mail:dr_kankuppi@usa.net

Key words: Wear,Surface deterioration,adhesive wear,running in, boundary lubrication.

1.0 INTRODUCTION

Studies on metals based on unlubricated sliding have been conducted on a wide range of ferrous and non-ferrous metals, as a basis for the development of materials for applications such as vehicles braking and space technology. With increasing operating speeds, there are several materials and lubricant combination that is becoming increasingly difficult to predict the effect of even a small variation in the operating condition. It is believed that an understanding of the unlubricated condition is a necessary pre-requisite to the more complex lubricated situation. The quality of most metal products depends upon the condition of their surfaces and on performance of machine components. Wear is one of the destructive influences to which metals are exposed.The displacement and detachment of metallic particles from a metallic surface may be caused by contact with

i) Another metal (adhesive/metallic Wear)

ii) Metallic/Non-metallic abrasive (abrasion)

iii) Moving liquids or gases (erosion)

Generally Wear occurs in combination.

2.0 MECHANISM OF WEAR

Adhesive wear and Abrasive wear occurs in most cases. A variety of conditions affect wear including environment, type of loading, relative speed of mating parts, lubricant, temperature, hardness, surface finish, presence of foreign particle, composition and compatibility of mating parts involved. Wear is basically unavoidable hence combination of hard and soft materials are used.

In adhesive wear, (also called Scoring, Galling, Siezing and Scuffing), tiny projections produce friction by mechanical interference with a relative motion of contacting surfaces. This increases resistance to further movement. If the driving force is sufficient to maintain movement, the inter locking particles are deformed. If they are of brittle material they may be torn off. This leads to the conclusion that Wear resistance will be improvrd by preventing metal to metal contact by increasing the hardness to resist initial indentation. Wear resistance can also be improved by increasing toughness to resist tearing out of metallic particles and increasing the surface smoothness to eliminate projections.

Abrasive wear occurs when hard particles slide/roll under pressure across a surface. The abrading particles forming the harder object tend to scratch the softer material. These harder particles may also penetrate the softer metal and cause tearing off metallic particles. Ease with which the deformed metal is torn off depends upon the toughness. Therefore Hardness and toughness also determine abrasive wear. However of these two, hardness is important.

3.0 GENERAL CHARACTERISTIC OF WEAR MATERIAL

The rate of wear in sliding pair depends upon the properties of parts in contact, treatment of the rubbing surfaces and their quality and also on the running conditions, i.e., load, temperature, lubrication and so on. Diverse changes occuring in the contact layer gives rise to various types of wear. The mechanism of surface destruction is varied. Depending upon the character of the interface medium, differentiation is made between dry wear, boundary – lubrication wear and abrasive wear.

Three phases of wear process takes place.
i)The running -in period.
ii)Period of steady –state wear.
iii)Period of severe wear.

The running-in period consists that the asperities on rubbing surfaces change their shape and material becomes work-hardened. Due to this. Elastic condition set in. Ensuring this is important because it provides for minimum wear and a stable magnitude of frictional force. Running in is characterised , as a rule, by more intensive wear of rubbing surfaces and by high heat generation. This is accompanied by changes both in surface geometry and in the after running-in (in various conditions for diverse sliding pairs), a stable surface roughness prior to given running conditions develops,which is duplicated rather than changed further on during the rubbing process.

Running-in is followed by the period of steady-state wear,over whih the wear rate of the joint in the given condition is minimum.Various investigations have shown that the wear particles break away as a result of numerous load cycles on a single frictional bond. The main difficulty in understanding wear of material is due to the ambient conditions. Considerations of the effect that physical,chemical and mechanical factors have on wear gives grounds for regarding wear as a cumulative process in which the effects of individual factors combine during repeated loading of the frictional bonds in separation of wear particle.

Materials for rubbing parts are selected in accordance with the operating conditions and cost. Wear resistance is determined by the mechanical and physical properties and by the electro-chemical properties of the metals medium system.Increased wear life can be achieved by the formation of passivating protective films, corrosion inhibitors or by selective materials with maximum wear resistance. Lubrication is an important contributing factor to wear resistance,especially in adhesive wear. A sufficiently thick film completely eliminates metallic contact reducing wear to a negligible amount. However more frequently, boundary lubrication occurs.This is the condition of intermittent metallic contact.Under boundary condition ,wear depends upon speed, pressure,nature of mating surfaces and efficiency of residual film.

4.0 EXPERIMENTAL SET UP AND PROCEDURE

In order to study the wear behavior of different mating parts, a compact, easy to operate experimental setup is designed and fabricated. The apparatus is rigidly set up on the machine with the help of bolts attached to the base, which can be put through the T-slots.(Fig.1). Wear is measured with the reduction in weight (in grams) of the test pins. Two surfaces, i.e., the pins and a base plate are made to be in contact. Due to the frictional resistance arising , as the pins are made to rotate against a stationary base, wear occurs. The loading of the apparatus is constrained to 300 Newtons. The speeds have been maintained at 80 r/min

and 160 r/min. The test is conducted for various materials (like brass, mild steel) and for a fixed time duration, After which the reduction in weight of the pins is measured.

5.0 RESULTS AND DISCUSSION

Fig. 2 shows the variation of wear as the applied load varies for different materials. Speed selected is 80 r/min. It was observed that wear increases with increase in load. In the same Fig. 2 the behavior of wear for material brass at two different speeds VIZ., 80 r/min and 160 r/min. is also shown. It is observed that for both the speeds the wear is directly proportional to the load applied. Also wear is more at higher speeds.

6.0 CONCLUSION

Referring to the Fig. 2 , it is observed that ,mild steel being a softer material than brass undergoes a higher wear for a specified speed. Thus wear not only depends upon the load but also on the type of material selected. Hence it is an important criteria when considering wear to give weightage to the conjunction of material employed. It is also observed from the Fig.2 that for higher speed wear is more.

Thus we can conclude that the

i) wear depends upon the load applied.
ii) Wear depends upon the material selected, and
iii) Wear depends upon the relative sliding speeds of metals in contact.

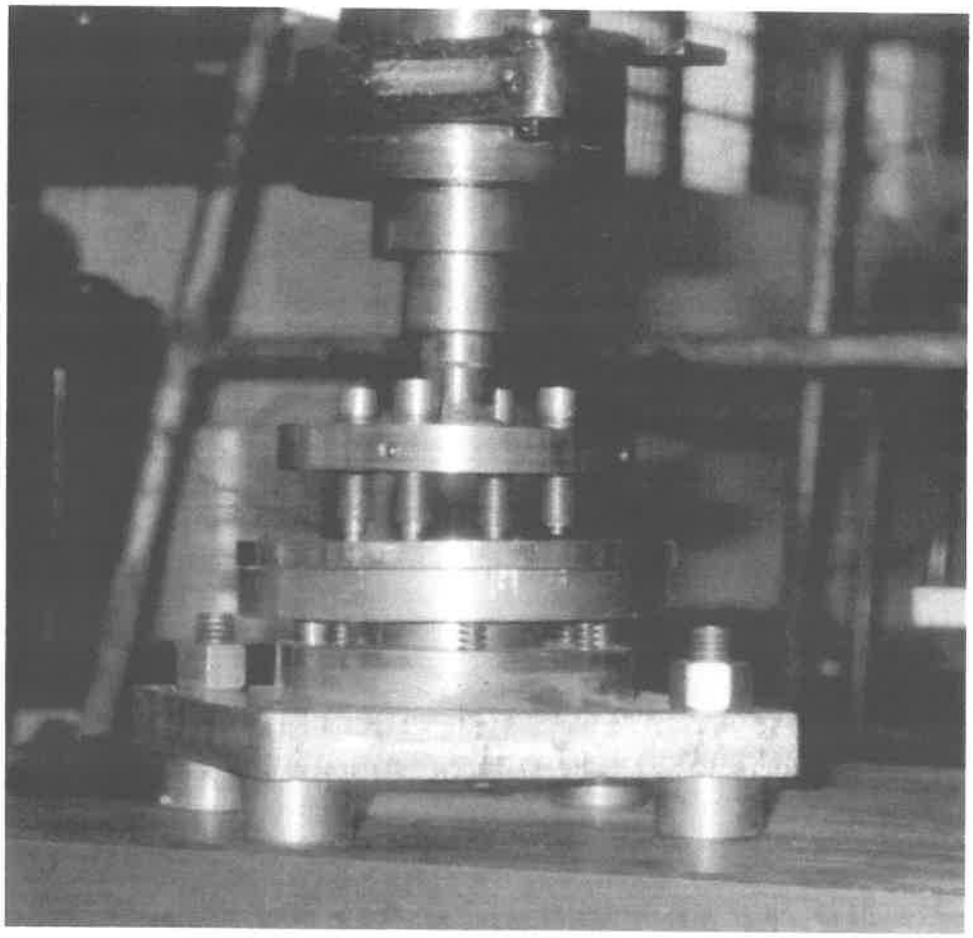

FIG. 1. EXPERIMENTAL SET UP

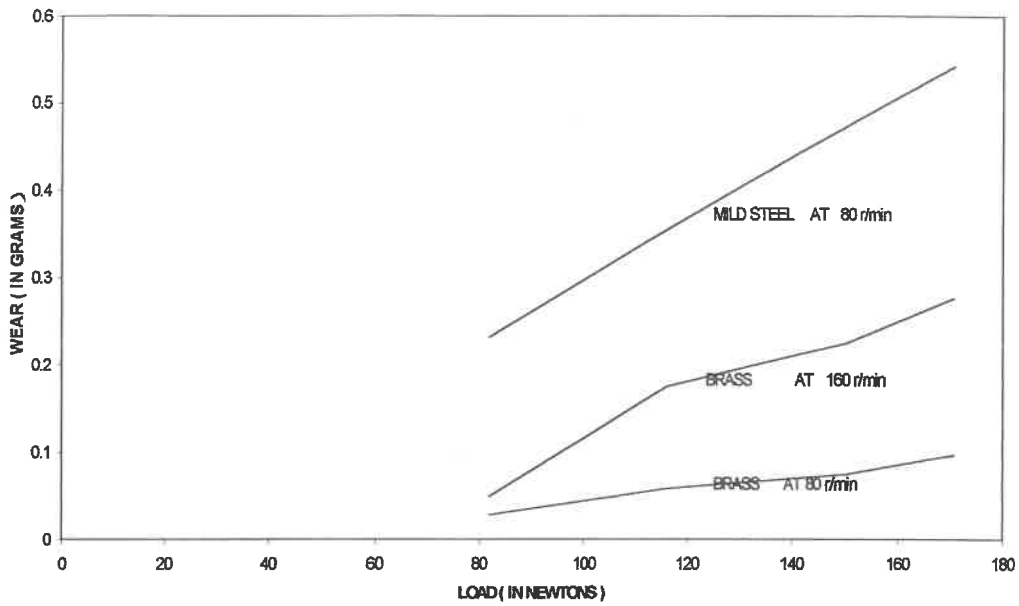

FIG. 2 WEAR BEHAVIOR OF DIFFERENT MATERIALS

REFERENCES

1. Introduction to Physical metallurgy- Sidney.H.Avner,Second Edition,1974. Mc-Graw Hill International Edition.
2. Basic Lubrication Theory- Alaister Cameron. First Wiley eastern May 1987.
3. 'Wear behavior of Different Mating parts by use of an Attachment in drilling machine' B.Tech. Project BIET, Davanagere.577 004, Karnataka State. India.

Automatic Surface Damage Exploring and Repairing System by Precise Micro Robots

Hisayuki Aoyama and Satoshi Miyamoto

Applied Micro Systems, Robotics Div.
Dept. of Mechanical Engineering & Intelligent Systems,
University of Electro-Communications, Tokyo 182-8585
Japan
[URL http://www.aolab.mce.uec.ac.jp]

1. INTRODUCTION

In recent years, many types of micro robots and locomotion mechanisms have been developed as high precision positioning tools and opened new application in the filed of not only precision engineering but biochemical one. Particularly the piezo driven mechanisms can allow the excellent positioning resolution of nanometer level within an infinite workspace although the feedback properties with external sensors are required to improve the coordinate accuracy over the working area[1]. Also the micro robot has the potential performance for the application in the special environment such in-pipe and in-chamber where it is difficult for the conventional mechanism to extend its arm. Surface investigation of the product and the facility with complex curved surface, in which small mechanical defect should cause the serious problem, needs much of efforts to do.

Our group have developed many small robots with micro tools and sensors on the precise locomotion platform which is composed of piezo elements and electromagnets. Basic structure and performance were reported in the previous papers[2].

In this report, the newly developed micro robots which can explore on the target surface in order to find out the mechanical damages such as crack and defect, and propagate the acoustic signal in order to indicate the damage location by the passive resonator are described. And another one which has dual microphones to detect the acoustic signal and maneuver itself automatically to repair the crack automatically is also explained.

As illustrated in Fig.1, these small robots can collaborate each other on the target to perform this unique task. This system can allow the low cost precise inspection and automatic repairing over night without any expensive facilities.

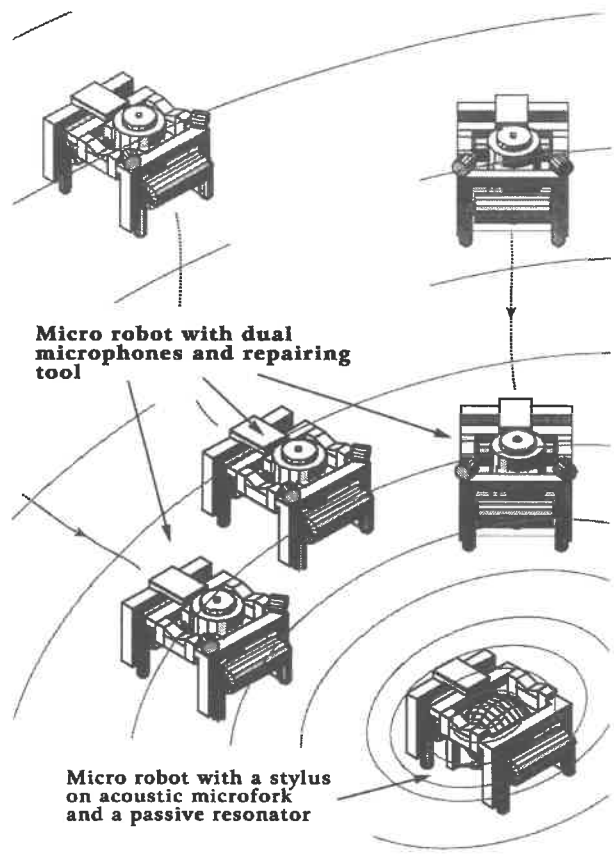

Fig.1 Conceptial schematic of micro robots for automatic surface damge inspection and reparation

2. MICRO ROBOTS FOR SURFACE DAMAGE INSPECTION AND REPARATION

2.1 Micro robot with stylus on U type micro fork and acoustic resonator

The micro robot which can explore on the target sample and detect the mechanical crack, and then propagate its acoustic signal by the

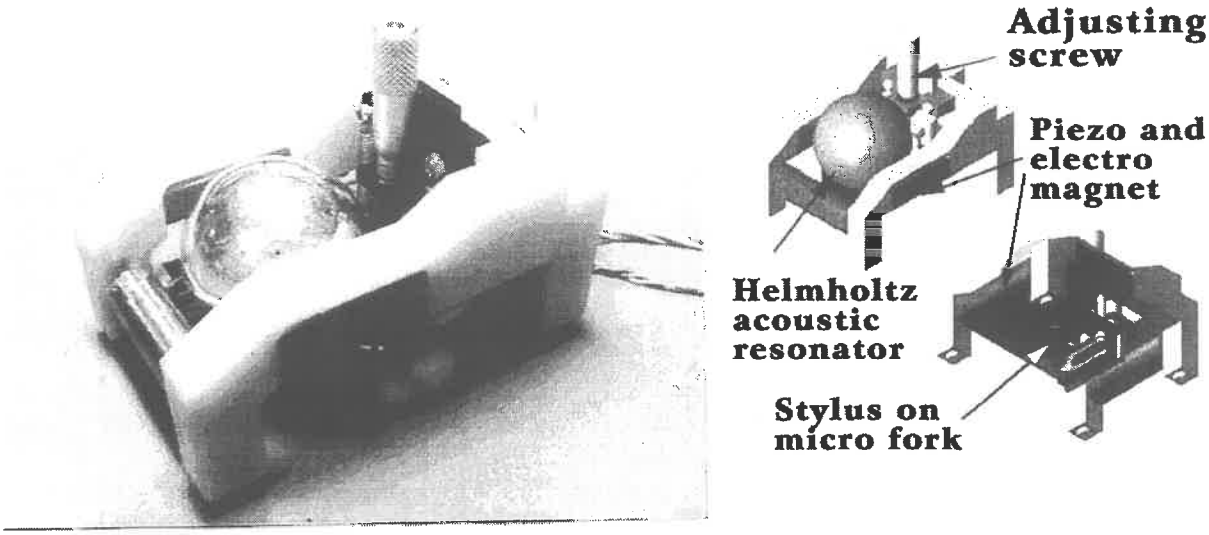

(a) Photograph of the developed small robot

(b) Isometric view of the small robot

Fig.2 Micro robot with a micro fork with stylus and a passive acoustic resonator

passive resonator is shown in Fig.2. This small robot, 40mm in height, 40mm in width and 60mm in length, has piezo element and electromagnet to move precisely based on an inch-worm principle. Furthermore it is incorporated with a stylus set at the end of the micro sound fork excited by the piezo film and a passive Helmholtz resonator.

When the stylus traverses over the small crack, it is free of contact so that it can start to vibrate at its resonance. However the vibration is suppressed so as to give no signal when keeping the contact with the plane surface, as shown in Fig.3. The amplitude of stylus vibration of several ten micron should be determined according to the depth of crack to be checked. For instance, the acoustic signal can be oscillated when the micro fork stylus with the amplitude of 20 micron goes over the defect of deeper than 20 micron.

A simple passive acoustic resonator is equipped with the robot in order to propagate this insignificant trigger signal to other small robots with repairing tools without any supplemental electronics and any wires. This idea partially comes from the insect world such a mosquito wing and a cicada's resonator. The volume of cavity and the diameter of orifice should be designed carefully to match to the micro fork resonance frequency.

In the experiment as mentioned below, the commercially available U type micro fork with the dimension of 1.5mm in width, 8mm in length, and 0.5mm in thickness is used for a

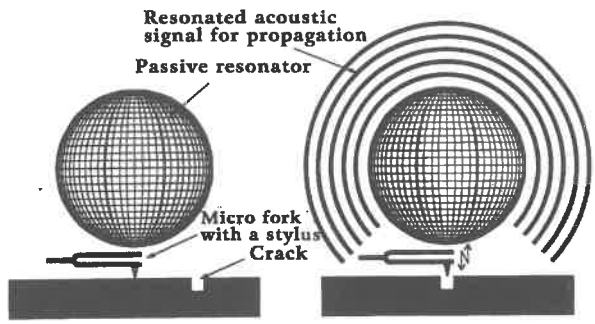

Fig.3 Principle of crack detection; a stylus set at the end of the micro fork excited by the piezo to scan the surface and its acoustic signal can be resonated by the passive resonator for wide propagation

pickup device, which has the resonance frequency of 1000Hz excited by piezo film. And a thin stylus of tungsten with 0.1mm diameter is attached at the end of this micro fork as an active feeler. To amplify this small vibration for propagation, a passive Helmholtz spherical resonator with the diameter of 25mm and 3.0mm orifice are designed and implemented close to the micro fork.

2.2 Micro robot with microphone and repairing tool

After the location of the defect is identified by the small robot with a stylus sensor, other small robots with a repairing tool have to move toward the destination automatically. To

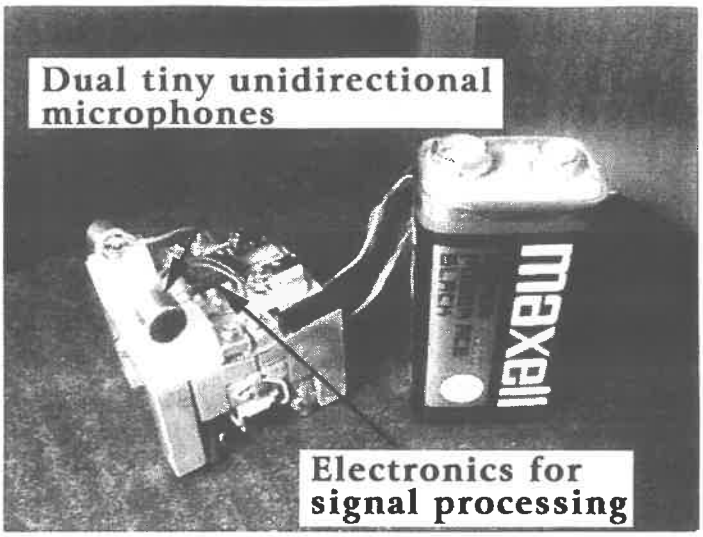

(a) Photograph of the small robot with dual tiny microphones to detect the signal source

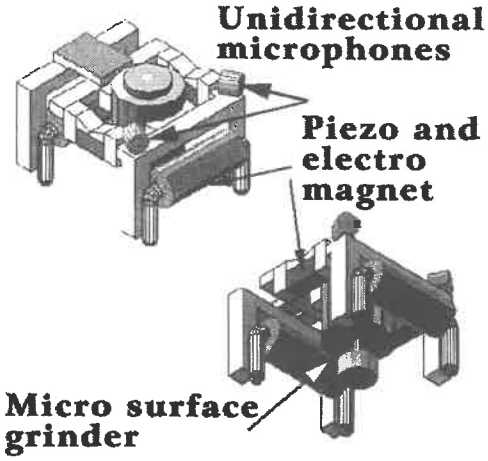

(b) Conceptual view of the robot with dual microphones and simple micro grinder to finish the surface on going development

Fig.4 Micro robot with dual unidirectional microphones to detect the signal source from the small robot with a vibrating feeler

prevent the system being complicated, each small robot is required to maneuver itself by the reflective manner based on the simple control sequence. So a pair of tiny unidirectional microphones with a primary electronics are embedded on the robot to detect the direction of signal source which is generated by the vibrating stylus as shown in Fig.4.

The detected acoustic signal from two microphones can be compared to the threshold and turn on the piezo actuation. And the differential amount from two sensors also can be used for switching either of two piezo elements to control the heading of the robot. This simple sensor and the primary signal processing device allow the small robot to move automatically toward to the source of acoustic signal which indicates the surface damaged point. Since there should be many kinds of damage and crack on the surface, we have to investigate these characteristics. Currently we are designing two small robots on going development, one of which has a micro electro discharge tip to mold the crack and the other has the micro grinder to finish the surface.

3. EXPERIMENTS

As a primary experiment, the sample with the several grooves of 30 micron to 120 micron depth is used to check the basic performance. The amplitude of the vibrating stylus as a threshold value can be controlled easily by the input voltage applied to the piezo film on the micro fork.

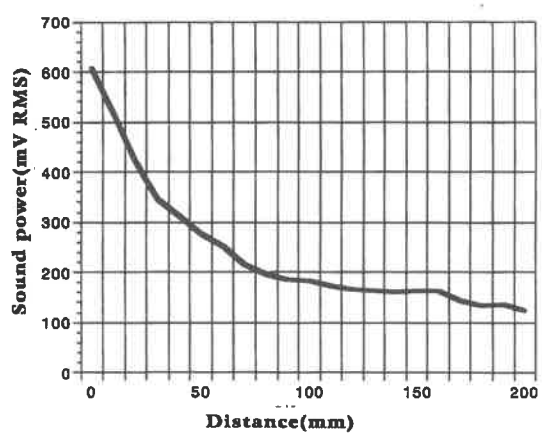

Fig.5 The relation between the distance from the resonator and the acoustic power which can shows the workable ranging by acoustic propagation

It was confirmed that the resolution is approximately 10 micron within the range from 30 to 120 micron. However the amplitude of vibration smaller than 50 micron causes the decrease of acoustic propagation range from the resonator, and consequently other robots with microphones should lose the signal destination. In the practical application on the desktop, the acoustic signal of the crack deeper than 50micron can be enough to be detected

given by

$$\omega_0 = \frac{\lambda}{\pi D} f = \frac{\lambda}{\pi} \frac{\sqrt{n^2 - NA^2}}{NA} \tag{1}$$

where λ is the wavelength of the laser beam, n is the refractive index, f is the focus length of the microscope objective, D is the diameter of the aperture and NA is the numerical aperture of the microscope.

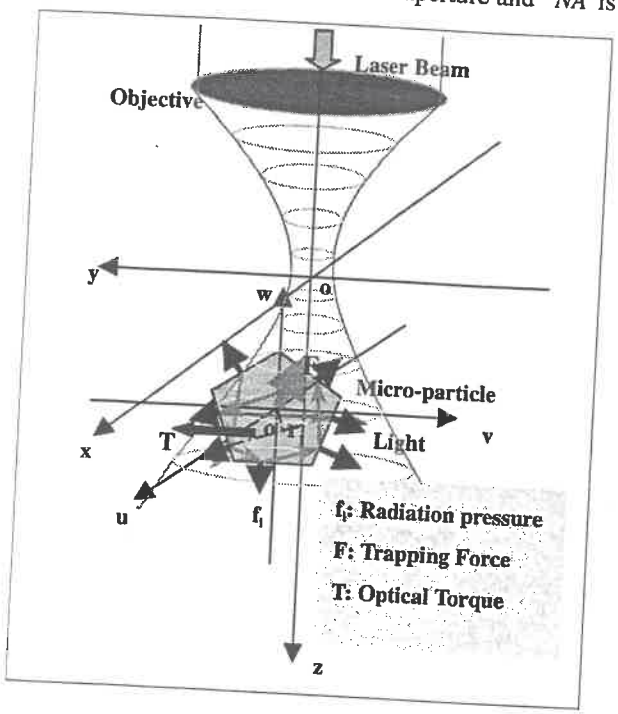

Fig.2 Schematic Diagram of Static Simulation

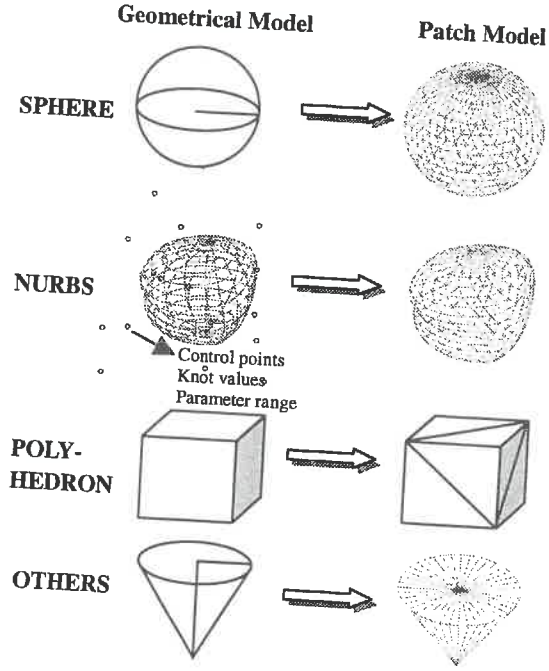

Fig.3 Model of Micro-Particle

2.2 MODEL OF MICRO-PARTICLE

In order to simulate the trapping on arbitrary shaped particles, we use two models to represent the micro-particles: the geometrical model and the patch model as shown in Fig.3. The geometrical model depends on the parameter of the particle shape. For example, the spherical particle is represented by its radius and the polyhedron particle is represented by faces and points. We also use closed non-uniform rational B-spline surface(NURBS) as geometrical model for other particles with smooth surfaces. The patch model is represented by many small triangles, which connected to each other to form a closed surface. The geometrical model is converted to the patch model by dividing the shape of the particle into very small triangles. We use the patch model for calculation because the it is more convenient for ray tracing.

2.3 SPEED CUBE

The calculation of the trapping force and the optical torque is a time-consuming task when the number of patches is very large because during ray tracing, each of the patch should be tested to see if it is intersected with the current light. In our simulation program, a speed cube is generated to accelerate this process.

For any particle shape, a rectangular box can be found which is just large enough to enclose the patch model. We can now divide the rectangular box into N ×N×N units with each having the information field filled by all the addresses of the patches, which are intersected with the unit as shown in Fig.4(a). If no patch intersects with it, the unit has nothing in its information field. During the ray tracing, only the units which are intersected with the current light are inspected one by one along the propagation of light. For the unit to be inspected, only the patches which are intersected with the unit are tested as shown in Fig.4(b). The tested patches are thus greatly reduced and the ray tracing greatly accelerated. This rectangular box is called speed cube.

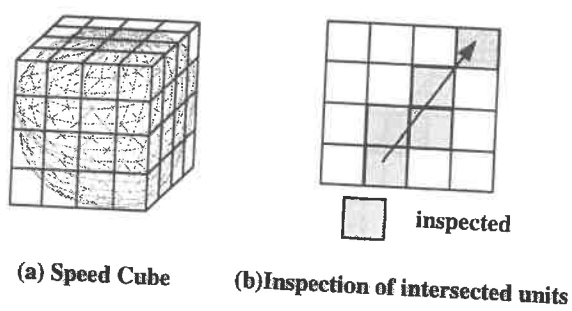

Fig.4 Establishment of Speed Cube and its application in Ray Tracing

3. DYNAMIC SIMULATION

A dynamic simulator, which can simulate the motion of the trapped particle, has been developed. It is based on the mathematical mode as shown in Fig.5. The coordinate system (x,y,z) gives the reference frame for the model of the laser beam with its origin at the focal point of the objective lens and its z axis opposite to the propagation of the laser beam. The coordinate system (u,v,w) gives the reference frame for the model of the particle and is established in such a manner that it always moves together with the particle.

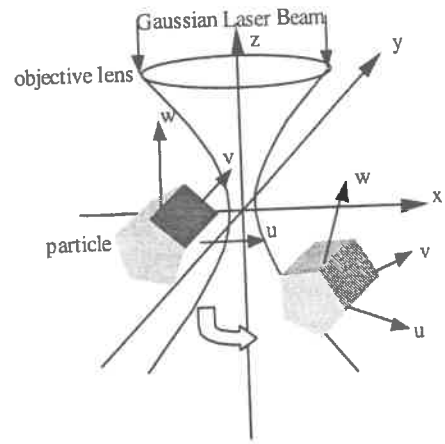

Fig.5 The Coordinate Systems for Dynamic Analysis of Laser Trapping. The Particle Coordination (u,v,w) Moves Together with the Particle.

The main procedure for dynamic analysis of laser trapping on micro-machine tools can be given as followings:

(1)The translation vector $\mathbf{s}$ and the rotation vector $\mathbf{a}$, whose direction represents the rotation axis passing through the center of mass and magnitude represents the angle it rotates, are determined by the equation of motion

$$\mathbf{F}_r(\mathbf{s},\mathbf{a})+k_f\frac{d\mathbf{s}}{dt}+\mathbf{F}_{gb}=m\frac{d^2\mathbf{s}}{dt^2} \qquad (2)$$

$$\mathbf{t}_r(\mathbf{s},\mathbf{a})+k_\tau\frac{d\mathbf{a}}{dt}=I\frac{d^2\mathbf{a}}{dt^2} \qquad (3)$$

where $\mathbf{F}_r(\mathbf{s},\mathbf{a})$ and $\mathbf{t}_r(\mathbf{s},\mathbf{a})$ represents the optical trapping force and the optical torques, respectively, which can be calculated based on static simulation mentioned before. $\mathbf{F}_{gb}$ represents the forces contributed by gravity and buoyancy. $k_f=-6\pi r\eta$ and $k_\tau=-8\pi\eta r^3$, where r is the effective radius of the particle and η is the viscosity of the fluid. m is the mass of the particle and I is the moment inertia of the particle.

The equation of motion is solved discretely by dividing the time domain into small time intervals.

(2)With the translation vector $\mathbf{s}_t$ and rotation vector $\mathbf{a}_t$ at different specific time t obtained, transform matrix $\mathbf{M}_t$, mapping the coordinates from (u,v,w) to (x,y,z), are established. Assuming that the coordinate system (u,v,w) has the same orientation as the coordinate system (x,y,z) with its origin at (x_0,y_0,z_0) and the center of gravity respect to the coordinate system (u,v,w) is (u_c,v_c,w_c). Denote the translation vector as $\mathbf{s}_t=(s_x,s_y,s_z)$, the unit direction vector of $\mathbf{a}_t$ representing the rotation axis as $\mathbf{n}=(a,b,c)$ and the magnitude of rotation $\mathbf{a}_t$ as $\theta=|\mathbf{a}_t|$, we obtain

$$\mathbf{M}_t=\begin{bmatrix}1&0&0&0\\0&1&0&0\\0&0&1&0\\-u_c&-v_c&-w_c&1\end{bmatrix}\begin{bmatrix}(b^2+c^2)\cos\theta+a^2 & -ab\cos\theta+c\sin\theta+ab & -ac\cos\theta-b\sin\theta & 0\\ -ab\cos\theta-c\sin\theta+ab & (a^2+c^2)\cos\theta+b^2 & -bc\cos\theta+a\sin\theta+bc & 0\\ -ac\cos\theta+b\sin\theta+ac & -bc\cos\theta-a\sin\theta+bc & (a^2+b^2)\cos\theta+c^2 & 0\\ 0 & 0 & 0 & 1\end{bmatrix}\begin{bmatrix}1&0&0&0\\0&1&0&0\\0&0&1&0\\u_c+x_0+s_x & v_c+y_0+s_y & w_c+z_0+s_z & 1\end{bmatrix} \qquad (4)$$

(3)The coordinates of particles respect to (u,v,w) at different specific time t are mapped to (x,y,z) by

$$[x\quad y\quad z\quad 1]=[u\quad v\quad w\quad 1]\mathbf{M}_t \qquad (5)$$

4. SIMULATION RESULTS

A designed-tool made of silica with shape structure as shown in Fig.6 was investigated. Our calculation was performed under the following conditions. Assume we have Ar^+ laser with power of 100mW operating at a wavelength of 0.488 μm and having a TEM_{00} mode structure. The numerical aperture of the microscope objective lens is 0.95. The surrounding medium is air with a refractive index of 1, and the refractive index of the particle is 1.44. The density of silica is 2.08 g/cm^3. The viscosity of air η is taken as $1.82\times10^{-5}\,Ns/m^2$. Assuming that at initial state, the designed-tool is positioned in the horizontal

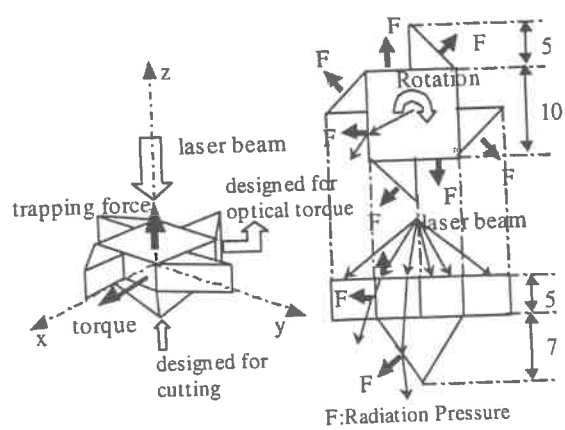

Fig.6 Designed Tool Trapped by Focused Laser Beam for Micro-machining. The Dimension of Length is μm.

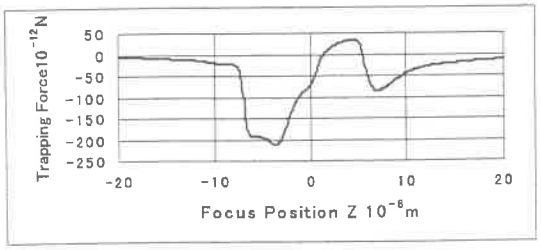

Fig.7 Trapping force on designed-tool changing with focus position along Z axis

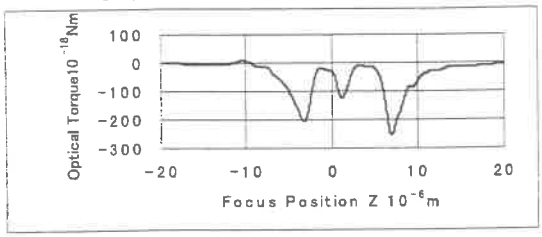

Fig.8 Optical Torque on designed-tool changing with focus position along Z axis

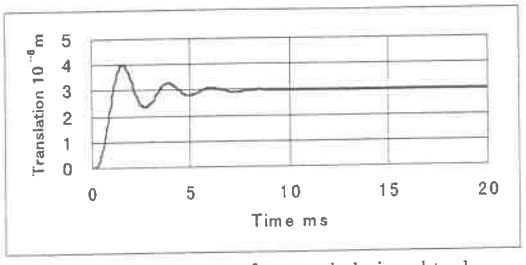

Fig.9 Translation of trapped designed-tool as function of time

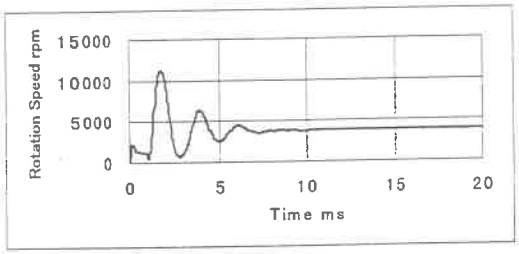

Fig.10 Rotation Speed of trapped designed-tool as function of time

plane as shown in Fig.6 and we began our simulation when the beam focus locates at 5.35 μm on the z axis. We investigated the motion of the designed-tool within the first 0.02 seconds and the time interval was taken as 10^{-4} seconds. Fig.7 shows the trapping force changing with the position of the laser beam. Fig.8 shows the optical torque changing with the position of the laser beam. Fig.9 shows the translation of the designed-tool as a function of time, giving a vibration up and down during the first 10 milliseconds and a stable state afterwards. Fig.10 shows the rotation speed of the trapped designed-tool changing with the time. Fig.11 shows the movement states of the designed-tool trapped by the focused laser beam at different times including its translation and rotation speed. Within the first 10 milliseconds, the maximum speed can excess 10000rpm and at stable state it can still rotate at the high speed of about 3800rpm. If the designed-tool hits on the surface of the workpiece, this rotation speed is high enough for micro-cutting and grinding.

5. CONCLUSION

Simulation for laser trapping on arbitrary shaped designed particles has been implemented. The trapping force and the optical torque can be calculated by static simulation and the motion of the trapped particle can be defined by dynamic simulation. Simulation results gives a verification that designed-particle can be trapped as a tool for nano-meter machining.

REFERENCE

1)Hiroki SHIMIZU, Takashi MIYOSHI, Yasuhiro TAKAYA, Satoru TAKAHASHI, "Study on Micro-Machining Using Optical Radiation Pressure," 1st International Euspen Conference, Bremen(1999), 199-202.

2)Jian BAI, Takashi MIYOSHI, Yasuhiro TAKAYA, Satoru TAKAHASHI, "Computer Simulation for Laser Trapping on Micro-particles with Arbitrary Shapes," Int. JSPE, Vol.33, No.4, (1999)363-368.

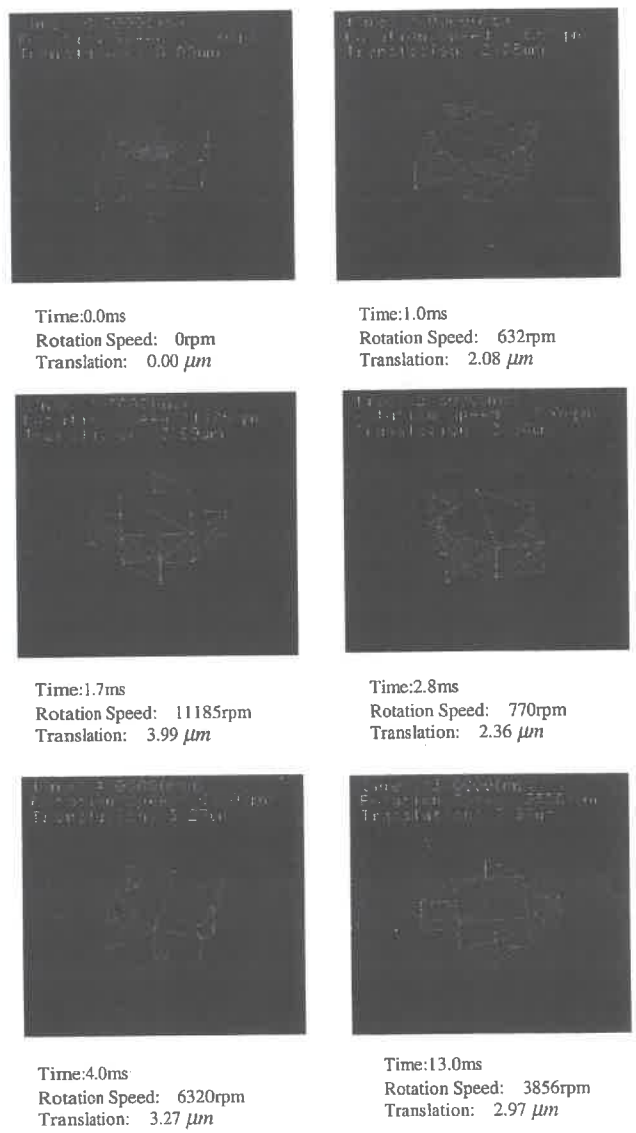

Fig.11 Movement states of the designed-tool trapped by the focused laser beam at different time

2. Structure of the fabricated microrobot

The section of the fabricated microrobot is shown in Fig. 1. The microrobot is able to move in pipes by imitating the motion of an earthworm. The microrobot is structured by three flexible nitrile butyl rubber bellows. A bellows-cell is 5 mm in outer diameter and 20 mm long. The total length of the microrobot is 60 mm. Three plastic air-tubes which feed pneumatic pressure to the microrobot are 1 mm in inner diameter, 2 mm in outer diameter and 1000 mm long. Eight friction rings which are 7 mm in outer diameter, 1.5 mm in inner diameter and 0.3 thick. The friction-rings are made of vinyl chloride for the acrylic pipe and made of rubber with small warts for the sheep's small intestine.

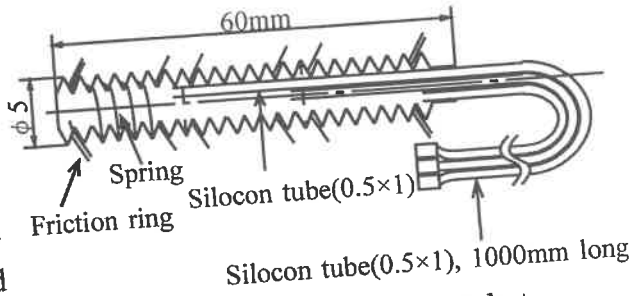

Fig.1 Structure of the microrobot

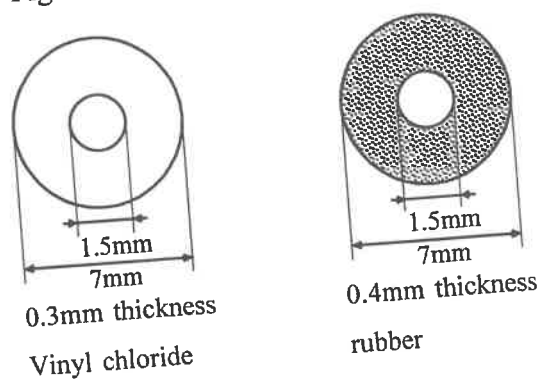

Fig.2 Friction ring

The friction-rings are shown in Fig. 2. The friction for creeping motion of the microrobot comes from these friction-rings. A friction-ring made of vinyl chloride for the acrylic pipe makes the friction force of 0.048 N in an acrylic pipe of 9 mm in inner diameter for the forward direction and 0.093 N for the backward direction of the microrobot. A friction-ring made of rubber with small warts for sheep's small intestine makes almost same friction force of 0.051 N for the forward direction and 0.093 N for the backward direction of the microrobot.

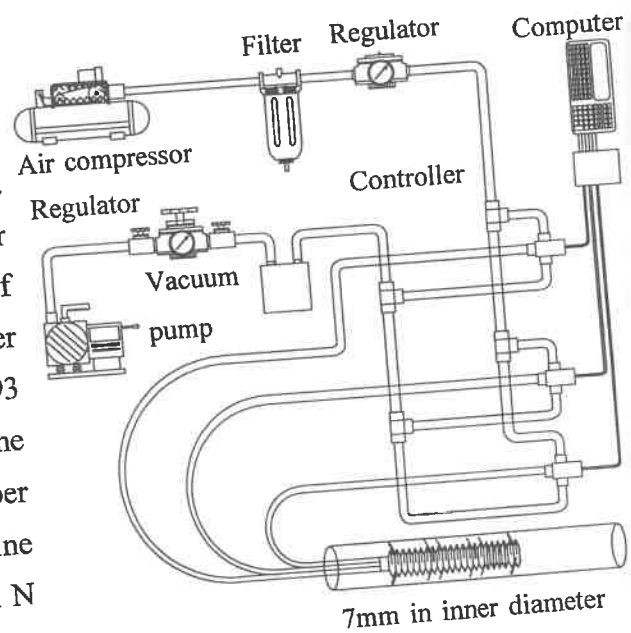

Fig.3 Experimental apparatus

3. Experimental apparatus of the fabricated microrobot

An experimental apparatus for measuring the speed of the microrobot is shown in Fig. 3. A computer controls three electromagnetic valves through a valve controller. Three feeding air-tubes are connected from the electromagnetic valves to three bellows-cells. The air-compressor is connected to the entrance port of the electromagnetic valves and the vacuum pump is connected to the exit port of the electromagnetic valves. The pneumatic and the vacuum pressure are independently feed to each bellows-cell.

The time-chart of the pneumatic pressure for the microrobot is shown in Fig. 4. First, the all bellows-cells are shrunk by the vacuum pressure. Then the pneumatic pressure pulses are sequentially supplied to the cell-1, the cell-2, and the cell-3. A tractile wave generated by the stretching and shrinking motion goes to the backward direction in the flexible bellows. Consequently, the in-pipe mobile microrobot is able to move to the forward direction.

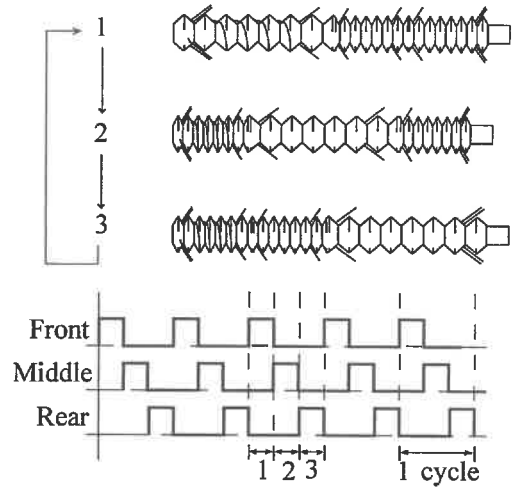

Fig.4 Time chart of the microrobot

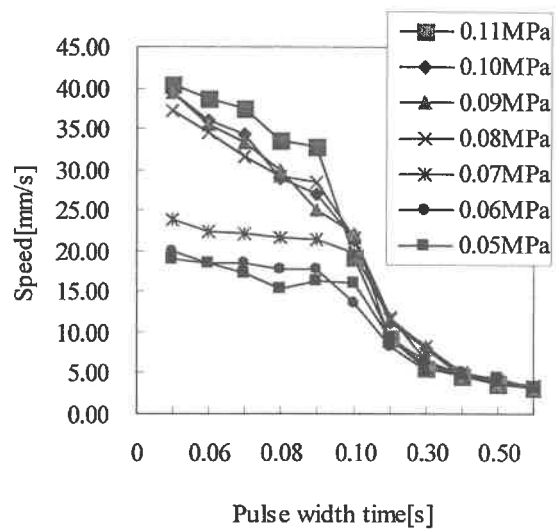

Fig.5 Speed of the microrobot

4. Moving characteristics of the fabricated microrobot in the acrylic pipe

The moving speed of the microrobot in the acrylic pipe is measured. The vacuum pressure is -0.08 MPa and the pneumatic pressure is changed from +0.05 MPa to +0.11 MPa. The pulse width time is changed from 0.05 seconds to 0.6 seconds. The relationship between moving speed of the microrobot in an acrylic pipe of 7 mm in diameter and the pulse width time is shown in Fig. 5. The maximum speed of 40 mm/s was obtained at the pneumatic pressure of +0.11 MPa and the pulse width time of 0.05 seconds.

5. Moving characteristics of the fabricated microrobot in the sheep's small intestine

The moving speed of the microrobot in the sheep's small intestine is measured. The vacuum pressure is -0.08 MPa and the pneumatic pressure is changed from +0.05 MPa to +0.11 MPa. The pulse width time is changed from 0.05 seconds to 0.6 seconds. The relationship between moving speed of the microrobot in the sheep's small intestine held in an acrylic pipe of 7 mm in diameter and the pulse width time is shown in Fig. 6. The maximum speed of 9 mm/s was obtained at the pneumatic pressure of +0.11 MPa and the pulse width time of 0.08 seconds.

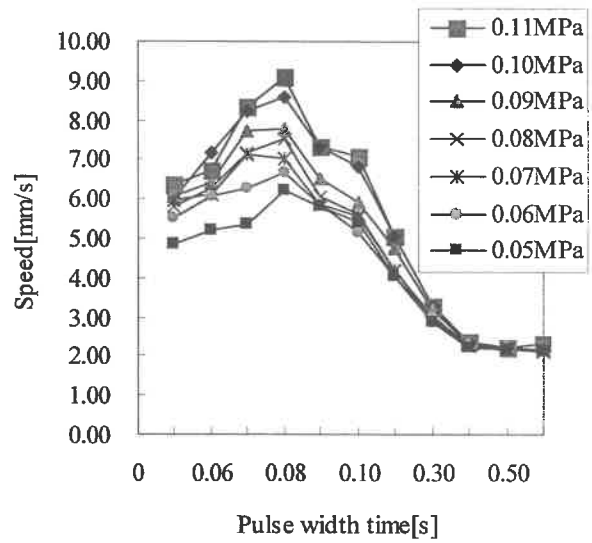

Fig.6 Speed of the microrobot

6. Conclusions

A fabrication of a prototype of a new in-pipe microrobot which move and inspect large or small intestines in the human body was performed. The followings are the conclusions of the fabrication.

1) We fabricated a new earthworm type microrobot which is constructed by three flexible nitrile butyl rubber bellows 5 mm in outer diameter and 60 mm long. The microrobot is able to move in an acrylic pipe of 7 mm, and 40 mm/s was obtained at the pulse width time of 0.05 seconds, -0.08 MPa of the vacuum pressure and 0.11 MPa of the pneumatic pressure.

2) The microrobot is confirmed to move in the sheep's small intestine held in an acrylic pipe of 7 mm in diameter and 9 mm/s was obtained at at the pulse width time of 0.08 seconds, -0.08 MPa of the vacuum pressure and 0.11 MPa of the pneumatic pressure.

References:

[1] S. Kato, M. Shirakawa, M. Ohno and M. Tabata: " Fabrication of Microrobot Movable in the Small Intestine of Pigs" Proc. of the ASPE 1999 Annual Meeting (1999) pp. 204-207.

[2] S. Kato, M. Shirakawa, S. Ozawa and T. Sugiura: " Moving Characteristics of an Earthworm type I-pipe Microrobot in Pig's Small Intestine" , Proc. of The 10th JSME Autumn Bioengineering Conference and Seminar (1999), pp. 71-72.

SELF-ALIGNMENT OF MICROPARTS USING LIQUID SURFACE TENSION – EXAMINATION OF THE ALIGNMENT CHARACTERISTICS –

Kaiji SATO*, Kentaro ITO*, Seiichi HATA** and Akira SHIMOKOHBE**
*Interdisciplinary Graduate School of Science and Engineering, Tokyo Institute of Technology
4259 Nagatsuta, Midori-ku Yokohama, 226-8502 Japan
** Precision and Intelligence Laboratory, Tokyo Institute of Technology

1. Introduction

MEMS technologies have become an important research field. In order to realize the systems composed of microparts as practical products, assembly technique of the microparts is necessary[1]. And the alignment is a very important task in the assembly. The purpose of this research is to establish the self-alignment technique for the microparts assembly using liquid surface tension. For this purpose, the self-alignment method using a liquid droplet and microparts which have two kinds of different characteristic areas in the surface, has been studied[2].

In this paper, the factors which influence the alignment performance are examined as the alignment characteristics. First, the states of the micropart and the droplet after the alignments are observed and the alignment errors are evaluated. Next, the relation between the theoretical restoring force and the alignment error is discussed. And then the effect of the high wettability area pattern change on the alignment performance is examined. In the experiments, water is used as liquid for alignment.

2. Self-alignment Method Using Liquid Surface Tension

Figure 1 shows the principle of the self-alignment method using liquid surface tension. The surface of each micropart used in the method is divided into two areas, high and low wettability ones. In the figure, the high wettability area pattern in the micropart 1 is similar to that in the micropart 2. Using these microparts, the self-alignment is carried out as follows.

(1) A droplet of liquid is put on the high wettability surface area of the micropart 1.
(2) The micropart 2 is put on the micropart 1 so that the droplet comes in contact with the high wettability surface area of the microparts.
(3) The micropart 2 is moved by the liquid surface tension so that the high wettability area pattern of the micropart 1 overlaps with that of the micropart 2 and the alignment is accomplished.

3. State of Micropart and Liquid in the Alignment and Alignment Accuracy

In this chapter first, the alignment experiments with six kinds of water volumes are made and their alignment errors are measured. Next, on the basis of the measured alignment errors and the observation result, the factors which affect the accuracy are discussed.

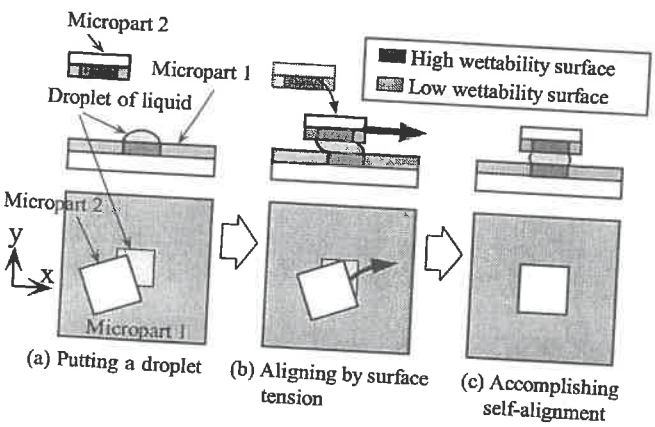

Fig.1 Principle of the self-alignment

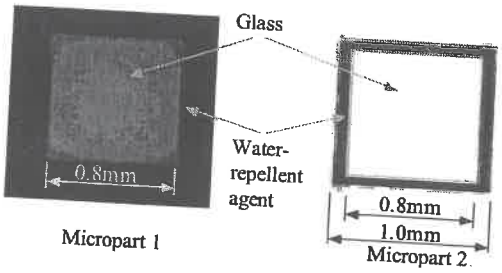

Fig.2 Experimental microparts

3.1 Experimental Equipment and Microparts

The position of the microparts is measured by using an image acquisition and processing system including a CCD camera connected to a microscope. Pixel pitch of the CCD represents about 3.6μm. The position and the incline angle of each microparts before the alignment can be adjusted by two fine stages.

Figure 2 shows experimental microparts used in this chapter. The microparts are fabricated using photolithography technique. They have a high wettability surface area which is made of glass, and a low wettability one on which the water-repellent agent is coated. The left side of the figure is the micropart 1 and the right side, the micropart 2. The size of the micropart 2 is 1mmx1mm. The high wettability area size of the both microparts is 0.8mmx0.8mm.

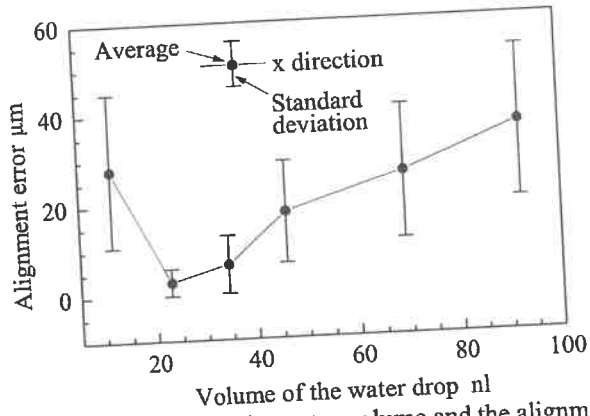

Fig.3 Relation between the water volume and the alignment error in the x direction

3.2 Effect of the Water Volume Change on Alignment Accuracy

By using six kinds of water volumes which are between 12nl and 92nl, the effect of the water volume change on the alignment accuracy was examined. Figure 3 illustrates the alignment errors in the x direction. Using each water volume, 10 similar alignments were made. In the experiments, the micropart 2 was dropped on the micropart 1 from a 500μm height after the initial errors were set at 100μm in the x direction, 0μm in the y direction and 0° in the θ direction. In case of the volume more than 23nl, the average and the standard deviation of the alignment errors become larger as the volume increases. However, the 12nl water volume causes larger average and standard deviation of the errors than 46nl one.

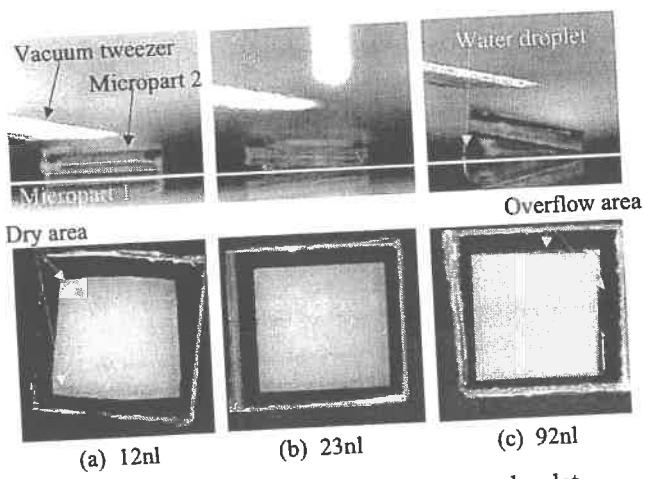

Fig.4 Behavior of micropart and water droplet after the alignment

Figure 4 illustrates the photograph of the states of the micropart 2 and the water droplet after the alignment. Upper parts of Fig.4 are the side views of the states and lower ones are the upper views. The upper parts show that the micropart 2 does not keep parallel to the micropart 1 and touches the micropart 1. So the alignment accuracy is considered to be influenced by friction force. The lower part of Fig.4(a) shows that the water does not cover all the high wettability area of the micropart 1 and the wetting area which supports the micropart 2 in Fig.4(a) is smaller than those in Fig.4(b) and (c).

In Fig.4(b), the water keeps in only the high wettability area of the micropart 1, but not in Fig.4(c). When the water does not keep in it like Fig.4(c), the surface tension force does not work so as to eliminate alignment errors exactly. Figure 5 shows the frequency in which the water overflows the low wettability area. When the volume is more than 35nl, the alignment error becomes larger as the frequency is larger. The fact shows that the overflow deteriorates the alignment accuracy. The alignment error by 23nl volume is better than that by 35nl though the water covers the high wettability area and does not overflow the low one in both cases of 23nl and 35nl. The reason is discussed

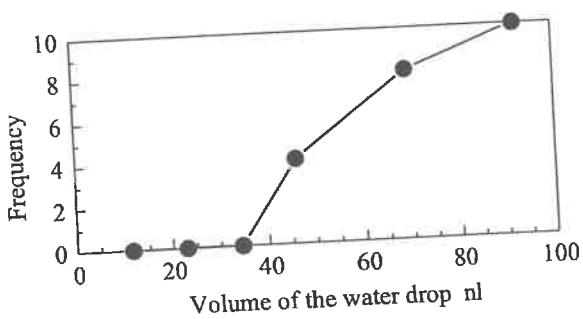

Fig.5 Frequency of water overflow in the alignment

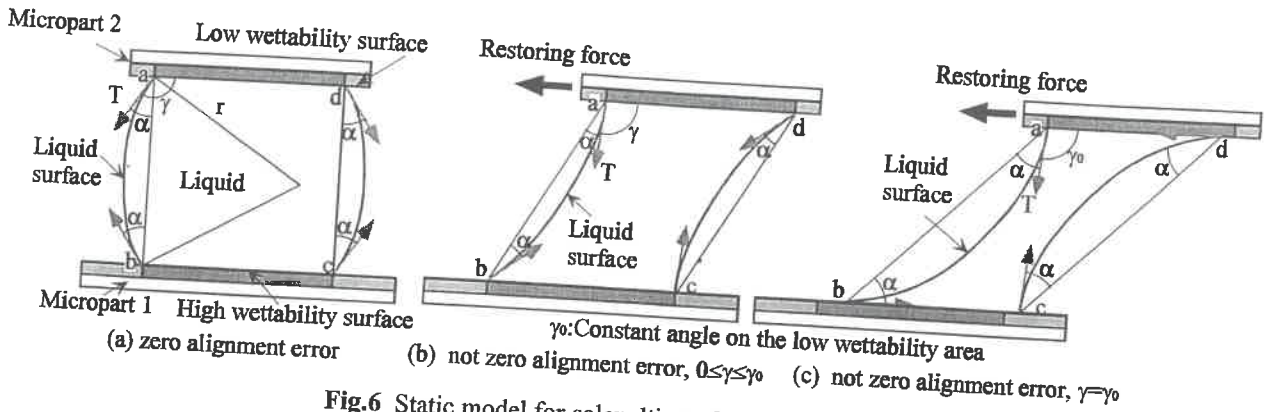

Fig.6 Static model for calcualtion of the restoring force

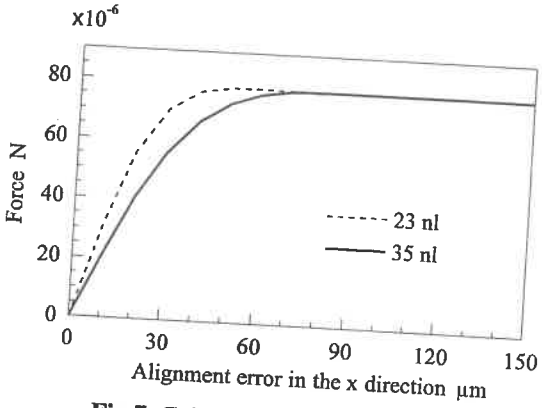

Fig.7 Calculated restoring force (I) (Square:0.8mmx0.8mm)

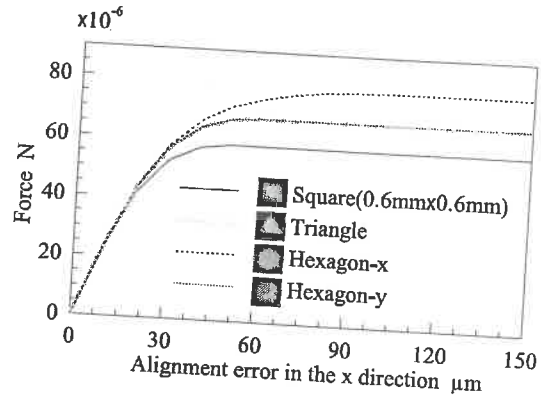

Fig.8 Calculated restoring force (II)

in next section.

3.3 Theoretical Analysis

Figure 6 illustrates a static model for calculation of the restoring force. In the model, the liquid droplet is modeled based on the following assumptions; (1) the radius of curvature of the liquid r is uniform, (2) the liquid exits only on the high wettability area surface and the thickness of liquid is uniform, (3) four angles of the tension from the straight lines ab or cd are equal to each other(see Fig.6), (4) the angle α changes or the liquid overflows only so that the wetting angle γ keeps in the range from 0 to the contact angle on the high wettability area (see Fig.6(b),(c)). Figure 7 shows theoretical restoring force in the linear direction with 23nl and 35nl based on the assumptions. When the alignment error is less than 60μm, the restoring force with the 23nl droplet is larger than that with the 35nl one. The experimental result with the 23nl droplet shows lower alignment error than that with the 35nl one. This fact indicates that the alignment error depends on the restoring force in case of no dry area on the high wettability one and no liquid overflow.

4. Effect of the High Wettability Area Pattern Change on Alignment Performance

In the alignment, the restoring force is generated on the boundary line between high and low wettability areas. Theoretically, its magnitude in each direction, depends on not only the total length of the line but also the area pattern. In this chapter, using three kinds of microparts which have different boundary patterns, the effect of the high wettability area pattern change on alignment performance is discussed experimentally and theoretically.

Theoretical restoring forces with three kinds of microparts which have different boundary patterns (square, triangle and hexagon), are shown in Fig.8. In this figure, two restoring forces by hexagon boundary patterns are illustrated. Hexagon-x pattern coincides with Hexagon-y one rotated 90°. All the microparts have the same length of boundary line. Each water volume used is determined so that each theoretical liquid thickness is similar to the other. When the initial error is larger than 20μm, Hexagon-x pattern produces the largest restoring force and the square pattern causes the smallest one.

Figure 9 illustrates the experimental alignment errors in the linear direction when the initial error is 100μm. The

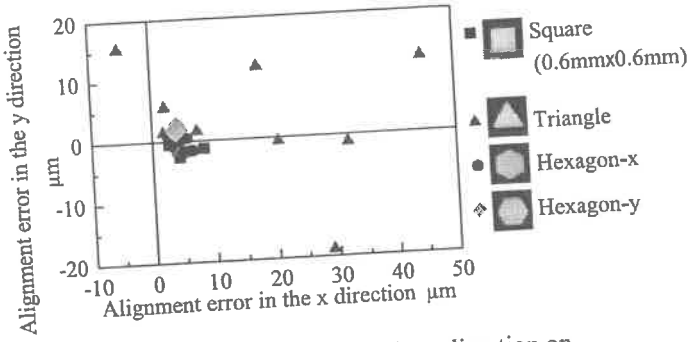

Fig.9 Effect of the initial error in the x direction on the alignment (I)

Fig.10 State of the water and the micropart after the alignment (triangle pattern)

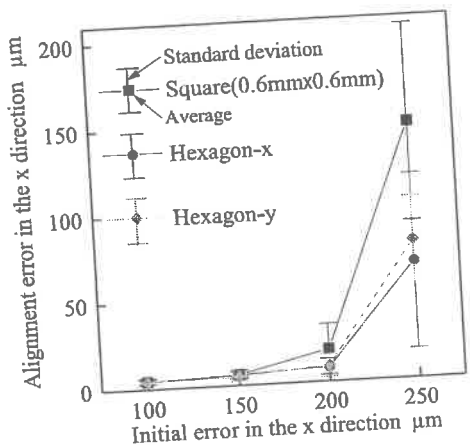

Fig.11 Effect of the initial error in the x direction on the alignment (II)

experimental average errors by two hexagon patterns and square one are smaller than 5μm. The average error by the triangle pattern is 15.4μm and larger than that by the others though the theoretical force by using triangle pattern is larger than that by the square one. Figure 10 shows the state of the water droplet and the micropart with the triangle pattern after the alignment. In the figure, an acute angle edge of the triangle in the circle is not covered with water and the water overflows the low wettability area. This behavior of the water droplet was observed using the micropart with the triangle pattern but not with the hexagon and the square ones. The results show that the difference of the high wettability area pattern can influence the behavior of the liquid droplet.

Figure 11 shows the average and the standard deviation of the alignment error when the initial error in the x direction is from 100 to 250μm. In each case, 10 similar alignments were made. In Fig.8, the restoring forces with the hexagon pattern microparts are larger than or equal to that with the square one. The difference between the forces increases with the increase of the error. In Fig.11, the alignment error using the microparts with the hexagon patterns is smaller than that with the square one, especially in case of the initial error lager than 150μm. The results show that the restoring force influences alignment performance well in case the water droplet does not behave like Fig.10.

5. Conclusions

In this paper, the factors which influence the alignment performance are examined experimentally and theoretically. The results indicate that the liquid overflow and the existence of dry area in the high wettability one cause low alignment accuracy, and that the alignment performance is influenced by the restoring force. Future work is to realize parallel alignment of many microparts.

Acknowledgments

This research was supported by a grant from JSPS Research for Future Program "Complex Integrated Machines" and carried out at the Vacuum Machining Laboratory in Tokyo Institute of Technology.

References

[1] T.Sato, K.Koyano, Y.Hatamura and M.Nakao: Construction and Evaluation of Micro-Object Manipulation System with Concentrated Motion, *Trans. Jpn.Soc.Mech.Eng.*, Vol.62, No.95-1125, (1996) 228-234 (in Japanese).

[2] K.Sato, S.Hata and A.Shimokohbe: Self-alignment for Microparts Assembly Using Water Surface Tension, *Pro. SPIE*, Vol.3892, (1999) 321-329.

Micro Multi-point Sheet Electrode for Auditory Brainstem Implant

Hirokazu TAKAHASHI[1], Takayuki EJIRI[1], Masayuki NAKAO[1],
Kiyoshi MATSUMOTO[1], Yotaro HATAMURA[1], Naoya NAKAMURA[2],
Kimitaka KAGA[2], and Thierry HERVE[3]

[1] Department of Engineering Synthesis, Graduate Shcool of Engineering, The Univ. of Tokyo
7-3-1 Hongo, Bunkyo-ku, Tokyo, JAPAN
[2] Department of otolaryngology, Graduate Shool of Medicine, The Univ. of Tokyo
7-3-1 Hongo, Bunkyo-ku, Tokyo, JAPAN
[3] TIMC-IMAG, Faculty of Medicine, Grenoble Univ.
38 706 La Tronche, Cedex, FRANCE

1. Introduction

For a future hearing rehabilitation of patients with bilateral acoustic neuromas, Auditory Brainstem Implant (ABI) has been on clinical trials. ABI is a prosthesis that bypasses a peripheral auditory pathway and directly stimulates the Cochlear Nucleus on the brainstem with an implanted electrode [1-3]. In order to improve the efficacy of ABI, medical and clinical knowledge for both stimulation and auditory functions are needed more, and several researches are being currently performed [4,5]. In conventional auditory physiological studies, however, glass pipet needle or silver ball recordings are common, which cannot provide enough spatiotemporal information [6,7]. In this paper, a multipoint sheet microelectrode for direct cortical recordings is proposed and its feasibility is tested on the Auditory Cortex of rats. Using this electrode, recordings of auditory evoked potentials (AEPs) and electrically evoked potentials (EEPs) with a high spatiotemporal resolution are reported.

2. Fabrication of the sheet electrode

The sheet microelectrode should satisfy following requirements: 1) It should have multiple recording points on the surface of the brain with a high spatial resolution. 2) It should not be invasive, and should be flexible enough to follow pulsation of the brain. 3) Its contact resistance should be small enough to detect microvolt-ordered evoked potentials. 4) It should be made of biomaterials, which do not react to brain tissues. The sheet electrode shown in Figure 1 has been fabricated with lithographic technologies. The cross section of the electrode is shown in Figure 2. The electrode has 32 recording points in a 2-mm-square area, which is the same size of the rat Auditory Cortex. An area opened for a recording site is 100-μm-square.

Figure 3 shows the process flow for the sheet electrode. A 25 μm thick polyimide film was spin coated with a 15 μm thick positive photoresist and then exposed to ultraviolet light through a photomask (a). After developing, the

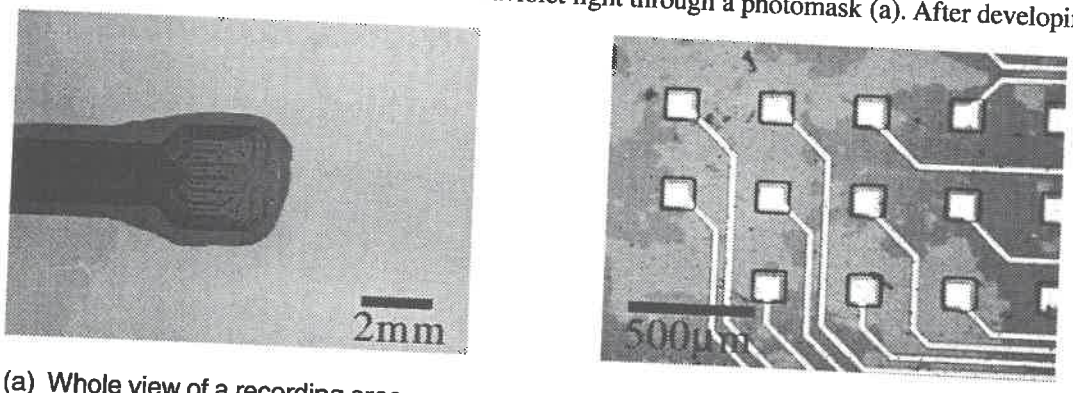

(a) Whole view of a recording area

(b) Magnification of the tip

Figure 1. Micro multi-point sheet electrode

laminante was etched with a fast atom beam to make 1 μm deep trenchs on the polyimide film (b). As a conducting layer, 0.2 μm thick gold was deposited, followed by the deposition of small quantity of chromium (c). By means of making the 1 μm deep trenchs on the polyimide film and the thin chromium layer beneath the gold layer, the gold-polyimide bond are promoted and the photoresist can be removed easily. After the photoresist layer was removed, photosensitive polyimide was spin coated on the whole surface as an insulator layer, and it was removed at recording points by ultraviolet exposure (d). Finally, the photosensitive polyimide at the recording points was removed completely through O_2 plasma etching (e).

The contacting resistance of the electrode is about 20-40 kΩ, which is proved to be small enough for cortical recordings of AEPs.

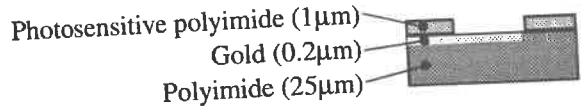

Figure 2 Cross section of a recording point of the electrode

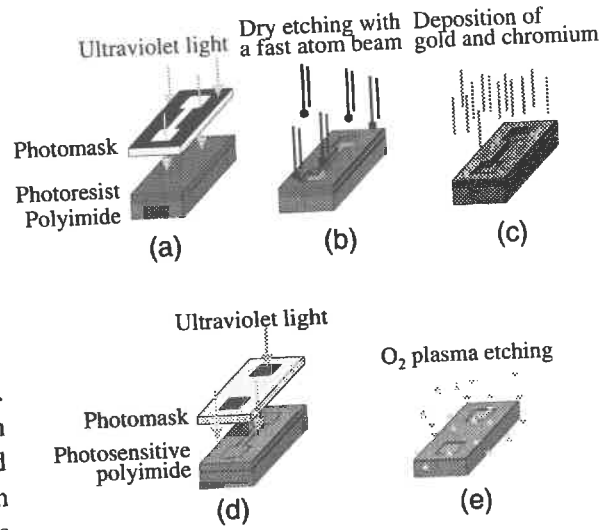

Figure 3 Process flow for the sheet electrode. For details, refer to the text.

3. Experimental setup

3.1 Animal preparation

10 Adult albino rats with normal ABR (Auditory Brainstem Response) and weighing 200-300g were used. Each animal was intraperitoneally anesthetized with pentobarbital (50 mg/kg). The temporal skull was removed to expose the Auditory Cortex, and then part of the cerebrum was aspirated to expose the Cochlear Nucleus. A hole was drilled at the vertex in order to insert the reference electrode and another hole was drilled 7 mm more frontally in order to insert the ground electrode. Those two electrodes are 0.5-mm thick pins of sockets used for integrated circuits. They were placed so as to make electrical contact with the dura, and they were fixed to the skull with dental cement. The rats' head was fixed in a stereotaxic holder. The sheet

(a) Whole View

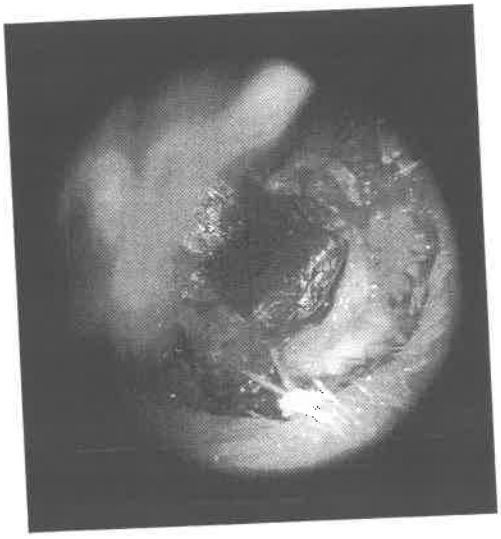

(b) Magnification

Figure4 Views of the electrode mounted on the Auditory Cortex of a rat under anesthesia.

electrode was mounted on the Auditory Cortex for recording as shown in Figure 4. Then, for stumulating a concentric circular needle electrode of whcih diameter at the tip is 0.2 mm was mounted on the Cochlear Nucleus.

3.2 Experimental protocol

Alternating clicks at 90 dB UHL were delivered through a speaker located at 20 cm of the rat's head at the rate of 1 click/sec. Following acoustic stimulation, the Cochlear Nucleus was stimulated electrically. The electrical stimuli were monophasic, bipolar, and constant-current pulses with a duration of 100 µs and an amplitude of 75 mA. The repetition rate used for evoked potential recordings was 1 click/sec.

A 32 channels amplifier (NEC, Biotop 6R12-4) was used for simultaneous recording of 32 vertex positive AEPs with the sheet electrode. Each signal was filtered with a bandpass of 50 Hz - 1500 Hz, -12 dB/oct. AEPs or EEPs were obtained by averaging over 100 responses.

The experiments were perfomed in accordance with the guidelines of "Animal Experiments Committee of Tokyo University".

4. Result

Figure 5 shows an example of 32 AEPs of 0 - 50 msec detected with the sheet electrode. A different recording point obtains a different response in amplitudes and latencies. Figure 6, which was built on the data of Figure 5, shows AEPs distribution patterns that are coded by circle sizes. Figure 7 shows an example of the EEPs and Figure

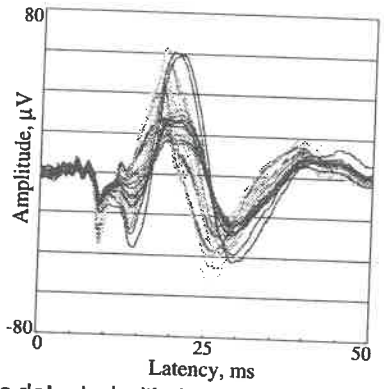

Figure 5 AEPs detected with the microelectrode. Each wave profile is coresponding to a response from each recording pad.

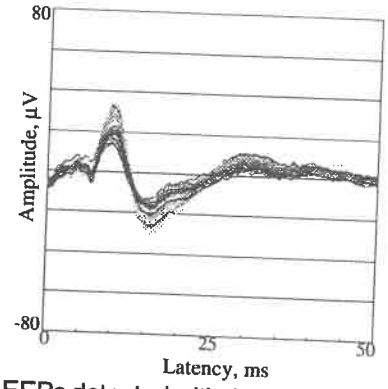

Figure 7 EEPs detected with the microelectrode. Each wave profile is coresponding to a response from each recording pad.

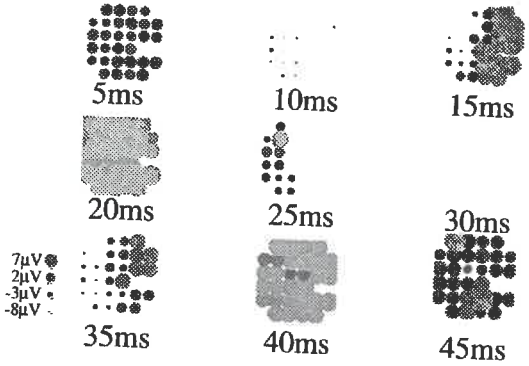

Figure 6 Potential distribution paterns of the AEPs on a rat auditory cortex. The amplitude of the response detected by each pad is coded by a circle size, and the latency from the onset of the stimule is shown below each respose representation.

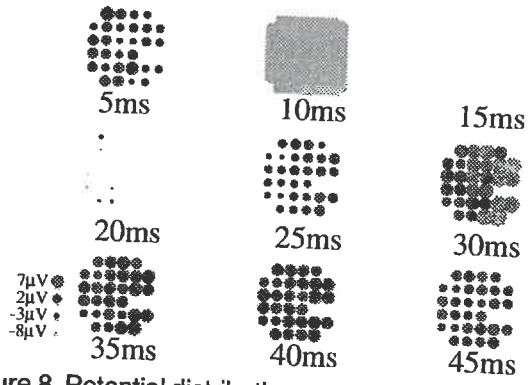

Figure 8 Potential distribution paterns of the EEPs on a rat auditory cortex. The amplitude of the response detected by each pad is coded by a circle size, and the latency from the onset of the stimule is shown below each respose representation.

8 shows the EEPs distribution patterns. A different recording point obtains a different response in amplitudes, but not in latencies.

5. Discussion

This result indicates that the multi-point sheet electrode can give us high-resolution spatiotemporal neuronal data of cortical activities, which could not be explored by conventional physiological methods. In order to discuss about functions of auditory pathways, relations between acoustic stimuli and cortical responses should be explored. Especially, Tonotopic organizations on the auditory cortex should be found out with the electrode [6,7].

EEPs and their distribution patterns can also be obtained with the sheet electrode, but the disparities between signals of each point are smaller than those of AEPs. It can be infered that the stimulating electrode was too large for functional stimulation. If the electrode were small enough to stimulate neurons more selectively at the Cochlear Nucleus, more dynamical responses could be recorded on the Auditory Cortex.

In order to provide useful information for designing the future ABI, AEPs and EEPs should be compared, and then efficient electrical stimulations for ABI should be discussed in our future works.

6. Summary

In this paper the sheet multi-point microelectrode is proposed, fabricated, and used for direct recording of AEPs on a rat auditory cortex. It is flexible enough, biocompatible, and has 32 recording points. Using the electrode, AEPs that were recorded simultaneously at 32 points showed significant disparities. EEPs were also recorded with the sheet electrodes, but did not show significant disparities.

Achknowledgement

This study was supported by the Promotion of Fundamental Studies in Health Science of the Organization for Drug ADR Relief, R & D Promotion and Product Review of Japan.

References

[1] Steven R. Otto, Robert V. Shannon, Derald E. Brackmann, et al: "The multichannel auditory brarin stem implant: Performance in twenty patients." Otolaryngology Head and Neck Surgery, 118, 3: 291-303, 1998

[2] Derald E. Brackmann, William E. Hitselberger, Ralph A. Neson, et al: "Auditory brainstem implant: I. Issues in surgical implantation." Otolaryngology- Head and Neck Surgery, 108: 624-633, 1993

[3] Robert V. Shannon, Jose Fayad, Jean Moore, et al: "Auditory brainstem implant: II. Postsurgical issues and performance." Otolaryngology- Head and Neck Surgery, 108: 634-642, 1993

[4] Douglas B. McCreery, Robert V. Shannon, Jean K. Moore, et al: "Accessing the tonotopic organization of the ventral cochlear nucleus by intranuclear micro stimulation." IEEE transactions on rehabilitation engineering, 6, 4: 391-399, 1998

[5] Hussam K. EL-Kashlan: "Multichannel cochlear nucleus stimulation." Otolaryngology- Head and Neck Surgery, 121, 3: 169-175, 1999

[6] Junsei Horikawa, Susumu Ito, Yutaka Hosokawa, et al: "Tonotopic representation in the rat auditory cortex." Proceedings of Japan Academy, 64, B: 260-263, 1988

[7] Sharon L. Sally and Jack B. Kelly: "Organization of auditory cortex in the albino rat: Sound Frequency." Journal of Neurophisiology, 59, 5: 1627-1638, 1988

Design of a Precision Electro Discharge Micro Milling Machine

King-Fu Hii, Xiaohui Zhao, and R. Ryan Vallance

Precision Systems Laboratory, University of Kentucky, Lexington, KY *

Abstract

This paper presents the design of a precision electro discharge micro milling machine being designed and built in the Precision Systems Laboratory at the University of Kentucky. This machine will use micro electrodes to mill complex 3D cavities with electrical discharges between an electrode tool (cathode) and a workpiece (anode) submerged in dielectric fluid. The machine entails three axes of motion consisting of a pre-existing XY stage and a new Z stage with spindle. The objectives in designing this machine are to achieve high precision for large workpieces and to develop an open architecture machine controller for micro EDM. The CAD data documenting this machine design is available free through the Open Design Foundation. These solid models can be downloaded by any party, and they may be used, modified, or redistributed as long as the machine remains an Open Design. This paper presents two concepts for the new z-stage and spindle. One concept uses a flexure for fine motion during micro machining, and the spindle is held on a plate that is guided with air bushings to accommodate a range of workpiece heights. The second concept is a conventional vertical column with a head and spindle. The two concepts are compared using error budgets.

Keywords: precision, machine design, micro EDM, micro machining, electro discharge machining

Introduction

Material-removal processes such as milling have been scaled to the micron scale [1], [2], [3]. The most successful accomplishment is probably single-point diamond machining [4], [5], which is commercially available. However, the challenge in cutting microstructures arises from the fragility or compliance of the microstructure and the tools being subjected to cutting forces. In addition, mechanical cutting produces burrs, and some applications require that the burrs be removed with post-machining processes. For these reasons, alternative micro-machining techniques [6] that produce little or no cutting forces and do not produce burrs can be favorable. One alternative is micro electro discharge machining (μEDM), an electro-thermal process where electrical sparks between an anode and cathode submerged in a dielectric fluid melt and erode material.

Practical machining with anode or cathode erosion from electrical discharges in a dielectric fluid began in the 1940s. Since then, wire EDM and sinking EDM have become standard techniques for manufacturing high-precision tooling. Since electrical discharges do not require mechanical contact, they are well suited for machining at the micro scale. In the early 1980s, researchers began applying EDM to drill microholes [7]. Then in 1985, Masuzawa described an innovative microfabrication process called wire electro discharge grinding (WEDG) [8]. WEDG machines a cylindrical workpiece with discharges between a traveling wire and the workpiece. This process enables the fabrication of a variety of shapes by controlling the position of the wire guide in the x and y directions and the position of the workpiece in the z direction. Microshafts

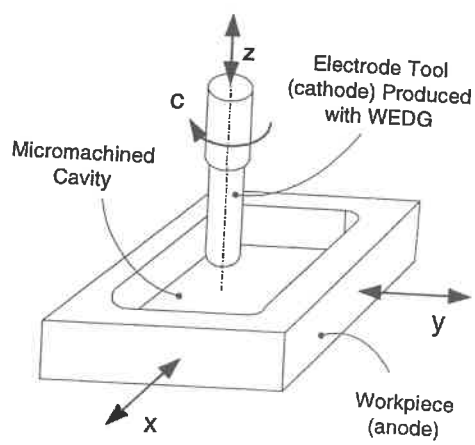

Fig 1: Micro Milling with Electrical Discharges

* *210-A CRMS Building, Lexington, KY 40506. http://www.engr.uky.edu/psl.*

manufactured with WEDG can subsequently be used for micro milling or drilling, as illustrated in Fig 1.

In 1990, Matsushita received a patent for a μEDM machine that integrated WEDG and drilling/milling into a single machine [9]. This machine is now available from Panasonic Factory Automation in the United States. The machine handles workpieces up to about 140 x 150 mm in size, and it is rated for a positioning accuracy of 1 μm over a 10 mm range and 2 μm over a 100 mm range.

This paper introduces a new machine for electro discharge micro milling being developed at the Precision Systems Laboratory at the University of Kentucky. This machine will be licensed as an Open Design with full documentation available through the Open Design Foundation. The Open Design license permits anyone to use, modify, improve, or distribute this machine as long as the machine remains an Open Design. Details of the license agreement are available at the Open Design Foundation's web site[†].

Overview of Machine

The objectives in designing this new machine are 1) to improve precision to less than 1 μm for large workpieces (around 200 x 150 mm) and 2) to develop an open architecture controller for integrating machine control, process monitoring, and motion planning.

The machine currently uses an XY positioning stage, illustrated in Fig 2, which was adopted from a surplus mask aligner. The XY Stage is built upon a granite slab (760mm x 1190mm x 200mm) that is pneumatically isolated from the floor. Y-axis motion is provided by a structural stage (y-stage) that is supported by five air bearing pads (with vacuum preload). Two of the bearings guide the y-stage along the edge of the granite, and three of the bearings float the y-stage on the top surface of the granite. The y-stage is positioned by a drive system that consists of a DC servomotor (mounted on the y-stage) that rolls along a friction drive link connected through a spherical joint to a stationary support on the granite. Position is sensed with a plane mirror interferometer.

The x-axis motion is provided by a structural stage (x-stage) on the granite's top surface that uses four air bearings on the bottom of the x-stage. Two additional air bearings preload the x-stage against the y-stage. The y-stage therefore acts similar to a drafting T-square. The x-stage is positioned with a drive system consisting of a DC servomotor (mounted on the y-stage) that pushes a friction drive link, attached to the x-stage through a flexure. Position is sensed with a plane mirror interferometer.

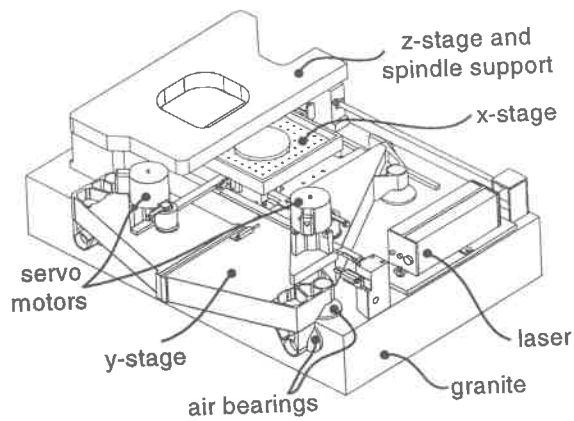

Fig 2: XY Stage in the Open Electro Discharge Micro Milling Machine

Concepts for the Z-Axis and Spindle

This section briefly describes two conceptual designs for adding z-axis motion to the xy-stage and a spindle for electrode rotation. The z-axis motion should accommodate a range of workpiece heights but still position the electrode or workpiece with high resolution and precision. Workpiece heights may vary from less than 6mm to around 25mm thick. When micro machining, the machine should be capable of positioning the electrode in the z-direction over a range of around 100 μm. These functions may be separated into two separate subsystems or be integrated into the same subsystem.

Flexure Concept for Z-Stage

A concept that uses a flexural bearing and PZT actuator for fine motion in the z-direction is illustrated in Fig 3. In this figure, the flexure and actuator are integrated into the x-stage. The flexure supports a round worktank for holding the dielectric fluid and workpiece. A circular flexure is located near the workpiece height in the z direction to reduce Abbe errors. The centers of the worktank, flexure, and actuator are coaxial. A PZT actuator with at least 100 μm travel can be used or a PZT with shorter stroke can be amplified with a mechanism. The electrode tool would be held above the workpiece and rotated with a motor driven, air bearing spindle. A variety of workpiece heights is accommodated by pre-adjusting the height of the spindle, which is supported on a plate guided with air bushings. Variants of this concept might locate the flexure on

[†] http://www.opendesign.org

of the spindle or support the spindle on top of a stiff flexure.

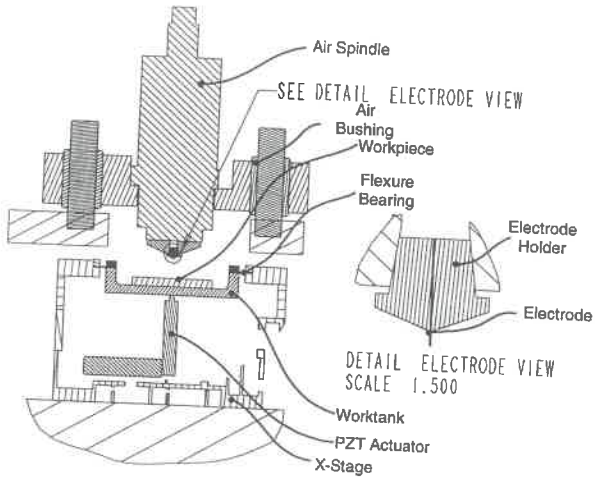

Fig 3: Flexure Concept

Column Concept for Z-Stage

As illustrated in Fig 4, this concept supports the motorized air bearing spindle on precision (±5 μm over 200 mm rail) linear guides with recirculating ball (or roller) bearings. The carriage is driven through a flexible coupling with a servomotor and screw that is mounted on the support column. In this concept, the course and fine motions are provided by a single bearing system and actuator in the z direction. The worktank is mounted directly on the x-stage. The air spindle will have more travel range (around 200 mm) along the z-axis. Additional Abbe error from the offset roller bearings reduces the accuracy of the machine. Variants on this concept could use other types of linear bearings (such as air bearings) or other drive system (such as friction drive).

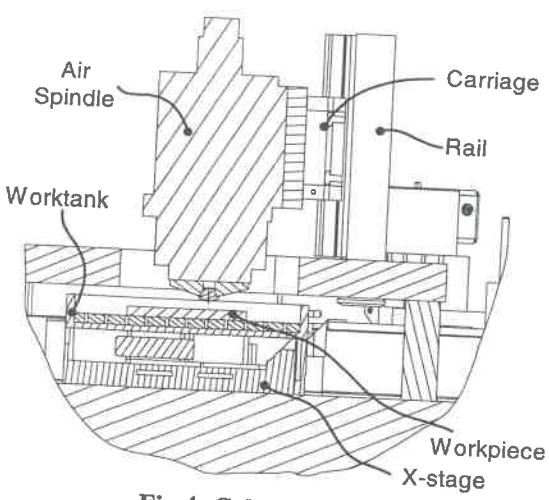

Fig 4: Column Concept

Error Budgets for Concepts

The random errors of the flexure concept are anticipated using an error budget. At this time, the error budget is predictive, but actual errors will be experimentally measured. The estimated errors are based on 6 standard deviations. Table 1 shows the error budget for the flexure concept. The error budget predicts a positioning error of 0.6 μm in the x direction and 0.7 μm in the y direction over a 200 mm range, and 0.7 μm in the z direction over a 10 mm range. The error budget for the column concept predicts a positioning error of 3.9 μm in the x direction and 4.5 μm in the y direction (over a 200 mm range), and 0.7 μm in the z direction (over a 10 mm range). Both of the design concepts are acceptable. However, the higher precision in the flexure concept is preferable for ultra precision machining.

Open Architecture Controller

An open architecture controller is being designed to control the motion of the workpiece and electrode. The controller will use a plane mirror interferometer, isolated in a separate metrology frame as shown in Fig 2, to measure the x and y position of the stages. Sensing in the z direction will be incorporated into the design of the z-stage. The controller consists of a motion I/O card with three 16-bit DACs and three encoder inputs for A-Quad-B signals (PMDi, Inc.). The motion I/O card is used in a PC running the QNX real-time operating system. Real-time motion control will be implemented in software running on the host CPU. The controller will be capable of reading and interpreting standard G&M codes for specifying tool paths.

Conclusions and Future Work

This paper introduced the electro discharge micro milling machine being designed and built by the Precision Systems Laboratory at the University of Kentucky. Two concepts for adding z-axis motion to a pre-existing x-y stage were described and compared using error budgets. An open architecture controller for the machine was also briefly described. The documentation for this machine is being licensed as an Open Design and is available free through the Open Design Foundation.

Future work for this machine includes the detailed design and fabrication of the z-axis stage, machine metrology and error assessment, and implementation of the machine controller.

BUDGET ERROR ANALYSIS FOR MEDM MILLING MACHINE (Flexure Concept)	X-AXIS (nm)	Y-AXIS (nm)	Z-AXIS (nm)	ANGLE (rad)	ABBE X (m)	ABBE Y (m)	ABBE Z (m)	Notes
ERROR SOURCES								
X-AXIS STAGE KINEMATICS								
Positioning inaccuracy in X, dxx	100.0							Mostly due to servo and feedback
Nonstraightness of X in Y, dxy		350.0						Mostly due to y-stage flatness
Nonstraightness of X in Z, dxz			347.7					Mostly due to granite flatness
Angular motion of X about X (roll), exx		0.0	208.6	1.37E-06		0.1524		Little Effect on Z Direction
Angular motion of X about Y (pitch), exy	0.0		208.6	1.37E-06	0.1524			Little Effect on X Direction
Angular motion of X about Z (yaw), exz	0.0	134.6		4.42E-07	0.3048			Little Effect on X Direction
Y-AXIS STAGE KINEMATICS								
Nonstraightness of Y in X, dyx	347.7							
Positioning inaccuracy in Y, dyy		100.0						Mostly due to servo and feedback
Nonstraightness of Y in Z, dyz		0.0	0.0					Little Effect on X Axis Stage
Angular motion of Y about X (pitch), eyx		0.0	0.0					Little Effect on X Axis Stage
Angular motion of Y about Y (roll), eyy	0.0		0.0					Little Effect on X Axis Stage
Angular motion of Y about Z (yaw), eyz	0.0	291.6		4.42E-07	0.6604			Effects Yaw and Y of X Stage
Z-AXIS STAGE KINEMATICS								
Nonstraightness of Z in X, dzx	20.0							
Nonstraightness of Z in Y, dzy		20.0						
Positioning inaccuracy in Z, dzz			20.0					
Angular motion of Z about X (pitch), ezx		20.0	20.0					
Angular motion of Z about Y (yaw), ezy	20.0		20.0					
Angular motion of Z about Z (roll), ezz	20.0	20.0						
SPINDLE KINEMATICS								
Radial motion in X, dcx	76.2							
Radial motion in Y, dcy		76.2						
Axial motion, dcz			76.2					
Tilt motion about X, ecx		7.0	0.0					
Tilt motion about Y, ecy	7.0		0.0					
TOOL AND WORKPIECE								
Tool position (tool set or measure.)	200.0	200.0	200.0					
Nonrepeatibilty of tool change	400.0	400.0	400.0					
THERMAL								
Expansion/Contraction in Z-Stage	0.0	0.0	177.6					X and Y expansion balanced up
Root Sum of Squares (RSS)	581.3	665.4	668.2					

Table 1: Error Budget for Flexure Concept [10]

Acknowledgements

This work is being conducted at the University of Kentucky with funding from the UK College of Engineering.

References

[1] Friedrich, C.R. and M.J. Vasile. "Development of the Micro Milling Process for High Aspect Ratio Microstructures". *Journal of MEMS*. Vol. 5, No. 1. 1996. p. 33-38.

[2] Vasile, M.J., C.R. Friedrich, B. Kikkeri, and R. McElhannon. "Micrometer-Scale Machining: Tool Fabrication and Initial Results". *Precision Engineering*. Vol. 19. 1996. p. 180-186.

[3] Schaller, Th., L. Bohn, J. Mayer, and K. Schubert. "Microstructure Grooves with a Width of Less than 50 µm Cut With Ground Hard Metal Micro End Mills". *Precision Enginerring*. Vol. 23, No. 4. Oct, 1999. p. 229-235.

[4] Brehm, P.D. "Diamond Turning and Flycutting for Precision". SME Technical Paper, No. MR770965. 1977.

[5] Bryan, J.B. "Design and Construction of an Ultra Precision 84 Inch Diamond Turning Machine". Precision Engineering. Vol. 1, No. 1. 1979. p.13-17.

[6] Masuzawa, T. and H.K. Tönshoff. "Three-Dimensional Micromachining by Machine Tools". Keynote Paper. *Annals of the CIRP*. Vol. 46, No. 2. 1997. p. 621-628.

[7] Sato, T., T. Mizutani, and K. Kawata. "Electro-Discharge Machine for Micro Hole Boring". *National Technical Report*. Vol. 81, No. 5. Oct. 1985. p. 105-113.

[8] Masuzawa, T. "Wire Electro-Discharge Grinding for Micro-Machining". *Annals of the CIRP*. Vol. 34, No. 1. 1985. p. 431-434.

[9] Masaki, T., T. Mizutani, K. Yonemaochi, and A. Tanaka. "Electric Discharge Machining Method and Apparatus for Machining a Microshaft". U.S. Patent #4,900,890. Issued Feb. 13, 1990.

[10] Hale, L. C. *Principles and Techniques for Designing Precision Machine*. Ph.D. Thesis. Massachusetts Institute of Technology. Cambridge, MA, USA. Feb, 1999.

The New Long Range Multi-axis Nanopositioner using Inertial Slider/Walking Method

Jong Y. Shim, Hewon Chung and Dae-Gab Gweon
Department of Mechanical Engineering, Korea Advanced Institute of Science & Technology 373-1 Kusong-Dong, Yusong-Gu, ME3265, Taejon 305-701, Korea

Introduction

Ultraprecision positioning mechanism with both long moving range and nanometer resolution is more and more required in the field of precision engineering and many efforts are made to meet this requirements such as inertial slider, inchworm, magnetic levitation stage etc [1][2][3]. In the precision sample measurement applications (STM, AFM, TEM, SEM), the positioning stability is also an important design consideration[4]. To meet these requirements a nanopositioner is designed using inertial slider and inertial walking method. The resulted travel range is 50mm×50mm and positioning resolution is a few nanometers.

The inertial slider motion is caused simply by a saw-tooth-like periodic acceleration of a piezoelectric element and the inertia of the moving stage. The body can travel long distance comprised of many small steps (nanometer to microns) by the stick-slip effect between two contact solids. The inertial walking method has an advantage of stability which is accomplished by the supporting rod. Instead of the tube PZT, the three rods support the moving body and good stability is obtained. Inertial walking method has expansion and contraction of the tube PZT in the voltage input sequence which is somewhat different from inertial slider.

The new nanopositioner has simple structure and can be operated with either method and is always on the base surface by the three contact points.

Operating Principle

The designed nanopositioner consists of three-tube-PZT (sapphire ball at the one end of each tube), three supporting rods, moving body, mirror surface base (See Fig.1). The three rods and three PZTs are located at the vertex position of the hexagon which is the body hole shape. Simple operation can make stage have three to six degree-of-freedom motion. The three planar motion(X,Y,Θ) have unlimited motion range and nanometer(micro radian) resolution and in the other three DOF motion travel range is limited by the expansion of tube PZTs. Two operating methods, inertial slider and walking, can be adopted. Inertial slider operation is the one which is the same as conventional operation except for the complexity

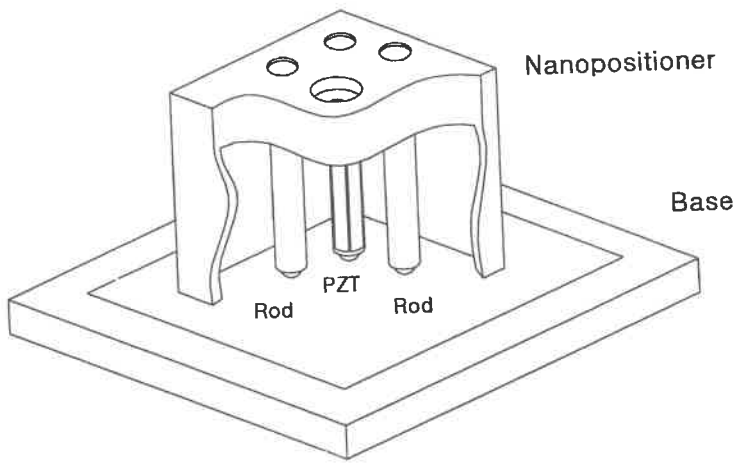

Fig. 1. Schematic view of the nanopositioner

of the actuation and inertial walking method is the new one of which cycle is composed of the actuation of three tube PZTs along with expansion and contraction. When the body is stationary phase, it is on the base by the supporting rod. The second method can eliminate PZT drift problems and will show more stable position maintaining characteristic.

Figure 2 shows the two operating principles. The left column sequence is the inertial slider operation and the right column is the inertial walking. Inertial slider method can make motion by the stick-slip effect between contact surfaces, sapphire ball and mirror-surface, and the slip motion phase is shown in the second figure(left column) and the slip can be made by the deflection of the tube PZTs. The third figure shows the stick phase, thus motion occurring, of which acceleration is relatively low.

In the inertial walking method, at first, expansion of the PZTs occurs (the second figure in the right column), and the next, the body moves by the deflection to the right(the third figure). In the last sequence contraction and deflection are followed and actuation sequence is repeated.

The fig. 2 is one dimensional movement principle schematic but the planar 3-DOF motion can be obtained by extend one dimensional movement to the planar motion. Figure 3 shows the motion direction(by deflection) of the tube PZTs and when signal inputs are applied for each PZT to have direction as shown in the figure, translational and rotational motion can be obtained.

Mechanical Design

The size of the mirror-surface base is 100mm x 100mm and the material is stainless-steel with hard chrome plated. The moving body weighs about 150g and has dimension of 50mm×50mm×48mm. The tube PZT[5] is four segmented type and has maximum contraction of 6μm. The outer diameter is 6.35mm and inner diameter is 5.15mm with 30mm tube length. Therefore the maximum deflection is about 20μm.

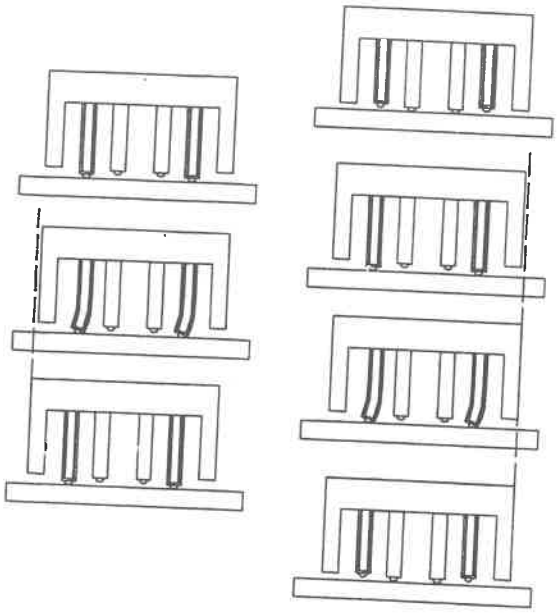

Fig. 2. Two operating methods (inertial slider and inertial walking)

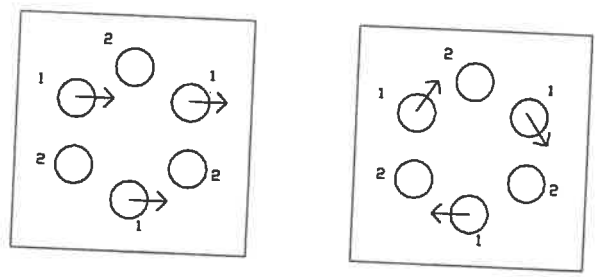

Fig. 3. Method of translational and rotational motion of the moving body

Considering charge constants and mechanical Q, the PZT material is selected to have good waveform-input following characteristic. For the stability and desirable inertial motion, a sapphire ball(6mm diameter), which has high hardness, is attached to the end of the tube PZT by the glue(Epoxy). Also the supporting rod has a hard steel ball at it's end.

Electrical Design

The tube PZT has a 500V maximum voltage input and the actuating waveform frequency is in the range of a few kHz. Therefore 15 channel (12 for outer electrode and 3 for inner electrode) PZT driver which has at least 10khz bandwidth is needed and must not have nonlinear characteristic as possible such as signal distortion. PA88 [6] op-amp is used for high voltage amplification and about 30khz bandwidth and negligible distortions are obtained with designed driver.

For generating waveform signals, PC-based waveform generators are adopted [7] and it can generate siganals at the rate of 1Msamples/sec.

Discussion

A multi-DOF nanopositioner was developed, having long moving range and nanometer resolution, and it

slider and inertial walking). Mechanical and electrical components was developed and experiments are being processed. Using laser interferometer and capacitive sensors, the control experiments of the nanopositioner are in the recent work.

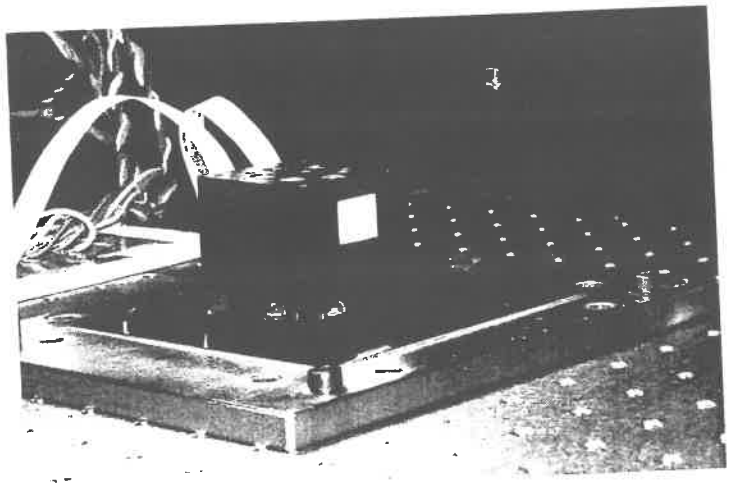

Fig. 4 Picture of the multi-axis nanopositioner

References

[1] K. Besocke, "An Easily Operable Scanning Tunneling Microscope", Surf. Sci., **181,** 145(1987)

[2] D. W. Pohl, "Dynamic piezoelectric translation devices", Rev. Sci. Instrum., **58**, 54(1987)

[3] Wonjong Kim and David L, Trumper, "High Precision magnetic levitation stage for photolithography" , Pre. Eng., **22**, 66(1998)

[4] L. Libioulle, A. Ronda, I. Derycke, J. P. Vigneron, J. M. Gilles, "Vertical two-dimensional piezoelectric inertial slider for scanning tunneling microscope", Rev. Sci. Instrum., **64**, 6(1993)

[5] PT130.14, Physik Instrumente, D-76337, Waldbronn

[6] PA88, Apex Microtechnology, 5890 N. Shannon Road, Tucson AZ 85741-5230

[7] PCI-6713, National Instrument, National Instruments Corporation 11500 N Mopac Expwy Austin, TX 78759-3504

New artifacts for calibration of large CMMs

Markus Bartscher, Konrad Busch, Matthias Franke, Heinrich Schwenke and Franz Wäldele
Physikalisch-Technische Bundesanstalt, CMM Section, 38116 Braunschweig, Germany

Contact: markus.bartscher@ptb.de

Key Words: coordinate measuring machines (CMMs), CMM calibration, dimensional artifacts

Abstract

Especially in car and aircraft industry large coordinate measuring machines (CMMs) are widely used. The calibration of these CMMs with conventional tools like lasers, level meters or straight edges is costly and scarcely practical. This paper deals with new 2D artifact-based techniques for the error mapping for large CMMs. This work is part of the European Standards, Measurements and Testing Programme[1]. Participants are Physikalisch-Technische Bundesanstalt PTB (Germany), Istituto di Metrologia "G. Colonnetti" IMGC (Italy), Brown & Sharpe DEA (Italy), Carl Zeiss (Germany), Trimek (Spain), Volkswagen Navarra (Spain) and Czech Metrological Institute CMI (Czech Republic).

Introduction

Calibration and numerical error correction of CMMs require a mathematical model of the error behavior and methods to assess the errors. While for small and medium-sized portal-type CMMs the rigid-body error model fits well with the real behavior, this is not so for large CMMs. Large horizontal arm CMMs and to some extent also large bridge type CMMs show elastic errors which cannot be properly modeled up to now. The assessment of the CMM error map for smaller CMMs can be performed by measuring calibrated ball or hole plates (up to 960 mm x 960 mm in size) in defined positions [1]. This method is time- and cost-effective compared to the use of lasers and other dedicated tools like levels and straight edges. Unfortunately ball plates cannot be simply upscaled for the error mapping for large CMMs because of among other things weight, elasticity and thermal problems. Hence the model and the error assessment have to be adapted to large CMMs.

Error model adapted to large horizontal arm CMMs

The rigid-body model is a good starting point for an effective model of large CMMs. It provides a clear idea of the error nature. Additionally, numerical correction algorithms based on the rigid-body model have been implemented in most CNC-driven CMMs. Therefore it suggests itself to keep this model as a basis and to expand single rigid-body error functions by additive elastic error terms. As elastic effects of horizontal-arm CMMs are related to the column, three elastic functions are found to be significant [2, 3]: the elastic roll error $xrx(x,z)$ of the x-slide, the elastic straightness error of the vertical axis $ytz(y,z)$ and the related pitch error $yrx(y,z)$. All elastic effects are proportional to the ram extension z:

elastic roll of x-slide	$xrx(x,z)$	$= C(x)\cdot z$	(column tilt)
elastic column straightness	$ytz(y,z)$	$= B(y)\cdot z$	(column bending)
elastic pitch	$yrx(y,z)$	$= A(y)\cdot z$	(column bending)

The designation of axes x, y, z follows the kinematic chain (cf. Fig. 1). The model is extended here to cover column tilt errors of horizontal arm CMMs with a long x-stroke [4]. Therefore the model parameter C is not treated as a constant [2, 3] but as an x-dependent function $C(x)$. All elastic model functions $A(y)$, $B(y)$, $C(x)$ (designation according to [2]) are specific to the design of the CMM. CMMs of the gantry type show different elastic errors and have to be treated separately.

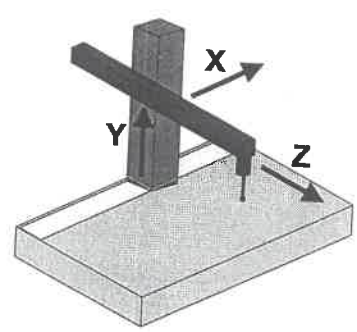

Fig.1: Designation of CMM axes according to the kinematic chain

[1] SMT4-CT97-2183: "MESTRAL"

New artifacts adapted for the error mapping of large horizontal arm CMMs

Design

The error mapping of large CMMs up to a certain size should be performed by calibrated material measures such as ball or hole plates as these present obvious advantages. The artifacts must be adapted in size to the large CMMs.

To overcome problems due to the required size, large artifacts should have certain features: They should be dismountable to overcome transport problems. Main components should be built from simple geometry elements to allow effective manufacture. Therefore L-shaped dismountable 2D artifacts [3] have been manufactured. They include two main tube components (Fig. 2, 3 m and 1,5 m), which carry precision spheres. Calibrated sphere positions provide length and straightness reference. The spheres are probed by the CMM in defined artifact positions for rigid-body and elastic error mapping [3]. The tubes of the 2D artifact can also be applied for CMM verification using only the given length information.

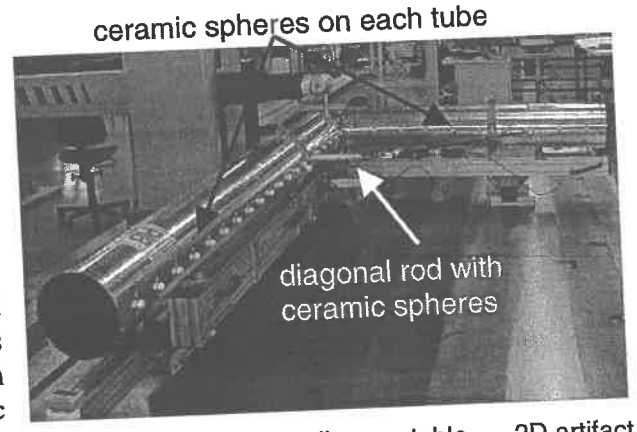

Fig. 2: L-shaped dismountable 2D artifact 3 m x 1,5 m with mounting equipment

Material

Due to the weight, the use of an artifact is limited by practical handling aspects and by the induced bending. Therefore carbon fiber reinforced plastics (CFRP) as a light weight material has been used for the artifact's main tube components. CFRP tubes can be manufactured by the fiber winding process, which is an industry-proven, cost-effective and variable process. Additionally, it allows the use of high modulus (HM)-fibers to make the structure as stiff as possible. CFRP components have been protected by aluminum foil to avoid air humidity-induced changes in the artifact dimensions [3]. The analysis of the length measurements shows that the stability of the CFRP material is sufficient for use as large CMM calibration artifacts (constancy over half a year: 5 µm over 3 m length). For measurements in facilities without air-condition, the CFRP length expansion coefficient of $+0.9 \cdot 10^{-6}\,K^{-1}$ has to be taken into account.

Mounting

The use of dimensional artifacts always requires stable mounting. Absolute minimization of bending and bending changes can be achieved by multiple-point mounting. Here a quite uncommon but most effective method is applied, which is both flexible and stable: a coupled passive hydraulic system provides the same force for every supporting point of the artifact (Fig. 3).

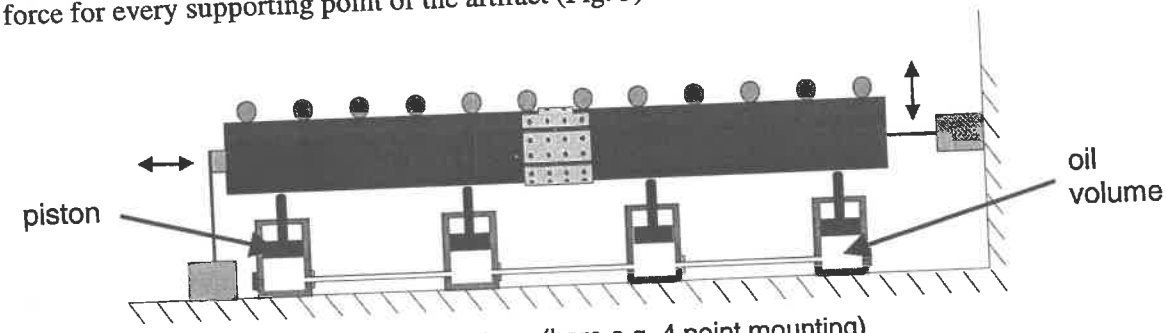

Fig. 3: Scheme of the hydraulic mounting system (here e.g. 4 point mounting)

Calibration

The calibration of larger artifacts is a difficult task. For handling and transport reasons, artifacts are not allowed to be extremely heavy, which itself might provide long-term calibration stability. Therefore environmental and transport effects can strongly influence large artifacts of reasonable dimensions and weight. One solution to this dilemma is to calibrate artifacts at the customer's site just before use (in-situ calibration). 2D artifacts embody length and straightness reference. Therefore we use a two-step calibration procedure: comparison of the 2D artifact sphere distances against a length standard with a mobile comparator (Fig. 4 and 5) and a reference-free straightness calibration on the CMM. The calibration data show that a procedure with a four-position reversal about both artifact sides yields best results. Three additional horizontal positions are required here, which is a reasonable effort considering the advantages of the in-situ calibration.

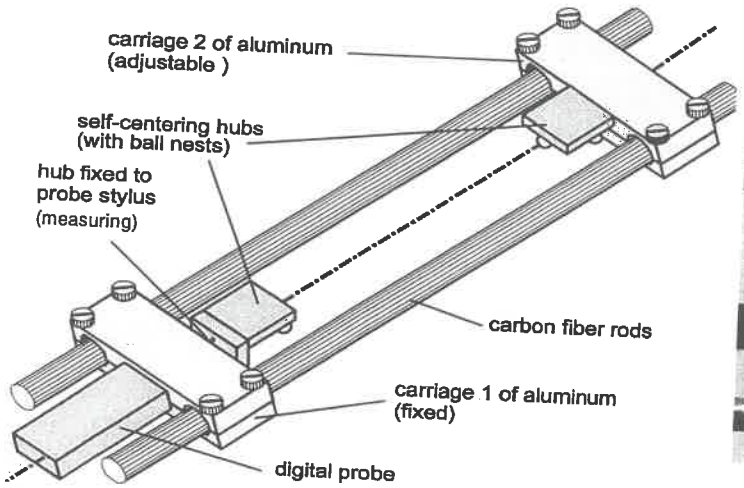

Fig. 4: Scheme of length comparator

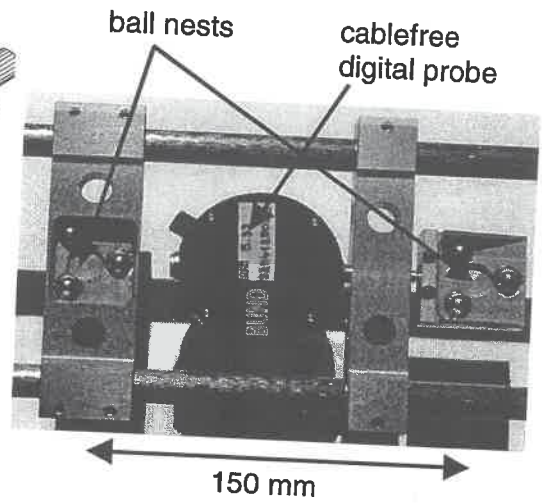

Fig. 5: Built up length comparator

Measurements

Measurements on large horizontal arm CMMs have been performed with the new L-shaped 2D artifact (Fig. 2) to test the handling, the error assessment procedures and the performance. Tests have been carried out in industrial environments to obtain realistic results.

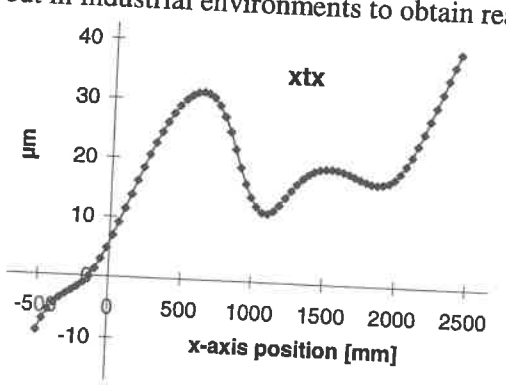

Fig. 6: Positional error xtx of horizontal arm CMM assessed with the new L-shaped 2D artifact

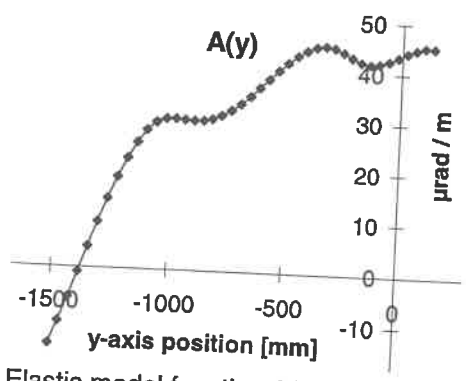

Fig. 7: Elastic model function A(y) of the elastic pitch $yrx(y,z) = A(y) \cdot z$ of horizontal arm CMM assessed with the new L-shaped 2D artifact

PTB developed analysis software (KALKOM) to assess CMM errors. The program features a graphical interface enabling the industrial use of the ball plate method with various 2D artifacts. KALKOM was extended to additionally extract the three horizontal arm CMM elastic errors from measurements with

L-shaped 2D artifacts. Fig. 6 and 7 show as an example the positional error *xtx* and the elastic model function *A(y)* [part of elastic pitch error *yrx(y,z)*] of a horizontal arm CMM. The evaluated error components can be directly used for the error correction of CMMs.

In order to prove the consistency of measurements, a test was performed to analyze the inconsistencies between the calibrated and the measured values. In this test KALKOM calculates the correction of the CMM using the 24 single error components just evaluated. The correction is applied to the original point measurement data for the error assessment (virtual correction). Differences between these values so corrected and the calibration values of the 2D artifact give an estimation of the contradictions in the measurements. Reasons for these discrepancies are the repeatability of the CMM itself, the stability of the artifact and its mounting and potential imperfection of the underlying kinematic model.

As a measure of the contradictions, the analysis of the length measurements is statistically evaluated. From this the standard deviation of the spread of all measured lengths amounts to 18 µm for the horizontal arm CMM under test. (Remark: It is to be noted that this standard deviation is calculated over all measured lengths up to 3200 mm!). In order to assess this value the repeatability of the sphere positions on the artifact has been used. This repeatability amounts to 12 µm (standard deviation). Assuming that the intrinsic repeatability of this CMM is not much below this value as further tests with other 2D artifacts have shown, the insufficiency of the error assessment with the new L-shaped 2D artifact is of the order of 10 µm.

From these results it can be derived that the mounting and the stability of artifacts have to be further optimized. Moreover, the experiments show how important it is to measure the temperatures of CMM scales during the CMM error assessment. Practical experience shows that the application of L-shaped 2D artifacts is limited in size for handling reasons. The authors estimate the artifact size limit for the use of L-shaped 2D artifacts to 3 m × 1,5 m. CMMs with one axis up to twice the greatest artifact length can be reasonably covered with these 2D artifacts.

Conclusion and outlook

This paper presents a new calibration set for making large horizontal arm CMMs traceable. The set consists of a new type of L-shaped 2D artifact, of error assessment procedures and of adapted error assessment software. Up to now tests have been performed at three industrial facilities. Handling experience with the new L-shaped 2D artifacts shows that full error assessment for a horizontal arm CMM with a 3 m x-stroke can be performed in two days, with the perspective of carrying out the procedure in nearly one day. First results will be cross-checked with CMMs of higher accuracy. Independent tests of the new artifacts with step gages or ball bars will validate the new system in the end. Final project results will be available in early spring 2001.

Acknowledgement

The authors acknowledge the support by EC Programme SM&T under contract SMT4-CT97-2183. We also thank our project partners for their contribution and cooperation.

References

1. Trapet, E. and Wäldele, F., Measurement, **9** No. 1, 17 (1991)
2. Trapet, E. and Arriba, L., SMT progress report, Trimek Annex Report, Project SMT4-CT97-2183, July 1999
3. Bartscher, M., Busch, K., Schwenke, H., Trapet, E., Wäldele, F., Proc. of the 9th METROLOGIE 99 conf., Bordeaux (France), 158 (1999)
4. Trapet, E., private communication (2000)

A Method of Optimal Design for Minimization of Force Rippie in Long Stroke Precision Linear Actuator with BLPMM

Myung J. Chung, Moon G. Lee and Dae-Gab Gweon
Department of Mechanical Engineering, Korea Advanced Institute of Science and Technology
373-1 Kusung-Dong, Yusong-Gu, Taejon, 305-701, Korea

Abstract-- A method of optimal design for minimization of force ripple in long stroke precision linear actuator without Finite Element Analysis (FEA) data is described. By this optimal design method, the force ripple is 78% reduced and minimum acceleration is 52% increased in compared with that of before optimal design of linear actuator. This linear actuator has 300mm traveling stroke and 20nm positioning resolution.

I. INTRODUCTION

There is an increasing requirement for controlling linear motion over several ten nanometer to hundreds of millimeter strokes, as in the semiconductor industries and precision manufacturing, for example [1]. Linear actuator with BLPMM (Brushless Permanent Magnet Motor) could offer significant advantages over conventional linear actuation technologies, such as motor driven cams, linkages and pneumatic rams - in terms of efficiency, operating bandwidth, speed and thrust control, stroke and positional accuracy with low kinematic complexity.

In linear actuator with BLPMM, there is force ripple, which is characteristic of BLPMM with salient-poles and acts as disturbance to positioning. For precision positioning of linear actuator, the force ripple has to minimize. The method for minimizing of force ripple has been studied by many researchers. Among the recipes, there are skewing of magnet [2], shifting of magnet pole pairs and changing the ratio of magnet pole width to slot pitch [3]. These methods have been conducted by FEA (Finite Element Analysis), which is time consuming work and hard to apply to optimal design.

In this paper, we claculated the force components, which are used in force ripple calculation, in the function of geometric parameters of linear actuator with BLPMM, and used the sequential quadratic programming (SQP) method for optimal design without FEA data. The linear actuator geometric parameters ısed in force ripple calculation selected as optimal lesign variable and ratio of force ripple to rated force is lefined as cost function.

By optimal design, the force ripple is 78% reduced nd minimum acceleration is 52% increased in ompared with that of before optimal design of linear ctuator. This linear actuator has 300mm traveling troke and 20nm positioning resolution. This analytic ıodel can be used in the position control of linear ctuator as estimator of force ripple.

II. GEOMETRICAL STRUCTURE

Fig. 1 shows the basic geometrical structure of linear BLPMM, where an iron core of armature is wound by coil with three phase and stator is attached to permanent magnets, which is faced with armature winding each other with N and S poles. Table I lists the value of geometrical parameters before optimal design of the linear brushless PM motor.

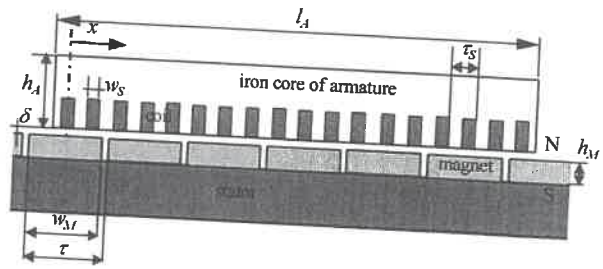

Fig. 1. Geometrical structure of linear BLPMM.

TABLE I
GEOMETRICAL PARAMETERS OF THE BLPMM

Parameter	Symbol	Value	Unit
Slot pitch	τ_S	8.0	mm
Slot depth	d_S	4.0	mm
Pole pitch	τ	24.0	mm
Armature length	l_A	144.0	mm
Magnet thickness	h_M	3.0	mm
Magnet width	w_M	20.0	mm
Air gap length	δ	3.0	mm

III. CALCULATION OF FORCE COMPONENTS

The force components of linear BLPMM is consisted with cogging force and mutual force. We can obtain the cogging force by integrating Maxwell stress tensor along the slot face on the iron core of armature. This force acting on each surface of the armature is given by

$$F_c = \frac{L}{2\mu_0}\int [B_n^2 - B_t^2]dl = \frac{L}{2\mu_0}\int B_n^2 dl \qquad (1)$$

The mutual force is obtained by summation of static thrust of the each one phase winding and is given by

$$\bar{F}_m = K_f [I_u \quad I_v \quad I_w][B_u \quad B_v \quad B_w]^T \qquad (2)$$

where K_f is a force constant, I_u, I_v, I_w are a current of each phase and B_u, B_v, B_w are a flux density of each phase. The detail expression of each force components are represented in reference [4].

IV. Optimal Design Method

A. Procedure of Optimal Design

The SQP is used for optimal design of BLPMM, this method uses an iterative procedure, and generates a quadratic programming (QP) sub-problem at each iteration and updates the estimates, the Hessian of Lagrangian [5].

The cost function is given by

$$F(x) = \left(\frac{f\max - f\min}{f\max + f\min} \right)^2 \qquad (3)$$

where $f\max - f\min$ is force ripple.

From (1)-(2), the force ripple is related with electric and geometric parameters. The parameters related with the force ripple are selected as design variables, and the other parameters are selected as fixed variables.

The design variables (x) are coil diameter (d_{co}), slot depth (d_s), armature length (l_A), magnet shift length (s_P), magnet width (w_M) and air gap length (δ). The fixed variables are active length (L), slot pitch (τ_S), pole pitch (τ), magnet remanence flux density (Br), magnet thickness (h_M) and applied voltage (V_{ap}).

The constraints are maximum flux density in teeth (B_{max}), minimum thrust acceleration (a_{thr}), temperature at coil (T_{coi}) and the ratio of normal force to rated thrust force (F_{nor}/F_{rate}). The constraint conditions are given by

$$g1(x) = B_{max} - G1 \leq 0, \qquad (4)$$

$$g2(x) = G2 - a_{thr} \leq 0, \qquad (5)$$

$$g3(x) = T_{coi} - G3 \leq 0, \qquad (6)$$

$$g4(x) = F_{nor}/F_{rate} - G4 \leq 0, \qquad (7)$$

where G1=1.5(T), G2=10(m/s^2), G3=100(℃), G4=2.

The flowchart of the optimal design is shown in Fig. 2. The flux density is calculated by the initial value (x) of design variables and fixed variables, and force components is calculated by using the flux density, design variables and fixed variables. The initial value of design variables is middle value of bound, and convergence tolerance (ε) is 0.01%.

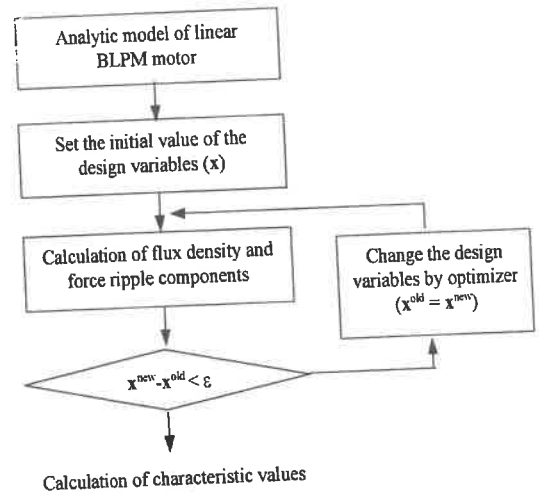

Fig. 2. Flowchart of the optimal design method of linear BLPMM.

Fig. 3 shows the optimization procedure of cost function and Fig. 4 shows the optimization procedure of design variables, where the coil diameter and air gap length is limited by bound.

B. Results of Optimal Design

Table II shows the optimal value of design and fixed variables and Table III is the performance of the motor calculated by the result of optimal design. By optimal design, the force ripple is reduced 33.09(N) from 42.41(N) to 9.32(N) and minimum acceleration is increased 8(m/sec^2) from 7.29(m/sec^2) to 15.29(m/sec^2) in compared with that of before optimal design.

Fig. 5 shows the force ripple, which is obtained by (1) -(2), of optimized BLPMM, where the main component of ripple is by end effect force, which is not exist in rotary PM motor. In this optimal method, the design variables related with end effect force are armature length and magnet shift length, which used to compress the first order component of end effect force.

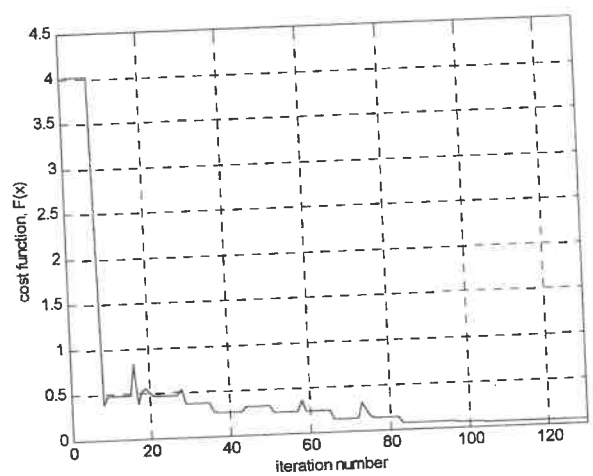

Fig. 3. Optimization procedure of the cost function.

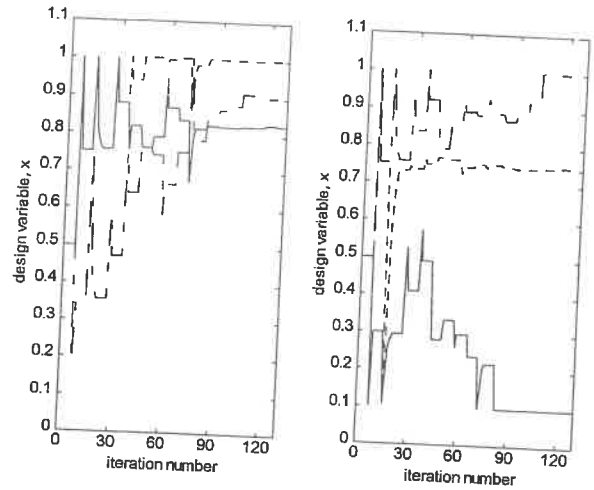

Fig. 4. Optimization procedure of the design variables.

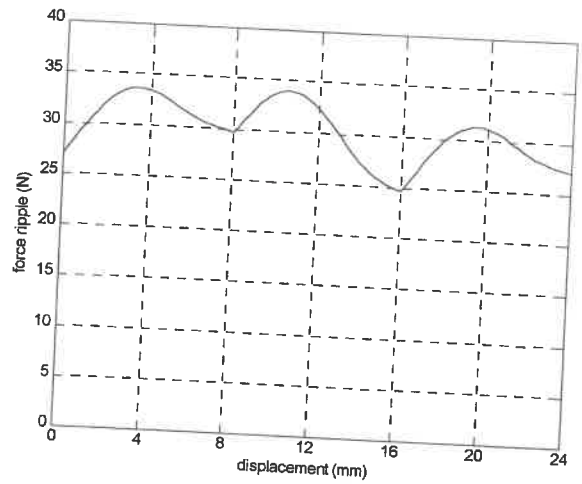

Fig. 5. Analytical force ripple of optimized BLPMM.

TABLE II
OPTIMAL VALUE OF THE DESIGN AND FIXED VARIABLES

Item	Symbol	Value	Unit
Rated current	I	1.0	A
Coil diameter	d_{co}	0.4	mm
Number of phase	n	3	
Number of pole	p	6	
Number of slot	Qs	18	
Pole pitch	τ	24.0	mm
Slot pitch	τ_S	8.0	mm
Slot depth	d_S	4.0	mm
Armature length	l_A	163.2	mm
Armature width	L	50.0	mm
Magnet shift length	s_P	0.1	mm
Magnet thickness	h_M	3.0	mm
Magnet width	w_M	17.5	mm
Remanence flux density	Br	1.17	T
Air gap length	δ	3.0	mm
Tooth ratio	tr	0.5	

TABLE III
CHARACTERISTIC VALUE OF THE MOTOR

Item	Value	Unit
Maximum thrust force	34.01	N
Rated thrust force	29.44	N
Minimum acceleration	15.29	m/s^2
Air gap flux density	0.55	T
Force constant	29.44	N/A
Maximum force ripple	9.32	N

V. EXPERIMENTAL RESULTS

The force ripple of BLPMM developed using the optimal value of design variables is obtained by using the experimental setup of the Fig. 6. In this set-up, the armature is fixed on air slide bearing and guided. Fig. 7 shows the force ripple of BLPMM obtained by experimental test when rated current is applied in armature coil. In Fig. 7, the force ripple contains cogging force, which has two components of tooth ripple and end effect, and mutual force. Among the force ripple components, tooth ripple component is suppressed effectively, but end effect component is suppressed ineffectively. The possible reason is that the end effect component is very sensitive to armature length, so the error is induced by the analytic solution adopted the assumption in analytical model.

The closed loop control is performed by feeding back the position information from laser interferometer as shown in Fig. 6. The control input is generated by PID controller. Fig. 8 shows the response of actuator when the system commanded to move 300mm stroke and Fig. 9 shows the positioning resolution of actuator for 20nm step motion.

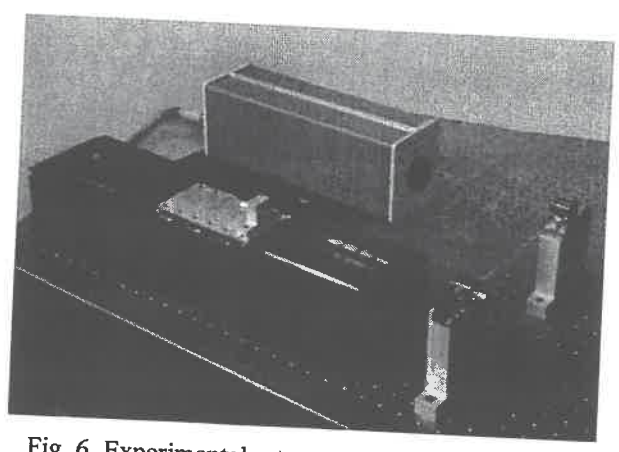

Fig. 6. Experimental set-up and designed BLPMM.

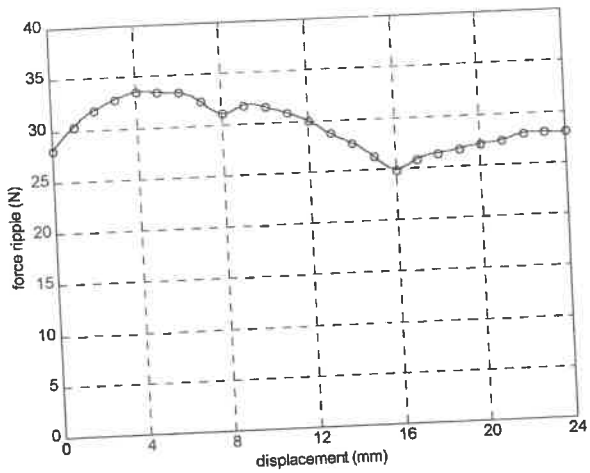

Fig. 7. Experimental force ripple of optimized BLPMM.

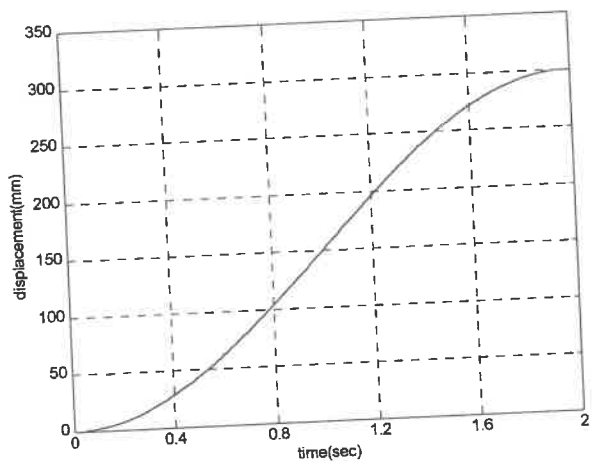

Fig. 8. Response of actuator: when the system commanded to move 300mm stroke.

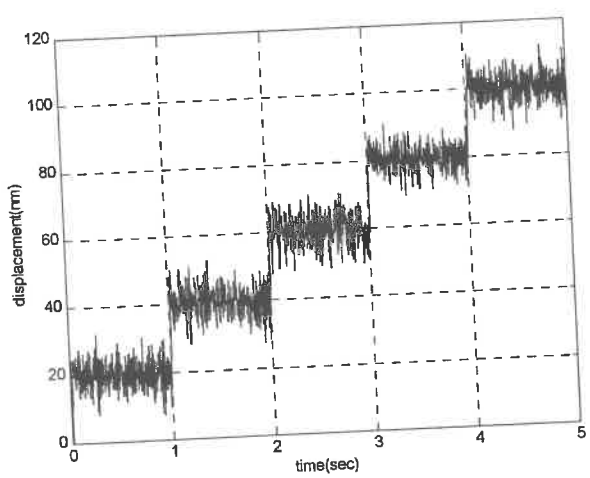

Fig. 9. Positioning resolution of actuator: when the system commanded to move 20nm step.

VI. CONCLUSION

The analytic model representing the force ripple in the function of geometric parameters of motor is developed and the optimal design is done by means of considering force ripple as cost function and electric and geometric parameters as design variables without FEA data. By optimal design, the force ripple is 78% reduced and minimum acceleration is 52% increased in compared with that of before optimal design of linear actuator. This linear actuator has 300mm traveling stroke and 20nm positioning resolution. This analytic model can be used in the position control of linear actuator as estimator of force ripple.

ACKNOWLEDGMENT

The work described in this paper was carried out at the Korea Advanced Institute of Science and Technology with the financial support of the Korea Research Foundation made in the program year of 1999 of the South Korea.

REFERENCES

[1] S.Q. Lee and D.G. Gweon, "A Long Stroke and Ultra-precision XYθ Stage using Simple Linear DC Servo Actuators," in *ASPE*, pp.4341-4344, 1997.

[2] G.H. Jang et al, "Performance of a Brushless DC Motor due to the Axial Geometry of the Permanent Magnet," in *IEEE Trans. on Magnetics*, vol. 33, no. 5, September 1997, pp. 4101-4103.

[3] Touzhu Li and Gordon Slemon, "Reduction of cogging torque in permanent magnet motors," in *IEEE Trans. on Magnetics*, vol. 24, no. 6, November 1988, pp. 2901-2903.

[4] Myung J. Chung et al., "Analytical Representation of Cogging Force in Linear Brushless Permanent Magnet Motor, " in *Proceedings of the ICMT'99*, Oct 1999, pp.310-314.

[5] A. Grace, *Optimization Toolbox User's Guide*. The Math Works Inc. 1990.

A High Precision Linear Measuring System

TaeBong Eom, JinWan Han
Length Group, Korea Research Institute of Standards and Science, Taejeon, Korea

1. Introduction

Most of demands for measuring dimension are related to the linear measurement. The national standards laboratories maintain the precision artifacts such as end standards and line scales. These length standards are usually calibrated using the laser interferometer. Several standards laboratories have the calibration systems for line standards or end standards. Some laboratories modified commercial machine such as coordinate measuring machine or universal measuring machine for their purposes, and others specially developed their own systems. Generally these are designed for calibrating one or two artifacts, so standard laboratories need several calibration systems to measure a variety of different artifacts.

To calibrate precision length standards and length measuring transducers, Korea Research Institute of Standards and Science (KRISS) has built the new linear measuring machine. The main requirement of machine is to achieve a flexibility to calibrate a variety of different standards such as step gages, long range linear transducers, line scales and end bars with high accuracy. This system is not designed for calibrating standard grade gauge block or graduated line scale, which is usually measured by specially, designed precise interferometers.

2. Structure of the linear measuring system

2.1. Description of the structure

System consists of four main parts: machine body, translating system, laser interferometer and detecting apparatus. The granite surface plate (3,000 mm x 700 mm x 600 mm) is used as a base of the machine body and a guide of the moving carriage. The translating system, which carries two interferometer reflectors and detecting apparatus, makes relative displacements between the measuring artifact and the detecting apparatus. This consists of horizontal global stage, micro-stage, tilting stage and z-axis stage. The global stage, which incorporates air bearings for smooth movement, is driven by the steel belt and the geared DC motor. It has a traverse length of 2,500 mm. The rotational errors (pitch and yaw) of global stage are smaller than 8 second over 2,500 mm moving range. The micro-stage, which the detecting apparatus is fixed at, is used for horizontal fine motion. To compensate the rotational errors of the global stage, two axes tilting stages are used. The yaw angle of tilting stage is servo-controlled to minimize the difference between reading values of two interferometers, and the pitch angle of tilting stage is adjusted using the look-up table stored at computer. Thanks to two tilting stages, the rotational errors of a carriage can be smaller than 1.5 second. A micro-stage and two tilting stages, which have the monolithic structure

and are made of high-strength aluminum alloy, are driven by PZTs. Z-axis stage which uses cross roller bearing can be vertically moved to focus the microscope on line standard measurement or move the electronic micrometer probe to other measuring face of end standard without crash. Z-axis stage is driven by motorized micrometer with rotary encoder.

The displacement measurement of carriage is realized by two laser interferometers (one HP5518 laser head and two home-built plane mirror interferometers) which have a resolution of 5 nm. The measuring axis of length standards is vertically on same height with two interferometer reflectors and horizontally on the center of two interferometer reflectors, so measuring object can be aligned coaxially with the center of two laser beams. Thanks to this arrangement, the errors caused by Abbe offset can be minimized, and two reflectors and an electronic micrometer probe can be moved vertically without losing the interferometer signal

The detecting apparatus is used to detect the measuring point of length standards. Two detectors are generally used. For probing the measuring surface of end standards, an inductive probe with a spherical ball is used. It is only used as a zero detector. For observing the scale of line standards and detecting its center, an optical microscope is also used.

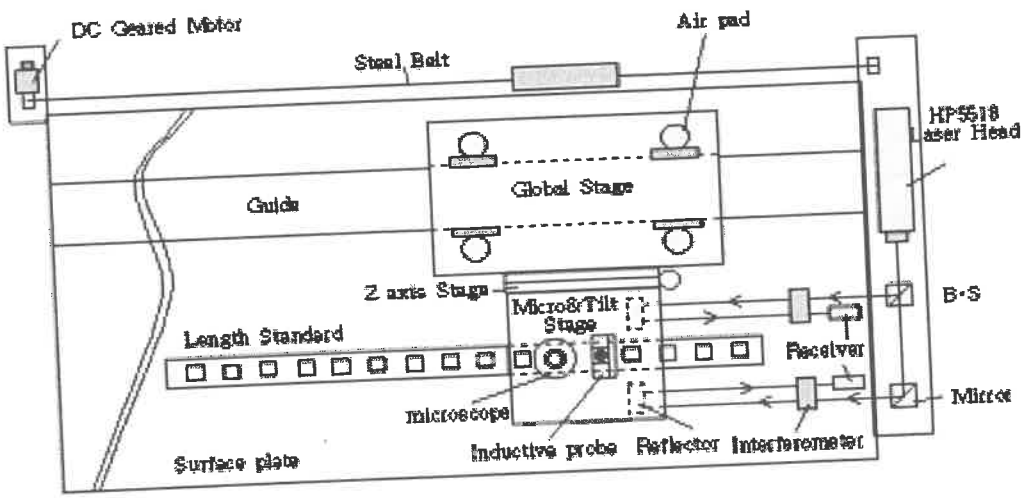

Fig. 1. Schematic diagram of the linear measurement system (top view).

2.2. Operation of the system

In order to reduce the dead path error and air turbulence effect, the measuring object is positioned as close as possible to the interferometer. And the measuring object must be aligned coaxially with center of two laser beams to minimize Abbe error and cosine error. In the system, measurement artifact can be usually aligned within Abbe offset of 2 mm and cosine deviation of 1 minute. Before and after each measurement, the air temperature, pressure and humidity are measured and the refractive index of the air

is calculated using the modified Edlen equation. And also material temperature is measured to compensate a thermal expansion. All sensors of HP compensator have been periodically calibrated. Especially, environmental measuring system with very high accuracy can be used to get more accurate compensation value.

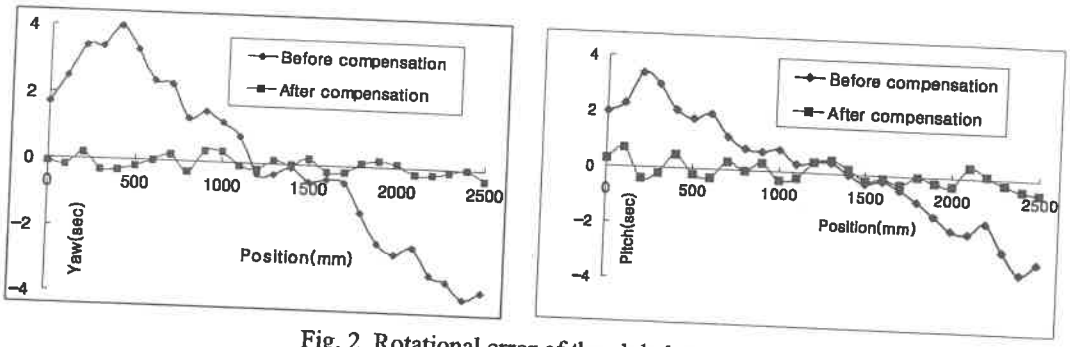

Fig. 2. Rotational error of the global stage.

On measuring the step gauge or the end bar, a reference gauge block (5 mm or 10 mm) is used to calculate the effective probe diameter. This gauge block has been measured on a gauge block interferometer with an uncertainty of 25 nm. The standard deviation of determined effective probe diameter is typically below 20 nm. The computer controls the position of a horizontal stage and a vertical stage to allow the electronic probe to touch the front or rear measuring face. On touching the face, the computer controls PZTs of a micro-stage for fine positioning and two tilting stages for angle adjusting. The system measures the front and rear faces of measuring blocks in sequence automatically.

For measuring the scale, an optical microscope with a CCD camera and an illumination system is used. The image processor board captures the image of the scale marker and displays it on the CRT monitor with reference cross line which is generated by computer. In order to coincide the image of the scale marker with the reference cross line, the fine positioning of the scale can be carried out manually using the micro-stage driven by PZT.

On calibrating the linear transducer such as linear encoder or long range potentiometer, Transducer is aligned coaxially with laser axis, and head (moving part) of transducer is fixed to micro-stage. The computer controls the global stage and micro-stage to move head of transducer to predefined positions. The reading values of linear transducer are compared with values of laser interferometer.

3. Uncertainty of the linear measuring system

Measurement uncertainty depends on type and quality of the measuring objects. Table 1 shows an example of uncertainty budget roughly evaluated for the calibration of a long gauge block. The expended uncertainty (k=2) of the system is (0.2 + 0.63 * L) μm, where L is in m. The system is in laboratory with temperature variation of ±0.5 °C, so the most significant sources of uncertainty are from wavelength compensation error and thermal expansion correction error.

To test the accuracy of the system, a set of gauge blocks from 300 to 1,000 mm was measured using the linear measuring machine. The results were compared with the reference values that were obtained by interferometry or comparison method as shown in fig.3. The uncertainty (k=2) of reference values is (0.02 + 0.1 * L) μm, where L is in m. The estimated uncertainty of measurement is in good agreement with reference values of the gauge blocks.

Table 1. Uncertainty budget evaluated for calibration of a long gauge block

Source of Uncertainty	**Standard Uncertainty**
Repeatability of gauge block measurement	0.05 μm
Uncertainty in probe diameter(master gauge block, repeatability and stability)	0.08μm
Laser frequency(center frequency and stability)	0.01ppm
Uncertainty in wavelength compensation(sensor accuracy and Edlen equation)	0.10ppm
Uncertainty in thermal expansion correction(sensor accuracy and expansion coefficient accuracy)	0.28ppm
Cosine error	0.07ppm
Abbe error	0.01 μm
Combined standard uncertainty Uc(L)	(0.1+0.31*L) μm, L: m
Expanded uncertainty(k=2) U(L)	(0.2+0.62*L) μm, L: m

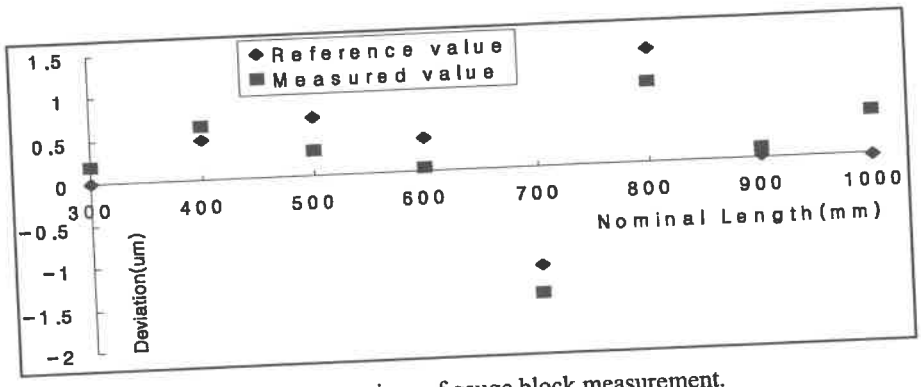

Fig. 3. A comparison of gauge block measurement.

DEVELOPMENT OF AN ULTARA-PRECISE POSITIONING STAGE TRAVELLING ON A GRATING

Satoshi Honda
Tokyo Metropolitan Institute of Technology, Tokyo, Japan

1. Introduction

Nowadays, an ultra-precise positioning stage is an indispensable component of a precise machine tool, a measuring instrument or a semiconductor manufacturing equipment. The ultra-precise positioning stages requires not only mechanical performance of high stiffness, accurate guidance, and the minimum lost motion but also control performance of precise positioning, minute resolution, dependable repeatability, and smooth driving. Some integrated ultra-precise positioning stages with a devised mechanism and an intelligent control system have been developed.[1)2)3)] One integrated stage consists of a ball screw, an air slider and a laser interferometer.[1)] Another stage is formed into a linear electric motor with a precise linear encoder.[2)] Other stage composes an inchworm mechanism moving on a guide rail.[3)] However, the first stage is bulky because individual instruments are assembled without merging. If stiffness of the ball screw and the air slider should be more rigid and if measurement accuracy of the laser interferometer should be higher, those instruments become bigger and heavier. The second stage is compact; yet a control system is complicated because the linear motor cannot control the position without regulating of electric current accurately. Control system of the third stage is constructed easily because inchworm motion is accomplished by using an open-loop control system; still, the stage can not position every step without slipping even if driving plates grip on the guide rail tightly.

In this paper, we present a novel ultra-precise positioning stage[4)] which table is travelling on a grating and is driven by an inchworm motion. The stage consists of three gratings. Two small gratings alternately meshed on anther grating in the inchworm motion. The stage is accurately positioned every one pitch of the grating by the inchworm motion. The stage does not need a feedback control system composed of a laser interferometer and a complicated control algorithm, so the structure of the stage becomes compact and its table is positioned by an open-loop control system. This paper describes the structure of the ultra-precise positioning stage and an adjusting method for the two small gratings assembled on an inchworm unit so that two small gratings must correctly and precisely mesh on the grating in the inchworm motion.

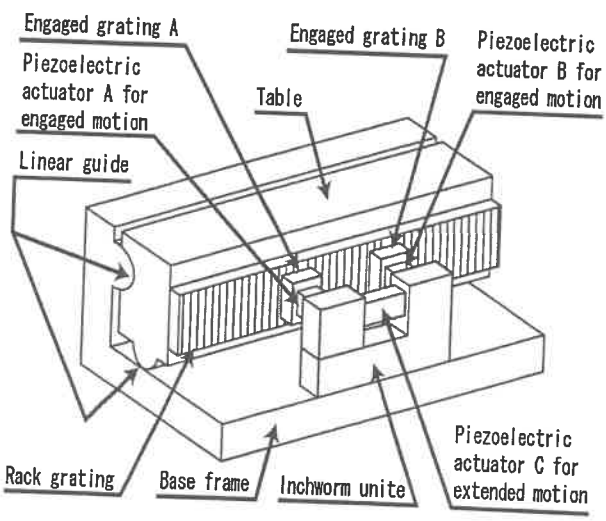

Figure 1. Structure of the ultra-precise stage

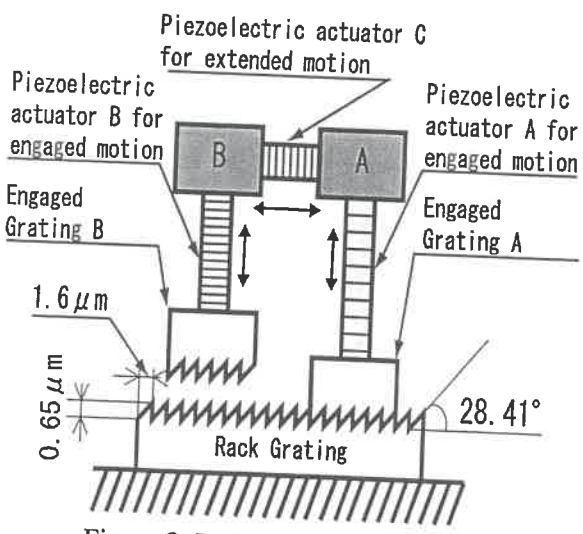

Figure 2. Inchworm mechanism

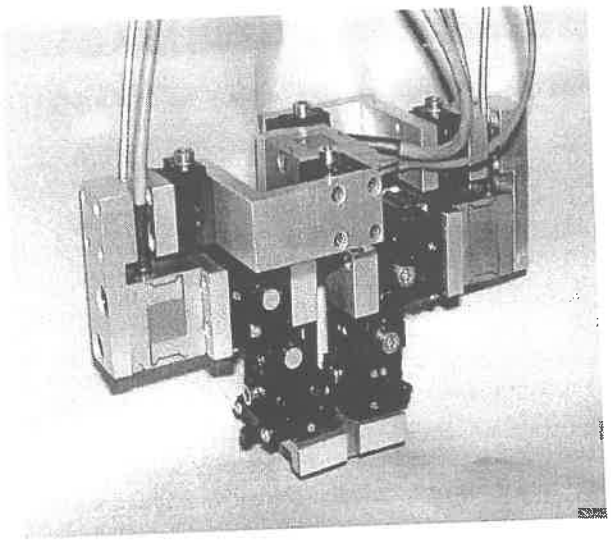

Figure 3. The inchworm units

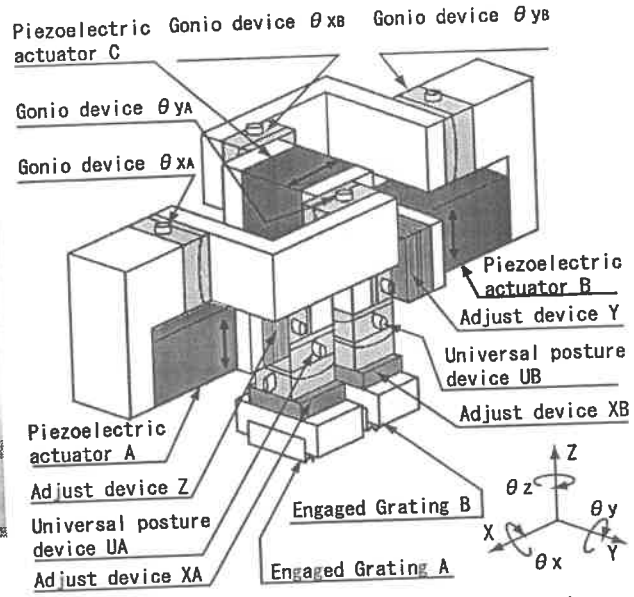

Figure 4. Structure of the inchworm unit

2. Structure of the ultra-precise positioning stage

The ultra-precise positioning stage consists of the table, the inchworm unit and a base frame as shown in figure 1. The table slides on the base frame and is guided along a linear guide formed into convex ridge and concave slot which intersections are semicircle. The grating is attached on the side of the table. The grating acts as a mechanical rack with pitch of 1.6 micrometer and depth of 0.65 micrometer. We call it a rack grating. The inchworm unit consists of two small gratings and three piezoelectric actuators. Both small gratings are meshed on the rack grating step by step in the inchworm motion as shown in figure 2. We call them engaged gratings.

The inchworm unit is shown in figure 3 and figure 4. One piezoelectric actuator (C) acts for an extended motion and other two piezoelectric actuators (A, B) act for an engaged motion. Four gonio devices are installed between three piezoelectric actuators. Two universal posture devices and position devices for x, y and z directions are assembled on the piezoelectric actuators (A, B). The engaged gratings are respectively attached on the position devices for x direction. Assembled angle of the piezoelectric actuators are ultra-precisely adjusted by using the gonio devices, so two pairs of the piezoelectric actuator (C) for extend motion and the piezoelectric actuators (A or B) for engaged motion are perpendicularly moved each other. Both surfaces of the engaged gratings are ultra-precisely adjusted into the same plane. Both grooves of the engaged gratings are adjusted in parallel by using two universal posture devices (UA, UB) and the position devices (Y, Z) for y and z directions. Both position devices (XA, XB) for x direction are used to adjust interval between both engaged gratings. Reference interval is the distance that is pitch of the grating multiplied by a certain integer. The adjust method mentioned above is appeared in the experimental result.

3. Adjusting method and Experimental results

The adjust method for the engaged gratings was confirmed in the experiment. Figure 5 shows the coordinate frame for the inchworm units and the engaged gratings. Firstly, four gonio devices were regulated as both piezoelectric actuators for engaged motion move into the z direction and the piezoelectric actuator for extend motion moves into the x direction. Secondly, two universal posture devices and position devices for x, y and z directions were regulated as the surfaces of the engaged gratings are correspond to the x-y coordinate plain and both grooves of the engaged gratings are parallel against y axis; and also, interval distance between both engaged gratings correspond to the distance multiplied pitch of the grating by a certain integer.

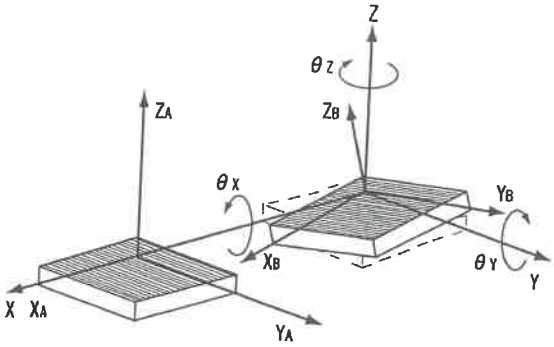

Figure 5. Coordinate frame of the gratings

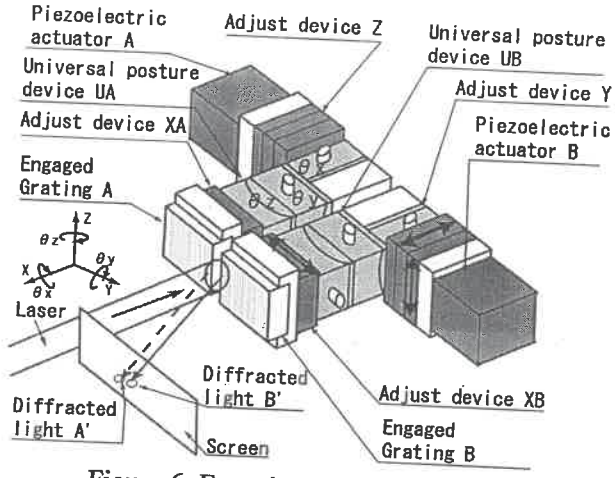

Figure 6. Experimental equipment

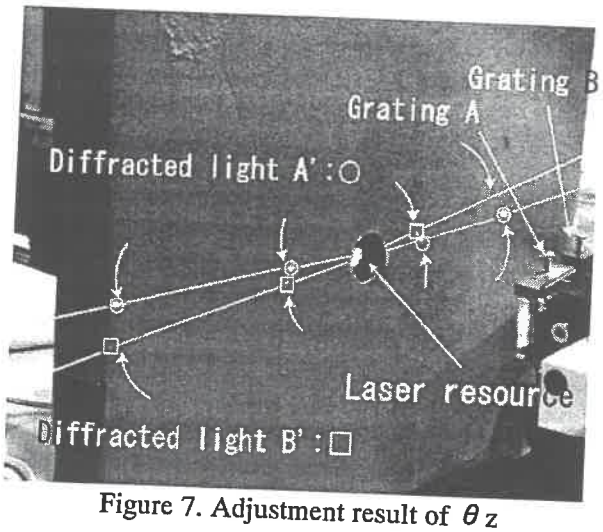

Figure 7. Adjustment result of θz

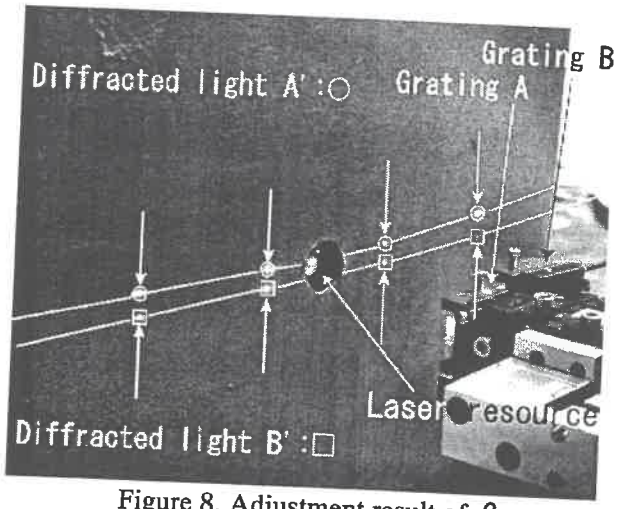

Figure 8. Adjustment result of θx

Diffracted lights were used for these adjustments as shown in figure 6. As the angle of θz was not regulated, a series of spots of the diffracted light B' crossed to a series of spots of diffracted light A' as shown in figure 7; therefore, an adjust screw of θz was regulated as both series of spots of the diffracted lights become parallel. As the angle of θx was not regulated, both series of spots of diffracted lights (B' and A') were separated in parallel as shown in figure 8; therefore, an adjust screw of θx was regulated as both series of spots of diffracted lights become the same line. As the position of z was not regulated, interval between each spot was not same as shown in figure 9; therefore, position z was regulated. As the angle of θy was not regulated, both spots of the diffracted lights did not corresponded as shown in figure 10; therefore, an adjust screw of θy was regulated as both spots become same point as shown in figure 11. If the procedure was accomplished, interference fringe appeared at the corresponded spot as shown in figure 12 and figure 13. As the interval distance was not regulated, the interference fringe did not correspond to the reference interference fringes, therefore, an adjust screw of x was regulated. Two engaged gratings could correctly and precisely mesh on the ruler grating in the inchworm motion.

4.Conclusions

Novel ultra-precise positioning stage travelling on the grating was developed. The stage can position at every one pitch of the grating by meshing the engaged gratings to the rack grating. The engaged gratings are ultra-precisely adjusted into the same plain and into parallel grooves by using diffracted lights, and

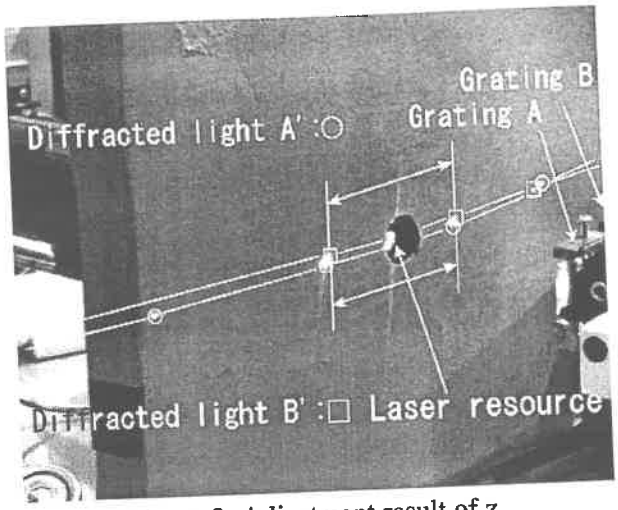

Figure 9. Adjustment result of z

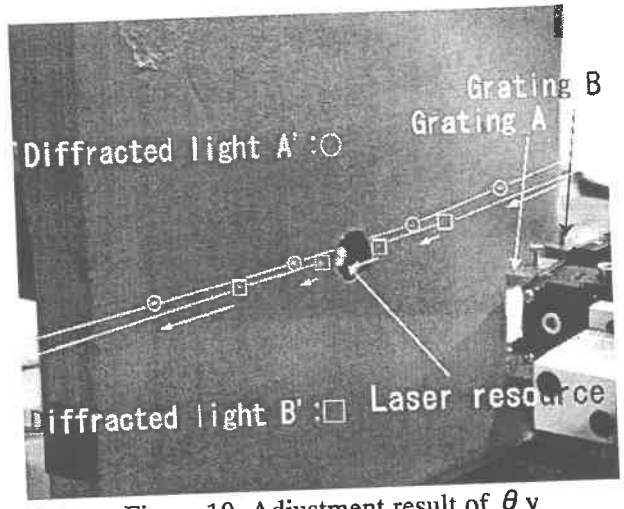

Figure 10. Adjustment result of θ y

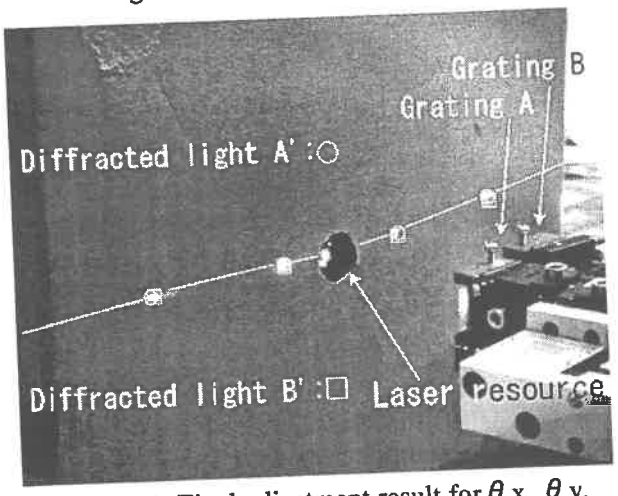

Figure 11. Final adjustment result for θ x, θ y, θ z, z

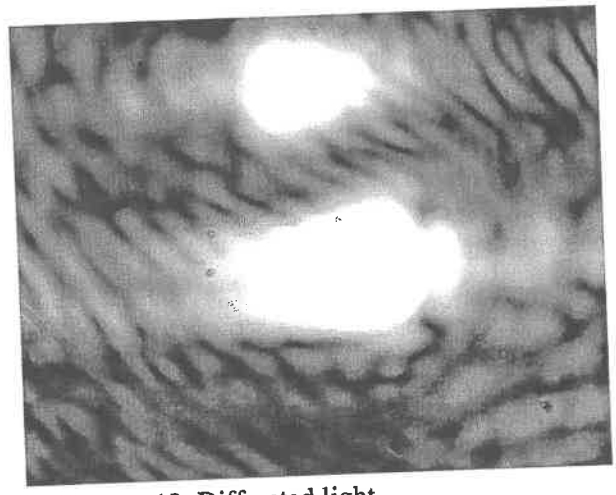

Figure 12. Diffracted light (Un-adjusted for θ x, θ y, θ z, z)

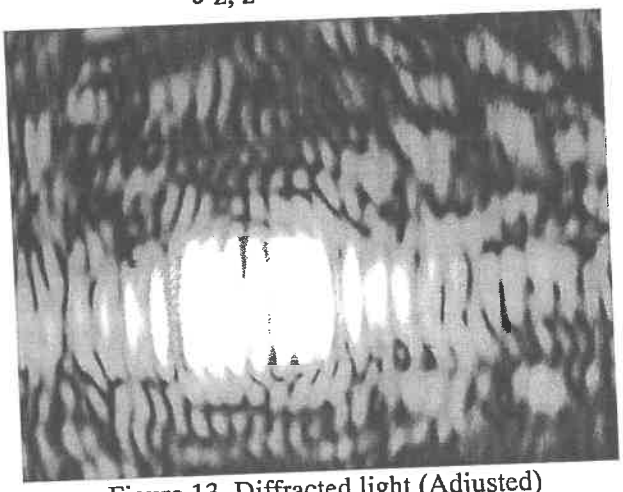

Figure 13. Diffracted light (Adjusted)

the interval distance between the engaged grating is regulated by corresponding to the reference interference fringes.

References

[1] Jiro Otsuka, et al.: Ultra-precision Positioning Using Lead Screw Drive, JSPE, 59, 10, pp1655-1661 (1993).

[2] Shigeru Futami, et al.: Nanometric Positioning Using AC Linear Motor and Rolling Guide, JSPE, 57, 10, pp1808-1813 (1991).

[3] Tetsuro Sakano et al.: Study on a Micro Piezoelectric Linear Actuator with Friction Drive Method", JSPE, 63, 9, pp1246-1250 (1997).

[4] Takashi Wada and Satoshi Honda: Development of an Ultra-Precise Positioning Stage Engaged with Gratings, Proceedings of 14th ASPE annual meeting, pp228-231(1999).

Development of a Measuring Instrument for Grinding Wheel Peripheral Shapes

Masumi IZUMI*, Hwa-Soo LEE*, Tadashi WAKABAYASHI* and Shigeru INOUE**
*College of Science and Technology, Nihon University, 1-8-14 Kanda-Surugadai, Chiyoda-ku, Tokyo, 101-8308, Japan.
**Makino Seiki, Co., LTD., 4029, Nakatsu, Aikawa-Machi, Aiko-Gun, Kanagawa, 243-0303, Japan.

Abstract

In the present paper, a precise measuring method of contours of rotating grinding wheel is proposed, in which a wire is used as a contact probe and wire touch signals to rotating wheel are detected by an acoustic emission sensor. Utilizing a wire as a probe, new wire part can be provided as a probe in every touching to wheel surface by reeling it. In this study, a driving system feeding the probe in the direction parallel to the wheel axis is developed, and wheel peripheral shapes are measured in a surface grinding machine. As the test results, it is clarified that rotating wheel peripheral shapes can be measured with the resolution in micron order. Furthermore, it is confirmed that this measuring method can be applied to monitor protruding abrasive grains causing scratches in grinding operations.

Key words: Grinding Wheel Peripheral Shape, AE sensor, Wire, Measuring Instrument.

1. Introduction

Since geometrical shape of grinding wheel periphery is directly copied to workpiece surface in grinding operation, it is very important to confirm that wheel periphery is generated as required. From such a viewpoint, authors have proposed a precise measuring method of wheel peripheral shape [1]. In this method, a wire is used as a contact probe to rotating wheel. Although the wire surface is ground by direct contact to rotating wheel, new part of wire as a touching probe is supplied by reeling wire before every contact. And then, probe geometry is not affected by contact to wheel. Their contact signals are monitored by an Acoustic Emission i.e. AE sensor. In reference [1], a measuring system of wheel peripheral shape is developed, in which coordinate system of numerical control machine is applied to obtain the wheel geometry for NC machines. In this study, a new measuring equipment for ordinary grinding machines without NC control is developed and its performance is clarified.

2. Measuring equipment and system

Figure 1 shows a newly designed measuring equipment. It consists of monitoring part for detecting wheel periphery and driving part feeding the monitoring part to wheel radius and rotating axis directions. The monitoring part consists of an AE sensor, a spool reeling wire, a wire guide and a stepping

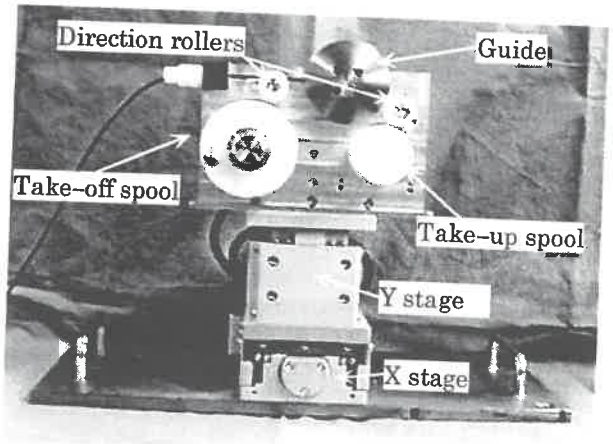

Figure 1 Measuring instrument

motor. Since this part is designed compact i.e. 220 mm high, 380 mm width and the weight is 50N, it can be located on tables of ordinary surface grinding machines.

Figure 2 shows a setup of the measuring system. An X-Y stage and a stepping motor are controlled by a personal computer in this system.

Measurement of wheel shape is carried out in the following procedure. The wire is fed upward by Y stage and approaching to wheel surface. A touching signal emitted by AE sensor due to their contact is rectified and transferred to a discriminator. In the discriminator, contact signal is evaluated whether on or not based on previously determined threshold signal level. In case of that contact signal is detected, upward feeding of Y stage is stopped. Simultaneously, the coordinate of X and Y at contact point are transferred form the feed controller to the personal computer. After that, Y stage is fed downward and the wire is reeled by stepping motor in order to supply a new part to contact point as a new probe.

On the other hand, X stage is feed to the previously determined next monitoring point in the wheel rotating axis direction, where Y stage is fed upward. Repeating this procedure, a series of contact coordinates are obtained. Finery, compensating the wire radius, the wheel shape can be obtained.

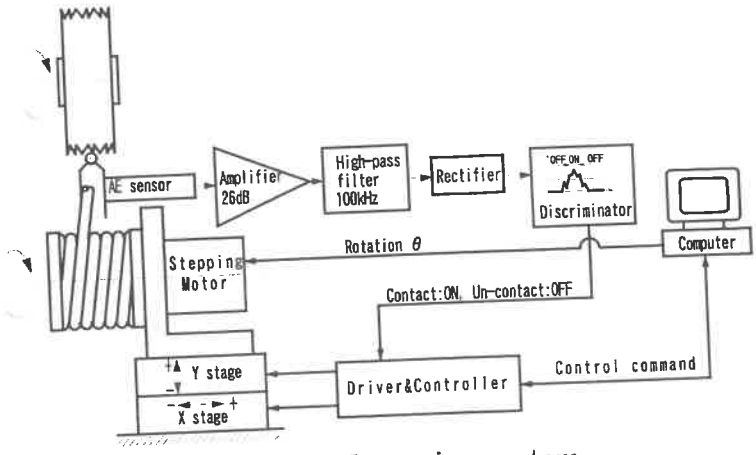

Figure 2 Measuring system

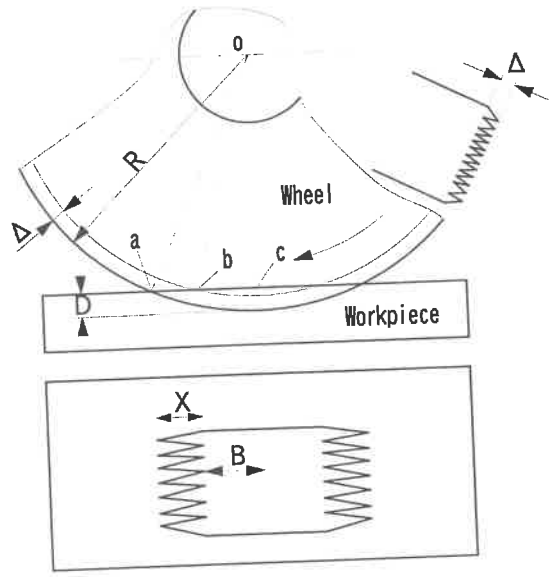

Figure 3 Copying method

Table1 Measuring conditions

Grinding wheel	WA46G8V (ϕ200×25×50.8)
Machine tool	Surface grinding machine
AE sensor	500kHz
Wire	Tungsten wire, ϕ0.1mm
X-stage resolution	0.001mm
Y-stage resolution	0.0005mm

3. Comparison with conventional copy method

In order to evaluate the measuring performance of the proposed method, measured results are compared with the results of conventional copy method. Conventional one is a method in which grinding an easy to grinding material, the surface of ground workpiece is measured with a contour measuring device. Since this method is easy and reliable, it is applied in this study.

On the other hand, a precise monitoring method of the distribution of abrasive grains height in rotating wheel surface is developed and their monitoring results are compared with the measuring results in the proposed wire method. Figure 3 shows a schematic diagram of monitoring the distribution of abrasive grains. In this method, a flat

workpiece is ground under the depth of cut D. A grinding mark depending on the surface geometry of wheel is made in the ground surface as shown in below in Figure 3. In this method, the surface roughness of wheel is expanded in the mark remained in the surface of ground workpiece.

The relation between actual roughness height of wheel Δ and copied height on workpiece X can be easily calculated by geometrical relations as follows.

$$\left.\begin{aligned} R^2 &= (R-D)^2 + B^2 \\ (R-\Delta)^2 &= (X-B)^2 + (R-D)^2 \end{aligned}\right\} \cdots\cdots\cdots\cdots\cdots 1)$$

$$X^2 + 2\sqrt{R^2-(R-D)^2}\,X + \Delta^2 - 2R\Delta = 0 \cdots\cdots 2)$$

Where, R is a wheel radius, D is a depth of cut and B is a distance from center to point b in Figure 3. From Equation (2), the expanding ratio, X/Δ, can be obtained as a function of Δ as shown in Figure 4. This is a calculated example when $2R$ is 200 mm. According to this calculation, it is easy to monitor the geometric shape of wheel surface in 20 magnification.

4. Measurement of wheel peripheral shape

Measured examples of a wheel peripheral shape by the proposed wire method and the copy method are shown in Figure 5(a). These measurements are carried out under the machining conditions as shown in Table 1. In these curves, two groves can be seen. They are previously made by a dresser in order to compare two measuring results. It can be confirmed that these two curves coincide each other well.

Figure 5(b) shows the deviation of these two curves. Dotted two lines in both side show the level of $\pm 10.0\ \mu$m. Deviation curves are less than $\pm 10.0\ \mu$m, it means that the proposed wire method can measure the detail of wheel surfaces as precise as the copy method.

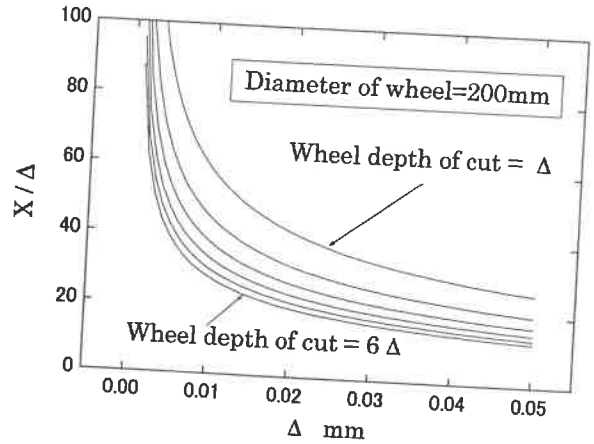

Figure 4 Relations between the wheel depth of cut and the magnification of height of a grit

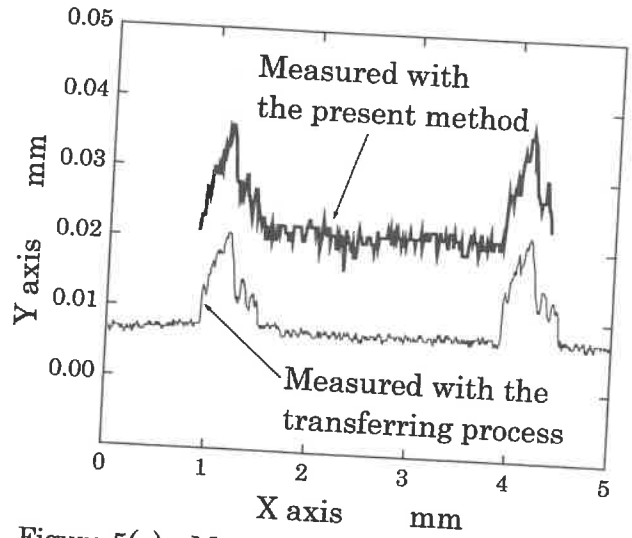

Figure 5(a) Measuring results of the wheel profiles and the deviation between these profiles

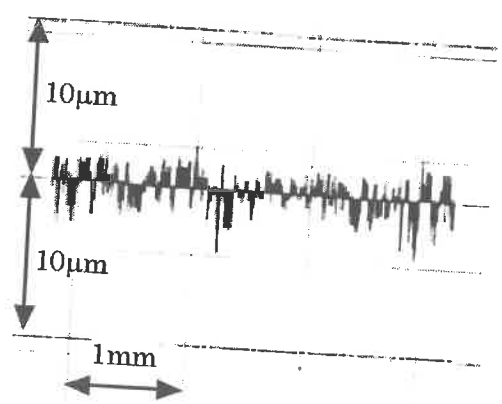

Figure 5(b) Deviation of the results

5. Measurement of abrasive grain height of wheel surfaces

The precise monitoring method of the distribution of abrasive grains height described above is applied to a wheel after grinding, and the microscope photograph is shown in Figure 6(a). In this figure, grinding marks of each abrasive grain can be monitored clearly. In this experiment, since wheel diameter $2R$ is 200 mm and wheel depth of cut D is 120 μm, the magnification rate is 20 from the calculation result shown in Figure 4. As shown in this figure, it can be seen that the height of abrasive grains are not average, and some of them are protruding about 20 μ m. Since these protruding grains cause scratching of ground surfaces in grinding, they must be monitored carefully.

Figure 6(b) shows the measuring results of the same part by the proposed wire method. This result shows that the proposed wire method can measure the wheel surface geometrical shape precisely. As these experimental results, it is clarified that the method proposed in this study can be applied to precise monitoring of abrasive grains in rotating wheel surface.

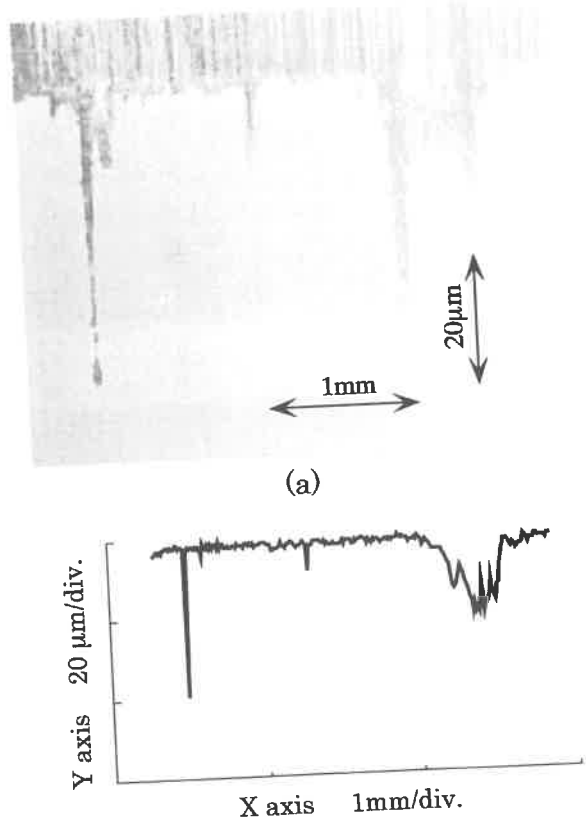

Figure 6 Wheel profiles enlarged by the transferring method and measured with the present method.

6. Conclusions

A measuring instrument for rotating wheel peripheral shapes using a wire touching probe is developed for ordinary surface grinding machine. Its measuring performance is evaluated experimentally. The results as follows are obtained.

1) This equipment can be applied to an ordinary surface machine which is not numerically controlled, and it may be used other type of grinding machines.
2) Using this equipment, protruding abrasive grains in rotating wheel surfaces can be monitored clearly. It means that it may be apply to analyze the generating algorithm of workpiece surface topography in grinding operations.

Reference

[1] Hwa-Soo LEE, Masumi IZUMI, Tadashi WAKABAYASHI, Shigeru INOUE, "Development of a Precision Measuring Method of Grinding Wheel Peripheral Shapes", Proceedings of 1st International conference and general meeting of the European society for precision engineering and nanotechnology, (1999), Volume 1, pp. 258-261.

Analysis of PZT tube scanner motion using newly designed sensing mechanism

Hewon Jung , Jongyoup Shim, Daegab Gweon
Department of Mechanical Engineering ME3265,
Korea Advanced Institute of Science and Technology
373-1 Kusung-Dong, Yusong-Gu, Taejon, 305-701, Korea

1. Introduction

PZT tube scanner was invented by Binnig and Smith in 1986.[1] It soon became the predominant design of piezoelectric scanner used in scanning tunneling microscopy(STM)[2], scanning force microscopy(SFM)[3] and near-field scanning optical microscopy(NSOM)[4]. A single PZT tube, with the outer(or inner) metal coating sectioned into four quadrants, with voltages applied on, can generate displacements in three dimentions. Its advantages over the other scanner is prevailing: higher electromechanical constant, higher resonance frequency, and much smaller size, which greatly simplifies vibration isolation. However, tube scanner has disadvantage that its behavior is unpredictable because it has not only nonlinearities such as a hysteresis and creep caused by the inherent characteristics in PZT but also has coupling effect between the axis caused by the tube structure.[5,6] To analyze this displacement behavior including the coupling effect, we need a sensing mechanim which can measure the displacement's change of tube scanner's end without interference between the axis. Therefore, in this study, we introduce a newly designed sensing mechanism for PZT tube scanner, which has decoupling capability for 3 axis by adopting the flexible hinge mechanism. Using this sensing mechanism, we investigate the tube scanner's coupling effect between the axis. This research will be foundation for the future work about the tube scanner's displacement control without nonlinearities.

2. Sensing Mechanism design for PZT tube scanner

Conventional PZT tube scanner has good mechanical properties because it is monolithic and symmetric. However, the tube moves the end effect using angular motion casued by tensile and compressive stresses generated on opposite sides of the tube, resulting the end effect tilting from the original horizontal plane. In order to analyze and compensate this tilt motion, it is necessarily needed to measure the end effect motion of PZT tube scanner precisely in 3 axis. General method to measure the end effect motion is the one using the interferometer in 3 axis. However, the tilt motion of the tube scanner make the beam of interferometer not aligned to the receiver like the Fig. 1.

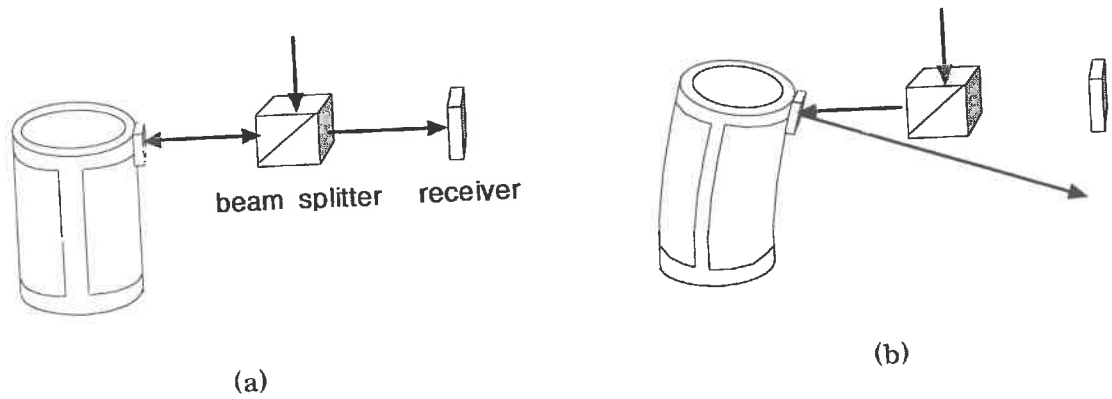

Fig. 1 (a) Measurement of the end effect of tube scanner using the interferometer (b) A schematic diagram of the illustration that the tilt motion of the tube scanner make the beam of interferometer not aligned to the receiver.

Therefore, new sensing mechanism for measurement of the tube scanner is required which is not affected by the tilt motion. To achieve this goal, new sensing mechanism shown in Fig. 2 is designed.

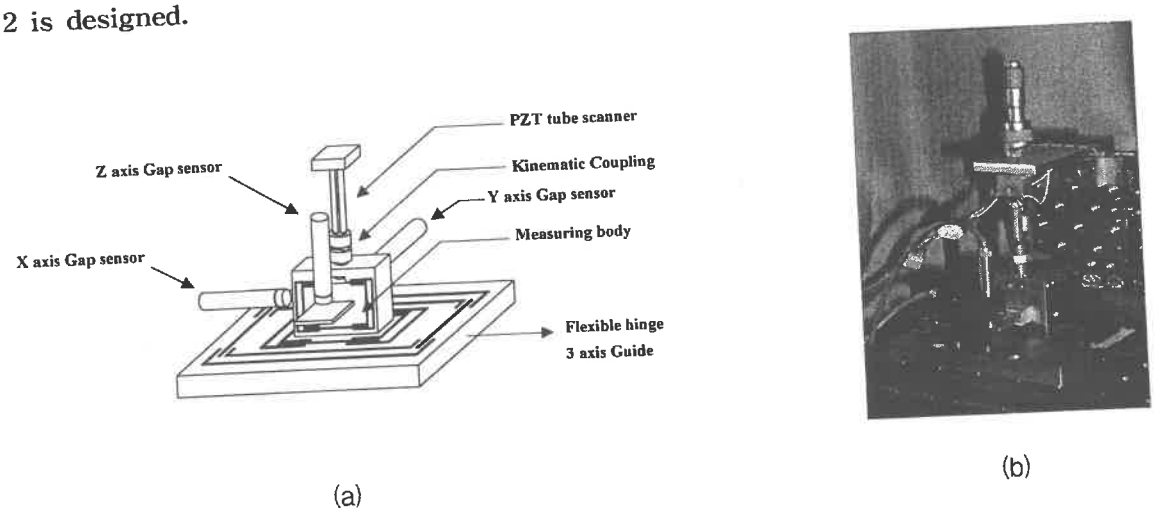

Fig. 2 PZT tube scanner displacement sensing mechanism (a) Schematic of PZT tube scanner displacement sensing mechanism (b) Photo of sensing mechanism

To measure the end effect of PZT tube scanner(PT130.14 Physik Instrumente) in 3 axis regardless of the tilt motion and be easy for measuring process, substitute measuring body is connected to the end effect by the kinematic coupling. Measuring process is performed to the measuring body instead of the end effect by 3 gap sensors(3890 system, ADE) with a 2.5 nm resolution. The measuring body has the same motion with the end effect by the kinematic coupling. However, since this measuring body is guided by 3 axis flexible hinge mechanism[7], this measuring body does not has the tilt motion and but only has the translation motion. Kinematic coupling is constituted to two hole with three sides wall and one ball shown in Fig. 3 It has six contact points which make the end effect and measuring body constrained exactly.

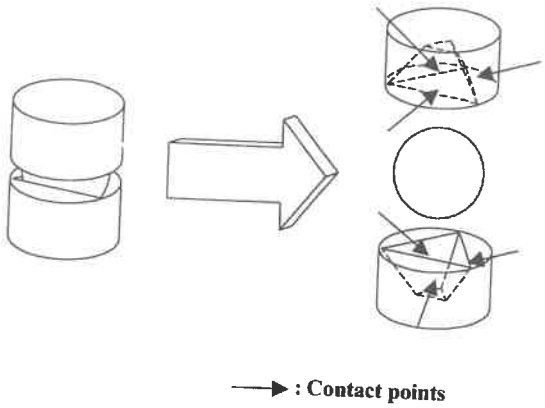

Fig. 3 Kinematic coupling of the sensing mechanism. It has six contact points which make the end effect and measuring body constrained exactly.

3. Experimental result

To test this sensing mechanism, triangular wave voltage is applied to the x electrode in PZT tube scanner. And the output displacement at x direction and displacement at z direction derived by the tilt motion is acquired(Shown in Fig. 4(a)).

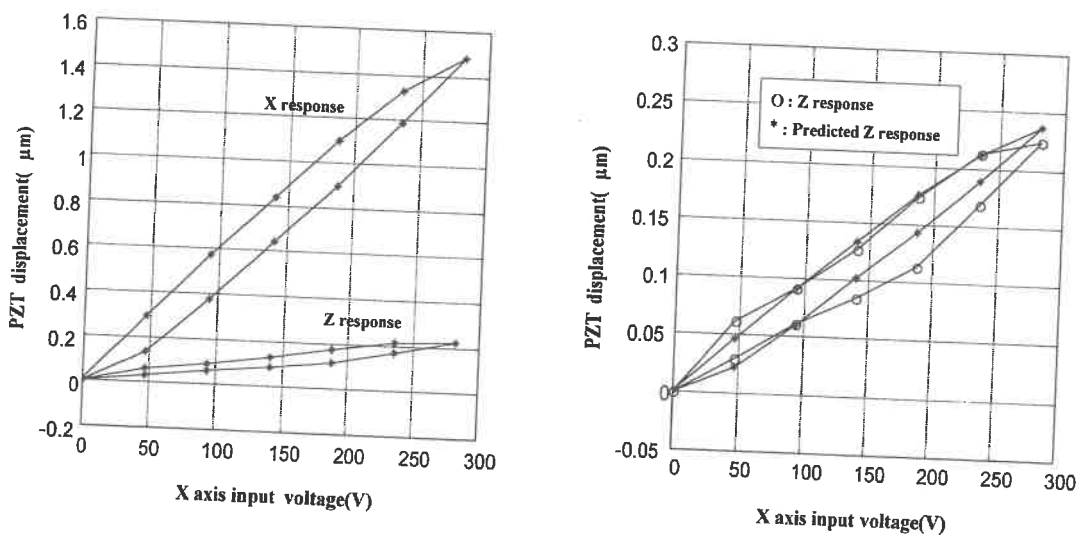

(a) (b)

Fig. 4 Experimental result when input voltage is applied at the x electrode of PZT tube scanner. (a) result of X displacement and derived Z displacement (b) Derived Z response and Predicted Z response

A simple analysis shows that the d_z of the z displacement is derived as follows[6] :

$$d_z = d_x \frac{r}{l} \tag{1}$$

where d_z is the derived Z displacement, d_x is the X displacement, r is the mean radius of the tube(5.75 mm) and l is the length of the tube(36mm). d_z calculated by this equation and d_z by the experiment is shown in Fig. 4(b). Shown in the figure, these two values are almost the same. This fact proves that our newly designed sensing mechanism is very appropriate to measure the PZT tube scanner's out displacement.

4. Conclusion

In this study, we introduce a newly designed sensing mechanism for PZT tube scanner. Using this sensing mechanism, we investigate the tube scanner's coupling effect between the axis. And it is shown that this sensing mechanism is very adequate to measure the PZT tube scanner's displacement. This research will be foundation for the future work about the displacement hysteresis and creep of the tube scanner and tube scanner's displacement control without nonlinearities.

References

[1] G.Binnig and D.P.E. Smith, Rev.Sci.Instrum. 57, 1986, pp. 1688~1689

[2] Y. Kuk and P.J. Silverman, Rev.Sci.Instrum., 60(2), 1989, pp. 165~180

[3] Dror Sarid and Virgil Elings, J.vac.Sci.Technol.B 9(2), Mar/Apr 1991, pp.431~437

[4] U.Durig., D.W.Phol and F.Rohner, J.Appl.Phys., 59(10), 1986, pp. 3318~3327

[5] R.G.Carr, J. of Microscopy, 152, Nov. 1988, pp. 379~385

[6] M. Locatelli and G. Lamboley, Rev. Sci. Instrum., 59, 1988, pp. 661~663

[7] Jong Y Shim, Hewon Chung and DaeGab Gweon, Proceedings from ASPE 1998 Annual Meeting, vol. 18, 1998, pp. 457~461

Comparative Analysis of Halbach and Conventional Linear Motors for Precision Positioning and High Speed Control

Moon G. Lee, Myung J. Chung, Sung Q Lee, and Dae-Gab Gweon

ME3265, Dept. of Mech. Eng., Korea Advanced Institute of Science and Technology
373-1 Kusung-Dong, Yusong-Gu, Taejon, 305-701, Korea

I. Introduction

The control of linear motion over short and long strokes is increasingly required in many applications, such as the semiconductor industry, precision manufacturing, and etc. Brushless permanent magnet (PM) linear motors could offer significant advantages over conventional actuation devices, such as motor driven cams, linkages and pneumatic rams - in terms of efficiency, operating bandwidth, speed and thrust control, stroke and positional accuracy. [1] The motors consist of the rotor with the permanent magnets and the stator with stator windings. Magnetic flux is guided by permeable material, which is used in the stator and backing iron of the rotor.

Conventionally, salient-poles are used to maximize magnetic flux density in air gap where stator coil is wounded. Brushless PM linear motors with salient-poles, however, have the force ripple originated from the reluctance between stator and rotor. The ripple is referred to cogging force. The force ripple is detrimental to precision positioning of the motor for its non-linearity. Non-salient stator can be adopted to remove the force ripple, however, traction force of the motor is not sufficient for it has lower magnetic flux density than salient motor.

The alternative to remove the ripple and to improve the traction force of linear motor is introducing Halbach magnet array (HMA). Using the magnet array, the magnetic flux density can be so highly confined to stator winging that traction force of the motor can be high. There is no salient-pole that there is no magnetic reluctance variation with respect to rotor motion. The reluctance variation is cause of the cogging force.

In this paper, we modeled conventional surface-mounted PM linear motor and HMA linear motor, and analyze the performance of the motors via finite element method (FEM). The conventional motors consist of the rotor with standard permanent magnet array and the stator with salient-poles. The HMA motor has HMA in rotor and non-salient permeable magnetic flux guide. And then we compare performances of the two motors under constraints of same exciting current, same coil windings, and small cogging force. The performances are actuating force production capability and ripple force suppressibility.

II. Conventional brushless PM linear motor with salient poles

Conventional BLPMLM with salient poles is constructed as Fig. 1. If the rotor moves there is force ripple, namely cogging force, without energizing current in coil. Rotor pulls stator so strongly that guide mechanism must support this attraction. If air bearing is used as guide mechanism load capacity of the bearing is about a few tens of kgf.

In order to suppress cogging force under 5% of maximum traction force and reduce the attractive force under 10 kgf, the specification of BLPMLM has selected ad table 1. In the motor the air gap is nearly same as magnet length. Cogging force and attraction becomes larger as the gap is smaller.

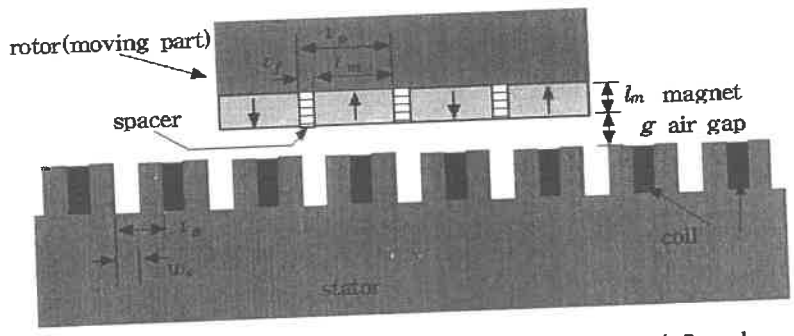

Fig. 1 2-dimensional model of BLPMLM: 2 phase/ 2 pole
(Only one phase coil is presented)

Table 1 Specification of presented BLPMDCM

parameters	nomenclature	value
pole pitch	τ_p	5.08 cm × 0.5
magnet width	τ_m $(=\alpha_m \tau_p)$	5.08 cm × 0.9
slot pitch	τ_s	τ_p × 0.5
slot width	w_s	τ_s × 0.5
magnet length	l_m	τ_p × 0.5
current of coil	i	2 A
winding number of coil	n	300 turns
motor depth	L	10 cm

Ⅲ. Halbach Magnet array linear motor without salient poles

Trumper has proposed HMA in Fig. 2.[2] The motor has no cogging force and attractive force between rotor and stator is very smaller than conventional BLPMLM for there is no high permeable material in rotor components. Therefore the air gap can be selected much smaller than BLPMLM. In the HMA linear motor air gap is selected as a quarter of magnet length.

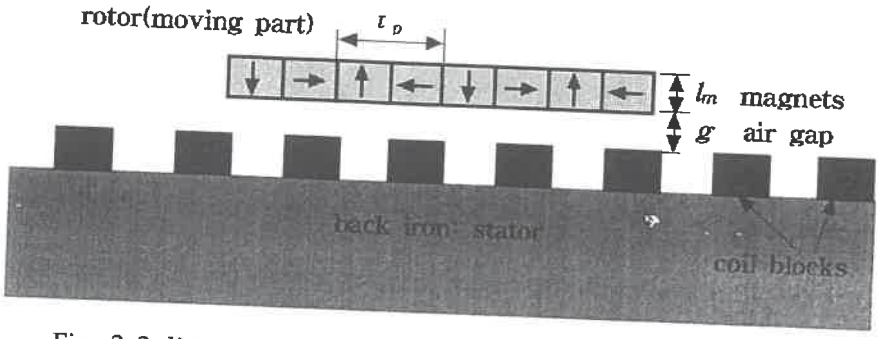

Fig. 2 2-dimensional model of HMA motor: 2 phase/ 2 pole
(Only one phase coil is presented)

Ⅳ. Comparative analysis: BLPMLM vs. HMA linear motor

We analyze the motor's performance using finite element method. The following Fig. 3 and 4 are magnetic flux line of each model.

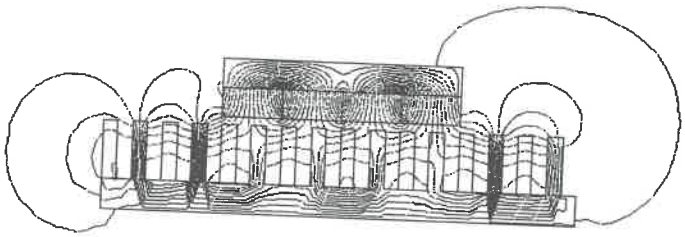

Fig. 3 Finite analysis result of BLPMLM:
magnetic flux line

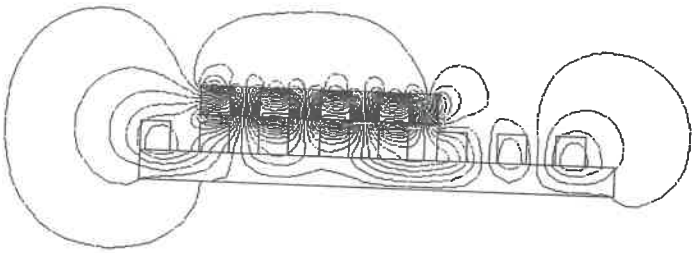

Fig. 4 Finite analysis result of HMA linear motor: magnetic flux line

In the analysis, traction force or actuating force of linear motor is calculated when only one phase coil is energized. Then the force with respect to rotor position is as Fig. 5. From the figure, the actuating force production capability is comparable under condition of small cogging force and attraction force. In BLPMLM, maximum cogging force is 4.9 % of maximum actuating force and maximum attraction force is about 6 kgf.

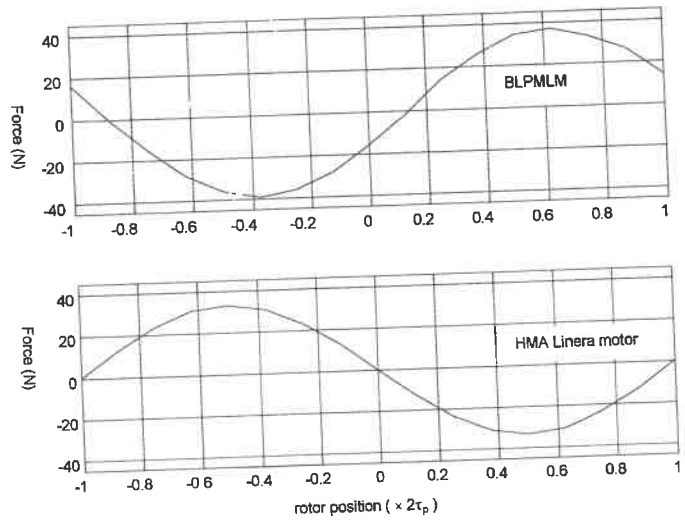

Fig. 5 Actuating force with respect to rotor position for each motor

Generally, actuating force of coreless motor is smaller than that of cored motor. If we must consider cogging force and attraction force, however, HMA linear motor can be strongly recommended even if the force is also important. So, HMA linear motor can be widely used in area precision positioning and high speed actuator needed.

Reference

[1] Z. Q. Zhu et al., Calculation of cogging force in a novel slotted linear tubular brushless permanent magnet motor, in IEEE Trans. on Magnetics, vol. 33, no. 5, September 1 997, pp 4098-4100.

[2] Trumper et. al., Design and Analysis Framework for Linear Permanent Magnet Machines, IEEE Trans. on Industry Applications, vol. 32, no. 2 March/April 1996.

Form and Length Measurements Using a Modified Commercial Form Measuring Instrument

Frank Lüdicke, Otto Jusko, Helge Reimann
Physikalisch-Technische Bundesanstalt (PTB), Braunschweig, Germany

INTRODUCTION

Often small uncertainties, of 0,1 µm and less, are today required in dimensional calibrations. Even the form of artifacts from high-precision manufacture deviates from the ideal shape, and these form deviations influence the uncertainties of length calibrations. At PTB, precise calibrations of the length are therefore always carried out together with form calibrations [1]. Economic as well as measurement uncertainty aspects require the combined measurement of length and form in a single set-up. The term "form" is to include among other things the measurands roundness, straightness and parallelism. As a measuring instrument capable of measuring length and form is not commercially available, a suitable set-up has been developed by PTB.

To satisfy the requirements of applicants from industry PTB had to meet the following conditions: a measuring range of approximately 200 mm x 400 mm and a target uncertainty of ≤0,1 µm for both length and form measurements.

SELECTED BASE INSTRUMENT AND ITS METROLOGICAL PROPERTIES

For economic reasons, a commercial cylinder form measuring instrument with specifications as close as possible to the defined measurement task has been selected. The instrument has a rotary table (C-axis, C-guide), a radial guide (R) and a vertical guide (Z). It was investigated with respect to its metrological properties:

- The measuring range of the guides meets the requirements. As is usual with an instrument of this type, the selected cylinder form measuring instrument was not equipped with a length measuring unit.
- The R-guide deviates from straightness by less than 0,1 µm. The R-guide is, therefore, well suited for installation of a displacement device to be used for length measurements.
- The most precise guide is the C-guide of the rotary table. Its radial deviations are smaller than 0,1 µm.
- Precise adjustments of the probe in the Y-direction were difficult, and it was impossible to move and adjust the probe by computer control in this direction.
- The straightness deviations of the Z-guide were found to be 0,15 µm. The angle between C-axis and Z-guide was about 2 arc seconds (''') and varied with time within 0,3''. On long cylinders the angle deviations would lead to deviations of few micrometers in measurements of the parallelism of the generating lines of cylinders.
- It was found that neither vibrations caused by the instrument itself nor vibrations transmitted by the building significantly affect the form and length measurements.

- The permanent heat generation of the electronics inside the rotary table presented serious problems. The temperature difference between the top of the rotary table and the surrounding space was 3 K.

Some remarks on the temperature influence on measurements:
If the object to be measured is made of steel (uncertainty of the thermal expansion coefficient: $\approx 0{,}4\ K^{-1}$, ambient temperature 20°C), the uncertainty component in length measurements, after correction of the thermal expansion, amounts to about 0,1 µm. The temperature influence on the result of form measurements is even more critical, because no temperature corrections are usually made in form measurements. The temperature gradients, therefore, significantly change the form of the objects to be measured. An ideal cylinder 100 mm in diameter and, for example, 300 mm in length changes approximately into taper shape, with the generating lines deviating from parallelism by about 3 µm, which is indicated by a temperature gradient of about 3 K in the cylinder's axial direction. This example shows the importance of constant temperatures inside the object to be measured and the importance of the minimization of any heat generated inside the form measuring equipment.

As a result some of the instrument's properties obviously needed to be improved to achieve the target uncertainty. These modifications will be described in the following.

METROLOGICAL IMPROVEMENTS

The photograph shows the selected and modified instrument based on the commercial cylinder form measuring instrument.

For length measurements and for the measurement of the probe's displacement in the R-direction a plane-mirror laser interferometer has been added, see photograph. The special three-bar construction (7) of the mechanical linkage of the mirror mount (5) ensures that distortions of the base do not influence the length measurement. To avoid Abbe errors, all laser beam parts had to be positioned in a single plane, including the contacting element and the C- and R-axes. The contacting element of the probing head (9) is positioned at the same height Z as the interferometer (3) (Abbe principle). All optical components of the laser interferometer are adjusted with the aid of a four-fold segment photo-diode to minimize the deviations of the laser beam parts from parallelism in relation to all axial directions. The cross-hair plate (11) is used to adjust the primary laser beam (1) crossing the C-axis on the top of the instrument. The cross-hair plate is positioned with the aid of a diode laser centered on the rotary table.

To eliminate the influence of the straightness and position deviations of the Z-guide the laser interferometer is not only used for length but also for straightness and parallelism measurements. The straightness profile of the interferometer reflector (plane mirror (6)) has been determined by the reversal method, by means of a straight edge standard with an optical surface finish. After elimination of the known deviations from straightness, the mirror is used as the straightness datum line in substitution for the Z-guide.

The arm of the probing head may be positioned horizontally (Y-direction). In this case, the diameter and form measurements of long artifacts can easily be performed because the

element can be brought to any point on the two opposite generating lines of an external cylinder to be measured.

The Y-guide now is replaced by a computer-controlled precise guide. Leveling and centering are also performed by computer control, as is cresting (adjustment to the zenith of the curve) which can be carried out using the newly installed motor-driven Y-guide.

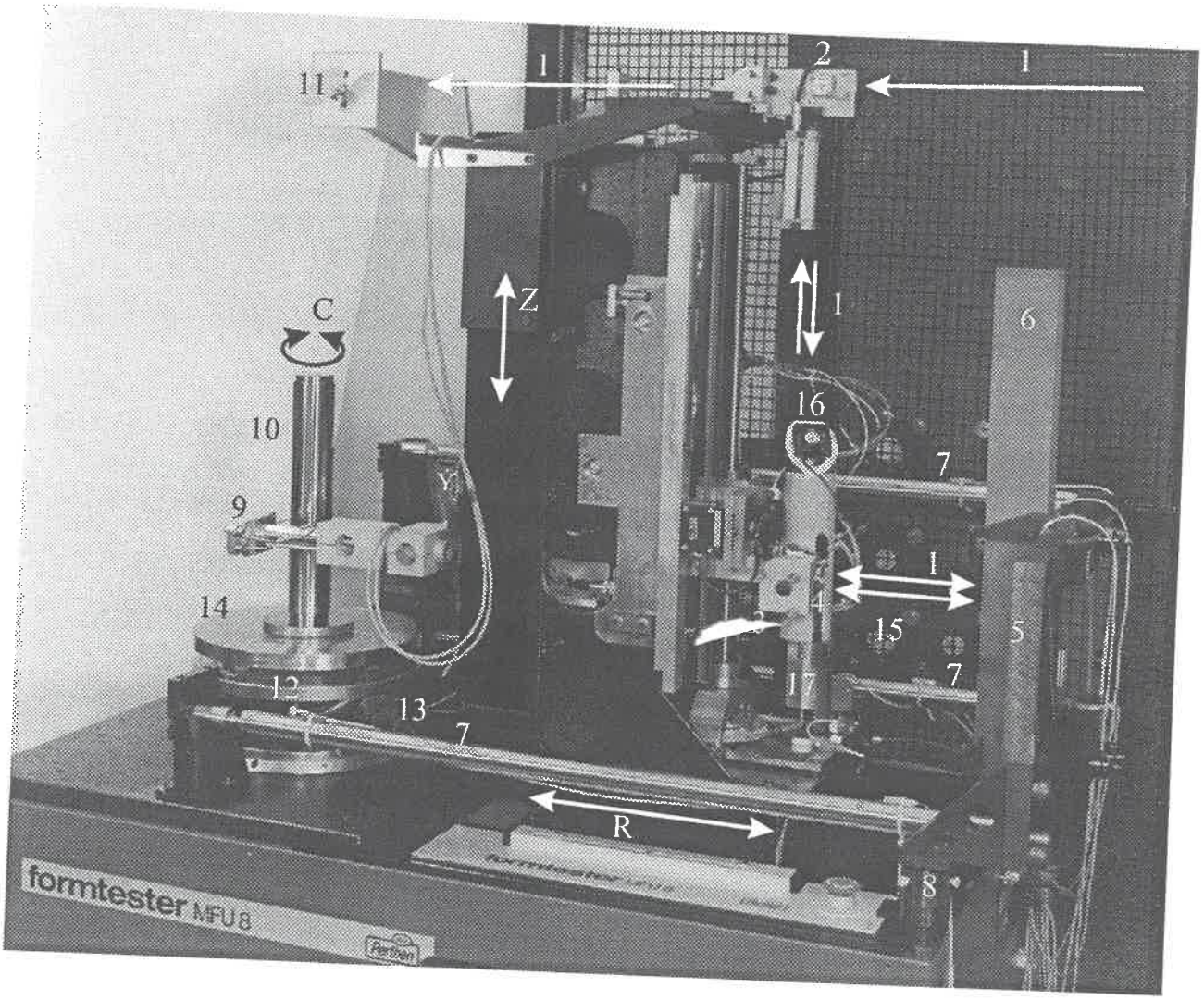

Photograph of the commercial form measuring instrument modified by PTB for form and length measurements

1 laser beams, 2 beam splitter, 3 optical interferometer, 4 quarter wave plate, 5 mirror mount, 6 plane mirror, 7 Invar bars with flexures at their ends, 8 ball in V-grooves in the R-direction (and on the other side of the instrument: a ball between flat faces), 9 probe, 10 object to be measured, 11 cross hair plate, 12 rotary table, 13,15,16 ventilators, 14 Invar plate, 17 motor of the vertical guide,
C rotary axis of the rotary table, R,Y,Z guides perpendicular to each other

During the initial phase of the project, ever increasing restrictions were detected in the commercial version of the instrument when additional data transfers had to be carried out during measurement operations, for example for the diameter measurements with the laser interferometer. This was the reason why a new data transfer system combined with the instrument control system was installed.

The temperature problem of the rotary table has been solved by ventilation. The cylindrical sheet metal side cover of the rotary table has been replaced by a perforated cover (12). In addition, four ventilators (13) have been mounted on this cover sheet, which ensure the supply of fresh air into the electronics of the rotary table. Finally, an additional solid plate (14) with small supports made of material of low thermal conductivity was mounted on the top face of the rotary table to reduce heat transfer. This arrangement reduces the local temperature gradient to 0,1 K.

Moreover, lower thermal gradients along the length measuring light path of the laser interferometer were ensured by the ventilators (15) blowing fresh air into the space between the plane mirror (6) and the interferometer (3). Additionally the temperature increase by a few kelvin during operation of the motor (17) of the vertical guide has been reduced by an exhauster system (16).

MEASUREMENT RESULTS AND OUTLOOK

The verification of the modified instrument regarding length and form measurement was performed by comparison measurements using artifacts whose length and form deviations were known. These were gage blocks, rings, plugs, a Moore type step gage, flicks, roundness standards and multi-wave standards [2] calibrated against PTB's reference instruments [1]. The results obtained for both length and form, agreed within < 0,1 µm with the calibrated values.

The investigation of the modified instrument has shown that the temperature influence due to heat generation and heat transfer has been reduced significantly and that a further reduction may be possible. It is intended to cover the whole instrument with a box and to move the air inside and outside by ventilators as proposed by [3].

As the target uncertainty has been achieved, routine form and length calibrations with the modified instrument will be performed in the very near future.

REFERENCES

[1] F. Lüdicke and H.-J. Rademacher, "Bestimmung von Maß und Form an Zylindern und Kugeln", PTB-Mitteilungen 6/89 (1989), p. 429-433.

[2] O. Jusko, F. Lüdicke, "Novel multi-wave standards for the calibration of form measuring instruments", Proc. 1st EuSPEN, Bremen, Vol. 2, ISBN 3-8265-6085-X, 1999, 299-302.

[3] R. Ziegenbein, F. Lüdicke, and G. Goch, "A New Ultra Precision Instrument for Calibration of Gauges and Measurements of High-Quality Products", Proceedings of 7th IPES (1993 Kobe, Japan), p. 24-27.

Development of Long Depth of Focus Optical Microscopy using Software-confocal Method and its Application to 3-D Profile Measurement

Kimiyuki Mitsui and Tetsuya Uno
Department of Mechanical Engineering
Keio University, Yokohama, Japan

Introduction

Optical microscopes are used for observation, profile and dimensional measurement and assembling the superfine parts of miniature machines or micromachines, but the limited depth of focus of the microscopes often obstruct these operations, so the development of a microscope with greater depth of focus is needed to meet the needs of workers and researchers in this field. Other than clear microscopic observation, long depth of focus optical microscopy is useful for 3-D shape measurements such as cutting tool wear [1].

Confocal laser microscopes, which eliminate defocused image of the object by pinhole, are used to obtain clear images for 3-D profiles, but confocal scanning units have very complicated optical systems and are also very expensive.

One of the authors has already reported a research on expanding depth of focus optical microscope [2]. In the research, the multiple focal images of the targets of observation were fed into a computer and only the images in focus synthesized. The computer was first sequentially input with numerous static images sent from a CCD camera while driving the microscope objective lens. Next, Hadamard transform method (frequency distribution comparison method) was introduced to discriminate and synthesize only the images in focus.

But in the algorithm based on Hadamard transform method, optical microscope picture image consists of 640 x 480 pixels must be divided into smaller segments, for example 16 x 16 or 8 x 8 pixels, and focus measure operation is done on each segments. Therefore, the drawback of the algorithm was exact representation for complicated surface structure was not possible. Furthermore, the algorithm has problem that the focused segment also contains diffused light that is introduced from defocused image of the other part of the object.

In this report we propose an algorithm to obtain focused picture image based on the principle of confocal microscopy. A diffused light introduced by defocusing of the image is removed by computer image processing from the microscope images obtained by CCD camera. The method does not need laser and confocal scanners, which are necessary for confocal laser microscope. The system is composed of only a optical microscope, a CCD camera and a personal computer. The long depth of focus picture images and 3-D profile of a measuring objects can be obtained. The new algorithm to remove a diffused light is proposed as the software-confocal method.

The proposed method is applied for actual image composition and 3-D profile measurements. Specimen, an inclined aluminum plate, miniature ball bearing and leg of an insect, were selected as the measuring objects, and the results show validity of the proposed method to the long depth of focus microscope observation and 3-D profile measurement.

Experimental setup and principle

Figure 1 shows the experimental setup. The system comprises a optical microscope, a CCD camera, a image frame grabber, a personal computer, a X-Y-Z micro stage. The CCD camera is a black and white type with 640 x 480 pixels.

Figure 2 shows image composition procedure proposed in this research. Incremental microscope displacement that correnponds to the depth of focus is used to obtain the image frame sequence of objects. Camera images are transffered to the computer as bit map files and processed. At each pixels, the image frame among the image sequence, which gives a maximum forcus measure, is determined. As the method to calculate maximum forcus measure, the Sum-Modified-Laplacian operator [3] can be used. But, in this study, the focus measure of a pixel is calculated simply as the difference of Intencity value of the pixle to the neighboring pixels (differential method).

Figure 3 shows the basic image formation geometry. Each point on the object

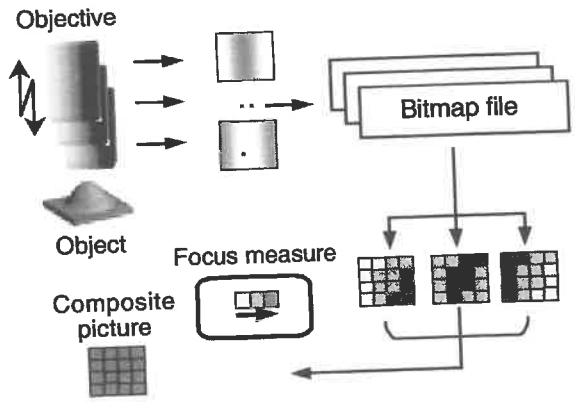

Figure 2: Procedure of picture composition

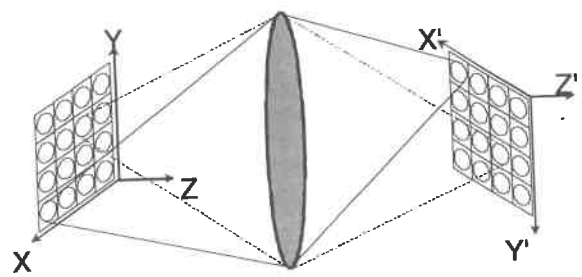

(a) Focused image

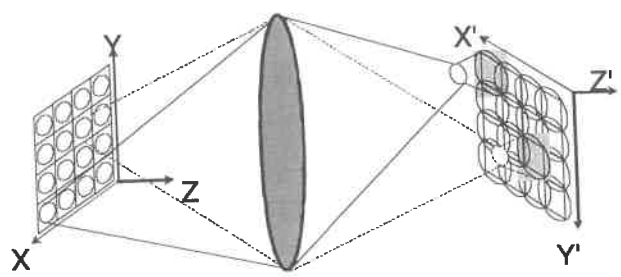

(b) Defocused image

Figure 3: Focused and defocused image

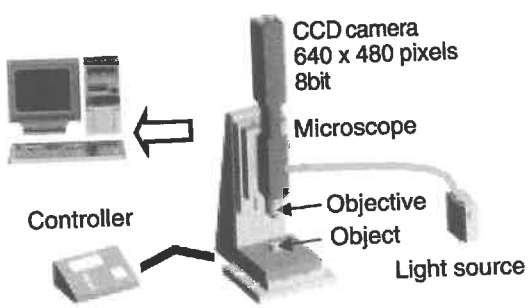

Figure 1: Experimental setup

plane is projected onto a single point on the image plane, thus causing a clear or focused image to be formed on the image plane (Fig. 3 (a)). If, however, the CCD sensor plane does not coincide with the image plane, the light received from the object by the lens is distributed over a circular patch on the sensor plane (Fig. 3 (b)). The distribution of light energy over the circular patch can be modeled as shown in Figure 4.

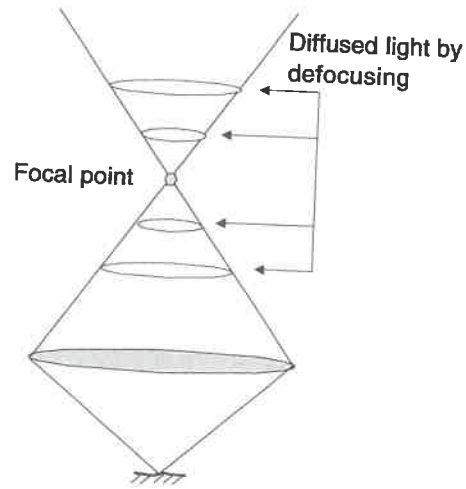

Figure 4: Diffused light by defocusing

Intencity value of each pixles must be compensated by removing diffused light that is introduced from defocused image of the other part of the object. Figure 5 shows the feature that the difussed light from the lower part of the surface does not affect the pixels corresponding to higher part of the surface. Therefore, we can remove the defused light from pixels of the CCD camera one by one from upper part to lower part of the surface. After diffused light is removed from all pixels, the focus level that maximizes the focus measure is calculated again at each pixels.

Experimental results

A tilted aluminum plate, the angle of obliquity is 39 degrees, is observed by the microscope. The aluminum plate was polished with sandpaper. The height difference of right and left endpoints in the microscope field of view corresponds to 350 μm. The 35 2-D parent images were obtained and 3 of them are shown in Figure 6 (a),(b), and (c). The images were taken with a 10x objective on a tool microscope. The height distance between the images was 10 μm. Figure 6 (d) and (e) show the composite picture images obtained by the differential method and proposed software-confocal method. Figure 6 (e) and (f) show 3-D shapes of the inclined plate obtained by these two methods. It is obvious that software-confocal method can provide far more accurate 3-D shape than conventional method. However, noise components are seen at the left and

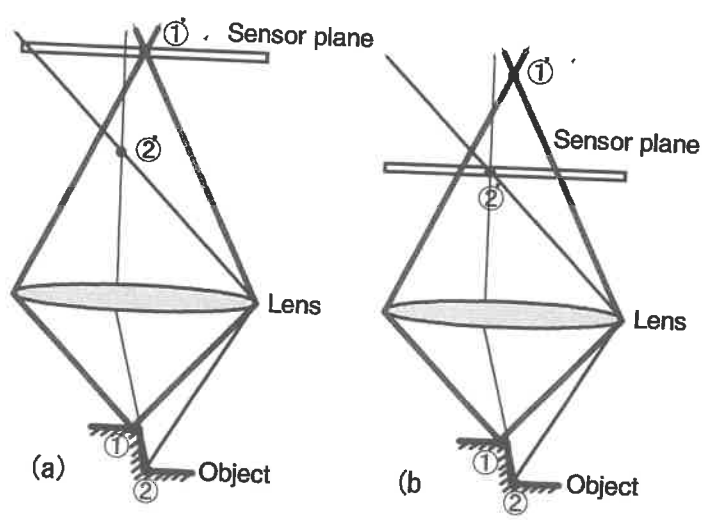

Figure 5: Overlap of the diffused light
(a) Diffused light from ② dose not affect on ①'
(b) Diffused light form ① affects on ②'

right endpoints in Figure 6 (f), further improvement of the image processing algorithm is needed.

Conclusion

The purpose of this study was to develop a 3-D shape measuring technique for micro components using a microscope, a CCD camera and a personal computer. Newly proposed software-confocal method can remove a diffused light due to defocusing images from individual pixels of a CCD camera. The proposed method is applied for actual image composition and 3-D profile measurement. Specimen, an inclined aluminum plate, was selected as the measuring object, and the results shows validity of the proposed method to the long depth of focus microscope observation and 3-D profile measurement.

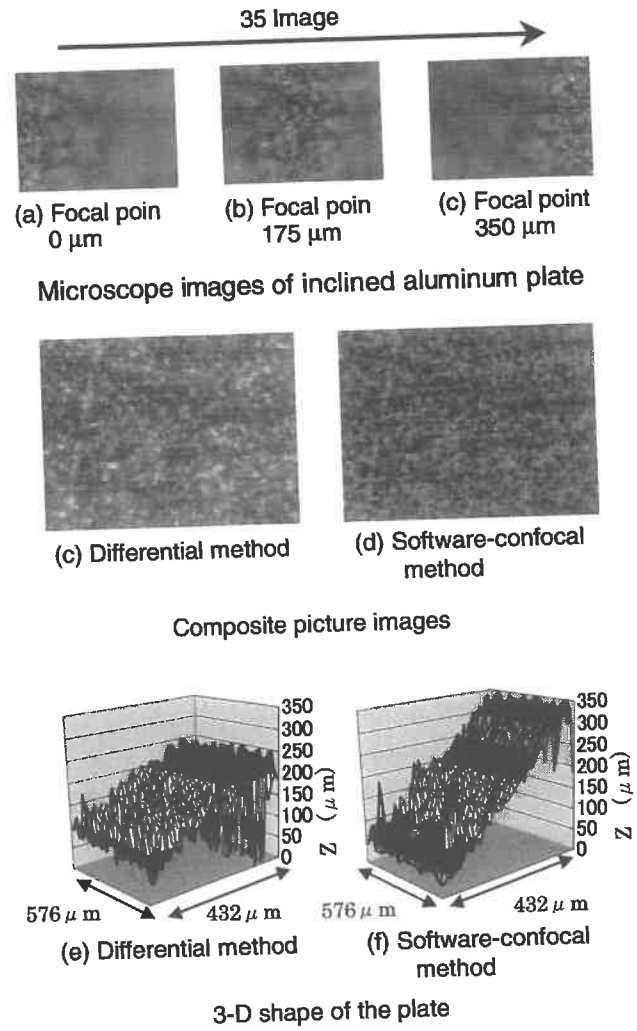

Figure 6: 3-D shape measurement of inclined plate

References

[1] K. S. Moon and Z. K. Ling: Measurement of Cutting Tool Wear with Shape-From-Focus (SFF) Method, Proceedings Vol. 20, ASPE (1999) 75.

[2] T.Shiraishi and K.Mitsui: Development of a Long Depth of a Focus Optical Microscopy Based on Computer Image Processing, Proceedings of ASPE Annual Meeting (1993) 392.

[3] S. K. Nayar and Y. Nakagawa: Shape from Focus - An Effective Approach for Rough Surfaces -, IEEE Int. Conf. on Robotics and Automation (1990) 218.

A Micro Coordinate Measurement System with Virtual Contact Probe

K. W. Ng*, K. S. Moon*, C. R. Friedrich* and Z. K. Ling**

* Department of ME-EM
Michigan Technological University
Houghton, Michigan
** Ford Motor Company
Dearborn, Michigan

Abstract

This paper presents a micro coordinate measurement system to provide 3-D coordinate measurement environment for very small and ultra precision manufactured parts. The system is based on the concept of "virtual contact probe". It consists of two main modules. They are computer-aided microscope module and geometric modeling module. In this study, a commercial version of white-light interferometric metrology microscope is used as the computer-aided microscope module where it provides the height data of an object. The system also uses a commercial CAD system (IDEAS) as the geometric modeling module. The potential of the proposed system is demonstrated by the results of the implementation, which shows 3-D metrology capability.

Key words: micro, coordinate measuring machine (CMM), virtual, CAD

Introduction

Manufactured parts usually consist of many geometrical features such as circles, lines, planes, spheres, cylinders and so forth. Coordinate measuring machines (CMM's) have been used to measure the features three dimensionally. In general, CMM's have been applied for measuring parts with medium or large volume. For the particular task of measuring small parts, specially designed CMMs also have been developed (Jansen et al., 1999). However, for the parts with measuring volume of less than $1cm^3$, CMM's with conventional touch probes may have limited applications.

There have been attempts to integrate CMM and CAD/CAM system. They use the CAD/CAD system and the CMM for planning and executing dimensional measurement of manufactured parts having complex and sculptured surfaces (Wong et al., 1991). In this paper, a micro coordinate measurement system to provide 3-D coordinate measurement environment with measuring volume of less than $1cm^3$ is presented. The key component of the proposed system is the "virtual contact probe". The concept of "virtual contact probe" is rather similar to that of the CMM. It uses the pointing tool of CAD system as the "virtual contact probe". It makes a measurement by acquiring points on the CAD screen using the probe.

The system consists of two main modules. They are computer-aided microscope module, and geometric modeling nodule. The computer-aided microscope module provides a non-contact and 3-D height measurement capability with he range from a few micrometer scales to over several millimeters. In this study, a commercial version of white-light nterferometric metrology microscope is used to provide the height data of an object. Next, an IGES (Initial Graphics Exchange Standards) file is generated based on the height data. The resultant IGES file serves as the bridge between the eight data and the geometric modeling module.

Computer-Aided Microscope Module

Several micro-measurement techniques can be used in the computer-aid microscope module. Recently, some special computer-aided microscopes have been developed such as white-light interferometric microscopes (Bruning et al., 1974, Bhushan et al., 1985). In this study, a commercial version of white-light interferometric metrology microscope has been used. The microscope (Phase Shift Technology MicroXAM) can produce sampling of 748 by 480 data points with the axial resolution of 2.5 nm (standard mode) and the lateral resolution of 690 nm (20X microscope objective). Micro milling and drilling processes at Michigan Tech produced the sample used for this study. Figure 1 is a photograph of the sample. The shape of an arc and the holes machined by end milling and drilling processes can be observed from the 2-D microscopic photo. The 3-D height data of the sample are given in Figure 2.

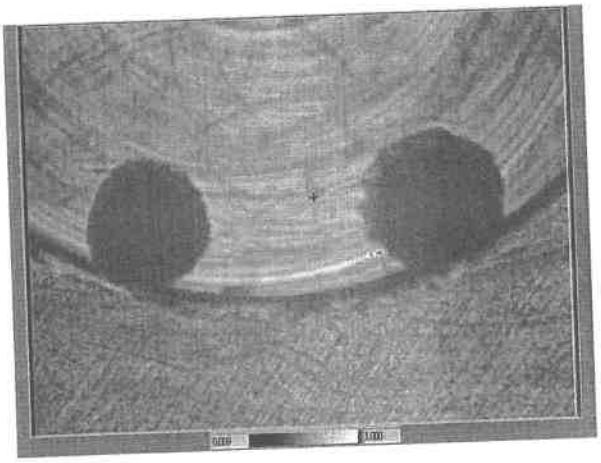

Figure 1. Microscopic photo of the sample

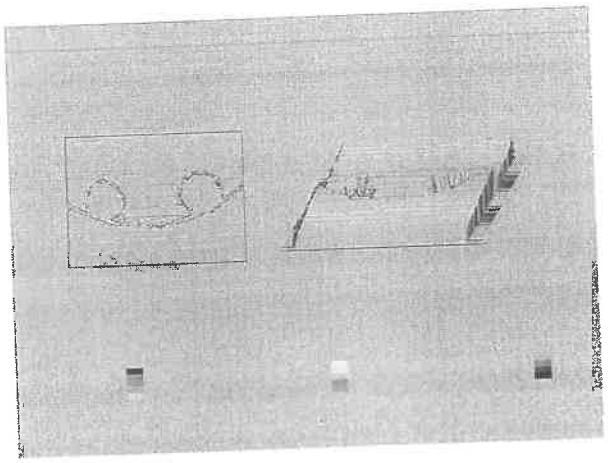

Figure 2. 3-D height plot from the white-light interferometric mi

Geometric Modeling Module

From the computer aide microscope module, a set of points that represent the shape (height data) of the sample has been generated. With the assistance of geometric modeling tools, such as determining distances between two geometric entities, setting up datum planes, the resultant model can be used to provide a virtual measurement environment. In this geometric modeling module, the system uses a commercial CAD system (IDEAS) as its platform. An IGES (Initial Graphics Exchange Standards) file is generated based on the height data from the previous module. This file represents the shape of the measured object. There are different ways to represent the shape model. In this system, the shape will be represented with methods that have various complexities. First, the shape is represented by elements with four vertices. Second, the shape is established with the lofting technique. In this study, a C-language based program has been developed to transform the height data generated by the microscope into an IGES file. Figure 3 provides an IDEAS screen snapshot generated by the IGES file. It can be noted that it is the same image as the one in Figure 2.

The available tools in the geometric modeling platform can be used as the coordinate measuring means. In particular, pointing tool can be used as a "virtual touch probe". Other tools include measuring linear and angula quantities, establishing datum lines, planes, and surfaces, determining surface normal, viewing the object from variou perspectives, zooming in and out of the surface, and etc. In this paper, circular and step height measurement has bee performed as an example. Selecting three points from the arc has performed for the circular measurement. The step

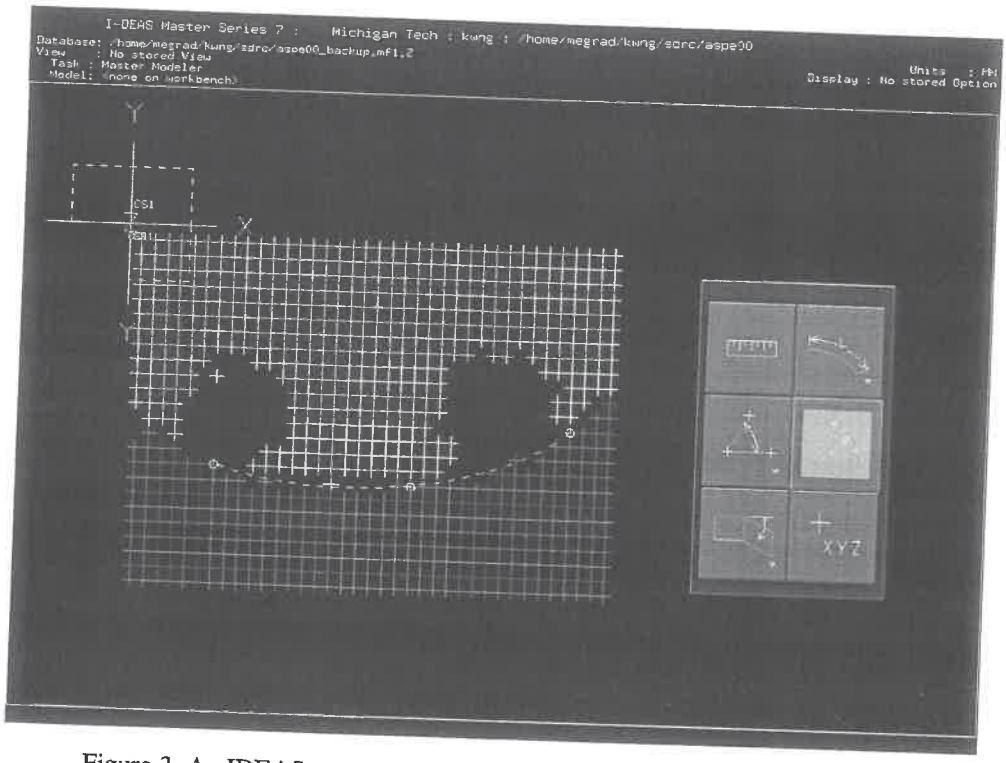

Figure 3. An IDEAS screen snapshot showing the same image as Figure 2

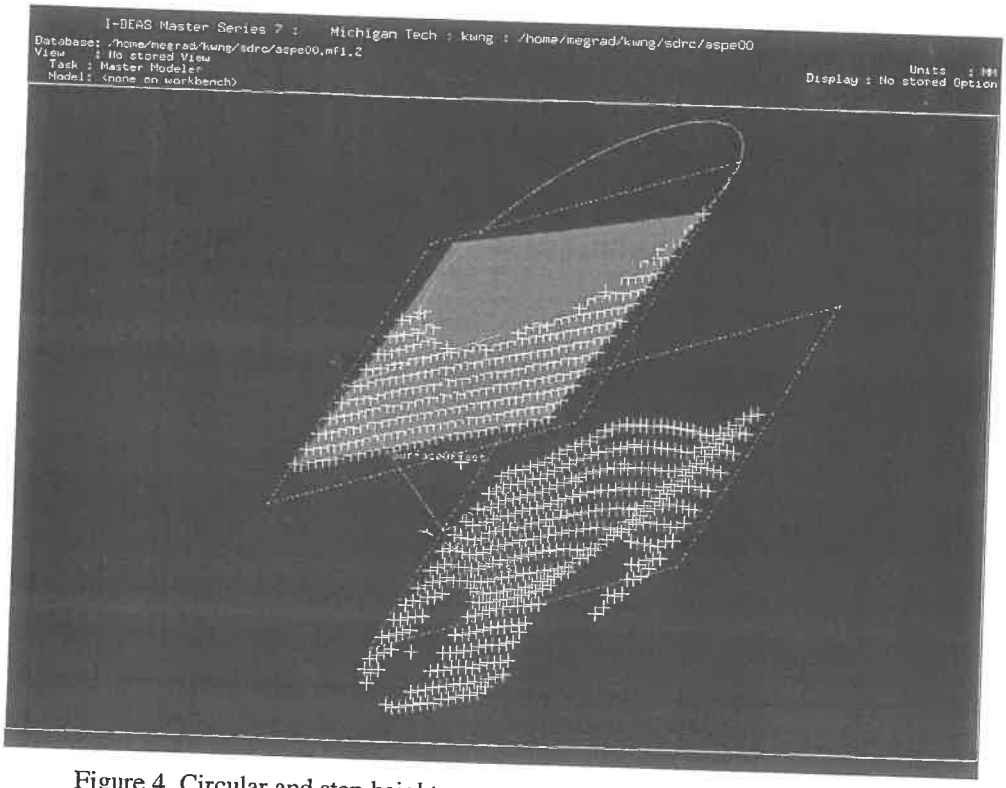

Figure 4. Circular and step height measurement using the virtual touch probe

height has been measured by establishing planes by selecting points and finding the distance between the two planes. The measurement results are given by

Coordinate of center point: (16.345 μm, 10.691 μm, 24.668 μm)

Radius: 16.400 μm

Datum plane equation: -0.04491 x –0.9023 y – 0.4286 z + 21.789 (μm)

Distance (step height): 16.876 μm

Conclusions

In this paper, a system for measuring 3-D coordinates of a part has been proposed. The system is appropriate for the micro coordinate measurement of very small part. The system includes precision surface height measuring instrument and geometric modeling platform. Its potential application in 3-D metrology has been demonstrated using a sample measurement. The proposed method requires extensive calculations to generate IGES file, especially for large size height data. For this study, it took about 30 minutes to perform all the required data processing using a workstation (SUN ULTRA10). However, the fast-improving performance of computers can make the technique attractive.

References

Bhushan, B., Wyant, J. C., and Koliopoulos, C. L., 1985, "Measurement of Surface Topography of Magnetic Tapes by Mirau Interferometry," Applied Optics, vol., 24, pp. 1489-1497.

Bruning J. H., D. R. Herriott, J. E. Gallagher, D. P. Rosenfeld, A. D. White, and D. J. Brangaccio, 1974, "Digital Wavefront Measuring Interferometer for Testing Optical Surfaces and Lenses," Applied Optics, vol. 13, pp. 2693-2703.

Jansen, A., N. L. Rosielle, P. Schellekens, 1999, "A Fully Elastically guided 3-D CMM With A Measuring Volume of 1 cm^3", Proceedings of the 14th The ASPE Annual Meeting, October, Monterey, California, pp. 452-460.

Wong, C. L., C.H. Menq, and R. Bailey, 1991, "Computer-Integrated Dimensional Inspection of Manufactured Objects Having Sculptured Surfaces," Advanced Manufacturing Engineering, vol. 3, no. 1, pp. 37-44.

Enhancements to the Pellissier H5 Hydrostatic Level

David H. Parker,* John W. Shelton,† Bill Radcliff,‡
The National Radio Astronomy Observatory§
Key Words: hydrostatic level, laser ranging, radio telescope

1 Introduction

The Pellissier H5 Hydrostatic Level is used for applications requiring an order of magnitude improvement in accuracy over conventional optical leveling. The H5 has been used on such applications as the 32-meter radius track for the National Radio Astronomy Observatory (NRAO) Green Bank Telescope (GBT) alidade, the Final Focus Test Beam (FFTB) project at Stanford Linear Accelerator Center (SLAC), the Superconducting Super Collider (SSC), measurements of the Golden Gate Bridge, etc. For the GBT alidade track, 16 benchmarks on a 32-meter radius were measured 3 times over a 2-week period. In each case, the levels closed to better than 0.050 mm over the 200-meter run. The H5 has been well described in the literature by Imfeld, Pellissier, Plouffe, and Ruland [1], so a description will not be repeated in this article.

The GBT metrology system [2,3] will employ 12 ground-based laser ranging instruments on a 120-meter radius, i.e., 12 monuments on 62-meter spacing (0.75 km loop). The metrology system will use measured distances only, so the 3-D coordinates of the instrument locations are required in order to do trilateration calculations. The goal is to establish the (x,y,z) coordinates to an accuracy of less than 0.1 mm. The x and y coordinates can be measured by the instruments, but due to the insensitivity of the monument geometry in the z direction, and the need to orient the ground instruments with respect to the gravity vector (to point the telescope), hydrostatic leveling is required.

2 Enhancements

While the H5 is semi-automated, two operators are required to work in synchronization to achieve accurate results. The sense probe is motor-driven down, but the return is manually operated. Touching the instrument to drive the probe up introduces small vibrations that can introduce errors by detecting the crest of a small wave instead of the steady state level. Operator fatigue can also be a problem for extended measurements. The H5 measurement heads are connected by a fixed 15-meter hose; thus, a measurement between a set of monuments would require 4 stable, temporary bench marks to span the 62-meter distances. Due to the 0.75-km run to close the circle, it was decided to extend the hose length to 63 meters, and automate the operation. The model NPH6 (the NRAO enhanced version of the Pellissier H5) includes: motor driven probes on digital indicators; modular coaxial hoses that are quickly removable from the measurement heads; electrically operated solenoid valves; 120 VAC operation; an external pump and reservoir (both measurement heads are identical); RTD temperature probes at each well and both sides of the pump; total computer control, with RS485 interface to all components, and real-time display of all parameters. See Figure 1.

3 Operation

There are two fundamental sources of error in a hydrostatic level. Due to the change in the density of water with temperature, any difference in temperature between two legs of a sag in the hose will result in a difference in the static height of the water at the two ends. The other source of error is the dilation of the connecting hose. When the water is pumped through the hose to purge air bubbles or equalize the temperature, the pressure dilates the hose

* Green Bank, WV, dparker@nrao.edu, (304) 456-2121
† Green Bank, WV, jshelton@nrao.edu, (304) 456-2117
‡ Green Bank, WV, bradclif@nrao.edu, (304) 456-2122
§ The National Radio Astronomy Observatory is operated by Associated Universities, Inc. under cooperative agreement with the National Science Foundation

slightly. As the hose relaxes after pumping the water level rises in the measurement wells. This dictates that a pair of measurements be made nearly simultaneously in order to minimize the error of the rising water level. Of course, there are many additional ways to go wrong.

With the NPH6, outdoor measurements are made in the evening to avoid temperature gradients introduced by the sun. The hose is supported and held level on a temporary strut rail, as defined by a masonry line, to avoid the "U" tube error. The water is circulated through a coaxial hose arrangement, with the inner hose acting as the sense line and the outer hose acting as a return and moderator.

The dilation problem is minimized by using a wire reinforced sense line, synchronizing the sense probes to contact within 0.5 seconds of each other, and signal processing. Due to the automation, it is easy to take data for 30 minutes or more. By plotting the data and looking at the individual well levels, the sum of the well levels, and the differential between the well levels, errors can usually be detected. For example, spikes easily detect contamination of the water in a well in one well level. Contamination always causes the probe to drive deeper in the water before making contact. A leak or drop of condensate into the well is seen in the sum of the well levels. Of course, the differential level is the ultimate goal of the measurement. By looking at trends over minutes, errors can be detected.

Synchronized measurements are made at the rate of about 2.5 per minute. Data is typically taken for about 30 minutes (75 points) and then plotted and analyzed. After an initial characteristic transient period of around 10 minutes, a section of data is selected as the actual measurement.

4 Calibration

The instrument zero point was calibrated in the lab, on a surface plate with a short hose, to minimize thermal errors. Repeatability of the zero point is around 0.002 mm. Repeatability of the measurement with a 63-meter hose is checked in the lab by coiling the hose on a table level to the surface plate. Repeatability of the 63-meter hose is around 0.006 mm. The differential was checked by raising one instrument on a gage block.

5 Results

Four outdoor monuments were measured in November 1999 on calm evenings (one pair each evening). Multiple sets of data were taken, after circulating the water between measurements. The standard deviations for the 63-meter distances were 0.0046 mm, 0.0038 mm, and 0.0075 mm — about the same as in the lab.

Figure 2 shows the well levels for 5 water circulation and measurement cycles. Note that a shorter length indicates a higher water level. Note that immediately after a circulation operation, the level shows a characteristic exponential decay (rising water level) as the hose relaxes. This is followed by a period of gently increasing or decreasing level. Figure 4 shows the differential level. Note that the sun set around 17:30 and there is a significant change (0.050 mm) in the differential for the following measurement cycles. Figure 5 shows an expanded version of the levels around 19:00.

6 Acknowledgement

The authors wish to acknowledge the contribution of Pierre Pellissier, the leading authority on hydrostatic leveling. who kindly taught us the tricks of the trade and provided the enabling technology to make the NPH6 a reality. Though he has passed on, his contribution to the science continues.

7 References

[1]. Hans L. Imfeld, Pierre Pellissier, Dan Plouffe, and Robert Ruland, Proc. Fifth International Workshop on Accelerator Alignment, Argonne Nat. Lab, Oct, 1997.

[2] David H. Parker and John M. Payne, "Metrology System for the Green Bank Telescope", Proc. ASPE 1999 Annual Meeting, Vol. 20, p.21-24.

[3] http://info.gb.nrao.edu

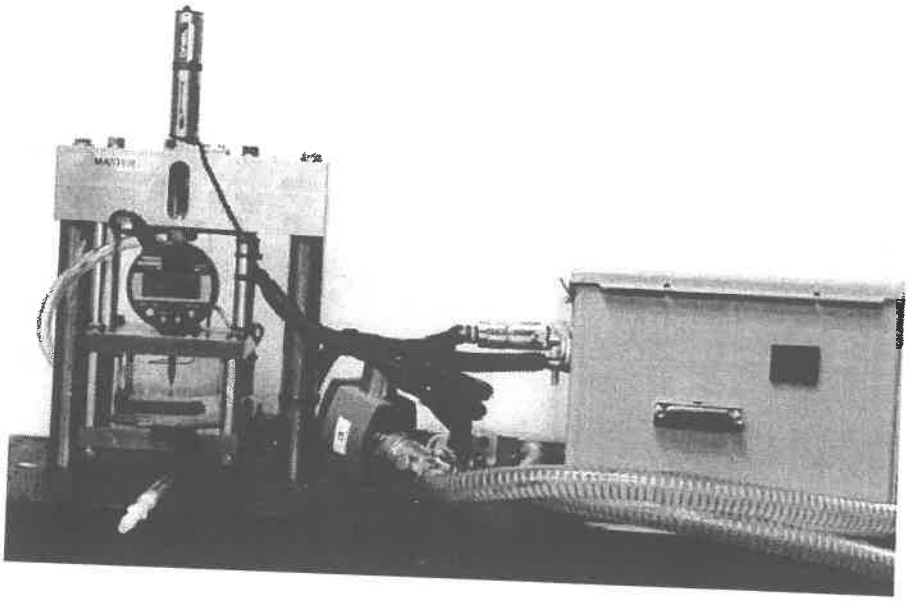

Figure 1

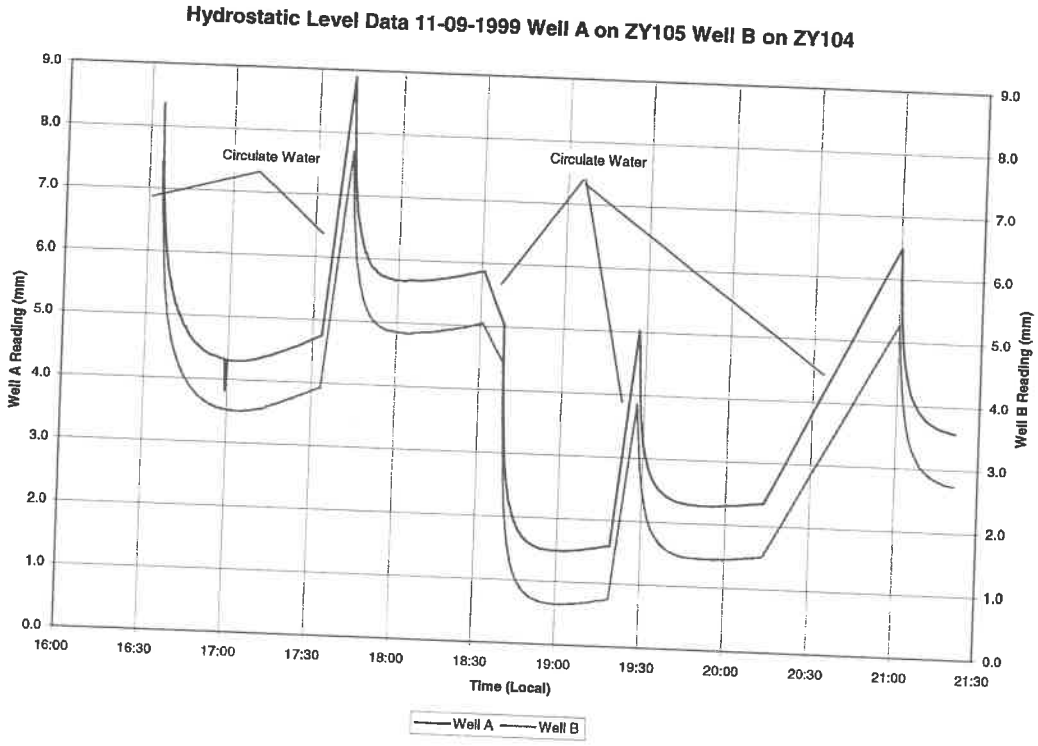

Figure 2

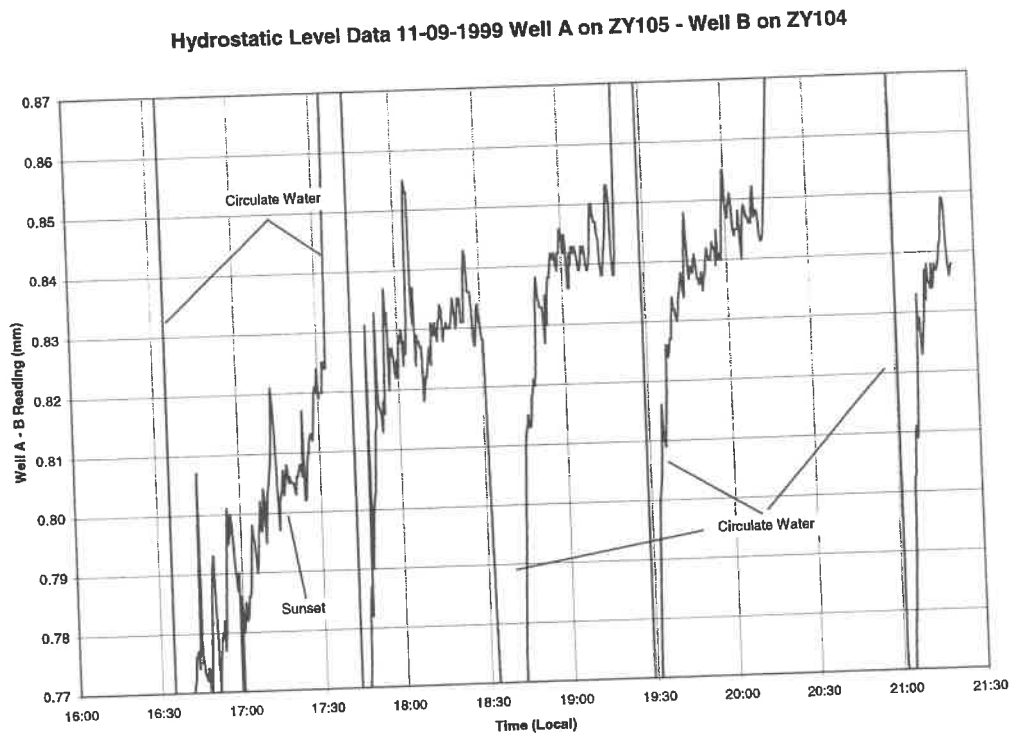

Figure 3

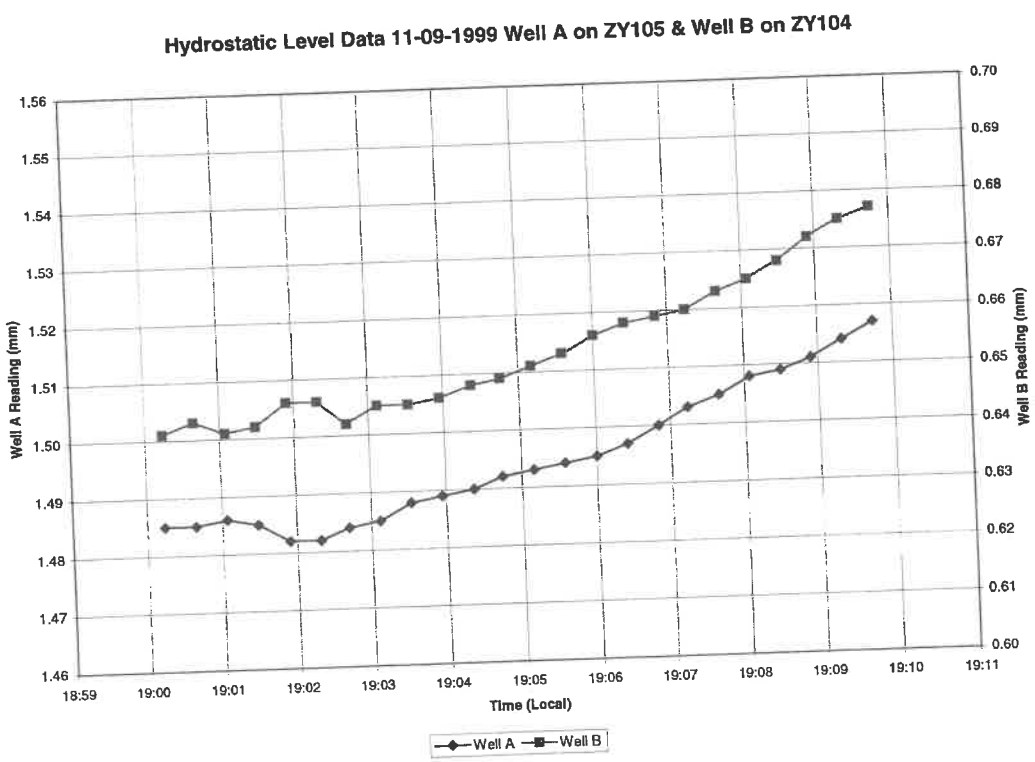

Figure 4

A DETACHABLE STEP GAGE FOR THE CALIBRATION OF VERTICAL MACHINING CENTERS AND BRIDGE TYPE COORDINATE MEASURING MACHINES

Sousa, A.R.[1]; Schneider, C.A.[2]
LABMETRO - Metrology and Automation Laboratory
UFSC - Federal University of Santa Catarina - Brazil
[1]ars@labmetro.ufsc.br and [2]cas@certi.ufsc.br

Abstract

The use of 2D calibrated artifacts (hole and ball plates) to verify the accuracy of Coordinate Measuring Machines and Vertical Machining Centers imposes some difficulties when testing vertical axis of such equipments, because of the need of measuring the plate vertically, parallel to the path of the machine axis. In this paper, a detachable step gage has been designed and tested to overcome this problem, particularly critical for testing purpose in Machining Centers. The results have shown a good dimensional stability of this artifact and repeatability of the positioning and the repositioning during the calibration. Comparisons with a laser interferometer device have shown better results and smaller uncertainty compared to a hole plate under the same test.

1. PROBLEMS DURING CALIBRATION OF MULTI-AXES MACHINES WITH CALIBRATED ARTIFACTS

The use of 2D calibrated artifacts to verify the accuracy of Coordinate Measuring Machines (CMM) has increased significantly in the last years, as a consequence of its metrological reliability and time efficiency, what makes it a more efficient alternative to CMM calibration and geometric tests on Machining Tools (MT) with touch probes **[1]**. However, in this calibration process it is necessary to measure the plate in the vertical position what cause some problems, due to the necessity of adaptation of a horizontal stylus on the touch probe and to the necessity of positioning the plate a distance away from the path of the vertical axis (usually Z-axis) **[2]**.

The necessity to place the plate away from the Z-axis increases significantly the uncertainty of the calibration, as the horizontal adaptation increases the probe uncertainty and the angular errors (row, pitch and yaw) have a greater influence because the artifact and the Z-axis are not aligned (*Abbe* off-set errors). These factors contribute to increase in more than 100% the uncertainty of the results in the calibration of CMM or in the geometric test of MT.

The problem is more critical when testing vertical machine tools, because its vertical column is larger than vertical columns of Coordinate measuring machines and, then, it is necessary to adapt long horizontal stylus to the touch probe as can be seen in the test shown in figure 1. In this test, a long horizontal stylus (300 mm) was adapted to the touch probe, in order to measure vertically a hole plate, in the geometric test of a vertical milling machine. Due to this adaptation, the uncertainty introduced by the touch probe increased significantly, when compared to the uncertainty of the touch probe in its original condition.

This problem would be overtaken only if the artifact could be positioned aligned with the vertical column of the machine and, this condition would be satisfied only if the artifact could be mounted/dismounted as the vertical axis moved along its vertical path. In this article, this solution was implemented with the use of a detachable artifacts described in the next section.

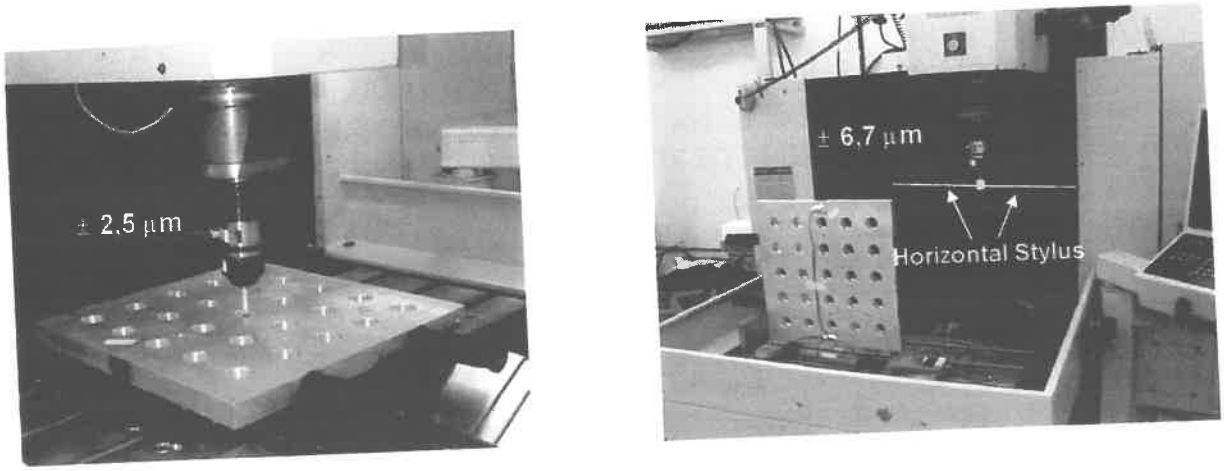

Figure 1 – Probe uncertainties (3D) in different measurement planes

2. A DETACHABLE STEP GAGE TO THE CALIBRATION OF VERTICAL AXES

A solution for the problem described above was reached using a vertical detachable artifact, as shown in figure 2 [3]. Triangular bases with spheres fixed in their centers are supported over inferior bases with kinematic mounting to assure a good repeatability in the positioning and repositioning of the bases [4]. During the calibration of the artifact on a CMM, the position of the sphere fixed on the inferior base is measured and the other bases are positioned over the inferior ones and the position of the central spheres determined. The measurements of the spheres are carried out in several cycles, upward and downward, in order to evaluate the repeatability of the kinematic mounting. The same experimental procedure is performed during the calibration of a CMM or during the geometrical test of a MT and, from the comparison between calibrated and measured positions, the geometrical errors are evaluated. It is possible to determine the errors of linear positioning in *Z* direction (zpz), straightness of the *Z*-axis in *X* (ztx) and *Y* (zty) directions, and squareness between *X* and *Z* (xwz), and between *Y* and *Z* (ywz).

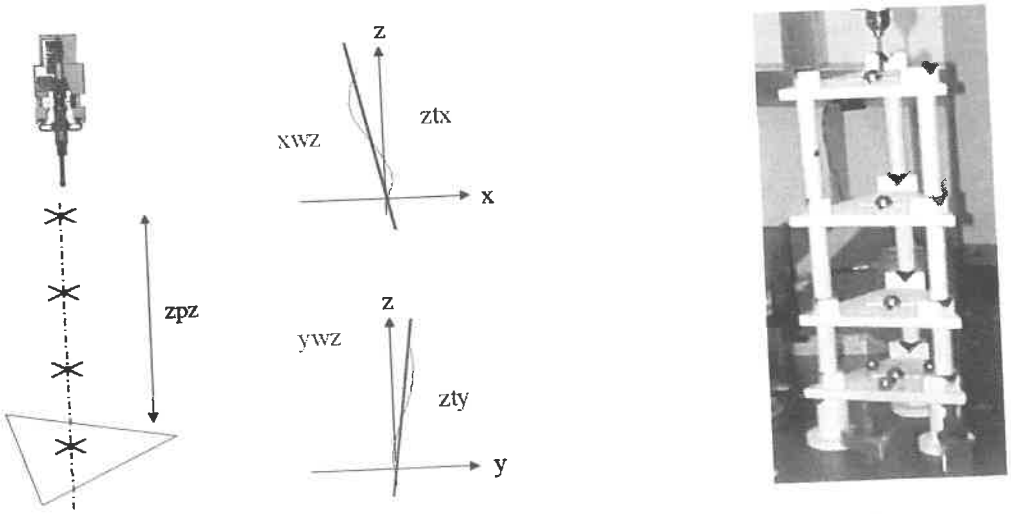

Figure 2 – A detachable step gage to the calibration of vertical axis of CMM and MT

3. EXPERIMENTAL RESULTS

The detachable step gage was calibrated on a CMM Zeiss ZMC550 measuring the reference spheres as the artifact was mounted and dismounted, in several cycles. Those results can be found at Figure 3, where it is possible to realize that the deviations in the sphere's center from the mean position are usually under 1 μm. The uncertainty (U95), considering other factors, was estimated in ± 2,2 μm.

		Cycles and Deviations [μm]									
		U	D	U	D	U	D	U	D	U	D
BASES		1	2	3	4	5	6	7	8	9	10
1	X	-0,4	0,0	0,0	0,2	0,1	0,0	0,2	0,0	0,2	-0,3
	Y	-0,3	0,1	0,0	0,0	0,3	0,0	0,1	0,1	-0,1	-0,2
	Z	0,2	0,1	-0,1	-0,2	-0,1	0,1	-0,1	0,1	0,0	0,0
1+3	X	0,2	0,0	-0,2	0,0	-0,1	0,2	-0,1	0,1	0,1	-0,2
	Y	0,3	-0,2	-0,2	0,2	0,0	-0,2	0,4	0,0	-0,3	0,0
	Z	0,2	-0,1	0,2	0,1	0,0	-0,4	-0,3	0,2	0,1	-0,1
1+3+4	X	0,2	-1,7	0,0	1,1	-0,1	-0,4	-0,1	1,0	0,1	0,1
	Y	0,2	-0,4	-1,0	0,2	0,5	-0,2	-0,3	0,5	0,2	0,2
	Z	0,3	-0,1	0,3	-0,2	-0,1	-0,6	0,1	-0,1	0,2	0,2
1+3+4+2	X	-0,4	-0,4	-0,4	0,6	-0,1	0,2	0,2	-0,1	0,2	0,2
	Y	-1,5	0,0	0,5	0,6	0,7	0,5	-0,3	0,0	-0,2	-0,2
	Z	-0,1	-0,2	0,1	0,2	0,6	-0,3	0,2	0,0	-0,3	-0,2
1+3+4+5	X	0,2	-0,2	0,1	0,3	0,1	0,1	-0,2	-0,3	0,1	0,1
	Y	0,7	0,7	-0,6	0,2	-0,2	0,2	-0,5	-0,2	-0,2	-0,1
	Z	0,1	0,1	0,3	-0,1	-0,4	-0,3	-0,2	0,1	0,1	0,2

U = Upward D = Downward

Figure 3 – Deviations from the mean position in mounting and dismounting cycles

After the calibration, the artifact was used in the geometric test of a vertical milling machine with a touch probe. The spheres were measured in several upward and downward cycles and the temperature from the artifact and form the machine tool were monitored for thermal compensation. Comparing the calibrated with the measured positions, the error of linear positioning in the Z-axis was estimated.

The same test was performed using a laser interferometer and a hole plate vertically positioned (with a horizontal stylus on the probe) and the results are found in figure 4. It is possible to verify a very good coincidence in the results of laser and the detachable step gage. When comparing the results obtained with the hole plate, it becomes clear that the long stylus adapted to the touch probe influenced significantly its metrological reliability. When analyzing only the laser and the detachable step gage, the artifact has operational advantages compared to the laser. The test of Z-axis was performed in 1 hour with the artifact and in 3 hours with the laser.

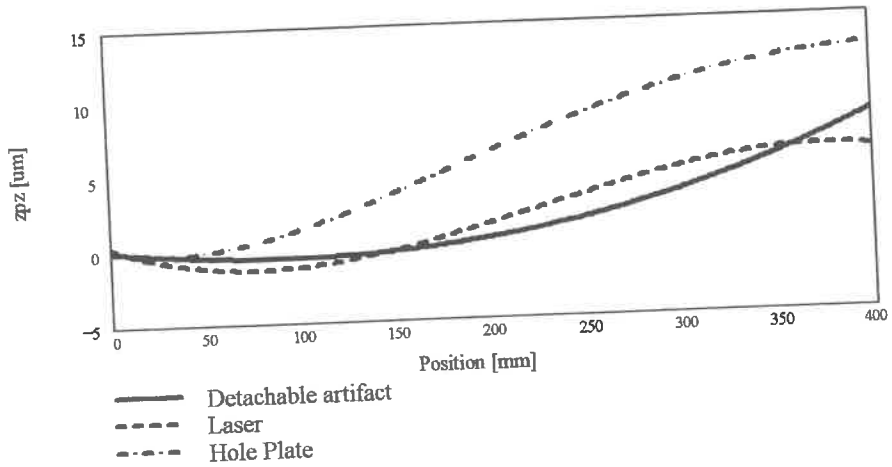

Figure 4 – Comparison of test methods in the test of a vertical axis of a CNC milling machine

4. CONCLUSIONS

Excellent results were obtained in this work, indicating that the kinematic mounting can be applied in calibrated artifacts to overcome limitations during the calibration process of vertical axis of Coordinate Measuring Machines and Vertical Machining Centers, when using hole and ball plates [5].

The detachable artifact showed a repeatability bellow 1 µm during repositioning operations, with an uncertainty of ± 2,2 µm (95 %) in the reference centers of the spheres, with a good flexibility. Its geometry assures a thermo-symmetric structure and the materials applied in the contact elements have a strong dimensional stability in more than two years of use.

Several developments have been implemented on this artifact to improve its metrological reliability to make it possible to verify volumetric accuracy (3D) of multi-axis machines, and not only along one axis (1D).

5. REFERENCES

[1] **Sousa, A. and Schneider, C. A.** *An indirect method to verify and enhance machine tool accuracy.* Proceeding of LAMDAMAP IV, Laser Metrology and Machine Performance, July 1999.

[2] **Trapet, E. and Wäldele, F.** *A reference object based method to determine the parametric error components of coordinate measuring machines* Measurement, Vol. 9, No 1, pp. 17 - 21, 1991.

[3] **Sousa, A.** *Calibrated artifacts with Coordinate Metrology innovating the Geometric tests of Machining Centers.* Doctor Thesis, Federal University of Santa Catarina - Brazil, 2000 (in Portuguese).

[4] *Introduction to Positioning Equipment.* Technical Report, Newport Inc, 1997.

[5] **Sousa, A. and Schneider, C. A.** *A comparison between laser interferometric and calibrated artifacts for the geometric test of machine tools.* Proceedings of the International Symposium on Laser Metrology for Precision Measurement in Industry, October 1999.

Design and Use of a Precision Bearing Analyzer

Vincent C. Vigliano, Eric R. Marsh
Machine Dynamics Research Lab
The Pennsylvania State University
University Park, Pa. 16802.

Introduction

For precision ball bearing analysis, careful design of structural and measurement loops is required for increased repeatability and accuracy. The computer-controlled bearing analyzer developed for this work is designed, manufactured, and programmed to take reliable error motion measurements with an accuracy of one microinch (25 nanometers). In addition to the development of the bearing analyzer, a study was performed on how fixed sensitive direction relates to inner race roundness and how rotating sensitive direction relates to outer race roundness.

Bearing Analyzer Hardware and Components

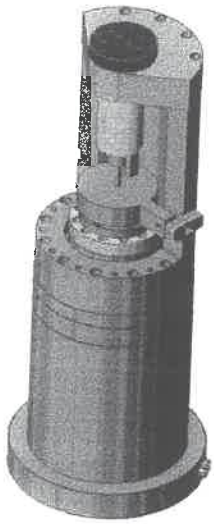

Figure 1. The Bearing Analyzer

The bearing analyzer spindle is a Professional Instruments® motorized 3R Blockhead with a linear brushless DC motor. A Heidenhain® ERO 1221 (1024 counts/rev) rotary encoder is attached to the base of the spindle. Lion Precision® capacitance gages with 50 V/0.001 in. sensitivities record radial displacements. The data acquisition setup includes a 5MHz, 12-bit National Instruments® data acquisition board, attached to one of the computer's PCI ports. National Instruments' LabWindows/CVI® software controls the data acquisition board and performs signal processing and data analysis. Professional Instruments® also manufactured the motor housing and air bearing load cell.

The outer race of the bearing being tested is fitted into a precision-made holder; the inner race is mounted on a spherical pilot attached to the motorized 3R. During a test, the inner race rotates while the outer race is restricted from rotation. The air bearing load cell imparts axial preload. Two capacitance gages (not shown) are then set to gage on the ground outer surface of the bearing holder in X and Y directions[1].

Data Acquisition and Analysis

The data acquisition is computer-controlled and uses simultaneous sample and hold capabilities of the board for analysis at 10,000 RPM. The maximum resolution of the board is 0.25 mV which is 1 LSB at an A/D range of ±0.5V. This is compatible with the high-resolution Lion Precision® capacitance gages.

For the software, LabWindows/CVI® has a user interface format that is capable of running as a stand-alone executable. The underlying code used for user interface controls and data analysis is C++®. After the raw data is acquired, the user has an option to run a digital, window-type low pass

[1] Tlusty, J., System and Methods of Testing Machine Tools, *Microtechnic*, vol. 13, 1959

filter with a linear phase. The user may specify the number of filter coefficients to be used and the cutoff (in upr). For fixed sensitive direction measurement, the fundamental frequency (1 upr) is removed from the data and the data is scaled to the appropriate units. The rotating sensitive direction measurement mathematics is described in ANSI B89.3.4M Axis of Rotation. Axial tests require that the fundamental frequency remain so the data is simply scaled to appropriate units and displayed. A fixed sensitive direction radial error motion test on a Fafnir 7204W® angular contact ball bearing is shown.

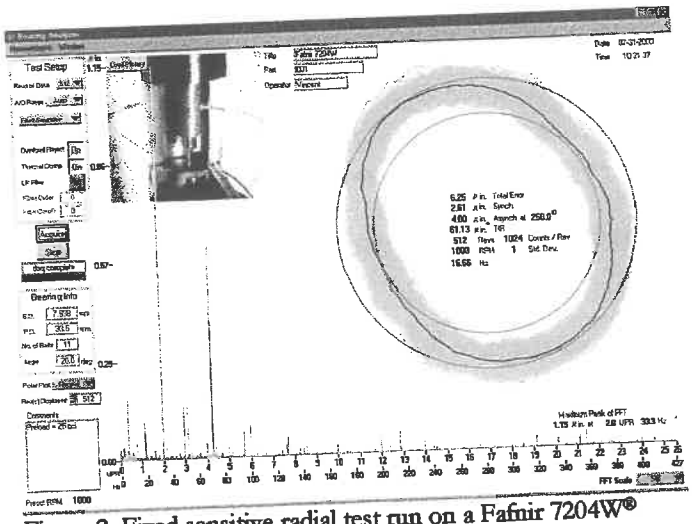

Figure 2. Fixed sensitive radial test run on a Fafnir 7204W® angular contact ball bearing. 18.2 µin Total Error, 4.3 µin Synchronous Error, 4.0 µin. Asynchronous Error.

The bearing analyzer software also has the ability to display the FFT spectrum of the data, which enables identification of certain ball bearing errors and defects[2]. The frequency calculations are available from a wide range of sources, the equations from Harris' Rolling Bearing Analysis are used in this case. Using given information from a bearing such as ball diameter, pitch diameter, and number of balls, the specific frequencies of cage rotation, ball spin, inner/outer race form errors and ball defects can be found.

Frequency Analysis of Ball Bearings

From the angular contact ball bearing frequency equations, several calculated frequencies are displayed on the bearing analyzer. A separate window is devoted to this frequency analysis where the specific frequency values are reported with a plot of the localized FFT spectrum.

The frequency analysis window is valuable for attaining specific information about a ball bearing, but lacks the ability for a quick comparison between several bearings of the same type. This would be accomplished by assigning a scaled value to each of the factors that represent the total error motion of the bearing so a user could ascertain which frequencies are contributing the most as well as perform a quality comparison between bearings in a batch.

---

2 Harris, T., *Rolling Bearing Analysis*, Wiley Interscience, 1991, p 950

Fixed and Rotating Sensitive Direction Measurements on the Bearing Analyzer

For spindle error analysis, the error motion test may be different depending on what type of sensitive direction the application uses. For instance, diamond turning on a lathe uses a fixed sensitive direction; the spindle rotates the workpiece while the tool is fixed. Therefore a fixed sensitive direction test on the lathe's spindle would be used to predict roundness in the parts. Likewise, a rotating sensitive test would be performed on a jig-borer, which rotates the tool while the workpiece remains fixed.

In terms of ball bearings, it has been postulated that rotating sensitive direction measurement is related to the outer race form while fixed sensitive direction measurement relates to the inner race form. An experiment was conducted on the bearing analyzer to study this relationship. Two Fafnir 7204W® were disassembled and the outer races were press fit into aluminum holders manufactured to be 2-lobed and 3-lobed. Two inner races were tested as received; one was 3-lobed and the other 2-lobed.

Results of the Fixed and Rotating Sensitive Tests

The following combinations of inner and outer races are shown with total, synchronous, and asynchronous radial error motions:

Inner Race	Roundness (µin.)	Outer Race	Roundness (µin.)	Total Radial Error Motion (µin.)	Synchronous (µin.)/Form	Asynchronous (µin.)
2-lobed	32.2	3-lobed	247.2	42.2	12.6/ 2-lobed	30.5
2-lobed	32.2	2-lobed	428.6	162.0	19.4/2,3,4-lobed	119.1
3-lobed	43.2	2-lobed	428.6	74.5	7.3/3-lobed	37.3
3-lobed	43.2	3-lobed	247.2	50.3	7.0/2,3,4-lobed	45.0

Table 1. Fixed Sensitive Direction

Inner Race	Roundness (µin.)	Outer Race	Roundness (µin.)	Total Radial Error Motion (µin.)	Synchronous (µin.)/Form	Asynchronous (µin.)
2-lobed	32.2	3-lobed	247.2	69.1	21.0/ 3-lobed	62.3
2-lobed	32.2	2-lobed	428.6	183.2	18.3/2,3,4-lobed	169.9
3-lobed	43.2	2-lobed	428.6	53.1	17.1/2 and 4-lobed	62.8
3-lobed	43.2	3-lobed	247.2	60.5	11.7/2,3,4-lobed	50.0

Table 2. Rotating Sensitive Direction

As an example, the first case (2-lobed inner race, 3-lobed outer race) comparison is shown below. The (a) plots represent the roundness traces of the specific races while the (b) plots are the resulting error motions.

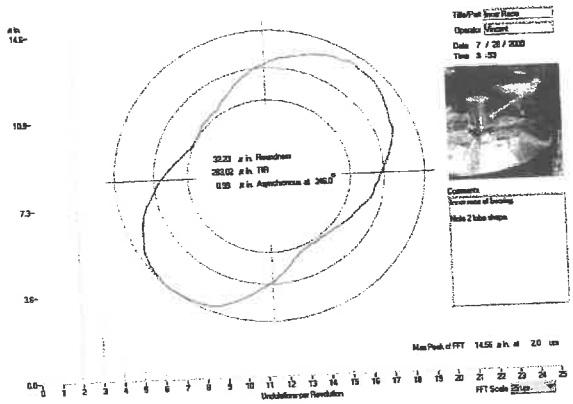

Figure 7a. Inner Race 32.2 µin. Roundness

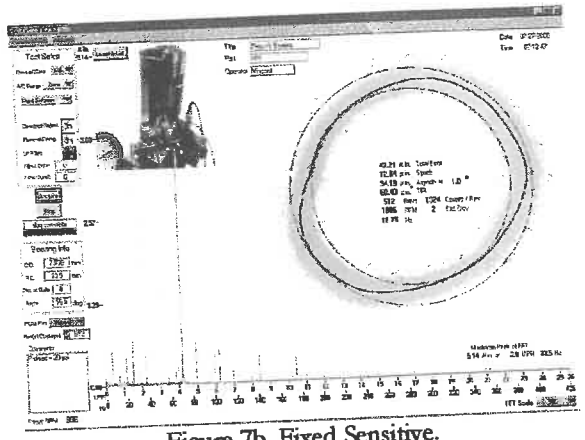

Figure 7b. Fixed Sensitive.
Total 42.2 µin., Synch. 12.6 µin., Asynch. 30.5 µin.

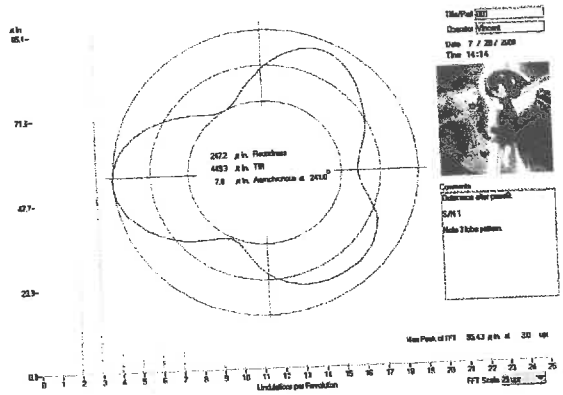

Figure 8a. Outer Race 247.2 µin. Roundness

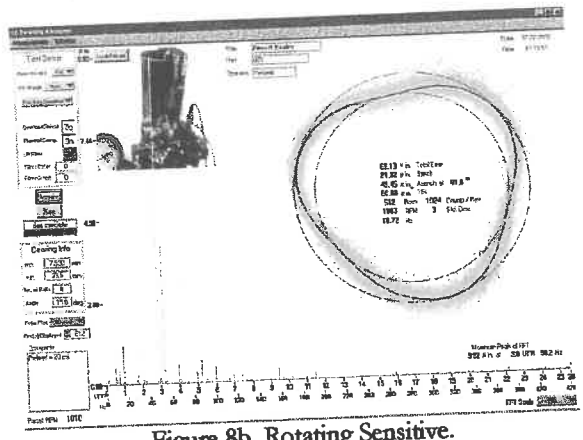

Figure 8b. Rotating Sensitive.
Total 69.1 µin., Synch. 21.0 µin., Asynch. 62.3 µin.

Conclusions and Future Work

In summary, the hypothesis was that the number of lobes on the inner race would match the number of lobes of the radial error motion in the fixed sensitive direction and similarly for the outer race and the rotating sensitive direction. This was the case when one race was 2-lobed and the other 3-lobed. However, when both races were 2-lobed or 3-lobed, the forms were not distinct in the polar plot of the radial error motion in either the fixed or rotating sensitive directions. The two or three undulations per revolution content were overshadowed by other frequencies.

Further examination of the resulting error motions from a 2-lobed inner race/2-lobed outer race and a 3-lobed inner race/3-lobed outer race will be performed. Also, the attenuation of the inner and outer race roundness in the bearing analysis will be explored as well as how preload affects total, synchronous, and asynchronous error motions.

Acknowledgments
The authors would like to personally thank Mel Liebers, Dave Arneson, Randy Hasser, and Dan Oss from Professional Instruments for their valuable input and assistance. Also, we'd like to thank Larry Tell for helping with several software issues.

A Convolved Multi-Gaussian Probability Distribution for Surface Topography Applications

J.David Cogdell
The Timken Company
Timken Research, RES-09
P.O. Box 6930
Canton, OH 44706-0930 U.S.A.

Introduction

Engineering surfaces, particularly those generated using multi-step manufacturing processes and intended for tribological applications like bearings and gears, rarely if ever have normally-distributed elevations. As Williamson and Greenwood observed over forty years ago, dual-process and worn surfaces often exhibit two or more distinct scales of texture - a relatively rough original structure with a finer-scale structure existing atop truncated ridges and peaks of the original structure. In the case of dual-process surfaces the original, primary structure is often generated by grinding and the smoother secondary structure by honing, lapping, or polishing. Both single and multi-process surfaces may be further modified in service by adhesive, abrasive, or corrosive wear mechanisms, all of which can generate additional fine-scale structure. Especially in the case of three-body abrasive wear, this tertiary structure may be generated primarily on the highest elevations of the as-manufactured secondary structure.

Quantification of multi-scale texture has relied primarily on one of two method, both involving plotting the cumulative distribution function on normal probability scales. If there is only one, perfectly Gaussian distribution the data plots as a straight line with slope proportional to the standard deviation of the elevations. Multiple, distinct distributions exhibit discontinuities in slope: the slopes on either side of a discontinuity can be related to the RMS roughness values of the constituent distributions. It is also possible to derive values for mean elevation of the discrete components. It must be noted, however, that because of the effects of convolution of the multiple textures, neither the RMS nor the mean elevation values derived in this manner are correct.

One alternative is the procedure described in DIN 4776-1990 for calculation of the Rk family of surface topography parameters. Basically this involves modeling the bearing area curve as a series of straight lines approximating the material and void volumes of the structure. There are, however, problems both with accuracy of representation and with numerical stability.

A convolved, multi-normal probability distribution model has been developed corresponding to the usual case of successively finer-scale Gaussian structure residing atop the worn upper extremities of the coarser structure immediately below - i.e. secondary structure existing on the worn peaks and ridges of the rougher primary structure, tertiary structure atop the secondary, etc. The model is fit to measured topography data using a Levenberg-Marquardt nonlinear regression routine inside an iterative loop. Normal practice is to obtain (3D) topography data using either interferometric or scanning probe microscopes, although the method works equally well for profile data from stylus instruments. The solution train begins with the global data mean and standard deviation as the initial guess for the primary structure parameters. It stops automatically upon failure to meet all of five validity criteria, and reports the previous (last valid) solution. The converged solution yields means, RMS values, and percent area coverage for all statistically significant structural components. The method is illustrated graphically with examples from common engineering surfaces covering two orders of magnitude of roughness – from 6 to over 600 nm RMS.

It is also possible – although not illustrated here - to replace selected Gaussian components in the model with non-Gaussian probability distributions, e.g. scallops corresponding to cutting tool nose radius - thereby allowing characterization of e.g. hard-turned or diamond-machined surfaces with honed or polished ridges.

It is anticipated that this characterization method will be useful primarily for surface generation process development applications.

Theory

The discrete probability distribution corresponding to a normally-distributed surface is given by the familiar Gaussian equation (1), expressing the probability f(z) in terms of the population mean and standard deviation μ and σ. In equation 1, f, μ and σ are written with subscipts: these will be used to denote the order of the Gaussian – primary, secondary, tertiary, etc.

$$f(z)_i = \frac{1}{\sigma_i\sqrt{2\pi}} e^{-0.5\left(\frac{z-\mu_i}{\sigma_i}\right)} \qquad (1)$$

$i=1,2 \ldots n$

The complementary distribution C(z) is given in equation 2 as one minus the integral of f(z) from minus infinity to z. C(z) can also be expressed for computational convenience in terms of the error function.

$$C(z)_i = 1 - \int_{-\infty}^{z} f(v)_i dv \equiv 0.5\left(1 - erf\left(\frac{z-\mu_i}{\sigma\sqrt{2}}\right)\right) \qquad (2)$$

$i=1,2 \ldots n$

The global discrete probability distribution G_2 for the case where the peaks of one (primary) distribution are truncated by the secondary distribution, both individually Gaussian, is given exactly by equation 3, i.e. as the sum of the product of f_1 *and* C_2 and f_2 *and* C_1. Note that the primary and secondary structure each truncate the other, so that both distributions are area-wise discontinuous. The complimentary distribution terms express the fraction of plan area over which the individual probability terms apply.

$$G_2 = f_1C_2 + C_1f_2 \qquad (3)$$

Equation 3 is readily extended to an arbitrary number of levels, where increasing levels are assumed to have increasingly smaller standard deviations and to reside entirely on the truncated peaks of the immediately preceding distribution. The basic concept has much in common with the concept of self-similarity.

Equation 4 extends Equation 3 to arbitrarily many Gaussian levels. The result can be expressed concisely as the sum of a series of products.

$$\begin{aligned} G_n &= f_1C_2 + C_1[f_2C_3 + C_2[f_3C_4 + C_3[f_4C_5 + \ldots C_{n-1}[f_nC_{n+1}]]]] \\ &= f_1C_2 + C_1f_2C_3 + C_1C_2f_3C_4 + \ldots C_1C_2C_3\ldots C_{n-1}f_nC_{n+1} \\ &= \sum_{j=1}^{n}\prod_{k=0}^{j-1} C_k f_j C_{j+1} \qquad \textit{where } C_0 = C_{n+1} \equiv 1 \end{aligned} \qquad (4)$$

Implementation

Equation 4 expresses the probability of finding solid material at a given elevation z, as a function of the n means and standard deviations corresponding to the equation being evaluated. The solution begins by grouping the elevation data into bins with equal numbers of data points in each bin. The bin widths and number of data points per bin are then converted to experimental probabilities, which are, assigned to the median elevation values for each bin.

Equation 4 is solved iteratively using a standard Levenberg-Marquardt nonlinear regression routine nested inside an outer iterative loop. The solution train begins by solving for σ_1 and μ_1 using the global sample standard deviation and mean as initial guesses. σ_1 Is then perturbed by a small negative amount and μ_1 by a small positive amount to generate initial guesses for σ_2 and μ_2. All four parameters - μ_1, σ_1, μ_2, and σ_2 - are re-evaluated in the second iteration. Similarly, μ_2 and σ_2 are perturbed to generate initial guesses for the third iteration and all six parameters are re-evaluated in the third iteration, etc.

The process continues to termination as indicated by the failure to meet one or more of five validity criteria:

- Maximum Gaussian order (number of convolved distributions): 6
- Maximum Levenberg-Marquardt iterations divided by Gaussian order: 100
- Minimum Levenberg-Marquardt solution accuracy: 1.0e-005
- Minimum area coverage (any Gaussian component): 1.0%
- Minimum improvement in standard error of estimate relative to previous iteration: 1.0%

The process yields means, standard deviations, and percent area coverage for each Gaussian component in the highest-order valid solution, together with standard errors of the estimate and R^2 (calculated relative to the Gaussian distribution defined by the global mean and standard deviation, however, rather than the global mean alone). One, two, or three-Gaussian solutions are common for a wide range of manufactured surfaces.

Examples

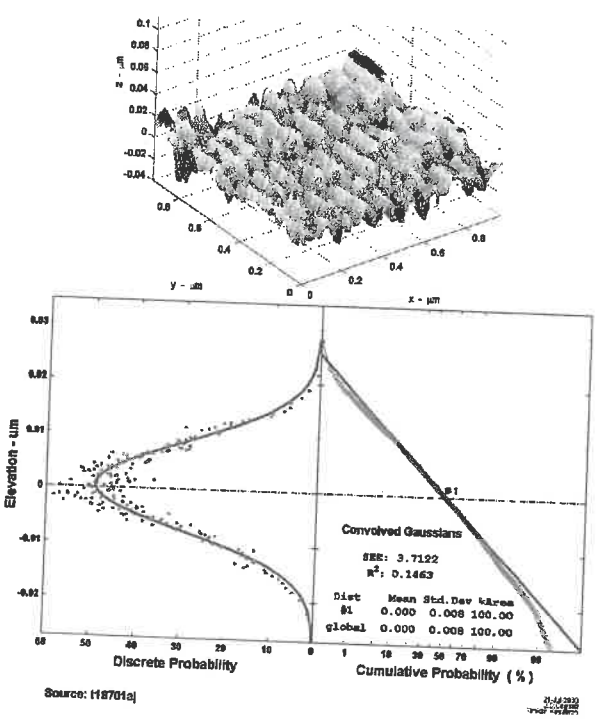

Figure 1. Single-Gaussian Surface

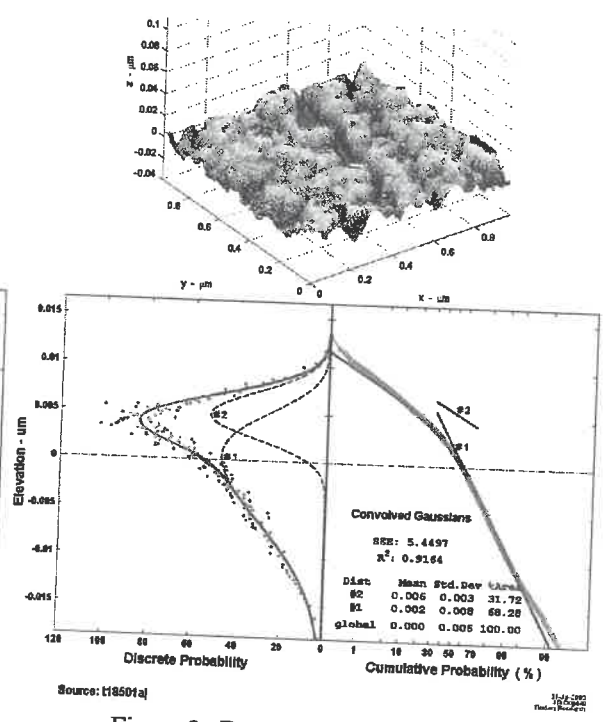

Figure 2. Dual-Gaussian Surface

Figures 1 and 2 illustrate solutions for typical PVD coated surfaces. The lower part of the figures shows observed (bin) probabilities as discrete data points and the best-fit solution as a heavy solid line. The surface in Figure 1, a 1 μm thick epitaxial coating over precision-ground steel, is well described by a single Gaussian. Figure 2 also shows a coated surface, but this time distinctly non-epitaxial. This surface is best described in terms of a dual-Gaussian probability distribution. The primary structure has a mean value located 2 nanometers above the global mean and a RMS roughness of 8 nm. The secondary mean is at 6 nm and the secondary RMS roughness is 3 nm. Global roughness is 6 nm. The 3 nm secondary occupies 32% of plan area. Note that in many tribological applications the effective roughness of this surface would be 3, not 6 nm.

The dashed, curved lines in the lower left side of Figure 2 are the convolved primary and secondary-structure probabilities, respectively: their sum equals G_2 from Equation 4. The short straight lines in the right-hand sub-figure depict the means and standard deviations: the # signs are over the means, and the slope of the lines in the probability-scale plot is proportional to standard deviation. The means and standard deviations correspond to the values in the small table included with each figure. The upper half of the figures consists of isometric views of the surfaces.

Figures 3 and 4 show two more surfaces – both with small but distinct secondary structure atop the primary peaks/ridges. Figure 3 is a rough-ground steel surface with a global RMS roughness of 0.64 μm. The tribologically important top 14% of the surface, however, has a roughness of 0.26 μm. The surface shown in Figure 4 has a global roughness of 150 nm with a 47 nm secondary occupying the top 12% of the structure.

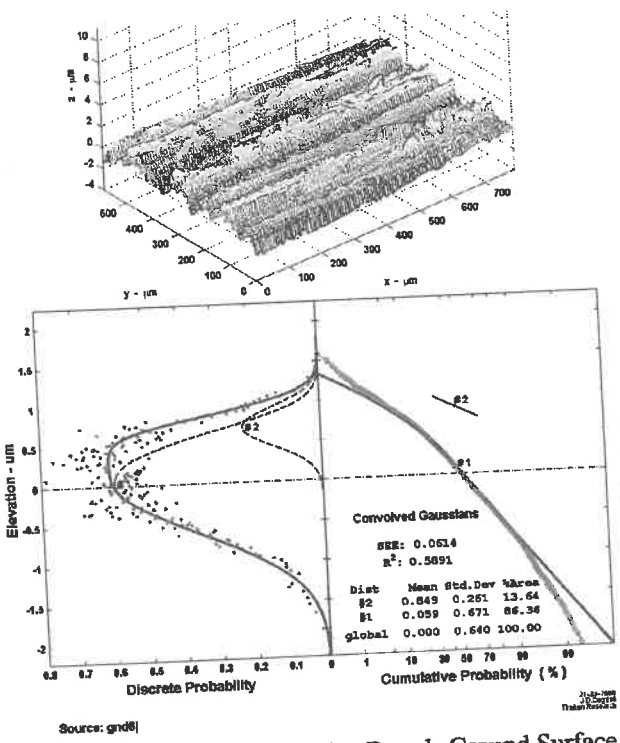

Figure 3. Dual-Gaussian Rough-Ground Surface

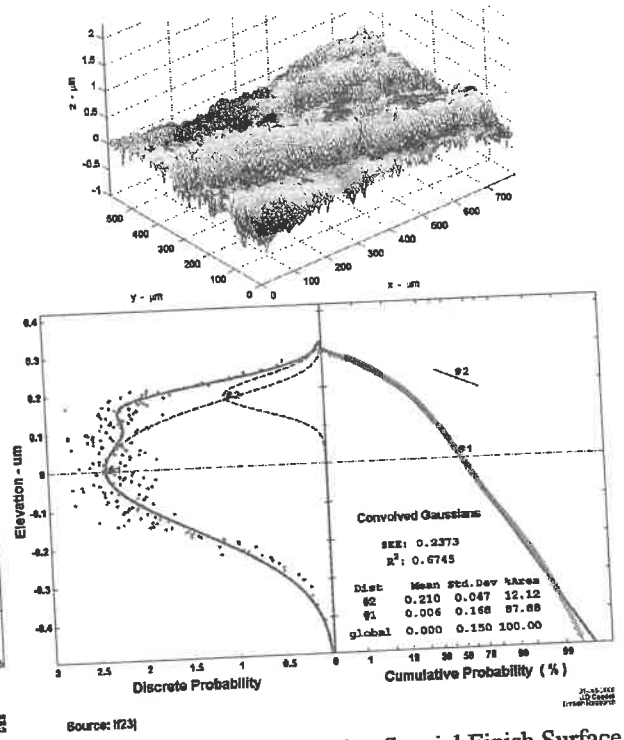

Figure 4. Dual-Gaussian Special Finish Surface

Conclusion

Multi-Gaussian analysis can yield tribologically relevant topography information, which may have particular utility for manufacturing process development.

SUBSURFACE MICROSTRUCTURE EFFECTS ON FREQUENCY CHARACTERISTICS OF POLISHED QUARTZ OSCILLATOR DISCS

T. Kaneeda, Y.Yokota, D. Nishiyama
Department of Mechanical Engineering, Okayama University of Science
1-1 Ridai-cho, Okayama city, Okayama 700-0005, JAPAN

T. Miyawaki
Wakou Kikou Co.Ltd.
3385-5 Kogushi, Okayama city, Okayama 702-8016, JAPAN

S.Yokomizo
Okayama Prefecture Office, Industry Development Division
2-4-6 Uchisange, Okayama city, Okayama 700-8570, JAPAN

1.Introduction

It is easy to find quartz oscillators as precision parts in such communication media devices as cellular phones, personal computers and GPS, because of their remarkable electric stability at high frequencies. In order to scale down these communication media devices, the quartz oscillator has to be reduced in size or made thinner. However, the machining of the oscillator often results in surface damage, such as cracks, on the oscillator disc surface[1]. These may subsequently produce fluctuations in the frequency, which leads to a lowering of the operation stability. In order to produce smaller communication media devices with higher precision and performance, the damaged surface layer of the oscillator disc should be critically examined by an appropriate method. However, to date few papers have discussed the evaluation of cracks on the oscillator disc surface.

In this paper, observations of cracks on the oscillator disc surface have been conducted with a high accelerating voltage transmission electron microscope (TEM) in order to recognize differences in microstructure between the damaged layer of lapped and polished oscillator discs. Then, frequency characteristics on both specimens were compared to clarify the effects of the damaged layer on frequency.

2. Experimental procedure

2.1 Quartz oscillator disc

AT cut [2] quartz oscillator discs with a diameter of 9mm were used as specimens, because of their high performance and stable frequency characteristics at room temperature. Two types of lapping were used, namely, conventional and fine lapping. The conventional lapping was conducted in order to improve the dimension and configuration accuracy, i.e., thickness, flatness and parallelism.

In this process, fused aluminum oxide WA#1000-3000 was used as the media.

In the fine lapping, the disc was thinned by WA#3000-8000 in order to be within the tolerance of the thickness measuring natural frequency. The appearance of the specimen at this stage was cloudy. After the fine lapping, the disc was polished with cerium oxide CeO_2 with less than 1 μm grain diameter. The finished disc was clear transparent.

2.2 Frequency characteristic measurement

The frequency of the quartz oscillator discs was measured using the reactance measurement apparatus. The apparatus was made by HUMO Laboratory, and is a non-contact electrode type manual frequency measurement apparatus, providing 2-100MHz frequency characteristics for a disc which has a 3.5-10.0mm diameter. The apparatus consists of electrodes, a network analyzer and a plotter. The disc is always charged by alternative voltage being supplied from the upper and lower electrodes.

3. Experimental results

3.1 Frequency characteristics

Fig.1 shows frequency characteristics of the disc lapped and polished. The results show that the resonance frequency for the lapped and polished discs were 11.39 and 10.175 MHz, respectively. In quartz, the thickness of the oscillator disc controls the resonance frequency as shown by equation (1).

$$f_0 \fallingdotseq 1650 / y_0 \qquad (1)$$

f_0: Resonance frequency (KHz)

y_0: Thickness of oscillator (mm)

Oscillator amplitudes for the lapped and polished discs were approximately 5 and 8 dB, respectively. One feature of an ideal oscillator disc is that the principal oscillation in the frequency

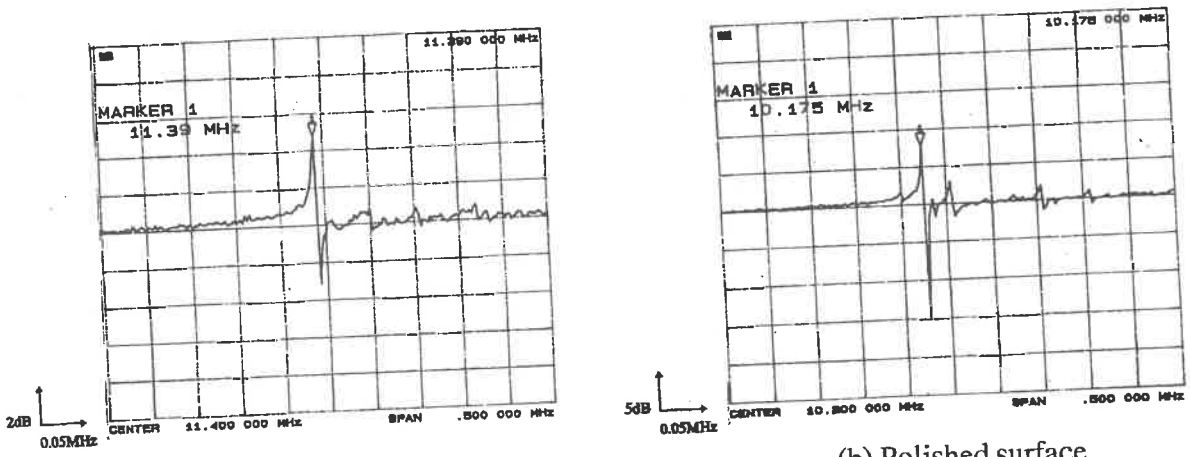

(a) Lapped surface (b) Polished surface

Fig.1 Frequency characteristics

characteristic curve is unique and there is no incidental oscillation around the resonance frequency. It is well known that the oscillation-frequency curve is positively affected by the surface profile and parallelism of the oscillator. Also, generation of the incidental oscillation is certainly dependent on the parallelism[3]. On the other hand, the oscillator amplitude is controlled by the surface roughness. In the frequency characteristics measurement, the thickness of both specimens was almost the same, and so the difference in the frequency characteristics was determined by the removal process.

3.2 Surface profile

The surface profile meter measurements showed that the roughness of the lapped disc was 0.62μm Ra and 5.0μm Ry. On the other hand, the surface profiles of the polished disc was measured using a ZYGO surface texture analyzer. The results are summarized as follows: Rrms=1.6nm, Ra=0.8nm and peak-to valley=91.8nm. The peak-to-valley value was much larger than any other value because some etch pits might have lowered the smoothness of the disc. In view of the surface roughness, it is evident that the polished surface was superior to the lapped surface.

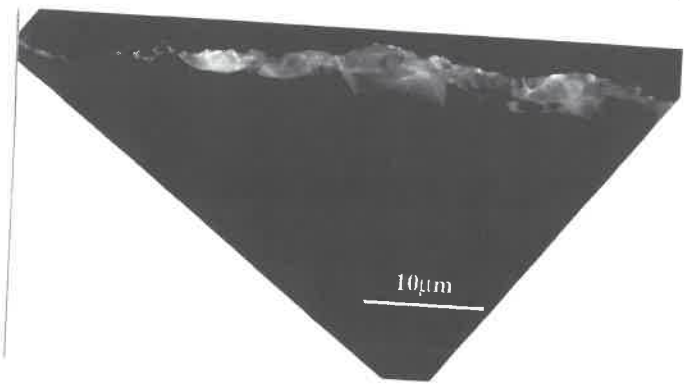

Fig.2 Dark field image of lapped surface

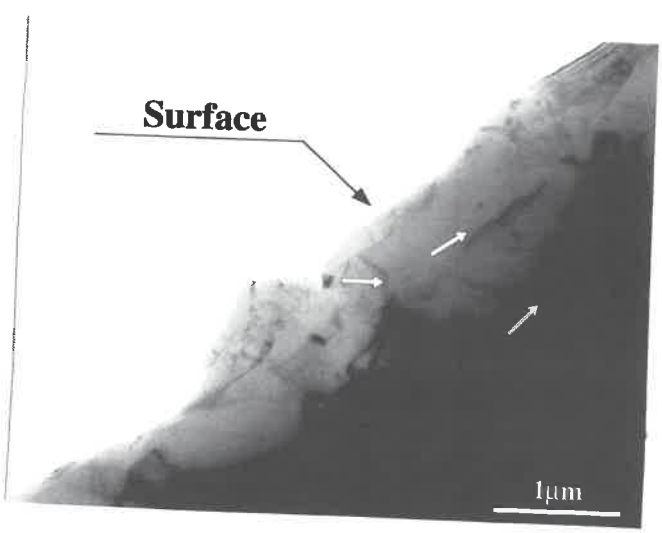

Fig.3 Typical median cracks in lapped surface

3.3 Damaged layer observation

The cross-section sandwich process[4] was adopted for preparing the TEM specimen.

Fig.2 shows a cross-sectional TEM micrograph of the lapped surface. This photo is a dark field image. The photo shows a rough surface and several microcracks which extend to below 10 μm depth from the surface.

Fig.3 shows a typical median crack in the deformed layer, and Fig.4 shows a typical lateral crack in the deformed layer. In the preparation of the specimen, the mechanical removal process might also generate microcracks. However, cracks generated during the operation would have wider openings and some plastic deformation, compared with the cracks already existing in the discs. Therefore, it is possible to recognize differences on the TEM image between originally generated cracks and cracks generated during the preparation.

Fig.4 shows a cross-sectional TEM micrograph of the polished surface. The

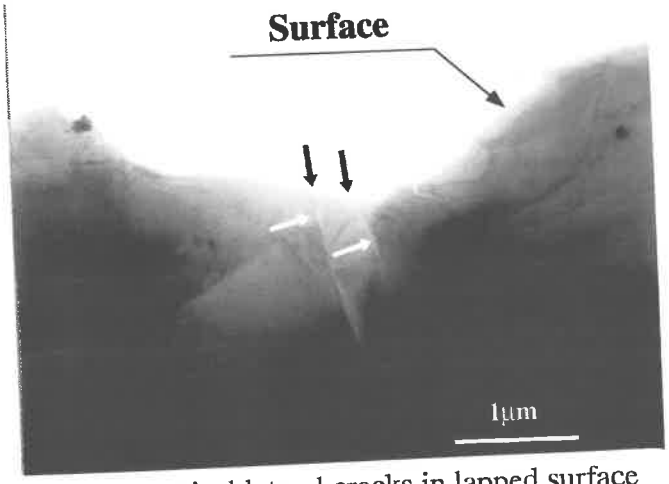

Fig.4 Typical lateral cracks in lapped surface

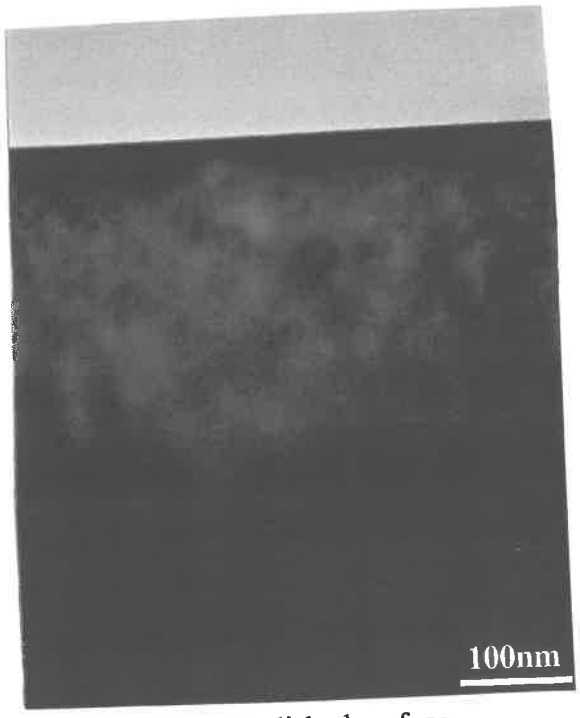

Fig.5 Polished surface

micrograph shows an ultra-smooth surface, less than a few nm Ra, which corresponds to the surface profile measurement shown in 3.2. The polishing process appears to eliminate surface roughness and microcracks. A less than 10nm thick-layer, shown as a dark contrast, can be observed at the top surface. This might be caused by plastic deformation.

4. Conclusions

TEM observations of quartz oscillator discs were conducted in order to evaluate the deformed layer. The relationship between surface properties and frequency characteristics was analyzed. The results are as follows:

(1) Differences in the damaged layer between the lapped and polished disc surfaces were clearly observed by the TEM.

(2) The lapped surface showed some lateral and median microcracks, within 10 μm depth from the top surface.

(3) The polished surface provided an ultra-smooth surface with no cracks, however, a few nm-thick contrast layer was observed, suggesting a damaged layer caused by plastic deformation.

(4) The frequency characteristics corresponded to the surface properties.

References

1. S. Sato, Lapping Technology of Quartz Blank for Mobile Telecommunication, *J. of Grinding Engineering*, 1997, **41** (4): 127-130.
2. Crystal Engineering Hand Book Editor Group, *Crystal Engineering Hand Book*, Kyouritu Shuppan, 1990: 377.
3. A. Chiba, K. Koizumi and M. Ikeda, Study on Precision of Quartz Composite Plates, *J. of Grinding Engineering*, 1999, **43** (5): 214-219.
4. R. B. Marcus, and T. T. Sheng, *Transmission Electron Microscopy of Silicon VLSI Circuits and Structures*, John Wiley and Sons, New York, 1983: 22.

SURFACE TOPOGRAPHY ANALYSIS OF SILICON WAFERS BY A CHROMAMETER

Ganesha Udupa and B.K.A. Ngoi

Precision Engineering Laboratory,
School of Mechanical & Production Engineering,
Nanyang Technological University,
Nanyang Avenue, Singapore–639798
Email: mgudupa@ntu.edu.sg

ABSTRACT: Silicon wafers are widely used in semiconductor and optical industries. With this material, there is an immense need to obtain nanometric surface finish owing to the advantage of improved performance of the components. The present research work is carried out in order to find a co-relation between the surface topography of silicon wafer and the corresponding brightness or lightness value. The wafers are subjected to various reclamation processes starting from lapping to final polishing stage. An approach of assessing surface topography based on measuring lightness (a measure of their reflectivity) is proposed which could be used for mass inspection of silicon wafers during processing. The measurement results of AFM are used to find a suitable relation using regression analysis. The equations for Ra, Rq and Rmax have been established and the calculated values are within ± 5 % error.

Key Words: Surface topography, Chromameter, Atomic force microscope.

1. INTRODUCTION

Silicon wafer is widely used in semiconductor and optical industries because of its excellent performance, which is used for fabricating high speed field-effect and bipolar transistors, infrared-emitting diodes, solid-state lasers and integrated circuits [1]. The silicon that is used by semiconductor manufacturers is obtained by removing oxygen from silicon dioxide (SiO_2), purifying it, then growing it into a single crystal and doping of the crystal. The single crystal, that may be up to 24 inches in length and 8 inches in diameter is ground to a cylindrical shape and cut mechanically into slices which are about 675 μm thick. Subsequently, the slices are sized, edge ground, lapped, etched and polished. The end product is known as the 'silicon wafer' that is used by the semiconductor device manufacturers. The surface roughness of the processed silicon wafer plays an important role in the performance of semiconductor devices. The semiconductor industries uses atomic force microscopy (AFM) to measure the surface roughness during product inspection, this is a rather expensive and time consuming in terms of labour and equipment expenses. The present research work is carried out in order to find a co-relation between the surface roughness of silicon wafer and the corresponding brightness or lightness value. The brightness value can be measured by a chromameter, which is less expensive, and measurement can be done in a few seconds. The Chromameter could be used to estimate the surface roughness of the wafers by finding a suitable relation in terms of roughness parameter and brightness value of the wafer. The measurement results of AFM are used to find a suitable relation using regression analysis.

2. EXPERIMENTAL PROCEDURE

The surface roughness of silicon wafers produced by lapping, etching and polishing processes are measured by AFM and the brightness value of the same are also measured by Chromameter. Atomic Force Microscope (AFM) consists of a micro –fabricated cantilever with an optical lever system to monitor the cantilever deflection (Fig. 1). It may resolve single molecules (more rarely single atoms) laterally and vertically. The AFM scans essentially van-der-Waals forces. It uses a fine tip to measure surface topography and properties through an interaction between the tip and surface [2]. Topographic images with a height resolution of 0.1 nm and lateral resolution down to nanometers can be measured. Compared with Scanning Electron Microscopes (SEM), the AFM provides extraordinary topographic contrast, direct height measurements and unobscured views of surface features.

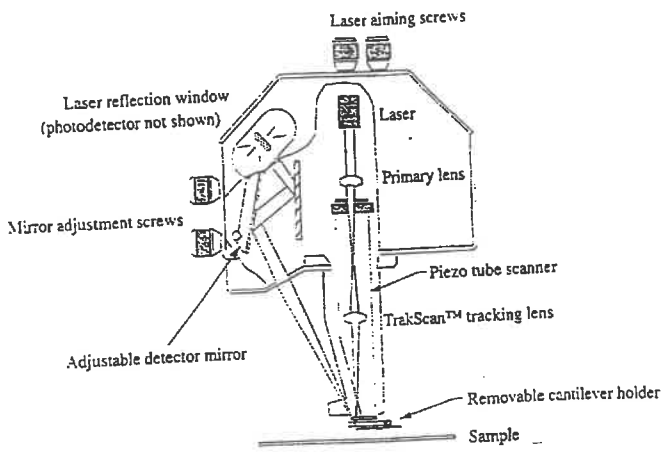

Fig.1 Principle of AFM

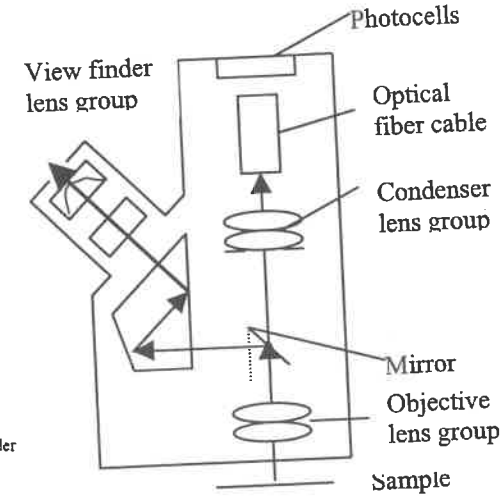

Fig.2 Principle of Chromameter

Another instrument used for the experiment is a Chromameter, which can express colors numerically according to international standards. In this experiment, L* a* b* color space (also referred to as CIELAB) is used. In this color space, L* indicates the lightness and a* and b* are the chromaticity co-ordinates (the color directions)[3]. The optical system for measuring the specimen and for viewing the specimen through the viewfinder is shown in Fig 2. When the specimen is looked at through the viewfinder, the mirror is inclined at 45° to allow the reflected light from the wafer surface (the specimen is illuminated by the focus lamp, not shown in the figure). When in measure mode, the mirror is moved to the vertical position (shown dotted) and the focus lamp is automatically switched off at the same time. The light received from the wafer sample and transmitted by the objective lens group and then passes through a condenser lens system to the receiving endface of the optical-fiber cable for measuring the sample. This optical–fiber cable transmits the light to the sensors (photo cells). The photocells convert the light received by them into a current whose strength is proportional to the brightness of the light. This signal is then converted to numerical values.

3. RESULTS AND DISCUSSION

The wafer roughness measurement results are obtained by AFM for the various Si-wafer surfaces and corresponding brightness value is obtained by a chromameter. The graphs of various parameters (Ra, Rq and Rmax) Vs lightness value (La) are drawn (Fig.3). The regression analysis is carried out to find suitable best-fit line to the data. Table 2 shows the average roughness (Ra) parameter (measured, calculated and error) for the various wafer surfaces. The best fit equations obtained from the analysis is given in Table 3.

Table 2: Average Roughness (Ra) based on AFM and Chronometer measurements

Final polished wafer				Etched wafer				Lapped wafer			
La	Ra - AFM	Ra- (chrom)	E %	La	Ra - AFM	Ra- (chrom)	E %	La	Ra- AFM	Ra- (chrom)	E %
3.32	0.048	0.046	3.15	63.73	65.45	62.61	4.34	56.51	105.62	106.05	0.41
3.34	0.065	0.067	3.24	63.01	52.28	54.84	4.89	56.61	110.52	107.60	2.64
3.30	0.027	0.025	4.22	64.76	75.89	75.69	0.26	57.11	113.63	115.66	1.79
3.32	0.045	0.046	3.29	65.06	79.42	79.99	0.72	56.81	112.87	110.75	1.87
3.30	0.027	0.025	4.22	63.71	64.55	62.38	3.36	56.32	101.39	103.18	1.76
3.35	0.080	0.077	3.22	64.49	72.32	72.01	0.42	56.50	105.62	106.05	0.41

These equations could be used to estimate the surface roughness parameters of the wafer by knowing their lightness value (La) by a chromameter This will greatly reduce the measuring time and cost involved in AFM measurements. To verify these equations, a set of new wafers are measured by a chromameter, and various roughness parameters are evaluated and it is observed that the results are within the 5% error. This approach of measurement of surface

roughness based on lightness value can be employed in mass inspection in semiconductor industries to check the quality of the wafer surfaces at every stage of the process.

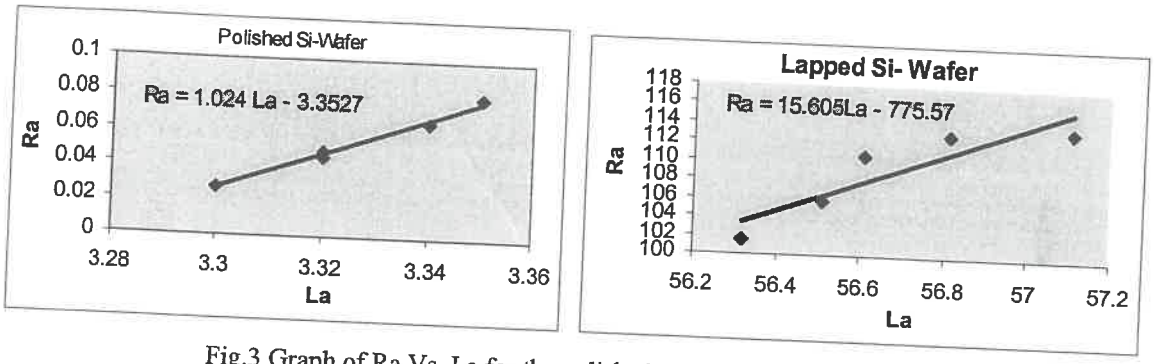

Fig.3 Graph of Ra Vs. La for the polished and the lapped Si-wafer surfaces

Table 3: Best fit equations obtained by regression analysis for the various roughness parameters:

Final polished wafer:	Stock polished wafer :
$Ra = 1.024\,(La) - 3.3527$	$Ra = 4\times10^{-34}\,(e)^{22.21\,(La)}$
$Rq = 3\times10^{-34}\,(e)^{22.341\,(La)}$	$Rq = -2.6074\,(La) + 11.972$
$Rmax = 7\times10^{-46}\,(e)^{31.119\,(La)}$	$Rmax = -5592.8\,(La)^2 + 38177\,(La) - 65013$
Etched wafer :	Lapped wafer surface
$Ra = 0.0003\,(e)^{0.1902\,(La)}$	$Ra = 15.605\,(La) - 775.57$
$Rq = 0.0231\,(e)^{0.1291\,(La)}$	$Rq = -71.231\,(La)^2 + 8118.2\,(La) - 231146$
$Rmax = 56.732\,(e)^{0.04\,(La)}$	$Rmax = 1520.1\,(La) - 84252$

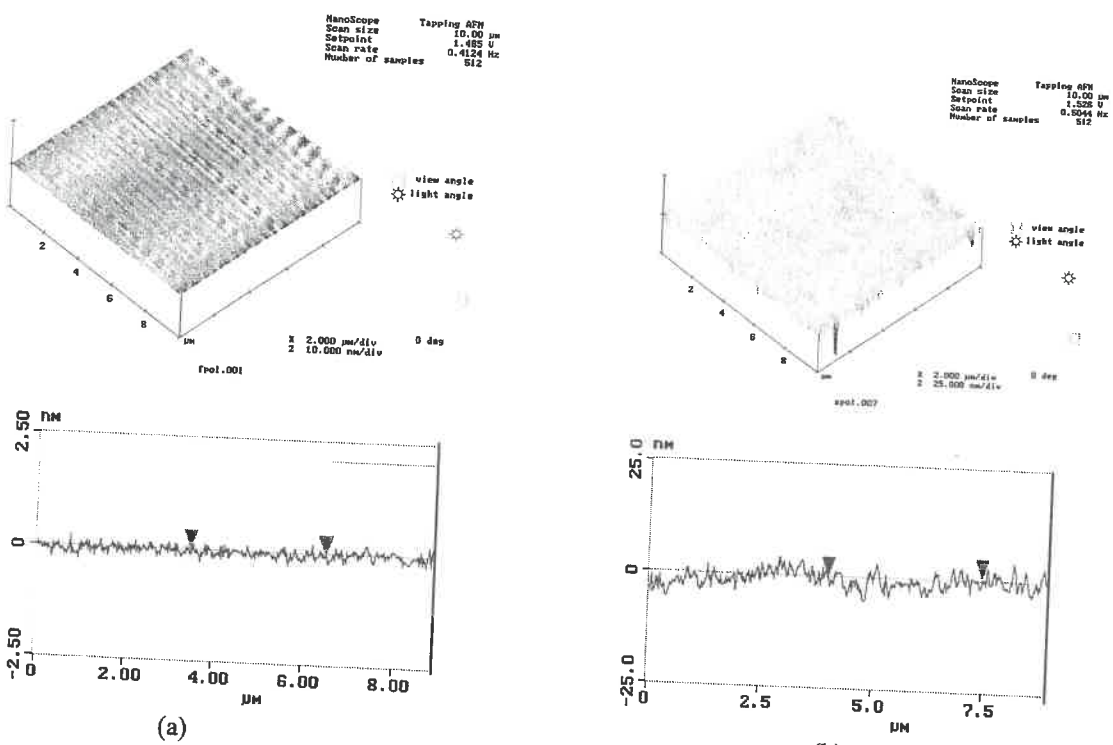

(a) (b)

Fig.4 2-D and 3-D Surface topographic features of Si wafer surfaces (a) final and (b) stock polished

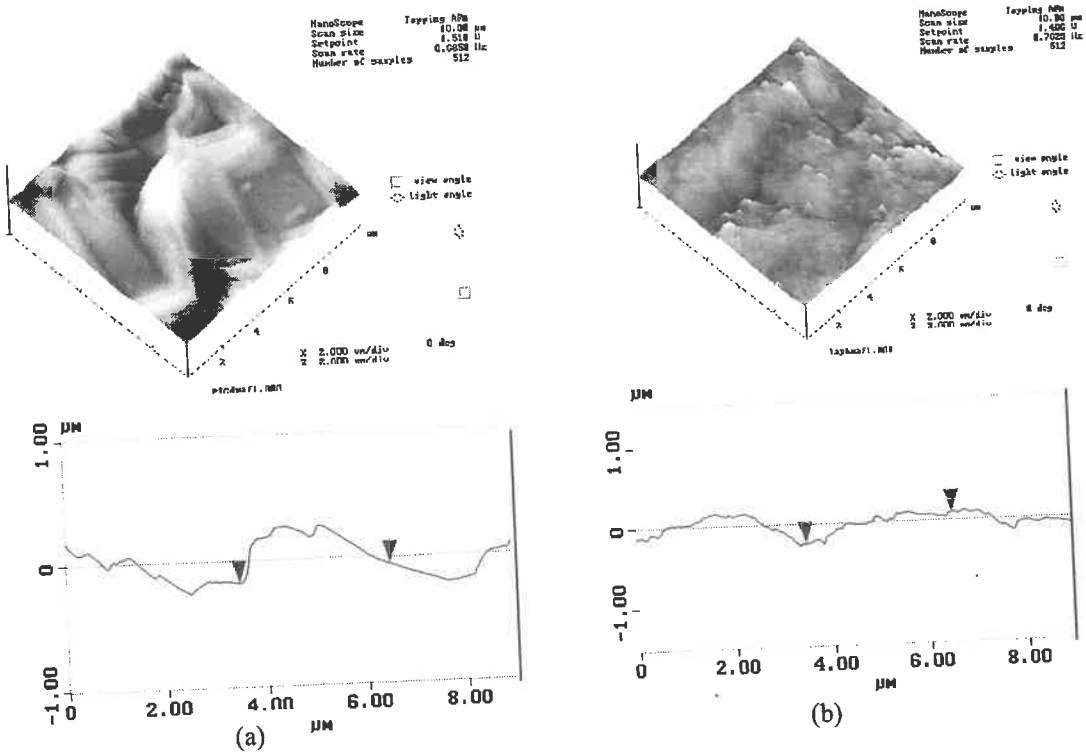

Fig.5 2-D and 3-D Surface topographic features of Si wafer surfaces (a) etched (b) lapped.

Figures 4(a) and (b) shows the 2-D and 3-D surface topographic features of polished and stock polished silicon wafer surfaces respectively measured by AFM. The figures shows the polishing marks in case of stock and final polishing and inturn needs optimisation of the process. Figures 5(a) and (b) shows the 2-D and 3-D surface topographic features of etched and lapped silicon wafer surfaces. The surface shows peaks and valleys due to cutting action of the abrasive particles during lapping process respectively. The etching improves the surface roughness of the wafer.

4. CONCLUSION

The wafer surface roughness measurement and analysis has been carried out in order to find a suitable relation between lightness value and roughness parameters. These relations could be used to find the surface roughness parameters of processed silicon wafers using the lightness or brightness results obtained by a chromameter. The measurement by Chromameter not only helps in reducing the measurement time but also reduces the measurement cost of the wafers due to an expensive AFM instrument being generally employed in semiconductor industries. The measurement error by chromameter using the parameter equations are within ± 5 %, which could be reduced by taking a large number of measurements.

References:

1. Venkatesh V.C et al, "Observations on polishing and ultraprecision machining of semiconductor substrate materials, Annals of the CIRP, Vol. 44/2, 611-618, 1995.
2. Scanning Probe Microscope Operating manual, Digital Instruments, Dimension 3000, 1995.
3. Chroma meter manual, Minolta Corporation, 1994.

Error Budget by Constraints

Stephen K. Eisenbies, Robert J. Hocken
Center for Precision Metrology
The University of North Carolina at Charlotte, Charlotte, NC

Abstract

Error Budget by Constraints is a method of error budgeting the design of a precision machine using Monte-Carlo simulations. Instead of using conventional methods of combining errors to predict the performance of a particular design, the Error Budget by Constraints Method creates a large set of virtual "possible" machines using a computer and evaluates distributions of errors that can occur. This approach can be used to clarify for the designer the effects of certain individual axis errors or design changes

Keywords: Error Budget, Monte Carlo Simulation, Parametric Model

Introduction

When designing and building precision machines, it is important to have a clear understanding of errors that are introduced in manufacturing and by the environment. One of the methods used to develop an understanding of the effects of these errors is error budgeting. Defined by Donaldson [1], "an error budget is a systems analysis tool, used for prediction and control of the total error of a system at the design stage for systems where accuracy is an important measure of performance. Given a system-error goal, an error budget can be used in a control mode to set individual subsystem error limits, while also making trade-offs that balance the level of difficulty among the subsystems. In a predictive mode, proposed subsystem designs can be assessed for error contributions, leading to a predicted overall system error."

Error budgets are tested by methods defined in the Guide to Uncertainty in Measurements [2]. In this approach, a root-mean-square (rms) value is determined for the set of the individual error limits. The rms value is an estimate of the total machine error caused by the individual errors. This method has worked well in many designs, but is conservative, and does not necessarily give a clear understanding of the effects of individual errors in more complex systems.

The method of Error Budget by Constraints is designed to address these problems by creating a set of virtual possible machines with a computer and evaluating the distribution of errors associated with a particular design. This is done using a variation on the Monte Carlo Simulation Method developed by Phillips [3] for calculating coordinate measuring machine (CMM) measurement uncertainty.

Principles

For the method of error budget by constraints, a large set of virtual machines created by a computer is evaluated for desired performance characteristics. Each virtual machine is given its own set of parametric errors. Each individual parametric error is itself constrained within specified limits. From the set of virtual machines, an error distribution can be determined for a desired machine characteristic. This information can be used to evaluate the probability that a design will meet specified requirements.

The first step in setting up an Error Budget by Constraints simulation is to put together a mathematical model of the machine. This is done by creating a full parametric model [4] of the design being evaluated. A parametric model is a tool used in online error compensation that determines the actual position of a machine tool in space based on the commanded position and the known axis errors. In this approach, since the axis errors are unknown, simulated errors are used instead to create a possible machine. Setting up the parametric model will clarify the set of axis errors that contribute to the total error in the machine. Axis errors, or individual errors, include all position and angular errors, whether

they are quasistatic or static. In some cases, individual errors may be ignored if, by inspection, they are found to have a negligible contribution to the total error. This will help to simplify the simulation.

With the parametric model complete, and the relevant error terms determined, the next step is to create a simulation of the individual errors. For each virtual machine created by the computer, a unique set of randomly generated error functions is created. The error functions are designed such that they simulate the types of errors and level of precision that is expected.

The way an error is simulated depends on the type of error being modeled. For static errors such as offsets and squareness, a random error is selected from a uniform distribution with a set of upper and lower limits. This type of error is a constant for each virtual machine and is not a function of machine axis position.

Quasistatic errors in an axis will change as a function of a machine's axis position. Thus these types of errors are modeled by randomly generated functions specifically designed to simulate a particular error. Linear positioning accuracy, straightness, and angular errors such as yaw, pitch, and roll are examples of quasistatic errors on a linear axis. Rotary positioning axes will have quasistatic errors including axial and radial motion, as well as tilt and angular positioning errors.

Quasistatic errors for linear axes are simulated by creating a tenth-order Legendre Polynomial [5] with random coefficients. Coefficients are chosen that do not exceed the maximum error expected along the range. Summing the absolute values of the coefficients gives a value equal to the maximum error. To test how well the polynomial simulates an actual error, distributions from 1000 generated functions are made at five points along the range of the polynomial: the start and endpoints, and three evenly spaced points in between. The test results in a distribution for each of the five points that are not all similar. At each of the endpoints the distributions have a 3-sigma value approximately equal to the maximum error. In the range of the function from one-quarter to three-quarters of the way through the function, the distributions are similar, but the 3-sigma value is closer to 25% of the maximum error. To take advantage of this linear range, the first and last quarter of the function is truncated and the remainder multiplied an appropriate factor. The definition of a Legendre polynomial sets its range from –1 to +1. To make the simulated error match the match range and start point on the machine axis, it is necessary to scale and offset the independent variable of the function.

Further changes are made to the Legendre polynomial depending on whether it is a straightness error or some other type such as a linear positioning or angular error. To simulate straightness measurements appropriately, a least-squares fit line is subtracted from the function. An example of a randomly generated straightness function is shown in Figure 1. Other types of errors will have their starting point set as having zero error.

Simulating quasistatic errors for rotary positioning tables is accomplished by using a fifth-order Fourier Series [5] with random coefficients and random phase shifts. Like the linear axes, the coefficients are chosen so that their absolute values sum to the maximum error expected along a range, with no individual coefficient exceeding the maximum error. A random phase shift is chosen for each term

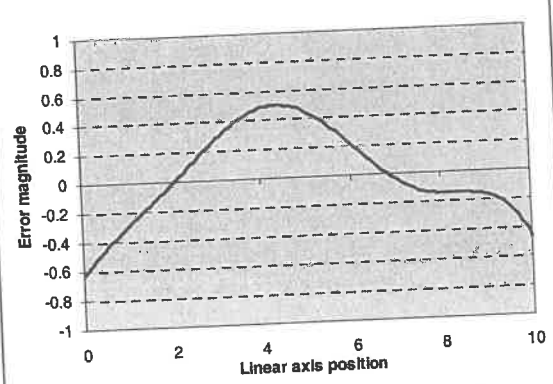

Figure 1: Simulated Straightness Error Function

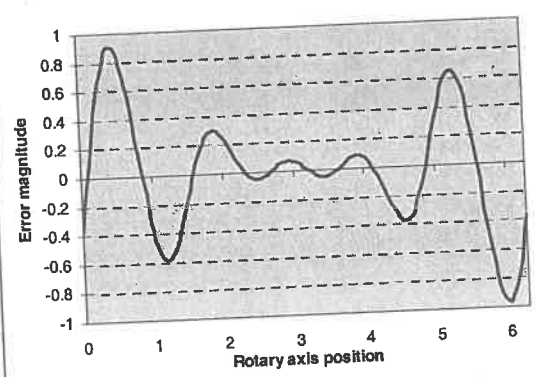

Figure 2: Simulated Rotary Axis Error Function

between zero and two Pi radians. Unlike the Legendre Polynomials, this approach gives good distributions at all points in its range and it is not necessary to alter the function further. An example of a randomly generated rotary table error function is shown in Figure 2.

Applying the simulated error functions to the parametric model, we now have a mathematical model of a simulated "possible" machine that can express the total error at any position in the machine's working volume. The result is a three-term vector describing the actual position of the machine coordinate system in the base coordinate system. By iterating the process a large number of times, distributions can be made of certain characteristics of the total error, such as magnitude or direction, or the location of a maximum error in the work volume. These distributions can be used to determine the probability that a particular design with specified constraints on error sources will fall within a set of limits for a particular characteristic. This method can also be used to predict how well a design may perform on a particular measurement task such as a cylinder, hemisphere, and other part geometries.

Experiment

To show the effectiveness of this method to predict the total error in a machine, a simulation will be completed of an existing machine and then compared to actual measurements. The measuring machine that will be simulated is a Shelton YZ CMM located at Oak Ridge National Labs. The Shelton Machine is a three-axis CMM with a stationary bridge supporting a carriage and a ram over a rotary table. A diagram of this machine can be seen in Figure 3.

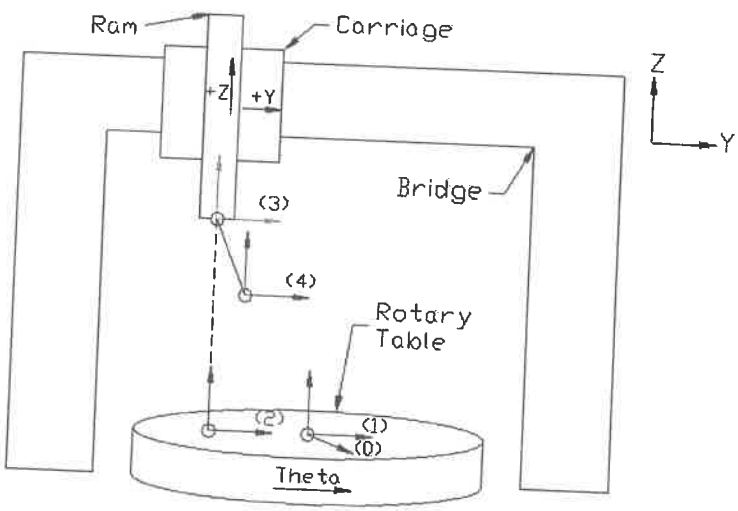

Figure 3: Schematic of Shelton YZ Machine

A mathematical model is developed for this machine that gives the position of the probe tip, coordinate system 4, relative to the base coordinate system, coordinate system 0, attached to the rotary table. Included in this model are relevant individual parametric errors that will have an effect on the total error. Because this machine is used for measuring cylindrical and spherical parts, some of the individual errors can be neglected since they cause cosine errors.

To set the limits on the individual errors, the specifications from the machines calibration charts will be used. Since the Shelton machine is somewhat large compared to many of the parts it is used to measure, the volume that will be evaluated on the machine is smaller than the whole working volume. Using the mathematical model and the error limits, a simulation of the specified working volume will be iterated one thousand times. For each virtual machine, the maximum total error seen over its entire range will be stored in computer memory. All of these maximums should make a normal distribution that

shows a mean maximum total error and an associated standard deviation. As an example, a simulation result for a stacked rotary axis machine design is shown in Figure 4.

To test the simulation results, measurements will be made of the actual machine. These actual errors will be inserted into the same mathematical model used for the simulation to determine the actual maximum total error in the evaluated range. It is expected that the actual maximum error measured on the machine will fall within the distribution determined by the simulation.

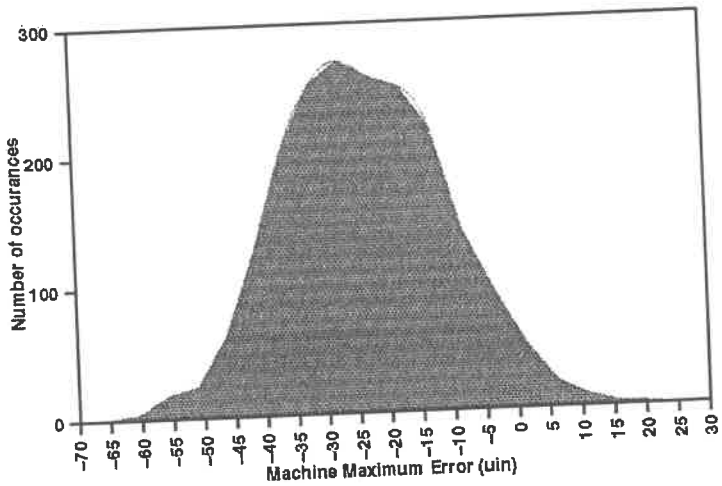

Figure 4: Example Error Budget by Constraints simulation result

Summary

When precision machines are being designed, it is imperative to have a good understanding of the effects of errors on the final performance. In more complex machines, it is sometimes difficult to understand such effects. Current methods used to evaluate the effects of errors become difficult to implement as complexity increases. The method of Error Budgets by Constraints addresses this issue by creating a large set of possible machines with a computer and evaluating them as a whole. By creating virtual machines, the effects of certain errors or changes in design can quickly be evaluated. This approach has the promise to be a powerful tool used in the design of precision machines in the future.

Acknowledgements

I would like to thank Mr. Bill Barkman of Oak Ridge National Labs for his input and ideas on this project. His thoughts have been a valuable resource in this work.

References

1. R.R. Donaldson, "Error Budgets", Technology of Machine Tools, vol. 5, October 1980, sec. 9.14, pp. 1-14.
2. Guide to the Expression of Uncertainty in Measurement, First Edition. International Organization for Standardization. 1993.
3. S.D. Philips et al., "A Constrained Monte Carlo Simulation Method for the Calculation of CMM Measurement Uncertainty." Not yet published.
4. G. Zhang et al., "Error Compensation of Coordinate Measuring Machines", Annals of the CIRP, Vol. 34/1, 1985.
5. E. Kreysig, Advanced Engineering Mathematics, 8th Edition. John Wiley & Sons, Inc. 1999.

A STUDY ON MODEL BUILDING OF FREE-FORM CURVES

Feng Guoxin, Zhang Guoxiong, Xie Zexiao, Wang Chunhai
National Key Lab of Measurement Technology & Instrument
Tianjin University, Tianjin, P. R. China

Key Words: B-Splines, free-form curves, equal-chordal-height sampling method

ABSTRACT

Based on the least-zones principle, a new mathematical modeling method established for free-form curves from the discrete sampling data, using one-parameter cubic non-uniform B-splines, is presented. Approximate errors with this method are the least. A new selection method of non-uniform fitting points, based on the equal-chordal-height method, is developed. It is proved that approximate errors of free-form curves, based on the new selection method of non-uniform fitting points, are greatly reduced. The new model building method can implement the requirement that approximate errors should be the least.

1. PREFACE

After performing fast and accurate measurement of free-form curves and surfaces with CNC-CMM in reverse engineering, a key task is to implement full and smooth reconstruction on the curves and surfaces with the acquired discrete data. At the same time, fitting accuracy of the curves and surfaces should be the best. The main method of the reconstruction on curves and surfaces is fitting method, which is divided into two methods--the interpolation method and the approximation method[1]. The approximation method, however, can perform smooth reconstruction on the curves and surfaces. Therefore, the approximate method is widely used in fitting curves and surfaces. Furthermore, the non-uniform B-Splines is one of the best tools, with which approximating errors are far less. In order to obtain a fine approximate method, we establish, based on the least-zones principle, a new mathematical model building method on curves with discrete data, using one-parameter cubic non-uniform B-splines.

2 MODEL BUILDING ON CURVES WITH LEAST APPROXIMATE ERRORS

Because of the requirements of high precision and high smoothness, it should be based on the least-zones principle in curves fitting or surfaces fitting. However, we widely use the least-squares method to substitute for the least-zones principle. Moreover, fitting performances of non-uniform B-Splines are better than those of uniform B-Splines[2][3][4]. Therefore, based on the least-squares method, we use one-parameter cubic non-uniform B-splines to establish a model building method on curves. The least-squares model building method on curves is as follows:

Given N sampling points in interval $[a,b]$: (x_i, y_i) $(i = 1, 2, \cdots, N)$, the usual fitting model of a curve with non-uniform B-Splines is

$$S(x) = \sum_{i=1}^{n+4} d_i B_{i,4}(x)$$

, where n is the number of fitting points and $B_{i,4}(x)$ is the base of the cubic non-uniform B-splines.

Then, we have the equation of residual errors at sampling points

$$
\begin{aligned}
r_k &= S(x_k) - y_k \\
&= d_1 B_{1,4}(x_k) + d_2 B_{2,4}(x_k) + \cdots + d_{n+4} B_{n+4,4}(x_k) - y_k \qquad (k = 1, 2, \cdots, N)
\end{aligned}
$$

The residual sum of squares is:

$$
F(d_1, d_2, \cdots, d_{n+4}) = \sum_{k=1}^{N} r_k^{\,2}
$$

Based on the least-squares method, the residual sum of squares should be the least i.e. $\frac{\partial F}{\partial d_2} = 0, \frac{\partial F}{\partial d_2} = 0, \cdots, \frac{\partial F}{\partial d_{n+4}} = 0$, namely,

$$
\begin{bmatrix}
\sum B_{1,4}^2 & \sum\sum B_{1,4}B_{2,4} & \cdots & \sum\sum B_{1,4}B_{n+4,4} \\
\sum\sum B_{1,4}B_{2,4} & \sum\sum B_{2,4}^2 & \cdots & \sum\sum B_{2,4}B_{n+4,4} \\
\cdots & \cdots & \cdots & \cdots \\
\sum\sum B_{1,4}B_{n+4,4} & \sum\sum B_{2,4}B_{n+4,4} & \cdots & \sum B_{n+4,4}^2
\end{bmatrix}
\cdot
\begin{bmatrix} d_1 \\ d_2 \\ \cdots \\ d_{n+4} \end{bmatrix}
=
\begin{bmatrix} \sum\sum B_{1,4} f_k \\ \sum\sum B_{2,4} f_k \\ \cdots \\ \sum\sum B_{n+4,4} f_k \end{bmatrix}
\quad \text{where} \quad
\begin{aligned}
\sum B_{i,4} B_{j,4} &= \sum_{k=1}^{N} B_{i,4}(x_k) \cdot B_{j,4}(x_k) \\
\sum B_{i,4} f_k &= \sum_{k=1}^{N} B_{i,4}(x_k) \cdot f_k
\end{aligned}
$$

3 EFEECTS OF DIFFERENT SELECTION METHODS OF FITTING POINTS ON APPROXIMATE ERRORS

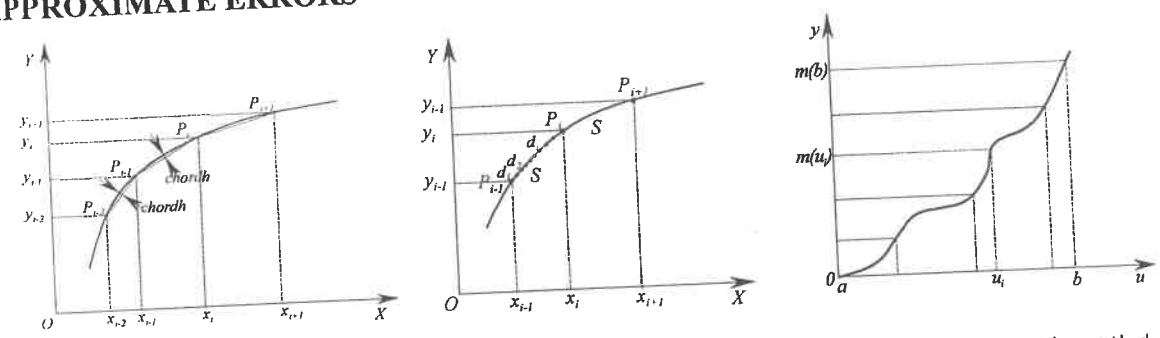

a) equal-chordal-height method b) equal-arc-length method c) interpolation method

Fig. 1 Schematic diagrams of selection methods of fitting points

Usually, in curve fitting, fitting points are evenly selected. This selection method of fitting points is adapt to even curves but for complex curves fitting accuracy of the method is poor because equidistant fitting points can not exactly reflect the characteristics of the patterns of curves. In order to obtain a perfect selection method of fitting points, which really reflects to the characteristics of the patterns of curves, three nonuniform selection methods, which are the equal-chordal-height method, the equal-arc-length method and the interpolation method respectively, are presented. The schematic diagrams are shown in Fig. 1.

5 COMPUTER SIMULATIONS OF FITTING CURVES WITH UNIFORM AND NONUNIFORM FITTING POINTS

The units of all the numbers in following figures are the same, and the values of all the numbers are absolute values.

5.1 Relations between Fitting Errors and The Number of Uniform Sampling and Fitting Points

For the curve defined as follows, we made two groups of simulations.

$$
f(x) = \frac{100}{\sqrt{80^2 + (x - 200)^2}}, \text{ where the range of variable } x \text{ is } x \in [-400, 400]
$$

We firstly keep n=12 equidistant fitting points and evenly take N=50 and N=80 sampling points in the interval respectively. Fitting error curves are shown in Fig. 4a) and 4b) respectively. Secondly, we keep N=80 equidistant sampling points and evenly take n=12 and n=25 sampling points in the interval. After

curves fitting, we've got series of fitting error curves shown in Fig. 5a) and 5b) respectively.

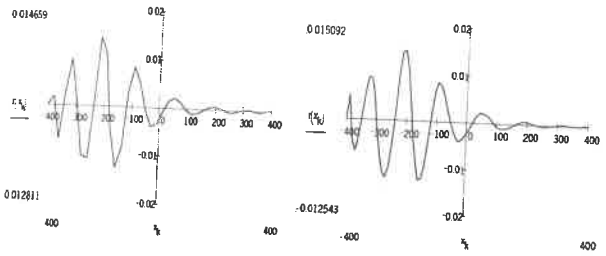

a) N=50 b) N=80

Fig. 2 fitting errors of the curve B

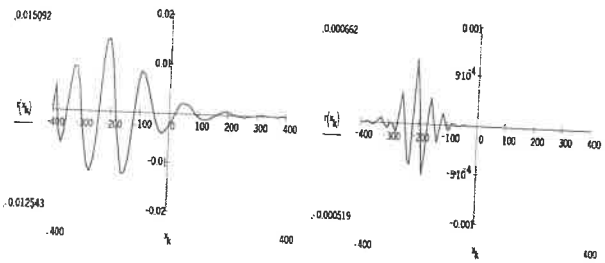

a) n=12 b) n=25

Fig. 3 fitting errors of the curve A

From Fig. 2, we can find the number of sampling points justly make curves more smoothly but fitting errors are not reduced significantly. From Fig. 3, we can see that the more the number of fitting points, the less fitting errors. However, the patterns of fitting error curves are not greatly changed, which fitting errors at the positions where the curvature of the curve varies greatly are great. This is to say that we can properly increase the number of fitting pints to improve the fitting accuracy of a curve.

5.2 Computer Simulations of Fitting Curves with Nonuniform Fitting Points

We use three kinds of nonuniform selection methods of fitting points, which are the equal-chordal-height method, the equal-arc-length method and the interpolation method respectively, to fit the following curve $f(x) = \sin x$, where the range of variable x is $x \in [0, \pi]$. To be compared, we also take the uniform selection method in fitting curves. Fitting results of the curve are shown in Fig. 8.

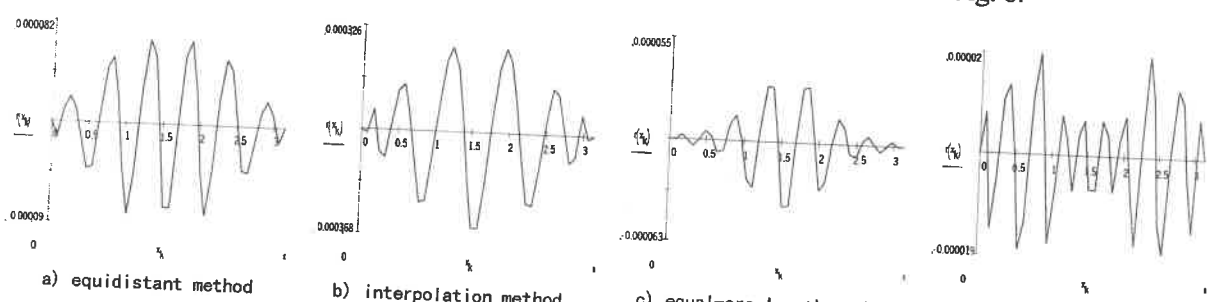

a) equidistant method b) interpolation method c) equal-are-length method d) equal-chordal-height method

图 4 Effects of selection methods of fitting points on fitting errors of curve

Compared with other methods, fitting points with the equal-chordal-height selection method can really reflect the pattern of the curve and fitting accuracy should be the best. Fitting errors shown in Fig. 4d) are the least. Because fitting points based on the method are self-adaptively densely distributed at the positions where the curvature of the curve varies hard, fitting errors are significantly reduced at those positions. Thus, the fitting accuracy is greatly improved and the pattern of the fitting error curve is different from those based on other selection methods.

6 EXPERIMENT OF THE APPROXIMAT MODEL BUILDING ON CURVES

In order to prove that the new model building method, we measured a standard cycloidal gear, using a trigger probe of which the diameter of the ball is $2.999mm$ on the CMM. The original function expression and measuring parameters of the cycloidal gear are as follows:

$$\begin{cases} x = R_z\left(\sin\alpha - \dfrac{K_1}{Z_b}\sin Z_b\alpha\right) + r_z \dfrac{K_1 \sin Z_b\alpha - \sin\alpha}{\sqrt{1 + K_1^2 - 2K_1\cos Z_b\alpha}} \\ y = R_z\left(\cos\alpha - \dfrac{K_1}{Z_b}\cos Z_b\alpha\right) - r_z \dfrac{-K_1\cos Z_b\alpha + \cos\alpha}{\sqrt{1 + K_1^2 - 2K_1\cos Z_b\alpha}} \end{cases}$$

$\alpha \in [-\frac{\pi}{Z_a}, \frac{\pi}{Z_a}]$, $K_1 = 0.5505$, $R_z = 109\,mm$, $r_z = 8.5\,mm$, $Z_a = 11$, $Z_b = 12$.

In fitting the curve, we took 41 sampling points and 11 fitting points. Fig. 5a)~d) are the fitting error curves with the equidistant selection method, the interpolation selection method, the equal-arc-length selection method and the equal-chordal-height selection method of fitting points respectively. The unit of numbers in each figure is mm and the values of all the numbers are absolute values.

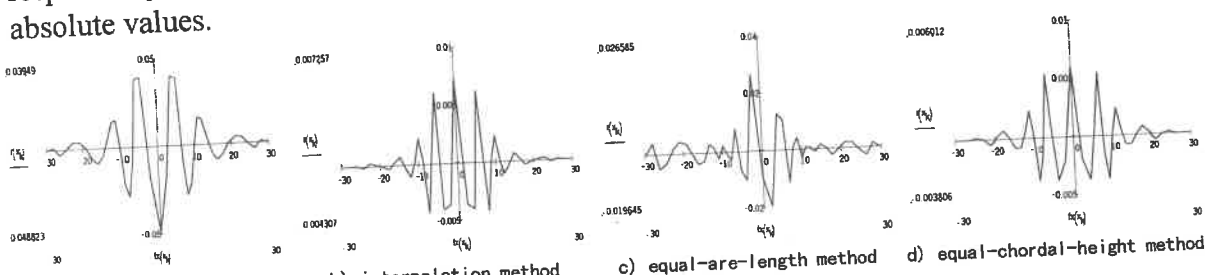

a) equidistant method b) interpolation method c) equal-are-length method d) equal-chordal-height method

Fig. 5 fitting errors on a cycloidal curve

From the results of the experiment, we can find that approximate errors of the curve with the equal-chordal-height selection method of fitting points are much less than others. Approximate errors on the curve are the least. At the same time, the fitting curve keeps the same pattern of the original curve and it is smooth enough.

7 CONCLUSIONS

With careful analyses of the theories and plenty of experiments, we can conclude:

Based on the least-zones principle, it is feasible for the new modeling method, using one-parameter cubic non-uniform B-splines and least–squares fitting algorithm, to implement the reconstruction on curves of which approximate errors are the least. The influences of the distributions of uniform and non-uniform fitting points on approximate errors of the new curve models are significant. Moreover, using the equal-chordal-height selection method of non-uniform fitting points, approximate errors of the curves can be reduced greatly. With the new method, the reconstruction of curves, which approximate errors are the least, is implemented.

ACKNOWLEDGEMENT

This research is supported by the 863 High Technology Research & Development Project of China（No. 863-511-942-024）.

REFERENCES

1 Shi F. Zh., CADG & NURBS, The Press of Beijing Aerospace University, Beijing, 1994

2 C.de Boor, On Calculation with B-spline, J. Approx. Theory., Vol. 6, pp.50-62, 1992

3 C.de Boor, Bicubic spline Interpolation, J. Math. and Phys., Vol. 41, pp.211-218, 1962

4 C.de Boor and R. E. Lynch, On spline and their minimum properties, J. Math. Mech., Vol. 15, pp.953-969, 1966

5 Alhanaty, M., Bercovier, M., Curve Fitting and Design by Optimal Control Methods, Proceedings of the IEEE Symposium on Information Visualization, IV, pp108-113, 1998

6 Gopi, M., Manohar, S, Unified Architecture for the Computation of B-Spline Curves and Surfaces, IEEE Transactions on Parallel and Distributed Systems, Vol. 8, No. 12, pp 1275-1287, 1997

7 Werner, A., Skalski, K., Reverse engineering of free-form surfaces, Journal of Materials Processing Technology, Vol. 76, No. 1-3 , pp 128-132, 1998

On-machine Profile and Straightness Measurement of a Linear Slide

Eric H.K. Fung, S.M.Yang
The Hong Kong Polytechnic University, Department of Mechanical Engineering
Hung Hom, Kowloon, Hong Kong, Hong Kong SAR, 99999, P. R. of China
BusinessPhone: (852)-2766-6647, Fax: (852)-2365-4703, email: mmhkfung@polyu.edu.hk

In this paper, a new system is proposed to measure the straightness error of a precision linear slide under on-machine conditions. Precision slides play an important role in machine tools and measuring machines. In precision turning machines, the workpiece is held in position by the spindle while the moving table carries the cutting tool. In order to enhance the performance of these machines, it is necessary to measure the motion errors of the tool or the table and correct these errors by means of a fast piezoactuator. In active error compensation (AEC), the motion errors of the table are determined on-line and fed to the controller for correction. Here, if the profile is known exactly, the motion error can be obtained simply by subtracting the profile data from the output of a displacement sensor. However, under on-machine conditions, such precalibrated profiles or references are not reliable, due to deviations from the calibration conditions. To overcome this difficulty, information on three displacement sensors are employed to construct an ideal software datum that can be used on-line in AEC. Such a software datum can act as an ideal reference for separating the profile from the motion errors. Measurements will be performed on an experimental lathe using the proposed system that consists of three capacitive displacement probes and their signal conditioning devices. The parameters of the profile used for measurement are measurement range = 36 mm, sampling period = 0.1 mm, separation between the central and edge sensor = 10.9 mm. The repeatability error of the profile obtained from the two measurements is found to lie within 1 m. The characteristics of this method are: (1) the profile is determined under on-machine conditions requiring no pre-calibrations and (2) a novel approach to represent the test section of the profile by one cycle of a periodic function is facilitated by specially arranging three sensors to form a stationary stage.

KeyWords: precision linear slide, straightness error, profile measurement, Fourier series

SELF-CALIBRATION FOR 2-DIMENSIONAL PRECISION STAGES BASED ON CIRCLE CLOSURE PRINCIPLE

Xiaoming Lu & Hy D. Tran *
Department of Mechanical Engineering
University of New Mexico
Albuquerque, NM 87131

Abstract

Self-calibration is one of the main approaches to obtain greater accuracy in precision engineering. By measuring a rigid artifact placed at different locations and orientations on a stage, it is possible to separate the stage error map from artifact errors by comparing the different views. However, it is impossible in practice to realize an exact 90° rotation about an exact pivot point, and achieve an exactly known translation with absolutely no rotation. The key issue is to decouple stage error when there are artifact errors, alignment errors, and measurement noise. Previous approaches are to isolate the alignment error first by using least squares, which is effective when the measurement noise has a normal distribution. Then, polynomial fitting, or Fourier series, or other orthogonal function decompositions are used to decouple the stage error from three measurement views, view 0, view 1(90^0 rotation) and view 2 (one interval translation). It is difficult to realize these three measurement views in practice.

We present a testbed physical realization of an X-Y stage for nanolithography. This stage is an air-bearing dc motor driven capstan drive system being retrofitted with a NanoGrid XY-grid-based encoder for feedback. The NanoGrid greatly reduces possible effects from air turbulence (as might be seen with laser interferometers) and Abbe offsets from using separate X and Y scales. However, the metrology is based on an artifact: The accuracy of the grid itself. We will present a circle-closure based self-calibration method for grid and stage calibration.

The principle of circle closure (the sum of the angles around any point in a plane equals 360) is for self-calibration of the rotation angle of the rigid artifact (e.g. XY encoder grid). When the mark position of rigid plate is measured in turn with about 90° rotation, difference between each rotation and an unknown reference angle x can be measured using a differential measurement (which can achieve better resolution). Circle closure provides a constraint that the sum of all the rotations must be 360°. This provides sufficient information for the solution for all unknown rotation angles. We only need to decouple the computation of the pivot point position in the self-calibration algorithm. The mathematical model is simpler, and may be easier to implement.

Redundant measurements may be used to improve calibration accuracy. Different combinations from the 4 measurement views (0, 90^0, 180^0, 270^0) can be used to calibrate the stage errors. The final calibration is calculated by using least square methods. The mathematical model and algorithm with and without additive measurement noise are simulated using MATLAB.

Keywords: self-calibration, nanolithography, calibration algorithm, two-dimensional stage

Introduction

Two-dimensional XY stages are used in many precision engineering applications. The specific application that we are interested in is nanolithography, where it is desirable to maintain nm to sub-nm accuracies over a 2-dimensional workspace spanning a wafer (e.g. 300 mm). There is generally a deviation between the measured stage position and its true position; this is called the stage position measurement error.

The stage position measurement error is the sum of random measurement noise and systematic measurement error, which is a function of the stage position. Calibration is the procedure used to

* Lu: luxm@unm.edu Tran: tran@me.unm.edu This work is supported by DOD/ARO DAAD-19-99-1-0196

determine the stage error map, to map the measured stage position to its position in a Cartesian reference frame. In conventional calibration method, two steps are needed: First, measure a standard artifact; i.e, an artifact plate that has marks with known positions. The difference between the measured position and the known position of the marks is the stage error at that mark location. Second, set up a mapping function (a stage calibration function) between the measured coordinates and the actual coordinates; e.g., using a piece-wise linear function or a polynomial. The stage calibration function is an approximation to the stage error map. The accuracy depends on the traceability of the artifact. Precision stages are tested against artifacts which have been certified by a calibration service whose "grand master" are traceable to national measurement or standard institutes which have realized and transferred the base units.

In our nanlithography application, there is no standard artifact available with the desirable nm accuracy. In fact, we are unable to fabricate an artifact with mark positions known better than the metrology system. Here we run into the chicken-or-egg problem: How do you construct an accurate measurement standard without an accurate standard to calibrate the machine that would make it? Therefore we need to do self-calibration.

Previous work on self-calibration of x-y stages

Self-calibration has a long history, and the advent of e-beam mask pattern generators has increased interest in its use. Raugh (1984) developed a mathematical theory for 2-dimensional self-calibration; however, the algorithm presented is not numerically robust, and is also sensitive to random measurement noise. Ye, Pease et al. (1997) developed a discrete Fourier transform-based algorithm, based on Raugh's theory, which is numerically robust. This approach extracts the stage measurement error from the artifact mark position measurements by comparing three different views of a measurement artifact plate. These three views are an initial set of measurements, a set of measurements with the artifact plate rotated 90 degrees with respect to the stage, and a set of measurements with the artifact plate translated by one grid interval with respect to the stage. The problem now is, how do you achieve an exact 90 degree rotation, and how do you translate the artifact plate one grid interval, without adding rotational motion. Finally, the discrete Fourier-transform based algorithm is complicated.

Testbed physical realization of x-y stage for nanolithography

Our interest is to develop a stage for imaging interferometric lithography (IIL, Brueck, 1998). This technique can help optical lithography approach the fundamental linear systems limit of optics of $\lambda/2$. Any lithographic technique will require more accurate and precise stage positioning (and dimensional stability) to enable registration across multiple levels. Hence, the motivation to investigate self-calibration. Current metrology for precision and ultraprecision stages is based on heterodyne laser interferometers; with a HeNe laser at 632.8 nm wavelength, interpolation of 2^{10} to 2^{11} ($\lambda/1024$ to $\lambda/2048$) is available for two-pass interferometers. This corresponds to resolutions of 0.6 to 0.3 nm. Unfortunately, the refractive index of air varies with CO_2 and water-vapor content, and air turbulence. This is the primary limitation on the accuracy with operation in air—while the resolution of the interferometers is nm, the actual accuracy may only be sub-μm. Other metrology systems have been proposed to reduce the errors due to air, such as holographic encoders and two-color interferometers; neither technology has yet been proven accurate. For metrology, we are using the OPTRA NanoGrid XY encoder system, which offers nm-level resolution, but with accuracy at the submicron level. The objective of the self-calibration research is to develop algorithms to improve the accuracy of the encoder to its resolution—from submicron to nanometer accuracy, and to implement these in a lithographic stage. We have obtained, courtesy of Sematech, an air-bearing, capstan drive interferometric lithography stepper, with HP laser interferometers for feedback (shown in Figure 1). This stepper will serve as a testbed for the stage development, which will primarily investigate self-calibration and thermal compensation methods.

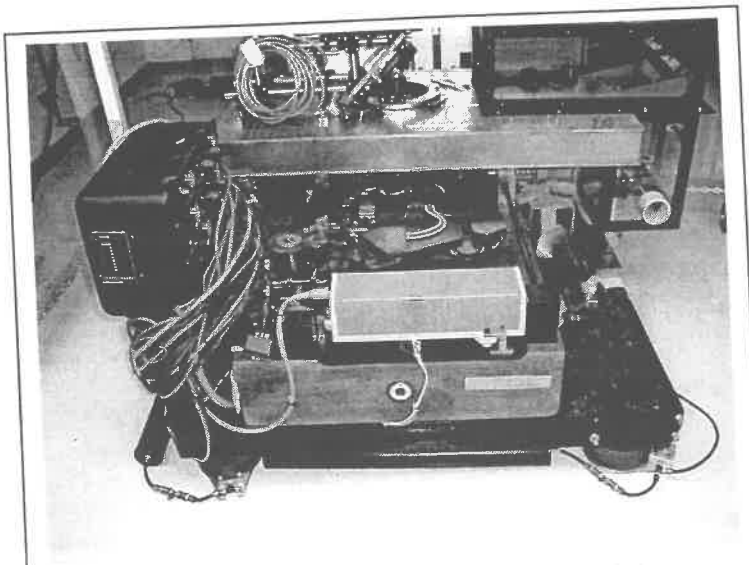

Figure 1. Testbed air-bearing stage for self-calibration research

This stage is configured as a stacked-slide X-Y stage, although the moving stage itself is supported by air bearings on the granite surface plate. The wafer chuck is mounted on a piezo-driven flexure stage. The existing laser interferometer will be retained for calibration purposes, although its basic resolution is 5 nm (e.g. coarser than the resolution of the NanoGrid metrology).

The X-Y encoder system resolution is 0.3 nm; it is insensitive to variations in the index of refraction of air—but its basic accuracy is on the order of 1 μm, since its accuracy is based on the absolute accuracy of the encoder artifact plate, whereas the laser interferometer accuracy is fundamentally dependent on the wavelength of the laser. We will mount the NanoGrid system on the stage, with the encoder plate parallel to, and in the same plane as the wafer chuck. The encoder plate will move with the wafer chuck, while the readheads are stationary. This will minimize Abbe offsets. At the same time, since there is a large planar area available around the wafer chuck, multiple encoder plates and readheads may be installed in order to obtain redundant measurements.

Stage error function and artifact plate error function

The stage error function S(x,y) is the systematic measurement error at (x,y), where (x,y) is the true location of the sample site in a Cartesian grid. Assume the field to be calibrated is L×L. The origin of the x-y axis is chosen at the center of this area. So,

$$S(x,y) = S_x(x,y)e_x + S_y(x,y)e_y$$

where ex and ey are the unit vectors of the stage axis. Sx(x,y) and Sy(x,y) are functions on the continous 2-D field L×L. Let the sample sites be in a N×N square array covering the field L×L (For simplicity, let N be odd). The sample site locations in the Cartesian grid are:

$$x_m = m\Delta$$

$$y_n = n\Delta$$

where m= – (N–1)/2,– (N–2)/2, … ,0 ,…, (N–2)/2 ,(N–1)/2, n= –(N–1)/2,–(N-2)/2, … ,0 ,…, (N–2)/2, (N–1)/2 and $\Delta = (L/N)$, which is called the sample site interval. So the discrete stage error function can be expressed as

$$S(x_m, y_n) = S_x(x_m, y_n)e_x + S_y(x_m, y_n)e_y$$

The artifact plate has a square (N×N) mark array of the same size as the stage sample site array. The origin of the plate x-y axis is located at the center on the mark array. The nominal mark locations in the plate coordinate system are the same as the sample site locations in the stage coordinate system. The plate is rigid; i.e, the relative positions between the marks on the plate do not change when we rotate it on the stage. However it is not perfect, which means that each actual mark at (x_m,y_n) deviates from its nominal location by $A(x_m,y_n)$.

$$A(x_m, y_n) = A_x(x_m, y_n)e_x + A_y(x_m, y_n)e_y$$

It should be noted that every mark on the artifact plate has an identification number (m,n). The mark's identification number does not change during the plate's motions on the stage.

Decoupling the alignment error based on angle calibration using circle closure

Circle closure is used to measure the rotation angle. The XY grid is placed on a rotation table which is mounted on the stage; a schematic is shown in Figure 2. There are two sensor heads above the XY grid which are used to get translation information in each measurement view. We can select two points on the four sides of xy grid plate to determine the direction of each side. The direction change of each side can be measured by an autocollimator or other high resolution sensor. According to circle closure, the sum of 4 inner angles is equal to 360 degrees. The principle of circle closure is a natural conservation law for plane angles in Euclidean geometry. Denoting the deviations from the nominal value by $\Delta\theta_i$ (i=0,1,2,3) and the actual rotation angle θ_i. We have

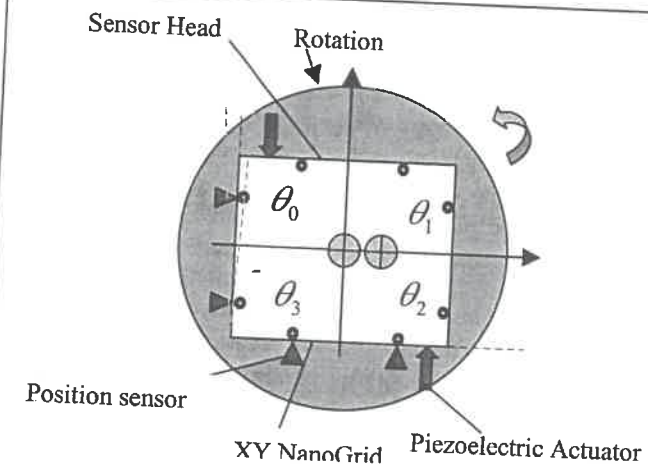

Figure 2. Decoupling alignment errors based on angle calibration via circle closure.

$$\theta_i = x + \alpha_i$$

$$\theta_i = 90^0 + \Delta\theta_i$$

$$\Delta\theta_i = x - 90^0 + \alpha_i$$

$$\sum_{i=0}^{3}\Delta\theta_i = 4(x - 90^0) + \sum_{i=0}^{3}\alpha_i$$

With the constraint of the circle closure $\sum_{i=0}^{3}\Delta\theta_i = 0$, we have $x = 90^0 + -\frac{1}{4}\sum_{i=0}^{3}\alpha_i$

With x, we can calculate the actual rotation angle θ_i with

$$\theta_i = 90^0 - \frac{1}{4}\sum_{i=0}^{3}\alpha_i + \alpha_i$$

We only need to decouple the computation of the pivot point position in the self-calibration algorithm. In this way, only two 90^0-rotation views are needed to exactly calibrate the stage errors at those sites sampled by the mark array. The mathematical model is simpler, and may be easier to implement.

Summary

The mathematical model and algorithm with and without additive measurement noise are simulated using MATLAB; the results of the simulation are shown in the poster. The algorithm gives an exact self-calibration on the discrete sample sites. When there is random measurement noise, different combinations from different rotations and two sensor head (4 rotation measurement views and 4 translation measurement views) are used to calibrate the stage errors. The final calibration is calculated by using least square methods.

References

Brueck, S. R. J., "Imaging Interferometric Lithography," *Microlithography World*, Winter 1998.

Evans, C. J., Hocken, R. J., and Estler, W. T., "Self-Calibration: reversal, redundancy, error separation, and 'absolute testing,' " *CIRP Annals*, Vol45(2), 1996.

Raugh, M.R. "Absolute two-dimensional sub-micron metrology for electron beam lithography" *Prec Eng* vol. 7(1), p. 3-13, 1985.

Ye, J., Takac, M., Berglund, C. N., Owen, G., and Pease, R. F., "An exact algorithm for self-calibration of two-dimensional precision metrology stages," *Prec Eng* vol. 20(1), p. 16-32, 1997.

Carlson, D., Dorval, R. K. , Gargas, J. A., Hercher, M., Mansur, D., and Tran, H. D., "A Versatile XY Stage with a Flexural Six-Degree-of-Freedom Fine Positioner," *Proc. 10th ASPE Annual Meeting*, p. 203-206, October 1995.

SHAPE ERROR MEASUREMENT OF A PARABOLIC MIRROR USING THE RAY TRACING AND THE FRINGE SCANNING METHOD

Takashi Nomura, Kazuhide Kamiya, Seiichi Okuda, Keishin Yamazaki,
Toyama Prefectural University, Kosugi-machi, Toyama, 939-0398, Japan
Hatsuzo Tashiro, and Kazuo Yoshikawa
Toyama University, Gofuku, Toyama, 930-8555, Japan

Abstract

A shape error measurement based on geometrical optics is proposed. The method uses grid lines with a sinusoidal transmittance distribution. The grid lines are displayed on a liquid crystal panel. The beam transmitted through the liquid crystal panel reflects on a mirror surface being tested and reaches a screen. A CCD camera detects the projected images. The images are analyzed by the fringe scanning method. Using the method, the spatial resolution with respect to the measuring points is improved. The shape error of an off-axis parabolic mirror made of plastic is measured by the proposed method.

Keywords: Ray tracing, Angle of reflection, Fringe scanning method, Phase analysis, Null test of an off-axis parabolic mirror, High spatial resolution, Liquid crystal panel

1. Introduction

Many reflection mirrors incorporated in illumination or display systems are manufactured. Several such mirrors are made of plastic. Errors in the shapes of the mirror surfaces occur depending on the manufacturing condition of these mirrors. To identify mirrors with an acceptable quality level, a method of rapidly and precisely measuring shape error is desired. When the entire mirror surface is measured, interferometers are ordinarily used. However, the use of the interferometers is difficult in this measurement, because the precision of the surface is low, that is, the interval of interferogram observed by the interferometers is too narrow. Consequently, the shapes are measured using a coordinate measuring machine. The method has the following problems. When a large number of points is measured, the measuring time is long. On the contrary, when the points are scarce, the spatial resolution limit becomes low. To rapidly and precisely measure the shape errors of mirror surfaces, a measurement using the ray tracing and the fringe scanning method[1)] is proposed in this paper.

2. Measurement method

2.1 Principle

The proposed method is based on geometrical optics; namely, it is an improved Hartmann test[2)]. In this paper, we discuss the surfaces with respect to off-axis parabolic reflectors. In the proposed optical arrangement, the source of illumination light is located at the focal point of a designed parabolic mirror surface. A liquid crystal panel is located between lenses L2 and L3, as shown in **Fig. 1**. A grid is displayed on the liquid crystal panel. Light passing through the panel is diffracted in many beams. Only one beam is selected by the spatial filter. The beam is reflected on the mirror surface to be tested and collimated. A projected image of the grid reaches the diffusing screen. The intensity of the projected grid image on the screen is detected with a charge-coupled device (CCD) camera. When the designed mirror surface or a standard one is measured, the projected image

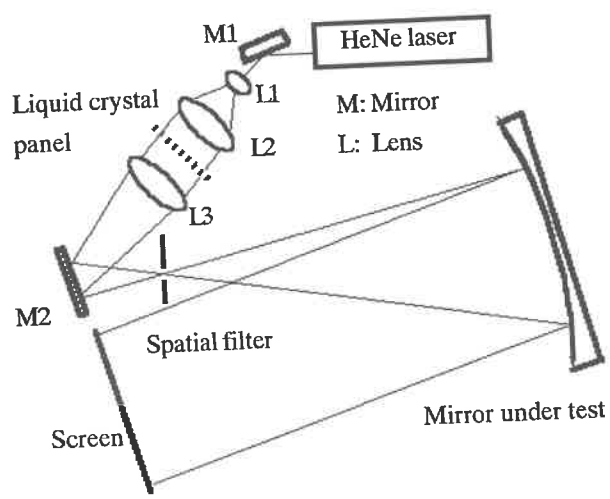

Fig.1 Optical arrangement

shown in **Fig. 2 (a)** is obtained. When the mirror to be tested has error in its shape, the projected image is modified as shown in **Fig. 2 (b)**. The coordinates of an intersection on the standard surface are defined as (x,y), and the coordinates of the same intersection on the surface being tested is defined as (x',y'), as shown in **Fig. 2 (c)**. The difference between the inclination of the designed surface and that of the surface being tested is obtained from the amount of shift of the intersection. The amount of shift of the intersection increases in proportion to the difference in the reflection angle θ and the distance L between the screen and the surface being tested. The difference in the reflection angle is twice the differences in the inclination angles θ_x and θ_y at the measuring position, where the subscripts indicate the direction of the inclination at the measuring point. Consequently, the differences of the inclination angles θ_x and θ_y are as follows:

$$\theta_x = \frac{x' - x}{2L} \cdots (1),$$

$$\theta_y = \frac{y' - y}{2L} \cdots (2).$$

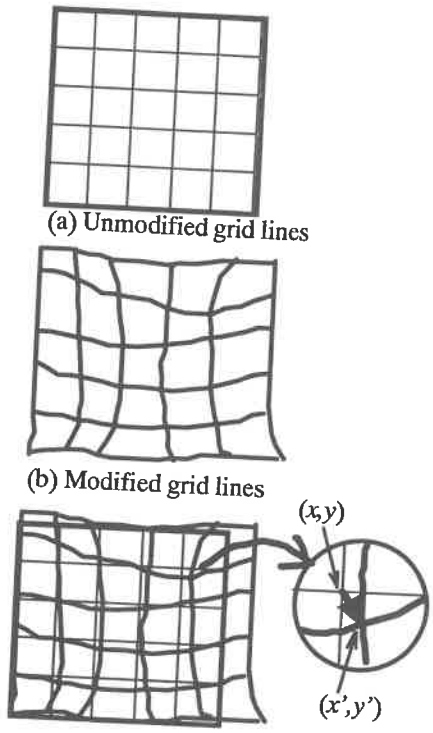

(a) Unmodified grid lines

(b) Modified grid lines

(c) Superimposed grid lines

Fig.2 Projected grid lines

The differences in the inclination angles over the entire surface being tested are calculated using these equations. All intersections are measured, and then the difference in the inclination of the surface at each intersection is analyzed. Then, all the differences in the inclinations are integrated, with the result that the error in the shape of the surface being tested is obtained.

The above-mentioned method has two problems. The first problem is low spatial resolution; that is, the differences in the inclinations are measured only at the intersections, therefore shape measurements with high spatial resolution cannot be performed. The second problem is the integration procedure. The integration has large error in the calculation because intervals between the intersections are wide. Furthermore, the calculation of the integration is difficult because the information on the inclinations is not aligned with the directions of the x-axis and y-axis. To achieve high resolution, to simplify the calculation, and to perform it precisely, there is a method in which intersections are shifted pixel by pixel of the CCD camera. However the method has the problems that huge images are captured and the measuring time is long. To solve these problems, the fringe scanning method is applied in the proposed method.

2.2 Measurements with high spatial resolution

In our proposed method, grid lines with sinusoidal transmissivity distribution are displayed on the liquid crystal panel shown in **Fig. 1**, and recording is done in two stages. The first stage is concerned with the x-direction; the grid lines are perpendicular to the x-axis. The grid lines are shifted every 1/4 interval of the grid perpendicular to the lines, by computer commands. Four projected images whose phases differ by $\pi/2$ are obtained. Each image is assumed to be an interferogram. The images are captured in a computer and analyzed by the fringes scanning method. By this procedure, phase distribution in the x-direction of the projected image is obtained. The second stage is concerned with the y-direction; the grid lines are rotated at a right angle and the same procedure as above is performed in the y-direction. And then the phase distribution in the y-direction of the projected image is obtained. Phase distributions in the two directions are superimposed. The same phase points are detected and used as intersections. As a result, many measuring points and, therefore high spatial resolution, are obtained.

3. Experiments

To verify the efficacy of the proposed method, an off-axial parabolic mirror made of plastic was measured using the optical system shown in **Fig. 1**. The dimensions of the mirror were 110 ×62 ×5 mm. The liquid crystal panel used in the experiments was an active matrix type and had 480×440 pixels. The dimensions of the panel were 26.9 ×20.2 mm. The grid lines with sinusoidal transmissivity distribution of 256 gray levels were displayed on the panel. A translucent white plastic panel with a thickness of 1 mm was used as a diffusing screen. From the back of the screen, the projection images on the screen were recorded with the CCD camera. The distance between the focal point and the mirror being tested was 338.8 mm, and the distance between the mirror and the screen was 398.6 mm. The interval between the grid lines displayed on the liquid crystal panel was 4.5 mm. The panel was inserted into the collimated beam. The grid lines were shifted every 1.1 mm perpendicular to the lines by computer commands. Four projected images whose phases differing by $\pi/2$ were obtained. Each image was analyzed as an interferogram with phases differing by $\pi/2$.

The phase distribution after calculation is shown in **Fig. 3**. The gray level indicates the phase. Black and white represent phase zero and 2π, respectively. Intersections were determined by the phase gaps shown in **Figs. 4 (a)** and **4 (b)**, which change from black to white in **Fig.3**. The grid lines with respect to the x-direction and the grid lines with respect to the y-direction were superimposed. In the result, intersections with respect to the mirror being tested were obtained. The intersections are marked by × in **Fig. 5**.

To detect intersections with respect to the standard mirror, computer simulations are performed. The intersections obtained by the simulations are marked by + in **Fig. 6**. **Figures 5** and **6** were superimposed and then the vector map indicating the shift of the intersections was obtained, as shown in **Fig. 7**. The vectors were analyzed to determine the inclination at each intersection with respect to the x-direction and y-direction. The inclinations were integrated over the mirror surface being tested to analyze the shape error of the mirror. The integration method based on the trapezoidal rule was used.

To increase the number of measuring points, the following method was used. Phase fraction ε explained below was added at the phase distribution map.

$$\phi_\varepsilon(x,y) = 2\pi \cdot \mathrm{Frac}\left\{\frac{\phi(x,y)+\varepsilon}{2\pi}\right\} \cdots (3)$$

where, $\phi(x,y)$ is the phase of the modified grid line before shifting and $\phi_\varepsilon(x,y)$ is the phase after shifting. And Frac(δ) is given a fraction of δ. Then the positions of the phase gaps were shifted by changing ε. A new intersections with respect to the phase fraction are obtained. When a finer phase fraction is used, higher spatial resolution is obtained.

In these experiments, the area of 64 × 46 mm was measured by the CCD camera with 512×512 pixels. The gray scale was in 256 steps and the spatial resolution was 0.22 mm/pixel. To simplify the explanation, the phase fraction ε was added every $\pi/4$. The three-dimensional plots analyzed by the proposed method are shown in **Fig.8**. The displayed area is 40 × 50 mm and the spatial resolution is 1.4 mm. The spatial resolution of the map was 64 times higher than in the experiments without the method. When the mirror was measured with the three-dimensional coordinates machine, the measuring time of 300 points was 40

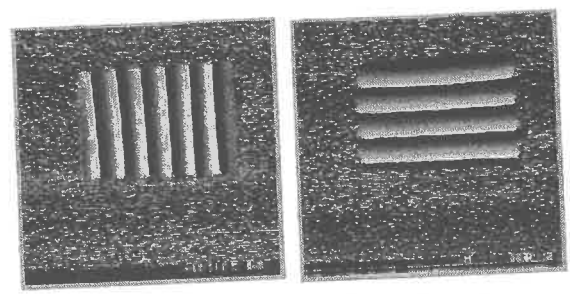

(a) Phase distiribution in the direction of the x-axis

(b) Phase distiribution in the direction of the y-axis

Fig.3 Phase distribution analyzed by the fringe scanning method

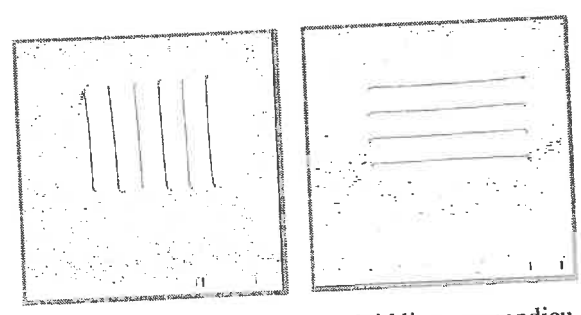

(a) Grid lines perpendicular to the x-axis

(b) Grid lines perpendicular to the y-axis

Fig.4 Grid lines of phase zero

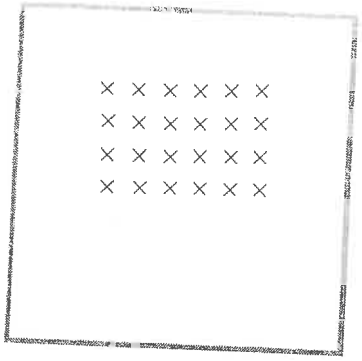

Fig. 5 Intersections of the grid lines obtained by measurement

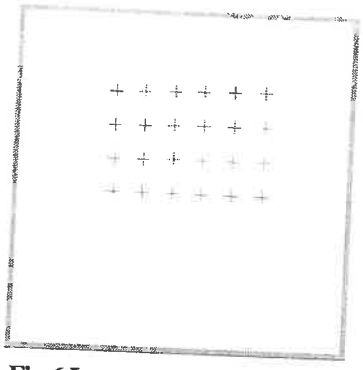

Fig.6 Intersections of the standard grid lines obtained by simulation

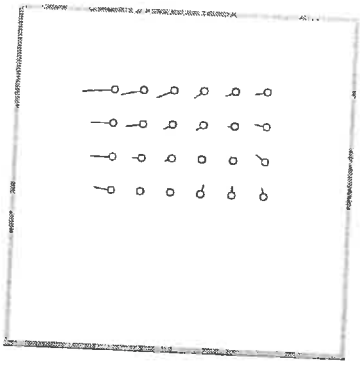

Fig.7 Vector map of the displacement of intersections

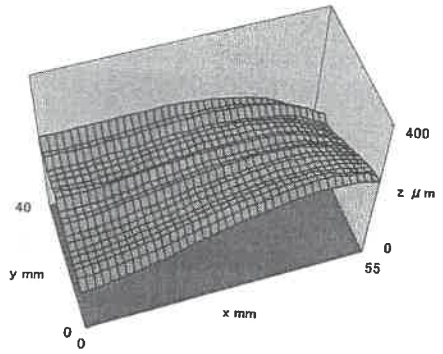

Fig.8 Three-dimensional plots of the error in the shape of the mirror surface analyzed by the proposed method

minutes. In the proposed method, the measuring time of 300 points was 3 minutes, which was 13 times shorter than that by the three-dimensional coordinates machine. When the numbers of measuring points were 1,536, the measuring time was 10 minutes. The spatial resolution obtained by the experiments was 1.4 mm.

4. Conclusions

The proposed method is a kind of shape error measurement based on geometrical optics; namely, it is an improved Hartmann test. Unlike the Hartman test, the proposed method uses grid lines with a sinusoidal transmittance distribution. The intersections of the projection grid of the standard surface and that of the surface being tested are superimposed. The difference between the inclination of the standard surface and that of the surface being tested is obtained from the shift of the intersections. The difference is integrated and the errors in the shape of the mirror being tested are analyzed. A liquid crystal panel displaying grid lines is used. The grid lines are shifted stepwise in the direction perpendicular to the grid lines. The beam transmitted through the panel reflects on the mirror surface being tested and reaches a screen. A CCD camera detects the projected images. The images are analyzed by the fringe scanning method. By this procedure, the phase distribution in the shifted direction is obtained. The grid lines are rotated at a right angle and the same procedure is performed in the other direction. The phase distribution in that direction is obtained similarly. Using the method, the spatial resolution with respect to the measuring points can be increased up to the resolution of the CCD camera. In these experiments, an area of 64×46 mm was measured by a CCD camera with 512×512 pixels. The spatial resolution obtained by the experiments was 1.4 mm. The shape error of an off-axis parabolic mirror made of plastic was measured by the proposed method. The efficacy of the method could be verified through these experiments.

Acknowledgements

This research was supported in part by a Grant-in-Aid for General Scientific Research (C2) (No. 126550119) from the Ministry of Education, Science, Sports, and Culture of Japan. We thank Professor O. Sasaki of Niigata University for his suggestions.

References

1) J.H.Bruning, *et al.*, Appl. Opt., 13,11, (1974) pp.2693-2703.

2) D. Malacara, *Optical Shop Testing*, 2nd ed. (*Wiley, New York,* 1992) pp. 367-396.

Profile tolerance zones with control points

T. M. Kethara Pasupathy, Robert G. Wilhelm and Gregory A. Hetland*

Center for Precision Metrology
Department of Mechanical Engineering and Engineering Science
The University of North Carolina at Charlotte
9201 University City Blvd., Charlotte, NC 28223-0001

*Hutchinson Technologies Ltd.
40 West Highland Park, Mail Stop 403
Hutchinson, MN 55350-9784

Introduction:

Controlling uncertainty in specification and verification grows more important as part feature size decreases. Specification uncertainty occurs when geometric characteristics are described and controlled to achieve portions of intended function but the specification is incomplete. With the growing impetus for smaller feature sizes, complete representation of tolerances is a key requirement for control of specification.

As an initial focus, we have studied specification uncertainty [1] related to the mathematical definitions for profile tolerances as defined in ANSI Y 14.5.M [2]. These definitions describe tolerance zones for individual features but they do not define zones between adjacent features. Hence, under certain conditions, the tolerance zones can be incomplete. Some blending curves are identified to modify and blend the tolerance zones of adjacent features.

Polynomial curves and surfaces that are generated by mapping from parametric space to Euclidean space are extensively used in computer aided geometric design (CAGD). These curves and surfaces are obtained by a linear combination of basis functions and control points. Examples include Bezier curves, B-Splines, and NURBS. Cardew et. al. [3] have described a suitable representation scheme to define tolerance zones for free-form surfaces associated with aerofoils and turbine blades. B-Splines are employed to define tolerance zones that have a varying form desirable for such curves and surfaces. Utpal Roy and Bing Li [4] in their scheme to simulate model variations for form tolerances have used a 16 point Bi-cubic interpolation method. The 16 point Bi-cubic interpolation model constrains the simulated curve to pass through the generated points.

This paper describes an approach for complete representation of profile tolerances that defines tolerance zones bounded by polynomial curves and surfaces. The specification described here is useful for the development of standard definitions for profile tolerance zones. By using polynomial curves, tolerance zones of adjacent features can be blended using suitable parameters and conditions. In the following sections, we first introduce the problem with some examples of the awkward zones that arise with the current standard. In the section on our approach, we show a method by which parametric curves can define profile tolerance zones. Also included are some basis functions for polynomial curves along with their applications and advantages in defining unambiguous zones. Finally, conclusions and future work are discussed. All Figures are printed after the section on references.

Profile tolerance zones from current definition:

The current ANSI mathematical standard for profile tolerances defines the profile tolerance zone by translating every point of the specified feature bilaterally by the same distance according to the tolerance value specified in the feature control frame. While the current definition satisfies requirements to specify the individual features, under certain conditions, ambiguities arise.

Consider Figure 1 where adjacent features are depicted with reasonable bilateral profile tolerance values as per the standard. The shaded areas indicate ambiguity in those areas that might be intended or required by the designer but cannot be implied for subsequent processes such as analysis, manufacturing or measurements. This is because there is no unique normal at the end points of the nominal feature. The ISO zone definitions result in different zones that may not be useful for particular design specification [1]. As another case, when multiple tolerance zones are indicated on a single feature, as shown in Figure 2, the boundary of the tolerance zone has sharp changes that may not be useful for preserving design function. Furthermore, considering the worst-case tolerance zone boundary as an offset of the nominal geometry, self-intersections and cusps can occur in the tolerance zone, as shown in Figure 2, and pose a problem [5]. Though the standard informally conveys the information that the offset distance has to be small compared to the dimensions of the nominal part, self-intersections and cusps often occur for practical offset distances. It is clear that these conditions are not desirable in the specification of precision-

engineered parts. In the absence of such ambiguities, worst-case performance and function can be guaranteed with a significantly lesser degree of uncertainty. The next section describes a general approach to define complete solutions.

Approach to define profile tolerance zones using parametric curves:

As a brief review, the general form of parametric curves is given by

$$B[P](t) = \sum_j B_j(t) P_j \qquad 0 \le t \le 1$$

Where $P = [P_j]$ is an array of control points and $B(t) = [B_j(t)]$ are the blending functions. The blending functions must satisfy identity and convex hull properties. The identity property, ensure that the blending function is independent of the choice of coordinate origin and requires that

$$\sum B_j(t) = 1 \ for \ all \ t$$

The convex hull property ensures that the convex hull of the control points contains the curve and requires that

$$B_j(t) \ge 0 \ for \ all \ j$$

Blending functions that were earlier applied [3,4] and useful for geometric tolerances can be grouped into two classes. One class of functions, the Hermite, requires the curves to pass through the control points. The other class, the B-Spline function, does not require the curve to pass through all the points. Bezier curves are a special case of the B-Spline function [6].

The designer with a prior knowledge on the requirement of the worst-case tolerance zone boundary of adjacent features can define the zone shape by projecting control points with respect to the nominal geometry. By manipulating these control points and suitable blending functions, the tolerance zones can be shaped to specify design requirements. In the example shown in Figure 3, the nominal geometry of two features at an obtuse angle with different tolerance values is shown. The control points (A through K in the figure) are projected from the nominal surfaces. The blending is performed with a B-Spline basis function. To demonstrate the application of the blending curves in defining the worst-case boundary, the figure shows different blending curves that range from straight lines to higher degree curves. The curves show the boundary of the t+ zone or the zone that is beyond the material of the part.

Hermite functions allow the interpolating curve to pass through the control points and have specific advantage in simulating the actual surface. The control points with the rational form of B-Splines and Bezier curves can also be used to define nominal geometry. Algorithms available for offsets of the above nominal curves can be directed to avoid self-intersections and cusps [5]. Of these several options, the non-uniform B-Spline basis function interpolates the end control points and gives better control of the tolerance boundary.

Figure 4 illustrates a suggestion on the information the specification can include. The 2D part has adjacent features controlled by a tolerance zone of varying form. The position of the control points is referenced from the intersecting point (indicated as Origin in Figure 4) of the two datum features, A and B. Necessary and sufficient conditions are provided in the feature control frame to specify the blending function, control points, and knot vector values. Such a definition could define the acceptable tolerance zone shown as a hatched area in the t+ zone. The inner worst-case boundary (t- zone) would be specified similarly.

Thus, with a suitable representation scheme, tolerance zones could be generated to meet specific requirements and specification communicated unambiguously.

Conclusions and future work:

We presented some shortcomings in using the current standard for profile tolerance definitions. We also presented an approach to solve the problems using parameterized curves. The parameterized curve form has distinct advantages such as tailoring the zones to requirements and providing unambiguous specification. Future work would include development of a model in a CAD environment that can provide a necessary framework to assist the designer with the choice of blending tools and in automatic detection of zones that require blending. As an important feature, the CAD system should be able to store the data of the modified zone for subsequent processes such as analysis and measurements.

References:
1. R.G. Wilhelm, "Geometric Tolerances for Three Dimensional Profiles", Engineering Design and Automation, 2(4): 231-242, 1996.
2. American Society of Mechanical Engineering, New York, N.Y., Mathematical Definition of Dimensioning and Tolerancing Principles ANSI Y14.5.1M, 1994.
3. M.J. Cardew –Hall, Lebans T, G. West, and P. Dench, A method of representing dimensions and tolerances on solid based freeform surfaces" Robotics and computer –Integrated manufacturing, vol. 10, No. 3 pp. 223-234,1993.
4. U Roy and Bing Li, Representation and interpretation of geometric tolerances for polyhedral objects – 1 Form tolerances, Computer Aided Design, vol. 30, no 2, pp. 151-161,1998.
5. T.Maekawa, An overview of offset cures and surfaces, Computer Aided Design, 31; 1999; pp. 165-173.
6. M.E.Mortenson, Geometric Modeling, 2e, Wiley Computer Publishing, 1997.

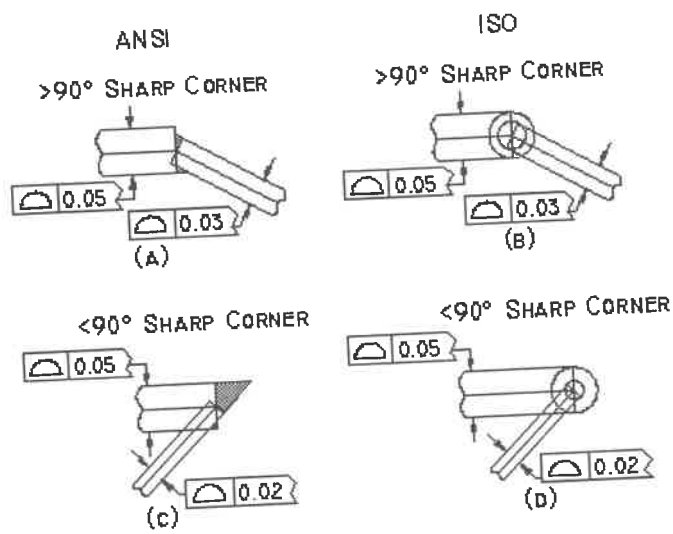

Figure 1

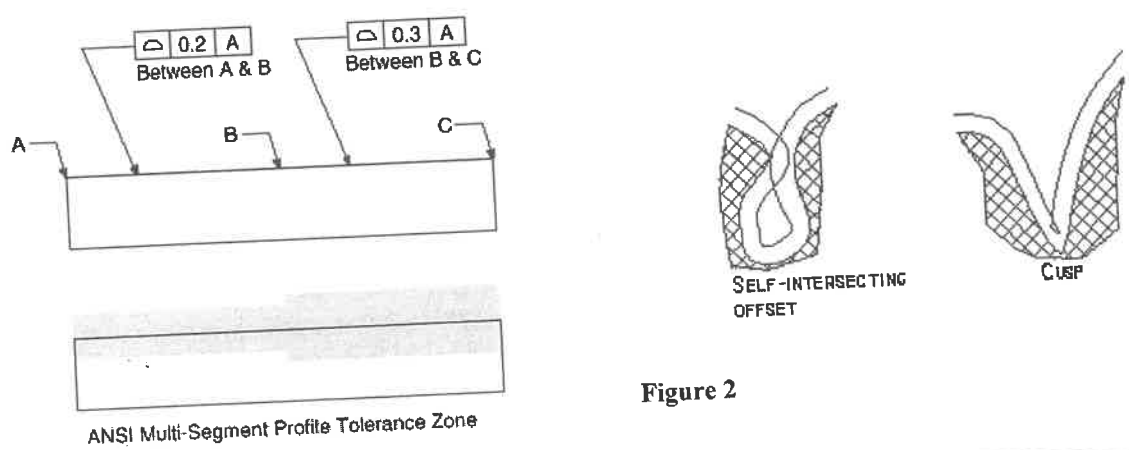

Figure 2

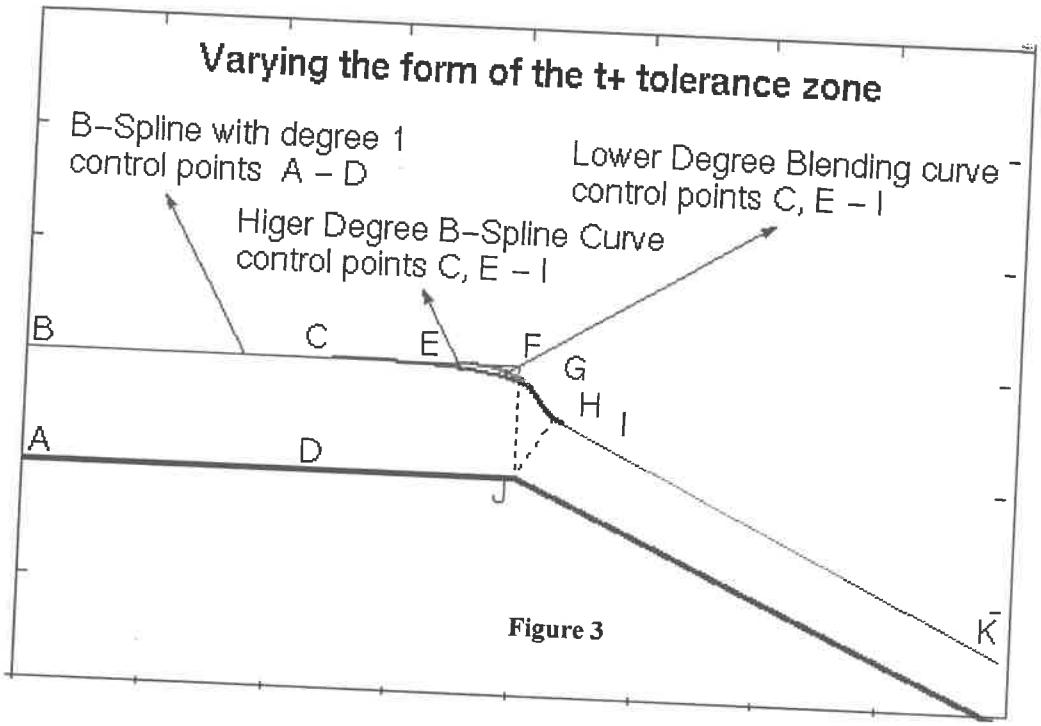

Figure 3

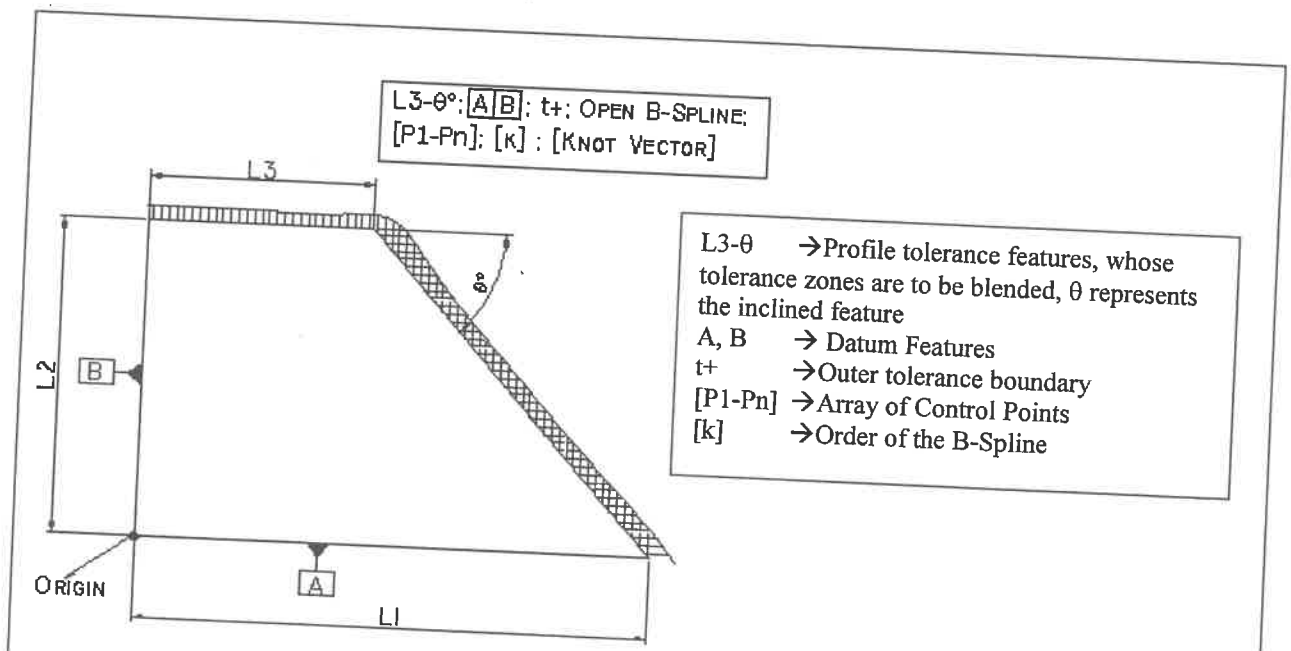

L3-θ →Profile tolerance features, whose tolerance zones are to be blended, θ represents the inclined feature
A, B → Datum Features
t+ →Outer tolerance boundary
[P1-Pn] →Array of Control Points
[k] →Order of the B-Spline

Figure 4

Precision Interferometer Measurement of Ultrahigh Precision Grate Base

Shuzhi Peng
Changchun Institute of Optics and Fine Mechanics, Chinese Academy of Science
22/5 Wilby Wilby, Bentley, Perth, W. A. 6102, AUSTRALIA
BusinessPhone: 08-94556868, email: shuzhipeng@netscape.net

The grate plate is wildly used in Ultrahigh precision instrument due to its various advantages such as high hardness, good processed technology, absorbing vibration, low coefficient of expansion, high abrasion hardness, corrosion-resisting, etc. Exacting flatness measurement is key to the success of precision equipment. The HP5529A Dynamic Calibrator is a well-established tool for the Ultrahigh precision measurement of flatness, linear, longitudinal displacement, etc. However, its outstanding disadvantage is that it can not measure by non-contact, a flexible, automated system is necessary to manufacturing process. By way of research and development of "Dual Optical Laser Direction Writing Equipment", a new sensor flexible automated system SFAS 2000 designed and made at CIOM is presented. The theory is that light from a HP5519A laser head passes through a pair of phase diffraction gratings to illuminate the test surface with two beams at different angles of incidence. The same pair of gratings recomines two beams, resulting in an interference pattern with an equivalent wavelength. During this measurement, a sensor will receive the signals and send them into the software package. Meanwhile a CCD camera captures a sequence of phase-shafted interference patterns, which the computer analyses to obtain an accurate map of the shape and topography of processing surface. The resulting measurement data can be displayed as high-resolution rotatable three dimension graphics, numeric displays or sliced cross section. By means of self-instructed mode and programmable attenuator, the sensoring system SFAS 2000 can automatically determine the attenuation degree and calculate the processing feed amount. The self-instructed mode is required only for the first of a configuration of workplace position. This allows the processor to instantly interact with the machine process and quickly identify scrap-production flatness error sources, then give crucial feedback at stage of the process, from milling and turning to grinding; from polishing to lapping and super-finishing. Powerful software package based on MATLAB running in a Microsoft windows 95,97 or 98 environment allows processor to set the parameters within which he wants to measure using a protocol that is comfortable to most users. The real-time, on-screen graphics is helpful of quickly identifying trends and variability within the whole production process. The precision and reliability of this new system ensure that the grate plate meets the demand of ultrahigh precision.

Key Words: Ultahigh precision; Flatness; Grate plate

Accurate Profile Measurement by an Interferometer

Xue-Feng QIANG , Wei GAO and Satoshi KIYONO
Department of Mechatronics and Precision Engineering, Tohoku University
Aobayama 01, Sendai 980-8579, Japan

1. Introduction

For the purpose of improving measurement accuracy in interferometry, a lot of methods have been proposed to separate the form error in the reference optics from that in the test optics. The best known one is the three-plate method[1][2] in which multiple measurements to three plates combined in pairs are carryed out. The unknown form error in the test optics can be evaluated through the calculation of the measurement results. However, multiple measurements across several lines and the combination of these individual sets of data are considered to lead to a loss of precision. In another method proposed by Schulz and Elssner[3], three positions, including the basic position, rotated position and cat's eye position, were used between the reference optics and the test optics. With a comprehensive calculation of data at these positions, the unknown form error in the test optics can be evaluated in spite of that in the reference surface. However, a device containing eight degrees of mechanical freedom is necessary to adjust tilts caused by the surface movement. In this method, the measurement precision is most likely limited by the moving precision of the device.

In contrast to these complicated methods, a simpled method called the 2-position method has been proposed by Itoh et al[4] for flatness measurement. In this method, a measurement combining two orientations with one along the circle and the other along the radius was attempted. Through movement in both of the orientations, the form error in the reference surface can be removed respectively.

In this paper, the 2-position method is applied to spheric surfaces along the circle. The form error in the reference surface along a closed circle can be removed by the combination of the measurements around the test surface rotation. Furthermore, The differential output is Fourier transformed and the true form error along the concentric circles of the profile are determined by phase operation. The algorithm is extended to test the influence of random errors in sampling and the positioning error when rotation the test surface associated with the measurement. Experimental results that confirm the effectiveness of this method in improving measuring precision are also presented.

2. Principle

In the interferogram evaluation for the spheric surface(see Fig.1), the parallel measuring rays penetrate the reference surface and illuminate on the test surface by convergent rays. The interference patterns can be formed by the translation of the rays reflected from both the test surface and the reference surface by which the form error (or deviations) in both of the surfaces can be obtained. In this method, the circles arraying along concentric circles are tested. The number of these circles is set as $i=1,2,\ldots,N_c$ from the center of concentric circles to the outest circle.

The principle of 2-point method[5] (see Fig.2) is used to separate the form error in the reference surface from that in the test surface. The interferometer output of the ith circle before and after the rotation can be expressed by Eq.(1) and Eq.(2).

$$m_{i1}(\theta_n) = f_i(\theta_n) + \varepsilon_i(\theta_n) = f_i(n\theta_s) + \varepsilon_i(n\theta_s) \tag{1}$$

$$m_{i2}(\theta_n) = f_i(\theta_n - \Delta\theta) + \varepsilon_i(\theta_n) + \Delta R_i(\theta_n) = f_i(n\theta_s - \Delta\theta) + \varepsilon_i(n\theta_s) \quad (n = 1, 2, \ldots N_r) \tag{2}$$

where $f_i(\theta_n)$ and $\varepsilon_i(\theta_n)$ repersent the form error in the test surface and the reference surface respectively. θ_n repersents polar coordinates of the surfaces along a single circle which is n times of the sampling interval θ_s. $\Delta\theta$ is the rotation angle.

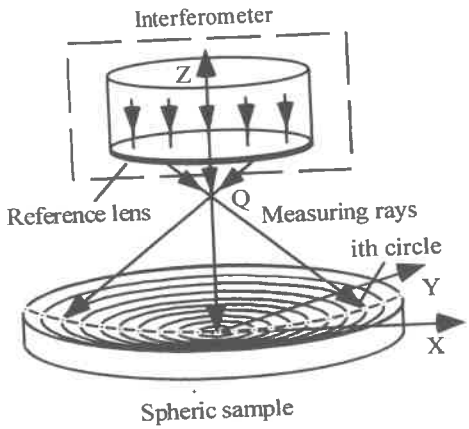

Fig.1 Profiles along circles on a test surface

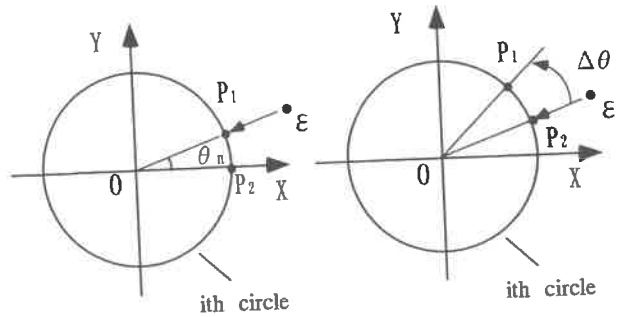

(a) Before rotation (b) After rotation

Fig.2 Principle of 2-position method

N_r is the number of the sampling points on the circle.

The following differential output, in which the form error in the reference surface is removed, can be obtained by taking the difference of Eq.(1) and Eq.(2).

$$m_{dc}(\theta_n) = m_{i1}(\theta_n) - m_{i2}(\theta_n) = f_i(\theta_n) - f_i(\theta_n - \Delta\theta) \tag{3}$$

The differential output is then Fourier transformed to get the true form error in the profile through phase operation. The calculated result of the test surface can be taken into Eq.(1) to obtain the form error in the reference surface.

True form errors in all concentric circles can be obtained respectively through the same way.

3. Simulation

The algorithm is extended to test the influence of random errors in sampling and the positioning error when rotating the test surface. The parameters for simulation are set as

1) Radius of curvature of the test optics: 519mm
2) Number of test circles N_c : 28 (radius: 50mm)
3) Number of sampling points N_r : 350
4) Sampling interval θ_S : $2\pi/350$
5) Rotary angle $\Delta\theta$: $29\theta_S$

Considering that high-frequency components of form errors are much small, the spatial frequency range for calculation is set to be lower than 20. Because the resolution of the interferometer used for experiment is ± 0.5nm , the PV value of random errors included in the interferometer output is set to be ± 0.5nm. From the compared result between the input profile and the calculated profile(see the result 1 of Fig.3), we can see that the influence of random errors is amplified by 6 times in the calculated result. The reason is that, the harmonic sensitivity of the 2-position method is close to zero at the frequency number of 12 and random errors in the interferometer output are amplified greatly in the calculation. To avoid this problem, the 12th frequency component is extracted in the calculation. From the compared result (see the result 2 of Fig.3), we can see the residual error(the difference between the input profile and the calculated profile) is about 0.5nm. Such operation is also taken in the following calcultion.

The influence of the positioning error when rotating the test surface is also investigated by simulation. A polygon mirror and an autocollimeter are used in the experiment as positioning instrument and the positioning precision is able to be kept in 2sec. The positioning error is thus set to be 2sec and 4sec in simulation respectively. Here, random errors sre set to be null. The PV value of the residual error due to the positioning error(see Fig.4) is 0.03nm and 0.07nm respectively. From these results, we can see the influence of the positioning error is negligible.

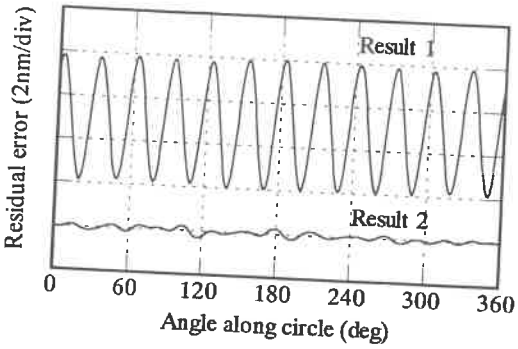

Fig.3 Influence of random error

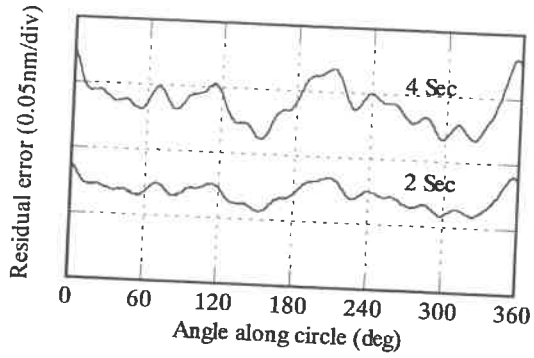

Fig.4 Influnce of positioning error

4. Experiment

The optical instrument used in experiment was ZyGo GPI-XP(see Fig.5), a Fizeau type interferometer. The spheric test optics was illuminated by the laser light from above. The stage system was used to fix the spheric test optics and rotate it along Z axis which was the same direction as the laser light. A polygon mirror and an autocollimeter were utilized jointly to guarantee the ratory precision. There were 24 mirrors in the utilized polygon mirror, and the interval of the negibouring mirrors was 15°. Thus, it is possible to calibrate angles larger than 15° with use of polygon mirror and autocollimeter jointly. In the experiment, the rotary angle was set to be $29\theta_s$ ($\theta_s=2\pi/350$) which was about 29°49'43". Since the set angle was near 30°, the polygon mirror must be rotated from the first mirror to the third mirror. The divide angular error of the polygon mirror about 3sec was compensated in the experiment.

The aperture of the spheric test optics was 100mm and the radius of curvature was 519mm. There were 28 concentric circles with the same interval to be calculated. Among these circles, the number of the outest circle was set to be the 28th. Fig.6 shows the measured profile of the outest circle (28th circle) by the 2-position method. The results of three repeated measurements are shown in Fig.8. The PV value was about 1.1μm and the repeatability error was about 6.5nm. Fig.7 shows the corresponding results of the reference surface. The PV value was about 9nm and the repeatability error was about 5nm(see Fig.9).

The calculated results of the profile in different circles are shown in Fig.10, and the corresponding results in the reference circles are shown in Fig.11. From Fig.10 and Fig.11, we can see that the PV values of the calculated profiles in the test circles decreased with the decreasement of the radius of these circles. But for the reference circles, the PV value was almost the same for all the circle. The repeatability in Fig.10 and Fig.11 changes in the range of 2nm~6.5nm.

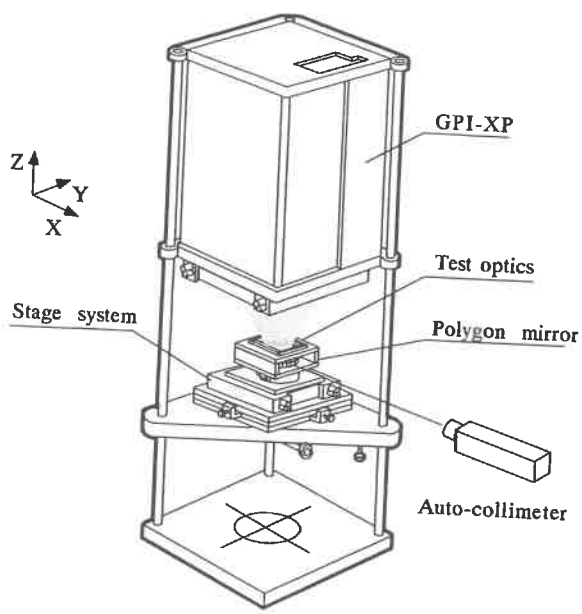

Fig.5 Measurement system

5. Conclusions

(1) The 2-position method has been applied to the measurement of spheric surfaces. The influence of random errors in sampling and the positioning error when rotating the test surface was investigated by simulation.

(2) A spheric optics has been measured by the 2-position method in a ZyGo Fizeau type interferometer. The PV value of

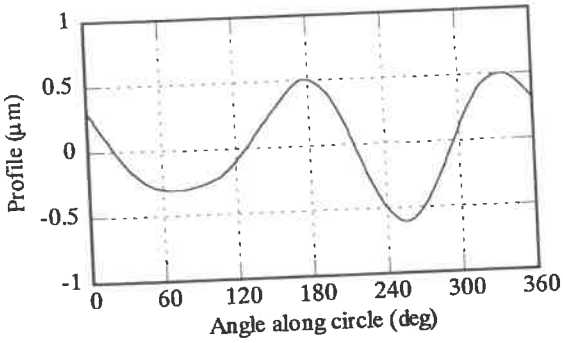

Fig.6 Measured profile of the test surface

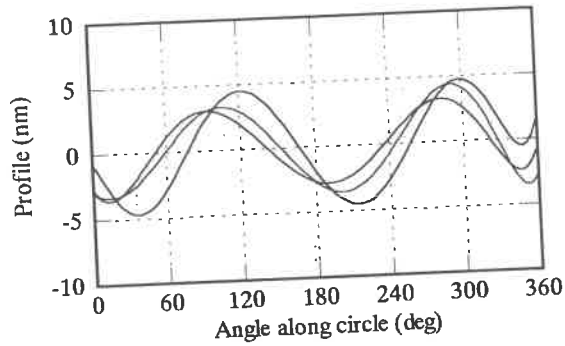

Fig.7 Measured profile of the reference surface

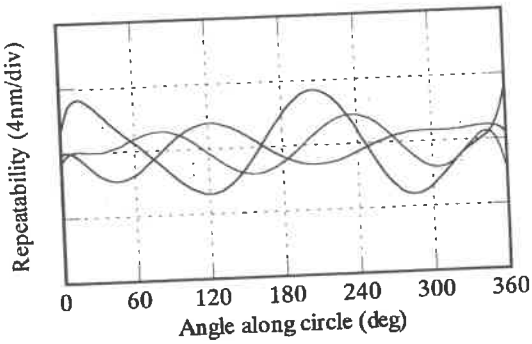

Fig.8 Repeatability error in the sample profiles

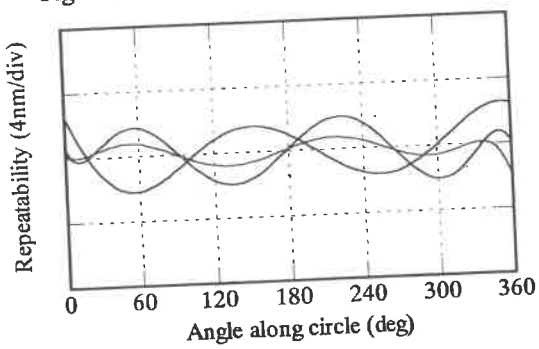

Fig.9 Repeatability error in the reference surface

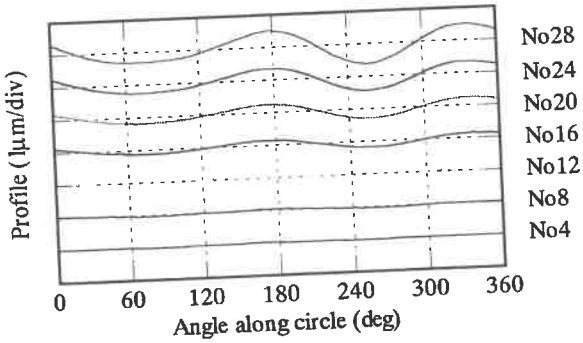

Fig.10 Test surface profiles of different circles

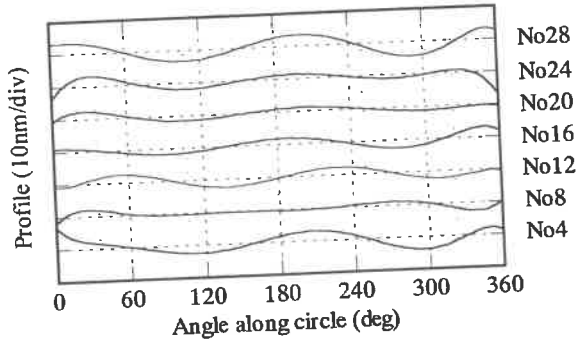

Fig.11 Reference surface profiles of different circles

the profile in the outest circle was about 1.1μm ,and the repeatability error was about 6.5nm. The form error in the reference surface was about 9nm.

References

(1) G.Shulz and J.Schweider : Precise Measurement of platness, *Appl.Opt.* 6, (1967), 1077-1084.

(2) G.Shulz, J.Schweider, C.Hiller and B.Kicker : Establishing an Optical Flatness Standard, *Appl.Opt.* 10-4, (1971), 929-934.

(3) K.E.Elssner, R.Burow, J.Grzanna and R.Spolaczyk : Absolute sphericity measurement, *Appl.Opt.* 28-21, (1989), 4649-4662.

(4) S.Itoh, T.Hinaji and O.Horiuchi : High precision flatness measurement by combining two-orientation method and radial shift method, *Proc.JSPE.* (in Japanese) 5, (1992), 883-886.

(5) H.Tanaka, H.Sato : A study on the basic characteristics of Straightness Measurement by Sequential-Two-Points Method, *J.Jpn.Soc.Pres.Eng. (Group C)* (in Japanese) 48- 436, (1982), 1930- 1935.

A method for non-contact measurement of free-form surfaces based on CMM

Xu Yuchun Zhang Guoxiong Xie Zexiao Feng Guoxin Wang Chunhai
State Key Laboratory of Precision Measuring Technology & Instruments, Tianjin University, P. R. China

Keywords: free-form surface, coordinate measuring machine, PH10 probe head, laser triangulation probe, calibration

1. Introduction

Free-form surfaces are widely used in aviation, space flight, automobile and household appliances industries. However, many mechanical parts with free-form surfaces are impossible to be presented by CAD models. Usually they are designed by digitizing a model or part, by means of a tactile or non-contact optical probe. To increase the speed of digitizing free-form surface, there has been rapid growth of interest in non-contact measurement technology in recent years. Laser triangulation probes have many advantages, so is often used for digitizing a three-dimensional model or part.

In this paper, a non-contact measuring method, based on coordinate measuring machine, PH10 probe head and laser triangulation probe, is proposed. By employing a PH10 probe head, the laser beam might keep in the direction almost normal to the surface measured. This system can measure the desired points on free-form surface automatically, and is able to measure the surfaces with large inclination.

2. Non-contact measuring system

This measuring system is shown in Figure 1. It consists of a LB-12 laser triangulation probe, PH10 probe head and ZOO2 CMM. The LB-12 laser probe is a one-dimensional sensor that measures the distance to surface, it is mounted on the PH10 probe head. The PH10 probe head has two axes A and B, the

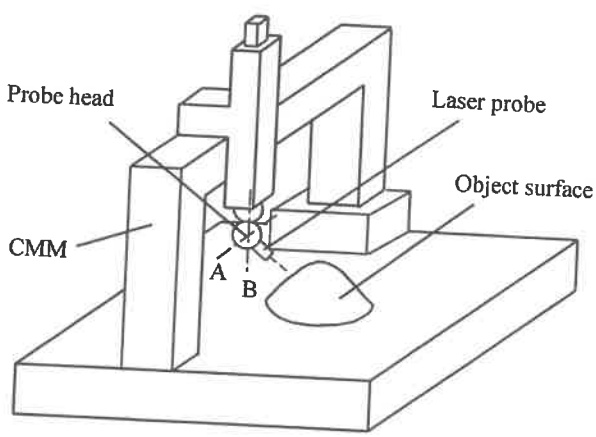

Fig.1 Non-contact measuring system

angular range of PH10 about A axis is 0 ~ 105 degrees, the range about B axis is –180 ~ 180 degrees, and the angular interval about both axes is 15 degrees. Whether or not to change the laser beam direction is determined based on the angle between the normal of surface and direction of present laser beam. The PH10 probe head is mounted on Z axis of the ZOO2 CMM. The scanning process for free-form surface is realized by the CMM.

3. Principle of measurement

Within the measuring volume of the CMM, the positional information of sampled point is obtained by integrating the reading encoders of the CMM and that of the laser probe. To find the geometric translation function and calculate the three-dimensional data points, a geometric model is established and shown in Figure 2. It involves five frames: (1) global reference frame $o_0x_0y_0z_0$ of the CMM, (2) Motion frame $o_1x_1y_1z_1$ of the CMM, (3) Original frame $o_2x_2y_2z_2$ of the PH10 probe head, (4) Work frame $o_3x_3y_3z_3$ of the PH10 probe head, (5) Frame o_4t of the LB-12 laser probe.

By using the established geometric model, the three-dimensional data points can be calculated.

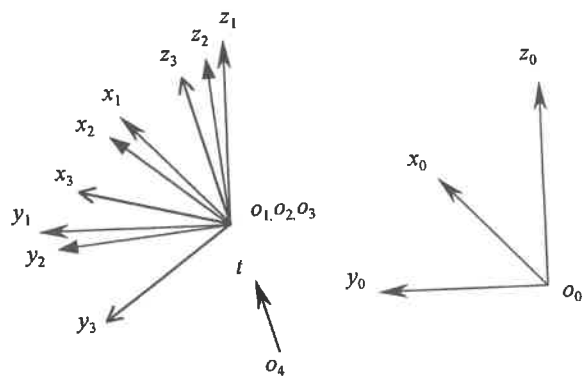

Figure2 Frames for non-contact measuring system

4. Calibration of the system

Calibration of the system can be implemented by measuring a fixed known or unknown point. Usually, the position of the fixed point is unknown, so the calibration can be performed by measuring a fixed point four times. There is a problem how to ensure the same fixed point is measured four times. To satisfy this requirement, a reference ball is used and the calibration of the system is implemented.

5. Measurement of a free-form surface

An experiment for measuring a gesso free-form surface is performed using above

developed system. The sampling points are distributed uniformly at horizontal plane with different altitudes. The conditions and results are given.

6. Conclusion

A non-contact measuring method is proposed and the system is developed. It consists of a LB-12 laser triangulation probe, a PH10 probe head and a CMM. During measuring a free-form surface, the laser beam direction can be changed by PH10 to keep it normal to surface. It enables the system to measure the surfaces with steep inclination.

7. Acknowledgement

The financial support from 863 High Technology Development Committee of China (No. 863-511-942-024) is gratefully acknowledged.

References

(1) C. Bradley and G. W. Vickers. Automated Rapid Prototyping Utilizing Laser Scanning and Free-Form Machining. Annals of the CIRP, Vol. 41/1, 1992: 437-440

(2) K. Saito and T. Miyoshi. Noncontact 3-D Digitizing and Machining System for Free-Form Surface. Annals of the CIRP, Vol. 40/1, 1991: 483-486

(3) Shao ZhiYong, Lu Jiechi, Lai Kangsheng, Wang Xiaoming and Yu Shuiran. Research on laser digitizing collecting system of 3-D surface. Journal of Dalian University of Technology 37/3, 1997: 301-305

(4) Theodoracators V. E. and Ranganath R. K. 1991, An automated and interactive approach for fitting B-spline surfaces through 3D planar visual data, ASME Computer in Engineering, 2: 23-31

In-process roundness measurement system for cylindrical machine parts of small diameter with run-out error compensation

Ryuichi YAMADA*, Takanori TAKEI** , Kazuhisa YANAGI **
*Nagaoka National College of Technology, Department of Mechanical Engineering, Nishikatakai 888, Nagaoka, 940-8532, Japan
** Nagaoka University of Technology, School of Mechanical Engineering, Kamitomioka 1603-1, Nagaoka, 940-2188, Japan

Introduction

A number of cylindrical machine parts of small diameter are widely used in the information storage devices and information processing instruments. The functional performances of such devices can be attributed to the overall accuracy of those mechanical components. It has been demanded that the diameter error and out-of-roundness of the cylindrical machine parts are small enough from a practical point of view. Quality control technology in the production line is an issue to meet the requirement. Not only the geometrical accuracy of the products but also the mechanical accuracy of the machine tools are important. An objective of our study is to develop an in-process measurement system which can evaluate both the roundness of turned cylinder and the rotational error of lathe spindle. Cylinders to be measured are smaller than 2 mm in diameter and the target measurement accuracy of the system is the range of sub-micrometer.

Measurement principle

The measuring instrument of the developing system consists of three optical sensing units. Each unit has a parallel light beam and twin photo diodes to detect the asymmetrical beam power distribution. The parallel light beam is produced using a super luminescent diode (SLD) and a collimator lens. A cylindrically turned work is set within the crossing of the three light beams, where two of them are orthogonal. The work displacement perpendicular to each beam axis can be detected from the difference signal of the related twin photo diodes. Then the run-out locus of the work can be drawn as a Lisajous figure using the two orthogonal sensing units. As to the roundness measurement of the work itself, so-called V-block method was adopted. The two sensing units may be regarded as an optical virtual V-block and the remaining sensing unit as a tangential type displacement sensor. Following the measuring principle of the V-block method, the roundness profile can be evaluated by knowing a series of correction factors for the corresponding numbers of undulation per revolution. A practical design procedure for the optical and mechanical configuration was shown in Fig.1

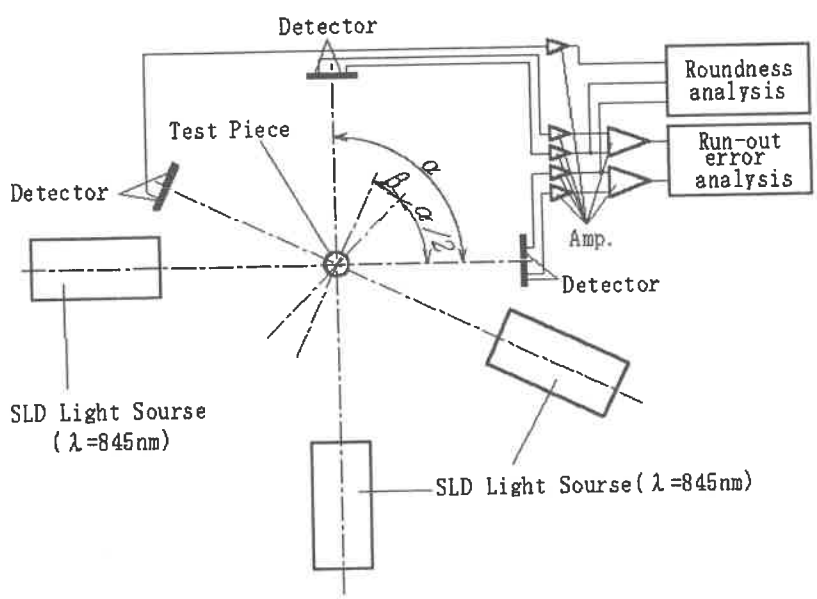

Fig.1 Schematic of measurement system

Effect of setting angle of the optical axes on the fluctuation of the correction factors

In roundness measurement by the V-Block method, the correction factor μ depends on the number of undulation per revolution of measured signal. When the value of μ is small, the signal of its undulation per revolution is reduced, and the measurement becomes difficult. Then, the effect of the measurement noise becomes easy to be received. The correction factor is expressed by the equation (1).

$$\mu_{n,\alpha,\beta} = \sqrt{\left(1+l_{n,\alpha,\beta}\right)^2 - f_{n,\alpha,\beta}{}^2} \qquad (1)$$

where

$$l_{n,\alpha,\beta} = \left[\frac{\cos\beta\cos\left(n\frac{\pi+\alpha}{2}\right)}{\sin\left(\frac{\alpha}{2}\right)}\right]\cos n\beta - \left[\frac{\sin\beta\sin\left(n\frac{\pi+\alpha}{2}\right)}{\cos\left(\frac{\alpha}{2}\right)}\right]\sin n\beta$$

$$f_{n,\alpha,\beta} = \left[\frac{\cos\beta\cos\left(n\frac{\pi+\alpha}{2}\right)}{\sin\left(\frac{\alpha}{2}\right)}\right]\sin n\beta - \left[\frac{\sin\beta\sin\left(n\frac{\pi+\alpha}{2}\right)}{\cos\left(\frac{\alpha}{2}\right)}\right]\cos n\beta$$

In equation (1), α is the angle which forms V- Block, and β is a tilting angle of displacement sensor in making bisector of α to be base line. α and β are shown in Fig.1.

In this study, α was fixed at 90°, because run-out error and roundness profile are measured simultaneously. After the decision of α value, adequate β was examined. Concretely, β at which a series of correction factors became over 0.5 was searched under the condition that the numbers of undulation per revolution were from 2 within 20. As a result, it satisfied this condition that the absolute values of β are 3.7° ~7.3°. For 3.7° ≤β≤7.3°, a series of correction factors for the numbers of undulation per revolution was calculated. The results are shown in Fig. 2 and Fig.3. The 19th undulation per revolution has the biggest fluctuation of a series of correction factors. However, the deviation of the value of μ is about 0.15 and small enough when the value of β is deviated by 0.5°.

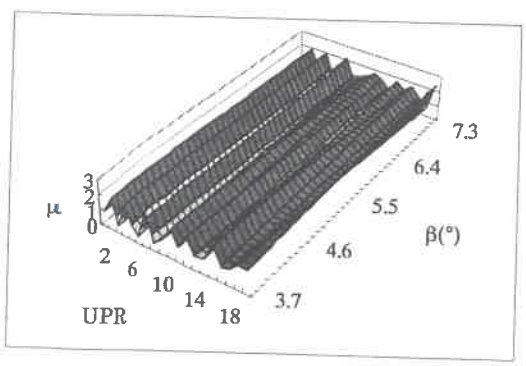

Fig.2 Correction factor

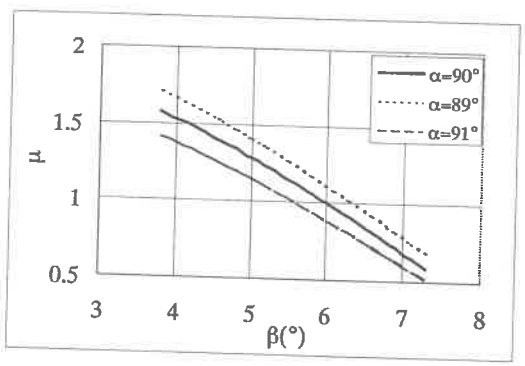

Fig.3 Correction factor (UPR19)

Selection of the light source

It is supposed that this measuring instrument measures cylindrical parts of 2mm diameter or less. Therefore, light source of the good blocking-off property was necessary when a pin gage was inserted on the cross section of light beam.

SLD was selected as a light emitting device which is able to satisfy above –mentioned property. SLD generates the stimulated emission light similarly to LD (Laser diode) and possesses fairly good wavelength-selectivity. However, it is an incoherent light source because there is no resonator. It has medium luminescent characteristics between LED and LD.

The intensity distribution along a normal line passing through the optical axis was measured for SLD

and LED. (The distance from the devices was 35 mm.) From the experimental results shown in Fig.4, we can see that SLD gives the maximum intensity near the optical axis and high frequency components with small amplitude are superimposed. For the case of LED, the intensity distribution is almost flat. When a pin gage was inserted on the cross section of light beam, the blocking-off property of SLD seems to be much better than LED as shown in Fig.5. It is obvious that SLD is suitable for the measurement of pin gage displacement in the horizontal direction, if the output signal and the displacement are practically linear to each other.

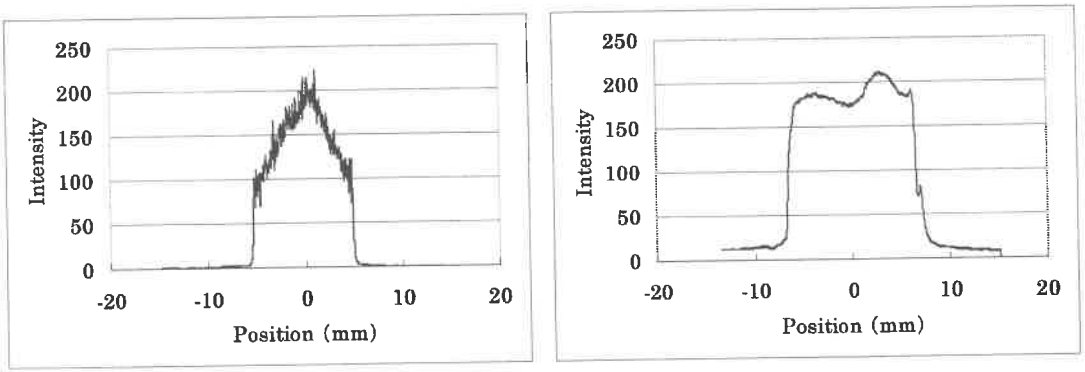

(a) SLD (b) LED

Fig.4 Intensity of light beam

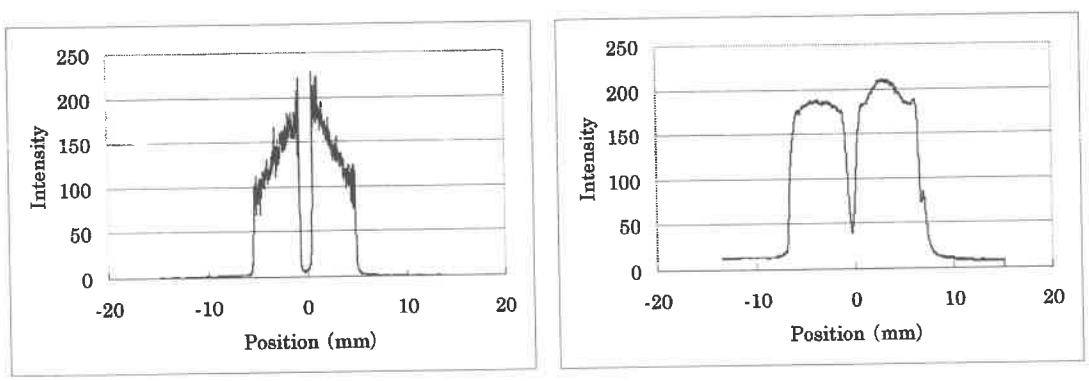

(a) SLD (b) LED

Fig.5 Intensity of light beam cut off by pin gage of the 1mm diameter

Modulation of the light source

To avoid the interference of the three light sources to each other, the lock-in measurement technique was adopted. First, the signal to be detected is distinguished from the noise by giving a modulation. Then, by synchronizing the modulated signal to the reference signal, the noise can be removed, and only desired frequency component is functionally taken out.

The electronic circuit structure for this measurement is shown in Fig.6. Function generator (MAX038) makes the square wave signal arise. This signal is used for the modulation of the light source and also as the reference signal of the phase detector (CD-505R2). First, the phase detector amplifies modulated signal, and it does the BPF processing. The BPF processing removes odd number harmonics by the square wave modulation. After the synchronization by the phase sensitive detector (PSD), the desired displacement signal can be obtained through a low pass filter (LPF).

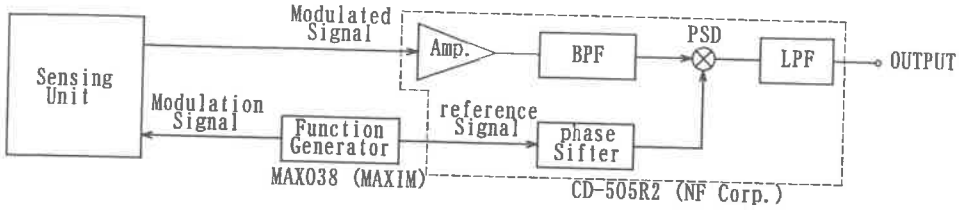

Fig.6 Block diagram of rock-in Amplifier and Sensing unit

Measurement result

Since the modulation limit of SLD light source is 10kHz, the modulation frequencies of 5,7 and 9kHz were adopted for the three beams. These can be no interference among the higher harmonics. The output signals of twin photo diode against pin gage position (1mm in diameter) are shown in Fig. 7 respectively corresponding to three modulation frequencies. The distance between the pin gage and the twin photo diodes to detect was 15mm, and that between the pin gage and SLD was 20mm. The three cases in Fig.7 show good linearity between the output signal and the pin gage position. Therefore, the run-out error can be measured from the difference signal of two twin photo diodes which are set orthogonal, and the roundness profile can be obtained by harmonic analysis of the output signal from the corresponding diode.

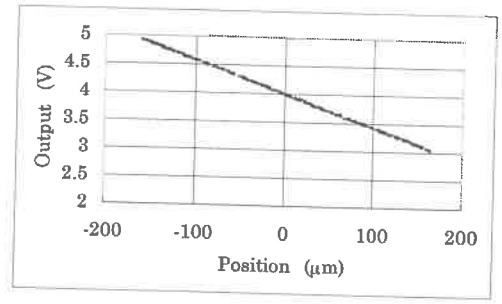

(a) 5kHz

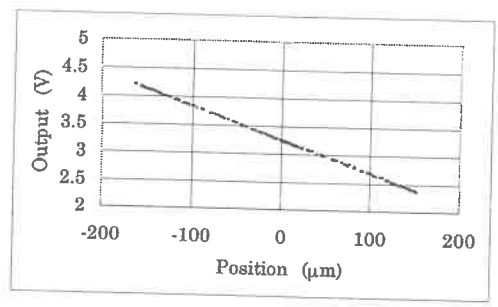

(b) 7kHz

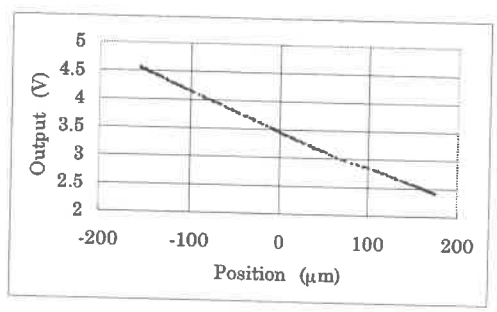

(c) 9kHz

Fig.7 Output signal against pin gage position

Conclusions

(1) An in-process roundness measurement system for cylindrical machine parts of small diameter with run-out error compensation was proposed.

(2) The adequate arrangements of the sensing units were found out theoretically for the measurement of roundness profile and run-out error simultaneously.

(3) The blocking-off property of SLD by a pin gage is much better than LED, and so SLD is suitable for the in-process roundness measurement.

(4) The lock-in measurement technique was utilized so that the three light sources might not functionally interfere to each other.

Reference

1) R.Yamada,K.Yanagi and C.W.Lee, "Optical Evaluation Method for Run-out Error of High Precision Spindle by Separating Rotation Error with Tool Chucking Error",Journal of The JSPE,Vol.64, No.12, 1785-1790 (1998).

2) A.Yokota,R.Yamada,K.Yanagi and M.Sakai, "Development of Roundness Measurement System by Optical V-block Method (1st Report) ",Journal of The JSPE,Vol.65,No.11, 1663-1667(1999).

AUTOMATIC MEASUREMENT OF LARGE SURFACE PLANENESS

Zhang Jingcai Lei Tianjue Chen Yuexiang

Academy of Machinery Science & Technology

Beijing 100044, P.R.China

1 INTRUDUCTION

Gradienter planeness measurement method is one in common used method. It uses horizontal as the measurement datum plane. The bridge-board with a Gradienter go along with some definite lines step by step. With the measurement date of the Gradienter, the relative height of the two points that the bridge-board standing on can be calculated. Processing the dates we can get the planeness error. Due to the size of the Gradienter is small it is portable. At same time it is easy to operate. So it is popular in manufactory, especially in the production plant. But, this method has some weaknesses: 1) This method is difficult to measure the discontinuous surface. Because the bridge board must move along with the definite lines, so if there some holes or slots on the lines the measurement will can't be made. 2) It is not automatic, so the measurement time is long and the accuracy of measurement result related with the operators.

In this paper we improve the Gradienter planeness measurement method by using modern technologies. The method is much modified by the mechanical and electronic control technology, grating measurement technique and automatic technology. The bridge-board with the Gradienter moves automatically on the measuring surface. At each time one end stop and the other turn around it. Through the step motors we can control the turning angle, so we can record the positions of the bridge. The bridge moves freely and needless measuring along the definite lines. All measuring dates are transformed into one coordinate by Homogeneous Matrix. Processing these dates the planeness error of the surface can be got. In this way we can measure the discontinuous surface and eliminate the measurement error made by manual operation.

2 MEASUREMENT PRINCIPLE

2.1 Homogeneous Matrix

There are two coordinates O and S (Fig 1), The position of S in coordinate O is (a,b,c). $\bar{n}, \bar{o}, \bar{a}$ are unit vectors of coordinate S. Matrix A is named as Homogeneous Matrix.

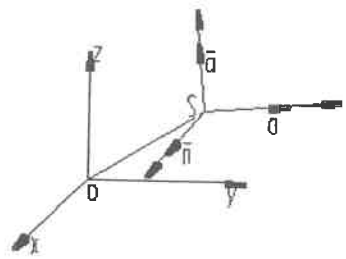

Fig 1 Coordinate transform

$$A=\begin{bmatrix} n_x & o_x & a_x & a \\ n_y & o_y & a_y & b \\ n_z & o_z & a_z & c \\ 0 & 0 & 0 & 1 \end{bmatrix} \tag{1}$$

It can express both the rotation and transiation of the coordinate. Following are the expressions for the rotations around Axis X, Y, Z and the transition of a coordinate:

$$R(x,\theta)=\begin{bmatrix} 1 & 0 & 0 & 0 \\ 0 & \cos\theta & -\sin\theta & 0 \\ 0 & \sin\theta & \cos\theta & 0 \\ 0 & 0 & 0 & 1 \end{bmatrix} \tag{2}$$

$$R(y,\theta)=\begin{bmatrix} \cos\theta & 0 & \sin\theta & 0 \\ 0 & 1 & 0 & 0 \\ -\sin\theta & 0 & \cos\theta & 0 \\ 0 & 0 & 0 & 1 \end{bmatrix} \tag{3}$$

$$R(z,\theta)=\begin{bmatrix} \cos\theta & -\sin\theta & 0 & 0 \\ \sin\theta & \cos\theta & 0 & 0 \\ 0 & 0 & 1 & 0 \\ 0 & 0 & 0 & 1 \end{bmatrix} \tag{4}$$

$$T(a,b,c)=\begin{bmatrix} 1 & 0 & 0 & a \\ 0 & 1 & 0 & b \\ 0 & 0 & 1 & c \\ 0 & 0 & 0 & 1 \end{bmatrix} \tag{5}$$

2.2 Transformation of measurement coordinate

The measurement bridge-board can move on the measuring surface like this: one end of it

stand and the other one go around it and the stand end is by turns. This movement can be expressed by the transformation of coordinate (Fig 2). So the positions of measurement points can be expressed in one original coordinate with the Homogeneous Matrix. After n times turns, the position of the n+1 measurement point can be get from equation (6).

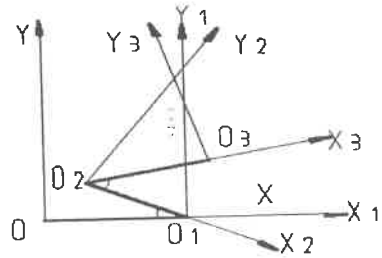

Fig 2 Coordinate transform of measurement bridge-board

$$\begin{bmatrix} x_{n+1} \\ y_{n+1} \\ z_{n+1} \\ 1 \end{bmatrix} = T(L,0,0)\cdot R(z,\theta_1)\cdot T(-L,0,0)\cdot R(z,\theta_2)\cdot T(L,0,0).....R(z,\theta_n)T((-1)^n L,0,0)\begin{bmatrix} 0 \\ 0 \\ 0 \\ 1 \end{bmatrix} \quad (6)$$

In the equation:

n=0,1,2...;

θ_n is the turn angle of the measurement bridge-board;

L is the length of the bridge-board.

The value of the error of every measuring point can be calculated as following:

$$z_0 = 0$$

$$z_n = \sum_{i=1}^{n-1} \cdot z_i + L \cdot \alpha_n \quad (7)$$

α_n is the value of the Gradienter at every measurement position.

We get the position coordinates and the error values of the measuring points. Process them we can get the planeness error of the measuring surface.

3 EXPERIMENT EQUIPMENT

Fig 3 is the experiment system diagram. An electronic Gradienter is on the measurement bridge-board. Under the bridge-board there are two supports. At the end of the supports there are two balls. Around each support there is an electromagnetism clutch. Between the support and the clutch there is a ball bearing. Next each support is a wheel which can move a little vertically. A motor connects with each wheel. A single piece computer is under the central of

the bridge-board.

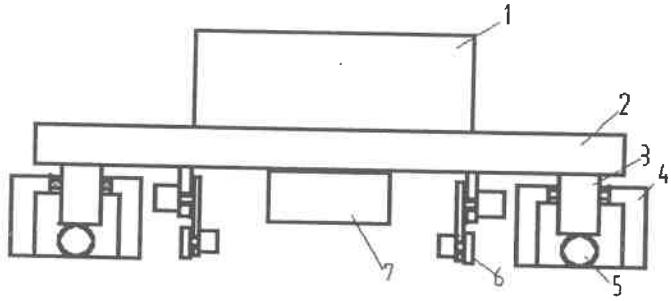

Fig 3 .Experiment equipment diagram

1. Gradienter 2 Bridge-board 3.Support 4 electromagnetism clutch 5.ball 6.Wheel 7. single piece computer

The measuring procedure is: Put the equipment on the surface for measuring. Two support balls support the bridge. Turn on the electromagnetism clutchs. The computer remembers the first value of the Gradieter. Turn off one electromagnetism clutch and the other one is still turned on. So the support at this end is fixed. Turn on the motor at this end. Drive the wheel and the bridge turn around. Turn off the motor and the bridge stops at the second position. The computer remembers the steps the motor has pasted for calculating the turned angle. Power on the clutch and remember the second value of the Gradieter. Go on as this we can measure the whole surface. It is easy to review the measurement because the computer has remembered the steps the motors moved at every time.

4 CONCLUSION

Applying the Homogeneous Matrix in Gradienter planeness measurement, make the method more convenient and efficient. The measuring accuracy is depended on the Gradienter. Using the angle meter of large scale, this method can also be applied on measuring the form of large crooked plane.

REFERENCE

1. M. Murray and Z. Li, A Mathematical Introduction to Robotic Manipulation, CRC Press, 1994.

2. N. Z. Liao and L. Qin, Planeness error measurement for mirror flat of water turbogenerator. Journal of Astronautic Metrology and Measurement, Vol.17, No.4.

A Proposed Method for the Dimensional Metrology of Non-Rigid Objects

Kenneth L Blaedel*, David W Swift, Hooman Tajbakhsh[1],
Steven R Patterson[2], and Daniel C Thompson[3]
Lawrence Livermore National Laboratory
PO Box 808 L-537, Livermore, CA

Keywords: Dimensional Metrology, FEA accuracy, Measurement uncertainty

Definition of Problem

The goal of this project is first, to understand methods of restraining or actuating non-rigid objects so that their resulting deformations are repeatable and predictable. By understanding the effect of restraints, we can specify, manufacture, measure and assemble non-rigid objects to high precision. The second goal is to develop a methodology for designing restraints or actuators so as to produce a specified deformation on the surface of a non-rigid object to high precision. Such a methodology allows us to design a non-rigid object for manufacture under one set of conditions, but for use under a different set. The first goal, while appearing to be a straightforward structural analysis problem, is subject to many sources of error that must be reduced in order to apply the analysis with high confidence. The second goal falls under the domain of design, for which the engineering tools are much less developed when compared to tools for analysis.

Some applications, such as fixturing components to be machined or mounting optical components in an assembly, seek to minimize the effect of the restraints on the deformation of the object. Much of our effort in restraining these objects treats the objects as rigid bodies and has resulted in well-disciplined expertise that is cultured throughout the precision engineering community[i]. In addition, methods of specifying and assembling rigid bodies are also addressed as specific disciplines within the precision engineering community. For example, the measured dimension of a rigid component is traceable at a specified level of confidence to a single source (e.g., NIST in the USA). Hence the independent measurement of one component of an assembly can be related to the measurement of the other components of that assembly. There is no generalized analog to this pedigreed process for dimensionally characterizing non-rigid bodies. This problem is often overcome for specific manufacturing problems by constructing rigid fixtures that over-constrain the non-rigid parts to be assembled and then performing the dimensional measurement of the contour of each component to check whether each meets the geometric specification given in a drawing. Note that, because the measurement confounds the shape of the part and the effect of the fixture, such inspection measurements will yield only an approximation to the assembled shape, which is a function of both the geometry and the relative compliance of the component parts of the assembly. As a result, non-rigid components are more difficult to specify and inspect and therefore are more difficult to purchase from outside vendors compared to rigid components. The problems are compounded as the requirements come to include higher and higher precision.

In contrast to the fixturing applications mentioned above, which attempt to minimize their effect on the deformation of the object, other applications, such as attaching actuators to deformable optics, seek to change the deformation in a precisely prescribed fashion. Understanding and modeling the effects of the attachments are common to both applications. But the second class of application goes beyond the first in that, given a prescription for a desired deformation, there may be no effective collection of actuators that will fulfill the prescription or there may be many such collections. The problem is to define candidate solutions and to choose the best one to implement. A design methodology is needed to help make the decisions when choosing what type of actuation is required (e.g., force, moment, pressure, surface traction), where to locate the actuators, and how

* E-mail address of corresponding author: blaedel@llnl.gov
[1] Currently at Etec Systems, Inc., Hayward, CA
[2] Center for Precision Metrology, University of North Carolina - Charlotte
[3] Production Technology Inc., Hanover, New Hampshire

few to include in order to achieve a given level of precision.

In summary, the problem that is addressed here is how to deal with non-rigid objects in a high-precision environment. That a body deforms does not in itself preclude high precision. This project seeks to develop a methodology to specify, manufacture, measure and assemble non-rigid objects to a level of precision that is beyond current capability. It will accomplish this by assessing the precision with which we can predict a deformation. It further seeks to provide methods to design constraints for non-rigid objects that effect a prescribed deformation to a high precision. It is interesting to note that while evolving tools such as improved finite element analyses and new methods of dimensional measurement will assist us in advancing our understanding of how to predict and control deformation, nothing has particularly prevented advancements in the past. Rather, the demand for higher precision has created the need to understand how to better constrain non-rigid bodies.

Technical Approach

A new method is proposed here for specifying and accepting non-rigid components, and which leads to a new ability to simulate their assembly to high precision. As shown in Fig. 1, the method begins with a measurement of the non-rigid part as it is exactly constrained under well-defined conditions and, in contrast to current convention, is not measured in an unknown, over-constrained condition. The deformation imposed by the well-defined constraints can then be removed by simulation to predict the "free-state" shape of the part as though it were free from external forces and constraints.

The free-state condition, which is not physically realizable, is then used to decide on the acceptability of the component. As shown in Fig. 2, the acceptability of the part now concerns not just how closely the geometry of the part is to the specified shape, but could include other metrics such as the magnitude of the energy required to force the free-state part into the specified shape. In essence, the part is measured and then compared to specification through the use of a "virtual" fixture embodied in software rather than being measured and then compared to a specification through the use of a hardware fixture.

This method is further used to estimate the shape of a component part as it is incorporated into an assembly of non-rigid components. As shown in Fig. 3, two such components can be assembled to each other by simulation because both the geometry and the compliance of the components are known and available to the simulation.

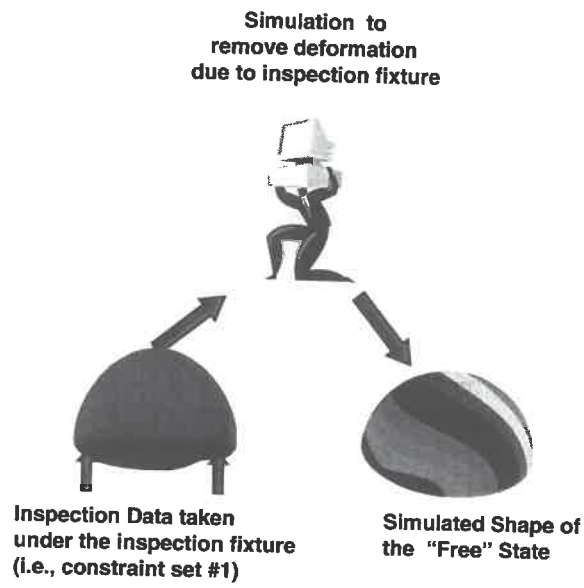

Figure 1: The shape of a non-rigid part that is free from external forces and constraints is simulated from a measurement of its constrained shape

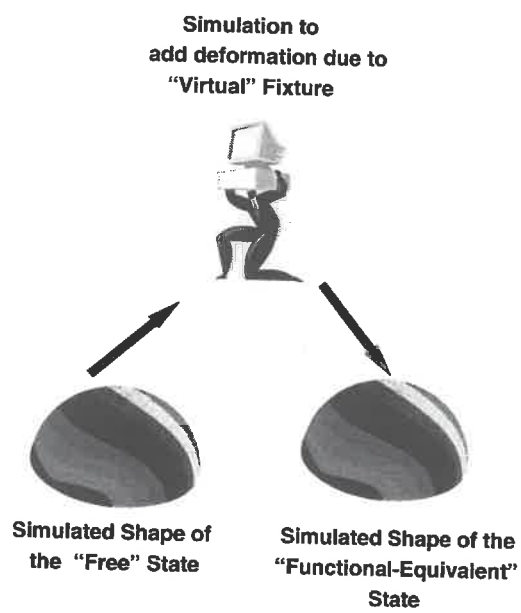

Figure 2: New measures of goodness, which are embodied as virtual fixtures in software, are used for the purpose of acceptance testing

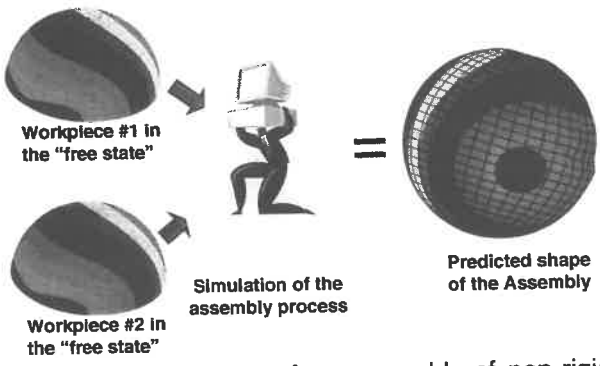

Figure 3: The shape of an assembly of non-rigid objects can be modeled from the free state shapes of the components

Error Budget

This project incorporates three major activities. First is an analysis activity to assess how well one can determine static deformation of a non-rigid body as a consequence of external forces and boundary conditions. While this solution should be easily calculable from the methods of either Finite Element Analysis or specific analytic solutions, predicting the accuracy of the calculated solution requires further work. What is needed is first a statement of uncertainty to accompany the calculated deformation and second to drive the uncertainty down. Hence, this phase largely constitutes a sensitivity analysis of deformation caused by constraints, which will then indicate where the largest error contributors lie. An outcome of this activity will be the ability to rank the goodness of classes of restraints for mounting non-rigid objects. For example, restraints that can trap frictional forces, such as conventional bolted joints, are known to be quite unpredictable and so such a class of restraints is unsuitable for the purpose of high-precision control of deformation.

The sensitivity study described above is an error budget for the uncertainty with which we can predict deformation and leads to the next activity, which is to reduce the larger error contributors. For example, a problem that often confronts us is knowing how to characterize a constraint for input into a finite element (i.e., the "contact algorithm"). As mentioned above, we may be limited to certain classes of constraints, such as frictionless constraints or perhaps we will have to measure force at the constraints in order have accurate contact algorithms. Another contributor is knowing to high precision what the material properties are. Reducing this uncertainty may require extra measurement procedures, such as measuring the deformation at different forces and then calculating a "best-fit" elastic modulus.

The third activity of this project will use experiments to corroborate the confidence levels of the analyses for the case of a thin cylinder. We will demonstrate the ability to accept measurements taken under one set of constraints and then estimate the deformation for comparison to the second set of measurements taken under the second set of constraints. Referring to the figures, we will obtain high-precision measurements of a part under two different, well-specified sets of constraints shown as the "inspection" state in Fig. 1. Next, from each of the "inspection" state measurements we will simulate the "free" state shown in Fig. 1. The degree to which the two simulated "free" state shapes agree is a measure of how well the simulations performed. Note that this method of verification is not complete in that it does not directly confirm the intermediate "free" state, which is not physically realizable.

---

[i] L C Hale, "Principles and Techniques for Designing Precision Machines," Ph.D. Thesis, MIT, Feb 1999 [also UCRL-LR-133066].

Data Filtering using Measured Surface Normals

Robert Edgeworth[2] and Robert G. Wilhelm[1]

[1]Center for Precision Metrology
Department of Mechanical Engineering and Engineering Science
The University of North Carolina at Charlotte
9201 University City Blvd., Charlotte, NC 28223-0001

[2]Intel Corporation
5000 W. Chandler Blvd.
Chandler, AZ, 85226

Invalid measurement data are phenomena that plague the reliability of Coordinate Measurement Systems. The best-fit algorithms used for feature computation all amplify the influence of the points most distant from the mean. As a result, a single invalid point can significantly skew the computed feature parameters, even for large data sets. If the feature happens to be a datum, the error propagates through the measurement of the entire part. A measurement consisting of thousands of measured points can be ruined by a single bad piece of data. It is therefore desirable that invalid data be identified and removed before feature evaluation is performed.

Three separate cases are considered. The first case is the problem of contact occurring on undesired surfaces. This type of problem can occur when measuring complex parts such as a gear hob or when using a non-spherical probe. This case is the best suited for solution through the use of surface normal data since the change in surface normal between surfaces is large and easily detected. The remaining problem, the detection of invalid data due to dirt, burrs, porosity or external factors, is divided into 2 cases. The division is made based upon the spacing of the data collected. If the spacing is large, each point can only be considered independently. If the measurement data are dense we can use the relationship between points to refine the analysis.

Complex Part Evaluation

Complex parts can be vulnerable to invalid data due to inadvertent contact with nearby surfaces that are not part of the data set. Cutting tools such as broaches or gear hobs are a particular instance of this problem. The teeth are closely spaced and each tooth is composed of a number of surfaces that need to be evaluated separately. Due to the small clearances between surfaces, it is common for a measurement that was targeting one surface to actually collect data from an adjoining surface. A small error in the rotational alignment used to collect the measurements can lead to large numbers of data points being attributed to incorrect features. A similar problem occurs when non-spherical probes are used for measurements. Figure 1 shows three types of non-spherical probes commonly used for coordinate measurement. These probes have a limited set of surfaces that are valid for metrology purposes. It is desirable to be able to recognize when data are collected from contact with invalid parts of the probe.

In both of these cases there is a large variation in surface normal values between each surface. The cutting tool example has surfaces that vary in direction by greater than 10 degrees. If the surface normal at each point is measured it is a simple matter to identify the actual contact surface for each point. The process to properly associate the measured data with each feature would be a two step process. First, the points would be separated into groups related to each tooth surface based upon the surface normal measured. Then the sets would be associated with the appropriate tooth number based upon the location of points in space.

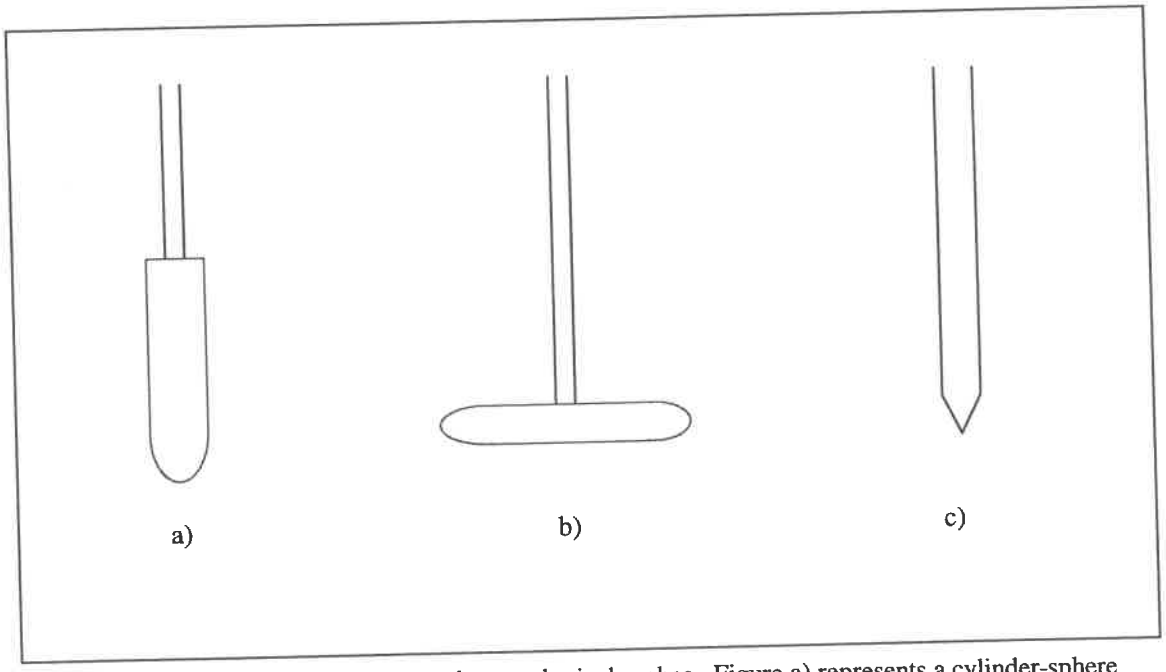

Figure 1: Profiles of commonly used non-spherical probes. Figure a) represents a cylinder-sphere probe, b) is a disk probe and c) is a point stylus

A similar approach could be applied for measurements using non-spherical probes of the type shown in Figure 1. Measurements collected using these probes can be divided into 3 categories based upon the value of the measured surface normal. The categories are valid 3D data, valid 2D data and invalid data. Consider the case of a cylinder sphere probe. The relevant categories as a function of the angle the measured surface normal makes with the axis of the probe cylinder would be:

Angle to Axis	Case
0° to 89.x°	Valid 3D data
90°	Valid 2D data
>90°	Invalid data

The transition value between 3D and 2D data would be found by subtracting the surface normal measurement repeatability from 90°.

Sparse Data Sets

With a sparse data set, it is not possible to make a comparison between adjacent points. There are still a number of invalid data conditions that can be detected by simply examining the measured surface normal of each point. Interference from burrs or incorrect surface contact, vibration triggering of the probe and large pieces of foreign material such as machining chips all produce large surface normal deviations. These kinds of probing errors can be detected and excluded by selecting a heuristic threshold value for the deviation of the surface normal from nominal. The threshold test would be applied after a surface fit is performed to remove the potential of a complete data set being flagged due to a tilt error in manufacturing. If any invalid points are detected and removed the fit would be computed a second time without the invalid

data. The size of such a threshold would vary depending upon the surface condition of the part under examination.

The objective is to select a threshold value sufficiently small to exclude invalid data but large enough to ensure a small probability of rejecting valid results. If the process accepts invalid data, the result will be a false report suggesting an out of tolerance condition. The cost of such a report at worst some lost production time while the error is investigated and, in most cases, the only cost will be the cost of a repeated inspection of the part in question. However a valid point flagged as invalid could potentially result in a false report indicated that an unacceptable part meets the design standard. The potential cost of this type of error is the production of numerous defective parts that will need to be scrapped at some future point in the manufacturing process. In the extreme, the production of defective parts could lead to the loss of a customer or insolvency of the producing company. The asymmetrical nature of this problem makes it clear that any choice of threshold value should be biased to ensure there is a negligible probability of rejecting valid data.

To select a suitable threshold value, an understanding of the magnitude of angular errors present on the surface is required. The magnitude is a function of 2 factors: the amplitude and wavelength of the surface error. Increasing the size of the surface errors results in larger angular errors. Smaller wavelengths produce larger angular errors as well. Amplitude and wavelength are not strictly independent since energy considerations tend to dictate that smaller wavelengths have relatively smaller amplitudes. However, for the purpose of selecting a threshold value, amplitude and wavelength will be considered to be independent. The result will be a slightly more conservative test value, but this satisfies the intent of biasing the threshold against rejecting valid data.

If the surface error is assumed to be a single sinusoid of wavelength L and amplitude A, the maximum angular error on the surface is:

$$\tan^{-1}\left(A\frac{2\pi}{L}\right)$$

The amplitude A should be set to ½ the largest error that can be reasonably expected from the manufacturing process for the surface in question. The wavelength parameter should be the width of the smallest deviation that is desired to be detected by the measurement process. A reasonable choice for this value would be the sample spacing. As an example using 0.050 mm for the error amplitude and 5 mm as the wavelength parameter yields an angular threshold value of 3.6°.

8.4 Dense Data Sets

In the case of dense data, the relation between adjacent points can be used to form a frequency filter to detect invalid data. Since the concern is with the exclusion of outlying points in the data set, the computational load can be reduced by only considering points that are in the outer quartiles of the total range of deviations in the set. The method works by comparing the error in the surface normal of the surface with the expected value of the second derivative of the surface based upon the assumption that the surface is locally smooth and continuous. If the surface normal error exceeds the second derivative criteria, the data point is flagged as invalid.

Consider the 3 points shown in Figure **2**, d_j is the deviation from nominal for the jth point, θ_2 is the tangent error angle found from measuring the surface normal at point 2, and s is the distance between sample points. Presuming a surface shape that approximates a sinusoid, the second derivative of the surface would be of the form:

$$\frac{\partial x^2}{\partial^2 y} = A^2\left(\frac{2\pi}{L}\right)^2 \sin\left(\frac{2\pi}{L}x\right)$$

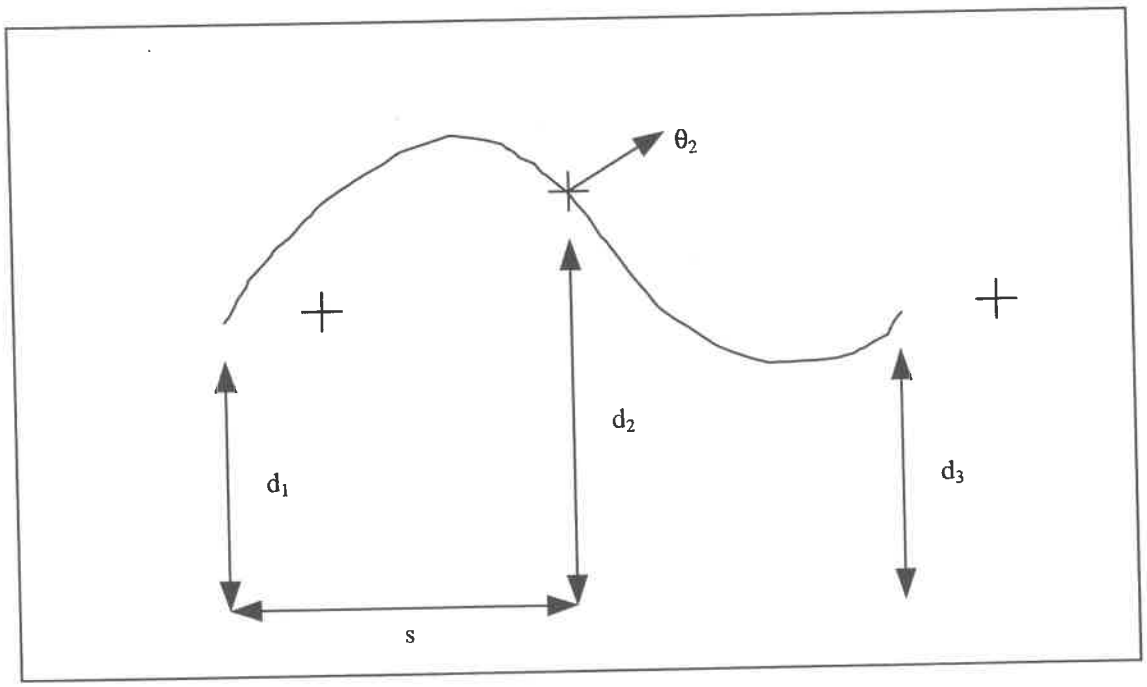

Figure 2: 3 point model for dense data sets.

To select suitable values for the amplitude of the surface A, and the wavelength, L we consider the measurement parameters. Since we have made the assumption that our data set includes the full range of deviations present on the part it is safe to set the value of A to be the range of deviations present in the set of three points under consideration. The wavelength parameter is set to be the distance across the group of points, $2s$. When s is particularly small, L may be set to be either of the minimum feature size based upon mechanical filtering of the probe sphere or a minimum wavelength cutoff specified by the user. Using this model, the maximum second derivative we would expect to encounter on a smooth continuous surface would be:

$$\frac{\partial x^2}{\partial^2 y} = (Range[d_1, d_2, d_3])^2 \left(\frac{2\pi}{2s}\right)^2$$

If the value of ε calculated above exceeds this test criteria, we can conclude that the point in question is not representative of a smooth, continuous, surface and should be excluded from the data set.

Acknowledgements:

This work has benefited greatly from the exceptional research environment provided by the Center for Precision Metrology at UNC Charlotte and the Cameron Center for Applied Research. This material is based upon work supported by the National Science Foundation, the UNC Charlotte Center for Precision Metrology Research Affiliates and the National Science and Engineering Research Council of Canada.

References:

Salsbury, J. G., "Uncertainty of the Coordinate Measurement Process Due to Unwanted Asperities", Proceedings of the ASPE, 1996, 15, 664-667.
Edgeworth R. and Wilhelm R.G., "Applications of Surface Normal Measurements to Coordinate Metrology", in Proceedings of the American Society for Precision Engineering, 1997, 16, 90-93.

Plate Calibration Methods for Two-Dimensional Stages

Jiyou Fu[1] G. X. Zhang[2] Robert Hocken[1]
[1]University of North Carolina at Charlotte, Charlotte, NC 28223
[2]Tianjin University, Tianjin 30072, China

Abstract: Plate self-calibration methods become good candidates for improving the position accuracy of two-dimensional stages. In this paper, the basic principles and the classification of plate calibration methods are introduced. Then, the assumptions of Stanford method and the reversal plate calibration method are discussed. Finally, the criteria for selecting plate self-calibration method are suggested.

Key words: plate calibration, self-calibration, metrology, two-dimensional stage calibration

1. Introduction

As the dimensions of micro-lithography features shrink, the need for improving the position accuracy of two-dimensional stages grows. Conducting a stage calibration and obtaining a two-dimensional position error map have become a crucial step to ensure the position accuracy of the stages. Since most two-dimensional stages also are two-dimensional metrology systems, the error map of the stage can be revealed by measuring the mark locations on a calibrated plate.

The most popular plate is the glass plate with evenly distributed cross chromium marks (Fig.1), as it is easy to write a program with X and Y loops to inspect all marks automatically. The position of each mark can be found at the intersection formed by one horizontal middle line and one vertical middle line. The distance between any neighboring marks is called an interval Δ, and often the intervals along both X and Y directions are the same.

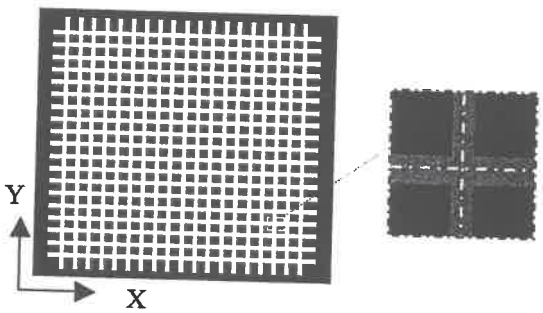

Fig.1 Grid plate and a focused mark

Depending on whether the plate is calibrated or un-calibrated, plate calibration methods can be classified as a non-self-calibration or a self-calibration method. However, it is not always possible to find an instrument sufficiently accurate to calibrate a plate as the accuracy of the intended machine increases. Thus, the self-calibration method, which utilizes an un-calibrated plate to obtain the stage's error map, becomes a good approach [1].

2. Principles of Plate Self-Calibration Methods

In the plate calibration, the position and orientation of the plate relative to the stage is usually called a "view". Many views have been designed and some of them are shown in Figure 2, where XOY and $X_pO_pY_p$ are the stage coordinate system and the plate coordinate system, respectively. In the first view (Fig.2.a), which is called "view 0" or "home view" and is represented by "H", the plate is aligned with the guide ways of the stage such that the angle between the X-axis of the plate and X guide way of the stage is nominally zero. The other views are obtained by rotating or translating the plate with respective to view 0. To facilitate the description of the views, we use letter "R" and "T" to denote "rotation" and "translation" motions respectively. For example, the rotation view (Fig.2.b) is represented by $R_z(-90°)$, where a plate is counter-clockwise rotated 90° around Z-axis; the translation view (Fig.2.c) is represented by $T_x(+m)$, where a plate is translated *m* intervals in the X-axis; the combined view (Fig2.d) is represented by $R_y(+180°)T_y(+1)T_x(+1)$, where a plate is clockwise rotated 180° around Y-axis and then followed by one interval translation along both X and Y axes.

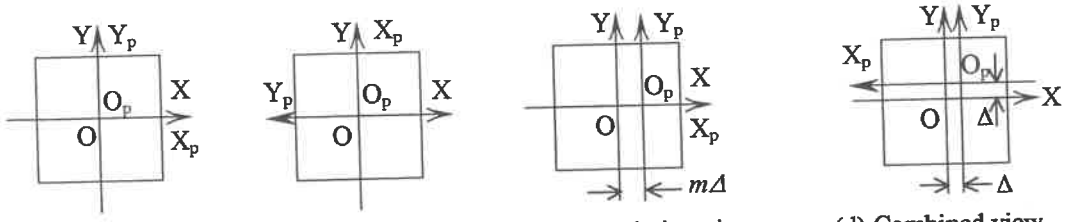

(a) Home view H (b) Rotation view $R_z(-90°)$ (c) Translation view $T_x(+m)$ (d) Combined view $R_y(+180°)T_y(+1)T_x(+1)$

Fig. 2 Various views

Self-calibration methods [2] are based on the properties of the invariant point sets and geometrical symmetries, which are held in different views. Suppose we have a plate with $N \times N$ lattice points (Fig.3), the total number of unknown position errors for the plate is $2N^2$, which includes N^2 unknown X position errors and N^2 unknown Y position errors. There are also $2N^2$ unknown stage errors. At each view, $2N^2$ equations can be obtained while three unknown alignment errors are introduced: two translation errors ΔO_x and ΔO_y and one angular error θ. Since the machine readings at the lattice points are defined as the sums of the position errors of the stage points and the plate marks, the equations for view 0 are:

$$V_{0x}(x_i, y_j) = M_x(x_i, y_j) + P_x(x_i, y_j) - y_j\theta_0 + \Delta O_{0x} \quad (1)$$

$$V_{0y}(x_i, y_j) = M_y(x_i, y_j) + P_y(x_i, y_j) + x_i\theta_0 + \Delta O_{0y} \quad (2)$$

where (M_x, M_y) and (P_x, P_y) are the position errors of the machine and the plate at point (x_i, y_j) respectively; $V_{0x}(x_i, y_j)$ and $V_{0y}(x_i, y_j)$ are the machine x and y readings at point (x_i, y_j) respectively; θ_0, ΔO_{0x} and ΔO_{0y} are the alignment errors; and $i, j = 0, 1 \ldots N\text{-}1$, usually $N > 10$. Notice that we assume the alignment angular error is very small such that $\sin\theta \approx \theta$ and $\cos\theta \approx 1$.

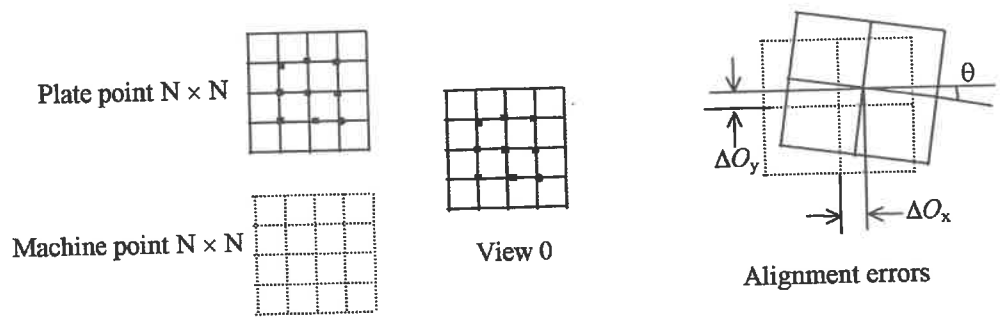

Fig. 3 View 0 and alignment errors

So, the total number of known data for one view is $2N^2$, whereas the total number of unknowns is $4N^2 + 3$. To solve the unknown position errors of both plate and stage, we need make more measurements at different views. Table 1 illustrates that at least three views are needed to make the expression $(4N^2+9 < 6N^2)$ happen as long as the machine point set and the stage point set are the invariant point sets in all views. Besides, it has been shown that at least one view must be a translation view relative to the view 0 [3].

Table 1 The relation between the view number and equation number

View number	Unknown number	Equation Number
1	$4N^2 + 3$	$2N^2$
2	$4N^2 + 6$	$4N^2$
3	$4N^2 + 9$	$6N^2$

3. Two Types of Plate Self-Calibration Methods

Since it is not easy to solve the non-linear $6N^2$ equations for the $(4N^2+9)$ unknowns, to reduce the computation requirement, properly manipulating the data set becomes necessary. There are two general

methods to model the point set of the machine, the point-to-point comparison method and the machine error method. In the plate calibration method based on the point-to-point comparison model, no relation is assumed between the errors at any two points on the machine. A successful example of this is the stage calibration method presented by Stanford University [4]. In the plate calibration method based on the machine-error model, the position errors of all points on the machine can be fitted into the homogenous transformation error matrix model [5]. The reversal plate calibration method [6] falls into this category.

Our computer simulation results have shown that both methods could give exact stage error map if there was no random error. But, these algorithms can not work correctly unless the stage errors or the plate errors meet their assumptions.

3.1 Stanford Method

In Stanford method, three views are used: H, $R_z(-90°)$ and $T_x(+1)$. A linear computation algorithm is designed to calculate the stage error map and the plate error map. The scale can be determined by matching any length standard after obtaining the stage error map. The assumptions include:

1) No x and y translations exist on the plate point set and stage point set. The translation is defined as the sum of the position errors on the whole point set. They can be expressed as:

$$\sum_{j=-(N-1)/2}^{(N-1)/2}\sum_{i=-(N-1)/2}^{(N-1)/2} M_x(x_i,y_j) = \sum_{j=-(N-1)/2}^{(N-1)/2}\sum_{i=-(N-1)/2}^{(N-1)/2} M_y(x_i,y_j) = 0 \tag{3}$$

$$\sum_{j=-(N-1)/2}^{(N-1)/2}\sum_{i=-(N-1)/2}^{(N-1)/2} P_x(x_i,y_j) = \sum_{j=-(N-1)/2}^{(N-1)/2}\sum_{i=-(N-1)/2}^{(N-1)/2} P_y(x_i,y_j) = 0 \tag{4}$$

Ideally, the translation errors of the stage will be zero if we can choose a proper point on the stage as the origin. Nevertheless, the origin point may be located at any place on the stage, instead of the lattice points.

2) No rotation exists on the plate point set and the stage point set. The rotation of the point sets is defined as:

$$\frac{\sum_{j=-(N-1)/2}^{(N-1)/2}\sum_{i=-(N-1)/2}^{(N-1)/2}(M_y(x_i,y_j)\cdot x_i - M_x(x_i,y_j)\cdot y_j)}{\sum_{j=-(N-1)/2}^{(N-1)/2}\sum_{i=-(N-1)/2}^{(N-1)/2}(x_i^2+y_j^2)} = 0 \tag{5}$$

$$\frac{\sum_{j=-(N-1)/2}^{(N-1)/2}\sum_{i=-(N-1)/2}^{(N-1)/2}(P_y(x_i,y_j)\cdot x_i - P_x(x_i,y_j)\cdot y_j)}{\sum_{j=-(N-1)/2}^{(N-1)/2}\sum_{i=-(N-1)/2}^{(N-1)/2}(x_i^2+y_j^2)} = 0 \tag{6}$$

Ideally, the rotation will be zero if a proper axis orientation can be found.

Because the x and y translation and the rotation values of the stage point set can not be given by the algorithm or known before the self-calibration, it is difficult to find the origin and the axis orientation which meet the above assumptions. Thus, the stage error map obtained from Stanford method has unknown coordinate system, which might not be directly related to the machine coordinate system. However, the stage error map obtained from this method does reflect the physical stage errors, which can be compared with the stage error maps obtained from other methods by the translation and rotation operations.

3.2 Reversal Plate Calibration Method

In the reversal plate calibration, three views are used: H, $R_z(-90°)$ and $R_y(180°)$. Besides, one of the scale errors, for example, x scale error, must be calibrated. A linear algorithm is designed based on the assumption that the position errors of all points on the machine can be fitted into the homogenous transformation error matrix model [7]. The x and y position errors of the XY stage of a XYFZ type machine [8] are given as:

$$M_x(x_i,y_i) = -\delta_{xx}(x_i) - \delta_{xy}(y_j) + y_j\alpha_{xy} - y_j\varepsilon_{zy}(y_j) \tag{7}$$

$$M_y(x_i,y_i) = -\delta_{yx}(x_i) - \delta_{yy}(y_j) + x\varepsilon_{zx}(x_i) + x\varepsilon_{zy}(y_j) \tag{8}$$

where x, y are the desired motions in the X, Y directions, and $\delta_{uv}(v)$ is the linear error motion in U direction under nominal V motion. $\varepsilon_{uv}(v)$ is the angular error motion of V motion about U axis, α_{uv} is the squareness error between U and V axes, and u, v can be x or y. The origin is defined at the center of the stage and all the error motions equal to zero at this point. The X guide way of the machine is the X-axis of the stage error map. Because the above assumptions assure that the algorithm can handle 4-fold symmetrical features, no translation view is selected in this method.

An un-calibrated plate has been measured with a vision based CMM, *Voyager*[9]. The experiment results showed that the machine parametric errors derived from the reversal plate calibration method were close to those directly measured by a laser interferometer [6]. And the stage error map obtained from the machine readings from the three views was similar as that created by the interferometer data. The reversal plate calibration method succeeds only when the stage error map can be closely described by the machine error model. Fortunately, the parametric machine error model has been successfully applied in the CNC (Computer Numerically Controlled) machines and CMMs for more than two decades, which proved that the machine error model can describe their machine error map. Therefore, the plate calibration method based on the machine error model can be applied in these areas. Whether or not the stage error map of any machine with x and y guide ways can be closely represented by the machine error model should be verified.

4. Conclusion

Plate self-calibration methods are promising to improve the stage position accuracy. They can be classified as into two categories based on how to model the stage point set. Stanford method is a good example of the point-to-point comparison method. The stage error map obtained from Stanford method can reveal the physical stage errors, but it is difficult to relate to the machine coordinate system because of its assumptions. The reversal plate calibration method belongs to the machine error method. The stage error map obtained from this method can be directly used for the error compensation. However, it won't succeed unless the stage errors can be closely described by the machine parametric errors. Therefore, by discussing the assumptions of these methods, we can understand the limitation of the methods, which helps us to choose a proper method in applications and design new methods in the future. A good plate self-calibration method should be simple and convenient in practical use and at the same time all the assumptions on the point sets of a plate and a stage should reflect the reality which means they introduce only negligible errors for the required task. The algorithm should be linear and error resistant.

Reference:

[1] Michael R. Raugh, Nov/Dec, 1997, Two-dimensional stage self-calibration: role of symmetry and invariant sets of points, J.Vac.Sci.Technol. B (15) 6:2193-2145

[2] Evans, Chris J., Hocken, R., Estler, W. Tyler, 1996, Reversal, redundancy, error separation, and 'absolute testing', Annals of the CIRP, 45/2:617-632

[3] Michael R. Raugh, Nov/Dec, 1985, Absolute two-dimensional sub-micro metrology for electronic beam lithography: a theory of calibration with application, Precision Engineering, 7:3-13

[4] Ye, J., 1996, Errors in High-Precision Mask Making and Metrology, PhD Thesis, Stanford Electronics Laboratory, Stanford University

[5] Hocken, R., Borchardt, B., May, 1979, On characterizing measuring machine geometry, NBSIR 79-1752

[6] Zhang, G. Fu J., 2000, A method for optical CMM calibration using a grid plate, Annals of the CIRP, 49/1:399-402

[7] Zhang, G., et al., 1985, Error Compensation of Coordinate Measuring Machines, Annals of the CIRP, 34/1:445-448

[8] ASME B89.4.1-1997, American National Standard (Revision of ASME B89.4.1-1995), 1997, Methods for performance evaluation of coordinate measuring machines, American Society of Mechanical Engineers

[9] GSI Lumonics Inc., 1997, Software manual: Voyager software version 5.0

COMPARISON STUDY OF AREAL FUNCTIONAL PARAMETERS FOR ROUGH SURFACES

X. Q. JIANG L. BLUNT K. J. STOUT

Centre for Precision Technologies, School of Engineering,
The University of Huddersfield, Huddersfield HD1 3DH, UK

ABSTRACT

Previously the use of conventional two-dimensional surface measurement was confined to process control and quality assurance. Some attempts were made to develop two-dimensional surface parameters from which functional inferences could be drawn but these were limited and not always successful. The advent of areal surface measurement has meant that areal surface parameters have been developed which have much greater functional significance.

The authors investigate the functional characterisation of different functional parameter families based on the Abbott-Firestone curve. A comparative study has then been followed to fully show the properties of these functional parameters. In this paper, a number of measurements of engineering surfaces have been carried out, and outcomes demonstrate that the volume parameters have enormous practical significance, and they can be used to better evaluate the bearing area ratio numerically and functionally.

Key Words: the bearing ratio, the volume family, functional parameters, rough surfaces

INTRODUTION

The initial functional parameters were extracted from the Abbott-Firestone length ratio in the 1930's. The peak roughness was defined as a range of heights embracing 2% ~ 25% of the bearing length, whilst the medial and valley roughness were defined to cover 25% ~ 75% and 75% ~ 98% of the bearing length respectively. At the beginning of the 1980s, Trautwein [1] developed a two-piece linear model of the Abbott-Firestone curve for characterising cylinder bore surfaces. A parameter called oil retention volume was derived from the model. In the 1990's the R_k family, parameter set appeared which split the bearing ratio into three by means of a secant to the region at the point of inflection corresponding to a 40% bearing ratio, being drawn to intercept the axes. The three parts describe the peaks, the valleys and the core roughness of the surface. The parameters are used exclusively for asymmetrical plateau-like surfaces, which assume that a digital valley suppression filter standardised in DIN 4776 is used to obtain a roughness profile [2].

In the present study two functional parameter families have been used to assess the areal surface. The first one is the S_k family, which is a straightforward extension of the R_k parameter set. The other is the index family that includes bearing index, core fluid retention index and valley fluid retention index, which are also based on the bearing area ratio [3]. The peak roughness was defined as a range of heights embracing 5% of the bearing area, whilst the core and valley roughness were defined to cover 75% and 20% of the bearing area respectively. The main advantage of the index family is that it is useful to develop a knowledge-based expert system for identification of different kinds of 3D surface topography. The problem of the index family, however, is that it can not very clearly describe material and core volume information on a absolvte scale.

In order to improve the index family as well as considering information about the material and void volume of a surface topography including the bearing area, an enhanced functional family has been proposed through the EC SMT4-CT98-2209 project [4]. This family is assumed to not only keep the benefits of the index family (identification of the shape features of surface waveforms), but also addresses the change of material and void volume for different roughness levels similar to the advantages of the S_k family.

INDEX FAMILY

With regard to 3D surface functional characterisation, a functional index family based on bearing area ratio was proposed in the primary parameter set. It includes the bearing index, S_{bi}, core fluid retention index, S_{ci} and valley fluid retention index, S_{vi}. In the analysis, the bearing area ratio curve is divided into three parts. The peak roughness

was defined as a range of heights embracing 5% of the bearing area, whilst the core and valley roughness were defined to cover 75% and 20% of the bearing area respectively. The index family is designed for a twofold purpose. One of the purposes is to identify the shape features of different types of surface waveforms by observing the location of three functional indexes in two pattern planes, S_{vi} vs S_{bi} and S_{vi} vs S_{ci}. The other attempts to deal with the topographical features of the surfaces, for instance, bearing, running in and fluid retention properties.

A series of experiments on engineering surfaces, such as ground, honed, lapped, and EDM surfaces have been carried out in order to verify the ability of the index family to characterise functional properties of the 3D surfaces. Examining Fig.1*a* to Fig.3*a*, obtained from parts of experiments of engineering surfaces, the results seem ambiguous. The values of index parameters are similar to each other whether different types of surfaces or different roughness levels are considered. This makes it difficult to interpret the load bearing capability and lubrication retention properties of these engineering surfaces. Practical work indicates that by using the index parameters it is impossible to clearly understand the nature of the development of surface topography.

The relationships between shape features of different surface topographies and their index family are shown in Fig.4*a* and Fig.5*a*. The positions of functional parameters of different types of surfaces are located at the pattern can be used to identification of shape features of these surfaces. Both pattern planes are constructed using S_{bi} versus S_{vi} and S_{ci} versus S_{vi}. Observing Fig.4*a* and Fig.5*a*, it is clear that index parameters can be used to qualitatively identify the shape features and discriminate different types of 3D surface topography. This is very useful when introduced to develop a knowledge-based expert system for the qualitative identification of 3D surface waveforms.

THE IMPROVED FUNCTIONAL PARAMETER SET – THE VOLUME FAMILY

As is well known, in industrial applications there are a wide range of functional requirements from contact phenomena (such as wear, friction, lubrication, sealing tightness, contact rigidity, contact stress, loaded area and thermal conductivity etc.) to non-contact phenomena (such as optical transmission, surface cleanliness and surface painting quality). It is impossible to propose a functional parameter set to meet all functional requirements. However, it is possible that a functional parameter set can be used to generally characterise the common functional properties; for instance, area and volume geometrical properties, or to describe wear and tribological properties. An improved functional family would not only keep the benefits of index family (identification of the shape features of surface waveforms), but also address the change of material and void volume for different roughness levels or analyse running-in procedure (similar to advantage of R_k family). The bearing area ratio function contains a great deal of information about the material and void volume of a surface topography, further area and volume are fundamental geometrical descriptors. Therefore, more natural functional properties can be directly derived from the volume information of a bearing ratio curve.

In terms of the above ideas, three improved functional parameters derived from the volume information of a bearing ratio curve are proposed. This parameter set is the so-called volume family, which is based on an assumption that the peak material embraces 0~10% of the bearing area whilst the core and valley ranges cover 10~80% and 80~100% of the bearing area.

THE VERIFICATION OF THE VOLUME FAMILY

A comparative study has been executed. In order to fully verify the properties of the improved functional parameters, the volume family is compared with both index family, and S_k family (which is a straightforward extension of the R_k parameter set). Fig.1*b* to Fig.3*b* shows the set of results. As far as the engineering surfaces are concerned, it is easy to see from the diagrams that the outcomes of the three groups of engineering surfaces shows that the values of volume family varied for the different roughness levels. The results can be used to interpret surface material and void volume properties of different kinds of surface with different roughness levels, and the value variation is similar to S_k family as shown in Fig.1*c* to Fig.3*c*.

Additionally, if values of volume family are scaled by the root-mean-square deviation, the results obtained when plotting two pattern planes as shown in Fig4*b* and Fig5*b* have the same relationship as the index parameters. The pattern structures are similar to Fig.4*a* and Fig.5*a* except for a little scalar change due to the S_m having a truncation level from 5% to 10%. Consequently, as well as the tribological advantages in terms of volume analysis, the volume family retain the ability to describe typical shapes of manufactured surfaces.

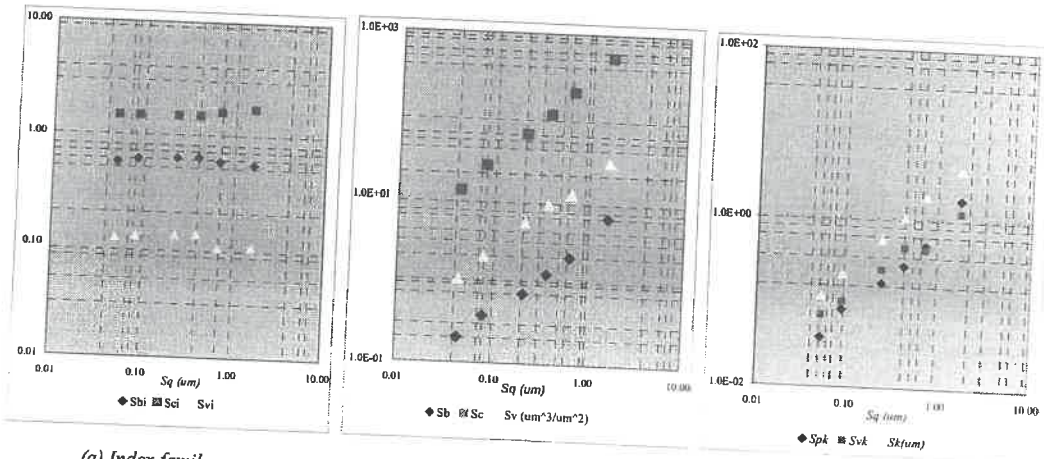

(a) Index family (b) Volume family (c) Sk family

Fig.1 functional parameter sets for the ground surface

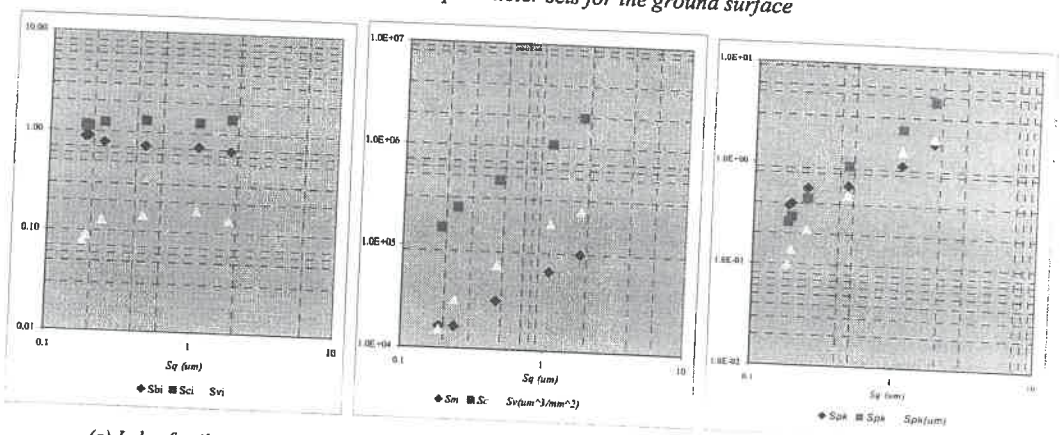

(a) Index family (b) Volume family (c) Sk family

Fig.2 functional parameter sets for the honed surface

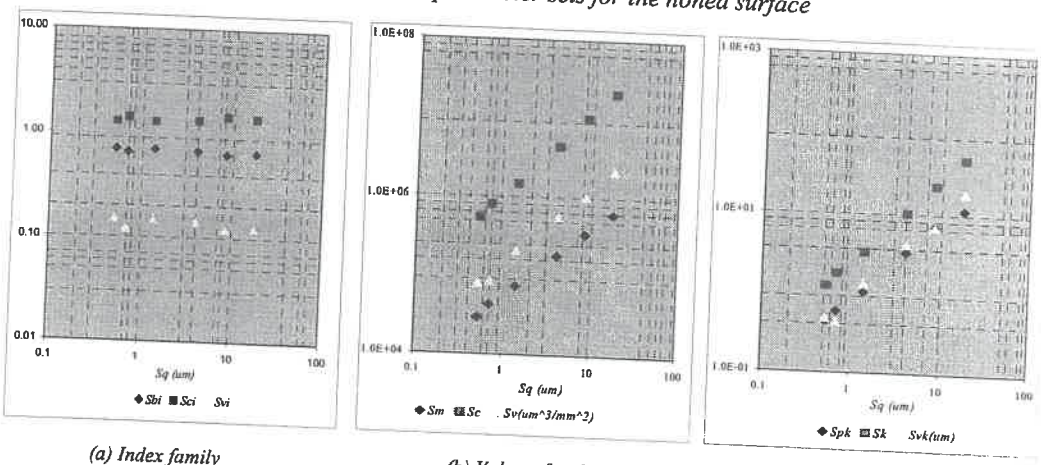

(a) Index family (b) Volume family (c) Sk family

Fig.3 functional parameter sets for the EDM surface

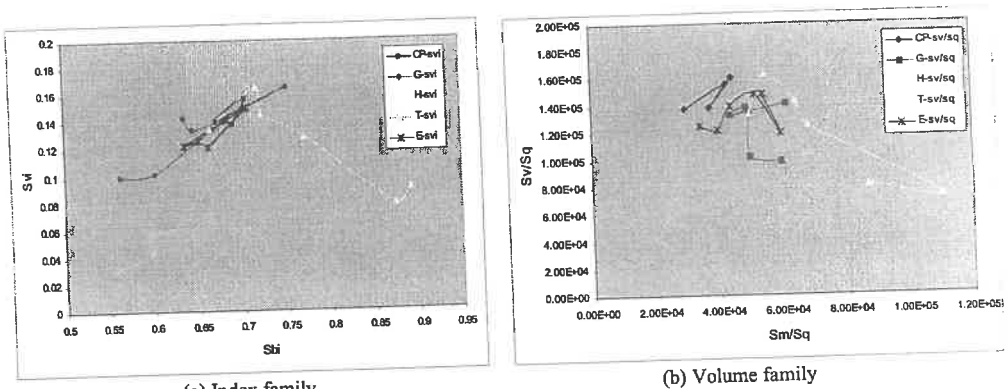

(a) Index family (b) Volume family

Fig.4 Svi vs. Sbi and Sv/Sq vs. Sm/Sq for pattern recognition of engineering surfaces

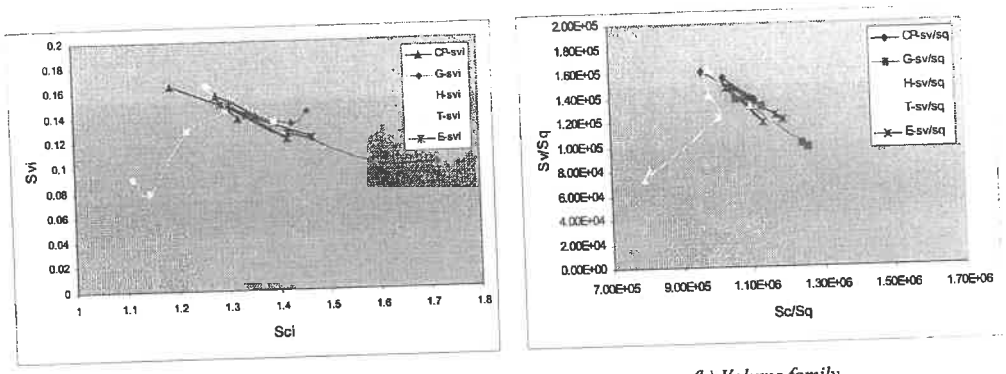

(a) Index family *(b) Volume family*

Fig.5 Svi vs. Sci and Sv/Sq vs. Sc/Sq for pattern recognition of engineering surfaces

CONCLUSIONS

As shown by these experiments, the values of the index parameters are similar to each other when different types of surfaces or different roughness levers are considered. This makes it difficult to interpret the load bearing capability and lubrication retention properties of these engineering surfaces particularly when the differences is the surfaces as only in scale. The volume family addresses the disadvantages of the index family. The practical work has shown that the values of the volume family (1) clearly vary with the different roughness levels; (2) interpret surface material and void volume properties of different kinds of surfaces with different roughness levels (the value variation is similar to the S_k family); (3) as scaled by the root-mean-square deviation, the results obtained when plotting two patterns have the same relationship as the index parameters. The results demonstrate that the volume parameters have enormous practical significance, and they can be used to better evaluate the bearing area ratio numerically and functionally.

REFERENCES:

1. R. Trautwein, characteristic values for determining and evaluating the surface of cylinder bores, Mahle GmbH, Stuttgart, 1981
2. DIN Measurement of surface Roughness; Parameters R_k, R_{pk}, R_{vk}, M_{r1}, M_{r2} for the description of the Material Portion in the roughness, German standard, DIN 4776, 1990
3. K.J. Stout, P.J. Sullivan, W.P. Dong, E. Mainsah, N. Luo, T. Mathia, and H. Zahyouani, *The development of methods for the characterisation of roughness in three dimensions,* 1st edn, Commission of the European Communities (ISBN 0 70441 313 2), 1993
4. L. Blunt and X.Q. Jiang, project report (1) of the work package 1, European Community SMT CT98-2209, 1999

An Accurate and Robust Stereo Algorithm with a Variable Window for Measurement of 3D Shapes

Gyung-Bum Kim and Sung-Chong Chung

MAnufacturing Systems & Control LABoratory
Department of Mechanical Design & Production Engineeering
Hanyang University, SungdongGu, Seoul 133-791, KOREA

Abstract: This paper describes the application of area-based stereo algorithm to the measurement of 3D shapes. Existing stereo algorithms tend to generate rather big matching errors due to large variations of disparity near depth discontinuities, and haven't taken into account the local deformations of rectangular window resulting from projective distortion. In order to deal effectively with these problems, the proposed stereo algorithm finds the variable window with a constant disparity in the 3d array constructed with the potential matching points, which are determined by proposed area-based correlation function. In addition, the local deformations of the variable window are taken into account, and then an accurate and robust sub-pixel disparities are estimated. Experiments with various synthetic images show the verification of the proposed algorithm.

Key Words: Depth discontinuity, Local deformation, Projective distortion, Stereo matching, Variable window

1. Introduction

Stereo vision which measures depths of 3d shapes using two images acquired from different viewpoints is one of the useful non-contact measurement techniques. It can be used effectively in terms of accuracy and application range. In stereo vision, the most challenging problem for shape measurements is to find corresponding image points. This problem is called stereo matching. Based on [1], stereo algorithms can be classified into three classes: feature-based, area-based, and pixel-based.

Among these, area-based stereo algorithms[2,3] have been widely used to practical stereo vision systems. They have an excellent matching accuracy in matching areas with both large intensity variations and continuously smooth disparities. To do this, the appropriate size selection of rectangular window is of importance. Generally, if the size of matching areas is determined as large as possible, enough intensity variations are included and then matching accuracy is improved in continuously smooth areas. However, large deformation of matching areas results from projective distortion, and smoothing in the vicinity of depth discontinuities occurs because area-based methods are based on the assumption that disparities within matching area are constant. Therefore, existing area-based stereo algorithms tend to generate many matching errors in depth discontinuities and have not taken into account deformed windows resulting from different viewpoint yet.

A lot of studies have been tried to solve these problems. The window size is adaptive to local intensity variations or determined to minimize uncertainties of estimated disparities[3]. This method deals effectively with depth discontinuities but can not consider local deformations of matching area, and also requires too much computation cost. On the other hand, the differential matching[4], which updates disparities iteratively using modified area-based correlation functions, results in relatively accurate matchings in continuously smooth surfaces, but is poor at treating depth discontinuities.

In this paper, an accurate and robust stereo algorithm applied to surfaces with depth discontinuities and continuously smooth areas are studied. To develop a robustness estimator against noise a decaying influence function is introduced for the correlation function. A variable window with a constant disparity in the 3d array is constructed for the potential matching points. It is also determined by the proposed area-based correlation function. In addition, the local deformations of the variable window are taken into account, and then an accurate and robust sub-pixel disparities are estimated. Experiments with synthetic images show the verification of the proposed algorithm.

2. An Accurate and Robust Stereo Algorithm

2.1 Selection of Potential Matching Points

The data which are arbitrarily distributed, not filling up normal distribution, are referred to outliers. The estimation techniques using robust estimators[5] have been applied to the cases of a few outliers. Fig. 1 shows the characteristics of robust estimators, of which weighting function $\rho_\sigma(n)$ converges a specific value gradually and influence function $\Psi_\sigma(n)$ converses zero, according to increase of intensity differences n. Therefore, these estimators have the property that effects of noise like outliers are not increased over a

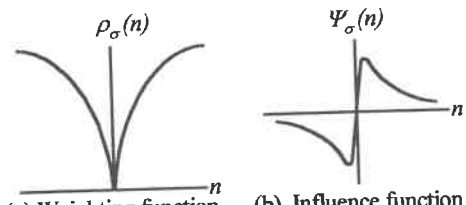

(a) Weighting function of robust ρ_σ- estimator (b) Influence function

Fig. 1 Shapes of robust estimator

certain limit, contrary to the quadratic estimator used widely by existing area-based method.

Effects of outliers due to noise and projective distortion appear highly in the intensity difference distributions of stereo images with depth discontinuities. So, a function with the robust estimator characteristics for matching candidate, which makes effects of outlier reduced, tries to be found. The proposed robust estimator and its derivative, influence function, is given by

$$\rho_\sigma(n) = \log\left\{1 + \frac{1}{2}\left(\frac{n}{\sigma}\right)^2\right\}, \Psi_\sigma(n) = \frac{d\rho_\sigma(n)}{dn} = \frac{2n}{2\sigma^2 + n^2} \quad (1)$$

Although these estimators make the effects of noise reduced using rectangular window Ω_1, smoothing is generally followed around depth discontinuities. 4 line masks $\Omega_2 \sim \Omega_5$ in which disparities along specific line direction are very likely to be constant, are devised to diminish the smoothing as much as possible.

In this paper, new area-based correlation function[6] is introduced for the selection of potential matching points that can decline noise effects and preserve depth discontinuities in detail, as follows:

$$\begin{aligned} n(u,v) &= I_L(u+i, v+j) - I_R(u+d+i, v+j) \\ NSSD(d) &= \sum_{(i,j)\in\Omega_1} \rho_\sigma(n(u,v)) + \lambda \sum_{(i,j)\in\Omega_2\cup\Omega_5} \rho_\sigma(n(u,v)) \quad (2) \\ \hat{d}_p &= \arg \min \; NSSD(d) \end{aligned}$$

where d and $n(u,v)$ are a disparity and noise at a pixel (u,v), respectively. However, these potential matching points are likely to have smoothing in depth discontinuities. This is regarded as because different disparities come into existence in matching area $\Omega_1 \sim \Omega_5$ and projective distortion has not been considered. Therefore, the formulation of stereo matching is tried to devise matching areas with a equal disparity and deal a little with problems of projective distortion.

2.2 Integer Disparity Estimation

The three-dimensional array composed of row and column of an image, disparity range, is defined as *3dPMP[u][v][d]*. This array is constructed by assigning "1" to the voxel($[u][v][\hat{d}_p]$) which corresponds to disparity candidate $\hat{d}_p$. Fig. 2 shows constructed three-dimensional array and potential matching points described by black color means pixels corresponding to minimum disparity $d_{\min}$.

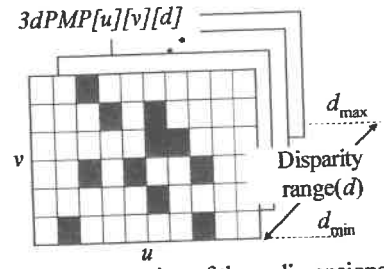

Fig. 2 Configuration of three-dimensional array

In the case of projecting three-dimensional shapes to stereo images, equal disparities are likely to exist centered at a interested pixel. To include this physical sense, 4-connectivity of a pixel is investigated through labeling technique, and then three-dimensional array is renewed at the array plane corresponding to each disparity. Here, connected potential matching points can be found and the connected number of the points can be computed. Integer disparities within a disparity range is estimated by determining the disparity with maximum connected number. This can be expressed by

$$\hat{d} = \arg \max_{d_{\min} \le d \le d_{\max}} \text{Number of connected pixels of } 3dPMP[u][v][d] \text{ at } (u,v) \quad (3)$$

2.3 The Definition of a Variable Window

The proposed variable window consists of the set of the potential matching points which correspond to not only intensity value but also intensity variation of corresponding points of stereo images, and is defined as W_v. The measure of intensity variation is intensity gradient-based similarity, S_G, as shown by Eq. (4) and S_G of corresponding potential matching points at least have to be positive. The first item of this similarity means average gradient magnitude and the second the magnitude of two gradient differences. The application of gradient-based similarity to the determination of the variable window makes the reliability of matching areas improved.

Fig. 3(a) shows the proposed variable window of three-dimensional array plane which corresponds to an estimated integer disparity at an interested pixel. The window has an arbitrary shape, contrary to rectangular window, and also equal disparity. These properties are

the main idea that can deal effectively with problems of existing area-based method.

$$W_v = \{w \mid w \in W_c, S_G > 0\} \quad at \ (u,v)$$

where

W_c : Set of connected pixels of $3dPMP[u][v][\hat{d}]$

$$S_G(u,v) = \frac{|\nabla I_L(u,v)| + |\nabla I_R(u+\hat{d},v)|}{2} - |\nabla I_L(u,v) - \nabla I_R(u+\hat{d},v)| \quad (4)$$

$$\nabla I_L = \begin{bmatrix} \partial I_L / \partial u \\ \partial I_L / \partial v \end{bmatrix}, \nabla I_R = \begin{bmatrix} \partial I_R / \partial u \\ \partial I_R / \partial v \end{bmatrix}$$

2.4 Sub-Pixel Disparity Estimation

In the case of projecting an arbitrary point of a shape to stereo images, there is generally an ambiguity of ±1/2 pixel in an image coordinate.[7] This ambiguity includes projective distortion resulting from different viewpoints, noise like outliers and so on. These problems make stereo matching get difficult.

In this paper, the projective distortion of devised variable window is formulated and then sub-pixel disparity estimation is performed. Fig. 3(b) shows that the region corresponding to a variable window centered at (u,v) in the left image is a sheared and slanted variable window centered at $(u+d(u,v),v)$ in the right image, due to the projective distortion. An approximation of this distorted window can be computed from the derivatives of the disparity. Here, if high order terms are assumed to be negligible, intensity relationship of corresponding points in the variable window can be expressed as

$$\begin{aligned} I_L(u,v) &\approx I_R(u+\hat{d}+d_0+d_u u+d_v v, v) + n(u,v) \\ &\approx I_R(u+\hat{d},v) + (d_0+d_u u+d_v v)\frac{\partial I_R}{\partial u}(u+\hat{d},v) \\ &\quad + n(u,v) \end{aligned} \quad (5)$$

where $d_u = \dfrac{\partial d(u,v)}{\partial u}, d_u = \dfrac{\partial d(u,v)}{\partial v}$

The formulation for sub-pixel disparity estimation is derived as Eq. (6) and sub-pixel disparity d_0 is determined to minimize the objective function E with respect to sub-pixel disparity and the first order derivatives of disparity d_u, d_v, using newton's method. For the implementation of this method, disparity maps by Eq. (3) is calculated and then the disparity map is used as the first component of the initialization vector for referencing the intensity and derivatives of corresponding points. The other components, which are the derivatives of disparity, are initialized at 0. Also, Existing estimated integer disparities are set at the pixels which a convergence don't be guaranteed.

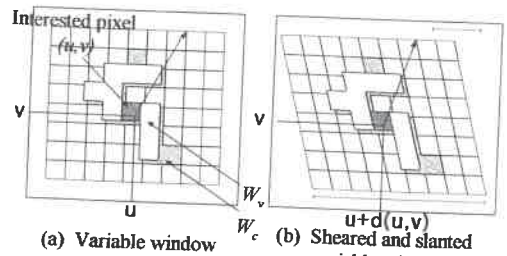

(a) Variable window (b) Sheared and slanted variable window

Fig. 3 The proposed matching areas

$$\begin{aligned} &Find \quad d_0 \\ &minimize \\ &E(u,v;d_0,d_1,d_2) = \sum_{(\alpha,\beta)\in W_v} \rho_\sigma\left(n(u+\alpha, v+\beta)\right) \end{aligned} \quad (6)$$

3. Experiments

Matching areas Ω_1 and $\Omega_2 \sim \Omega_5$ were used as 9×9 and 25 respectively, and weighting factor λ was 1. Fig. 4 shows the random dot stereograms which have the properties of depth discontinuities and smooth areas and are constructed with the disparity range of 0 to 12 pixels. Three-dimensional plots of disparities computed by several methods are compared as shown in Fig. 5-6. The larger the disparity, the brighter the figures are described. The proposed method makes smoothing reduced a little and has a closer description in both depth discontinuities and continuously smooth areas, compared with existing methods.

In order to compare the performances of several algorithms quantitatively, the means of absolute matching errors per a pixel are computed as shown in Table 1. Matching errors of SSD are less than those of NCC, and matching errors of the proposed algorithm relative to those of SSD are reduced about 48%, 10% in pulse train, sine function images, respectively. In addition, several algorithms are applied to each image, which is mixed with the noise of uniform distributions equivalent to 5%, 10% and 20% of maximum intensity

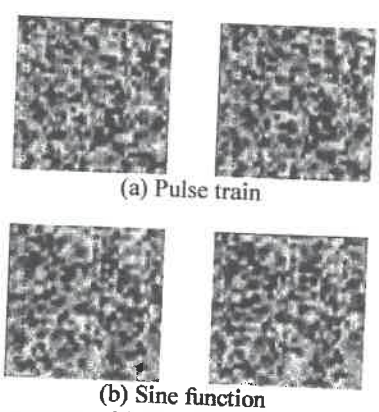

(a) Pulse train

(b) Sine function

Fig. 4 Stereograms with discontinuities and smooth areas

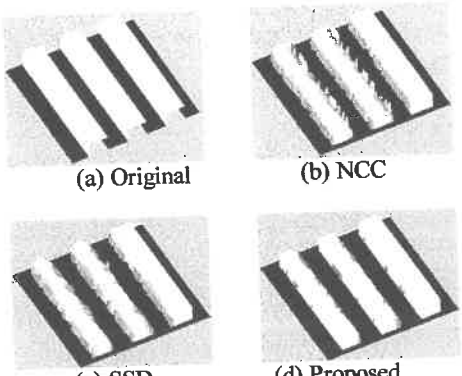

(a) Original (b) NCC

(c) SSD (d) Proposed

Fig. 5 Comparisons of computed disparities for Fig. 4(a)

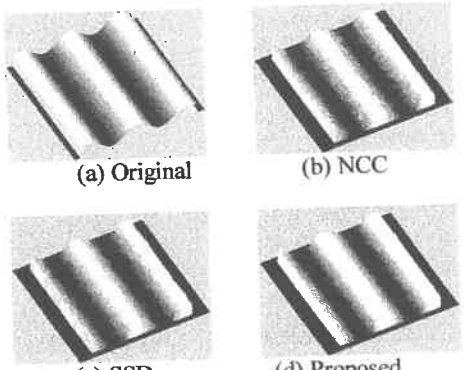

(a) Original (b) NCC

(c) SSD (d) Proposed

Fig. 6 Comparisons of computed disparities for Fig. 4(b)

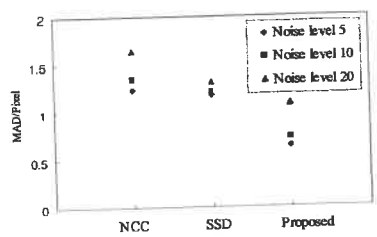

(a) Pulse train

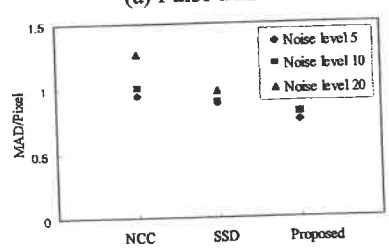

(b) Sine function

Fig. 7 Performance evaluations of robustness to noise

Table 1 Means of absolute matching errors per a pixel

	Pulse train	Sine function
NCC (9×9)	1.20	0.92
SSD (9×9)	1.17	0.88
SSD with $\Omega_1 \sim \Omega_5$	1.34	0.95
Proposed	0.60	0.80

in order to show robustness against noise, as shown in Fig. 7. As a result, the proposed method outperforms previous ones in terms of accuracy and robustness to noise.

4. Conclusions

An accurate and robust stereo algorithm with a variable window has been proposed. The application of the variable window to stereo matching satisfied the basic assumption of existing area-based stereo methods, and also projective distortions of the window resulting from different viewpoints were considered. The proposed stereo method makes matching errors reduced in both depth discontinuities and continuously smooth areas, and has robustness against noise drastically. The verification of proposed method has been confirmed through several experiments.

Acknowledgement

The authors would like to acknowledge financial supports of the SAMSUNG ELECTRO-MECHANICS Co., LTD.

References

(1) Dhond, U. R. and Aggarwal, J. K., 1989, "Structure from Stereo: A Review," *IEEE Trans. Syst. Man Cybernetics*, Vol. 19, No. 6, pp. 1489~1510.

(2) Kanade, T., Yoshida, et al., 1996, "A Stereo Machine for Vidio-rate Dense Depth Mapping and Its New Applications," *In Proc. of Computer Vision and Pattern Recog.*, pp. 196~202.

(3) Kanade, T. and Okutomi, M., 1994, "A Stereo Matching Algorithm with an Adaptive Window: Theory and Experiment," *IEEE Trans. Pattern Anal. Machine Intell.*, Vol. 16, No. 9, pp. 920~923.

(4) Dervernay, F. and Faugeras, O., 1994, "Computing Differential Properties of 3D Shapes from Stereoscoptic Images without 3D Models," *In Proc. of Computer Vision and Pattern Recog.*, pp. 208~213.

(5) Meer, P., Hintz, D., Rosenfeld, A. and Kim, D. Y., 1991, "Robust Regression Methods for Computer Vision: A Review," *Int. J. Computer Vision*, Vol. 6, No. 1, pp. 59~70.

(6) Chung, S. C. and Kim, G. B., 2000, "A New Area-Based Stereo Algorithm for Measurement of 3D Shapes," *Trans. of NAMRI/SME*, Vol. 28, pp. 383~388.

(7) Rodrigue, J. J. and Aggarwal, J. K., 1990, "Stochastic Analysis of Stereo Quantization Error," *IEEE Trans. Pattern Anal. Machine Intell.*, Vol. 12, No. 5, pp. 467~470.

Volumetric Error Identification and Measured Data Correction for On-Machine Measurement and Inspection Systems

Kyung-Don Kim and Sung-Chong Chung

MAnufacturing Systems & Control LABoratory
School of Mechanical Engineering
Hanyang University, SungdongGu, Seoul 133-791, KOREA

Abstract : Needs for higher accuracy on machined components are always on the rise. Inspection of parts *in situ* has the significant advantage to rapidly rework the part based upon inspection results. Objectives of this research are quick calibration of volumetric errors of machine tools and proper assessment of machined shapes distorted by machine tool error sources by correction of measured data. In order to realize the objectives a three-dimensional reference artifact is invented and fabricated. Measurement results on the machine tool can be corrected according to the identified volumetric error map. The accuracy of the proposed method is verified by comparing the identified volumetric error map with the diagonal test results of ANSI/ASME B.5 using a laser interferometer.

Keywords : Invar, Measured data correction, On-machine measurement and inspection systems, Reference artifact, Touch trigger probe, Volumetric error identification.

1. Introduction

In the conventional quality control system, a workpiece machined on a machining center requires to be moved to a coordinate measuring machine (CMM) for checking its dimensional accuracy. After developing touch trigger probes, on-machine probing has found a broad range of applications where it is vital to automated production processes. The inspection of parts *in situ* has the significant advantage of possibly being able to immediately rework the part based upon the inspection results. On-machine measurement and inspection systems (OMMIS) can allow manufacturers in many industries to deliver precise components, minimize scraps, and maximize productivity.[1-3]

The use of a machine tool as a CMM has some significant liabilities that need to be carefully considered before employing this measurement technique. In particular, the on-machine inspection process is oblivious to all error sources common to both the production and inspection processes. For example, if the machine tool's axes are out-of-square, the cutting process will produce an out-of-square part. The inspection process, using the same out-of-square axes, will consequently measure the part to be perfect. The key component of the OMMIS, therefore, is a proper assessment of machined shape by correction of measured data that is distorted by machine tool error sources. For this purpose, a method for quick and accurate assessment of dominant error sources of the machine tool is needed at the moment of measurement.

If a machine tool is to be made use of a measuring system like a CMM, calibration of machine tool errors with reference artifacts such as step gauges, ring gauges, hole and ball plates, and so on are required. However, above mentioned artifacts are one or two dimensional gauges, and therefore more than two setups are required for identification of volumetric errors. Fixed head type probes that are mainly used for machine tools cannot access to the artifacts.

In this paper, a three-dimensional reference artifact is invented and fabricated. A volumetric error identification method is also proposed for quick and accurate assessment of machine tool errors by direct measurement of the artifact on the machine tool. Measurement results are accurately corrected according to the identified volumetric error map. Accuracy of the proposed method is confirmed by comparing the identified volumetric error map with the diagonal test of ANSI/ASME B.5 using a laser interferometer.

2. Simple Volumetric Error Model

A correction process of measured data on the machine tool requires a volumetric error model that can calculate correction amounts at measured positions. Previous works for volumetric error models mainly focus on accurate prediction of volumetric errors that will arise during the whole machining processes.[4-5] These models include complex model parameters. Experiments required for the parameter estimations are impossible jobs or difficult and time-consuming processes.

The on-machine inspection technique aims to use a machine tool as a measuring machine. It can be used to assure workpiece accuracy for a moment on the way of the machining processes. Since the machine

conditions are not changed drastically during the short measurement time and thermal errors have slowly time varying characteristics, a simple volumetric error model that contains dominant error sources of the machine tool is more effective for correction of measured data rather than the complex prediction model. A simple volumetric error model is developed as follows:

$$
\begin{aligned}
dX &= \delta_x(x) + \sum_{i=1}^{4} \Delta a_i + P_1 x + PZXz \\
dY &= \delta_y(y) + \sum_{i=1}^{4} \Delta b_i + P_2 y + PXYx - PYZz \\
dZ &= \delta_z(z) + \sum_{i=1}^{4} \Delta c_i + P_3 z
\end{aligned}
\qquad (1)
$$

where dX, dY and dZ are components of volumetric errors according to working coordinates of a machine tool, x, y and z. $\delta_x(x)$, $\delta_y(y)$ and $\delta_z(z)$ are positioning errors along X-, Y- and Z-Axis respectively. $\sum \Delta a_i$, $\sum \Delta b_i$ and $\sum \Delta c_i$ are thermal drifts of the workspace origin of machines in direction of X-, Y- and Z-Axis respectively. P_1, P_2 and P_3 are thermal expansions, and PXY, PYZ and PZX are squareness errors between axis pairs due to the thermal distortion. This model can be easily constructed by the error synthesis method.[2,5]

3. Error Identification

For quick identification of the model parameters, PXY, PYZ, PZX, $\sum \Delta a_i$, $\sum \Delta b_i$, $\sum \Delta c_i$, P_1, P_2, P_3, a three-dimensional reference artifact is designed and fabricated, and then measured on machine tool using a touch trigger probe. Identification of positioning errors will not considered in this paper, because these errors can be easily calibrated using equipments such as a laser interferometer or a step gauge, and then automatically compensated for by machine controllers.

Fig. 1 shows the reference artifact composed of a square, a metrology block and two columns. The metrology block is fixed on the table close to machine's workspace origin. The square and two columns can be quickly installed on the table without interfering with the workpiece machined when the on-machine measurement is required. The reference artifact is calibrated by a CMM, and then referenced in the measurement on the machine tool. The artifact is made of invar – a material with an extremely low thermal expansion coefficient. So we can minimize thermal variation of the artifact.

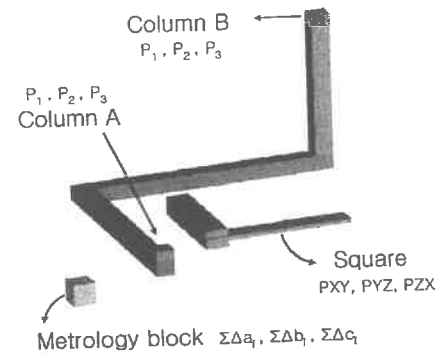

Fig. 1 Designed reference artifact

3.1 Identification of PXY, PYZ, PZX

A square can be installed on the machine table in different posture according to the parameters to be identified. Fig. 2 shows schematic diagrams to calibrate squareness errors, PXY, PYZ, PZX. To identify the parameter PXY when X- and Y-Axis of the machine tool have an inclination of α_Z and β_Z respectively, and also the square has an inclination angles of δ_1 and δ_2 due to misalignment, four measurement points, $A(a_1, y, z)$, $B(a_2, y, z)$, $C(x, b_1, z)$, $D(x, b_2, z)$, have to be successively measured from the square lying on a X-Y plane. In this case, the stylus tip is moved along X′- and Y′-Axis, respectively. Real

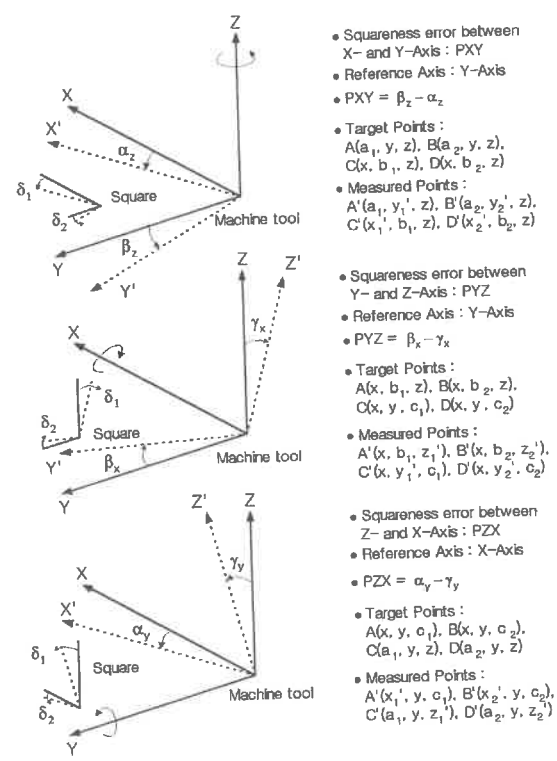

Fig. 2 Squareness errors of a machine tool

contact points become $A'(a_1, y_1', z)$, $B'(a_2, y_2', z)$, $C'(x_1', b_1, z)$ and $D'(x_2', b_2, z)$. The squareness error between X- and Y-Axis, PXY, can be derived from geometric relationships between the square and the stylus tip, and then expressed as follows:

$$PXY = \beta_Z - \alpha_Z = \frac{x_2' - x_1'}{b_2 - b_1} + \frac{y_2' - y_1'}{a_2 - a_1} + (\delta_2 - \delta_1) \quad (2)$$

where $\delta_2 - \delta_1$ is the error of the square. It was calibrated on a CMM.

In a similar way, PYZ and PZX can be obtained as eqs. (3)~(4) by assumption that Y- and Z-Axis of machine tool have an inclination of β_X and γ_X, and X- and Z-Axis have an inclination of α_Y and γ_Y respectively as shown in Fig. 2.

$$PYZ = \beta_X - \gamma_X = -\frac{z_2' - z_1'}{b_2 - b_1} - \frac{y_2' - y_1'}{c_2 - c_1} + (\delta_2 - \delta_1) \quad (3)$$

$$PZX = \alpha_Y - \gamma_Y = \frac{z_2' - z_1'}{a_2 - a_1} + \frac{x_2' - x_1'}{c_2 - c_1} + (\delta_2 - \delta_1) \quad (4)$$

Therefore, substituting both the measured values of the square on the machine tool and the calibrated value by a CMM into the eqs. (2)~(4), the squareness errors between axis pairs can be calibrated.

3.2 Identification of $\sum \Delta a_i, \sum \Delta b_i, \sum \Delta c_i$

Fig. 3 shows a schematic diagram for coordinate frame acquisition established on the metrology block for thermal drifts identification. Fifteen points (five points per each plane) are measured and then transformed to three plane equations as follows:

$$\begin{aligned} i_1 x + j_1 y + k_1 z &= l_1 \\ i_2 x + j_2 y + k_2 z &= l_2 \\ i_3 x + j_3 y + k_3 z &= l_3 \end{aligned} \quad (5)$$

where $(i_i, j_i, k_i)_{i=1,2,3}$ is a unit normal vector to the ith plane, and l_i is the distance of the ith plane from the workspace origin of machine. The workpiece coordinate origin, O_W, is the intersection of the primary, secondary and tertiary planes, and can be determined as follows:

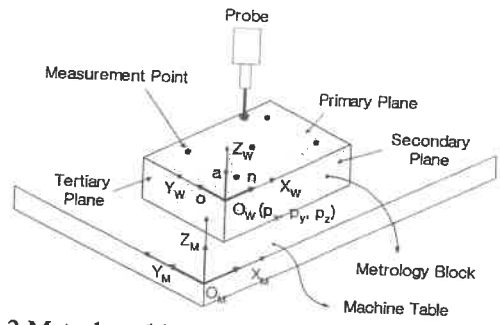

Fig. 3 Metrology block for thermal drift identification

$$\begin{bmatrix} p_x \\ p_y \\ p_z \end{bmatrix} = \begin{bmatrix} i_1 & j_1 & k_1 \\ i_2 & j_2 & k_2 \\ i_3 & j_3 & k_3 \end{bmatrix}^{-1} \begin{bmatrix} l_1 \\ l_2 \\ l_3 \end{bmatrix} \quad (6)$$

Since metrology block is fixed close to the workspace origin, $\sum \Delta a_i$, $\sum \Delta b_i$ and $\sum \Delta c_i$ are able to be considered to the thermal drifts of the workpiece coordinate origin established on the metrology block, and then expressed as follows:

$$\begin{aligned} \sum \Delta a_i &= p_x' - p_x \\ \sum \Delta b_i &= p_y' - p_y \\ \sum \Delta c_i &= p_z' - p_z \end{aligned} \quad (7)$$

where p_x, p_y, p_z and p_x', p_y', p_z' are the origin of workpiece coordinate system before and after the variation of thermal conditions respectively.

3.3 Identification of P_1, P_2, P_3

Fig. 4 shows two position vectors that represent the distance between two columns as shown in Fig. 1. One position vector of column B relative to the column A, ${}^A P_B$, is a calibrated value by a CMM. The other position vector, ${}^A P_B'$, is a measured value on machine tool, which can be obtained by measuring two columns and establishing workpiece coordinate systems as described in section 3.2. The difference between the two position vectors can be represented as follows:

$$\Delta P = {}^A P_B' - {}^A P_B = [\Delta P_X \quad \Delta P_Y \quad \Delta P_Z]^T \quad (8)$$

where ΔP_X, ΔP_Y and ΔP_Z can be represented as volumetric error components like the eq. (1). However, the thermal drifts of the workspace origin of machine, $\sum \Delta a_i, \sum \Delta b_i, \sum \Delta c_i$, can be eliminated because the

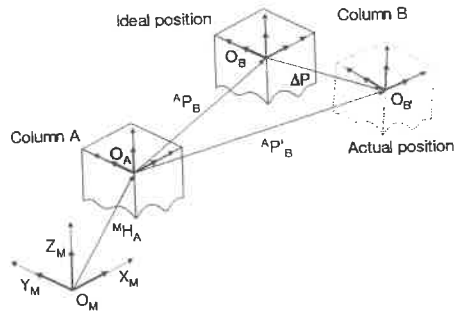

Fig. 4 Relative deviation of two columns

position vector ${}^{A}P'_{B}$ is a difference between two column positions. Therefore, the thermal expansion of each axis, P_1, P_2, P_3, can be expressed as follows:

$$P_1 = (\Delta P_X - PZXz)/x$$
$$P_2 = (\Delta P_Y - PXYx + PYZz)/y \qquad (9)$$
$$P_3 = \Delta P_Z / z$$

Since the squareness errors due to the thermal distortion of each axis, PXY, PYZ, PZX, can be calibrated as described in section 3.1, the thermal expansion of each axis, P_1, P_2, P_3, can be identified by substituting the calibrated values into eq. (9).

4. Experiments

In order to verify the accuracy of the proposed method, the diagonal test of ANSI/ASME B.5 using a laser interferometer has been performed. After warming up the vertical machining center, the reference artifact is measured on the machine tool and the volumetric error map is constructed by substituting the identified model parameters into eq. (1). It takes about 6 minutes to measure the artifact. A software-based compensation system is implemented for the diagonal test, which can modify the current position based on the identified error map. Fig. 5 shows the result of the diagonal test. The positioning errors in diagonal direction have been reduced from 22μm to 10μm after compensation. And then, the machine tool is heated up by moving X-, Y-, and Z- Axis at 6m/min and rotating the spindle at 3000rpm at the same time to simulate the actual machining conditions that include the thermal interactions among error sources. The artifact is measured again and the model parameters are updated. The positioning errors in diagonal direction after the heating process have been reduced from 45μm to 10μm after compensation of volumetric errors based on the updated error map.

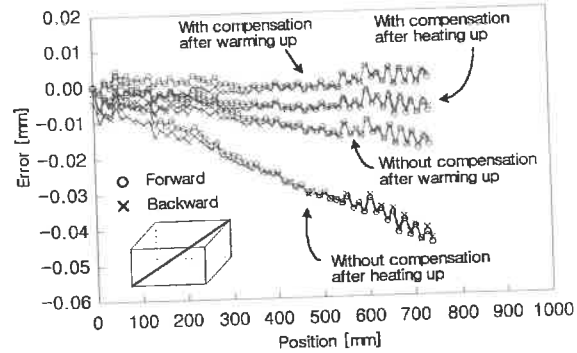

Fig. 5 Positioning errors in diagonal direction

5. Conclusions

A method for a proper assessment of machined shape by correction of on-machine measured data has been studied. A simple volumetric error model that contains dominant error sources of the machine tool is adopted for correction of the measured data. A three-dimensional reference artifact is invented and fabricated to identify the model parameters through the process-intermittent measurement using a touch trigger probe. A volumetric error identification method is also proposed for the quick and accurate assessment of the present machine conditions by direct measurement of the artifact on the machine tool. The diagonal test of ANSI/ASME B.5 using a laser interferometer has confirmed the validity of the proposed method.

Acknowledgement

The authors would like to acknowledge the financial supports from the Keonwoo Precision Co., LTD.

References

1. J. A. Bosch, 1995, *Coordinate Measuring Machines and Systems*, Marcel Dekker, Inc., New York, New York.
2. J. Mou and C. R. Liu, 1992, "A method for Enhancing the Accuracy of CNC Machine Tools for On-Machine Inspection", *Journal of Manufacturing Systems*, Vol. 11, No. 4, pp. 229-237.
3. S. C. Chung and K. D. Kim, 1999, "Design and Analysis of 2½ Dimensional Measurement and Inspe-ction System on the Machine Tool", *Transactions of NAMRI/SME*, Vol. 27, pp. 281-286.
4. M. Weck, P. Mckeown, R. Bonse and U. Herbst, 1995, "Reduction and Compensation of Thermal Errors in Machine Tools", *Annals of the CIRP*, Vol. 44, No. 2, pp. 589～598.
5. J. Ni, 1997, "CNC Machine Accuracy Enhance-ment Through Real-Time Error Compensation", *Journal of Manufacturing Science and Engineering*, Vol. 119, No. 11, pp. 717-725.

THE INTERACTION OF MEASURING ERRORS AND WORKPIECE ERRORS IN FEATURE EVALUATION ALGORITHMS

Edward P. Morse* and James G. Salsbury†

*Center for Precision Metrology
The University of North Carolina at Charlotte

†Mitutoyo America Corporation

Keywords: CMMs, Measuring Errors, Error Analysis, Fitting Algorithms, Uncertainty

Research in coordinate metrology may be classified in two broad categories: *sample set sufficiency* (i.e. have we collected enough points to adequately represent the surface), and *algorithms* (i.e. how do we manipulate the data we've collected). In this paper we assume that our data are sufficient to represent the surface under consideration, and we focus on the manipulation of these data. Most algorithmic studies assume some systematic error in the workpiece and either no error or some random error in the measurement process. In other words, it is assumed that the data collected are perfect or that some random variation is added to each point individually, representing measuring error. The values reported by different algorithms are compared to determine either differences between the reported results or the influence of the pointwise random variation on the results.

In this paper we consider systematic errors in both the measuring system and the workpiece, and random errors in the measuring process. In addition, we examine algorithm selection for not only the evaluation of the workpiece, but also the calibration of the measuring system. Of particular importance to our work is the *residual probing error* after probe calibration. The influence of these errors is studied for two of the four algorithms commonly used in evaluating round features on workpieces. These are the least squares circle (LSC), minimum zone circle (MZC), maximum inscribed circle (MIC), and minimum circumscribed circle (MCC). The much-used and oft-maligned LSC algorithm is the most common for many applications, but is now being replaced by the other algorithms for certain evaluations where the others "better capture the spirit of the (Y14.5) standard."

Our contention is that a fundamental piece of the analysis is usually overlooked when discussing the choice of the "appropriate" algorithm for a particular measurement. We have found that the fitting algorithm used to establish the nominal probe geometry is critical to the successful assessment of workpiece geometry. It is often claimed that the MIC algorithm is the most appropriate for determining the "fit size" of an internal feature, but this claim is suspect if the average probe radius was found using a least-squares algorithm. In this paper we examine the influence of probing errors and calibration algorithms on the reported values of workpiece measurements. We discuss how the choices for calibration algorithms and feature fitting algorithms interact, and provide examples that illustrate our findings.

1. *Calibration*

In the calibration of the Coordinate Measuring Machine's (CMMs) probing system, a sphere of known diameter – and small form error – is measured, and the difference between the machine motion and the sphere size are used to calculate the *effective* diameter of the probe stylus. This effective stylus diameter is then used to compensate subsequent measurements taken with the CMM. The algorithm used to calculate the stylus diameter is most often of the least squares type. This means that, for any point collected on the calibration sphere, the distance from this point to the stylus center may be less or more than the average stylus radius which is calculated.

In Figure 1 below we plot the pre-travel variation of a common (Renishaw TP-6) touch trigger probe with different stylus lengths (10, 60, and 100 mm), and in Figure 2 we show the influence of this variation on the

measurement of a ring gage. These plots are complementary, as the ring gage does not introduce significant error to the radial deviations.

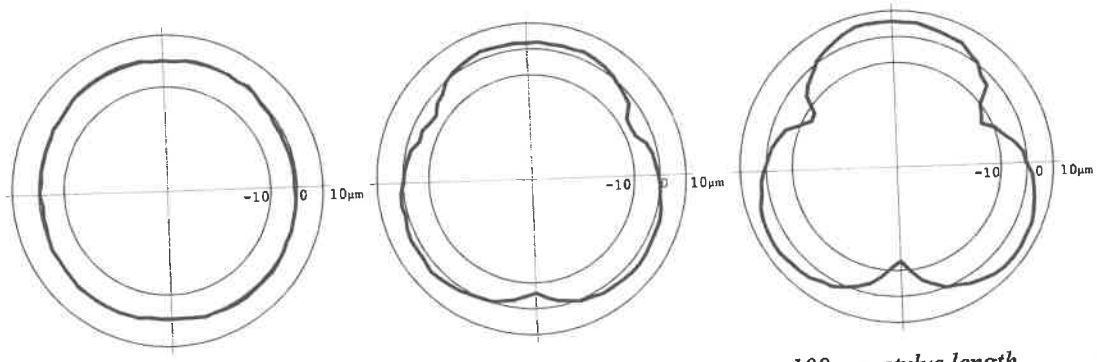

10 mm stylus length *60 mm stylus length* *100 mm stylus length*

Figure 1: Apparent stylus shape (at the "equator").

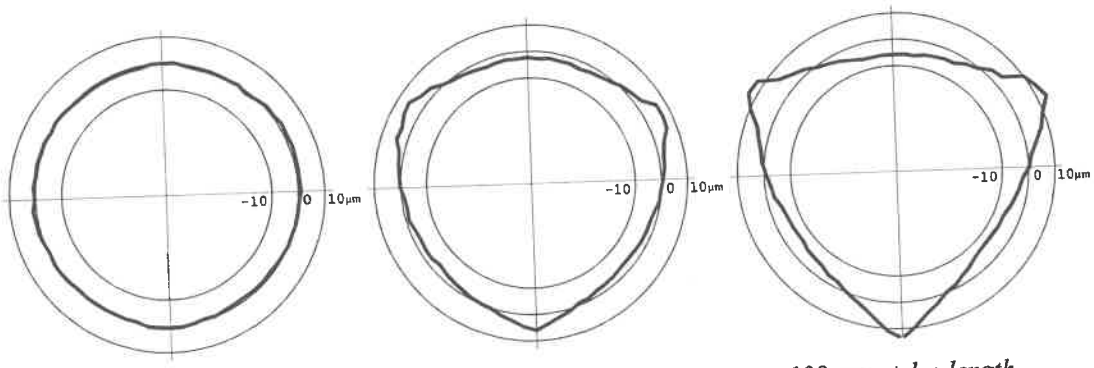

10 mm stylus length *60 mm stylus length* *100 mm stylus length*

Figure 2: Data obtained from measuring ring gage.

In each of the figures above, the zero-level of deviation corresponds to the LSC fit. The centers for the LS and MI circles are quite close, so the plots for the MIC fit are very similar except that the zero-deviation diameter is the inscribed circle, and all deviations are positive.

2. *Workpiece Errors*

In this abstract we address mainly errors of form in the workpiece. That is, how does the shape of the feature (a subset of the workpiece surface) being measured differ from the ideal geometric element to which it is fit. Errors in the form of the feature may influence significantly the size calculated for the feature. Measurements of two artifacts are described in this abstract: an XX-class ring gage and a machined aluminum testpiece (or puck), each with an internal bore of about one inch in diameter. The ring gage will not have errors of form that we can distinguish from the uncertainty of our measuring machine and method, while the aluminum puck has form errors that we can easily measure. The actual form of the puck, determined with a Mahr MFU7 roundness machine and correlated to the CMM data, is shown in Figure 3. The puck provides an interesting example case, because the measuring system and the workpiece both exhibit distinct three-lobe patterns of errors, and the interaction of these errors depends upon the "phase relationship" of these patterns.

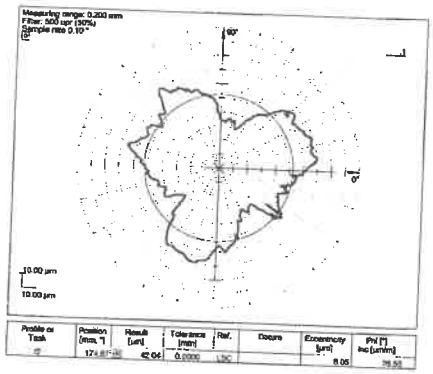

Roundness machine results

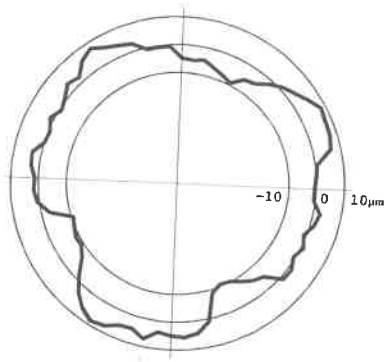

CMM results

Figure 3: Actual form error of an aluminum testpiece (the "puck").

3. *Interaction of errors*

We assume that the errors of the CMM and the workpiece are independent and additive. This is reasonable on a point-by-point case, but the introduction of fitting algorithms masks this property. For example, if the measuring system and the workpiece each introduce 20 μm of radial error, the resulting data *may or may not* show 40 μm of error. From the data summarized in Table 1 we can infer from the "long stylus" case that this particular combination of two ~20 μm error sources results in a residual radial error of less than 30 μm.

Table 1: Influence of systematic measuring errors on reported size and form of artifacts.

Probe Setup		Algorithm(s)	Residual Error (range of radii, or circularity / 2)	Random Point Error (average std. dev. of individual points)	Fitted Diameter
XX Ring Gage	Short Stylus	Least Squares	2.5 μm	0.49 μm	25.3983 mm
		Maximum Inscribed	3.0 μm	0.56 μm	25.3951 mm
	Medium Stylus	Least Squares	9.9 μm	0.76 μm	25.3982 mm
		Maximum Inscribed	10.3 μm	0.86 μm	25.3907 mm
	Long Stylus	Least Squares	20.2 μm	1.08 μm	25.3979 mm
		Maximum Inscribed	20.4 μm	1.22 μm	25.3839 mm
Aluminum "Puck"	Short Stylus	Least Squares	20.5 μm	0.48 μm	25.7432 mm
		Maximum Inscribed	20.7 μm	0.75 μm	25.7226 mm
	Medium Stylus	Least Squares	22.2 μm	0.62 μm	25.7418 mm
		Maximum Inscribed	22.3 μm	0.78 μm	25.7208 mm
	Long Stylus	Least Squares	28.3 μm	0.68 μm	25.7424 mm
		Maximum Inscribed	26.9 μm	1.12 μm	25.7197 mm

Both artifacts were measured several times with each probe setup. The *Residual Error* column shows the range of the average radii for the point measurements. The *Random Point Error* column shows the standard deviation of the points' radii averaged over all (72) of the sample point locations.

4. *Influence of algorithm choice*

While the algorithm choice for feature evaluation is a frequent subject of discussion, the use of different algorithms for the calibration is usually ignored. While the popular LS algorithm provides robust, repeatable results, the influence of this choice on later inspection routines can be significant. In this section, we focus on the computed diameter as a function of the feature evaluation algorithm.

If the same algorithm and sampling strategy are used for calibration and measurement, we expect there to be a minimal bias in the measurement results due to the repeatability of errors in the measuring system. Because the LS algorithm was used for calibration, the LSC diameters calculated for our artifacts show little variation, as seen in Figure 4.

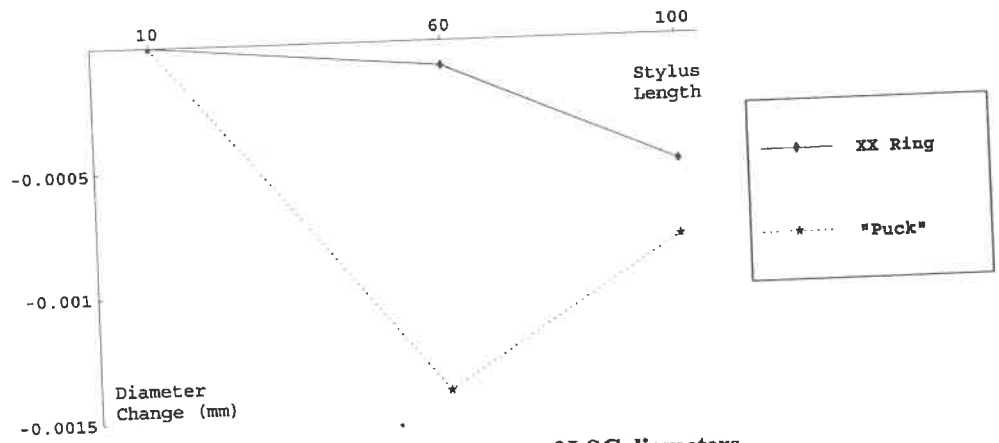

Figure 4: Comparison of LSC diameters.

However, if we use different algorithms for calibration and measurement, there can be a significant bias in the resulting diameter. In Figure 5 below, we see the effects of "mixing" an LS calibration routine with an MI feature evaluation algorithm. The ring gage data show the under-estimation of the fitted internal diameter becoming more severe as the stylus length increases. The diameter values calculated for the puck are far less sensitive to the change in stylus length (and the associated probing errors). The bias between the LS and MI diameters for the puck is due entirely to the algorithms, as the same measurement points are used in the calculations.

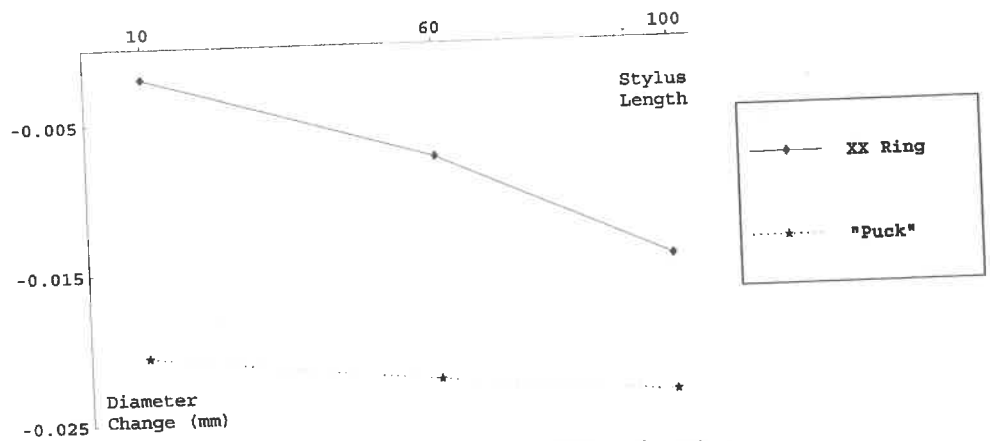

Figure 5: Comparison of MIC diameters.

5. *Conclusions*

The primary objective of this short abstract is to call attention to the importance of the probe calibration fitting algorithm. The use of different algorithms for calibrating and measuring may have adverse effects, but the uncertainty and bias introduced by the algorithm choice must be identified for each case. In Figure 5 we see two different effects due to the differences between LSC and MIC for feature diameter calculation. The MIC ring gage diameters are affected significantly by measurement errors, which may lead us to choose the LSC algorithm for estimating the diameter of the gage. The LSC algorithm introduces a significant bias if we wish to find the "fit diameter" of the puck and the MIC algorithm may be preferred to correlate CMM measurements to size as described in the Y14.5M standard, or to estimate the "true geometric counterpart" of this feature.

A novel practical approach to cylindricity evaluation: An experimental report *

G. Singh,† O. Devillers,‡ and F. P. Preparata§

Evaluating cylindricity is a very important application in metrology, since cylindrical surfaces are ubiquitous in industrial machining. Cylindricity is normally evaluated by measuring radial form (in sections normal to the nominal axis), or axial form (along nominal generatrices), or a combination of the two. In this note, we focus on radial form measurements. Reliable measures of the quality of a cylindrical surface therefore is of paramount importance, essentially to avoid overly conservative criteria that may lead to costly unnecessary rejection of surfaces perfectly complying with specifications. *Cylindricity*, a single parameter with the physical dimension of a length, is this measure of quality.

The definition of cylindricity that best conforms with the standards ISO 1101 and DIN 7184 derives from the notion of *minimum zone cylinder*, i.e., the region of space contained between two co-axial cylinders with minimum radial separation containing all the data points. Cylindricity is the radial separation of a minimum zone cylinder. Unfortunately, the construction of the zone cylinder is a much more difficult geometric problem than the better understood construction of the zone circle in two dimensions. There are several reasons for the mentioned difficulty. The minimum zone cylinder is, in general, defined by six points, but there may be several 6-point subsets of the point set yielding minimum zone cylinders; in addition, given six points, it can be shown that constructing the zone cylinder through these points involves the solution of a system of six degree-4 equations, a task requiring

* *This work was partially supported by the U.S. Army Research Office under grant DAAH04-96-1-0013.*

†Mahr Federal, Providence, RI

‡INRIA, BP93, 06902 Sophia-Antipolis, France.

§Computer Science Department, Brown University, Providence, RI 02912, USA

sophisticated algebraic geometry tools. Due to this substantial geometric and algorithmic difficulty, it is obviously a frequent metrological practice to resort to simpler, but less effective, surrogates, such as reduction of cylindricity to circularity, or optimizations based on least square fits. Reductions to circularity involve an estimate of the axis, projection of all data points on a plane normal to this axis, and the computation of the minimum zone-circle in this plane. Alternatively, the axis is estimated as the least-square-fit of the centers of a set of normal sections, and the optimization aims at obtaining a "small" perturbation of this axis which minimizes radial separation [Ch85]. Noteworthy is an iterative approximation method [CF95], which shares with our approach the use of linear programming but is based on basically different criteria. The same paper contains a good survey of the literature on the subject.

Recently a new method has been proposed [DP00] that, as a number of previous optimization approaches, avoids the direct construction of the zone cylinder of a point set, and approximates it with controlled accuracy through a computationally very efficient process. The approach is based on the following idea. A cylinder of near-vertical axis is replaced (approximated) by a one-sheet hyperboloid with the same axis and such that its sections in planes normal to the z-axis are circles. Correspondingly, a zone cylinder is replaced by a zone hyperboloid, analogously defined. Clearly, the cylinder and its associated hyperboloid are two distinct geometric objects, but if their common axis is brought to coincide with the z-axis by a rigid motion, the hyperboloid tends to a cylinder and in fact cylinder and associated hyperboloid become provably the same object. This property is the key to the approach, since, rather than the set of zone cylinders, we perform the much easier search of the set of zone hyperboloids. The latter task is a computationally much simpler, since it is implemented as a linear programming in six dimensions and runs in time nearly proportional to the size of the point set. Each measured point gives rise to two linear constraints, corresponding to lying on the correct sides of the inscribed and the circumscribed hyperboloids, and the objective function is the radial separation. Since the LP-optimization also returns the axis of the zone hyperboloid (as an offset with respect to the origin and a direction), the values of the axis parameters are an excellent measure of the quality of the approximation.

As it normally happens, the axis of the minimimum zone cylinder is not vertical, because both of the imperfections of the artifact being evaluated and of the misalignment of the measuring apparatus. Our objective is the

determination of this axis. Therefore, we take the axis of the computed zone hyperboloid as a first approximation to it, and subject the point set to a rigid motion bringing the z-axis to coincide with the axis of the hyperboloid. By this coordinate transformation the (unknown) axis of the minimum zone cylinder is brought closer to the z-axis than it was initially. Iterating this process, we can approach the cylinder axis with excellent precision. Typically, 2-3 iterations obtain a satisfactory solution of the original problem. The theory of the method was presented in detail in [DP00]; the purpose of this paper is to corroborate the theory with actual metrological experiments on physical objects.

We shall refer to the common metrological set-up where the test object is positioned with nominally vertical axis on a rotating platform and a probe takes samples in chosen horizontal planes. For each specimen, the measurement data consist of 256 angularly evenly spaced points on three evenly spaced horizontal slices. Each data point is measured using an off-the-shelf commercial instrument, which yields a triplet (R, θ, z), of radius, angle, and elevation. This data, converted into cartesian form constitutes the input to the LP-optimization. The axis information returned by the LP-algorithm is used to change the frame of reference (by identifying the obtained axis with the z-axis), and the procedure is iterated on the modified data set.

We have performed experiments on an large set of test parts, of which we shall report below results on the following typical examples:

1. part 1: a master disc of radiurs 0.625in, a high precision object.
2. part 2: an aluminum bar stock, a very coarse object.
3. part 3: a brass bushing, a medium quality object damaged by two grooves on opposite sides.
4. part 4: a cylindrical spacer, slightly tapered in the middle section.

For each of these four objects we report below the following data:. the nominal radius (in inches), the cylindricity as the deviation from the least-square cylinder (LS-method), the cylindricity as the minimum-zone optimization starting from a least-square axis (LS-MZC), the cylindricity as obtained by the hyperboloid method (Hyperb.), the number of performed iterations, and a measure of quality expressed the the "relative offset", which is defined as the sum of the offsets of the centers at the three section normalized by the

radius. Cylindricities are expressed in μinches.

object	radius	LS – method	LS – MZC	Hyperb.	iterat.	offset
part 1	0.625	33.42	21.41	15.39	4	2.4×10^{-6}
part 2	2.00	3035	2463	2066	4	0
part 3	1.50	41756	36423	26128	3	7.2×10^{-11}
part 4	1.50	68.31	58.87	52.22	2	2.1×10^{-6}

References

[CF95] K. Carr and P. Ferreira, Verification of form tolerances Part II: Cylindricity and straightness of a median line, *Precision Engineering*,17,2,145-155;1995.

[Ch85] D.G. Chetwynd, Application of linear programming to engineering metrology, *Proc. Inst. Mech. Eng*, 199, 93-100; 1985.

[DP00] O. Devillers and F.P.Preparata, Evaluating the cylindricity of a nominally cylindrical point set, *Symposium on Discrete Algorithms*, January 9-11, 2000.

An Artificial Intelligent Measuring-Sequence Path Planning for CMM

Wu Yongqing Liu Shugui Zhang Guoxiong
(College of Precision Instruments and Opto-Electronics Engineering, Tianjin University, P.R.China)

1. Introduction

Although Coordinate Measuring Machine (CMM) have a considerable level of automation over traditional methods, they still have to be manually operated to conduct the first part inspection, in case of an on-line inspection planning. And the DMIS (Dimensional Measurement Interface Specification) program provides a neutral interchange format between the CAD of systems and the dimensional measuring equipment. In case of an off-line inspection planning, the whole procedure can be simulated by the CAD software. In order to achieve a higher level of automation, CAD-directed inspection planning is essential. In the CMM inspection path planning, optimization of the inspection path plays a major role in increasing the throughput of the CMM. The path planning for a CMM is similar to that of a Cartesian robot path planning, the goal being to generate an optimum collision-free path. In the inspection process, the CMM probe has to move in the workspace to touch different areas of the part for measuring purposes. Thus, the planning of measuring sequence becomes vital, because the efficiency of inspection is determined by the distance probe traveling.

2. Variation of factors affecting the total measurement time

Optimizing measuring sequence is a problem of sequence arrangement. Its purpose is to obtain the shortest measuring time possible. It must first consider all factors that affect the measurement time during the entire measurement process. The time required for measurement by a CMM includes:

1. Time for workpiece assembly and probe correction;
2. Time for the designation of the reference coordinate system;
3. Time for the CMM probe movement;
4. Time for rotating the probe angle when designating the probe direction after it moves to each measurement point positions;
5. Time for measurement test;
6. Time for movement from the original measuring point to the initial measurement position, and from the final measurement point back to the original measuring point.

3. Basic Assumptions of the Measuring Sequence

Among the six aforementioned factors, certain assumptions are made for certain factors to ensure a collision-

free condition, as described below: T_s, T_{bac}, only occupying one action or movement time. T_{ref}, the reference coordinate system is designated only once. T_{pro}, according to past measurement experience, it is best to avoid changing the probe during the measurement process, which not only increases the measurement time, but also affects the precision. In this paper, the measurement path planning was completed by a single probe. Thus, T_{pro}=0.

4. Basic Approach

The TSP demands that one find the best order among the n cities to be visited that minimizes the total distance traveled. Here, a cost function, which is dependent on the order of a finite number of objects, has to be minimized. In this analogy, each measured point would be viewed as a "stop" along the path of inspection. The complexity of the requisite scheduling analysis would increase on the order of $(n-1)!$, where n is the number of the measured points. When the weights is determined in the above analysis, the distance between two measured points seems to be one and only considerable factor.

The application of a connectionist model to provide rapid solutions to the TSP problem would be desirable. However, the large number of potential solutions makes the training of more traditional neural networks, such as standard back propagation, a formidable task. Fortunately, an intelligent algorithm for solving TSPs already exists in the form of Hopfield networks (Fig.1). Hopfield networks are inherently recurrent because of the feedback connection of network outputs to input vectors. The recurrent network ability to function as an associative memory makes possible the selection of an optimal solution given incomplete data.

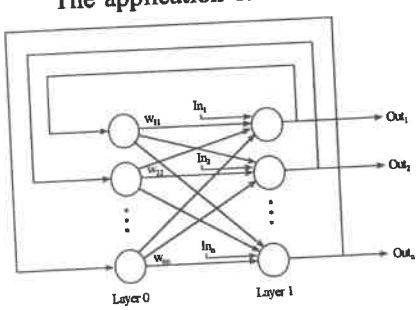

Fig.1 Typical Hopfield network

For a stable network, each iteration diminishes the change in the output until a steady state is achieved. Unstable networks, however, iterate endlessly and are thus treated as chaotic systems. Recurrent networks are stable if the weight matrix is symmetrical with zeros on the main diagonal. If one denotes the elements of the weight matrix by w_{ij}, where $i=1,\cdots,n$ stands for the measured point and $j=1,\cdots,n$ indicates the point position in the measuring sequence, such a network would have an associated Liapunov function of the form:

$$E=-\frac{1}{2}\sum_{i}\sum_{j\neq i}w_{ij}x_i x_j+\sum_{i}x_i T_i \tag{1}$$

Where E is network energy; x_i is the output of the i th neuron, and T is the threshold value. The expression of the cost function to be minimized in the form of the Liapunov function ensures network stability, as any change in the state of a neuron will either reduce the network energy or maintain its current value.

It is seen easily that constructing the energy function is the key to apply the neural network technology. The entire inspection process must be mapped onto the computational network by expressing the associated cost function in the form of the Liapunov function. In this application, the energy function must satisfy two requirements: (1) it must be low for only those solutions that produce a single neuron activation (each measured point can only be inspected once) and (2) it must favor solutions that satisfy system constrains (the shortest path). The first

requirement is satisfied by an energy function of the form:

$$E_1 = \frac{A}{2}\sum_{x=1}^{n}\sum_{i=1}^{n}\sum_{\substack{j\neq i\\ j\in[1,n]}}^{n} V_{xi}V_{xj} + \frac{B}{2}\sum_{i=1}^{n}\sum_{x=1}^{n}\sum_{\substack{y\neq x\\ y\in[1,n]}}^{n} V_{xi}V_{yi} + \frac{C}{2}\left(\sum_{x=1}^{n}\sum_{i=1}^{n} V_{xi} - n\right) \tag{2}$$

where A, B, and C are Lagrange multipliers, and V_{xi} indicates the ith position of the xth point in the inspection sequence. The resulting set of rules is as follows. The first term is zero if, and only if, each point is inspected only once. The second term is zero if, and only if, that position in the sequence is not occupied by another measured point. The third term is zero if, and only if, that the sum of the measured points is n. Otherwise, this allows the second requirement, when only considering the length of inspection path, to be satisfied by adding an additional term to the energy function in the following fashion:

$$E_2 = \frac{1}{2}D\sum_{x}\sum_{y\neq x}\sum_{i} d_{xy}V_{xi}(V_{y,i+1} + V_{y,i-1}) \tag{3}$$

where d_{xy} is the distance between the xth and yth points.

5. Application

In actual inspection, there are less than ten measured points in every measured surface in general way; several points, even exceeding one hundred points, are included in the entire workpiece. Based on the above method, the shortest path in the inspection can be determined, however, the calculation of Hopfield neural network is computationally expensive because of the excessive measured points as the network inputs. Otherwise, due to the requirement of DMIS, the element surfaces of workpiece are thought as the basic unit in the measuring procedure. It is needed that a new cost energy function is constructed. However, the function is a weighted, nonlinear combination of system constraint such as the aforementioned factors. So the difficulty of computation is further increased. In order to make the method feasible, its improvement can be developed to simplify the computational complexity. Thus, in the original structure of Hopfield neural network, according to the different conditions of workpieces, the problem of path planning can be divided into two parts: the sequence of the measured surfaces and the sequence points in every measured surface.

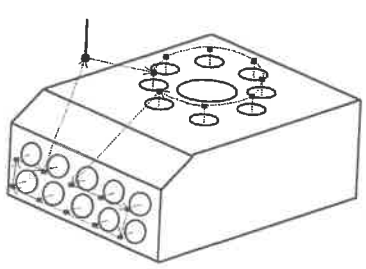

Fig.2 Example of a sample workpiece

To the surfaces included in some workpieces, as shown in Fig.2, it is relatively simple to determine the sequence of the measured points in them. Thus, the considerable attention should be paid to the sequence of the measured surfaces. Their sequence can be determined by Hopfield neural network, when the measured surfaces chosen as the inputs of the network. In this method, the distance between two measured surfaces is thought as the shortest distance between two measured points in the two different measured surfaces respectively. Otherwise, when the sequence of the measured surfaces is determined, that is, the starting and ending points in the sequence of the measured points in their surface are determined, the arrangement of the measured points in their surface can be solved by the nearest neighbor method. The nearest neighbor method can usually be applied to certain points in a space with a definite

staring point. The position of the point closest to the present planning point (as present initial measurement point) is used as the next sequence point planned. However, according to the method, the final point in the sequence may not be the ending point. In order to solve the problem in the nearest neighbor method, the path is found from the starting point in the positive direction; at the same time, the another path is also found from the ending point in the negative direction until all measured points are marked. In the end, the sequences of the measured surfaces and the measured points in every surface can be combined into an integrated path.

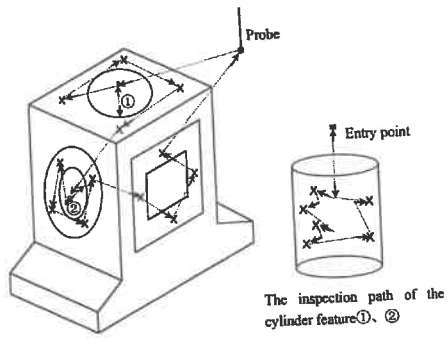

Fig.3 Example of a housing case

On the other hand, some measured surfaces of workpiece might be intersected mutually, for example workpiece shown as in Fig.3, unlike the previous condition that every surface is separate and independent. In the condition, the measured points in their surface should be considered firstly. Based on Hopfield neural network, the sequence of the measured points in every measured surface can be determined when these points chosen as the inputs of the network. The result, the sequence of the measured points, forms a ringed structure. According to the nearest neighbor method, the position of the point closest to the initial position of the probe can be found, and the point is thought as the starting point of its surface. Then the ending point can also be determined with the formed ringed structure. Repeat the process until all measured surfaces are marked. Finally the inspection path of the entire workpiece is obtained.

6. Conclusion

To eliminate human interaction in determining the path planning in inspection, a heuristic approach utilizing recurrent neural networks is proposed. Based on the Hopfield neural network method, a near optimal solution to the path planning, if not optimal, can be reached. Although this list of the cost parameters is by no means complete, it serves to sufficiently illustrate the application of TSP to inspection task scheduling. At the same time, for the reason of the element surface treated as basic unit in DMIS, the new cost equation might be determined hardly to plan the inspection sequence of the element surface. However, because of the excessive measured points chosen the inputs of networks and limitation of network structure, the advantage of Hopfield neural networks could be taken reasonably. From the practical view, further discussion about the neural network method is given. The entire neural network is divided into several small networks, and an improved nearest neighbor method is applied. Consequently, the computational complexity of the algorithm to path planning is decreased greatly.

References

1. A.C.Lee, D.P.Chen and C.L.Lin, "A CAD/CAM system from 3D coordinate measuring data", The First International Conference on Automation Technology, Taipei, Taiwan, pp.479-485, 1988.
2. K.Lau, N.Duffie and J.Bollinger, "Automatic contour measurement for three-dimensional geometry", SME, Journal of Manufacturing Systems, 66(1), pp.535-541, 1985.
3. Zong-Ching Lin and Chein-Chung Chen, "Measuring-Sequence Planning by the Nearest Neighbour Method and the Refinement Method", Int J Adv Manuf Technol 13:271-281, 1997.
4. Steven M.Ruegsegger, "Intelligent Scheduling Optimization Using a Rule-Based Artificial Neural Network", Proceedings-IEEE International Conference on Robotics and Automation, v.1, May, 16-20, 1998.

Investigation of Subsurface Damage of II-VI Semiconductors Using Photoluminescence

D. W. Hamby and D. A. Lucca

School of Mechanical and Aerospace Engineering
Oklahoma State University
Stillwater, OK 74078

1. Introduction

The ultraprecision finishing of II-VI semiconductors with minimized subsurface damage continues to be of significant interest. The need for ultra-fine finishing of the II-VI compound ZnO is driven by its role in the development of short wavelength light emitters, either as a substrate material for GaN based devices [1] or as the optically active material [2]. Subsurface damage resultant from wafer sawing, lapping and polishing is of particular importance in terms of its detrimental effect on device performance. The objective of the present work is to demonstrate the applicability of photoluminescence (PL) spectroscopy as a technique for the assessment of subsurface damage in polished II-VI bulk semiconductors. PL spectroscopy is a sensitive, non-destructive technique that can provide information on the type and distribution of defects and/or impurities in a semiconductor and has been used to examine the bulk quality of II-VI crystals [3]. In this work, (0001)-oriented ZnO was chemomechanically polished and the PL results were compared to as-grown and etched wafers. Low temperature (77 K) PL for an etched wafer was also measured and compared to the room temperature results.

2. Photoluminescence

In direct bandgap semiconductors, PL is the result of photo-excited electrons returning to their ground state and emitting photons characteristic of the material. PL has been used extensively to investigate optical properties and electronic band structure of semiconductors [4]. Because the band structure of a semiconductor is sensitive to the presence of defects and impurities, the PL response is altered according to the type and density of defects or impurities. Figure 1 shows a schematic representation of PL in a simplified energy level diagram of a typical direct bandgap semiconductor. In the figure, an incoming photon (with energy larger than the bandgap) is absorbed and as a result, an electron in the valence band is excited into the conduction band (a and b). The photo-excited electron nonradiatively releases energy to the crystal until it reaches the bottom of the conduction band (c), where it recombines with a hole in the top of the valence band (d), resulting in the emission of a photon with energy equivalent to the bandgap energy, E_g (3.3 eV for ZnO) (e). The figure also illustrates the presence of an allowed energy level within the "forbidden" gap due to a defect within the crystal. The recombination of an electron and a hole associated with this particular defect would result in a photon with an energy of E_d. While defects or impurities in the crystal may result in new PL spectral peaks resultant from the recombination of electrons and holes at the defect [5], they may also introduce nonradiative mechanisms that do not result in photons (e.g., an Auger-type process). Such nonradiative mechanisms compete with the radiative luminescence and effectively lower the relative intensity of the spectral peaks. As a result, the spectral content of PL measurements combined with the overall PL intensity can provide important information regarding the crystalline quality of the semiconductor [3]. The best resolution of PL spectra occurs at temperatures well below room temperature since lower temperatures reduce the thermal broadening of the photo-excited carriers. Cooling the semiconductor to 4 K (liquid He) reduces the thermal broadening from 25 meV at room temperature to <1 meV [6].

3. Experimental

We have designed, built and tested a system (Figure 2) that will enable the investigation of the PL spectral response of II-VI materials. Our goal is to use the spectrally-resolved PL to assist in developing a basic understanding of the subsurface damage that results from ultra-fine finishing processes. The PL is

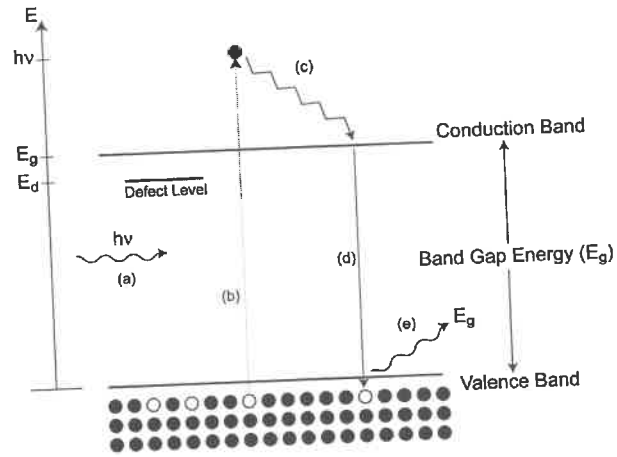

Figure 1. Electronic band structure of a typical direct bandgap semiconductor illustrating: (a) and (b) photo-excitation of electron into the conduction band, (c) nonradiative decay of electron to the bottom of the conduction band, (d) and (e) radiative decay of electron across the "forbidden" bandgap resulting in the emission of a photon of energy E_g. Also shown is an allowed energy level within the bandgap due to a defect in the crystal (Defect Level).

excited with a cw Ar^+ laser, capable of 250 mW output power at 351.1 nm. The spectra are analyzed using a 0.5 m monochromator with a 2400 g/mm holographic diffraction grating blazed at 400 nm. The monochromator is equipped with a LN_2 cooled 1024x128 (26.6 mm x 3.3 mm) CCD array for the measurement of both the UV and visible spectral response and a LN_2 cooled InGaAs single channel detector for measurement of IR spectral response. Using wavelength selective optics, the 351.1 nm and 351.4 nm emission lines (TEM_{00} mode) from the laser are isolated as the excitation wavelengths. The output power of the laser is 125 mW and the beam is focused to a spot size of 100-200 µm. The beam is passed through a set of color filters to reject the plasma lines associated with the spontaneous Ar^+ emission. Any scattered light from the sample surface is also filtered using a sharp cut-off glass filter prior to entering the monochromator. The spectral resolution of the detection system (monochromator with 2400 g/mm grating and CCD array) is computed to be 0.06 nm. For low temperature studies, the sample is mounted on a cold finger in a continuous flow liquid He cryostat. The temperature of the cold finger can be varied from 4 K to 300 K using an autotuning temperature controller.

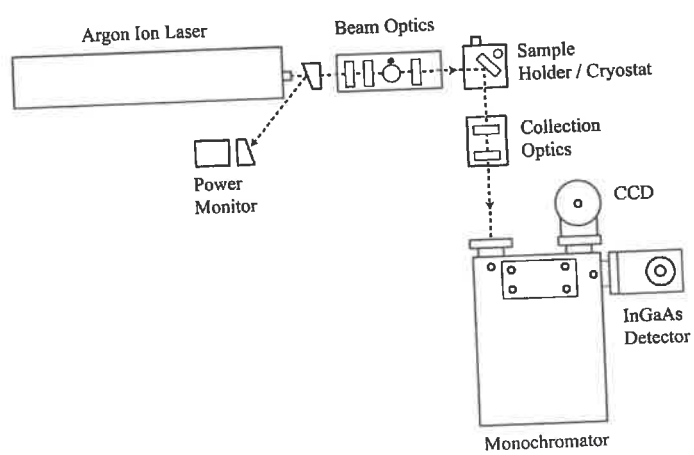

Figure 2. Schematic of photoluminescence system.

We have performed initial room temperature experiments on as-grown, etched and chemomechanically polished single crystal hexagonal (wurtzite) ZnO grown by the seeded chemical vapor transport (SCVT) method. All experiments were performed on the (0001) Zn-terminated face. A set of four wafers of nominal dimensions 10 x 10 x 0.45 mm were prepared on both sides by first lapping and then chemomechanical polishing. Lapping was achieved using a commercial lapping machine with a cast iron wheel and a 9 μm Al_2O_3/de-ionized H_2O slurry resulting in 25 μm of material removal. This was followed by chemomechanically polishing the surface using a commercial polishing machine and a slurry of a 1:8 ratio of sodium hypochlorite:colloidal silica (9.1 pH). Approximately 60 μm of material was removed under low loading conditions of 1.7 x 10^{-2} MPa. Two of the wafers were then "relief-etched" using a 5% trifluoroacetic acid/de-ionized H_2O solution at 95-100 °C for 2 minutes to remove any polishing damage and provide a measure of original crystal quality. The results were then compared to the PL response of an as-grown crystal. A preliminary comparison was also made between room temperature and low temperature PL of an etched crystal.

4. Results

Figure 3 shows room temperature PL for as-grown, etched and polished ZnO and low temperature PL for an etched surface (inset). From the room temperature PL spectra of the polished surfaces it was found that there is a decrease in the mean integrated intensity as compared to both the relief-etched material and the as-grown sample. The decreased intensity of the polished surface versus that of the as-grown material points to the presence of defects not found in the as-grown material. The observed higher PL intensity of the etched crystal versus the as-grown sample suggests that chemomechanical polishing and subsequent etching may have reduced or eliminated near surface defects and/or residual stresses present in the as-grown crystal. Each of the measured room temperature PL spectra was found to contain an intense near band edge (NBE) peak at 380 nm. The PL spectra from the etched samples contained an additional peak at 396 nm and a weak, broad peak at about 512 nm, whereas the polished and as-grown samples showed no peak at 396 nm and no significant peak at 512 nm. Although the origin of the peak at 396 nm is unknown at present, one plausible explanation may be the emission of photons due to exciton-exciton collision [2]. The peak at 512 nm, commonly referred to as the green luminescent peak, has been widely

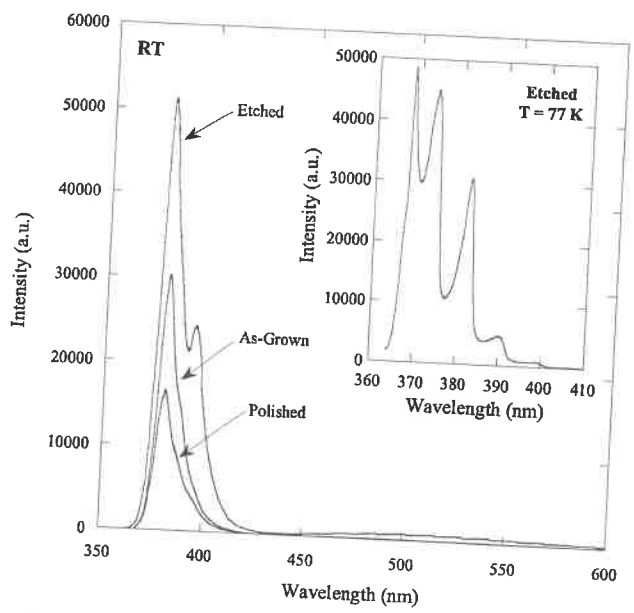

Figure 3. Room temperature PL spectra obtained for as-grown, etched and polished surfaces of the Zn-terminated face of (0001) ZnO. Inset: Low temperature (77 K) PL response for an etched surface.

reported in the literature [7] and is attributed to point defects in the crystal such as O vacancies. The ratio of the NBE peak to the green peak is one method for assessing the quality of the material. Typical ratios reported in the literature are on the order of 1-10:1 [4]. Our results show a ratio of about 150:1 for the polished samples at room temperature, indicating both high virgin material quality and minimal polishing damage. The inset shows an initial low temperature spectrum from an etched ZnO wafer. The individual peaks have not yet been identified, but additional peaks within the NBE band are clearly resolved demonstrating the reduction in thermal broadening.

5. Conclusions

Photoluminescence spectroscopy has been shown to be capable of assessing the subsurface damage of polished single crystal ZnO. The PL response of chemomechanically polished (0001)-oriented wafers was compared to both etched and as-grown samples. All samples exhibited a 380 nm peak, with the polished samples consistently having the lowest intensity. Our results indicate that the as-grown surface does not represent the best crystalline surface condition. Etched samples contain an additional peak at 396 nm that may be attributed to exciton-exciton collision. Further work is required for complete identification of both the room and low temperature peaks.

Acknowledgements

The authors thank G. Cantwell and B. Haskins of Eagle Picher and L. Robins of NIST for their significant help. Support by the National Science Foundation, Division of Design, Manufacture and Industrial Innovation is gratefully acknowledged. We thank Drs. L.A. Martin-Vega, D. Durham and K.P. Rajurkar for their interest and support. Funding by the Oklahoma Center for the Advancement of Science and Technology is also gratefully acknowledged.

References

[1] Hamdani, F., Botchkarev, A., Kim, W., Morkoc, H., Yeadon, M., Gibson, J.M., Tsen, S.-C.Y., Smith, D.J., Reynolds, D.C., Look, D.C., Evans, K., Litton, C.W., Mitchel, W.C., Hemenger, P., Optical Properties of GaN Grown on ZnO by Reactive Molecular Beam Epitaxy, *Applied Physics Letters*, **70**, 467-469 (1997).

[2] Bagnall, D.M., Chen, Y.F., Zhu, Z., Yao, T., Koyama, S., Shen, M.Y., Goto, T., Optically Pumped Lasing of ZnO at Room Temperature, *Applied Physics Letters*, **70**, 2230-2232 (1997).

[3] Vij, D.R., Singh, N., *Luminescence and Related Properties of II-VI Semiconductors*, Nova Science Publishers, New York, 1998.

[4] Srikant, V., Clarke, D.R., On the Optical Band Gap of Zinc Oxide, *Journal of Applied Physics*, **83**, 5447-5451 (1998).

[5] Swaminathan, V., Young, M.S., Caruso, R., Mechanical Damage Induced Luminescence Band in GaAs, *Journal of Applied Physics*, **57**, 1387-1390 (1985).

[6] Perkowitz, S., *Optical characterization of Semiconductors: Infrared, Raman, and Photoluminescence Spectroscopy*, Academic Press, London, 1993.

[7] Reynolds, D.C., Look, D.C., Jogai, B., Van Nostrand, J.E., Jones, R., Jenny, J., Source of the Yellow Luminescence Band in GaN Grown by Gas-Source Molecular Beam Epitaxy and the Green Luminescence Band in Single Crystal ZnO, *Solid State Communications*, **106**, 701-704 (1998).

Second Order Distortion of Grazing Incidence Interferometric Measurements

Paul D. Knight, Jr, Steven R. Patterson
Center for Precision Metrology
The University of North Carolina at Charlotte, Charlotte, NC

I. Introduction

A dual diffraction grating grazing incidence interferometer for the measurement of artifacts with cylindrical geometry has been developed. [1-4] Figure 1 shows a schematic of this type of interferometer. A cylindrical test artifact produces annular fringes that, to first order utilizing geometrical raytracing, result from deviations of the sample from a true cylinder. This interferometric configuration has previously measured axial sinusoidal artifacts for determination of instrument spatial frequency response.[5] Since a periodic structure that produces repetitive changes in phase, amplitude, or both of an impinging wavefront can be considered as a diffraction grating [6] the effect of diffraction on the resultant fringe pattern was examined. Because any surface profile can be deconvolved into its Fourier components, a surface can be modeled as a sum of individual sinusoidal profiles with each spatial frequency introducing some degree of diffraction upon an incident light beam. An investigation was undertaken to determine how a second order approximation of diffraction from an axially sinusoidal artifact influence profile reconstruction.

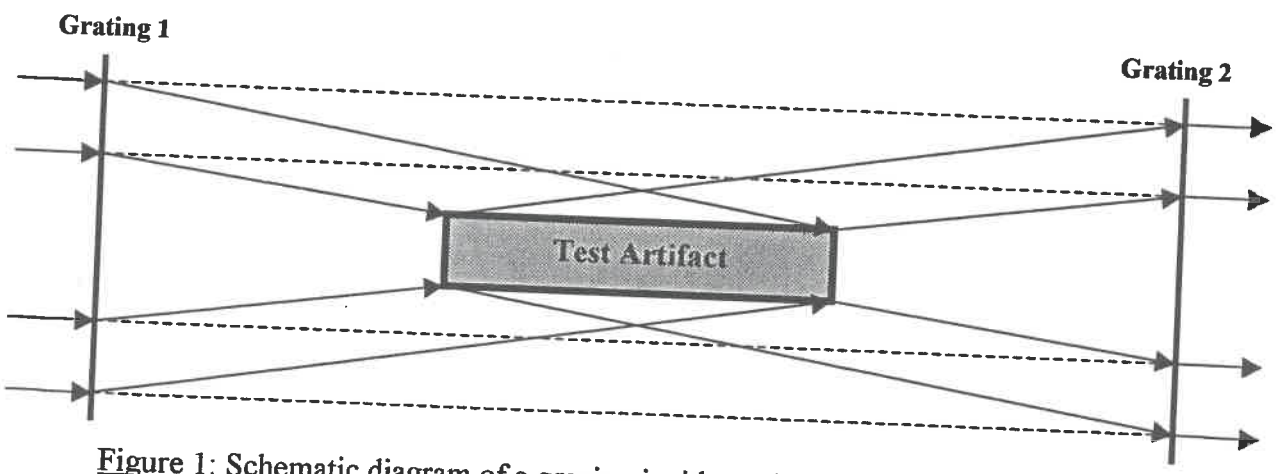

Figure 1: Schematic diagram of a grazing incidence interferometer for the measurement of cylindrical artifacts incorporating radial diffraction gratings as beamsplitters and combiners.

II. Theoretical Analysis

Assume a single frequency, axially sinusoidal artifact of amplitude m/2 and wavelength d, where d is smaller than the length of the part, z_0, is tested by a diffractive grazing incidence interferometer (the derivation is the same for both planar and rotational symmetry parts). An example of this is shown in Figure 2.

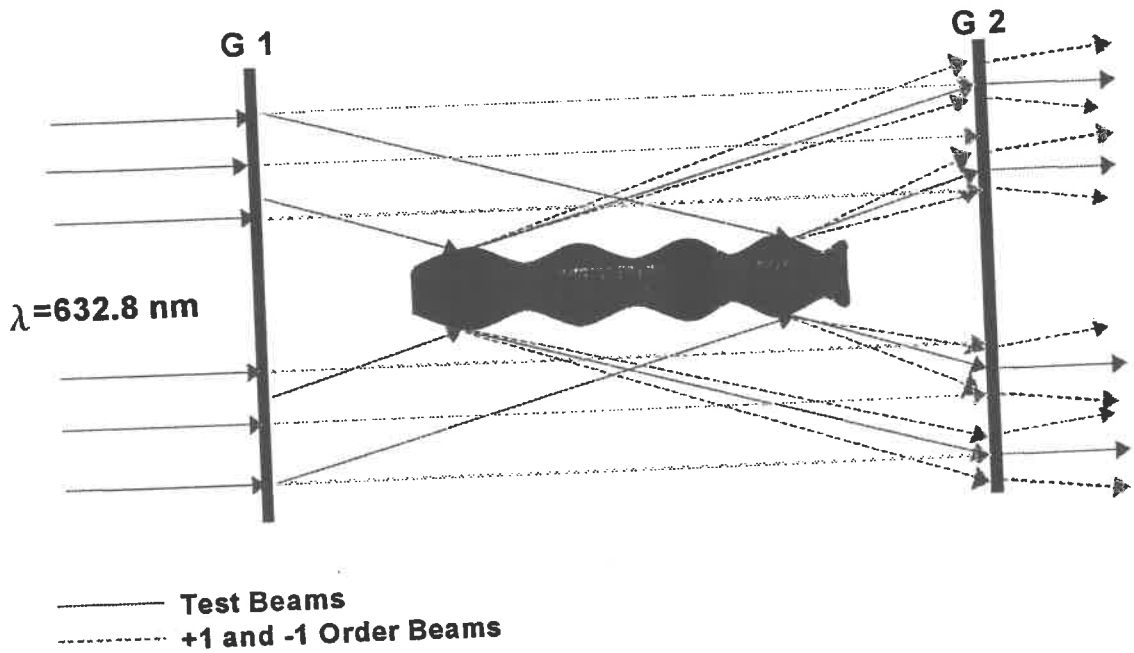

Figure 2: Diagram demonstrating diffraction from a cylindrical test artifact for a dual grating grazing incidence interferometer

The measurement artifact acts as a reflective phase grating on the impinging wavefront diffracting the reflected light. Employing plane wave diffraction theory [7], the field U as a function of position x on the second grating for a single frequency phase grating, keeping only the zeroth and first diffracted orders from the part and neglecting aperture effects, is

$$U(x) = J_0\left(\frac{m}{2}\right) + J_1\left(\frac{m}{2}\right)\left[e^{ikx \sin\theta_{-1}} - e^{ikx \sin\theta_{+1}}\right] \tag{1}$$

where J_0 and J_1 are the zeroth and first order Bessel functions [8] respectively, k is the wave number, and θ_{-1} and θ_{+1} are the -1 and $+1$ diffracted angles from the artifact with respect to the artifact surface normal respectively. Inserting the transformation $\tan\theta_0 = x / z$ and a first order Taylor series expansion of $\sin\theta_{-1}$ and $\sin\theta_{+1}$ into equation 1, the field as a function of the z axis along the length of the measurement artifact becomes

$$U(z) = J_0\left(\frac{m}{2}\right) + 2J_1\left(\frac{m}{2}\right) i \sin(k_d z) \tag{2}$$

with k_d the profile spatial frequency and z the axial position on the part. This form of U(z) reproduces the single frequency axial sinusoid on the measurement artifact and is the expected first order approximation of measuring the artifact by the grazing incidence interferometer. Inserting a second order Taylor series expansion of $\sin\theta_{-1}$ and $\sin\theta_{+1}$ into equation 1 and again transforming to z coordinates, the field now becomes

$$U(z) = J_0(\frac{m}{2}) + 2J_1(\frac{m}{2})\left[e^{ik_d(\frac{\alpha}{2})z}\right]\left[i\sin(k_d z)\right] \tag{3}$$

where α is the factor $g^2/d\lambda$ with g being the pitch of grating 1 and 2 (assuming symmetric grating pitch). To a second order approximation of $\sin\theta_{\pm 1}$, there is an enveloping function distorting the artifact profile reconstruction. For a part with a total length of 30 mm and an axial wavelength d of 3 mm with g being a nominal 8 microns and a λ of 0.6328 microns, αk_d is approximately $0.02k_d$. The enveloping function has a wavelength about 50 times longer than the part profile. Depending on the spatial frequency of the axial profile and the position of the sinusoid along the envelope (at a peak, valley, or midpoint), the amplitude of the axial profile is a dependent on the position of the enveloping function. Generally, if we include n diffractive orders from the part, the field of the reconstructed profile, transformed to part coordinates can be written as

$$U(z) = J_0(\frac{m}{2}) + \sum_{n=1}^{\infty} 2J_n(\frac{m}{2})\left[e^{ik_d(\frac{n^2\alpha}{2})z}\right]\left[i\sin(nk_d z)\right] \tag{4}$$

The enveloping wavelength is a function of n^2 but also a function of J_n which approaches zero very fast for small values of m/2. Values of m/2 are less than 0.01 for form measurements of many parts tests by this interferometer. For a surface profile that can be decomposed into p sinusoids along the direction of the optical axis, the field of the reconstructed profile normalized to the zeroth order, can be shown to be

$$U(z) = 1 + \sum_{p=1}^{p}\left[\frac{J_1(\frac{m_p}{2})}{J_0(\frac{m_p}{2})}\right]\left[e^{ik_p(\frac{\alpha_p}{2})z}\right]\left[2i\sin k_p z\right] \tag{5}$$

neglecting intermodulation and higher order terms that are much smaller than those listed in the equation above. Each of the previous calculations assumed the focus position of the imaging system is the position of the second grating. Transforming the focus position to a position z' between grating 1 and grating 2, the field along the axis of the part can be written as

$$U(z) = [e^{ikz'}]\{J_0(\frac{m}{2}) + 2J_1(\frac{m}{2})\left[e^{ik_d(\frac{\alpha}{2})(z-z'(1-\frac{\alpha^2}{4}))}\right]\left[i\sin(k_d(z - z'\frac{\alpha^2}{2})\right]\} \tag{6}$$

The focus shift has the effect of changing the position of the enveloping function by an amount $z'\alpha/2$ (to first order) and to a lesser extent changing the position of the axial sinusoid by a factor $z'\alpha^2/2$ (this effect is second order). The change in field for multiple frequency parts is analogous to the change for single frequency components. Since the position of the enveloping function can be changed, multiple measurements at different focal positions allow the calculation of the

enveloping function wavelength for each spatial frequency. This would enable correction for second order diffractive distortions of an artifact measurement.

III. Conclusions

Measurement of axially sinusoidal artifacts by a dual diffractive grating grazing incidence interferometer was theoretically described to a second order approximation. An enveloping function of the original profile was predicted. The phase of the focal plane was shown to change as a function of the imaged focal plane. A compensation method to correct for the second order distortion was presented. Future work involves verifying the existence of the second order enveloping function and the ability to change its position by varying the imaged focal plane.

IV. References

1. Dresel, T., Schwider, J., Wehrhaln, A., and Babin, S., "Grazing incidence interferometry applied to the measurement of cylindrical surfaces," *Opt. Eng.*, **34**, 3531-3535 (1995).
2. ATP Project Brief 95-01-0022, "Non-contact optical metrology of complex surface forms for precision industrial manufacturing," General Competition (July 1995).
3. Knight, P. D. and Patterson, S. R., "Repeatability and calibration of a grazing incidence cylindrical interferometer," *Proceedings of the ASPE*, **16**, 106-109 (1997).
4. Lindlein, N., Schreiner, R., Brinkmann, S., Dresel, T., and Schwider, J., "Axicon-type test interferometer for cylindrical surfaces: systematic error assessment," *Appl. Opt.*, **36** (13), 2791-2795 (1997).
5. Knight, P. D. and Patterson, S. R., "Sensitivity Analysis of a Cylindrical Interferometer," *Proceedings of the ASPE*, **20**, 436-9 (1999).
6. Hecht, E., *Optics*, Addison-Wesley, Reading, MA, 424-434 (1987).
7. Rayleigh, L., "On the theory of optical images, with special references to the microscope," Phil. Mag., (5) 42:167 (1896).
8. Abramowitz, M. and Stegun, I., Eds., Handbook of Mathematical Functions, U. S. Department of Commerce, National Bureau of Standards, Washington, DC (1968).

Compensation of Phase Change upon Reflection in White Light Interferometry

Min-Cheol Park and Seung-Woo Kim
Korea Advanced Institute of Science and Technology
Department of Mechanical Engineering
Science Town, Taejon, 305-701, South Korea

In this paper we presents a compensation method of the phase change upon reflection with a particular aim of measuring step heights using white light interferometry. Figure 1 shows the geometry of the Michelson interferometer being considered in this investigation, where the variable z denotes the relative displacement between the objective and target surface during scanning. The phase change upon reflection ϕ depends upon surface materials, and even for a given material, its value varies with the wavelength λ and incident angle of rays θ within the numerical aperture (NA) of the objective [1]. In this investigation, for simplicity of analysis, the θ-dependency of the phase change is not considered by assuming the NA value of the objective to be used is small less than 0.15, which is usually the case in the Michelson interferometer with low magnification. The phase change is consequently regarded to be dependent upon the wavelength only, i.e., $\phi=\phi(k)$ where k is the wavenumber, i.e., $k=2\pi/\lambda$.

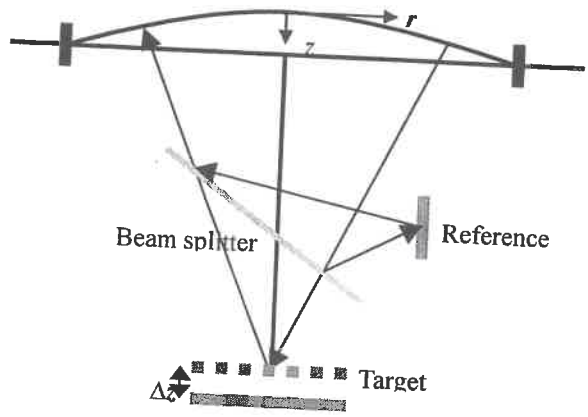

Figure 1. Schematic of the Michelson interferometer.

White light interferograms may generally be thought of incoherent superposition of interferences occurring on individual monochromatic rays comprising the light source. This reasoning leads to the general expression of the intensity distribution of

$$I(z) = I_0 \int_{k_0-\Delta k/2}^{k_0+\Delta k/2} [1+\gamma(k)\cos(2k(z-z_0)+\phi(k))]F(k)dk \qquad (1)$$

where I_0 is the mean intensity; z_0 the surface height; $\gamma(k)$ the modulation; and $F(k)$ denotes the spectral distribution of the light source centered at k_0 with a spectral width of Δk. The phase term of the integrand of Equation (1) is extracted as

$$\Phi(k) = \phi(k) + 2k(z-z_0) \qquad (2)$$

where $\phi(k)$ represents the variation of phase change in the spectral frequency domain for a given target material. If $\phi(k)$ is constant, the slope of $\Phi(k)$, i.e. $d\Phi(k)/dk$, becomes exactly twice the height variance z-z_0. For most metal surfaces $\phi(k)$ varies with k as some representative curves computed in electromagnetic theory are shown

in Figure 2 [4]. The variation of $\phi(k)$ is generally not drastic in the frequency region of visible light [4], thus it may be approximated as

$$\phi(k) \cong \phi(k_0) + (k - k_0)\frac{d\phi}{dk}. \qquad (3)$$

This first-order estimate of $\phi(k)$ is substituted into Equation (2) to allow the phase term to be written as

$$\Phi(k) \cong \phi(k_0) - k_0 \frac{d\phi}{dk} + 2k\left(z - \left(z_0 - \frac{1}{2}\frac{d\phi}{dk}\right)\right). \qquad (4)$$

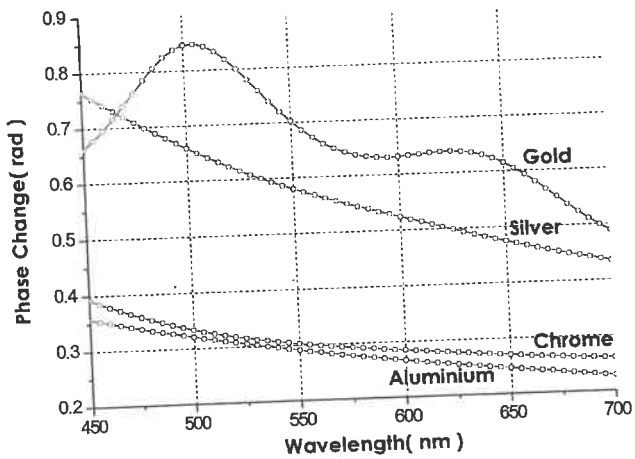

Figure 2. Variation of phase change upon reflectio with wavelength for different metals.

The intensity distribution of Equation (1) is then worked out by substituting Equation (4) and subsequently performing the integral operation concerned. In doing that, the modulation $\gamma(k)$ and the spectral distribution of the light source $F(k)$ are presumed to undergo no radical variations with k as previously assumed for $\phi(k)$. Finally the intensity distribution is obtained in the form of

$$I(z) = g(z - z_m)\cos(2k_0(z - z_m) + \phi_m) \qquad (5)$$

where $g(z\text{-}z_m)$ is referred to as the visibility function, ϕ_m is the mean of the phase change and z_m is the envelope peak of white light interferogram [1]. The background intensity I_0 in Equation (1) is omitted in Equation (5) since it requires no further considerations. The above result indicates that there are two different peaks that provide mathematical convenience in locating the relative position of the resulting fringe pattern. One is the so-called envelope peak located at $z=z_m$ where $g(z\text{-}z_m)$ reaches its crest, while the other is the fringe peak $z=z_m-\phi_m/2k_0$ where the harmonic variation of fringes hits the maximum. Currently available fringe processing algorithms of 3-D mapping determine the relative locations of the sampled interferograms by detecting the envelope peak [5,6] and/or the fringe peak [7,8]. Even though the two peaks do not precisely coincide with the true height z_0, no measurement error occurs in profiling target surfaces of uniform material as long as z_m and ϕ_m remain constant. However, this is not the case when profiling composite targets comprised of dissimilar materials whose optical properties are not known.

Equation (4) depicts that there is an offset between the envelope peak z_m and the true height z_0, which amounts to $\frac{1}{2}\frac{d\phi}{dk}$, i.e.,

$$z_m = z_0 - \frac{1}{2}\frac{d\phi}{dk} = z_0 - z_\phi. \qquad (6)$$

This consequence points out that the surface height z_m determined from the peak of envelope function $g(z)$

deviates from its true height z_o by the amount z_ϕ. Accordingly, the numerical value of z_ϕ needs be identified for compensation, which may be obtained by elaborate experimental work or be computed by using experimental data of phase changes available from optical handbooks [4]. It would however be practical and even more reliable if the effect of z_ϕ were corrected through a sensible strategy of compensation without actual identifying process of z_ϕ.

The compensation proposed in this investigation is based upon the fact that most 3-D surface mapping instruments of white light interferometry are also capable of performing the quasi-monochromatic phase measuring interferometry simply by inserting spectral filters of narrow band with subsequent modification of PZT control. Let k_1 and k_2 be two different spectral frequencies of the filters prepared with the condition of $k_1 < k_2$. Then the procedure of compensation is explained through an example shown in Figure 3, which illustrates a step height made of material A on a substrate of material B. The first step is two separate measurements of monochromatic phase measuring interferometry performed against materials A and B, whose results are expressed as

$$h_1 = h - \frac{\phi_1^A - \phi_1^B}{k_1} \text{ and } \qquad h_2 = h - \frac{\phi_2^A - \phi_2^B}{k_2} \tag{7}$$

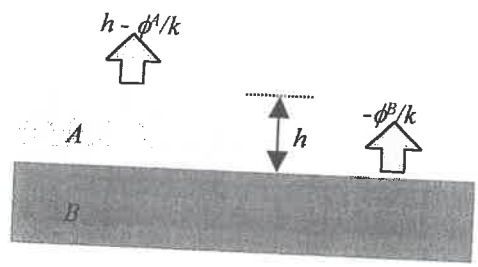

Figure 3. Step height made of dissimilar metallic materials.

where the superscripts A and B indicate the materials A and B, respectively. In addition, the subscripts 1 and 2 designate the spectral frequency k_1 and k_2, respectively. The measured heights h_1 and h_2 have different offsets from the true height h, which are not identified because the phase changes ϕ_1^A, ϕ_1^B, ϕ_2^A, and ϕ_2^B are not known. Now, the offset term z_ϕ of white light interferometry defined in Equation (6) may be approximated such as

$$z_\phi \equiv \frac{1}{2}\frac{d\phi}{dk} \cong \frac{1}{2}\frac{\phi_2 - \phi_1}{k_2 - k_1}. \tag{8}$$

Then, the second step is one measurement of white light interferometry without using the filters, whose measured height H is worked out such as

$$H = z_m^A - z_m^B = (z_0^A - z_0^B) - (z_\phi^A - z_\phi^B) = h - \frac{1}{2}\frac{(\phi_2^A - \phi_1^A) - (\phi_2^B - \phi_1^B)}{k_2 - k_1}. \tag{9}$$

The key idea of the compensation is that the offset term of white light interferometry expressed in Equation (9) is estimated from the measurement results of the quasi-monochromatic phase measuring interferometry. For this, Equation (7) may be converted into

$$\Delta h = h_2 - h_1 \cong -\frac{1}{k_c}[(\phi_2^A - \phi_1^A) - (\phi_2^B - \phi_1^B)] \tag{10}$$

in which the spectral frequencies frequency k_1 and k_2 are replaced with central frequency k_c for simplicity without introduction of significant errors. Finally, the true height h is determined by substituting Equation (10) into (9) such as

$$h = H - \frac{1}{2}\frac{k_c(h_2 - h_1)}{k_2 - k_1}. \tag{11}$$

where the true height h can be determined using only known and measured variables.

Table 1 demonstrates two representative experimental results that were obtained to verify the compensation algorithm of phase change described so far. Target #1 is a step height made of two dissimilar metals, which was in fact manufactured by VLSI Co. and subsequently certified by the National Institute of Standards and Technology to have a true height of 94.0 nm. Target #2 is another step height made of chrome on glass, whose height was measured 76.0 nm by a stylus instrument (α-Step). A Michelson interferometric objective with 5X magnification and 0.13 NA was used to carry out the compensation technique proposed in this investigation. Two supplementary phase-shifting measurements were performed using quasi-monochromatic lights of λ_1=660 nm, and λ_2=500 nm. The envelope peak of white light interferograms was detected by the QPFA algorithm described in Ref. [9] with a scanning interval of $\lambda/12$. The compensated results were finally obtained as 97.9 nm for Target #1 and 71.8 nm for Target #2, which deviate from the known nominal values as much as 3.9nm and 4.2nm, respectively. This indicates that the proposed compensation method is capable of reducing the step height measurement error within ±5 nm.

Table 1. Measurement results of two different step heights.

Targets	h_1 (nm)	h_2 (nm)	H (nm)	h (nm)
Target #1: 94.0nm Step Height (VLSI Co.)	43.1	69.5	144.7	97.7
Target #2: 76nm Step Height (Chrome-doped glass)	48.9	43.1	61.5	71.8

h_1, h_2 : PSI Measurements (λ_1=660nm, λ_2=500nm),
H : WSI Measurement, h: Compensated result.

References

1. J. Biegen, Opt. Lett. **19**, 1690 (1994).
2. T. Doi, K. Toyoda, Y. Tanimuira, Appl. Opt. **36**, 7157 (1997).
3. G. D. Feke, D. P. Snow, R. D. Grober, P. J. Groot, L. Deck, Appl. Opt. **37**, 1796(1998).
4. E. Palik, *Handbook of Optical Constants of Solids Vol I*, Academic Press (1985).
5. P. de Groot, L. Deck, Opt. Lett. **18**, 1462 (1993).
6. P. de Groot, L.Deck, J. Mod. Opt. **42**, 389(1995).
7. K. Larkin, J. Opt. Soc. Am. A. **13**, 832 (1996).
8. P. Sandoz , R. Devillers, A. Plato, J. Mod. Opt. **44**, 519 (1997).
9. M. C. Park, S. W. Kim, Opt. Eng. **39**, 952(2000).

A COMPACT INTERFEROMETRIC SURFACE CHARACTERIZATION DEVICE

Andrew D. Woodfin, Faramarz Farahi, Robert J. Hocken
University of North Carolina at Charlotte
9201 University City Blvd. Charlotte, NC 28223

Introduction

Conventional interference microscopy has been superseded in numerous applications, particularly three-dimensional surface profiling, with the greater range afforded by scanning white light interferometry (SWLI).[1,2] Monotonic path modulation of one optical arm in an interference microscope, along the imaging axis and perpendicular to the surface under study, allows for creation of interference fringes whose visibility is dependent on the coherence of the light source and the distance between reference and sample reflecting surfaces. Conventional phase measuring methods, as employed in laser interferometry, are fundamentally limited to phase modulo 2π. Incoherent illumination, on the other hand, allows for discrimination of a distinct optical path difference at which the interference contrast is at a maximum. The measurement range thereby becomes effectively infinite, though practically limited by the accuracy with which the position of maximum interference contrast can be fixed and correlated with an axial position.

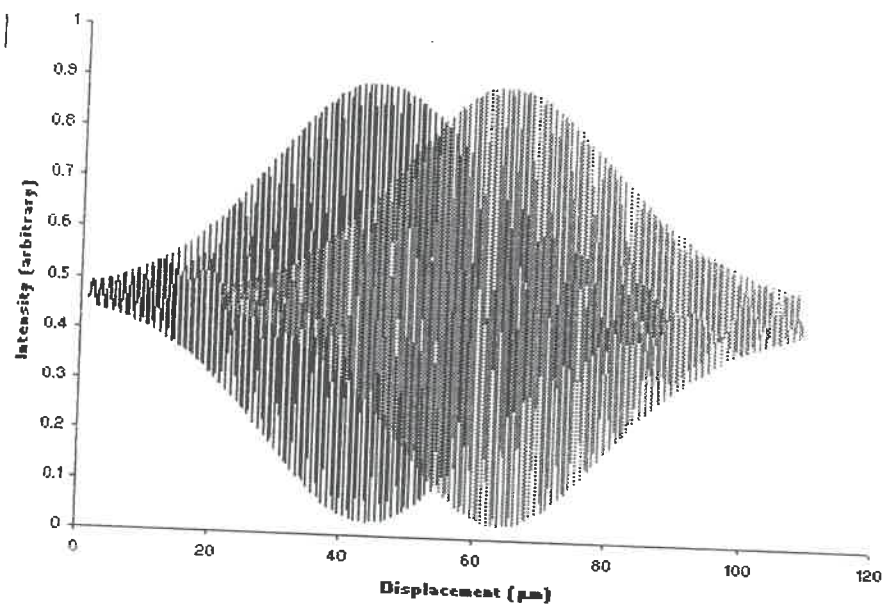

Figure 1 Illustration of two displaced low-coherence interferometric transfer functions

Available commercial instruments which exploit the unique aspects of SWLI have heretofore been large apparatus requiring significant vibration isolation. The general design is built around a benchtop microscope, with the addition of imaging electronics and mechanical scanning mechanisms for effecting the optical path modulation. A small number of slightly more compact instruments have become available, though for limited and specialized applications. Moreover, these smaller instruments still incorporate incandescent light sources and their commensurate size, along with bulk mechanical path displacement mechanisms. The instruments typically are large, requiring that parts be brought to the instrument, rather than allowing for the converse. As

small-scale mechanisms become increasingly integrated into larger systems, the need for a versatile device capable of in-situ inspection becomes evident. Assessment of surfaces and integrated mechanisms, without requiring disassembly and part fixturing, allows for a more accurate evaluation of the system characteristics under operating conditions. Furthermore, a sufficiently compact instrument can be employed in configurations where the constraining dimensions would otherwise preclude a benchtop device.

Significant reduction in the size of the active instrument region is facilitated through the implementation and integration of a solid state light source and fiber-optic transmission media. By decoupling the light source from the imaging optics, several enhancements are realized. The heat generated by a conventional incandescent source is removed from the metrology loop, as the fiber coupled source can be located at an arbitrary distance from the surface under study; the only source-induced heat contribution then comes from the radiant flux directly incident on the surface. Furthermore, by allowing transmission through optical fiber, the transmission media itself (i.e., the fiber) may be manipulated to effect the requisite optical path modulation. In so doing, the path modulation mechanism can also be separated from the imaging optics, thereby requiring no mechanical motion in the imaging system. The net result is a compact probe capable of versatile in-situ inspection, with no moving parts.

Experimental Setup

The low-coherence light source used in the device is a superluminescent diode operating at a central wavelength of 833 nm with a linewidth of 20 nm. The true benefit for our purposes lies in the diode's ability to be coupled into a single-mode optical fiber, thereby permitting arbitrary non-rigid separation between the interferometric instrument and the heat generated by the source. An extended incandescent broadband source cannot be successfully coupled into a single-mode fiber, precluding its use for interferometric imaging. The SLD is pigtailed to a 1-meter length of optical fiber in order to reduce coupling sensitivity to misalignment between the source and fiber. A 3 dB directional coupler splits the light into two fiber paths, which subsequently serve as the two interferometer arms. One length of the fiber is wound around a cylindrical piezoelectric element to perform the optical path modulation, necessary for scanning the interferometric transfer function. The PZT drive voltage is provided by two separate servo controllers. By performing all path length modulation in-fiber, the optical probe at the surface under study requires no moving parts, thus allowing for lower mass and higher device resonant frequency and stiffness (through elimination of material interfaces). The probe carries only imaging and collimating optics, as well as a bulk beamsplitter to redirect and recombine the optical signals from the fiber and the surface under study, thus completing a Mach-Zehnder configuration.

The optical fiber itself presents both unique problems as well as benefits to the instrument design. Its inherent sensitivity to environmental variations, particularly the effect of temperature fluctuations on refractive index and axial dimensions, produces an obvious obstacle to the stability requirements placed on the optical path lengths in an interferometric configuration. However, the ability of fiber to yield long optical path lengths in a relatively small volume affords the opportunity for the requisite path modulation in scanning white light interferometry to be performed with very little physical actuation. By wrapping the optical fiber around a cylindrical piezoelectric element, the necessary monotonic path length modulation may be performed while simultaneously compensating for the environmental sensitivity of the fiber. The environmental compensation is achievable by exploiting the ability of the fiber to transmit

multiple optical signals on one path, thus allowing for a secondary wavelength to track the path variations in the fiber alone and having the resulting error signal used as compensation feedback to the piezoelectric actuator.

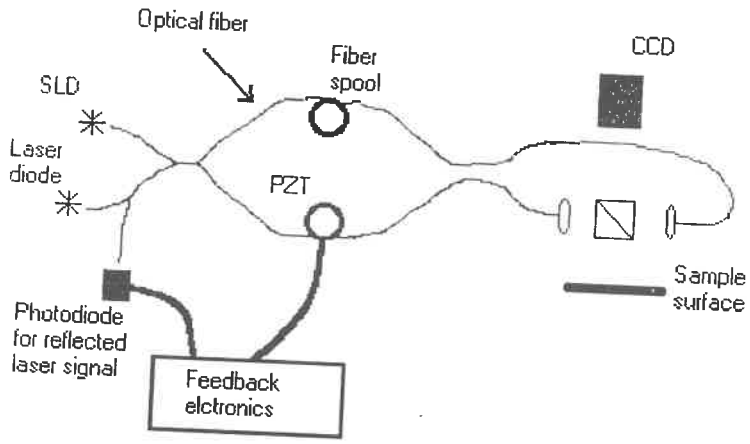

Figure 2 Schematic of experimental setup

Undesired environmental sensitivity in the fiber interferometer is circumvented through the use of a secondary light source, namely a laser, which is coupled into the two lengths of optical fiber simultaneously with the low-coherence source. A filter at the instrument side detection optics prevents introduction of the laser signal into the low-coherence measurement, but allows the laser to traverse the full length of the fiber's sensitive region. Back reflections of the laser signal from the fiber endfaces yields a Michelson interferometric configuration. As the environmentally induced phase variations manifest at a lower frequency than those produced by the deterministic path modulation, the laser signal is monitored under a low-pass frequency cutoff in order to correct for the environmental fluctuation while allowing for the requisite low-coherence transfer function modulation. The resulting laser interference signal is tracked and fed back into the PZT modulator through a servo loop.

To allow for in situ inspection away from an isolated environment, a vibration insensitive device is necessary. A large part of the vibration insensitivity is afforded in the reduced size alone, as the significantly reduced mass allows for a higher resonant frequency. As the path modulation is performed in-fiber, the need for bulk movable mechanisms is also eliminated. This allows for the elimination of potentially unstable interfaces, thereby significantly increasing the device stiffness. Further increase in the overall stiffness is afforded by preloading the device against the surface under study, through the use of an external frame and elastic elements. This serves to increase the interface stiffness between the largely monolithic probe assembly and the surface under study.

Conclusions and Future Work

The mechanical design of a compact interferometric surface analysis device has been performed. The ability to separate the light source and requisite path modulation mechanism from the imaging components through the use of fiber optic transmission media have allowed for a significant size reduction in the elements which must remain in proximity to the sample under study.

The introduction of optical fiber warrants further inspection of characteristics peculiar to it with regard to its effect on a hybrid interferometric system. Work is ongoing in assessing the effect on overall system performance from parasitic factors such as polarization drift and deformation induced variable fiber dispersion.

1. L. Deck and P. de Groot, Appl. Opt., **33**, 7334-7338 (1994).
2. P. J. Caber. Appl. Opt., **32**, pp.3438-3441, (1993).

Dual Mode Phase Measurement of Heterodyne Optical Interferometry

Noh-Bin Yim[1], Min-Suk Kim[1], and Seung-Woo Kim[1]

[1]*Dept. of Mechanical Engineering, Korea Advanced Institute of Science and Technology*

Science Town, Taejon 305-701 Korea

Abstract

We present a new digital phase measuring scheme for optical heterodyne interferometry, hich provides high measurable velocity up to 6 m/s with a fine displacement resolution of 0.1 nanometer. The main idea is combining two distinctive digital phase measuring techniques with complementing characteristics to each other; one is the Doppler shift frequency counting with 20 MHz beat frequency for high velocity measurement and the other is the synchronous phase demodulation with 2.0 kHz beat frequency for extremely fine displacement resolution. The two techniques are operated in switching mode in accordance with the object speed in a synchronized way. Experimental results prove that the proposed dual mode phase measuring scheme is realized with a set of relatively simple electronic circuits for beat frequency shifting, heterodyne phase detection, and low-pass filtering.

Keywords: Optical heterodyne interferometry; dual mode phase measurement; displacement measurement; beat frequency shifting; Doppler shift.

1. Introduction

Nowadays high performance precision machines are increasingly adopting heterodyne laser interferometers as position feedback transducers to attain sub-micrometer resolutions over a long travel of machine axis movement. However, the task of achieving high velocity measurement together with sub-micrometer resolutions is not easy because currently available phase measurement techniques for optical heterodyne interferometry suffer degeneration in measuring resolution when the bandwidth of phase detection is increased. Many techniques demand a tradeoff between the maximum measurable velocity and the displacement resolution, because the two performance criteria conflict with each other to be attained simultaneously due to limitations of individual measuring principles. To cope with the problem, in this investigation, we propose a new digital phase measuring scheme based on the hybrid concept of adopting two distinct techniques with complementing characteristics to each other; one is the Doppler shift frequency counting with high velocity measurement capabilities and the other is the synchronous phase demodulation advantageous for extremely fine resolutions. The two techniques are concurrently operated in accordance with a switching strategy regarding the object velocity to be measured. This dual mode concept allows a low cost, but high performance phase measurement as will be demonstrated in detail through a series of relevant experiments.

2. Measurable Velocity and Displacement Resolution

If a laser source of 600 MHz beat frequency is used, the maximum measurable velocity

reaches above 200 m/s . However, increasing beat frequency for high velocity measurement deteriorates the measuring resolution in return. The reason is that the bandwidth of phase detection is usually fixed in the absolute time scale in most phase measuring techniques.

3. Dual Mode Phase Measurement

The concept of dual mode phase measurement proposed in this investigation is to combine two different but complementing phase measurement techniques. One is the high Doppler shift frequency counting with 20 MHz beat frequency technique that performs high speed measurement up to 6.7 m/s. The other is the high resolution displacement measurement of synchronous phase demodulation with 2.0 kHz beat frequency that is aimed for an extremely fine resolution of 0.1 nanometer within the speed limit of 0.67 mm/s . When the object speed is low at the onset of acceleration and also in the final positioning of deceleration, both the techniques are operated in the "high resolution phase mode." In this mode, the total displacement L is measured as

$$L = \frac{\lambda}{2} \times \{N + (\frac{\varphi_2 - \varphi_1}{360^\circ})\} \qquad (1)$$

where N is the total number of frequency count of Doppler shift, and φ_1 are φ_2 are the initial and final phase values respectively measured by the high resolution phase measurement of synchronous demodulation.

Realizing the dual mode phase measurement proposed so far requires identifying by experiment the exact phase value of the phase meter right at the precise instance when actual up/down counting of the frequency counter takes place.

4. Experimental Results

Firstly, the measurement resolution and stability of the high resolution phase meter were examined in comparison with commercially available high performance function generators whose phase accuracy had been guaranteed as 0.05° through external standardized calibration procedures. Considering that the overall noise level of the circuits was measured 0.3 mV, it is concluded that the resolution of the phase meter is in the level of 0.01°. In addition, as for the long term stability of the circuits, it was found that the output of the phase meter fluctuates only within the limit of 0.1° over a period of 6 hours.

Secondly, the whole electrical circuits for both the phase meter and frequency counter were evaluated as an assembly. For this, the function generators were used in the same way as previously to generate the reference and measurement signals. In addition, for accurate digital determination of the displacement following Equation (1), the analog output of the volt meters were connected to an IBM PC via GPIB interface. Repeated measurements were taken to reveal that the mean deviation of phase readings from the assembly is –0.045° with 0.027° standard deviation. For comparison, the beat frequency shifter in the phase meter was

deactivated and then measurements were taken again with the original 20 MHz beat frequency. This comparison confirms that the beat frequency shift from 20 MHz to 2.0kHz improves measuring accuracy by a factor of 4.

Thirdly and finally, actual displacement measurements were performed after integrating the developed circuits with necessary optics for heterodyne interferometry. For evaluation of test results, a capacitive displacement sensor was installed after calibration as the reference in computing measurement errors of the laser interferometer.

5. Conclusions

We have proposed and tested a new dual mode phase measurement method for optical heterodyne interferometers, which is specially devised to provide advantages in measuring resolution and speed at the same time. This new method is realized with relatively simple electronic circuits of beat frequency shift, high resolution phase detection, and high bandwidth frequency counting. Repeated experimental results show that measurement resolution is improved by a factor of 10, while measurement repeatability is enhanced from 1.47 ± 0.083 nm to 0.34 ± 0.061 nm in terms of standard deviation.

Reference

[1] F.C. Demarest , "High-resolution, high speed, low data age uncertainty, heterodyne displacement measuring interferometer electronics", Meas. Sci. Tech. **9**, 1024-1030, 1998.

[2] P.G. Charette, L.W. Hunter, and C.J.H. Brenan, "A complete high performance heterodyne interferometer displacement transducer for microactuator control", Rev. Sci. Instrum. **63** (1), 241-248, 1992.

[3] Krohn-Hite Co., "IEEE-488 programmable precision phase meter model 6620 operation manual", section 6. Circuit description, 1986.

[4] H.P Lio and M.S. Young, "New digital phase meter concept and its application", Rev. Sci. Instrum. **68** (4), 1894-1901, 1997.

[5] G.E. Sommargren, "A new laser measurement system for precision metrology," Precision Engineering **9**, 179-184, 1987.

[6] S. Yokoyama, "Intermode beat stabilized laser with frequency pulling", Appl. Opt. **33**(3), 358-363, 1994.

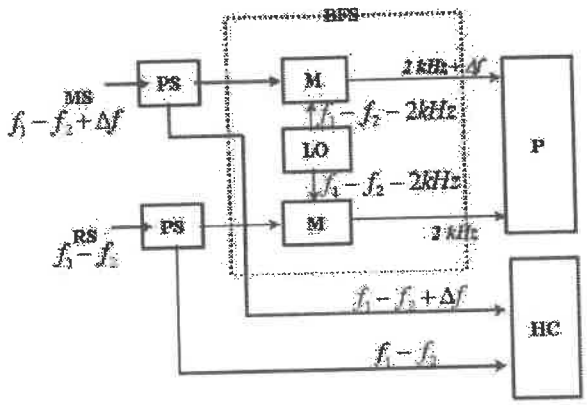

MS : measurement signal
PS : power splitter
LO : local oscillator
P : high resolution phase meter using PSD
HC: high bandwidth phase counter
RS: reference signal
M: mixer
BFS : heat frequency shifter

Figure 1
Electronic configuration of the dual mode phase measuring method

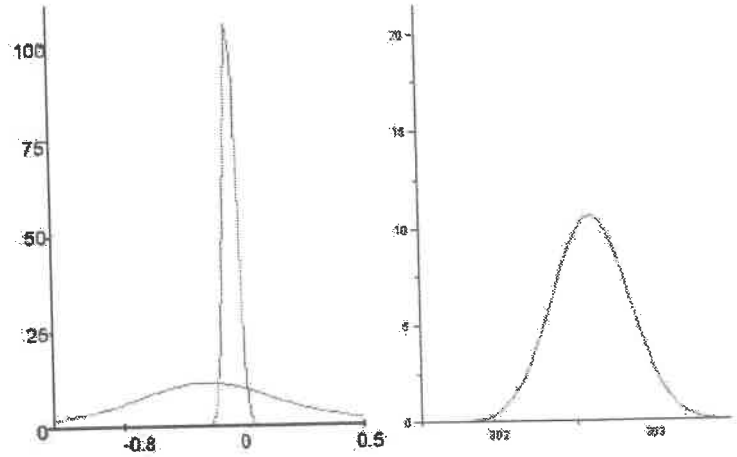

Figure 2 Evaluation result
(a) phase detection variation (nm)
between conventional method and "dual mode phase measurement"
(b) Variation (°) of the phase value at the up/down counting point

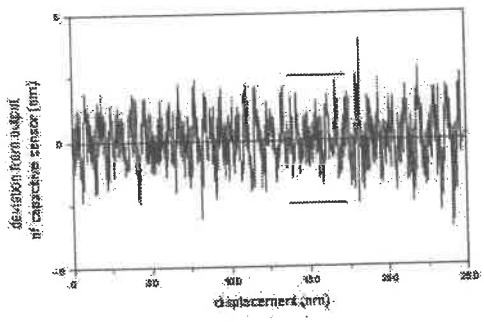

(a) example of deviation with a conventional phase meter

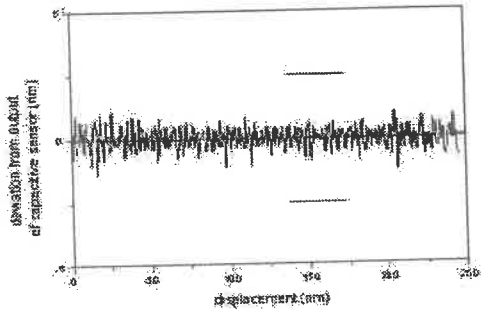

(b) example of deviation with the dual mode phase measurement

Figure 3 Results of the dynamic test

Nikon Electron Projection Lithography System: Mechanical and Metrology Issues

W. Thomas Novak, Douglas Watson,
Nikon Research Corporation of America
Belmont, California

Yasushi Yoda
Nikon Corporation
Tokyo, Japan

Electron Projection Lithography (EPL) is one of the leading candidates to replace optical lithography for the patterning of the fine integrated circuit (IC) patterns that will be produced in the near future. This technology is expected to be used in production at the so-called "70 nm Node," where the patterns on the IC's can be as small as 70 nm lines and 70 nm spaces. This technology is expected to be in production beginning in the year 2005.

Nikon has been working in collaboration with IBM on this technology for several years, beginning prior to 1995. Now, several key technology areas have been developed and the design of a prototype system is in process.

In the EPL system the exposure process is accomplished by directing a beam of electrons through a reticle or mask, and imaging the reticle pattern onto a silicon wafer at a demagnification of 0.25 X. The electron optics between the reticle and wafer precisely deflect the electron beam to sequential positions on the reticle and wafer, and make corrections to the beam positioning to correct for stage location errors. The beam is electronically deflected mainly in the X direction while the stages are scanned in the Y direction, simultaneously correcting for the relative stage motion and any known position errors. See Figure 1.

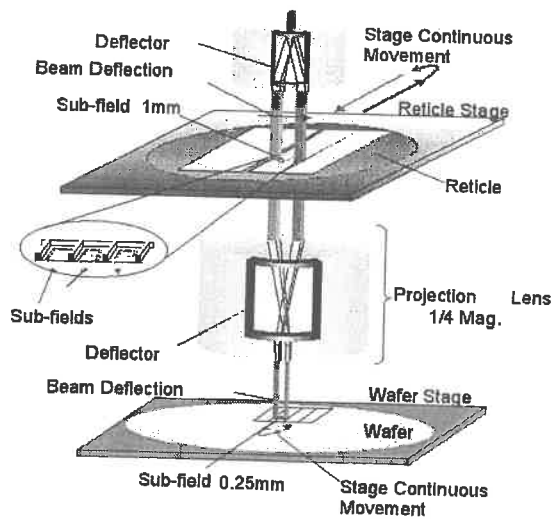

Figure 1. EB stepper exposure process

The reticle itself is made from a 200 mm diameter silicon wafer. The reticle pattern is a 2 dimensional grid of 1x1 mm patterns, subsequently reduced to 1/4 mm x 1/4 mm patterns on the wafer. These reticle patterns consist of a thin membrane supported on a grill structure etched into the silicon (Figure 2).

Electron beam columns have been built at Nikon and IBM to obtain test data and to demonstrate the viability of the electron optics system concept. These columns have been used to demonstrate the excellent resolving ability, shown in the Figure 3, as well as many other basic performance characteristics needed for the next generation of IC's.

In addition to resolution, one of the essential requirements of IC lithographic patterns is the ability to align a pattern being exposed to other patterns on the wafer. As a general rule, the total alignment tolerance is about 1/3 of the linewidth being patterned. For 100 nm lines, this amounts to about 35 nm total from all error sources. Making a system error budget by dividing this error into allowable

errors from various sources results in an allowable positioning error from any given source which is very small, typically around 1 to 10 nm. This places a severe challenge for the machine design. In addition,

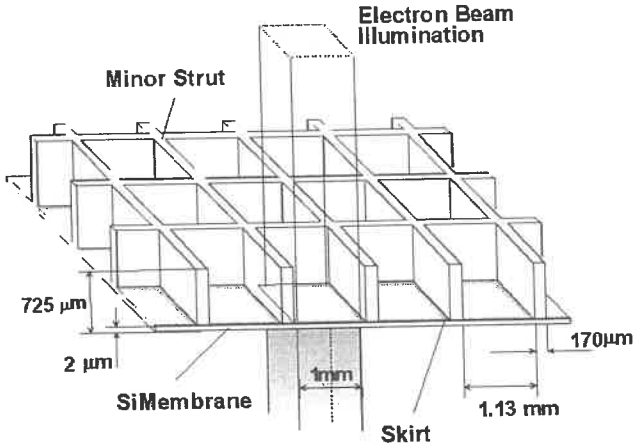

Figure 2. Local structure of Silicon stencil reticle

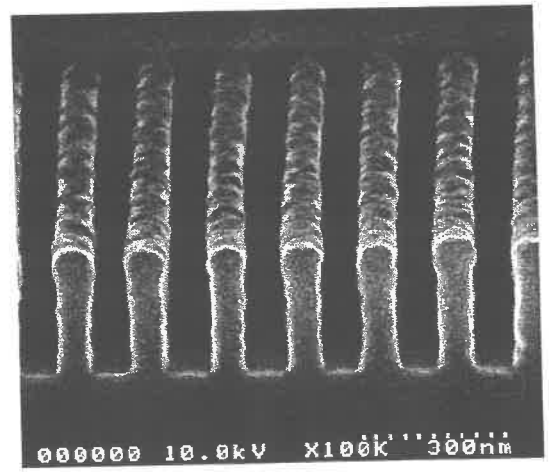

Figure 3. SEM of 80 nm lines and spaces

the stages must move at high velocities and be capable of high acceleration in order for the system throughput to be high enough for the machine to be marketable.

Nikon has a long history of over 22 years of precision stage development for their lithography systems. Recently, the stages have been based on air bearings and linear motor technology. It is desirable for Nikon to utilize this technology for the EB systems, but the requirements for the EB stages are much different than their optical counterparts.

The stages must operate in a vacuum and cannot cause deterioration to this environment because of gas leakage or outgassing. Air bearings cannot be used without elaborate methods to remove the air escaping from the bearings and effectively prevent air release into the vacuum chamber.

Another major consideration is that the electron beam is extremely sensitive to magnetic fields. Any motors or actuators must be designed properly and be well-shielded to prevent stray magnetic fields, which will shift the X-Y placement of the beam.

Additional considerations make the EB stages more difficult to design and manufacture compared to the optical counterparts. However, a key mitigating factor makes the system design reasonable. The ability to deflect the electron beam acts as a high bandwidth fine stage to make corrections to the stages' position. Thus the stages can have micron level positioning ability compared to the optical system stages' nanometer positioning ability. Figure 4 shows a computer rendering of the electron optics column and the reticle and wafer stages.

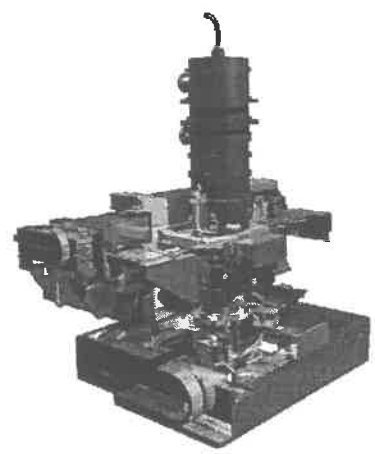

Figure 4. EB column with stages

In order for the electron optics to correct for the stages' positioning errors, the system metrology must still have nanometer level accuracy. The system must be able to determine these errors precisely. This requires considerable attention in the design of the metrology subsystems. Error sources can include component thermal expansion, component and body distortion due to moving stages, vibration, electronic noise, and electronic drift. The laser interferometer system must be extremely stable, and the data timing must be stable and known precisely. If the wafer stage is moving at 200 mm/second, a 5 nsec timing error can cause 1 nm position error, which is considered significant.

Our goal is to maintain a system vacuum level of 10^{-6} Torr. Nikon built a chamber to test and evaluate vacuum compatible air bearing designs. One test fixture is shown in Figure 5. Using this test fixture, data were obtained and the results compared to analytical models. From this, vacuum compatible designs have been made which we think will have acceptable performance in the Nikon EPL system. The bearings perform like a conventional air bearing with typical flows, gaps, and stiffness. In addition a series of pump out grooves are used to scavenge the air escaping from the bearing before it leaks into the main vacuum chamber.

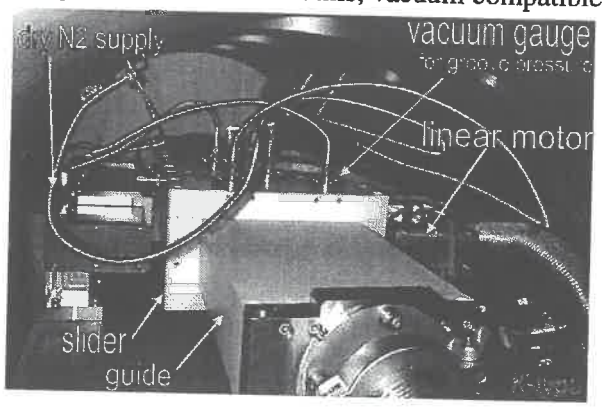

Figure 5. Vacuum air guide test fixture

The management of the magnetic fields near the electron beam is another key design consideration. Electron beams are very sensitive to magnetic fields: AC fields perturb the e-beam while DC fields can, in principle, be calibrated out. However, DC fields can perturb the e-beam if any magnetically permeable materials near the column move. When these materials change position, the DC fields change in position and magnitude, thereby causing the beam to be deflected some amount. If this change is not measured or calibrated out, the result is a beam positioning error. The exposed image is then incorrectly aligned on the wafer. The fields can be external to the system or can come from actuators within the system (eq. Stage motors, loaders, vibration/isolation actuators). For moving magnetic material, even the DC lens fields are a potential problem. Positioning accuracy puts severe limits on beam motion, while throughput almost certainly require stage motors much closer to the column than in previous e–beam systems. These conditions require a system level approach to magnetic shielding.

Both AC and DC magnetic fields from linear motors have been measured by performing experimental studies and have been modeled with computer modeling software (FEA). These magnetic characteristics have been incorporated into the magnetic shielding design. One mitigating factor is that during scanning, the stage moves at constant velocity with low currents to the motor windings. Therefore AC fields from the motors during scan are expected to be much less than during stage acceleration.

The EPL System main body structure has been designed to minimize overall distortion under vacuum loading and stage movement, and particularly the distortion of the stage and metrology components. The vacuum chambers containing the stages are accessible for maintenance via large panels and smaller windows. A version of the main body design is shown in Figure 6.

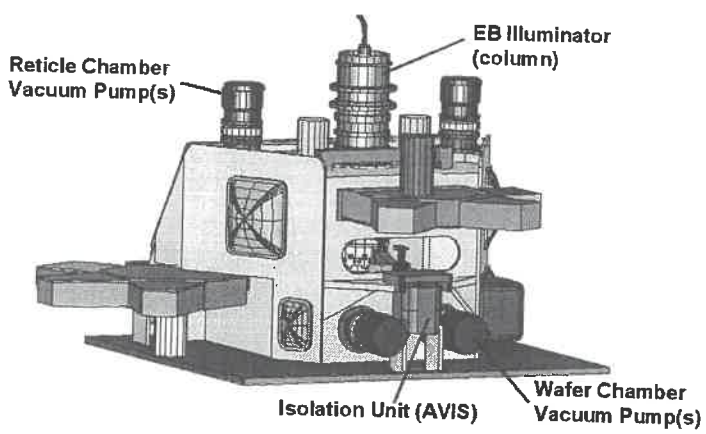

Figure 6. EB body with main components

In order to reduce body vibration and distortion, the reaction forces from the wafer and reticle stages are isolated, and brought out to a reaction frame. This reaction frame is independent from the main body, and is attached to ground. As the stages accelerate and decelerate, these forces are not applied to the body structure containing the metrology and the electron optical components.

Figure 7 shows a simplified block diagram of Nikon's EB system mechanics. As can be seen from this diagram, there are many subsystems that are inter-related and must perform in synchrony to achieve acceptable final results. In addition to the electron optics and the stages, there are substrate

handling subsystems and vacuum pumps and components. Additional key elements that relate to substrate positioning are optical alignment microscopes, autofocus and autoleveling sensors (AF/AL) and a backscattered electron detector. This last unit can be used to determine the position of the electron beam relative to alignment targets on the silicon wafer substrate or wafer stage.

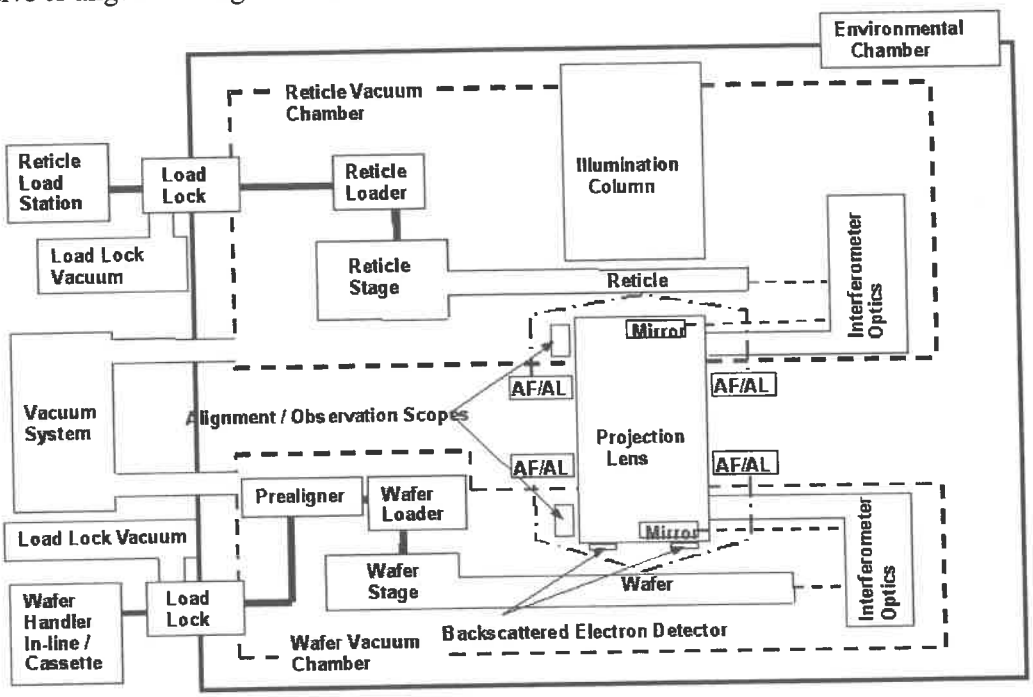

Figure 7. System block diagram of Nikon's EB system mechanics

Many man-years of engineering effort have been spent by Nikon together with IBM developing this next generation lithography tool. The concept and design model for the EB structure and configuration have been developed. FEA modeling of various parts of the structure has been done to optimize vibration modes, structural rigidity and distortion under loads. Thermal analysis has been done to understand and improve the design of the stages, actuators, and electron optics components. Experimental tests, theoretical analysis, and FEA models have been used to study and optimize the magnetic components of the system and the air bearings used in the stages. Further development and modification of the entire concept is being done to address cost reliability, throughput, and production issues. This effort together with IBM's electron optics expertise and Nikon's system and precision stage experience will ensure the achievement of a high throughput and high performance EPL system.

ACKNOWLEDGEMENT

The authors wish to thank M. Sogard and A. Hazelton of Nikon Research Corporation (NRCA); T. Miura, K. Suzuki, T. Yamaguchi, K. Okamoto and Y. Okubo of Nikon Corporation; and H. Pfeiffer, R. Dhaliwal, M. Gordon, R. Kendall, W. Stickel, and J. Rockrohr of IBM Corporation for their contributions both directly and indirectly to this paper.

REFERENCES

K. Okamoto, et al., "E-beam stepper lithography," Solid Stage Technology, May, 2000.

K. Suzuki, et al,. "Nikon EB stepper; its system concept and countermeasures for critical issues," SPIE 3997, pp. 214-224.

High–NA Camera for an EUVL Microstepper

Layton C. Hale, Russell M. Hudyma, John S. Taylor, Richard L. Thigpen, Carl A. Chung
Lawrence Livermore National Laboratory, Livermore, CA 94550

Introduction

Extreme ultraviolet lithography (EUVL) is a promising next-generation technology for extending the ability of microelectronics manufacturers to make ever denser circuits with smaller features, a trend known as Moore's Law. A major EUVL program, involving three national laboratories and members of an industrial consortium,* is underway to demonstrate full-field scanned printing with 70 to 100 nm feature sizes using a four-mirror camera with a modest 0.1 numerical aperture (NA).[1] Within our program, a complementary project sponsored by International Sematech will provide an important capability to print 30 nm features using a two-mirror 0.3 NA small-field camera, see Figure 1. Known as the Micro-Exposure Tool (MET), this development tool will enable high-resolution printing several years before high-NA, pre-production (or beta) tools are available.

EUV systems operate at a much shorter wavelength than current and proposed deep-ultraviolet systems, for example, 13.4 nm versus 157 nm. This allows proportionally better optical resolution, which is often estimated using Equation 1, where k_1 is a constant related to process parameters and the source coherence, and λ is the wavelength. The NA, defined as the sine of the half cone angle of light exiting the camera, is an important optical design parameter that will likely be between 0.2 and 0.3 for EUVL production tools. Increasing the NA improves resolution but the depth of focus decreases even faster, indicated by Equation 2. Results from EUVL printing experiments lead to these estimates for the constants: $0.5 < k_1 < 0.7$ and $k_2 \approx 1$.

$$R = \frac{k_1 \lambda}{NA} \tag{1}$$

$$DOF = \pm \frac{k_2 \lambda}{NA^2} \tag{2}$$

The high absorption of EUV light in optical materials requires the use of reflective optics within a vacuum environment. This is a major departure from traditional optical lithography, which predominantly uses refractive optics. The multilayer coating technology developed within our program provides adequate reflectivity approaching 70% for normal-incidence optics, and the coating uniformity is within budgeted figure tolerances. However, the production of optical substrates to sub-nanometer figure and finish remains extremely challenging now and into the future.

Carl Zeiss is the optical fabricator contracted to produce two sets of MET optics using their own interferometers. We will install the optics into two LLNL-designed cameras and return them to Zeiss for optical system alignment. Zeiss will assume ownership of one camera for their internal use and the other will eventually be installed into the MET.†

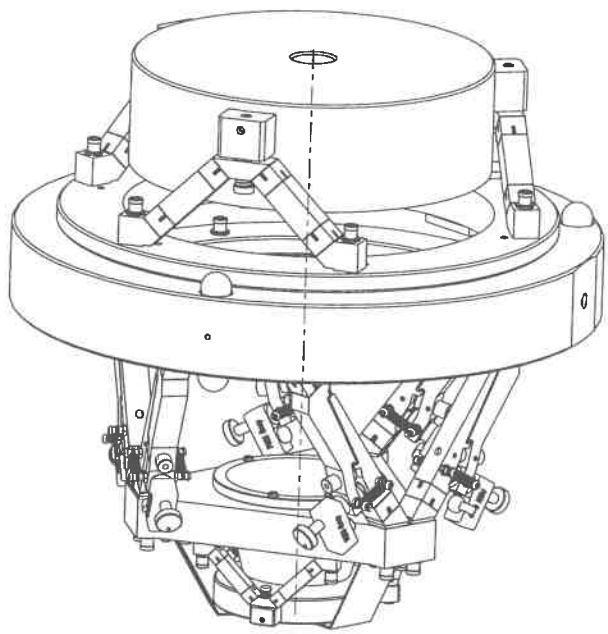

Figure 1 Solid model of the MET camera design.

Overview of the Optical Design

The MET camera employs two mildly aspheric mirrors: a convex primary (designated M1) and a concave secondary (designated M2) having nearly the same radius of curvature. This "equal radii" concept enables the field curvature to be corrected to a value significantly better than other two-mirror cameras such as the Sandia 10x camera, a Schwarzchild configuration.[2] As Figure 2 shows, each optic has a central hole to permit ray bundles to pass through. The optical design is rotationally symmetric about the optical axis except for 4° and –0.8° tilts of the mask and wafer planes, where

This work was performed under the auspices of the U.S. Department of Energy by University of California, Lawrence Livermore National Laboratory under contract No. W-7405-Eng-48.

* The Virtual National Laboratory (VNL) is a cooperative partnership between Sandia National Laboratory, Lawrence Berkeley Laboratory and Lawrence Livermore National Laboratory. The Limited Liability Company (LLC) is a consortium of microelectronics manufacturers who sponsor and participate in EUVL research.

† At the time of this writing, the optics and camera hardware are nearing completion. Full assembly is anticipated by the publish date with optical alignment to follow. The Micro–Exposure Tool is just entering the conceptual design phase. The MET will be located in the US.

the ratio is equal to the 5:1 magnification. Tilted planes are required when using a reflection mask in the way anticipated for EUVL production tools. In this case, the field size projected onto the x-y plane is 3 x 1 mm at the mask and 600 x 200 μm at the wafer.

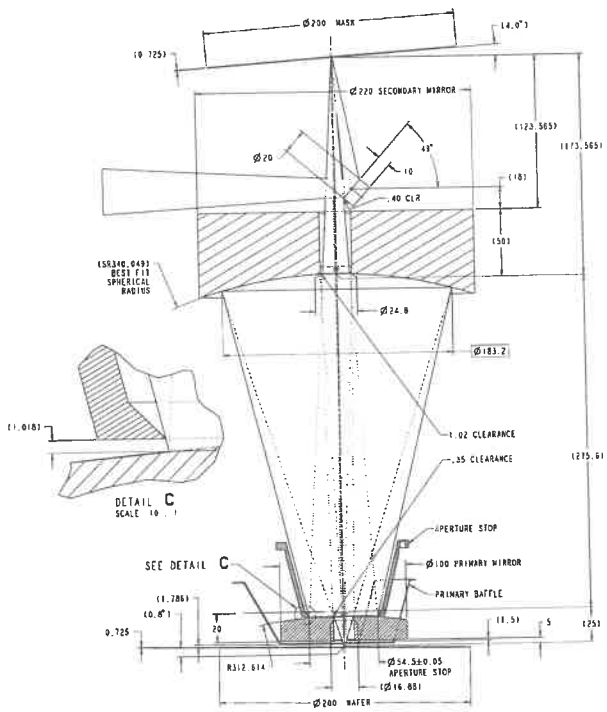

Figure 2 Cross section of optical components with all ray bundles shown. The dimensions are in millimeters.

While the wavefront error is well corrected for tilted planes, the magnification varies across the tilted field, resulting in significant image distortion. However, distortion is not a concern for the process development studies planned for the MET. Without tilted planes, the MET camera may be used with a transmission mask for printing devices that require low distortion. Table 1 summarizes the errors inherent to the optical design, that is, assuming perfect optics. Figure errors on the optics cause twice the error in reflected wavefront and are assumed to combine in quadrature. Since several low-order error functions are compensable at system alignment, quadrature becomes a realistic assumption.

Error Type	Tilted	Not Tilted
Composite RMS Wavefront	0.42 nm	0.28 nm
Maximum RMS Wavefront	0.72 nm	0.36 nm
Minimum RMS Wavefront	0. 24 nm	0.15 nm
Peak Distortion	242 nm	2.24 nm

Table 1 Errors inherent to the optical design computed over the full 600 x 200 μm wafer field.

Optic Specification

The optic specification for the MET is identical to that of the four-mirror camera mentioned previously.[3] The advantage of fewer optical surfaces in the MET is partially offset by the more stringent printing requirements for 30 nm. The specification comprises three measures of surface error integrated over consecutive regimes of spatial frequency as listed in Table 2. These are tied closely to performance requirements and the bandwidth of various measuring instruments. The figure specification relates to high-resolution, low-distortion imaging across the full field. Figure error is measured using full-aperture interferometry. MSFR (mid-spatial-frequency roughness) causes near-angle scattering such that the scattered light remains in the image field. MSFR causes background illumination superimposed on the desired image, thus reducing image contrast and process window. In addition, nonuniform contrast over the image field causes the critical dimension of printed features to vary over the field. MSFR is measured using phase-shifting interference microscopy with several objectives to cover the frequency range. HSFR (high-spatial-frequency roughness) scatters light outside the image field, thus reducing throughput and also decreasing contrast. HSFR is measured using atomic force microscopy.

Error Regime	Specification	Spatial Period
Figure	0.25 nm rms	> 1 mm
MSFR	0.20 nm rms	1 mm – 1 μm
HSFR	0.10 nm rms	< 1 μm

Table 2 Specifications for MET projection optics.

The degree of difficulty in meeting the figure and MSFR specification depends largely on the asphericity of the optics. The peak aspheric departure for the smaller M1 is reasonable at 3.82 μm but the maximum aspheric slope is rather large at 1.18 μm/mm. The peak aspheric departure for M2 is 5.61 μm with a maximum aspheric slope of 0.47 μm/mm. The substrates are Zerodur™ to minimize thermal distortion.

Functional Requirements of the Camera Body

The camera body must satisfy three functional requirements extraordinarily well: 1) low-distortion support of the optics, 2) precision adjustments for aligning the optics, and 3) dimensional stability, both long term for alignment and short term for image placement. In addition, the camera must function in a vacuum environment and define the boundaries of ray bundles passing through it.

Description of Structural Components

Figure 1 shows the complete camera design from which the key structural components are visible. The support ring provides upper and lower kinematic mounting interfaces available to the MET and the alignment interferometer. In addition, the support ring has a 360° rotational interface to the M2 cell for the clocking adjustment and it provides attachment points for six actuation flexures. The triangular-shaped M1 cell attaches to the opposite ends of the actuation flexures, and together they provide high-resolution adjustment in

the five degrees of freedom critical for optical alignment. The M1 and M2 cells each support three flexures that combine to constrain six degrees of freedom for each optic. In addition, the flexures each provide a quick-disconnect interface to three lugs that are permanently bonded to each optic. The support ring, actuation flexures, cells, flexures and lugs are manufactured from Super Invar, a low-CTE (coefficient of thermal expansion) alloy of iron, nickel and cobalt.

Aperture Stop and Baffles

The boundaries of ray bundles through the camera are controlled by the aperture stop on the outer dimensions and a pair of baffles on the inner dimensions. As Figure 2 shows, the aperture stop is located just above optic M1 and is easily replaced if there is an experiment need to change its size. The purpose of the baffles is to block the direct light path from mask to wafer allowed by the central holes in the optics. The hole baffle, located below M1 and above the wafer, reduces the effective size of a direct ray bundle from the 16.6 mm hole size through M1 to just 4 mm. The plug baffle, located and attached via a single cantilever to the central hole area in optic M2, actually blocks the direct ray bundle. The hole and plug baffles combine to block all light emanating within a 4 mm circle on the mask.

Optic Mounts

The optic mounts must reproduce the same optic figure in the camera as achieved during fabrication metrology, within about 10% of the optical figure specification. We could not reasonably use the camera mount also for fabrication metrology due to space constraints within the interferometer. Instead, separate metrology mounts for M1 and M2 were constructed to provide a constraint state nominally identical to the respective camera mounts. Each mount is kinematic providing exactly six constraints that fully arrest the degrees of freedom of the optic without overconstraint. Neglecting friction, each mount carries the weight of the optic through three points that are geometrically defined at the centers of spherical surfaces on the bonded lugs. The reaction force at each point is nominally vertical but may vary due to friction, manufacturing tolerances in the mounts and misalignment to the gravity vector. The error budget process identified sliding friction as a significant error source to contend with in the mount designs.

The camera mount uses three, two-constraint flexures to support each optic. The flexures are arranged as three vees with their vertices coincident with spherical interfaces each formed between a conical seat on the flexure and the spherical surface on the bonded lug. This arrangement is evident in Figure 1. The optic is placed in the mount with full freedom to align to the mount constraints while minimizing sliding friction at the sphere-cone interfaces. Once fully constrained in the mounts, preload springs are applied in a way that does not disturb the interfaces. The metrology mount duplicates the same constraints as the camera mount using rolling-element bearings to reduce fiction to an acceptable level. Figure 3 shows the M1 metrology mount and the M2 metrology mount is similar.

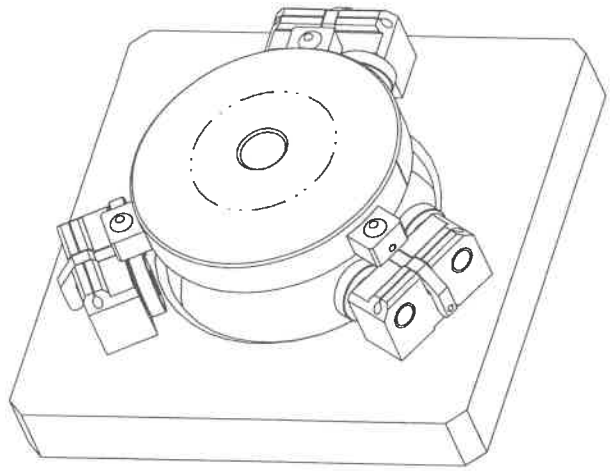

Figure 3 The M1 metrology mount uses pairs of rolling-element bearings to form a three-vee kinematic coupling.

Actuation System

The actuation system shown in Figure 1 has six actuation flexures that support and move the M1 optic and cell relative to the support ring. Often called a Stewart platform, this type of system is classified as a parallel-link mechanism since the active members act as structures in parallel as opposed to serial or stacked actuation stages. All six members are required to provide rigid constraint, and any pure motion of the stage requires coordinated motion of all six flexures. The coordination may be described with sufficient precision using a linear matrix equation since the required motions are small with respect to the overall size of the links.

The range and resolution requirements flow down from optical alignment needs. Table 3 summarizes the requirements and the capability of the actuation system. The actuator resolution for x-y translation is set to match the need to affect the transmitted wavefront at the 0.05 nanometer level. The geometry of the actuation system is such as to surpass the need in the other degrees of freedom. The most significant margin is in z translation because the interferometer will refocus as part of the alignment, thus relaxing the actuation requirement. However, this direction is the most sensitive for stability of the focal plane. The required alignment range comes from a Monte-Carlo simulation using anticipated manufacturing tolerances. It was reasonable to provide an actuator range having nearly a 5x margin. This requires the dynamic range of the sensors to be 4000:1 or 12 bits. The actuation system is capable of somewhat larger moves in single directions than those stated in Table 3. A three-way RSS combination: ±150 μm Δx-Δy, ±100 μm Δz, ±1000 μr θx-θy, uses the full ±149 μm travel of one or more actuation flexures.

Stage Motion	0.05 nm Sensitivity	Actuator Resolution	Tolerance Model	Actuator Range
Δx	0.10 μm	0.10 μm	± 34 μm	± 150 μm
Δy	0.10 μm	0.10 μm	± 34 μm	± 150 μm
Δz	0.61 μm	0.05 μm	± 21 μm	± 100 μm
θx	1.20 μr	0.80 μr	± 120 μr	± 1000 μr
θy	1.20 μr	0.80 μr	± 120 μr	± 1000 μr

Table 3 Range and resolution for actuated degrees of freedom.

Actuation Flexure

The function of the actuation flexure is to provide a single, adjustable constraint along its axis. It is remotely actuated during alignment corrections but otherwise functions as a passive constraint. Figure 4 is a cross section through the actuation flexure that shows the piezo-screw actuator and LVDT position sensor. A computer controller closes the loop on each actuator and computes the decoupling relation for coordinated motion. Effectively the piezo-screw actuator operates an 11:1 lever that is cut into the actuation flexure.

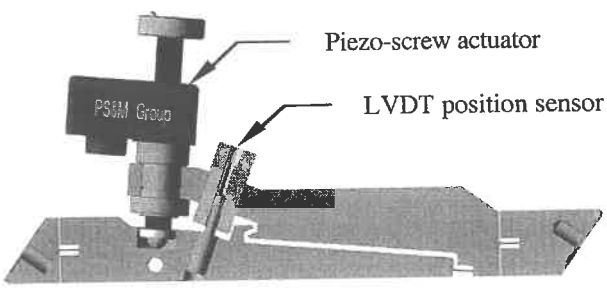

Figure 4 The section shows three of five blade flexures formed by a series of EDM cuts. The two blades near each end have identical companions that are rotated 90° about the constraint axis and are not visible in the section. Each pair acts as a ball joint. The single off-axis blade allows the flexure freedom to actuate within the travel stop. The screw axis, the constraint axis and a straight-line extension of the off-axis blade all intersect at a common point.

A number of factors are considered and balanced in the design of the actuation flexure. It must provide stiff axial constraint, sufficient compliance and range of motion in the non constraint directions, low actuation force, and bending stresses below yield. The axial stiffness governs the modal frequencies associated with the M1 optic and cell. Modes of vibration within the flexure, so called flexure modes, are of little consequence because associated optic motion is second order. However, the desire to keep these frequencies relatively high (> 200 Hz) limits the flexibility of the blades and ultimately the travel and lever ratio of the actuator.

A finite element analysis of the actuation flexure shows that the maximum actuation force and bending stress are 2.74 N and 178 MPa, respectively, which are within the design constraints. The total compliance along the constraint axis is 37.85 nm/N and is fairly well distributed with the lever arm and column being the greatest contributors. Both could easily be made stiffer but the increased mass would lower the flexure-mode frequencies, particularly the torsional mode at 250 Hz (not including the actuator or LVDT in the model). Further gains could be made by optimizing individual blade flexures for their expected ranges of travel, but instead they were all given the same proportions: 0.5 mm thick, 16 mm wide and 5 mm long.

Dynamic System Modeling

The need for steady image placement over the length of an exposure drives the dynamic stability requirement to be only a few nanometers of relative motion. Since the MET tool body and vibration isolation system heavily influence the performance of the whole lithography system, the strategy used in the camera design has been to maximize modal frequencies involving optic motion, thus deferring rigorous dynamic response modeling to the full MET system design.

A fairly detailed finite element model was developed to obtain the modal analysis results given in Table 4. Two boundary conditions were considered: 1) rigid kinematic constraints to identify flexibility within the camera assembly; and 2) kinematic constraints with modeled compliance to estimate a realistic system response. For the rigid case, optic M2 is the first to show motion at 353 Hz followed by M1 at 418 Hz. On real kinematic mounts, the camera moves nearly as a rigid body at 208 Hz.

Mode No.	Frequency	Mode Shape Description
Results for a rigid kinematic constraint		
1-6	250 Hz	Torsion of actuation flexures
7-12	344 Hz	Torsion of M2 flexures
13 & 14	353 Hz	X-Y motion of M2
15 & 16	418 Hz	X-Y motion of M1 optic/cell
17	525 Hz	Z motion of M2
18 & 19	530 Hz	Combined X-Y, θ_x-θ_y motion
Results for a compliant kinematic constraint		
1 & 2	208 Hz	Nearly rigid X-Y motion, all
9 & 10	310 Hz	Nearly rigid θ_x-θ_y motion, all

Table 4 Summary of the modal analysis results for rigid kinematic constraints and also three-vee kinematic constraints assuming silicon nitride as the ball material and tungsten carbide as the vee material.

References

1 Tichenor, Daniel A., et al., "EUV Engineering Test Stand," SPIE Emerging Litographic Technologies IV, 2000, **3997**

2 Goldsmith, J. E. M., et al., "Sub-100 nm Imaging with an EUV 10x Microstepper," SPIE Emerging Litographic Technologies III, 1999, **3676**

3 Taylor, Sommargren, Sweeney, Hudyma, "The Fabrication and Testing of Optics for EUV Projection Lithography" *Proc ASPE*, 1998, **18**

Nullifying Acceleration Forces in Nano-Positioning Stages for Sub-0.1μm Lithography Tool for 300 mm Wafers

Y.B. Patrick Kwan, Erik L. Loopstra
ASM Lithography B.V., De Run 1110, 5503 LA Veldhoven, The Netherlands.

Introduction

The transition of the semiconductor industry from the current 200 mm wafers to the larger 300 mm wafers has presented considerable challenges to all equipment suppliers, in particular the lithography tool manufacturers. Not only are the moving masses of nanometer-positioned wafer stages increases by up to a factor of 3.4, but accelerations are also to be doubled in order to maintain the same number of exposed wafers per hour. The driving forces in nanometer-positioned stages have to be increased by a factor of 5 or more, even with extensive weight reduction by use of unconventional structural materials. For example, the maximum driving force in the scan direction in the latest 300mm-wafer lithography platform exceeds 1kN. This level of actuation forces is close to the limit of conventional dynamic architecture of lithographic equipment, in which the reactions are connected to 'ground' via a so-called force frame (Fig. 1).

To design a machine platform that is extendable well beyond the 70-nm node, means of nullifying the acceleration forces is highly desirable if not essential.

Theory

The use of a frictionless, counter-moving mass for nullifying reactions to acceleration forces is not new, as has been implemented for decades in firearms and artilleries. The application of this simple concept in nano-positioning stages not only has the same effect of reaction force cancellation, but also has the additional advantage that the centre of mass of the combined system remains stationary, thus also significantly reducing vertical disturbances to the rest of the machine.

Working principle is simple -- reactions to acceleration forces are channelled to a so-called balance mass free to move, in the specific degree(s) of freedom, in the opposite direction with min. friction. The ratios of accelerations and displacements between the moving object and the balance mass both equal the inverse of the mass ratio :

$$m_1 . \ddot{y}_1 = m_2 . \ddot{y}_2 \quad \text{or} \quad m_1 . y_1 = m_2 . y_2$$

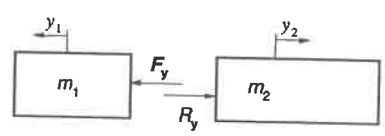

The challenge is to implement such an inertia balancing system in multiple degrees of freedom.

Embodiment 1 -- Reticle Stage Balancing in 6 Degrees of Freedom

While the latest generations of wafer and reticle positioning stages are servo-controlled to nanometer accuracies in all six degrees of freedom, movements with long ranges and high forces rarely exceed 2 or 3 degrees of freedom. For example, the reticle stage essentially move in long range and high acceleration only in the scanning (y) direction, while movements and forces in the other five degrees of freedom are small. As such a single balance mass as shown above with friction-free movement in the same direction would suffice. The use of two balance masses on each side, however, offers additional balancing possibilities against yawing moments through differential movements between the two balance masses. Minute movements in the other 4 degrees of freedom can also be effected on the same masses by supporting them in those directions compliantly.

The embodiment can be summarised as follows:

Transmission of Forces & Moments from Reticle Stage to Balancing System

F_x	via thrust bearings between Long Stroke Module (LoS) & Balance Mass (BM)
F_y	through linear motor in scan direction (mover on LoS, magnet plates on BM)
F_z	via thrust bearings between LoS & BM
T_x	differential vertical forces on thrust bearings between LoS & BM
T_y	differential vertical forces on thrust bearings between LoS & BM_1.
T_z	differential Y-forces between LoS & BM, as in F_y.

Balancing Methods

F_x	compliant support for BM	F_y	long-range balance-mass movements
F_z	compliant support for BM	T_x	compliant support for BM
T_y	compliant support for BM	T_z	diff. balance-mass movements

Embodiment 2 -- Wafer Stage Balancing in 3 Degrees of Freedom

A similar scheme can also be applied to the wafer stage. The latter has, however, major movements in at least 2 degrees of freedom (two orthogonal directions in the plane of the wafer). An open-frame type balance mass, free to move in the above-mentioned plane in a frictionless manner, can be used for the said balancing purposes. An additional freedom for yaw movement has to be allowed for to accommodate off-centre reaction forces.

The embodiment can be summarised as follows:

Transmission of Forces & Moments from Wafer Stage to Balancing System

F_x	via thrust bearings between Long Stroke Module (LoS) & Balance Mass (BM)
F_y	through linear motor in scan direction (mover on LoS, magnet plates on BM)
F_z	via thrust bearings between LoS & BM
T_x	differential / off-centre vertical forces between LoS & BM (thrust bearings)
T_y	differential / off-centre vertical forces between LoS & BM (thrust bearings).
T_z	differential Y-forces between Long Stroke & Balance Masses.

Balancing Methods

F_x	long-range balance-mass movements	F_y	long-range balance-mass movements
F_z	(optional) compliant support for BM	T_x	(optional) compliant support for BM
T_y	(optional) compliant support for BM	T_z	balance-mass yaw movements

Experimental Verification

Figure 4 shows unfiltered servo error plots superimposed on velocity profiles. The first chart shows reticle stage (RS) servo error in the scan direction, with RS at standstill and wafer stage (WS) at full acceleration. The second chart shows the reverse. As can be seen, no obvious cross talk between RS and WS can be observed, demonstrating the effectiveness of the balancing systems.

Conclusions

The use of inertia balancing results in much improved machine dynamics and simplifies the design of the machine structure considerably. Experimental results have demonstrated the effectiveness of the balancing system in reducing the cross talk of different moving stages sharing a common machine platform. It has been demonstrated that such a balancing system can be implemented with long-range movements in at least 3 degrees of freedom.

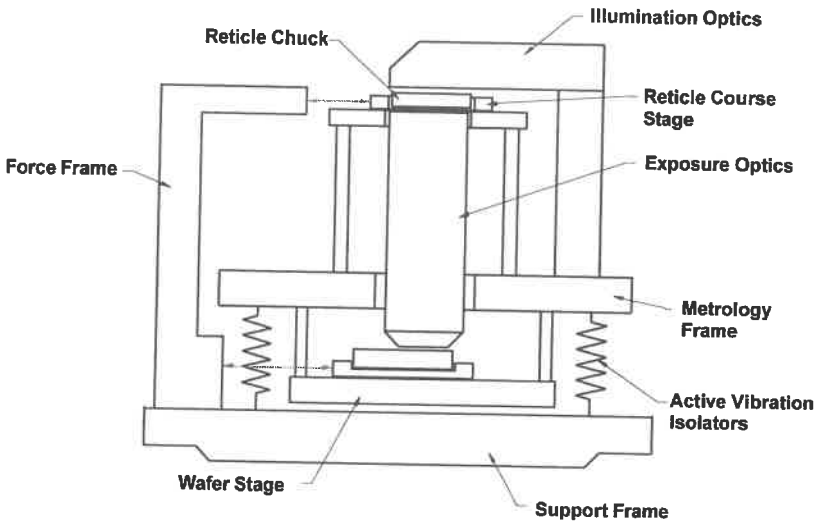

Fig. 1 Dynamics Architecture of an ASML PAS 5500 Scanner
(Actuator Forces transmitted to a Force Frame)

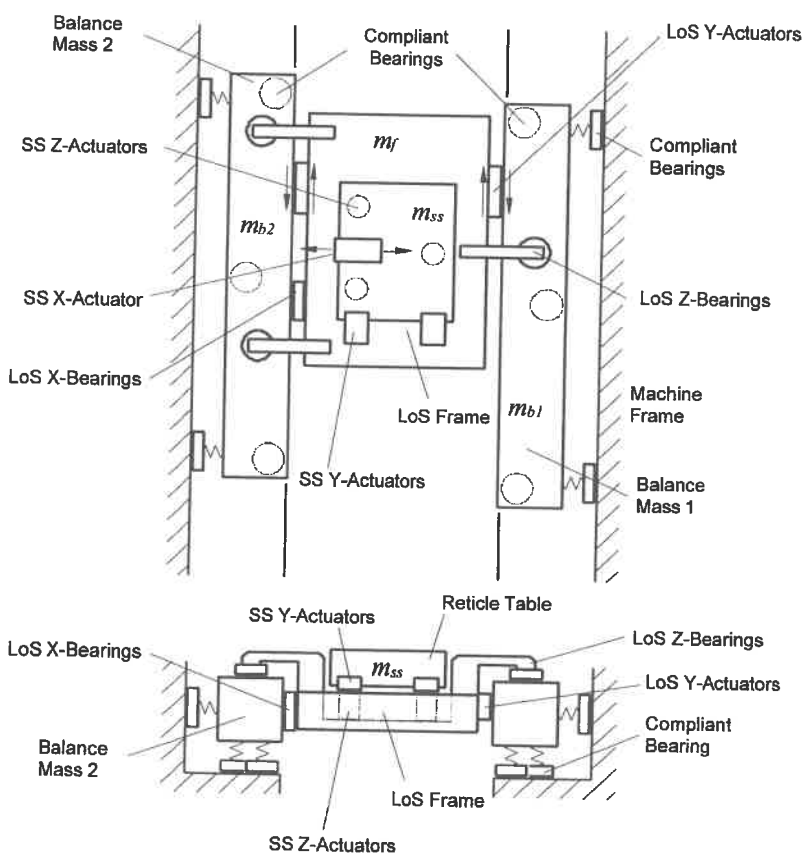

Fig. 2 6 Degrees-of-Freedom Balancing for a Reticle Stage

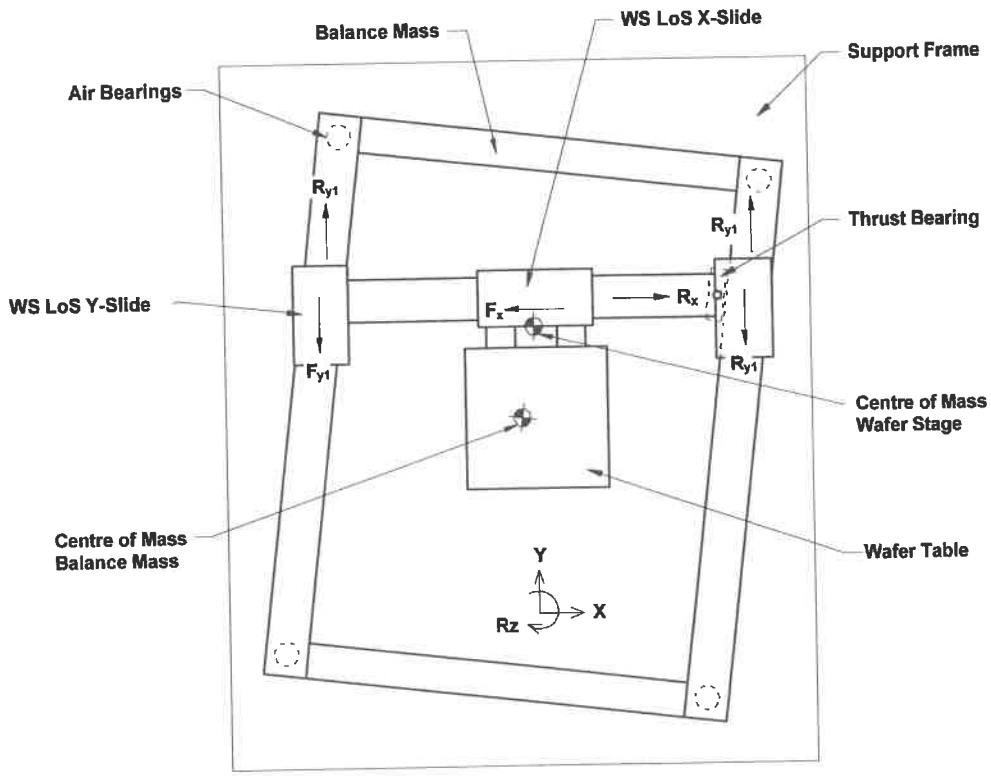

Fig. 3 Long-Range Balancing in 3 Degrees of Freedom for a Wafer Stage

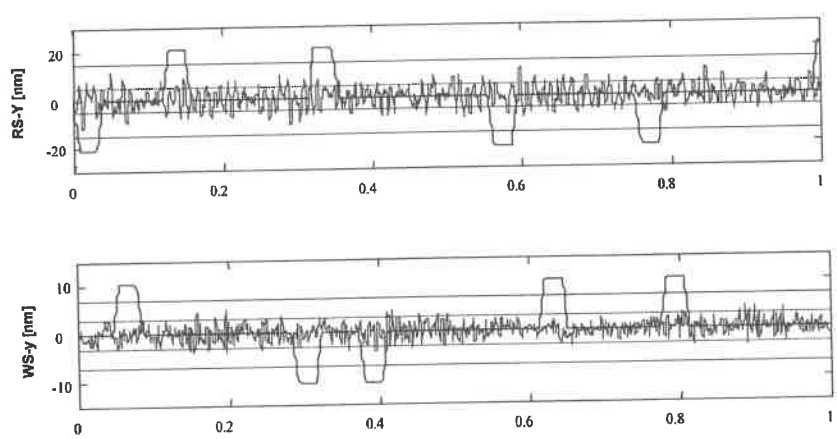

Fig. 4 Servo Error Plots for Reticle and Wafer Stages

Development of a Vertical Wafer Stage for High-Vacuum Applications

Erik Beckert, Andrew Hoffmann, Christoph Schäffel
IMMS gGmbH, Ilmenau, Germany

Eugen Saffert
Technical University of Ilmenau, Germany

Ulf-Carsten Kirschstein
Leica Lithography Systems GmbH, Jena, Germany

1 Introduction

Several new lithography approaches for semiconductor manufacturing require the redesign of current wafer step- and scan-systems leading to new concepts of high precision and dynamic movement under severe conditions such as high vacuum. Additionally non-optical lithography techniques usually show high sensibility to stray magnetic fields. This paper presents the concept, design issues and first evaluation results of a wafer stage designed for the ion-beam based lithography process.

2 Stage Specification

The goal was to develop a wafer positioning stage with step- and scan capabilities for a test bench to investigate the ion-beam lithography process. This process uses an ion source and a large column of electrostatic lenses to form the wafer exposing ion beam. This arrangement results in several challenging issues for the stage:

- Due to the risks of mask distortion and mask pollution with particels from the ion source area it was decided to arrange the ion-optics column horizontally, which means that the stage needs to position the wafer in a vertical plane making weight compensation a problem.
- The high sensitivity of the ion beam to magnetic and electrostatic fields requires not only the removal of possibly disturbing field sources near the ion beam but also careful shielding of field sources that are further away like the drives of the stage.
- The exposure process takes place under high vacuum conditions ($7.5e^{-7}$ Torr). A stage designed for this environment faces two major problems: heating and out-gassing. Power consumption optimized drives together with cooling equipment and careful material selection are a must for the stage design. Wear and friction needs to be reduced or even eliminated to prevent failure.

With its application in a future lithography process the wafer stage must be able to handle wafers of up to 12" diameter resulting in a travel area of at least 310 x 310 mm^2 in a vertical plane. The capability of moving in all six degrees of freedom should allow the stage to compensate wedge and thickness deviations of the wafer. The stage has to achieve a positioning accuracy in the sub-µm and µrad range which is enhanced to the nanometer range by the electronic ion beam tracking system. For wafer mark scans that connect the wafer in metrology and alignment terms to the ion-beam the stage must sustain a scanning speed accuracy below 2%.
Finally, the stage concept has to show high throughput capabilities in order not to be the bottle neck in cost-of-ownership considerations.

3 *Design Concept*

The solution for this complex motion problem was split up into two drives. A stepper motor acts as rough drive for a vertical Y-motion of 320mm. A magnetically guided, precise electrodynamic direct drive realizes a horizontal X-motion of 320mm as well as fine positioning in all other five degrees of freedom. **Figure 1** shows the overall structure. A shortcoming of it is the large base distance of the direct drives leading to large air gaps within the magnetic guidance to provide a required rotational motion.

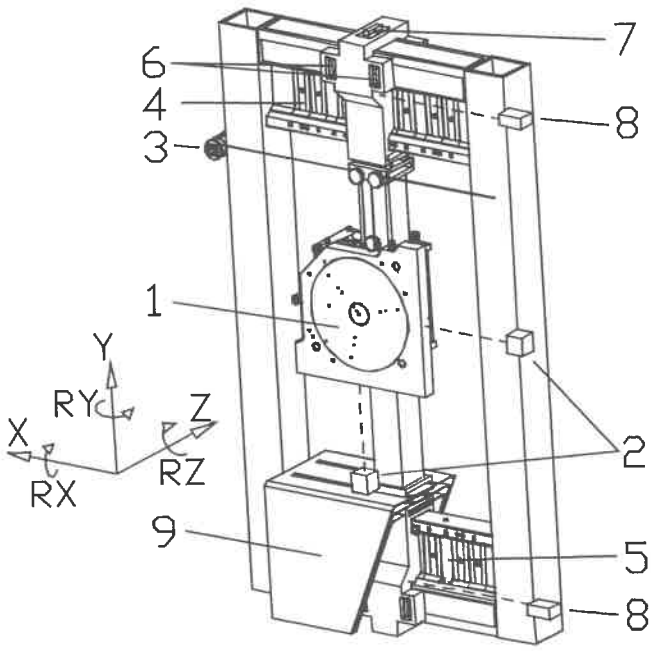

Figure 1: Design concept of the vertical wafer stage

The wafer is chucked onto a ZERODUR™ metrology unit (1) by electrostatic forces. The position of this unit is measured by three capacitance gauges in the Z-direction and a 0.6nm resolution 6-beam laser interferometer (2) in the other 5 degrees of freedom (providing twice RZ). The metrology unit is mounted onto a frame that glides along a 1 m long vertical ceramic ruler supported by a block and tackle mechanism driven by a fast stepper motor (3) through a cable winch. With the help of piezoelectric stacks the frame can be clamped to the ruler at any vertical position within a range of ±160mm with an accuracy of ±10µm in Y and a reproducibility of a few microns / µrad in the other axes. After reaching a desired vertical position the cable is relaxed to minimize its disturbing effects on the X-motion.

The main drive consists of an upper (4) and lower (5) direct drive with active magnetic guidances in Z (6) and Y (7) implementing the horizontal X-motion measured by two local laser interferometers (8) with a resolution of 5nm. These drives are more then half a metre away from the exposure spot on the wafer so the magnetic field leaking through the shielding of the drives will subside significant. Each magnetic guidance of the drives, arranged according to **figure 2**, has its own capacitance gauge to control the gap of the bearing between ±0.5mm, while the upper Y-bearing has built-in permanent magnets to compensate the static weight of the stage of around 50kg. According to the geometrical data of figure 2 and a resolution of 20nm of the capacitance gauges this leads to the following travel areas and theoretical position resolutions: X:±160mm (5nm), Y:±160mm (20nm), Z: ±0.5mm (20nm), RX:±0.4mrad (16nrad), RY: ±4mrad (160nrad), RZ: ±5mrad (6nrad). The advantages of this concept are the following: a single high precision stage can be moved in all six degrees of freedom. It is magnetically guided, floats freely (neglecting the influence of the electric cables) and thus without wear and friction. Potential field emitting sources are relatively far away from the exposing beam, a large area around the exposure spot on the wafer is iron-free. A three-layer magnetic shielding additionally decreases the field emitted from the drives of the stage. The weight compensation allows to drive all electromagnets of the guidance with low static current leading to low heat generation. The coils for the two linear drives are fixed and can, therefore, be easily water-cooled.

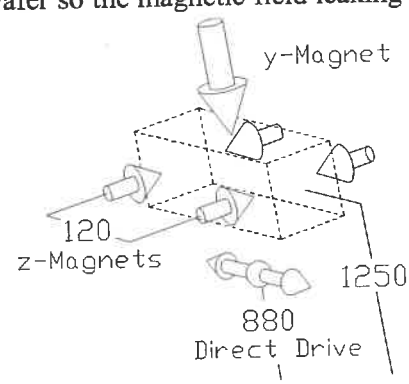

Figure 2: stage geometry, only upper drive shown

4 *Realization*

Figure 3 shows the setup of the drives in a segment of the large vacuum chamber of the test bench system. It depicts the upper and the lower drive each mounted in a steel chassis that also serves as first layer of the magnetic shielding. Two additional layers of magnetic shielding can be mounted around each chassis after the drives have been installed and adjusted. The layers are designed to form a labyrinth seal for the magnetic field inside. An advance study, carried out in a shielding chamber usually used for biomagnetic studies, showed that a three layer shielding with the described labyrinth seal reduces the magnetic field emitted from a drive down to 10nT (static) and 5pT (dynamic) at the exposure spot.

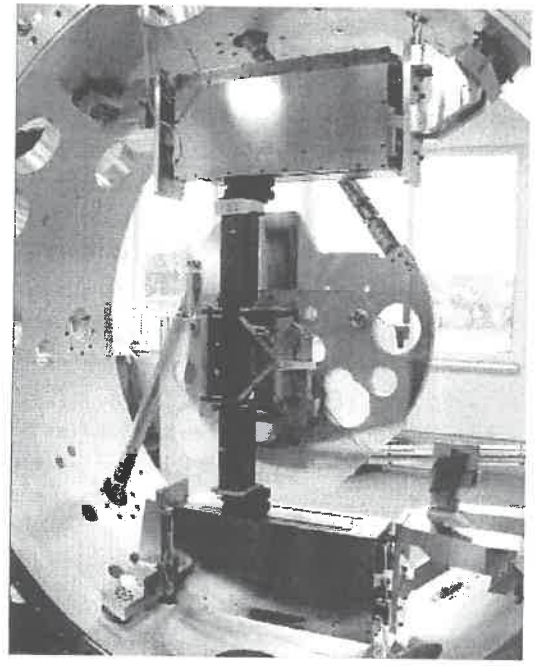

Figure 3: vacuum chamber setup

A major concern while designing the actuators of the drives were out-gassing and heating issues of the coils for the direct drive and the magnetic bearing. To prevent out-gassing an aluminum foil with an oxide coating of 5μm thickness is used as conductor for the coils. The oxide coated coil cores are designed in a way that reduces eddy-currents resulting in a lower time constant of the coils. The problem of heating due to the coil current is critical especially under vacuum conditions. Copper blocks with large cooling channels on top of the stators of the direct drives give them not only a stable double-T-shape but also withdraw heat from the direct drive coils. Since it seems not advantageous to connect the stage to a cooling equipment the electromagnets inside the stage were designed to have small current to force and a large force to mass ratio. The results are z-magnets with a weight of 0.6kg and a power consumption of 3W for 100N at an air gap of 1mm, while the y-magnets parameters are 1.4kg and 1.3W (100N at 1mm). Of course, these maximal forces are only required during peak accelerations. Since the magnetic guidances are driven only with low static currents to provide static torque compensation their mean power consumption is much lower and estimated to be 0.5W overall only. Thermal calculations showed that a maximum over-temperature of 3K will occur at the electromagnets coil cores, reduced to below 1K overall. Additionally, the actuators and stators of the direct drives are coated with black alumina to provide heat transfer via radiation from the stage to the cooled stator.

The control system of the stage consists of an industrial PC equipped with an TMS320C40 DSP-System sampling at a frequency of 2kHz. A/D-converters read the guidance air gaps from the capacitance gauges and a 64x interpolating encoder card services the two local X-interferometers. The wafer stage can be completely controlled with these "local" signals. They don't, however, provide exact position of the wafer. This is provided by the "global" 6-beam laser interferometer that measures directly at the wafer metrology unit. Its readings are transferred to the DSP control system via a high-speed parallel interface. The control system commands four power stages for the phases of the two direct drives and 12 power stages for the electromagnets of the magnetic guidance. Additional digital outputs command the stepper motor for the Y-motion and the clamp mechanism of the wafer metrology unit.

5 *Results*

A first evaluation of the wafer stage took place under industrial environment conditions. A major shortcoming of the test bench visible in figure 3 was the lack of a vibration isolation. As a consequence the environmental noise deteriorates the position stability of the wafer stage. Despite these aggravating circumstances the following positioning noises (3σ) at the wafer metrology were realized.

X [nm]	Y [nm]	Z[nm]	rotX [μrad]	rotY [μrad]	rotZ [μrad]
110	140	220	0.2	0.8	0.3

Table1: Realized position stability (deviation 3σ)

A general problem for all axes is the elasticity between the wafer metrology unit and the drives. The control model for the system assumes rigid couplings there, leading sometimes to vibrations with amplitudes below 1μm. In a further optimization the modeling of the elasticity with spring constants is planned.

To scan control marks on the wafer the stage needs to perform a motion in both the X- and Y-coordinate with a very constant speed. This is necessary for the beam - wafer alignment optics to obtain constant frequency signals while scanning the grid structure of the marks. **Figure 4** shows the speed deviation in percent while scanning with a speed of 1mm/s in the X-axis (along 4mm, performed by the direct drive) and the y-axis (along 0.2mm, performed by the y-magnetic guidance). The results clearly show that it is much easier to realize a uniform movement with direct drives (X) than by varying the air gap of a magnetic guidance (Y). Major problems for a uniform movement in the Y-direction lie in the short motion length, the varying influence of the weight compensation during the motion and a still too big time constant of the Y-electromagnets. Nevertheless a movement with deviations below 3% was realized at least for ±30μm around the desired spot which is sufficient to detect the control marks.

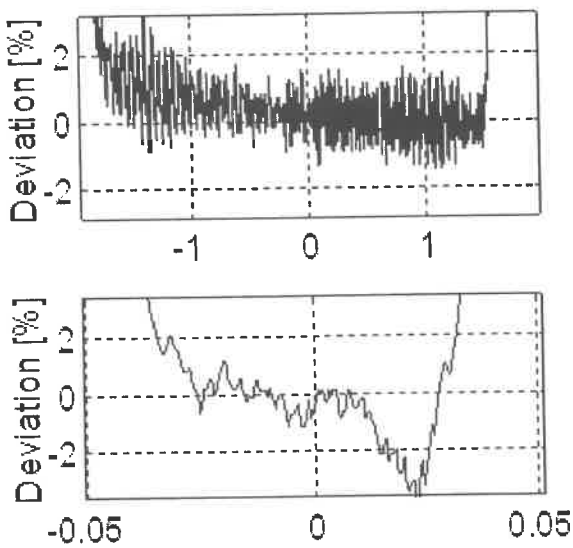

Figure 4: Speed deviations while scanning with 1mm/s in X (top) and Y (bottom)

6 *Conclusion*

A wafer positioning stage was built that a) is suitable to perform a vertical positioning process, b) can be used under vacuum conditions and c) realizes very low magnetic flux densities at the exposure spot on a wafer. It was shown that it is possible to reach a sub-micron accuracy with this stage in all degrees of freedom.

7 *References*

[1] Risse, S.; Peschel, T.; Damm, C.; Kirschstein, U.: A new metrology stage for Ion Projection Lithography made of glass ceramics, Optomechanical Engineering and Vibration Control (SPIE Proceedings Series 3786), p. 330-338

A giant magneto resistive (GMR) eddy current sensor for use as a zero width coordinate measuring machine probe

Stuart T. Smith and Teodor Dogaru, Center for Precision Metrology, UNC Charlotte, NC 28223

Summary

This abstract presents the working principle and some early results of using a GMR eddy current sensor as a CMM probe for detecting interfaces and edges. Two sets of factors effect accuracy and precision of this technique, these being the geometry and operational parameters of the probe and the assembly being measured. The influences of these variable parameters on the measurement are briefly discussed. As an example, it is shown that the location of the contact interface between two aluminum plates can be measured from the magnitude and/or phase response of the probe as it traverses over the surface. Analytic methods for interface location are also discussed.

Introduction

Preliminary results using a giant magneto resistance (GMR) based eddy current sensor for the directional detection of edges and discontinuities in solid surfaces are presented in this paper. An example of such a surface might be the surface that is created after the shrink fitting of a shaft in a hole, the wringing together of gage blocks or clamping of multiple components into an assembly. Clearly in this case it is not possible to use a conventional coordinate measuring machine (CMM) probe which relies on mechanical contact of a sphere of finite radius. The eddy current probe presented herein consists of a pancake-type excitation coil that creates circular eddy currents confined in a region near the surface of the specimen under test, figure 1. Dimensions of the excitation coils used in experiments range from mean radii of 1 to 8 mm. The sensing element consists of either a unipolar GMR or bipolar spin dependent tunneling (SDT) GMR sensor both in a Wheatstone bridge configuration. This represents a very directional device, detecting only the field vector along its sensitive axis. The GMR sensor is placed at the end of the coil on its symmetry axis, while the sensor's sensing axis is coplanar with the surface of the specimen. In this way, the sensor is insensitive to the excitation field that is oriented perpendicular to the

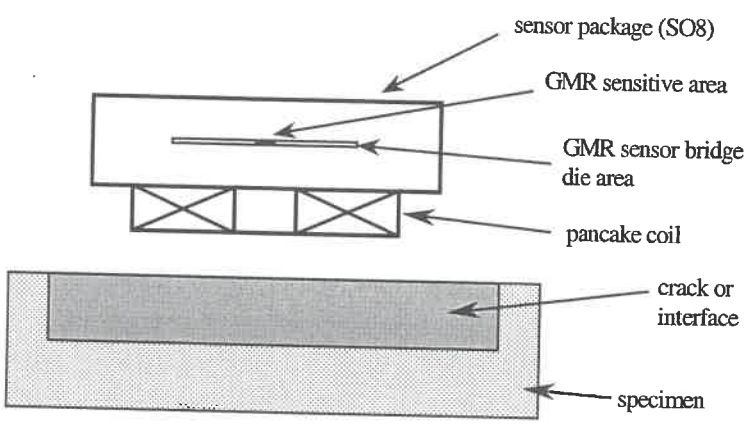

Figure 1: Schematic diagram indicating probe configuration

specimen surface. Moreover, when the probe is placed above a defect-free specimen, because of the circular symmetry of the induced eddy currents, the magnetic fields at the sensor's location

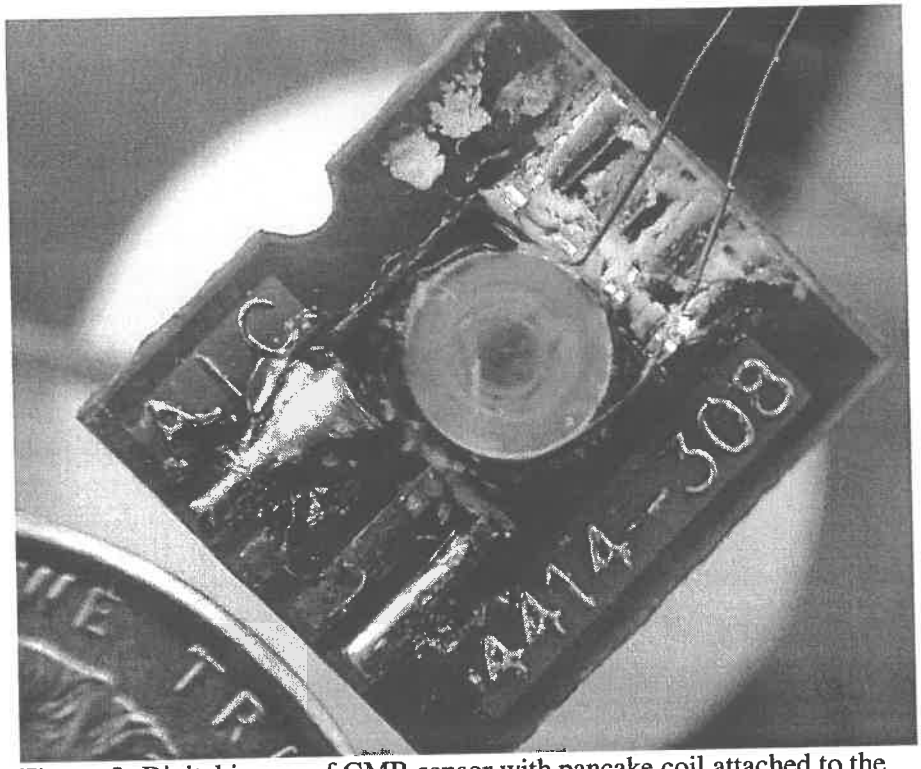

Figure 2: Digital image of GMR sensor with pancake coil attached to the lower face. A US penny (1 cent coin) is shown in the lower left corner for scale.

cancel. As a consequence, the sensor's output is zero in the case of a defect-free specimen. Figure 2 shows a digital image of a typical eddy current probe.

In general, induced eddy currents will form loops confined to the surface by the skin effect and concentrated mainly in a path corresponding to the mean coil diameter[1]. As the probe is traversed towards an edge, a crack or any other electrical discontinuity, the circular eddy current field will be perturbed thereby producing a signal at the sensor proportional to the asymmetry of the eddy current loops. Because of the change in impedance across contacting surfaces, a mechanical interface can be modeled as a thin crack. Consequently, there will be two current loops confined either side of the interface with the currents following the mean circumference of the coil and also along the interface. Because the eddy current loops will circulate in the same direction, the two currents flowing either side of the interface will be in opposite directions or 180 degrees phase shifted. During measurement, the sensor is oriented to be sensitive to fields produced by the currents flowing along the interface, its output will be proportional to the net field at the sensor. As the small sensor traverses over the crack, the single eddy current loop will be split to form a chordal "D" shaped loop on one side and a circular loop on the other that is cut by the interface. As the sensor approaches the interface, the current following the 'crack' on the side nearest to the sensor will produce the largest field. When the axis of the coil is located directly above the crack, there will be equal and opposite current loops, each a perfectly semi-circular "D", either side. Because the currents are of equal magnitude and opposite phase, the magnetic field in the plane of the sensor will be zero. Continuing across the interface the currents on the opposite side will begin to dominate thereby producing a steadily increasing signal that tends towards 180 phase shift relative to that produced on the opposite side.

[1] Dogaru T. and Smith S.T., 2000, A GMR based, eddy-current sensor, *IEEE Trans. On Magnetics*, submitted

Results

To illustrate the operation of such a probe, a pair of aluminum plates of similar thickness and with ground edges were placed in intimate contact on the bed of a Bridgeport milling machine. An SDT eddy current probe similar to that shown in figure 2 was then mounted in the spindle with the lower face of the pancake coil about 0.1 mm above the surface. The sensor was then rotated to maximize sensitivity to the interface (rotating the sensor by a further 90 degrees would effectively make the crack invisible). Future probes will incorporate bi-directional sensing elements to determine the vector of the field in the plane of the sensor. The specimen was then traversed under the probe at increments of 0.0254 mm and the amplitude and phase was measured at excitation frequencies of 20, 30 and 40 kHz using an SRS 850 lock-in amplifier.

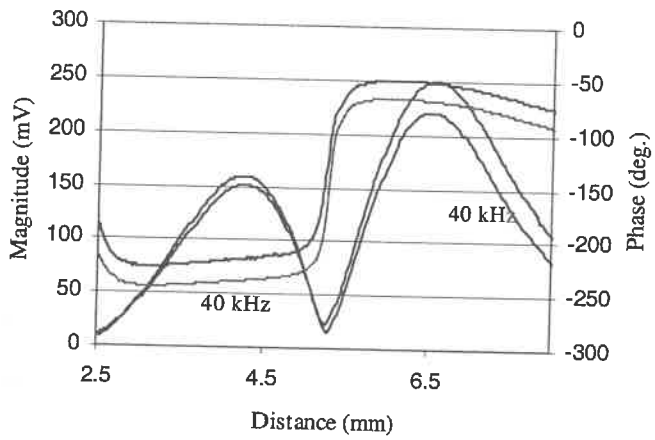

Figure 3: Magnitude and phase response of the eddy current probe at excitation frequencies of 30 and 40 kHz as it is traversed over a interface between two aluminum plates

Figure 3 shows the magnitude and phase of the output from the probe as it traverses over the surface of the two plates across the interface between them. A minima and a rapid phase change tending to 180 degrees can be seen as the probe passes the interface located at a position approximately 5.3 mm from the start of the scan. The asymmetry in the magnitude and phase responses is caused by misalignments between the sensor, coil and specimen.

A number of analytical methods may be used to determine the position of the interface. Tracking the minima, which, for a perfect probe, should tend to zero, is a simple method that may be used to determine the location of the edge. By location, it is inferred that this would be a point that would traditionally be considered the trigger event of a conventional CMM probe.

However, there are analytic methods that might provide a more precise location of the interface. A full representation of magnitude, phase and displacement requires a 3_D plot showing the response as a continua of points in space (i.e. a string). Figure 4 shows the three orthogonal views of such a three dimensional plot for the response measured at an excitation frequency of 40 kHz. The first figure is traditionally called a polar plot and this exhibits a characteristic figure "8". In this figure the displacement is along an axis perpendicular to the plane of the page. As the sensor moves over the interface the phase shift rapidly changes by 180 degrees and can be seen as the relatively straight line at –45 degrees. The position of the interface can be considered to occur at the point of intersection in the figure "8". Alternatively, the plot can be viewed along the displacement axis from two directions to yield the real and imaginary parts of the response, figure 4(b). Theoretically, the real and imaginary parts of the response should cross the axis of the graphs when the sensor is located above the interface. In reality, the intersection of the two plots will be shifted by offsets caused by manufacturing tolerances in the probe and specimens (the effects of which are currently under investigation). Closer examination of the data reveals that the crossing occurs at a position 5.295 mm from the start of the scan.

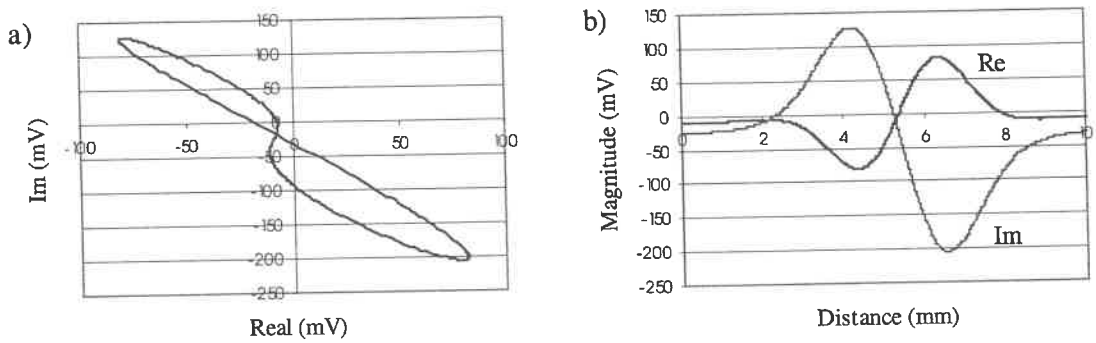

Figure 4: Three orthogonal views of the eddy current probe response, a) polar plot, b) real and imaginary parts of the response. Excitation frequency 40 kHz

Another method can be derived if it is assumed that the most rapid phase change will occur when the probe is traversing directly over it. Hence it may be possible to locate the interface at the peak value of the first derivative of the phase with respect to the scan distance. Additionally, it may be argued that the rate of the phase change is related to the separation of the two opposing eddy currents running along either side of the interface and the relative lift-off of the probe. In general, for a particular material, the eddy currents will be concentrated towards a surface at a depth inversely proportional to the square root of the excitation frequency. In general, the sensitivity of the peak phase slope measurement will be increased with increasing excitation frequency and reduced probe – specimen separation. Figure 5 shows the phase slope as a function of the displacement of the probe. A nonlinear curve fit of a Lorentzian function is also shown for the 40 kHz plot. It is clear that the phase slope is significantly enhanced at the higher frequency. From the non-linear curve fit, the peak is found at a displacement of 5.295 mm a value equal to the location of the intersection of the real and imaginary loci. However, it is also noted that the peak for the phase slope measured with a 30 kHz excitation is slightly shifted. This illustrates that the location of the interface is relative.

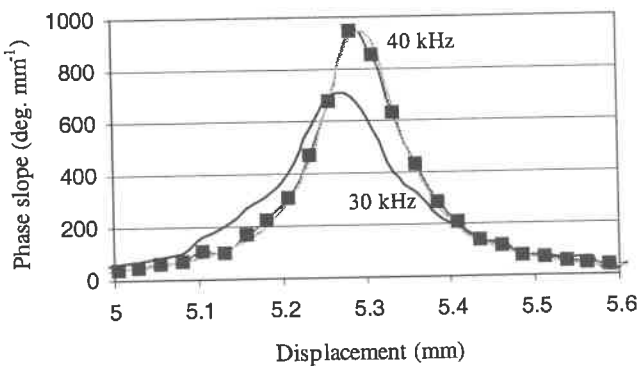

Figure 5: Phase slope as a function of displacement

Although, the principle of operation of an eddy current probe for the location of interfaces has been demonstrated, there clearly remain a number of outstanding issues. In particular, effects of probe and specimen geometry as well as operating parameters such as excitation frequency, coil current and specimen material are to be assessed in future studies.

Acknowledgements

The authors would like to acknowledge the support of the Affiliates Program of the CPM and continued support from Non Volatile Electronics, MN, in particular Dr's Carl Smith and Bob Schneider. Thanks also go to Hua Yang and Mark Lederman for assembling probes and collecting data.

A NEW DESIGN FOR A THREE-DIMENSIONAL MEASUREMENT PROBE

Alexander Sohn, Thomas A. Dow, Edward A. Marino*
North Carolina State University
Precision Engineering Center
Campus Box 7918, Raleigh, North Carolina 27695

An Electronic Three-Dimensional measurement probe (E3D) was developed to be low cost, flexible, rugged, sensitive and accurate to ±0.25 μm in all three directions over its 250 μm measuring range. The unique diaphragm flexure design reduces the problem of force lobing while maintaining a low probing force of 20 mN/μm (2 gf/μm).

Design

E3D is a mechanically simple device designed for analog scanning. As shown in Figure 1, the sensors for the probe are three orthogonally mounted Linear Variable Differential Transformers (LVDT's) that provide frictionless measurement and are suited for sensing nanometer

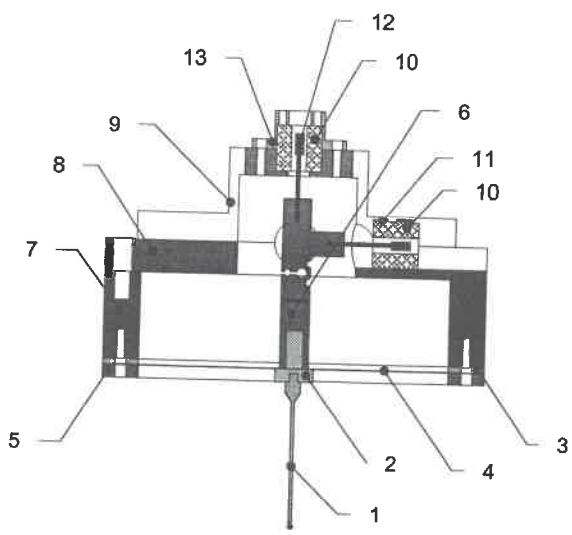

Figure 1 Schematic cross section of 3-D Probe 1. Stylus 2. Connecting Nut 3. Outer Clamping Spacer 4. Diphragm flexure 5.Middle Spacer 6. Triad 7. Shell 8. LVDT Support (bottom) 9. LVDT Support (top) 10. LVDT Coils 11. LVDT Cover (X Shown) 12. LVDT Core 13. LVDT Cover (Z)

* Current Address: UTC-Pratt & Whitney,400 Main St., East Hartford, Conn. 06108.

displacements. These sensors are rigidly coupled to a probe tip through a Triad and inconel beam. The system is free to rotate in two dimensions (X and Y) and translate in a third (Z) via a thin pretensioned diaphragm flexure. The diaphragm flexure and orthogonal arrangement of the three LVDT's allows independent sensing of the three directions. The diaphragm flexures also have the advantage that they can be easily substituted in different configurations to suit the measurement application.

Testing

The device has been tested on several standards: a flat plate, a step height standard and a gauge block to characterize its performance. Accuracy, repeatability and resolution all currently lie within the measurement noise band (±0.25 μm).

The most demanding of the tests - scanning a step height standard with multiple steps totalling 75 μm in height - revealed a measurement error of ±0.18 μm rms. All three axes were used over a substantial portion of their ranges in thesetests. Figure 2 shows the raw data output of each probe axis, specified as X', Y', and Z'. The raw data was then combined to evaluate the vertical displacements on the stepped sample and calculate the error in the measurement as shown in Figure 3.

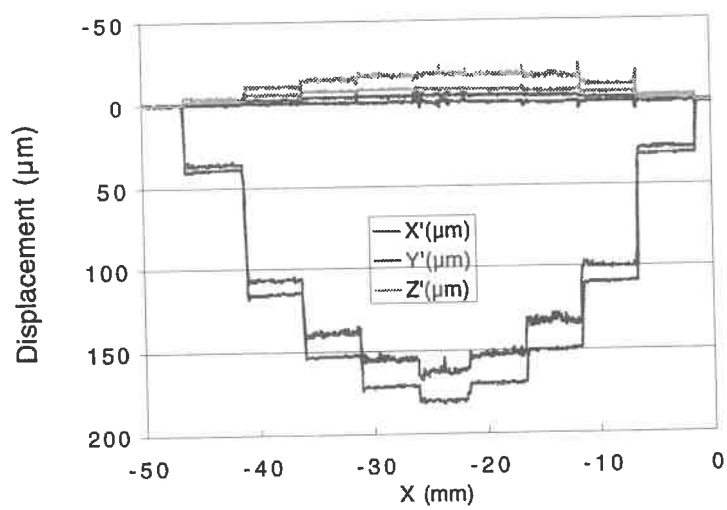

Figure 2 Raw Data obtained from the three axes of the probe upon measuring a stepped sample. The two traces for each axis represent a forward and reverse scan.

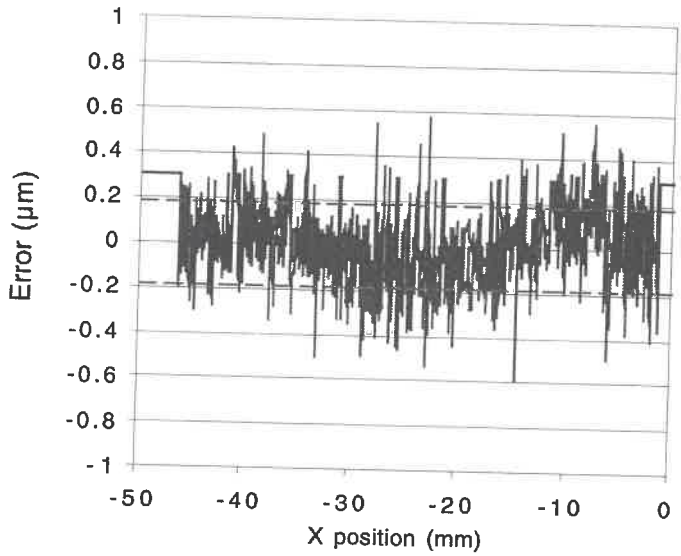

Figure 3 Error plot for stepped sample measurement. All three axes of the probe were used to generate a part profile, which was subsequently subtracted from the part's true profile to obtain the error in the Z- Direction. The dashed line indicate the RMS Value of 0.19 µm

Double Diaphragm Flexures

Since these tests were performed with the probe in the single-diaphragm configuration, force lobing presented complications. As can be seen in Figure 2, when the stylus was drawn across the surface of the sample, frictional forces caused large X- deflections since this measurement axis was about ten times more compliant than the Z- direction. Oftentimes, the X-axis exceeded its measurement range, even for modest Z- deflections. This would certainly present significant difficulties for many types of measurements.

From the outset of this project, multiple diphragms were seen as an avenue for equalizing probing forces in different directions. The flexure design evolved through several configurations: from a machined aluminum diphragm, to one of steel and finally to a self-contained, pretensioned membrane. To eliminate the need for a tensioning mechanism on the probe, the flexure was pretensioned by soldering a 25 µm (.001") brass diaphragm to a copper ring. The difference in Coefficient of Thermal Expansion (CTE) between Copper (17 ppm/°C) and brass (20 ppm/°C) causes a strain on the diaphragm, pretensioning it. This flexure design allows a wide range probing forces to be obtained as well as the use of multiple flexures in a stacked configuration.

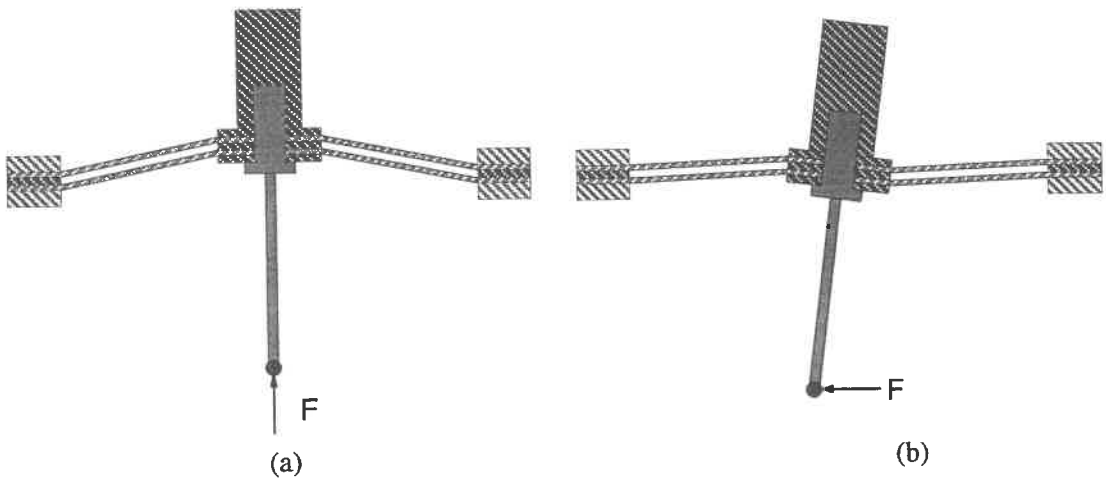

Figure 4 Schematic cross section of probe with double diaphragm. (a) shows deflection in the axial (Z') direction and (b) shows deflection in the radial (X' or Y') direction.

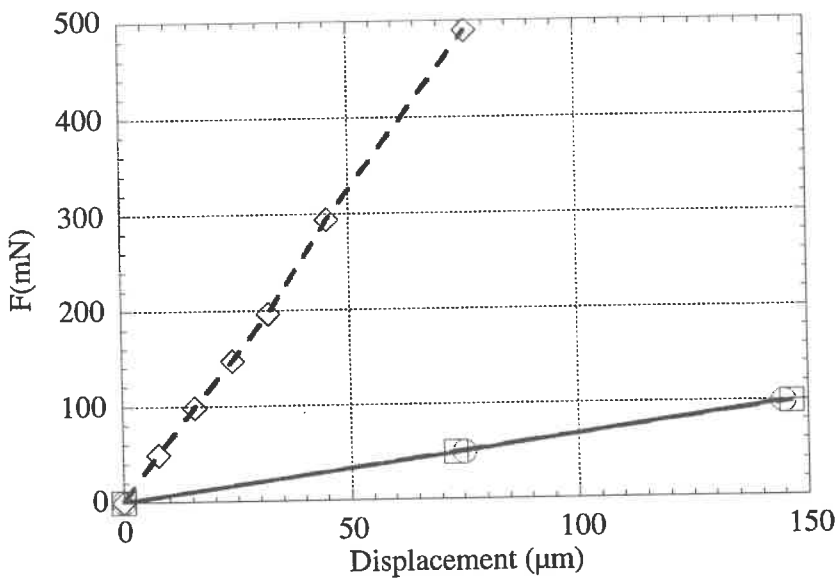

Figure 5 Force/Displacement curves with single. G, E, and A represent the X', Y' and Z' directions, respectively. The slopes of these curves represent the stiffness in each direction with a ratio of approximately 10:1 between the radial (X', Y') and axial (Z')

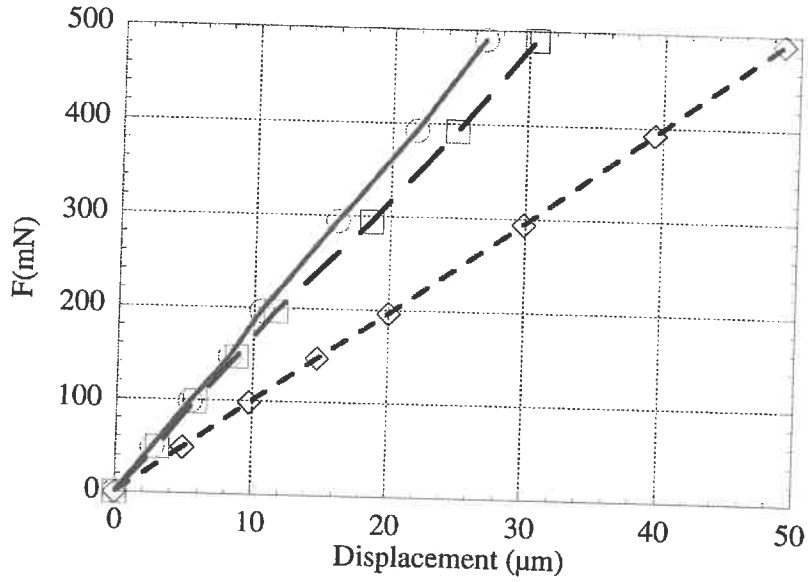

Figure 6 Force/Displacement curves with double diaphragms spaced 2.5 mm apart. G, E, and A represent the x', y' and z' direction, respectively. The stiffnesses in all directions lie within a factor of two of each other.

The use of Dual flexures as shown in Figure 4 allows a substantial increase in stiffness to be obtained in the radial direction, while only doubling the stiffness in the axial direction. The spacing of the flexures is then a independent parameter that can be adjusted to eliminate force lobing in all directions. The reduction in force lobing is illustrated in Figures 5 and 6.

Conclusions

E3D is ready for implementaion into 3-D measurement systems. The current version of the device is shown in Figure 7. A commercial incarnation of it is being developed for installation on an ultraprecision 3-D measurement system developed at Eastman Kodak Co.

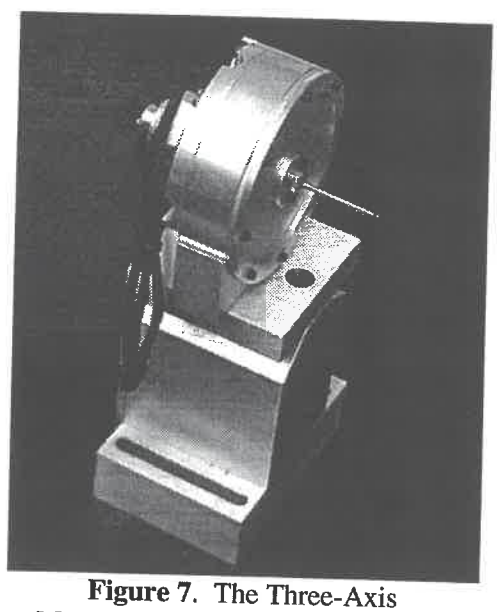

Figure 7. The Three-Axis Measurement Probe mounted on an aluminum stand.

Development of a special CMM for dimensional metrology on microsystem components

Uwe Brand, Thomas Kleine-Besten, Heinrich Schwenke
Physikalisch-Technische Bundesanstalt (PTB)
Braunschweig, Germany

INTRODUCTION

Further miniaturization and modularization are current trends in microsystem technology, which require 3D-coordinate measurements to be performed with measurement uncertainties in the range of 0.1 µm. With conventional coordinate measuring machines sub-centimeter structures usually can be measured only optically, i.e. in two dimensions with measurement uncertainties of about 1 µm. Therefore activities were started to develop special measurement equipment which satisfies the described requirements. Moreover the equipment to be developed will also allow to perform measurements on other challenging objects, like e.g. small setting ring standards, small diameter wires etc.

The PTB started a project to develop a special CMM for dimensional metrology on microsystem components with an uncertainty of < 0.1 µm. At first an opto-tactile 3D-sensor with an optical fibre as a "probe pin" will be used. The sensor allows to use very small probing balls with diameters down to 25 µm and probing forces as low as 1 µN. 2D probing uncertainties of 0.15 µm were already obtained with this system [1].

The second tactile sensor to be used is based on a silicon boss-membrane with piezo resistive transducers [2]. First probing experiments have been carried out showing its resolution and 1D-reproducibility of the contacting points to be better than 10 nm.

In parallel to the instrument development new precision diamond turned depth setting standards for topography measuring instruments with depths in the mm range have been developed [3]. The standards are made of OFHC copper and are covered with a wear-reducing nickel coating. The calibration uncertainty of the deepest grooves (currently 900 µm) amounts to 54 nm. Under good conditions, these standards allow to perform traceable measurements of topography measuring instruments with a maximum uncertainty of 78 nm for the range of 1 mm.

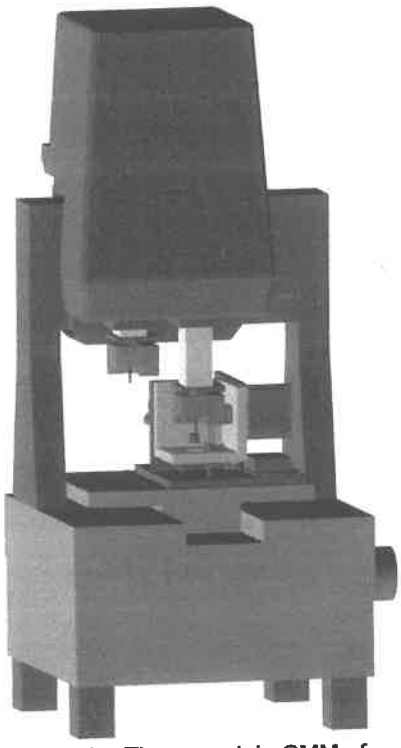

Fig. 1: The special CMM for dimensional measurements on microsystem components

THE SPECIAL CMM

The PTB develops a special CMM for dimensional metrology on microsystem components with an uncertainty of < 0.1 µm. The measurement range will be 25 mm x 40 mm x 25 mm. The instrument is based on a commercial CMM [4] with improved capabilities through the use of high resolution scales (10 nm resolution) and optimised air bearings. A stability of < 20 nm between ram and the basic setup in all axes was aimed at. The instrument will consist of an optical coordinate measurement system and two tactile 3D-micro-sensing systems. Both tactile sensing systems will be mounted at different z-columns of the coordinate measuring machine (see Fig. 1). To improve the measurement uncertainty of the instrument the translational displacement and the guiding deviations are measured by laser interferometry. A metrology frame including three minaturised plane mirror laser interferometers [5] for simultaneous measurement of displacement and angle is added to the CMM. Each of the two tactile sensors is enclosed by a zerodur cuboid that is mounted to the CMM ram. The metrology frame consists of an outer aluminium frame, supporting the compact laser interferometers and an inner frame, made of invar, that supports the reference mirrors of the interferometers and the specimen to be measured.

The first tactile sensor to be used will be an opto-tactile 3D-sensor [6] with an optical fibre as a "probe pin". The 2D version of this sensor [6] is commercially available with smallest probing ball diameters of 25 µm and probing forces down to 1 µN. The functional principle is based on the determination of the probing ball position by an optical imaging system and a CCD camera (Fig. 2). The "probe pin" used is an optical fibre whose tip is provided with a spherical probing element which is illuminated through the fibre. The optical fibre is mounted in the optical axis of the system such that the probing element is kept in the focussing plane of the optical system. The backscattered light of the ball is imaged on the CCD sensor as a bright light spot, whereas the rest of the fibre remains largely invisible to the camera as it is outside the focussing plane. When the probing element comes into contact with the workpiece surface (i.e. when shifting with respect to the camera), the light spot changes its position on the sensor. This change in position can be evaluated with subpixel accuracy. 2D probing uncertainties of 0.15 µm have already been obtained with this system [1]. Recently a modified 3D version has been realized and tested [6] that is planned to be used on the special CMM for first measurements. The 3D sensor (Fig. 2) uses a second imaging system that is mounted perpendicular to the probing fibre and images a second target mark (1). As a target mark for measuring the z-deflection a glass sphere was used. Illumination can be made optionally as vertical illumination or as transmitted light.

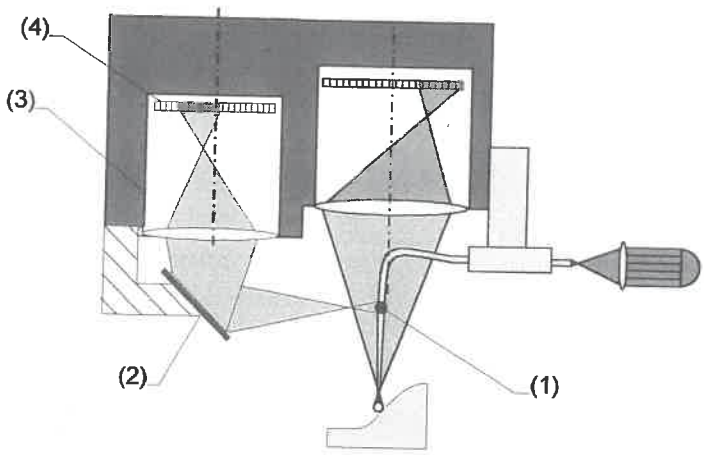

Fig. 2: Principle of the 3D-opto-tactile micro-probe: (1) second target mark (2) mirror, (3) second camera for measuring the z-deflection of the target mark, (4) CCD-chip

The second tactile sensor to be used with the special CMM is a completely different type of tactile 3D-sensor. It is based on a silicon boss-membrane that acts as a membrane spring and a stylus in the center [2] (see Fig. 3). The probing element of the sensor consists in this early stage of development of a stiff stylus, 500 µm in diameter and 4 mm long. It is fixed to the boss by epoxy resin. On the backside of the membrane there are piezo resistive elements that locally detect deformations of the membrane. Deflection of the stylus during probing of a workpiece deformes the membrane and causes local resistance changes of the piezo resistive elements. Connecting the piezo resistive elements to Wheatstone bridges allows to measure stylus deflections in x-,y- and z-direction. Probing experiments have been carried out showing a resolution of the sensor of a few nanometers and 1D-reproducibility of the probing points to be better than 10 nm (see Table 1).

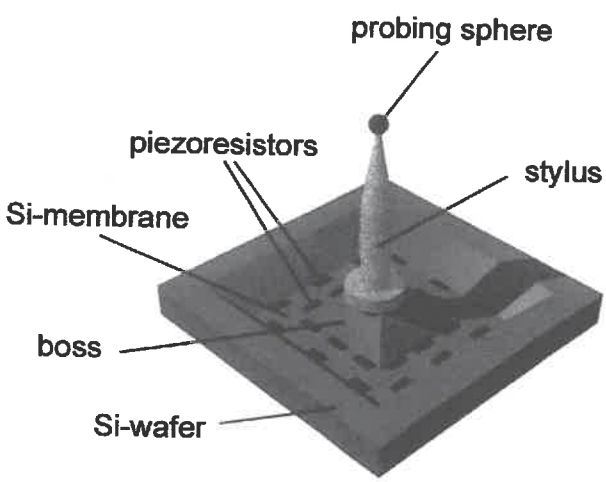

Fig. 3: 3D-Si-boss-membrane sensor with piezo resisitve elements

For a maximum deflection of the probing sphere of 3 µm and a deflection velocity of 100 nm/s a high linearity (R > 0,99997) of the probing curves and no hysteresis deformation was found. With

deflections up to 20 µm in x-y-direction and a slow deflection velocity of 100 nm/min hysteresis due to the relaxation of the epoxy resin was observed. The maximum deflection in z-direction should not exceed 6 µm because of possible mechanical destruction of the boss-membrane.

	x-, y-probing direction	z-probing direction
resolution	*3 nm*	*5 nm*
repeatability of contact point position	*< 10 nm*	*< 20 nm*
stiffness	*2.5 mN/µm*	*55 mN/µm*
measuring range	*20 µm*	*6 µm*
crosstalk x-y-direction	*< 15 $nm_y/\mu m_x$*	*< 120 $nm_x/\mu m_z$*
crosstalk z-direction	*< 15 $nm_z/\mu m_x$*	-

Table 1: Specifications of the tactile 3D Si-boss-membrane sensor

In the following, measurement results with the 3D-Si-boss-membrane sensor will be described that were obtained at the PTB with a probing ball diameter of ≈ 160 µm and a shaft diameter of 500 µm. The maximum penetration depth into boreholes is only 200 µm according to the conical shaft. To demonstrate the capabilities of the system, 2D-measurements on a setting ring standard (1 mm diameter) were carried out. Probing direction was x-direction and it was analyzed the x-axis of the sensor. From the x-probing curves the probing points (probing force zero) were calculated. Fitting a circle to the measured probing points and calculating the deviations for each point gives the measured form errors. These form errors are due to form errors of the ring, due to form errors of the probing sphere used, due to contributions of the 3D-Si-boss-membrane sensor and due to geometric errors of the x-,y-positioning table. The ring measurement was repeated several times in order to determine the measurement repeatability. The standard deviation reached for unidirectional probing at PTB is appr. 0.1 µm; It is to be expected that for the two- and three-dimensional case comparable results can be achieved.

DEPTH SETTING STANDARDS FOR MEASUREMENT RANGES FROM 1 µM TO 1 MM

At PTB, ultraprecise surface figuring by diamond turning has proved its worth in the manufacture of superfine roughness standards. This technique not only allows synthetic roughness profiles [7] to be manufactured with great precision, but also surfaces of optical quality. Surfaces with arithmetical mean deviations of $R_a \approx 1$ nm and flatness errors smaller than 100 nm over ranges of a few millimeters are today the state of the art. Achieving this surface quality requires, however, a lot of time and effort. Special attention must, for example, be paid to the purity of the materials to be machined (for example, OFHC-Cu (oxygen-free copper) or highest grade aluminium), and the environmental conditions around the finishing machine must be very stable. Manufacture may take several days. For the manufacture of the new depth setting standards, a commercial CNC diamond turning machine controlled by a laser interferometer (resolution: 10 nm) was used. The material selected was very pure copper (OFHC-Cu), as the best surface qualities (arithmetical mean deviation $R_a = 1$ nm, waviness $W_t = 50$ nm, flatness 50 nm over a measuring length of 20 mm) have been obtained with this material. The copper disks used are 90 mm in diameter and 10 mm in thickness. A mono-crystalline natural diamond with a tip radius of 5 µm was used as a cutting tool. The feed rate was 0,1 mm/min on the plane surfaces and 0,03 mm/min on the flanks, with the spindle rotating at 1000 revolutions/min. Feed motion was 10 – 20 µm, only the final cut was carried out at a feed motion of 1 µm. After the rotationally symmetric grooves have been produced on the disk, the latter is cut into twelve parts of identical size using wire-EDM. To reduce wear the surface is covered with a nickel coating (thickness 5 µm). The surface hardness of the standards then is approx. 500 HV and corresponds to that of medium-hard steel. The surface is resistant to wear even if conventional contact stylus instruments are used whose measuring force is relatively great (in the mN range). As a result of the nickel coating the roughness of the surface increases, however, so that the arithmetical mean deviations then are $R_a = 9$ nm. Limited by the layer thicknesses which can be

produced in practice, profiles with a depth down to 100 µm can be cut into the Ni layer also directly and used as standards without additional coating. This allows the roughness originally produced in the turning process (which is a little lower) to be maintained. For the grooves deeper than 100 µm it is planned to apply an additional cut after coating the disk with the wear reducing Ni layer in order to achieve a better surface quality. The aperture angle of the grooves is (70 ± 1)°, the width of the grooves at the root 0.3 mm, and the range between the v-grooves 0.4 mm in length. As an example, Figure 4 shows a selection of groove depths. As the grooves can be manufactured with any depth desired, grading of their depths can be adapted to specific measuring instruments. It is moreover possible to manufacture any aperture angle greater than 70° and, thus, edges with flatter slope. Even optical measuring instruments such as, for example, fringe projection measuring instruments for which continuous tracing of the fringes is essential for evaluation, can be calibrated with such grooves.

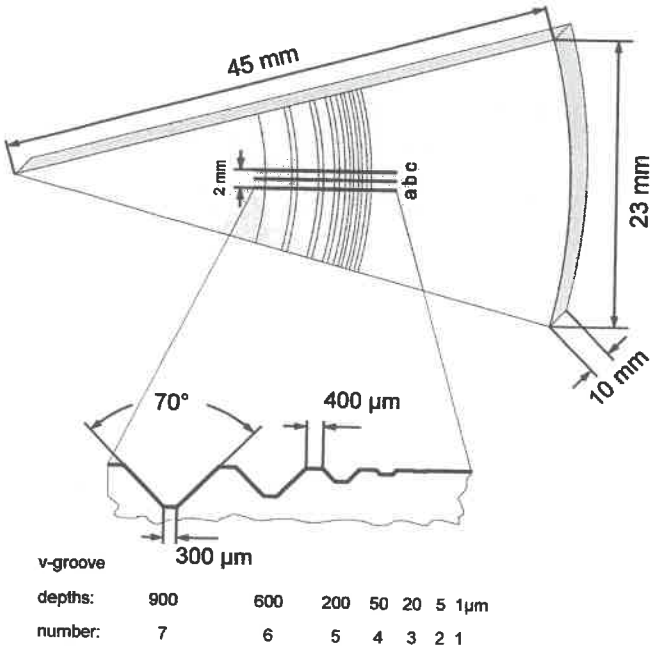

Fig. 4: Details of the new diamond-turned depth setting standard

Calibration can be carried out very efficiently, as all calibration grooves can be measured in a single measurement. The length of the profile to be measured amounts to only 8 mm for seven grooves between 1 µm and 1 mm in depth. The groove depths (d) have been calibrated using a Form Talysurf stylus instrument. The expanded uncertainty for the deepest groove (900 µm in depth) is U = 54 nm. The main contributions to the uncertainty follow from the repeatability of the FTS calibration ($u = 2.5 \cdot 10^{-5} \cdot d$), from the uncertainty of the step heights of the standard used to calibrate the FTS (7.5 nm) and from the deviation of the feed unit from the level plane and the drift of the FTS during the measurement (6.1 nm).

The uncertainties obtained here are typical of the diamond-turned depth setting standards presented. Deviations are within the range of a few per cent.

Which uncertainties of measurement can be obtained in the calibration of a measuring instrument when the new diamond-turned depth setting standards are used? To answer this question it is assumed that the properties of the measuring instrument to be calibrated are similar to those of a Form Talysurf stylus instrument. The uncertainty of measurement of the measuring instrument to be calibrated can then be calculated, assuming a standard uncertainty of the calibration standard of 54/2 nm. From this follows an uncertainty value of the calibrated topography values 38.4 nm when a groove 1 mm in depth is to be measured. When an uncertainty contribution caused by the alignment of the profile is taken into account, and on the assumption that four repeat measurements are performed, an expanded uncertainty of measurement of U = 78 nm results. Thus under good conditions, allows link-up of topography measuring instruments to a material standard with a maximum uncertainty of measurement of 78 nm in the measurement range of 1 mm.

In the case described here, the grading of the groove depths has been adapted to the measurement ranges of a contact stylus instrument; however, the manufacturing process allows any grading desired. Nominal values can be complied with with tolerances of a few thousandths.

LITERATURE

[1] Guijun, Ji, Schwenke, H; Trapet, E: Opto-tactile sensor for measuring small structures on coordinate measuring machines. ASPE (1998)

[2] Kleine-Besten, T; Loheide, S; Brand, U; Bütefisch, S; Büttgenbach, S: Development and characterization of

new probes for dimensional metrology on microsystem components. Proc. EUSPEN (1999), 387-390
[3] Brand, U; Krüger-Sehm, R; Stuht, P; Koender, L; Hinzmann, G; Feist, C; Jäger, V: Depth setting standards for profilometers and interference microcopes. Surface Colloquium Chemnitz 2000, Germany
[4] Coordinate Measuring Machine Video Check IP400 from Werth Messtechnik GmbH, Siemensstr. 19, 35394 Gießen, Germany
[5] Miniature plane mirror interferometer for simultaneous measurement of path and angle, SP 500 D from SIOS Messtechnik GmbH, Am Vogelherd 46, 98693 Ilmenau, Germany
[6] Schwenke, H; Weiskirch, C; Kunzmann,H: Opto-taktiler Sensor zur 2D- und 3D-Messung kleiner Strukturen mit Koordinatenmessgeräten. Technisches Messen 12 (1999), 485-489 (in german)
[7] Hillmann, W; Jäger, V.; Krystek, M: Superfine roughness standards with irregular profile for the calibration of mechanically and optically scanning surface measuring instruments. Qualität und Zuverlässigkeit, 42 (1997), 76-79 (in german)

DESIGN AND TESTING OF A HIGH SPEED, 5-DOF, COORDINATE MEASURING MACHINE WITH PARALLEL KINEMATIC STRUCTURE

John C. Ziegert
Department of Mechanical Engineering
University of Florida

1.0 Introduction

During the past several years, a great deal of attention has been paid to parallel kinematic machines as an alternative structure for machine tools and other robotic equipment. Numerous claims have been made about the inherent advantages of this type of architecture, including superior stiffness and positioning accuracy. Despite these claims, and substantial effort by many research groups and industrial concerns, at this time few if any PKM machine tools are in use in daily manufacturing activities.

The goal of the work reported here was to examine the parallel kinematic architecture as applied to coordinate measuring machines, and to explore the accuracy attainable with this type of structure. In the following sections, we will describe a novel 5-DOF parallel structure with self-calibration capabilities which we are developing for use as a CMM. We will describe the basic design features, the kinematic relations which govern its motion, the metrology system, and the self-calibration algorithms. Finally, we will report on the results of accuracy tests of the assembled machine.

2.0 Design Concept

The basic structure of the hexapod coordinate measuring machine (HCMM) is shown in Figure 1. Kinematically, HCMM can be thought of as two tetrahedrons with a common base[1]. The apexes of the tetrahedrons are joined by a rigid center rod, which carries the CMM probe. At the three base joints, pairs of struts meet in double Hooke joints with a common center. At the apexes, three struts are joined to the center rod by spherical 4-bar linkages with common centers. Since the six struts all connect to the center rod at two points, the center rod cannot be rotated about its own axis by the extension of the struts. Therefore, the machine has only 5-DOF, and requires only 5 actuators. The sixth strut is passive (non-actuated) and serves only to carry a redundant measurement system, which is used for self-calibration. HCMM is designed to be able to measure objects within a cylindrical workspace 400 mm in diameter and 400 mm tall.

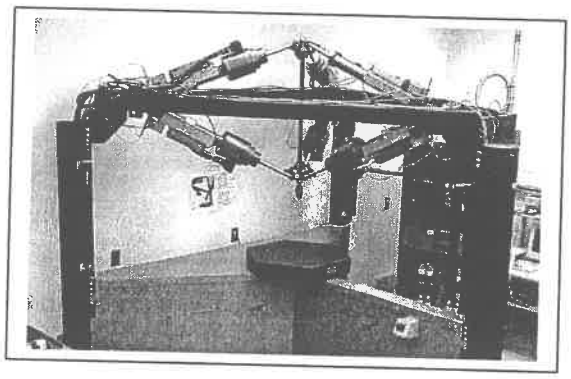

Figure 1. Hexapod Coordinate Measuring Machine

3.0 Base Design

The base structure of HCMM is assembled from structural steel components and consisting of three vertical stands with appropriate connections to support the work table and maintain their position. Atop the stands, an equilateral triangular weldment is kinematically supported by a ball and v-groove system. The 3 base joints are attached to this triangle, which has a side length of approximately 2175 mm. .

3.0 Strut Design

The 5 actuated struts of HCMM are designed to provide rapid movement of the center rod and attached probe by extended and retracting rotating nut

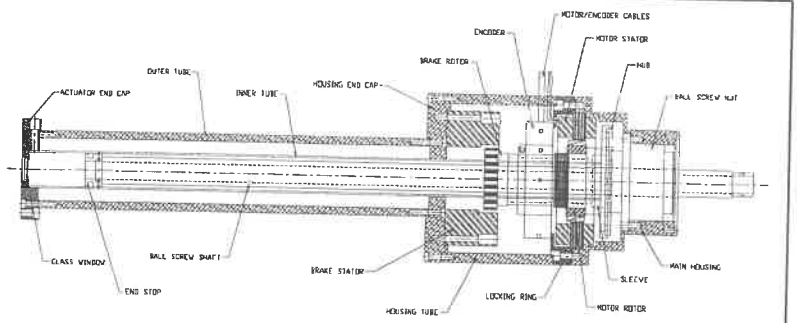

Figure 2. Schematic of HCMM actuated strut.

ballscrews under servo control. The rotating nuts are actuated by frameless DC servomotors with the rotor directly attached to the nut and the stator attached to the strut body. The body of the strut also houses a brake and a rotary encoder. The ballscrews have a 15mm hole through their length to permit co-axial strut displacement metrology using laser interferometry. The screw has friction seals and travels within an outer tube which enables the laser path to be evacuated. The struts can extend from a minimum length of approximately 900 mm to a maximum length of 1425mm. Tests of a single strut show it to be capable of extensional accelerations of 30 m/s^2 (3 g), and extensional speeds of up to 3 m/s at maximum motor rpm. A schematic of the actuated strut is shown in Figure 2. The response to a commanded motion with 3g acceleration is shown in Figure 3. The passive strut is similar in construction except that it has no motor and utilizes a recirculating ball spline instead of a ballscrew.

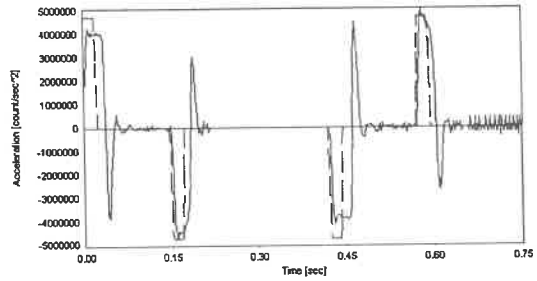

Figure 3. Response of HCMM strut to a commanded 3g acceleration. (Dashed line is commanded, and solid line is actual response)

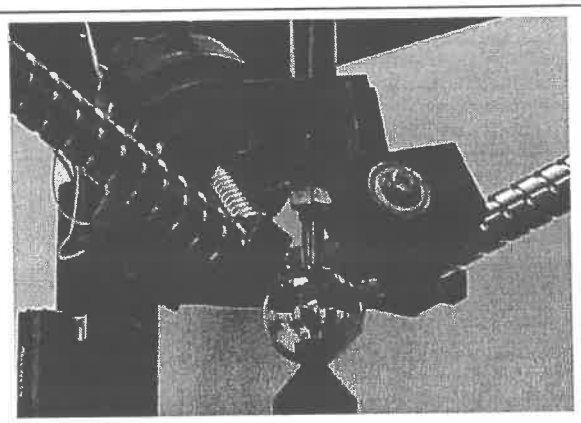

Figure 4. HCMM center joint design, showing reference sphere.

4.0 Joint Design

The kinematic model used to control HCMM assumes that the joints at the ends of each strut provide perfect spherical motion. Furthermore, it assumes that each pair of base joints and each set of three center rod joints is perfectly concentric. This is analgous to the assumption of axis straightness and orthogonality in serial cartesian machines. As a practical matter, it is very difficult to construct such joints with satisfactory accuracy. Therefore, HCMM employs the parallel kinematic machine equivalent of a "metrology frame", by incorporating a precision reference sphere at the center of each joint. (Figure 3). These spheres are mounted to the base and center rod in a manner which places them outside of the structural load path of the machine. The strut metrology system uses these sphere surfaces as kinematic references, thus allowing the requirement for accuracy of joint motions to be relaxed.

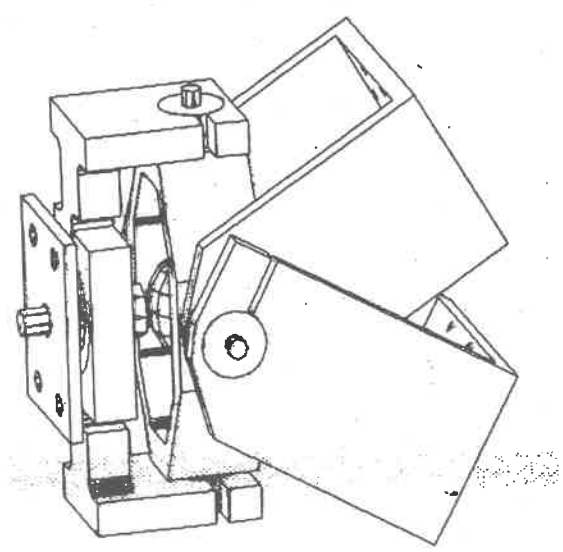

Figure 5. Schematic of HCMM base joint design.

5.0 Strut Metrology System

Each strut carries a laser and the associated optics necessary to measure the change in strut length interferometrically. (Figure 4) The metrology system is mounted to the strut body via a 4-DOF kinematic adjustment system which allows the measurement beam to be directed down the strut axis. The interferometer itself is carried on a flexure mounted stage with

a flat faced follower which rides against the reference sphere on the base joint. The target retroreflector is also spring mounted to ride against the reference sphere on the center rod. The laser beam is brought to the interferometer via a system of mirrors and another 4-DOF adjustment system which allows the laser beam to be properly aligned to the interferometer optics. After leaving the interferometer, the laser beam enters the evacuated strut through a window. The use of an evacuated beam path for the laser measurement beam obviates the need for correction of wavelength variations due to atmospheric conditions.

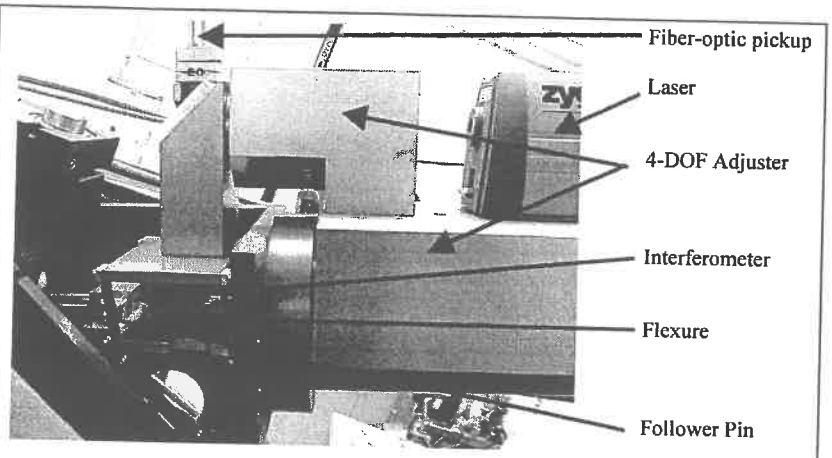

Figure 6. Closeup of HCMM strut metrology system

6.0 Kinematics

The kinematic structure of HCMM was chosen to reduce the number of parameters in the kinematic model to a minimum. In general for parallel kinematic machines (PKMs) it is straightforward to compute strut lengths corresponding to a given position and orientation of the moving body (inverse positional solution). However, for most machines of this architecture, the computation of the platform pose corresponding to a given set of strut lengths is more difficult (forward positional solution). In general, multiple forward solutions are possible and iterative techniques are needed to find them. When a PKM is used as a CMM, the computation of the probe tip coordinates from the strut displacements requires the forward positional solution. Since this computation needs to be performed hundreds of times in the measurement of a typical part, it is critical for a CMM with parallel kinematic structure to have a forward positional solution which is computationally efficient, and preferably in closed form..

One of the reasons for choosing the kinematic architecture of HCMM was that its forward and inverse positional solutions are both easily obtained in closed form. Since HCMM is essentially composed of two tetrahedra with a common base, the simple algebraic equations for the solution of a tetrahedron given in Ziegert and Mize [2] can be used to solve for the coordinates of the upper and lower reference spheres on the center rod. For each of these tetrahedra, the only information needed to compute the coordinates of the apex relative to a coordinate system defined by the base triangle is the absolute length of each of the six edges. These lengths consist of the three base lengths, which are assumed to be constant, and the lengths of the three struts. Since the laser interferometers used for strut metrology can only measure changes in the strut lengths, the total length of each strut is obtained by adding the initial length to the change in length measured by the interferometer. Therefore, for each tetrahedron, six kinematic parameters (3 base lengths and 3 initial strut lengths) are needed to compute the coordinates of the apex. Since the two tetrahedral share a common base, there are only 9 independent kinematic parameters. However, the center rod length remains constant during motions of HCMM. This fact is used to allow self-calibration as described in the next section. Therefore, the center rod length becomes a 10th kinematic parameter which is determined in the self-calibration procedure. Once the numeric value of these ten parameters is determined, the probe tip coordinates are obtained by projecting a line through the apexes of the two tetrahedra to the probe tip. During operation, each time the probe tip coordinates are computed, the length of the center rod is also computed. If this value deviates excessively from the calibrated value, it is a sign that the data are suspect, and it may be time to perform a new self-calibration.
The equations used to compute the apex coordinates of the two tetrahedral and project a line through them to the probe tip, constitute the kinematic model of HCMM. This model and its inverse may be used to transform from strut coordinates to cartesian world coordinates and vice-versa. The 10 kinematic parameters used in the model are all nominally constant, and must be determined via calibration of the fully

assembled machine. The accuracy of these parameter values strongly affects the positioning accuracy of the machine.

7.0 Self-calibration

As explained above, HCMM has 5-DOF of motion, and therefore has 5 actuated struts. The sixth strut is passive and is simply a telescoping tube arrangement which extends and retracts as the HCMM is moved throughout its workspace, and which carries a laser interferometer system to measure its length changes. This redundant measurement information is used to by the self-calibration procedure in the following manner:

1. The machine is moved to its home position, and each of the strut laser interferometers is electronically zeroed. Note that at this position, the 3 base lengths, the lengths of the 6 struts, and the center rod length are known only approximately.
2. The machine is moved to a pre-selected set of poses in the workspace. At each pose, the change in length of each strut from its initial length is recorded.
3. Using an initial guess of the kinematic parameters, and the recorded strut displacements, the coordinates of each tetrahedron apex is computed. The length of the center rod is then computed as the distance between these points. If the kinematic parameters used to compute these coordinates and lengths are correct, the center rod length should be constant for every pose of the machine.
4. A search is performed for the set of kinematic parameters which minimizes the sum of squares of differences in the predicted center rod length over the pose set.

An extensive simulation [3] of the self-calibration procedure has been performed to determine the optimal pose set, and the effect of measurement noise on the quality of the calibration results. The results of this simulation showed that satisfactory calibration can be obtained using as few as 30 separate poses in the calibration set if they are properly selected.

Since the time required to collect the self-calibration data is very short (approximately 2 minutes), semi-automatic compensation for thermal deformations of the machine structure may be achieved by simply performing the self-calibration at intervals determined by the fluctuations in the thermal environment and the thermal time constant of the machine structure. Another indication which may be used to determine the need for recalibration is the computed center rod length. Each time a coordinate is measured, the coordinates of the upper and lower tetrahedron apexes is computed prior to computing the probe tip coordinates. The center rod length is computed as the distance between these points. Excessive variation in the computed center rod length is an indication that recalibration is needed.

8.0 Machine accuracy

Accuracy testing of HCMM is currently underway. Results of these tests will be reported in future publications.

Acknowledgements

This work was supported in part by the National Science Foundation under grants DDM-9358138 and DMI-9522845. The author also wishes to acknowledge the following students who have contributed greatly to the design and construction of this machine: Kamal Bhojwani, David Bruns, Chin Chou Huang, Eric Ingram, Bernhard Jokiel, Edmund Loftus, Mark Mevoli, Chris Mize, Yunjun Mu, Chuck Perry, Tony Schmitz, Doug Yeager

References

1. Jokiel, B.*, and Ziegert, J.C., "Modelling and Simulation of a Parallel Architecture Five-Axis Coordinate Measuring Machine", *Proceedings of ASPE 1996 Annual Meeting*, Monterey, CA, November, 1996, pp. 233-237.
2. Ziegert, J.C., and Mize, C.D.*, "The Laser Ball Bar: A New Instrument for Machine Tool Metrology", *Precision Engineering: Journal of the American Society for Precision Engineering*, v.16, no. 4, October 1994, pp. 259-267.
3. Huang, C.C., and Ziegert, J.C., "Self Calibration of a Hexapod Coordinate Measuring Machine", *Proceedings of ASPE 1997 Annual Meeting*. Norfolk, VA, October, 1997, pp. 361-364.

Multi-Layered Circuit Board Precisely Pressed / Damascened on Glass Plates

Masayuki Nakao, Jinyo Kumaki, Kiyoshi Matsumoto and Yotaro Hatamura
Department of Engineering Synthesis, Graduate School of Engineering, The University of Tokyo
7-3-1 Hongo, Bunkyo-ku, Tokyo, 113-8656 Japan
TEL + 81-3-5841-6360, FAX + 81-3-5800-6993, E-mail nakao@hnl.t.u-tokyo.ac.jp

1. Introduction

Modern VLSI production requires mapping precise circuit pattern on glass plates. Such processes include pattern impression on, for example, the optical circuit of light processing units, electrical circuit boards, flat panel displays and the fluidic circuit of μ -TAS (Micro Total Analysis Systems).

Currently available processes for fabricating such precise circuit patterns, with thin lines of 5 -50 μ m in width, include MEMS type processes such as HF wet-etching [1] or SF6 dry-etching [2] with photo-lithography masking on the glass plates. However, an alternative inexpensive reproduction process will further reduce the cost.

The authors introduce a precision engineering type reproduction process, namely a pressed/damascened process. We first 1) fabricate a precise circuit pattern on a ceramic mold (male), 2) press the pattern of the ceramic mold on a glass plate (female), and lastly 3) damascene metal on the female pressed pattern on the glass plate.

We experimented with a multi-layered circuit board as an example of such precise circuit patterns. For the multi-layered circuit board fabrication, we further experimented with two sub-processes; 4) opening through holes in the glass plates, and 5) stacking and fixing of the damascened glass plates.

Our pressing process for circuit boards accomplishes much higher precision in reproduction compared to conventional screen print processes and dramatic cost reduction from the most recent semi-conductor lithography processes.

This paper reports our prototyping with the new process and evaluates the results.

2. Design of the pressed/damascened process

Fig. 1 illustrates the multi-layered circuit board process.

The process (a) prepares glass plates and a WC (tungsten carbide) mold, next (b) opens through holes by electrolyzation in the glass plates, and (c) sand-blasts a male-pattern on the WC mold.

The WC mold then (d) presses against a glass plate to produce a female-pattern on the glass. Then the process (e) deposits Cu on the pressed glass and (f) flattens it with CMP (chemical mechanical polish) to reproduce the same Cu pattern as the female pattern. We then (g) stack and fix the damascened plates, and finally (h) produce a multi-layered circuit board.

The pressing sub-process (d) has, in the past, been applied to optical glass gratings or optical lenses [3]. The glass forging at 500 - 700 °C requires heat resisting material such as SiC, WC or Pt/Ni plated steel for the mold.

We have also tried the mold-pattern sub-process (c) to molds of optical fiber connectors by grinding with a slitting tool. The method, however, only applies to simple patterns of line-and-space.

From these experiences, we adopted a WC mold and sand-blasting. Sand-blasting is now available for producing precise patterns such as in DFR (dry film resist) lithography for PDP (plasma display panel) walls [4].

The Cu deposition sub-process (e) and CMP (f) are well known for multi-layered wiring processes of semi-conductors. In synthesizing the process, we designed the process variables empirically for glass plates. The next section describes our synthesis.

3. Prototyping the multi-layered circuit board

3.1 Glass plates and WC molds

For the glass plates, we used two types; one with material property of low heat-expansion and low specific inductive capacity (Corning Pyrex 7740, 3.25 ppm/°C, 5.1, 821°C) and the other with low softening temperature (Ohara PBM3, 9.5 ppm/°C, 8.0, 586°C). The former better suites circuit boards; low heat-expansion and specific inductive capacity is similar to conventional ceramic circuit boards. The PBM3 (30 × 30 x 0.2 mm) mainly served the stacking and fixing sub-processes for its easy bonding.

We used WC bonded by 10 wt% Co (Toshiba Tungaloy EM10) for WC molds. Sand-blasting realizes higher removal rate with larger Co composition.

3.2 Opening through holes

We employed electrolyzation method to glass plates. Fig. 2 explains the method; the bath is NaOH 8 mol/l solution, voltage is 40-60 V, and the tool is a ϕ 0.14 mm insulated wire. In a short process time of about 1 second, a ϕ 0.17 mm hole opened through the 0.2 mm thick PBM3 as Fig. 3(a) shows. The hole form, however, was conical as Fig. 3 (b) shows.

3.3 Mold patterning

As a precision pattern, we used an L-shaped, 20 μ m wide line pattern.

The process used a contact UV exposure machine for lithographic machining the pattern on a 30 μ m thick DFR (manufactured by Nippon Gousei). Then a powder-beam machine (Sony HJ-1500) sand-blasted the EM10 surface with ϕ 5.5 μ m SiC particles, and 1 minute blasting eventually dug 1.5 μ m deep trenches.

Fig. 4 shows the ridges and trenches on the mold. The ridges have flat unblasted surfaces, which coincide with the metal wiring area. Rough blasted surfaces on the trench match the insulated area.

3.4 Pressing

A hot press machine (Toshiba Machine TS-112) then pressed the mold to the glass plate with a pressure of 15 MPa for 30 seconds at 530°C. Infrared heating enabled quick heating rate; the total pressing time was 7.5 minutes including cooling to 220 °C.

Fig. 5 shows the grooves produced on the glass plate. The 20 μ m wide pattern precisely copied to 1.5 μ m deep grooves. The magnified view in Fig. 6 shows that even the mold texture reproduced on the glass.

3.5 Cu deposition and CMP

We deposited a 3 μ m thick copper on the pressed glass plate by sputtering and vapor deposition. Generally, sputtering has strong adhesion but low deposition rate, whereas vapor deposition features weak adhesion and high deposition rate. Sixty minutes of sputtering under 73W RF and 4.0×10^{-3} torr produced a 0.3 μ m thick Cu layer, followed by vapor deposition under 1.0×10^{-6} torr to add 2.7 μ m to the Cu layer. One minute of heating with 10V-4A took place during the deposition process.

Next the selective copper removal process makes flat surfaces as Fig. 7 shows. The process conditions were ϕ 0.18-0.23 μ m Al_2O_3 particles and H_2O_2 pH 3.7-4.1 solvent (Rodel-Nitta QCTT 1010) on a polyurethane pad (Rodel-Nitta IC-1000/S-400, ϕ 200 mm) under 22.8 kPa, 120 r.p.m. for 20 minutes on a table-top machine (Maruto ML-180).

The copper should remain only in the grooves because the chemically stable glass functions as a stop layer. However, the process polished copper in the grooves by 0.3 μ m in excess because we had to completely remove copper from the rough and pressed blasted glass area.

3.6 Stacking and fixing

The final process included stacking three damascened glass plates (PBM3, each 0.5mm thick), and a 30 second pressing in the press machine under 1.5 MPa at 530°C for fixing the plates. We then inserted a

soldering ball (Sn-37wt%Pb, ϕ 0.074 mm, 183 °C melting temp.) through the ϕ 0.3 mm holes for better electrical contact.

Fig. 8 (a) and (b) show the transparent two-layered and three-layered patterns, respectively.

The circuit resistance measured 100 Ω whereas the theoretical value was 24 Ω . The higher resistance is due to insufficient nitrogen gas flow during the pressing process causing oxidization on the soldering contacts.

4. Evaluation of the process

As a measure of our reproduction process, we evaluated the precision. Fig. 7 shows a slightly wider than expected Cu pattern due to roughness in the pressed blasted glass area. Longer polishing, for completely removing Cu on that area, caused the resulting line width to widen by 2 μ m from the target. Other problems like pattern distortion or unevenness of the groove depth were not observed. We conclude that our hot press process accomplished a precise reproduction with only a 10% variation in the line width.

Our pressed/damascened process can be applied to other designs. As an example, we prototyped an electrode that can be used for brain science or a fluidic chip for immunization tests. This pressed/ damascened process can also apply to replication on plastic plates, and it is a promising technology for future biochemical/medical devices.

5. Summary

For reproducing precise 20 μ m wide circuit patterns, the authors developed a pressed/damascened process on glass plates. The mechanical process demonstrated its precision through prototyping of a multi-layered circuit board, with only 2 μ m error in the line width. The process is applicable to production and other scientific fields and also realizes low cost reproduction of fine patterns.

Reference:

[1] H. Nakanishi, proc. of MEMS '97, p.299 (1997)

[2] K. Matsumoto, et al., proc. of MEMS '98, p.127 (1998)

[3] E. G. Loewen et al; Diffraction Gratings and Application , p.577 (1997)

[4] T. Shinoda, et al; Journal of Japan Applied Physics, 65-7, p.723 (1996)

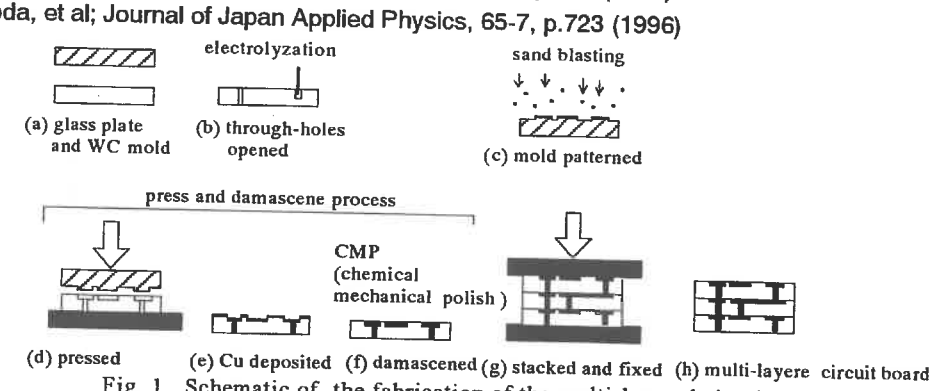

Fig. 1 Schematic of the fabrication of the multi-layered circuit board

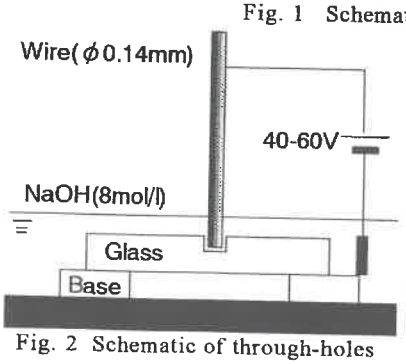

Fig. 2 Schematic of through-holes opening

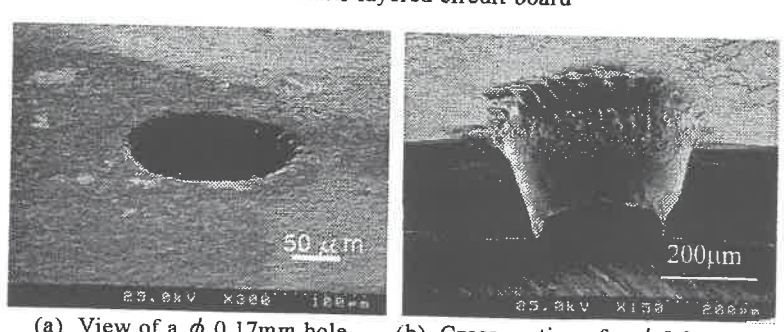

(a) View of a ϕ 0.17mm hole (b) Cross section of a ϕ 0.3mm hole

Fig. 3 SEM views of the through-hole

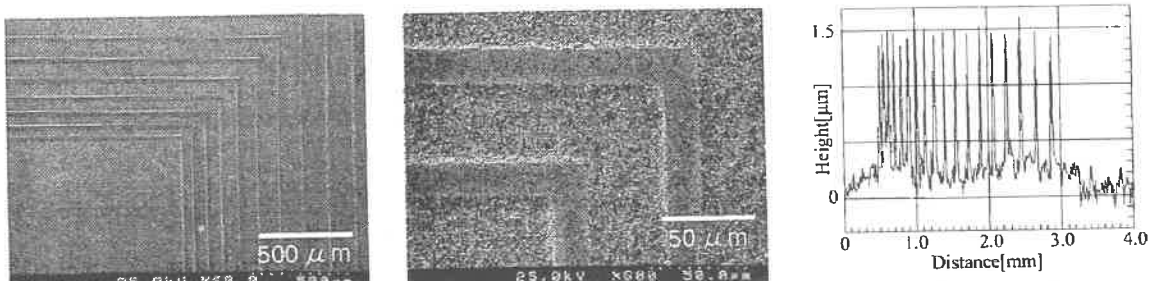

(a) SEM view (b) SEM view (magnified) (c) Surface profile

Fig. 4 SEM views of the mold surface

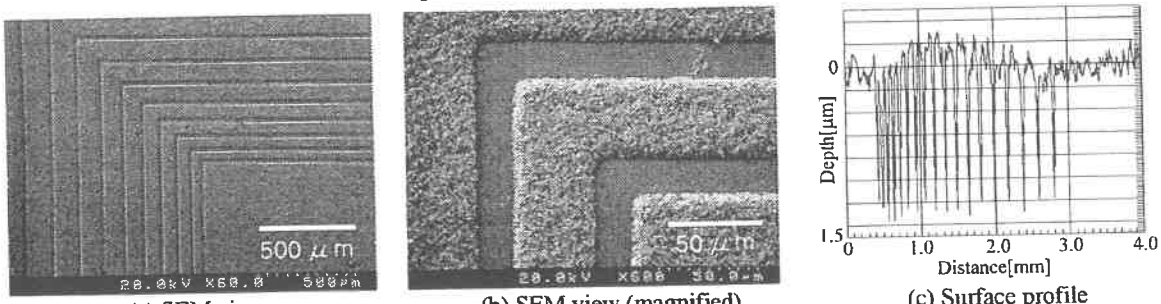

(a) SEM view (b) SEM view (magnified) (c) Surface profile

Fig. 5 SEM views of the pressed glass surface

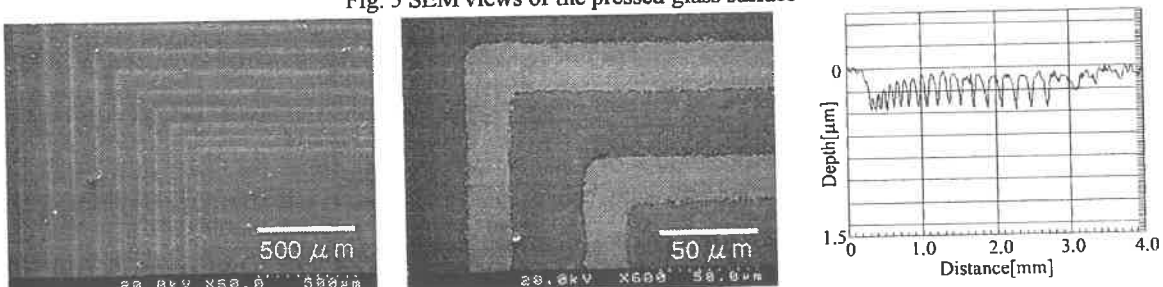

(a) SEM view (b) SEM view (magnified) (c) Surface profile

Fig. 7 SEM views of the damascened glass surface

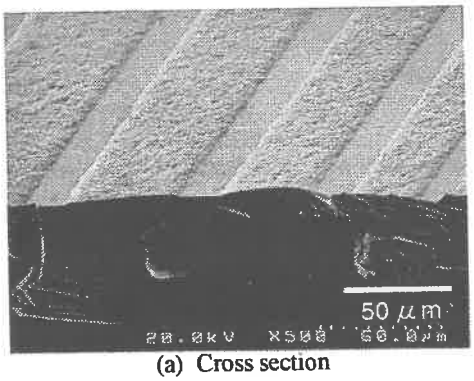

(a) Cross section

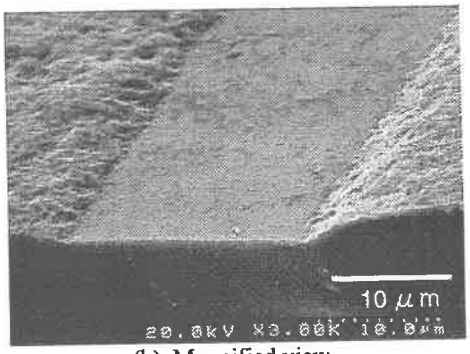

(b) Magnified view

Fig. 6 SEM views of the pressed glass surface

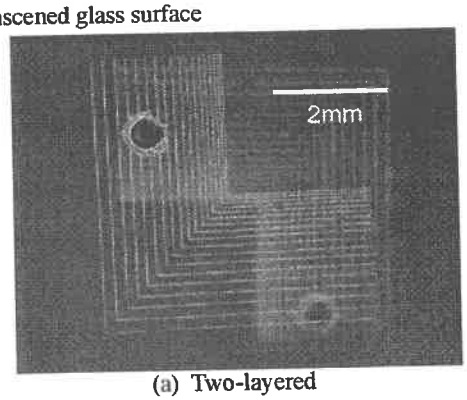

(a) Two-layered

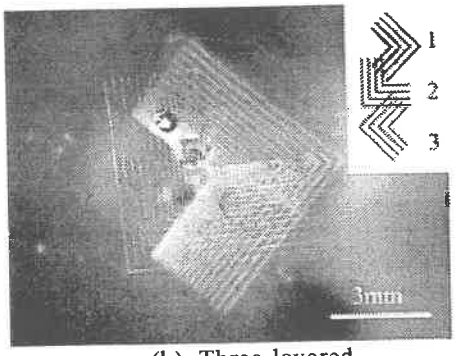

(b) Three-layered

Fig. 8 Photographs of the multi-layered glass circuit board

PRODUCTION OF A RAYLEIGH-TAYLOR INSTABILITY TARGET

Robert D. Day, Norman Elliott, Joyce Elliott, Veronica Gomez, Timothy Pierce, Douglas Hatch, Gerald Rivera, Elfino Armijo, Peter Gobby, Mike Brooks, Brian Hennike, Lawrence Rodriguez, Jake Bartos

Los Alamos National Laboratory

INTRODUCTION

Rayleigh-Taylor (RT) instabilities occur when a low-density fluid attempts to accelerate a high-density fluid. The instability manifests itself by forming bubbles of the low-density that percolate through the high-density fluid. Concurrently, spikes of the high-density fluid "jet" into the low-density fluid. This instability is seen in familiar occurrences such as the growth of icicles and the draining of sinks. If the interface between the two fluids remains perfectly smooth the instability will not occur; that is, it must be "seeded" by a wave-like perturbation. For the two cases mentioned above, a vibration can be sufficient to perform the "seeding".

The implosion of an Inertial Confinement Fusion (ICF) target often requires that a low-density fluid accelerate a high-density fluid. This leads to the possibility of developing RT instabilities that can produce a non-uniform implosion and drastically reduce the energy coming from the target. The "seed" for these instabilities comes from manufacturing defects such as surface finish or form errors. An illustration of manufacturing-induced RT instabilities is seen in figure 1[1] where the magnetic field acts as a low-density fluid that was imploding an aluminum cylinder. The high-density fluid in this case was the aluminum cylinder wall. The interface between the fluids was "seeded" by two different sine waves that were machined into the aluminum surface. The wavelength of the sine wave seen in the left portion of the cylinder shown in figure 1 was 2 mm. The wavelength of the sine wave on the right was 0.75 mm. Both sine waves had an amplitude of 25 μm. An examination of the data presented in figure 1 shows that as time increases the instabilities grow; however, the longer wavelength sine wave grows at a faster rate than the one with the shorter wavelength. These data, along with other data, have shown that there is both a wavelength and amplitude dependence on RT instability growth [2]. Since there will always be manufacturing defects in ICF targets and since RT instability growth is a rather complicated physical phenomena, a significant theoretical and experimental effort has been dedicated to understanding this phenomena.

TARGET FOR OBSERVING RT INSTABILITY GROWTH LATE IN TIME

A series of experiments have been performed at the Omega and Nova lasers to understand RT instability growth during the initial growth stages [2]. Since the laser used to illuminate the x-ray backlighters is only on for a time-duration of one nanosecond, observation of a fully developed instability can not be accomplished. Therefore, a target needed to be produced that would adequately simulate the geometry of a RT instability midway through its development. Drawings of the experimental package are shown in figure 2. It was anticipated that the 30 μm tall by 10 μm thick spikes and the 5 μm thick base would be difficult to fabricate. It was decided to begin two methods of production: machining and photolithography.

MACHINED TARGET PACKAGE

The machined targets were made according to the drawing in figure 2b. Approximately 10 targets of this style were needed for these experiments. It was decided to approximate the straight spikes by machining them on the rim of a disc that was 70 mm in diameter. An aluminum disc was machined with the needed reference surfaces being diamond turned so that the tool location

could be determined to within a few micrometers. Copper was then deposited onto the rim of the disc. The disc was then remounted onto the diamond turning machine so the grooves could be machined into the copper.

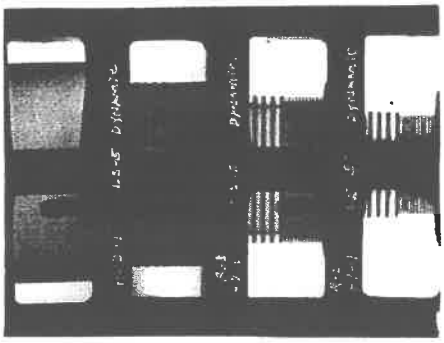

Time 0 6.25 μs 8.00 μs 9.25 μs

Figure 1 – A series of radiographs taken perpendicular to the axis of an imploding aluminum cylinder showing the RT instability growth.

(a) (b)

Figure 2 – Drawings of the two packages that were needed for the RT experiments.

The primary concern for the machined package was that the machining stresses would deform the thin spikes. After numerous discussions, it was decided to use a form-tool to produce the grooves. The design of the form-tool necessitated the 7.5° angles that are shown on the drawing in figure 2b. Initially every other groove was machined, then these grooves were filled with wax to support the thin wall while the remaining grooves were being machined. After machining all of the grooves the wax was removed leaving a ring of copper material with the appropriate grooves machined into it. This process worked very well. All the critical dimensions were held to within 2 μm of the desired amount. A cutaway view of the aluminum disc and the copper rim with the machined grooves is shown in figure 3.

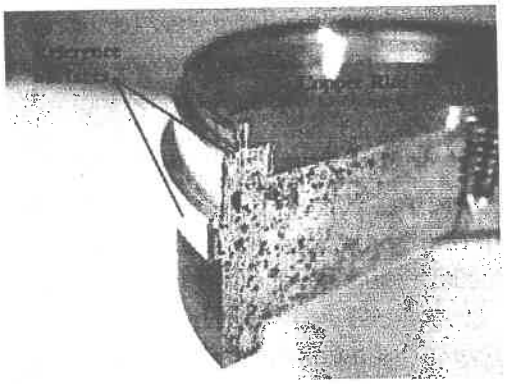

Figure 3 – A Photograph of the aluminum disc showing the copper rim with the machined grooves.

After machining the grooves, the parts needed to be cut to the proper width. This was performed with an Electron Discharge Machine to minimize machining stresses. There was considerable concern that the residual stresses from the machining operation would cause the packages to deform to such an extent that they could not be integrated into the entire target assembly. Therefore, it was decided to build the package supporting structure, as shown in figure 4, while the package was on the aluminum substrate. This structure would provide the necessary structural integrity to the package and make target assembly much easier. The package and its supporting structure would then be removed from the substrate. The supporting structure consisted of 150 μm-thick stand-offs that were glued to a 50 μm thick gold washer. Each of the above steps required great care because of the delicate nature of the packages and the extremely small size of the components involved (particularly of the gold stand-offs). This assembly process, although tedious, worked very well. Figure 4 shows a package that has been EDMed to the correct width adjacent to an assembled package that is ready to be leached.

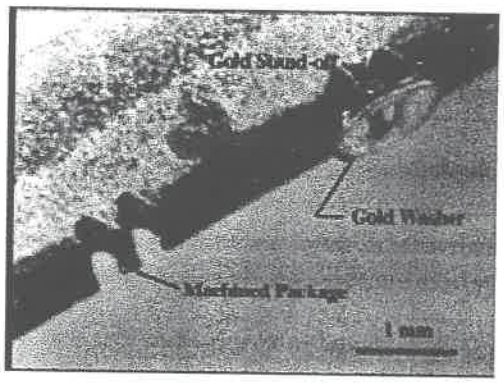

Figure 4 – Photograph of package EDMed to width adjacent to an assembled package ready to be leached

PACKAGES PRODUCED USING ELECTRON DISCHARGE MACHINING (EDM)

Fabrication problems with the packages produced by photolithography caused their delivery to be too late to be used in these experiments; therefore, they will not be discussed. A photograph of some of packages that eventually arrived is shown in figure 5. The photolithography fabrication problems caused a third fabrication approach to be used. This approach was to use the EDM process to make the entire package described in figure 2a. The same copper/aluminum substrate combination was used to produce these parts as was used for the machined packages. A Panasonic Micro EDM was used for these parts. It was decided to use this machine in a manner similar to a milling machine to produce these packages. This process is very labor intensive; however, the very tight schedule dictated that this approach should be attempted. This technique produced very good spikes; however the bottom web was estimated to be 15 μm. It is thought that an unknown amount of electrode wear was responsible for the thicker web. These packages did deliver very useful data [3].

FINAL TARGET ASSEMBLY

After the package assemblies were completed, they were mounted to the side of a sphere that had laser entrance holes machined into it that formed a tetrahedral geometry. The package, along with the backlighter and shield, needed to be mounted along a specific direction so that it would be illuminated properly. The accuracy of mounting was about 0.5°. A view of one of the final target assemblies is shown in figure 6.

CONCLUSIONS

All of the fabrication methods described above worked well for producing the target packages desired. Great care and attention to detail was required at each step. Considerable forethought made the process proceed well even when unforeseen difficulties arose. The parts were produced in about two weeks from the making of the substrate to final target metrology. Photolithography is probably the optimum way to make this type of part if the schedule will allow it. The usefulness of having a Computer Numerically Controlled EDM for producing small quantities of these types of structures was also demonstrated by this project.

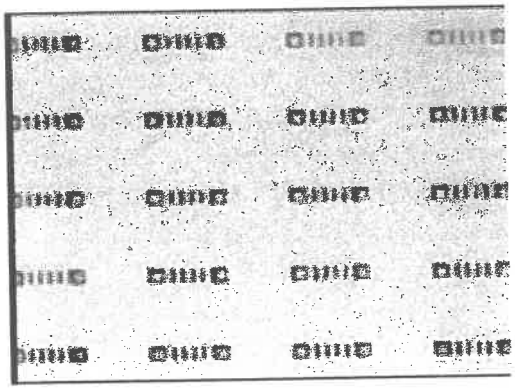

.Figure 5 – Packages made by photolithography process.

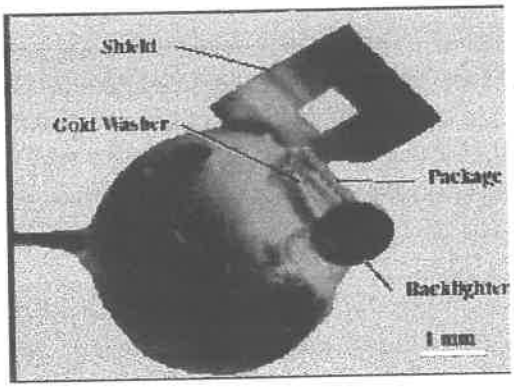

Figure 6 – Photograph of final target assembly

Assembly, along with fabrication, can be very difficult. Forethought and the ability to handle very small parts facilitated being able to assemble these targets in very timely fashion.

In summary, the experimenters and theoreticians were very pleased with these targets. This set of experiments confirmed the theoretical calculations used to simulate RT instabilities.

ACKNOWLEDGEMENTS

We are grateful for the useful discussions with Bill May of Chardon Tool Company. He helped us think-through the machining process and his company produced the diamond tools. Dawn Skala of Sandia National Laboratory made sure the photolithography was performed very well and about as rapidly as was possible. A special thanks is also extended to Brian Hennike, Larry Rodriquez, and Bob Springer of Los Alamos National Laboratory for coating the aluminum substrates. This work was supported by the U.S. Department of Energy, office of Inertial Fusion, under the contract number W7405-ENG-36. This support is gratefully acknowledged.

REFERENCES

[1] Keinigs,R. K., Atchison, W. L., Faehl, R. J., Mclenithan, K. D., Trainor, R. J., "One-and Two-Dimensional Simulations of Liner Performance at Atlas Parameters," Proceedings VIII International Conference on Megagauss Magnetic Field Generation, Tallahassee, Florida, 1998.

[2] Hsing, W. W., Barnes, C. W., Beck, J. B., Hoffman, N. M., Galmiche, D., Richard, A., Edwards, J., Graham, P., Rothman, S., Thomas, B., "Rayleigh-Taylor Instability Evolution in Ablatively Driven Cylindrical Implosions," Phys. Plasmas, 4, (5), May 1997.

[3] Schappert, G., Batha, S., Klare K., Hollowell, D., Mason, R., "Rayleigh-Taylor Spike Evaporation," to be published.

BENDING DEFLECTIONS DUE TO SCRIBE-INDUCED RESIDUAL STRESSES

B. Austin, B. Love, T. Dow, J. Eischen and R. Scattergood
Precision Engineering Center, NCSU, Raleigh, NC 27695-7918

Introduction

When a sharp diamond tip is translated across the surface of a specimen, a scribe trace will be generated. This is a source of residual stress. The stress is due to the elastic-plastic constraint associated with the deformed material that is displaced from the trace. When scribes are made across a plate sample, the residual stresses will cause bending distortions orthogonal to the scribe trace. This effect can be used to produce nanometer-scale shape changes that can be useful in manufacturing applications such as disk read-write heads [1]. The objective of the work reported here was to produce a model for the bending effect. The model uses the elastic stresses caused by a line-force dipole to approximate the scribe-induced residual stresses. Scribing experiments were made to verify the accuracy of the model.

Model

Consider a line-force dipole acting on the surface of an elastic half-space shown in Figure 1. The force dipole lies along the z-axis. F is the line force per unit length, a is the force spacing and B = Fa is the dipole strength. A force-dipole model consisting of two orthogonal pairs of discrete dipole forces acting on the surface of an elastic half space was introduced by Yoffe [2] as a model for the residual stresses due to a single indentation. The scribe can be viewed as the superposition of a series of indentations that produce a line-force dipole [3]. The stresses due to a line-force dipole acting on an elastic half space can be evaluated using the equations given by Johnson [4].

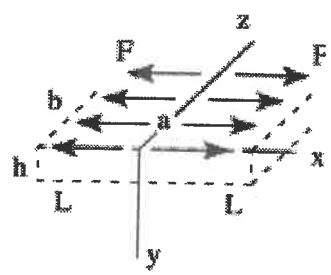

Fig. 1. Line-Force dipole

For the analysis of the bending effect, consider a finite rectangular plate with a central scribe along the z-axis in Figure 1. The finite-body stress solution requires that the stress field due to the half-space line-force dipole vanish on the plate surfaces. If the plate thickness h is small compared to its length 2L and width b, the magnitude of the stress acting on the plate edges is negligible. However, the normal and shear stresses, σ_{yy} and σ_{xy}, which act on the bottom surface cannot be ignored. The equilibrium configuration (bending effect) is obtained by applying the reversed dipole stresses to the bottom surface of the plate and then solving a beam-bending problem with these stresses as the loading functions [5]. This is not an exact solution for the internal stresses, however, the relevant force and moment equilibrium conditions are satisfied. FEM calculations showed that the shape profile errors are negligible using this approximation. Equation (1) is the solution of the beam-bending problem for the bend angle, ϕ (X), and the displacement, δ (X). The normalized distance along the plate is X = x/h, B is the dipole strength (taken in the limit F -> ∞ and a -> 0 such that B is fixed), E is the elastic modulus and h is the

thickness. After shifting the functions given in equation (1) by multiples of the scribe spacing, superposition can be used to obtain the equivalent results for multiple scribes.

$$\phi(X) = -\frac{6B}{\pi E h^2}\left[\tan^{-1}(X) + \frac{X}{1+X^2}\right] = \frac{6B}{\pi E h^2} f(X)$$
$$\delta(X) = -\frac{6B}{\pi E h}\left[X \tan^{-1}(X)\right] = \frac{6B}{\pi E h} g(X) \qquad (1)$$

Figure 2 shows the form of the functions f(X) and g(X) defined in equation (1) for a single central scribe (only half of the symmetric profile is shown). By definition, $\phi(X)$ and $\delta(X)$ are the tangent angle and the displacement at X measured downward (negative) from the x-axis, hence, g(X) is equivalent to the profile shape. The bend-angle function f(X) approaches $-\pi/2$ as X increases and the displacement function g(X) becomes linear. Therefore, the bending effect appears as a localized "hinge" around the scribe trace at X = 0. Similar features are obtained for multiple scribes symmetrically placed around a central scribe. In order to compare the predictions of the model to actual profiles, the dipole strength B in equation (1) must be evaluated. For a given scribe tip geometry and material, the normal load applied to the scribe is the dominant parameter determining the residual stresses and the dipole strength. In order to calibrate the model for verification purposes, the procedure adopted here was to measure the average bend angle as a function of the scribe load W. By equating $\phi(X)$ in equation (1) to the measured angles, a relation between B and W can be obtained. This will be the calibration curve for the given scribing geometry and material parameters.

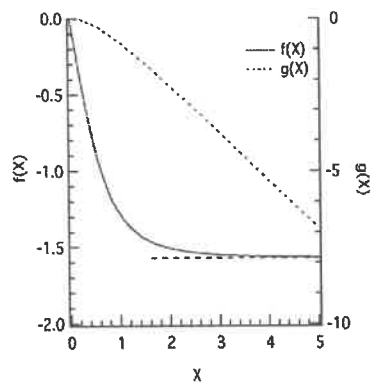

Fig. 2. f(X) and g(X) functions.

Scribing Tests and Model Verification

The scribing tests were done using Dynatex V4-64 diamond scribing tips, with the scribe axis tilted 32° from vertical, and the modified Zwick hardness tester shown in Figure 3. The samples were translated in the scribing direction using a motorized x-y stage. The test material was Al_2O_3-TiC (30 volume % TiC) and for most of the tests the samples were ceramic plates measuring approximately 1 mm x 1 mm x 0.3 mm thick. Displacement profiles were measured using a New View optical profilometer. The difference between the initial sample profile and the profile after scribing, adjusted for tilt, produced the bend profile for the given scribing conditions. A series of tests were made using scribing loads in the range $0.031\ N \leq W \leq 1.71\ N$ to establish the bend angle vs. scribe load relationship. This data was used to establish the dipole

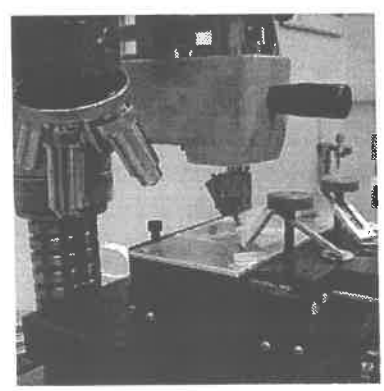

Fig. 3. Setup for scribing tests.

strength vs. scribe load relationship shown in Figure 4 ie., the B vs. W calibration curve [5]. Verification of the model was based on a comparison of the measured displacement profiles with the model prediction for $\delta(X)$ given in equation (1) using the B values from Figure 4. This comparison is considered to be a primary benchmark since the displacements are usually the quantities of interest for applications [1]. Figures 5a and 5b show typical examples of the measured displacement profiles (solid) and the model predictions (dashed) for test samples used to generate the calibration curve in Figure 4. The spikes on the measured curves are profilometer dropouts that correspond to the positions of the three scribes made per test sample. The agreement is very good over the range of the loads used. Figure 6 shows an example of the measured displacement profile (solid) and the model prediction (dashed) for a sample tested under different conditions (5 mm sample length and five scribes). The agreement is again very good which verifies the fact that the calibration curve shown in Figure 4 is a master curve for the given scribing conditions and material properties.

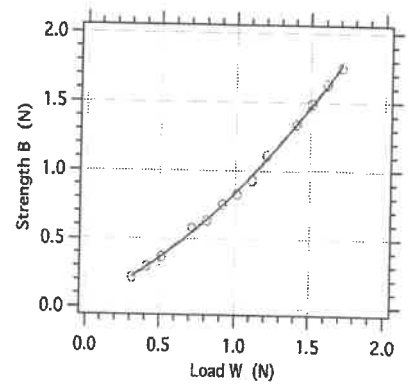

Fig. 4. B vs W calibration curve.

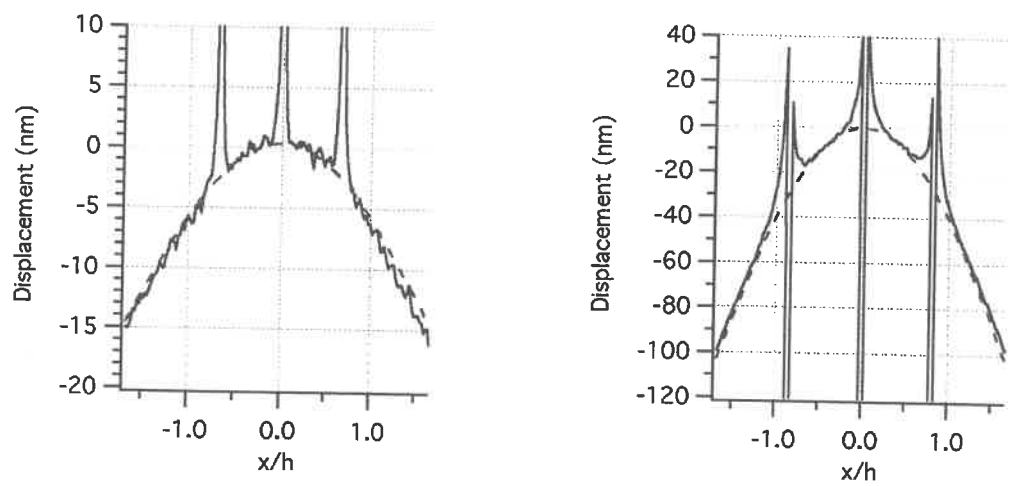

Fig. 5. a) W = 0.31 N, B = 0.22 N. b) W = 1.61 N, B = 1.75 N.

For the model calculations and the verification results shown in Figures 5 and 6, scribes were made across the entire width of a plate sample. This is essentially a 1D problem, which is suitable for calibration and verification of the force-dipole model based on Figure 1 and equation (1). However, in practical applications where scribing is used to either produce a certain shape on a component or correct a form error [1], scribes of various lengths and orientations will be required. This becomes a 2D problem that is more difficult to solve and, in general, is not amenable to simple analytical results of the kind obtained in equation (1). The approach in this case requires the use of FEM to obtain solutions for displacement profiles due to partial scribes

(line-force dipoles) on the surface of plate samples. For given scribing conditions, calibration data like that shown in Figure 4 can be used to obtain the dipole strengths required as input for the FEM calculations. Studies are currently underway to implement and verify an FEM-based 2D model using line-force dipoles [6]. Figure 7 shows a typical FEM result for a partial scribe made across a plate sample. In this case there are curvatures around two principal axes.

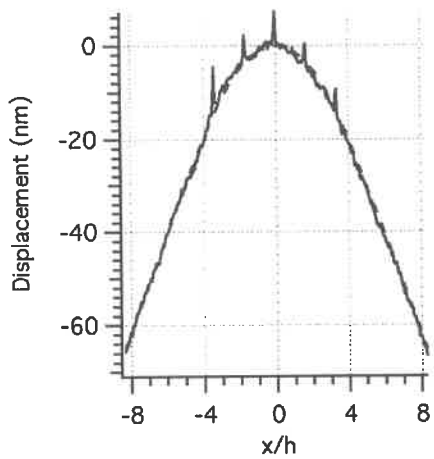

Fig. 6. W = 0.16 N, B = 0.0864 N. Five scribes indicated by the peaks were made on a 1 mm x 5 mm x 0.3 mm Al_2O_3-TiC sample.

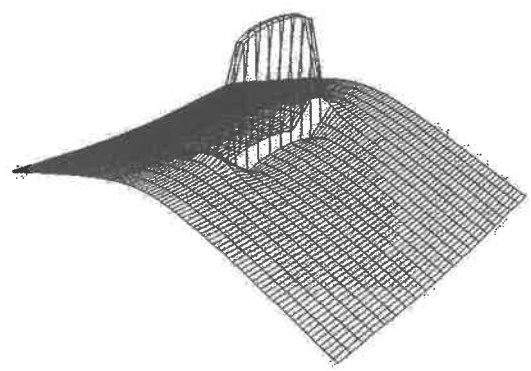

Fig. 7. FEM calculation for the displacement profile due to a partial scribe. The discrete peak is an artifact showing the scribe location.

Conclusions

The comparisons of the measured and model displacement profiles presented in Figures 5 and 6 show that the line-force dipole model provides a very good representation of scribe-induced residual stresses and the associated bending effects. Processes that produce similar types of residual stress, for example, grinding or laser-melt scribing, may also be amenable to force-dipole models provided that the models are suitably modified to account for the differences in the elastic-plastic constraints.

References

1. A. C. Tam, C. C. Poon, L. Crawforth and P. M. Lundquist, "Stress on the Dotted Line", Data Storage, vol. 6, issue 13, 29 (1999).
2. E. H. Yoffe, "Elastic Stress Fields Caused by Indenting Brittle Materials", Phil. Mag. A, vol. 46, no. 4, 617 (1982).
3. Y. Ahn, T. N. Farris and S. Chandraskar, "Elastic Stress Fields Caused by Sliding Microindentation of Brittle Materials", Proc. of the Int. Conf. On Machining of Advanced Materials, S. Jahanimir, ed., NIST Spec. Publ. 847, 71 (1993).
4. K. L. Johnson, "Contact Mechanics", Cambridge Univ. Press, p.17 (1985).
5. B. Austin, MS Thesis, North Carolina State University (2000).
6. B. Love, MS Thesis, North Carolina State University (in progress).

Investigations on the Tool Plate Preparation for Nanogrinding

Hans H. Gatzen, Heiko Siekmann
Institute for Microtechnology, Hanover University, Germany

Key words: Nanogrinding; fixed abrasive lapping; advanced ceramics; grinding plate creation; diamond embedding.

Abstract --- Nanogrinding (also known as fixed abrasive lapping), a surface grinding process using a lapping kinematic but no loose grain, is lending itself to ultraprecision machining of advanced ceramics. The process is capable of creating surfaces with minimized surface damages and average roughnesses R_a in the subnanometer range. The creating of the plate surface, embedding the diamond grains, as well as aligning their summits, is substantially influencing the nanogrinding process. Therefore, studying it, particularly the diamond embedding, seems very rewarding and is the subject of this paper. To analyze the location of diamonds, a combination of scanning electron analysis (SEM), energy dispersive x-ray spectrometry (EDS), and atomic force microscopy (AFM), was applied. As a result, both the location of diamonds as well as conditioning grains could be determined.

Introduction

The surface machining of ceramic mini- and microparts requires processes capable of creating surfaces with average roughness values R_a in the subnanometer range and minimal subsurface damages [1]. Flatnesses smaller than 10 nm/mm are additional requirements, e.g. for the machining of air bearing surfaces (ABS) for read/write heads of rigid disk drives. The nanogrinding process fulfills these requirements. It is based on a lapping process but in contrast to the loose lapping abrasives only fixed abrasive grains are applied for the material removal. Like lapping, the nanogrinding process uses a fluid to separate tool and workpiece. To achieve a sufficient film thickness, nanogrinding requires a significant grinding plate roughness [2]. This roughness is accomplished by conditioning the plate with a conditioning medium, e.g. pumice, as a first step to create the plate. After the conditioning, loose diamond grains are added and embedded into the plate surface. Both, the embedding of the diamonds as well as the coplanar arrangement of their summits are achieved through a conditioning ring. After diamond impregnation the plate is cleaned and all loose grains are removed.

Grinding Plate Topography

Figure 1 sheds some light on the nature of surface topography change after the different process steps. It presents AFM micro topography graphs of exactly the same region of the plate surface. Left, it depicts the virgin plate after conditioning, at the center it shows the plate after diamond impregnation, and right it presents the plate in a used condition after 60 min. of nanogrinding.

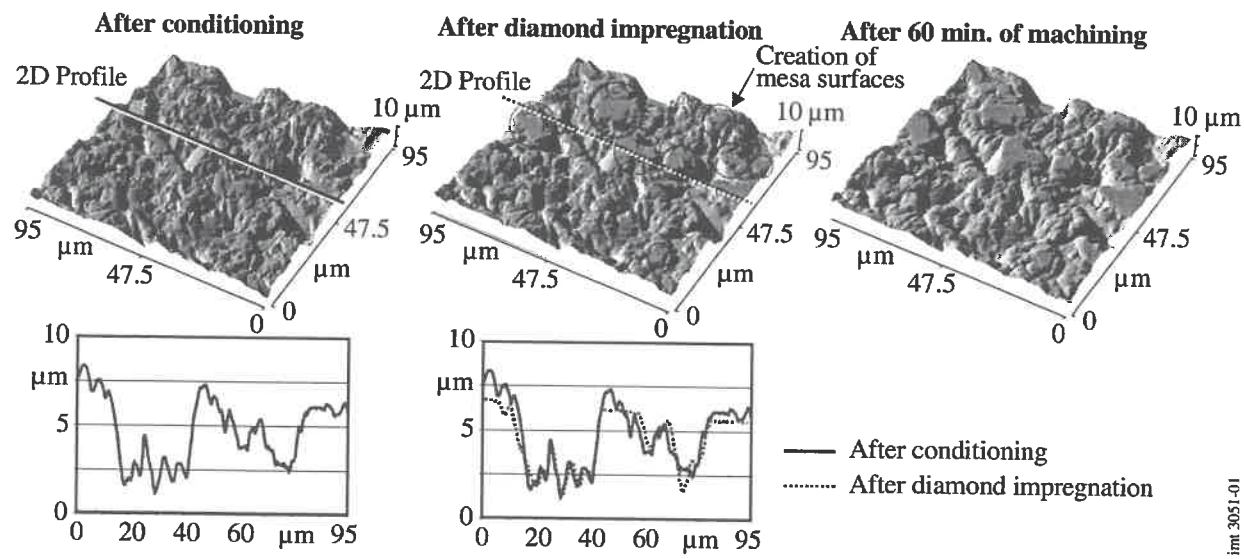

Fig. 1 Different states of the plate´s surface topography (AFM measurements)

After conditioning, the plate started out with a random profile. The conditioning process resulted in an average and peak-to-peak plate roughness of $R_a = 1.4$ µm and $R_t = 12$ µm, respectively. The gouges in the tin surface with a

depth of up to 8 µm are caused by conditioning grains. They represent the space for storing nanogrinding fluid and removed material during workpiece machining.

However, the diamond impregnation process causes a very distinctive change to the topography. The conditioning ring and the loose diamonds during this process step apparently truncate the peaks, creating some mesa type plateau surfaces in which the diamond grains are embedded. The size of the mesa surfaces is in the range of 5 µm x 5 µm to 30 µm x 30 µm. Deeper parts of the plate's roughness profile are not influenced. During the 10 min. of diamond impregnation approximately 1 µm of material is removed in the peak area of the roughness profile.

The consecutive machining process results only in a very slight further flattening of the peaks and thus in an increase of the mesa surface areas as is depicted after 60 min. of workpiece machining. Only mechanical contact between plate and workpieces and the abrasive action of the removed material particles (with sizes smaller than 5 nm) cause a further material removal of the plate material and therefore plate topography wear.

Detection and Topographical Analysis of Embedded Abrasives

For nanogrinding, typically a two-phase machining process using two different diamond grain sizes has been applied. The first "rough grinding" phase was conducted with 1.5-3 µm diamond, with the grain size chosen for maximal material removal. Optimal surface finish was achieved in the "fine grinding" phase with a 0.5-1 µm diamond grit. One of the key questions unresolved in the past has been at what location the diamonds are being embedded in the surface. To pinpoint these spots, the plate surface was subjected to a combination of scanning electron microscopy (SEM), energy dispersive x-ray spectrometry (EDS), and atomic force microscopy (AFM). Since even detecting diamonds with a size of 1.5-3 µm with EDS was a major challenge (carbon is on the borderline of detectability), the plate analysis was performed for the first phase of the nanogrinding process. Furthermore, local surface changes occurring through the conditioning process had to be observed and followed.

To do so, a method had to be devised to pinpoint a certain area. This was accomplished by marking a test field with a size of 100 µm x 100 µm at the tin surface. It was accomplished by scratching a frame around it using a diamond tip with a 2 µm tip radius (Figure 2, top). Afterwards, this test field was subjected to an SEM/EDS to detect the abrasives embedded in the tin surface (Figure 2, bottom left). Aside from diamond, pumice grains were found, which were used to roughen up the plate in the conditioning process and remained in the plate. Their portion of the total surface area was determined to be 10-15%. Nevertheless, it was shown that the abrasive pumice grains do not take part in the material removal process during workpiece machining since they do not result in any removal rate. In the example, six pumice grains and two diamonds are embedded in the enlarged part of the marked field. The results equal a density of diamond grains N_A of 3,500 per mm^2.

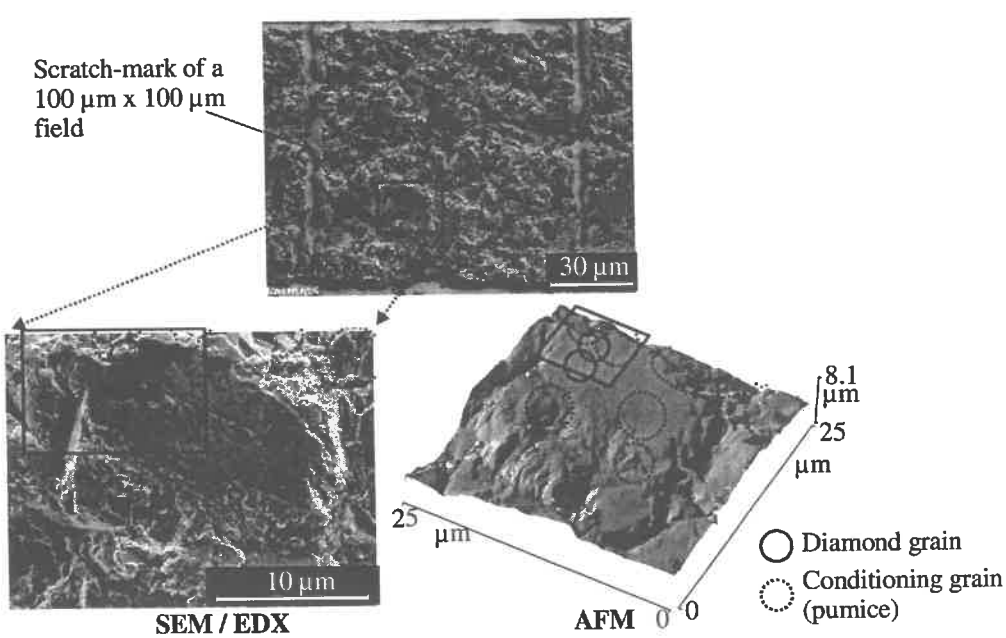

imt 3051-02

Fig. 2 Combination of SEM/EDX and AFM analyses for the detection and topographical analysis of embedded abrasive grains

After the SEM/EDS analyses, the test field was subjected to high resolution topographical AFM measurements (Figure 2, bottom right). The 3D AFM picture shows that the two diamond grains are embedded in one of the plate's mesa surfaces which in this case had a size of approximately 18 µm x 18 µm.

Grain Protrusion and Grain Location in the Plate

By performing a 2D analysis, i.e. looking at the plate cross section of the AFM plate measurements, the protrusion of abrasive grains beyond the binding material could be determined. For instance, this is demonstrated in Figure 3 which shows an enlarged view of the upper diamond grain previously presented in Figure 2. The scans show a protrusion in excess of 110 nm in the A-B and 150 nm in the C-D profile.

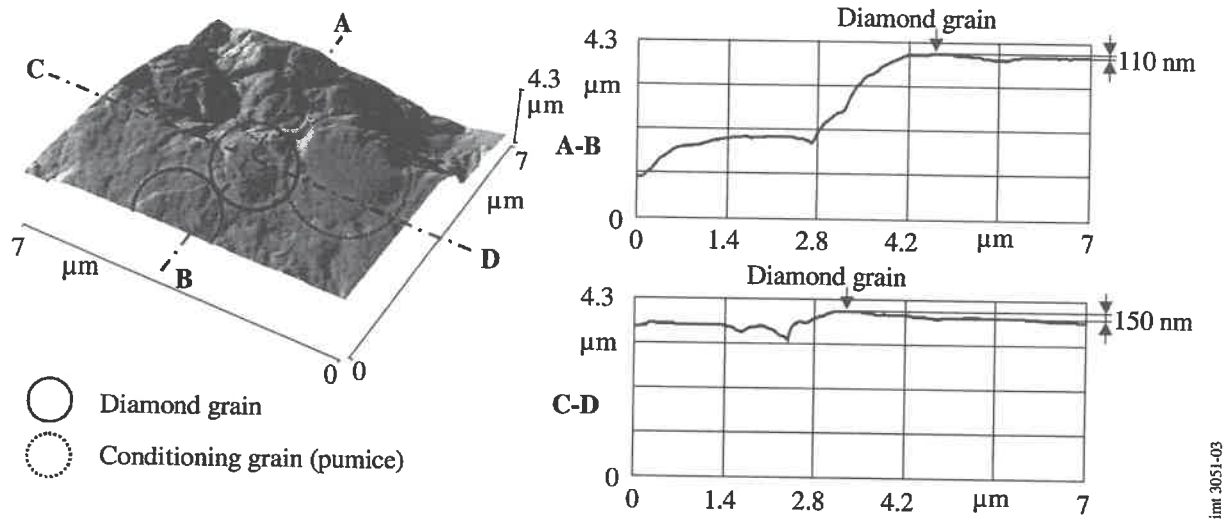

Fig. 3 2D surface cross sections of an embedded diamond grain

The pumice grain at the right hand side of Figure 3 shows significant wear marks. Figure 4 depicts a schematic view of its recession. The conditioning grain was not only truncated, it also ended up with a plateau surface recessed at least 100 nm below a neighborhood diamond grain's cutting edge. This view clearly indicates why pumice as a conditioning grain does not participate in the material removal process during workpiece machining: it already wears during the diamond impregnation process step by contact wear with the impregnating diamond, due to its low hardness (Figure 4).

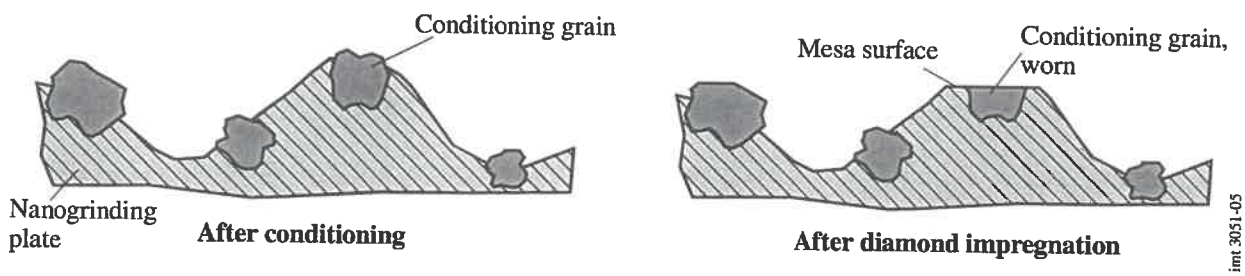

Fig. 4 Wear of conditioning grains during diamond impregnation

As result of analyzing different diamond grains in the nanogrinding plate, a protrusion above the mesa surfaces in the order of 50-200 nm was observed for the 1.5-3 µm grit diamond. Preferably, the diamonds embed themselves at the rim of the mesa surfaces as is depicted in Figure 5. Due to the high plastic deformations caused by the embedding processes the tin-matrix increases in hardness in the sub-surface zone by work hardening. This was proven by nanohardness measurements. The hardness increased by a factor of seven from 0.05 GPa to 0.34 GPa. Due to the work hardening, a deeper penetration of diamonds into the plate during workpiece machining seems to be avoidable. Therefore, a long plate life is achieved.

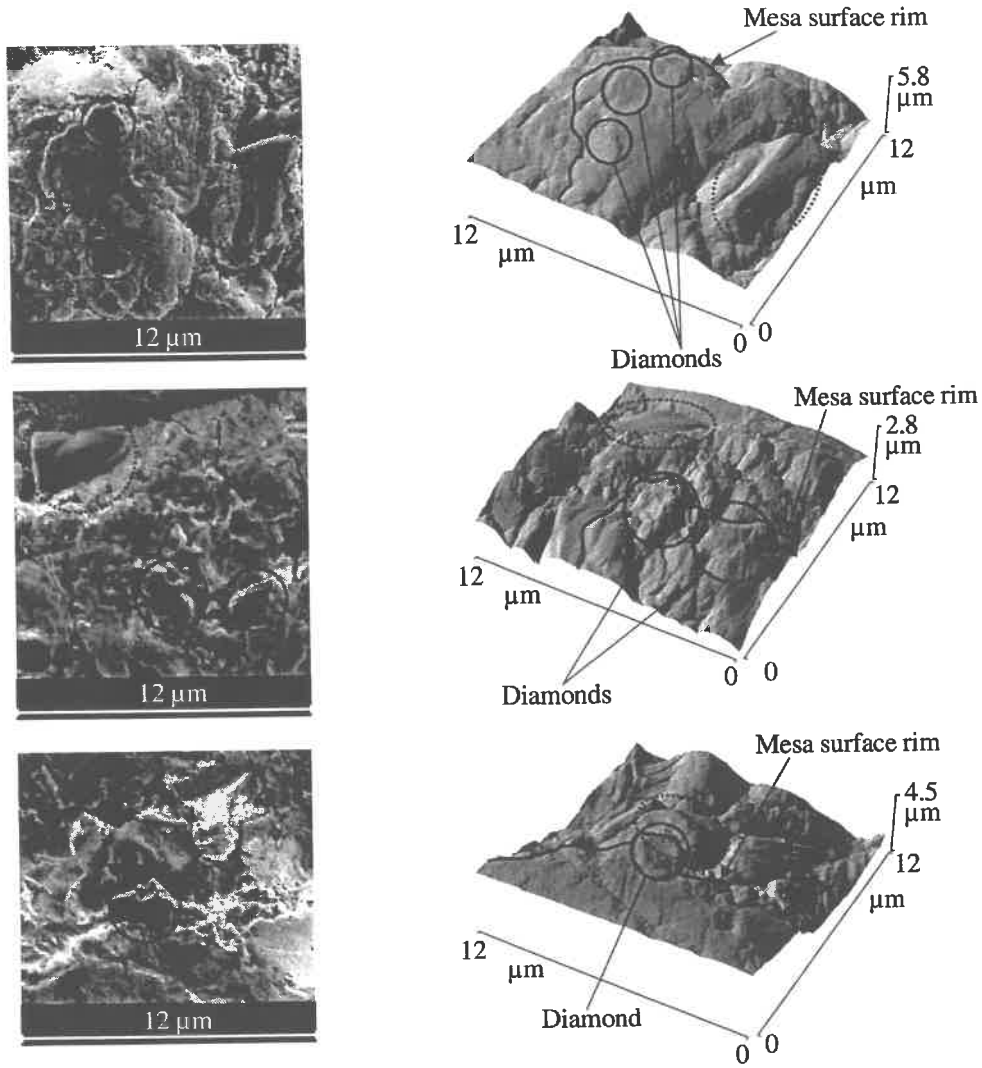

Fig. 5 Examples for embedded diamonds in the nanogrinding plate; SEM (left) and AFM (right) analyses

Conclusion

During the different steps of a nanogrinding process, the nanogrinding plate's microtopography is subject to change. After conditioning, the plate had an average and peak-to-peak plate roughness of $R_a = 1.4$ µm and $R_t = 12$ µm, respectively. During conditioning, mesa type plateau surfaces were created in which the diamond grains were embedded. The consecutive machining process hardly changed the mesa surface, just increased it minutely. By a combination of SEM/EDS and AFM analyses, diamond grains embedded in the plate could be detected and topographically analyzed. The grain density for a 1.5-3 µm grit is approximately $N_A = 3{,}500$ mm^2, the grain protrusions above the plate's tin surface were in the range of 50-200 nm. The diamonds preferably embed themselves at the mesa surfaces' rims. Aside from diamond grains, conditioning grains also embed themselves into the plate during conditioning. Due to their low hardness, these grains already wear during the diamond impregnation process and therefore do not take part in the material removal process.

References

[1] Gatzen, H.H.; Maetzig, J.C.: Nanogrinding. Precision Engineering, Journal of the ASPE, Vol. 21, No. 2/3, pp. 134-139, 1997

[2] Gatzen, H.H.; Siekmann, H.: Plate Topography Influence on the Nanogrinding Process. Proceedings of the 1999 Annual Meeting of the ASPE, pp. 83-86, 1999

Microfactory and a Design Evaluation Method for Miniature Machine Tools

Nozomu Mishima, Kiwamu Ashida, Tamio Tanikawa,
Hitoshi, Maekawa, Kenji Kaneko and Makoto Tanaka
Mechanical Engineering Laboratory, 1-2 Namiki, Tsukuba, Ibaraki, JAPAN

1. INTRODUCTION

Mechanical Engineering Laboratory, MITI, Japan proposed a concept of a microfactory which consists of tiny machine tools and robots. In terms of energy efficiency, a large machine represents considerable waste. Miniaturization of machine tools to size compatible to the target products without compromising machining tolerance lead to enormous savings in energy, space, and resources. Recent progress of control and fabrication technologies of microstructures has made those small machines possible to prototype. MEL developed a miniature lathe; the micro-lathe [1]. Although the micro-lathe was only 1 cubic inch large, it was capable to cut metal more accurate than a conventional lathe. The success of the micro lathe was the driving force to prototype a whole factory that performs a series of fabrication and assembly on a desktop.

For the machine tools of the microfactory, the existing experience of machine tool design may not be applicable. Machine tool designers will need a general design guideline to appropriately reduce the size of machine tools. The latter half of this study combines an analytical procedure representing the machining motions known as form-shaping theory [2] with a well-known robust design procedure; the "Taguchi method" [3], [4]. The effort identifies critical design parameters that have significant influence on the machining tolerance [5]. The paper applies the method to analyze the effect that the machine tool structure has on its machining performance. From two design candidates of the micro milling machine, the method can tell which design has a better theoretical performance, in terms of machining tolerances. The result leads us to conclude that the design evaluation method is applicable to a systematic miniaturization of a machine tool from its conceptual design stage.

2. THE MICROFACTORY

2.1 General concept

The concept of the microfactory is to fabricate small products using small amount of energy and space. Production rate has not been a critical issue by now. On the other hand, the configuration change of the factory corresponding to the product requirement will be flexible. Because of these features, the microfactory can commit some high value, large variation and small volume manufacturing, in future. The first performable component of the factory, aforementioned micro lathe (fig. 1) can cut brass within 1.5μm surface roughness and 2.5μm roundness error. It means that the micro lathe is more accurate than a conventional lathe. The next issue was to design and prototype a whole microfactory that consists of several components, and collaboratively fabricates a product. The effort has achieved as a prototype machining microfactory. Figure 2 shows the overview of the prototyped microfactory that consists of three machine tools and two manipulators. It can produce a tiny ball bearing assembly on the single desktop.

2.2 Components of the microfactory

The microfactory consists of three machine tools and two small manipulators. The components are the micro lathe, a micro press machine, a micro milling machine, a micro transfer arm and a micro two-fingered hand. The following images (figure 3 through 6) are the components of the factory.

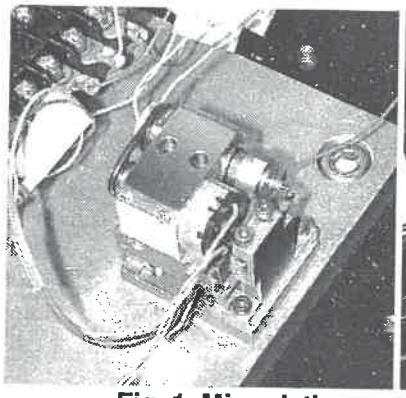

Fig. 1 Micro lathe

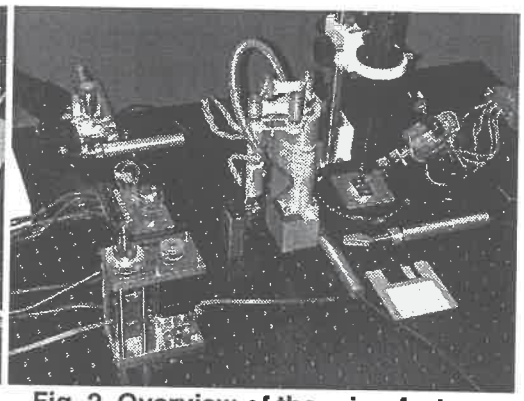

Fig. 2 Overview of the microfactory

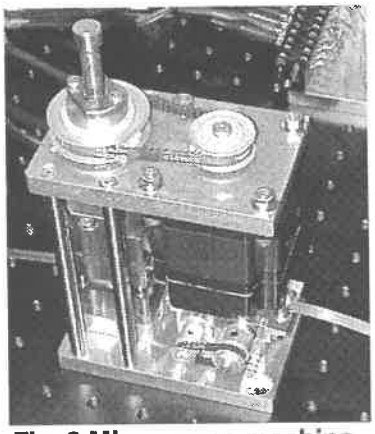

Fig. 3 Micro press machine

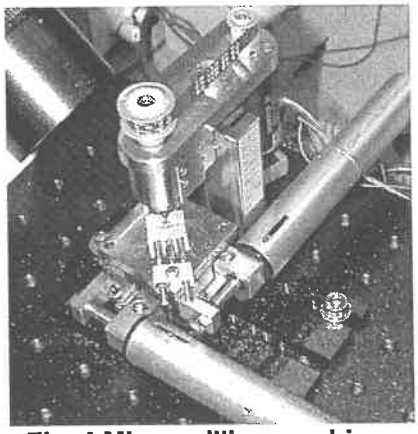

Fig. 4 Micro milling machine

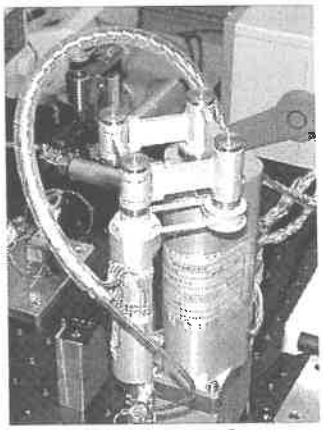

Fig. 5 Micro transfer arm

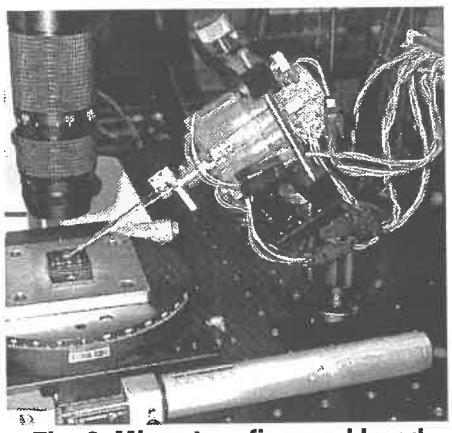

Fig. 6 Micro two-fingered hand

2.3 Test product of the microfactory

To prove that the microfactory is capable to machine and assemble a "product", we choose an extra small ball bearing as the test product. Following procedure is the manufacturing process for the product.

a) The micro press machine punches the top cover of the bearing.
b) The micro lathe turn-cuts the rotary shaft.
c) Micro milling machine mills the top and bottom surfaces of the bearing housing and drills the inner surface.
d) The micro transfer arm transfers the parts from the stockyard to the assemble yard.
e) The micro two-fingered hand assembles the machined parts and purchased steel balls.

Figure 7 shows the assembled ball bearing that has 100μm rotary shaft diameter and 900μm housing diameter.

2.4 Result of the test production

As the result of the fabrication of the ball bearing, the microfactory was capable to assemble the test product on a single desktop that is approximately 50 by 70cm. In addition, because of its extremely small size, it would be easy to reconfigure the system corresponding to the large variety of the products. Therefore, the microfactory has a future possibility as a manufacturing system to produce many varieties of extra small machine parts. However, it still remains some problems, such as the low production rate or the difficulty of the fixture of the product To apply the microfactory or similar small manufacturing systems to actual productions, those problems have to be overcome.

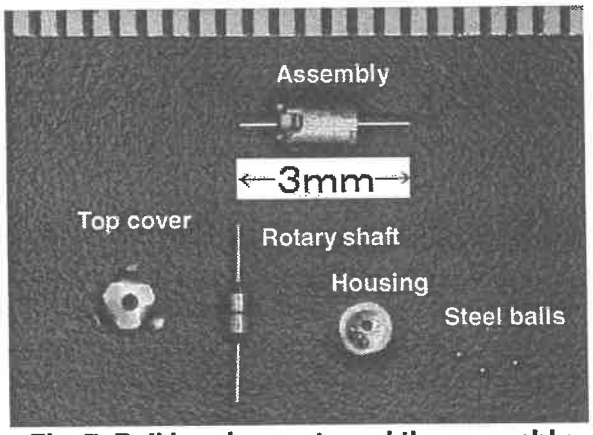

Fig. 7 Ball bearing parts and the assembly

3.CONCEPTUAL DESIGN EVALUATION OF MICRO MILLING MACHINES

3.1 Representation of cutting motions

A machine tool structure is considered as a chain of directly linked rigid components extending from the product through the cutting tool. We defined an orthogonal coordinate system S_i correspondingly to element i (i=0 to k). The transformation from S_i to S_{i+1} represents a coordinate transformation between components. We represent these respective coordinate transformations by homogeneous transformation matrices [6]; A_i. In an ordinary machine tool, A_i is represented by one of either parallel transformation along the x, y or z axes or rotation around the axes. Each of these six coordinate transformations is assigned a number to distinguish them, with parallel movement along the x-axis being 1, and so on. When the homogeneous transformation matrices A_i are represented by the transformations j_i, (=1 to 6), and the amounts

of motions are represented by l_i, we define $A(i)(j_i)(l_i)$ as the expressions of the matrices. Vector $\vec{r}_0$ represents the relative displacement between the product and the tool, and the tool shape vector $\vec{r}t$ is also defined. The relation between $\vec{r}_0$ and $\vec{r}t$ is as given by eq. (1), and $\vec{r}_0$ is the definition of the form-shaping function that expresses the cutting motions of the machine tools mathematically. Actual machine tools have assembly tolerances, thermal deformation, wear and many other sources of errors. In order to describe actual cutting motions, one must consider these errors. Such errors may for convenience's sake be treated as errors in transformations between elements. We define another homogeneous transformation matrix $A_{\varepsilon i}$ to generally represent transformation error between elements. By inserting the error component matrix $A_{\varepsilon i}$ between $A(i)(j_i)(l_i)$ and $A(i+1)(j_{i+1})(l_{i+1})$ in eq. (1), the form-shaping function including errors, $\vec{r}_{\varepsilon 0}$ is written as eq. (2). And the form-shaping error function $\Delta\vec{r}_{\varepsilon 0}$, expressing the shift from the target value of the machine tool motions, is defined as the difference between the form-shaping function not containing errors and that containing the errors, as eq. (3).

$$\vec{r}_0 = A(0)(j_0)(l_0)\cdot\cdot A(i)(j_i)(l_i)A(i+1)(j_{i+1})(l_{i+1})\cdot\cdot A(k-1)(i_{k-1})(l_{k-1})\vec{r}_t \quad (1)$$

$$\vec{r}_{\varepsilon 0} = A(0)(j_0)(l_0)A_{\varepsilon 0}\cdot\cdot A(i)(j_i)(l_i)A_{\varepsilon i}A(i+1)(j_{i+1})(l_{i+1})\cdot\cdot A(k-1)(j_{k-1})(l_{k-1})A_{\varepsilon k-1}\cdot\vec{r}_t \quad (2)$$

$$\Delta\vec{r}_0 = \vec{r}_{\varepsilon 0} - \vec{r}_0 \quad (3)$$

3.2 Two design candidates of the micro milling machine

By using the form-shaping theory, it has become possible to evaluate the effects of design parameters of an existing design. However, the method does not provide a design suggestion to choose one design from design candidates, or to create an alternative design when the performance of the old design is insufficient. This stage of a design procedure is often called "Conceptual Design". Although the Taguchi method does not mention about the conceptual design, one can compare performance of several designs by the method. This paper applies the method to two design candidates of the micro milling machine which was used in the microfactory. To obtain a design guideline, we compared two different designs with same machine parts, same dimensions and different distribution of degrees of freedom (DOF). Following the machine tool elements from the product towards the cutting tool, one has two axes before the static part, whereas the other has all three axes concentrated. Figure 8 shows the two design candidates. Tables 1 through 3 show the design parameters, product dimensions and local errors for the two designs.

3.3 Form-shaping error function

The form-shaping function of the micro milling machines including errors; $\vec{r}_{\varepsilon 0}$ can be expressed using the design parameters and local errors. The form-shaping error functions for the two designs that indicate the positioning errors from the target points can be expressed as equations (4) and (5).

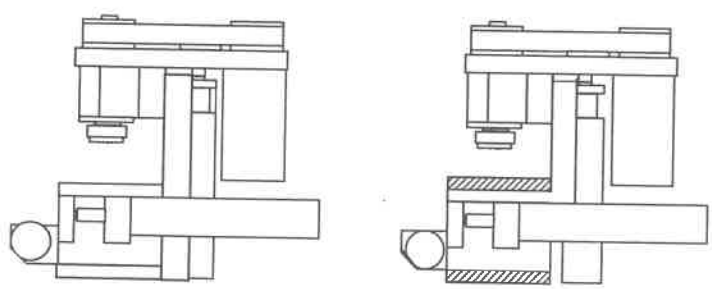

(a) Type 1 with distributed DOF (b) Type 2 with concentrated DOF

Fig. 8 Two design candidates

Table 1 Design parameters

Design parameters	Variable
Tool length	lt
Spindle overhung	ld
Thickness of the stages	ls

Table 2 Product dimensions

Dimensions	Variable
width	l
depth	d
height	h

3.4 Applying the Taguchi method

To achieve machining tolerance that is stable under a variety of machining conditions, a method is needed for obtaining a design which is robust with respect to unknown local errors. The Taguchi method is widely used in the field of quality engineering, and provides an environment for robust design. This study uses the Taguchi method to evaluate the dimensional effect imposed on machining errors by the machine structure, when local errors are unknown. Simulations were performed applying the method to the form-shaping error function. The Taguchi method allows us to calculate combinations of values of control factors to optimize an evaluation function, given noise factors fluctuating within given ranges. In this study, the

primary objective is to determine the effect on machining performance of structural design, when some local errors exist in the various components of the machine tool. Therefore, it is appropriate to take the design parameters and product dimensions to be control factors and the local errors to be noise factors. We also define Δx, Δy, Δz to be the error amounts in each axis direction. Then, we take $(\Delta x^2+\Delta y^2+\Delta z^2)^{1/2}$ to be the evaluation function. The number of independent local errors being 15, an L16 orthogonal array [4] is applicable for systematic inclusion of 15 factors at two levels. The two of the design parameters in table 1 being fixed, we, therefore conduct an analysis using an L9 orthogonal array.

Table 3 Defined local errors

Parameter	Variable
Angular errors of the XY stages	α1,β1,γ1
Scale error of the XY stages	δx1
Straightness error of the XY stages (horizontal)	δy1
Straightness error of the XY stages (vertical)	δz1
Angular errors of the Z slide	α3,β3,γ3
Scale error of the Z slide	δz3
Straightness error of the Z slide (horizontal)	δx3
Straightness error of the Z slide (vertical)	δy3
Angular error of the spindle axis	α4
Eccentricity of the spindle	δx4
Expansion of the spindle	δz4

$$\bar{r}\varepsilon = \begin{bmatrix} \delta x1+\delta y1+\delta x3+\delta x4-\gamma 1d-(\beta 3+\alpha 4)lt+(\gamma 1-\gamma 3)d+(\alpha 1+\beta 1)(2ls+h) \\ \delta x1+\delta y1+\delta y3+\delta x4+(\alpha 3+\alpha 4)lt-\beta 1(2ls+h)-\alpha 1(ls+h) \\ 2\delta z1+\delta z3-\delta z4+\alpha 1d-(\beta 1+\alpha 3)d \\ 1 \end{bmatrix} \quad (4)$$

$$\bar{r}\varepsilon = \begin{bmatrix} \delta x1+\delta y1+\delta x3+\delta x4-(\beta 3+\alpha 4)(lt+2ls)-(2\gamma 1+\gamma 3)d-\alpha 1(ls-h)-\beta 1(2ls-h) \\ \delta x1+\delta y1+\delta y3+\delta x4+(\alpha 3+\alpha 4)(lt+2ls)-\alpha 1(2ls-h)-\beta 1(ls-h)+\gamma 1l \\ 2\delta z1+\delta z3-\delta z4-\alpha 1l-(\alpha 1+\beta 1+\alpha 3)d \\ 0 \end{bmatrix} \quad (5)$$

3.5 Comparison of the theoretical performance

We implement the same ranges of the local errors to two machines, which are given in catalogs of actuators, slides and motors. The ranges of the control factors and the noise factors are substituted to equations (4) and (5) to clarify the effect of each factor on the machine performance. Under these assumptions, the results based on the Taguchi method is expected to show the priority of the designs directly. Figure 9 shows the comparison of the theoretical performances calculated by the Taguchi method. The figure leads us to conclude the one design with distributed DOF (type1) has evidently better theoretical performance than the other with concentrated DOF.

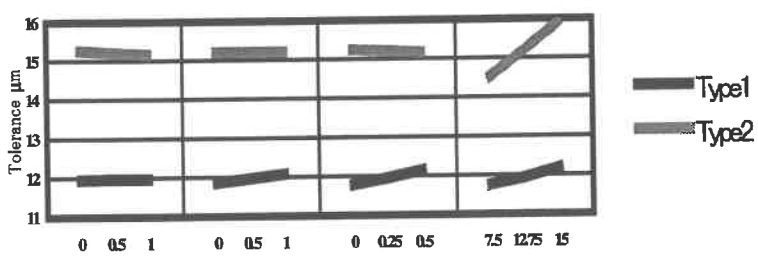

Fig. 9 Machining error comparison

4. CONCLUSIONS

The microfactory: The prototyped microfactory successfully showed the capability as a space and energy-saving machining system for small products.

The design evaluation method: Proposed design evaluation method was effective to identify a design that has a better theoretical performance from two design candidates.

References

[1] Kitahara, T., Ishikawa, Y., Terada, K., Nakajima, N., and Furuta, K. (1996). *Development of Micro-lathe,* Journal of Mechanical Engineering Laboratory, Vol. 50, No. 5, p. 117-123.

[2] Reshtov, D.N., and Portman, V.T. (1998). *Accuracy of Machine Tools,* ASME Press, New York.

[3] Taguchi, G. and Konishi, S. (1994) *Quality Engineering Series* Vol.1-4, ASI Press.

[4] Folkes, W.Y. and Creveling, C.M. (1995). *Engineering Methods for Robust Product Design*, Addison Wesley.

[5] Mishima, N. and Ishii K. (1999). *Robustness Evaluation of a Miniaturized Machine Tool*, Proceedings of DETC99, 25th Design Automation Conference.

[6] Paul, R.P. (1981). *Robot Manipulators --Mathematics, Programming and Control--*, THE MIT press, Cambridge.

Performance Evaluation of a Parallel Cantilever Biaxial Micropositioning Stage

Edward Amatucci, Nicholas G. Dagalakis, John A. Kramar, and Fredric E. Scire
National Institute of Standards and Technology
Gaithersburg, Maryland 20899

1. System Overview

The phenomenal growth of opto-electronic manufacturing and future applications in micro and nano manufacturing has raised the need for low-cost high performance micro-positioners. The National Institute of Standards and Technology (NIST) Advanced Technology Program (ATP) funded a team of NIST scientists and engineers to address the performance, testing and calibration needs of micropositioners. As a result of this effort various performance testing and calibration techniques are being developed on a new generation of micro-positioners with low crosstalk, good lateral resolution and strong load capabilities for delicate sub-micron automated assembly and positioning applications. The Parallel Cantilever Biaxial Micropositioning Stage (Figure 1.) is composed of two piezo-electric translators (PZTs) with internal capacitance sensors, two flexure joint couplings, a monolithic mechanical flexure baseplate, two capacitance sensors measuring the inner stage motions, control software and supporting commercial electronics. Inspired from the PiezoFlex[1] Stage [1] which has only one cantilever flexure mechanism on each axis, this new micropositioning stage has a novel configuration and design in that it has two parallel sets of cantilever beam flexures. This design reduces crosstalk in the X and Y translations and creates motions that are more linear and independent from each other in the X and Y directions.

Figure 1. Parallel Cantilever 2D Micropositioning Stage

The other improvement includes the addition of sensors on axis with the actuator of the system. This is designed to reduce Abbe offset errors for precision measurement and control of the stage. Our new design has the potential to reduce the error caused by the rotation of the cantilever and also provide room for on-axis sensing of the moving x-y stage. It has two micro actuators and two sensors to directly monitor the actuator and stage motions respectively.

One of the more important performance characteristics of any planar micro-positioner is its angular cross talk error. All other errors can be compensated with the use of sensors and closed-loop feedback control. Correcting angular error cross talk can often require the use of expensive sensors and additional micro-positioners, which would then have to be connected in series with the planar micro-positioner to induce equal and opposite sign angular displacements. Our first generation micro-positioner has an unqualified (uncertainties yet to be determined) angular error of 0.3" to 0.4" ((1/12000)° to (1/9000)°).

2. Micro-positioner Controller

A simple motion controller of the micro-positioner has been developed. Figure 2 shows a schematic block diagram of the controller. The controller is running on a PC and issues motion commands to the controller of two piezoelectric PZT actuators, through a serial line connection. The actuators are Queens Gate (QG) 17 μm capacity PZTs (Q1 and Q2 in Figure 2) and are mounted into machined holes within the structure of the micro-positioner. The actuators are equipped with embedded capacitive gauges, which measure the change in the length of the PZT stacks. This information is used by the QG controller to close the feedback loop. Our controller monitors and

[1] PiezoFlex is a trademark associated with Wye Creek Instruments design of a flexure stage. This and certain commercial products are identified in this paper to specify experimental procedures adequately. Such identification is not intended to imply recommendation or endorsement by the National Institute of Standards and Technology, nor is it intended to imply that the products identified are necessarily the best available for the purpose.

displays the actuator elongation information. The micro-positioner is equipped with two capacitive gauges described in the previous section (C1 and C2 in Figure 2), which monitor the absolute position of the moving stage along its two orthogonal axes. The outputs from these two gauges are digitized, by a data acquisition card (DAQ) and plotted on the control panel of the controller. The QG controller is not using these signals for feedback information. The operation of the controller is open loop in order not to mask the performance of the micro-positioner.

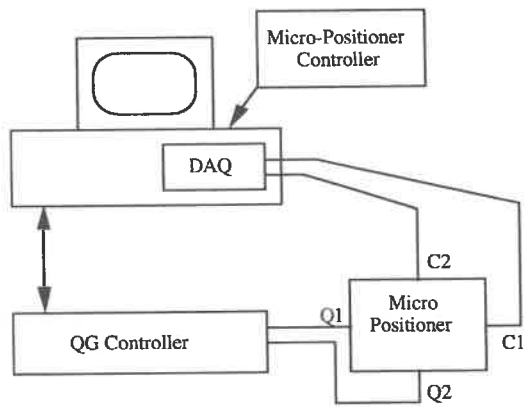

Figure 2. Schematic Block Diagram of the Controller

3. Mechanical Lumped Parameter Model

Figure 3 shows a simple mechanical lumped parameter model of the micro-positioner along a single axis direction.

In Figure 3, M_s represents the mass of the moving stage and M_c the mass of the actuator-to-stage coupling mechanism. K_{lo} and K_{li} are the stiffness of the two levers that support the moving stage. K_c represents the stiffness of the coupling mechanism. B_{lo}, B_{li} and B_c represent the constants of dashpots, which model the losses due to structural damping and any other energy dissipating mechanism that might be used to dampen oscillations of the moving stage.

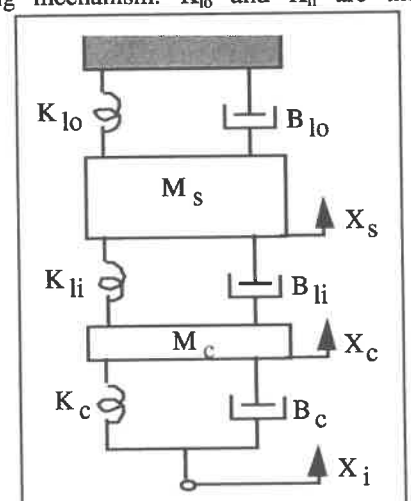

Figure 3. Lumped parameter model

If X_i represents the input displacement generated by the actuator and X_s represents the displacement of the moving stage it is easy to show that the following relation is true:

$$X_s = GR\ X_i \quad (1)$$

where,

$$R = \frac{K_{li} K_c}{K_{li} K_{lo} + K_{li} K_c + K_{lo} K_c} \quad (2)$$

We call R the transmission ratio of the coupling mechanism and G the lever gain . It is obvious from eq. (2) that $R < 1$ since all stiffness values are positive. That means that the moving stage displacement will always be less than the displacement range of the actuator. R should be as large as possible to utilize as much of the available input displacement as possible. Increasing the stiffness K_c of the coupling mechanism will increase R. A very stiff coupler could transmit moments and shear forces that could destroy a piezoelectric stack actuator.

4. Square Trajectory Performance Test

During testing of a micro-positioner the coupling between the actuator and the cantilever beams was damaged. In one case the coupling was bent and in another case the clamping ball sheared through the shaft of the coupler. In both cases the damage was difficult to detect, because the deformation was small and hidden from view. To avoid operating under defective conditions a simple and fast square trajectory performance test was developed. This is a simple test that can easily spot problems with the operation of the micro-positioner. The micro-positioner is commanded to move its stage equal displacements sequentially along the X and Y orthogonal axes directions. The output displacement along the X and Y directions is measured, scaled and plotted on the controller monitor screen. The lengths of the sides of the trajectory plotted on the screen must be equal to the commanded displacement times the transmission ratio of the

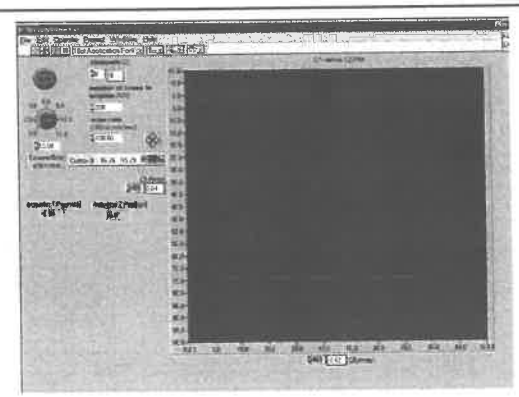

Figure 4. Output from a Square Trajectory Test

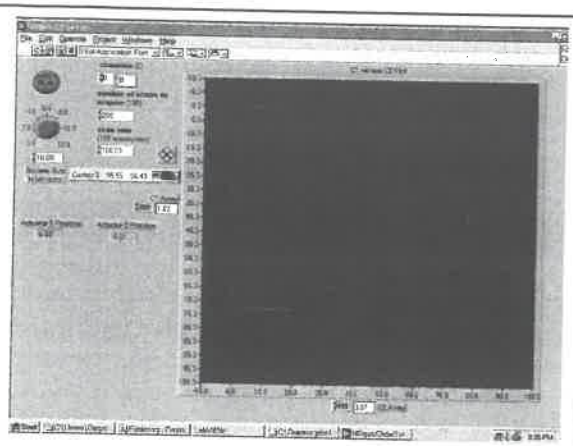

Figure 5. Output showing a defective coupling.

coupling times the micro-positioner gain. For example, if the commanded input displacement is 10 μm, the transmission ratio is 0.7, and the gain is 10, the measured output displacement would be 70 μm. This is a simple test to perform and can provide an easy measurement of the micro-positioner couplings transmission ratios. Figure 4 shows the output from such a test.

This type of test can be performed when the micro-positioner is in good operating condition and then used as a baseline to monitor the operation of the micro-positioner. Figure 5 shows the result from a test when one of the couplings of the micro-positioner was defective. This particular coupling was not capable of transmitting high actuation forces. Overloading or repeated rapid changes in the direction of motion resulted in deformation and slippage. As can be seen from Figure 5 the output displacement along axis #2 is much smaller than that expected from the base line test. This defect would have gone undetected if it were not for the square trajectory test.

5. Calibration

Very often micro-positioners are run open loop without feedback position sensors. In that case it is important to perform a careful calibration in order to determine the correct command signals for the desired output position of the moving stage. One way to calibrate these devices is to develop a mathematical model of the kinematic mechanism, perform the proper experiments, and then use the results to estimate the parameters of the mathematical model. The model can then be used to solve the inverse kinematic problem, to estimate the motion command signals that correspond to the desired positions of the moving stage.

$$\begin{bmatrix} X_o \\ Y_o \\ \Theta_o \end{bmatrix} = \begin{bmatrix} -\frac{L_{1x}}{2H_{1x}} & -\frac{L_{2x}}{2H_{2x}} & 0 & 0 & 0 & 0 & -\frac{L_{1y}}{2H^2_{1y}} & \frac{L_{2y}}{2H^2_{2y}} \\ 0 & 0 & -\frac{L_{1y}}{2H_{1y}} & -\frac{L_{2y}}{2H_{2y}} & -\frac{L_{1x}}{2H^2_{1x}} & \frac{L_{2x}}{2H^2_{2x}} & 0 & 0 \\ \frac{L_{1x}}{W_xH_{1x}} & -\frac{L_{2x}}{W_xH_{2x}} & \frac{L_{1y}}{W_yH_{1y}} & -\frac{L_{2y}}{W_yH_{2y}} & 0 & 0 & 0 & 0 \end{bmatrix} \begin{bmatrix} X_{1i} \\ X_{2i} \\ Y_{1i} \\ Y_{2i} \\ X^2_{1i} \\ X^2_{2i} \\ Y^2_{1i} \\ Y^2_{2i} \end{bmatrix}$$

Figure 6. Kinematic model equations

Figure 6 shows the kinematic model equations of the parallel cantilever biaxial micro-positioner. X_i and Y_i are the input displacements generated by the actuators and X_o, Y_o, are the output displacements. Θ_o is the yaw rotation angle of the moving stage. The subscripts 1 and 2 correspond to the individual levers for the cases where they are activated by separate actuators. The subscripts x and y correspond to the directions of the two orthogonal axes. L is the distance between the lever pivot point flexure and the flexure that transmits the force to the moving stage. H is the distance between the lever pivot point flexure and the flexure that transmits the force from the actuator to the lever. W is the distance between the two flexures that transmit forces to each side of the stage along the one axis direction. Figure 7 shows the dimensional symbols marked on a picture of the micro-positioner.

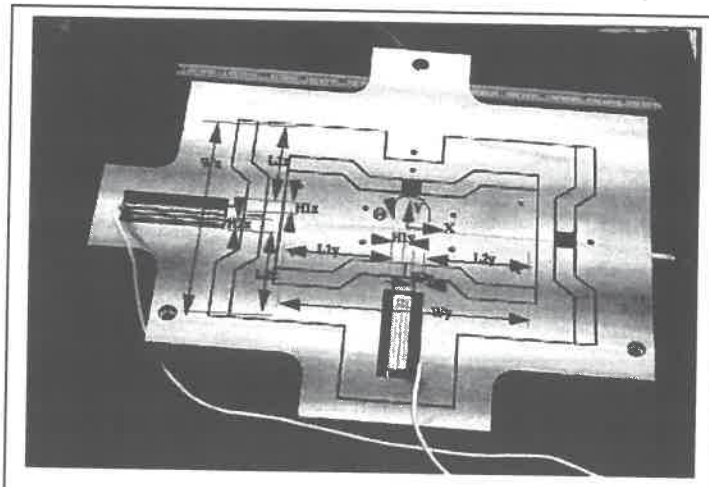

Figure 7. Picture of micro-positioner with dimension symbols

The accuracy of the calibration algorithm depends on several parameters. We are currently investigating the effects of the following: 1) the level of complexity of the mathematical model, such as the effect of non-linear terms

in the mathematical equations of Figure 6.; 2) the number and location of the calibration test positions; 3) the noise in the stage position measurement sensors; and 4) the curve fitting algorithm of the mathematical equations. The suitability of a calibration algorithm can be judged by its ability to predict experimental data. Figure 8 shows a plot of the magnitude of the calibration model vs. experimental x and y position error.

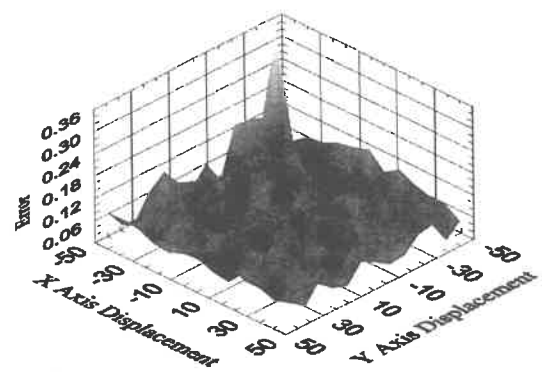

Figure 8. Calibration model vs. actual x, y error vector mapping. All units are in μm.

6. Roll-Pitch-Yaw Error Test

Two Elcomat autocollimators were employed with an optical square to provide simultaneous measurement of pitch, roll and yaw. Resolution of the Elcomat is at least 0.01". Accuracy is limited to perhaps an order of magnitude worse if care is not taken to enclose the optical beam path within a tube and average at least 20 s of data for each data point. By combining autocollimator measurements with microstage displacement measurements, straightness of travel may be estimated by using a numerical integration algorithm. A LabView program was written to move the stage through a serpentine pattern along a 10 x 10 matrix of positions. At each position, approximately 1000 autocollimator measurements were collected and averaged together. Figure 9 shows the result for yaw determined from one autocollimator's measurements. The yaw scale has been offset about its mean value for clarity The yaw is approximately 0.3" or 0.4". Note that we are only showing the worst set of our data and also determined data for pitch, roll and yaw with both autocollimators. Bottom line, the cross couplings from these small yaw angles are going to be approximately 0.2 μm over the whole work zone. For small areas we will have excellent performance.

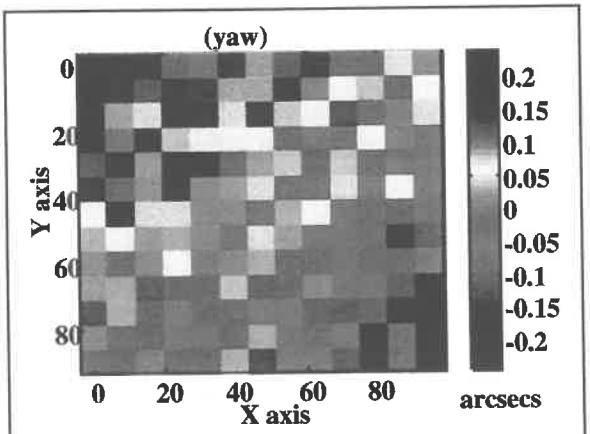

Figure 9. Colormap of micro-positioner yaw error taken on a 10 x 10 position grid. All XY axis units are in μm.

7. Conclusions

In conclusion, performance measures and calibration techniques used on the prototype designs are critical for industry to fabricate larger numbers of these devices. This will provide a low cost system backed by sound calibration, performance measures and design principals. Reduction in size can be accomplished with the use of special metals or composites and/or the use of special fabrication techniques and design modifications [2,3]. The durability of the stage will be enhanced with mechanical stops that will protect the flexure elements from being damaged from accidental abrupt contact by robotic end-effectors placing assembly components on the stage. Also, various configurations of this stage will be developed including a three, four and six axis version.

8. Acknowledgements

We would like to thank Dr. Lowell Howard, Dr. E. Clayton Teague, Jason Marcinkowski, James Gilsinn, Chris Nowakowski, Brian Weiss, and NCMS Optoelectronics Consortium Members for their contributions.

9. References

1. Scire, Fredric E., Teague, Clayton E., "Piezodriven 50-μm range stage with subnanometer resolution", *Rev.Sci.Instrum., 49(12),* December 1978, pp. 1735-1739
2. Smith, S. T. and Chetwynd, D. G., "Foundations of Ultraprecision Mechanism Design", *Gordon and Breach Science Publishers,* 1992, Volume 2
3. Slocum, Alexander H., "Precision Machine Design", *Prentice-Hall, Inc.,* 1992, pp. 1-743

NC MICRO-LATHE TO MACHINE MICRO-PARTS

Yuichi Okazaki
Mechanical Engineering Laboratory
Namiki 1-2, Tsukuba, 305-8364, Japan

Tokio Kitahara
Shonan Institute of Technology
Tsujido-Nishikaigan 1-1-25, Fujisawa, 251-0046, Japan

1. Development and revision of the Micro-Lathe

The original micro-lathe, a palm-top machine tool, was developed in 1996 by Mechanical Engineering Laboratory, as a component of micro-factory [1][2]. It has demonstrated the machining capability of small parts and possible advantages of the extreme downsizing of machine tools. For example, power consumption directed to the material removal was estimated to be a very small portion of the total consumption. Even in the case of the micro-lathe, it was calculated to be several percent of the power consumed at the spindle driven by a 1.5W motor. It means that regular-sized machine tools are in many cases consuming power just for running. Therefore, downsizing of machine tools results in cutting the running power, including that for air conditioning, as well as renovated space factor. Downsizing can also reduce the machine price, and induce agility in reconfigurability of manufacturing systems. Intention of downsizing leads us to design criteria of machine tools different from the conventional one.

On the other hand, as a practical machine tool, the original micro-lathe was lacking machining capacity in sense of form generation, because it had a limited slide feed function. Therefore, the objective of the second step development was to equip the micro-lathe with a precision numerical control like regular NC machine tools, as well as to secure machining accuracy.

2. Mechanical Design

The revised micro-lathe succeeded the original mechanical design: It sizes 32 x 28 x 30 mm, and weighs 98 grams (**Fig. 1**). Two micro-sliders are driven by a set of embedded PZT actuators sizing 2 x 3 x 9 mm from Tokin. The slide block is of a monolithic structure manufactured by wire EDM out of brass. The main slide and the clamp slide are connected to each other via thin blades with 0.15 mm thickness. Two parts of the clamp slide are also connected with a blade on one side, and on the other sides connected to a block by two short cantilevers. The two actuators are embedded and glued into the slide block. The actuators expand or bend the blades or the cantilevers. The clearance at the clamp slide is set slightly positive when the clamping actuator is not activated.

The micro-sliders are operated in stepwise manner. However, unlike the conventional "inchworm" mechanism, the slide uses only one actuator for clamping and one for feed action, and friction is positively used (**Fig. 2**). In the stationary state in the step motion cycle, the main stage is held tightly between the countering guide-ways by friction. In the feed phase following the clamping phase, the feed actuator breaks the friction, and pushes the main slide forward referred to the clamp stage, followed by the releasing the clamp. This mechanical configuration provides with guiding- and hold rigidity. The two slides are stacked orthogonally and connected to each other on the top of the each main slider.

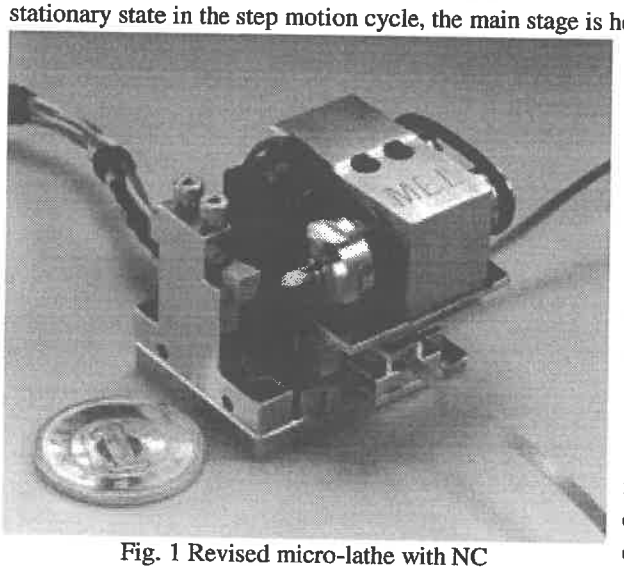

Fig. 1 Revised micro-lathe with NC

The friction at the main slide is as large as about 5 N in thrust force, so that the clamping actuator should generate clamping force greater than 25 N, provided friction coefficient is 0.2. Actual net thrust was measured as about 1 to 2 N.

The spindle unit is using two ball bearings of 10 mm outer diameter, and holding a 2 mm diameter collet chuck. The spindle is indirectly driven by a 1.2 W DC coreless motor up to 15,000 rpm. The spindle unit and

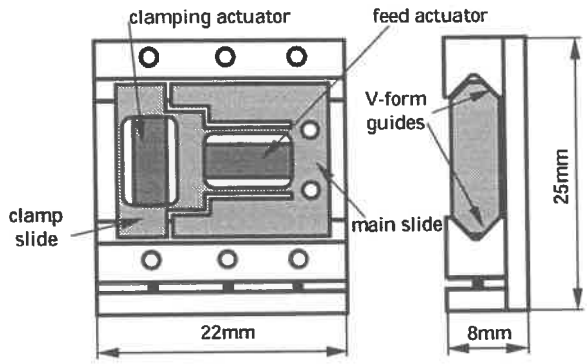

Fig. 2 PZT driven micro-slider

drive motor are mounted on the top of the X-slide. One additional tool can be optionally mounted for combined operation, e.g., left-hand-side turning or cut-off.

3. Slide Drive

By optimising the drive waveforms fed to the two actuators, sufficiently smooth feed movement was obtained. Feed rate is controlled by changing the feed amplitude. Feed direction is alternated by reversing the drive waveforms (**Fig. 3**). In that case, the feed actuator pulls the main stage. Although the feed actuator acts differently in forward and reverse movement, the response is almost same.

The step feed cycle is fixed to 200 Hz. The maximum feed rate and the minimum step size achieved was 400 μm/s and 50 nm. These values are dominated by calculated maximum step feed amount of 2 μm and stick-slip motion in the feed phase. It is preferable that the friction coefficient drops from the static value when the stiction is broken. Very slightly-lubricated condition resulted best. As the step feed amount is changed, the average velocity responds almost linearly, but small deadzone around zero

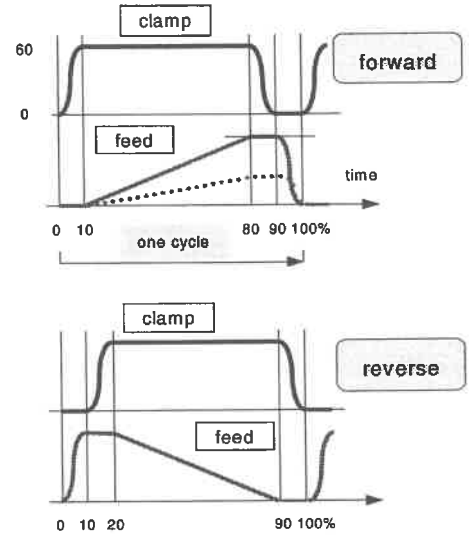

Fig. 3 Drive waveforms

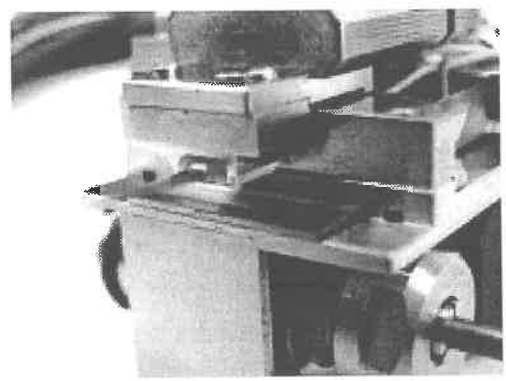

Fig. 4 Close-up of the micro-linear encoder

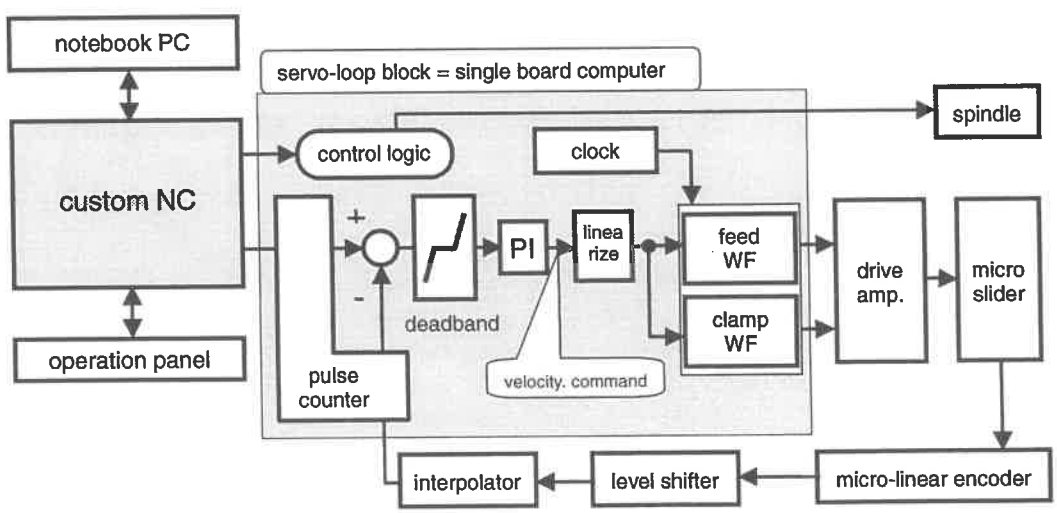

Fig. 5 Block diagram of the closed-loop NC system (single axis and spindle control illustrated)

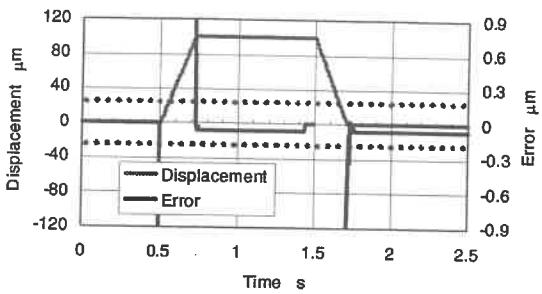

Fig. 6 Step response (100 µm step)

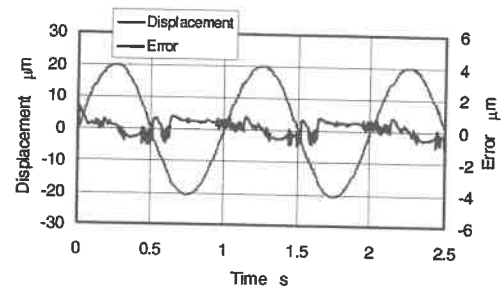

Fig. 7 Sinusoidal response

velocity was observed. It has been compensated for by a linearizer. The drive amplifier uses high-voltage operational amplifiers, swinging 0 to 80 volts.

4. Full Closed-Loop Numerical Controller

A full closed-loop feedback has been composed by using embedded micro-linear encoders developed by Olympus Optical Co. Ltd (**Fig. 4**). It comprises of Surface Emitting Laser (SEL) diode, and is based on unique diffracted image projection principle. The head sizes 4.5 x 5.5 x 2.1 mm and outputs quadrature sinusoidal signal of 25 µm pitch. A resolution of 62.5 nm was achieved after 400X interpolation by microE M400 interpolator.

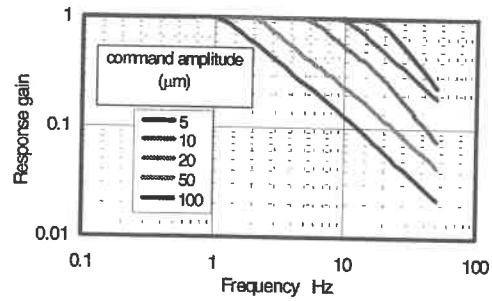

Fig. 8 Frequency response

The total control system is illustrated in **Fig. 5**. A custom numerical controller based on a microprocessor feeds servo loop block with position command pulse train, processing motion codes of part programs or manually given commands. Notebook PC is used for monitoring the status and for handling part programs. The operation panel is full-sized for a secure HMI. The servo-loop block is realized by a single board computer with 5x86-133 CPU, together with pulse counters and D/A converters. The servo-loop program is operated on MS-DOS.

spindle rotation	: 7500rpm
depth of cut	: 20mm
feedrate	: 25µm/s
workpiece	: brass ø2mm
tool	: R0.1 diamond
lubricant	: none

Table 1 Machining conditions

At the beginning of every step cycle of 5 ms, the following error, i.e. the position command subtracted by the actual position, is converted into velocity command via PI (proportional-integral) controller. Then according to the velocity command, the drive waveforms are generated based on the principle described in the previous section, and in turn fed to the high-voltage drive amplifier. The command resolution is set to 0.1 µm, and the actual positioning resolution is 0.2 µm by a deadband component to maintain stability. Total occupying desktop space of the system is about 550 x 450 mm, including the lathe, a custom NC and electronics.

5. Motion Control

A typical step response is shown in **Fig. 6**. The positioning error converges within the deadband of 0.2 µm without overshoot, because the moving mass is negligibly small compared to the drive force and the friction in this region. A typical sinusoidal tracking response is shown in **Fig. 7**. For small command amplitude, the following error is small, while for large amplitude or high frequency command, the following error bursts because of the available maximum velocity. In terms of frequency response, the bandwidth depends on the command amplitude (**Fig. 8**). No dynamics is ruling the response. The contouring error can be reduced by tuning servo-parameters or introducing other control algorithm.

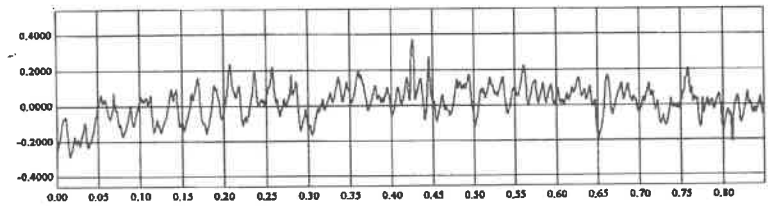

Fig. 9 Surface roughness along the generator line

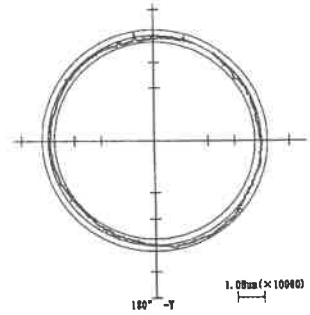

Fig. 10 Roundness

6. Machining

Workpieces made of brass of 2 mm diameter were machined using a diamond tool. Surface roughness of the cylinder in the generator line direction and radial direction were measured by stylus roughnessmeter. Those values are 0.5 μm Ry or 60 nm Ra (**Fig. 9**), and 0.8 μm Ry or 126 nm Ra. Roundness error was smaller than 0.5 μm (**Fig. 10**). These values are better than those of the original micro-lathe, and are comparable to those of regular-sized machines. Component of the surface roughness is not related to the theoretical tool mark. It is because of guiding irregularity. When the motion of the both axis are combined, the surface roughness becomes worse due to feed fluctuation.

Taking advantage of the accurate feed control, a thin needle of 50 μm diameter and 600 μm long was successfully machined out of brass rod. NC motion control enables programmed shape generation. In **Fig. 11** and **Fig. 12**, the machined samples are shown.

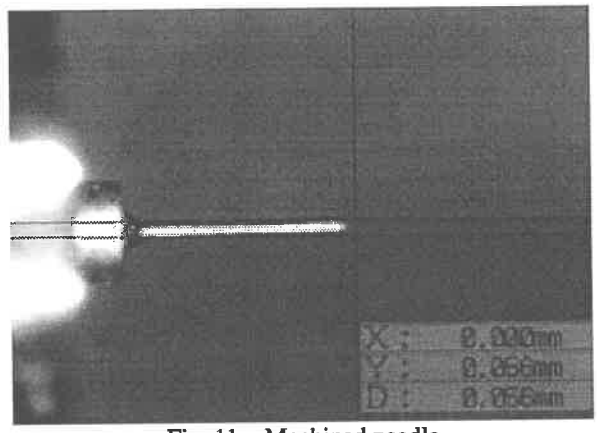

Fig. 11 Machined needle

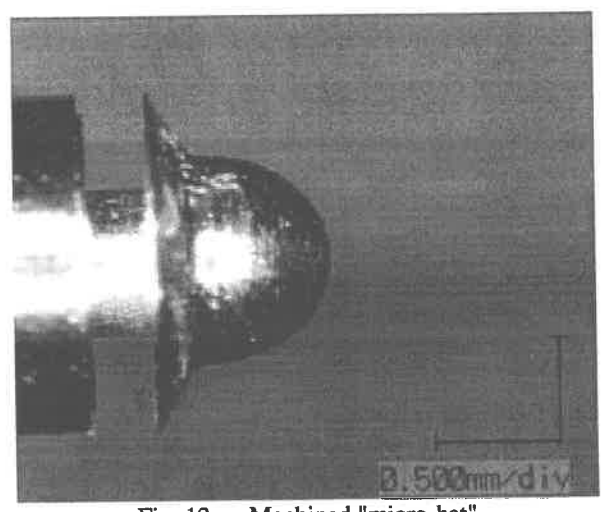

Fig. 12 Machined "micro-hat"

7. Conclusion

The micro-lathe, a palm-top machine tool, has been developed and revised, integrated with PZT-driven micro-sliders, micro-linear encoders and a custom numerical controller. The micro-lathe has potential to machine mechanical parts with precision comparable to regular-sized machine tools.

On the other hand, the micro-lathe has still shortcomings in material handling, chip handling, tool change, and machining throughput. It is not ready to be introduced into manufacturing system. However, its unique design and capability would stimulate design of various machineries. The integrated key components will be potentially used in some positioning devices or instrumentation.

8. Acknowledgements

The authors would express great thank to Dr. E. Yamamoto, Olympus Optical Co. Ltd., Mr. K. Furuta, Seiko Instruments Inc., and Mr. Y. Fuda, Tokin Corporation for their support.

9. References

1. T. Kitahara, et.al. : Development of micro-lathe, Journal of Mechanical Engineering Laboratory, 50-5 (1996) 117-123
2. T. Kitahara, et.al. : Microfactory and microlathe, Proceedings of International Workshop on Microfactories (1999) 1-8

MICROFLUIDIC CONTROL USING MEMS

John Collier, Donald Wroblewski, Thomas G. Bifano
Boston University, Boston, Massachusetts 02215

A microelectromechanical system (MEMS) for gas flow control has been designed, fabricated, and tested at Boston University. The device uses an array of 61 coordinated but independent binary microvalves (μ-valves) in parallel to control flow. Flow rate across the μ-valve array is proportional to the number of microvalves open, yielding a scaleable, high precision, fluidic control system. In this paper, performance of the μ-valve array in a closed-loop, compact flow control system is detailed.

The μ-valves are thin film silicon diaphragms that have been fabricated using surface-micromachining processes. Each diaphragm is supported several micrometers above a port extending through the substrate. Electrostatic attraction is used to deflect the diaphragm to seal off the corresponding port.

Each μ-valve is either fully-open or fully-closed; flow rate is regulated by controlling the number of valves that are open. Performance measurements on fabricated devices confirm feasibility of the fluidic control concept and robustness of the electro-mechanical design. Air flow rates of 50 ml/min for a pressure differential of ~10 kPa were demonstrated. Linear flow control was achieved over a wide range of operating flow rates. For constant-pressure systems, this technique provides a linear relationship between flow rate and the number of open valves. The array is addressed in a binary fashion to reduce the number of off-chip connections. The μ-valve array is installed in a small package along with a microprocessor-based controller and a micro flow sensor. A chip-based control system digitally regulates the number of open valves in response to an analog flow sensor signal. Advantages of the digital μ-valve array include low fabrication costs, low power consumption, and scalable precision.

KeyWords: mems, fluid, valve, control, flow, pressure

Precision Generation of Optical Elements Using Drop-on-Demand Technology

H.-J. Trost, W.R. Cox, C. Guan, D.J. Hayes, R. Hoenigman, and D.B. Wallace
MicroFab Technologies, Inc.; 1104 Summit Ave., Ste 110; Plano, Texas 75074; USA

1 Overview

Optical methods and elements are playing a large and ever more increasing role in communications and computing applications. At MicroFab Technologies, Inc., we have developed drop-on-demand technology capable of handling a large variety of materials, including polymers suitable for optical elements. This permits the direct, data-driven construction of, e.g., lenses and fiber sections at the location of use, unlike photolithographic and other machining techniques which shape elements through removal of material. These process advantages provide an opportunity for significant cost reductions that will help the expansion of the use of high-speed communications technologies. We are working with a number of companies and research institutions on specific applications.

The most common use of drop-on-demand technology is found in ink-jet printers. While that application is highly specialized for specific inks, with precision requirements characterized by a few tens of microns, the optics field demands a variety of fluids to be dispensed (Figure 1) with precisions down to 1-3 μm (3 std. dev.). To date, we have accomplished a relative placement accuracy of less than 2 μm (1 std. dev.) in arrays of microlenses (Figure 2). It appears that this result is still dominated by the properties of the motion system and the currently used software corrections. Thus, there is room for improvement by using better motion equipment and control procedures. Applications include microlenses on pixel arrays for collimating laser beams, lenslets on fiber ends for increased efficiency in couplings, and lenses with an axial gradient index of refraction (AGRIN) for creating small focal spots. On arrays, solder balls for electrical connections may be needed alongside the lenses. Ink-jet technology can provide these, too, and optical polymers are available that will allow the solder process to be performed without damage to the optical elements nearby.

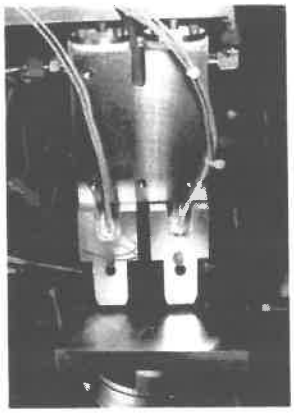

Fig. 1: Heated dual drop-on-demand print head.

Beyond placement accuracy, requirements arise on focal length, focal spot size and lens speed, which translate into performance requirements for the dispensing system, i.e., control of drop sizes and spreading behavior on the target substrate. Required microlens diameters range from tens of microns to millimeters, depending on the specific application. For lenses of diameters in the order of 300-330 μm, we have achieved errors on diameter of less than 0.6%, and on focal length (also around 300-330 μm) of less than 1.1% (both 1 std.dev.). We have produced microlenses with speeds as fast as f/1.2 which is very hard to do with any other manufacturing technology.

2 Technical Implementation

Our core technology is the development of drop-on-demand fluid dispensing technology for applications ranging from printing of biomedical arrays to optical elements to solder balls to controlled creation of aromatic odors. The fundamental element consists of a piezoceramic cylinder fitted around a small glass tube with a narrow orifice (as is the case for the applications discussed here) or a piezoceramic block with a number of fluid channels directly machined into it. The underlying principle of operation is the

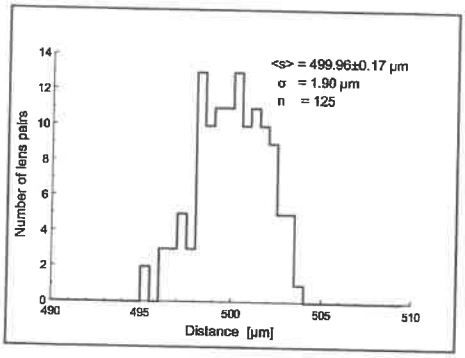

Fig. 2: Distribution of spacings in a lens array.

creation of acoustic waves in the fluid column by the piezo actuator which then, under proper shaping of the stimulating pulse to the piezo element, leads to controlled ejection of single droplets (Figure 3)[3].

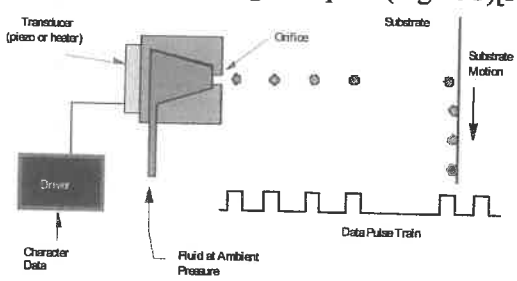

Fig. 3: Principle of drop-on-demand dispensing.

We build print stations in which the dispensing head is held in a fixed position and the substrate is moved to produce the desired pattern. By convention, the substrate (glass for experiments, glass, silicon and other substrates for custom applications), moves horizontally in the x-y plane. The print station on which the patterns and results of the present paper were created uses Parker Daedal 806000CT type motorized stages (150 mm travel) for the x and y motion. The stages are driven by with Parker Compumotor LN57-83 stepper motors and drives which are operated in microstepping mode at 20000 steps per turn of the 1 mm pitch lead screw. Position feedback is obtained through optical linear encoders made by RSF Elektronik, of their MSA670 class with 0.25 μm resolution. A Parker Compumotor AT6400 motion controller is set to employ position maintenance with a deadband parameter of 7 encoder counts or 1.75 μm. A third stage parallel to the x stage allows to position either of the two print heads show in Figure 1 as well as a downward looking camera over the center of the x-y region of motion. Its accuracy characteristics are very similar to those of the x and y stages; however, we need only the reproducibility of a few positions. Manual motion capabilities allow vertical adjustment of the print heads and camera, and rotational adjustment of the substrate. (The latter can also be accommodated in software.) The print station is controlled from an elderly PC (Intel 486DX 66 MHz processor, Windows 95 operating system) using a custom program written in-house.

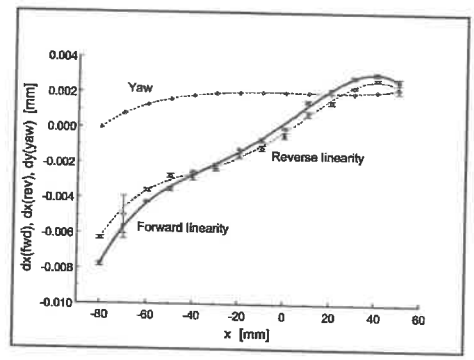

Fig. 4: Linearity and yaw for x axis.

The x and y stages have been surveyed by an outside contractor with a laser interferometer for linearity and yaw. Given that the carriages and their supports are longer than the total travel, we have assumed that the yaw can be translated into a transverse displacement of the center of the carriage by integrating it along the path of travel. The surveys have recorded data every 10 mm for each axis and quantity, with three runs forth and back for the linearities. The three runs are averaged and the resulting data approximated by polynomials up to 5th degree (Figure 4). The yaw angle is then used again to translate from the center of the carriage to the fixed location of the active print head. These corrections are employed in the control software on the host PC which feeds corrected postion information to the motion controller. Our a priori expectation was to shrink the positioning errors from about ± 10 μm (the typical range of linearity errors reported by the manufacturer for the type of stages used) to the order of ± 2 μm, i.e., close to the position maintenance bandwidth we are demanding from our motion

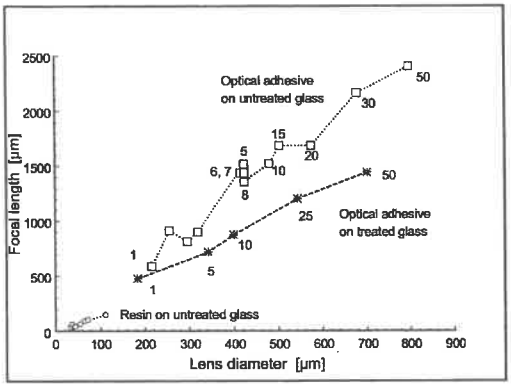

Fig. 5: Control of lens diameter and focal length. Numbers are numbers of droplets per lens.

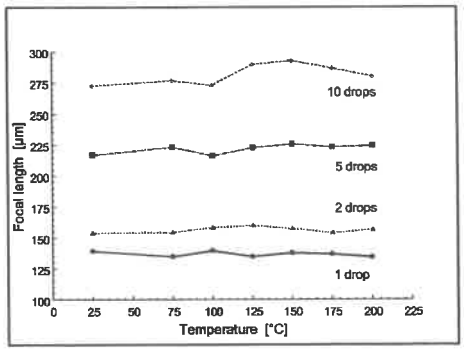

Fig. 6: Focal lengths vs baking temperature for different lens size (numbers of drops).

system.

As described, the surveys give us good accuracy for reaching any point on the substrate once we have picked a starting point. The absolute placement of droplets then still depends on some additional effects: the accuracy of finding a starting point, i.e., the home position for the x and y stages, the positioning and orientation of the print head, and the directionality of the dispensed droplets with respect to the center axis of the print head. We circumvent any inaccuracies induced by these sources by using a CCD camera looking down on the substrate, tied to a monitor outfitted with a Boeckeler VIA-100 screen calibration system. This allows us to pick up a suitable first position for a printing project, e.g., from survey marks, and by performing test prints and inspecting those with the camera, to summarily compensate for all error sources related to the fluid dispensing. Experience has shown that dispensing of optical polymers at elevated temperatures (needed foremost to make and keep them liquid) is quite stable and reproducible over long periods of time.

3 Printing Optical Elements

Our custom projects in the optics sector are centered around creating small lenses on flat substrates like glass plates or on the ends of fibers. The former are useful for building massively parallel optical switches while the latter include, e.g., efficient and stable couplings for single fibers. The basic lens is spherical, coming about quite naturally when one or a few droplets are dispensed at a fixed location. The drop-on-demand technology does allow us to also make quite odd-shaped lenses, e.g., hemielliptical or even nearly-square based ones. Tools to influence diameter and focal length include the choice of material and treatment of the substrate surface. Data from an early study in Figure 5 show both options at work.

Once printed, the optical material is cured by exposure to ample heat or UV light. The curing process is quite uncritical in terms of maintaining a specified focal length; e.g., a wide variation of the baking temperature will affect the focal length only to within a very few percent (Figure 6). This also implies that the lenses remain unaffected by large temperature variations in their operating environment.

A good example for the requirements set by applications is demonstrated by the coupling of light from an edge emitting diode laser (Figure 7) into fibers. Using an air gap is the most stable choice available. Its backdraw is that exiting light is diverging, leading to loss of signal intensity if the capturing element does not cover the full cross section of the light cone. In turn, increasing the capturing element increases the amount of background noise, so there may be a balance between two evils to be made. Placing a focussing lens onto the laser and the end of the fiber can narrow the cone significantly, improving the quality of the signal transfer. In figures 8 and 9, the estimated effect of the lens radius (and with it, the focal length), and of the displacement between the fiber and lens axes is shown. Without lenses, efficiencies of order of 10-15% are obtained. Thus

even a lens of 40 μm diameter, which we have produced successfully already some time ago, will yield an improvement by a factor of two. In general, with drop-on-demand technology a wide range of focal lengths from tens to hundreds of microns is available to accomplish the task at hand. We also note the significant loss in efficiency for lenses on fibers misaligned by more than about 2 μm.

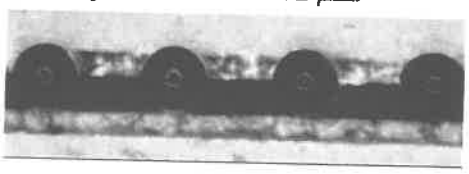

Fig. 7: Edge emitting laser with 200 μm lenses.

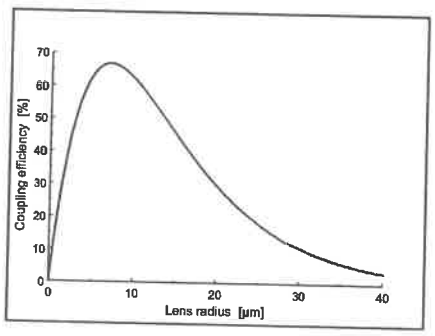

Fig. 8: Coupling efficiency vs. lens radius.

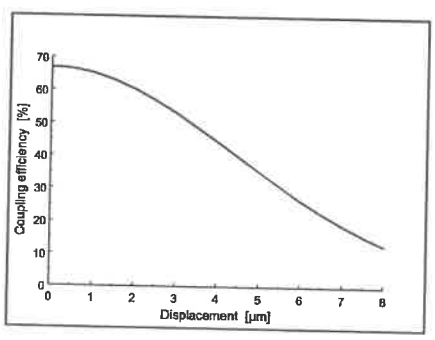

Fig. 9: Efficiency vs. lens-fiber displacement.

The curve in Figure 8 shows that the radius of curvature of the lens has to be maintained to a few microns in order to accomplish a well-defined coupling efficiency. We have inspected random subsets of lenses in a planar array of 2700 lenses for their diameters and back focal lengths (measured on the flat side of the lenses) and find both quantities to behave satisfactorily (Figures 10, 11). To maximize the efficiency for the case shown in Figure 8, we will have to reduce the diameters of the droplets which form the lenses. We are developing and tuning our technology to do this reliably.

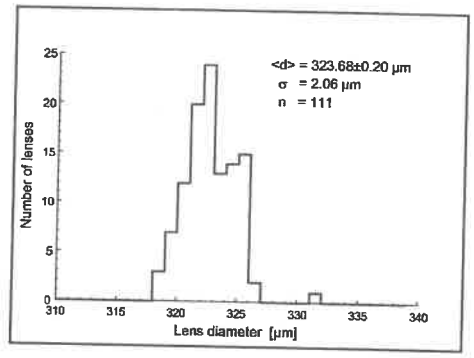

Fig. 10: Distribution of lens diameters in an array.

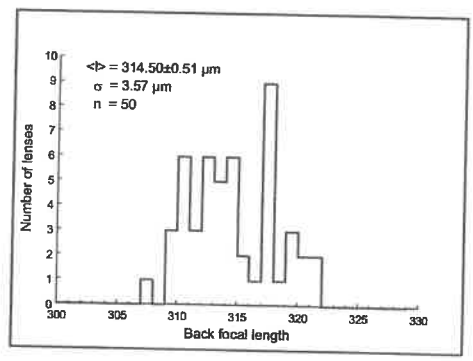

Fig. 11: Distribution of focal lengths in an array.

In summary, drop-on-demand technology offers new avenues in the development and production of optical devices, and combines challenges for control of fluid dispensing with those of more mechanical machining techniques.

[1] W.R. Cox et al., SPIE Proceedings 2382 (1995) 110-115.

[2] W.R. Cox et al., IMAPS International Journal of Microcircuits & Electronics Packaging 20 (1997) 89-95.

[3] D.B. Wallace, ASME Pub. 89-WA/FE-4 (1989).

NANO-POSITIONAL DETECTION USING LASER TRAPPING PROBE FOR MICROPARTS

Yasuhiro Takaya, Satoru Takahashi and Takashi Miyoshi
Department of Mechanical Engineering and Systems, Osaka University
2-1 Yamadaoka Suita, 565-0871 Osaka, JAPAN

1. INTRODUCTION

Over the recent years, steady progress of micro-fabrication or micromachining technology is seen with the enhancement of photolithography technology for creating miniature three-dimensional (3D) structures with dimensions ranging from millimeters to submicrometers. In order to obtain and maintain compatibility of standardized microcomponents in practical use, it is necessary to assess the geometrical properties of micromachined 3D shapes based on coordinate metrology at an accuracy of the nanometer order. For this a nano-CMM (Coordinate Measuring Machine)[1] is required, and a nano-CMM which is 1/100 or 1/1000 the size of a conventional CMM has been proposed for the coordinate metrology of microparts by positional probing. Fig. 1 shows the concept of the nano-CMM. In the use of the nano-CMM, the dimensions and other geometrical properties of the microscale 3D shapes of microcomponents must be evaluated in the nanometer order by probing the measurement points using a three-dimensional sensing microprobe. The microprobe must satisfy harsh specifications such as probe sphere size in the micrometer order, 3D positional detection sensitivity of higher than 10nm and measuring force of less than 10^{-5} N. New probing techniques for achieving nano-positional detection using a microprobe are therefore required. To answer to this need, the authors have developed a new probing technique for the nano-CMM, called a laser trapping probe [2] whose principle is based on the single-beam gradient-force optical trapping technique [3] and microscope interferometers. The work reported in this paper deals with the fundamental characteristics of the practical positional detection and measurements of a glass microsphere with a NIST traceable mean diameter of about 160μm using the laser trapping probe.

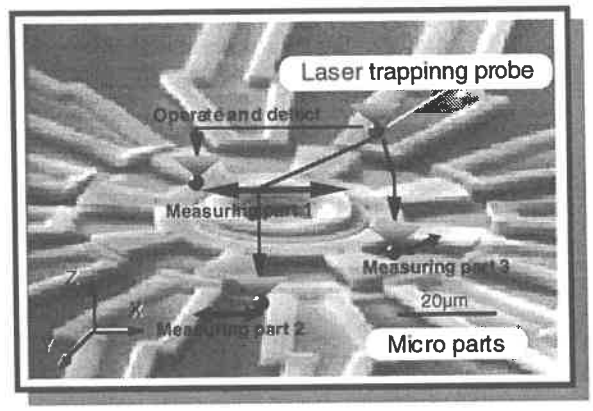

Fig. 1 Conceptual drawing of nano-positional detection using laser trapping probe

2. PRINCIPLE OF 3D POSITIONAL SENSING

An optically trapped small dielectric particle in air [4] is used as the microprobe sphere. It is sensitive to external force generated by interactions with a workpiece and has the same dynamical properties as a positional detection probe. Fig. 2 shows the dynamical behavior of an optically trapped small dielectric particle. The probe sphere retains a stable position when applied with trapping force $\mathbf{F}_t$, which is the resulting force of all radiation pressures $\mathbf{f}_i$ produced by the focused laser beam, as shown in Fig. 2(a). When an external force $\mathbf{F}_e$ is applied to the probe sphere (Fig. 2(b)), the dynamical balance is broken and the probe sphere shifts. At this moment, the trapping force changes with the radiation pressure distribution depending on the illumination conditions of the probe sphere position. When $\mathbf{F}_e$ is released (Fig. 2(c)), the probe sphere is accelerated in the direction of the stable position and is finally returned to the initial position precisely. As discussed above, an optically trapped small dielectric particle has the same dynamical properties as a probe sphere, which is sensitive to external force generated by interactions with a workpiece.

3D positions in the coordinate system can be measured by detecting the shift of a probe sphere caused by the external force $\mathbf{F}_e$ at the position approximating to the workpiece. The Linnik type microscope interferometer senses displacement with high accuracy;for example detecting displacement δ of P_0 on the probe sphere's top surface indicates a shift Δ in an arbitrary direction as shown in Fig.4. Fig. 4(a) shows the fundamental configuration of the Linnik type microscope interferometer. The two waves divided by a beam-splitter are united and a concentric circular fringe pattern is produced on the detector. A microprobe sphere with a diameter of less than 8.0μm as shown in the SEM image of Fig.4(b) is used as the probe sphere. The fringe pattern employed which reflects displacements at not just one point but everywhere on a probe sphere's top surface promises high sensitivity.

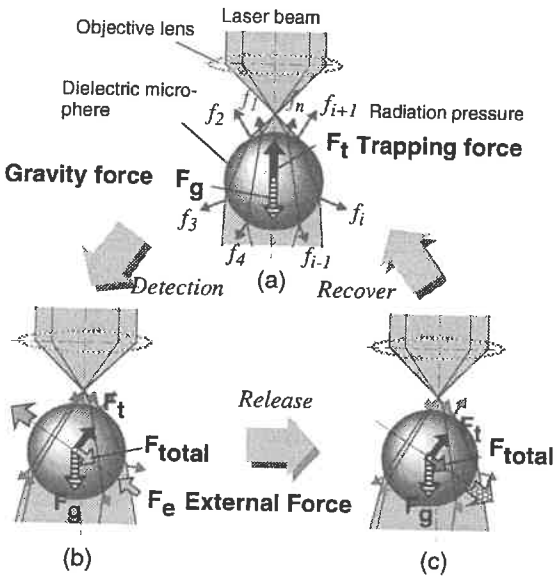

Fig. 2 Dynamical behavior of laser trapping probe

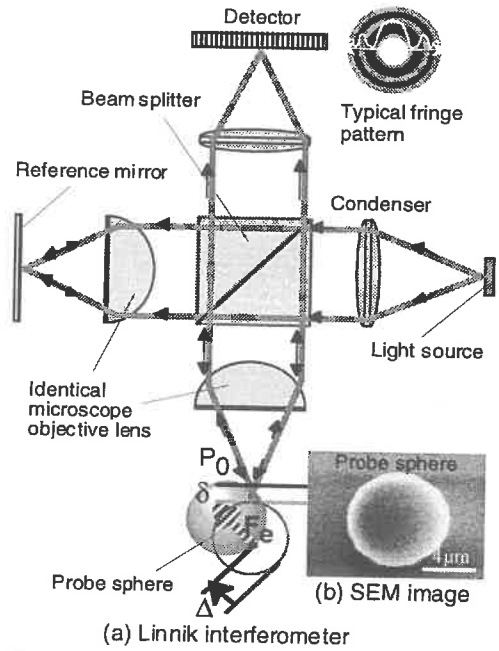

Fig. 3 Configuration of Linnik interferometer

3. LASER TRAPPING PROBE SYSTEM

Fig. 5 shows the schematic diagram of the measurement system specifically designed for trapping particles in air, observing the trapped particles and measuring the fringe pattern. The system is composed of a laser trapping optical system with a Q-switch/Nd:YAG laser with wavelength of 1064nm, Linnik type microscope interferometer consisting mounting a microscope objective lens 1 with a numerical aperture (N.A.) of 0.95 and an xyz-stage with positioning accuracy of 5nm, which is driven by PZT actuators. The YAG laser beam is deflected by a dichroic mirror toward the microscope objective lens 1, then focused on silica particle used as a probe sphere. The silica particle can only be levitated in air with the concentration of the high energy of the Q-switch pulse emission, after which the probe sphere can be maintained at a stable position in the CW emission mode with a low power of less than 100mW. A He-Ne laser with a wavelength of 633nm is utilized as the interference light source. The beam travels through an optical fiber and is deflected by a cube beam-splitter. A dichroic mirror divides the wave into two; one segment travels to a reference mirror with a flatness of 1/10 the wavelength and the other to the probe sphere. The reference mirror is positioned using a PZT stage with the same positioning accuracy as the xyz-stage. The top view of a trapped probe sphere with the fringe is obtained using the microscope component with a magnification rate of 500X. The fringe image data detected by the CCD area sensor is processed by a personal computer with an image memory. Manipulation of the probe is observed using the microscope unit in the lateral direction.

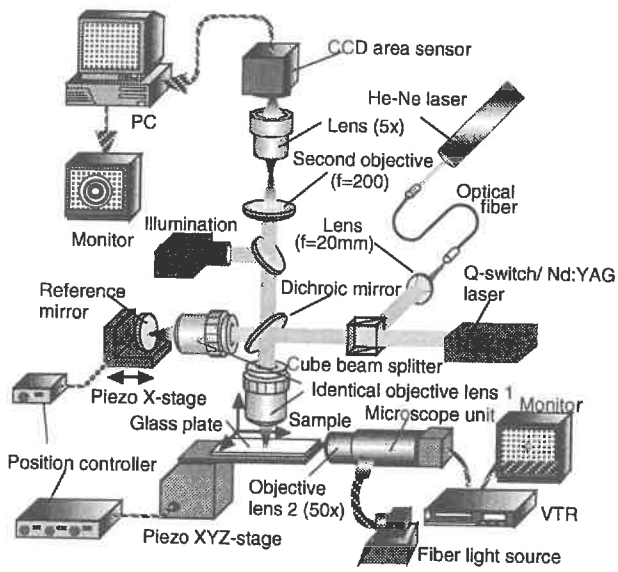

Fig. 4 Schematic diagram of laser trapping probe experimental system

4. FUNDAMENTAL EXPERIMENTS

Fundamental experiments were carried out to find the fringe properties with a probe approximated to the workpiece. A glass microsphere (see Chapter 5) was used as the workpiece. Fig. 5 shows the microscopic images of the three-dimensional trapped probe sphere in air and the approach to the workpiece with the corresponding fringe pat-

terns. The probe moves in the z-direction to the workpiece as shown in Fig. 5 (a). When the probe sphere is at the nearest position to the workpiece as shown in Fig. 5(b), the fringe intensity meets the turning-over indicated in Fig. 5(c). The initial position was set at about 20μm away from the workpiece surface, and the first bright fringe intensity B1 changing with distance L from the initial position was measured. Fig. 6 shows the measured results. The normalized intensity was found to decrease steadily from about L=10μm as the probe was about to come in contact with the surface. Finally the intensity reached the minimum value at about L=18μm. These fringe properties enable non-contact sensing of the position of the workpiece. The laser trapping probe can detect position according to changes in the fringe intensity such as the turning-over of the first bright fringe.

5. MEASUREMENTS OF A GLASS MICROSPHERE

To verify the validity of the positional detection method based on changes in the fringe intensity, the coordinate measurement of a uniform glass microsphere was carried out. Figs. 7(a) and (b) show the measured cross sections and nominal values of a uniform glass microsphere as the workpiece. The probe position was fixed and the workpiece was moved relatively by the xyz-stage on which the workpiece was set. Each position was measured twice by probing in the z-direction. Five cross sections of parts A to E were measured. The glass microsphere had a calibrated mean diameter of 168±8.48μm traceable to the Standard Meter through the National Institute of Standards and Technology (NIST). Fig. 8 shows the measured point data plot, the regression circle calculated using the least square method and deviations of the individual measured points from the regression circle. Fig. 8(a) shows that the diameter d1=121.7μm of the regression circle for the measured part A (Y=60μm) agrees with the nominal circle diameter of D1=117.6μm within uncertainty range. The measured points more or less fit the regression circle within the maximum deviation of 2.0μm. Figs.8 (b) and (c) show the measured results for part B (Y=50μm) and part C (Y=40μm) respectively. The regression circle diameter, the nominal circle diameter, and maximum deviation obtained were as follows; d2=157.8μm, D2=135.0μm, 4.0μm for part B and d3=157.9μm, D3=147.7μm, 6.0μm for part C. A regression sphere with diameter of 168.4μm was obtained from 60 measured points. This agreed well with the nominal diameter of 168±8.48μm within uncertainty range. Consequently, these measured results demonstrate the potentials of the laser trapping probe as a positional detection probe for the nano-CMM, which can measure submillimeter size 3D shapes of microparts with nanometer order accuracy.

6. CONCLUSIONS

To establish a nano-positional detection probe technique for evaluating the geometrical properties of the microscale 3D shapes of microcomponents, a laser trapping probe applying an optically trapped small dielectric particle in air and Linnik interferometer has been developed. The fringe properties with probe access to the workpiece were experimentally investigated. A microprobe sphere was displaced by less than 160nm by interactions between the microprobe sphere and workpiece. To verify the validity of the positional detection method based on changes in the fringe intensity, measurements of a glass microsphere with a NIST traceable mean diameter of 168±8.48μm were carried out. A regression sphere with a diameter of 168.4μm was obtained from 60 measured points. This agreed well with the nominal diameter within uncertainty range. The measured results demonstrate the potential of the laser trapping probe as a nano-positional detection probe for evaluating the submillimeter size 3D shapes of microparts with nanometer order accuracy.

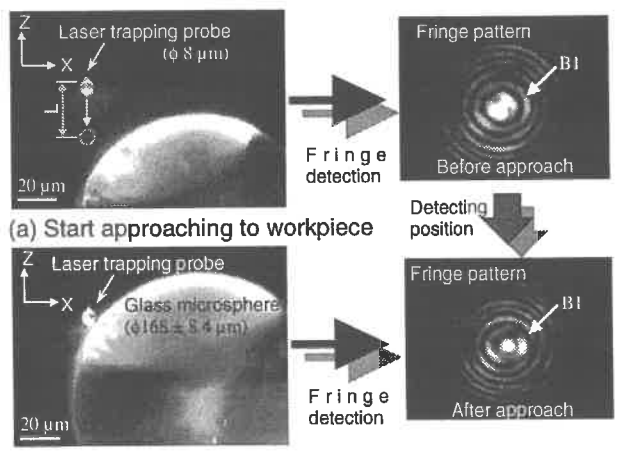

(a) Start approaching to workpiece

(b) Almost contact with workpiece

(c) Fringe shift

Fig. 5 Change in fringe pattern while close to glass microsphere

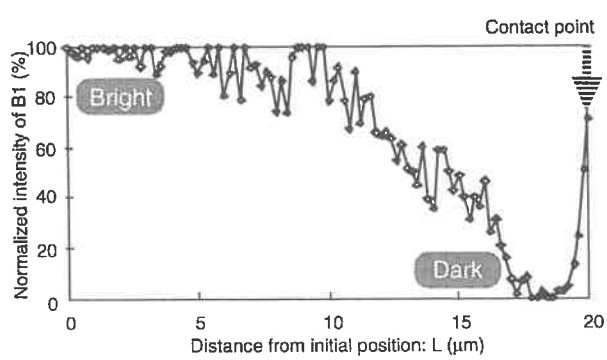

Fig. 6 Changes in fringe intensity according to probe approach

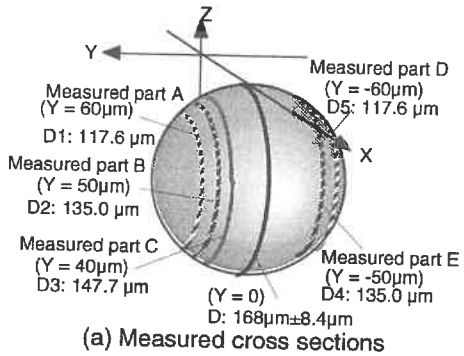

(a) Measured cross sections

(b) Specification of glass microsphere

Certified Mean Diameter	168μm±8.4μm
Standard Deviation	7.5μm
Index of Refraction	1.51@589nm
Composition	Soda lime glass

Fig. 7 Measured cross sections and nominal values

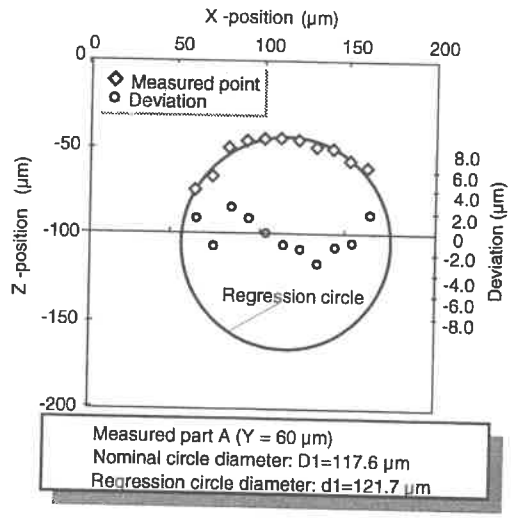

(a) Measured result of measured part A

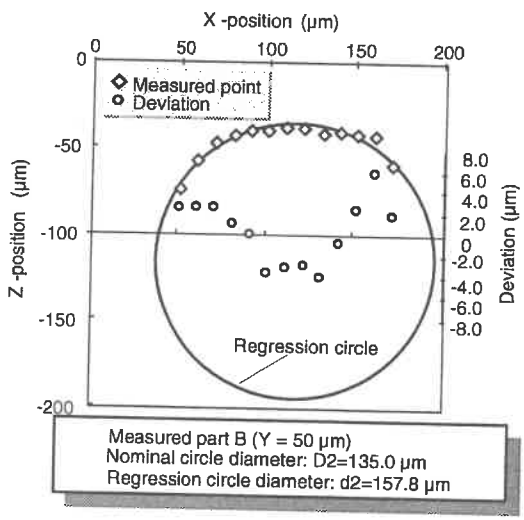

(b) Measured result of measured part B

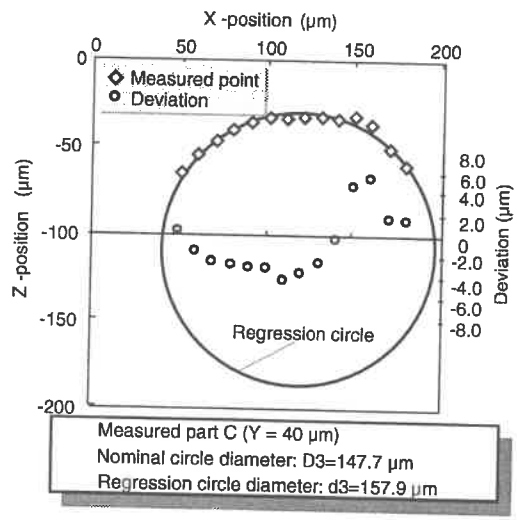

(c) Measured result of measured part C

Fig. 8 Measured results of glass microsphere using laser trapping probe

ACKNOWLEDGMENTS

This work was partly supported by the Ministry of Education, Science, Sports and Culture under the Grant-in-Aid for Scientific Research (B)(2)(Contact No. 09555044) in 1997 and Mitutoyo Association for Science and Technology(MAST)(Contact No. R9907) in 1999.

REFERENCES

[1] K. Takamasu, et al., "Basic Concepts of Nano-CMM (Coordinate Measuring Machine with Nanometer Resolution)", *Proc. of The Japan-China Bilateral Symposium on Advanced Manufacturing Engineering*, pp.155-158(1996).

[2] Y. Takaya, H. Shimizu, S. Takahashi, T. Miyoshi, "Fundamental Study on The New Probe Technique for The Nano-CMM based on The Laser Trapping and Mirau Interferometer", *Measurement*, **25**/1, pp.9-18(1999).

[3] A. Ashkin, J. M. Dziedzic, J. E. Bjorkholm and S. Chu, "Observation of a single-beam gradient force optical trap for dielectric particles", *Opt. Lett.*, **11**, pp.288-290(1986).

[4] Y. Takaya, S. Takahashi, T. Miyoshi and K. Saito(2), "Development of The Nano-CMM Probe based on Laser Trapping Technology", *CIRP ANNALS* , **48**/1, pp.421-424(1999).

RAPID PROTOTYPING OF MICROFLUIDIC COMPONENTS

William C. Jackson[+], Wayne Leger[*], Gabriel P. Lopez[+], and Hy D. Tran[* §]
*Dept. of Mechanical Engineering
[+]Dept. of Chem. & Nuc. Eng.
University of New Mexico
Albuquerque, NM 87131

Abstract

Microfluidic devices are receiving considerable attention in the fabrication of micro-electro-mechanical systems for biotechnological applications (e.g. BioMEMS). Microscale total analysis systems can reduce cost and increase speed of analysis, especially through reduced use of reagents and reduced system size. A key factor in developing new microfluidic applications is the development of prototyping technologies for fabricating and testing new system designs that incorporate fluidic networks, microreactors, separation, and detection systems. One technique for fabricating microfluidic networks is based on replica molding of microchannels with poly(dimethyl siloxane) (PDMS). Microchannel networks with feature size down to 5 μm have been demonstrated with PDMS replica molding. PDMS replica molding can fabricate microchannel networks with a turnaround period of hours to days using inexpensive, benchtop equipment. However, valves and pump technologies are still macro-scale (e.g. external syringe pumps, peristaltic pumps, or power supplies for electro-osmotic pumps). We present a rapid prototyping technique for fabrication of microfluidic networks and active components (e.g. valves) based on PDMS replica molding combined with magnetic actuation. This technique allows embedding of magnetically actuated, mechanically active polymers within the PDMS microchannel network. By activating the microchannels, the channels may be closed or opened (e.g. valving action). Multiple valves and reservoirs may be actuated in order to create pumping via peristaltic action. Magnetic actuation may be achieved by incorporating a magnetically active material into the PDMS (whether permanent magnet, or high permeability material), and applying an external magnetic field from a printed circuit board. Both valves and pumps have been demonstrated. Using inexpensive benchtop equipment, we can fabricate actual devices with sizes on the order of a few millimeters, with channel sizes on the order of a few hundred micrometers. We have demonstrated active valves that close leak-tight, and withstand back pressures on the order of 1.5 kPa.

Introduction

Recent years have witnessed an explosion in the types and proposed uses of microfabricated fluidic systems, especially in bioanalytical applications. A significant impediment to the incorporation of microfluidic devices is the difficulty of designing, building, and testing microfluidic systems. We describe a convenient method for creating new microfluidic systems that incorporate active microfluidic components (namely valves) that combine magnetic actuation with elastomeric materials. This method can be easily extended to allow the rapid fabrication of a variety of other active microfluidic components such as pumps, injectors, flow controllers and mixers, thus allowing the rapid design, fabrication, testing and utilization of complete microfluidic systems (e.g., within a day).

This work is an extension of methods for rapid prototyping of fluidic microchannels based on replica molding of elastomers, such as poly(dimethyl siloxane) (PDMS). Microchannel networks with feature sizes down to ~5 μm can easily be formed by replica-molding of three-dimensional patterns formed by simple photolithographic methods. Silicone polymers such as PDMS have high compliance, high elongation, and good sealing properties, making them useful valving materials. Elastomer-based valving strategies have recently been reported by Unger et al., who described pneumatic methods for deforming elastomeric microchannels to form microvalves and micropumps.

[§] Lopez: gplopez@unm.edu Tran: tran@me.unm.edu
Support provided by ONR N00014-95-1-1315, and NIH Bioengineering Consortium Program 1R24GM60799-01

By combining elastomers with magnetic materials and using electromagnets in the substrate, active valves can be fabricated. This approach is simpler and allows miniaturization, by removing the need for macroscopic, externally switched pneumatic supplies.

Theory

Electromagnetism is frequently used for actuation. Force production is either due to the interaction between the applied field and magnetic domains in a ferromagnetic material (e.g. an electromagnet lifting scrap metal), or to the interaction between an applied field and an electric current (e.g. a voice coil speaker). A magnetic field may be generated by an electric current (e.g. a coil, or electromagnet), or may be intrinsic in a material (e.g. a permanent magnet). Modulation of force, or control of force is achieved through the control of current in an electromagnet.

There are three complications:

- the force of magnetic attraction between an electromagnet and a ferromagnetic material drops off quickly with distance,
- elastomers (being non-ferromagnetic) have magnetic permeabilities several orders of magnitude smaller than ferromagnetic materials, and
- ferromagnetic materials are typically ceramics or metals, and do not have satisfactory elastic properties.

A solution to these problems is to create microfluidic systems that contain areas of "magnetic elastomer" which serve as actuation points for processes such as valving, pumping, and mixing. The magnetic polymer can be permanently magnetized or not, and can be created by blending ferromagnetic powder (such as magnetically soft materials such as iron or silicon iron; or high hysteresis, magnetically hard alloys such as NdFeB, strontium oxides or iron oxides) with the elastomer precursor at the desired locations before curing. Thus, the magnetic elastomer will have a combination of the necessary magnetic permeability and the needed elastic properties. Alternatively, a nonmagnetic elastomer forming a microfluidic channel can be over-coated with a magnetic material; however, this increases the distance from the electromagnet, and hence, decreases the magnetic force that can be applied to it.

For materials without permanent magnetization, reversing action is due to the elastomeric nature of the composite material: When the electromagnet is deactivated, the elastomer returns to its initial, undeformed shape, thus opening the channel for fluid flow. If an elastomeric magnetic composite is permanently magnetized, it should be possible to control both forward and reverse action in an actuator by switching the direction of the current in an external electromagnet.

Forces on ferromagnetic materials are based on aligning the magnetic moments within the materials. The magnetic pressure F/A (force per unit area)between an electromagnet and a ferromagnetic material is approximately

$$\frac{F}{A} = \frac{B^2}{2\mu_0}$$

where B is the flux density, and μ_0 is the permeability of free space. The flux density B can be calculated using finite element analysis software, estimated by using magnetic circuit theory, or measured empirically. Permanent magnet materials such as NdFeB alloys can support flux densities on the order of 1 tesla at the magnet face, and transformer laminations can support about 1 T before saturation occurs; therefore, the practical upper limit on the amount of pressure which may be generated with readily available materials is approximately 400 kPa. In practice, we would expect to see less pressure, since the magnetic elastomer needs to work against the elastomer modulus, and the magnetic circuits are not optimized.

Experimental procedure

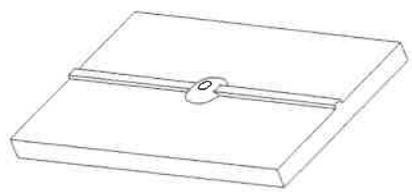

Figure 1. Master form, which serves as replica mold for a microfluidic channel and valve.

The fabrication of components is based on replica molding of a master form (which is a negative of the microfluidic networks). Figure 1 shows a sample master form. These masters may be fabricated by any convenient means, such as machining, rapid prototyping, or photolithography. For "small" (μm size) microchannels, typical master fabrication is by spinning photoresist on a flat surface (e.g. a silicon wafer), and generating a pattern by exposing the photoresist through a laser-printed or linotronic-printed transparency. For convenience, the masters described here were fabricated by machining aluminum, with channel widths of 250 μm and height of 100 μm.

The typical PDMS elastomer used for replication in these experiments is Dow Sylgard 184, though many silicone elastomers may be used. Standard Sylgard 184 preparation is mixing 10:1 elastomer to curing agent by weight, degassing, then, pouring on the master form. After cross-linking (either 24-48 hours room temperature cure, or 2 hours to 30 minutes at 70-150 C in a convection oven), the replica may be peeled off of the master, and adhered to a flat substrate to form microfluidic channels and networks. The resulting elastomer is quite compliant, with a Young's modulus measured at 0.48 MPa.

To make valves, we need to make a magnetically active elastomer. This is done by making a more elastic polymer (32:1 elastomer to curing agent; measured modulus 0.29 MPa), and mixing this with a magnetic material (in this case, 50% by weight of iron powder. Adding the filler can result in increasing the modulus by as much as a factor of 4). This magnetic elastomer is cured in the locations where the dimples are on the master. Our procedure is to actually cut away the cured non-magnetic elastomer from the dimple area; pouring in magnetic elastomer over the dimple; and curing the magnetic elastomer. The resulting elastomer network with magnetic elastomer is then peeled from the master, and adhered to a flat substrate. Electromagnets (extracted from Radio Shack relays) are placed under the substrate, which can then be used to turn the valves on or off. The measured magnetic field with the electromagnets energized, at the level of the elastomer, is 87 mT (870 gauss) A schematic of the process is shown in Figure 2, and photographs of the master part and the resulting microfluidic network with two valves are shown in Figure 3.

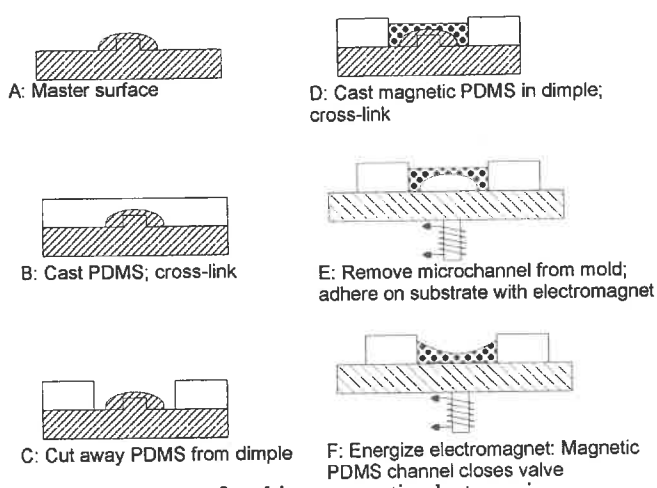

Figure 2. Process of making magnetic elastomeric microvalves

PDMS tends to adhere more to itself than to other materials before cross-linking, this makes mold releases unnecessary. The downside is that the microchannels will not adhere very well to the substrate either, unless the substrate is carefully cleaned, or unless a layer of PDMS is also applied to the flat substrate prior to adhering the molded microchannel. This, and the low physical strength of the elastomer, will limit the microchannel fluidic systems to low pressure applications.

Results

Experimental results with these micro-channels show leak-tight seals to water

and to air. When an external pressure of greater than 1.5 kPa is applied to one side of a closed micro-valve, the PDMS fails. When the valve is open, flows of 250 μL/min are accommodated with a pressure drop of 0.55 kPa across a length on the order of 100 mm of microchannel and valve. Figure 4 shows some results from two-valve switching to select between a fluorescent and a clear flow.

Figure 3. (Left) Master aluminum part, which has raised channels, wells, and dimples. (Right) After replica molding, the elastomer microchannel is peeled from the master. Two magnetic valves are shown.

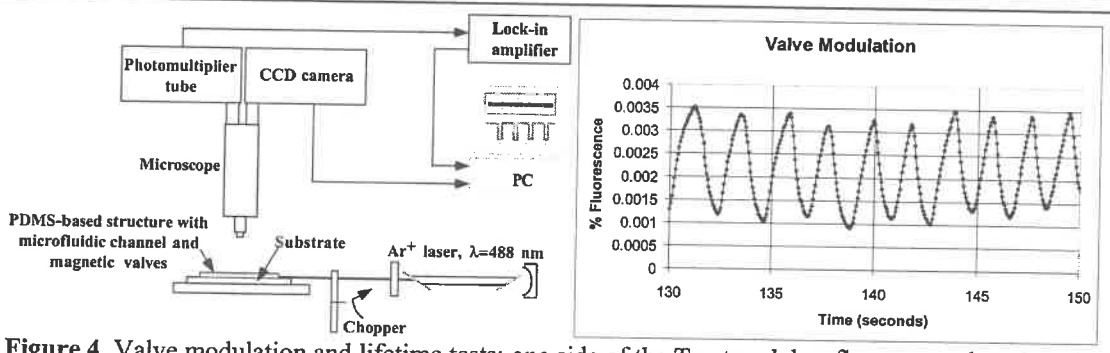

Figure 4. Valve modulation and lifetime tests; one side of the T network has fluorescent dye; the other, plain water. The fluorescence is detected as the two valves on the T are switched on/off off/on every second for several hours

Conclusions

We have demonstrated a simple, inexpensive approach for rapid prototyping of microfluidic components. Although the pressure capability of our current process is not very high, we are optimizing material properties, magnetic designs, and processing methods. Complementing development of microfluidic fabrication methods, collaborations with sensor development, assay development, fluid dynamics analysis, and biological tests are ongoing.

References

Delamarche, E., Bernard, A., Schmid, H., Michel, B., and Biebuyck, H., "Patterned Delivery of Immunoglobulin to Surfaces Using Microfluidic Networks," *Science* v. 276, p. 779-781, May 2, 1997

Jackson, W. C., Tran, H. D., O'Brien, M. J., Rabinovich, E., and Lopez, G. P., "Rapid Prototyping of Active Microfluidic Components Based on Magnetically Modified Elastomeric Materials," submitted to *J. Vac. Sci. Tech B.*

Unger, M., Chou, H., Thorsen, T., Scherer, A., and Quake, S., "Monolithic Microfabricated Valves and Pumps by Multilayer Soft Lithography," *Science* v. 288, p. 113-116, April 7, 2000.

Xia, Y., and Whitesides, G. M., "Soft Lithography," *Ann. Rev. Mat. Sci.* v.28, p.153-184, 1998.

Dynamic forces and energy dissipation in vibration diamond cutting of copper

E. Brinksmeier, J. Schmütz

Laboratory for Precision Machining (LFM), University of Bremen
Badgasteiner Straße 2, D-28359 Bremen, Germany

Keywords: vibration cutting, dynamic forces, energy dissipation

Introduction

In this paper we introduce a method for studying the interaction between tool and workpiece in elliptical vibration cutting at ultrasonic frequencies. The method is based on recording process force signals from a piezoelectric transducer synchronously with the tool displacement. The workpiece-sensor-system is modeled as a harmonic oscillator with known mass, resonance frequency and damping. An interpretation of the recorded data is suggested by means of an harmonic analysis.

Experimental set-up

The kinematics of elliptical vibration cutting and the set-up used in the machining experiments is shown in figure 1. An ultrasonic resonator operating at 20 kHz is mounted vertically with the tool fixed at the lower end of the sonotrode. Although the primary excitation is in the vertical direction (x-axis), a horizontal movement of the tool is superimposed due to periodic bending of the resonator resulting in an elliptical tool path [1]. The ratio of the major to the minor axis of the ellipse approximately is $a/b \approx 20$.

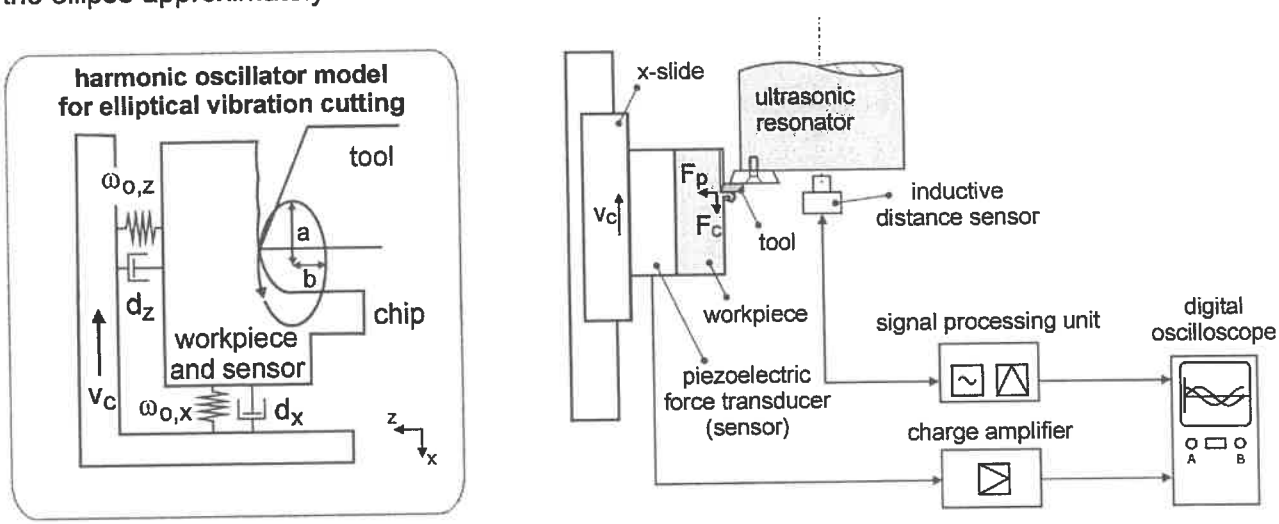

Fig. 1: Harmonic oscillator model for elliptical vibration cutting process and experimental set-up

An OFHC-copper specimen is fixed on a numerically controlled precision xyz-table. A continuous cutting speed v_c is obtained by moving the workpiece along the negative x-direction. The displacement of the tool is monitored by an inductive distance sensor (µ-epsilon), while the displacement of the workpiece-sensor-system is measured with a Kistler type 9251A piezoelectric force transducer in both cutting- and thrust-force direction. All three signals are recorded with a digital oscilloscope sampling at a rate of 3 MHz (Fluke View). The resolution of the measuring device is determined by the limiting frequency of the charge amplifiers (100kHz).

The resonance frequency and damping rate of the workpiece-sensor-system, consisting of workpiece, fixture, transducer and preloading plate have been determined experimentally by recording transients after impulse exciation. The following values were obtained:

$\omega_{o,x}$ = 1.3 kHz and d_x = 0.05 in the cutting force direction

$\omega_{o,z}$ = 1.27 kHz and d_z = 0.06 in the thrust-force direction

In a vibration cutting process, the system can be regarded as a pendulum which is excited at a frequency far beyond its own resonance frequency. In this case, the exciting force is phase shifted by π with respect to the pendulums' reaction. Moreover, the exciting force at a given circular frequency is transformed into an vibration amplitude according to the amplitude resonance function [2]. Therefore, the output signals of the transducer do not directly convert into a force, but have to be corrected accordingly. The figures below show the uncorrected output signals as received on the digital oscilloscope in volts.

Experimental results

If the workpiece is fed in at a very low speed v_c, cutting- and thrust force are sinusoidal and in phase. This is also the case, if the motion of the workpiece is stopped altogether (v_c = 0). The frequency of the sinusoidal force signals is equal to the excitation frequency (20 kHz).

In the cutting force direction, the tool displacement runs ahead of the displacement of the workpiece-sensor-system by $\pi/2$ or – in other words – the tangential speed of the resonator is phase shifted by π with respect to the displacement of the workpiece-sensor-system (cf. fig. 2). This is due to the fact that the friction vector is always opposed to the velocity of the relative movement.

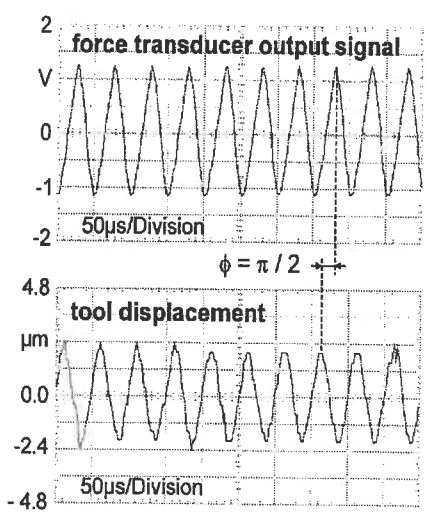

process parameters:

cutting speed:	: v_c = 0.1 mm/s
vibration frequency	: f = 20 kHz
vibration amplitudes:	a = 2.5 µm
	b ≈ 0.125 µm

diamond tool:

nose radius	: r_ε = 50 µm
rake angle	: γ = 0°
clearance angle	: α = 8°

Fig. 2: Displacement of workpiece-sensor-system versus tool displacement

Analysis of the process forces in the frequency domain

Generally, one would expect the engagement of tool and chip to occur before the lower reversal point of the tool. The lower reversal of the tool conicides with the positive flank of the 20 kHz sinewave signal attributed to clearance face friction. With an increasing cutting speed v_c, a saddle point appears in the output signal of the force transducer in the cutting force direction. An analysis in the frequency domain reveals higher order harmonic waveforms in the transducer output signals (cf. figure 3). In the cutting direction, the displacement of the workpiece-sensor-system exhibits the second harmonic of the excitation frequency. The output signal in the thrust force direction also comprises a significant fraction of the third order harmonic.

Elastic loading occurs in both the cutting- and thrust force direction, because the elastic recovery of the force transducer is much slower than the resonator movement. Elastic loading results in a static off-set of both signals, if recorded in the DC-mode of the oscilloscope (cf. fig. 3, left).

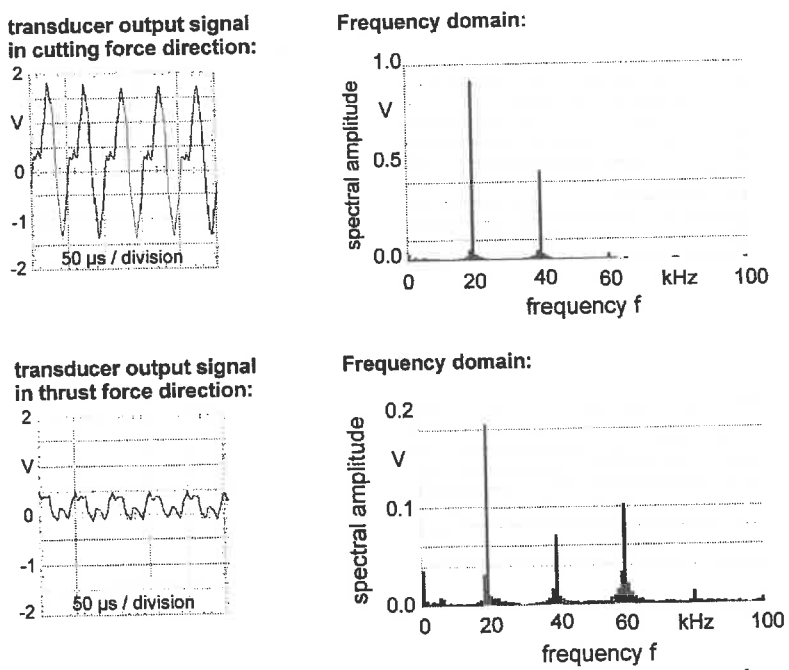

process parameters:

cutting speed:	: v_c = 10 mm/s
depth-of-cut	: a_p = 20 µm
vibration frequency	: f = 20 kHz
vibration amplitudes:	a = 2.5 µm
	b ≈ 0.125 µm

diamond tool:

nose radius	: r_ε = 50 µm
rake angle	: γ = 0°
clearance angle	: α = 8°

Fig. 3: Frequency spectra of transducer output signals

Discussion of results

The observations of the force-transducer output signals indicate that there is little cross-talk between the cutting- and thrust-force direction. Therefore, the workpiece-sensor-system is considered an harmonic oscillator with separate resonance and damping properties in each direction (cf. fig.1).

If the workpiece motion is stopped in vibration cutting, no chip formation is to be expected, but still a sinusoidal displacement of the workpiece-sensor-system is observed. The first harmonic in the force transducer output signal can be attributed to clearance face friction. Since the minor axis of the tool oscillation is very small with the ellipse being almost tangential to the workpiece, the clearance face is continuously in contact with the machined surface.

Higher harmonics appear, when the chip formation is initiated by increasing the cutting speed v_c. Thus, the harmonic workpiece vibrations with frequencies larger than the excitation frequency are caused by the chip formation process. In the cutting force direction, the chip is compressed once per tool oscillation. At low vibration frequencies in a quasistatic regime, the thrust force is known to change sign, when the chip is pulled off by rake face friction [3]. This may explain, why we see more complex harmonics in the workpiece displacement in the thrust force direction.

Based on the assumption that the harmonics with order >1 are related to chip formation, we can compare the energy stored in the higher order harmonic vibrations to that contained in the first order harmonic. This determines the minimum energy consumed in the chip formation process:

$$E_{chip} \sim \sum_{n=2}^{\infty} n^2 A_n^{\ 2} \omega_n^{\ 2} \qquad \text{(eq. 1)}$$

where A_n is the amplitude of the nth harmonic and n = 1 is the fundamental vibration (20 kHz). The energy stored in the fundamental vibration of the workpiece-sensor-system contains fractions of both clearance face friction and chip formation. The overall energy transmitted from tool to workpiece is given by the sum of the energies contained in all harmonic vibrations.

From the practical point of view, a harmonic analysis of the workpiece-sensor vibrations allows to monitor the process in many ways: The beginning of the chip formation is indicated by higher order harmonics in the frequency spektra of the transducer output signals in both cutting- and thrust-force direction. Moreover, the energy consumed in the chip formation can be compared to the overall energy transmitted to the workpiece without explicit knowledge of the interaction forces.

References

[1] Brinksmeier, E.; Gläbe, R.: Elliptical Vibration Cutting of Steel with Diamond Tools. Proceedings of the 14th ASPE Annual Meeting, Volume 20, 1999: pp. 163 - 166.

[2] Thomson, W. T.: Theory of Vibration with Applications. Chapman and Hall, London, 4th Edition, 1993: pp. 51 - 60.

[3] Shamoto, E.; Moriwaki, T.: Study on Elliptical Vibration Cutting. Annals of the CIRP, Volume 43/1/1994: pp. 35 - 38.

CHARACTERISTICS OF MICRO GROOVE MACHINING FOR THE MOLD OF PDP BARRIER RIBS

Hae-Do Jeong *, In-Ho.Cho** , Sang-Cheol Jeong**, Jun-Min Park**
* School of Mechanical Engineering, Pusan National University, Pusan, Korea
**Graduate School of Precision Mechanical Engineering, Pusan National University, Pusan, Korea

Corresponding author. Fax: +82-51-510-3210 ; e-mail: inhoy2k@yahoo.co.k

ABSTRAC

Plasma display panel (PDP) is a type of flat panel display utilizing the light emission that is produced by gas discharge. Barrier Ribs of PDP separating each sub-pixel prevents optical and electrical crosstalk from adjacent sub-pixels. Mold fo forming barrier ribs has been newly researched to overcome the disadvantages of conventional manufacturing process such as screen printing, sand-blasting and photosensitive glass methods. A mold for PDP barrier ribs has stripes of micro grooves transferring stripes of glass-material wall . In this paper , Stripes of grooves of which width 48 μm, depth 124μm , pitch 274 μm was acquired by machining the material of WC with dicing saw blade. Maximum roughness of the bottom and sidewall of the grooves was 120 nm and 287 nm respectively. Maximum tilt angle caused by difference between upper-most width and lower-most width was 2°. Maximum Radius of curvature of bottom was 7.75 μm. These results meet the specification fo barrier ribs of 50 inch XGA PDP.

Keywords: micro groove, tungsten carbide , plasma display panel, barrier rib, dicing saw blade

1. Introduction

Market of Plasma Display Panel (PDP) is expected to be 10 billion dollars in the year of 2001 starting High Definition Television (HDTV) [1]. PDP is well known to be the best candidate for over 40 inch flat display panel which have strong points such as 160° view angle, 500 cd/m² luminance etc. Though PDP costs 20-30 thousands yen per inch, Reduction of manufacturing cost and time should be steadily achieved for PDPs to survive as wide flat display panel.

PDP is flat panel display utilizing light emission that i produced by gas discharge. As Fig. 1 shows, each pixel i separated by barrier ribs which shape is stripes of glass wall. In case of 40" VGA AC PDP, Width and depth of Barrier ribs are about 80μm and 150μm respectively.

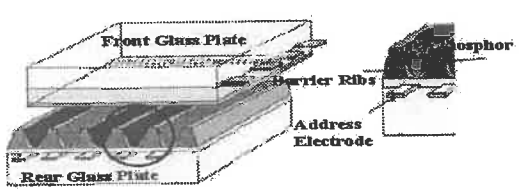

Fig. 1 Schematic structure of AC PDP

There are several kinds of conventional manufacturing process for barrier ribs having each of shortcomings. Sandblasting method laminating selective protecting layer over glass paste takes severe material consumption rates (Fig. 5a). Screen printing method of laminating each glass paste layer 10-15 times is complicated causing uneven edge profile(Fig. 5b . Photosensitive glass method etching selectively open glass causes bottom problem (Fig. 5c).

Forming Press forming method (Fig. 5d) using negatively shaped mold is being newly researched to acquire simple process that overcomes all the above mentioned shortcomings[2].

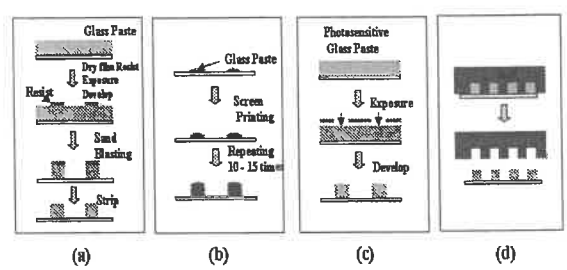

Fig. 2. Conventional method for Barrier Rib and Press

Mold having micro grooves is able be manufactured by LIGA, Wire EDM. But LIGA is not cost effective and Wire EDM does not meet the requirements of roughness and wear resistance due to thermall stressed surface layer. Other method for micro grooving is reported to have used single point diamond tool for only soft metal, Al, Cu for plastic mold but glass mold.

In this paper, Micro-grooving materials of WC and Alumina was tried to get the mold for PDP barrier ribs. Micro -grooving by using dicing blade is tried for hard and wear resistant material although dicing blade is conventionally used for dicing Silicon, GaAs wafer to each chips.

2. Grooving Characteristic

2.1. Preparation for Mold

Materials of WC and SiC are reported to have been used for mold of presnel lens[3]. WC material have high wear resistance enough to be appropriately used for glass mold. WC and Alumina were chosen to be experimental materials as highly wear -resistant and chemically-stable mold. Designed dimensions are 50 μm width , 127 ±5μm depth, 224 μm space between grooves which satisfies a specifications of 50 inch XG PDP.

	WC	Alumin
Spec.	V2(CIS019)	99.8 (Purity)
HRC	76	74.5
Surface	Ground by Resin Bond Wheel #2000	Ground by Resin Bond Wheel #400

Table 1 Experiments Material and Preparation

2.2. Experimental results

Micro Automation, Model 1006 Dcing Saw was used under the conditions as below.

Blade Speed	30000 rpm
Depth of Cut	100-150μm
Cutting Type	Down Cut
Coolant	Tap Water
Kerf	48 , 45 μm
Line Pitch	225 μm
Feed Rate	0.5, 1, 2, 3, 4, 5, 7 mm/s

Table 2 Experimental Conditions

The narrow gap between barrier ribs and front glass plate is about 10μm. Exhausting process followed b sealing takes usually 4-6 hours because of the top surface roughness of barrier ribs. So the better roughness mean shorter exhausting process in PDP manufacturing. So bottom surface quality of grooves in negatively shaped mold is important factor. Also the sidewall surface of groove is important since it affects releasing glass paste from mold.

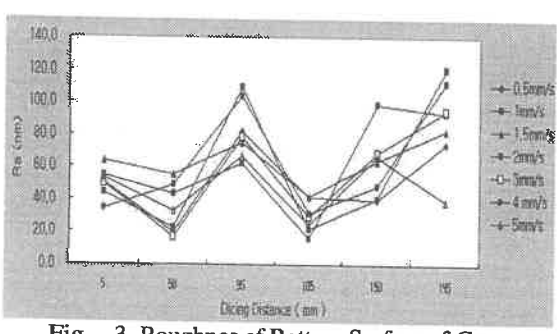

Fig. 3. Roughnes of Bottom Surface of Grooves

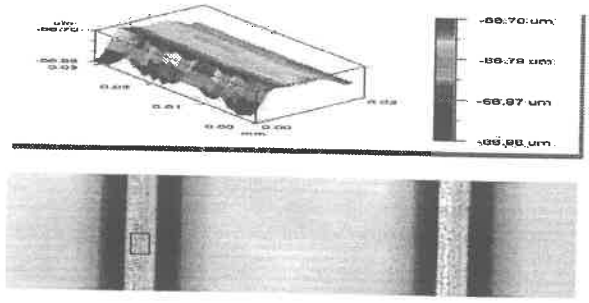

Fig. 4. Example of Roughness of Boxed Area of Bottom Surface

Fig.3 shows the roughness of bottom surface of grooves of mold according to feed rates. It was measured by Optical Dimesional Metrology Center, Intek Engineering Co. Fig.4 shows 3D roughness data of a bottom surface that is boxed in lower optic photograph (box 20μm ×67μm).

Roughness has no apparent dependency on feed rate, but feed rate 5 mm/s results in lowest average Ra of all the measured points. Maximum and minimum roughness were 120 nm and at 2mm/s and 16.5 nm at 3 mm/s, respectively.

In the case of WC material, feed rate over 7 mm/s result in crack of dicing blade. Minimum and maximum of surface roughness are Ra = 16.4 nm at 1 mm/s, Ra = 109.2 nm at 2 mm/s, respectively.

When grooving Alumina, Feed rate 3 mm/s results in severe crack propagation from pore (Fig.5).

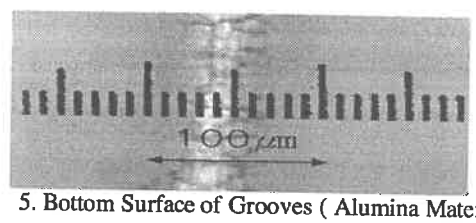

Fig. 5. Bottom Surface of Grooves (Alumina Material)

2.3. Roughness of Groove Sidewall and Measuring

Roughness of side wall surface is related with released side wall surface of barrier ribs formed by mold. Better roughness of side wall means better releasing.

In measuring, it has been difficult to measure roughness of the sidewall of high aspect ratio grooves. In this paper, new method is applied to measuring (Fig.6).

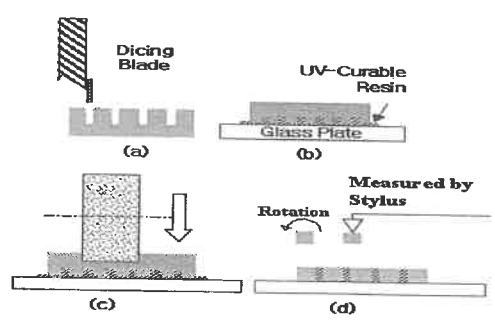

Fig. 6. Preparation for measuring roughness of side wall of grooves

Lamination of UV-curable resin on the ground glass plate is followed by pressing mold upon it. UV exposure through the glass plate makes resin cured bonding mold and glass plate(Fig. 6a, b). Precision backside grinding is followed until bottom of grooves appears(Fig. 6c,d). After Ultrasonic cleaning in chemical, methylene chlorid removes UV-curable resin between separated wall. Ultrasonic cleaning in DI water rinses the residual chemical and makes each rectangular-shaped separated wall.. The surface roughness of side wall machined b above described method is measur ed by Form Talysurf Series 2 (Fig.7). The position of the stylus was confirmed by attached optic microscope (500x). Its roughness is Ra=297nm in scanning length 644μm .

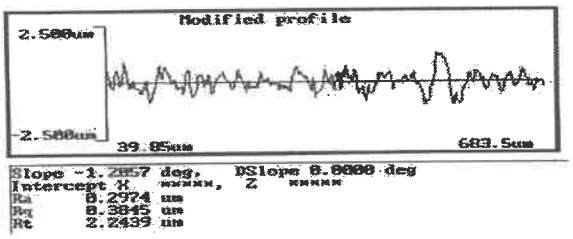

Fig. 7. Roughness of Sidewall of Grooves

2.4. Shapes of Grooves and Blade Wear

Blade wear is measured indirectly by measuring groove depth variance for radial wear and groove width for axial wear. Fig.8 shows shapes of grooves that were machined under conditions of 1mm/s feed rate and 1300 mm total grooving distance. It was measured point to point by optical microscope Olympus 500x (X-Y table resolution 0.5 μm).

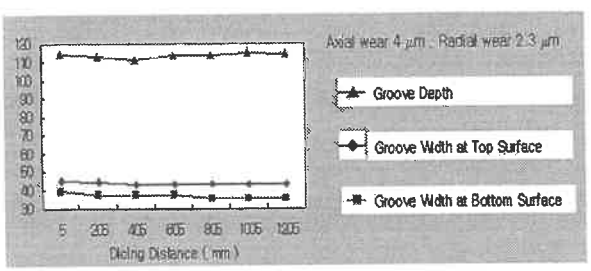

Fig. 8. Variance of Groove Dimension According to Dicing Distance (WC material)

The variance of groove width of upper most width and bottom width are 2.5μm and 4.5μm , respectively at dicing distance 1205 mm. This variance means axial wear of blade indirectly.

Since ariance of groove depth was affected by thickness variance of test materials and attachments (upper most line in Fig.8), radial wear of blade was 2.3 μm by measuring the difference between the pre-processed and post-processed exposure of blade. Radius curvature (R) of bottom surface and tilt angles (•) of sidewall are shown in Fig. 9. The tilt angle of sidewall and radius of curvatu e are calculated by

Tilt angle , $\theta = \arctan [(Wb-Wa) / 2d]$

Radius curvature, $R = (Wb-Wa) / 2$

Wa : measured linear length on the bottom surface

Wb : measured width of tip surface, d : groove depth.

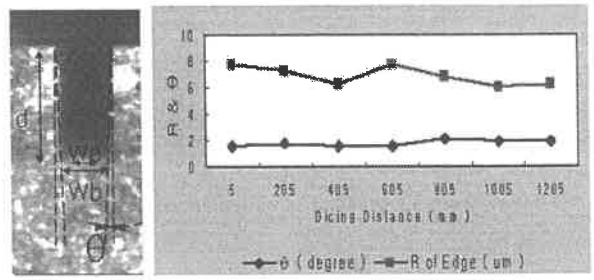

Fig. 9. Radius of Curvature(R) and Tilt Angle (•) of Grooves according to Dicing Distance (WC material)

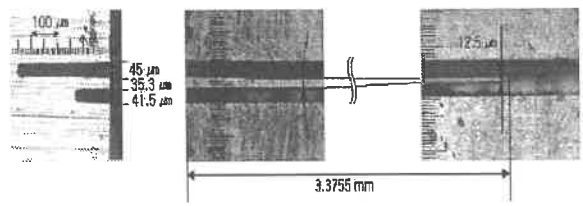

(a) (b) (c)

Fig. 10. High Aspect Ratio groove and minimum distance between grooves (WC material)

Fig. 10(a) is side view of (b). High aspect ratio grooving and minimum spacing between grooves w ere experimented. Angle(β) between upper groove and lowe groove was set 0.19 ° voluntarily to acquire minimum spacing. The aspect ratio of 7.8 (width 35.3μm depth 355.5μm) groove was acquired. And minimum spacing was measured 12.5μm at dicing distance 3.3755 mm.

In case of Alumina, feed rate below 5 mm/s results in no crack of blade. Radial blade wear in grooving Alumina continuously with a blade varying feed rates from 1 mm/ – 5mm/s is shown inTable 3. As the diamond retention of Electroplated Ni bond is weak, diamond grits are easil knocked off by the strong impact force generated during cutting[4]. It is thought that pore of Alumina causes strong impact on diamond abrasives that are bonded by electroplated Ni, which results in severe wear of diamond saw blade.

Feed Rate	Axial Wear at 300 mm of Dicing Distance
1 mm/s	25 μm
2 mm/s	12 μm
3 mm/s	20 μm
5 mm/s	10 μm

Table 3 Axial wear of blade (Alumina)

2.5. Chipping Characteristics

In silicon wafer dicing, chipping is reported to increase as feed rate increases in the rage of 30-60 mm/s [5]. Chipping characteristics on WC material ha ve not such a tendency since experiments in this paper was made in th small and short range of feed rate, 0.5 - 5 mm/s. These chipping data were distinguished from defect induced b surface grinding. Maximum chipping was 4.5 μm at feed rate of 5mm/s. Chipping on the mold affects the quality of released barrier rib and phosphor printed on it. As a result, chipping can affect the discharge characteristics of PDP.

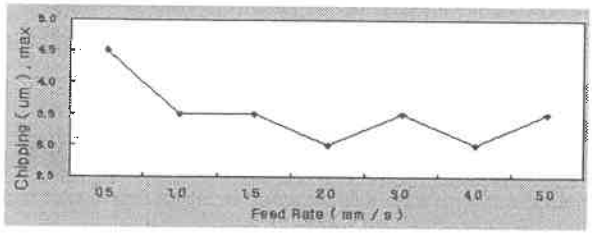

Fig. 11. Chipping according to dicing distance (WC)

Material of silicon can be used as mold. But its chipping characteristics were worse than WC as Fig. 12 shows.

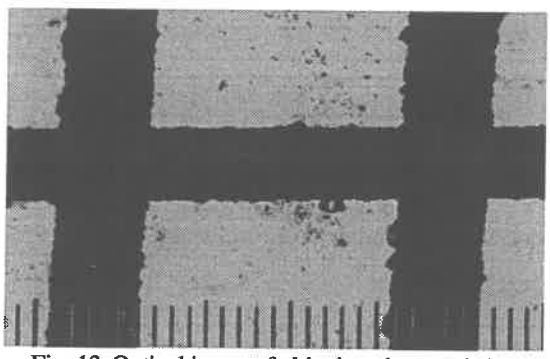

Fig. 12. Optical image of chipping characteristics (Silicon material)

Maximum chipping induced by grooving silicon was about 10 μm. The chipping was generated continuousl along the dicing path.

3. Conclusions

This paper demonstrated the fabrication of Mold fo PDP barrier ribs. The mold was fabricated by dicing method. Alumina was not appropriate as ceramic mold since dicing causes severe micro-crack. Silicon was not appropriate as mold either according to its chipping characteristics. WC showed a good feasibility for dicing method. Process featured that dicing is well applied on the material which is not ductile but brittl and has less porosity. In the view of groove shape, maximum tilt angle of sidewall was 2° and maximum radius curvature of rounded bottom was ca lculated 7.75μm. In the view of surface quality, bottom surface has maximum roughness Ra = 120 nm , surface of sidewall has roughness Ra=297nm. Maximum axial wear and radial wear were 4 μm and 2.3μm, respectively. Dicing force measuring would be made for better understanding of WC grooving.

Acknowlege

This work was supported by Milli-Structure Production Technology Developing Project. The authors like to thank Mr.Yoon, president of Kordis Ltd. for experimental support.

Reference

[1] J.S.Lee, Display Technology Roadmap and its trends, Vol. 1, NO.1.200 KIDS

[2] J.H.Ryu, PDP Cell Structure and Barrier Rib Forming Technology, Flat Display Tech. Sym.

[3] H.Suzuki , Ultra Precesion Grinding of Micro Fresnel shape . pp 59-64 . ABTEC'99

[4] C.-M. Sung, "Brazed diamond grind: a revolutionary design for diamond saws", Diamond and Related Materials 8 (1999) 1540-1543

[5] Toshiharu MIWA, "Blade wear and wafer chipping in dicing process", ICPE'97 Taipei, Taiwan, pp401

Chipping of Sintered Cutting Tools
- Mechanism and its Prediction -

Kunio Uehara, Toyo University, Saitama, Japan
Junji Herai, Kiriu Machine Mfg. Co. Ltd., Gunma, Japan
Tomio Ishikawa, Mikasa Sangyo Co. Ltd., Saitama, Japan

1. Introduction

The geometrical irregularity of cutting edge due to chipping is a significant factor that affects the quality of surface finish in precision machining. The single crystal diamond cutting tools are widely used for precision machining of aluminum and copper. The reason of the use of single crystal material is to assure the smoothness of the cutting edge. Besides, the sintered polycrystalline cutting tools are also used increasingly in an extended field of precision machining such as cutting of hardened steel. The cutting edge of sintered tool is tends to chip in this case because the cutting force is big and the cutting tool has a heterogeneous structure. Chipping of cutting edge is a significant problem for to assure the quality of surface finish in this type of machining.

Many research works (e.g. [1],[2],[3]) have been reported on the phenomena and the mechanism of chipping of cutting tools so far, and also many on-line methods that detects tool wear and chipping have been reported. Most methods use a monitoring principle that detects the abnormality of cutting signals such as cutting force. A big problem of this principle is that the monitoring equipment acts after chipping occurred. It has been pointed out that an important cause of tool chipping is the deterioration or the fatigue of the tool material in interrupted cutting [1],[2]. The deterioration of tool material at the cutting point should accompany the change of physical and chemical properties of the tool material at the same point.

From this point of view, the authors have contrived and tested a prediction method of chipping that measures the electric contact resistance between the tool point and an electrode [4],[5]. In this method, the detection is done prior to the occurrence of chipping. Afterwards, this method has been improved and a new non-contact method that measures the impedance of high frequency coil has been contrived. The object of this paper is to clarify the mechanism of the deterioration of the tool material through finite element analysis and microscopic structure observation, and to propose two prediction methods that detect chipping before its occurrence.

2. Finite Element Analysis

Most sintered cutting tools are composite material that is consisted of hard particles and ductile binding metal. A finite element analysis was carried out assuming that the principal cause of the deterioration or the fatigue is the in-homogeneity of the structure of sintered cutting tools.

Fig.1 shows the nose part of the cutting tool schematically. In the plane A, the normal stress σ and shear stress τ will act at the under part of contact zone when the cutting tool is exposed to the cutting force. Similarly,

the normal stress σ will act in the plane B. The finite element analysis was applied to these sections assuming that the stress distribution is uniform when the structure of the cutting tool is homogeneous. Fig.2 shows the finite element model used in this calculation. It was confirmed that the result of calculation agrees well with the theoretical one when the material is uniform, and when loading and supporting conditions are given as is shown in the figure. Fig 3 shows some results of the calculation. In these figures, ① shows the binding material, and ② shows the hard particles. The material constants are as follows:

① E=210000 N/mm^2, Poisson's ratio: 0.3. ② E=550000 N/mm^2, Poisson's ratio: 0.2.

The calculation is carried out as a problem of plane stress though the plane strain condition is also tried. The result of the calculation shows that the in-homogeneity of the structure of sintered cutting tool induces tensile stress near the grain boundary and inside of the hard particles. The generation of the tensile stress is repeated by interrupted cutting. Thus, the fatigue phenomenon or the deterioration of the structure will proceed. They are, the formation of cracks, development of cracks, formation of vacant places (holes) in the structure. These changes of the structure bring about the change of physical and chemical properties. This is the result and the implication of the finite element analysis.

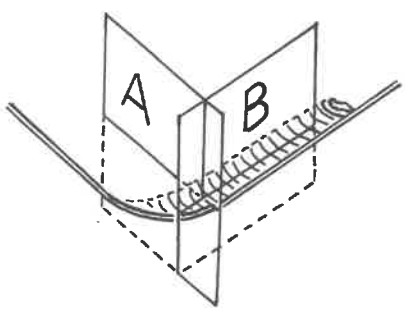

Fig.1 Nose of the cutting tool

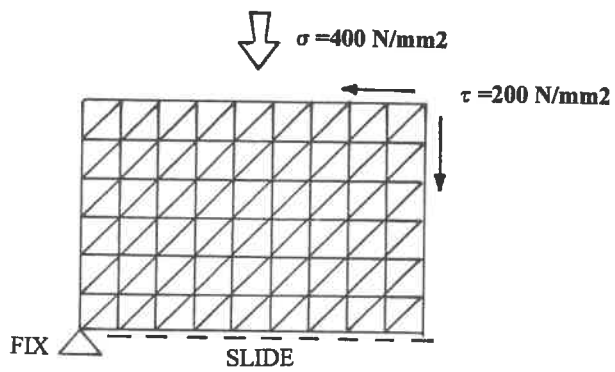

Fig.2 Model of Finite Element Analysis

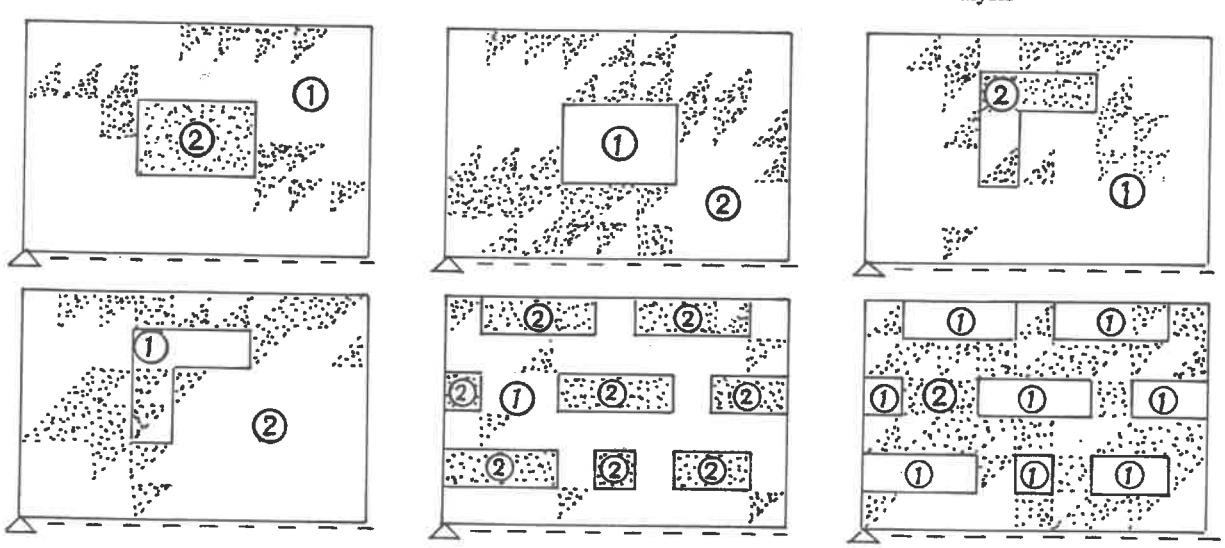

Fig.3 Results of calculation (at section **A**, Dotted Zone: **σ1>100 N/mm2**)

3. Change of Microscopic Tool Structure in Interrupted Cutting

The chipping phenomena and accompanied change of tool structure was examined with wide combination of tool materials and cutting conditions. In the test, the interrupted turning test was carried out using 0.55% carbon steel round bar as the work-piece. Four longitudinal grooves of 5mm width were cut on the work-piece previously for the above purpose. The cutting tool materials used in the tests are: (1) sintered carbide P10, (2) sintered carbide K10, (3) TiC,TiN cermet, (4) Al_2O_3, TiC ceramic and (5) TiCN coated tool.

The tool geometry and cutting conditions are as follows:

Tool geometry: -6,-6,6,6,15,45,0.8mmR, Cutting speed: 95, 135,200 and 300m/min.,

Feed: 0.1mm/rev., Depth of cut: 1mm, Cutting fluids: none.

The cutting test is stopped when chipping is observed, the rake face of the cutting tool is then polished by abrasive paper of #3000 slightly and examined under an Scanning Electron Microscope. A typical result of these tests is shown in Fig.4. In this case, the P10 tool is used and cutting speed is 300m/min, the cutting time is 2.4minutes. According to the pictures, the change of the tool structure is clearly observed near the fractured part, that is, the formation of small cracks and vacant parts (many small holes) are observed as is predicted by the finite element analysis. This phenomenon is observed widely in the above combinations of cutting tools and cutting conditions.

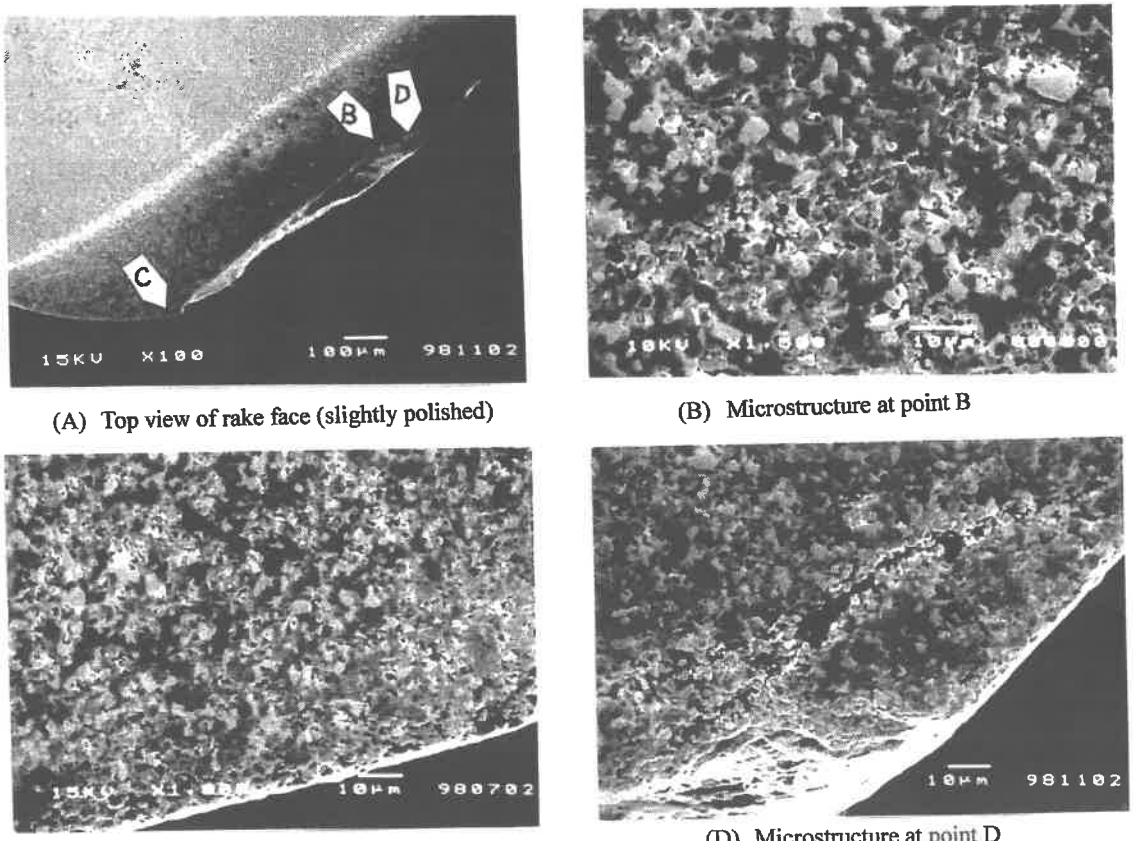

(A) Top view of rake face (slightly polished)

(B) Microstructure at point B

(C) Microstructure at point C

(D) Microstructure at point D

Fig..4 Microstructure of chipped cutting tool (rake face)

4. Prediction of Chipping

Two prediction methods are contrived and tested based on the above stated results. The change of the structure of cutting tools at tool point should accompany the increase of the electric resistance at that point. To detect the increase of the electric resistance, two methods were tested. The first one is a method that measures the electric contact resistance as is shown in Fig.5. The performance of this method was already reported in the literature [5]. According to the test, this method has high sensitivity to the deterioration of cutting tools, however, it is not suitable for coated cutting tools. The second method is then tested. This is shown in Fig.6 schematically. The tip of the cutting tool is inserted in the center hole of a detecting coil. The high frequency electric current (e.g. 300KHz) is applied to the coil and its impedance is measured. A bridge circuit is used for detecting the difference of the impedances of two coils. According to the test, it is found that this method has many advantages but it is important to raise the sensitivity by focusing the magnetic field.

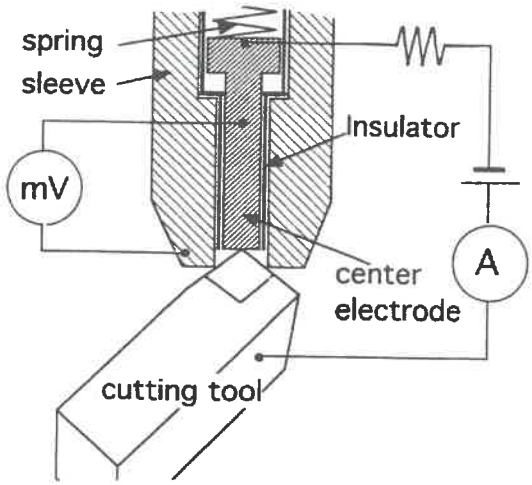

Fig.5 Chipping prediction method (1)

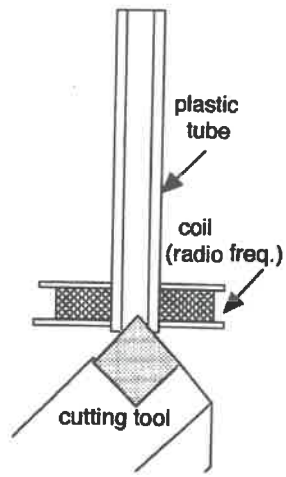

Fig.6 Chipping prediction method (2)

5. Conclusions

The mechanism of chipping of sintered cutting tools in interrupted cutting is clarified through finite element analysis and microscopic observations. It is verified that the deterioration of the tool structure is the significant cause of tool chipping. Two chipping prediction method are proposed based on the above findings.

6. References

[1] Uehara K., Kanda Y, On the Chipping Phenomena of Carbide Cutting Tools, Annals of the CIRP, 25/1, 1977.

[2] Shirakashi T. et al., Analytical Prediction of Cutting Edge Chipping in Interrupted Turning Operation, (5th report), J. of the Japan Soc. of Precision Engineering, 48/10, 1982.

[3] Bouzakis K.D. et al., Experimental and FEM Analysis of the Fatigue Behavior of PVD Coatings on HSS Substrate in Milling, Annals of the CIRP, 47/1, 1998,

[4] Uehara K., Takeshita H., Prognostication of the Chipping of Cutting Tools, Annals of the CIRP, 38/1, 1989.

[5] Uehara K., Obitsu N, Relationship between Catastrophic Fracture and Electric Resistance of Cutting Tools, Proc. of the American Society for Precision Engineering, Vol. 12, 1995.

The Effects of Fluids on the Deformation and Ductile-to-Brittle Transition of Silicon

John A. Patten, Sherman V. Mumford
The University of North Carolina at Charlotte, Charlotte, NC

This research evaluates the effect of fluids on the deformation and ductile to brittle transition of silicon. Scratches were made on a polished silicon wafer surface by using a diamond stylus under increasing loads until the brittle transition was detected. The scratches where drawn while the diamond–silicon point of contact was completely submerged in one the following fluid environments: air, de-ionized water, acidic chemical mechanical polishing (CMP) slurry or an alkaline CMP slurry. The CMP slurry environments produced a suppression of the brittle transition compared to the air environment resulting in an apparent increase in toughness. Under higher loads, the de-ionized water and both CMP slurries resulted in an apparent increase in hardness compared to air.

Keywords: Silicon, ductile machining, brittle transition, CMP, single-point diamond turning

Introduction

The search for a better understanding of brittle material behavior led to the discovery of a "ductile regime" of operation.[1] Precision machining of brittle materials in the ductile regime is well documented.[1-3, 5-7] Cutting fluids are often used in silicon processing to achieve favorable results. Water is a cooling agent for high speed, high temperature grinding operations and during single-point diamond turning (SPDT). Chemical mechanical polishing (CMP) uses slurries to mechano-chemically effect the material removal rate. The CMP fluid is thought to soften the silicon surface, thereby allowing ductile material removal. Cutting fluids that promote ductile cutting can also negatively impact the machining process by increasing tool wear.[4] Cutting fluids and their effect on silicon machining is the focus of this research. Silicon scratching experiments in previous research revealed an "apparent increase in hardness" due to the presence of water and polishing slurries when compared to dry air abrading.[5] The present research more than doubles the number of data points of the original experiments and offers additional insight to the mechanisms involved with the ductile to brittle transition of silicon.

Experimental Procedure

This experimental procedure involves scratching an N-typed, (100), arsenic doped, 0.005 ohms-micrometer, single crystal polished silicon wafer. The scratches were created in four different fluid environments: air, de-ionized water, Klebesol 30H50 chemical slurry and Klebesol 30N50 chemical slurry. *Table 1* shows comparative data. The scratches were drawn by a profilometer at a constant velocity of 0.5 mm/s. A two-micron radius, diamond-tipped, stylus was used to create the scratch. The scratches were drawn in the $<0\bar{1}1>$ and $<01\bar{1}>$ directions. Finally, the silicon wafer was imaged in an AFM. A minimum trace area of 40 x 40 microns was used to gather sample data. The scratch topography was then analyzed using two and three-dimensional AFM images.

Table 1 Characteristics of fluids

Fluid Description	Chemical Property	pH Level	Particle	Particle size
Air	N/A	N/A	N/A	N/A
De-ionized water	Neutral	6	N/A	N/A
Slurry 30H50	Acidic	2	Colloidal silica	50 nm
Slurry 30N50	Alkaline	10	Colloidal silica	50 nm

Results

Identification of the ductile material behavior was qualitatively characterized by scratch topography. Evidence of ductile regime scratching was characterized as being continuous, rounded and smooth with pile-up on either side of a well-defined groove. *Figure 1* shows a typical ductile scratch. The dependent variable for this research was scratch depth, which was measured by use of AFM imaging. The ductile-brittle transition in silicon under each of the fluid condition was also determined from the AFM images. Under applied loads of up to 20 mN, all of the fluid environments yielded a ductile response. When comparing the scratch profiles of the air, de-ionized water, and both slurry environments at these loads minimal form/shape variation was noticeable. The distinguishing feature in the resulting geometry at these loads is the scratch depth. The scratch depth, at each applied load, is an indication of the material's hardness.

Discussion

Figure 2 charts the scratch depths of each fluid at 20 and 30 mN loads where ductile deformation occurred. Scratching in air resulted in the most penetration. The CMP slurry did not produce the softening expected, based upon commonly accepted practices. The use of the CMP slurry during scratching resulted in less penetration compared to air under equivalent loads. Scratching the silicon in the slurry environments at loads of 20 mN and 30 mN clearly exhibits a material behavioral change. The depth of penetration, while scratching the silicon under these conditions, is up to 40% less than the depth of penetration of the air and water environments. Resistance to scratch penetration is analogous to material hardness. Both slurry environments induced what may be characterized as an apparent increase in hardness of the silicon surface. The depth and degree of this reaction is not known and is viewed simply as a near surface change. In addition to the slurries being resistive to penetration, they also withstood greater loads before the initiation of the ductile to brittle transition. A 50-mN load was needed to induce the brittle transition in the 30H50 slurry compared to a 30-mN load for air. See *figure 3* for a summary of all brittle transition loads. The load induced ductile to brittle transition is analogous to the material's toughness. Toughness is the ability to withstand a load without fracture. Load can be viewed as an indicator of toughness. CMP slurries produced both a hardening and

toughening effect compared to air. Not only did the slurries resist penetration but also they retarded the onset of the ductile to brittle transition and thus retarded cracking.

The present experiments were not refined enough to show the well-documented phenomenon that machining in water promotes brittle fracture when compared to air[6]. The load increment of 10 mN was too large to differentiate the ductile to brittle transition in air and water. The apparent increase in hardness, in a water environment compared to air environment, is supported by the shallower depths of penetration at higher loads. *Figure 4* shows a progression of silicon scratches from a ductile deformation into an increasingly more brittle zone. *Figure 5* shows the geometric changes in a scratch as the silicon goes through the ductile to brittle transition. The scratch groove is no longer smooth and continuous.

Conclusion

Topographical conditions of scratches drawn on n-type, (100), single-crystal, polished, silicon wafers have been analyzed. Scratches were made on the wafer surface in one of four fluid conditions: air, de-ionized water, acidic polishing slurry or alkaline polishing slurry. The scratches were performed under increasing loads until the ductile to brittle transition occurred. This research measured scratch depths from the purely ductile zone until a definite presence of the brittle transition was observed. The use of CMP slurry, and to a lesser extent water, reduced the deformation of the silicon, at higher loads, compared to the air, i.e. an apparent increase in hardness. The CMP slurries also allowed for higher loads before the onset of brittle fracture, i.e. an apparent increase in toughness.

Acknowledgements

This research was funded in part by a National Science Foundation REU grant and the Ronald E. McNair Post Baccalaureate Achievement Program.

References

1. Blake, P. N., Scattergood, R. O. "Ductile-Regime Machining of Germanium and Silicon," *J. Am. Ceram. Soc.*,73[4]949(1990).
2. Patten, J., "Cutting Tool Edge Radius and Depth of Cut Influence on the Generation of the High Pressure Phase Transformation During Ductile Machining," *Proceedings of the ASPE Spring Topical Meeting on Silicon Machining*, 1998, 17, 88-91.
3. Morris, J. C., Callahan, D. L., Kilik, J., Patten, J. A. and Scattergood, R. O. "Origins of the Ductile Regime in Single-Point Turning of Semiconductors," *J. Am. Ceram. Soc.* 78[8] 2015-20 (1995).
4. Chargin, D., "Cutting Fluid Study for Single Crystal Silicon," *Proceedings of the ASPE Spring Topical Meeting on Silicon Machining*, 1998, 17, 59-62.
5. Patten, J, "The Effect of Fluids on the Ductile Response of Silicon During Abrading," *Proceedings of the ASPE Spring Topical Meeting on Silicon Machining*, 1998, 17, 28-31.
6. Uhlmann, E., Engel, H. and Paesler, C. "Chip Formation and Sub-surface Damage in Ductile Mode Grinding of Semiconductors," *ASPE Proceedings*, 1998, 18, 626-631.
7. Ikeda, M., Yamada, A., Shiratori, S., Kokaji, Y. "Investigation into the Microplastic Deformation Mechanisms of Si Single Crystal by Light Load Scratching," Proceedings of the International Conference on Production Engineering, part 1, Tokyo 1974.

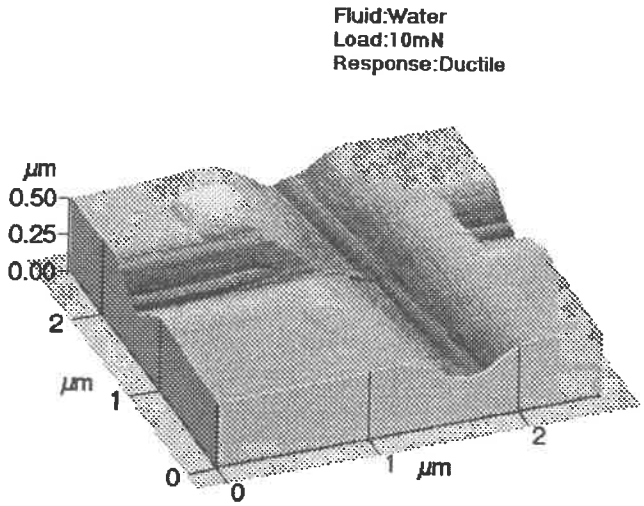

Figure 1 Smooth, rounded, and continuous surface typical of ductile regime scratching

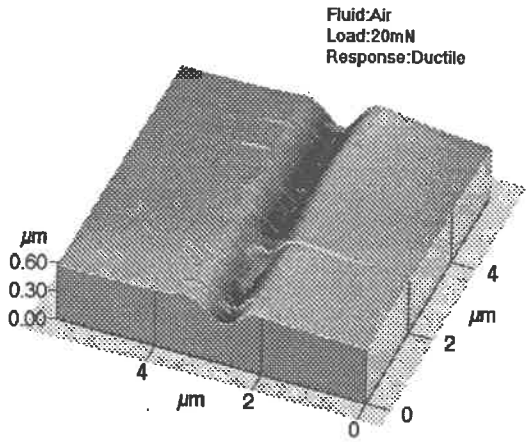

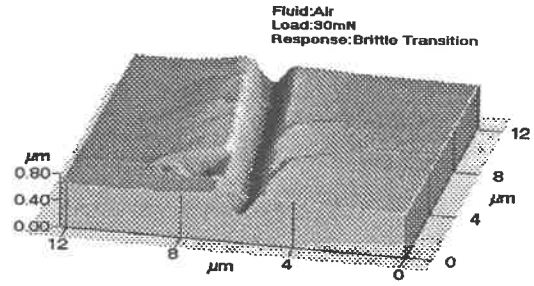

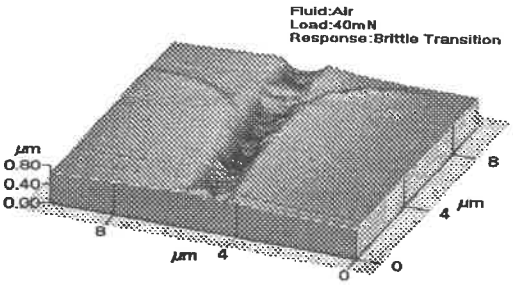

Figure 4 AFM Images showing the change in scratch topography as silicon goes through the ductile to brittle transition.

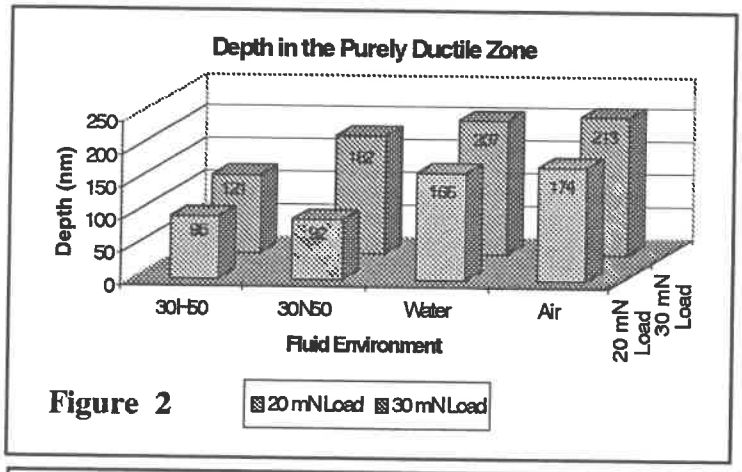

Figure 2

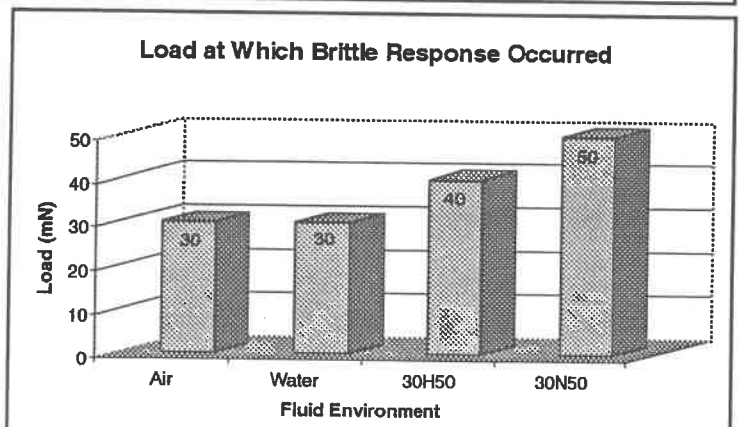

Figure 3

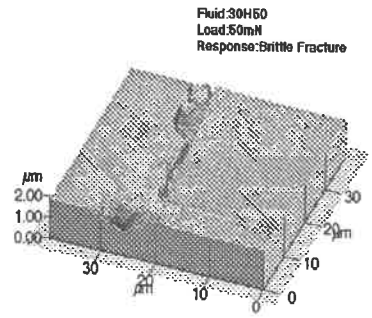

Figure 5 Scratch resulting in brittle fracture

Authors Index

Adams, David P. 176
Ahn, Joong-Yong 304
Ahn, Jung Hwan 41*
Ajao, Dotun 252
Akita, Haruki 341
Amatucci, Edward G. 571
Andersson, Clarence A. 264
Aoki, Takayuki 78
Aoyama, Hisayuki 332
Armijo, Elfino 555
Asakawa, Yohei 62
Ashida, Kiwamu 567
Austin, Brad 559
Badami, Vivek G. 31, 280
Bai, Jian 336
Bamberg, Eberhard 308
Bartos, Jacob J. 555
Bartscher, Markus 361
Barylski, Adam 110
Bauer, Markus G. 180
Beckert, Erik 529
Bieg, Lothar F. X. 316
Bifano, Thomas G. 579
Bittner, Douglas 195
Blaedel, Kenneth L. 462
Blunt, Liam 473
Bohart, Allen D. 184
Booij, Silvia M. 132
Braasch, Jan 260
Brand, Uwe 542
Brinksmeier, Ekkard 74, 592
Brooks, Mike 555
Bruning, John H. 31
Bui, Son H. 144
Busch, Konrad 361
Campos Rubio, J. C. 268
Cerniway, Matthew A. 42
Chandra, Abhijit 86
Chandrasekaran, Nagasubramaniyan 78
Chang, Fuh-Yu 82, 114, 128
Chao, C. L. 82
Chen, Ping 86
Chen, Yuexiang 458
Chino, Shinichiro 296
Cho, In-ho 596
Choi , Hon-Zong 102
Choi, Kee-Bong 240
Chung, Carl A. 521
Chung, Hewon 357
Chung, Myung J. 365, 385
Chung, Sung-Chong 50, 272, 276, 304, 477, 481
Clark, Stephan R. 39
Clarke, Michael 187
Cogdell, J. David 413
Collier, John 579
Collins, Pat 184
Cortesi, Roger S. 191
Cox, W. Royall 580
Cuttino, James F. 231
Dagalakis, Nicholas G. 571
Damazo, Bradley N. 199
Day, Robert D. 555
Devillers, O. 489
Di Giacomo, Benedito 227
Dogaru, Teodor 533
Donmez, Alkan 199
Dow, Thomas A. 42, 136, 180, 203, 537, 559
Duduch, J. G. 268
Eda, Hiroshi 140
Edgeworth, Robert 465
Eischen, Jeff 559
Eisenbies, Stephen K. 425
Ejiri, Takayuki 349
Elliott, Joyce 555
Elliott, Norman 555
Emmons, Craig 264
Enikov, E. 20*
Ensz, Mark 316
Eom, TaeBong 369
Fähnle, Oliver W. 132
Farahi, Faramarz 509
Faulk, Scott 184
Feng, Guoxin 429, 451
Fesperman, Ronnie 106
Franke, Matthias 361
Friedrich, C. R. 397
Fu, Jiyou 469
Fu, Shengyu 25
Fujishima, Mokoto 260
Funaki, Yoshio 340*
Fung, Eric H. K. 433*
Gaines, J. 20*
Gao, Wei 35, 106, 447
Gatzen, Hans H. 90, 563
Gee, Anthony E. 115, 268
Gill, David D. 136
Gobby, Peter 555
Gomez, Veronica 555
Greene, Philip 195
Greivenkamp, John E. 39
Grejda, Robert D. 94
Griffin, Robert 252

*Extended abstract not available at press time.

**Abstract unavailable at press time.

Guan, C. 580
Gweon, Dae-Gab 207, 357, 365, 381, 385
Hale, Layton C. 521
Halvorson, Craig 184
Hamano, Toshiaki 223
Hamby, David W. 497
Han, JinWan 369
Hara, Seiichiro 312
Harper, Kari 199
Hata, Seiichi 345
Hatamura, Yotaro 349, 551
Hatch, Douglas 555
Hayes, Donald J. 580
Heinrich, Matias D. 203
Heitkamp, Red . . . . . **
Hennike, Brian 555
Herai, Junji 600
Herve, Thierry 349
Hetland, Gregory A. 442
Hidai, Hirofumi 148
Hii, King-Fu 353
Hillesheim, Jeffrey . . . . . **
Hirano, Tameyoshi 172
Hocken, Robert J. 425, 469, 509
Hoenigman, R. 580
Hoffmann, Andrew 529
Hoffmeister, Hans-Werner 152
Honda, Satoshi 219, 340*, 373
Horio, Ken'ichiro 46
Hoshino, Yoshihiro 296
Hosokawa, Akira 70
Huang, Peisen S. 35
Hudyma, Russell M. 521
Iijima, Chihiro 240
Ikawa, Naoya 324
Inoue, Hideaki 296
Inoue, Shigeru 377
Ishikawa, Tomio 600
Ito, Kentaro 345
Ito, Yujiro 98
Izumi, Masumi 377
Jackson, William 588
Jayadevappa, K. V. 328
Jeong, Hae-Do 102, 160, 596
Jeong, Jae-Hwa 207
Jeong, Sang-Cheol 160, 596
Jeong, Seong-Min 119
Jiang, Xiang-Qian 473
Jokiel, Jr., Bernhard 316
Joseph, Vince 164
Jung, Hewon 381
Jusko, Otto 389
Kaga, Kimitaka 349
Kagawa, Yoshihito 260
Kamiya, Kazuhide 438

*Extended abstract not available at press time.

Kanai, Edward T. 35
Kanda, Yuichi 54
Kaneeda, Toshiaki 417
Kaneko, Kenji 567
Kasai, Youhei 341
Kato, Norihiko 341
Kato, Shigeo 223, 244, 341
Kawada, Masaki 70
Kawahara, Yasuhiro 260
Ketahara Pasupathy, Trichy M. 442
Kikuchi, Motohiro 62
Kim, Gyung-Bum 477
Kim, Jung-Hwan 288
Kim, Kyung-Don 481
Kim, Min-Seok 272
Kim, Min-Suk 513
Kim, Nam-Kyu 50
Kim, Seung Woo 505, 513
Kim, Seung-Cheol 272, 276
Kim, Suck 292
Kim, Sung-Heon 160
Kim, Tae-Hoon 304
Kirschstein, Ulf-Carsten 529
Kitahara, Tokoi 575
Kiyono, Satoshi 35, 447
Kleine-Besten, Thomas 542
Knapp, Byron R. 211
Knight, Jr., P. Douglas 501
Knuefermann, Markus M. W. 187
Kobayashi, Yoshikazu 168
Koguchi, Yoshio 62
Komanduri, Ranga 78
Kondo, Ryo 140
Kondo, Sumihisa 70
Kotilainen, Markku S. 215
Kozak, Jerzy 124
Kramar, John A. 571
Kulawiec, Andrew W. 31
Kumaki, Jinyo 551
Kuriyagawa, Tsunemoto 66
Kurosaki, Yasuo 156
Kwan, Y. B. Patrick 525
Lawton, Kevin M. 280
Lee, Chang-Ha 288
Lee, Hong-Lim 119
Lee, Hwa-Soo 98, 377
Lee, Moon G. 365, 385
Lee, Seok-Woo 102
Lee, SukWon 292
Lee, Sung Q 385
Leger, Wayne 588
Lei, Tianjue 458
Lim, Han-Seok 41*
Lin, Hung-Yi 82, 114, 128
Lin, Jing-Chie 128

**Abstract unavailable at press time.

Ling, Z. K. 397
Liu, Jiancheng 260
Liu, Shugui 493
Liu, Xiangyang. 25
Loopstra, Erik L. 525
Lopez, Gabriel P. 588
Love, Bryan 559
Lu, Xiaoming 434
Lucca, Don A. 497
Lüdicke, Frank 389
Luttrell, Dan E. 15*
Ma, K. J.. 82
Maeda, Yukio 62
Maekawa, Hitoshi 567
Malz, Rüdiger 74
Marino, Edward A.. 537
Marsh, Eric R. 94, 211, 409
Matsumoto, Kiyoshi 349, 551
McClellan, Michael 184
Miller, Michele H.. 86
Mishima, Nozomu 567
Mitsui, Kimiyuki 393
Miyajima, Katsunori. 341
Miyamoto, Satoshi. 332
Miyawaki, Tatsunori 417
Miyoshi, Takashi 336, 584
Moon, Jun Hee 288
Moon, K. S. 397
Moon, Y. H. 160
Mori, Mosahiro 260
Morse, Edward P. 485
Mumford, Sherman V. 604
Muralikrishnan, Bala 25
Nabeshima, Masaru 46
Nagasawa, Hirokazu 219
Nakamura, Naoya 349
Nakano, Fumiaki 54
Nakano, Hirotami. 140
Nakao, Masayuki. 349, 551
Nelson, B. J.. . . . . 20*
Ng, K. W. 397
Ngoi, Bryan K. A.. 421
Nishiyama, Daisuke. 417
Nomura, Takashi 438
Novak, W. Thomas. 517
O'Connor, Brian P.. 211
Ogura, Ichiro 58
Oh, Han-Seog 119
Okada, Akira 172
Okamoto, Yasuhiro 172
Okazaki, Yuichi 58, 575
Okuda, Seiichi 438
Omari, Mohammed 252
Ono, Manabu. 223, 244
Onozuka, Hideaki 62

*Extended abstract not available at press time.

Oosone, Tomoaki. 312
Ouyang, Jian 284
Pahk, Heui Jae 288, 292
Park, J. W. 160
Park, Jun-Min 160, 596
Park, Min-Cheol. 505
Park, Sung-Eun 119
Park, Sung-Lim 207
Parker, David H. 21, 401
Patten, John A. 106, 604
Patterson, Steven R. 236, 280, 462, 501
Payne, John M. 21
Peng, Shuzhi 446
Picard, Yoosuf N. 176
Pierce, Timothy 555
Pierse, Michael G.. 187
Piratelli-Filho, Antonio 227
Porto, A. V.. 268
Prakash, E. S. 164
Preparata, F. P. 489
Preuß, Werner. 74
Qiang, Xue-Feng. 447
Qiao, Feng. 16
Qu, Weimin 86
Radcliff, Bill 401
Raja, Jay 25, 144
Rajurkar, Kamlakar P. 124
Rakuff, Stefan 231
Read, Roger R. F. 187
Reimann, Helge. 389
Richard, Ralph M. 39
Rivera, Gerald 555
Rodriguez, Lawrence 555
Sadashivappa, K. 164, 328
Sadasue, Kojiro 98
Saffert, Eugen 529
Sakamoto, Shigehiko 70
Salsbury, James G. 320, 485
Santoro, F. G.. 268
Sasián, Jose M.. 39
Sato, Kaiji 240, 345
Sato, Kimitoshi. 156
Sawa, Masashi 62
Scattergood, Ronald O.. 559
Schäffel, Christoph 529
Schinstock, D. 231
Schmütz, Jörg 592
Schneider, Carlos Alberto 405
Schwenke, Heinrich. 361, 542
Scire, Frederic E.. 571
Shang, Zongren. 195
Sharma, Aditya K. 236
Shelton, John W. 21, 401
Sheu, S. C. 82
Shillito, Keith 184

**Abstract unavailable at press time.

Shim, Jong Youp 357, 381
Shimada, Shoichi 324
Shimizu, Jun 140
Shimokohbe, Akira 240, 345
Shinshi, Tadahiko 240
Shirai, Kenji 168
Shirakawa, Mizuyuki 223, 244
Shivakumar, J. 328
Siekmann, Heiko 563
Singaperumal, M. 164
Singh, Gurpreet 489
Singh, Jai R. 264
Slocum, Alexander H. 191, 215, 248, 308
Smith, Stuart T. 256, 533
Sohn, Alexander 136, 537
Son, Seong-Min 41*
Sousa, André Roberto 405
Stout, Kenneth J. 473
Sugaya, Takayuki 341
Suzuki, Hirofumi 66
Swift, David W. 462
Syoji, Katsuo 66
Tajbakhsh, Hooman 462
Takahashi, Hirokazu 349
Takahashi, Satoru 336, 584
Takai, Hideyoshi 324
Takaya, Yasuhiro 336, 584
Takei, Takanori 454
Tanaka, Hiroaki 324
Tanaka, Kenji 66
Tanaka, Makoto 567
Tani, Yasuhiro 54
Tanikawa, Tamio 567
Tashiro, Hatsuzo 438
Taylor, John S. 521
Thigpen, Richard L. 521
Thompson, Daniel C. 462
Tokura, Hitoshi 148
Ton-Nu, Phuong-Thao 284
Tran, Hy D. 284, 474, 588
Trost, Hans-Jochen 580
Tsai, Chih-Chang 128
Udupa, Ganesha 421
Uehara, Kunio 600
Ueno, Shigeru 296
Uneme, Masayoshi 296
Uno, Tetsuya 393
Uno, Yoshiyuki 172
Vallance, R. Ryan 248, 353
van Brug, Hedser 132
van der Bijl, Robert-Jaap M. 132
Vasile, Michael J. 176
Venkataraman, P. 31
Vigliano, Vincent C. 409
Vikramaditya, B. J. 20*
Vrushabhendrappa, Y. 328
Wakabayashi, Tadashi 98, 377
Wäldele, Franz 361
Wallace, David B. 580
Wang, Charles P. 252
Wang, Chunhai 300, 429, 451
Watanabe, Kazushi 140
Watson, Douglas 517
Weadon, Timothy L. 21
Wenda, Andreas 152
Wilhelm, Robert G. 442, 465
Williams, David F. 115
Woodfin, Andrew D. 509
Woody, Shane C. 256
Wroblewski, Donald 579
Wu, Tung-Chuan 114, 128
Wu, Yongqing 493
Wurmus, Helmut 16
Xie, Zexiao 429, 451
Xu, Yuchun 451
Yamada, Ryuichi 454
Yamaguchi, Hitomi 54
Yamazaki, Kazuo 260
Yamazaki, Keishin 438
Yan, Jiwang 66
Yanagi, Kazuhisa 454
Yanagihara, Kiyoshi 54
Yang, G. 20*
Yang, S. M. 433*
Yasui, Heiji 70
Yim, Noh-Bin 513
Yoda, Yasushi 517
Yokomizo, Seiichi 417
Yokota, Yasuhiro 417
Yoon, Sung Won 292
Yoshikawa, Kazuo 438
Yoshino, Masahiko 78
Zeadan, Jeihad 90
Zhang, Guoxiong 429, 451, 469, 493
Zhang, Jingcai 458
Zhang, Xiaoyou 240
Zhao, Fuzhang 264
Zhao, Xiaohui 353
Zhou, Libo 140
Ziegert, John C. 547

*Extended abstract not available at press time.

**Abstract unavailable at press time.